OCRWM	SCIENTIFIC ANALYSIS COVER SHEET	1. QA: QA Page 1 of 552

2. Scientific Analyses Title

In Situ Field Testing of Processes

3. DI (Including Revision Number)

ANL-NBS-HS-000005 REV02

4. Total Attachments	5. Attachment Numbers - Number of pages in each
9	I-6, II-18, III-16, IV-10, V-8, VI-8, VII-4, VIII-22, IX-22

	Printed Name	Signature	Date
6. Originator	J.S.Y. Wang	SIGNATURE ON FILE	12/5/2003
7. Checker	C. Campbell	SIGNATURE ON FILE	12/5/2003
8. QER	S. Harris	SIGNATURE ON FILE	12/5/03
9. Responsible Manager/Lead	J.S.Y. Wang	SIGNATURE ON FILE	12/5/2003
10. Responsible Manager	P. Dixon	SIGNATURE ON FILE	12/5/03

11. Remarks

Block 6. Additional contributors to this report are:

6.1 – P.J. Cook; 6.2 – R.C. Trautz, S. Flexser; 6.3 and 6.4 – Q. Hu; 6.5 – P.J. Cook; 6.6 through 6.9 – R. Salve; 6.10 – R. Salve, D.B. Hudson, P.J. Cook, Q. Hu, M. Conrad; 6.11 – Y. Tsang, P.J. Cook; 6.12 – R. Salve, D.B. Hudson, K. Williams; 6.13 – W. Soll, H.J. Turin, K. Williams, S.S. Levy, T.T. Vandergraaf; 6.14 – Z.E. Peterman, J.B. Paces, G.L. Patterson, J.F. Whelan, L.A. Neymark, B.D. Marshall, R.C. Roback.

Revision History

12. Revision/ICN No.	13. Description of Revision/Change
REV00	Initial Issue
REV01	Complete revision. Numerous changes have been made throughout the document. Table and figure identifiers have been changed throughout. The main revisions are: • Section 4 "Inputs" has been revised to update data inputs and to associate subsections with the various analyses presented in the Section 6 subsections. • Section 5 "Assumptions" has been revised to update assumptions and to associate subsections with the various analyses presented in the Section 6 subsections. • Section 6.1 is revised (1) to include air-permeability data of Niche CD 1620 - Section 6.1.2.2, and (2) to analyze the permeability changes - Section 6.1.2.3. • Section 6.2 is revised (1) to present flow path observations at Niche CD 1620 - Section 6.2.1.2, (2) to present long-term seepage-test data - Section 6.2.1.3, and (3) to compare the seepage threshold data from Niche 4788 with short-term seepage threshold data from Niche 3650 - Section 6.2.2. • Section 6.3 is revised to present additional tracer distribution data on samples collected from the ceiling of Niche 3650 - Section 6.3.1.2. • Section 6.4 is revised to present laser ablation - induced coupled plasma mass spectrometry data for chemical tracer transport and sorption - Section 6.4.3. • Section 6.5 to Section 6.9 are not revised.

2. Scientific Analyses Title
In Situ Field Testing of Processes
3. DI (including Revision Number)
ANL-NBS-HS-000005 REV02

Revision History

12. Revision/ICN No.	13. Description of Revision/Change
REV01 (continued)	• Section 6.10 is revised (1) to present data of construction water tracer migration below invert Section 6.10.1.3, and (2) to present observations of non-ventilated Cross Drift - Section 6.10.2. • Section 6.11 on systematic hydrologic characterization is a new section. • Section 6.12 on fault test at Alcove 8 and Niche 3107 is a new section. • Section 6.13 on Busted Butte unsaturated zone transport test is a new section.
REV02	Analysis documentation was revised and changes were too extensive to use sidebars per AP-SIII.9Q/Rev. 1/ICN 2, Step 5.6c)1). The following Sections are modified: • Sections 1, 2, 3, 5, 6, 6.1—entire documentation as applicable to AP-SIII-9Q. • Section 4.1 to 4.2 as applicable to AP-SIII.9Q. • Section 6.1 to include air-permeability data for Alcove 8. • Section 6.2.1.3 to include additional seepage test data for Niche CD 1620 (Niche 5). • Section 6.10.1.2.1, 6.10.2, and 6.10.3 to include additional ESF main drift and cross drift observations. • Section 6.11.2.7 through 6.11.2.11, 6.11.3, and 6.11.3.4 to include new tests at boreholes LA#3 and LA#4. • Section 6.12.4 to include new available data from the Alcove 8/Niche 3107 (Niche 3). • Section 6.13 to add neutron probe moisture studies. • Section 6.14 is new from REV01 and includes geochemical and isotopic observations and analysis of the unsaturated zone. • Section 7 is revised to address the new material and modified as applicable to AP-SIII.9Q. • Attachment III to discuss details of seepage tests in Section 6.2. • Attachment VIII to include more information on geology. • Attachment IX to include calculations. All other sections have been modified for editorial purposes, to remove instances of the word "proposed" or "potential" before repository, and to adjust information as applicable to AP-SIII.9Q.

CONTENTS

Page

CONTENTS (CONTINUED)

CONTENTS (CONTINUED)

CONTENTS (CONTINUED)

CONTENTS (CONTINUED)

CONTENTS (CONTINUED)

CONTENTS (CONTINUED)

CONTENTS (CONTINUED)

CONTENTS (CONTINUED)

INTENTIONALLY LEFT BLANK

FIGURES

Page

FIGURES (CONTINUED)

Page

FIGURES (CONTINUED)

Page

FIGURES (CONTINUED)

Page

FIGURES (CONTINUED)

Page

FIGURES (CONTINUED)

Page

FIGURES (CONTINUED)

Page

FIGURES (CONTINUED)

Page

FIGURES (CONTINUED)

Page

FIGURES (CONTINUED)

Page

TABLES

TABLES (CONTINUED)

Page

TABLES (CONTINUED)

Page

INTENTIONALLY LEFT BLANK

ACRONYMS AND ABBREVIATIONS

1-D	one-dimensional
2-D	two-dimensional
3-D	three-dimensional
ACC	Accession Number
AMR	Analysis/Model Report
AMS	Accelerator Mass Spectrometry
AP	Administrative Procedure (DOE)
AR	Activity Ratio
ATDT	Automated Technical Data Tracking
B	Bottom borehole
BBTF	Busted Butte Test Facility
BST	Borehole Sensor Tray
CAMS	Center for Accelerator Mass Spectrometry
CD	ECRB Cross Drift
CDCS	Cross Drift Construction Station
CHn	Calico Hills Non-welded Hydrogeologic Unit
CRWMS	Civilian Radioactive Waste Management System
CS	Construction Station (ESF main loop)
CWAT	Construction Water
DOE	U.S. Department of Energy
DTN	Data Tracking Number
ECM	Effective Continuum Method
ECRB	Enhanced Characterization of Repository Block
ERP	Electrical Resistivity Probe
ERT	Electrical Resistance Tomography
ESF	Exploratory Studies Facility
FBA	Flourobenzoic Acid
FD&C	Food, Drug and Cosmetics
FEP	Features Events and Processes
FI	Fluid Inclusion
FIAs	Fluid Inclusion Assemblages
FY	Fiscal Year
GPR	Ground Penetrating Radar
GPR-T	Ground Penetrating Radar Tomography
HPZ	High Permeability Zone

ACRONYMS AND ABBREVIATIONS (CONTINUED)

ICPAES	Inductively Couples Plasma Atomic Emission Spectrometry
IMP	Ion Microprobe
LA	License Application
LA-ICP-MS	Laser Ablation analyzed by Inductively Coupled Plasma-Mass Spectrometry
LANL	Los Alamos National Laboratory
LBNL	Lawrence Berkeley National Laboratory
LPZ	Low Permeability Zone
M	Middle borehole
MC	Moisture Content
M&O	Management and Operating Contractor
M&TE	Measuring and Test Equipment
ML	Middle Left borehole
MFC	Mass Flow Controller
MR	Middle Right borehole
NRC	Nuclear Regulatory Commission
NTS	Nevada Test Site
OCRWM	Office of Civilian Radioactive Waste Management
PA	Performance Assessment
PMR	Process Model Report
PTn	Paintbrush Non-welded Hydrogeologic Unit
PVC	Polyvinyl Chloride
Q	Qualified
QA	Quality Assurance
QAP	Administrative Procedure (M&O)
QARD	Quality Assurance Requirements and Description
QIP	Quality Implementing Procedure
RH	Relative Humidity
RIS	Records Information System
SDOM	Standard Deviation of the Mean
SMOW	Standard Mean Ocean Water
SR	Site Recommendation
SLPM	Standard Liter Per Minute

ACRONYMS AND ABBREVIATIONS (CONTINUED)

TBM	Tunnel Boring Machine
TBV	To Be Verified
TCO	Test Coordination Office
TCw	Tiva Canyon Welded Hydrogeologic Unit
TDMS	Technical Data Management System
TDR	Time Domain Reflectometry
T_h	Homogenization Temperature
TIMS	Thermal-Ionization Mass Spectrometry
TSPA	Total System Performance Assessment
TU	Tritium Units
TWP	Technical Work Plan
U	Upper borehole
UL	Upper Left borehole
UM	Upper Middle borehole
UR	Upper Right borehole
USGS	United States Geological Survey
UV	Ultraviolet
UV/Vis	Ultraviolet and Visible
UZ	Unsaturated Zone
UZTT	Unsaturated Zone Transport Test
VS	Validation Study
WP	Work Packages
YAP	Administrative Procedure (YMP)
YMP	Yucca Mountain Site Characterization Project
YMRP	Yucca Mountain Review Plan

INTENTIONALLY LEFT BLANK

1. PURPOSE

The purpose of this scientific analysis report is to update and document the data and subsequent analyses from ambient field-testing activities performed in underground drifts through unsaturated zone (UZ) tuff rock units. This scientific analysis report supports Total System Performance Assessment (TSPA) of Yucca Mountain for Licensing Application (LA).

This report is the second revision (REV 02), with the initial issue (REV 00) prepared in March 2000 and the first revision (REV 01) in December 2001. This revision was developed in accordance with the *Technical Work Plan (TWP) for: Performance Assessment Unsaturated Zone* (BSC 2002 [160819], Section 1.10.6, under Work Package (WP) AUZM06) to document available data collected in tests described in the same UZ TWP:

- Moisture studies (in TWP Section 1.1 under WP AUZG01)
- Isotope hydrology (in TWP Section 1.2 under WP AUZG02)
- ESF/ECRB UZ testing (in TWP Section 1.23 under WP AUZT08)
- UZ Seepage Laboratory Testing (in TWP Section 1.24 under WP AUZT09)
- Radionuclide transport laboratory testing (in TWP Section 1.25 under WP AUZT10)
- UZ Busted Butte Transport Test (in TWP Section 1.26 under WP AUZT11).

ESF and ECRB are abbreviations for two existing drifts at Yucca Mountain where testing activities are performed: the Exploratory Studies Facility and the Cross Drift for Enhanced Characterization of Repository Block.

Documentation in this report includes descriptions of how and under what conditions the tests are conducted. The descriptions and analyses provide information useful for refining and confirming the understanding of flow, drift seepage, and transport processes in the UZ. The analyses include the impact of excavation (including use of construction water and effect of ventilation) on the UZ processes. This report is intended to support preparations and revisions of model reports in the UZ TWP (BSC 2002 [160819]) associated with:

- Climate, infiltration, and flow (in TWP Section 1.10 under WP AUZM06)
- Radionuclide mountain scale transport (in TWP Section 1.11 under WP AUZM07)
- Ambient drift seepage (in TWP Section 1.13 under WP AUZM09)
- Drift-scale radionuclide transport (in TWP Section 1.15 under WP AUZM11).

In general, the results discussed in this report are from studies conducted using a combination or a subset of the following three testing approaches: (1) air-injection tests, (2) liquid-release tests, and (3) moisture monitoring. The air-injection tests quantify spatial variability (heterogeneity) of permeability. The liquid-release tests provide an evaluation of *in situ* fracture flow and the

competing processes of matrix imbibition. In addition to active testing, sensors in boreholes and along drifts are used to monitor the *in situ* and perturbed conditions, evaluating the impact of excavation, ventilation, and construction-water usage on the surrounding rocks. The field studies are supplemented by laboratory testing, with addition (in this revision) of hydrochemical data from samples collected in underground drifts. Variabilities and uncertainties in both field and laboratory data are presented for cases with sufficient data to be amenable for statistical analyses.

1.1 OBJECTIVES AND PROCESSES ANALYZED BY THE AMBIENT FIELD TESTING ACTIVITIES

The field-test findings and their implications for drift seepage, fracture flow, matrix imbibition, moisture evolution, and radionuclide transport can be used to address Performance Assessment (PA) uncertainties and repository design issues. The UZ Flow and Transport Model (UZ Model) and the drift-scale models require field data for partitioning UZ flux into a fast fracture-flow component and a slow matrix-flow component (CRWMS M&O 2000 [151940]). This partitioning is controlled by fracture-matrix interaction. The damping of infiltration pulses and diversion by the Paintbrush nonwelded tuff unit (PTn) above the Topopah Spring welded tuff unit (TSw) are potential mechanisms for infiltration and percolation flux redistribution. In the vicinity of the repository, perturbations by drift excavation, air ventilation, and water usage can change the hydrological regime in the UZ. Retardation by rock mass and dispersion through fractures are processes affecting the migration of tracers and the dilution of radionuclides below the drifts to the water table. Some of these processes and related uncertainties, issues, and concerns are addressed by the ambient testing program at underground test sites at Yucca Mountain, further documented in Section 6. The data uncertainties are integral parts of overall model uncertainties in the understanding of processes and in constraining model assessments.

1.2 LOCATIONS OF TEST SITES

The ESF provides underground access to tuff units at and above the repository level. *In situ* testing and monitoring studies are being conducted to directly assess and evaluate the waste emplacement environment and the UZ natural barriers to radionuclide transport at Yucca Mountain. This scientific analysis report summarizes the progress and status of ambient studies of UZ flow conducted at various test sites along the ESF, as illustrated in Figure 1.2-1. The ECRB Cross Drift over the repository block provides access to different subunits of the TSw for ECRB, as illustrated in Figure 1.2-2 and Figure 1.2-3.

Figure 1.2-1 illustrates the locations of four alcoves (Alcoves 1, 2, 3, and 4) along the North Ramp, and three alcoves (Alcoves 5, 6, and 7) and four niches (Niches 3107, 3566, 3650, and 4788) along the Main Drift of the ESF. The numerical identification for each niche denotes the distance in meters from the North Portal. These niches are also referred to as Niches 1, 2, 3, and 4, in accordance to the time sequence of excavation (so that Niche 1 = Niche 3566, Niche 2 = Niche 3650, Niche 3 = Niche 3107, and Niche 4 = Niche 4788, along the ESF Main Drift). The ECRB Cross Drift branches out from the ESF North Ramp, crosses over the Main Drift near Niche 3107 (Niche 3), and reaches the western boundary of the repository block, as illustrated in Figure 1.2-2. Figure 1.2-3 illustrates how the ECRB accesses four hydrogeologic units encountered by the repository: through the entrance in the Topopah Spring upper lithophysal (Tptpul), followed by the middle nonlithophysal (Tptpmn), the lower lithophysal (Tptpll), and

the lower nonlithophysal (Tptpln) units (stratigraphic nomenclature of Buesch et al. 1996 [100106], Table 2, pp. 5–8). In comparison, the ESF Main Drift penetrates predominately the Tptpmn unit.

Many emplacement drifts will be in the lower tuff units. The lower units Tptpll and Tptpln have hydrological characteristics different from Tptpmn, with spatially variable lithophysae and fracture densities affecting the amount of seepage and fracture-matrix flow partition. A systematic study with transient air injection and pulse liquid release along four boreholes drilled into the crown of the ECRB Cross Drift has been conducted to evaluate spatial heterogeneity effects. One alcove (Alcove 8) in Tptpul and one niche (Niche CD 1620 or Niche 5, with CD denoting ECRB Cross Drift) in Tptpll have been excavated in the ECRB Cross Drift. Note that Alcove 8 in the ECRB Cross Drift (illustrated in Figure 1.2-3) is located directly (~ 20 m) above Niche 3107 (Niche 3) in the ESF Main Drift (illustrated in Figure 1.2-1).

The ECRB Cross Drift penetrates the Yucca Mountain block to reach the Solitario Canyon fault. The ECRB Cross Drift has four bulkheads, as illustrated in Figure 1.2-3, to hydrologically isolate particular sections of the Cross Drift, such as the portion which contains the fault. Figure 1.2-4 provides a panoramic view of the Yucca Mountain ridge, with Solitario Canyon in the foreground and Busted Butte in the background to the southeast of the repository block. The Calico Hills tuff unit, not accessible by either the ESF Main Drift or the ECRB Cross Drift, is exposed at Busted Butte, 8 km southeast of the repository area. This Busted Butte outcrop is the site of the Unsaturated Zone Tracer Test (UZTT), which is described in Section 6.13 of this report. The geochemical information collected underground from various experiments and test locations is summarized in Section 6.14 to support hydrological understanding of the *in situ* conditions at the Yucca Mountain site.

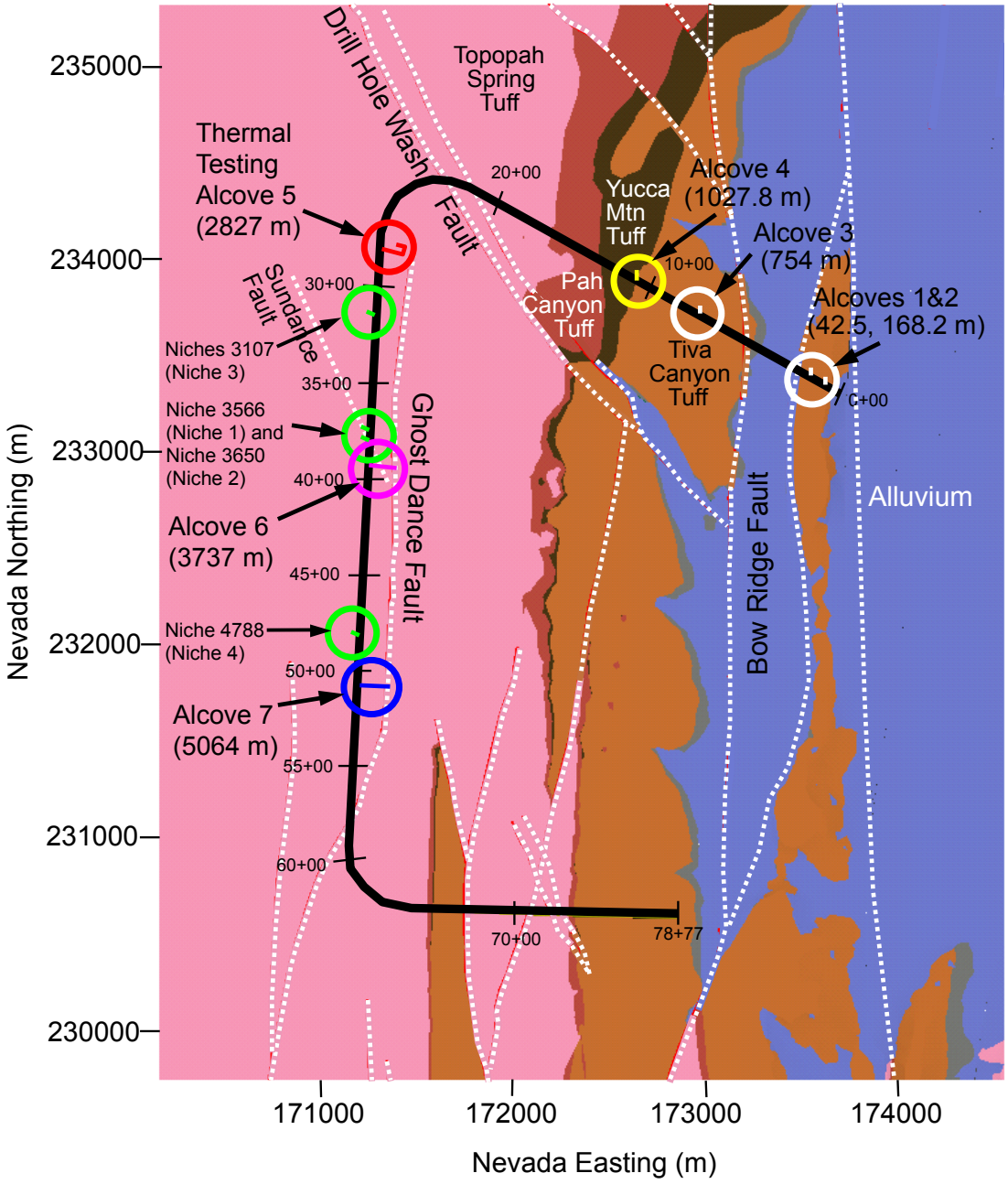

Figure 1.2-1. Schematic Illustration of Alcove and Niche Locations in the Exploratory Studies Facility at Yucca Mountain

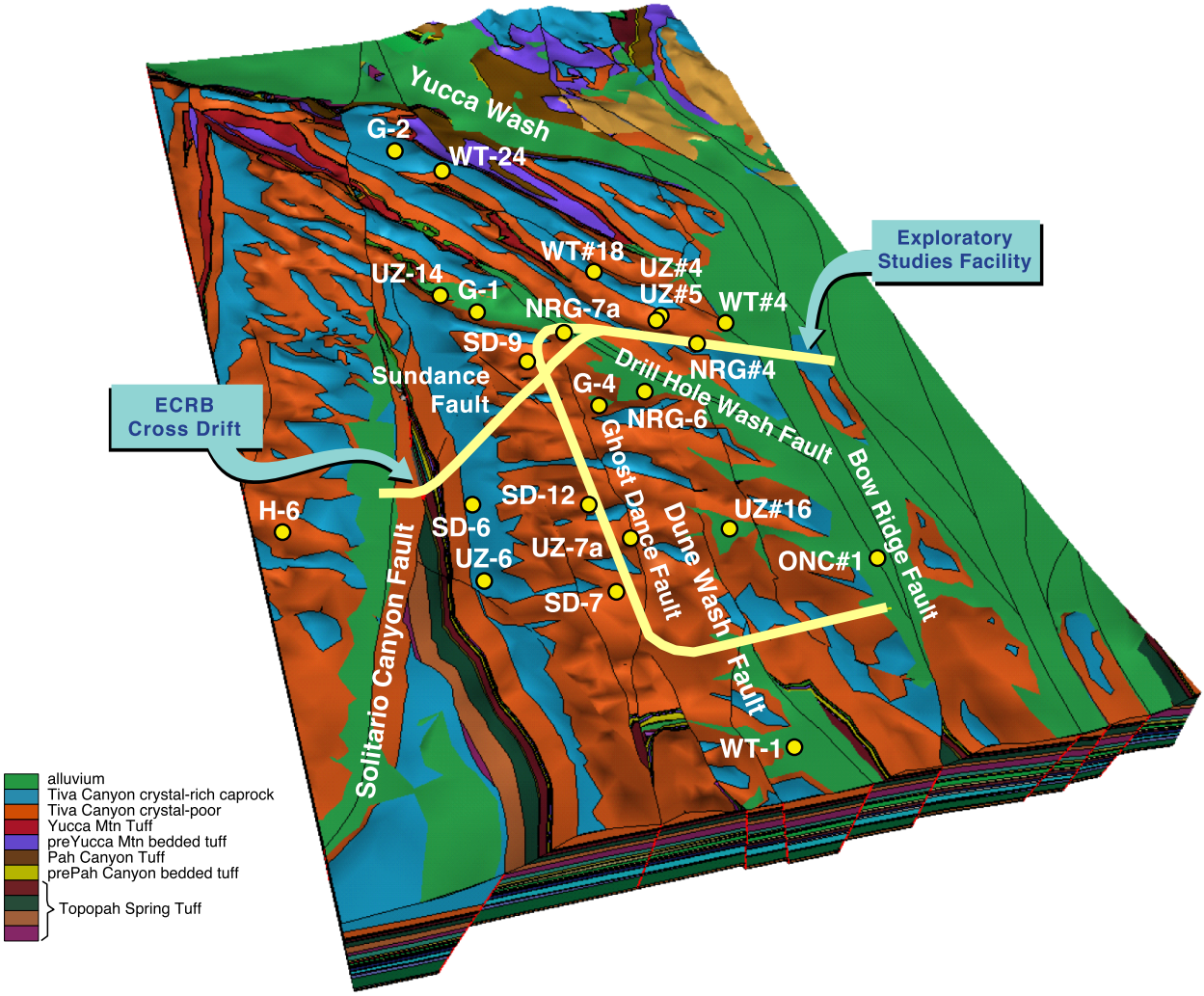

NOTE: The ECRB Cross Drift branches out from the North Ramp of the Exploratory Studies Facility, crosses over the Main Drift, and accesses the western fault boundary of the repository block at Yucca Mountain. Alcoves and niches are illustrated in Figure 1.2-1 for the ESF and in Figure 1.2-3 for the ECRB Cross Drift.

Figure 1.2-2. Schematic Illustration of the ESF and ECRB Cross Drift

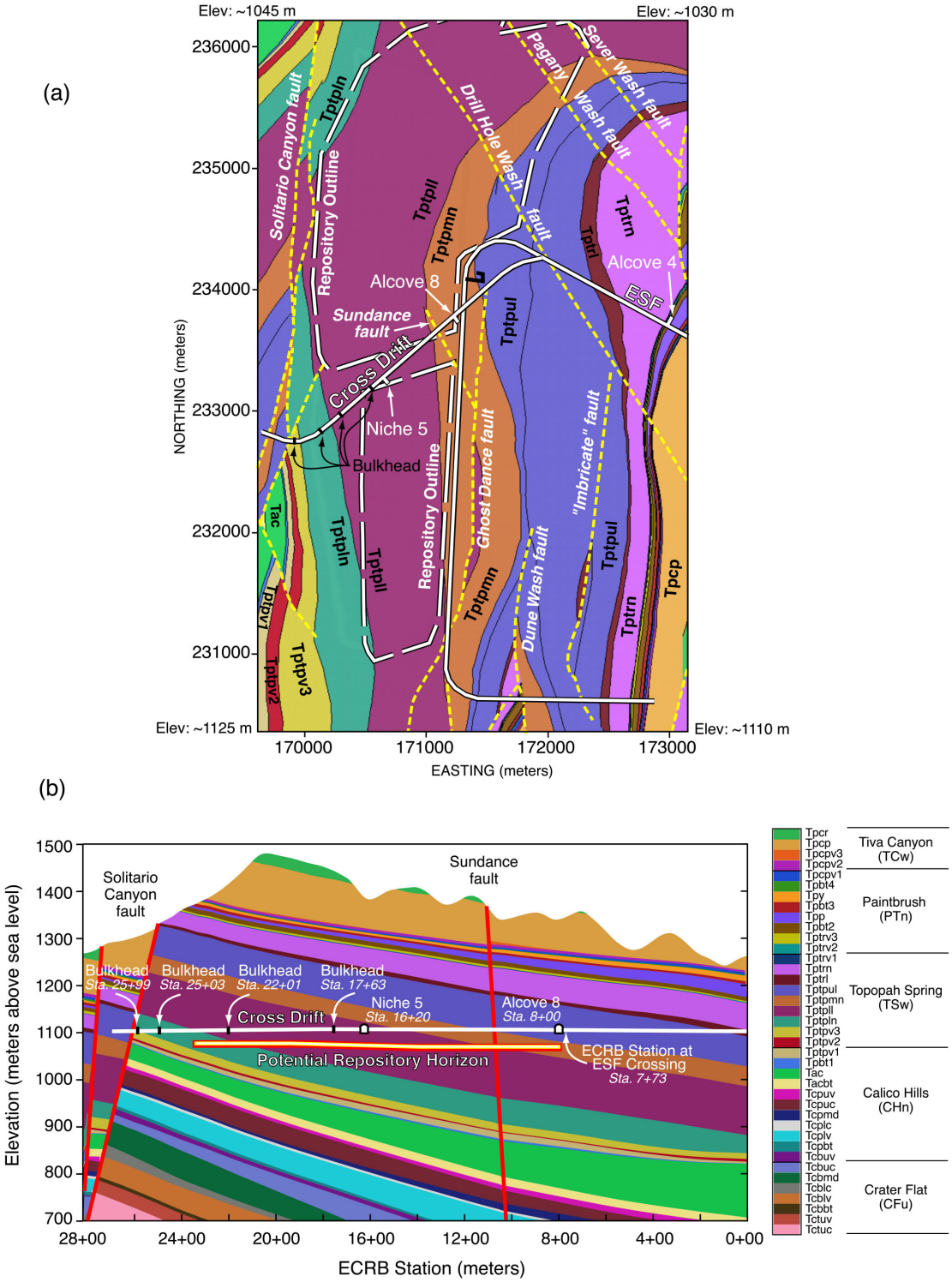

Note: The vertical cross-section in Figure 1.2-3(b) is along the ECRB Cross Drift in nominally the northeast to southwest direction.

Figure 1.2-3. Schematic Illustration of Spatial Distribution of Hydrogeologic Units Intersected by the Repository Horizon (Tptpul, Tptpmn, Tptpll, and Tptpln)

Figure 1.2-4. Photo of Yucca Mountain Ridge and Busted Butte, Taken from the Northwest across the Solitario Canyon Fault

1.3 SUPPORT TO FEP ANALYSIS AND TECHNICAL ISSUE RESOLUTION

This scientific analysis report provides summaries of information which could be used in modeling and abstraction reports (listed in Section 7) and to support the Features, Events, and Processes (FEP) analysis. The following table of FEPs was taken from the LA FEP List (DTN: MO0307SEPFEPS4.000 [164527]). The LA FEP List is a revision to the previous project FEP list (Freeze et al. 2001 [154365]). The selected FEPs are those taken from the LA FEP List associated with the subject matter of this report, regardless of the anticipated status for exclusion or inclusion in TSPA-LA as represented in BSC (2002 [160819]). The results of this analysis are part of the basis for the treatment of FEPs as discussed in the report *Features, Events, and Processes in UZ Flow and Transport* (BSC 2003 [164873]). The UZ FEP report, together with other UZ model reports listed in Section 7, are downstream reports of this scientific analysis report. These reports, rather than this report, provide direct inputs to address issues discussed in *Total System Performance Assessment–License Application Methods and Approach* (BSC 2002 [160146], Section 3.2.2). The cross-reference for each FEP to the relevant sections of this report is also given in Table 1-1 below.

Table 1-1. Features, Events, and Processes Addressed in this Scientific Analysis Report

LA FEP Number	FEP Name	Description Section
1.2.02.01.0A	Fractures	Section 6.1, Section 6.2, Section 6.6, and Section 6.9
1.2.02.02.0A	Faults	Section 6.7 and Section 6.12
2.2.01.01.0A	Mechanical effects of excavation/construction in the near field	Section 6.1
2.2.07.08.0A	Fracture flow in the UZ	Section 6.2, Section 6.6, and Section 6.9
2.2.07.09.0A	Matrix imbibition in the UZ	Section 6.4, Section 6.7
2.2.07.15.0B	Advection and dispersion in the UZ	Section 6.4 and Section 6.12
2.2.07.18.0A	Film flow into the repository	Section 6.2
2.2.07.20.0A	Flow diversion around repository drifts	Section 6.2 and Section 6.11
2.2.08.01.0B	Chemical characteristics of groundwater in the UZ	Section 6.14
2.2.08.03.0B	Geochemical interactions and evolution in the UZ	Section 6.14
2.2.08.08.0B	Matrix diffusion in the UZ	Section 6.3, Section 6.4, Section 6.6, Section 6.7, and Section 6.12
2.2.08.09.0B	Sorption in the UZ	Section 6.3, Section 6.4, Section 6.7, Section 6.12, and Section 6.13
2.2.08.10.0B	Colloidal transport in the UZ	Section 6.13
2.2.09.01.0B	Microbial activity in the UZ	Section 6.10
2.2.11.03.0A	Gas transport in geosphere	Section 6.1 and Section 6.5
2.3.11.03.0A	Infiltration and recharge	Section 6.12

This scientific analysis report also supports the resolutions of technical issues, including: ECRB moisture monitoring, in Section 6.10; Alcove 8/Niche 3107 (Niche 3) testing, in Section 6.11; flow through the Calico Hills nonwelded vitric, in Section 6.13; and analog radionuclide data from test blocks at Busted Butte, in Section 6.13.

1.4 CONSTRAINTS AND LIMITATIONS

The field-testing activities and the associated analyses are subject to the constraints and limitations of spatial locations and temporal durations for tests conducted in the underground drifts. One niche, Niche CD 1620 (Niche 5), has been excavated in the Tptpll unit. Most of the other existing testing alcoves and niches in the ESF (shown in Figure 1.2-3) are located at and

above the horizon of the Tptpmn unit. Test results and analyses from these sites provide information for the upper and middle tuff units. Some of the active flow tests were conducted within a few hours to a few days of each other because of limited accessibility to the test beds in the evenings and on weekends. Depending on system characteristics, the establishment of steady-state conditions requires longer tests. Some tests used automatic data acquisition systems for long-term monitoring and liquid releases, subject to power interruptions and equipment malfunctions. These constraints and limitations are addressed in the analyses of Section 6, if applicable.

The technical scope, content, and management of this scientific analysis report are controlled by the TWP (BSC 2002 [160819]). The update of the LA FEP list from the UZ TWP list is documented in Section 1.3. One deviation from the TWP on YMRP acceptance criteria is documented in Section 4.2. The deviation from the TWP on the status of the ^{36}Cl validation study is documented in Section 6.14.2.

INTENTIONALLY LEFT BLANK

2. QUALITY ASSURANCE

Development of this scientific analysis report and the supporting testing activities have been determined to be subject to the Yucca Mountain Project's quality assurance (QA) program as indicated in *Technical Work Plan for: Performance Assessment Unsaturated Zone,* TWP-NBS-HS-000003 REV 02 (BSC 2002 [160819], Section 8.2, Work Packages (WPs) AUZM06, AUZG01, AUZG02, AUZT08, AUZT09, AUZT10, AUZT11). Approved QA procedures identified in the TWP (BSC 2002 [160819], Section 4) have been used to conduct and document the activities described in this scientific analysis report. The testing and documentation activities follow the TWP for the methods used to control the electronic management of data (BSC 2002 [160819], Section 8.4, WPs AUZM06, AUZG01, AUZG02, AUZT08, AUZT09, AUZT10, AUZT11). There were no variances from the planned methods.

This scientific analysis report provides data for flow, seepage, and transport in natural barriers are classified in the Q-list (BSC 2003 [165179]) as Safety Category because they are important to waste isolation, as defined in AP.2.22Q, *Classification Analyses and Maintenance of the Q-List*. The report contributes to the analyses and modeling data used to support performance assessment (PA). The conclusions of this scientific analysis report do not affect the repository design or permanent items as discussed in AP-2.22Q, *Classification Criteria and Maintenance of the Monitored Geologic Repository Q-List*.

INTENTIONALLY LEFT BLANK

3. USE OF SOFTWARE

The software used in this study are listed in Table 3-1. All qualified software were obtained from Software Configuration Management (SCM), is appropriate for its intended use, and is used only within the range of validation in accordance with AP-SI.1Q, *Software Management.*

For data collection, only acquired software embedded as an integral part of the Measuring and Test Equipment (M&TE) were utilized. The M&TE software were controlled by AP-12.1Q, *Control of Measuring and Test Equipment and Calibration Standards*. Embedded software are exempted from AP-SI.1Q requirements. Software developed or modified for data collection are discussed in the data document associated with each DTN and associated software management reports.

Table 3-1. Software and Routines

Software Name and Version	Software Tracking Number (STN)	DIRS Reference Number	Platform and Operating System
EARTHVISION V4.0	30035-2-V4.0	152835	SGI, IRIX 6.4
ECRB-XYZ V.03	30093-V.03	147402	PC, Windows 98

No models were used for the analyses performed in this scientific analysis report.

Microsoft Excel 97, Microsoft Excel Version 7, Microsoft Excel 2002, CorelDRAW v11.633, Adobe Illustrator 10.0.3, Igor Pro 4.08, Photoshop 7.0.1, MacGPS Pro 4.0.3, DataDesk 6.2, and NOeSYS 2.0 were used for visual display or graphic representation of data; with simple calculations such as mean and standard deviations documented in Attachment IX of this scientific analysis report. These programs are exempted from the requirements of AP-SI.1Q. No developed or modified software is associated with the preparation of this scientific analysis report.

INTENTIONALLY LEFT BLANK

4. INPUTS

Field data collected from underground drifts that characterize ambient and *in situ* field testing conditions include the following:

- Pneumatic pressure and air-permeability data (pre- and post-excavation) for ESF niches
- Pneumatic pressure and air-permeability data from Alcove 4, Alcove 6, and Alcove 8
- Seepage and liquid-release data
- Laboratory dye measurements and sorptivity data
- Water-potential data and electrical resistivity probe data from drift walls and boreholes
- In-drift relative humidity and temperature data (under ventilated and nonventilated conditions)
- Chemical analysis data
- Geologic mapping data
- Unsaturated Zone (UZ) transport testing data from Busted Butte
- Geochemical data and isotope data from underground drifts and boreholes.

The properties resulting from the analyses of the above field data include air-permeability distribution, fracture network connectivity, fracture flow-path distribution, seepage percentage, seepage threshold, fracture characteristic curve, formation intake rate, wetting-front travel time, fracture porosity, fracture volume, fracture flow fraction, tracer distribution, matrix imbibition, retardation factor, fault and matrix flow, water-potential distribution, construction-water migration, relative humidity, moisture conditions, and hydrochemical distributions.

4.1 DIRECT INPUTS

The Q-status of all inputs and a description of the data are shown in the Technical Data Management System (TDMS). The direct inputs to the scientific analysis report were obtained from the TDMS. This scientific analysis report was revised to document recent available *in situ* field-testing data. Results from early revisions with no updates are retained. The input data used in this scientific analysis report are summarized in the tables, which are organized to correspond to equivalent subsections in Section 6.

Since one of the main objectives of this scientific analysis report is to document the data, both direct inputs and collaborating information are summarized together in this section, using separate tables to clearly distinguish different categories. Direct inputs are key data collected, interpreted, illustrated, or tabulated in this scientific analysis report. All other Data Tracking Numbers (DTNs) identified for collaborative information are tabulated in tables without the "direct input" designation.

With the focus of this scientific analysis on the ambient field-testing activities performed in underground drifts through unsaturated zone (UZ) tuff rock units (Section 1), some data collected from monitoring activities, data from surface-based field activities, and data from laboratory testing activities are not included in the "direct input" tables. These data may be important for downstream users for different modeling purposes. The downstream users can make different category selections based on different criteria. If collaborative data are not presented immediately following the direct input data, they are less informative than presentation of the inputs in separated sections.

The direct inputs are presented in the following sections and tables:

- Section 4.1.1.1, Table 4.1-1a on Data and Information Used to Illustrate Air-Permeability Distributions and Excavation-Induced Enhancements
- Section 4.1.2.1, Table 4.1-2a on Data Used to Illustrate Niche Liquid-Release and Seepage-Test Results
- Section 4.1.3, Table 4.1-3 on Data Used to Illustrate Tracer-Migration Delineation at Niche 3650 (Niche 5)
- Section 4.1.4, Table 4.1-4 on Data Used to Illustrate Tracer Penetration and Water Imbibition into Welded Tuff Matrix
- Section 4.1.5, Table 4.1-5 on Data Used to Illustrate Crosshole Analysis of Air-Injection Tests
- Section 4.1.6, Table 4.1-6 on Data Used to Illustrate Fracture Flow in Fracture-Matrix Test Bed at Alcove 6
- Section 4.1.7.1, Table 4.1-7a on Data Used to Illustrate Flow through the Fault and Matrix in the Test Bed at Alcove 4
- Section 4.1.8, Table 4.1-8 on Data Used to Compile Water-Potential Measurements in Niches
- Section 4.1.9, Table 4.1-9 on Data Used to Illustrate Observations of Construction-Water Migration
- Section 4.1.10.1, Table 4.1-10a on Data Used to Illustrate Moisture Monitoring and Water Analysis in Underground Drifts
- Section 4.1.11.1, Table 4.1-11a on Data Used to Illustrate Systematic Hydrological Characterization Results
- Section 4.1.12.1, Table 4.1-12a on Data Used to Illustrate Flow and Transport Test Results at Alcove 8/Niche 3107 (Niche 3)
- Section 4.1.13.1, Table 4.1-13a on Data Used to Illustrate Busted Butte Unsaturated Zone Transport Test Results
- Section 4.1.14.1, Table 4.1-14a on Data Used to Support Geochemical Interpretations

Other associated information are also summarized in different tables.

The uncertainties related to input data and parameters are presented in Section 6 of this scientific analysis report.

4.1.1 Data and Information of Air-Permeability Distributions and Excavation-Induced Enhancements

4.1.1.1 Data Used to Illustrate Air-Permeability Distributions and Excavation-Induced Enhancements (Direct Input)

Table 4.1-1a. Data Used to Illustrate Air-Permeability Distributions and Excavation-Induced Enhancements (Direct Input)

Inputs	Used in			Description
	Section	Figure	Table	
*LB0011AIRKTEST.001 [153155]	Attach. IX.3	6.1.2-1 6.1.2-2 6.1.2-3 6.1.2-4	6.1.2-1 6.1.2-5 IX.3-1	Air-permeability measurements in Niche 3566 (Niche 1) and Niche 3650 (Niche 2) of the ESF
LB980901233124.101 [136593]		6.1.2-5 6.1.2-6 6.1.2-7 6.1.2-8	6.1.2-1 6.1.2-5	Pneumatic-pressure and air-permeability data from Niche 3107 (Niche 3) and Niche 4788 (Niche 4) in the ESF (pre-excavation)
*LB990601233124.001 [105888]		6.1.2-5 6.1.2-7	6.1.2-1 6.1.2-5	Pneumatic-pressure and air-permeability data from Niche 3107 (Niche 3) and Niche 4788 (Niche 4) in the ESF (post-excavation)
LB980912332245.001 [110828]			6.1.2-5	Air-injection data from Niche 3107 (Niche 3) of the ESF (radial boreholes)
*LB0012AIRKTEST.001 [154586]		6.1.2-9	6.1.2-2 6.1.2-5	Air-permeability testing in Niche CD 1620 (Niche 5 upper boreholes, pre-excavation)
*LB0110AKN5POST.001 [156904]		6.1.2-9	6.1.2-2 6.1.2-5	Air-permeability measurement in Niche CD 1620 (Niche 5 upper boreholes, post-excavation)
*LB002181233124.001 [146878]		6.1.2-10	6.1.2-3 6.1.2-5	Air-permeability and pneumatic-pressure data collected from Niche CD 1620 (Niche 5 side boreholes, pre-excavation)
*LB0110AK23POST.001 [156905]		6.1.2-10	6.1.2-3 6.1.2-5	Air-permeability measurement in Niche CD 1620 (Niche 5 side boreholes, post-excavation)
LB980901233124.009 [105856]			6.1.2-5	Pneumatic-pressure and air-permeability data from Alcove 4 in the ESF
LB980901233124.004 [105855]			6.1.2-5	Pneumatic pressure and air-permeability data from Alcove 6 in the ESF
LB0302ALC8AIRK.001 [164748]		6.1.2-11	6.1.2-4 6.1.2-5	Air-permeability data from Alcove 8

NOTE: * Input DTNs for DTN: LB0310AIRK0015.001 [Output].

4.1.1.2 Information Used to Corroborate Analysis of Air-Permeability Distributions and Excavation-Induced Enhancements (For Reference)

Table 4.1-1b. Information Used to Corroborate Analysis of Air-Permeability Distributions and Excavation-Induced Enhancements (For Reference)

Inputs	Used in			Description
	Section	Figure	Table	
MO0008GSC00269.000 [166198]	6.1.1.2		6.1.1-5	As-built ECRB Alcove 8, construction observation alcove boreholes (#1 through 7)
*LB990901233124.004 [123273], Data Table S00017_002			6.1.2-5	Statistical analyses of air-permeability data from Niche 3650 (Niche 2), Niche 3107 (Niche 3), and Niche 4788 (Niche 4), as well as Alcove 4 and Alcove 6.

NOTE: * Other data tables also used as input in Section 6.5 on crosshole connectivity as shown in Table 4.1-5.

4.1.2 Data and Information of Niche Liquid-Release and Seepage-Test Results

4.1.2.1 Data Used to Illustrate Niche Liquid-Release and Seepage-Test Results (Direct Input)

Table 4.1-2a. Data Used to Illustrate Niche Liquid-Release and Seepage-Test Results (Direct Input)

Inputs	Used in			Description
	Section	Figure	Table	
*LB980001233124.004 [136583]	6.2.1.1 6.2.1.2, 6.2.1.3.1 6.2.2.1 6.2.2.3 6.2.2.4 Attach. IV.2 Attach. IV.3.2	6.2.1-2 6.2.2-2	6.2.2-4 II-1 II-4 IV.3-1	Liquid-release test data from Niche 3566 (Niche 1) and Niche 3650 (Niche 2) of the ESF
*LB980901233124.003 [105592]	6.2.1.1 6.2.1.2 Attach. IV.2 Attach. IV.3.2	6.2.1-2 6.2.2-1 6.2.2-2 6.2.2-3 6.2.2-4 IV.2-1	6.2.2-1 6.2.2-2 6.2.2-3 6.2.2-4 II-1 II-4 II-5 II-7 II-8 IV.3-1	Liquid-release and tracer tests in Niche 3566 (Niche 1), Niche 3650 (Niche 2), Niche 3107 (Niche 3), and Niche 4788 (Niche 4) in the ESF, as well as fracture flow and seepage testing in the ESF
*LB0010NICH3LIQ.001 [153144]	6.2.1.3.2	6.2.1-4	II-3a	Niche 3107 (Niche 3) seepage test
*# LB0010NICH4LIQ.001 [153145]	6.2.1.3.3	6.2.1-5 6.2.1-6 6.2.2-2	II-2 II-3b II-8	Niche 4788 (Niche 4) seepage tests measuring injected and captured water masses over time. Time spans include considerations for pumping time, wetting-front arrival time, and dripping duration.
*LB0102NICH5LIQ.001 [155681]	6.2.1.1 6.2.1.2	6.2.1-2	II-1	Niche CD 1620 (Niche 5) seepage tests–pre-excavation
*LB990601233124.001 [105888]			6.2.2-2 II-4	Seepage data feed to UZ drift-scale flow model for TSPA-SR
LB0211NICH5LIQ.001 [160792]	Attach. III.4 Attach. VI Attach. IX.6.1	6.2.1-14 6.2.1-15 6.2.1-17 6.2.1-18 6.2.1-19 6.2.1-20 6.2.1-21 6.2.1-22 6.2.1-23	IV.4-1 IX.6-1	Liquid-release and tracer tests in Niche CD 1620 (Niche 5) in the ECRB

NOTE: * Input DTN for DTN: LB0110LIQR0015.001 [Output].
Input DTN for DTN: LB0110NICH4LIQ.001 [Output].

4.1.2.2 Information Used to Corroborate Analysis and Interpretation of Niche Liquid-Release and Seepage Tests (For Reference)

Table 4.1-2b. Information Used to Corroborate Analysis and Interpretation of Niche Liquid-Release and Seepage Tests (For Reference)

Inputs	Used in			Description
	Section	Figure	Table	
MO0107GSC01069.000 [156941]			II-2	ESF Niche 4788 (Niche 4) borehole as-built information
MO0107GSC01061.000 [155369]	6.2.1.3.5.2 Attach. III.1		6.2.1-13	As-built profile Niche CD 1620 (Niche 5) bat-wing excavation
MO0209GSC02116.000 [160407],	6.2.1.3.5.2			ECRB Niche CD 1620 (Niche 5) borehole as-built information

4.1.3 Data Used to Illustrate Tracer-Migration Delineation at Niche 3650 (Niche 5) (Direct Input)

Table 4.1-3. Data Used to Illustrate Tracer-Migration Delineation at Niche 3650 (Niche 5) (Direct Input)

Inputs	Used in			Description
	Section	Figure	Table	
LB990601233124.003 [106051]		6.3.2-1 6.3.2-2 6.3.2-3 6.3.2-4 6.3.2-5 6.3.2-6 6.3.2-7 6.3.2-8	6.3.2-1	Tracer detection data from core samples for tracers injected in Niche 3650 (Niche 2) in the ESF

4.1.4 Data Used to Illustrate Tracer Penetration and Water Imbibition into Welded Tuff Matrix (Direct Input)

Table 4.1-4. Data Used to Illustrate Tracer Penetration and Water Imbibition into Welded Tuff Matrix (Direct Input)

Inputs	Used in			Description
	Section	Figure	Table	
LB980001233124.004 [136583]			6.4.1-1 6.4.1-2	Liquid-release tests in Niche 3566 (Niche 1) and Niche 3650 (Niche 2)
LB980901233124.003 [105592]			6.4.1-1	Liquid-release and tracer tests in Niche 3566 (Niche 1), Niche 3650 (Niche 2), Niche 3107 (Niche 3), and Niche 4788 (Niche 4) in the ESF.
LB990901233124.003 [155690]	6.4.1.4	6.4.1-2 6.4.1-3 6.4.2-1 6.4.2-2 V-1 V-2	6.4.1-2 6.4.2-1	Tracer lab analyses of dye penetration in Niche 3650 (Niche 2) and Niche 4788 (Niche 4) of the ESF
LB0110TUFTRACR.001 [156979]		6.4.3-1 6.4.3-2		Spatial distribution of applied tracers and the distribution of intrinsic tuff elements profiled using LA-ICP-MS

4.1.5 Data Used to Illustrate Crosshole Analysis of Air-Injection Tests (Direct Input)

Table 4.1-5. Data Used to Illustrate Crosshole Analysis of Air-Injection Tests (Direct Input)

Inputs	Used in			Description
	Section	Figure	Table	
LB980901233124.004 [105855]		6.5.1-2		Pneumatic-pressure and air-permeability data from Alcove 6 in the ESF
LB980901233124.009 [105856]		6.5.2-2		Pneumatic-pressure and air-permeability data from Alcove 4 in the ESF
LB990901233124.004 [123273]		6.5.1-1 6.5.1-3 6.5.2-3 6.5.2-4		Air-permeability crosshole connectivity in Alcove 6, Alcove 4, and Niche 4788 (Niche 4) of the ESF

4.1.6 Data Used to Illustrate Fracture Flow in Fracture-Matrix Test Bed at Alcove 6 (Direct Input)

Table 4.1-6. Data Used to Illustrate Fracture Flow in Fracture-Matrix Test Bed at Alcove 6 (Direct Input)

Inputs	Used in			Description
	Section	Figure	Table	
LB990901233124.002 [146883]		6.6.2-1 6.6.2-2 6.6.2-3 6.6.2-4 6.6.2-5 6.6.2-6 6.6.2-7 6.6.2-8	6.6.1-1 6.6.2-1	Alcove 6 flow data, including electrical resistance, water injection, intake rate, and water-potential measurements
LB990901233124.001 [155694]		6.6.2-8		Alcove 6 tracer tests: the breakthrough of tracers, relating to the volume and the measured tracer concentration of the collected liquid at four collection trays in Alcove 6 experiments

4.1.7 Data and Information of Flow through the Fault and Matrix in the Test Bed at Alcove 4

4.1.7.1 Data Used to Illustrate Flow through the Fault and Matrix in the Test Bed at Alcove 4 (Direct Input)

Table 4.1-7a. Data Used to Illustrate Flow through the Fault and Matrix in the Test Bed at Alcove 4 (Direct Input)

Inputs	Used in			Description
	Section	Figure	Table	
LB990901233124.005 [146884]		6.7.2-1 6.7.2-2 6.7.2-3 6.7.2-4 6.7.2-5 6.7.2-6	6.7.1-1	Alcove 4 flow data, including electrical resistance, water injection, intake rate measurements

4.1.7.2 Data Used to Corroborate Analysis of Flow through the Fault and Matrix in the Test Bed at Alcove 4 (For Reference)

Table 4.1-7b. Data Used to Corroborate Analysis of Flow through the Fault and Matrix in the Test Bed at Alcove 4 (For Reference)

Inputs	Used in			Description
	Section	Figure	Table	
GS960908314224.020 [106059]	6.7.1.1			Analysis report: geology of the north ramp–stations 4+00 to 28+00 data: detailed line survey and full-periphery geotechnical map–Alcoves 3 (UPCA) and 4 (LPCA), and comparative geological cross section–Stations 0+60 to 28+00

4.1.8 Data Used to Compile Water-Potential Measurements in Niches (Direct Input)

Table 4.1-8. Data Used to Compile Water-Potential Measurements in Niches (Direct Input)

Inputs	Used in			Description
	Section	Figure	Table	
LB980001233124.001 [105800]		6.8.2-1 6.8.2-2 VII-1 VII-2	6.8.2-1 6.8.2-2 6.8.2-3	Water-potential measurements in Niche 3566 (Niche 1), Niche 3650 (Niche 2), and Niche 3107 (Niche 3) of the ESF

4.1.9 Data Used to Illustrate Observations of Construction-Water Migration (Direct Input)

Table 4.1-9. Data Used to Illustrate Observations of Construction-Water Migration (Direct Input)

Inputs	Used in			Description
	Section	Figure	Table	
LB980901233124.014 [105858]		6.9.2-1 6.9.2-2 6.9.5-3 6.9.5-4	6.9.2-1 6.9.2-2	Borehole monitoring at the single borehole in the ECRB and ECRB crossover point in the ESF

4.1.10 Data and Information of Moisture Monitoring and Water Analysis in Underground Drifts

4.1.10.1 Data Used to Illustrate Moisture Monitoring and Water Analysis in Underground Drifts (Direct Input)

Table 4.1-10a. Data Used to Illustrate Moisture Monitoring and Water Analysis in Underground Drifts (Direct Input)

Inputs	Used in			Description
	Section	Figure	Table	
LB990901233124.006 [135137]		6.10.1-1 6.10.1-2	6.10.1-1	Moisture data from the ECRB cross drift; relative humidity data from various cross-drift stations
LAJF831222AQ98.007 [122730]		6.10.1-3		Chloride, bromide, and sulfate analysis of salts leached from ECRB-CWAT#1, #2, and #3 drillcore.
GS990908314224.010 [152631]		6.10.2-3		Comparative cross section along the ECRB Cross Drift
GS990408314224.006 [108409]			6.10.2-1	Full periphery geological maps for Station 20+00 to 26+81, ECRB Cross Drift
LB0110ECRBH2OP.001 [156883]		6.10.2.4		Measurements of water potential at three locations between successive bulkhead doors in the ECRB
LB0307ECRBRHTB.001 [164843]	6.10.2.3	6.10.2-5 6.10.2-6 6.10.2-7 6.10.2-17 6.10.2-18		Measurements of relative humidity, temperature, and barometric pressure at four locations between successive bulkhead doors in the ECRB
LB0301ECRBRHTB.001 [164605]	6.10.2.2 6.10.2.2.2 6.10.2.2.3	6.10.2-9 6.10.2-10 6.10.2-11 6.10.2-12 6.10.2-13 6.10.2-14 6.10.2-15 6.10.2-16		Observations of entries made on June 23, 2001, and October 1–2, 2001
LB0110ECRBH2OA.001 [156886]		6.10.3-1 6.10.3-2	6.10.3-1	Anion-cation measurements for water samples from nonventilated sections of the ECRB
LB0110ECRBH2OI.001 [156887]		6.10.3-3	6.10.3-1	Deuterium and DEL O-18 measurements for water samples from nonventilated sections of the ECRB

4.1.10.2 Additional Information on Drift Moisture Monitoring and Water Analysis (For Reference)

Table 4.1-10b. Additional Information on Drift Moisture Monitoring and Water Analysis (For Reference)

Inputs	Used in			Description
	Section	Figure	Table	
LB960800831224.001 [105793]	6.10.1.2.1		6.10.1-1	Relative humidity, temperature, and pressure in ESF monitoring stations
LB970300831224.001 [105794]			6.10.1-1	Moisture data report from October 1996 to January 1997
LB970801233124.001 [105796]	6.10.1.2.1		6.10.1-1	Moisture monitoring data collected at ESF sensor stations
LB970901233124.002 [105798]			6.10.1-1	Moisture monitoring data collected at stationary moisture stations
GS970208312242.001 [135119]			6.10.1-1	Moisture monitoring in the ESF, Oct. 1, 1996, to Jan. 31, 1997
GS970708312242.002 [135123]			6.10.1-1	Moisture monitoring in the ESF, Feb. 1, 1997, to July 31, 1997
GS980908312242.024 [135132]			6.10.1-1	Moisture monitoring in the ESF, August 1, 1997, to July 31, 1998
GS980908312242.035 [135133]			6.10.1-1	Moisture monitoring in the ECRB
GS021008312242.003 [162178]	6.10.1.2.2			Temperature and water-potential data from Alcove 3 and Alcove 4
GS030608312231.002 [165547]	6.10.2.2			Digital image data from the moisture monitoring tests in the ECRB bulkheaded Cross Drift from January 22, 2001, to February 3, 2003
MO0006J13WTRCM.000 [151029]		6.10.3-2		J-13 well water composition
LB0108CO2DST05.001 [156888]		6.10.3-3		Concentration data for CO_2 from gas samples collected from hydrology holes in drift-scale test
LB0011CO2DST08.001 [153460]		6.10.3-3		Contents of gas samples collected from the following drift-scale test holes: 57, 58, 59, 60, 61, 74, 75, 76, 77, 78, 185; and the following control areas: Heater Drift #2 and AO drift air

4.1.10.3 Additional Information on Water Potential and Saturation Measurements (For Reference)

Table 4.1-10c. Additional Information on Water Potential and Saturation Measurements (For Reference)

Inputs	Used in			Description
	Section	Figure	Table	
*LB980001233124.001 [105800]			6.10.1-2	3 main boreholes, 5 lateral boreholes in Niche 3566 (Niche 1) water potential
GS980908312242.022 [135157]			6.10.1-2	Heat-dissipation-probe drill holes water potential
GS980908312242.033 [107168]			6.10.1-2 6.10.1-3	1 core hole in Alcove 3, 2 core holes in Alcove 4 water potential and saturation
GS980908312242.032 [107177]			6.10.1-2 6.10.1-3	1 core hole in Alcove 3, 2 core holes in Alcove 4 water potential and saturation
GS980308312242.004 [107172]			6.10.1-2	18 North Ramp boreholes, 3 Alcove 4 boreholes, and 46 South Ramp boreholes, HQ, 2 m length water potential
GS980308312242.002 [135163]			6.10.1-2	Heat-dissipation-probe drill holes water potential
**LB980901233124.014 [105858]			6.10.1-2 6.10.1-3	43 psychrometers on ESF drift walls, 1 slant borehole below the invert, 43 TDR probes on ESF drift walls
GS980908312242.036 [119820]			6.10.1-2	6 heat-dissipation-probe drill holes water potential
GS970808312232.005 [105978]			6.10.1-2	USW NRG-7a, UE-25 UZ#4, UE-25 UZ#5, USW UZ-7a and USW SD-12 water potential
GS971108312232.007 [105980]			6.10.1-2	USW NRG-7a, UE-25 UZ#4, UE-25 UZ#5, USW UZ-7a and USW SD-12 water potential
GS980408312232.001 [105982]			6.10.1-2	USW NRG-7a, UE-25 UZ#4, UE-25 UZ#5, USW UZ-7a and USW SD-12 water potential
GS981208312232.002 [156505]			6.10.1-2	USW NRG-7a, UE-25 UZ#4, UE-25 UZ#5, USW UZ-7a and USW SD-12 water potential
GS980908312242.018 [135170]			6.10.1-3	3 main boreholes, 6 lateral boreholes in Niche 3566 (Niche 1) and 7 main boreholes in Niche 3650 (Niche 2)
GS980908312242.020 [135172]			6.10.1-3	3 main boreholes, 6 lateral boreholes in Niche 3566 (Niche 1) and 7 main boreholes in Niche 3650 (Niche 2)
GS980908312242.029 [135175]			6.10.1-3	3 boreholes in Alcove 6, 1 borehole in Alcove 7 saturation
GS980908312242.028 [135176]			6.10.1-3	3 boreholes in Alcove 6, 1 borehole in Alcove 7 saturation
GS980308312242.005 [107165]			6.10.1-3	PTn Borehole core saturation
GS980308312242.003 [135180]			6.10.1-3	South Ramp core saturation
GS980308312242.001 [135181]			6.10.1-3	TDR measurements of saturation
GS980908312242.030 [135224]			6.10.1-3	1 slant borehole core saturation

NOTE: * Also used as input in Section 6.8 on niche water-potential measurement, as shown in Table 4.1-8.
** Also used as input in Section 6.9 on construction-water migration, as shown in Table 4.1-9.

4.1.11 Data and Information of Systematic Hydrological Characterization Results

4.1.11.1 Data Used to Illustrate Systematic Hydrological Characterization Results (Direct Input)

Table 4.1-11a. Data Used to Illustrate Systematic Hydrological Characterization Results (Direct Input)

Inputs	Used in			Description
	Section	Figure	Table	
*LB00090012213U.001 [153141]	6.11.2.1	6.11.2-1 6.11.3-2	6.11.2-1	Two sets of air-k (pneumatic conductivity) tests at 3 intervals in title borehole. Air-k derived from steady-state pressure response.
*LB00090012213U.002 [153154]		6.11.2-2 6.11.2-3 6.11.2-4 6.11.2-5 6.11.2-6 6.11.3-2		Eleven sets of seepage tests. Liquid-release tests from borehole SYBT-ECRB-LA#2 at CS 17+26 in cross drift.
*LB0110ECRBLIQR.003 [156877]		6.11.2-7 6.11.2-8 6.11.2-9 6.11.3-2		Measurements of seepage from injection tests in boreholes located in the drift crown of the ECRB
*LB0110ECRBLIQR.001 [156878]		6.11.2-10 6.11.3-2		Measurements of seepage from injection tests in boreholes located in the drift crown of the ECRB
*LB0110ECRBLIQR.002 [156879]	Attach. IX.6.2	6.11.2-11 6.11.3-2	IX.6-2	Measurements of seepage from injection tests in boreholes located in the drift crown of the ECRB
LB0203ECRBLIQR.001 [158462]	Attach. IX.6.3 Attach. IX.6.4 Attach. IX.6.5	6.11.2-12 6.11.2-13 6.11.2-14 6.11.3-2	IX.6-3 IX.6-4 IX.6-5 IX.6-8	Systematic testing in SYBT-ECRB- LA#3 (May–July 2001)
LB0301SYTSTLA4.001 [165227]	Attach. IX.6.4	6.11.2-15 6.11.2-16 6.11.2-17 6.11.3-2	IX.6-6 IX.6-7	Measurements of seepage from injection tests in boreholes located in the drift crown of the SYBT-ECRB-LA#4

NOTE: * Input DTNs for DTN: LB0110SYST0015.001 [Output].

4.1.11.2 Information Used to Corroborate Analyses and Interpretations of Systematic Hydrological Characterization (For Reference)

Table 4.1-11b. Information Used to Corroborate Analyses and Interpretations of Systematic Hydrological Characterization (For Reference)

Inputs	Used in			Description
	Section	Figure	Table	
LB980912332245.002 [105593]	6.11.3.1			Gas tracer data from Niche 3107 (Niche 3) of the ESF
LB0110COREPROP.001 [157169]	6.11.3.1			Data measured from cores drilled in the ECRB: porosity, saturation, bulk density, gravimetric water content, particle density

4.1.12 Data and Information of Observations from the Test at Alcove 8/Niche 3107

4.1.12.1 Data Used to Illustrate Flow and Transport Test Results at Alcove 8/Niche 3107 (Niche 3) (Direct Input)

Table 4.1-12a. Data Used to Illustrate Flow and Transport Test Results at Alcove 8/Niche 3107 (Niche 3) (Direct Input)

Inputs	Used in			Description
	Section	Figure	Table	
GS020508312242.001 [162129]	6.12.2.1	6.12.2-1 6.12.2-2		Trenched fault infiltration in Alcove 8, 3/5/2001–6/1/2001
GS020908312242.002 [162141]	6.12.2.1	6.12.2-1 6.12.2-2		Trenched fault infiltration in Alcove 8, 6/1/2001–3/26/2002
GS030208312242.003 [165544]	6.12.2.1	6.12.2-1 6.12.2-2		Trenched fault infiltration in Alcove 8, 3/26/2002–8/20/2002
LB0110A8N3LIQR.001 [157001]	Attach. IX.6.5	6.12.2-3 6.12.2-4 6.12.2-5 6.12.2-7 IX.6-1	IX.6-9a IX.6-9b IX.6-10	Preliminary observations from the fault test at Alcove 8/Niche 3107 (Niche 3).
LB0204NICH3TRC.001 [158478]		6.12.2-7 6.12.2-8		Fault infiltration test tracer sampling April 2001–March 2002
LB0209A8N3LIQR.001 [165461]		6.12.2-4 IX.6-1	IX.6-9c IX.6-10	Resistance measurements from borehole 10 in Niche 3107 (Niche 3, 5/23/2001–9/3/2002)
LB0303A8N3LIQR.001 [162570]		6.12.2-4 6.12.2-6 6.12.2-8 IX.6-1		Alcove 8/Niche 3107 (Niche 3) seepage data compilation
LB0110A8N3GPRB.001 [156912]		6.12.3-1 6.12.3-2		Pre-seepage test ground penetrating radar tomography in radial borehole arrays between Alcove 8 (ECRB) and Niche 3107 (Niche 3, ESF)
GS031008312242.007 [166089]	6.12.4	6.12.4-2 6.12.4-3		Large plot infiltration in Alcove 8, 8/20/2002–11/19/2002
GS030608312242.005 [166200]		6.12.4-2		Surface infiltration in a large plot in Alcove 8 using permeameters from 11/19/2002–03/24/2003.
LB0306A8N3LIQR.001 [165405]		6.12.4-4 6.12.4-5		Fault infiltration test from Alcove 8 to Niche 3107 (Niche 3, 9/18/2002–10/16/2002)
LB0308A8N3SEEP.001 [166090]		6.12.4-5		Measurements of seepage at Niche 3107 (Niche 3) from injection tests in an infiltration plot located at Alcove 8 of the ECRB, 10/16/2002–4/2/2003

4.1.12.2 Additional Information for Alcove 8/ Niche 3107 (Niche 3) Tests and Summary of the Alcove 1 Tests (For Reference)

Table 4.1-12b. Additional Information for Alcove 8/ Niche 3107 (Niche 3) Tests and Summary of the Alcove 1 Tests (For Reference)

Inputs	Used in			Description
	Section	Figure	Table	
GS030508312242.004 [165545]	6.12.1.2			Photographs from Niche 3107 (Niche 3) of the Alcove 8/Niche 3107 (Niche 3) seepage experiment during construction showing construction water in Niche 3107 (Niche 3), 3/6/2000
*MO9901MWDGFM31.000 [103769]	6.12.1.2			Geologic Framework Model, Version GFM 3.1
GS010608312242.004 [165542]	6.12.1.3.1			Crossover Alcove/Seepage into Niche 3107 (Niche 3): small plot infiltration using a cylinder permeameter, 8/9/2000–8/21/2000
GS010608312242.002 [165543]	6.12.1.3.1			Crossover Alcove/Seepage into Niche 3107 (Niche 3): small plot infiltration using a box permeameter, 8/28/2000–12/14/2000
GS990108312242.006 [162979]			6.12.5-1	Pulse flow meter data for infiltration on surface, Phase I, May 9, 1998–December 4, 1998
GS000308312242.002 [156911]	6.12.5.1		6.12.5-1	Seepage data for water collected in Alcove 1, Phase I, 5/5/1998–9/27/1998
GS000808312242.006 [162980]			6.12.5-1	Pulse flow meter data for infiltration on surface, Phase II, 2/19/1999–6/20/2000
GS000399991221.003 [147024]			6.12.5-1	Preliminary infiltration, seepage, tracer data, Phase II, 2/19/1999–12/15/1999
GS001108312242.009 [165202]			6.12.5-1	Tracer data for water collected in Alcove 1, Phase II, 5/9/1999–7/5/2000

*Note: The TDMS shows DTN: MO9901MWDGFM31.000 [103769] to be superseded by DTN: MO0012MWDGFM02.002 [153777]; however, the new DTN does not include the data used for development of this analysis. The comment section on the Technical Data Information Form for the more recent DTN also states: “GFM2000 does not invalidate GFM3.1.” This scientific analysis report maintains the use of the original DTN.

4.1.13 Data and Information of Busted Butte Unsaturated Zone Transport Test Results

4.1.13.1 Data Used to Illustrate Busted Butte Unsaturated Zone Transport Test Results (Direct Input)

Table 4.1-13a. Data Used to Illustrate Busted Butte Unsaturated Zone Transport Test Results (Direct Input)

Inputs	Used in			Description
	Section	Figure	Table	
LA0302WS831372.001 [162765]		6.13.2-1 6.13.2-2		Fluorescein plumes observed in Phase 1a mineback
LA9909WS831372.001 [122739]	6.13.2.2	6.13.2-4a 6.13.2-4b 6.13.2-4c 6.13.2-4d 6.13.2-4e		Busted Butte UZ transport test: Phase I collection pad extract concentrations
LA9909WS831372.002 [122741]	6.13.2.2	6.13.2-4a 6.13.2-4b 6.13.2-4c 6.13.2-4d 6.13.2-4e		Busted Butte UZ transport test: Phase I collection pad tracer loading and tracer concentrations
LA0112WS831372.001 [157100]		6.13.3-3 6.13.3-4 6.13.3-5 6.13.3-6 6.13.3-7		Busted Butte UZ transport test: Phase II collection pad tracer loading.
LA0112WS831372.002 [157115]		6.13.3-3 6.13.3-4 6.13.3-5 6.13.3-6 6.13.3-7		Busted Butte UZ transport test: Phase II collection pad tracer concentrations.
LA0112WS831372.003 [157106]		6.13.3-3 6.13.3-4 6.13.3-5 6.13.3-6 6.13.3-7		Busted Butte UZ transport test: Phase II normalized collection pad tracer concentrations.
LB00032412213U.001 [149214]		6.13.4-1 6.13.4-2 6.13.4-3 6.13.4-4		Busted Butte ground-penetrating-radar data collected June 1998 through February 2000 at the unsaturated zone transport test (UZTT): GPR velocity data.
LB0110BSTBTGPR.001 [156913]		6.13.4-3 6.13.4-4		Time sequence ground-penetrating-radar tomography for the Busted Butte tracer imbibition test
LL990612704244.098 [147168]	6.13.4.2.1	6.13.4-7 6.13.4-8		ERT data for Busted Butte, electrical properties of the rock were measured during water infiltration.
LA0201WS831372.004 [165422]		6.13.5-1 6.13.5-2 6.13.5-3		Calculated moisture content for the Busted Butte site Phase II collection boreholes
LA0311SD831372.001 [166197]		6.13.5-2		*In situ* air permeability measurements at Busted Butte
LA0008WS831372.001 [156582]		6.13.5-4 6.13.5-5		Calculated daily injection rates for the Busted Butte unsaturated zone transport tests

4.1.13.2 Information Used to Corroborate Busted Butte Unsaturated Zone Transport Test (For Reference)

Table 4.1-13b. Information Used to Corroborate Busted Butte Unsaturated Zone Transport Test (For Reference)

Inputs	Used in			Description
	Section	Figure	Table	
LA9909WS831372.016 [140093]	6.13.1.11			Ion chromatography pore-water analysis for rock samples from Busted Butte (used in AMR as reference for pore-water composition)
LA9909WS831372.017 [140097]	6.13.1.11			pH pore water in rock samples from Busted Butte (used in AMR as reference for pore-water composition)
LA9909WS831372.018 [140101]	6.13.1.11			Gravimetric moisture content of rock samples from Busted Butte (used in AMR as reference for pore-water composition)
LA9910WS831372.008 [147156]	6.13.2.1		6.13.2-1	Busted Butte UZTT: gravimetric moisture content and bromide concentration in selected Phase 1A rock samples
LA9912WS831372.001 [156586]	6.13.3.9			Sorption of fluorinated benzoic acids and lithium on rock samples form Busted Butte
MO0004GSC00167.000 [150300]		6.13.4-1 6.13.4-2		As-built coordinates of boreholes in the test alcove and running drift, Busted Butte test facility (BBTF)
LA0108TV1221313U.001 [161525]	6.13.6			Static batch sorption coefficients and retardation coefficients
GS990708314224.007 [164604]	Attach. VIII.6			Detailed line survey data for Busted Butte access drift and Busted Butte cross drift
LA0204SL831372.001 [164749]	Attach. VIII.7		VIII-1	Mineralogy of the Busted Butte Phase 2 test block
LA0207SL831372.001 [160824]			VIII-3	Lithostratigraphic classification of hydrological-property core-sampling depths, Busted Butte Phase 2 test block
GS990708312242.008 [109822]			VIII-3 VIII-6	Physical and hydraulic properties of core samples from Busted Butte boreholes
GS960808312231.004 [108985]			VIII-4	Physical properties, water content. and water potential for samples from lower depths in boreholes USW SD-7 and USW SD-12. Submitted: 08/30/96.
GS960808312231.005 [108995]			VIII-5	Saturated hydraulic conductivity of Busted Butte.
GS951108312231.009 [108984]			VIII-5	Physical properties, water content, and water potential for borehole USW SD-7. Submitted: 09/26/95.
GS990308312242.007 [107185]			VIII-6	Laboratory and centrifuge measurements of physical and hydraulic properties of core samples from Busted Butte boreholes

4.1.14 Data and Information of Geochemical Interpretations

4.1.14.1 Data Used to Support Geochemical Interpretations (Direct Input)

Table 4.1-14a. Data Used to Support Geochemical Interpretations (Direct Input)

Inputs	Used in			Description
	Section	Figure	Table	
GS020408312272.003 [160899]			6.14.1-1	Collection and analysis of pore-water samples for the period from April 2001 to February 2002. Water chemistry analyses for physical parameters; common anions and cations from 15 ECRB-SYS-Series boreholes, USW SD-9 and USW NRG-7/7A.
GS030408312272.002 [165226]			6.14.1-1	Analysis of water-quality samples for the period from July 2002 to November 2002. Water chemistry analyses for physical parameters; common anions and cations; and trace metals.
GS000308313211.001 [162015]	6.14.1.2 Attach. IX.5		6.14.1-2 6.14.1-3 6.14.1-4	Geochemistry of repository block—chemical composition of rock from ECRB Cross Drift
LAJF831222AQ98.004 [107364]		6.14.2-1	6.14.2-1	Chloride, bromide, sulfate, and chlorine-36 analyses of salts leached from ESF rock samples.
LAJF831222AQ98.009 [145650]		6.14.2-1		Chlorine-36 analyses of salts leached from ESF Niche 3566 (Niche 1) drillcore.
GS951208312272.002 [151649]			6.14.2-2	Tritium analyses of porewater from USW UZ-14, USW NRG-6, USW NRG-7A and UE-25 UZ#16 and of perched water from USW SD-7, USW SD-9, USW UZ-14 and USW NRG-7A from 12/09/92 to 5/15/95.
GS990183122410.001 [146125]			6.14.2-2	Tritium data from pore water from ESF borehole cores, 1997 analyses by USGS. Tritium abundance data from boreholes ESF-AL#3-RBT#1, ESF-AL#3-RBT#4, ESF-AL#4-RBT#1, ESF-NAD-GTB#1A, ESF-NDR-MF#1, ESF-SAD-GTB#1, ESF-SR-MOISTSTDY#1, ESF-SR-MOISTSTDY#2 and ESF-SR-MOISTSTDY#13, for the period 1/16/97 through 11/6/97.
GS990183122410.004 [146129]			6.14.2-2	Tritium data from pore water from ESF borehole cores, 1998 analyses by University of Miami. Tritium abundance data from boreholes ESF-NAD-GTB#1A, ESF-NDR-MF#1, ESF-SR-MOISTSTDY#1, ESF-SR-MOISTSTDY#2, ESF-SR-MOISTSTDY#4, ESF-SR-MOISTSTDY#5, ESF-SR-MOISTSTDY#6, ESF-SR-MOISTSTDY#7, ESF-SR-MOISTSTDY#13 and ESF-SR-MOISTSTDY#16, for the period 3/31/98 through 8/20/98.
GS020408312272.002 [162342]			6.14.2-2	Tritium abundance data from pore water in core samples from Yucca Mountain ESF boreholes for the period of 4/30/1998–3/21/2001
GS021208312272.005 [162934]			6.14.2-2	Tritium abundance data from pore-water in core samples from Yucca Mountain ESF ECRB. May 20, 2001 to July 23, 2002.

Table 4.1-14a. Data Used to Support Geochemical Interpretations (Direct Input, Continued)

Inputs	Used in			Description
	Section	Figure	Table	
GS030208312272.001 [162935]			6.14.2-2	Gas and water vapor chemistry data in Yucca Mountain ESF ECRB bulkheads
GS010808315215.003 [164844]		6.14.2-2 6.14.2-5		Fluid inclusion homogenization temperatures from the ESF, ECRB, and EWCD, 12/99 to 4/01
GS020908315215.003 [164846]		6.14.2-2 6.14.2-3 6.14.2-4 6.14.2-5		Fluid inclusion homogenization temperatures from ESF and ECRB calcite and fluorite samples, 10/01 to 5/02
GS970208315215.005 [107351]		6.14.2-3 6.14.2-4 6.14.2-5		Carbon and oxygen stable isotope kiel analyses of calcite from the ESF and USW G-1, G-2 AND G-4, UE-25 A#1, USW NRG-6 and NRG-7/7A, and UE-25 UZ#16, April 1996–January 1997
GS970808315215.010 [145920]		6.14.2-3 6.14.2-4 6.14.2-5		Carbon and oxygen stable isotope analyses of calcite from the ESF and USW G-1, G-2, AND G-3/GU-3, from 01/16/97 to 07/18/97
GS980908315213.002 [146088]		6.14.2-3 6.14.2-4 6.14.2-5		Carbon and oxygen stable isotopic compositions of Exploratory Studies Facility secondary calcite occurrences, 10/1/97 to 8/15/98
GS990908315213.001 [153379]		6.14.2-3 6.14.2-4 6.14.2-5		Stable carbon and oxygen isotope macro and micro analysis of calcite from the ESF between 2/96 and 5/99.
GS020908315215.004 [164847]		6.14.2-5		Stable carbon and oxygen isotope analyses of ESF/ECRB calcite and USW SD-6 and USW WT-24 whole rock; 1/1999–6/2002.
GS010808315215.004 [164850]		6.14.2-5		Uranium and lead concentrations, lead isotopic compositions, and U-Pb isotope ages for the ESF secondary minerals determined at the Royal Ontario Museum between April 20, 2000 and April 19, 2001
GS021008315215.005 [164848]		6.14.2-5		Uranium, thorium, and lead concentrations, lead isotopic compositions, U-Pb isotope ages and $^{234}U/^{238}U$ and $^{230}Th/^{238}U$ activity ratios for the ESF and ECRB secondary calcite, opal, chalcedony and fluorite determined at the Royal Ontario Museum between 11/16/01 and 4/7/02.
GS021208315215.008 [164851]		6.14.3-1 6.14.3-2 6.14.3-3	6.14.3-1	^{238}U-^{234}U-^{230}Th-^{232}Th isotope ratios and calculated ages for opal hemispheres from sample hd2074 (spc00506577) at Station 30+51 in the Exploratory Studies Facility determined using ion-probe mass spectrometry.

Table 4.1-14a. Data Used to Support Geochemical Interpretations (Direct Input, Continued)

Inputs	Used in			Description
	Section	Figure	Table	
GS021208315215.009 [164750]	Attach. IX.5	6.14.3-4 IX.5-1	6.14.3-2 IX.5-1	U abundances, ^{238}U-^{234}U-^{230}Th-^{232}Th activity ratios, and calculated $^{230}Th/U$ ages, and initial $^{234}U/^{238}U$ activity ratios determined for sequential *in situ* microdigestions of opal hemispheres from the ESF by thermal ionization mass spectrometry
GS021208312272.008 [164609]	6.14.3.2	6.14.3-5 6.14.3-6 6.14.3-7 6.14.3-8 6.14.3-9	6.14.3-3	Uranium and thorium concentrations and ^{234}U-^{230}Th-^{238}U-^{232}Th isotopic compositions from whole rock samples from the ECRB Cross Drift and ESF collected between December 5–6, 2001 and analyzed between February and June 2002.
GS020608315215.002 [162126]	6.14.1.2	6.14.4-1 6.14.4-8 6.14.4-9		Carbon dioxide abundances, carbon dioxide concentrations, and normative calcite concentrations for cuttings from borehole USW SD-6, USW WT-24, and ECRB Cross Drift boreholes, Area 25, Nevada Test Site, determined by carbon dioxide evolution between May 25, 2000 and September 8, 2000.
GS021008315215.007 [162127]	6.14.1.2	6.14.4-1 6.14.4-8		Carbon dioxide abundance, carbon dioxide concentration and normative calcite concentrations in 333 powdered cuttings samples from borehole USW WT-24 determined by CO_2 evolution between July 1998 and August 1999
GS980308315215.008 [107355]		6.14.4-2 6.14.4-3 6.14.4-4 6.14.4-5 6.14.4-7 6.14.4-10		Line survey information from the Exploratory Studies Facility obtained to estimate secondary mineral abundance.
GS030808315215.001 [165426]		6.14.3-5 6.14.4-3 6.14.4-9 6.14.4-10		Calcite and opal mineralization occurrences in lithophysal cavities, fractures, and breccia zones from the line survey in the east-west Cross Drift
GS030908315215.002 [166097]		6.14.4-1 6.14.4-8 6.14.4-9		XRF fluorescence elemental compositions determined on cuttings from USW SD-6 and USW WT-24

4.1.14.2 Information Used to Corroborate Geochemical Interpretations (For Reference)

Table 4.1-14b. Information Used to Corroborate Geochemical Interpretations (For Reference)

Inputs	Used in			Description
	Section	Figure	Table	
LA0002JF12213U.001 [154760]	6.14.1.1			Chemistry data for pore water extracted from drillcore from surfaced-based boreholes USW NRG-6, USW NRG-7A, USW UZ-7A, USW UZ-14, UE-25 UZ#16, USW UZ-N55, USW SD-6, USW SD-7, USW SD-9, and USW WT-24.
LA0002JF12213U.002 [156281]	6.14.1.1			Chemistry data for pore water extracted from ESF, Cross Drift, and Busted Butte drillcore.
LAJF831222AQ98.011 [145402]	6.14.1.1			Chloride, bromide, sulfate, and chlorine-36 analyses of springs, groundwater, perched water, and surface runoff.
LA9909JF831222.012 [122736]	6.14.1.1			Chloride, bromide, and sulfate analyses of porewater extracted from ESF Niche 3566 (Niche 1) and Niche 3650 (Niche 2) drillcore.
LL030408023121.027 [162949]			6.14.2-1	Cl concentrations and Cl ratios obtained from YM rock samples and analyzed by accelerator mass spectrometry and ion chromatography.
LL030605223121.030 [163827]		6.14.2-1	6.14.2-1	Chlorine concentrations and chlorine ratios obtained from YM rock samples and analyzed by accelerator mass spectrometry.
LA0305RR831222.001 [163422]			6.14.2-1	Chlorine-36 and Cl in salts leached from rock samples for the chloride-36 validation study
LA0307RR831222.001 [164091]			6.14.2-1	Chloride, bromide, sulfate, and chlorine-36 analyses of salts leached from Cross Drift samples in FY99 and FY00
LA0307RR831222.002 [164090]			6.14.2-1	Chloride, bromide, sulfate, and chlorine-36 analyses of salts leached from ESF ^{36}Cl validation drillcore samples in FY99
GS990408314224.001 [108396]		6.14.3-5		ESF, ECRB Cross Drift, detailed line survey data collected from stations 00+00.89 to 14+95.18
GS990408314224.002 [105625]		6.14.3-5		ESF, ECRB Cross Drift, detailed line survey data collected from stations 15+00.85 to 26+63.85
GS971108314224.020 [105561]		6.14.3-5 6.14.4-5 6.14.4-6		Revision 1 of detailed line survey data, Station 0+60 to Station 4+00, North Ramp starter tunnel, Exploratory Studies Facility
GS971108314224.021 [106007]		6.14.3-5 6.14.4-5 6.14.4-6		Revision 1 of detailed line survey data, Station 4+00 to Station 8+00, North Ramp, Exploratory Studies Facility
GS950508314224.003 [107488]		6.14.3-8		Provisional results: geotechnical data - full periphery map data from North Ramp of the Exploratory Studies Facility, Stations 0+60 to 4+00.

Table 4.1-14b. Information Used to Corroborate Geochemical Interpretations (For Reference, Continued)

Inputs	Used in			Description
	Section	Figure	Table	
GS960708314224.008 [105617]		6.14.4-6		Provisional results: geotechnical data for Station 30+00 to Station 35+00, Main Drift of the ESF. Detailed line survey data
GS000608314224.004 [152573]		6.14.4-6		Provisional results: geotechnical data for Station 35+00 to Station 40+00, Main Drift of the ESF.
GS960708314224.010 [106031]		6.14.4-6		Provisional results: geotechnical data for Station 40+00 to Station 45+00, Main Drift of the ESF. Detailed line survey data. VA supporting data.
GS960908314224.014 [106033]		6.14.4-5 6.14.4-6		Provisional results - ESF Main Drift, Station 50+00 to Station 55+00. Detailed line survey data
GS970208314224.003 [106048]		6.14.4-5 6.14.4-6		Geotechnical data for Station 60+00 to Station 65+00, South Ramp of the ESF. Provisional results; detailed line survey data.
GS971108314224.022 [106009]		6.14.4-5 6.14.4-6		Revision 1 of detailed line survey data, Station 8+00 to Station 10+00, North Ramp, Exploratory Studies Facility
GS971108314224.023 [106010]		6.14.4-5 6.14.4-6		Revision 1 of detailed line survey data, Station 10+00 to Station 18+00, North Ramp, Exploratory Studies Facility
GS971108314224.024 [106023]		6.14.4-5 6.14.4-6		Revision 1 of detailed line survey data, Station 18+00 to Station 26+00, North Ramp, Exploratory Studies Facility
GS971108314224.025 [106025]		6.14.4-5 6.14.4-6		Revision 1 of detailed line survey data, Station 26+00 to Station 30+00, North Ramp and Main Drift, Exploratory Studies Facility
GS971108314224.026 [106032]		6.14.4-5 6.14.4-6		Revision 1 of detailed line survey data, Station 45+00 to Station 50+00, Main Drift, Exploratory Studies Facility
GS971108314224.028 [106047]		6.14.4-5 6.14.4-6		Revision 1 of detailed line survey data, Station 55+00 to Station 60+00, Main Drift and South Ramp, Exploratory Studies Facility

4.2 CRITERIA

Technical requirements to be satisfied by performance assessment (PA) are based on 10 CFR 63.114 [156605] (*Requirements for Performance Assessment*) and identified in the Yucca Mountain *Project Requirements Document* (Canori and Leitner 2003 [161770]). The acceptance criteria that will be used by the Nuclear Regulatory Commission (NRC) to determine whether the technical requirements have been met are identified in the *Yucca Mountain Review Plan, Final Report* (YMRP; NRC 2003 [163274]). The pertinent requirements and acceptance criteria for this scientific analysis report are summarized in Table 4.2-1.

The only Acceptance Criteria for this scientific analysis report listed in Table 3-1 of the TWP (BSC 2003 [160819]) was Criterion 2 from Section 4.2.1.3.6.3 (*Flow Paths in the Unsaturated Zone*) of NRC (2003 [162418]). NRC (2003 [162418]) has since been superseded by NRC (2003 [163274], with Criterion 2 from Section 2.2.1.3.6). Additional appropriate criteria for this scientific analysis report are Criterion 3 from Section 2.2.1.3.6, Criteria 2 and 3 from Section 2.2.1.3.3.3 (*Quantity and Chemistry of Water Contacting Engineered Barriers and Waste Forms*), and Criteria 2 and 3 from Section 2.2.1.3.7.3 (*Radionuclide Transport in the UZ*) of NRC (2003 [163274]). These criteria are listed in Table 4.2-1. This change of acceptance criteria is one deviation from the TWP (BSC 2002 [160819]) listed in Section 1.4.

Table 4.2-1. Project Requirements and YMRP Acceptance Criteria Applicable to This Scientific Analysis Report

Requirement Number[a]	Requirement Title[a]	10 CFR 63 Link	YMRP Acceptance Criteria
PRD-002/T-015	Requirements for Performance Assessment	10 CFR 63.114(a-c) [156605]	Criteria 2 and 3 for *Quantity and Chemistry of Water Contacting Engineered Barriers and Waste Forms* [b] Criteria 2 and 3 for *Flow Path in the UZ*[c] *Criteria 2 and 3 for Radionuclide Transport in the UZ*[d]

NOTES: [a] from Canori and Leitner (2003 [161770])
[b] from NRC (2003 [163274], Section 2.2.1.3.3.3)
[c] from NRC (2003 [163274], Section 2.2.1.3.6.3)
[d] from NRC (2003 [163274], Section 2.2.1.3.7.3)

The acceptance criteria identified in Section 2.2.1.3.3.3 of the YMRP (NRC 2003 [163274]) are given below, followed by a short description of their applicability to this scientific analysis report.

- Acceptance Criterion 2, *Data Are Sufficient for Model Justification*:

The data on seepage into drifts are collected, described, interpreted, and synthesized.

- Acceptance Criterion 3, *Data Uncertainty Is Characterized and Propagated through Model Abstraction*:

The parameter values and distributions are developed based on Yucca Mountain data for cases of field measurements and laboratory experiments with sufficient data. The results of this report provide information which could be used by, and uncertainties propagated through, UZ process and abstraction models (for a complete list, see Section 7).

The summaries of measurement results are discussed in Section 6.

The acceptance criteria identified in Section 2.2.1.3.6.3 of the YMRP (NRC 2003 [163274]) are given below, followed by a short description of their applicability to this scientific analysis report.

- Acceptance Criterion 2, *Data Are Sufficient for Model Justification*:

The data on hydrology and geochemistry of the unsaturated zone are collected using acceptable techniques.

- Acceptance Criterion 3, *Data Uncertainty Is Characterized and Propagated through Model Abstraction*:

Uncertainties in the characteristics of the natural system are considered.

The summaries of measurement results are discussed in Section 6.

The acceptance criteria identified in Section 2.2.1.3.7.3 of the YMRP (NRC 2003 [163274]) is given below, followed by a short description of their applicability to this scientific analysis report.

- Acceptance Criterion 2, *Data Are Sufficient for Model Justification*:

Data on the transport in the UZ are collected using appropriate techniques.

- Acceptance Criterion 3, *Data Uncertainty Is Characterized and Propagated through Model Abstraction*:

Uncertainty is adequately represented in process evaluation.

The summaries of measurement results are discussed in Section 6.

YMRP criteria are further discussed in Section 7.

4.3 CODES AND STANDARDS

No specific formally established standards have been identified as applying to this analysis.

5. ASSUMPTIONS

This scientific analysis report on ambient field testing of processes presents data collected in underground drifts at Yucca Mountain and its vicinity. No assumptions of parameters were used to supplement the measured data. Discussions on issues related to analysis approximation are included in Section 6. Other than supportable approximations required to utilize various analytic formulas and established scientific methods, physical assumptions were unnecessary, because no predicted values or simulated information was presented.

INTENTIONALLY LEFT BLANK

6. SCIENTIFIC ANALYSIS DISCUSSION

This section describes the field-testing results pertaining to unsaturated zone (UZ) processes in underground drifts at Yucca Mountain and its vicinity. The field activities range from decimeter-scale drift-seepage tests above niches, to meter-scale, fracture-matrix-interaction tests above slots in alcoves, to decameter-scale flow and transport tests in test blocks or between drifts, and to kilometer-scale moisture-monitoring studies along drifts. Niches are room-size excavations, slots are excavations below test beds in alcove walls, and alcoves are side drifts along the ESF Main Loop and ECRB Cross Drift.

Specifically, this section contains data and analysis related to the following topics.

- Section 6.1 and Section 6.5 present the test-site characteristics of niches and alcoves from pneumatic air-permeability test results (with Section 6.1 on permeability profiles and Section 6.5 on crosshole connections).

- Section 6.2 shows that drift-seepage thresholds exist and that seepage threshold data can be interpreted using the capillary barrier theory. It also presents liquid-flow-path data for niche sites.

- Section 6.3 and Section 6.4 present laboratory-measurement results for tracer migration and matrix imbibition for welded tuff samples from the ESF (with Section 6.3 on tracer distribution in the field and Section 6.4 on tracer and fluid penetration into the rock matrix).

- Section 6.6 presents the results of two series of fracture-matrix interaction tests to quantify the partitioning of flux into fast and slow components.

- Section 6.7 presents the results for flow tests in the Paintbrush nonwelded tuff (PTn) test bed.

- Section 6.8 summarizes data collected on ambient water-potential distribution in niches.

- Section 6.9 summarizes observations on construction-water migration.

- Section 6.10 presents data collected on moisture monitoring and water analyses in open drifts under the influence of ventilation and in closed drifts behind bulkheads, including ECRB Cross Drift and Alcove 7.

- Section 6.11 presents the results from systematic hydrological characterization using slanted boreholes along the ECRB Cross Drift.

- Section 6.12 presents the results of drift-to-drift tests from liquid releases in Alcove 8 and wetting-front and seepage detection at Niche 3107 (Niche 3), and on available information of Alcove 1 infiltration tests.

- Section 6.13 presents the results of different phases of transport tests at Busted Butte.

- Section 6.14 summarizes geochemical and isotope data in pore water, rocks, and fracture in-fill minerals collected from test locations in different tuff units.

The tests performed in niches and alcoves along the ESF are illustrated in Figure 6-1. Seepage into drifts at the repository level is related to water percolating down from the ground surface. Drift seepage tests at niche sites quantify the seepage from liquid pulses released above the niches. Percolation flux has a fast fracture-flow component and a slow matrix-flow component. This partitioning of flow is evaluated at the fracture-matrix test bed in Alcove 6. The heterogeneous hydrogeologic setting (with alternating tuff layers) determines the percolation distribution throughout the UZ, with input from infiltration at the ground surface boundary. The mechanism of redistributing near-surface fracture flow by the porous PTn, especially the flow-damping process by the PTn unit, is studied in a test bed in Alcove 4. The PTn unit examined at Alcove 4 consists of layered, altered, and bedded tuffs transected by a fault. Wetter climate conditions increase the infiltration, as quantified in an artificial infiltration test in Alcove 1 and in moisture monitoring at depth in Alcove 7. The seepage threshold data from niches and from systematic hydrological characterization are inputs to the Model Report *Seepage Calibration Model and Seepage Testing Data (U0080)* (BSC 2003 [162267]).

Figure 6-1 lists major TSPA issues (DOE 1998 [100550]) related to UZ flow processes of seepage, percolation, and infiltration. The tests illustrated in Figure 6-1 focus on different issues to quantify the functional relationships among these processes. Seepage is smaller than the percolation flux because of capillarity-induced drift diversion (BSC 2003 [162267], Section 6), and percolation may be smaller than infiltration because of lateral diversion of percolating water along tuff interfaces to bounding faults (BSC 2001 [156609], Section 6.4.3). All tests use tracers to assist the characterization of plume migration.

Figure 6-2 illustrates the ECRB Cross Drift to ESF Main Drift seepage collection system to study the migration of water and tracer flow from one drift to another. The crossover point is located in the northern part of the ESF, as illustrated in Figure 6-2 and Figure 6.1.1-1. In 1998, the seepage monitoring system was used to monitor the migration of construction water from the ECRB Cross Drift. Niche 3107 (Niche 3), originally excavated and used for the drift seepage study, is currently part of the drift-to-drift study as a seepage collection site. The existing horizontal boreholes at Niche 3107 (Niche 3) are used for wetting-front monitoring for liquid released from Alcove 8, excavated from the ECRB Cross Drift and directly above Niche 3107 (Niche 3).

Since neither the ESF Main drift nor the ECRB Cross Drift reaches the Calico Hills hydrogeologic tuff unit (CHn) below the repository block, a dedicated drift complex was excavated at Busted Butte, 8 km southeast of Yucca Mountain, to evaluate flow and transport processes in vitric CHn. Early results were first reported in the AMR *Unsaturated Zone and Saturated Zone Transport Properties (U0100)* (CRWMS M&O 2001 [154024]). The different field-testing phases and recent updates are presented in Section 6.13.

Geochemical and isotope data have been collected from laboratory analyses of samples from various experiments in different test locations. These data have been used to refine the conceptual understanding of the site and for inputs to process models. Early results were reported in the AMR *Analysis of Geochemical Data for the Unsaturated Zone (U0085)* (BSC

2002 [160247]). The updates of geochemical and isotope data are presented in Section 6.14 on pore water and rock compositions; isotope geochemistry examination on chlorine-36 validation studies, tritium distributions, and fluid inclusions for thermal history; uranium isotope studies for UZ flow record and flow zone delineation; and fracture mineral distribution and mineralogy.

Each testing activity has unique findings to contribute to the assessment of unsaturated flow and transport processes at Yucca Mountain. The progress and analyses of field-test results are presented in the following fourteen subsections for fourteen testing activities. Key (and verifiable) scientific notebooks (with relevant page numbers) used for recording the ESF Field Testing activities and analyses described in this scientific analysis report are listed in Table 6-1.

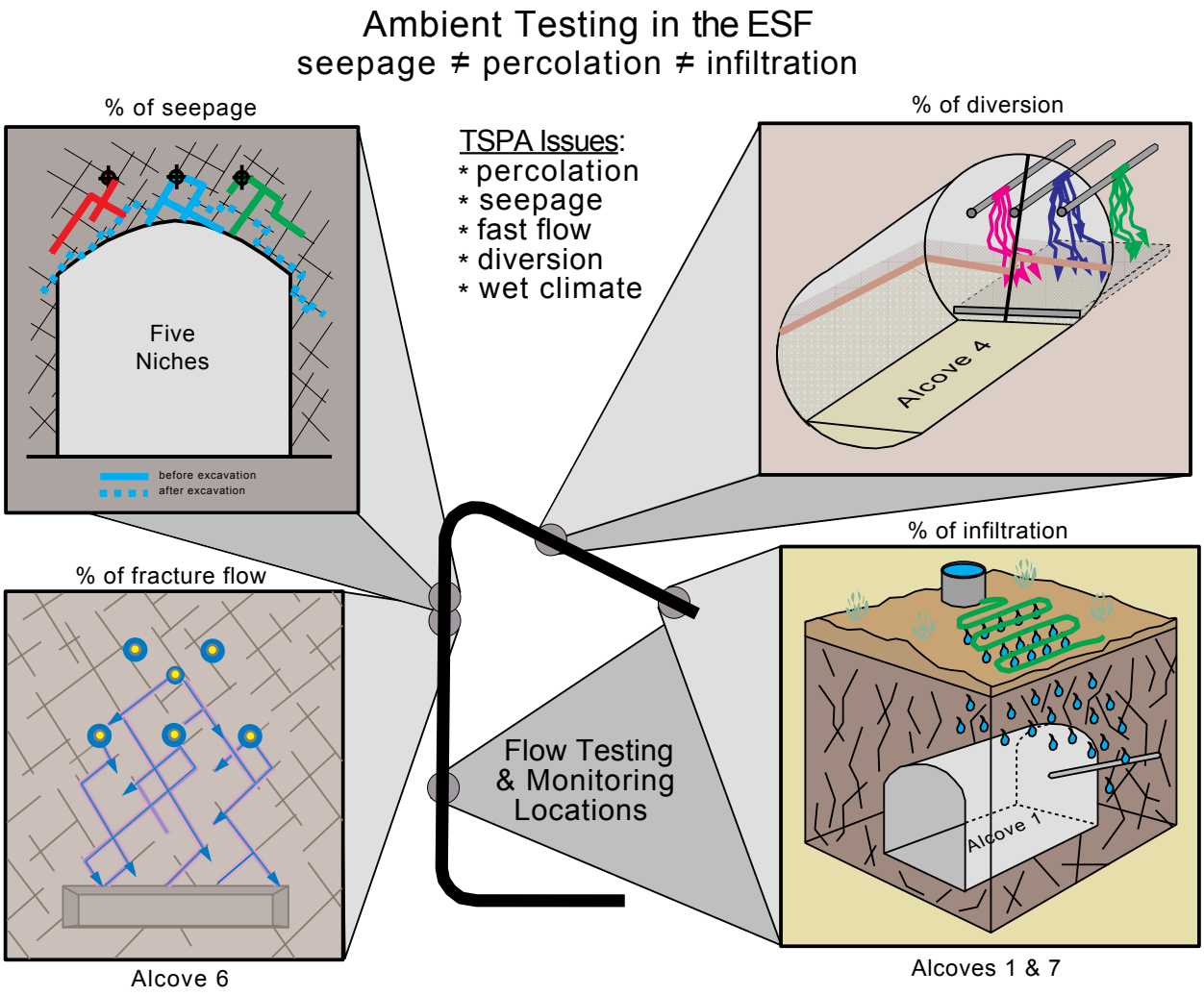

NOTE: The tests evaluate functional relationships between unsaturated zone processes to resolve TSPA issues.

Figure 6-1. Schematic Illustration of Flow Tests in the Exploratory Studies Facility at Yucca Mountain

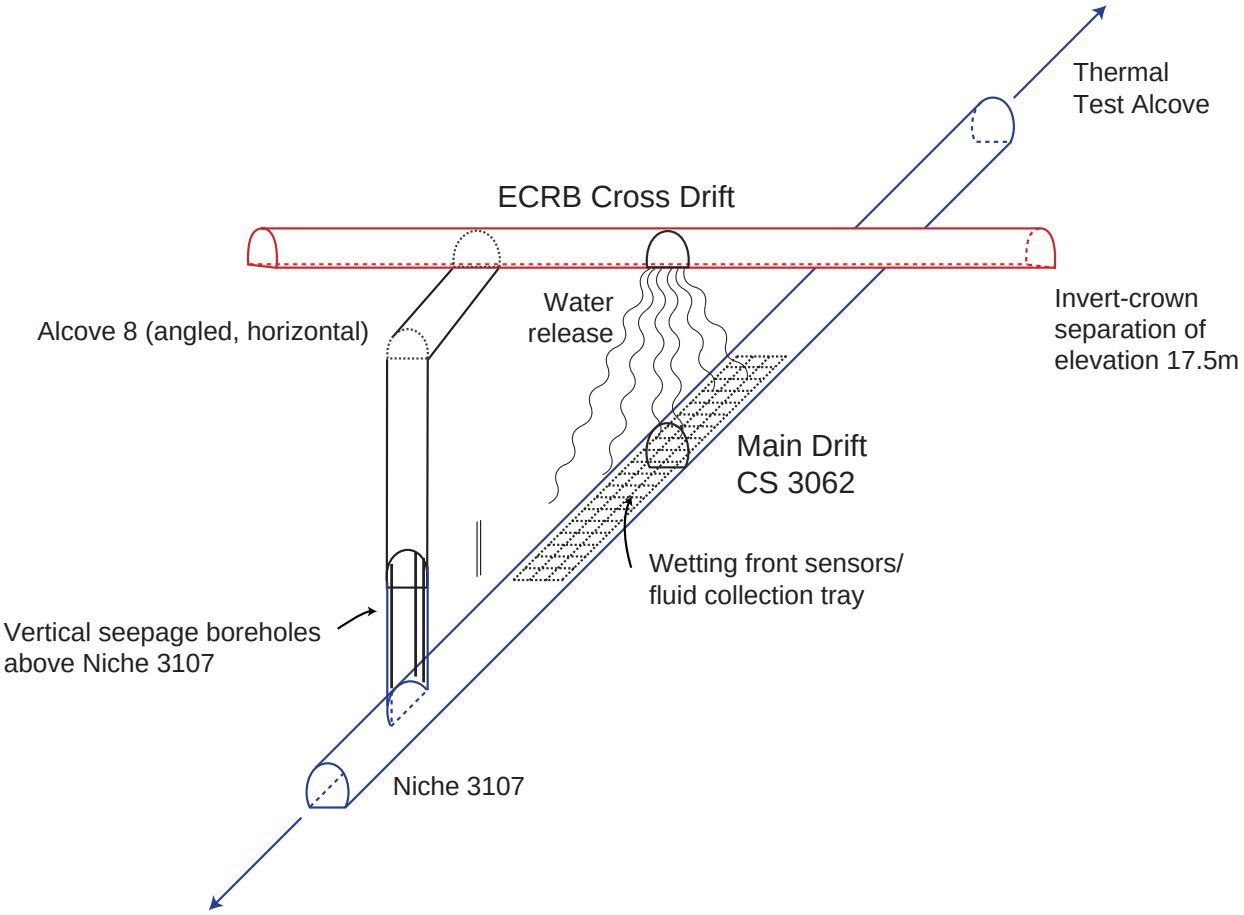

NOTE: Wetting-front sensors and fluid collection trays monitored the construction-water migration. Both the ECRB Cross Drift and the Main Drift, together with Alcove 8 and Niche 3107 and its boreholes, are horizontal in this illustration. Alcove 8 is directly above Niche 3107.

Figure 6-2. Schematic Illustration of the Cross-Over Point of ECRB Cross Drift with the Main Drift

Table 6-1. Scientific Notebooks*

M&O Scientific Notebook ID	Lab Scientific Notebook ID	Cited Pages or Page Range of Scientific Notebook	Relevant AMR Sections	Citation
SN-LBNL-SCI-065-V1	YMP-LBNL-JSW-6	1–158	6.1 (air-K), 6.2 (seepage)	Wang 1997 [156530]
SN-LBNL-SCI-066-V1	YMP-LBNL-JSW-6A	1–159	6.1 (air-K), 6.2 (seepage)	Wang 1997 [156534]
SN-LBNL-SCI-121-V1	YMP-LBNL-JSW-6B	1–159	6.1 (air-K), 6.2 (seepage)	Wang 1999 [156538]
SN-LBNL-SCI-122-V1	YMP-LBNL-JSW-6C	1–159	6.1 (air-K), 6.2 (seepage)	Wang 1999 [153449]
SN-LBNL-SCI-078-V1	YMP-LBNL-JSW-PJC-6.2	1–110, 115–125, 133–135, 144–146, 149–157	6.1 (air-K), 6.5 (cross-hole)	Cook 2001 [156902]
SN-LBNL-SCI-113-V1	YMP-LBNL-RCT-1	62–73, 80–157	6.2 (seepage)	Trautz 1999 [156563]
SN-LBNL-SCI-156-V1	YMP-LBNL-RCT-2	27–160	6.2 (seepage)	Trautz 2001 [156903]
SN-LBNL-SCI-177-V1	YMP-LBNL-RCT-3	4-94	6.2 (seepage)	Trautz 2001 [157022]
SN-LBNL-SCI-177-V2	YMP-LBNL-RCT-4	88–91, 116–117, 120, 130–159, 190–195, 198–221, 298–299	6.2-Attach III.4 (seepage)	Trautz 2001 [161208]
SN-LBNL-SCI- 221-V1	YMP-LBNL-RCT-5	154-160, 162-234, 239-301	6.2-Attach III.4 (seepage)	Trautz 2003 [166248]
SN-LBNL-SCI- 221-V2	YMP-LBNL-RCT-6	14–67	6.2-Attach III.4 (seepage)	Wang 2003 [165376]
SN-LBNL-SCI-089-V1	YMP-LBNL-JSW-QH-1	1–153	6.3 (tracer migration), 6.4 (imbibition)	Hu 1999 [156539]
SN-LBNL-SCI-090-V1	YMP-LBNL-JSW-QH-1A	20–22, 37–48, 54, 68–82, 86–99, 103–126	6.3 (tracer migration), 6.4 (imbibition)	Hu 1999 [156540]
SN-LBNL-SCI-091-V1	YMP-LBNL-JSW-QH-1B	9, 27, 35, 40, 42, 48–73, 77, 81–94, 107–110, 115, 118–119, 123–142, 149, 154–155	6.3 (tracer migration), 6.4 (imbibition)	Hu 1999 [156541]
SN-LBNL-SCI-092-V1	YMP-LBNL-JSW-QH-1C	13, 16–25, 39–41, 51–102, 105–112, 116, 128–133, 139–140, 143–145	6.3 (tracer migration), 6.4 (imbibition)	Hu 1999 [156542]
SN-LBNL-SCI-093-V1	YMP-LBNL-JSW-QH-1D	3–153	6.3 (tracer migration), 6.4 (imbibition)	Hu 1999 [155691]
SN-LBNL-SCI-154-V1	YMP-LBNL-JSW-QH-1E	130-136, 145-146	6.3 (tracer migration), 6.4 (imbibition)	Hu 2000 [156473]

Table 6-1. Scientific Notebooks* (Continued)

M&O Scientific Notebook ID	Lab Scientific Notebook ID	Cited Pages or Page Range of Scientific Notebook	Relevant AMR Sections	Citation
SN-LBNL-SCI-102-V1	YMP-LBNL-JSW-RS-1	1–117	6.6 (fracture-matrix interaction Alcove 6)	Salve 1999 [155692]
SN-LBNL-SCI-104-V1	YMP-LBNL-JSW-RS-1A	1–39	6.6 (fracture-matrix interaction Alcove 6)	Salve 1999 [156547]
SN-LBNL-SCI-105-V1	YMP-LBNL-JSW-RS-2	1–7, 8-127	6.6 (fracture-matrix interaction Alcove 6) 6.7 (PTn Alcove 4)	Salve 2000 [156548]
SN-LBNL-SCI-042-V1	YMP-LBNL-JSW-CMO-1	1–15, 18, 22, 45–-54	6.7 (PTn Alcove 4)	Oldenburg 2000 [156558]
SN-LBNL-SCI-088-V1	YMP-LBNL-JSW-JJH-1	1–71	6.7 (PTn Alcove 4)	Hinds 2000 [156557]
SN-LBNL-SCI-048-VI	YMP-LBNL-JW-1.2	103–152	6.8 (water potential) 6.9 (construction water migration)	Salve 1999 [156552]
SN-LBNL-SCI-133-V1	YMP-LBNL-JW-1.2A	1–43	6.8 (water potential) 6.9 (construction water migration)	Salve 1999 [156555]
SN-LBNL-SCI-116-V1	YMP-LBNL-JSW-4.3	1–24, 61–67, 74–81	6.10 (ESF moisture)	Wang 2000 [156559]
SN-LBNL-SCI-150-V1	YMP-LBNL-JSW-JS-1	18, 148	6.10 (ECRB moisture)	Stepek 2000 [156561]
SN-LBNL-SCI-182-V1	YMP-LBNL-JSW-RS-4	1–147	6.10.1 (ECRB moisture)	Salve 2002 [165378]
SN-LBNL-SCI-182-V2	YMP-LBNL-JSW-RS-6	1–59	6.10.1 (ECRB moisture)	Wang 2003 [165376]
SN-USGS-SCI-110-V1	N/A	1–99	6.10 (Niche Moisture)	Guertal 2000 [165384]
SN-USGS-SCI-128-V1	N/A	1–301	6.10.1 (ECRB moisture)	Hudson 2002 [165391]
SN-USGS-SCI-128-V2	N/A	1–297	6.10.1 (ECRB moisture)	Hudson 2002 [165392]
SN-USGS-SCI-128-V3	N/A	1–141	6.10.4 (Alcove 7)	Hudson 2003 [165273]
SN-USGS-SCI-133-V1	N/A	1–157	6.10.1 (ECRB moisture)	Hudson 2002 [163398]
SN-USGS-SCI-133-V2	N/A	1–147	6.10.1 (ECRB moisture)	Hudson 2003 [165393]
SN-LBNL-SCI-179-V1	YMP-LBNL-JSW-YWT-1	1–44	6.11 (ECRB systematic)	Tsang and Wang 2000 [165375]
SN-LBNL-SCI-179-V2	YMP-LBNL-JSW-YWT-2	8–48, 72–73, 98–99, 114–129	6.11 (ECRB systematic)	Wang 2003 [165376]
SN-LBNL-SCI-216-V1	YMP-LBNL-JSW-PJC-6.3	7–19, 22–27, 46, 58–60, 70–76	6.11 (ECRB systematic)	Wang 2003 [165376]

Table 6-1. Scientific Notebooks* (Continued)

M&O Scientific Notebook ID	Lab Scientific Notebook ID	Cited Pages or Page Range of Scientific Notebook	Relevant AMR Sections	Citation
SN-LBNL-SCI-181-V1	YMP-LBNL-JSW-RS-5	1–156	6.12 (Alcove 8-Niche 3107 [Niche 3])	Salve 2003 [165377]
SN-LBNL-SCI-181-V2	YMP-LBNL-JSW-RS-5.1	1–24	6.12 (Alcove 8-Niche 3107 [Niche 3])	Wang 2003 [165376]
SN-USGS-SCI-120-V1	N/A	1–172	6.12 (Alcove 8-Niche 3107 [Niche 3])	Hudson 2002 [165385]
SN-USGS-SCI-120-V2	N/A	1–182	6.12 (Alcove 8-Niche 3107 [Niche 3])	Hudson 2002 [165386]
SN-USGS-SCI-120-V3	N/A	1–179	6.12 (Alcove 8-Niche 3107 [Niche 3])	Hudson 2002 [165387]
SN-USGS-SCI-120-V4	N/A	1–190	6.12 (Alcove 8-Niche 3107 [Niche 3])	Hudson and Guertal 2002 [165388]
SN-USGS-SCI-120-V5	N/A	1–157	6.12 (Alcove 8-Niche 3107 [Niche 3])	Hudson 2002 [166103]
SN-USGS-SCI-120-V6	N/A	1–147	6.12 (Alcove 8-Niche 3107 [Niche 3])	Hudson 2002 [165389]
SN-USGS-SCI-120-V7	N/A	1–148	6.12 (Alcove 8-Niche 3107 [Niche 3])	Hudson 2003 [165390]
SN-USGS-SCI-108-V1	N/A	1-98	6.12.5 (Alcove 1)	Guertal 2001 [164070]
SN-LANL-SCI-038-V1	LA-EES-1-NBK-99-005	1–161	6.13 (sample analyses)	Bussod 2001 [165281]
SN-LANL-SCI-039-V1	LA-EES-5-NBK-98-020	1–161	6.13 (UZTT)	Bussod 1999 [146978]
SN-LANL-SCI-040-V1	LA-EES-5-NBK-98-010	1–156	6.13 (UZTT)	Bussod 1998 [149129]
SN-LANL-SCI-041-V1	LA-EES-5-NBK-98-011	1– 38	6.13.2 (UZTT injection)	Soll et al. 2001 [165296]
SN-LANL-SCI-042-V1	LA-EES-5-NBK-98-012	1–130	6.13.3 (UZTT injection)	Dunn 2001 [165297]
SN-LANL-SCI-043-V1	LA-EES-5-NBK-98-013	1–26	6.13.5 (UZTT air-K)	Bussod and Stockton 1999 [165324]
SN-LANL-SCI-044-V1	LA-EES-5-NBK-98-014	1–11	6.13.5 (UZTT air-K)	Wyckoff 1999 [165298]
SN-LANL-SCI-046-V1	LA-EES-5-NBK-98-016	1–44	6.13.5 (UZTT air-K)	Lowry 2001 [164632]

Table 6-1. Scientific Notebooks* (Continued)

M&O Scientific Notebook ID	Lab Scientific Notebook ID	Cited Pages or Page Range of Scientific Notebook	Relevant AMR Sections	Citation
SN-LANL-SCI-106-V1	LA-EES-5-NBK-99-003	1–120	6.13 (UZTT)	Soll and Bussod 2001 [165299]
SN-LANL-SCI-127-V1	LA-CST-NBK-99-002	1–7	6.13.1 (tracers)	Bussod and Turin 2000 [165300]
SN-LANL-SCI-133-V1	LA-CST-NBK-98-018	1–7	6.13.3 (tracer analyses)	Bussod and Wolfsberg 2000 [165301]
SN-LANL-SCI-136-V1	LA-CST-NBK-98-017	1–7	6.13.3 (tracer analyses)	Bussod and Wolfsberg 2000 [165303]
SN-LANL-SCI-145-V1	LA-CST-NBK-98-001	1–159	6.13.1 (tracers)	Bussod et al. 2000 [165305]
SN-LANL-SCI-159-V1	LA-CST-NBK-98-002	1–9	6.13.3 (tracer analyses)	Bussod and Wolfsberg 2000 [165306]
SN-LANL-SCI-160-V1	LA-CST-NBK-98-012	1–7	6.13.3 (tracer analyses)	Bussod and Wolfsberg 2000 [165308]
SN-LANL-SCI-161-V1	LA-CST-NBK-98-015	1–7	6.13.2, 6.13.3 (tracer analyses)	Bussod and Wolfsberg 2000 [165310]
SN-LANL-SCI-163-V1	LA-CST-NBK-98-016	1–10	6.13.2, 6.13.3 (tracer analyses)	Bussod and Wolfsberg 2000 [165311]
SN-LANL-SCI-169-V1	LA-CST-NBK-98-009	1–7	6.13.2, 6.13.3 (tracer analyses)	Bussod and Wolfsberg 2000 [165312]
SN-LANL-SCI-184-V1	N/A	1–6	6.13.2, 6.13.3 (tracer analyses)	Soll and Wolfsberg 2000 [165313]
SN-LANL-SCI-188-V1	N/A	1–7	6.13.2, 6.13.3 (tracer analyses)	Soll and Wolfsberg 2000 [165316]
SN-LANL-SCI-191-V1	LA-CST-NBK-99-004	1–10	6.13.2 (sorption)	Bussod et al. 2000 [165317]
SN-LANL-SCI-192-V1	LA-CST-NBK-99-003	1–8	6.13.2, 6.13.3 (tracer analyses)	Bussod and Wolfsberg 2000 [165319]
SN-LANL-SCI-193-V1	N/A	1–8	6.13.3 (tracer analyses)	Soll and Wolfsberg 2000 [165320]
SN-LANL-SCI-199-V1	LA-CST-NBK-98-004	1–810	6.13 (pad collection)	Bussod and Turin 2001 [165321]
SN-LANL-SCI-205-V1	N/A	1–56, photos 1–31	6.13.6 (BBTF block)	Drew 1999 [166105]
SN-LANL-SCI-206-V1	N/A	86326–86406	6.13.6 (BBTF block)	Drew 2001 [165323]
SN-LANL-SCI-206-V2	N/A	99176–99254	6.13.6 (BBTF block)	Drew 2001 [165325]
SN-LANL-SCI-206-V3	N/A	99326–99405	6.13.6 (BBTF block)	Drew 2002 [165326]
SN-LANL-SCI-206-V4	N/A	99551–99630	6.13.6 (BBTF block)	Drew 2002 [165328]
SN-LANL-SCI-206-V5	N/A	99701–99779	6.13.6 (BBTF block)	Drew 2002 [165330]
SN-LANL-SCI-206-V6	N/A	92851–92930	6.13.6 (BBTF block)	Drew 2002 [165333]

Table 6-1. Scientific Notebooks* (Continued)

M&O Scientific Notebook ID	Lab Scientific Notebook ID	Cited Pages or Page Range of Scientific Notebook	Relevant AMR Sections	Citation
SN-LANL-SCI-206-V7	N/A	100226–100303	6.13.6 (BBTF block)	Drew 2003 [165335]
SN-LANL-SCI-207-V1	N/A	83101–83181	6.13.6 (BBTF block)	Drew 2001 [165336]
SN-LANL-SCI-207-V2	N/A	83326–83406	6.13.6 (BBTF block)	Drew 2001 [165348]
SN-LANL-SCI-207-V3	N/A	83476–83556	6.13.6 (BBTF block)	Drew 2001 [165349]
SN-LANL-SCI-207-V4	N/A	97976–98055	6.13.6 (BBTF block)	Drew 2001 [165350]
SN-LANL-SCI-207-V5	N/A	98051–98130	6.13.6 (BBTF block)	Drew 2001 [165351]
SN-LANL-SCI-207-V6	N/A	98126–98205	6.13.6 (BBTF block)	Drew 2001 [165352]
SN-LANL-SCI-207-V7	N/A	99251–99329	6.13.6 (BBTF block)	Drew 2001 [165354]
SN-LANL-SCI-207-V8	N/A	99401–99480	6.13.6 (BBTF block)	Drew 2002 [165356]
SN-LANL-SCI-207-V9	N/A	99626–99705	6.13.6 (BBTF block)	Drew 2002 [165358]
SN-LANL-SCI-207-V10	N/A	99776–99854	6.13.6 (BBTF block)	Drew 2002 [165338]
SN-LANL-SCI-207-V11	N/A	92776–92855 6.13.6	(BBTF block)	Drew 2002 [165340]
SN-LANL-SCI-207-V12	N/A	100151–100229	6.13.6 (BBTF block)	Drew 2002 [165344]
SN-LANL-SCI-207-V13	N/A	100451–100528	6.13.6 (BBTF block)	Drew 2003 [165346]
SN-LANL-SCI-208-V1	N/A	91276–91356	6.13.6 (BBTF block)	Drew 2001 [165360]
SN-LANL-SCI-208-V2	N/A	86701–86780	6.13.6 (BBTF block)	Drew 2001 [165361]
SN-LANL-SCI-208-V3	N/A	99476–99542	6.13.6 (BBTF block)	Drew 2002 [165362]
SN-LANL-SCI-220-V1	LA-EES-1-NBK-94-002	1–101	6.13.1, Attach VIII (CHn mineralogy)	Levy 2001 [165363]
SN-LANL-SCI-228-V1	LA-EES-5-NBK-98-019	1–4	6.13.2 (injection)	Bussod and Wolfsberg 2000 [165364]
SN-LANL-SCI-232-V1	N/A	1–9	6.13.3 (tracer analyses)	Soll and Wolfsberg 2000 [165365]
SN-LANL-SCI-239-V1	N/A	1–103, 290–291	6.13.3 (tracer analyses)	Soll et al. 2002 [165366]
SN-LANL-SCI-241-V1	N/A	1–90	6.13.3 (tracer analyses)	Soll and Wolfsberg 2002 [165367]
SN-LANL-SCI-252-V1	N/A	1–77	6.13.3 (overcore)	Turin 2001 [165368]
SN-LANL-SCI-253-V1	N/A	1–168	6.13.2, 6.13.3 (tracer analyses)	Haga 2001 [165369]
SN-LANL-SCI-256-V1	N/A	1–75	6.13.1, Attach VIII (CHn mineralogy)	Levy 2002 [165370]
SN-LANL-SCI-257-V1	N/A	1	6.13.3	Soll 2001 [165371]

Table 6-1. Scientific Notebooks* (Continued)

M&O Scientific Notebook ID	Lab Scientific Notebook ID	Cited Pages or Page Range of Scientific Notebook	Relevant AMR Sections	Citation
SN-LANL-SCI-261-V1	N/A	1–53	6.13.1, Attach VIII (CHn mineralogy)	Soll and Aldrich 2002 [165372]
SN-LBNL-SCI-119-V1	YMP-LBNL-ELM-KHW-1	1–48	6.13.4 (ground penetrating radar)	Williams 2000 [165373]
SN-LBNL-SCI-119-V2	YMP-LBNL-ELM-KHW-2	1–32	6.13.4 (ground penetrating radar)	Williams 2002 [165374]
SN-LBNL-SCI-193-V1	YMP-LBNL-ELM-JP-1	1–25	6.13.4 (ground penetrating radar)	Peterson 2002 [165379]
SN-LLNL-SCI-421-V1	N/A	1–155	6.13.4 (electrical resistance tomography)	Daily and Buettner 2002 [165380]
SN-USGS-SCI-117-V1	N/A	1–75	6.13.1, Attach VIII (hydrological properties)	Flint 2001 [165381]
SN-USGS-SCI-117-V2	N/A	1–98	6.13.1, Attach VIII (hydrological properties)	Flint 2001 [165382]
SN-USGS-SCI-117-V3	N/A	1–73	6.13.1, Attach VIII (hydrological properties)	Flint et al. 2002 [165383]

* Note: The list of scientific notebooks is sorted first by different tests (represented by the subsection number to the second heading in the fourth column), and then by the scientific notebook IDs (listed in the first column). The listed scientific notebooks contain relevant and corroborating information for testing activities discussed in Section 6. Some scientific notebooks have test pages specified, while others have the whole notebook ranges listed. In addition to data collection, the scientific notebooks in general contain information about test configuration, test design, equipment set-up, sensor calibration, review records, and other test-related information. While data analyses are mostly developed from information in the scientific notebooks, data interpretations are supplemented by open literature surveys and professional exchanges, with the results documented in publications and in the scientific analysis report. Some investigators use technical procedures instead of scientific notebooks in data collections. The technical procedures, together with other information such as test-site configurations and sensor accuracies, are in site-investigation test plans and field work packages governing the testing activities, documented in the UZ TWP (BSC 2002 [160819]).

Alternative scientific approaches and technical methods are evaluated in Section 6. For example, analytic solutions are use to analyze seepage data instead of numerical models, in Section 6.2; psychrometer data are compared with electrical resistivity probe data in Section 6.9; and ion-microprobe results are compared with microdigestion results in Section 6.14. These comparisons are presented for rationales in selection of different methods by the readers of this report. No other identifiable methods are evaluated or used.

Variability and uncertainty are also evaluated in Section 6. The variability and uncertainty, as described in BSC (2002 [158794], Section 4.1), are:

> *Variability*, also referred to as aleatory uncertainty, arises due to natural randomness or heterogeneity. This first type of uncertainty cannot be reduced through further testing and data collection; it can only be better characterized. Thus, this first type of uncertainty is also referred to as irreducible uncertainty. It is typically accounted for using geostatistical approaches, e.g., using appropriate probability distribution functions.
>
> *Uncertainty*, also referred to as epistemic uncertainty, arises from lack of knowledge about a parameter because the data are limited or there are alternative interpretations of the available data. This second type of uncertainty can be reduced because the state of knowledge can be improved by further testing or data collection. As a consequence, this second type of uncertainty is also referred to as reducible uncertainty.

The term *variability* is used for aleatory uncertainty, and the term *uncertainty* is used for *epistemic* uncertainty.

Uncertainty may have different sources depending on how the parameter in question is derived (e.g., whether derived from measurements, analyses, or models), as follows:

> *Measurement uncertainty* refers to the exactness of the actual measurement method and related data processing.
>
> *Spatial variability uncertainty* refers to the uncertainty in parameters describing the spatial variability of data, typically arising from the limited number of samples.
>
> *Conceptual model uncertainty* arises when the most appropriate conceptual model for a system is uncertain.
>
> *Estimation uncertainty* arises if the resulting parameter is estimated from a random process (e.g., from noisy data or from a Monte Carlo analysis), giving a range of possible results.

This scientific analysis report focuses on spatial variability uncertainty of data collected from testing of processes.

The softwares are used for graphic display of data and for simple calculations as documented in Attachment IX. Once the results are acceptable, no other software are needed to be considered.

INTENTIONALLY LEFT BLANK

6.1 AIR-PERMEABILITY DISTRIBUTIONS AND EXCAVATION-INDUCED ENHANCEMENTS

Pneumatic air-permeability tests were undertaken at various locations in the ESF to characterize the potential fluid flow paths in the rock. The repository host rock consists predominantly of unsaturated, fractured welded tuff. Airflow occurs mainly through the fractures. Therefore, air-permeability tests efficiently characterize fractured systems and may be utilized to study fracture heterogeneity. Once the air injections stop, the pressure field returns to ambient conditions within minutes, under most field-test conditions.

To determine fracture location within boreholes at the test sites, packer assemblies were installed along boreholes to isolate intervals in clusters of boreholes drilled into the fractured rock to perform pneumatic testing. In these tests, air is injected into specific intervals at constant mass flux while pressure responses are monitored in other intervals. The specific objectives for pneumatic testing include:

- Profiling the air permeability of boreholes along their length.
- Investigating the effects of nearby excavation on the permeability of a rock mass.
- Enabling a site-to-site comparison of air-permeability statistics and related scale effects.

Two basic types of data are readily available from pneumatic testing and are used to satisfy these testing objectives: (1) single-borehole air-permeability profiles, which are used for borehole-to-borehole and site-to-site comparisons, and (2) crosshole pressure-response data, which enable a determination of connectivity (through fracture networks) between locations at a given site. This section focuses on the permeability profiles for boreholes in niche and alcove sites. Permeability profiles before niche excavation are compared with profiles measured after niche and alcove excavation. In addition, factors such as borehole orientation and host rock type are considered. Section 6.5 focuses on crosshole data analyses.

6.1.1 Niche Test Site and Borehole Configuration

Extensive air-permeability measurements have been made in borehole clusters at five niches and at three alcoves within the ESF tunnel, as part of a program to select locations for liquid-release tests. The air permeability along each borehole in a cluster serves as a guide to the selection of the liquid-release intervals.

6.1.1.1 Site Selection

Various niche and alcove sites were selected for study, based on fracture and hydrological data collected in the ESF, as illustrated in Figure 6.1.1-1. Four niches were excavated along the Main Drift of the ESF and a fifth in the ECRB Cross Drift. The first niche site is located at Construction Station (CS) 35+66 (hereafter referred to as Niche 3566 [Niche 1], located at 3,566 m from the ESF north portal), in a brecciated zone between the Sundance fault and a cooling joint, where a preferential flow path is believed to be present (based on elevated $^{36}Cl/Cl$ ratios described in BSC 2001 [154874], the report on geochemistry data). Niche 3566 (Niche 1) was

sealed with a bulkhead to conduct long-term monitoring of *in situ* conditions. The second niche site is located at CS 36+50 (Niche 3650 [Niche 2]) in a competent rock mass with lower fracture density than Niche 3566 (Niche 1). The third niche is located at CS 31+07 (Niche 3107 [Niche 3]) in close proximity to the crossover point located at CS 30+62. A test alcove (Alcove 8) has been excavated from the ECRB Cross Drift to a position immediately above Niche 3107 (Niche 3), so that a large-scale drift-to-drift test can be conducted at this location. The fourth niche site is located at CS 47+88 (Niche 4788 [Niche 4]) in a 950 m long exposure of the middle nonlithophysal zone, referred to by Buesch and Spengler (1998 [101433], p. 19) as the intensely fractured zone. The fifth niche is located at ECRB Cross Drift CS 16+20 (Niche CD 1620 [Niche 5]) near the center of the repository block. The first four niches described above were excavated on the west side of the ESF Main Drift within the middle nonlithophysal zone (Tptpmn) of the Topopah Spring welded tuff unit (TSw). The fifth niche in the ECRB Cross Drift is excavated in the lower lithophysal zone (Tptpll) of TSw, which is the tuff unit where most of the repository emplacement drifts are planned to be located. Alcove 8 is excavated in the upper lithophysal zone (Tptpul) of the ECRB Cross Drift.

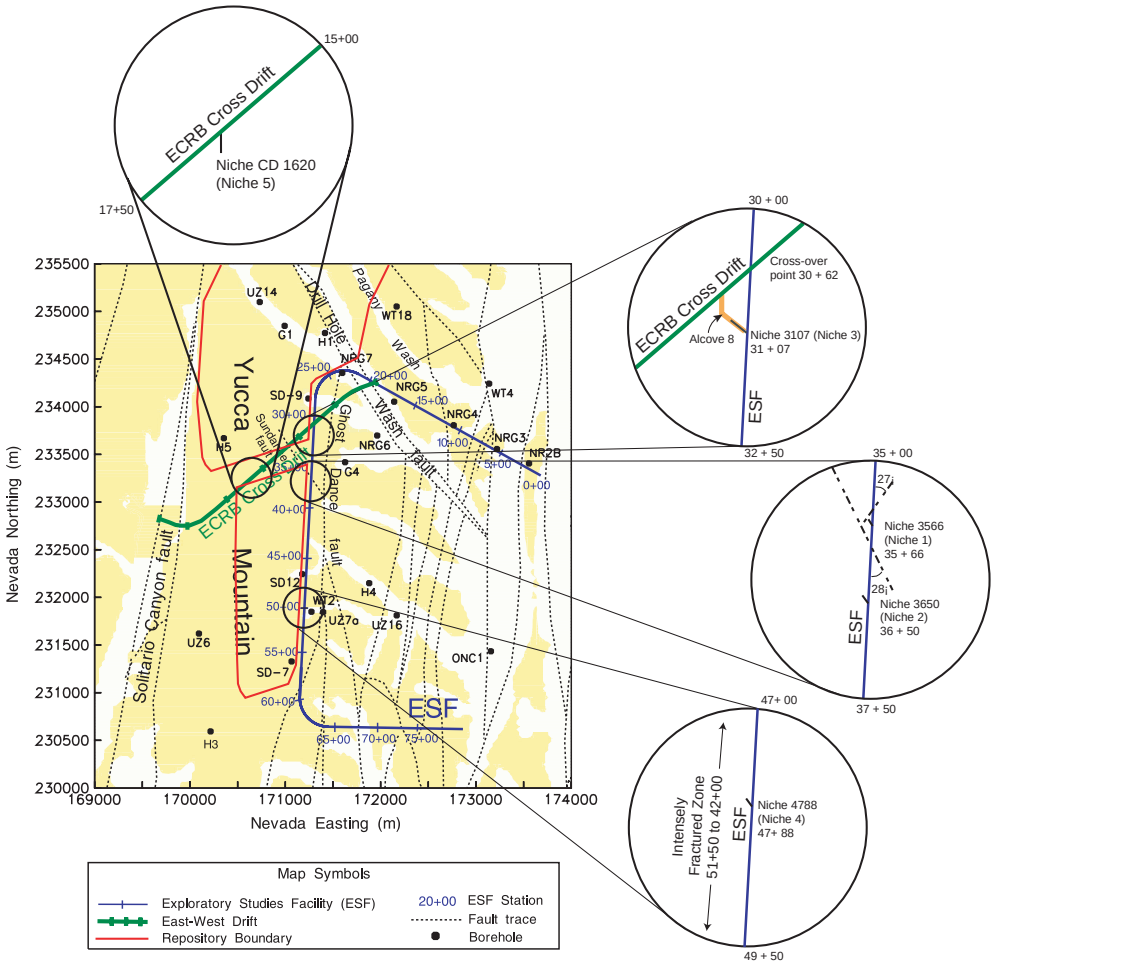

Repository Layout is from BSC (2003 [161726])

Figure 6.1.1-1. Schematic Illustration of Location Map for Niche 3107 (Niche 3), Niche 3566 (Niche 1), Niche 3650 (Niche 2), Niche 4788 (Niche 4) and Niche CD 1620 (Niche 5)

6.1.1.2 Borehole Configuration

Prior to niche excavation, three boreholes were drilled at Niche 3566 (Niche 1), and seven boreholes per niche were drilled at Niche 3650 (Niche 2), Niche 3107 (Niche 3), and Niche 4788 (Niche 4). Boreholes were drilled before excavation into both the rock to be excavated and the surrounding rock to gain access to the testing and monitoring area. Figure 6.1.1-2 shows the schematics of borehole clusters tested at the first four niche sites. Both types of boreholes were tested before niche excavation, and the surrounding boreholes were retested after excavation, allowing a study of excavation effects on the permeability of the surrounding rock. All boreholes shown in Figure 6.1.1-2 are parallel to the niche axis, as illustrated in Figure 6.1.1-3.

Three boreholes were originally drilled at Niche 3566 (Niche 1) along the same vertical plane coincident with the center of the niche (Figure 6.1.1-2a and Figure 6.1.1-3a).[1] The three boreholes were assigned the designation U, M, and B, corresponding to the upper, middle, and bottom borehole, respectively. Borehole M and borehole B were subsequently removed when the rock was mined out to create the niche, and borehole U still remains.

Figure 6.1.1-2b and Figure 6.1.1-3b show the location of the seven boreholes drilled at Niche 3650 (Niche 2). Three of the boreholes, designated UL, UM, and UR (upper left, upper middle, and upper right), were drilled approximately one meter apart and 0.65 m above the crown of the niche in the same horizontal plane. The remaining boreholes (ML, MR, BL, and BR) were drilled within the boundaries of the proposed niche and were subsequently mined out when the niche was excavated as planned.

Figure 6.1.1-2c and Figure 6.1.1-3c contain the final configuration of the seven boreholes drilled at Niche 3107 (Niche 3). The original intent was to drill the middle borehole ML and borehole MR beyond the limits of the proposed excavation to monitor the movement of moisture around the niche during subsequent testing. Unfortunately, the middle boreholes were not drilled at the correct elevation above Niche 3107 (Niche 3) and were partially mined away during excavation.

The final configuration of the seven boreholes drilled at Niche 4788 (Niche 4) is illustrated in Figure 6.1.1-2d and Figure 6.1.1-3d. A misinterpretation of a survey mark, along with bad ground conditions (i.e., falling rock or collapsing ground conditions) at Niche 4788 (Niche 4), also resulted in the partial loss of borehole ML at this site. The original plan was to drill the U and M series boreholes outside the excavation.

After the excavation of Niche 3566 (Niche 1), a special set of horizontal boreholes was drilled from within the niche into the walls and end of the niche in a radial pattern. A similar scheme was used at Niche 3107 (Niche 3) after its excavation. These are not shown on the plan views.

Air-permeability testing has been performed at Niche CD 1620 (Niche 5). Special boreholes to discern the effects of excavation on permeability were drilled alongside the proposed excavation

[1]Figures 6.1.1-2, 6.1.1-3, and 6.1.1-4 were generated using field measurements recorded in Scientific Notebooks (Wang 1997 [156530], Wang 1997 [156534]), Wang 1999 [156538], Wang 1999 [153449], and Trautz 1999 [156563]) and/or using pre-built plans for niche excavation. Therefore, these figures show the idealized shape of the niches and approximate locations of the boreholes. Figure 6.1.1-5 was generated using the as-built information (DTN: MO0008GSC00269.000 [166198]).

site, parallel to the niche wall to-be. These boreholes were designated "AK" because they were intended primarily for air permeability (K) use. Figure 6.1.1-4a and Figure 6.1.1-4c show in plan and elevation view respectively, these three boreholes designated AK1, AK2 and AK3 that were drilled 1 m apart in a horizontal plane, with the first borehole 1 m from the proposed niche wall level with the elevation of the ECRB springline. Before the inner excavation at Niche CD 1620 (Niche 5), seven additional boreholes were drilled as shown in Figure 6.1.1-4b, Figure 6.1.1-4d, and Figure 6.1.1-4e in plan, elevation, and side view respectively, designated B1.75, ML, MM, MR, UL, UM, and UR. All of these boreholes except B1.75 were drilled above the proposed inner-niche location. Subsequent excavation of the inner part of the niche mined out borehole B1.75.

After testing was completed at Niche CD 1620 (Niche 5), air-permeability measurements were performed in the near-vertical boreholes drilled from the invert of Alcove 8 towards Niche 3107 (Niche 3). These boreholes were drilled to surround the area designated for the pond experiment, as described in Section 6.12, to be performed in Alcove 8. These air-permeability tests were made to provide correlation with the ground penetrating radar imaging in the same boreholes, as opposed to providing direct location data for borehole water release experiments (as with the other air-permeability measurements). They were also intended to allow retesting to observe changes in relative permeability caused by possible partial saturation as a result of the pond experiment. The alcove plan and face views are shown with approximate borehole locations, designated as #1 to #6, in Figure 6.1.1-5a and Figure 6.1.1-5b respectively.

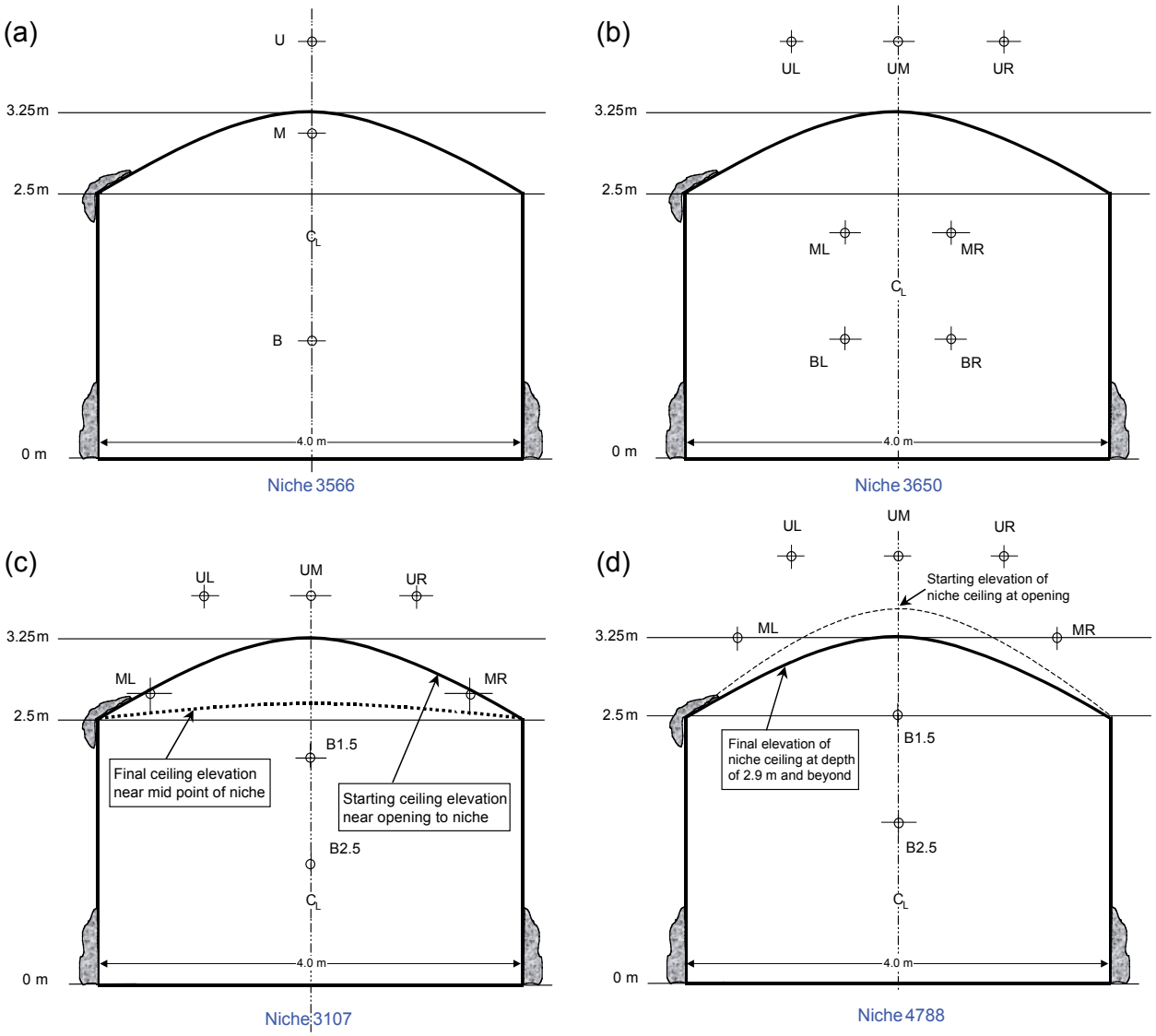

NOTE: All measurements are approximate and do not represent surveyed as-built conditions. The niche faces are on the west wall of the Main Drift of the Exploratory Studies Facility. See Figure 6.1.1-4 for borehole notations. C_L denotes centerline.

Figure 6.1.1-2. Schematic Illustration of the End View of Borehole Clusters at Niche Sites

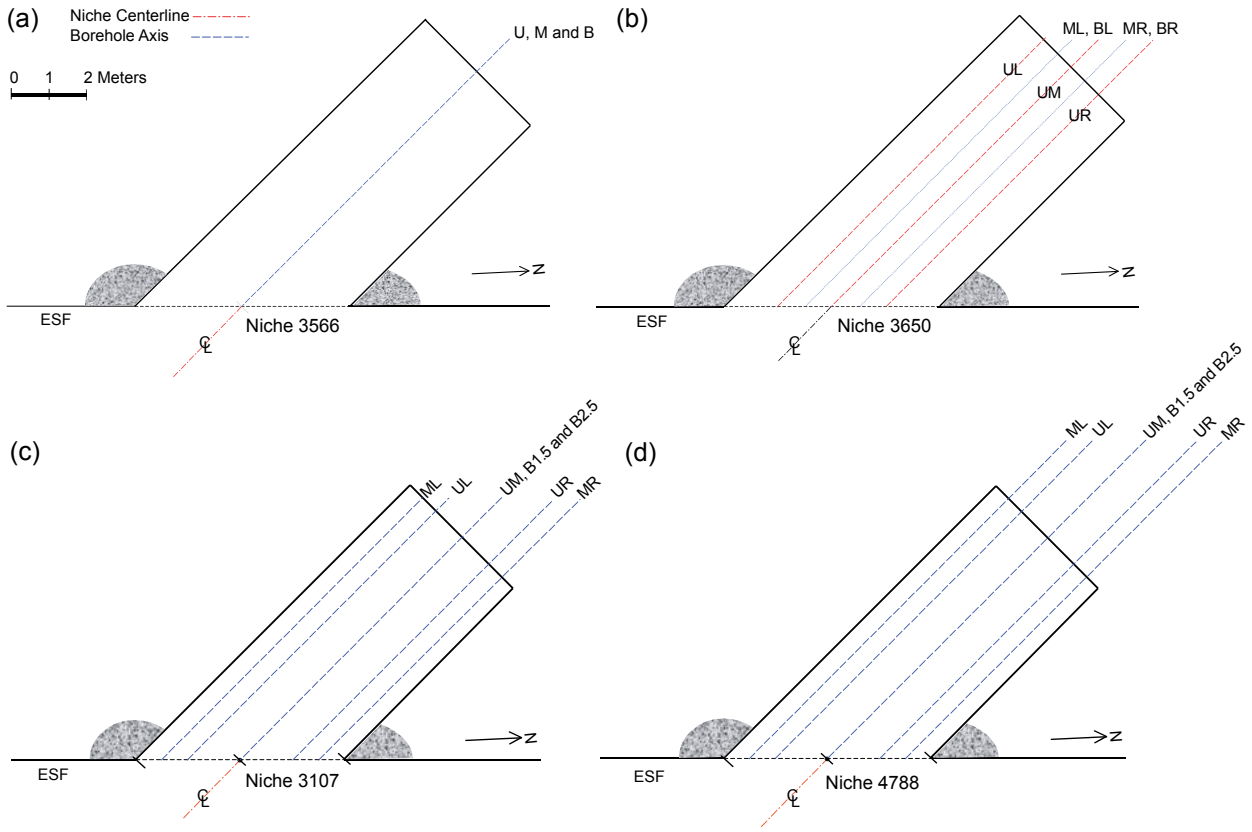

NOTE: All measurements are approximate and do not represent surveyed as-built conditions. The boreholes shown are oriented horizontally in the northwestern direction parallel to the niche axis. See Figure 6.1.1-4 for borehole notations. C_L denotes centerline.

Figure 6.1.1-3. Schematic Illustration of the Plan View of Borehole Clusters at Niche Sites

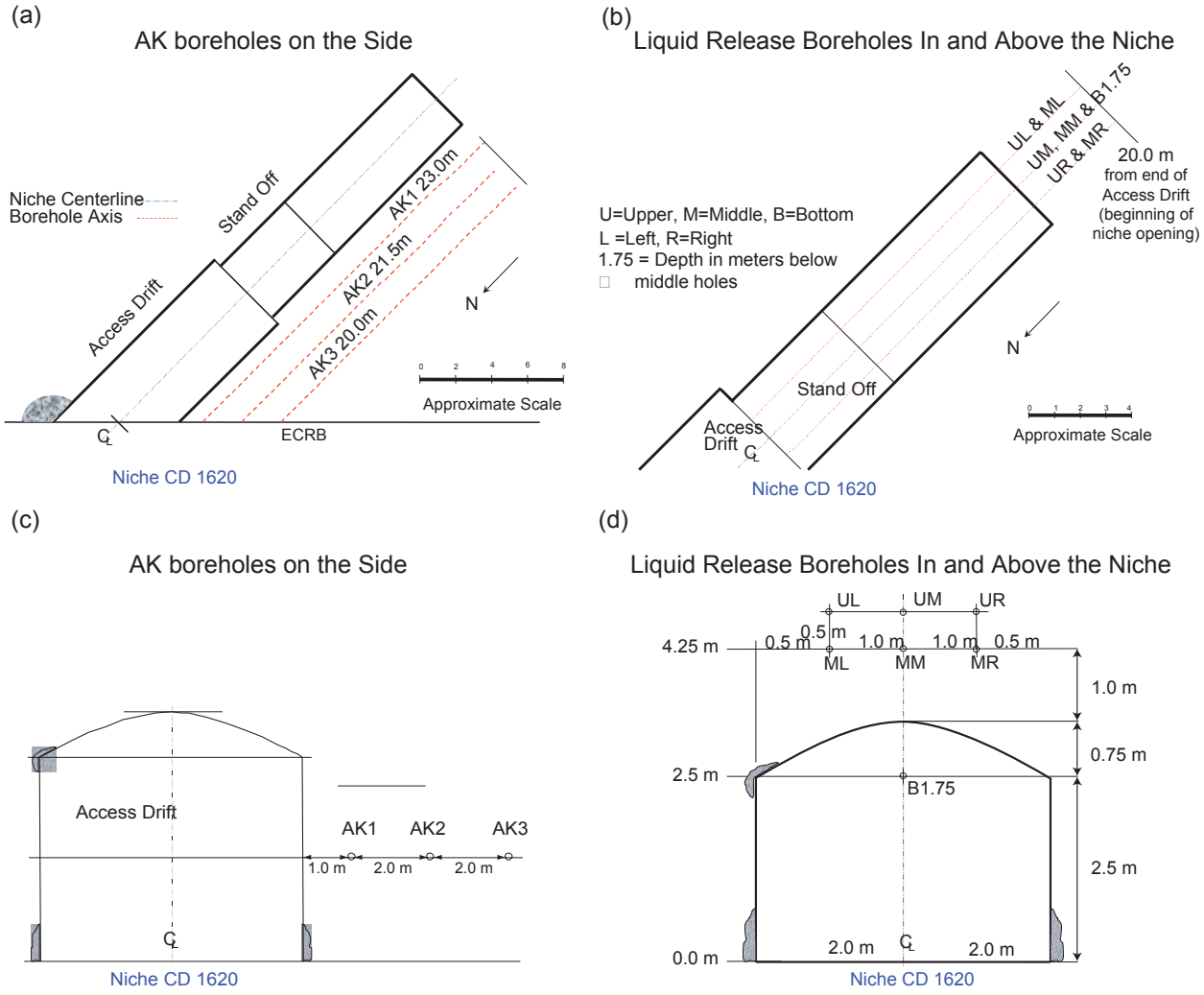

NOTE: All measurements are approximate and do not represent surveyed as-built conditions.
The niche face is on the southeast wall of the ECRB Cross Drift.
C_L denotes centerline.

Figure 6.1.1-4. Schematic Illustration of the End and Plan Views of Borehole Clusters at Niche CD 1620 (Niche 5)

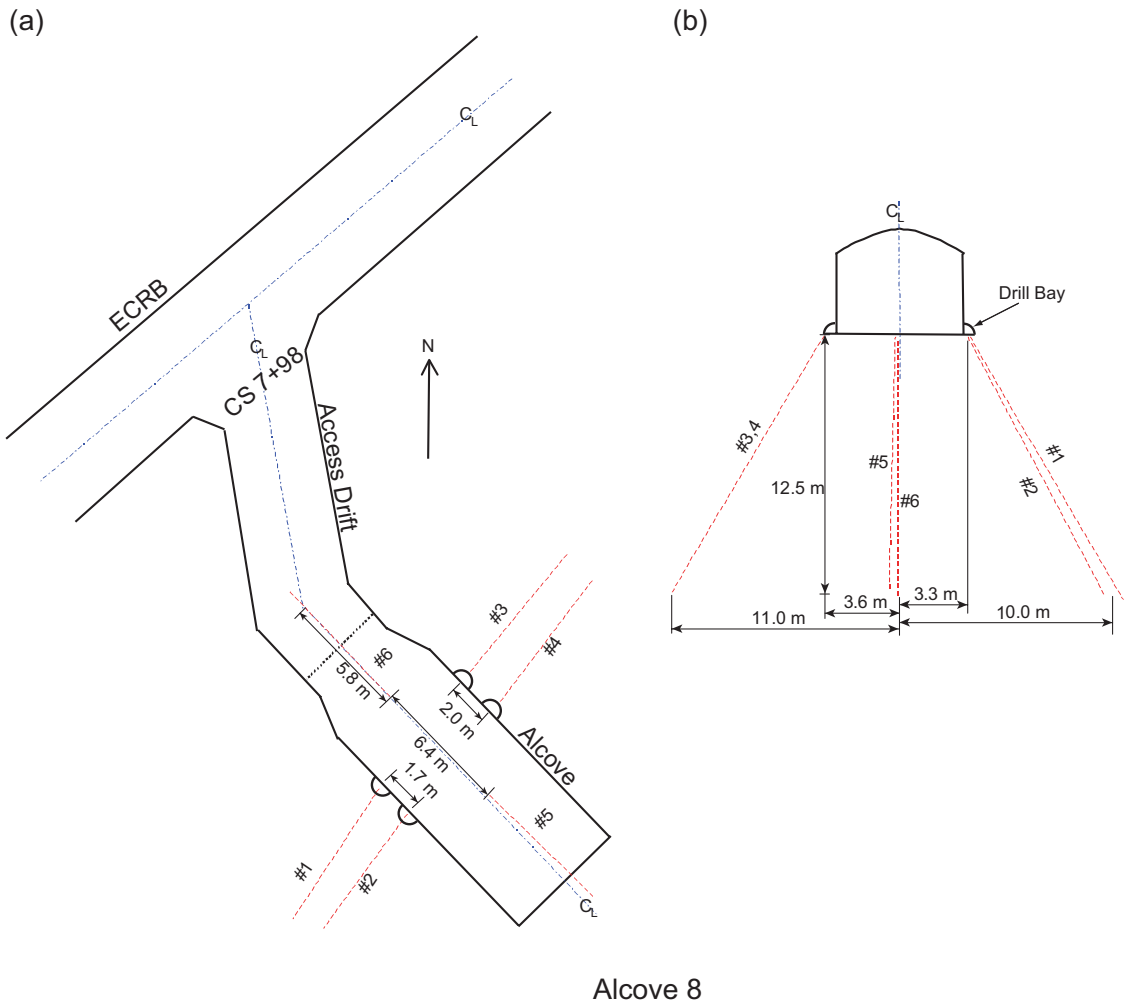

Alcove 8

NOTE: All measurements are approximate. Borehole as-built information is in DTN: MO0008GSC00269.000 [166198].
The niche face is on the southeast wall of the ECRB Cross Drift.
C_L denotes centerline.

Figure 6.1.1-5. Schematic Illustration of the Plan and End Views of Borehole Clusters at Alcove 8

6.1.2 Air-Permeability Testing, Spatial Distribution, and Statistical Analysis

To date, an estimated 3,500 separate air injections have been undertaken in the *in situ* studies underground at Yucca Mountain. Nearly a quarter-million pressure-response curves have been logged in the studies. The number of tests lends itself to visualization and statistical comparison of the flow connections and distributions of permeability in the rock mass. The specially designed equipment for pneumatic testing is described in Attachment I. With the equipment, it is feasible to conduct tests for site-to-site and borehole-to-borehole comparisons both before and after nearby excavations.

6.1.2.1 Data Reduction and Air-Permeability Determination

Data in the field were acquired in the form of voltage output from the various instruments and converted in real time or post-test time to physical units, using each instrument's calibration data. At Niche 3107 (Niche 3), Niche 4788 (Niche 4), Niche CD 1620 (Niche 5), and Alcove 8, data acquisition was fully automated, so that log entries for each individual injection test could be done by computer and correlation with the data files linked. Each of these tests was given three minutes to reach steady state. To maximize the signal-to-noise ratio, the maximum flow rate obtainable with the system that did not cause the interval pressure to exceed the packer leak-by pressure was chosen for the purpose of the permeability calculation.

Because each injection test was repeated to accommodate two different observation-packer configurations, there are two tests for each injection location from which to choose flow and pressure data for the single-borehole results. When graphed, the two are usually indistinguishable. Preference is given to the lower of the two if there is a significant difference, because this higher value is likely caused by leaks in the packer sealing.

Reported data consist of the acquisition filename, test location, time, date, channel or interval number, flow rate, ambient pressure, and steady-state injection pressure. The derived steady-state single-borehole permeability can be obtained using the expression described below.

In air-permeability tests to characterize the fracture heterogeneity of the test sites, permeability values are obtained from pressure changes and flow rates using the following modified Hvorslev's formula (LeCain 1995 [101700], Equation 15, p. 10):

$$k = \frac{P_{sc} Q_{sc} \mu \ln\left(\frac{L}{r_w}\right) T_f}{\pi L \left(P_2^2 - P_1^2\right) T_{sc}} \qquad \text{(Eq. 6.1.2-1)}^{a}$$

k permeability, m^2

P_{sc} standard pressure, Pa

Q_{sc} flow-rate at standard conditions, m^3/s

μ dynamic viscosity of air, Pa-s

L length of zone, m

r_w radius of bore, m

T_f temperature of formation, K

P_2 injection zone pressure at steady-state, Pa

[a] The solution is derived for the steady state ellipsoidal flow field around a finite line source. If the length L in the natural logarithm term in Equation 6.1.2-1 is replaced by an external radius R_e, this formula is identical to the cylindrical flow solution with an ambient constant pressure boundary at the external radius (Muskat 1982 [134132], p. 734). This replacement is used in Section 6.2.2.1 to estimate the saturated hydraulic conductivity for post-excavation liquid flow paths from the borehole interval to the niche ceiling.

P_1 ambient pressure, Pa

T_{sc} standard temperature, K

ln natural log

For the purpose of calculation, standard pressure is 1.013E+05 Pa (one atmosphere). The dynamic viscosity of air used is 1.78E-05 Pa-s. Temperature contributions to Equation 6.1.2-1 are negligible, with $T_f \sim T_{sc}$ for ambient-temperature testing conditions. See Attachment IX.3 for details on how this calculation was performed.

The Hvorslev's equation requires that air behave as an ideal gas. This stipulation is approximately true at the ambient temperatures and pressures used in the air-permeability tests. In addition, a finite line source is used to represent a borehole injection interval. This representation is applied to the borehole injection interval, where all air flow is approximated to be in the radial direction (none in the axial direction). This is justified because in the air-permeability tests, the length of injection zone was 0.3048 m and the radius of the borehole was 0.0381 m. The injection zone is a long, thin cylinder. Flows along axial directions were blocked by packers, and occurrences of packer leaks were monitored by pressures in adjacent borehole intervals, as described in Attachment I.

Although the fractured tuff of the niches is not a homogeneous or infinite medium, the Hvorslev equation provides a consistent method of calculating permeabilities, enabling comparison of the test results for various injection locations. Because the heterogeneity of the surrounding medium is not known *a priori*, the permeabilities calculated by analytic formula are estimates of effective values around the injection borehole intervals. The results of the air-permeability tests are used to characterize the heterogeneity of the medium of niche sites and test beds. Another requirement of this approach is that air flows are mainly through fractures and governed by Darcy's law. Darcy's law is used to relate flux to pressure gradients (Bear 1972 [156269]). The justification for this is that: under the ambient unsaturated conditions in fractured tuff at Yucca Mountain, capillary forces confine the liquid mainly to the matrix. This leaves the fracture network, which is more permeable than the tuff matrix, available for gas flow.

Deviations from Darcy's law may result from either turbulent flow or from the gas slip-flow phenomenon (Klinkenberg 1942 [106105]) but both these effects are considered to be negligible. Slip flow is significant only in pores with dimensions similar to the mean free path of air molecules (Bear 1972 [156269]). Apertures of the fractures in Yucca Mountain are much larger than the molecular mean free path. Pressure drop is proportional to flow rate in laminar flow, which is required for Darcy's law, but not in turbulent flow (Bear 1972 [156269]. These experiments were conducted at multiple flow rates to detect any evidence of deviation from Darcy's law due to turbulence, and none was found. Finally, small effects potentially associated with movement of residual water within the fractures and the multirate approach to check packer leak-by and other nonlinear effects (e.g., turbulence) are discussed in Attachment I.4.

6.1.2.2 Permeability Profiles

All boreholes at niches as illustrated in Figure 6.1.1-2 and Figure 6.1.1-3 are nominally 10 m long and 0.0762 m in diameter. Those in Figure 6.1.1-4 and Figure 6.1.1-5 were nominally 15 m long and 0.0762 m in diameter. The boreholes were drilled dry with compressed air to remove

drill cuttings. Both the packer interval length and the test interval length are 0.3 m in all cases. Further details of equipment configuration and test execution are discussed in Attachment I.

Whereas most of the niches were excavated so as to preserve certain boreholes surrounding them (in order to remeasure the air permeability in these holes after excavation), Alcove 8 was constructed before any drilling near it, so this opportunity did not occur there.

6.1.2.2.1 Pre- and Post-Excavation Permeability Profiles

Permeability profiles along boreholes at the five niches show the permeability value from each test interval, plotted against the location of the middle of the test interval (zone). Figure 6.1.2-1 illustrates three Niche 3566 (Niche 1) permeability profiles along the upper, middle, and bottom boreholes, which are parallel to the niche axis. The air-permeability tests were conducted before niche excavation. Niche 3566 (Niche 1), the first niche excavated in the ESF, is located in the vicinity of the Sundance fault. All three boreholes penetrated brecciated zones in the last one-third of their lengths, with broken rock pieces preventing packer insertion beyond this depth. A wet feature in a brecciated zone was observed at the end of this niche, right after completion of dry excavation (Wang et al. 1999 [106146], Figure (4c), p. 331). The width of the wet feature is comparable to the borehole-interval length of 0.3 m, used in the air-permeability tests (this section) and liquid-release seepage tests (Section 6.2).

After niche excavation, six additional horizontal boreholes were drilled from the inside of the niche, fanning out radially in different directions. Only two radial holes were tested and analyzed in this niche. This niche was sealed for moisture monitoring after testing these two boreholes, and further seepage testing in this niche has been deferred. The permeability profiles for two radial boreholes on the left side of the niche are illustrated in Figure 6.1.2-2. These boreholes also penetrated brecciated zones. The absence of data from the deeper portion of one of the boreholes in Figure 6.1.2-2 is related to the intrinsic difficulties of brecciated zone testing due to poor borehole conditions, which prevent the maintenance of a proper seal (see also Attachment I.4 for discussion about issues of packer leak-by in testing).

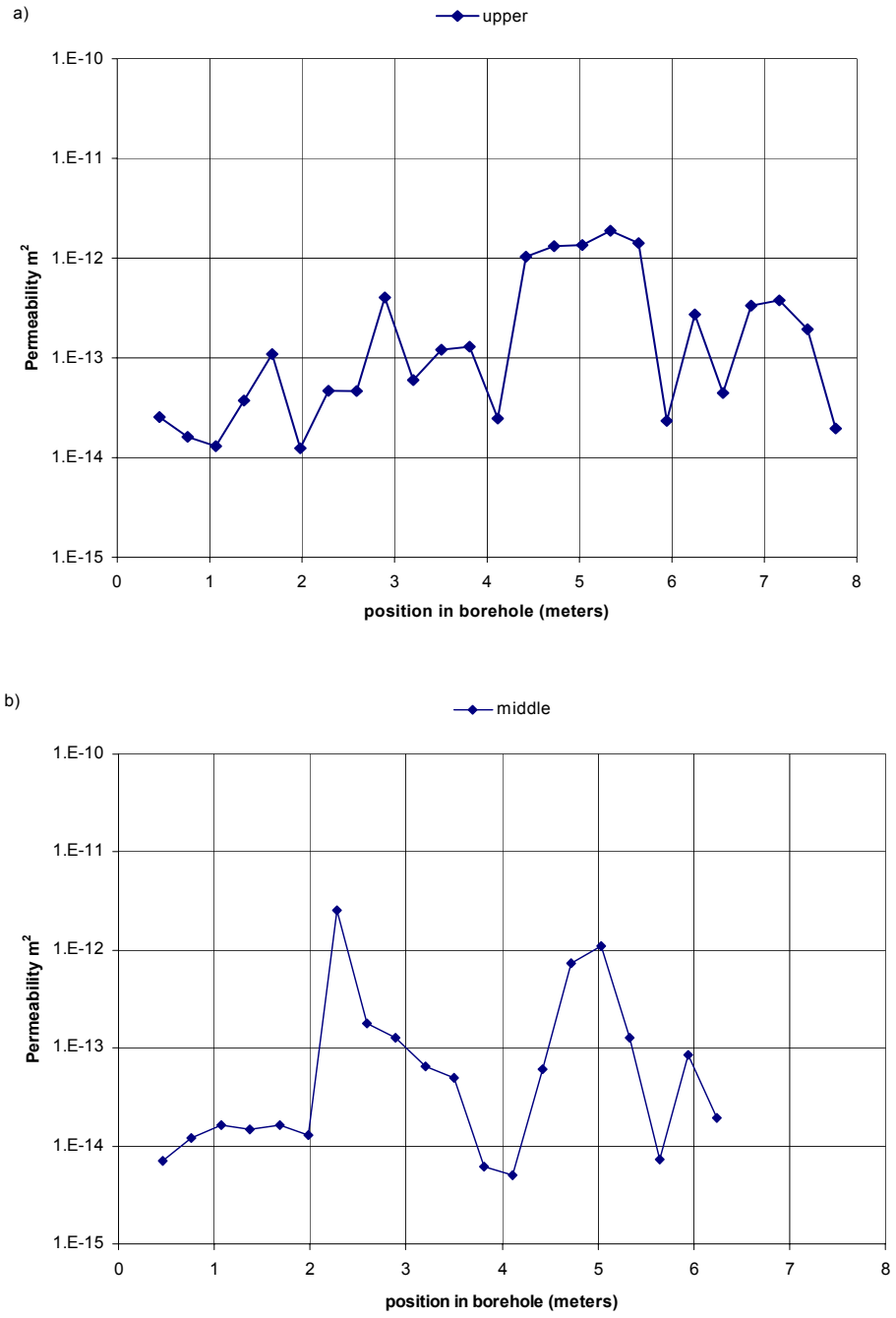

DTN: LB0011AIRKTEST.001 [153155]

NOTE: In DTN: LB0011AIRKTEST.001 [153155], zone numbers are reported, rather than actual position in the borehole. Zone 1 is centered at 0.5 m, and each successive zone is 0.3 m farther into the borehole (e.g., zone 2 is centered at 0.8 m).

Figure 6.1.2-1. Pre-Excavation Air-Permeability Profiles along Axial Boreholes at Niche 3566 (Niche 1)

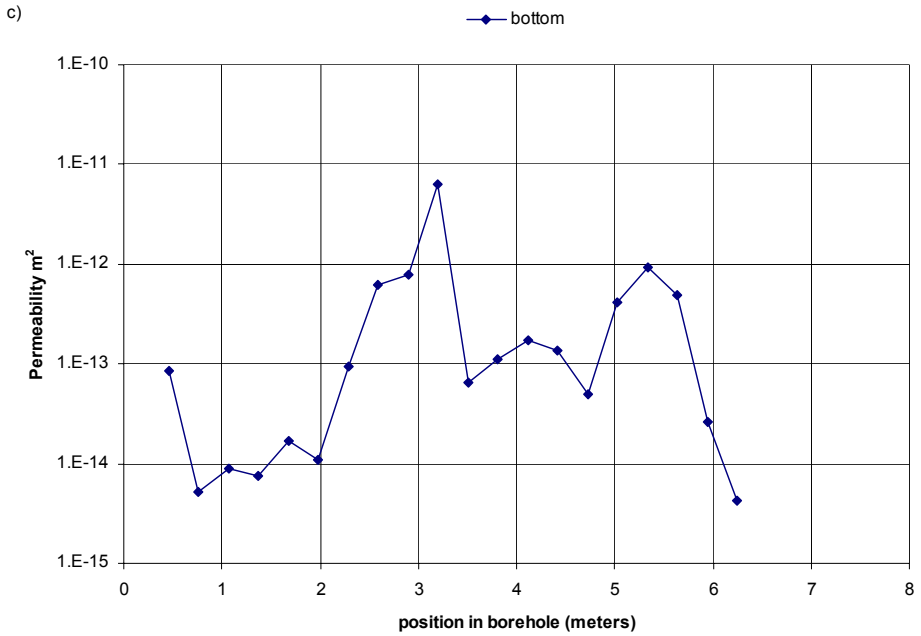

NOTE: In DTN: LB0011AIRKTEST.001 [153155], zone numbers are reported, rather than actual position in the borehole. Zone 1 is centered at 0.5 m, and each successive zone is 0.3 m farther into the borehole (e.g., zone 2 is centered at 0.8 m).

Figure 6.1.2-1. Pre-Excavation Air-Permeability Profiles along Axial Boreholes at Niche 3566 (Niche 1) (continued)

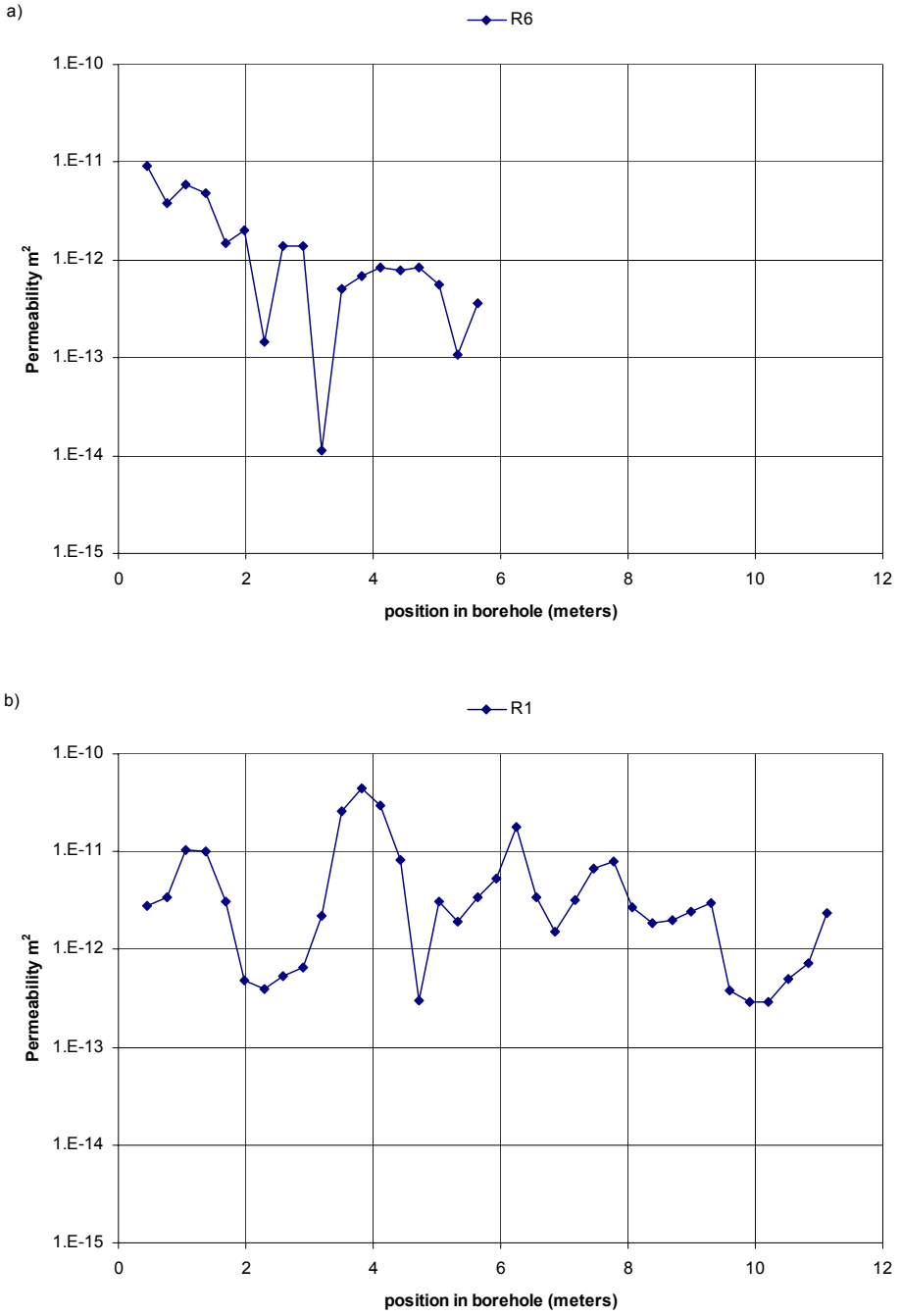

DTN: LB0011AIRKTEST.001 [153155]

NOTE: In DTN: LB0011AIRKTEST.001 [153155], zone numbers are reported, rather than actual position in the borehole. Zone 1 is centered at 0.5 m, and each successive zone is 0.3 m farther into the borehole (e.g., zone 2 is centered at 0.8 m).

Figure 6.1.2-2. Post-Excavation Air-Permeability Profiles along Radial Boreholes at Niche 3566 (Niche 1)

Figure 6.1.2-3 illustrates both the pre- and post-excavation permeability profiles along three upper boreholes at Niche 3650 (Niche 2). On all the plots with both pre- and post-excavation data, a line is drawn through the profiles to indicate the geometric mean of each (see Attachment IX.1 for calculations). This mean includes only intervals that were tested in common both before and after excavation.

The permeability increases could be interpreted as the opening of pre-existing fractures induced by stress releases associated with niche excavation (Wang and Elsworth 1999 [104366], pp. 751–757). The niches were excavated using an Alpine Miner, a mechanical device with a rotary head (as opposed to drill and blast) cutting the rocks below the upper-level boreholes, so that excavation damage itself would not alter permeability.

Intervals with high pre-excavation permeability recorded the smallest post-excavation permeability changes. In additional to mechanical effects, some of the permeability increases can be related to the intersection of previously dead-ended fractures with the excavated free surface. For borehole intervals, beyond the extent of the niche excavation, the permeability values are less altered. Figure 6.1.2-4 illustrates the pre-excavation permeability profiles of the other four boreholes. The middle- and bottom-level boreholes were available for air-injection testing only before niche excavation, since they were subsequently removed by excavation.

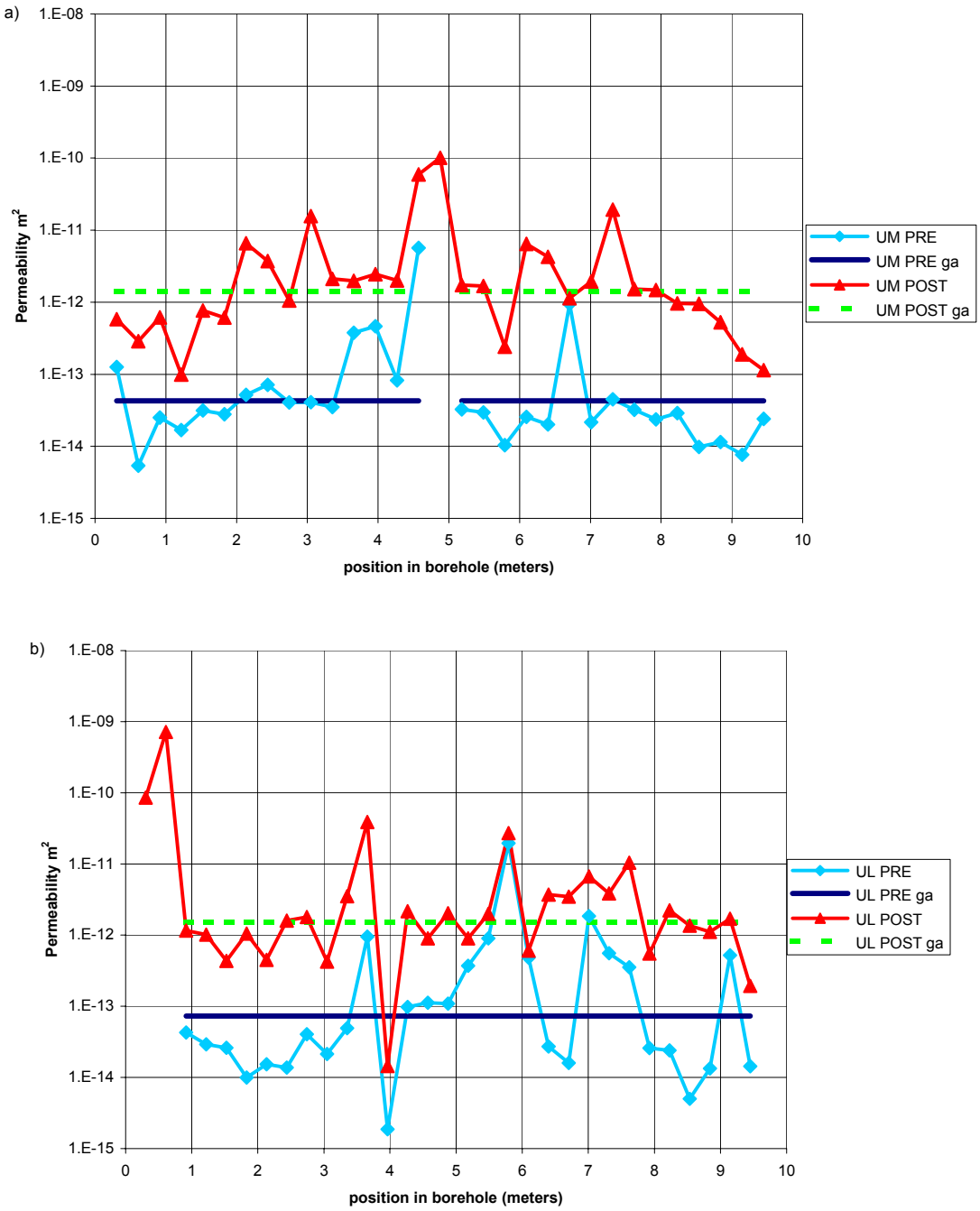

DTN: LB0011AIRKTEST.001 [153155]

NOTE: "ga" is the geometric average.

In DTN: LB0011AIRKTEST.001 [153155], zone numbers are reported, rather than actual position in the borehole. Zone 1 is centered at 0.5 m, and each successive zone is 0.3 m farther into the borehole (e.g., zone 2 is centered at 0.8 m).

Figure 6.1.2-3. Pre- and Post-Excavation Air-Permeability Profiles along Upper Boreholes at Niche 3650 (Niche 2)

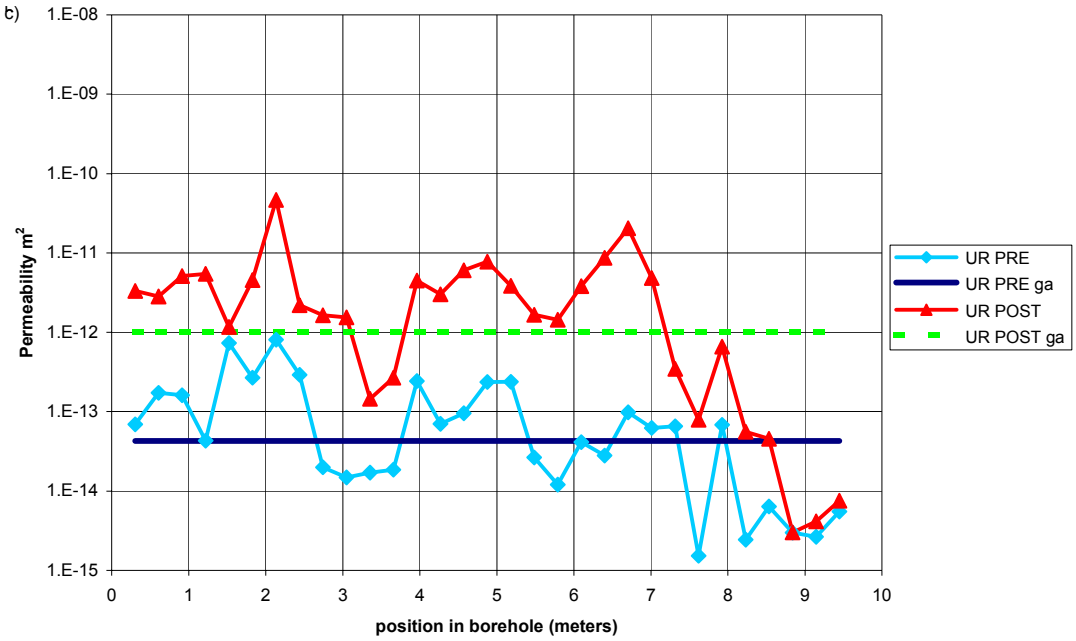

NOTE: "ga" is the geometric average.

In DTN: LB0011AIRKTEST.001 [153155], zone numbers are reported, rather than actual position in the borehole. Zone 1 is centered at 0.5 m, and each successive zone is 0.3 m farther into the borehole (e.g., zone 2 is centered at 0.8 m).

Figure 6.1.2-3. Pre- and Post-Excavation Air-Permeability Profiles along Upper Boreholes at Niche 3650 (Niche 2) (continued)

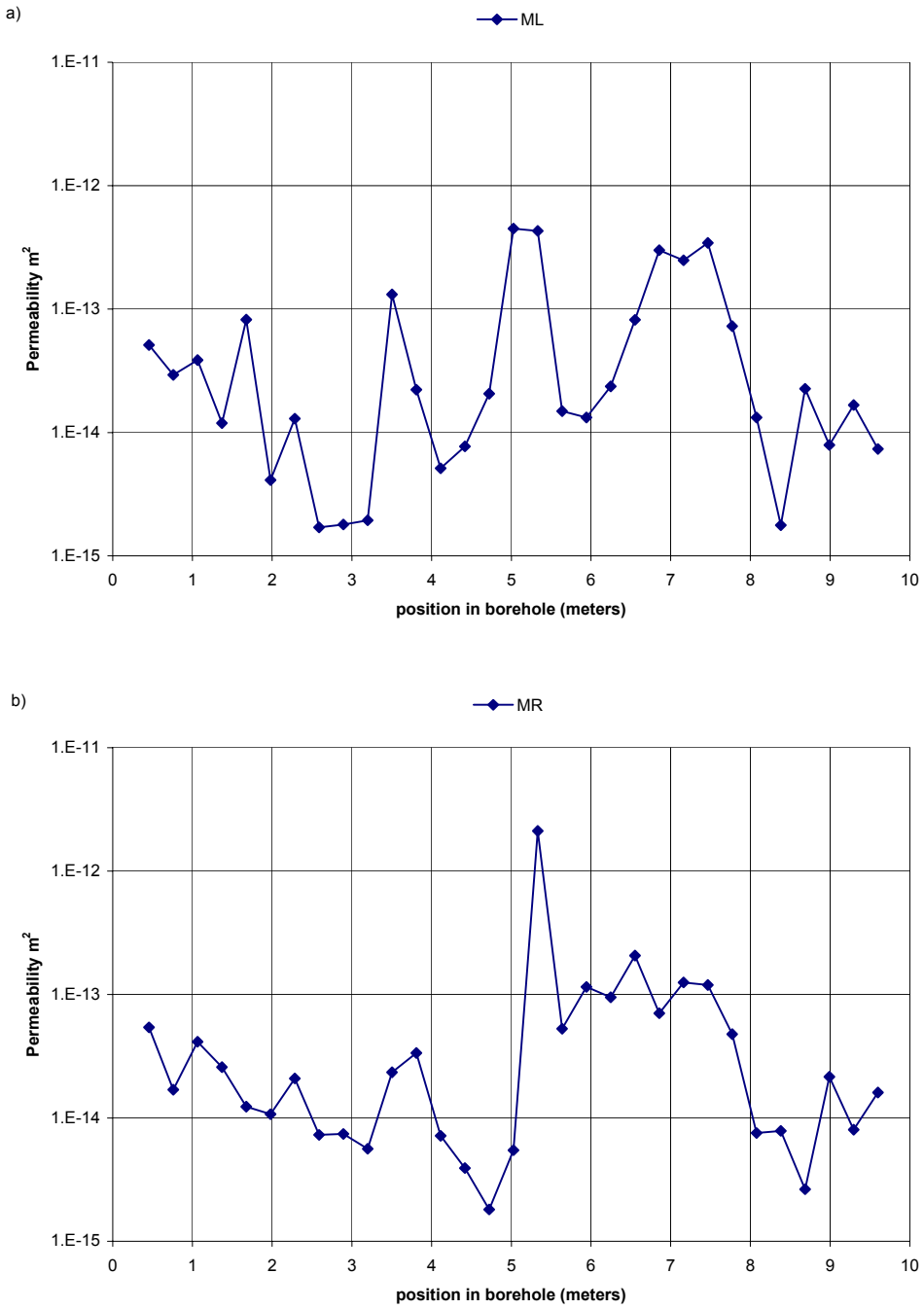

DTN: LB0011AIRKTEST.001 [153155]

NOTE: In DTN: LB0011AIRKTEST.001 [153155], zone numbers are reported, rather than actual position in the borehole. Zone 1 is centered at 0.5 m, and each successive zone is 0.3 m farther into the borehole (e.g., zone 2 is centered at 0.8 m).

Figure 6.1.2-4. Pre-Excavation Air-Permeability Profiles along Middle and Bottom Boreholes at Niche 3650 (Niche 2)

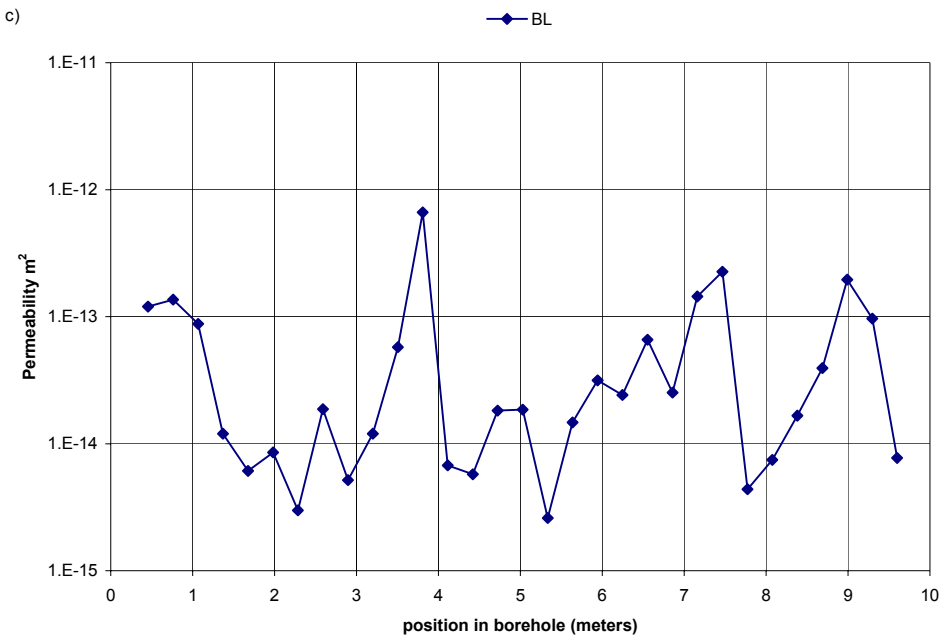

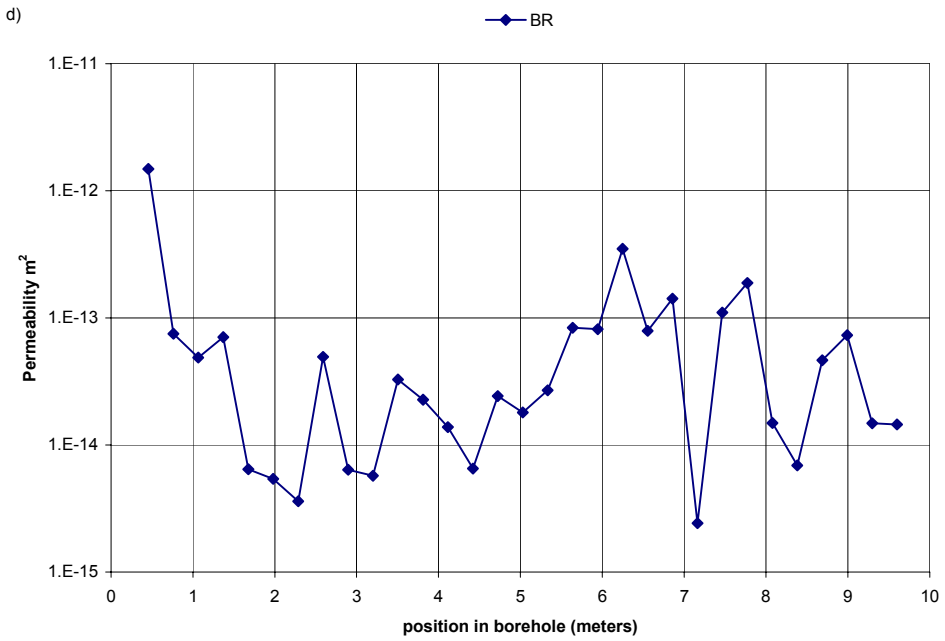

DTN: LB0011AIRKTEST.001 [153155]

NOTE: In DTN: LB0011AIRKTEST.001 [153155], zone numbers are reported, rather than actual position in the borehole. Zone 1 is centered at 0.5 m, and each successive zone is 0.3 m farther into the borehole (e.g., zone 2 is centered at 0.8 m).

Figure 6.1.2-4. Pre-Excavation Air-Permeability Profiles along Middle and Bottom Boreholes at Niche 3650 (Niche 2) (continued)

To compare with Niche 3650 (Niche 2), the corresponding results of the permeability profiles are presented for Niche 3107 (Niche 3) in Figure 6.1.2-5 and Figure 6.1.2-6, and for Niche 4788 (Niche 4) in Figure 6.1.2-7 and Figure 6.1.2-8. Figure 6.1.2-5 and Figure 6.1.2-7, similarly to Figure 6.1.2-3, are for the upper boreholes, with both pre-excavation and post-excavation values presented for the evaluation of excavation-induced enhancements in permeabilities. Figure 6.1.2-6 and Figure 6.1.2-8 are pre-excavation permeability profiles for the middle- and lower-level boreholes that were subsequently mined out from Niche 3107 (Niche 3) and Niche 4788 (Niche 4). The borehole layouts for these two niches are modified from the layout in Niche 3650 (Niche 2), as illustrated in Figure 6.1.1-2.

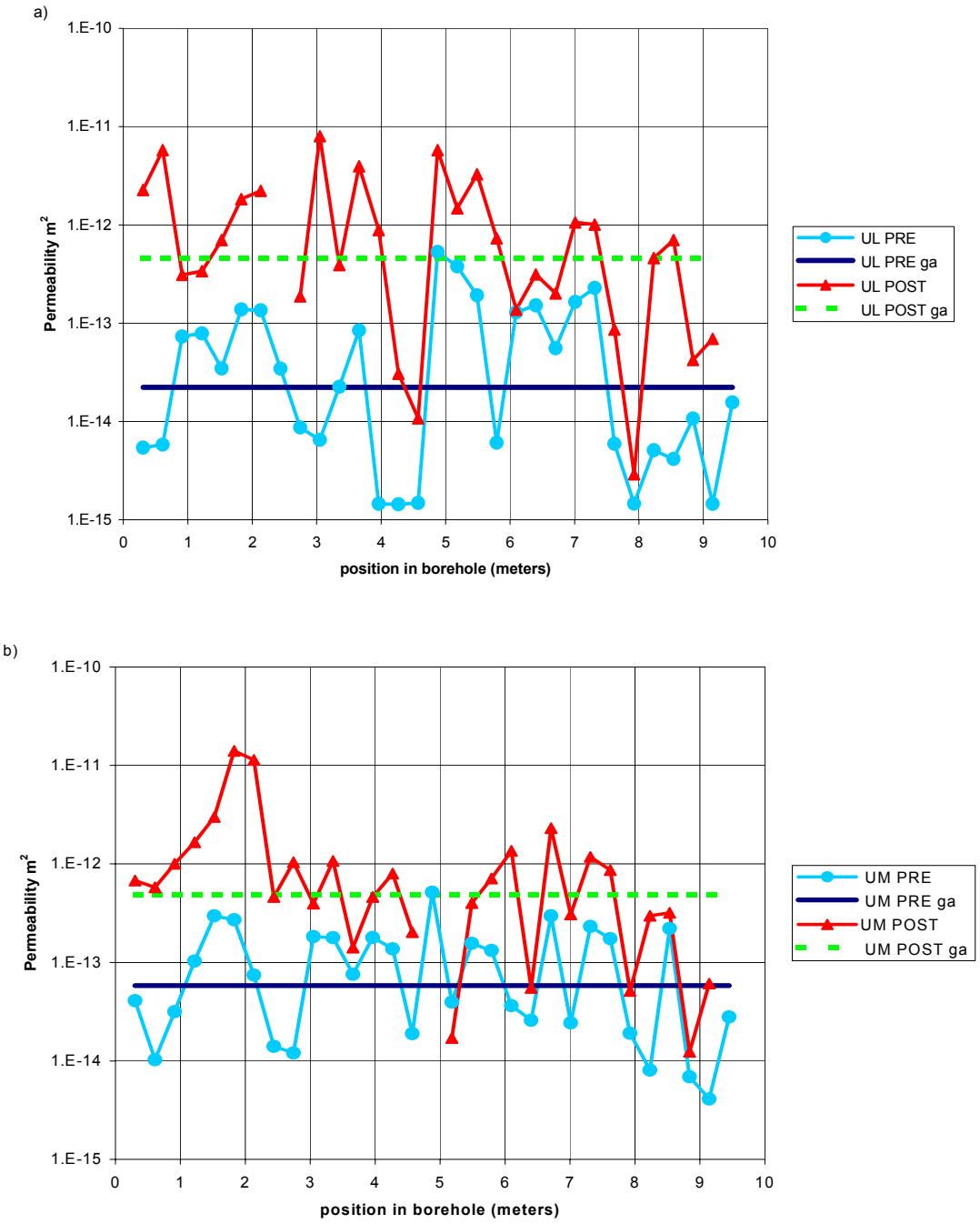

DTNs: LB980901233124.101 [136593] for pre-excavation data,
LB990601233124.001 [105888] for post-excavation data

NOTE: Intervals tested are 0.3 m long; position plotted is at farther end of tested interval.

Figure 6.1.2-5. Pre- and Post-Excavation Air-Permeability Profiles along Upper Boreholes at Niche 3107 (Niche 3)

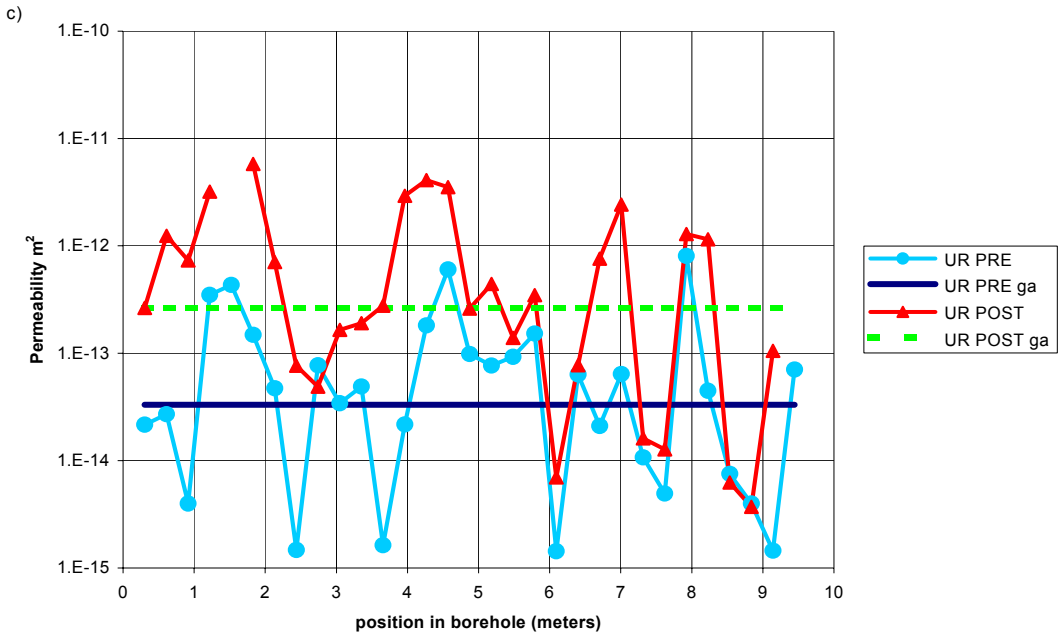

DTNs: LB980901233124.101 [136593] for pre-excavation data,
LB990601233124.001 [105888] for post-excavation data

NOTE: Intervals tested are 0.3 m long; position plotted is at farther end of tested interval.

Figure 6.1.2-5. Pre- and Post-Excavation Air-Permeability Profiles along Upper Boreholes at Niche 3107 (Niche 3) (continued)

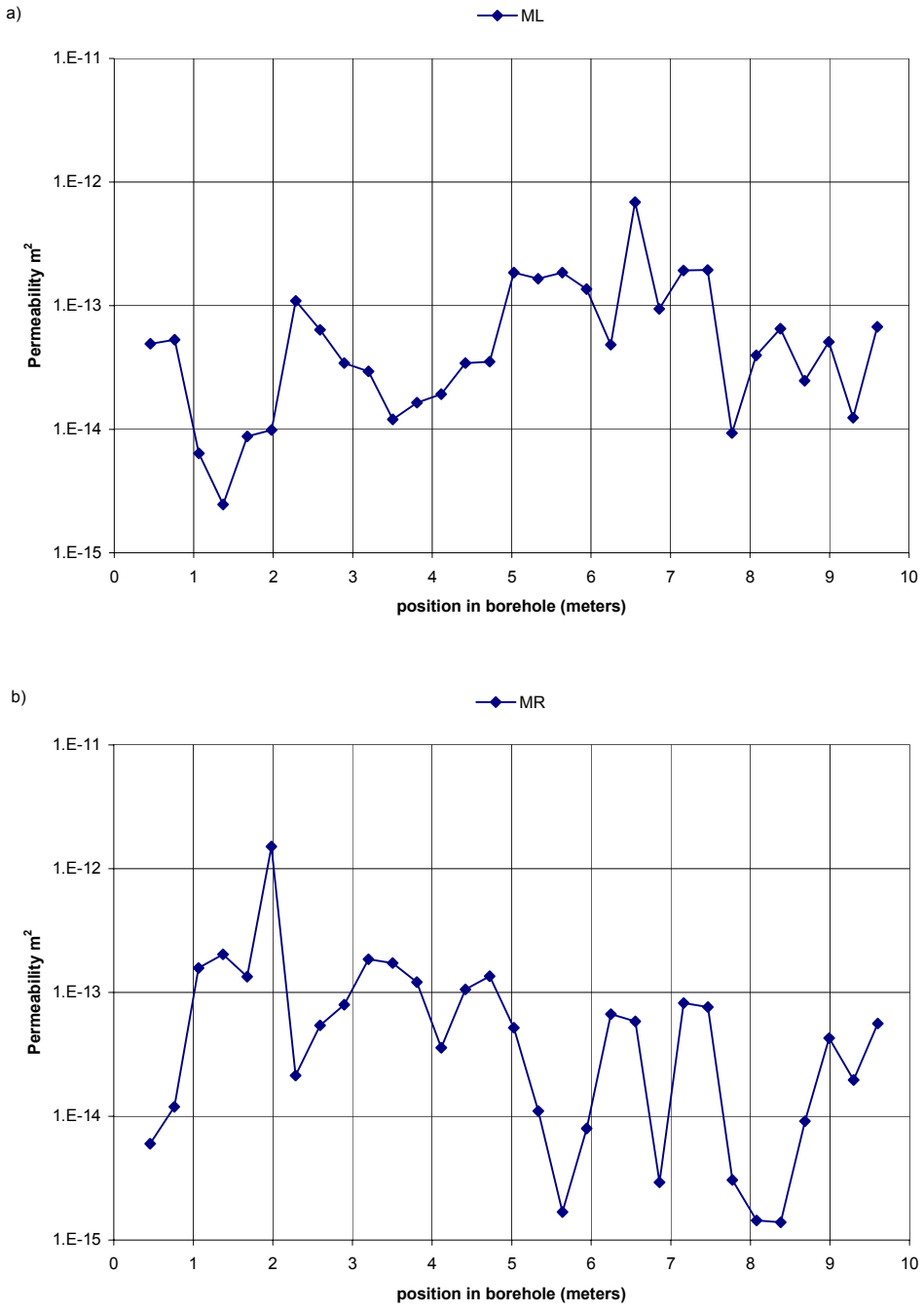

DTN: LB980901233124.101 [136593]

Figure 6.1.2-6. Pre-Excavation Air-Permeability Profiles along Middle and Bottom Boreholes at Niche 3107 (Niche 3)

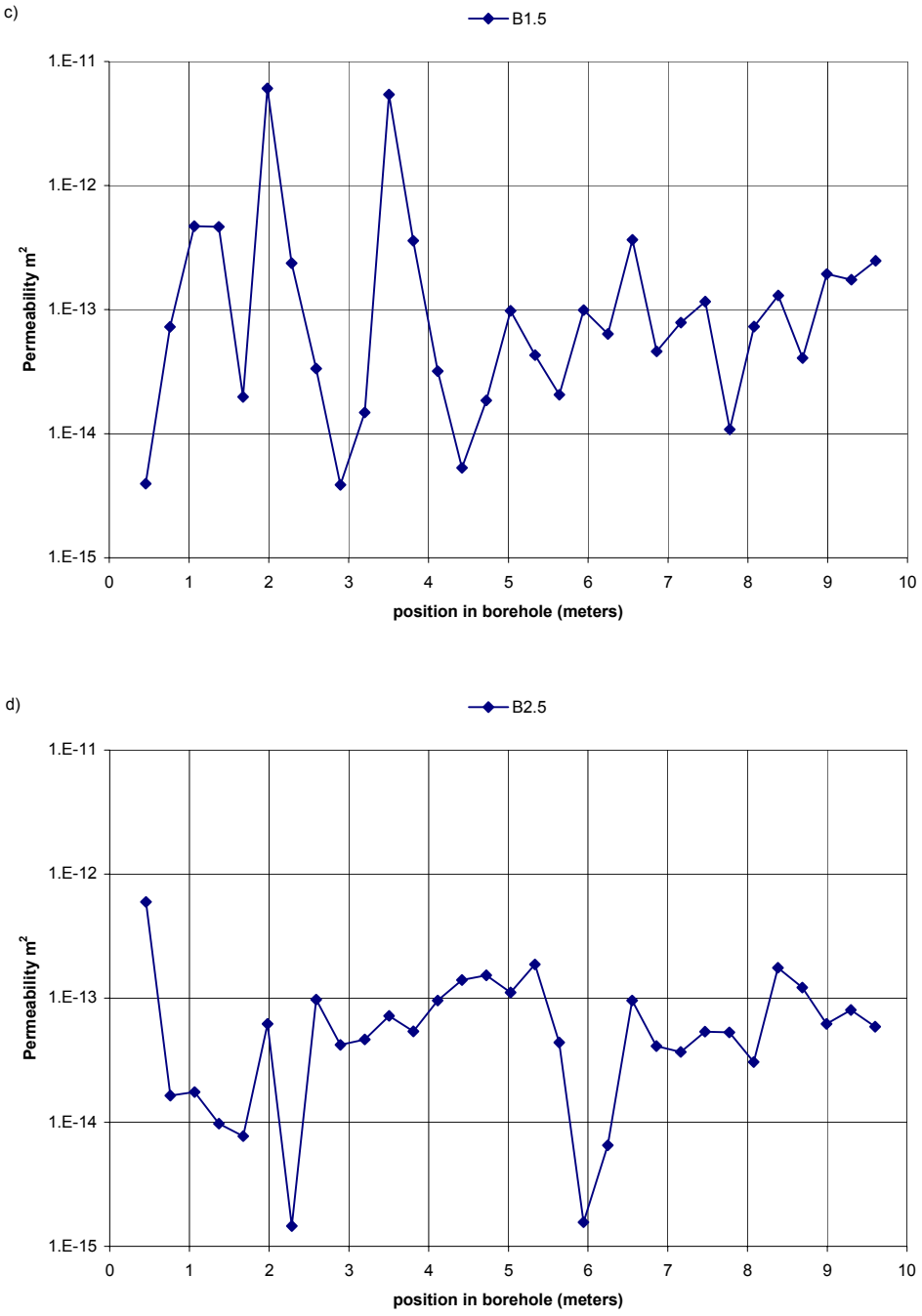

DTN: LB980901233124.101 [136593]

Figure 6.1.2-6. Pre-Excavation Air-Permeability Profiles along Middle and Bottom Boreholes at Niche 3107 (Niche 3) (continued)

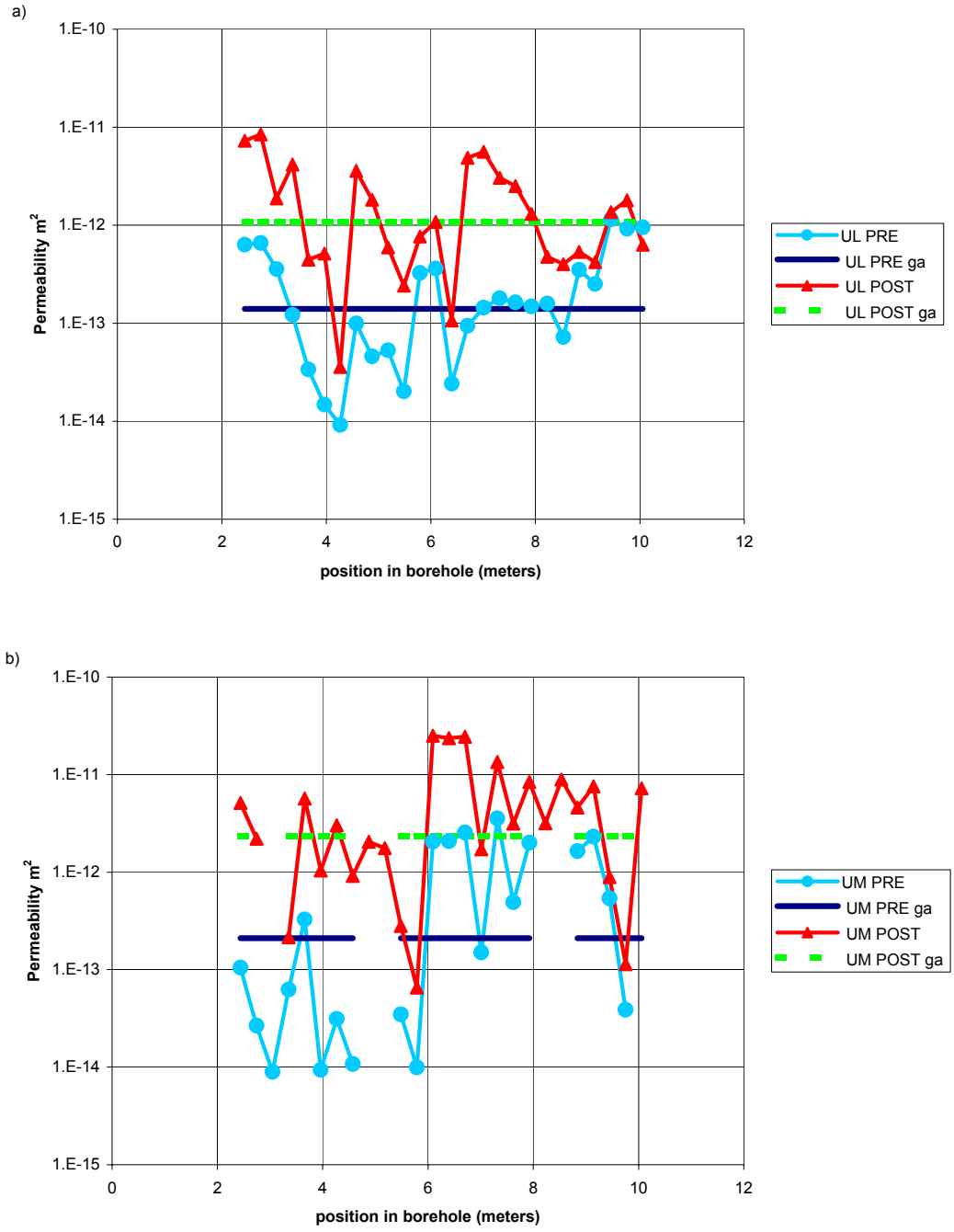

DTNs: LB980901233124.101 [136593] for pre-excavation data,
LB990601233124.001 [105888] for post-excavation data

Figure 6.1.2-7. Pre- and Post-Excavation Air-Permeability Profiles along Upper Boreholes at Niche 4788 (Niche 4)

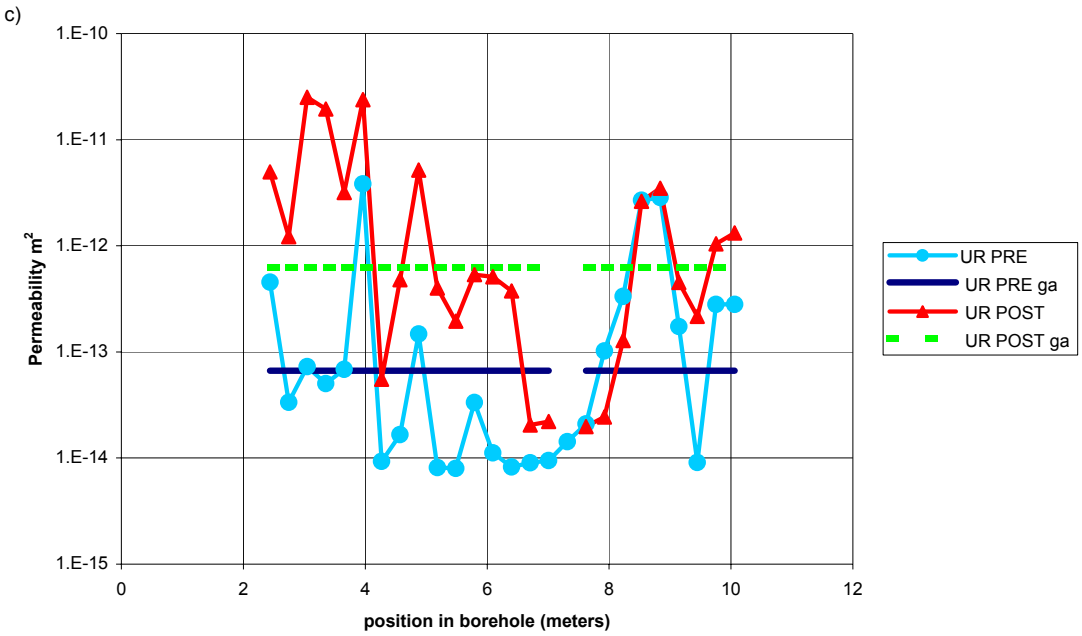

DTNs: LB980901233124.101 [136593] for pre-excavation data,
LB990601233124.001 [105888] for post-excavation data

Figure 6.1.2-7. Pre- and Post-Excavation Air-Permeability Profiles along Upper Boreholes at Niche 4788 (Niche 4) (continued)

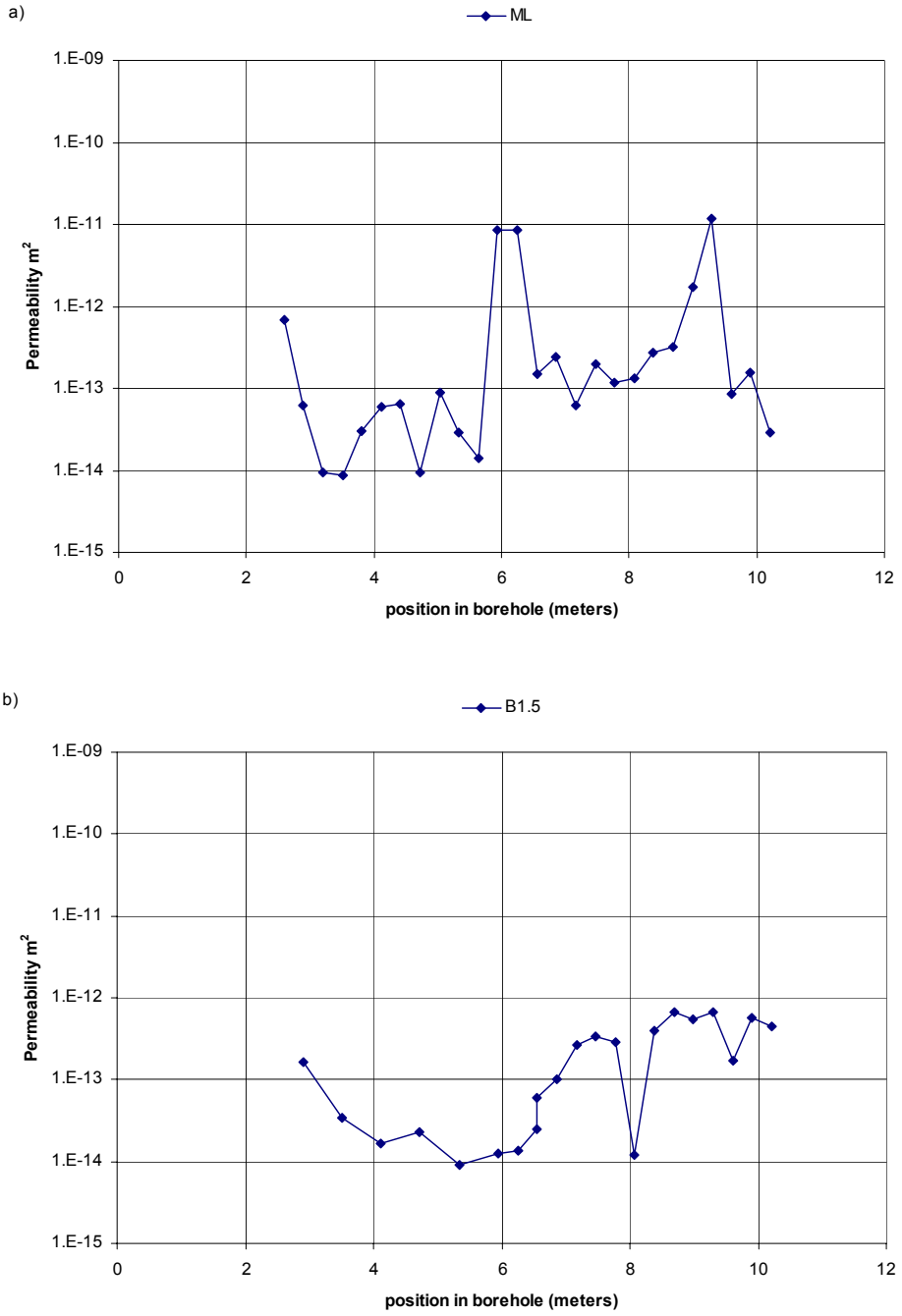

DTN: LB980901233124.101 [136593]

NOTE: Two or more measurements were made at each position. The least value of calculated permeability is reported here as being the most likely to be unaffected by leak-by.

Figure 6.1.2-8. Pre-Excavation Air-Permeability Profiles along Middle and Bottom Boreholes at Niche 4788 (Niche 4)

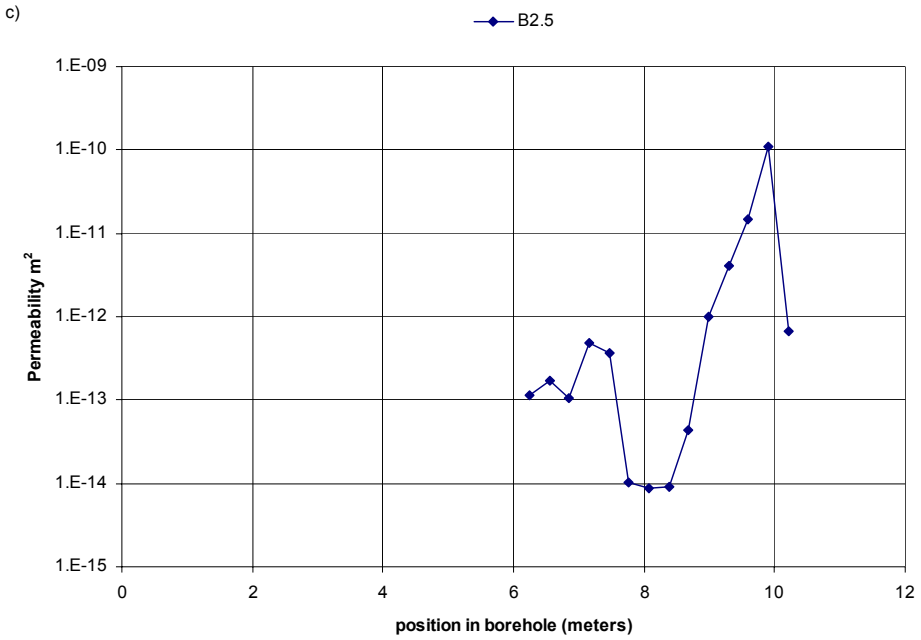

DTN: LB980901233124.101 [136593]

NOTE: Two or more measurements were made at each position. The least value of calculated permeability is reported here as being the most likely to be unaffected by leak-by.

Figure 6.1.2-8. Pre-Excavation Air-Permeability Profiles along Middle and Bottom Boreholes at Niche 4788 (Niche 4) (continued)

At Niche CD 1620 (Niche 5), measurements taken before and after excavation at the inner niche area and alongside the outer niche area allowed comparison of excavation effects on permeability profiles for boreholes situated above excavation versus those situated alongside excavation. Profiles were taken of borehole UL, borehole UM, and borehole ML over the inner niche area both before and after the inner niche excavation, as illustrated in Figure 6.1.2-9. (Only these particular holes out of the overhead holes were testable. The rest were blocked by borehole debris.) Likewise, the AK borehole closest to the proposed niche wall became blocked close to the collar before any measurements could be taken. The other two, AK2 and AK3, were successfully profiled with air-k measurements at 0.3 m intervals. After excavation of the outer niche, the AK boreholes were again profiled. In Figure 6.1.2-10, comparison of the profiles for the two AK boreholes does not show as big a change as the boreholes above the niche in Figure 6.1.2-9. For the overhead boreholes, certain borehole sections change permeability more than others, whereas the change in geometric average (subscript “ga” in figures) for the AK boreholes alongside the excavation is smaller than it is for the overhead boreholes. The UL borehole and the AK2 borehole are roughly the same distance from their respective mined surfaces of the niche, but show a marked difference in change of geometric average of permeability.

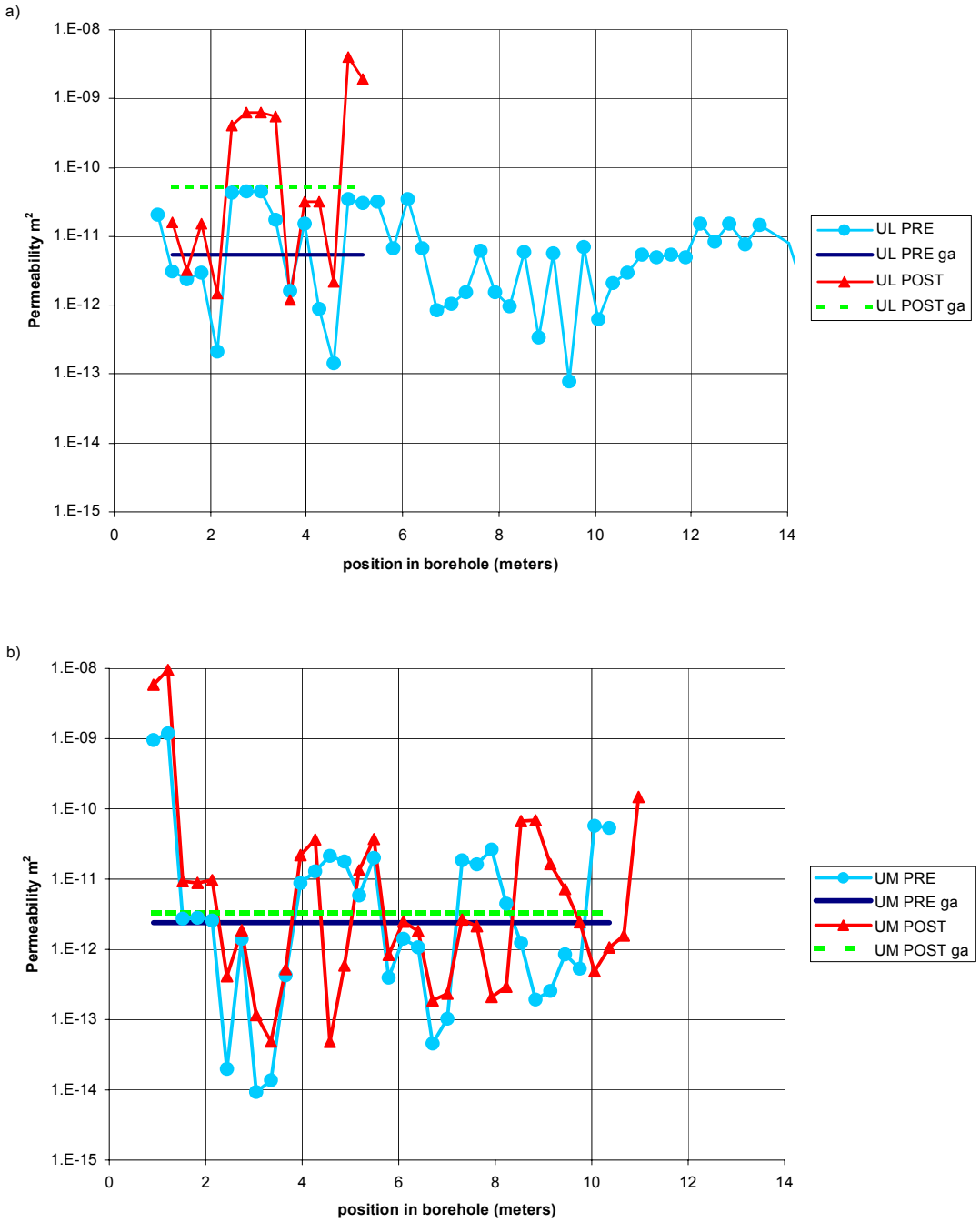

DTN: LB0012AIRKTEST.001 [154586] for pre-excavation data;
LB0110AKN5POST.001 [156904] for post-excavation data

Figure 6.1.2-9. Pre- and Post-Excavation Air-Permeability Profiles along Upper Boreholes at Niche CD 1620 (Niche 5)

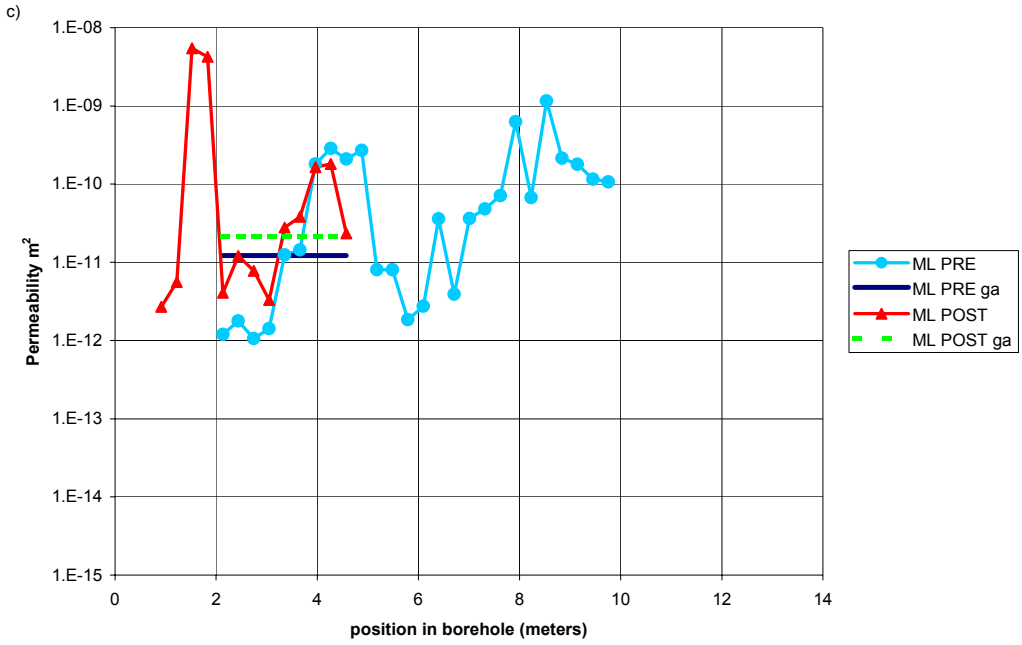

DTN: LB0012AIRKTEST.001 [154586] for pre-excavation data;
LB0110AKN5POST.001 [156904] for post-excavation data

Figure 6.1.2-9. Pre- and Post-Excavation Air-Permeability Profiles along Upper Boreholes at Niche CD 1620 (Niche 5) (continued)

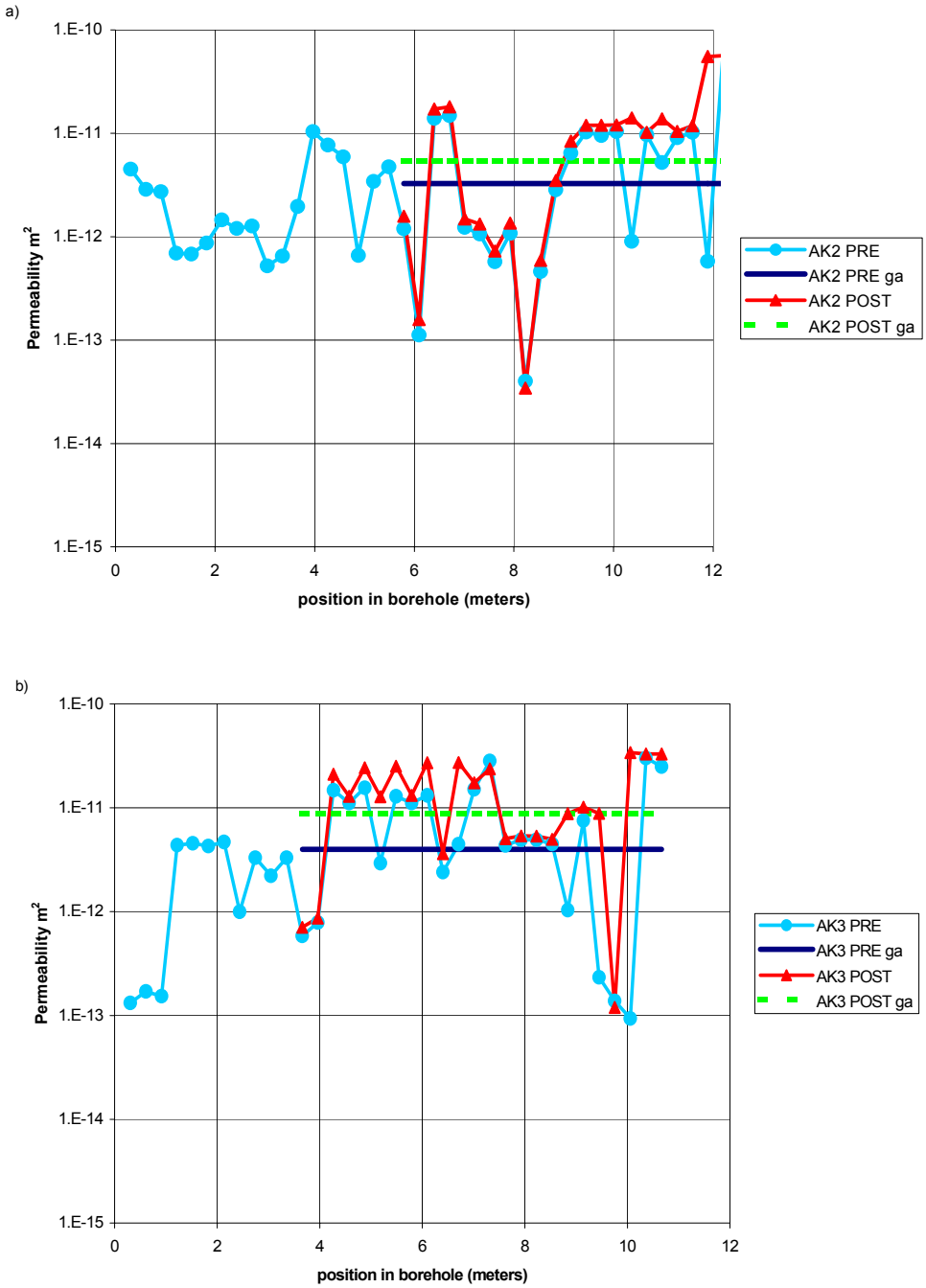

DTNs: LB002181233124.001 [146878]; LB0110AK23POST.001 [156905]

Figure 6.1.2-10. Pre- and Post-Excavation Air-Permeability Profiles along AK Side Boreholes at Niche CD 1620 (Niche 5)

6.1.2.2.2 Vertical Permeability Profiles

Alcove 8 afforded the first opportunity to obtain near-vertical borehole air-permeability profiles in any of the drifts at Yucca Mountain. Figures 6.1.2-11 (a–f) show the permeability as a function of depth for each of the boreholes drilled from the invert of Alcove 8. All boreholes have local peaks and sections of relatively uniform permeabilities along their depths, and high permeabilities towards the bottom. Boreholes 1, 3, and 4 exhibit relatively long sections of low permeability followed by a 3 to 5 order-of-magnitude increase starting at about 6 m for Borehole 1, 10 m for Borehole 3, and 8 m for Borehole 4. These permeability increases could be locally associated with the Tptpul-Tptpmn interface which is approximately midway between Alcove 8 and Niche 3107 (Niche 3), as discussed in Section 6.12.1.2 on the geometry and in Section 6.12.3 on the results of geophysical imaging of the drift-to-drift test bed.

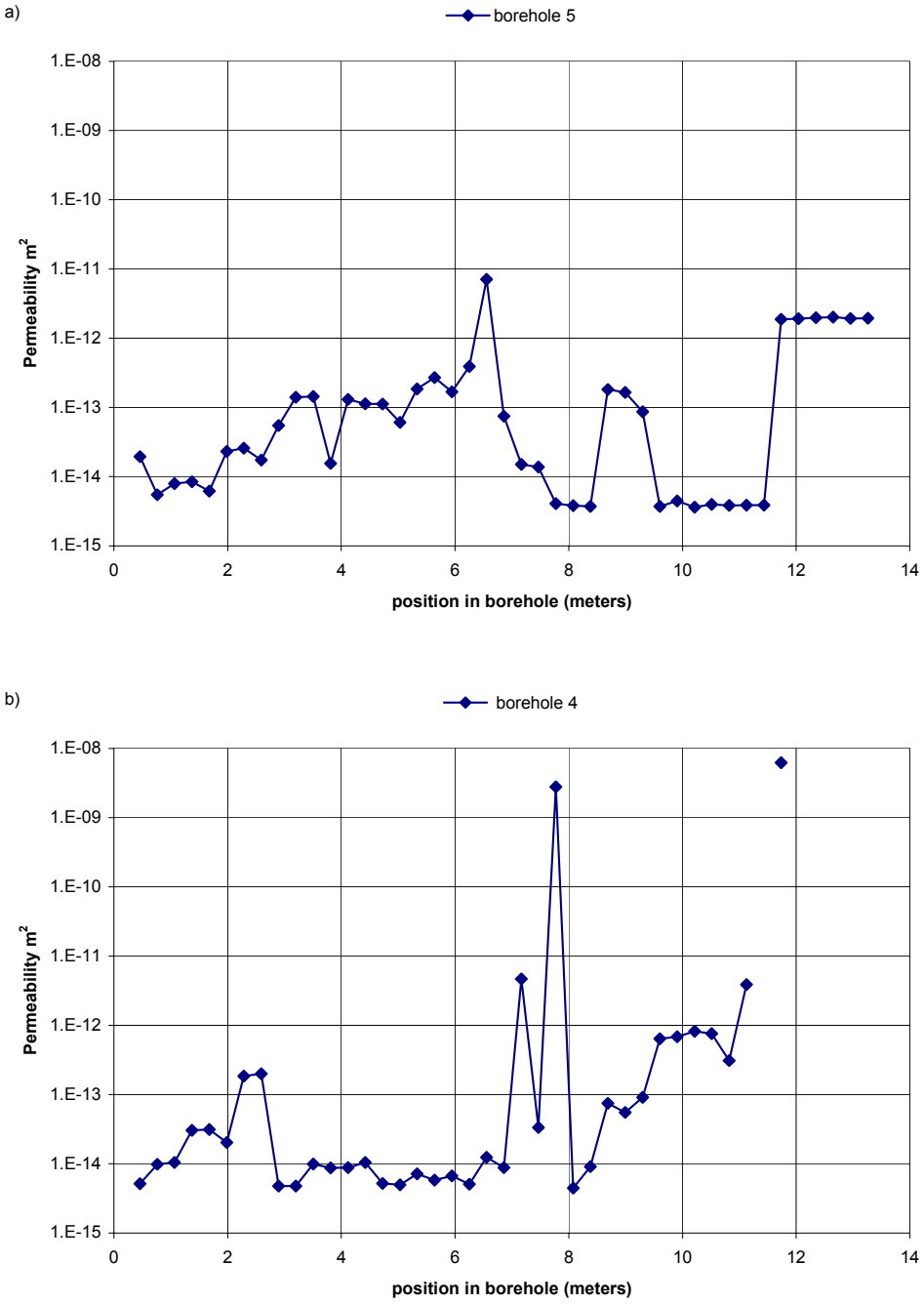

DTN: LB0302ALC8AIRK.001 [164748]

Figure 6.1.2-11. Air-Permeability Profiles down Boreholes in Alcove 8

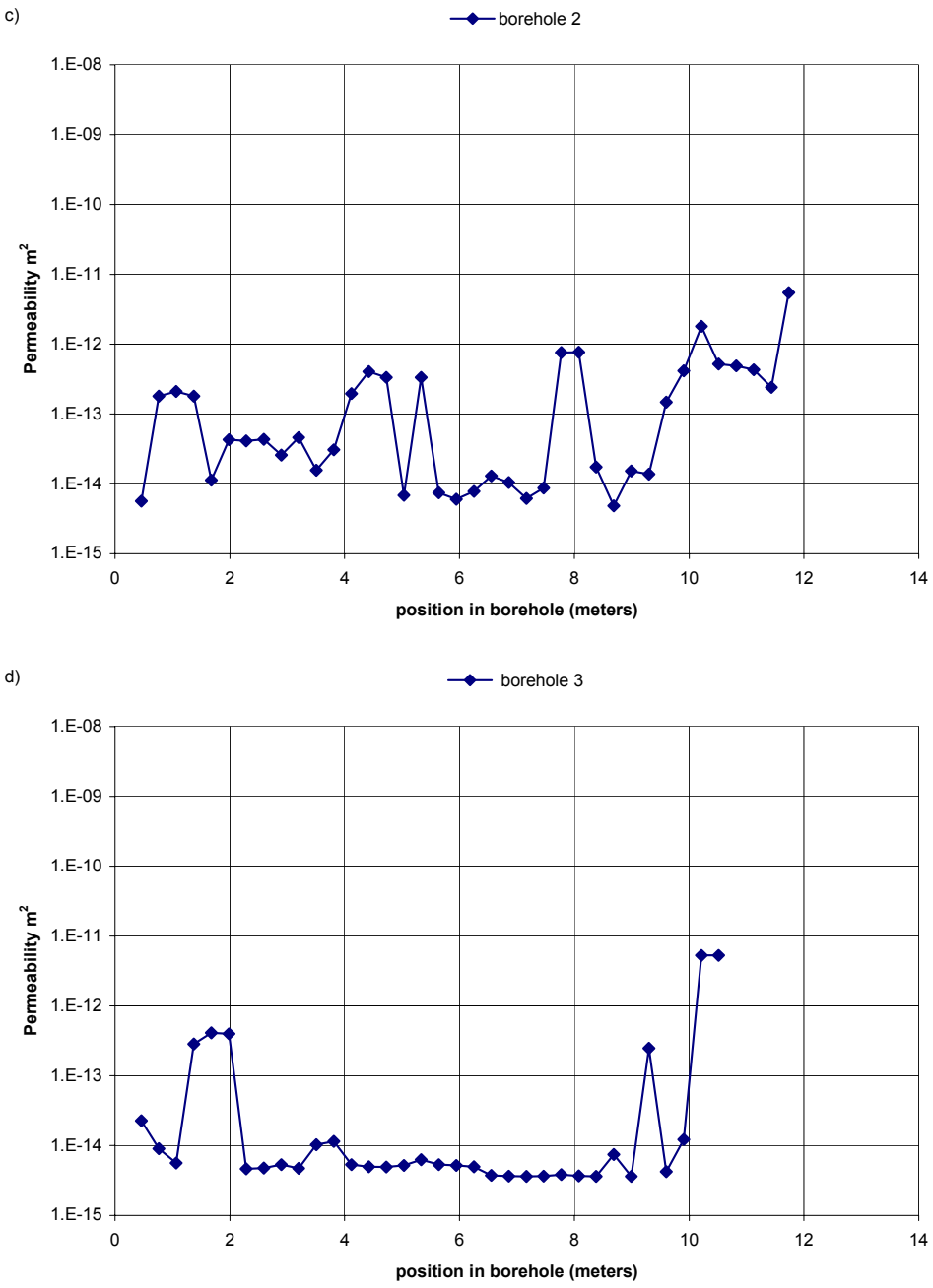

DTN: LB0302ALC8AIRK.001 [164748]

Figure 6.1.2-11. Air-Permeability Profiles down Boreholes in Alcove 8 (continued)

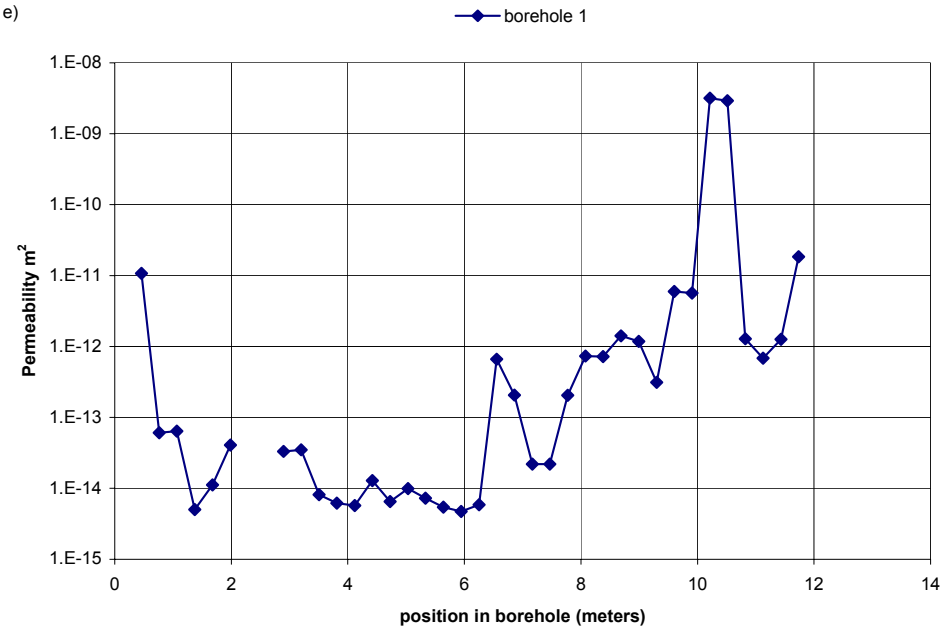

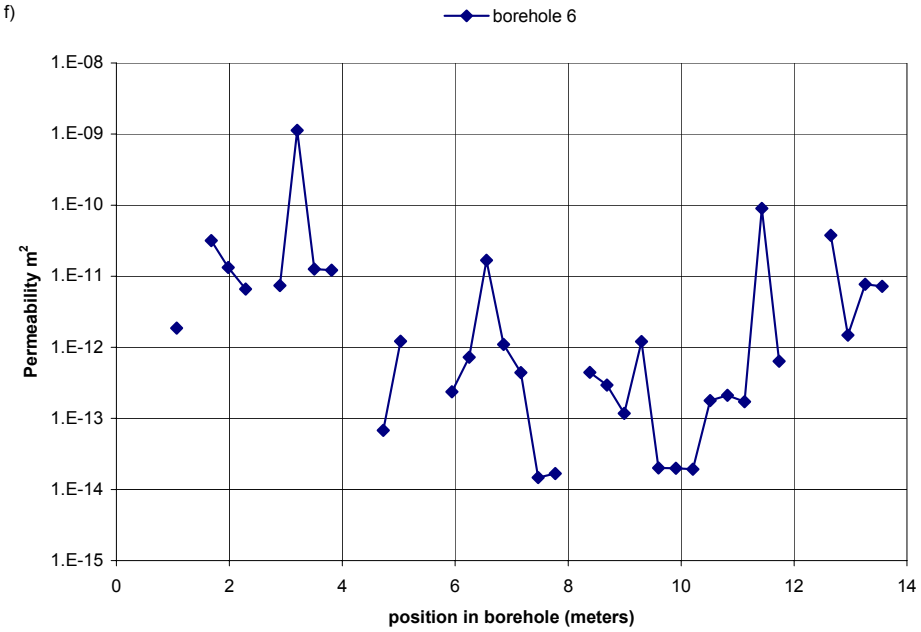

DTN: LB0302ALC8AIRK.001 [164748]

Figure 6.1.2-11. Air-Permeability Profiles down Boreholes in Alcove 8 (continued)

6.1.2.3 Permeability Change as a Function of Initial Permeability

Another type of plot can highlight the difference in the character of borehole permeability changes (caused by nearby excavation). The post-excavation permeability for a particular interval in a borehole, divided by the pre-excavation permeability for the same interval in a borehole, is the interval change ratio caused by excavation. A plot of the log change ratio versus the log pre-excavation permeability value can show a dependence of the change on the initial value. Figure 6.1.2-12 and Figure 6.1.2-13 show the changes for three of the overhead boreholes at Niche CD 1620 (Niche 5) and for two of the side boreholes, respectively. The overhead boreholes show some correlation to the notion that the initially low permeability zones change the most. For the side boreholes, however, there is a much weaker overall trend. See Attachment IX.5 for details on ratio, trend, and slope calculations. The slopes of the trend lines on the change ratio plots indicate some measure of correlation. Two individual slopes can be made out on the plot for the AK holes, one indicating a small population of intervals with strong change dependency, and one indicating a larger population with no dependency. The populations themselves are each evenly distributed over the initial permeabilites.

Change ratios for the pre- and post-excavation testing previously undertaken at Niche 3650 (Niche 2), Niche 3107 (Niche 3), and Niche 4788 (Niche 4) (all in overhead boreholes) are shown in Figure 6.1.2–14, Figure 6.1.2-15, and Figure 6.1.2-16, respectively. The change-ratio plots for these niches in the middle nonlithophysal zone of TSw show stronger correlation between initial permeability and the change ratio. Additionally, from the geometric averages in the profile plots, it can be seen that all these middle nonlithophysal niches show a larger average excavation effect than the boreholes at Niche CD 1620 (Niche 5) in the lower lithophysal zone of the TSw.

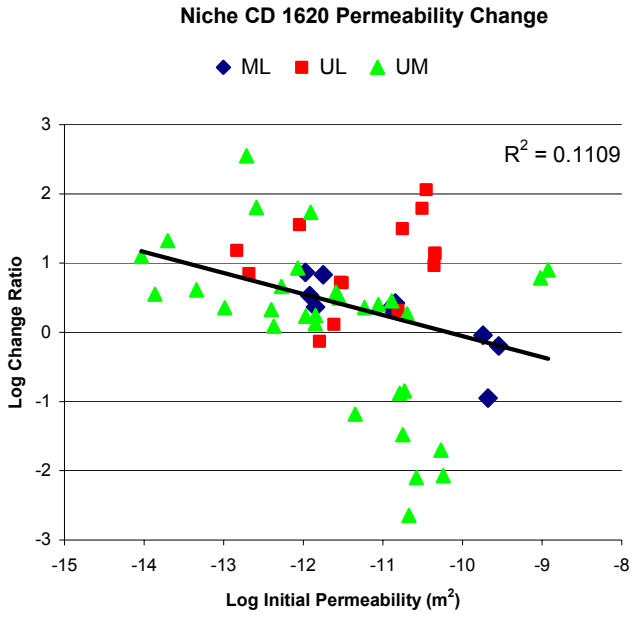

DTN: LB0310AIRK0015.001 [OUTPUT]

Figure 6.1.2-12. Change-Ratio Plot for Niche CD 1620 (Niche 5) Overhead Boreholes

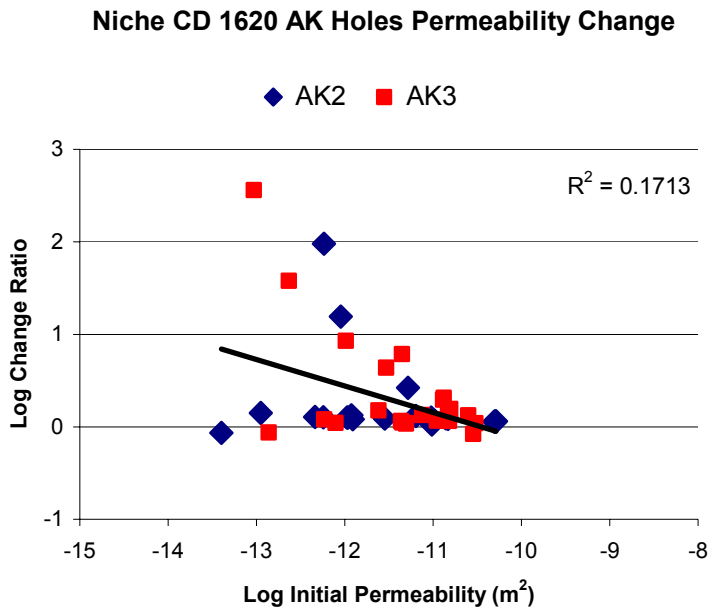

DTN: LB0310AIRK0015.001 [OUTPUT]

Figure 6.1.2-13. Change-Ratio Plots for Niche CD 1620 (Niche 5) AK Boreholes

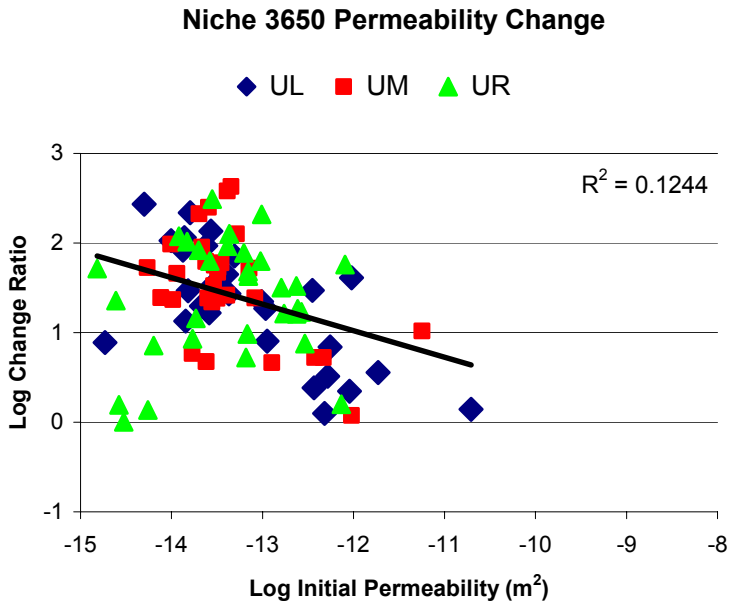

DTN: LB0310AIRK0015.001 [OUTPUT]

Figure 6.1.2-14. Change-Ratio Plot for Niche 3650 (Niche 2)

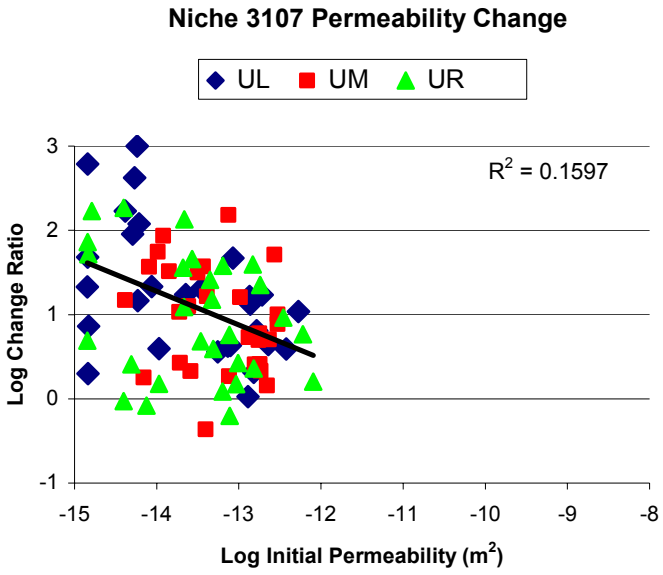

DTN: LB0310AIRK0015.001 [OUTPUT]

Figure 6.1.2-15. Change-Ratio Plot for Niche 3107 (Niche 3)

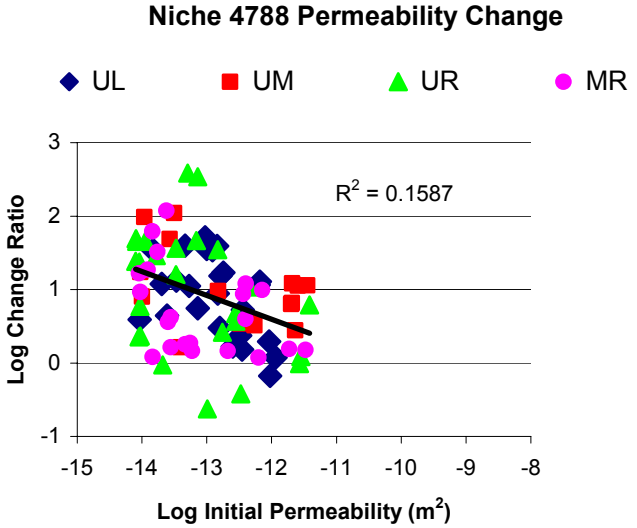

DTN LB0310AIRK0015.001 [OUTPUT]

Figure 6.1.2-16. Change-Ratio Plot for Niche 4788 (Niche 4)

6.1.2.4 Statistical Summary of Air-Permeability Distributions

Table 6.1.2-1 summarizes the average (arithmetic and geometric) values, standard deviations, and ranges of variations in pre- and post-excavation permeability of individual boreholes and of whole niche sites (see Attachment IX.1 for calculations). Also included are the averages, deviations, and ranges of interval change ratios for individual boreholes and whole niches. (The ratios are calculated from the pre- and post-excavation permeability values for each interval before the statistical analyses.) Table 6.1.2-2 shows similar information for the overhead boreholes at Niche CD 1620 (Niche 5). Table 6.1.2-3 shows this information for the side holes at Niche CD 1620 (Niche 5). For assessing the excavation-induced impacts, the analyses in Table 6.1.2-1, Table 6.1.2-2, and Table 6.1.2-3 incorporate retested boreholes only. Drift-scale variations along boreholes and among different boreholes within the same niche test site are larger than differences among different sites. Table 6.1.2-4 shows the statistics from the single data set for Alcove 8. Variability among intervals within boreholes in this case straddle that for the whole site. Also, Alcove 8 shows the largest range of values of any site yet tested.

Table 6.1.2-5 summarizes the geometric means and standard deviations of all clusters of boreholes tested in the ESF as a function of site location and rock type. The permeability values from the excavated boreholes are included in these averaging results. Pre-excavation (log geometric) means and standard deviations were derived from averaging over all possible boreholes in each niche or alcove cluster. (The middle- and lower-level boreholes supplement the upper boreholes to characterize the 3-D space in the test beds and locate flow paths under pre-excavation conditions. After excavation with only upper boreholes in a horizontal plane remaining, the air-permeability tests can characterize only the zones above the niche ceilings.) Because the pre-excavation holes at Niche CD 1620 (Niche 5) are the same set as those for post-excavation testing, both types of tests are included for this case.

Each borehole cluster has a distinct air-permeability character. The spatial variability in permeability is considerable at the borehole-interval scale of 0.3 m before averaging over the 10 m scale along the boreholes and the 100 m^3 volume over the borehole clusters (3 to 7 boreholes). Niche 3107 (Niche 3) and Niche 3566 (Niche 1) each have a "radial" entry in the table, which indicates boreholes that are drilled from inside the niches after excavation. Permeability values from these boreholes for Niche 3107 (Niche 3) (profiles not shown) vary little from those of the pre-excavation boreholes, indicative of the uniformity of the formation around Niche 3107 (Niche 3). For Niche 3566 (Niche 1), however, the radial boreholes that were tested ran through the brecciated zone within the niche wall, and thus exhibited higher permeability than that for the pre-excavation boreholes. The results for the borehole cluster at Alcove 8 show highest standard deviation, which may result from the boreholes' traversal of the contact. The entries in Table 6.1.2-5 for Alcove 4 and Alcove 6 are included for completeness and will be discussed in Section 6.5.

Standard deviation from the statistical analysis is a measure of variability, also referred to as aleatory uncertainty, for natural randomness or heterogeneity (as discussed in Section 6 and in BSC 2002 [158794]). The air-permeability measurement is one of the most effective methods to quantify the natural variability of unsaturated fractured rocks (Cook 2000 [165411]).

Table 6.1.2-1. Summary Statistics of Air Permeability (m^2) along Boreholes above Niches

Borehole	Niche 3650 (Niche 2)			Niche 3107 (Niche 3)			Niche 4788 (Niche 4)		
	Pre-Excavation	Post-Excavation	Post/Pre Ratio*	Pre-Excavation	Post-Excavation	Post/Pre Ratio*	Pre-Excavation	Post-Excavation	Post/Pre Ratio*
Geometric Mean									
UL	7.26E-14	2.09E-12	20.75	2.22E-14	4.55E-13	20.51	1.41E-13	1.07E-12	7.62
UM	4.29E-14	1.64E-12	33.29	5.81E-14	4.82E-13	8.72	1.81E-13	2.56E-12	11.09
UR	4.27E-14	1.01E-12	23.56	3.32E-14	2.64E-13	8.94	6.27E-14	6.27E-13	9.42
All 3	5.07E-14	1.51E-12	25.38	3.50E-14	3.87E-13	11.69	1.05E-13	1.20E-12	9.42
Arithmetic Mean									
UL	8.59E-12	2.98E-11	47.06	8.12E-14	1.46E-12	135.48	2.82E-13	2.07E-12	14.28
UM	1.01E-12	7.78E-12	72.98	1.14E-13	1.55E-12	21.36	8.59E-13	6.19E-12	26.43
UR	1.27E-13	4.59E-12	53.62	1.14E-13	1.04E-12	30.95	4.42E-13	3.79E-12	45.09
All 3	3.24E-12	1.40E-11	57.89	1.03E-13	1.35E-12	62.60	5.05E-13	3.99E-12	28.55
Minimum Value									
UL	1.86E-15	1.45E-14	0.67	1.44E-15	2.90E-15	1.06	9.16E-15	3.57E-14	0.67
UM	5.40E-15	9.88E-14	1.19	4.10E-15	1.24E-14	0.43	8.99E-15	6.56E-14	1.64
UR	1.53E-15	3.02E-15	1.01	1.43E-15	3.72E-15	0.63	8.01E-15	1.98E-14	0.24
All 3	1.53E-15	3.02E-15	0.67	1.43E-15	2.90E-15	0.43	8.01E-15	1.98E-14	0.24
Maximum Value									
UL	1.27E-10	7.15E-10	271.15	5.32E-13	7.99E-12	1229.23	1.15E-12	8.44E-12	51.54
UM	2.28E-11	1.01E-10	427.91	5.15E-13	1.40E-11	153.02	3.56E-12	2.50E-11	110.52
UR	8.07E-13	4.66E-11	310.67	8.06E-13	5.80E-12	184.13	3.83E-12	2.51E-11	386.90
All 3	1.27E-10	7.15E-10	427.91	8.06E-13	1.40E-11	1229.23	3.83E-12	2.51E-11	386.90
Range of Log									
UL	4.83	4.69	2.61	2.57	3.44	3.06	2.10	2.37	1.89
UM	3.63	3.01	2.56	2.10	3.05	2.55	2.60	2.58	1.83
UR	2.72	4.19	2.49	2.75	3.19	2.47	2.68	3.10	3.21
All 3	4.92	5.38	2.80	2.75	3.68	3.45	2.68	3.10	3.21
Std. Dev. of Log									
UL	1.18	0.84	0.69	0.81	0.83	0.83	0.58	0.57	0.54
UM	0.80	0.70	0.62	0.57	0.71	0.61	0.95	0.70	0.58
UR	0.73	1.05	0.66	0.79	0.90	0.74	0.85	0.94	0.84
All 3	0.93	0.88	0.66	0.74	0.82	0.75	0.79	0.78	0.67

Input: Niche 3650 (Niche 2) Pre- and Post-Excavation DTN: LB0011AIRKTEST.001 [153155]

Niche 3107 (Niche 3) Pre-Excavation DTN: LB980901233124.101 [136593], Post Excavation DTN: LB990601233124.001 [105888]

Niche 4788 (Niche 4) Pre-Excavation DTN: LB980901233124.101 [136593], Post-Excavation DTN: LB990601233124.001 [105888]

Summary: DTN: LB0310AIRK0015.001 [OUTPUT]

NOTE: *The post/pre ratio is the ratio of post-excavation to pre-excavation permeabilities. This ratio was calculated for each interval in each borehole. Values reported are the statistical measures (maximum, minimum, mean, etc.) of all post/pre ratios calculated for each borehole. For example, mean of (post/pre) ratio is not the same as the ratio of mean(post)/mean(pre).

*Where more than one measurement of permeability was made at a position, the least value is used in averaging.

Table 6.1.2-2. Summary Statistics of Air Permeability (m^2) along Boreholes above Niche CD 1620 (Niche 5)

Niche CD 1620 (Niche 5) Overhead			
Borehole	**Pre-Excavation**	**Post-Excavation**	**Post/Pre Ratio**
Geometric Mean			
ML	1.23E-11	2.14E-11	1.75
UL	5.54E-12	5.48E-11	9.89
UM	2.40E-12	3.32E-12	1.38
All 3	3.88E-12	9.19E-12	2.37
Arithmetic Mean			
ML	7.88E-11	5.15E-11	2.93
UL	1.75E-11	5.90E-10	22.75
UM	7.58E-11	4.90E-10	17.84
All 3	6.14E-11	4.44E-10	16.65
Minimum			
ML	1.06E-12	3.30E-12	0.11
UL	1.46E-13	1.19E-12	0.74
UM	9.28E-15	4.82E-14	0.00
All 3	9.28E-15	4.82E-14	0.00
Maximum			
ML	2.86E-10	1.82E-10	7.33
UL	4.53E-11	4.03E-09	115.10
UM	1.19E-09	9.51E-09	354.12
All 3	1.19E-09	9.51E-09	354.12
Range of Log			
ML	2.43	1.74	1.82
UL	2.49	3.53	2.19
UM	5.11	5.30	5.19
All 3	5.11	5.30	5.19
Std. Dev of Log			
ML	1.03	0.63	0.57
UL	0.87	1.22	0.63
UM	1.25	1.25	1.19
All 3	1.14	1.27	1.04

DTN: LB0012AIRKTEST.001 [154586] for pre-excavation data; LB0110AKN5POST.001 [156904] for post-excavation data

DTN: LB0310AIRK0015.001 [OUTPUT]

Table 6.1.2-3. Summary Statistics of Air Permeability (m^2) in Boreholes alongside Niche CD 1620 (Niche 5)

Niche CD 1620 (Niche 5) Side			
Borehole	**Pre-Excavation**	**Post-Excavation**	**Post/Pre Ratio**
Geometric Mean			
AK2	3.28E-12	5.41E-12	1.65
AK3	3.98E-12	8.81E-12	2.22
Both	3.61E-12	6.90E-12	1.91
Arithmetic Mean			
AK2	1.09E-11	1.58E-11	5.79
AK3	9.00E-12	1.50E-11	18.53
Both	9.93E-12	1.54E-11	12.16
Minimum			
AK2	4.01E-14	3.44E-14	0.86
AK3	1.46E-13	1.19E-12	0.84
Both	4.01E-14	3.44E-14	0.84
Maximum			
AK2	5.14E-11	5.88E-11	95.51
AK3	3.01E-11	3.40E-11	363.64
Both	5.14E-11	5.88E-11	363.64
Range of Log			
AK2	3.11	3.23	2.05
AK3	2.51	2.45	2.64
Both	3.11	3.23	2.64
Std Dev of Log			
AK2	0.82	0.83	0.44
AK3	0.72	0.61	0.61
Both	0.77	0.73	0.53

DTNs: LB002181233124.001 [146878] for pre-excavation data; LB0110AK23POST.001 [156905] for post-excavation data.

Table 6.1.2-4. Summary Statistics of Air Permeability (m^2) along Boreholes under Alcove 8

Alcove 8		
Borehole	**Geometric Mean**	**Arithmetic Mean**
BH1	1.76E-13	1.71E-10
BH2	6.41E-14	3.48E-13
BH3	1.33E-14	3.55E-13
BH4	6.29E-14	2.44E-10
BH5	5.11E-14	4.93E-13
BH6	1.11E-12	4.19E-11
All 6	8.67E-14	7.52E-11
	Minimum	**Maximum**
BH1	4.72E-15	3.17E-09
BH2	4.83E-15	5.46E-12
BH3	3.61E-15	5.28E-12
BH4	4.45E-15	6.25E-09
BH5	3.60E-15	7.06E-12
BH6	1.48E-14	1.13E-09
All 6	3.60E-15	6.25E-09
	Range of log	**Std Dev of log**
BH1	5.83	1.51
BH2	3.05	0.83
BH3	3.17	0.89
BH4	6.15	1.46
BH5	3.29	0.98
BH6	4.88	1.20
All 6	6.24	1.29

DTN: LB0302ALC8AIRK.001 [164748]

Table 6.1.2-5. Comparison of Geometric Means and Standard Deviations of Niches and Alcoves in the Exploratory Studies Facility at Yucca Mountain

Borehole Cluster	Type of Site	log(k) (m^2)	
		Mean	Standard Deviation
Niche 3566 (Niche 1) Pre-Excavation	Intersects brecciated zone	-13.0	0.92
Niche 3566 (Niche 1) Radial	Predominantly within brecciated zone	-11.8	0.66
Niche 3650 (Niche 2) Pre-Excavation	Moderately fractured welded tuff	-13.4	0.81
Niche 3650 (Niche 2) Post-Excavation	Post-excavation welded tuff	-11.8	0.88
Niche 3107 (Niche 3) Pre-Excavation	Moderately fractured welded tuff	-13.4	0.70
Niche 3107 (Niche 3) Post-Excavation	Post-excavation welded tuff	-12.4	0.82
Niche 3107 (Niche 3) Radial	Moderately fractured welded tuff	-13.8	0.92
Niche 4788 (Niche 4) Pre-Excavation	Highly fractured welded tuff	-13.0	0.85
Niche 4788 (Niche 4) Post-Excavation	Post-excavation welded tuff	-11.9	0.78
Niche CD 1620 (Niche 5) Pre-Excavation side	Highly porous lithophysal cavities; holes on side of excavation	-11.4	0.77
Niche CD 1620 (Niche 5) Post-Excavation side	Highly porous lithophysal cavities; holes on side of excavation	-11.2	0.73
Niche CD 1620 (Niche 5) Pre-Excavation overhead	Highly porous lithophysal cavities; holes above of excavation	-11.4	1.14
Niche CD 1620 (Niche 5) Post-Excavation overhead	Highly porous lithophysal cavities; holes above of excavation	-11.0	1.27
Alcove 4	Discretely faulted and fractured non-welded tuff	-13.0	0.93
Alcove 6	Highly fractured post-excavation welded tuff	-11.9	0.67
Alcove 8	Transition from upper lithophysal to welded fractured nonlithophysal in near-vertical boreholes	-13.1	1.29

DTNs: LB0011AIRKTEST.001 [153155], LB980901233124.101 [136593], LB990601233124.001 [105888], LB980901233124.004 [105855], LB980901233124.009 [105856], LB980912332245.001 [110828]; LB0302ALC8AIRK.001 [164748]; LB0012AIRKTEST.001 [154586]; LB002181233124.001 [146878]; LB0110AK23POST.001 [156905]; LB0110AKN5POST.001 [156904]

Summary: DTN: LB990901233124.004 [123273] (enhanced with Niche CD 1620 [Niche 5] and Alcove 8 results)

INTENTIONALLY LEFT BLANK

6.2 ANALYSIS AND INTERPRETATION OF THE NICHE LIQUID-RELEASE AND SEEPAGE-TEST DATA

The ESF Drift Seepage Test and Niche Moisture Study characterizes the seepage process and furthers our understanding of how moisture could seep into drifts. Specific objectives of the study include:

- Measuring *in situ* hydrological properties of the repository host rock for use in *Seepage Calibration Model and Seepage Testing Data* (BSC 2003 [162267]) and *Seepage Model for PA Including Drift Collapse* (BSC 2003 [163226])
- Providing a database of liquid-release and seepage data that can be used to evaluate seepage and other related UZ processes
- Evaluating drift-scale seepage processes to quantify the extent to which seepage is excluded from entering an underground cavity
- Determining the seepage threshold below which percolating water will not seep into a drift.

The objectives of the study are realized through a combination of field experiments, including air-injection, liquid-release, and seepage tests.

Analytic solutions are used in the data analyses presented in this section to estimate the seepage thresholds, capillary barrier strengths, water-potential values, and characteristic relationships along seepage flow paths. Local homogeneity is the main approximation in the analytic solutions used in estimating the air-permeability values and liquid seepage flow field. Numerical models have been formulated in the Model Report *Seepage Calibration Model and Seepage Testing Data* (BSC 2003 [162267]) to evaluate the effects of spatial heterogeneity on the effective seepage parameters, with the heterogeneity field based on the air-permeability distribution (described in Section 6.1). The seepage calibration model is the basis for other model reports in estimating the seepage fraction and distribution over the potential waste-emplacement drifts. The subsequent model reports include *Seepage Model for PA Including Drift Collapse* (BSC 2003 [163226]) and *Abstraction of Drift Seepage* (BSC 2003 [165564]).

Some of the early results based on short-duration releases of pulses above the first niche tested are enhanced by later tests in other niches with long durations, so that the liquid-release rates and seepage rates can approach steady state. The short-duration tests, originally designed to simulate the arrivals of episodic percolation events through fast flow paths into ventilated drifts, do not provide the data sets needed by the seepage calibration model and other PA models, which emphasize steady-state conditions in sealed drifts under post-emplacement conditions.

6.2.1 Review of Data Obtained from Liquid-Release and Seepage Tests Conducted at Niches

This section provides a general overview of the tests, including field activities performed prior to, during, and after the niches were excavated.

6.2.1.1 Pre-Excavation Liquid-Release Test Data

Before seepage tests in excavated niches, the niche test sites are characterized by air-permeability tests (Section 6.1) and by liquid-release tests. The pre-excavation liquid-release tests introduce a finite amount of dyed water to characterize the flow paths within the niche space. The main objective is to determine the relative strength between the gravity force that moves the liquid downward and the capillary forces that tend to spread the liquid laterally. The characterization of the flow paths is conducted during niche excavation (Section 6.2.1.2).

Hundreds of air-injection tests were conducted in the boreholes at niche sites prior to excavation. The test results were used to determine the distribution of single-borehole air permeabilities within the rock mass (refer to Section 6.1 in this scientific analysis report). These data were then used to select test intervals for subsequent liquid-release tests. The intervals selected for liquid-release testing exhibited a wide range of air permeabilities, including both high and low values.

Liquid-release tests were conducted in the same boreholes as the air-injection tests by pumping water containing colored or fluorescent dyes at a constant rate into various 0.3 m long test intervals. A finite amount of dye-spiked water, typically 1 liter, was introduced into each test interval, slowly to minimize buildup of fluid pressure in the test interval. Various colored and fluorescent tracers were used during the study to document the flow path traveled by the wetting front. Hereafter, the term "water" will be used to describe the test fluid, which may or may not have contained tracer.

Pre-excavation liquid-release tests were performed during early June and early August 1997, in boreholes installed prior to the excavation of Niche 3566 (Niche 1) and Niche 3650 (Niche 2), respectively. Pre-excavation liquid-release tests were performed at Niche 3107 (Niche 3) and Niche 4788 (Niche 4), starting in late April and late June 1998, respectively. Pre-excavation liquid-release tests were also performed at Niche CD 1620 (Niche 5) in the lower lithophysal zone in April 2000. The data from these pre-excavation tests, including the mass of water released, pumping rates and times, and liquid-release rates, were tabulated and entered into the TDMS, and assigned DTN: LB980001233124.004 [136583] for Niche 3566 (Niche 1) and Niche 3650 (Niche 2); DTN: LB980901233124.003 [105592] for Niche 3107 (Niche 3) and Niche 4788 (Niche 4); and DTN: LB0102NICH5LIQ.001 [155681] for Niche CD 1620 (Niche 5). The tables include directly measured mass, pumping rates, return flow rates, and derived quantities of average liquid release rates from the differences of the measured rates.

6.2.1.2 Niche Excavation Activities

The niches were excavated with an Alpine Miner, a mechanical device, using minimal water to observe and photograph the distribution of fractures and dye within the welded tuff. As reported in DTN: LB980001233124.004 [136583], dye was observed along individual fractures as well as along intersecting fractures to depths ranging from 0 to 2.6 m below the liquid-release points at the Niche 3566 (Niche 1) and Niche 3650 (Niche 2) sites. Dye was observed at a maximum depth of about 1.2 m below the release point at Niche 3107 (Niche 3) and about 1.8 m at Niche 4788 (Niche 4), as reported in DTN: LB980901233124.003 [105592]. Dye was observed at a maximum depth of about 1.4 m below the release point at Niche CD 1620 (Niche 5), as reported in DTN: LB0102NICH5LIQ.001 [155681]. (In this scientific analysis report, TDMS DTN and data report table name are both identified if many files are in a given DTN.) Flow of water through a relatively undisturbed fracture-matrix system was documented in this manner.

During the mining operation at Niche 3566 (Niche 1) and Niche 3650 (Niche 2), two types of flow paths were observed in the field, based on the observed pattern of dye: (1) flow through individual or small groups of high-angle fractures; and (2) flow through several interconnected low- and high-angle fractures, creating a fracture network. Dye was observed along individual fractures and fracture networks to a maximum depth of 2.6 m below the release points in the middle nonlithophysal zone (Tptpmn) of TSw. The vertically elongated dye pattern suggests that water is predominantly flowing downwards. In contrast, an approximately spherical dye pattern centered at the release point was observed at Niche CD 1620 (Niche 5), located in the lower lithophysal zone (Tptpll) of TSw. Dye was observed in fractures and lithophysae to a maximum depth of 1.4 m. Here, the dye patterns were more symmetric, with the lateral edges of the wetted area lying about equal distance from the release point.

Figure 6.2.1-1 compares examples of flow paths observed in the Tptpmn at Niche 3566 (Niche 1) with dye patterns observed in the Tptpll at Niche CD 1620 (Niche 5) (See Section 6.1.2.2 for the observation of a damp feature included in the figure). The observed damp feature and the dye patterns suggest that flow through fractures in the Tptpmn is predominately gravity-driven. In contrast, the symmetry of the dye patterns observed in the Tptpll suggests that capillary forces may be more important in this zone.

Dye was observed in numerous lithophysae in the Tptpll. There was no direct field evidence that water accumulated and dripped into the cavities, even though the liquid-release fluxes applied during the test were 1,000 times greater than the natural flux estimated at 10 mm/yr. No dye stains on the ceiling were observed to line up directly above stains on the floor of the cavities. An example of dye observed on the floor of a lithophysal cavity is illustrated in Figure 6.2.1-1d, suggesting capillary-induced upward fluid movement is a likely mechanism to introduce fluid into the cavity.

It is surprising that capillary forces appear to be stronger in the Tptpll, because the average air-permeability of the Tptpll is greater than the Tptpmn. Typically, capillary forces are less important in higher-permeability media than in lower-permeability materials. This may indicate that the air-permeability measurements performed in the Tptpll are influenced by the lithophysal cavities, which may connect relatively large fractures with smaller fractures, effectively contributing to the relatively strong capillarity.

Note that some of the lithophysae had a thick layer of drill cuttings (i.e., dust) coating their surfaces. This layer of dust could influence the flow (dye) patterns and depth of wetting-front migration observed in the Tptpll. This dust was introduced into the cavities intersecting the borings when the boreholes were air cored. The dust could act as a highly transmissive surface zone (compared to the rock matrix) that could enhance the uniform spread of the wetting front. The dust could also impede the movement of water and dye through the fractures by imbibing and retaining the moisture close to the point of release.

In general, the maximum distance that the wetting front traveled through the Tptpmn from the point of injection to the furthest point of observation increased with the mass of water injected. The data did not show that the type of flow (i.e., network or vertical fracture flow) had any significant influence on the maximum travel distance. Figure 6.2.1-2 shows that on average, the wetting front traveled much deeper (i.e., had a larger aspect ratio) for tests conducted in the Tptpmn compared to tests performed in the Tptpll. Computation of the aspect ratio was performed in the Excel spreadsheet documented in Attachment II, Table II-1. The average line for Tptpll in Figure 6.2.1-2 is influenced by a single data point with high aspect ratio (possibly associated with a fracture or fractures connected to the borehole—Trautz 2001 [157022] p. 69). Without this data point, the average is much closer to 1 (i.e., the aspect ratio of a spherical pattern.)

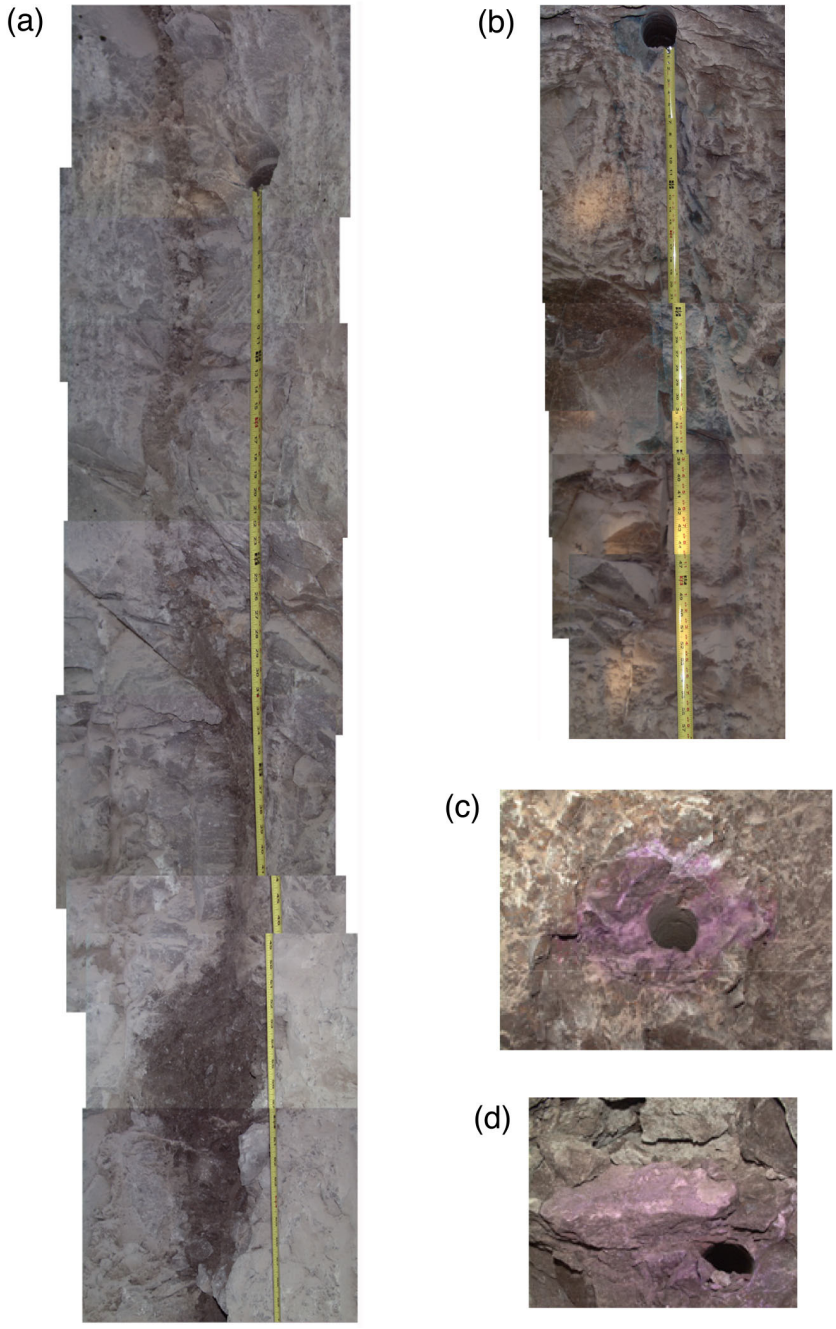

Source: Wang et al. (1999 [106146], Figures 4a, 4c); Trautz (2001 [157022] pp. 79, 84).

Figure 6.2.1-1. Photographic Illustrations of Flow Paths Observed During Niche Excavations: (a) Ambient Flow Path at Niche 3566 (Niche 1), (b) Blue-Dyed Flow Path at Niche 3566 (Niche 1), (c) Pink-Dyed Flow Path at Niche CD 1620 (Niche 5), (d) Pink Stain on the Floor of a Lithophysal Cavity at Niche CD 1620 (Niche 5)

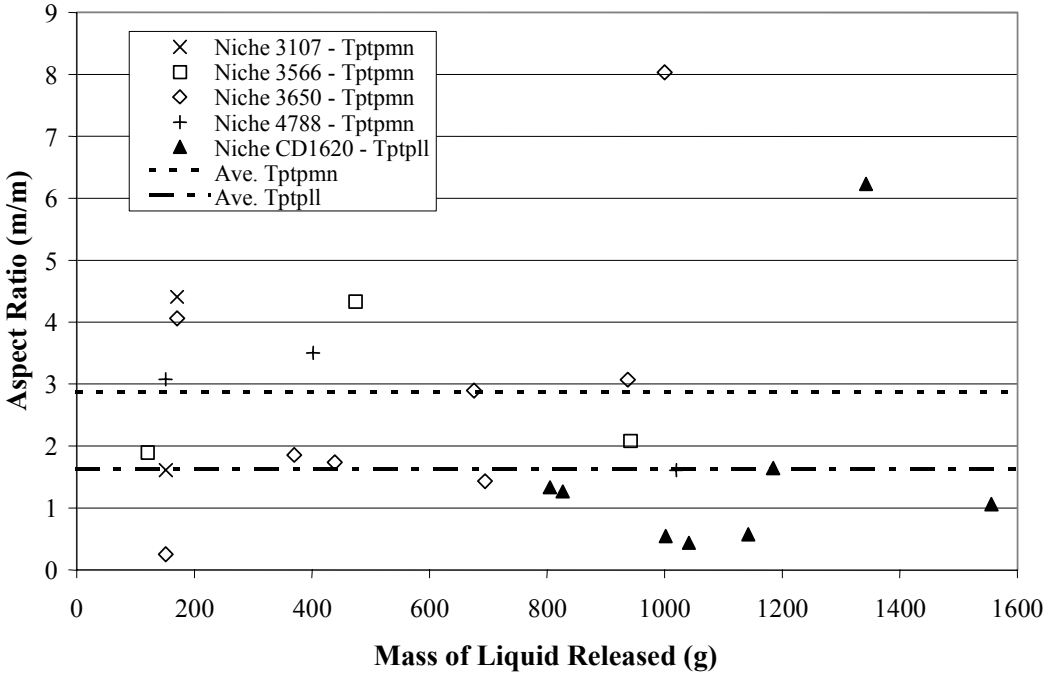

DTN: LB980001233124.004 [136583], DTN: LB980901233124.003 [105592],
DTN: LB0102NICH5LIQ.001 [155681].
DTN: LB0110LIQR0015.001 [OUTPUT]

Figure 6.2.1-2. Mass of Water Released Versus Aspect Ratio

6.2.1.3 Post-Excavation Seepage Tests

A series of seepage tests was performed at Niche 3107 (Niche 3), Niche 3650 (Niche 2), and Niche 4788 (Niche 4). In general, the tests were used to quantify the amount of water seeping into the drift from a localized water source of known duration and intensity. The tests were also used to establish the niche seepage-threshold (K_o^*), defined as the largest flux of water that can be introduced into the test borehole without resulting in seepage into the niche. The borehole flux values were derived from the pumping rate and the wetted area estimated for the borehole interval. This definition of niche seepage threshold is different from the definition used by PA, in which the seepage threshold related to the steady-state background percolation flux averaged over drift scale and site scale areas.

The seepage tests were conducted after the niches were excavated by pumping water into select test intervals in borehole UL, borehole UM, and borehole UR located above each niche. The distance from the test intervals to the niche ceiling ranges from 0.58 to 1.23 m for all the niche sites. (Computation of the distance is inserted in an Excel spreadsheet documented in Attachment II, Table II-2.) The tests were performed by sealing a short interval of borehole using an inflatable packer system, similar to the system used in air-injection tests as described in Attachment I. Any water that migrated from the borehole to the niche ceiling and dripped into the opening was captured and weighed.

For each packer interval, a liquid-return (overflow) line prevented buildup of excess pressure. If the liquid injection rate was high and return flow was observed, the liquid-release rate was

determined by the difference between injection flow rate and return flow rate (if any). The observation of return flows would indicate that the pumping rate exceeded the saturated hydraulic conductivity of the borehole interval. (For tests with small liquid volume in cases with significant storage in the borehole interval, no return flow did not imply that the pumping conditions represented unsaturated conditions.)

6.2.1.3.1 Niche 3650 (Niche 2) Seepage-Test Data

Forty niche seepage tests were performed on 16 test intervals positioned above Niche 3650 (Niche 2) beginning in late 1997 and ending in early 1998. Water migrated through the rock and seeped into the niche in 10 out of the 16 zones tested. The niche seepage threshold was determined for the 10 zones that seeped. Seepage and liquid-release data were tabulated and entered into the TDMS, where it was assigned DTN: LB980001233124.004 [136583].

The mass of water released to the formation was computed by mass balance. In turn, the liquid-release rate (Q_s) for each test was computed by dividing the mass released by the respective duration of each test; thus, these values represent time-averaged rates. The rate at which water was released to the formation ranged from 0.007 to 2.892 g/s, and the total mass released ranged from 274.5 to 5597.5 g per test, as summarized in DTN: LB980001233124.004 [136583].

When water appeared at the niche ceiling during a test and dripped into the opening, it was collected in the capture system and weighed. Figure 6.2.1-3 shows the approximate location of the capture system and test intervals relative to the niche boundaries, and the sequence of dyes and number of tests performed on each test interval. The wetting front typically arrived at the niche ceiling directly below the test zone. Most of the water was typically captured in only one or two 0.3 × 0.3 m cells located directly beneath the test interval.

In the immediate vicinity of locations where the niche ceiling and the conducting fractures intersect, the relative humidity could be high from local evaporation. However, the localized humid conditions were not met everywhere within the niche and/or the ESF Main Drift. Maintenance of high relative humidity conditions was important for long-term seepage tests, since the evaporation effects could have a substantial impact on the analysis of seepage data, with models setting post-emplacement high-humidity conditions in seepage threshold estimation. The potential impact of evaporation effects are discussed in Section 6.7 of the Model Report U0080 *Seepage Calibration Model and Seepage Testing Data* (BSC 2003 [162267]).

The mass of water captured ranged from 0.0 to 568.6 g per test, as reported in DTN: LB980001233124.004 [136583]. The niche seepage percentage is defined as the mass of water that dripped into the capture system, divided by the mass of water released to the rock:

$$\textit{Niche Seepage Percentage} = 100 \times \frac{\text{"}\textit{Mass Captured}\ (g)\text{"}}{\text{"}\textit{Mass Released}\ (g)\text{"}} \qquad \text{(Eq. 6.2.1-1)}$$

The niche seepage percentage ranged from 0% for zones that did not seep, to 56.2% for a predominantly gravity-driven flow through a highly saturated fracture (DTN: LB980001233124.004 [136583]).

The niche seepage tests at Niche 3650 (Niche 2) were conducted with a relatively small amount of liquid over short duration, with multiple tests over multiple borehole intervals. To address the model needs of steady-state data in controlled relative humidity conditions, the later tests in Niche 3107 (Niche 3) and Niche 4788 (Niche 4) were conducted in selected borehole intervals with large amounts of liquid over a long duration, as described in the following two sections.

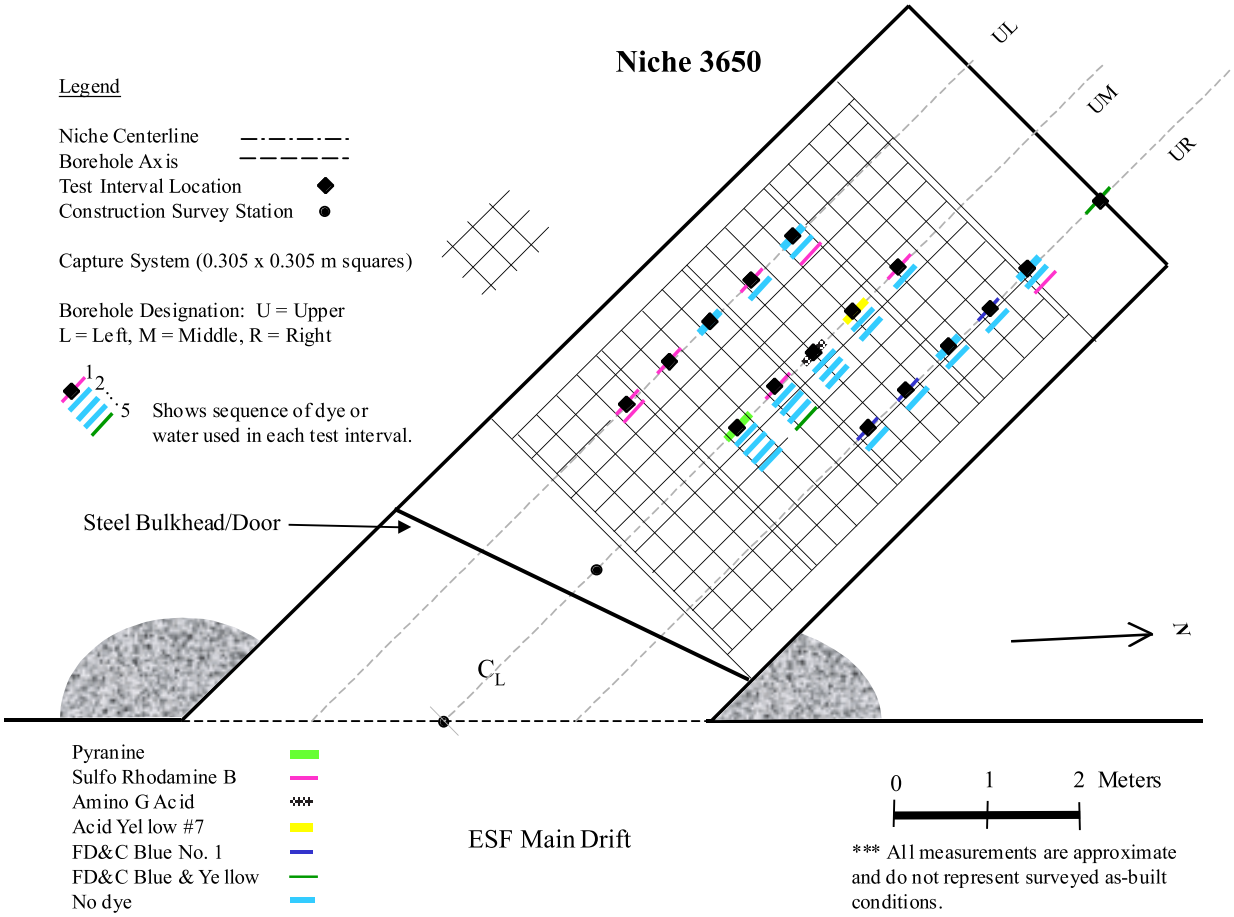

Figure 6.2.1-3. Schematic Illustration of Seepage Capture System and Test Intervals at Niche 3650 (Niche 2)

6.2.1.3.2 Niche 3107 (Niche 3) Seepage-Test Data

Beginning in early 1999 and ending in late 1999, twelve niche seepage tests were performed on two test intervals positioned above Niche 3107 (Niche 3). Water migrated through the rock and seeped into the niche for one out of the two zones tested. Niche seepage threshold was determined for the zone that seeped. The seepage and liquid-release data were tabulated and entered into the TDMS, where it was assigned DTN: LB0010NICH3LIQ.001 [153144]. As noted in Section 6.2.1.3.1, the borehole flux values were derived from the pumping rate and the wetted area estimated for the borehole interval. This definition of niche seepage threshold is different from the definition used by PA, with the seepage threshold related to the steady-state background percolation flux averaged over drift scale and site scale areas.

As with Niche 3650 (Niche 2), the mass of water released to the formation was computed by a mass balance. The liquid release-rate (Q_s) for each test was computed by dividing the mass released by the respective duration of each test; thus, these values represent time-averaged rates. The rate at which water was released to the formation ranged from 0.014 to 0.102 g/s for all of the tests, and the mass released ranged from 4,229.5 to 23,831.4 g per test.

When water appeared at the niche ceiling during a test and dripped into the opening, it was collected in the capture system and weighed. The wetting front typically arrived at the niche ceiling directly below the test zone. Most of the water was typically captured in only one or two 0.3 × 0.3 m cells located directly beneath the test interval. The mass of water captured ranged from 0.0 to 15,715.1 g per test. The seepage percentage defined by Equation 6.2.1-1 ranged from 0% for zones that did not seep to 70.1%.

The niche seepage tests were conducted with the bulkhead doors at the entrance to the niche closed and sealed. Also, the air space within the niche was artificially humidified to increase the relative humidity as high as practical to minimize the effects of evaporation resulting from ESF ventilation. One open-faced water bath was placed inside the niche to freely supply moisture to the niche space. The water loss volume resulting from evaporation was used to estimate the average evaporation rate over the niche space. The test conditions (e.g., high humidity and low evaporation rates) are representative of steady seepage into a drift that could potentially occur after the repository is closed, the heat load and temperature rise from the decaying waste have dissipated, and air in the sealed repository equilibrates with the surrounding rock is at or near 100% relative humidity. The relative humidity and temperature within Niche 3107 (Niche 3) is shown in Figure 6.2.1-4.

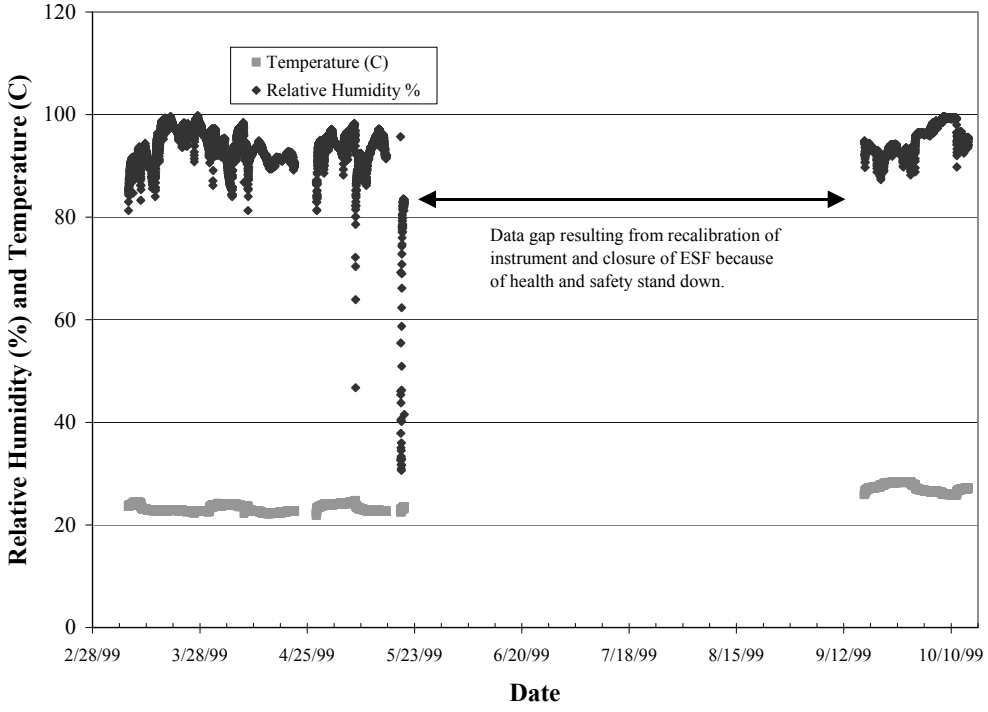

DTN: LB0010NICH3LIQ.001 [153144]

Figure 6.2.1-4. Relative Humidity and Temperature Inside Niche 3107 (Niche 3)

6.2.1.3.3 Niche 4788 (Niche 4) Seepage-Test Data

Beginning in late 1999 and ending in mid-2000, 13 niche seepage tests were performed on three test intervals positioned above Niche 4788 (Niche 4). Water migrated through the rock and seeped into the niche from all zones tested. The niche seepage threshold was determined for two of the three zones that seeped. The seepage and liquid-release data were tabulated and entered into the TDMS, where it was assigned DTN: LB0010NICH4LIQ.001 [153145]. As noted in Section 6.2.1.3.1 for Niche 3650 (Niche 2) and Section 6.2.1.3.2 for Niche 3107 (Niche 3), the borehole flux values for Niche 4788 (Niche 4) were derived from the pumping rate and the wetted area estimated for the borehole interval. This definition of niche seepage threshold is different from the definition used by PA, with the seepage threshold related to the steady-state background percolation flux averaged over drift scale and site scale areas.

The long-duration data from Niche 4788 (Niche 4) were analyzed in Section 6.6 of the Model Report U0080 *Seepage Calibration Model and Seepage Testing Data* (BSC 2003 [162267]). The seepage calibration model analyzed the transient behavior, storage effects, and memory effects between separate tests to determine the effective seepage parameters. The parameters were then used in the Model Report U0075 *Seepage Model for PA Including Drift Collapse* (BSC 2003 [163226]) to determine the seepage threshold flux relative to percolation flux. The final

input to TSPA is evaluated in the Model Report *Abstraction of Drift Seepage* (BSC 2003 [165564]).

As with Niche 3107 (Niche 3) and Niche 3650 (Niche 2), the mass of water released to the formation was computed by a mass balance. The liquid-release rate (Q_s) for each test was computed by dividing the mass released by the respective duration of each test; thus, these values represent time-averaged rates. The rate at which water was released to the formation ranged from 0.008 to 0.092 g/s for all of the tests, and the mass released ranged from 1,474.9 to 39,514.6 g per test.

When water appeared at the niche ceiling during a test and dripped into the opening, it was collected in the capture system and weighed. The wetting front typically arrived at the niche ceiling directly below the test zone. Most of the water was typically captured in only one or two 0.3 × 0.3 m cells located directly beneath the test interval. The mass of water captured ranged from 0.0 to 15,555.1 g per test. The niche seepage percentage defined by Equation 6.2.1-1 ranged from 0% to 68.7%.

Again, the seepage tests were conducted with the bulkhead doors at the entrance to the niche closed and sealed, and the air space within the niche was artificially humidified to minimize evaporation. Figure 6.2.1-5 shows the relative humidity and temperature inside of Niche 4788.

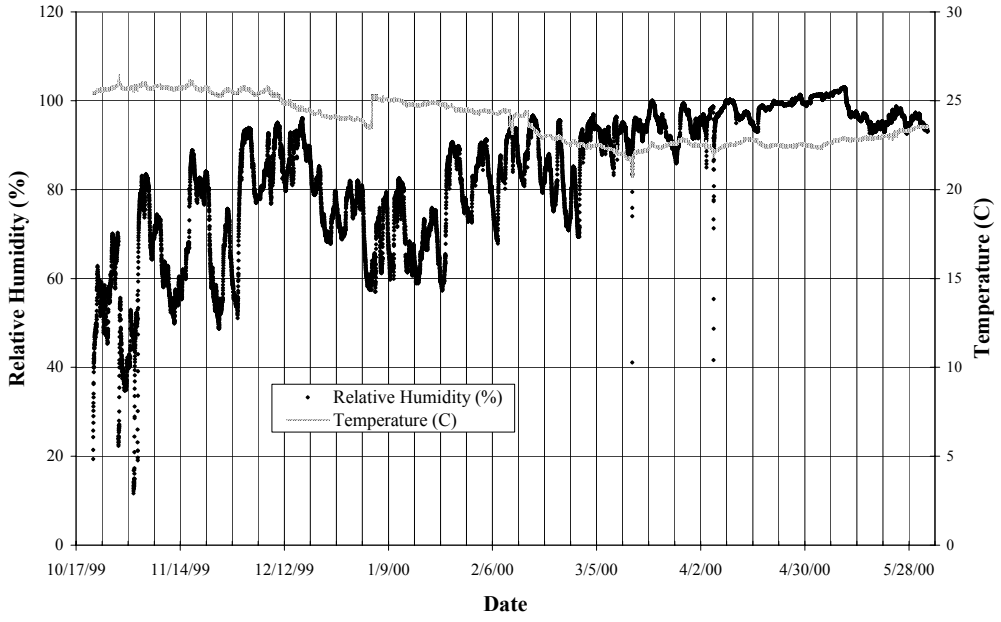

DTN: LB0010NICH4LIQ.001 [153145]:
native data file Niche4 h&T 3-10-00.csv,
Niche4 RH&T 4-1-00.csv, and
Niche4788 R&T 6-8-00.csv;
data report S00429_007.

Figure 6.2.1-5. Relative Humidity and Temperature Inside Niche 4788 (Niche 4)

Figure 6.2.1-6 illustrates the release rate into a borehole interval, the return rate, and the stabilization of niche seepage rate of water collected in the niche trays. If tests were not long enough before niche stabilization, the niche seepage ratio was not well defined. Various operating conditions and niche moisture conditions may contribute to the fluctuations observed in the early time data. The execution of long-duration tests to ensure quasi-steady conditions contributed to the robustness of seepage quantification at selected borehole intervals.

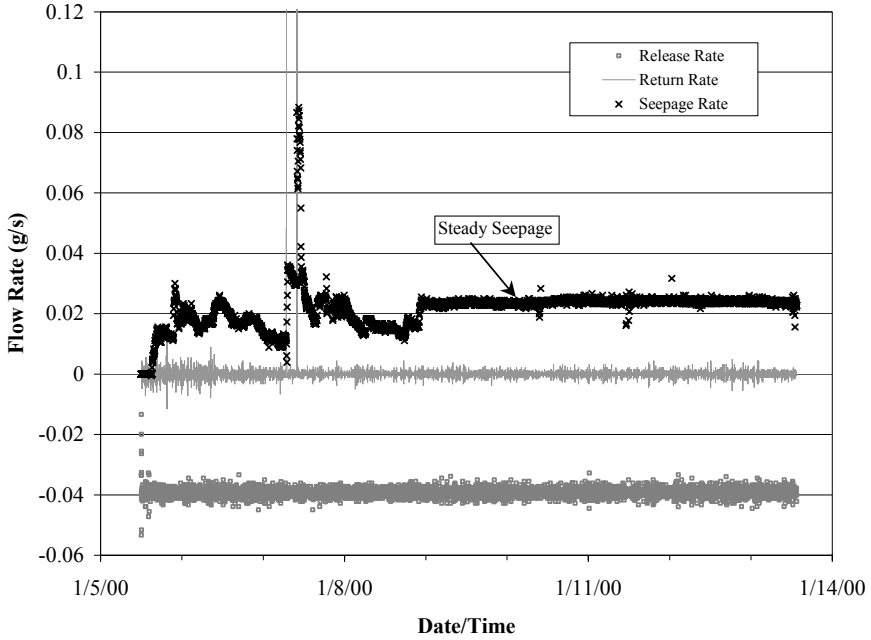

DTN: LB0010NICH4LIQ.001 [153145]:
native data file Niche 4788 UR 5.18-5.48m 1-5-2000.csv,
data report S00429_007.

Figure 6.2.1-6. Stabilized Flow Rates Observed during Test #1 1-5-00 Conducted on Test Interval UR at Niche 4788 (Niche 4)

6.2.1.3.4 Niche 4788 (Niche 4) Wetting-Area Data

In this section, an example of niche wetting-area data from a seepage test run in Niche 4788 (Niche 4) is discussed. The progression of the wetting fronts with time was recorded on videotape, and still images from the videos were captured and digitized. Wetting fronts were traced from these captured still images; they were later adjusted by reference to marked grid points and other features on the niche crown, and to sketches made during the tests, to correct for distortion caused by the camera's oblique angle of view to the niche crown. They were then superimposed over corresponding areas of a fracture map of the niche crown (Trautz 2001 [156903], pp. 57–62).

Figure 6.2.1-7 shows the wetting-front sequence for a seepage test begun June 26, 2000, with water released from the interval 7.62–7.93 m from the collar of the borehole UL. The release rate at the borehole interval was 0.02 g/s, and the seepage into the niche corresponded to 14% of the water released.

Several observations can be made from Figure 6.2.1-7. With regard to fractures, their presence has a variable impact on the progress of the wetting fronts. Influence of fractures appears relatively minor in the June 26, 2000, test (although a general upper-left-to-lower-right elongation of the fronts may reflect preferred fracture orientation). Also, the initial wetting fronts in these tests are displaced laterally from the vertical projections (the shortest paths) of the release intervals onto the crown, and the wetting fronts overall are not symmetrical about those projections, which suggest a role for fractures in directing flow in the niche crown.

Figure 6.2.1-8 shows the wetting-front growth with time for the seepage test. Each data point corresponds to one of the numbered contours in Figure 6.2.1-7. The x-axis refers to time elapsed since the first wet spot appeared on the crown, rather than from the first release of water.

The plot in Figure 6.2.1-9 pertains to the shape progression of the wet spot. If a front's 2-D shape remained constant as it grew, with subsequent fronts expanding uniformly and maintaining shape similarity between them, the slope of its line in Figure 6.2.1-9 would be constant. This is nearly the case through the early part of the test, with somewhat greater irregularity seen after the eight or ninth front (or data point). The average value of the slope for this test is ~0.25, somewhat less than the 0.28 slope, which would apply for a circle; this reflects the slightly elongated wetting fronts observed for this test.

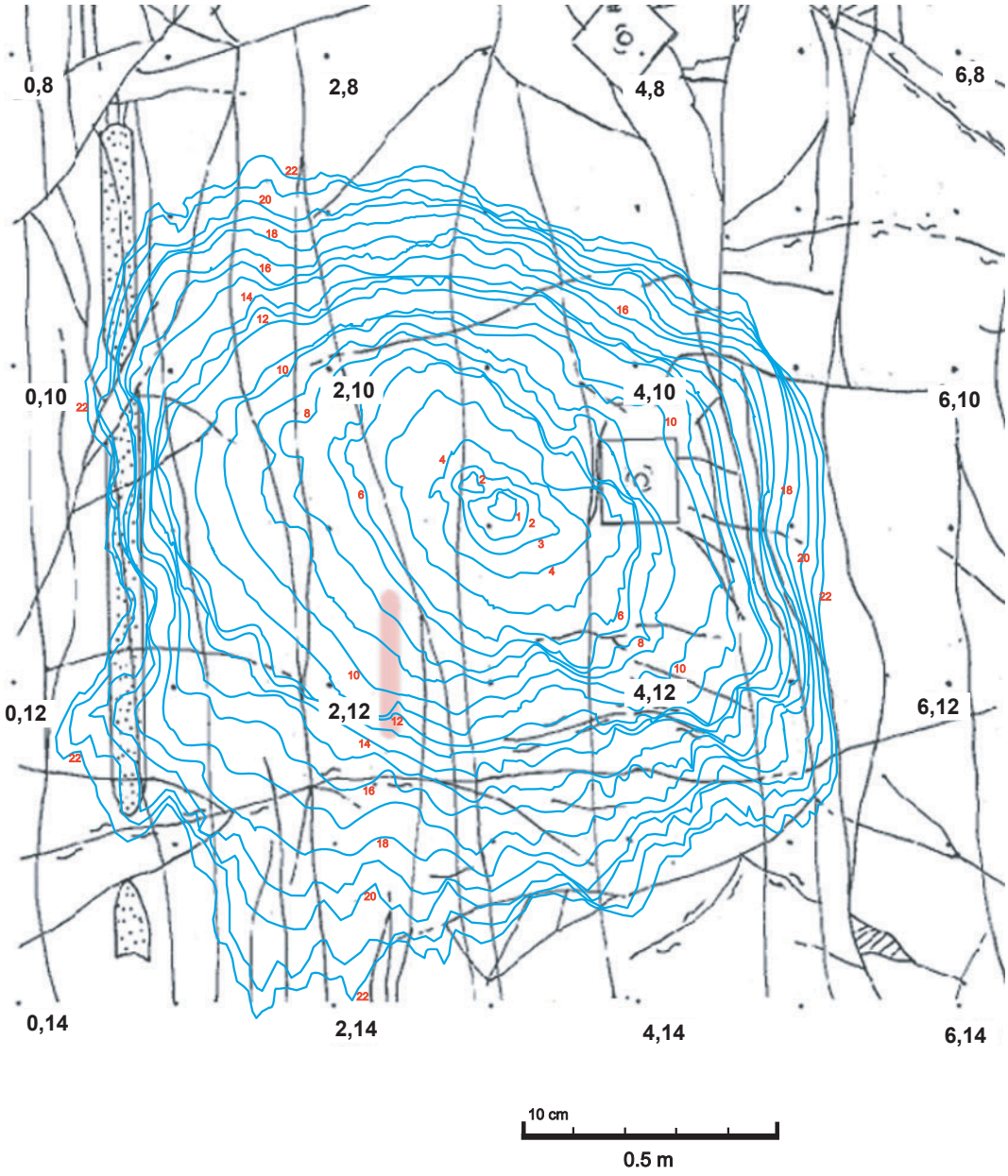

DTN: LB0110NICH4LIQ.001 [OUTPUT]

NOTE: Blue contours are outlines of wetting fronts. Numbers along wetting fronts correlate with the order of data points in Figure 6.2.1-8, and the time corresponding to each front can be determined from that figure. Pink bars indicate approximate positions of release intervals in boreholes above niche, projected onto crown.

Figure 6.2.1-7. Wetting-Front Sequences Overlying Fracture Map of Niche 4788 (Niche 4) Crown from Seepage Test Begun June 26, 2000

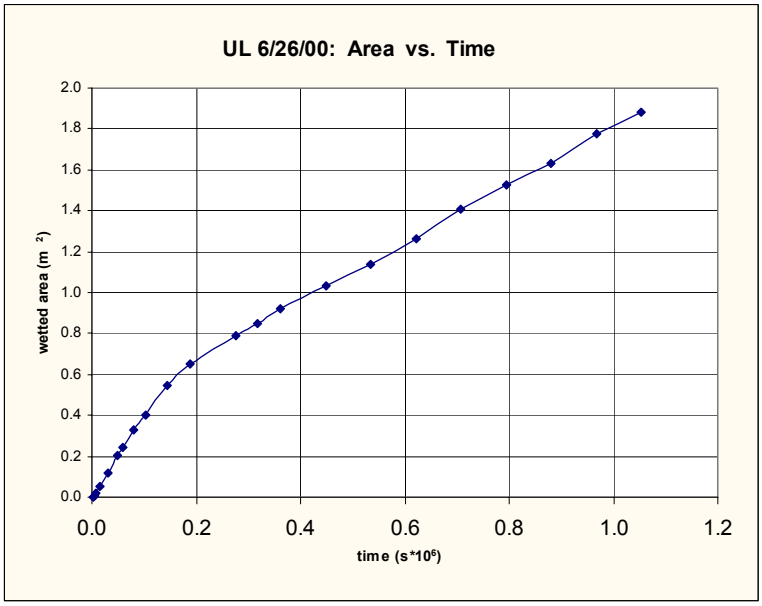

DTN: LB0110NICH4LIQ.001 [OUTPUT]

NOTE: Each plotted point represents data for one of the numbered curves shown in Figure 6.2.1-7.

Figure 6.2.1-8. Wetting-Front Area (m^2) versus Time (s) for the Seepage Test Shown in Figure 6.2.1-7

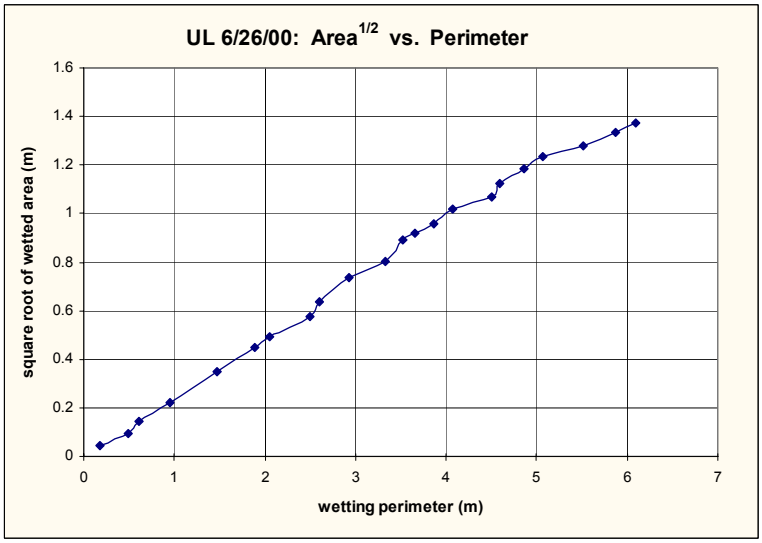

DTN: LB0110NICH4LIQ.001 [OUTPUT]

NOTE: Data points correspond to those in Figure 6.2.1-8.

Figure 6.2.1-9. Square Root of Area (m) Plotted versus Perimeter (m) for Each of the Wetting Fronts in the Niche 4788 (Niche 4) Seepage Test

6.2.1.3.5 Niche CD 1620 (Niche 5) Slot and Seepage-Threshold Tests

6.2.1.3.5.1 Background Information

The study site is located at cross-drift construction station (CD) 16+20 near the center of the ECRB and the repository block shown in Figure 6.1.1-1, and is known as Niche CD 1620 or Niche 5. The site was selected because it is located near the center of the repository block within the lower lithophysal zone (Tptpll) of the Topopah Spring welded tuff (TSw). Approximately 80% of the repository would be constructed within the Tptpll zone, given the current design (BSC 2003 [164491], 800-IED-WIS0-00103-000-00Ab; BSC 2003 [164889] Attachment VIII for area fractions: Tptpul: 4.5%, Tptpmn: 12.4%, Tptpll: 80.5%, Tptpln: 2.6%). Thus, characterization of seepage into waste emplacement drifts constructed in this zone is important to the performance and design of natural and engineered barriers.

The Tptpll contains large naturally occurring cavities called lithophysae that are attributed to gas and vapor-phase constituents entrapped and redistributed during the initial deposition, compaction, and gas migration out of the TSw (Buesch and Spengler 1998 [101433], p. 21). Lithophysae cavities are quite large at the site, with some ranging from 0.5 to 0.75 m in length and 0.2 to 0.3 m in height. Fractures are also present, but the majority of these appear to be cooling features associated with lithophysae cavities. These fractures primarily form halos or rinds around the cavities. Very few through-going fractures of significant length were mapped. However, given the high permeability of the rock observed at Niche CD 1620 (Niche 5) and reported in Section 6.1.2, the fracture rinds and lithophysae cavities do not appear to be dead-end features. Rather, short fractures appear to link the cavities and rinds, giving the entire network a larger overall average permeability than was observed in the densely welded, middle nonlithophysal zone (Tptpmn) of the TSw, where fractures dominate and lithophysae are sparse.

As noted in Section 6.2.1.1, liquid-release tests were performed at Niche CD 1620 (Niche 5) in April 2000 prior to the construction of the access drift and niche in May 2000 described in Section 6.2.1.2. Bulkhead doors were installed across the entrance to the excavation and sealed immediately upon construction to minimize evaporation and drying of the rock surrounding the drift. An initial post-excavation seepage test was performed in late February 2001 and ended approximately 39 days later in April 2001. Water did not seep, nor did the wetting front appear at the niche ceiling during this test after releasing approximately 300 liters of water. (Data are not provided for this test because, with the exception that no seepage was observed after releasing a large volume of water, they are inconsequential.) This test showed that the Tptpll had a high storage capacity (because of the large lithophysae) or was able to divert large quantities of water laterally around the drift through preferential flow paths not connected directly to the opening.

The lack of seepage and the failure of the wetting front to appear at the niche ceiling during the initial test prompted significant changes to the objectives of the seepage-testing program planned for Niche CD 1620 (Niche 5). A slot was constructed in the sidewall of the original niche that could be used to accomplish the following objectives, supplementing those described in Section 6.2:

- Demonstrate that the capillary barrier moves water laterally around the opening to the walls of the niche, where it would collect in the slot.

- Provide a water mass balance. The mass balance was intended to show that the flow field had reached steady state by demonstrating that the amount of water released to the formation was balanced by the amount of water recovered as seepage from the niche ceiling and slot, plus the unrecovered amount of water lost to evaporation as the wetting front spread across the niche ceiling.

The sections that follow describe the test configuration, operation, and equipment used to address these objectives and provide representative test results showing the type of data collected.

6.2.1.3.5.2 Description of Post-Excavation Seepage Tests

Test Configuration

Seven 15 to 17 m long boreholes were drilled in January 2000 at the Niche CD 1620 (Niche 5) site (shown in Figures 6.2.1-10 through 6.2.1-12) prior to niche construction. Each borehole is nominally 0.0762 m (3 inches) in diameter, with the exception of borehole ECRB-Niche1620#7, which was mistakenly drilled to a nominal diameter of 0.1016 m (4 inches) using a larger-diameter core bit. (Boreholes will be referred to hereafter by number only [e.g., #7] and not by their full designation [e.g., ECRB-Niche1620#7].) Post-excavation seepage tests were not performed on borehole #7, because the straddle packer system used to isolate the injection zone was not designed to fit the larger diameter hole.

The first borehole (#1) was installed at the approximate position shown in Figure 6.2.1-10 through Figure 6.2.1-12. Dye-spiked water was released into eight 0.3 m long test intervals within this borehole prior to niche construction, as noted in Section 6.2.1.1. The position of the dye within the rock was then photographed and mapped during niche excavation, and borehole #1 was intentionally removed during the mining process described in Section 6.2.1.2. A set of three boreholes (designated #2, #3, and #4) were drilled parallel to the axis of the niche in the same horizontal plane, located about 1.0 to 1.3 m above the opening of the niche. These boreholes are collectively referred to as the horizontal boreholes. The horizontal boreholes are spaced approximately 1 m apart.

A second set of three boreholes (designated #5, #6, and #7) were drilled parallel to the niche axis, but at a 6 to 8º angle upward (based on as-built information in DTN: MO0209GSC02116.000 [160407], approximately 1º higher than the designed angle in Figure 6.2.1-10). These boreholes are collectively referred to as the inclined boreholes. The collar of the inclined boreholes is located directly above and within 0.4 to 0.5 m of the horizontal boreholes. The upper boreholes are inclined so that the distance between the boreholes and the niche ceiling varies from about 1.4 to 3.0 m. In combination with the horizontal boreholes, the scale of the post-excavation seepage tests can vary from 1.0 to 3.0 m, the latter measurement being slightly larger than the radius of the niche.

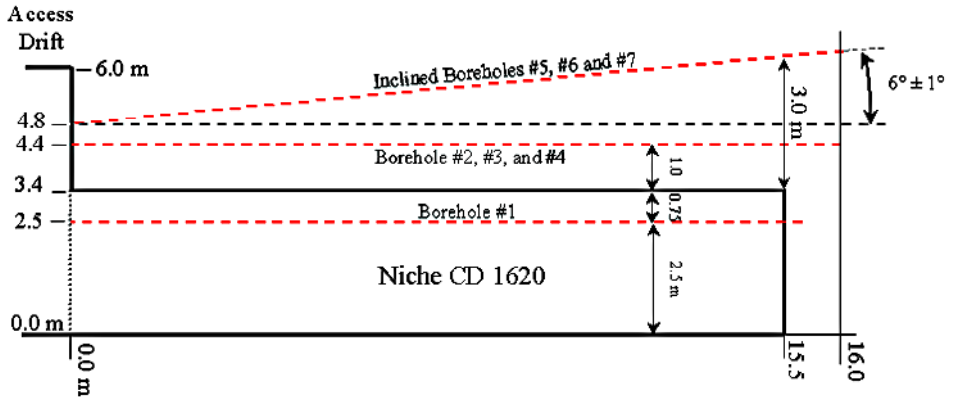

Source: BSC 2001 [158200] Figure 2.

Figure 6.2.1-10. Side View Schematic Illustration of the Boreholes at Niche CD 1620 (Niche 5)

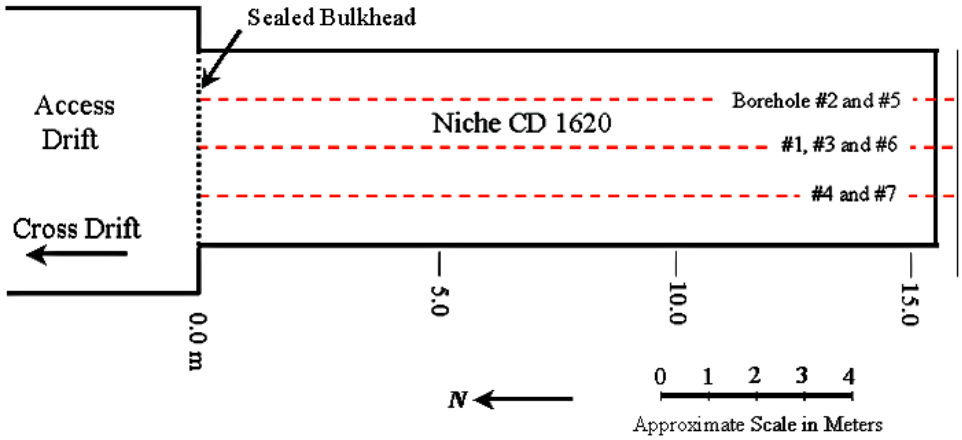

Source: BSC 2001 [158200] Figure 3.

Figure 6.2.1-11. Plan View Schematic Illustration of the Boreholes at Niche CD 1620 (Niche 5)

In May 2000, a mechanical excavator was used to mine out the rock to create Niche CD 1620 (Niche 5). The niche is approximately 15.5 m long by 4 m wide by 3.3 m high (Figure 6.2.1-10 through Figure 6.2.1-12). Niche CD 1620 (Niche 5) was constructed along the south side of the Cross Drift (at the location shown in Figure 6.1.1-1) within the lower lithophysal zone of the Tptpll. Water was used during niche construction to suppress dust generated during mining activities. Split-set rock bolts were installed in the ceiling of the niche immediately following construction to provide ground support for the excavation.

In May 2001, construction began on two slots located in the side walls of the niche called the "bat wing," as shown in Figure 6.2.1-12. The original intent was to construct a 6 m long by 1 m high by 1.5 m deep slot in each wall of the niche to aid in the collection of water. The slot design was based on the premise that, because of the capillary barrier, water would move laterally around the opening, where it would collect at a low spot and drip into the slot (Point A on Figure 6.2.1-12). The initial design was to slope the ceiling of the slot back toward the niche to produce

a low point for water to collect and by creating a capillary barrier, to prevent water from flowing around the backside of the slot.

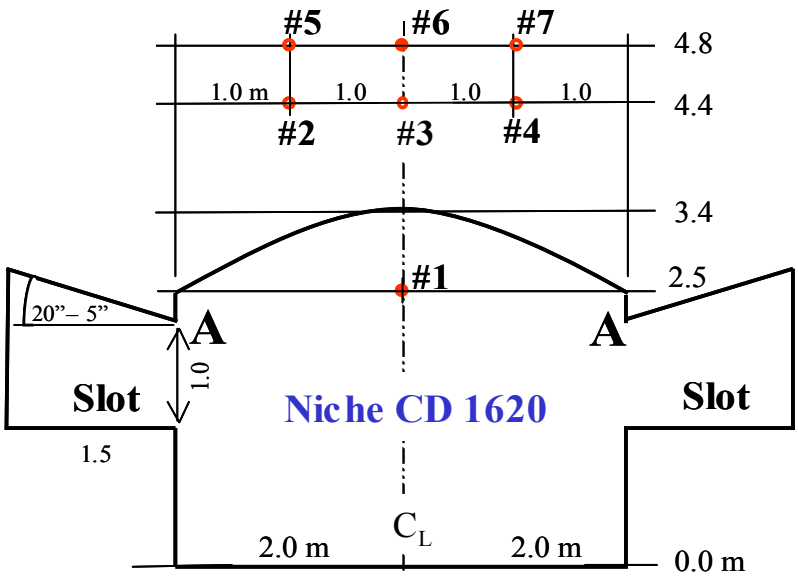

Source: BSC 2001 [158200] Figure 4.

Figure 6.2.1-12. Schematic Illustration of Front View of Niche CD 1620 (Niche 5) Facing South, Showing Location of Boreholes (#1–7)

Additional ground support consisting of Williams' rock bolts was installed in the ceiling of the niche prior to slot construction, to help stabilize the underground opening. These bolts supplemented the split-set rock bolts already in place, effectively doubling the number of bolts and decreasing the rock bolt spacing to about 0.5 m. Even with additional ground support, the unstable rock conditions at Niche CD 1620 (Niche 5) caused sections of the initial slot ceiling (Point A) to collapse during its construction, resulting in an excavation that did not meet the desired construction and testing specifications described above. Slot construction activities were halted after creating a 3.3 m long irregular-shaped excavation in the left rib and a short (< 1m) excavation in the right rib of the niche. Improvements to the 3.3 m long slot were made after construction by installing a wooden header and post system to support the brow of the slot excavation (i.e., Point A) keeping it from collapsing further (Figure 6.2.1-13 through Figure 6.2.1-15). The rock behind the header was then chipped away by hand to create the best sloping ceiling possible, given the circumstances. Additional ground support, consisting of metal house jacks, was installed further back in the slot to provide more stability.

Figure 6.2.1-13 shows the final size and shape of the slots. Note that there are five profiles numbered 2 through 6 in Figure 6.2.1-13, showing the irregular shape of the longest slot. Profile 2 and 6 define the lateral ends of the slot. The remaining profiles (3–5) are spaced sequentially by number between the two lateral ends with a distance of about 0.5 to 1.3 m separating the profiles.

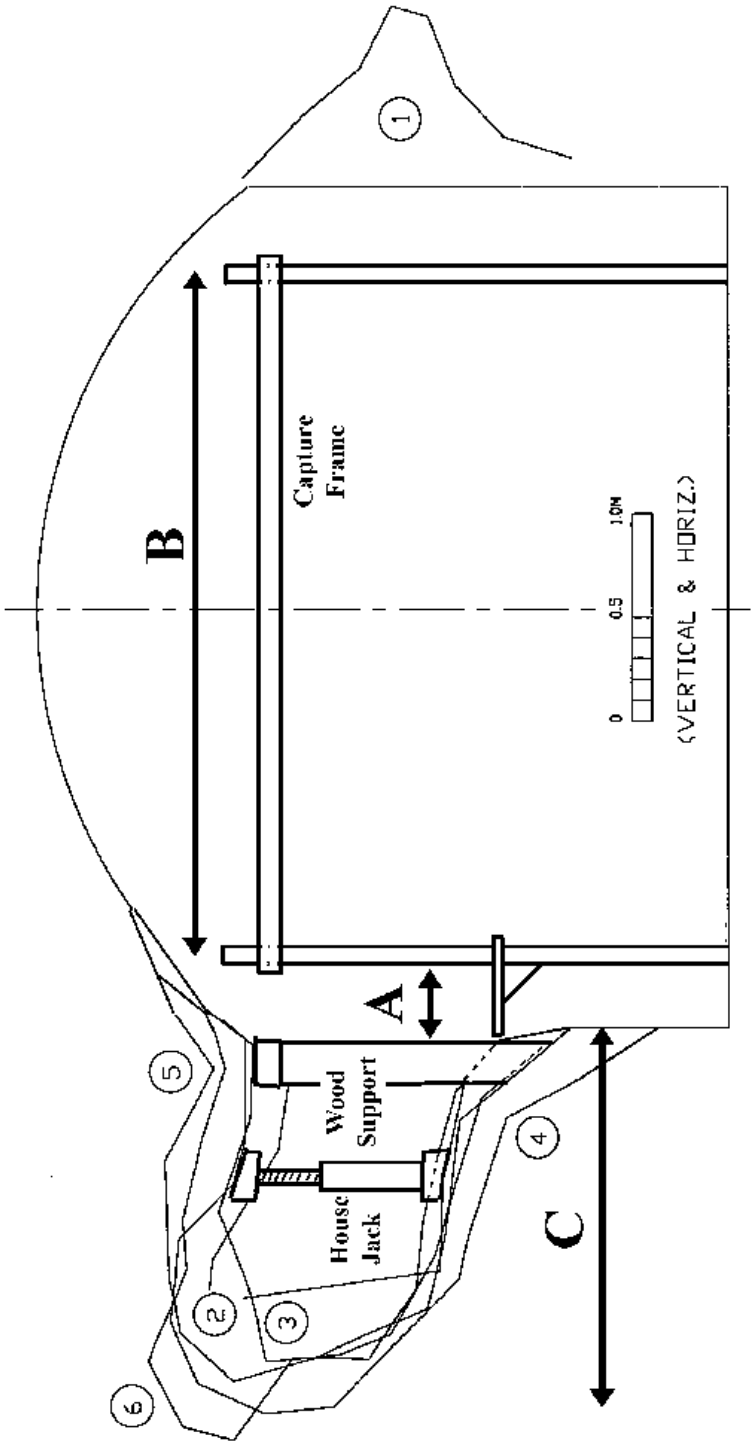

NOTE: Profile #2 is located closest to the niche entrance and # 6 is farthest away, after DTN: MO0107GSC01061.000 [155369].

Figure 6.2.1-13. Schematic Illustration of Front View of Niche CD 1620 (Niche 5) Facing South Showing Profile #1–7–Slot C

DTN: LB0211NICH5LIQ.001[160792]

Figure 6.2.1-14. Photograph of Left (East) Rib of Niche CD 1620 (Niche 5) Facing the Opening of a 3.3-m Long Slot and Showing Ground Support

DTN: LB0211NICH5LIQ.001 [160792]

Figure 6.2.1-15. Photograph of Left (East) Rib of Niche CD 1620 (Niche 5) Showing Ceiling of Slot and Ground Support

‚For additional detail on the slot profiles, refer to the surveyor's drawing (DTN: MO0107GSC01061.000 [155369]) provided in Attachment III.1.

The pilot hole from one of the rock bolts struck test boreholes #2 and #5. A rock bolt was subsequently installed in the pilot hole, blocking both test boreholes at a depth of 5.6 m from their collars, rendering the remaining 10 m of each borehole inaccessible. The rock bolts were subsequently removed by cutting through them laterally from within the test boreholes. This improved the depth available for testing from 5.6 to 7.9 m in borehole #2 and from 5.6 to 10 m in borehole #5. A straddle-packer assembly also got stuck in borehole #4 when air-injection tests were conducted on this hole. Numerous attempts to recover the packer were unsuccessful.

Unstable ground conditions, resulting in loose rock and debris sloughing off the walls of lithophysal cavities intersecting the boreholes, also contributed to several "natural" borehole blockages. The boreholes were vacuumed out to remove as much debris as possible before testing began. Boreholes #3, #4 and #6 were blocked at approximately 12.0, 9.0, and 10.5 m, respectively, by large rocks and debris that could not be extracted during the cleaning process. Table 6.2.1-1 summarizes the total depth and length of boreholes available for testing.

Table 6.2.1-1. Borehole Depth Summary

Borehole Designation	Available for Testing (m)	Total Depth (m)
ECRB-Niche1620#1	--	15.4
ECRB-Niche1620#2	0–7.9	16.0
ECRB-Niche1620#3	0–12.0	15.5
ECRB-Niche1620#4	0–9.0	15.0
ECRB-Niche1620#5	0–10.0	15.9
ECRB-Niche1620#6	0–10.5	16.0
ECRB-Niche1620#7 *	NA	14.8

Source: BSC 2001 [158200] Table 1.

NOTE: -- borehole was intentionally removed during niche construction
NA = not available
* borehole diameter is too large to accommodate test equipment.

Test Operation and Control Equipment

Custom-designed and built test equipment described in this section was used to operate and control the tests. In general, a seepage test is performed by pumping water at a known rate from a release reservoir sitting on an electronic balance through the release line, release manifold, and downhole straddle packer to the release or test interval located in the borehole (Figure 6.2.1-16). The straddle packer consists of a series of rubber glands that the test operator inflates with compressed air (like a balloon) inside the borehole. When inflated with air, the packers create a 0.3 m test interval, isolated from up and downhole sections of the borehole, thus preventing water from migrating throughout the length of the borehole during the experiment.

In the event that the pumping rate exceeds the infiltration capacity of the rock, water may begin to pond in the borehole and pressurize the test interval. An outlet located in the test interval (called the *return port*) prevents this from occurring. Water may rise to the level of the return

port where it will flow by gravity back through the return line, straddle packer, and return manifold, to the return reservoir, where it accumulates and is weighed by the return balance. The overflow line limits the maximum ponding depth of water within the borehole to about 0.05 m, thus preventing overpressurization of the test zone by the pump.

Water that enters the test interval percolates down through the rock, where it may eventually seep into the opening. A capture manifold or seepage collection system is used to capture the water seeping into the drift and to route it to the capture reservoir, where it accumulates and is weighed by the capture balance(s).

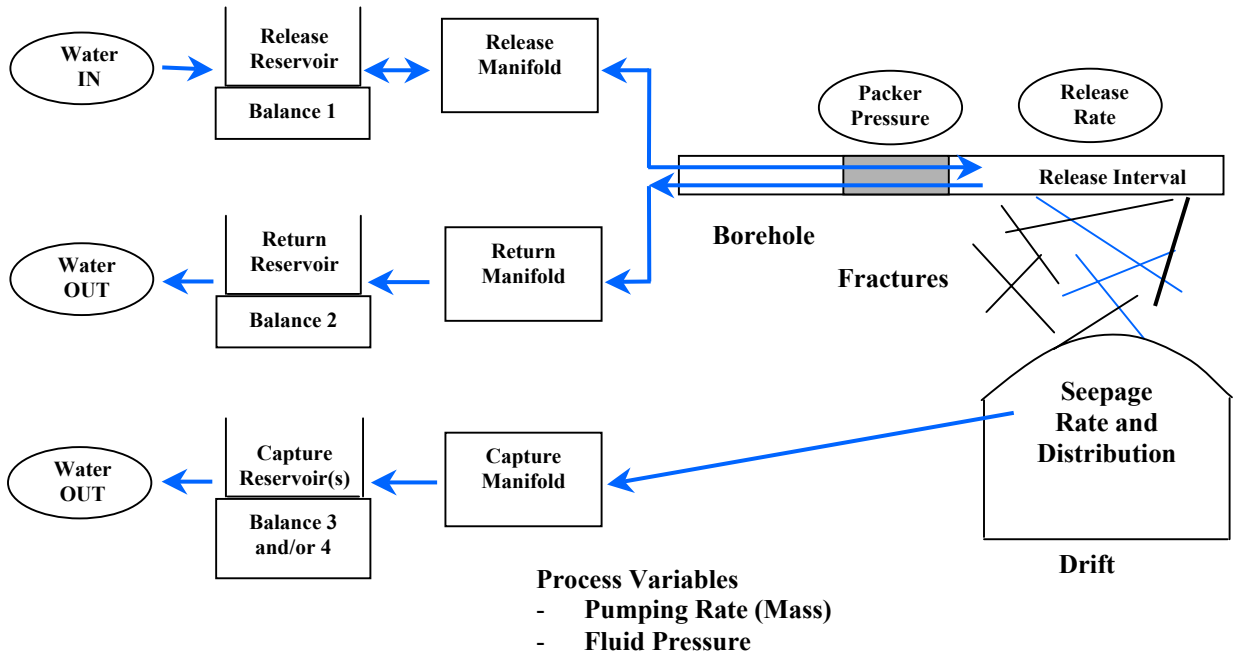

Figure 6.2.1-16. General Process Diagram for Seepage Testing at Niche CD 1620 (Niche 5)

Figure 6.2.1-16 provides a summary of the general processes that the test operator attempts to control during a seepage test, including the release, return, and capture rates. Control variables represent parameters that the operator is attempting to control. These are represented by ovals labeled in Figure 6.2.1-16. Control variables are affected by process variables (e.g., pump speed, valve position) manipulated by the operator. Additional detail on the test operation and control equipment is provided in Attachment III.2.

A plastic tarp was hung from the outside of the aluminum frame (shown in Figures 6.2.1-17 and 6.2.1-18) to the wooden supports at the edge of the slot shown in Figure 6.2.1-13 through Figure 6.2.1-15 to collect water seeping into the slot. The outlet from the slot seepage collection system drained through a pinch valve (that could also be controlled by the operator) to the capture balance.

Field personnel were not allowed to enter the slot, or hang the tarp off of the wooden and steel ground support system inside the slot, because of health and safety issues concerning rock instability. This restriction prevented the entire slot area (corresponding to depth C in Figure 6.2.1-13) from being covered by the slot seepage collection system. Instead, a much smaller area (with corresponding depth A in Figure 6.2.1-13) was covered by the slot seepage collection system. The majority of the slot seepage collection system was not beneath the slot ceiling itself, but rather beneath the sharply curved section of the niche where the niche ceiling meets the wall.

Data Acquisition Equipment

Calibrated instruments and data loggers were used to collect mass (g), mass rate (g/s), temperature (ºC), humidity (%) and pressure (pounds per square inch gauge, psig) data during the tests.

Mettler Toledo model PG, PG-s, and SG series electronic balances were used to measure the mass and rate that water was pumped into the test interval, that flowed back through the return line, and was captured as seepage. Initially, during the early stages of testing (5/3–5/16/02), two Mettler Toledo balances were used to measure the seepage mass and rate into the niche. Starting on 5/16/02, only a single balance was used to measure these same data. Mettler Toledo balances were also set up inside and outside the niche to measure the rate of evaporation from an open pan of water sitting on the balance. The data acquisition software listed in Attachment III.3 were used to query the balance for the mass and to calculate the mass rate on a user-defined time interval.

A calibrated Campbell Scientific, Inc. model CR10x datalogger was used to measure and record the measurements made by 12 calibrated Vaisala model HMP45C temperature and humidity probes located inside and outside the niche. Eleven of the probes were installed at various distances from the bulkhead to measure the air humidity and temperature distribution inside the niche. The twelfth sensor was installed outside the bulkheaded area of the niche to measure the temperature and humidity of the air in the ECRB (Trautz 2003 [166248], p. 162) for a detailed description of the probe locations).

The same calibrated Campbell datalogger was used to measure and record the measurements made by Setra model C204 pressure transducers (0–25 psig). The transducers were used to measure liquid pressures (air or water) inside the release and return lines leading to the test interval during the tests. These data were collected primarily for the purpose of monitoring and controlling the test equipment.7

DTN: LB0211NICH5LIQ.001 [160792]

Figure 6.2.1-17. Capture System Installation Showing Plastic Capture Trays and Tarp in Slot

DTN: LB0211NICH5LIQ.001 [160792]

Figure 6.2.1-18. Capture System Showing Tarp Installed Adjacent to Slot

Time-lapse video recordings of the niche ceiling and bottom of the capture trays were made during the tests to record the spread of the wetting front across the ceiling and dripping into the capture system. Sony model DCR-TRV900 video camcorders (mini-DV format) were utilized for this purpose.

Test Operating Conditions

A seepage test was typically conducted by pumping water at a constant rate through an injection line into a 0.3 m isolated test interval, located in one of the boreholes described in Table 6.2.1-1. Electronic balances were used to monitor the cumulative mass and rate at which water was pumped into the borehole, as well as return flow (if any occurs). Return flow occurs when the pumping rate exceeds the infiltration capacity of the rock.

Water migrating from the release point through the rock to the niche ceiling may drip into the niche, where it is collected in a capture system consisting of plastic trays and a tarp in the slot. Water drains by gravity through a network of tubes into a closed container, resting on an electronic balance. The balance is used to measure the cumulative mass of water that seeps and the seepage rate. One or more containers and balances may be employed for collecting seepage water.

Evaporation of water from the containers, the capture system, and the wetted area of the niche ceiling during seepage tests can influence the outcome of the seepage experiments. The effects of evaporation on the test results were minimized by employing the following techniques:

1. The bulkhead door at the entrance to the niche was closed and sealed during the seepage tests. This helped limit the exchange of dry air in the ECRB (typically <40% relative humidity) with moist air found within the niche (typically >85%).

2. Access to the interior of the niche during testing was limited to authorized field test personnel. Remote monitoring of the niche ceiling, and the capture trays, using digital video and remote monitoring of test equipment, minimized the number of trips inside the niche, thus limiting the exchange of air.

3. Fluid containers and transmission lines are closed systems, minimizing the effect of evaporation.

4. The potential exists for water to evaporate from the niche ceiling and diffuse into the air within the niche. Seepage water may potentially evaporate from the capture trays before the water has time to accumulate and drain into the tubing connecting the trays to the closed container on the seepage balance(s). Therefore, the relative humidity of the air inside the niche was artificially elevated to minimize evaporation, using a centrifugal-type humidifier capable of producing water vapor at a rate of about 1 kg per hour. Humidification occurred 24 hours per day, 7 days a week, under the condition that electrical power was available to operate the humidifier.

5. Electrical lighting within the niche was minimized to limit sources of heat that enhance evaporation. Sufficient lighting was provided, however, for video imaging of the wetted area spreading across the niche ceiling.

6. A small pan, resting on an electronic balance, was set inside the drift to directly measure the mass evaporative flux.

6.2.1.3.5.3 Test Summary

This section provides an overview of the seepage tests performed at Niche CD 1620 (Niche 5) and summarizes the type of data collected by evaluating and interpreting data for Test #2 9-17-02 conducted from 9/17/02 through 10/28/02. The analysis of the Niche CD 1620 (Niche 5) seepage test data for model calibration can be found in the Model Report U0080, *Seepage Calibration Model and Seepage Testing Data* (BSC 2003 [162267]).

Attachment III.4 summarizes general test information, including borehole number, depth of the test interval measured in meters from the datum near the borehole collar, test name, and test start and end dates. Seepage tests were initiated at Niche CD 1620 (Niche 5) in early May 2002 and ran through late May 2002, when the instruments and sensors were removed for routine calibration. Testing resumed in mid-July 2002, upon reinstalling the calibrated instruments, and continued through late October 2002 with seven tests performed over this time period.

Evaporation Pan Data

Evaporation pan data were measured using a single balance loaded with a container filled with water. Figure 6.2.1-19 shows the evaporation flux inside and outside the niche during Test #2 9-17-02. The plot indicates that the average evaporation flux outside of the niche is about a factor of 20 greater than the average evaporation flux inside the niche. (Note that the evaporation data collected during the study and contained in the original data files are the evaporation rates [g/s]. These were converted to evaporation fluxes [g/s-m^2] shown in the Figure 6.2.1-19 by dividing the evaporation rate by the surface area of the evaporation pan [i.e., πr^2, where r is the radius of the pan].) The radius of the evaporation pan inside the niche was 0.075 m (0.15 m diameter reported in Trautz (2003 [166248], p. 187) divided by 2) and outside the niche was 0.244 m (9 5/8 in. diameter reported in Trautz (2003 [166248], p. 187), converted as follows to r in meters (9 5/8 in. * 2.54 cm/in. * 1/100 m/cm)/2). Details of this calculation may be found in Attachment IX.6.1.

The peak evaporation rates associated with the saw-tooth pattern, observed in the evaporation pan data collected outside the niche, correspond to refilling the evaporation container with fresh warm water from the mine's water supply system.

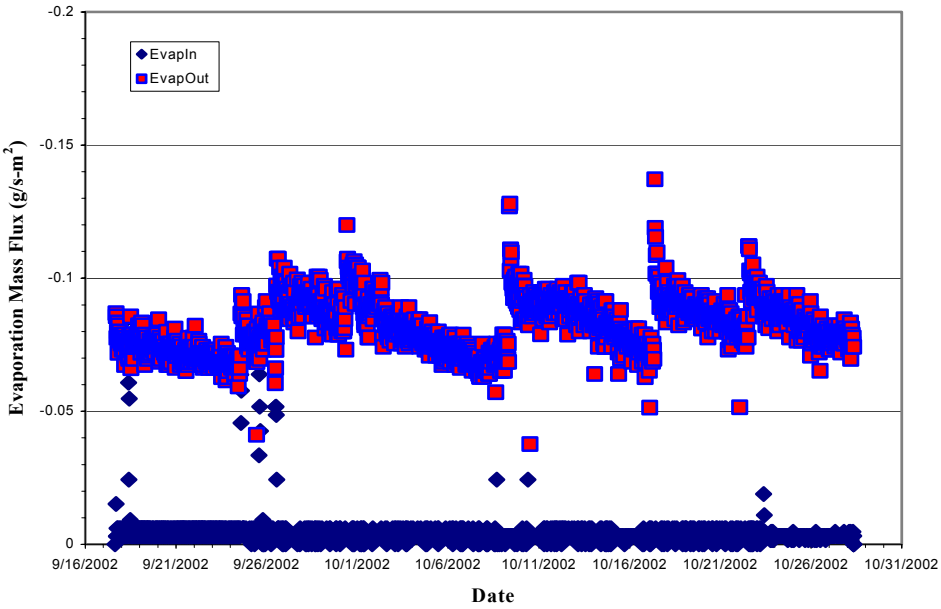

DTN: LB0211NICH5LIQ.001 [160792] Test #2 9-17-02:
native data files Test#1_BH#4_10-11_ft_9-17-02_#1.csv and Test#2_b5_20-21_ft_9-17-02_#1.csv].

Figure 6.2.1-19. Evaporation Rate Inside and Outside Niche CD 1620 (Niche 5) during Test #2 9-17-02

Relative Humidity and Temperature

The data filenames containing the relative humidity and temperature data from inside and outside the niche, and the liquid pressure data measured in the release and return lines during the test, are identified in Attachment III.4. (The pressure in the release and return lines were relatively constant during a given test, so these results will not be discussed further.) These data were collected using the sensors and Campbell Scientific, Inc., dataloggers described in the Data Acquisition Equipment subsection above.

Figure 6.2.1-20 shows the relative humidity and temperature of the air inside and outside the niche during Test#2 9-17-02 (9/17/02–10/28/02). The relative humidity and temperature inside the niche are very stable, ranging from about 90 to 94% and 24 to 25ºC, respectively. The sudden drop in relative humidity observed in mid- and late-September was caused by the exchange of cool moist air inside the drift with dry warm air outside the niche when field personnel opened the bulkhead and entered the niche. A slight rise in inside air temperature is noted over the measurement period. This is probably caused by the cooler inside temperatures slowly equilibrating with the warming temperature outside the niche.

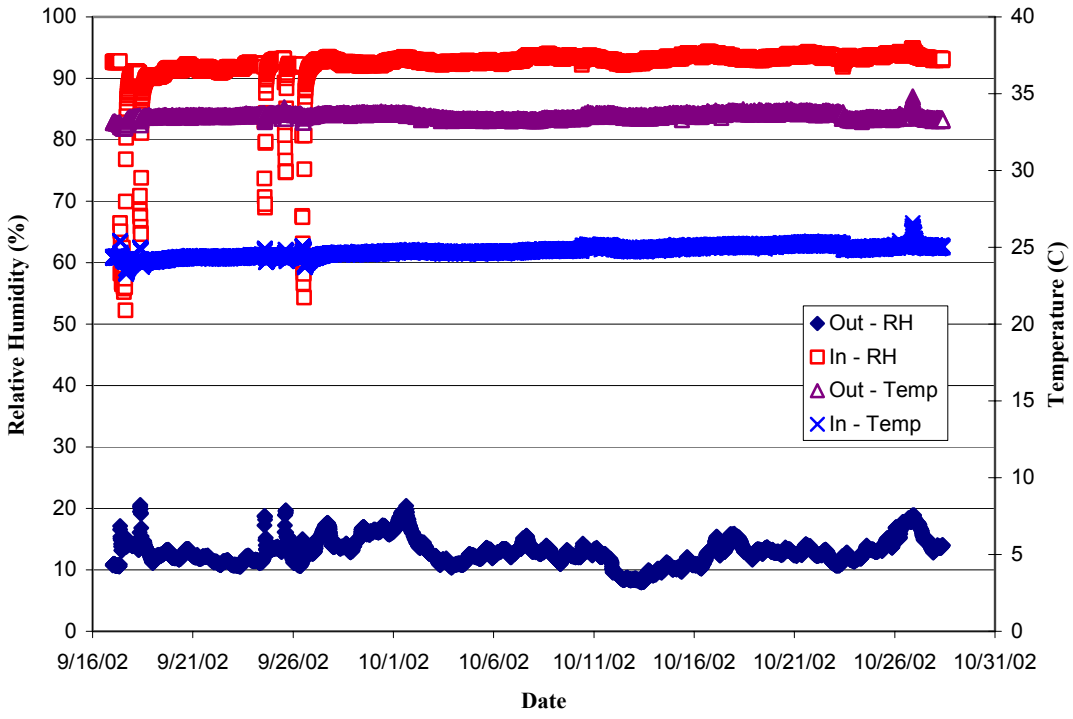

DTN: LB0211NICH5LIQ.001 [160792] Test#2 9-17-02:
native data files N5_RH-T-p_9-18-02.csv, N5_RH-T-p_10-18-02.csv, and N5_RH-T-p_10-29-02.csv.

Figure 6.2.1-20. Relative Humidity and Temperature of Air Inside and Outside Niche CD 1620 (Niche 5) during Test#2 9-17-02

The air temperature outside the niche in the ECRB is also quite stable (33 to 34ºC), but the relative humidity fluctuates from 8 to 21%. The fluctuation in relative humidity can be attributed to the tunnel ventilation system that draws moisture into the ECRB from outside the ESF. Relative humidity conditions in this case are influenced by outside weather conditions.

Test Data–Liquid Release and Seepage Rates

Figure 6.2.1-21 shows a plot of the liquid-release mass flow rate into the formation from the borehole and the total seepage mass flow rate entering the niche during Test #2 9-17-02. A peristaltic pump was used to pump water into the borehole, creating small surges in the rate that give the appearance that the release rate varies with time (i.e., double-line appearance to the release rate in Figure 6.2.1-21). The average release rate (about 0.023 g/s) was quite constant from 9/17 to 10/19/02, and then it steadily declined between 10/20/02 to 10/28/02 to a rate of 0.019 g/s.

Seepage into the niche began on 10/1/02, based on a definitive increase in mass observed on the capture balance. The seepage rate continued to increase through 10/20/02, when it suddenly started to decline and stopped seeping on 10/23/02. This corresponds within a day to the decline in the liquid release rate noted above. The sudden halt in seepage caused by a 10 to 20%

reduction in the release rate suggests that a seepage threshold exists in the Tptpll that is very sensitive to the release mass flow rate.

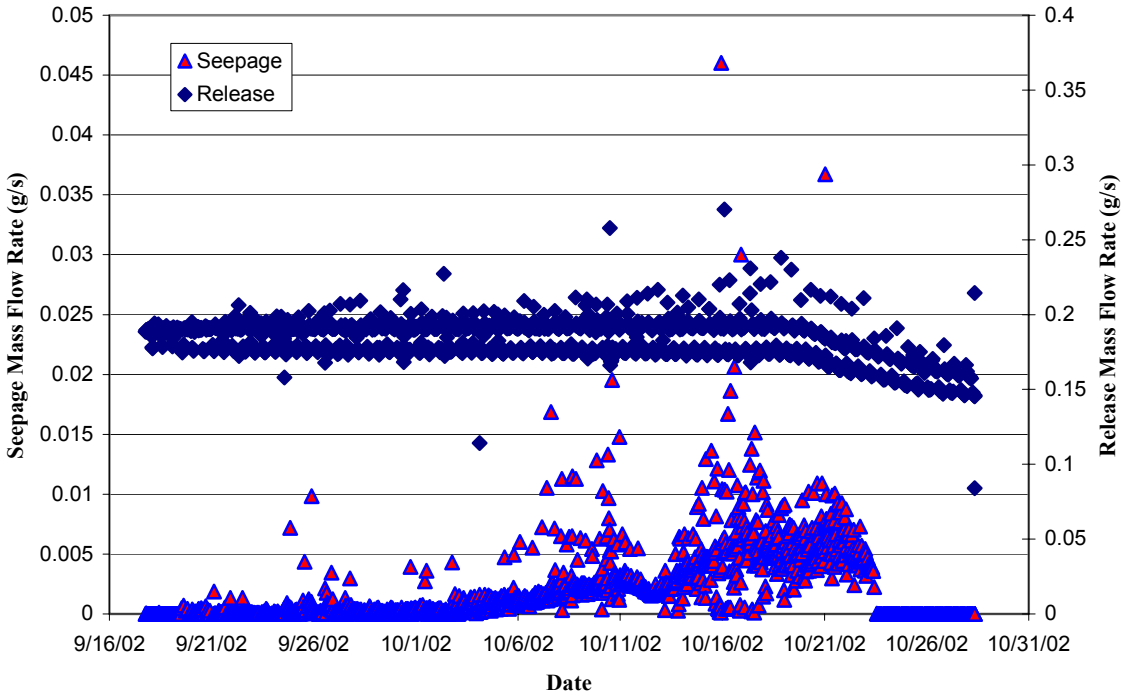

DTN: LB0211NICH5LIQ.001 [160792] Test#2 9-17-02:
native data files Test#2_b5_20-21_ft_9-17-02_#1a (srate).csv and Test#2_b5_20-21_ft_9-17-02_#2 (srate).csv.

Figure 6.2.1-21. Liquid-Release Rate into Borehole #5 and Seepage of Water into the Capture System of Niche CD 1620 (Niche 5) during Test #2 9-17-02

Figure 6.2.1-22 shows a plot of the total seepage rate into the niche (triangles) and the seepage rate captured by the tarp (diamonds) installed at the entrance to the slot (Area A, Figure 6.2.1-13). Seepage captured by the tarp follows the same pattern over time as the total seepage, the latter of which represents water collected from all the capture compartments. Seepage captured by the tarp is a large component of the total seepage into the drift, approaching 80 to 90% of the total during specific periods of time. Both seepage and the seepage captured by the tarp declined and dropped off to zero as the release rate declined after 10/20/02.

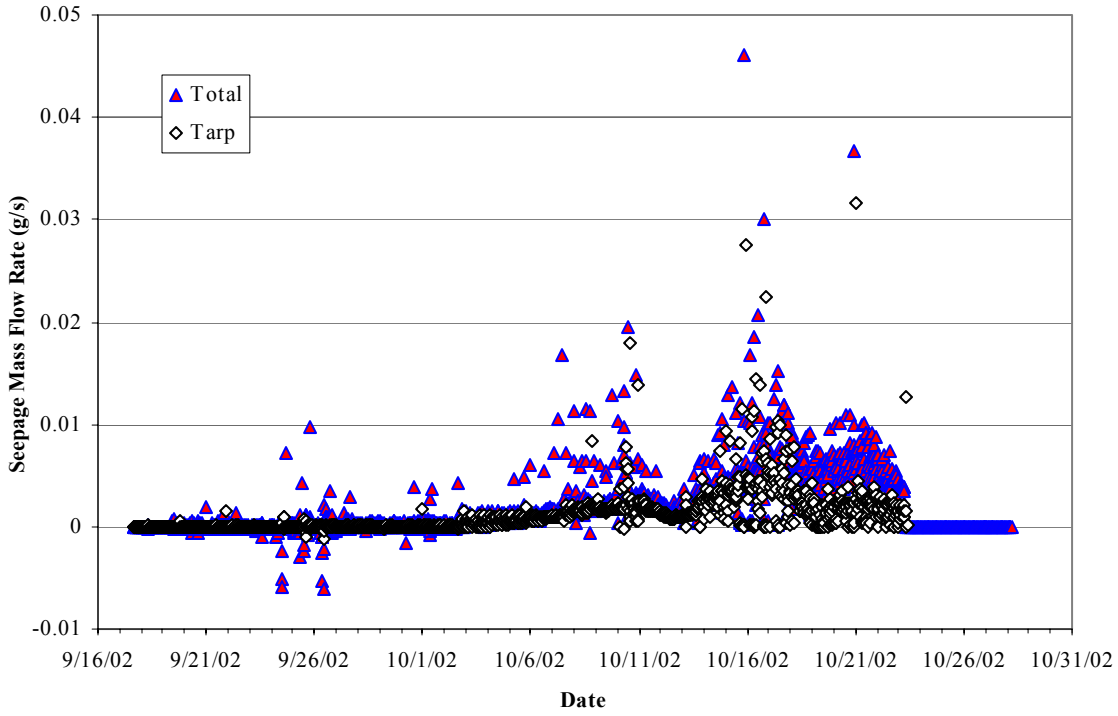

DTN: LB0211NICH5LIQ.001 [160792] Test#2 9-17-02:
native data files Test#2_b5_20-21_ft_9-17-02_#1.csv, Test#2_b5_20-21_ft_9-17-02_#1a (srate).csv, and Test#2_b5_20-21_ft_9-17-02_#2 (srate).csv.

Figure 6.2.1-22. Total Seepage and Seepage into the Tarp Area at the Entrance to the Slot

6.2.1.3.5.4 Summary–Niche CD 1620 (Niche 5)

Tests performed during the study (including the example experiment, Test #2 9/17/02) indicate that a measurable seepage threshold exists for the Tptpll–a stated objective of the niche study. Unfortunately, because of the constraints associated with installation of the slot collection system described in Section 6.2.1.3.5.2.2, investigators were unable to determine whether the water seeping onto the tarp during Test #2 9/17/02 and Test #1 7/15/02 (the only two tests where seepage onto the tarp occurred) originated from the slot or from the niche ceiling adjacent to the slot. Several attempts to observe seepage (i.e., dripping) were made, but the seepage rates were so slow that visual evidence of seepage from the slot was not possible. With the approximation that all of the seepage was derived from the slot, the results of Test #2 9/17/02 demonstrate that the slot did not effectively capture lateral movement of water around the niche, because seepage into the slot ceased when the seepage threshold was reached. The lack of seepage into the slot implies that the revised objectives of the test stated in Section 6.2.1.3.5.1 were not met in this study. Specifically, a mass water balance was not achieved because the lateral movement of seepage water was not collected in the slot. Photographic evidence has been collected in Niche CD 1620 (Niche 5), showing the wetted area spreading down the sidewall during the test (Figure 6.2.1-23), providing qualitative evidence that flow was diverted around the niche. Trautz and Wang (2002 [160335]) showed (using photographic evidence) that the wetted area spreads across the ceiling and down the terminal face and sidewall of Niche 4788 (Niche 4) in Tptpmn.

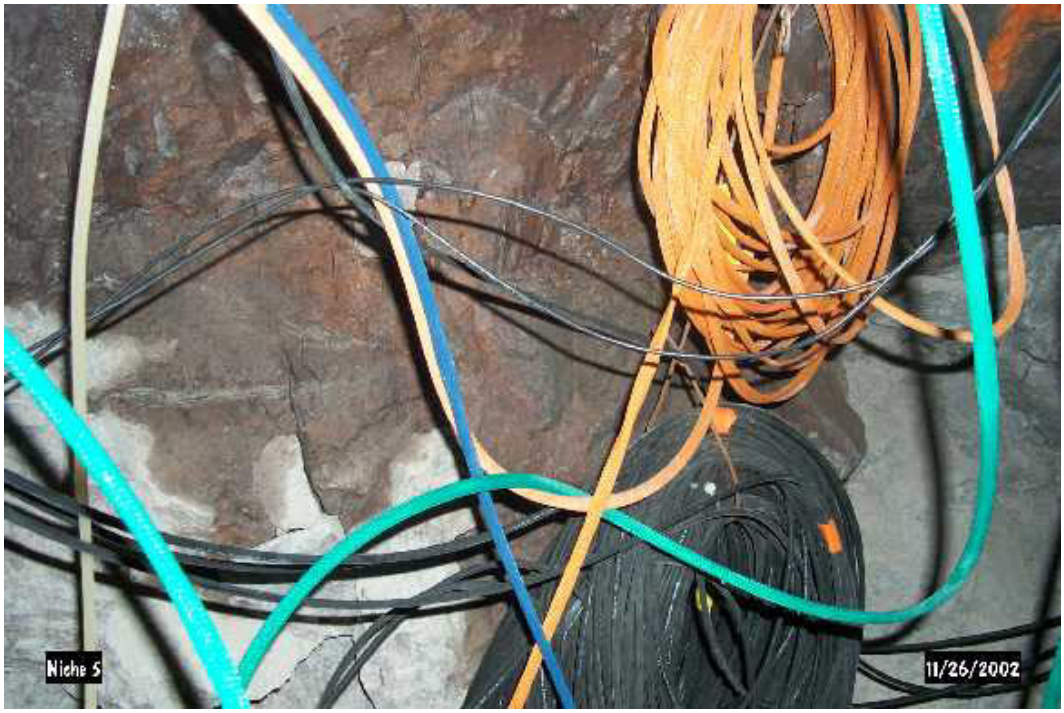

DTN: LB0211NICH5LIQ.001 [160792]

Figure 6.2.1-23. Wetted Area Spreading Down the Sidewall in Niche CD 1620 (Niche 5)

6.2.2 Niche Seepage Threshold and Fracture Characteristic Curves

The niche seepage data collected from short-duration tests in ten intervals at Niche 3650 (Niche 2), long-term tests in one interval at Niche 3107 (Niche 3), and long-term tests in three intervals at Niche 4788 (Niche 4) are analyzed in this section. As stated in Section 6.2.1.3.1, Section 6.2.1.3.2, and Section 6.2.1.3.3, the niche seepage threshold is defined in terms of the pumping rate and the wetted area estimated for the borehole interval. This definition of niche seepage threshold is different from the definition used by PA, which relates the seepage threshold to the steady-state background percolation flux averaged over drift-scale and site-scale areas.

6.2.2.1 Post-Excavation Liquid-Release and Niche Seepage Threshold

For a given test interval, seepage tests were initially conducted at high liquid-release rates (injection rates into borehole interval without excessive pressure buildup). Subsequent tests were performed at lower liquid-release rates to determine whether a threshold could be estimated below which seepage into the cavity would no longer occur.

Figure 6.2.2-1 shows a plot of the seepage percentages observed during four tests conducted at different q_s in borehole UM at the same interval, located 5.49–5.79 m from the borehole collar at Niche 3650 (Niche 2). A linear regression was performed on the four data points to compute the equation for the trendline and the R-squared values (R^2) reported in Figure 6.2.2-1 and tabulated in Table 6.2.2-1. This exercise was repeated for the intervals tested at all the niches to produce the regression data reported in Table 6.2.2-1 for all the zones that seeped. The R-squared values

were computed separately for each interval and are listed for those intervals where three or more data points are available. (The linear regression was performed in an Excel spreadsheet documented in Attachment II, Tables II-3a through -4e.) For the purposes of this analysis, liquid release flux (q_s) is approximately equal to the net downward flux K_o. This approximation is a conservative estimate of K_o (Trautz and Wang 2002 [160335]).

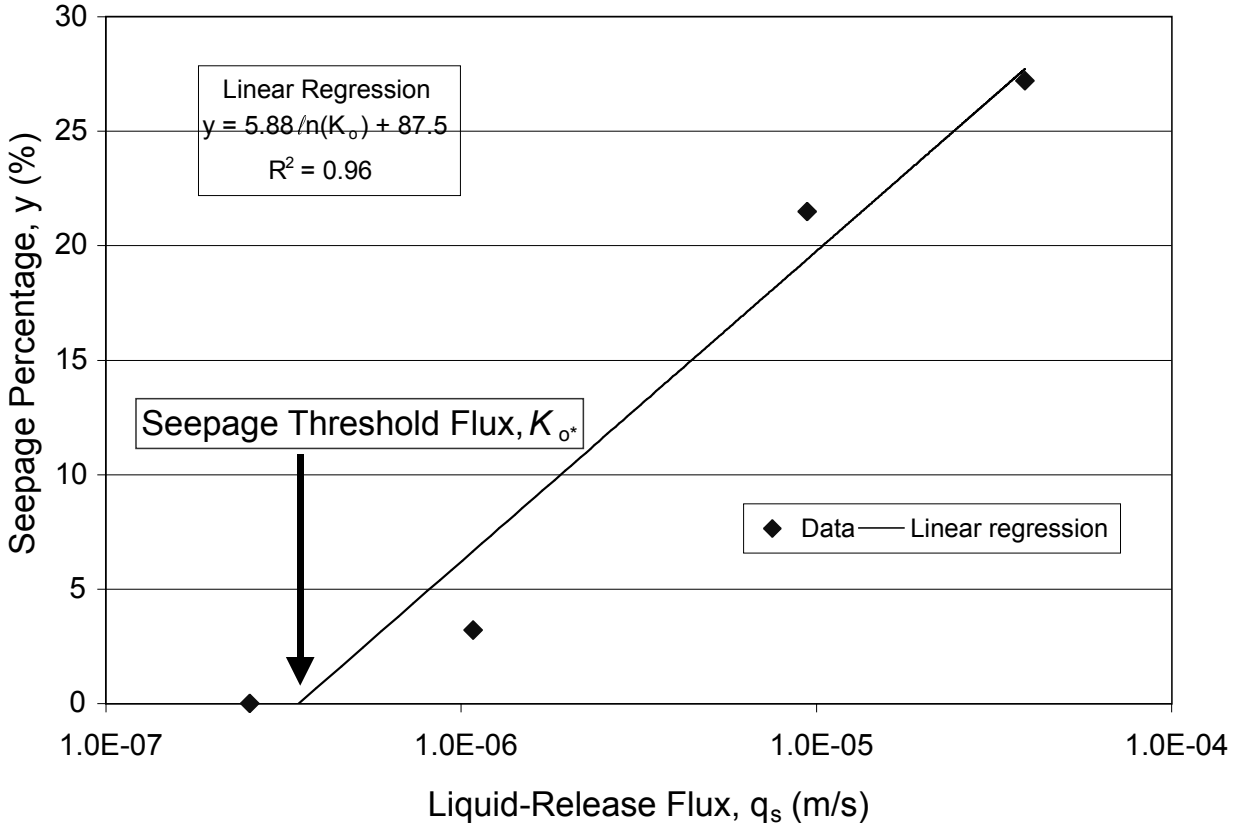

DTN: LB980901233124.003 [105592]

NOTE: Seepage tests were conducted for the interval 5.49–5.79 m from the collar for the upper middle borehole at Niche 3650 (Niche 2).

Figure 6.2.2-1. Liquid-Release Flux versus Seepage Percentage

Table 6.2.2-1. Seepage Threshold Fluxes (K_o^*).

Niche	Borehole and Depth (m)	Linear Regression Equation	Data Points	Correlation Coefficient (R^2)	Niche Seepage Threshold K_o^* (m/s)	Saturated Hydraulic Conductivity K_l (m/s)
3107	UM 4.88-5.18	$y = 30.440\ln(K_o) + 456.085$	8	0.820	3.11E-07	NA
3650	UL 7.01-7.32	$y = 0.6833\ln(K_o) + 8.5742$	2	NR	3.55E-06	8.98E-05
	UL 7.62-7.92	$y = 5.7394\ln(K_o) + 92.627$	3	0.979	9.80E-08	1.51E-04
	UM 4.27-4.57	$y = 5.2757\ln(K_o) + 79.443$	4	0.921	2.89E-07	2.62E-05
	UM 4.88-5.18	$y = 2.304\ln(K_o) + 31.767$	3	0.975	1.03E-06	2.52E-03
	UM 5.49-5.79	$y = 5.8876\ln(K_o) + 87.528$	4	0.963	3.50E-07	2.16E-05
	UR 4.27-4.57	$y = 0.314\ln(K_o) + 4.3283$	2	NR	1.03E-06	4.08E-05
	UR 4.88-5.18	$y = 0.3165\ln(K_o) + 4.3751$	2	NR	9.92E-07	9.87E-05
	UR 5.49-5.79	$y = 28.419\ln(K_o) + 351.09$	2	NR	4.31E-06	1.71E-05
	UR 6.10-6.40	$y = 4.2169\ln(K_o) + 79.596$	2	NR	6.35E-09	3.01E-05
	UR 6.71-7.01	$y = 10.574\ln(K_o) + 165.28$	3	0.974	1.63E-07	2.28E-04
4788	UL 7.62-7.93	$y = 9.273\ln(K_o) + 148.119$	4	0.929	1.16E-07	2.46E-05
	UM 6.10-6.40	$y = 15.697\ln(K_o) + 243.611$	4	0.980	1.82E-07	2.45E-04
	UR 5.18-5.48	$y = 25.415\ln(K_o) + 410.285$	3	0.970	9.75E-08	3.92E-06

DTN: LB980901233124.003 [105592] and LB0110LIQR0015.001 [OUTPUT]

NOTES: Various data sets were used to generate Table 6.2.2-1. Refer to Tables II-3 and II-4 in Attachment II, and Attachment IX.5 for details.
NA = not applicable, the test could not be completed as planned because of rock properties outside the equipment's measurable range.
NR = not reported because two data points result in perfect correlation (R^2 =1.0), therefore, correlation coefficient is meaningless.
y = predicted seepage percentage (%)
K_o = net downward liquid-release flux from regression model (m/s)
ln = natural logarithm

Table 6.2.2-1 also summarizes the niche seepage threshold (K_o^*), defined as the liquid-release flux below which water will not seep into the drift (i.e., see K_o^* defined on Figure 6.2.2-1). The K_o^* values were determined using the regression equations provided in Table 6.2.2-1 by setting the seepage percentage, y, equal to 0, and then solving for $K_o = K_o^*$ [$K_o^* = K_o(y=0)$]. Details on this analysis and calculation procedures may be found in Attachments II and IX. Here, the symbol K_o is used to denote the liquid-release flux used in the regression model to distinguish it from the liquid-release flux computed using the field data (q_s). In terms of K_o and K_o^*, the niche seepage threshold is defined as follows:

- If the liquid-release flux exceeds the seepage threshold flux ($K_o > K_o^*$) for the given interval, then water will seep into the drift.
- If the liquid-release flux is less than the seepage threshold flux ($K_o < K_o^*$), then water will not enter the cavity.

Figure 6.2.2-2 shows a log-log plot of K_o^* versus the saturated hydraulic conductivity (K_l) for 10 test intervals at Niche 3650 (Niche 2) and three test intervals at Niche 4788 (Niche 4) where seepage occurred. For each test interval, multiple tests with different release rates were conducted to estimate the niche seepage threshold. The air permeabilities obtained from the post-excavation gas-injection tests were converted into equivalent saturated hydraulic conductivities (DTN: LB980001233124.004 [136583]) as shown in Wang (1999 [153449], pp. 34–38) for Niche 3650 (Niche 2), to produce the values recorded in Table 6.2.2-1 and plotted in Figure 6.2.2-2. (Computation of K_o^* and K_l was performed in an Excel spreadsheet documented in Attachment II, Table II-4. K_l could not be calculated for Niche 3107 [Niche 3] because the air-permeability test could not be completed as planned: the rock properties were outside the equipment's measurable range.) The straight line in Figure 6.2.2-2 is derived from an analytic solution described in Section 6.2.2.2. The estimation of saturated hydraulic conductivity using air-permeability test data is evaluated in Attachment IV.2.

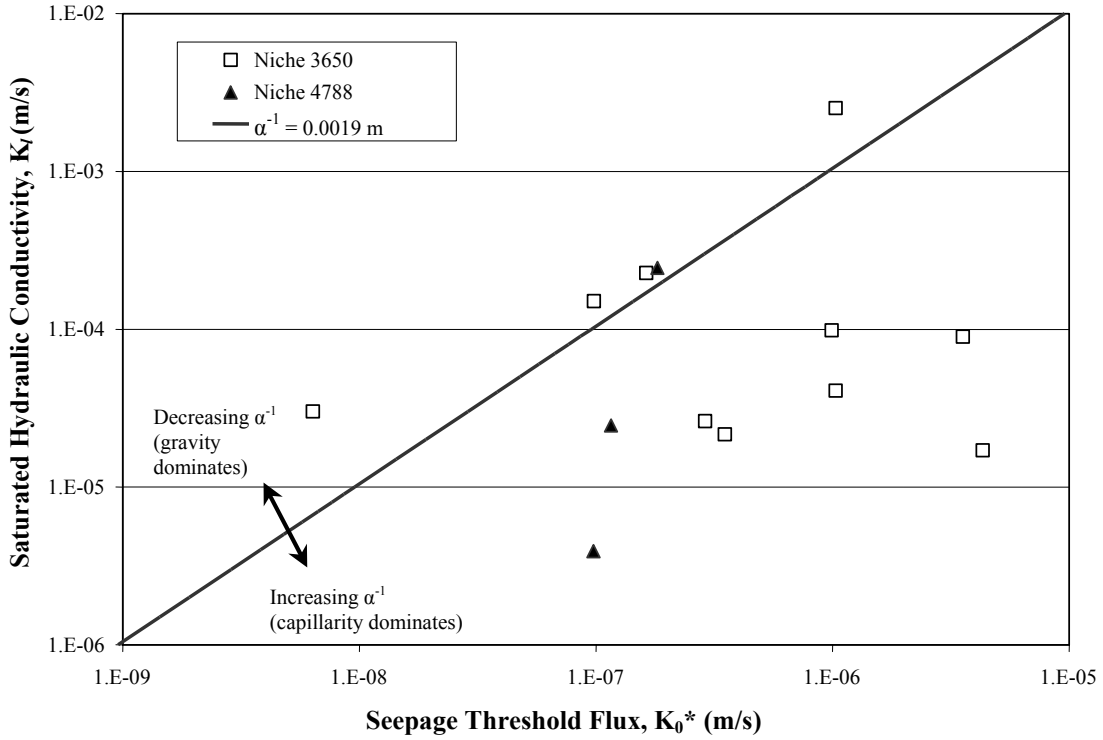

DTN: LB980001233124.004 [136583]; LB0010NICH4LIQ.001 [153145]; LB980901233124.003 [105592]; LB0110LIQR0015.001 [OUTPUT]

NOTE: Various data sets were used to generate this figure. Refer to Table II-4 and Table II-6 in Attachment II for details.

Figure 6.2.2-2. Niche Seepage Threshold

6.2.2.2 Capillary Strength (α^{-1}) of Fractures

Philip et al. (1989 [105743]) recognized that buried cylindrical cavities are obstacles to flow, preventing water from entering the cavity. The following theoretical relation between K_o^* and K_l was provided by Philip et al. (1989 [105743], Section 3.4, p. 19):

$$K_o^* = K_l \left[\vartheta_{\max}(s)\right]^{-1} \quad \text{(Eq. 6.2.2-1)}$$

where s is the value of the dimensionless cavity length and ϑ_{max} is the maximum value of the dimensionless potential ϑ at the boundary of the cavity. Philip et al. (1989 [105743], Equation 56, p. 20) show that ϑ_{max} occurs at the apex or crown of a cylindrical cavity. The dimensionless cavity length, s, is a measure of the relative importance of gravity and capillarity in determining flow. As $s \to 0$, capillarity dominates, whereas gravity dominates as $s \to \infty$.

An exponential functional relation between unsaturated hydraulic conductivity, $K(\psi)$, and water potential, ψ, is used (Philip et.al. 1989 [105743], Equation 12, p. 18):

$$K(\psi) = K_l e^{\alpha(\Psi - \Psi_e)} \quad \text{(Eq. 6.2.2-2)}$$

K_l is the saturated hydraulic conductivity (Pullan 1990 [106141], p. 1221), ψ_e is the air-entry potential, K_l is the conductivity at $\psi = \psi_e$, and α^{-1} is the capillary-strength parameter.

This Gardner exponential functional relation is used by Philip et al. (1989 [105743], Equation 12, p. 18) and by Braester (1973 [106088], Equation 5, p. 688) to transform and linearize the unsaturated governing equations. Equation 6.2.2-2 is also used in Section 6.2.2.4 to estimate water potential.

Another model for unsaturated hydraulic conductivity and water potential is the van Genuchten model with its own capillary-strength parameter and pore-size distribution parameter (BSC 2003 [162267], Section 6.3.2.3). The distinction between model-dependent capillary-strength parameters should be noted in comparing results from the analysis presented in this section and the results from the seepage calibration model and other PA models.

Philip et al. (1989 [105743], Equation 14, p. 18) note that the dimensionless cavity length s in Equation 6.2.2-1 is related to the capillary strength parameter α^{-1} (Equation 6.2.2-2) and a characteristic length of the cavity ℓ by the following expression:

$$s = 0.5\alpha\ell \quad \text{(Eq. 6.2.2-3)}$$

When s is large, Philip et al. (1989 [105743], Section 6, pp. 23–25) demonstrate that a boundary layer adjoining the ceiling of the cavity surface will develop. This allows the steady flow equation to be replaced by a boundary-layer equation that is readily solved. The asymptotic expansion of ϑ_{max} for large values of s yields (Philip et al. 1989 [105743], Equation 84, p. 23):

$$\vartheta_{max} = 2s + 2 - \frac{1}{s} + \frac{2}{s^2} - \ldots \quad \text{(Eq. 6.2.2-4)}$$

Philip et al. (1989 [105743], Table 1, Section 6, p. 25) note that when $s \geq 1$, the first three terms on the right-hand side of Equation 6.2.2-4 produce an adequate estimate that is within 12% or better of the exact value of ϑ_{max}. Therefore, using appropriate values for K_o^*, ℓ, and K_l, we can estimate the capillary strength (α^{-1}) for the porous medium from Equation 6.2.1-1, Equation 6.2.1-3, and the first three terms in Equation 6.2.2-4. This technique was utilized to compute the α^{-1} values reported in Table 6.2.2-2, using the values for K_o^* derived in Section 6.2.2.1. The K_l values were derived from post-excavation air-injection tests summarized in Table 6.2.2-1, and a value of 2 was used for ℓ, which is approximately equal to the radius of the curvature of the niche ceiling. By taking the reciprocal of the α^{-1} reported in Table 6.2.2-2, which in our case also equals s, all the s-values (with the exception of Niche 3107 [Niche 3] UM 4.88–5.18 m) are greater than one, justifying the use of Equation 6.2.2-4. The s-value for Niche 3107 (Niche 3) UM 4.88–5.18 m is slightly less than one (i.e., 0.43), implying that the use of Equation 6.2.2-4 will result in a larger error in α^{-1} for this test.

Table 6.2.2-2. Alpha (α) Values Estimated for the Fractures

Niche	Borehole and Interval (m)	Output Capillary Strength α^{-1} (m)
3650	UL 7.01-7.32	0.0855
	UL 7.62-7.92	0.0013
	UM 4.27-4.57	0.0225
	UM 4.88-5.18	0.0008
	UM 5.49-5.79	0.0334
	UR 4.27-4.57	0.0532
	UR 4.88-5.18	0.0205
	UR 5.49-5.79	0.71
	UR 6.10-6.40	0.0004
	UR 6.71-7.01	0.0014
4788	UL 7.62-7.93	0.0095
	UM 6.10-6.40	0.0015
	UR 5.18-5.48	0.0523
Theoretical limit		0.0019

DTN: LB980901233124.003 [105592]; LB990601233124.001 [105888]

NOTE: Various data sets were used to derive α^{-1}. Refer to Attachment II, Table II-5 for detail.

An early analysis based on visual inspection and straight-line fitting of Niche 3650 (Niche 2) short-duration test data in Figure 6.2.2-2 is documented in Trautz and Wang (2000 [165419]). In

this section of this scientific analysis report, the Niche 3650 (Niche 2) data analyses are compared with the results of long-duration tests at Niche 4788 (Niche 4).

Philip (1989 [156974]) reports that α^{-1} ranges from 0.05 m or less for coarse-grained soils to 5 m or more for fine-textured soils. In comparison, the values reported in Table 6.2.2-2 range from 0.001 to 0.71 m for the fractures tested, with the lower bound below that normally reported in the literature for soils. Philip (1989 [156974]) and White and Sully (1987 [106152], p. 1514) recognized that α^{-1} is a K-weighted mean soil-water potential directly related to the macroscopic capillary length, or pore radius r of the medium, as follows:

$$2\alpha^{-1} = \frac{2\gamma\cos(\theta)}{\rho g r} \qquad \text{(Eq. 6.2.2-5)}$$

where γ, ρ, and θ are the surface tension, density, and contact angle of the fluid, respectively, and g is gravitational acceleration. The right-hand-side of Equation 6.2.2-5 is known as Laplace's capillary formula, which is equal to the height of fluid rise in a small diameter cylindrical tube. Equation 6.2.2-5 can also be used to estimate the height of fluid rise between two smooth parallel plates (analogous to a fracture) by substituting the aperture b, or separation distance between plates for r in Equation 6.2.2-5.

Bouwer (1966 [155682], p. 733) and Raats and Gardner (1971 [155683], p. 922) described the macroscopic capillary length, and hence $2\alpha^{-1}$, as a "mean" height of capillary rise above a water table, or the "mean" air-entry head. In our case, the significance of $2\alpha^{-1}$ is that it represents the mean height that water can be retained in the fractures above the drift (without seeping) because of the capillary barrier.

Figure 6.2.2-2 was generated by plotting the K_o^* values derived in Section 6.2.2.1 along with their corresponding K_l values reported in Table 6.2.2-1. The significance of the line in Figure 6.2.2-2 is that it corresponds to the smallest value of α^{-1} that can be obtained, given the limited range of validity for the capillary mechanism using Laplace's formula. Wang and Narasimhan (1993 [106793], p. 329) show that when the fracture aperture is very large, the radial curvature of the fluid meniscus between two parallel plates will be very large and the capillary effect will be negligible. Using Laplace's formula, they determined for a wetting fluid of contact angle zero (i.e., $\theta = 0$ in Equation 6.2.2-5) that the capillary mechanism is no longer valid when the maximum aperture b_{max} between two smooth-walled parallel plates exceeds

$$b_{max} = \left(\frac{2\gamma}{\rho g}\right)^{1/2} \qquad \text{(Eq. 6.2.2-6)}$$

For $\gamma = 0.072$ kg/s^2, $\rho = 998$ kg/m^3, and $g = 9.8$ m/s^2 the nominal aperture size is 3.84 mm, which, using Equation 6.2.2-5, corresponds to a limiting value for α^{-1} equal to 0.0019 m. The line in Figure 6.2.2-2 represents the practical limit of Equation 6.2.2-1 calculated using the limiting value of α^{-1} derived from Equation 6.2.2-5 and Equation 6.2.2-6. Therefore, values of α^{-1} less than 0.0019 m correspond to nominal apertures that are greater than 3.84 mm, the point at which capillary forces vanish and gravity forces dominate flow. Several data points are

slightly above the line in Figure 6.2.2-2. This implies that gravity forces dominate fluid flow through these features.

6.2.2.3 Estimated Volumetric Water Content (θ) of Fractures

Another useful piece of information that can be derived using the niche seepage data includes estimates of the change in volumetric water content θ, where θ = (volume of water in fractures)/(bulk volume of fractured tuff) of the fractures. Direct measurement of fracture θ in the field is difficult at best using conventional hydrological techniques (e.g., using neutron moisture logs). Therefore, an alternative method of measuring average volumetric water contents indirectly, using wetting-front arrival times observed at the niche ceiling during the seepage tests, is described below.

Based on mass conservation along the vertical flow path, the depth of the wetting front below the water source is:

$$z_p = \frac{q_s\, t}{(\theta_{ave} - \theta_n)} \qquad \text{(Eq. 6.2.2-7)}$$

where z_p is the depth from the water-supply surface to the leading edge of the wetting front, t is the arrival time of the front at depth z_p, q_s is the constant flux of water supplied at the source, and θ_n is the initial or antecedent (or residual) water content.

Using the arrival time for the wetting front observed at the niche ceiling (DTN: LB980001233124.004 [136583]) and the q_s data (DTN: LB980001233124.004 [136583]), it is possible to estimate the change in volumetric water content change $\Delta\theta = \theta_{ave} - \theta_n$ for each seepage test by applying Equation 6.2.2-7. (Computation of $\Delta\theta$ was performed in an Excel spreadsheet documented in Attachment II, Table II-8 for Niche 4788 [Niche 4]. The $\Delta\theta$ was not computed for Niche 3107 [Niche 3]—refer to Section 6.2.2.4.) Table 6.2.2-3 provides a summary of the estimated $\Delta\theta$ values for zones where three or more seepage tests were conducted. With the approximation that the initial, antecedent, or residual moisture content θ_n is negligible compared to θ_{ave}, then $\Delta\theta$ becomes a measure of the average volumetric water content.

The water-content values shown in Table 6.2.2-3 range from 0.09 to 5.0%. Surprisingly, this indicates that the saturated water contents or porosities of the fractures could be as high as 5.0%, which is greater than expected. In turn, these values could influence travel-time calculations computed for the unsaturated zone, since travel time is proportional to water content. Using larger water content for the fractures would result in longer travel times.

The approach used to estimate water contents for the fractures are evaluated in Attachment IV.1 and Attachment IV.3.

Table 6.2.2-3. Estimated Changes in Volumetric Water Content ($\Delta\theta$)

Niche	Depth (m)	Test Name	Liquid Release Flux q_s, (m/s)	Average Water Content Change $\Delta\theta = \theta_{ave} - \theta_n$ (m^3/m^3)
3650	UL 7.62-7.92	Test #2 1-6-98	9.49E-06	0.0101
	UL 7.62-7.92	Test #1 2-12-98	1.89E-06	0.0017
	UL 7.62-7.92	Test #1 3-4-98	2.33E-07	0.0009
	UM 4.27-4.57	Test 5 Niche 3650 (11-13-97)	3.78E-05	0.0242
	UM 4.27-4.57	Test #1 12-3-97	9.42E-06	0.0146
	UM 4.27-4.57	Test #2 12-3-97	9.47E-06	0.0075
	UM 4.27-4.57	Test #1 1-7-98	8.82E-07	0.0120
	UM 4.27-4.57	Test #2 2-10-98	3.09E-07	0.0063
	UM 4.88-5.18	Test 1 Niche 3650 (11-12-97)	5.41E-05	0.0150
	UM 4.88-5.18	Test #1 12-4-97	9.49E-06	0.0043
	UM 4.88-5.18	Test #2 12-5-97	2.70E-06	0.0040
	UM 4.88-5.18	Test #1 1-8-98	8.75E-07	0.0082
	UM 4.88-5.18	Test #1 3-6-98	2.48E-07	0.0083
	UM 5.49-5.79	Test 4 Niche 3650 (11-13-97)	3.87E-05	0.0124
	UM 5.49-5.79	Test #2 12-4-97	9.43E-06	0.0061
	UM 5.49-5.79	Test #1 1-9-98	1.08E-06	0.0046
	UM 5.49-5.79	Test #1 2-11-98	2.55E-07	0.0040
	UR 6.71-7.01	Test #1 1-13-98	3.68E-06	0.0024
	UR 6.71-7.01	Test #1 2-3-98	1.91E-06	0.0018
	UR 6.71-7.01	Test #1 3-5-98	2.48E-07	0.0017
4788	UL 7.62-7.93	Test #1 11/3/99	1.65E-06	0.0200
	UL 7.62-7.93	Test #1 11-30-99 Niche 4788	9.22E-07	0.0057
	UL 7.62-7.93	Test #1 6-26-2000	3.59E-07	0.0101
	UL 7.62-7.93	Test #1 01-24-00	1.46E-07	0.0115
	UM 6.10-6.40	Test #1 Niche 4788 11/16/99	1.72E-06	0.0489
	UM 6.10-6.40	Test #1 Niche 4788 12-10-99	7.33E-07	0.0503
	UM 6.10-6.40	Test #1 06-08-2000	3.83E-07	0.0331
	UM 6.10-6.40	Test #1 3-14-2000	1.66E-07	0.0355
	UR 5.18-5.48	Test #1 Niche 4788 12/7/99	1.69E-06	0.0092
	UR 5.18-5.48	Test #1 1/5/2000	7.11E-07	0.0055
	UR 5.18-5.48	Test #1 02-14-2000	1.65E-07	0.0055

DTN: LB980901233124.003 [105592] and DTN: LB0110LIQR0015.001 [OUTPUT]

6.2.2.4 Estimated Water Potentials (ψ) of Fractures

The direct measurement of water potentials is difficult to make in unsaturated fractures because hydrological instruments are not readily adaptable to measuring such small features. Therefore, an indirect measure of the water potential (ψ) was formulated using the α-values computed in Section 6.2.2.2, the liquid-release fluxes, air-derived saturated hydraulic conductivities, employing Equation 6.2.2-2 with $q_s = K(\psi)$, and solving for ψ as shown below:

$$\psi = \frac{\ell n(q_s / K_l)}{\alpha} \qquad \text{(Eq. 6.2.2-8)}$$

Using the values for q_s and K_l reported in DTN: LB980001233124.004 [136583] and the α-values from Table 6.2.2-2, ψ was computed for several Niche 3650 (Niche 2) tests by employing Equation 6.2.2-8. (Computation of ψ was performed in an Excel spreadsheet documented in Attachment II, Table II-7 for Niche 4788 [Niche 4; ψ was not computed for Niche 3107 [Niche 3] because a value for K_l could not be computed: the corresponding air k value was not measurable with the equipment used). A summary of the resulting ψ values is provided in Table 6.2.2-4.

Table 6.2.2-4. Estimated Water Potential (ψ) for the Fractures

Niche	Borehole/Depth (m)	Test Name	Absolute Value of the Water Potential ψ (m)
3650	UL 7.62-7.92	Test #2 1-6-98	3.59E-03
	UL 7.62-7.92	Test #1 2-12-98	5.68E-03
	UL 7.62-7.92	Test #1 3-4-98	8.39E-03
	UM 4.27-4.57	Test 5 Niche 3650 (11-13-97)	8.26E-03
	UM 4.27-4.57	Test #1 12-3-97	2.30E-02
	UM 4.27-4.57	Test #2 12-3-97	2.29E-02
	UM 4.27-4.57	Test #1 1-7-98	7.64E-02
	UM 4.27-4.57	Test #2 2-10-98	1.00E-01
	UM 4.88-5.18	Test 1 Niche 3650 (11-12-97)	3.13E-03
	UM 4.88-5.18	Test #1 12-4-97	4.56E-03
	UM 4.88-5.18	Test #2 12-5-97	5.58E-03
	UM 4.88-5.18	Test #1 1-8-98	6.50E-03
	UM 4.88-5.18	Test #1 3-6-98	7.53E-03
	UM 5.49-5.79	Test 4 Niche 3650 (11-13-97)	1.95E-02
	UM 5.49-5.79	Test #2 12-4-97	2.77E-02
	UM 5.49-5.79	Test #1 1-9-98	1.00E-01
	UM 5.49-5.79	Test #1 2-11-98	1.48E-01
	UR 6.71-7.01	Test #1 1-13-98	5.90E-03
	UR 6.71-7.01	Test #1 2-3-98	6.84E-03
	UR 6.71-7.01	Test #1 3-5-98	9.76E-03
4788	UL 7.62-7.93	Test #1 11/3/99	2.56E-02
	UL 7.62-7.93	Test #1 11-30-99 Niche 4788	3.12E-02
	UL 7.62-7.93	Test #1 6-26-2000	4.01E-02
	UL 7.62-7.93	Test #1 01-24-00	4.86E-02
	UM 6.10-6.40	Test #1 Niche 4788 11/16/99	7.38E-03
	UM 6.10-6.40	Test #1 Niche 4788 12-10-99	8.65E-03
	UM 6.10-6.40	Test #1 06-08-2000	9.61E-03
	UM 6.10-6.40	Test #1 3-14-2000	1.09E-02
	UR 5.18-5.48	Test #1 Niche 4788 12/7/99	4.41E-02
	UR 5.18-5.48	Test #1 1/5/2000	8.93E-02
	UR 5.18-5.48	Test #1 02-14-2000	1.66E-01

DTN: LB980001233124.004 [136583]; DTN: LB980901233124.003 [105592]

NOTE: Various data sets were used to generate this table. Refer to Table II-7 in Attachment II for details.

6.2.2.5 Fracture-Water Characteristic Curves

The volumetric water-content values from Section 6.2.2.3 and the water-potential values derived in Section 6.2.2.4 are plotted on Figure 6.2.2-3 to create a water-characteristic curve for the fractures. Only those test intervals where three or more tests were conducted are included in the figure. (Inclusion of zones having only two data points joined by a straight line contributes little to understanding of the functional relation between θ and ψ.).

Note that the data fall into two groups, exhibiting similar water-retention characteristics. The first group (N3650 UL 7.62-7.92 m, N3650 UR 6.71-7.01 m and N3650 4.88-5.18 m) consists of high-permeability fractures that drain over a narrow range of water potentials and appear to have low residual water contents of about 0.001 to 0.002. The second group (N3650 UM 4.27-4.57 m, N3650 UM 5.49-5.79 m, N4788 UM 6.10-6.40 m, N4788 UL 7.62-7.93 m, and N4788 UR 5.18-5.48 m) consists of lower-permeability fractures that drain over a relatively larger range of water potentials and appear to have a slightly larger residual water content of about 0.005.

Residual water remaining in the fracture after the initial test can cause subsequent test data (collected during a test performed at a similar rate) to shift to the left, parallel to the x-axis, as shown in Figure 6.2.2-4 for zone N3650 UM 4.27-4.57 m. The second and third tests from this interval were conducted at nearly identical fluxes (9.42E-06 versus 9.47E-06 m/s) separated in time by less than 2 hours. The wetting front arrived at the niche ceiling during the second test in about half the time as the first test, resulting in a $\Delta\theta$ value that is half that for the second test compared to the first. The fourth and fifth tests in the sequence were performed approximately one and two months later, respectively. Evidence of the effects of wetting history is not readily apparent for these tests, which were conducted at lower fluxes (corresponding to lower water contents), indicating that the fractures drained or dried out prior to retesting.

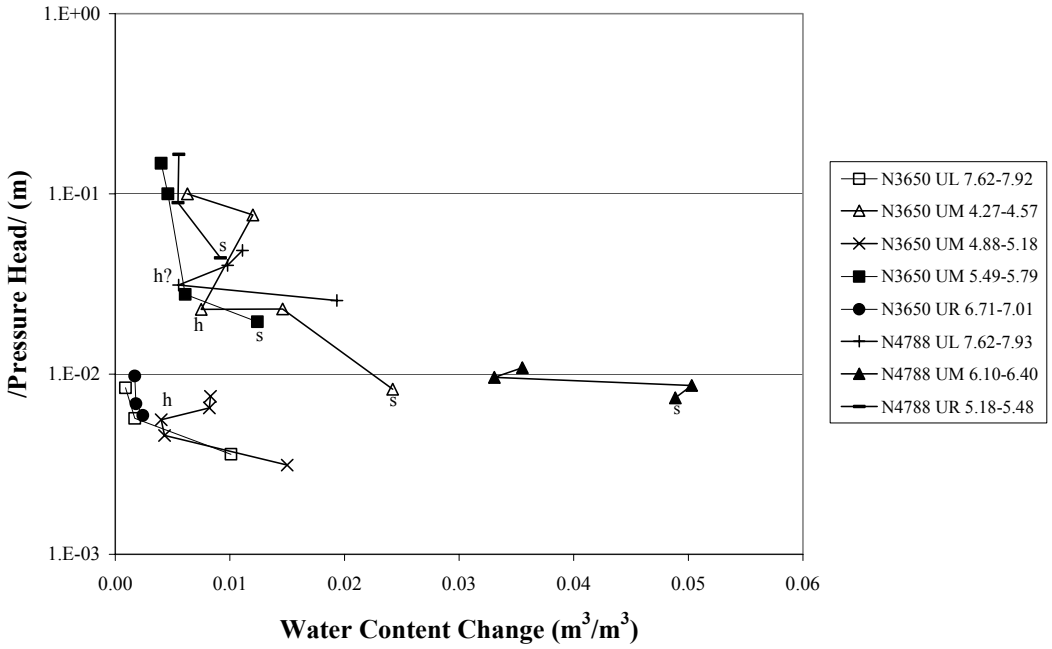

DTN: LB980901233124.003 [105592] and LB0110LIQR0015.001 [OUTPUT]

NOTE: Various data sets were used to generate this Figure. Refer to Table II-7 and Table II-8 in Attachment II for details.

s = saturated conditions
h = data point influenced by wetting history

Figure 6.2.2-3. Water Retention Curves for Fractures

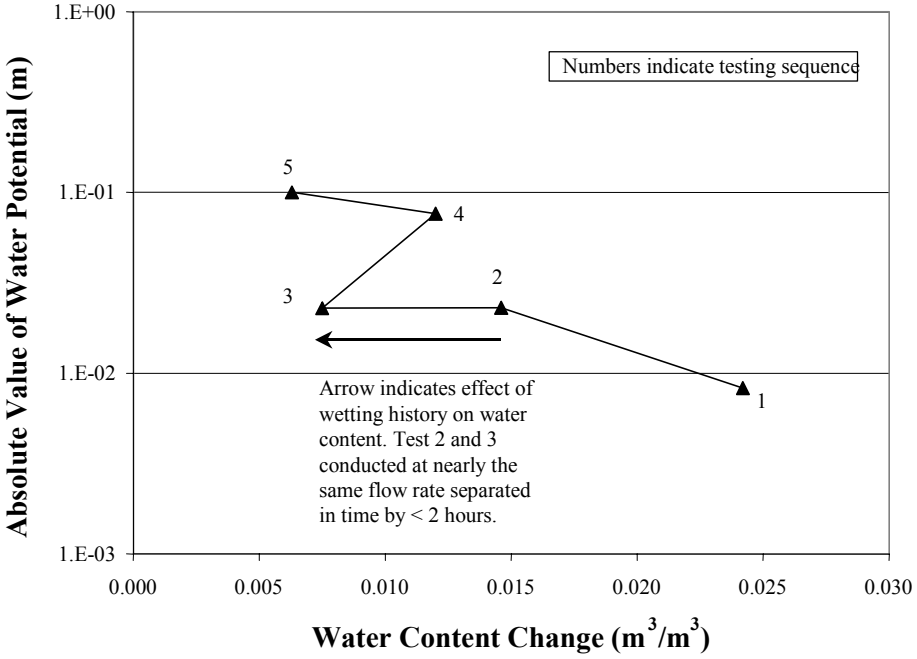

DTN: LB980901233124.003 [105592]

NOTE: Various data sets were used to generate this Figure. Refer to Table II-7 and Table II-8 in Attachment II for details.

Figure 6.2.2-4. Effect of Wetting History on Water Retention Curves for Test Interval N3650 UM 4.27–4.57 m

INTENTIONALLY LEFT BLANK

6.3 ANALYSES OF TRACER-MIGRATION DELINEATION AT NICHE 3650 (NICHE 2)

An additional episodic tracer migration test was conducted at drift-seepage test site Niche 3650 (Niche 2) in the ESF to elucidate the flow paths above the niche ceiling. The distribution of tracers from both the tracer migration test and previous liquid-release and seepage-threshold tests are presented in this section.

6.3.1 Tracer Distribution from the Tracer-Migration Test

6.3.1.1 Field Studies at Niche 3650 (Niche 2)

Seven 0.0762 m diameter boreholes were drilled at Niche 3650 (Niche 2). Three of these boreholes, designated UL, UM, and UR, were drilled approximately one meter apart and 0.65 m above the niche ceiling in the same horizontal plane as shown in Figure 6.1.1-2b. An array of twelve sampling boreholes was drilled to collect core samples for tracer analyses, as shown in Figure 6.3.1-1. The core analyses delineated the extent of tracer migration from an episodic liquid-release event as well as for all tracer and liquid-release tests.

Liquid-release tests were conducted prior to the niche excavation to evaluate how far a finite pulse of liquid would travel through unsaturated fractured rock (Section 6.2.1). Water containing colored dyes was used to mark the wetted area and flow paths resulting from each test. The niche was then excavated dry (using an Alpine Miner) to observe and photograph the distribution of fractures and dye within the welded tuff (Section 6.2.1 and Wang et al. 1999 [106146], pp. 329–332). After niche excavation, a series of short-duration seepage tests were performed to determine the amount of liquid that would seep into the mined opening (Section 6.2.2).

Along the three upper boreholes (UL, UM, UR), two Food, Drug & Cosmetics (FD&C) dyes were released before niche excavation: FD&C Blue No. 1 and FD&C Red No. 40. Blue and red bars in Figure 6.3.1-1a on the upper-left side of test-interval locations represent the pre-excavation liquid-release tests. Post-excavation liquid-injection tests, both with and without tracers, were conducted at various intervals along the boreholes to measure seepage into the niche. Post-excavation tracers included FD&C Blue No. 1, Sulpho Rhodamine B, Pyranine, FD&C Yellow No. 6, Acid Yellow 7, and Amino G Acid. The post-excavation seepage test sequences are summarized schematically on the lower right side of test-interval locations in Figure 6.3.1-1a.

6.3.1.2 Tracer Migration Test

The tracer migration test was conducted at Niche 3650 (Niche 2) six months after the seepage tests. From September 16–18, 1998, water containing six tracers (4.60 g/l NaI, 4.60 g/l CaI_2, 4.60 g/l $CaBr_2$, 1.56 g/l FD&C Blue No.1, 1.76 g/l FD&C Yellow No. 5, 0.019 g/l 2,3-difluorobenzoic acid, and 0.018 g/l pentafluorobenzoic acid) was released into a highly permeable zone located in borehole UM 4.88–5.18 m from the borehole collar. Iodide, bromide, and fluorinated benzoic acids were used as nonreactive tracers, while the others were applied as sorbing tracers. The release rate was 0.013 g/s, with a total released volume of about 1.52 liters.

The wetting front was observed to reach the niche ceiling in a large fracture/breakout, but water did not drip into the niche.

Between September 23 and October 1, 1998, twelve sampling boreholes, nominally 1.5 m long, were drilled into the niche ceiling around and below the liquid-release interval to determine the extent of the tracer migration. Rock-core samples were collected during the drilling process for subsequent laboratory chemical analyses. (Refer to Wang 1999 [153449], p. 99–107, 123, and 124 for detailed description of this tracer migration test.)

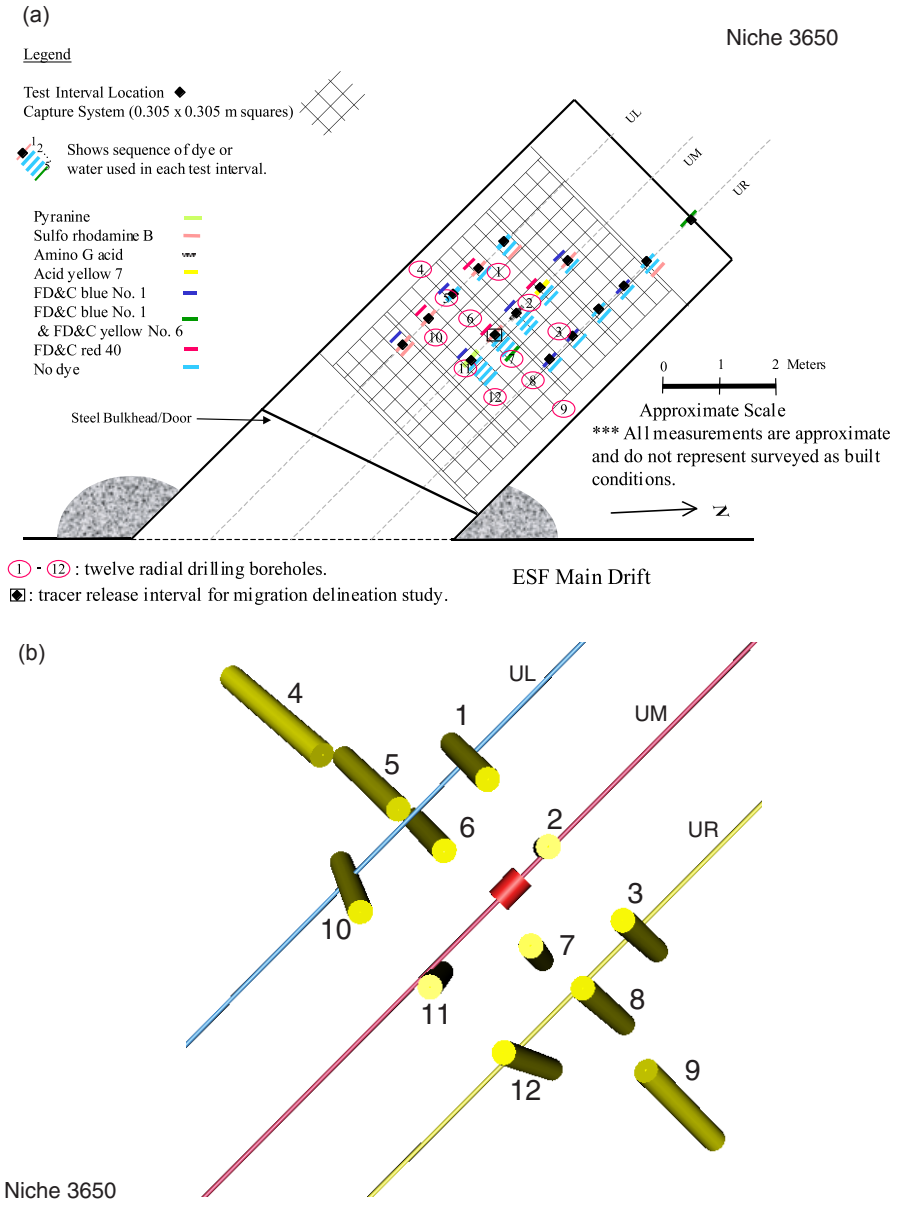

NOTE: The red-colored cylinder denotes the release interval of the tracer migration test.

Figure 6.3.1-1. Schematic of Sampling Borehole Array: (a) Plan View with Liquid-Release/Dye-Application History, and (b) Three-Dimensional View from inside the Niche

Figure 6.3.1-1b shows a 3-D perspective view of the sampling borehole array. The cores from the boreholes were 4.47 cm in diameter and were divided into sections during coring, with each section separately wrapped in Saran wrap. Each wrapped sample was placed inside a Lexan liner (with tape wrapping sealing both ends of the liners) and sealed in a Protecore® packet. The interval for each section was noted on the packet, which was assigned a unique numeric identifier.

The tracer chemical information is shown in Hu 1999 ([156541], pp. 154–155), and Hu 1999 ([155691], p. 151). Tracer analysis results and discussions are presented as concentration ratios (independent of chemical purity). Attachment V describes core sample processing and aqueous tracer measurement for the analyses of tracer distribution.

Iodide and FD&C Yellow No. 5 concentrations were not detected above background levels in the samples collected from the twelve boreholes drilled around the release interval. Iodide and FD&C Yellow No. 5 were applied only during the tracer migration test and were not used in earlier seepage tests at Niche 3650 (Niche 2). These results indicate that the sampling borehole array did not capture the tracer plume of the tracer migration test. Liquid migration was most likely localized and very possibly confined within the 1.0 m × 1.6 m area directly below the liquid-release interval.

Several rock-chip samples were collected from the ceiling of Niche 3650 (Niche 2) in March of 2001. These samples were obtained directly under the release interval of the tracer migration test (within a radius of about 20 cm), and within the twelve sampling boreholes. Six samples have been processed for chemical concentration measurements as documented in Hu 1999 ([155691], pp. 143–144), and Hu 2000 ([156473]). Iodide was detected in all six of the analyzed samples, confirming the arrival of iodide from the wetting front observed at the niche ceiling during the tracer migration test. FD&C Yellow No. 5 was not found among the samples, possibly because of its higher sorption compared to iodide.

6.3.2 Delineation of Tracer Distributions from Previous Liquid-Release Tests

Tests prior to the tracer migration test were conducted at different borehole intervals at various flow rates to determine the seepage thresholds for each interval. A total of 40 liquid-release tests over 16 borehole intervals were conducted at Niche 3650 (Niche 2), using both water with and without dye tracers as shown in Figure 6.3.1-1a. The distributions of these tracers were evaluated through the analyses of cores from the twelve sampling boreholes drilled into the flow domains. Examples of measured dye concentration versus borehole interval are shown in Figure 6.3.2-1 and Figure 6.3.2-2. The distribution of the tracers above the niche is used to assess the extent of tracer spreading and to provide data for the evaluation of seepage processes.

Tracer data are presented as dimensionless ratios of the detected tracer level to the background level. A higher ratio indicates the stronger presence of the tracer in the particular interval of a borehole. These detection ratios provide sufficient information about the spatial distributions of tracers, reconcile the difference in measurement techniques (i.e., ultraviolet/visible and fluorescence spectrophotometers), and eliminate the need to use and verify chemical purity information provided by the manufacturers. In Section 6.3.2.2, the measured dye distributions

are illustrated in three dimensions, based on as-built borehole survey coordinates using EARTHVISION-2 V4.0 software (LBNL 1998 [152835]).

6.3.2.1 Detection of Tracers

Several dyes from previous applications of seepage tests (Section 6.2.1.3.1) were detected within the borehole samples, as summarized in Table 6.3.2-1. FD&C Blue No.1 was present in seven out of 12 boreholes, with some of the boreholes containing relatively high concentrations of the tracer. Sulpho Rhodamine B was detected within four borehole samples. Overall, the dye distribution pattern was relatively spotty, reflecting the complex interplay of preferential flow paths and liquid application history. All of the previous liquid-release and seepage tests were conducted at least six months prior to the tracer migration test (Section 6.3.1).

Table 6.3.2-1. Compilation of Tracer Detection versus Borehole Location

Borehole ID	FD&C Blue No. 1	Sulpho Rhodamine B	FD&C Yellow No. 6	Pyranine	Acid Yellow 7	Amino G Acid
1	-	+++	-	-	-	-
2	+++	-	-	-	+++++	+
3	+++	-	-	-	-	-
4	-	-	-	-	-	-
5	-	-	-	-	-	-
6	-	-	-	-	-	-
7	+++++	+++++	+++	-	-	-
8	+++	-	-	-	-	-
9	+	-	-	-	-	-
10	+++	+++++	-	+	-	-
11	+++++	+	-	+++	-	-
12	-	-	-	-	-	-

DTN: LB990601233124.003 [106051]

NOTES: -: detection ratio < 3 (treated as absent)
+: The highest detection ratio is between 3–100 within this particular borehole.
+++: The highest detection ratio is between 100–1000 within this particular borehole.
+++++: The highest detection ratio is >1,000 within this particular borehole.

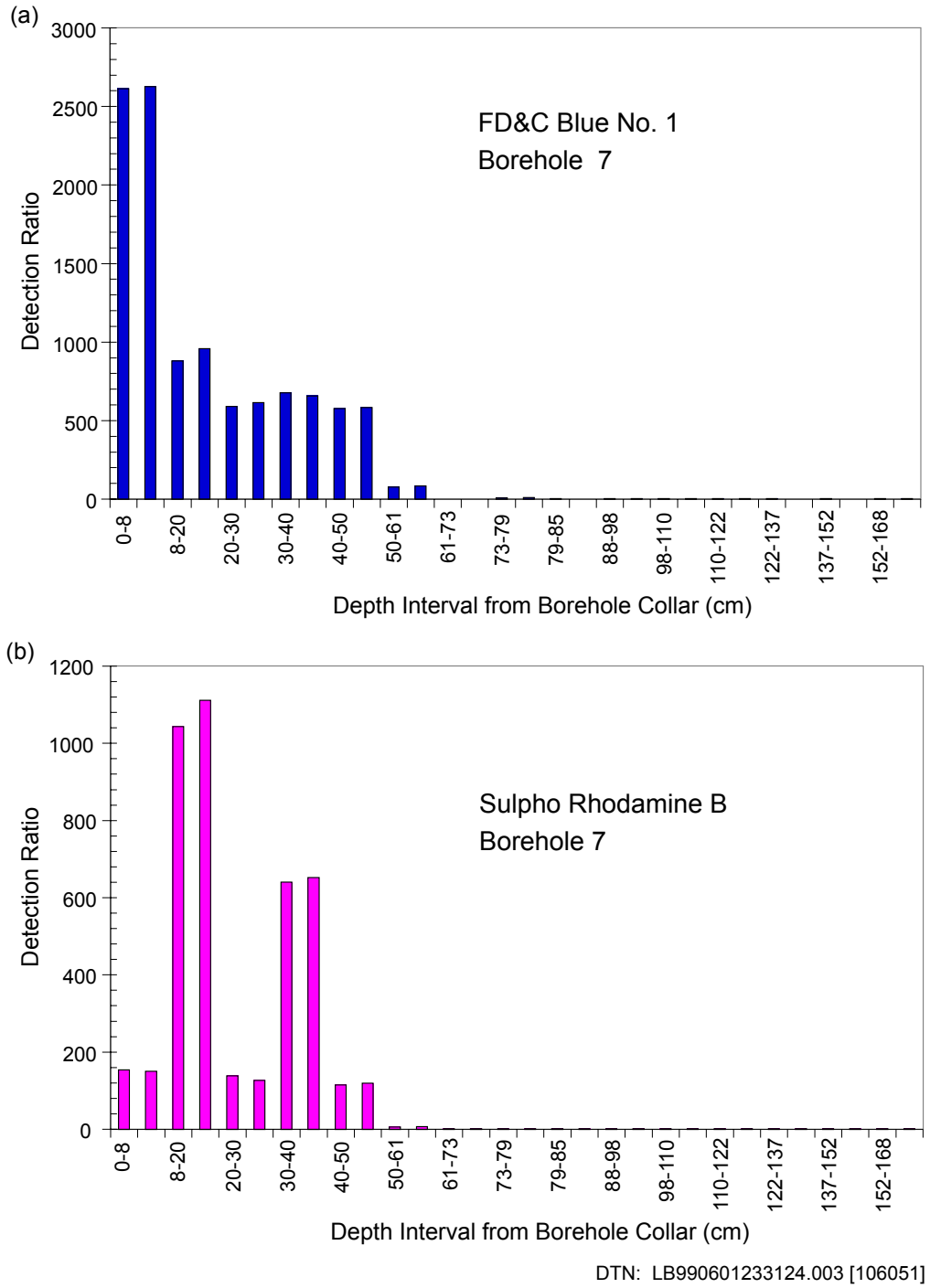

DTN: LB990601233124.003 [106051]

NOTE: Duplicate measurements were conducted in each specific interval.

Figure 6.3.2-1. Dye Detection along Borehole 7: (a) FD&C Blue No. 1 and (b) Sulpho Rhodamine B

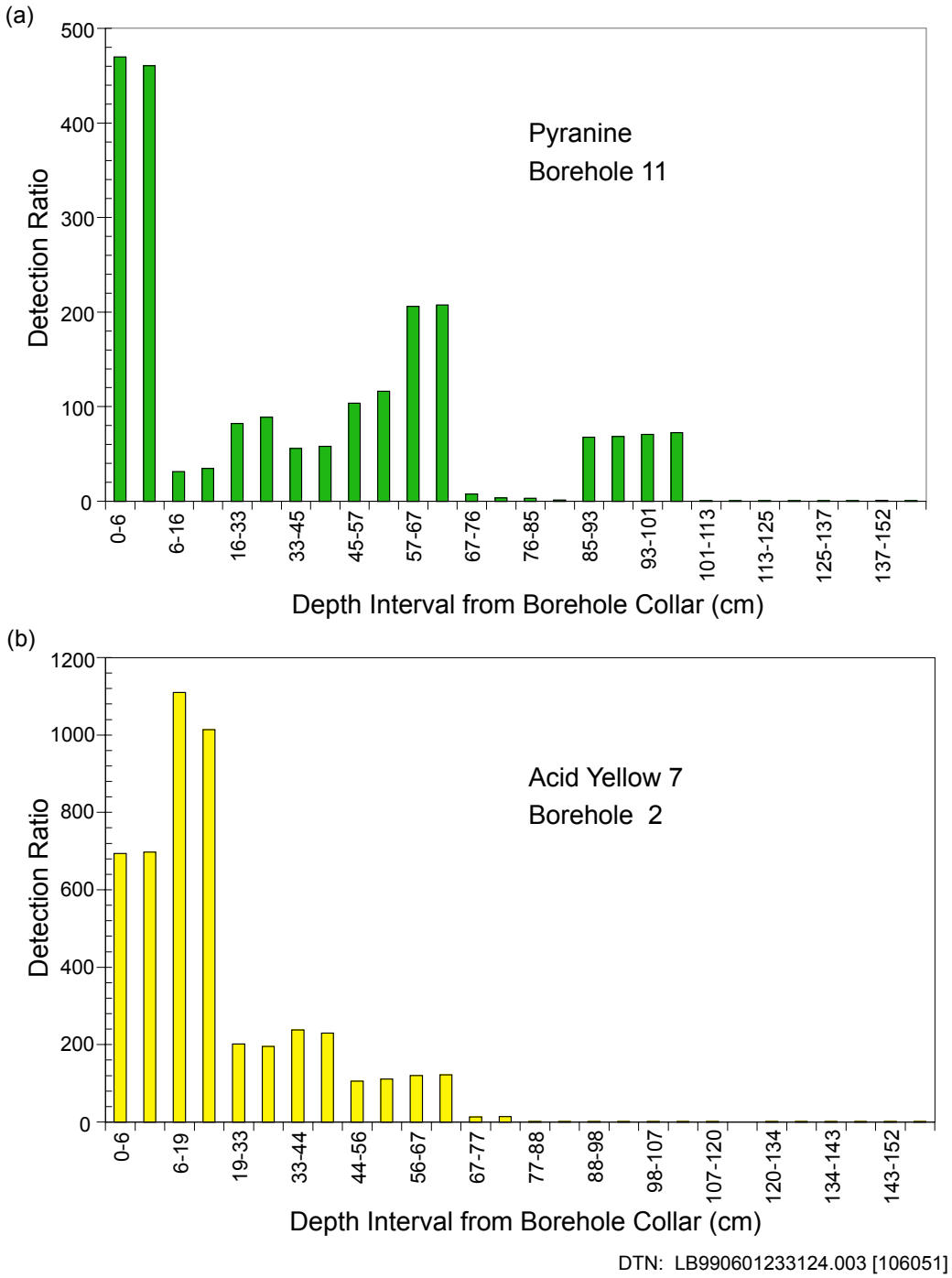

Figure 6.3.2-2. Dye Detection of: (a) Pyranine Along Borehole 11 and (b) Acid Yellow 7 along Borehole 2

6.3.2.2 Distribution of Dyes

FD&C Blue No. 1 was released in six intervals during pre-excavation liquid-release tests and in four intervals during post-excavation seepage tests (including one with a mixture of blue and yellow dyes). The blue dye distributions, together with release-interval locations, are illustrated in Figure 6.3.2-3. Boreholes where the tracer was not detected are represented by narrow lines. The multiple releases and dilutions introduced a complex application history. Overall results suggested that most regions containing blue dye were associated with tracer tests from nearby release intervals.

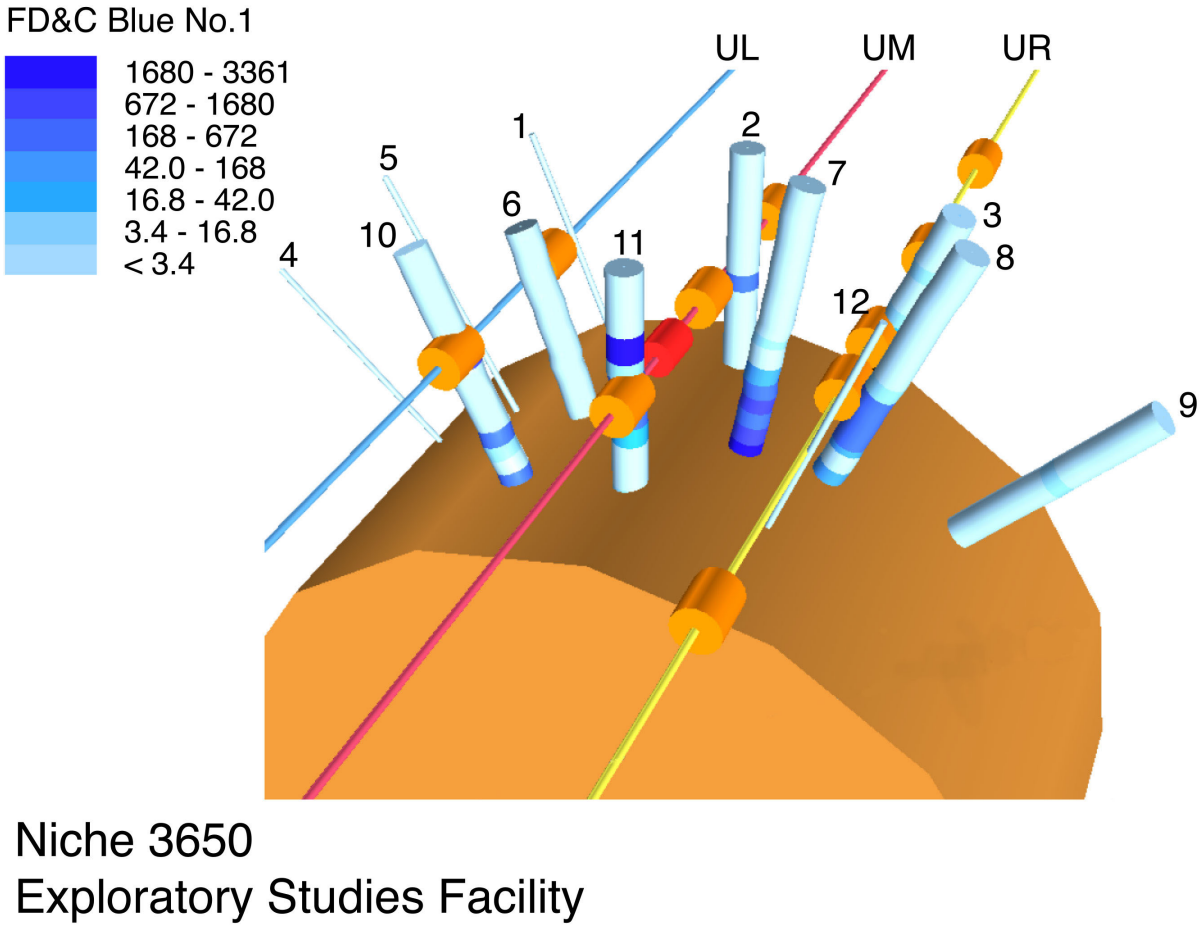

DTN: LB990601233124.003 [106051]

NOTE: The red cylinder denotes the tracer release interval of the tracer migration test and the other orange cylinders for intervals of early-release events. The sampling boreholes are individually identified. Detection ratios (dimensionless) are presented in the legend. Tracer concentrations are presented in dimensionless detection ratios as described in Section 6.3.2.

Figure 6.3.2-3. Three-Dimensional View of FD&C Blue No. 1 Detection Related to the Release Intervals above the Niche

Sulpho Rhodamine B was used in eight seepage tests along seven borehole intervals. Figure 6.3.2-4 illustrates the results for Sulpho Rhodamine B. Near borehole 7, Sulpho Rhodamine B was released once (in the interval UM 4.88–5.18 m), followed by three releases of water without dyes, and once with a mixture of FD&C Blue No. 1 and FD&C Yellow No. 6. The Sulpho Rhodamine B in borehole 7, and near the niche ceiling in borehole 8, most likely originated from this release episode. There was no Sulpho Rhodamine B detected in boreholes 3, 9, and 12. This suggested that the Sulpho Rhodamine B was likely migrating downward, rather than spreading laterally.

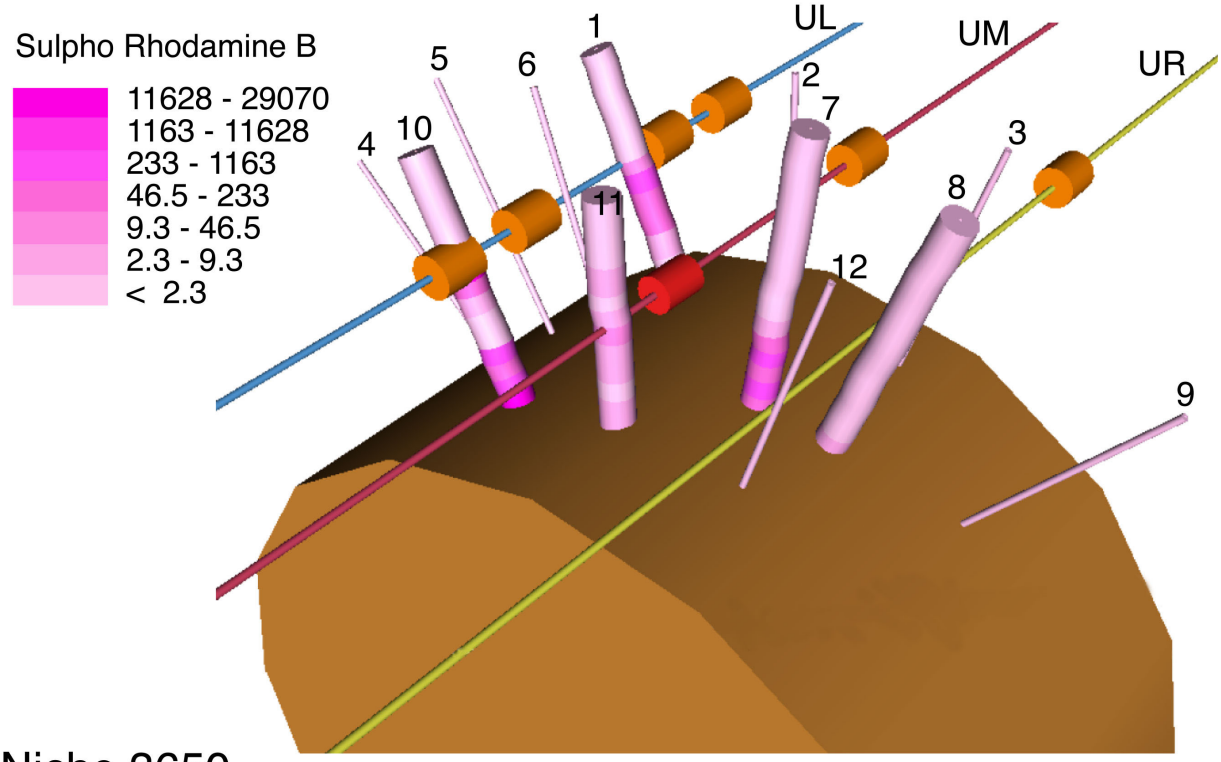

DTN: LB990601233124.003 [106051]

NOTE: The red cylinder denotes the tracer release interval of the tracer migration test and the other orange cylinders for intervals of early-release events. The sampling boreholes are individually identified. Detection ratios (dimensionless) are presented in the legend. Tracer concentrations are presented in dimensionless detection ratios as described in Section 6.3.2.

Figure 6.3.2-4. Three-Dimensional View of Sulpho Rhodamine B Detection Related to the Release Intervals above the Niche

In Niche 3650 (Niche 2), Pyranine, Acid Yellow 7, and Amino G Acid were used only once. Pyranine, Acid Yellow 7, and Amino G Acid are fluorescent dyes, and the low detection limits achievable with the fluorescence spectrophotometer provide confidence for the delineation of dye-stained flow paths within the sampling borehole array. Additionally, FD&C Yellow No. 6 was used once at UM 4.88–5.18 m within the sampling borehole array, and another time at Interval UL 7.62–7.92 m outside the borehole array (Figure 6.3.1-1a). The observations from

these tracer distributions also showed localized distributions of tracers, confirming downward migration (as opposed to the lateral spreading observed in the earlier tests).

Pyranine, for example, was detected at neighboring boreholes 10 and 11, with its presence much lower at borehole 10 than that at borehole 11 (Table 6.3.2-1 and Figure 6.3.2-5). Borehole 11 is located almost exactly below the interval of UM 4.27–4.57 m where Pyranine was released. Four episodes of water-only seepage tests were conducted following this Pyranine application. These liquid releases did not seem to enhance extensive lateral spreading. Overall, the lateral spreading of Pyranine was observed to be about 0.75 m to the left (i.e., borehole 10), resulting from these five release tests. However, its presence at borehole 10 was only slightly above the background level.

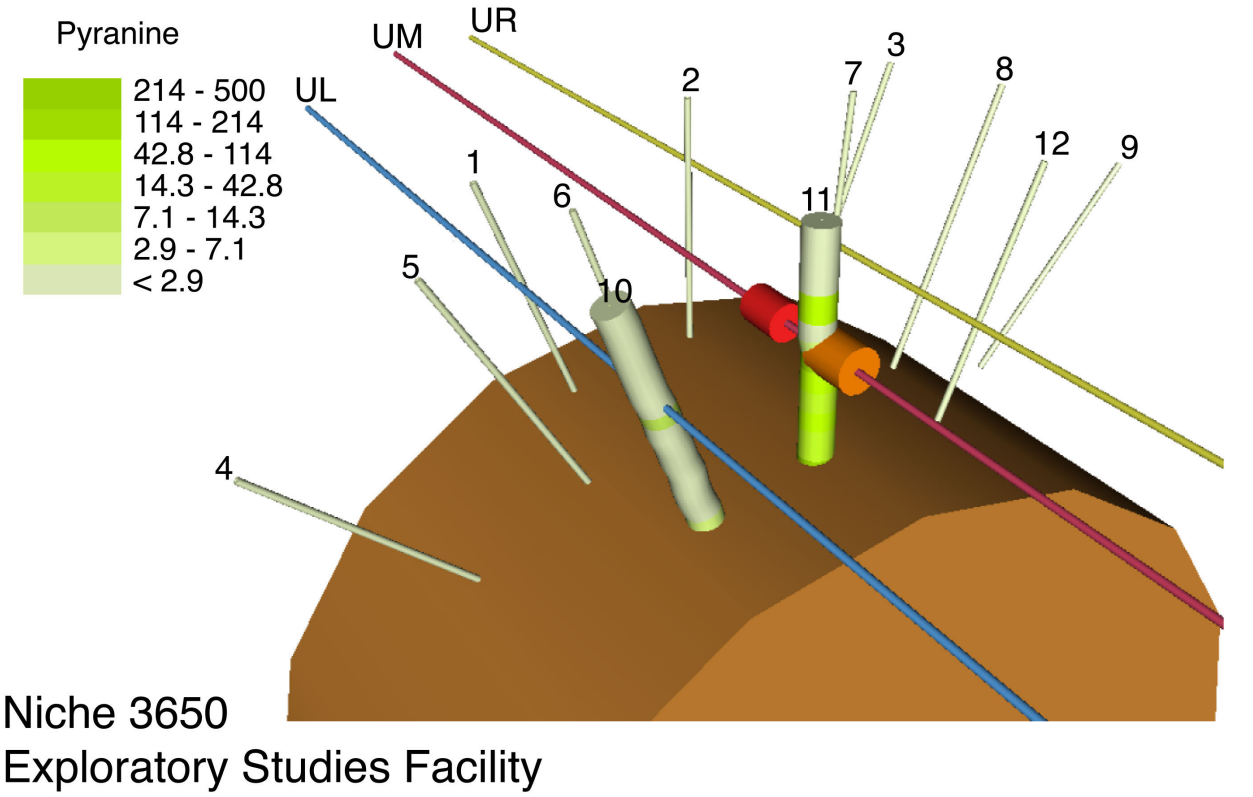

DTN: LB990601233124.003 [106051]

NOTE: The red cylinder denotes the tracer release interval of the tracer migration test and the other orange cylinder for interval of an early-release event. The sampling boreholes are individually identified. Detection ratios (dimensionless) are presented in the legend. Tracer concentrations are presented in dimensionless detection ratios as described in Section 6.3.2.

Figure 6.3.2-5. Three-Dimensional View of Pyranine Detection Related to the Release Interval above the Niche

Acid Yellow 7 was detected only at borehole 2, about 0.3 m from Interval UM 6.10–6.40 m where it was released (Figure 6.3.2-6). Amino G Acid was also detected near the detection limit at borehole 2, about 0.3 m from Interval UM 5.49–5.79 m where it was released (Figure 6.3.2-7). Note that although the Interval UM 5.49–5.79 m was encompassed within the sampling borehole array, Amino G Acid was not detected in any other borehole.

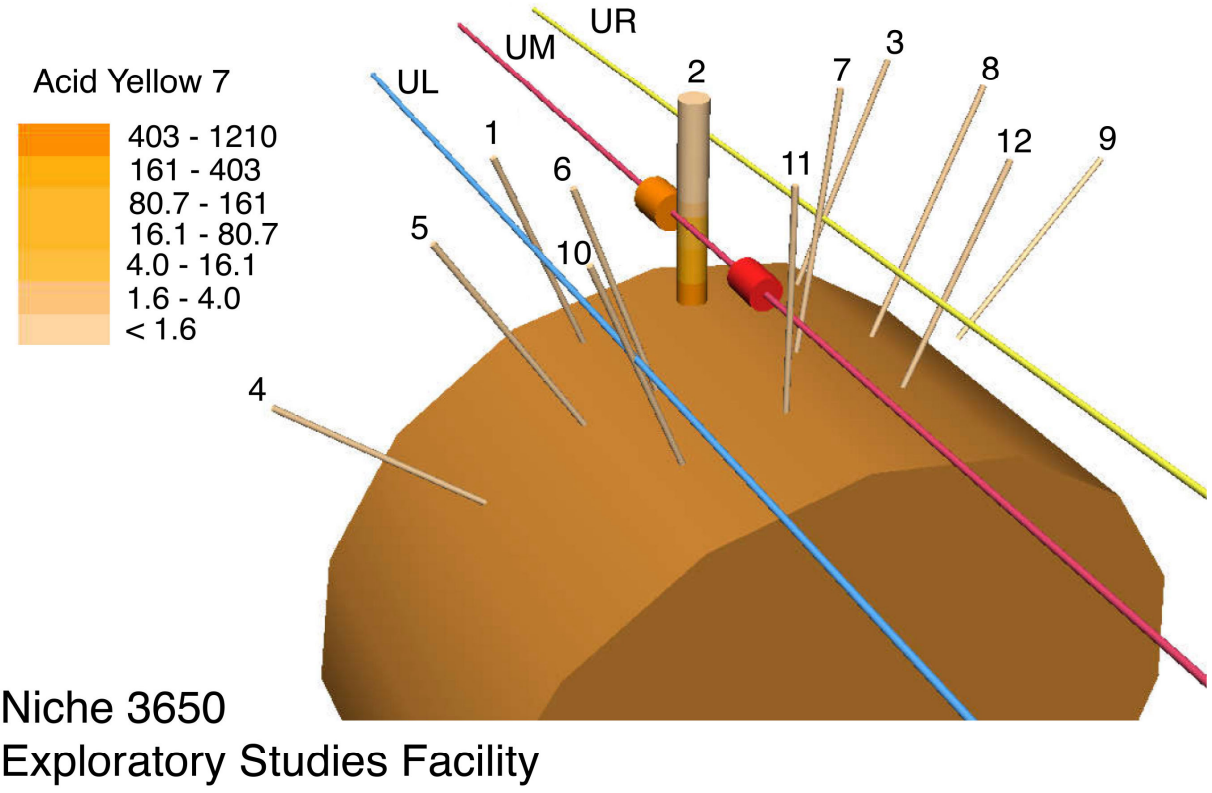

DTN: LB990601233124.003 [106051]

NOTE: The red cylinder denotes the tracer release interval of the tracer migration test and the other orange cylinder for intervals of an early-release event. The sampling boreholes are individually identified. Detection ratios (dimensionless) are presented in the legend. Tracer concentrations are presented in dimensionless detection ratios as described in Section 6.3.2.

Figure 6.3.2-6. Three-Dimensional View of Acid Yellow 7 Detection Related to the Release Interval above the Niche

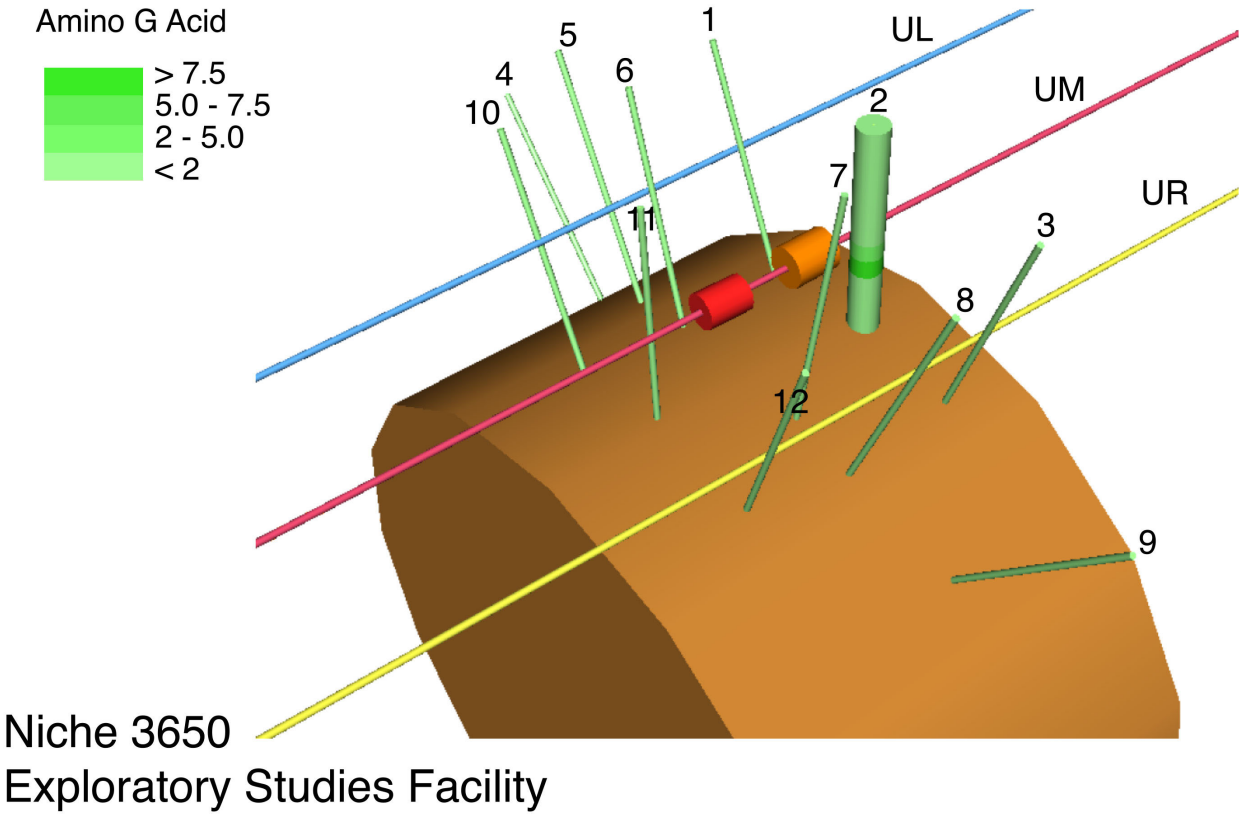

DTN: LB990601233124.003 [106051]

NOTE: The red cylinder denotes the tracer release interval of the tracer migration test and the other orange cylinder for interval of an early-release event. The sampling boreholes are individually identified. Detection ratios (dimensionless) are presented in the legend. Tracer concentrations are presented in dimensionless detection ratios as described in Section 6.3.2.

Figure 6.3.2-7. Three-Dimensional View of Amino G Acid Detection Related to the Release Interval above the Niche

The last dye distribution shown is for FD&C Yellow No. 6 (Figure 6.3.2-8). The dye was present at borehole 7. Borehole 7 was about 0.5 m from Interval UM 4.88–5.18 m where both FD&C Yellow No. 6 and FD&C Blue No. 1 were simultaneously released. This release episode had one of the lowest release rates (0.013 g/s) with one of the largest release volumes (5,597 g) among all the liquid-release tests conducted at Niche 3650 (Niche 2) (see Section 6.2 of this report). Borehole 7 is located in the middle of the sampling borehole array. The observation that FD&C Yellow No. 6 was only present in borehole 7 further demonstrated the localized characteristics of liquid flow with limited lateral spreading, even in this case with comparatively large release volume.

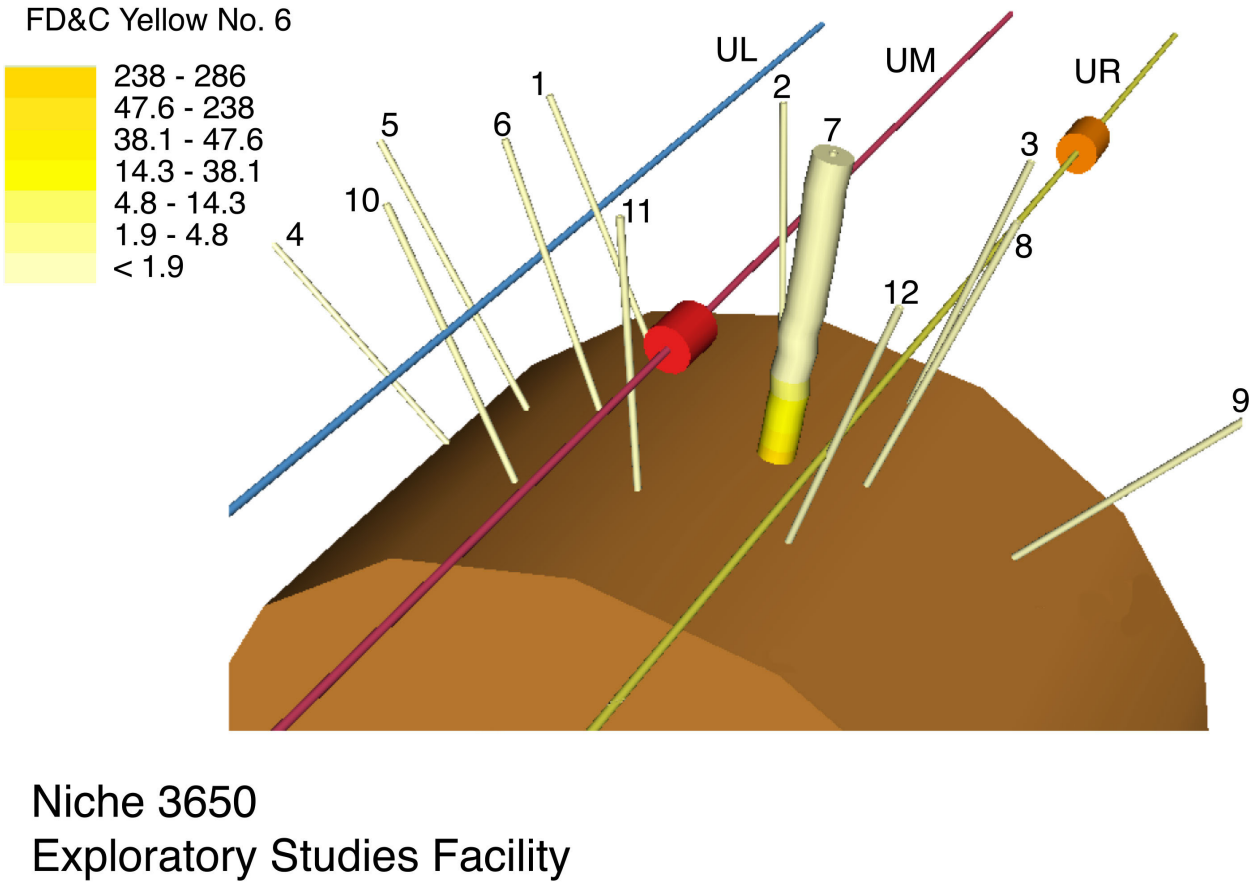

DTN: LB990601233124.003 [106051]

NOTE: The red cylinder denotes the tracer release interval of the tracer migration test and the other orange cylinders for intervals of early release events. (One of the two release intervals is the same as the last release event, represented by the red cylinder.) The sampling boreholes are individually identified. Detection ratios (dimensionless) are presented in the legend. Tracer concentrations are presented in dimensionless detection ratios as described in Section 6.3.2.

Figure 6.3.2-8. Three-Dimensional View of FD&C Yellow No. 6 Detection Related to the Release Intervals above the Niche

The dye distribution plots also indicated that some dyes have migrated above the injection intervals, as illustrated in Figure 6.3.2-3 for FD&C Blue No. 1, in Figure 6.3.2-5 for Pyranine; and to a lesser degree in Figure 6.3.2-4 for Sulpho Rhodamine B, in Figure 6.3.2-6 for Acid Yellow 7, and in Figure 6.3.2-7 for Amino G Acid. This is an interesting observation, indicating that fairly strong capillary forces may induce upward movements against gravity. Similar behavior was also observed in the Busted Butte test, as described in Section 6.13.3.1.1. However, further verification would be needed to determine the exact spatial extents of upward suction and tracer distribution. The locations of subsamples were derived from sample packets, and the spatial resolutions were poor, especially for fragmented core samples. The tracer subsample locations could be further checked against borehole logs (digital version if available) and core logs to improve spatial resolution.

6.4 ANALYSES OF TRACER PENETRATION AND WATER IMBIBITION INTO WELDED TUFF MATRIX

The objectives of this study are to investigate water flow and tracer transport, focusing on the relative extents of fracture flow and fracture-matrix interaction in the unsaturated, fractured tuff through a combination of field and laboratory experiments. Fieldwork was conducted in the ESF niches with liquid containing tracers released at specified borehole intervals. Tracer-stained rock samples were collected during niche excavation for subsequent laboratory analyses. Clean rock samples, collected from the same stratigraphic unit, were machined into cylinders for laboratory studies of tracer penetration into the rock matrix under different initial water-saturation levels. The use of laser-ablation inductively coupled-plasma mass spectrometry (LA-ICP-MS) to investigate chemical transport and sorption in unsaturated tuff is also presented.

6.4.1 Penetration of Dyes into Rocks from the Niches

Samples for laboratory analyses were collected from Niche 3650 (Niche 2) and Niche 4788 (Niche 4). The niche test sites, borehole configurations, liquid-release tests, and tracers used in the field are described in Section 6.2 and Section 6.3. Laboratory tests under controlled conditions were conducted to compare the travel front behavior of moisture, nonreactive bromide, and sorbing dye tracers (FD&C Blue No. 1 and Sulpho Rhodamine B). Sample drilling and tracer profiling techniques were developed. The descriptions and evaluations of laboratory analyses are presented in Attachment V.

6.4.1.1 Field Observations

During the niche excavation, as described in Section 6.2.1.2, dye was observed along individual fractures and intersecting fractures to a maximum depth of 2.6 m below the liquid-release points at Niche 3650 (Niche 2), and to a maximum depth of about 1.8 m at Niche 4788 (Niche 4). In general, the dye remained relatively close to the release interval and did not spread laterally more than 0.5 m. Figure 6.4.1-1 is a photograph taken during the excavation of Niche 4788 (Niche 4), showing the wall face with the fracture network stained by FD&C Blue No. 1. Results of post-excavation liquid-seepage tests at Niche 3650 (Niche 2) also indicated fast fracture flow with limited lateral spreading, since seepage water was captured directly below in trays beneath or immediately adjacent to the test interval.

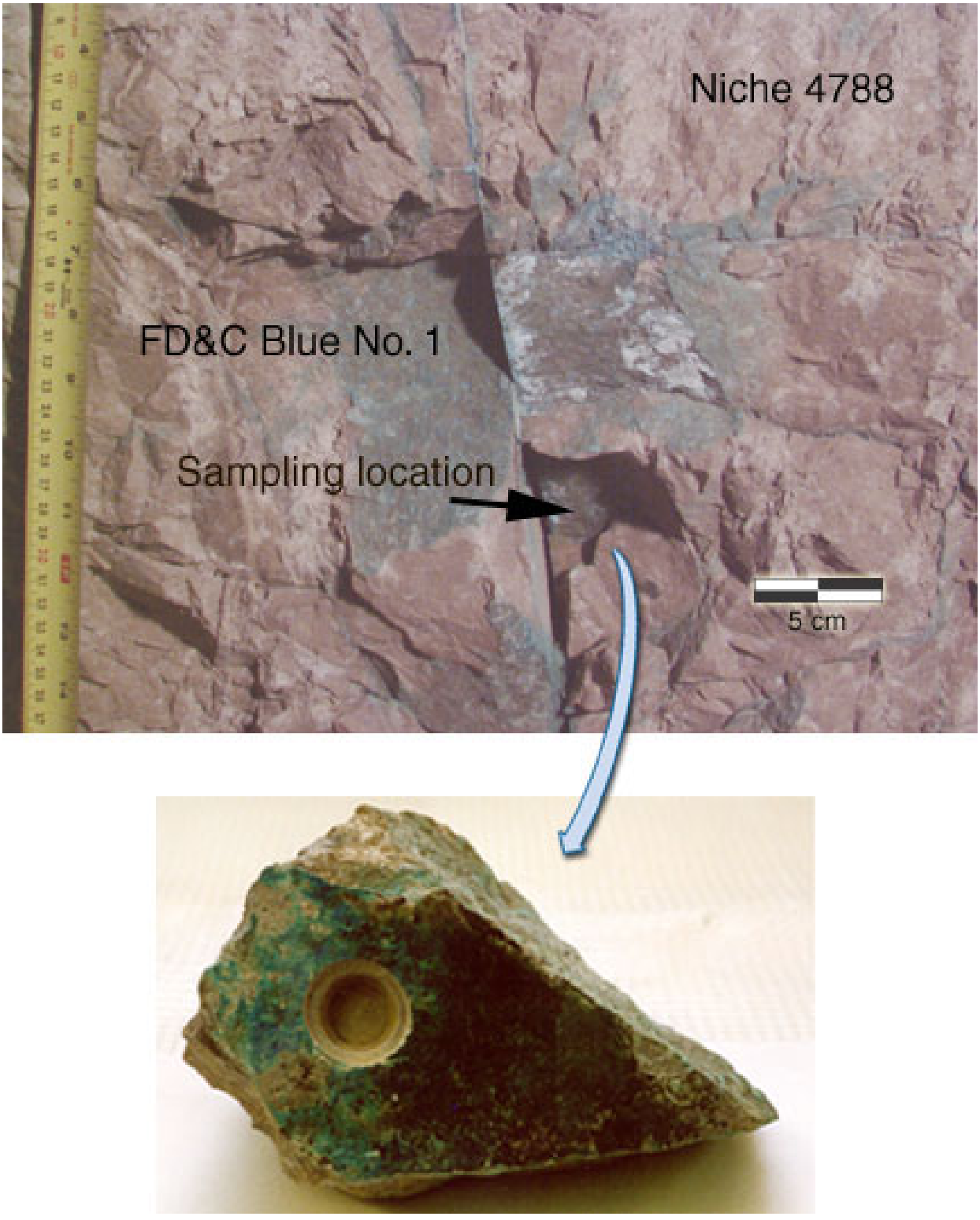

SOURCE: Hu et al. 2002 [165412], Figure 2.

Figure 6.4.1-1. Photograph Showing the Wall Face with Fracture Network and Sampling Location of Rock. Stained by FD&C Blue No. 1 during Niche Excavation at Niche 4788 (Niche 4)

6.4.1.2 Dye Penetrations into Rocks

Visual inspection of dyed rocks collected from the field studies showed that the dye stained the fracture surfaces and the color decreased with the distance and disappeared within a few millimeters from the fracture surfaces (Figure 6.4.1-1). The plot of Sulpho Rhodamine B detection ratio versus depth from the fracture surface is shown in Figure 6.4.1-2. (The dimensionless detection ratio is the measured tracer level divided by the background level.) The depth on the x-axis denotes the mid-point of the drilling interval. For example, the measured tracer concentration from a 1–2 mm drilling interval is shown at the 1.5 mm location from the sample surface. For three rock samples stained with either FD&C Blue No.1 or Sulpho Rhodamine B, each dye concentration decreased from the highest concentration to the background level in less than 6–7 mm. These results quantify the noticeable tracer matrix imbibitions from liquid flowing through the fractures.

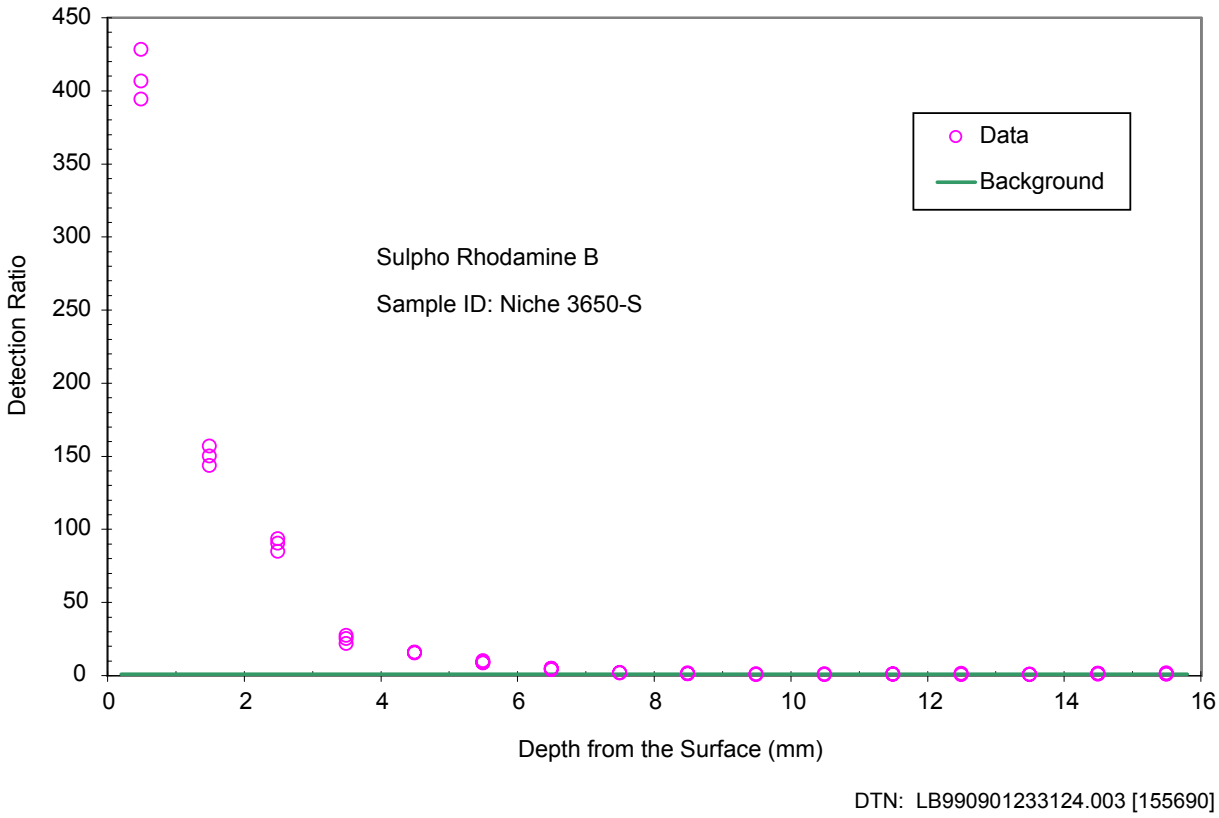

Figure 6.4.1-2. Sulpho Rhodamine B Penetration Profiles into Rock Matrix from the Fracture Surface

Table 6.4.1-1 provides relevant experimental conditions used during the liquid-release tests resulting in the three dyed rock samples collected during excavation. The samples were collected 7–13 days after the dye-spiked water was released into the formation. Water flow in post-excavation seepage tests was found to be very rapid, traversing 0.65 m in 4 minutes under the release rate of about 1.9 g/s (Table 6.4.1-2). It is therefore expected that the fluid-rock contact time is relatively short. Short travel times, together with high ratios of dye concentration in seepage water versus release water (in the far-right column of Table 6.4.1-2), indicated that the

contacts between flowing water in the fractures and the adjacent tuff matrix were highly transient. The exact duration of contacts on the fracture surfaces could not be measured.

Table 6.4.1-1. Liquid-Release Tests and Experimental Conditions

Tracer	Test Date	Test Location [c]	Tracer Conc. (g/l)	Release Rate (g/s)	Release Duration (min)	Mass Released (g)	Sampling Date
Sulpho Rhodamine B [a]	8/8/97	ML 6.71–7.01 m	2.0	2.0	8.22	170.9	8/19/97
FD&C Blue No. 1 [a]	8/6/97	UM 6.71–7.01 m	7.7	1.9	8.20	438.7	8/19/97
FD&C Blue No. 1 [b]	7/2/98	UM 6.40–6.70 m	6.77	0.49	35.0	1019.7	7/9/98

DTN: LB980001233124.004 [136583], LB980901233124.003 [105592]

NOTES: [a]Tests conducted at Niche 3650 (Niche 2) location

[b]Test conducted at Niche 4788 (Niche 4) location

[c]UM: upper middle borehole; ML: middle left borehole. Depth measurement (in meters) is from the collar of the borehole to the test interval.

Table 6.4.1-2. Post-Excavation Tracer-Release Tests at Niche 3650 (Niche 2)

Tracer	Test Location [a]	Release Rate (g/s)	Mass Released (g)	Mass of Seepage Recovered (g)	Wetting Front Arrives at (min:sec) [b]	Ratio of Seepage vs. Release Conc. (%)
Sulpho Rhodamine B	UL 7.01 – 7.32 m	1.949	1005.5	16.0	4:00	95.6
FD&C Blue No. 1	UR 4.27 – 4.57 m	0.198	995.7	4.0	56:08	77.0
FD&C Blue No. 1	UR 4.88 – 5.18 m	0.190	1016.4	4.0	29:50	103.9

DTN: LB980001233124.004 [136583]

NOTES: [a]UL: upper left borehole; UR: upper right borehole. Depth measurement (in meters) is from the collar of the borehole to the test interval.

[b]Time wetting front arrives at niche ceiling following the start of water release to the formation

Summary data are contained in DTN: LB990901233124.003 [155690]

6.4.1.3 Fast Fracture Flow

Fast fracture flow was demonstrated during the post-excavation seepage tests where dye-spiked water was released and collected, if possible, at the collection system below the niche ceiling. The last column of Table 6.4.1-2 shows the ratios of collected to released concentrations for FD&C Blue No. 1 and Sulpho Rhodamine B. Average seepage versus release-concentration ratio is 92.2 ± 13.8% over three tests with dyes. The seepage solution is a composite sample, which could be diluted from the resident water, if any, in the flowing fractures. Also, note that the release concentrations were obtained from the known dye mass dissolved in the known liquid, and no liquid sample was collected for the released solution during these tests. This uncertainty could contribute to the ratio of 103.9% (over the theoretical limit of 100%) for one of the FD&C Blue No. 1 tests. Significant dilutions (about 1,000 times), needed to bring down the sample

concentration within the linear standard curve needed for measurement, could also contribute to the uncertainty. More accurate ratios could be obtained if both the seepage and release solutions were measured simultaneously.

6.4.1.4 Concentration Profiles of Dye Tracer

For the dye-stained samples from the field, tracer concentrations were measured on rock powders collected from drilling intervals of the rock. Two FD&C Blue No. 1 dye profiles are illustrated in Figure 6.4.1-3. The scales of detection ratios described in Section 6.4.1.2 are plotted on the left-hand side. The scales of concentration ratios of measured concentration C divided by the released concentration C_o, C/C_o, are plotted on the right-hand side. The first few millimeters from the fracture surface contain the key portion of the tracer concentration profiles that indicate the extent of fracture-matrix interaction (Hu et al. 2002 [165412], p. 106).

Figure 6.4.1-3a for the sample Niche 3650-F has relative low values of C/C_o (compared with those obtained with Core D and Core H to be discussed in Section 6.4.2) for the first millimeter (i.e., 0–1 mm from the fracture surface). This sample could be associated with fast transient flow. Noticeable water and tracer imbibition into the surrounding matrix was observed, even though fracture flow could be fast.

In contrast, Figure 6.4.1-3b for the sample Niche 4788 has high value of C/C_o in the first millimeter. This sample was collected adjacent to a vertical flowing fracture that apparently dead-ended near the sampling location (Figure 6.4.1-1). For this sample, the fluid-rock contact time could have been longer, contributing to the higher concentration ratio at the first interval. The measured concentration ratio in the second (1–2 mm) interval drops drastically to the level similar to the samples in Figure 6.4.1-3a. With longer contact time, stronger surface sorption of the dye might also have occurred in this rock sample.

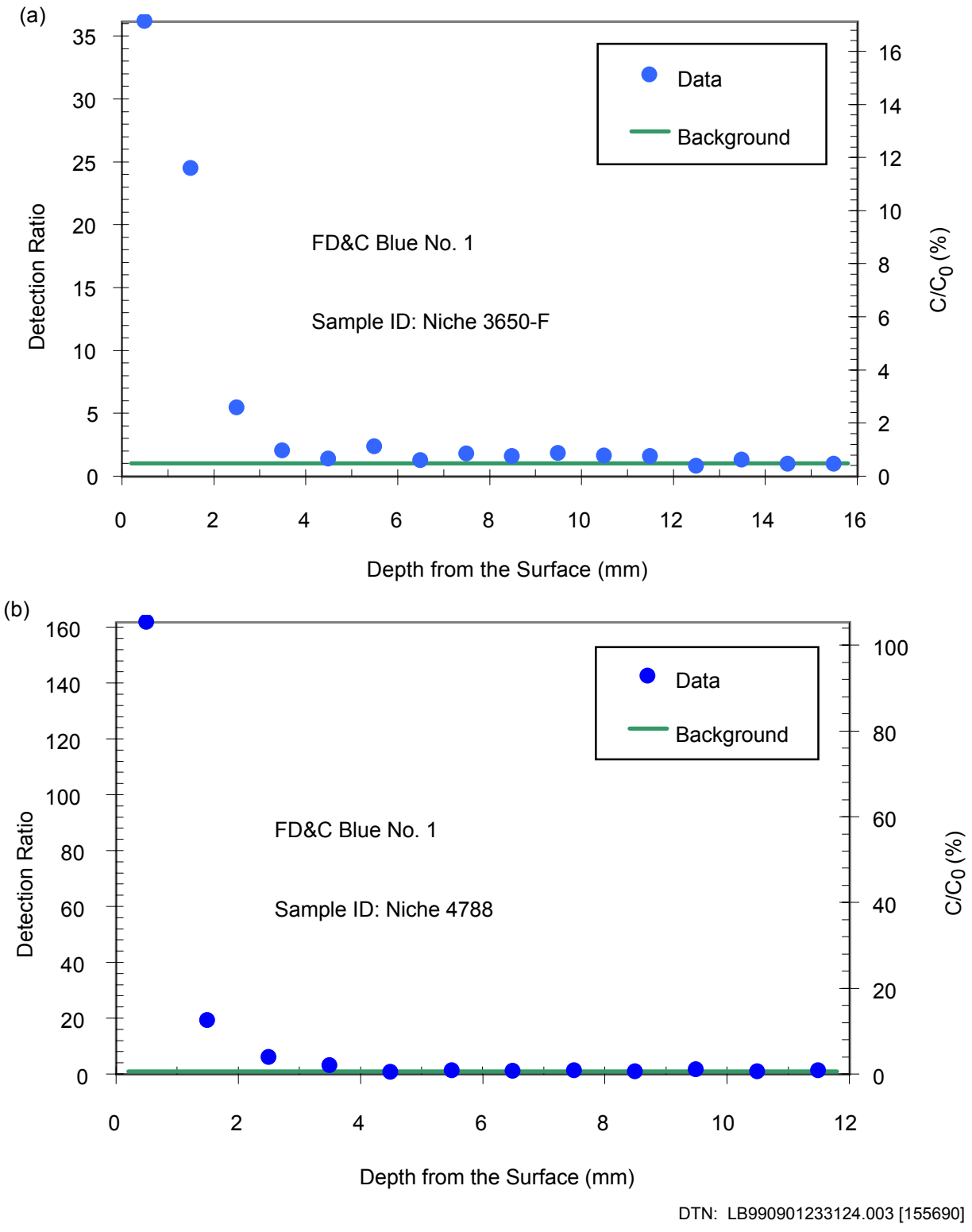

Figure 6.4.1-3. Tracer Penetration Profile into Rock Matrix from the Fracture Surface: (a) FD&C Blue No.1 at Niche 3650 (Niche 2); (b) FD&C Blue No.1 at Niche 4788 (Niche 4)

6.4.2 Retardation and Tracer Front Movement

Laboratory tests were conducted to quantify the imbibition of water and the retardation of tracers into rock cores. In the laboratory, tests can be conducted under controlled conditions, with concentrations in rock samples and in the core reservoir measured simultaneously. The flow paths along cores are well defined compared to the flow paths in the field. The laboratory test results can assist in interpreting data collected on dye-stained samples from the field tests.

There are two approaches presented for measuring the retardation factor: front separation and local 'saturated' measurements at the core-reservoir contact. The consistency between these two approaches lends credence to the quantification of retardation factors on core samples.

6.4.2.1 Dye Retardation Factor Determined by Front Separation

The descriptions and evaluations of laboratory tracer tests on core samples are presented in Attachment V. Figures 6.4.2-1 and 6.4.2-2 compare the concentration profile of nonreactive bromide with the concentration profiles of both FD&C Blue No. 1 and Sulpho Rhodamine B, relative to the moisture fronts obtained from visual inspection. The dyes lag behind the bromide front, indicating dye sorption to the rock. FD&C Blue No. 1 and Sulpho Rhodamine B were the most visible in the tuffs of the tested dyes. Sorption of these dyes on rock is not surprising, considering their complex chemical structure with various functional groups, even though they are negatively charged under normal pH conditions.

From the tracer profiles, the retardation factor R can be derived as the ratio of travel distance of nonreactive tracer divided by the travel distance of sorbing tracer. Bromide is approximately a nonreactive tracer in tuff, as indicated by its nearly coincident front with the wetting front at low initial water saturation. In Figure 6.4.2-1 for Core D at low initial saturation, the bromide front is located at 17–18 mm from the core bottom ($d_{0.5}$ = 17.5 mm, where $d_{0.5}$ is the depth at which the concentration is half of the steady-state concentration in the profile). The first data point at the 0-1 mm interval was excluded for bromide front determination. The 0–1 mm interval measurement was systematically higher than deeper intervals and was consistently observed for bromide in all core measurements. Because the 0–1 m interval at the core-reservoir interface is in direct contact with the tracers, it is not included in the calculation of the travel distance used to determine the retardation factor R. This does not seem to affect the sorbing tracers (FD&C Blue No. 1 and Sulpho Rhodamine B), as evident in the steady-state concentration of the first three intervals in Core D (Figure 6.4.2-1). For the sorbing tracers, $d_{0.5}$ is located at 3.5 mm (Figure 6.4.2-1). The retardation factor for both dyes is estimated to have the value 5 (= 17.5 mm/3.5 mm). Similarly, R is estimated to be 2.33 (= 3.5 mm/1.5 mm) for both dyes in Core H with high initial S_w (Figure 6.4.2-2).

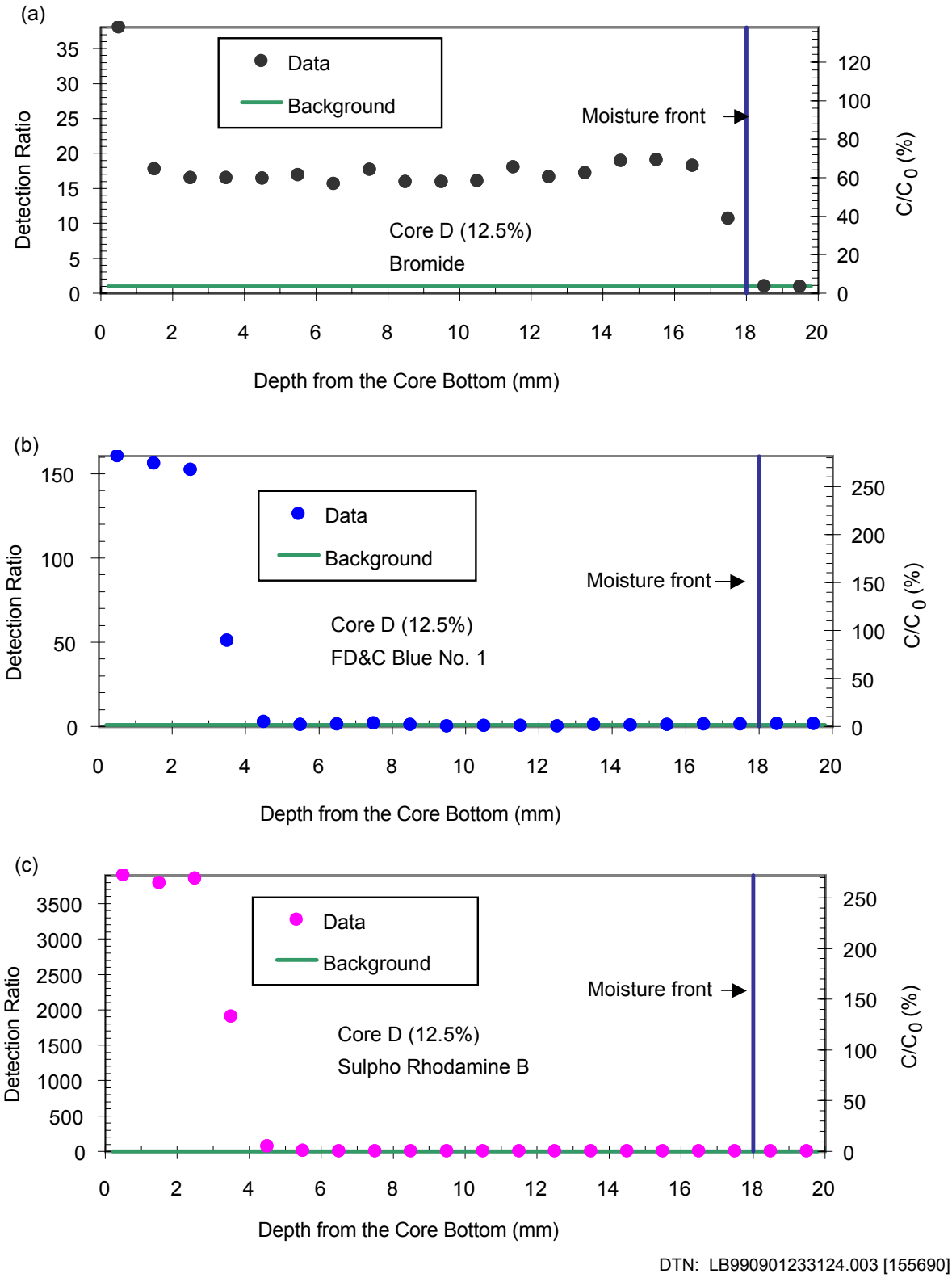

Figure 6.4.2-1. Comparison of Tracer Concentration Profiles in a Low-Initial-Saturation Core: (a) Bromide, (b) FD&C Blue No. 1, (c) Sulpho Rhodamine B. Core D had initial saturation of 12.5% and was in contact with saturated boundary for 19.5 hours.

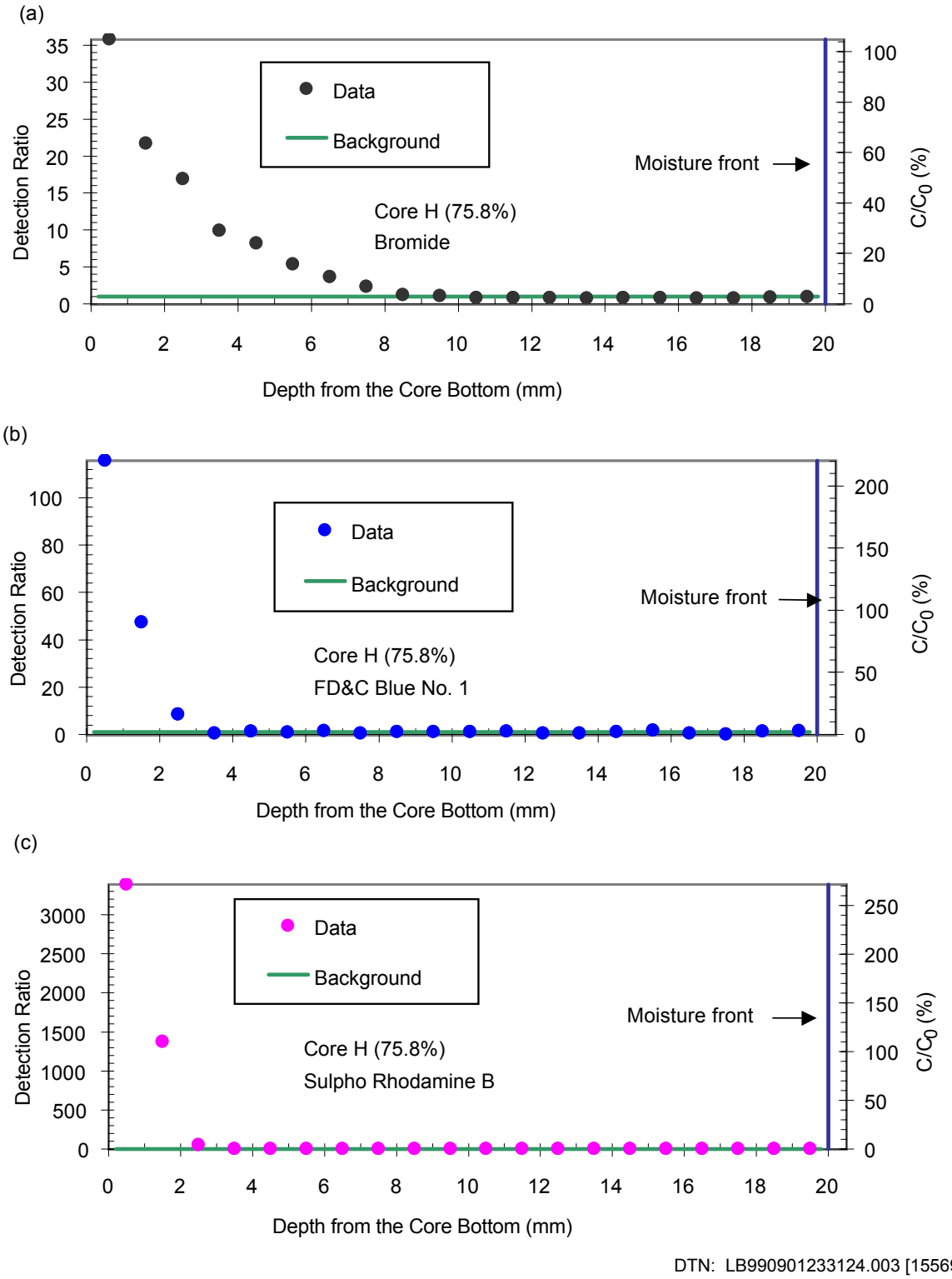

DTN: LB990901233124.003 [155690]

NOTE: Core H had initial saturation of 75.8% and was in contact with saturated boundary for 17.9 hours.

Figure 6.4.2-2. Comparison of Tracer Concentration Profiles in a High-Initial-Saturation Core: (a) Bromide, (b) FD&C Blue No. 1, (c) Sulpho Rhodamine B

The saturation dependence of the retardation factor is derived from the following functional relationship (Porro and Wierenga 1993 [134083], pp. 193–194):

$$R = 1 + \rho_b \times K_d / \theta \qquad \text{(Eq. 6.4.2-1)}$$

where K_d (mL/g) is the sorption distribution factor representing the distribution of solutes between aqueous and solid phase, ρ_b is the bulk density (g/mL), and θ is the water content. This equation explicitly shows that solute retardation is inversely related to water content. If the effective θ value is estimated as the average of the initial water content and the final water content (here set to be the measured porosity), the K_d value can be derived from the R-value. For the two core samples, the K_d value was calculated to be 0.089 mL/g for Core D and 0.047 mL/g for Core H (Attachment IX.3). The bulk density and porosity values for each core were measured independently, with values listed in Table 6.4.2-1. These measured values in Table 6.4.2-1 were used in calculating K_d values from measured R values.

Table 6.4.2-1. Measured Properties for Core Samples

Sample ID	Porosity (cm^3/cm^3)	Bulk Density (g/cm^3)
Core D	0.0888	2.248
Core E	0.0849	2.251
Core F	0.0890	2.239
Core H	0.0896	2.245
Core J	0.0823	2.266

DTN: LB990901233124.003 [155690]

As an additional consistency check, the calculations can be inverted and the R values derived from the K_d values for a fully saturated condition (i.e., 100% saturation). The $R_{100\%}$ is 3.25 for Core D and 2.17 for Core H from the inverse calculations. The average $R_{100\%}$ is 2.71 ± 0.76 for both FD&C Blue No. 1 and Sulpho Rhodamine B. Both K_d value and $R_{100\%}$ are constants independent of saturation. The simple checking verifies the functional relationship of Equation 6.4.2-1. For comparison, Andreini and Steenhuis (1990 [106071], pp. 85, 98) found that the retardation factor for FD&C Blue No. 1 ranged from 1.5 to 7 in a fine, sandy loam soil.

Note that the core measurements presented in this study can generate K_d values for intact rock under *in situ* partially saturated conditions. Most of the K_d values for sorbing solutes have been acquired by batch experiments using crushed rock, with the sizes chosen more or less arbitrarily and mainly for experimental convenience. The batch experiments were performed under saturated conditions with large water/rock ratios. There are concerns regarding the use of crushed-rock samples versus solid-rock samples in batch experiments on tuff rocks. The water/rock ratios used in the sorption experiments with crushed samples were large in comparison with the water/rock ratios likely to exist in the UZ. This unsaturated transport-sorption approach can be used to check the results commonly obtained from batch sorption experiments as well as to provide a more representative sorption under field conditions (Hu et al. 2002 [165412], p. 111).

6.4.2.2 Travel-Front Separation

As a nonreactive tracer, bromide is frequently used for flow tracking. The bromide front is comparable to the moisture front in the rock core at the initial water saturation of 12.5%, as illustrated in Figure 6.4.2-1a. The bromide front lags significantly behind the moisture front at the higher initial water saturation of 75.8%, as shown in Figure 6.4.2-2a. Note that the core top (20 mm) was wet when the experiment was ended, although the moisture front is shown at the 18 mm location in Figure 6.4.2-1b. This observation of nonreactive solute front lagging behind the moisture front agrees with the findings in moist soils (Warrick et al. 1971 [106150], pp. 1216, 1221; Ghuman and Prihar 1980 [106099], pp. 17, 19; Porro and Wierenga 1993 [134083], pp. 193, 196). Warrick et al. (1971 [106150]) first reported that the advance of a solute front was highly dependent on the soil moisture content during infiltration. During infiltration, no solute was found in the advancing wetting front where soil moisture contents were increasing, although the initially infiltrating water contained nonreactive tracer. The importance of this front separation, observed under a transient flow condition, might be more pronounced for low porosity materials under high moisture saturation, such as tuff at Yucca Mountain. Under these circumstances, a relatively small amount of invading solution can push the antecedent water further into the matrix.

For the imbibition experiment in Core D with low initial water saturation, the bromide front is sharp, with the strong capillary force driving the advection-controlled transport. Conversely, for the Core H with high initial water saturation, the bromide front is quite diffuse, since dispersion and dilution become important processes (on account of weaker capillarity) compared to advective flow. Sharp and diffused front separations between the bromide nonreactive tracer front and the moisture front, as well as between sorbing tracer front and bromide front, would provide the data for elucidating flow and transport in unsaturated, fractured tuff.

6.4.3 Application of LA-ICP-MS to Investigate Chemical Transport and Sorption

Laser ablation refers to the process in which an intense burst of energy delivered by a short laser pulse is used to vaporize a minute sample from a specific location. Chemical composition of the vaporized sample is then analyzed with inductively coupled plasma-mass spectrometry (ICP-MS). Laser ablation, coupled with ICP-MS (LA-ICP-MS), has recently evolved as a powerful analytical tool for solid samples (Russo et al. 2000 [155697]). LA-ICP-MS can determine simultaneously a large number of chemical elements, with very low detection limits. The applications of LA-ICP-MS have been recently reported in studies of tree rings, airborne particulates, and geochemistry. However, we are not aware of any studies where transport, sorption, or diffusion of contaminants in rocks are investigated by LA-ICP-MS. The high spatial resolution achieved by a focused laser beam makes LA-ICP-MS a very attractive approach to such environmental pollution studies.

This section describes the investigation of transport and sorption of chemicals that are of interest to the Yucca Mountain Project in unsaturated tuff. Laboratory tracer imbibition tests are similar to those presented in Attachment V, except that an initially dry tuff cube (1.5 cm in each side) was used in this LA-ICP-MS work, compared to core cylinders used in the drilling work as described in Section 6.4.1 and Section 6.4.2. Compared to the drilling technique presented in Attachment V, employment of LA-ICP-MS provides a quick way of profiling tracer chemical

concentration with high spatial resolution. Surrogate compounds are chosen based on their chemical similarity to radionuclides of interest. The tracer solution used in this study contained a mixture of NaBr, $NaReO_4$, CsBr, and RbBr. Both Br^- and perrhenate (ReO_4^-) are used as nonsorbing tracers, with perrhenate serving as an analog to technetium, which exists in a form of pertechnetate ($^{99}TcO_4^-$). Cesium (Cs^+) and rubidium (Rb^+) were used as cationic tracers to examine the sorption effect on delayed transport of radionuclides in unsaturated tuff. Non-radioactive cesium is directly used for radioactive ^{137}Cs. Experimental conditions and analyses are recorded in Hu (2000 [156473] pp. 130–136, 145–146).

Figure 6.4.3-1 shows the spatial-distribution results obtained from LA-ICP-MS profiling for the tuff cube face in contact with the tracer solution. Intensity in the y-axis indicates the signal, measured by ICP-MS, from the laser-abated mass for both the applied tracers and elements (Al, K, Ce, Th) intrinsic to the tuff sample. Peterman and Cloke (2001 [155696]) reported a very uniform distribution of elemental compositions in tuff. Signals shown in Figure 6.4.3-1 are in direct relationship to the reported elemental compositions: percent weight level for Al and K, trace (parts per million) level for Ce and Th. As expected, the spatial distribution of all elements measured is fairly uniform, because this cube face was in contact with the tracer solution throughout the imbibition test duration.

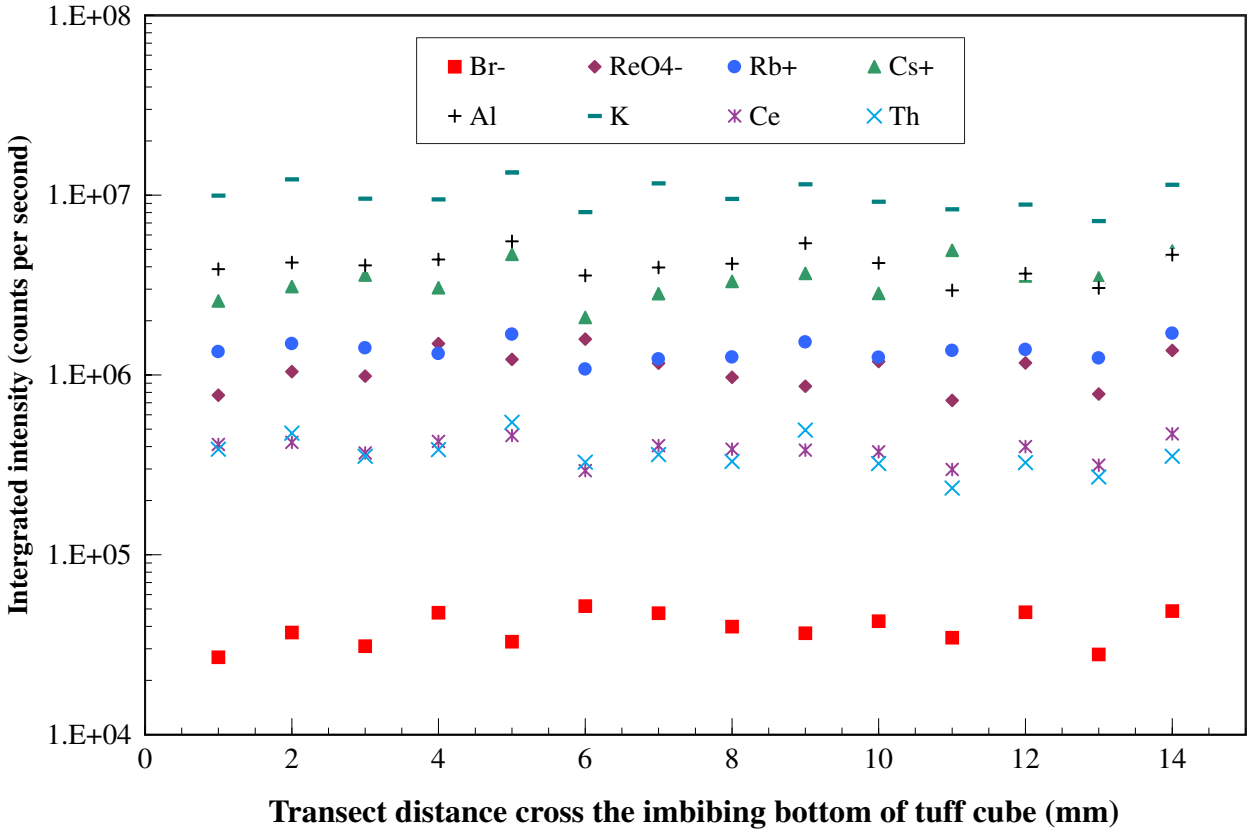

DTN: LB0110TUFTRACR.001 [156979]

Figure 6.4.3-1. Spatial Distribution along the Tracer Solution Contact Surface of Applied Tracers and the Distribution of Intrinsic Tuff Elements Profiled Using LA-ICP-MS

Figure 6.4.3-2, on the other hand, presents the spatial distributions of applied tracers, as well as uniform distribution of element K as it exists inherently in the tuff sample, for a side cube face parallel to the direction of imbibition. Anionic tracers, Br^- and ReO_4^-, travel much further than cationic tracers (Cs^+ and Rb^+) that sorb to the tuff. This is similar to those tracers discussed in Section 6.4.2.1, where sorption of dyes is observed. By the same approach, $d_{0.5}$ is located at about 10.15 mm for both Br^- and ReO_4^-, and $d_{0.5}$ is located at about 2.95 mm and 3.50 mm for Cs^+ and Rb^+, respectively. The retardation factors for Cs^+ and Rb^+ are, therefore, estimated to have the value of 3.44 (= 10.15 mm/2.95 mm) and 2.90 (10.15 mm/3.50 mm), respectively. Similar behavior is observed from the measurements made on another side cube face parallel to the direction of imbibition. Overall, LA-ICP-MS provides a useful way of sampling and understanding tracer, and by extension radionuclide, imbibition and transport in the rock matrix at small spatial scales and reasonable sampling times.

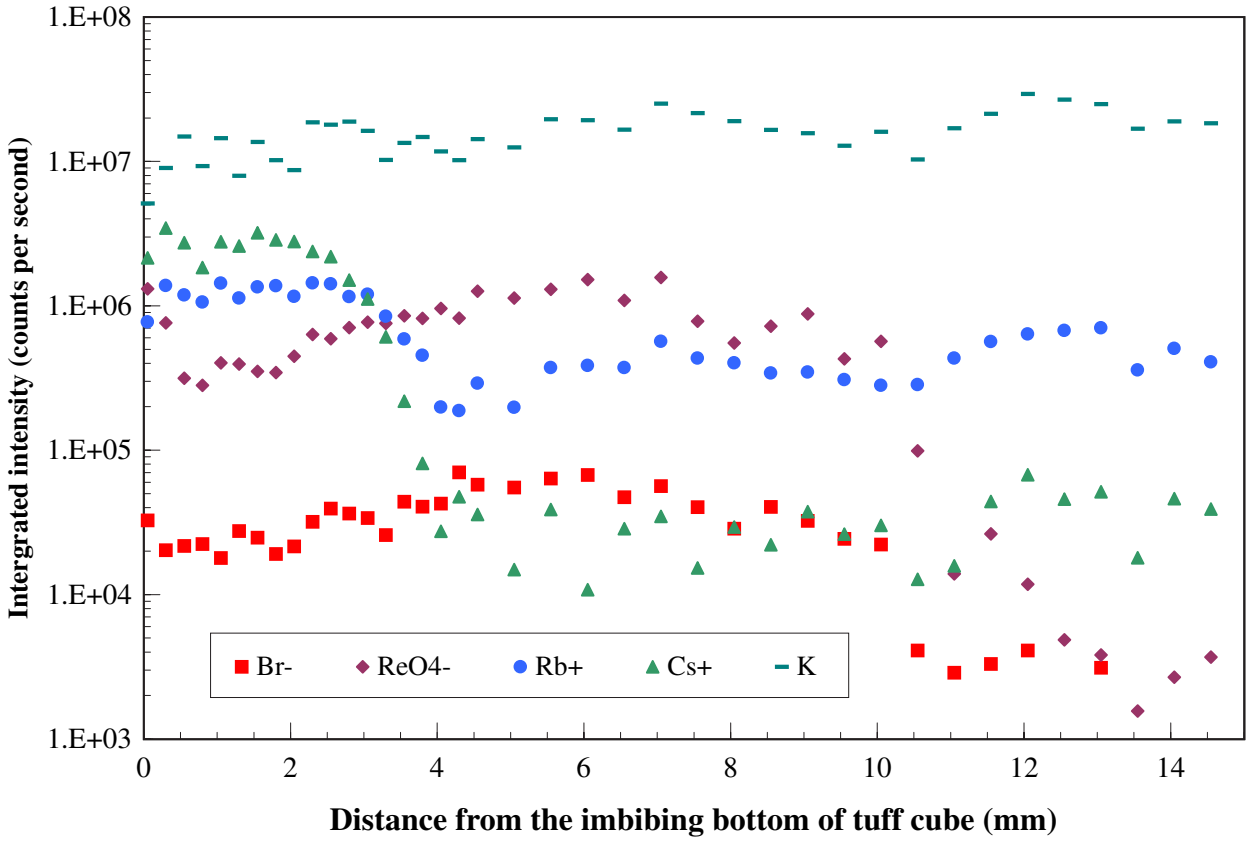

DTN: LB0110TUFTRACR.001 [156979]

Figure 6.4.3-2. Spatial Distribution Normal to the Tracer Solution Contact Surface (in the Direction of Liquid Imbibition) of Applied Tracers and Distribution of Intrinsic Tuff Elements Profiled Using LA-ICP-MS

INTENTIONALLY LEFT BLANK

6.5 ANALYSES OF CROSSHOLE AIR-INJECTION TESTS

This section continues the pneumatic air-permeability test analyses first presented in Section 6.1. Section 6.1 focuses on the air-permeability variations along boreholes in niches. The permeability profiles provide initial inputs to liquid-release-test interval selection, as described in Section 6.2. The permeability profiles were also used in a seepage-calibration study documented in the Model Report, on seepage calibration in defining the heterogeneity of the permeability structure used in modeling.

This section focuses on analyses of crosshole data for fracture-network connectivity. Fracture-network connectivity is one of the most important characteristics in evaluating flow paths from the inlets to the outlets of a given regime. The larger the system, the more elusive it is to determine the dominant flow paths. Air flow paths elucidated in this section are used to characterize test beds for liquid-flow test design and analysis, as described in Section 6.6 and Section 6.7 below for two slotted test beds in the ESF.

Crosshole tests used the same pneumatic testing equipment described in Attachment I. Up to seven identical packer strings were fabricated and installed in the boreholes to test a rock volume in the niches and in the test beds. The packer can isolate 0.3 m intervals along its length. Each interval can become either an observation or response zone, used to monitor pressure, or an injection zone, where air is introduced under pressure during the test. The automation system controls the permutations through pre-assigned sequences of injection tests in all borehole intervals in the borehole cluster.

Crosshole data is acquired at the same time as single-borehole data, by logging the steady-state pressure response in all observation zones while performing an injection. The observation response pressure is divided by the injection pressure to provide a measure of how well a response zone is connected to an injection zone in relation to that response zone's connections to the rest of the site. The normalization with injection pressure enables all the observation responses from all injections at a site to be directly compared. The crosshole connections can all be viewed on a single 3-D diagram instead of individual diagrams for each tested injection zone.

The niches and Alcove 6 are located within the TSw unit in the repository horizon. The Alcove 4 test site is in the PTn unit along the North Ramp of the ESF. Both the fractured TSw and the predominately porous PTn were evaluated by the pneumatic air-permeability tests.

6.5.1 Crosshole Responses in Welded Tuff

In Section 6.1.2, the single-borehole permeability profiles were presented for niches as the bases for selecting liquid-release intervals for drift seepage testing. The first example of crosshole analysis in fractured rock is on Niche 4788, located in an intensely fractured zone. The crosshole analysis for Niche 4788 is illustrated in Figure 6.5.1-1. The single-borehole permeability values (presented in Section 6.1 as profile plots in Figure 6.1.2-7 and Figure 6.1.2-8) are represented by circles in the crosshole plot, with each circle centered along the test interval within each of the boreholes. The size of the circles scales with the single-borehole permeability at each interval. Grayscale pins are shown with their points at the centers of the circles of the injection zones and heads intersecting through the centers of other circles at the observation zones. Direction of flow

is towards the pinhead, and the grayscale indicates the normalized response ratio ("Resp. Ratio" in the figure) from zero to one.

Figure 6.5.1-1 for Niche 4788 is fairly representative of a fractured site, showing discrete connections. It should be noted that very few of the connections have an opposite counterpart; the connections are predominantly one-way. This observation by no means indicates that flow is limited to one direction between points in the rock, but rather that the influence of local connections on the pressure response is strong. The pressure at a response zone discretely connected to the injection zone (and no other zone) will yield a large response. However, if the original injection zone in the reversed injection-observation combination is also well connected to the fracture network or a free surface, then it will not respond strongly to an injection in the original observation zone.

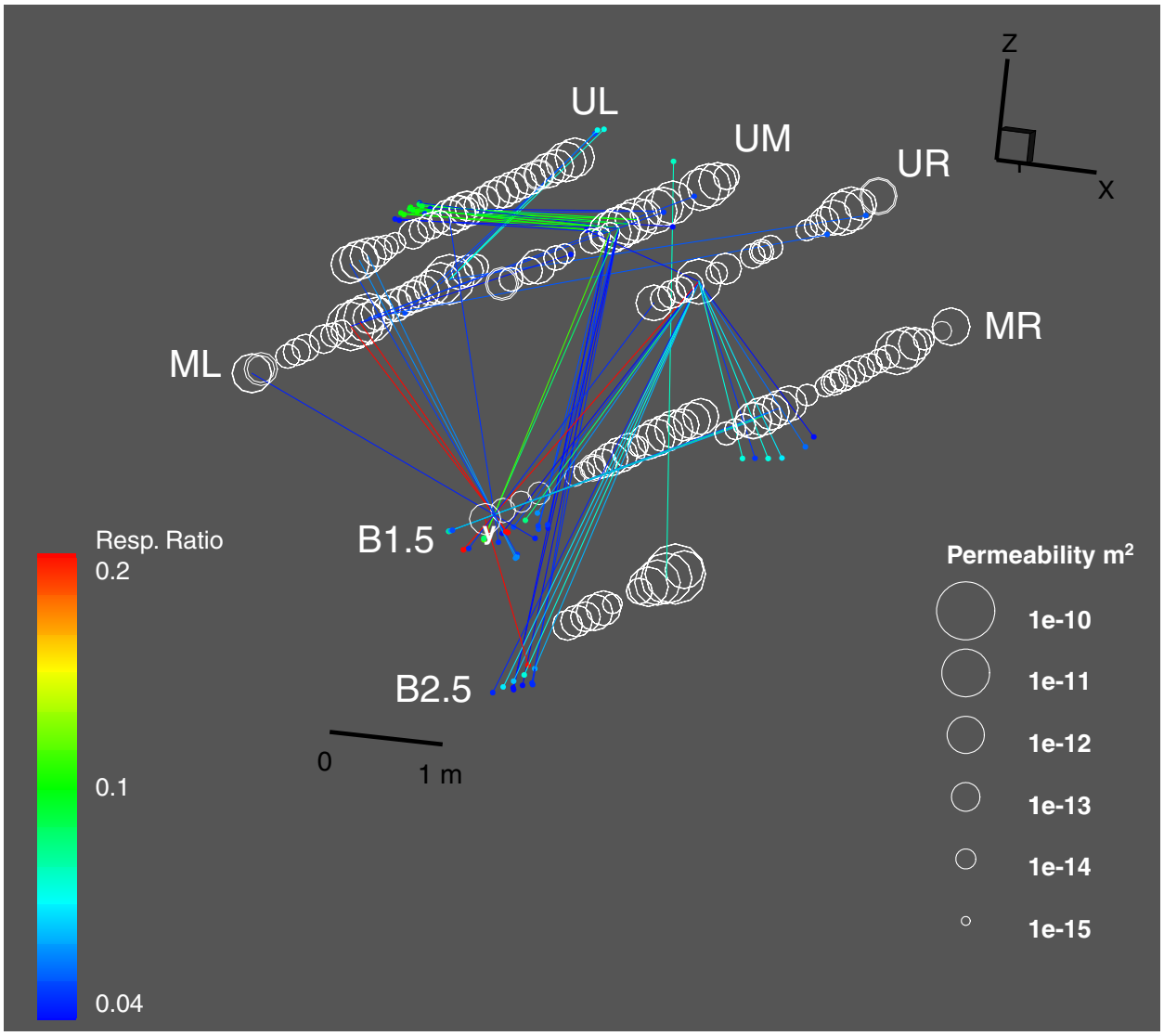

DTN: LB990901233124.004 [123273]

Figure 6.5.1-1. CrossHole Responses for the Borehole Cluster in Niche 4788

The fracture-matrix interaction test site in Alcove 6 of the ESF is in rock that is fractured, with discrete, subvertical fractures and relatively few subhorizontal fractures. The single-borehole permeability profiles for three boreholes tested in Alcove 6 are illustrated in Figure 6.5.1-2. Borehole A was used for a series of liquid-release tests, as described in Section 6.6. Boreholes C and D were used for wetting-front monitoring. Boreholes C and D are located 0.7 m and 0.6 m below Borehole A, respectively, and 0.7 m apart. The crosshole responses for this triangular cluster of boreholes are illustrated in Figure 6.5.1-3. Both Figure 6.5.1-2 and Figure 6.5.1-3 correspond to the first series of tests conducted in the region between 1.3 m and 5.3 m from the borehole collars. Another series of tests was conducted with a straddle packer system (two-packer string to isolate one zone for liquid releases) right before liquid-release tests along the injection borehole.

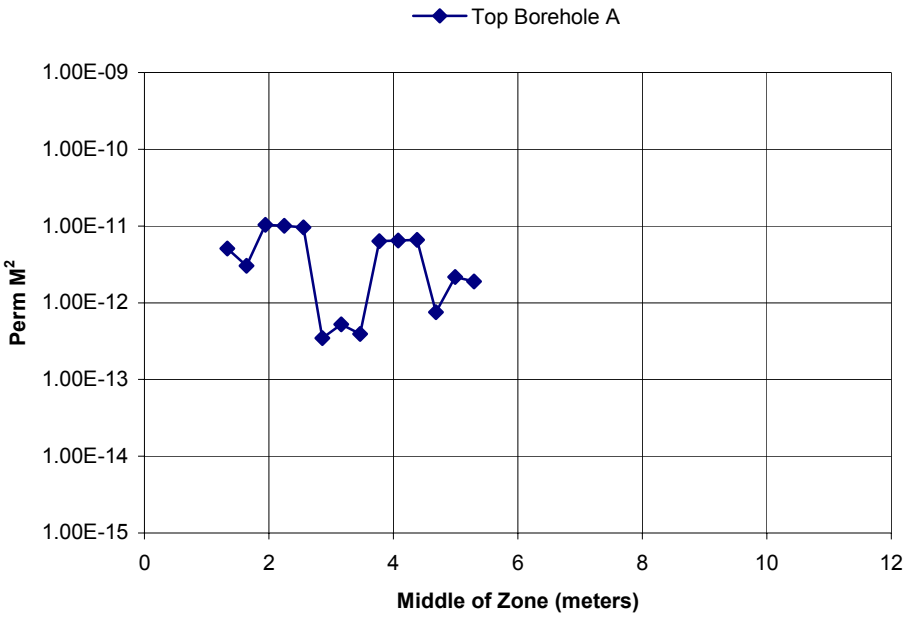

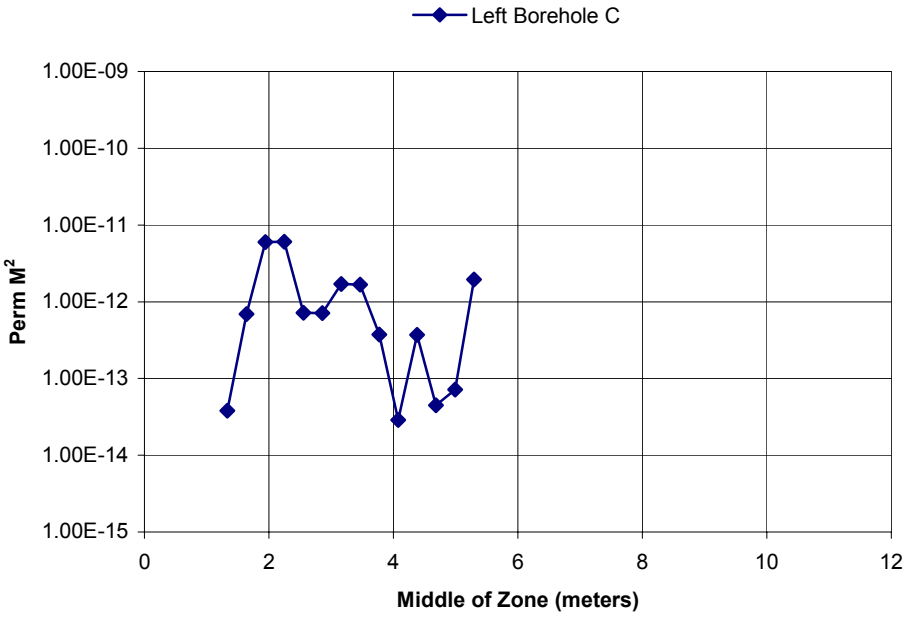

DTN: LB980901233124.004 [105855]

Figure 6.5.1-2. Air-Permeability Profiles along Boreholes in Alcove 6

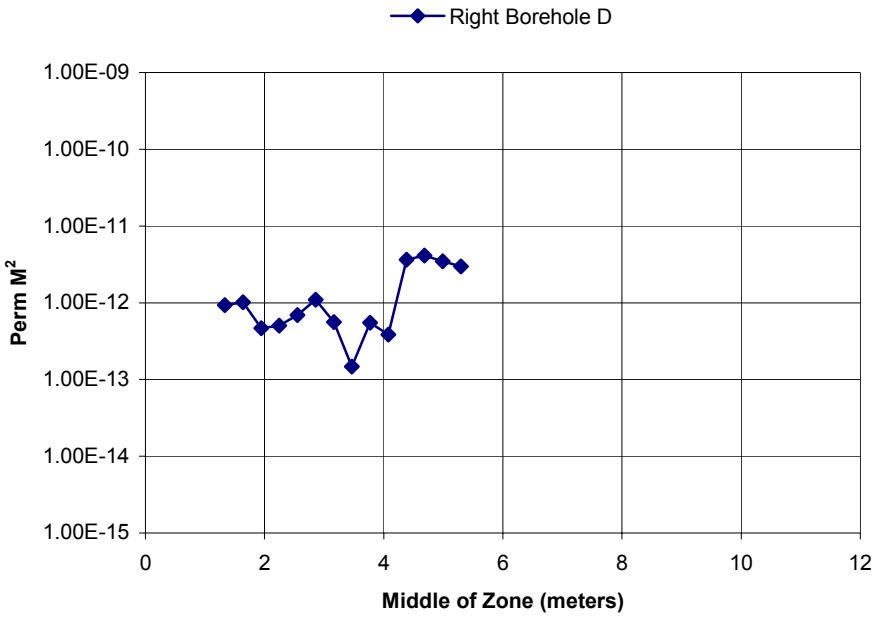

DTN: LB980901233124.004 [105855]

Figure 6.5.1-2. Air-Permeability Profiles along Boreholes in Alcove 6 (continued)

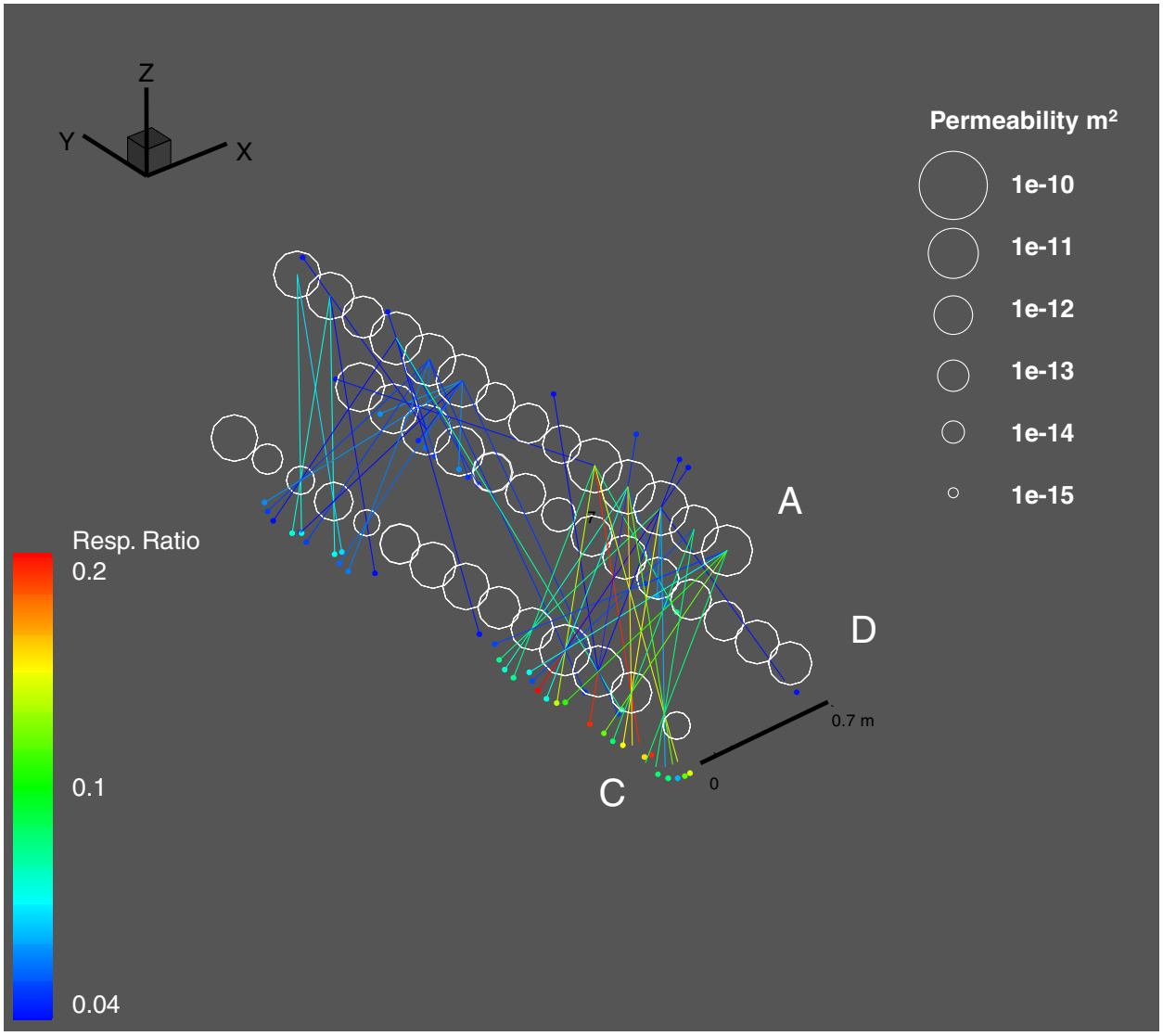

DTN: LB990901233124.004 [123273]

Figure 6.5.1-3. Crosshole Responses for the Borehole Cluster in Alcove 6

Both Figure 6.5.1-1 for Niche 4788 and Figure 6.5.1-3 for Alcove 6 represent crosshole responses in fractured rock. The ratios of pressure response in the observation borehole interval to pressure in the injection borehole interval (Resp. in figure scales) were displayed in the figures for the maximum value of 0.2 (or 20%). Niche 4788, in an intensely fractured zone, has wider range (or larger standard deviation, as shown in Table 6.1.2-3) of distribution in permeability than the variations over a smaller scale at Alcove 6. Both fracture sites contain discrete and well-defined flow paths between boreholes.

During liquid-release tests in the welded tuff (Section 6.2 on niche seepage tests and Section 6.6 on fracture flow tests), it was observed, in some cases, that liquid flux at certain zones was not always commensurate with the air-permeability values at these zones (see Attachment IV.2). Besides the capillary mechanism (that water will prefer smaller aperture fractures), another

possible explanation for this observation is that liquid tries to flow downward following gravity and is thus more sensitive to the directionality of permeability than is air. Directionality of flow is not available from single-borehole data and requires crosshole data analyses.

6.5.2 Permeability Distributions and Crosshole Responses in Nonwelded Tuff

The Alcove 4 test bed is located in the PTn unit. The test bed contains several nonwelded and bedded subunits, including a pinkish-colored argillic layer. The test bed contains a fault plane as illustrated in Figure 6.5.2-1. Section 6.7 below describes in more detail the borehole configuration and specifications. In this section, the focus is on the cluster of seven boreholes. Boreholes 1, 4, 11, and 12 intersected the projected fault plane in the front part of the test block, while boreholes 2, 15, and 16 penetrated other features in the test block, with potential fault zone influences (if any) confined near the ends of the boreholes. If the fault is perfectly planar, the last three holes would not be intercepted by the fault.

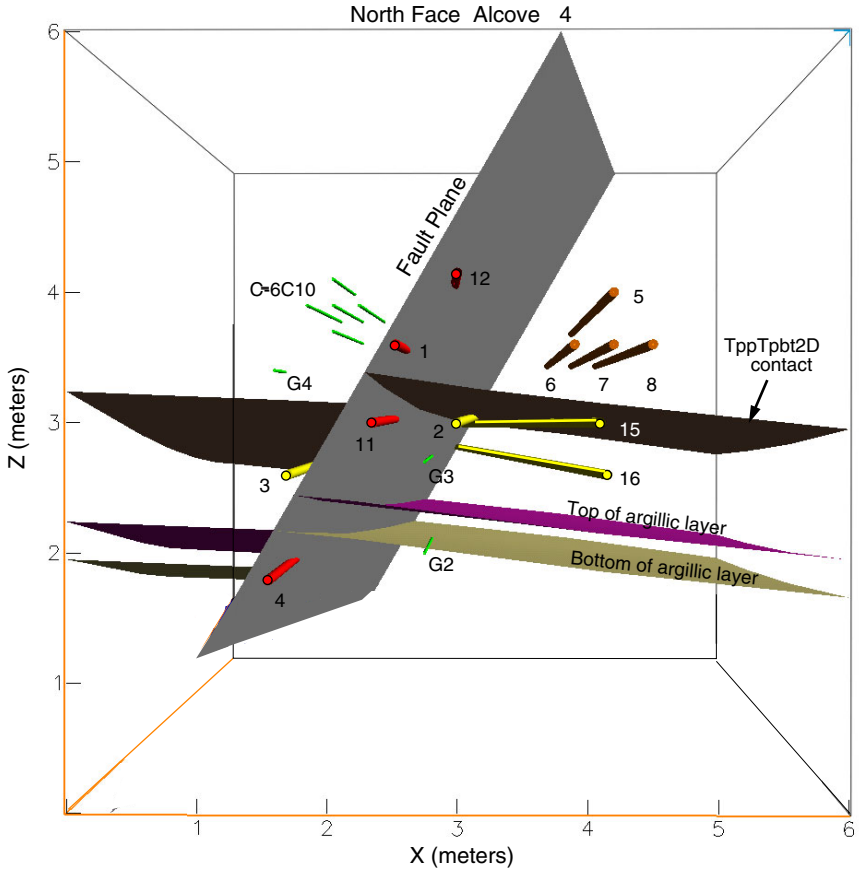

Figure 6.5.2-1. Perspective Illustration of Alcove 4 Test Bed

Figure 6.5.2-2 illustrates the single-borehole air-permeability profiles along the boreholes. Layer variations and the influence of faults could contribute to the widely distributed set of permeabilities over a broad range, both along individual boreholes and among different boreholes. With the exception of borehole 12, the other six boreholes penetrate a high-permeability zone near the end of the boreholes. Among all the borehole clusters tested in the ESF to date, the Alcove 4 PTn cluster shows the largest standard deviation of any of the sites (see Table 6.1.2-3 in Section 6.1.2.3). Even the cluster at the intensely fractured site at Niche 4788 has lower standard deviation of log permeability (0.85) than the value at Alcove 4 (0.93). The mean permeabilities of these two distinctly different sites (in lithological, geological, and fracture characteristics) are incidentally nearly identical. In comparison, the standard deviation for the Alcove 6 cluster was 0.67, and mean was nearly one order of magnitude higher.

Figure 6.5.2-3 shows the connections for Alcove 4 at the same shading scale used in welded tuff plots (Figure 6.5.1-1 and Figure 6.5.1-3). The number of connections is much higher for this nonwelded tuff site. To better display the stronger connections, Figure 6.5.2-4 portrays the data at Alcove 4 on a more appropriate scale legend and trims off the weaker connections. The salient features of the site now become apparent. Strong vertical connections are apparent between the upper and middle boreholes, but very little connectivity exists between the middle borehole and the lower-left borehole, despite similar flow rates and distances. The argillic layer exists between these locations, and the slot provides a nearly impermeable barrier. The single strong connection running from left to right is most likely associated with a high-permeability zone identified by the single-borehole profiles. The high-permeability zone could be associated with the fault intersecting the boreholes near the end. Interceptions were not identified in pre-test design in Figure 6.5.2-2. The connections were identified by crosshole analyses of pneumatic air-permeability test data.

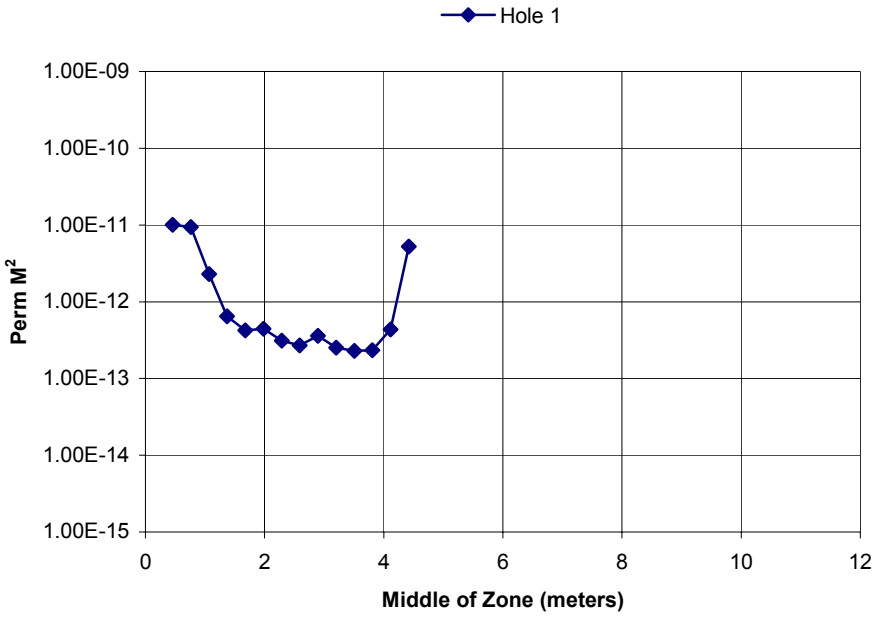

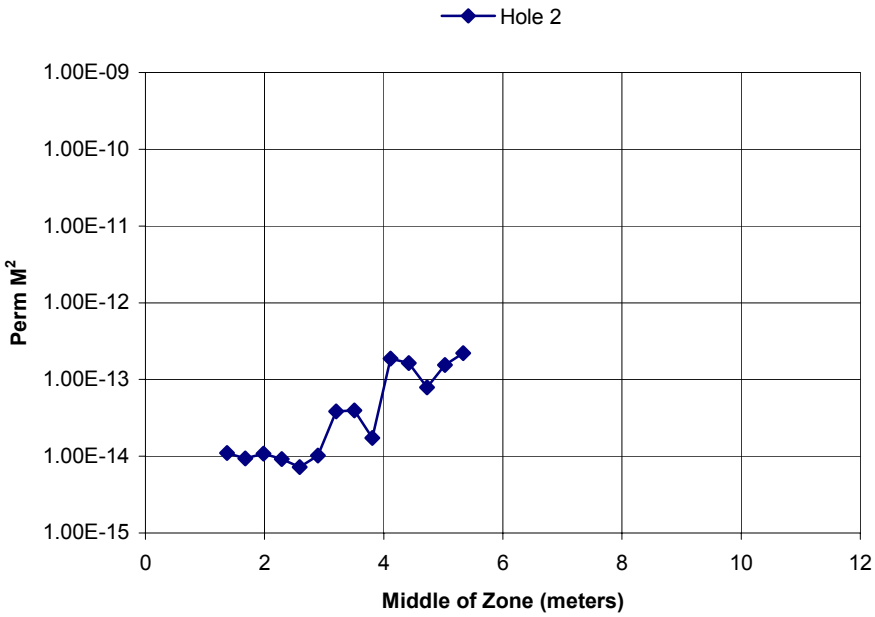

DTN: LB980901233124.009 [105856]

Figure 6.5.2-2. Air-Permeability Profiles along Boreholes in Alcove 4

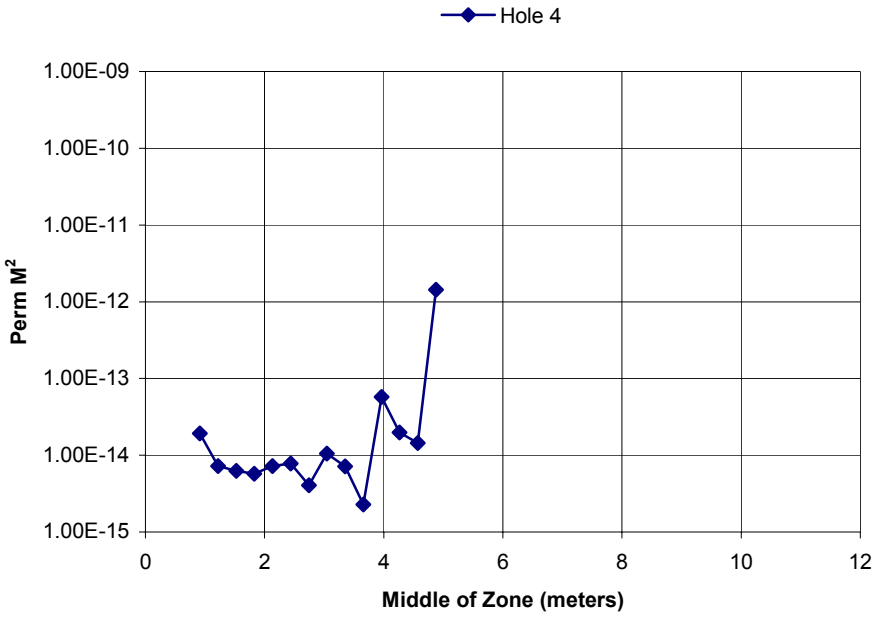

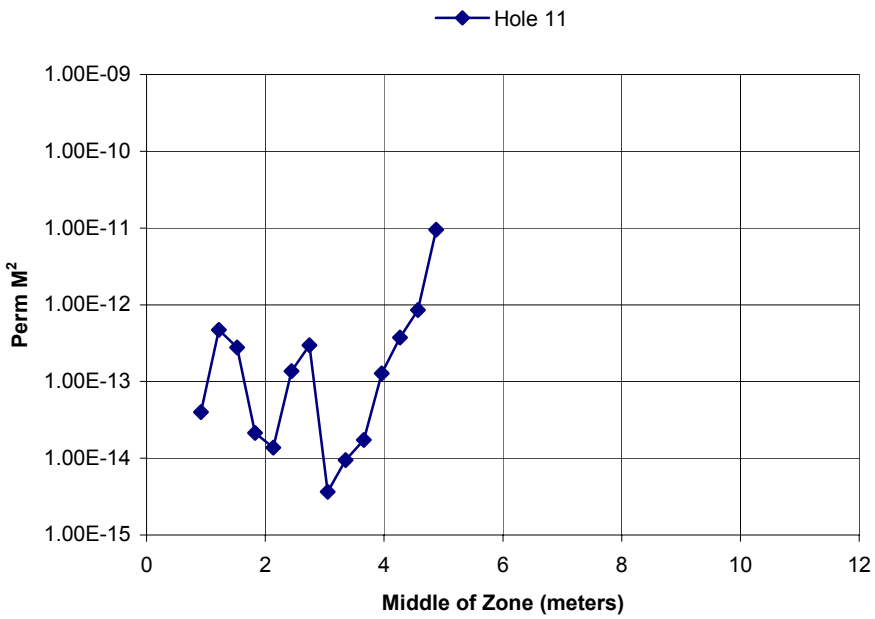

DTN: LB980901233124.009 [105856]

Figure 6.5.2-2. Air-Permeability Profiles along Boreholes in Alcove 4 (continued)

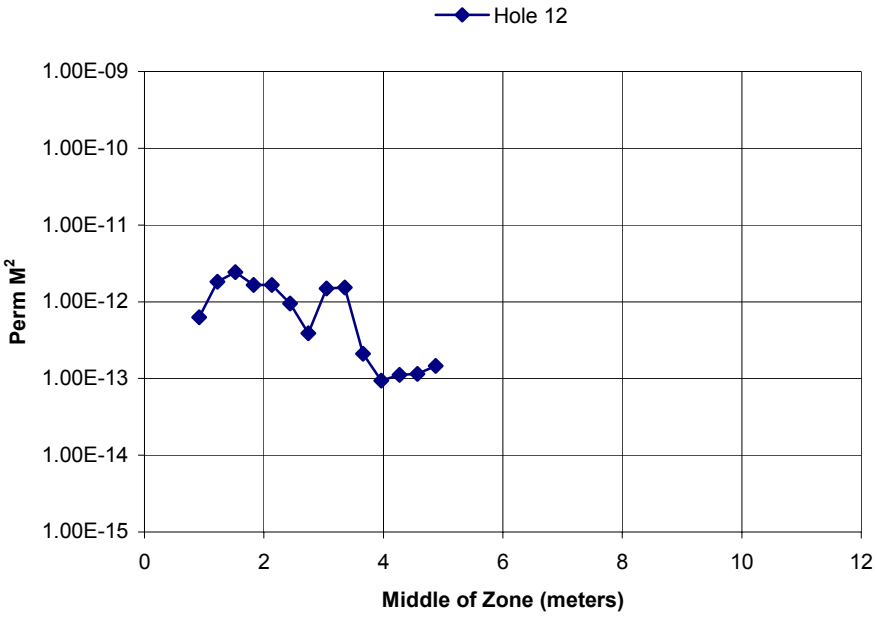

DTN: LB980901233124.009 [105856]

Figure 6.5.2-2. Air-Permeability Profiles along Boreholes in Alcove 4 (continued)

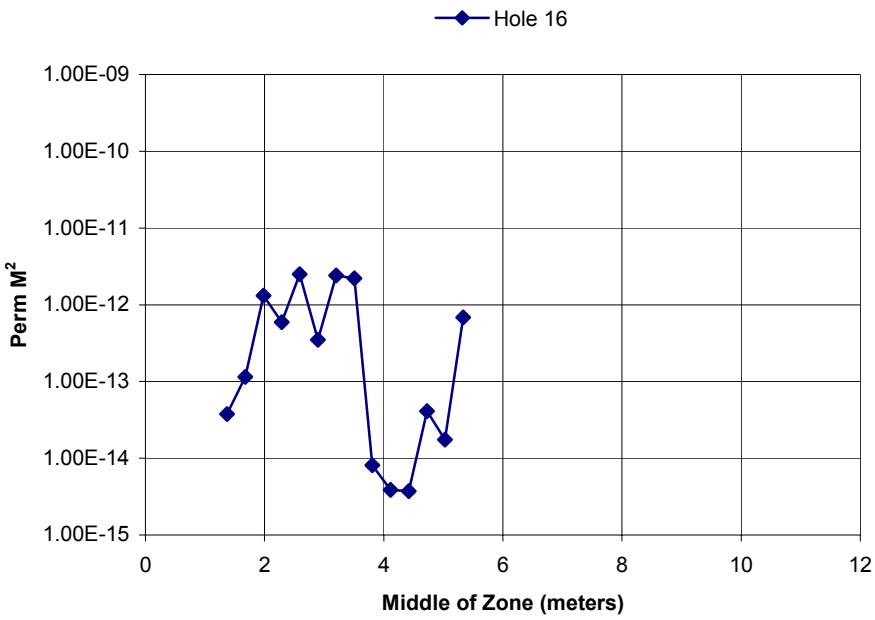

DTN: LB980901233124.009 [105856]

Figure 6.5.2-2. Air-Permeability Profiles along Boreholes in Alcove 4 (continued)

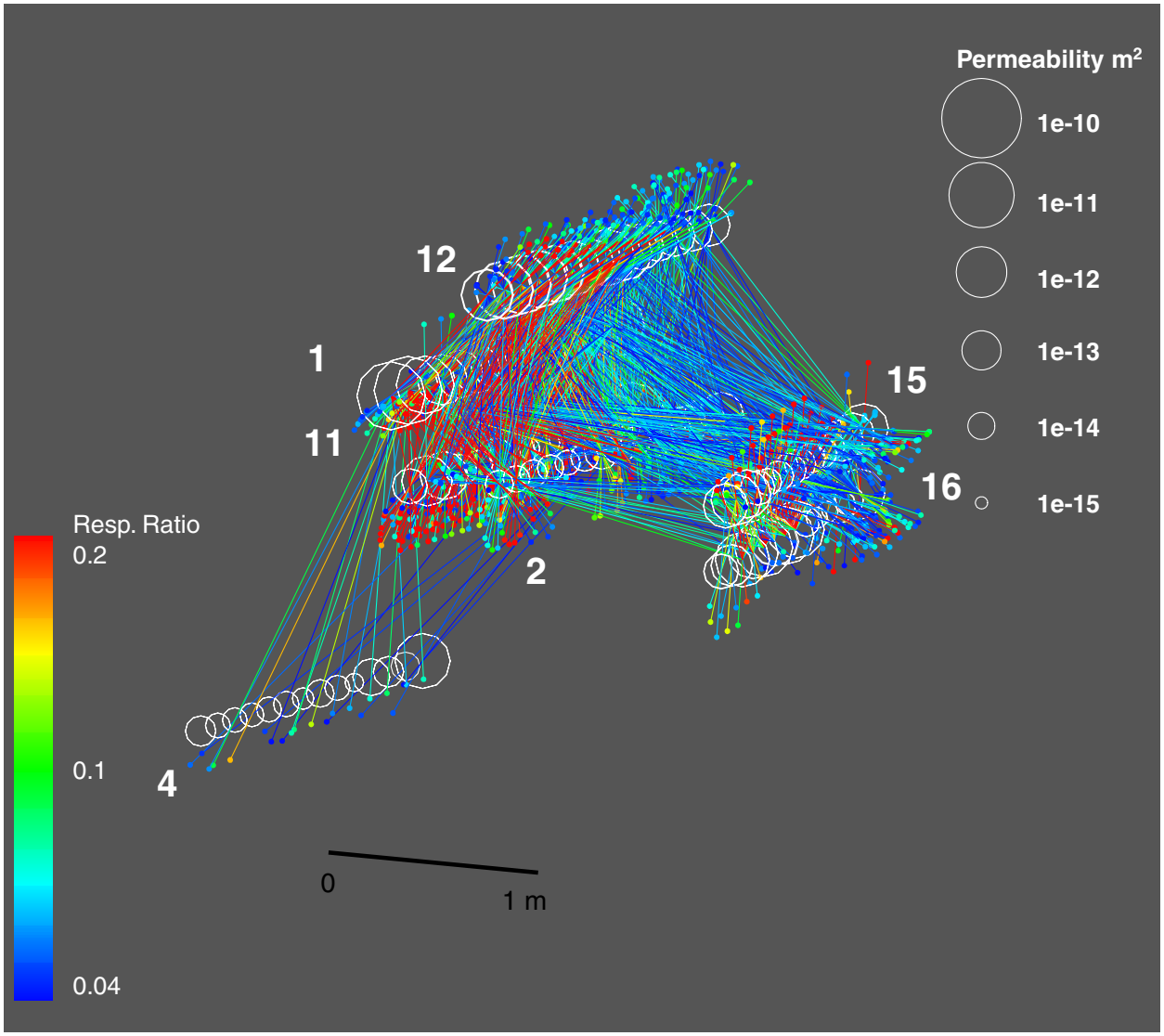

DTN: LB990901233124.004 [123273]

Figure 6.5.2-3. Crosshole Responses for the Borehole Cluster at Alcove 4 PTn Test Bed with All Response Pressure (Resp.) Ratios below 0.2 Included

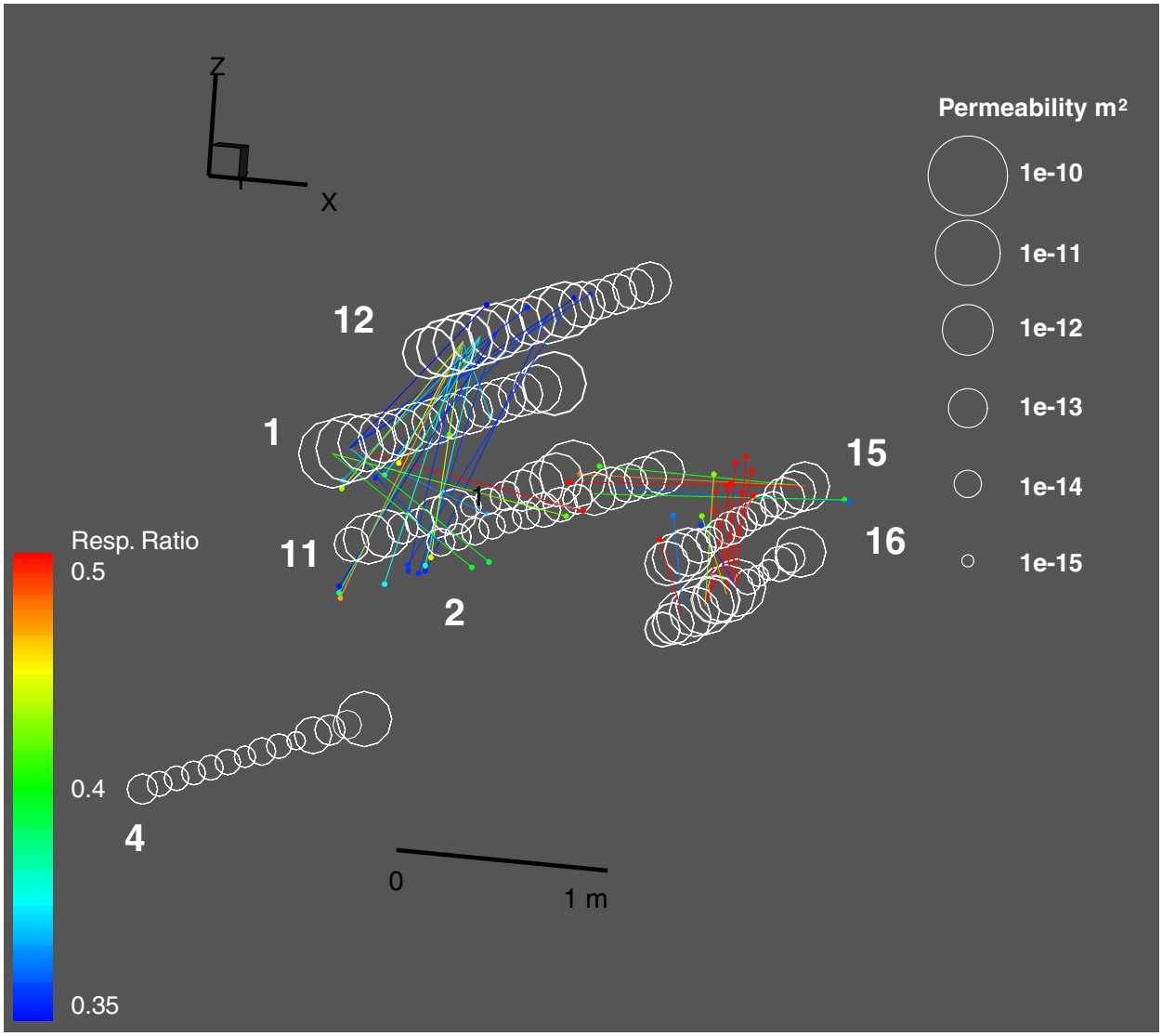

DTN: LB990901233124.004 [123273]

Figure 6.5.2-4. Crosshole Responses for Borehole Cluster at Alcove 4 PTn Test Bed with Small Response Pressure (Resp.) Ratios Filtered

6.6 ANALYSES OF FRACTURE FLOW IN FRACTURE-MATRIX TEST BED AT ALCOVE 6

Wetting-front movement, flow-field evolution, and drainage of fracture flow paths were evaluated in a test bed with a slot excavated below a cluster of boreholes. The slotted test bed is located within the Topopah Spring welded tuff (TSw) at Alcove 6 in the ESF at Yucca Mountain, Nevada. Hydraulic parameters such as formation intake rates, flow velocities, seepage rates, and fracture volumes were measured under controlled boundary conditions, using techniques developed specifically for *in situ* testing of flow in fractured rock. Below, the test-bed configuration and field instrumentation are described, followed by the results.

6.6.1 Liquid-Release Tests in Low- and High-Permeability Zones

Field tests were conducted at Alcove 6 over a period of six weeks, starting in late July 1998. These included multiple releases of tracer-laced water in one high-permeability zone (HPZ) and one low-permeability zone (LPZ) along an injection borehole. The permeabilities of these zones were determined from air-permeability measurements conducted over 0.3 m sections along the borehole, using a straddle packer that also was used for liquid releases. The HPZ had an air-permeability value of 6.7×10^{-12} m^2, and the LPZ had an air-permeability value of 2.7×10^{-13} m^2 (Salve 1999 [155692], pp. 48–49 and Cook 2001 [156902], pp. 51–53). During and following liquid-release events, changes in saturation and water potential in the fractured rock were measured in three monitoring boreholes, with changes continuously recorded by an automated data acquisition system. The water that seeped into the excavated slot below the injection zone was collected, quantified for volumes and rates, and analyzed for tracers.

6.6.1.1 The Test Bed

The test bed was located at Alcove 6 in the ESF (Figure 6.6.1-1a), lying within the middle nonlithophysal zone of the TSw. The rock was visibly fractured, with predominantly vertical fractures and a few subhorizontal fractures. The relatively wide fracture spacing (on the order of tens of centimeters) facilitated the choice of injection zones, allowing discrete fractures and well-characterized fracture networks to be isolated by packers for localized flow testing.

A horizontal slot and a series of horizontal boreholes are the distinct features of the test bed (Figure 6.6.1-1b). The slot, located below the test bed, was excavated by an over-coring method. The excavation sequence required (first) the drilling of parallel pilot holes, 0.10 m in diameter, over 4 m in length with a 0.22 m spacing, normal to the alcove wall. The pilot holes were then over-cored by a 0.3 m drill-bit to excavate the 2.0 m wide, 4.0 m deep and 0.3 m high slot located approximately 0.8 m above the alcove floor. Three I-beam supports were installed along the length of the slot for support. Four horizontal boreholes, 0.1 m in diameter and 6.0 m in length, were drilled perpendicular to the alcove wall above the slot. Boreholes A and B were located 1.6 m above the slot ceiling, while boreholes C and D were 0.9 m and 1.0 m above the slot ceiling, respectively, and 0.7 m apart (Figure 6.6.1-1b).

Borehole A was used for fluid injection, while boreholes B, C, and D were monitored for changes in moisture conditions. The slot was used to collect water seeping from the fractured

rocks above. A flexible plastic curtain 3.0 m wide and 0.9 m high was installed to cover the slot face and to minimize air movement between the alcove and the slot.

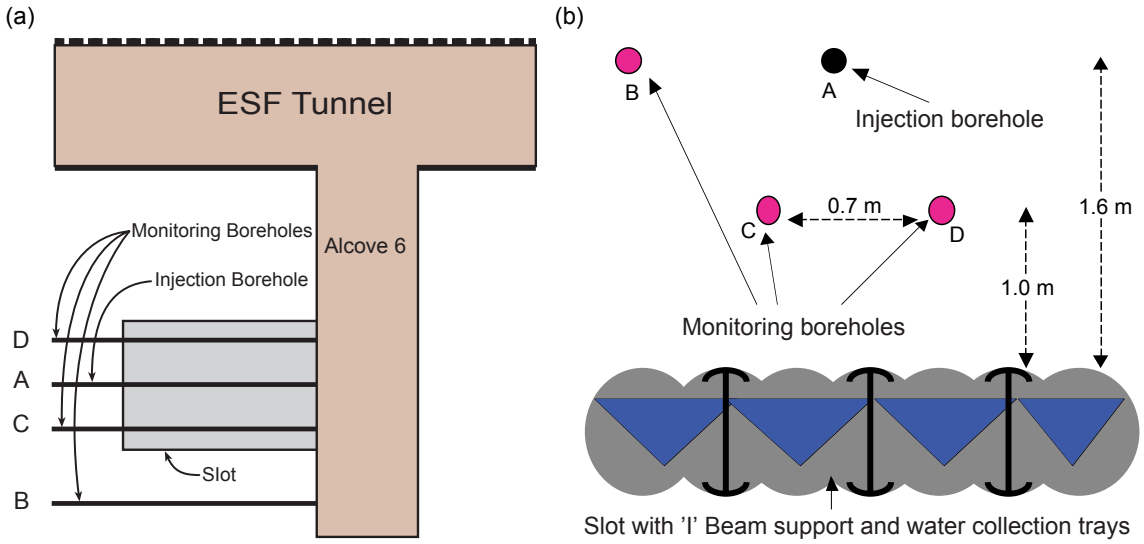

NOTE: Figures are not drawn to scale.

Figure 6.6.1-1. Schematic Illustration of (a) Plan view of Location and (b) Vertical View of Layout of Test Bed at Alcove 6 in the ESF at Yucca Mountain

6.6.1.2 Instrumentation

There were three distinct components to the flow investigation: (1) controlled release of water into isolated zones, (2) borehole monitoring for changes in saturation and water potential, and (3) collection of seepage from the slot ceiling. The key features of new instruments developed for this field investigation are presented in Attachment VI.

6.6.1.3 Liquid-Release Experiments

Air-permeability measurements were done along 0.3 m sections of the injection borehole as described in Section 6.1 and Section 6.5. The HPZ is located 2.3–2.6 m from the borehole collar, whereas the LPZ is 0.75–1.05 m from the collar. In both HPZ and LPZ, a series of constant-head tests were conducted to determine the temporal changes in the rate at which the formation could take in water. In the HPZ, a second series of tests was conducted with different injection rates. Tests conducted in this field investigation are summarized in Table 6.6.1-1. Seepage rates into the slot were monitored.

All the water used in the ESF was spiked with lithium bromide for mining-related activities and for most of the scientific investigations. Additional tracers were added to the water injected into the LPZ and during the first set of experiments in the HPZ (Table 6.6.1-1). During the tests, water that seeped into the slot was periodically sampled and analyzed for tracer concentrations.

Water was released into the LPZ three times over a period of two weeks, starting on July 23, 1998 (Table 6.6.1-1). For the first release, water was injected at a constant pump rate of approximately 56 mL/min. At 66 minutes, water was observed in the overflow line, indicating

that water was being injected at a rate higher than the intake capacity of the zone. At this time, the flow rate on the pump was immediately reduced to approximately 6.0 mL/min. Within 22 minutes, return flow ceased, and water was injected continuously at this rate for the next 4 hours and 23 minutes. Based on the actual flow rate determined from transducers located at the bottom of the water reservoir (see Attachment VI.1), a total of 6.3 liters of water was injected into the zone, of which 0.7 liters was recovered as return flow. The other 5.6 liters was released into the formation. Average net release rate into the formation rate was approximately 17 mL/min.

For the second liquid release in the LPZ, the constant-head injection system was used. The constant-head chamber was located adjacent to the injection borehole, such that the head of water was 0.07 m in the injection zone. This constant head was maintained for 4 hours in the injection zone, while the water level in the reservoir was continuously monitored. At the end of this constant-head period, water supply to the injection zone was discontinued, resulting in a falling-head boundary condition inside the injection zone. A total of 1.4 liters of water was introduced into the LPZ from both the constant-head and falling-head periods.

The final release into the LPZ was initiated on July 29, 1998, when water was introduced into the formation under a constant head (of 0.07 m) maintained for 43 hours, after which the ponded water in the injection zone continued to percolate into the formation under a falling-head condition. During the test, 1.0 liters of water were released under the constant-head boundary, whereas 1.2 liters were released under the falling head.

Summing up all three tests in the LPZ, 9.2 liters of water were released to the formation under a combination of constant and falling-head boundary conditions at the point of injection.

Water was injected into the HPZ during two groups of tests over a period of two weeks (Table 6.6.1-1). The first group of four tests was conducted during August 4–6, 1998, and the second group of four tests were conducted during August 25–28, 1998. The first two tests (Test HPZ-1 and Test HPZ-2) in the first group were constant-head tests (of head 0.07 m) that served to establish the intake rates at which the injection zone could release water to the formation. The HPZ-1 constant-head test rate was ~119 mL/min. The HPZ-2 constant-head test rate was ~98 mL/min. After the HPZ-2 test, tests were conducted at constant flow rates. During the third test (Test HPZ-3) conducted on the next day, water was injected at approximately half the intake rates observed with the constant-head system (i.e., ~53 mL/min). During the fourth test (Test HPZ-4) on August 6, 1998, water was injected at a constant rate of ~ 5 mL/min over 12 hours. During the second group of tests (Tests HPZ-5 through HPZ-8) over a period of four days starting on August 25, 1998, the injection rate was sequentially reduced from ~69, ~38, ~29, and finally to ~14 mL/min.

Table 6.6.1-1. Amount of Water and Types of Tracers Released into the Injection Borehole

Date	Test #	Injection type	Infiltration rate (mL/min)	Volume of water injected (l)	Additional Tracer *
7/23/98	LPZ-1	Constant rate	~16	5.6	Sodium Bromide 2,3,6 Trifluorobenzoic acid
7/24/98	LPZ-2	Constant head	~1.2	0.3	2,4,5 Trifluorobenzoic acid
7/24-25/98	LPZ-2	Falling head		1.1	2,4,5 Trifluorobenzoic acid
7/29-30/98	LPZ-3	Constant head	~0.5	0.4	3,5 Difluorobenzoic acid
7/30-31/98	LPZ-3	Constant head	~0.5	0.6	3,5 Difluorobenzoic acid
7/31-8/4/98	LPZ-3	Falling head		1.2	3,5 Difluorobenzoic acid
8/4/98	HPZ-1	Constant head	~119	16.3	Potassium Fluoride Pentafluorobenzoic acid
8/4/98	HPZ-2	Constant head	~98	17.3	2,3,4 Trifluorobenzoic acid
8/5/98	HPZ-3	Constant rate	~53	17.5	3,4 Difluorobenzoic acid
8/6/98	HPZ-4	Constant rate	~5	3.4	2,3,4,5 Tetrafluorobenzoic acid
8/25/98	HPZ-5	Constant rate	~69	18.4	
8/26/98	HPZ-6	Constant rate	~38	18.4	
8/27/98	HPZ-7	Constant rate	~29	18.2	
8/28/98	HPZ-8	Constant rate	~14	9.4	

DTN: LB990901233124.002 [146883]

NOTES: LPZ located 0.75-1.05 m from borehole collar
HPZ located 2.30-2.60 m from borehole collar
* All injected water was tagged with lithium bromide

6.6.2 Observations of Wetting-Front Migration and Fracture Flow

Water released in the injection borehole flowed through the fractured rock and, in the case of the HPZ, some of the water seeped into the slot located 1.6 m below. Liquid-release rates in the injected zone were measured, saturation and water-potential changes were observed along monitoring boreholes, and seepage water into the slot was collected.

6.6.2.1 Liquid-Release Rates

Measurements of liquid-release rates in the LPZ in this fractured-welded-tuff test bed exhibited a response similar to that observed for (unfractured) porous media. The initially high rates asymptotically approached low steady-state values of ~0.35 mL/min (Figure 6.6.2-1a). Near continuity was observed in the decreasing liquid-release rates, even with a five-day gap between liquid releases into the formation (Figure 6.6.2-1b).

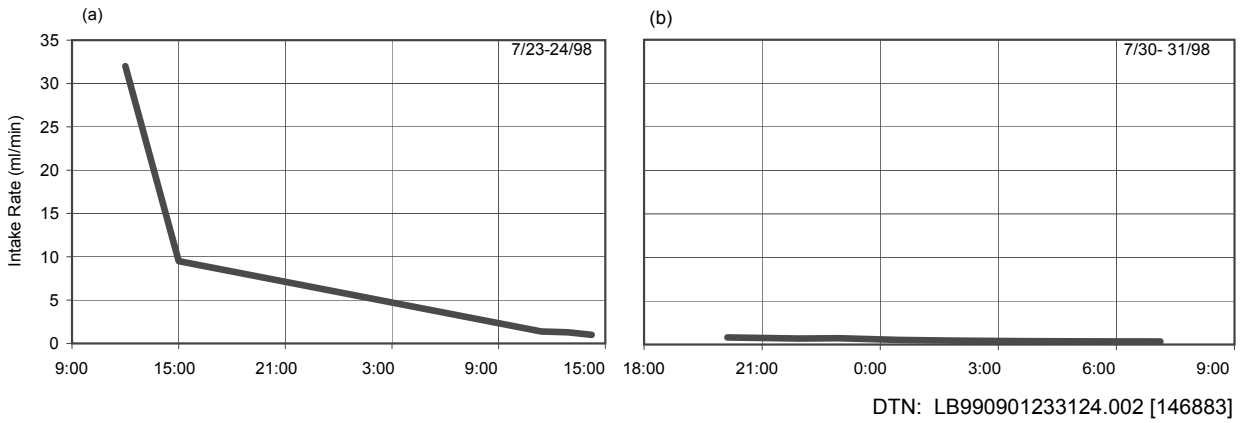

Figure 6.6.2-1. Water Intake Rates Observed in the Low Permeability Zone

For the first two constant-head tests conducted in the HPZ, the rates of liquid release varied significantly during and between tests (Figure 6.6.2-2). In the first test, the liquid-release rate continued to climb for the first sixty minutes and then remained steady for the next 15 minutes before briefly increasing sharply. For the remainder of the test it continued to fluctuate between 70 and 160 mL/min. In the second test, the liquid-release rate rapidly increased for the first 15 minutes. The rate then slowly decreased and steadied off to ~100 mL/min. Ninety minutes into the test, the liquid-release rate briefly fell to 35 mL/min, sharply increased to 130 mL/min, and slowly decreased to a quasi-steady rate of 90 mL/min in the next 80 minutes.

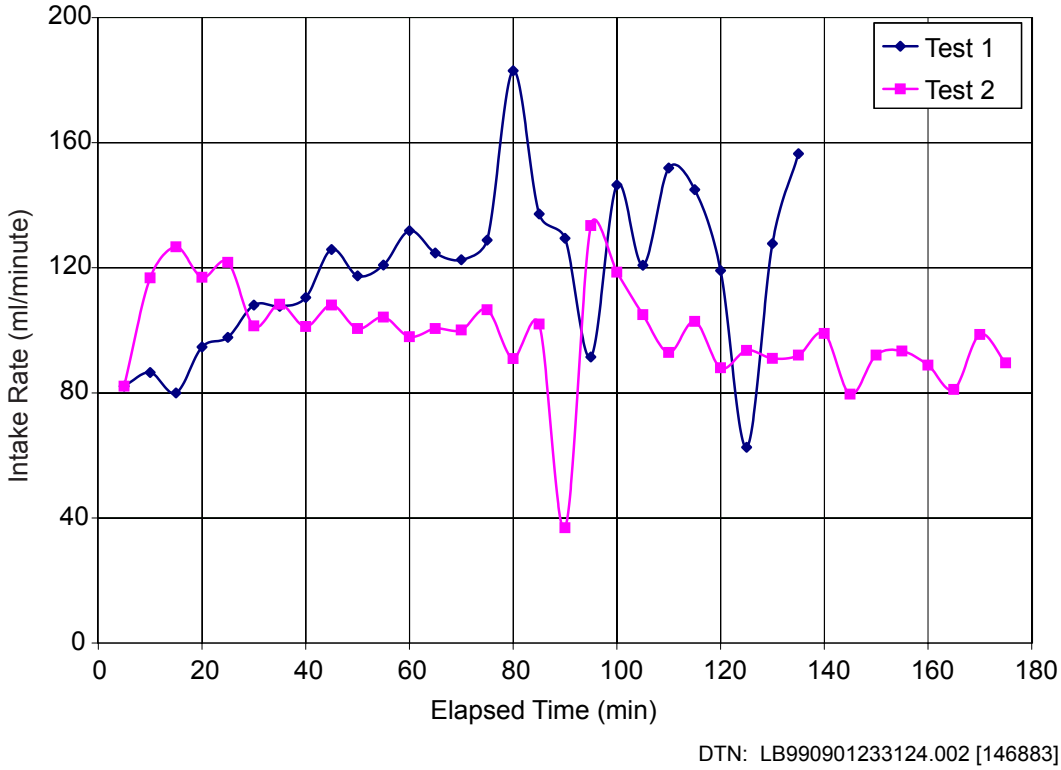

Figure 6.6.2-2. Water Intake Rates Observed in the High Permeability Zone

6.6.2.2 Formation Wetting and Drying

In the two monitoring boreholes (C and D, shown in Figure 6.6.1-1b) located below the injection borehole (A), changes in saturation were detected both by the electrical-resistivity probes (ERPs), as shown in Figure 6.6.2-3a and Figure 6.6.2-3c, and by the psychrometers, as shown in Figure 6.6.2-3b and Figure 6.6.2-3d. The ERPs consisted of two electrical leads sandwiched between pieces of filter paper. The results in Figure 6.6.2-3 are the responses to liquid release in the LPZ located 0.75–1.05 m from the borehole collar. In both boreholes, large changes in saturation were detected by either ERPs or psychrometers or both, located between 0.9 and 1.9 m from the collar. At a distance of 2.15 m from the borehole collar, the changes were much smaller.

The wetting process reduces electrical resistance and increases the water potential (making it less negative). The drying process induces the opposite changes. In borehole C, the first drying response was detected by the ERP 0.90 m from the borehole collar, as illustrated in Figure 6.6.2-3a. A step increase in resistance was observed 30 minutes after water had been released, suggesting some initial drying with dry air preceding a wetting front. Two hours later, an abrupt increase in wetting was indicated by a stepped decrease in resistance. ERPs located at 1.15, 1.40, and 1.65 m also detected the arrival of a wetting front within 2 to 4 hours of liquid release. In borehole D (Figure 6.6.2-3c), the ERPs located at 0.9 and 1.15 m from the collar were first to detect increases in saturation, 30 minutes after the first release of water. At distances of 1.40 and 1.65 m, the wetting front arrived 6 hours later.

In both boreholes, the probes that had the largest and quickest responses (i.e., probes located between 1.15 and 1.65 m) were also the ones that showed some drying between the two injection events. Probes located at a distance of 0.90–1.15 m detected a continuous drying trend after the initial period of injection.

The borehole C psychrometer data in Figure 6.6.2-3b supported the ERP data in Figure 6.6.2-3a with smoother and more systematic changes induced by wetting-front arrivals. The sensors closer to the release point had larger changes in water potential. At distances between 1.40 and 2.15 m from the collar, water potentials were between -140 and -75 m before the first injection. Immediately after water was introduced, water potentials began to rise steadily for the next four days, reaching values between -70 and -30 m. In response to the second injection period (i.e., July 29–August 4, 1998, in Table 6.6.1-1), the most noticeable increases in potentials were observed in the psychrometer located at 1.40 m, where water potentials increased from -40 to -15 m after the second injection period. In borehole D, illustrated in Figure 6.6.2-3d, changes in water potential were observed between 0.90 and 1.90 m following the first injection. However, the extent of drying, as seen in the decrease in water potentials at 1.40 and 1.65 m, was greater than observed in borehole C. During the second wetting event, water potentials in this zone were similar to those observed following the first event. Oscillatory responses could be related to variations of drift conditions for sensors near the borehole collars. This is a speculative interpretation, to be substantiated or refuted.

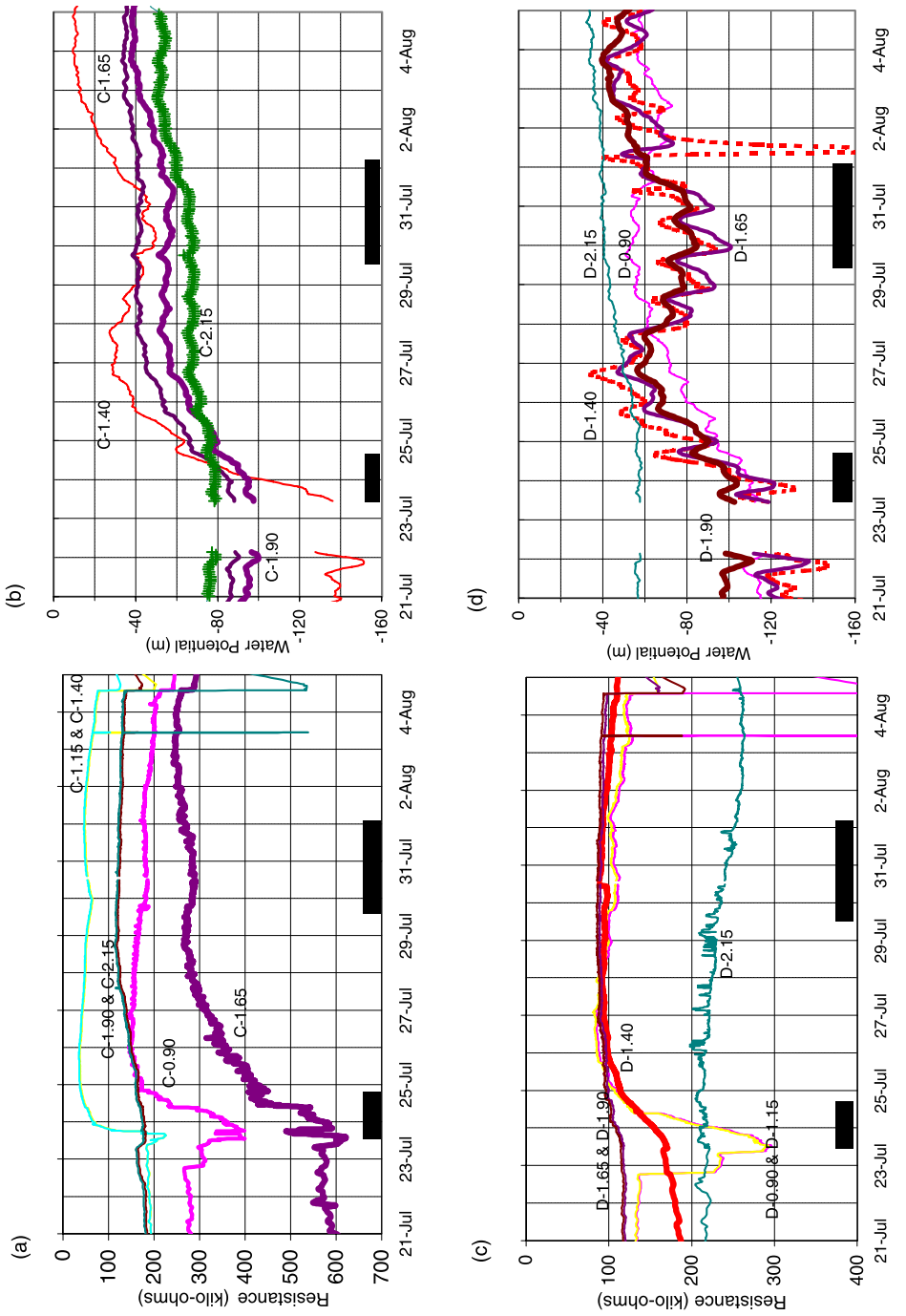

DTN: LB990901233124.002 [146883]

NOTE: The legend identifies the sensor location in borehole (C & D) and distance of sensor from the borehole collar. Shaded zones indicate the duration of liquid-release events. Note resistance axis is inverted.

Figure 6.6.2-3. Changes in Electrical Resistance and Water Potential Detected during Liquid Release into the Low Permeability Zone

Similar to the injection response in the LPZ, changes in saturation were detected both by the ERPs and psychrometers in the monitoring boreholes (Figure 6.6.2-4) from liquid releases into the HPZ located 2.30–2.60 m from the borehole collar. In borehole C, changes in saturation were observed between 1.9 and 3.4 m from the borehole collar, with the largest changes observed between 2.15 and 3.15 m. Both the ERPs and the psychrometers detected the changes. The largest changes in water potentials were detected between 2.15 and 2.40 m from the borehole collar in borehole C, where pre-injection water potentials, which were between -70 to -60 m, climbed to between -20 and -10 m after the first set of releases. These values persisted after the second set of releases. In borehole D, saturation changes were observed over a slightly wider span along the borehole (i.e., 1.65 to 3.65 m from the borehole collar), with the noticeable changes observed between 1.90 and 3.40 m from the borehole collar. After the initial release of water in the HPZ, water potentials between locations 2.15 and 2.90 m increased over a period of a week. These were between -15 to -5 m for the duration of the remaining liquid releases.

In both boreholes, the psychrometer data suggest that after the first batch of water releases (i.e., August 4–6, 1998), water potentials significantly increased (e.g., -60 to -20 m), which then persisted until the start of the second period of injection (August 25–28, 1998). During this second set of injections, more water was retained by the formation, resulting in further increases in water potentials. The ERP and psychrometer data indicate that the zones between 2.15 and 2.40 m in borehole C, and between 2.15 and 2.65 in borehole D, showed the largest changes during active testing.

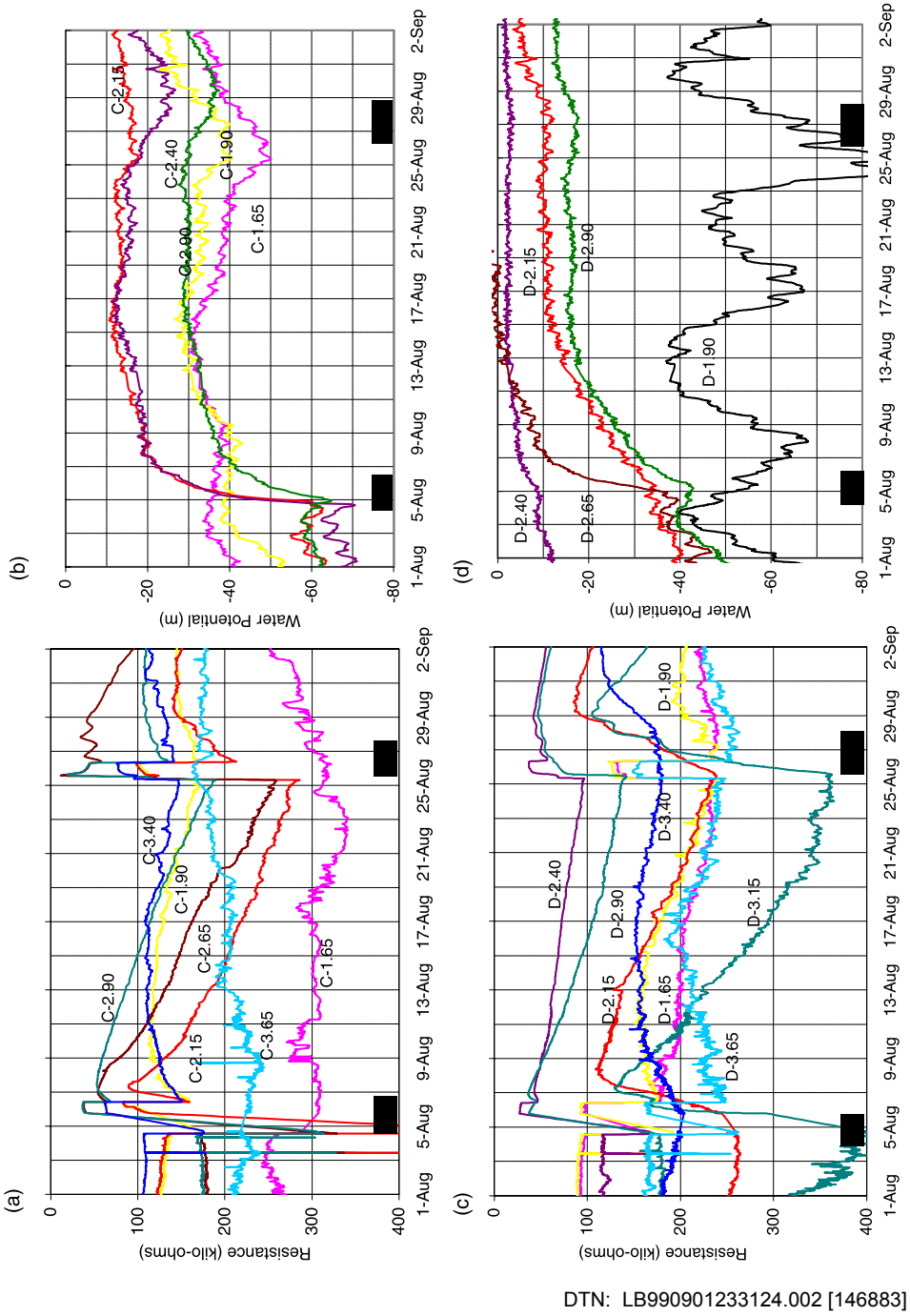

DTN: LB990901233124.002 [146883]

NOTE: The HPZ is located between 2.30 and 2.60 m from the borehole collar. The legend identifies the sensor location in borehole (C & D) and distance of sensor from the borehole collar. Shaded zones indicate the duration of two groups of liquid-release events. Note resistance axis is inverted.

Figure 6.6.2-4. Changes in Electrical Resistance and Water Potential Detected during Liquid Release into the High Permeability Zone

6.6.2.3 Seepage into the Slot

Seepage into the slot was observed during all eight tests in the HPZ (and none in the LPZ tests). The eight tests were conducted in two groups (Table 6.6.1-1). The test results are summarized in Table 6.6.2-1 and illustrated in Figure 6.6.2-3 and Figure 6.6.2-4 as two shaded test duration zones. During the first test in the first group (Test HPZ-1), water was first observed on the slot ceiling five minutes after the start with 0.41 liters of water released under constant-head conditions. In the HPZ-2 and HPZ-3 tests, water appeared in the slot within 3 minutes after 0.17 and 0.14 liters, respectively, had been released. In the HPZ-4 test, water appeared in the slot after five hours with 1.50 liters of water injected at a rate of 5 mL/min.

In the second group of tests, travel time for the first drop of water was 3 minutes after 0.14 liters was injected at a rate of ~69 mL/min (Test HPZ-5). In the HPZ-6 and HPZ-7 tests, the arrival time of the wetting front was 7 minutes after 0.26 and 0.20 liters of water were injected at a rate of 38 and 29 mL/min, respectively. In the final HPZ-8 test, water first appeared in the slot after 1:08 hr, with 0.90 liters injected into the formation at a rate of 14 mL/min.

Table 6.6.2-1. Summary of Liquid-Injection Tests in the High Permeability Zone.

Test Number	Injection Rate (mL/min)	Duration of Injection (hh:mm)	Volume Recovered (liters)	Travel Time of First Drop (hh:mm)	Volume of Water In Formation (liters)		Water Retained in Formation (%)
					At First Drop	At End of Injection	
HPZ-4	5	11:54	0.36	5:00	1.51	3.03	89
HPZ-8	14	11:19	4.56	1:08	0.90	4.82	51
HPZ-7	29	10:36	13.21	0:07	0.20	5.02	28
HPZ-6	38	8:00	14.73	0:07	0.26	3.71	20
HPZ-3	53	5:25	11.14	0:03	0.14	6.31	36
HPZ-5	69	4:26	11.47	0:03	0.14	6.90	38
HPZ-2	98	2:56	12.17	0:03	0.17	5.15	30
HPZ-1	119	2:17	11.61	0:05	0.41	4.67	29

DTN: LB990901233124.002 [146883]

The fraction of injected water recovered in the slot continued to increase as each test progressed. Significant variability was observed in the percentage of water recovered and the seepage rate during and between tests (Figure 6.6.2-5a and b). Seepage variability was related to both the amount of water injected and the rate at which water was released into the formation. Early in each test, the amount of water recovered sharply increased. The percentage of injected water recovered approached relatively constant values after approximately 10 liters of water had been injected. Intermittent seepage behavior (Figure 6.6.2-5b) was observed during all the tests.

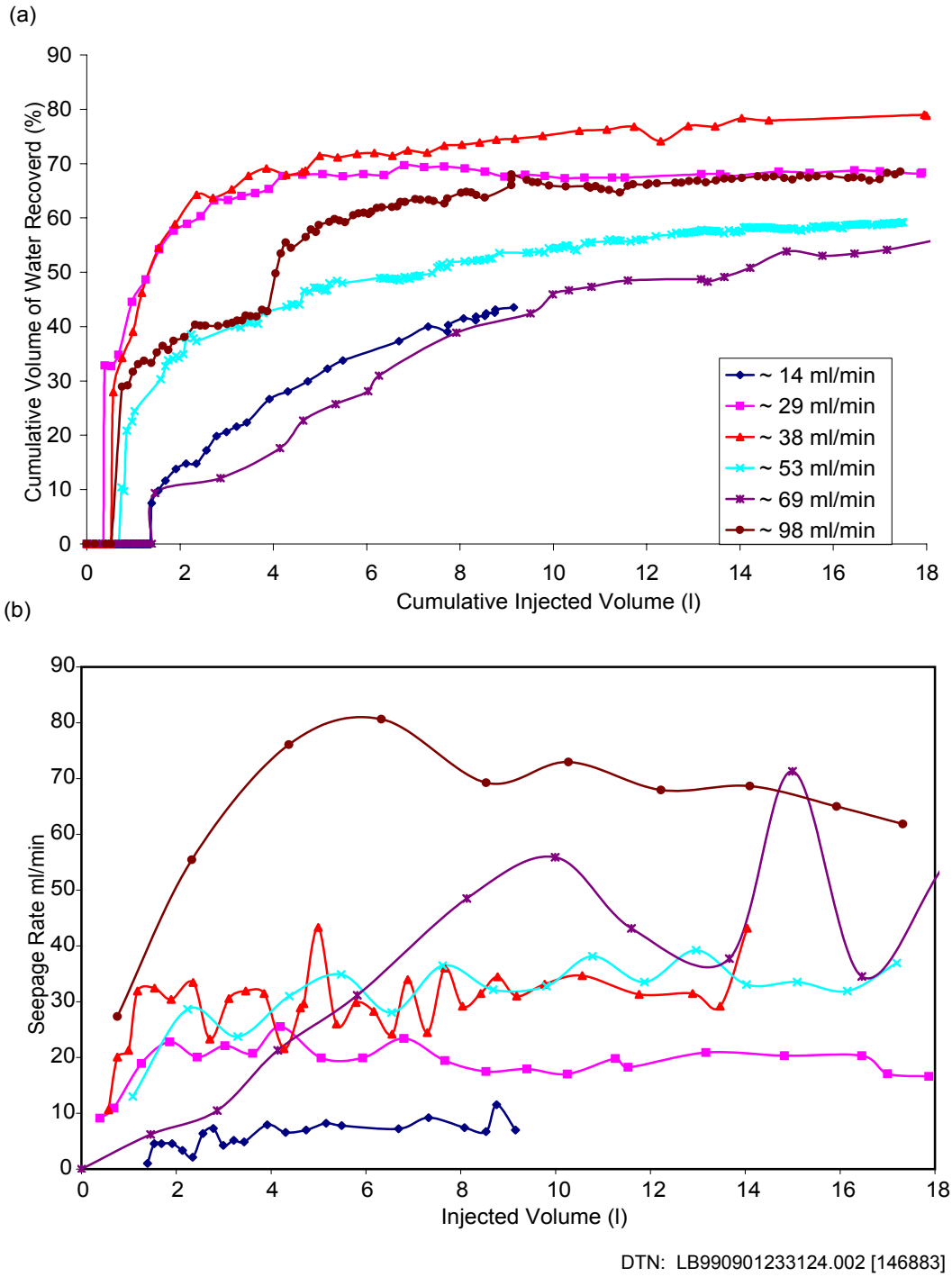

Figure 6.6.2-5. Seepage into Slot: (a) Percentage of Injected Water Recovered and (b) Seepage Rates for Various Release Rates

As illustrated in Figure 6.6.2-6, the percentage of the amount of injected water recovered at the release rate of 38 mL/min was higher than the percentages at other injection rates. The first maximum percentage could be associated with the dominant flow path connecting the injection zone with the outflow slot boundary. With increasing injection rate, additional flow paths, either through other fractures or through other areas in the same fracture, could contribute to the storage and flow of additional water.

Figure 6.6.2-6 also illustrates the distribution of seepage among the collection trays in the slot. As each test progressed, water initially appeared on the slot ceiling at one single point directly below the injection zone, and seepage water was collected from four trays located around the point of entry. During these tests, water seeping into the slot was largely concentrated in a single tray, with the three other trays collecting significantly smaller amounts of water. Slight increases at higher injection rates were noticeable in some of the secondary trays. The remaining 24 trays stayed dry during all the liquid-release tests.

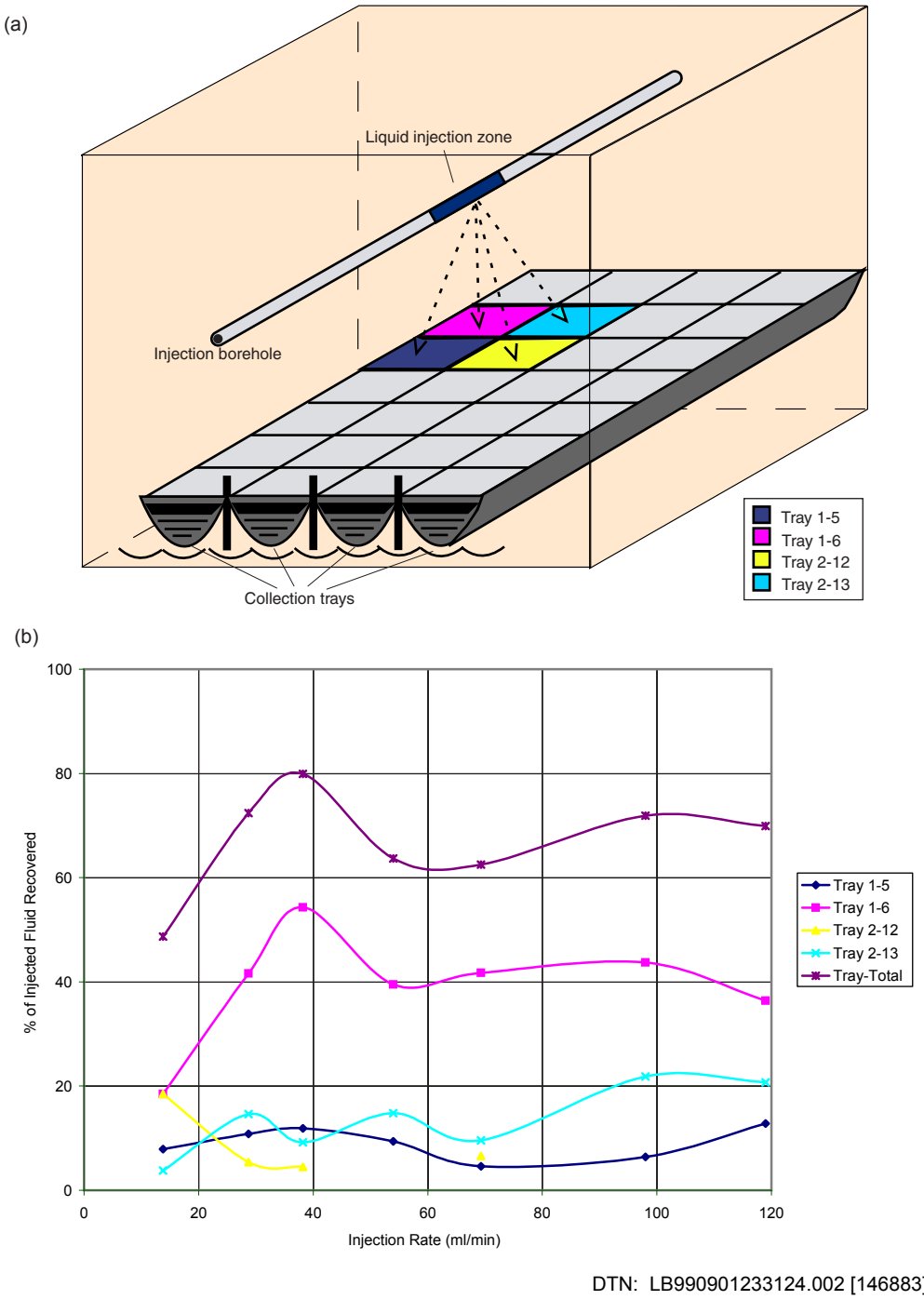

DTN: LB990901233124.002 [146883]

Figure 6.6.2-6. Seepage into Collection Trays in the Slot: (a) Tray Configuration and (b) Percentages of Injected Water Recovered for Different Trays

In all the tests during which there was seepage, 0.5 to 1.3 liters of water entered the slot after the water supply to the formation was switched off (Figure 6.6.2-7). Most of this water was collected within one hour, with recovery rates being largest immediately after the test. The constant-head test with ~98 mL/min release rate had a "stepped" nature to the post-injection recovery. During the first fifteen minutes, the 0.8 liters of collected water appeared in four bursts, each containing 0.1–0.3 liters of water. Changes of similar magnitudes were observed in the tests with injection rates of ~53 mL/min and ~14 mL/min (with one late burst each shown in Figure 6.6.2-7).

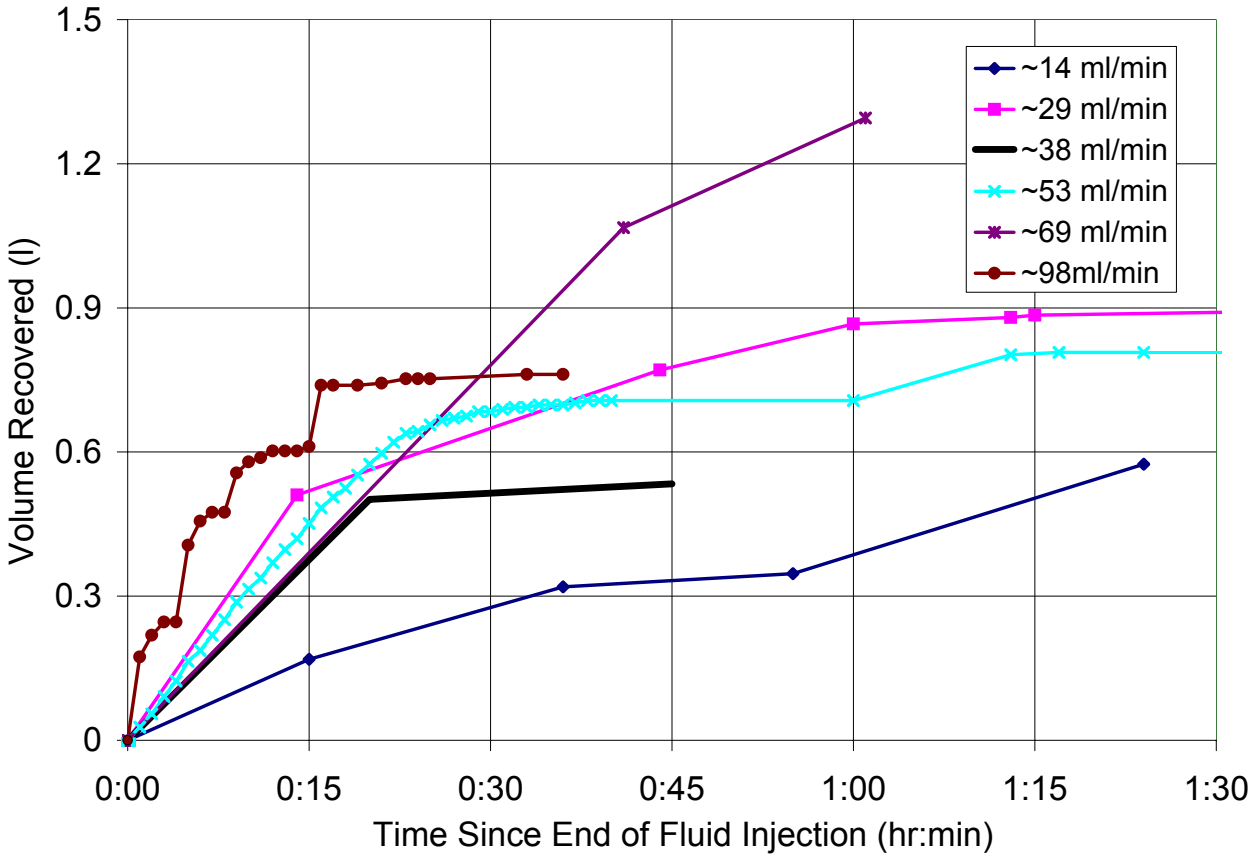

DTN: LB990901233124.002 [146883]

Figure 6.6.2-7. Volume of Water Recovered in the Slot after Liquid Injection at Various Rates into the High Permeability Zone was Stopped

6.6.2.4 Tracer Recovery

Tracers injected in the HPZ were detected in the water samples collected in the slot. (None of the traced water introduced in the LPZ was recovered.) Typically, tracers introduced in one test were rapidly flushed out of the system during the subsequent test (Figure 6.6.2-8). The pattern of recovered concentrations of tracers suggests that plug flow was the dominant process by which "new" water replaced "old" water from the previous test. Some recovery of tracers from the formation was observed during subsequent tests.

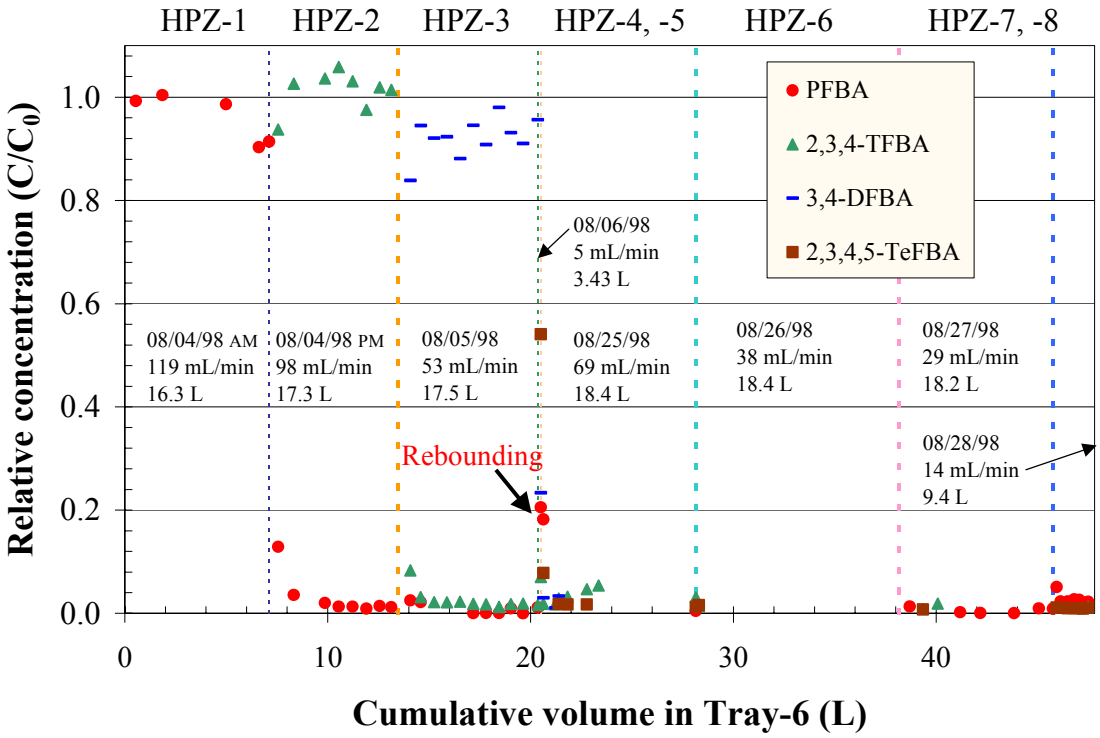

DTN: Flow Rate Data: LB990901233124.002 [146883] and Chemical Data: LB990901233124.001 [155694]

Figure 6.6.2-8. Tracer Concentrations in Seepage Water Following Injection into the High Permeability Zone

INTENTIONALLY LEFT BLANK

6.7 ANALYSES OF FLOW THROUGH THE FAULT AND MATRIX IN THE TEST BED AT ALCOVE 4

To investigate the potential for damping fast flow through the Paintbrush nonwelded tuff (PTn), the evolution of a flow field and the migration of a wetting front following the release of liquid into a fault and matrix were evaluated in a test bed using a cluster of horizontal boreholes at Alcove 4.

6.7.1 Flow Tests in Paintbrush Tuff Unit Layers and Fault

Field experiments were conducted in the PTn within the ESF at Yucca Mountain. These experiments included multiple releases of tracer-laced water in isolated zones along three horizontal boreholes. The zones into which water was released were selected based on air-permeability measurements conducted over 0.3 m sections of borehole (Section 6.5.2). The plumes that developed from these releases were monitored in six separate horizontal boreholes. During and following liquid-release events, changes in saturation and water potential along horizontal monitoring boreholes were continuously recorded by an automated data acquisition system.

6.7.1.1 The Test Bed

The test bed is located at Alcove 4 in the ESF. It is accessed through an alcove excavated (by an Alpine miner) at approximately 67 degrees to the central axis of the ESF North Ramp. Alcove 4 transects portions of the lower Pah Canyon Tuff (Tpp) and the upper pre-Pah Canyon bedded tuffs (Tpbt2) of the PTn (nomenclature of Buesch et al. 1996 [100106], p. 7). The central axis of the alcove has an azimuth of 6 degrees, which coincides with the approximate strike of the PTn units in the vicinity. The north face of the alcove, in which the test bed is located, is approximately 6 m wide and 5.3 m high (Figure 6.7.1-1).

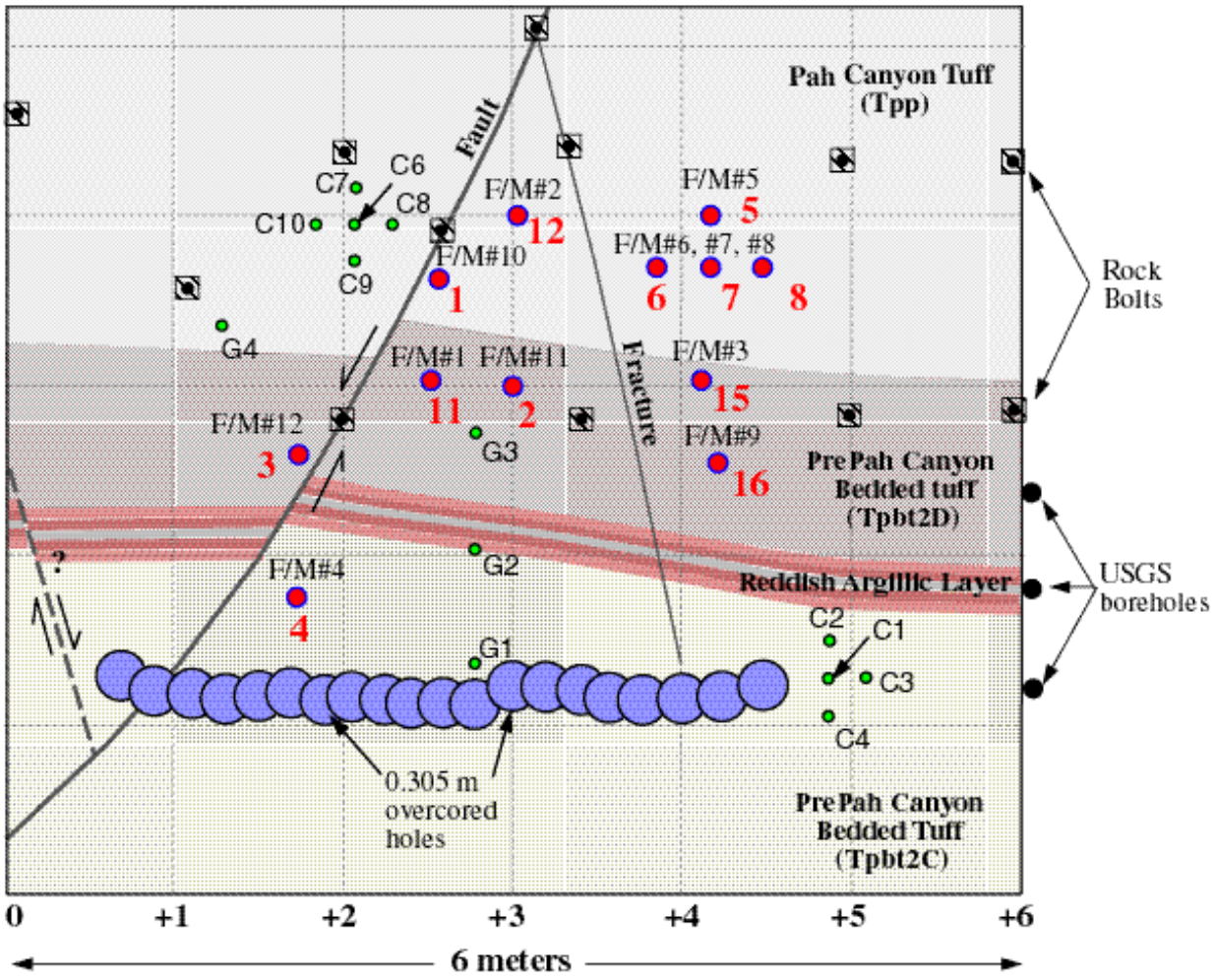

- 0.0762 m diameter (NQ) boreholes, approximate depth = 6 m
- 0.0254 m diameter boreholes, depth of "G" holes = 1 m, depth of "C" holes = 2 m

NOTE: Also included are location of boreholes and the slot.

Figure 6.7.1-1. Geological Sketch and Schematic Illustration for the North Face of Alcove 4 in the ESF at Yucca Mountain

The lower Tpp and upper Tpbt2 units D and C (units from Moyer et al. 1996 [100162], pp. 46-50) are exposed along the north face of Alcove 4. Tpp is nonwelded and pumice-rich. It exhibits a chalky-white color and is apparently zeolitically altered (based on destruction of the texture of the matrix ash and destruction of the integrity of the glass shards, Moyer et al. 1996 [100162], p. 46). Zeolitic alteration in the North Ramp of the ESF commonly follows fractures and faults that cut through the Tpp and Tpbt2 units (Barr et al. 1996 [100029], p. 44). The contact between the lower Tpp and upper Tpbt2D is sharp in Alcove 4, marked by distinct color changes. Tpbt2D is also nonwelded, possibly reworked, and has variably abundant (while zeolitically altered) pumice within a fine- to coarse-grained, medium-brown matrix.

Below Tpbt2D, lying in the upper Tpbt2C, is a thin (0.20–0.30 m), light-pink-to-red argillically altered layer that is almost completely offset by a small, westward-dipping normal fault. Alteration within this layer can be traced from the end of Alcove 4 out into the North Ramp. It is uncertain whether the argillic alteration seen in Alcove 4 is laterally continuous, though reddish alteration is commonly observed in several boreholes and in outcrops across Yucca Mountain at the same stratigraphic horizon (Moyer et al. 1996 [100162], pp. 54–55). The remaining Tpbt2C exposed along the north face below the argillic layer is massive and nonwelded, has very pale tan coloring, and contains abundant, coarse pumice and lithic fragments.

Cutting the north face of Alcove 4 is a normal fault with a small offset (0.25 m). As mapped along the crown at the end of the alcove (Barr et al. 1996 [100029], full-periphery geological map OA-46-289, DTN: GS960908314224.020 [106059] for the crown, but not for the end face), the fault has a strike of approximately 195 degrees and a westward dip of 58 degrees. The fault is open in the ceiling and is closed, with knife-edge thickness, near the invert on the north face. Intersecting the fault near the alcove crown along the north face is a high-angle fracture. The cause of the fracture is uncertain and could have been induced by drilling or drying, considering the location of rock bolts and the clay content of the rocks. The orientation of the fracture is unknown, though it has an apparent eastward dip of about 75 degrees. Similar to the fault, the fracture appears to have a large aperture near the ceiling and a much smaller aperture (eventually becoming undetectable) near the invert.

Two distinct features that were imposed on the formation define the layout of the field experiment, i.e., a horizontal slot and a series of horizontal boreholes. The slot, located immediately below the test bed, was designed to capture any seepage resulting from gravity drainage. It was excavated by a drilling sequence that required 0.10 m diameter pilot holes drilled parallel at 0.22 m spacing, perpendicular to the alcove wall. These pilot holes were then over-cored by a 0.3 m drill-bit to excavate a 6.0 m wide, 4.0 m deep and 0.3 m high cavity located approximately 1.5 m above the alcove floor. I-beam supports were installed along the length of the slot to prevent it from collapsing during the duration of the field tests.

Twelve 6.0 m long, 0.1 m diameter boreholes were drilled into the alcove face, as illustrated in Figure 6.7.1-1 and Figure 6.7.1-2. Borehole 1, borehole 4, borehole 11, and borehole 12 were positioned to intersect the fault for the purpose of conducting flow tests within the fault. Borehole 2 was located to detect moisture that could migrate through the matrix below borehole 12. Borehole 12 was the injection borehole for the fault flow tests conducted. The configuration of borehole 5, borehole 6, borehole 7, and borehole 8 was designed to investigate the nature of matrix flow in the Tpp, with borehole 5 serving as the injection borehole and borehole 6, borehole 7, and borehole 8 equipped with probes to detect changes in moisture conditions. Borehole 3 on the left side of the fault, and borehole 15 and borehole 16 away from the injection boreholes, were not instrumented for the tests conducted. (Borehole 9, borehole 10, borehole 13, and borehole 14 were planned but not drilled.)

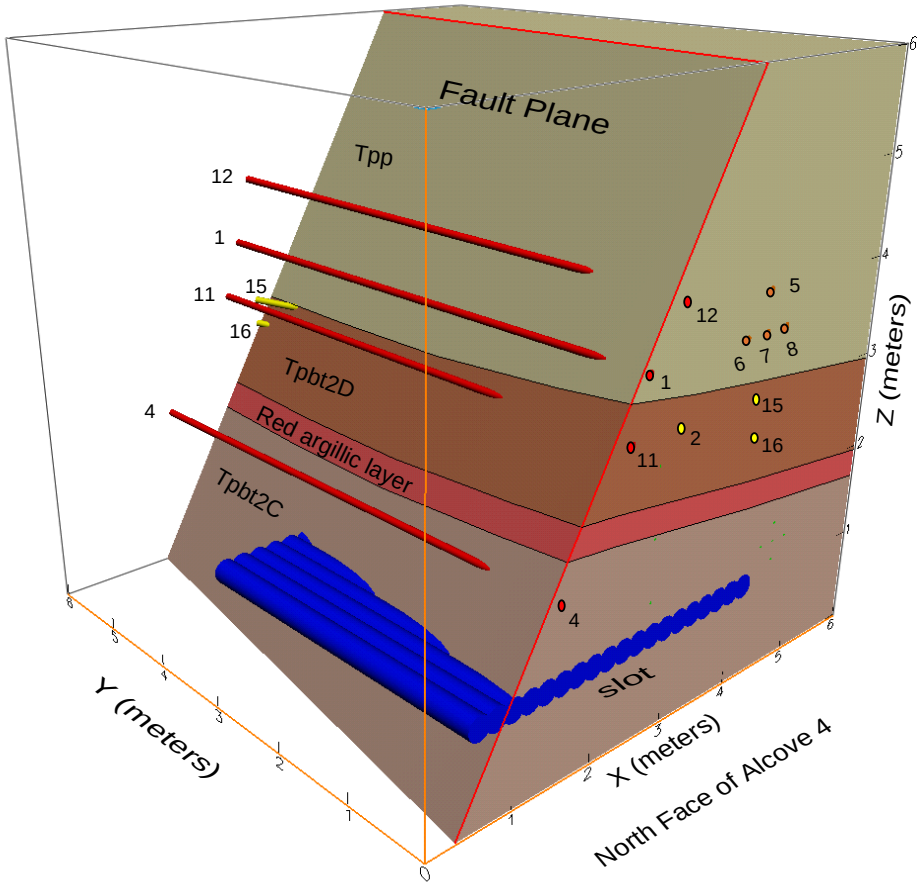

Figure 6.7.1-2. Perspective Illustration of Three-Dimensional View of the Boreholes, Slot, and Lithological Unit Contacts in the Alcove 4 Test Bed

6.7.1.2 Instrumentation

The flow investigation had three distinct components: (1) controlled release of water into isolated zones, (2) borehole monitoring for changes in saturation and water potential, and (3) the monitoring of seepage from the slot ceiling. For each component, new instruments were developed, details for which are described in Attachment VI. Because water did not seep into the slot, the seepage monitoring system was not used. Key features of the liquid-injection and borehole-monitoring system are presented in the following subsections.

6.7.1.2.1 Fluid Injection

The liquid-release experiments required water to be injected into the formation over a 0.3 m section of borehole with a constant-head boundary condition to determine the maximum rates at which the zone could take in water. The main components of the fluid-release apparatus included an inflatable packer system used to isolate the injection zone, a pump to deliver water to a constant-head chamber from which water was introduced into the injection zone, and a reservoir to provide a continuous supply of water. To capture the temporal variability in vertical flux of

water from the injection zone, an automated liquid-release system was developed to measure changing flow rates on a ponded surface. This system allowed for continuous measurement of local liquid-release rates during the entire experiment.

6.7.1.2.2 Borehole Monitoring

In six monitoring boreholes (borehole 1, borehole 2, borehole 11, borehole 6, borehole 7, and borehole 8 in Figure 6.7.1-2) located above the slot, changes in saturation and water potential were continuously recorded during the entire investigation. Changes in saturation along boreholes were measured with ERPs located at 0.25 m intervals along a 6.0 m length of each borehole. Water–potential measurements were made with psychrometers, as described in Attachment VI.2 for Alcove 6 testing. The psychrometers and ERPs were housed in special Borehole Sensor Trays (BSTs) installed along the length of each monitoring borehole.

6.7.1.3 Liquid-Release Experiments

Air-permeability measurements were made along 0.3 m sections of all nine boreholes to determine the exact location of the fault in borehole 4, borehole 11, and borehole 12, as discussed in Section 6.5.2. All water used in the ESF (for mining-related activities and scientific investigations) was spiked with the same concentration of lithium bromide. For the entire duration of the experiments, saturation and water-potential changes along the monitoring boreholes were continuously measured.

A total of 193 liters of water was released into borehole 12 during seven events, under constant-head conditions, between October 21 and November 5, 1998, as summarized in Table 6.7.1-1. In this borehole, as in all others, water was released over a 0.30 m interval. Here, the injection interval was centered at a distance 1.4 m from the borehole collar, determined from air-permeability measurements to be the location of the fault.

Table 6.7.1-1. Summary of Liquid Releases into the Fault Zone in Borehole 12

Test Number	Date (mm/dd/yy)	Volume Injected (l)	Duration (hh:mm)	Average Intake Rate (mL/min)
1	10/21/98	42.90	5:12	138
2	10/22/98	41.44	5:59	115
3	10/26/98	21.34	4:22	81
4	10/27/98	29.53	6:59	70
5	10/28/98	22.16	6:10	60
6	11/04/98	17.08	5:48	49
7	11/05/98	18.85	6:31	48

DTN: LB990901233124.005 [146884]

In borehole 5 away from the fault, water was released into two zones. In the first zone (located 1.50 to 1.80 m from the collar) 1.37 liters of water were released to the zone on October 19, 1998, and a similar volume was released on October 20, 1998. Because a problem was detected with the constant-head system, no more water was injected into this zone. On October 27, 1998, after the injection system was repaired, water was released into borehole 5 at a distance of 2.44–2.74 m from the borehole collar. In this zone, 6.5 liters of water were released under constant head conditions over a period of 23 days.

6.7.2 Observations of Fault Flow and Matrix Flow

During and following the release of water into the test bed, intake rates (rates of water moving into the formation during constant-head tests), travel times, and lateral dispersion of the plume (as seen along the length of horizontal boreholes) were continuously monitored. In the following section, the observed hydrological responses to liquid releases in the three zones as detected by ERPs and psychrometers are presented.

6.7.2.1 Fault Responses

6.7.2.1.1 Intake Rates

Water was injected into the section of borehole 12 that intercepted the fault approximately 1.40 m from the collar. Here, 193 liters of water were released into the formation during seven events that extended over a period of two weeks, as illustrated in Figure 6.7.2-1. Each event lasted between 4 and 7 hours, during which 20–43 liters of water entered the injection zone. Each release event began with water filling the 1.37-liter injection cavity in about 3 minutes, after which the liquid-release apparatus kept the injection zone filled by maintaining a constant-head boundary for the period of injection. After water was injected into the formation, the 1.37 liters of water occupying the injection zone were released to the formation under falling head conditions.

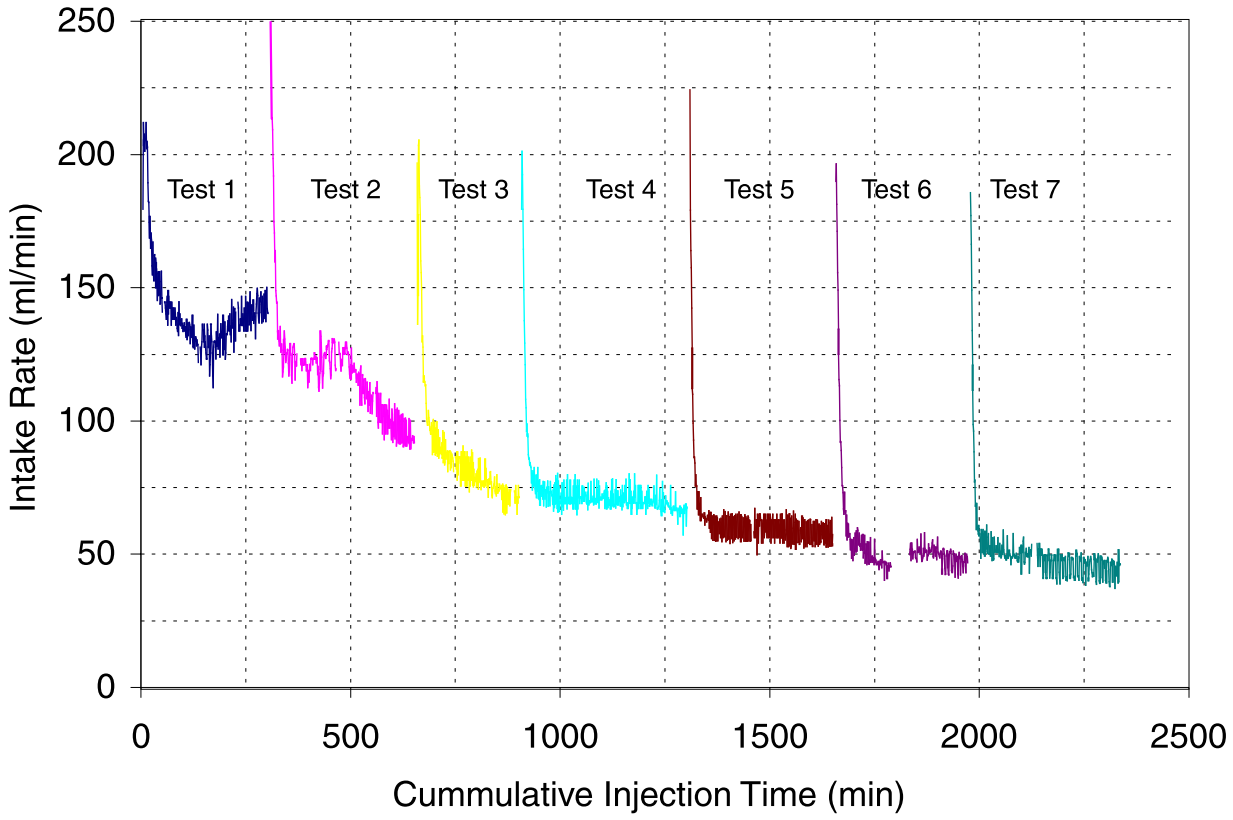

DTN: LB990901233124.005 [146884]

Figure 6.7.2-1. Intake Rates along the 0.3 m Zone Located on the Fault in Borehole 12

During Test 1 into the fault, the intake rate dropped from 200 mL/min to 120 mL/min over a period of 180 minutes, before recovering to 145 mL/min in the next 120 minutes. In Test 2, conducted one day later, the intake rate dropped from 200 mL/min to 120 mL/min over a period of 80 minutes before remaining fairly constant for the next 100 minutes. Approximately 180 minutes after this release event started, the intake rates began to drop steadily, reaching a rate of 95 mL/min by the end of the test. In Test 3, which was initiated four days later, the intake rates rapidly dropped to 95 mL/min during the first 40 min and then continued to decrease at a more gradual rate for the next 200 minutes to a rate of 70 mL/min. During Test 4 and Test 5, conducted during the next two days, the pattern of rate change was similar, with an initially high intake rate quickly dropping to a near constant value (70 to 60 mL/min, respectively). In Test 4, this constant value persisted 300 minutes into the test, after which there was a gradual decrease in intake rates for the remainder of the test. During Test 6, which began after a six-day hiatus, water was injected during two intervals. During this test, water was introduced under constant-head conditions for 140 and 158 minutes periods with a gap of 22 minutes, during which water imbibed into the formation under a falling head. The intake rates rapidly dropped to 50 mL/min. In Test 7 into this zone, the intake rates again dropped to 50 mL/min after 100 minutes of release. The rates gradually decreased during the 200 minutes of injection, which approached 40 mL/min after 18 liters of water had been injected.

6.7.2.1.2 Travel Times in Fault

When water was introduced into borehole 12, the time taken for the wetting front to travel 1.07 m along the fault to borehole 11 varied among the seven tests (Figure 6.7.2-2). In the first test, water was detected in the lower borehole ~300 minutes after the first release, while in the second test, the travel time was reduced to ~200 minutes. For the third test, this travel time was ~250 min; in the fourth test, water appeared in the fault in borehole 11 within ~150 minutes. The fastest travel time was observed for the fifth test, when the front arrived within ~120 minutes in borehole 11. In the last two tests, the travel times were significantly slower, with increasing saturations observed 400 and 700 minutes after the initial release of water.

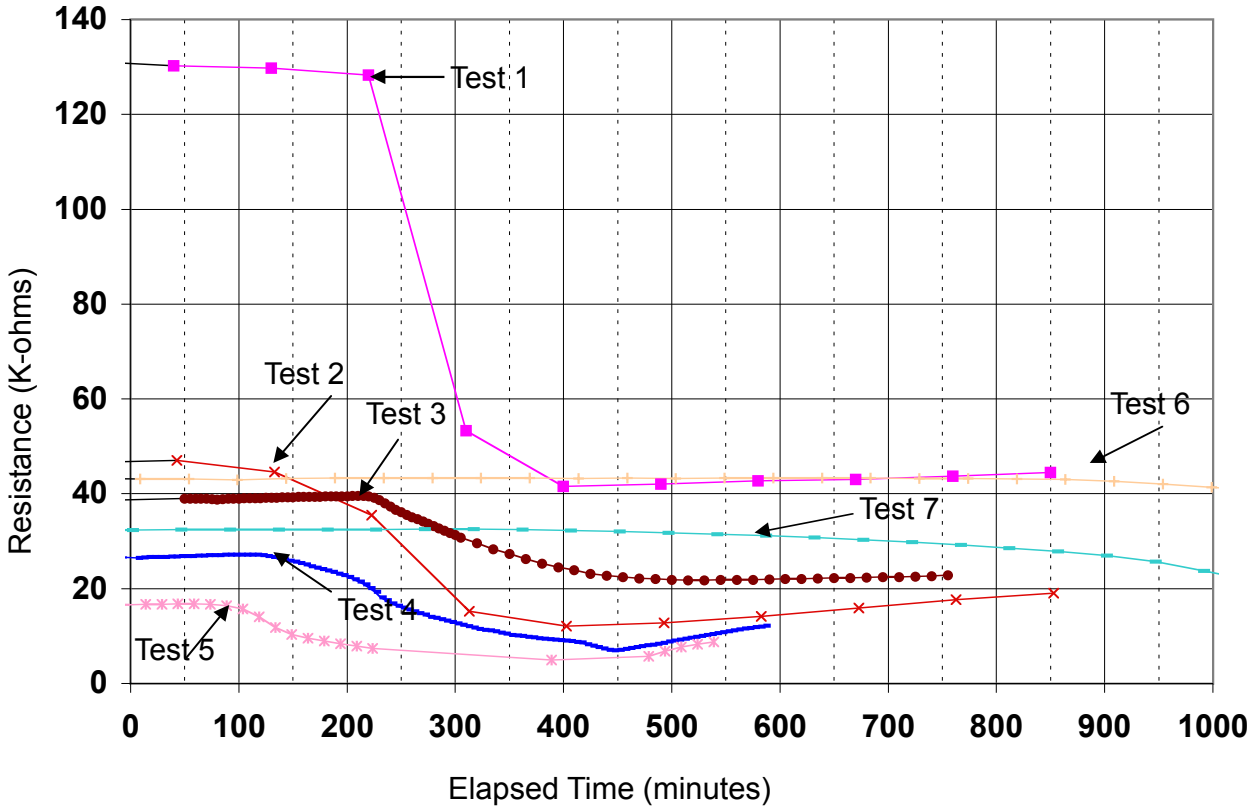

DTN: LB990901233124.005 [146884]

Figure 6.7.2-2. Wetting Front Arrival in Borehole 11 Following Liquid Released into the Fault in Borehole 12

6.7.2.1.3 Dispersion

Water injected into the fault in borehole 12 was detected along the length of borehole 11 by ERPs located between 0.65 and 2.40 m (Figure 6.7.2-3). Unlike the ERP located on the fault (1.40 m from the collar), which showed a stepped response to individual release events, these other ERPs showed a slow, gradual decrease in resistance measurements. The first response was seen in the ERPs located on either side of the fault, with the one at 1.65 m responding first. ERPs located between the alcove face and the fault appeared to be significantly drier at the start of the experiment than those located deeper in the test bed. These ERPs responded with larger decreases in resistance measurements following the start of the release water. The largest response to the injection events in borehole 12 was detected between 0.9 and 1.65 m from the collar in borehole 11.

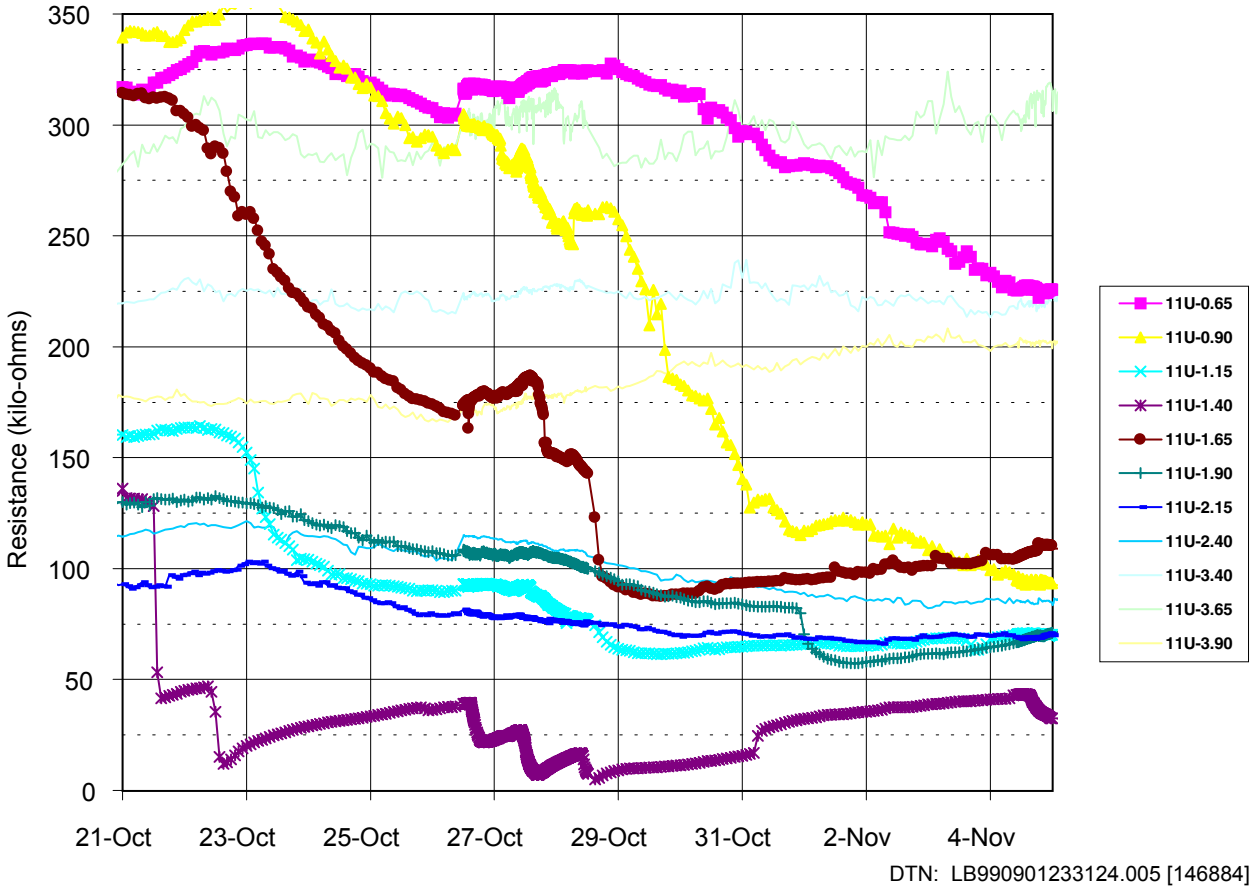

DTN: LB990901233124.005 [146884]

NOTE: The legend indicates the location of the measurement (in meters) from the collar. The 'U' indicates that these are measurements from the upper BSTs in the borehole.

Figure 6.7.2-3. Changes in Electrical Resistance in Borehole 11 in Response to Liquid Released into the Fault in Borehole 12

In borehole 2 located 0.97 m vertically below borehole 12, the first ERPs to detect the wetting front were centered immediately below the fault (Figure 6.7.2-4). Here, at a distance of 1.15 to 1.65 m from the borehole collar, changes in saturation were detected almost one week after the first injection event on October 21, 1998. Over the next three weeks, ERPs at 1.15 and 1.40 m continued to detect increasing saturations, while the ERP at 1.65 m wetted for four days before maintaining a relatively constant saturation level for the next 18 days. At depths between 1.90 and 2.40 m, the response was delayed very slightly.

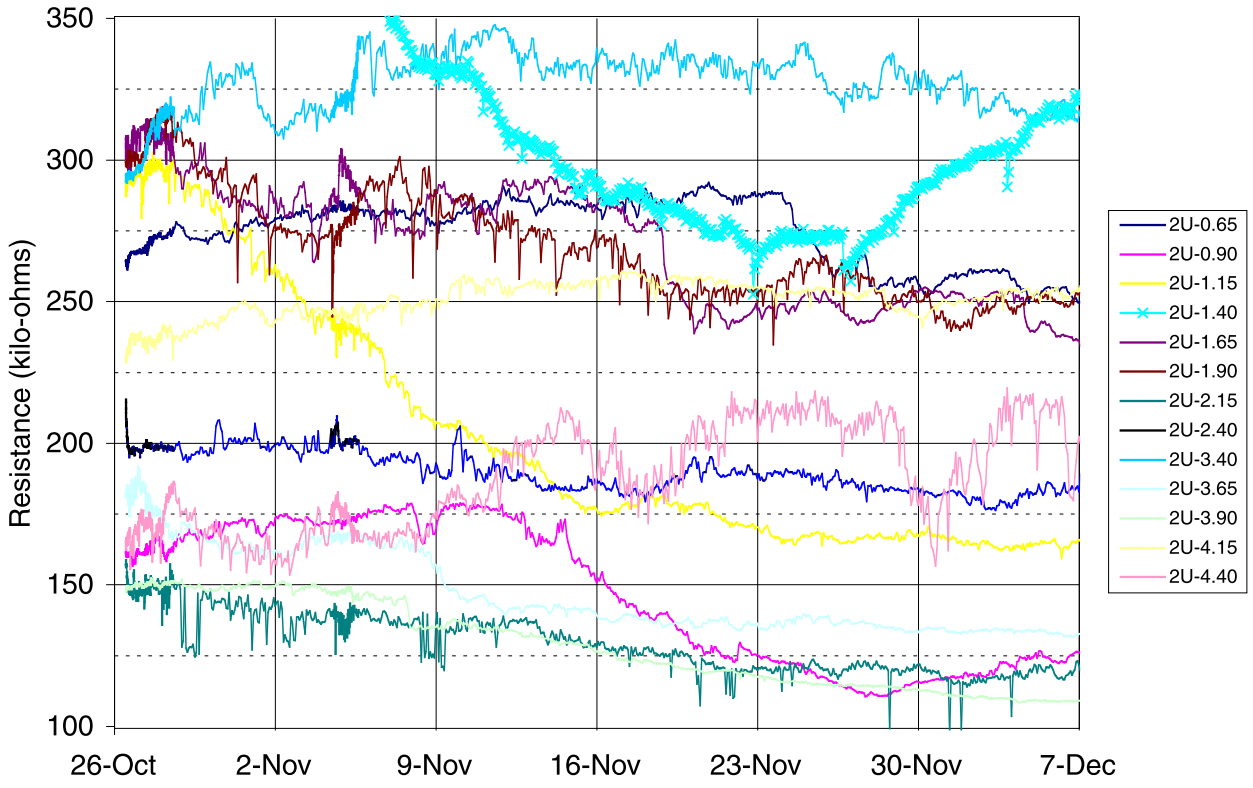

DTN: LB990901233124.005 [146884]

NOTE: The legend indicates the location of the measurement (in meters) from the collar. The 'U' indicates that these are measurements from the upper BSTs in the borehole.

Figure 6.7.2-4. Changes in Electrical Resistance in Borehole 2 in Response to Liquid Released into the Fault in Borehole 12

6.7.2.2 Matrix Responses

6.7.2.2.1 Intake Rates

When water was released into borehole 5, in the zone 2.44–2.74 m from the collar, the intake dropped steeply to 1 mL/min within 150 minutes (Figure 6.7.2-5). The intake rate then continued to gradually decrease over the next 2,000 minutes before reaching a constant rate of ~0.1 mL/min. This rate remained approximately constant for the entire duration of the test.

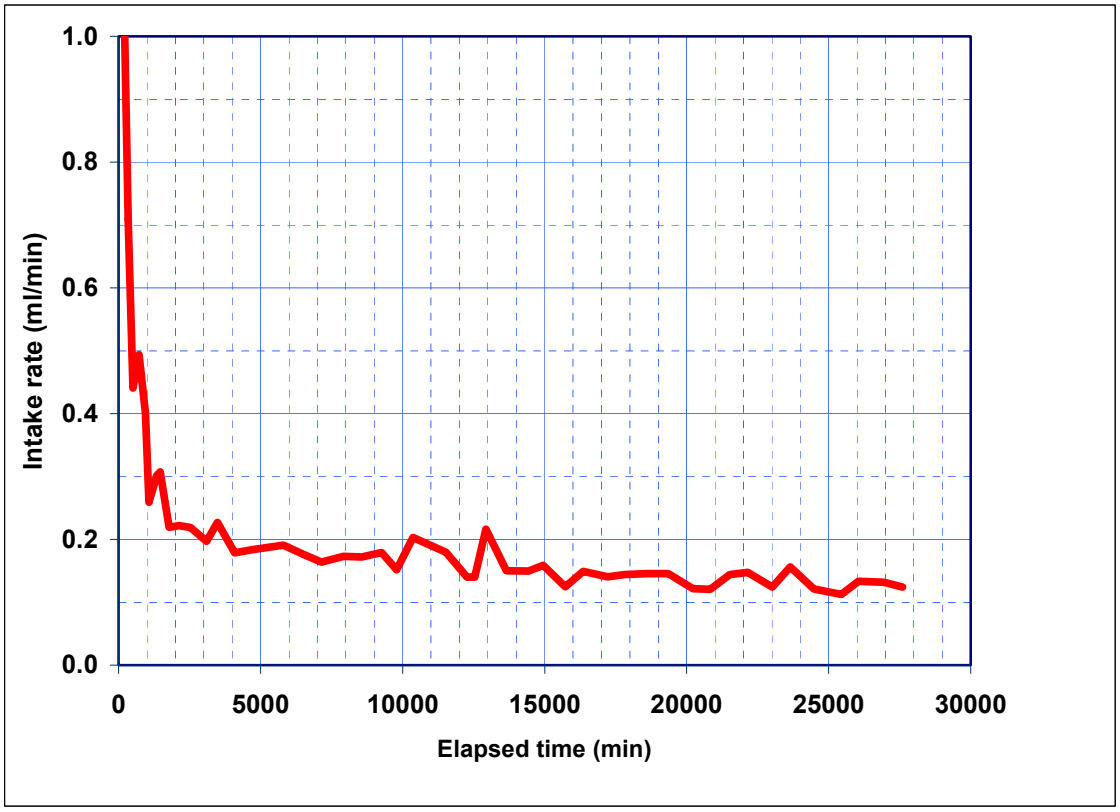

DTN: LB990901233124.005 [146884]

Figure 6.7.2-5. Intake Rates along a 0.3 m Zone in the Matrix Located 2.44–2.74 m from the Collar in Borehole 5

6.7.2.2.2 Wetting Front Migration

Following the first release of water in borehole 5 on October 27, 1998 (at 2.44–2.74 m from the collar), the wetting front was detected in the upper section of borehole 6 (located 0.45 from borehole 5) after a period of 14 days on November 10, 1998, at a distance of 2.90 m from the collar (Figure 6.7.2-6). Some of the sensors near the collar had high resistance values and fluctuating changes that might represent responses to additional drying and wetting processes near the borehole collar.

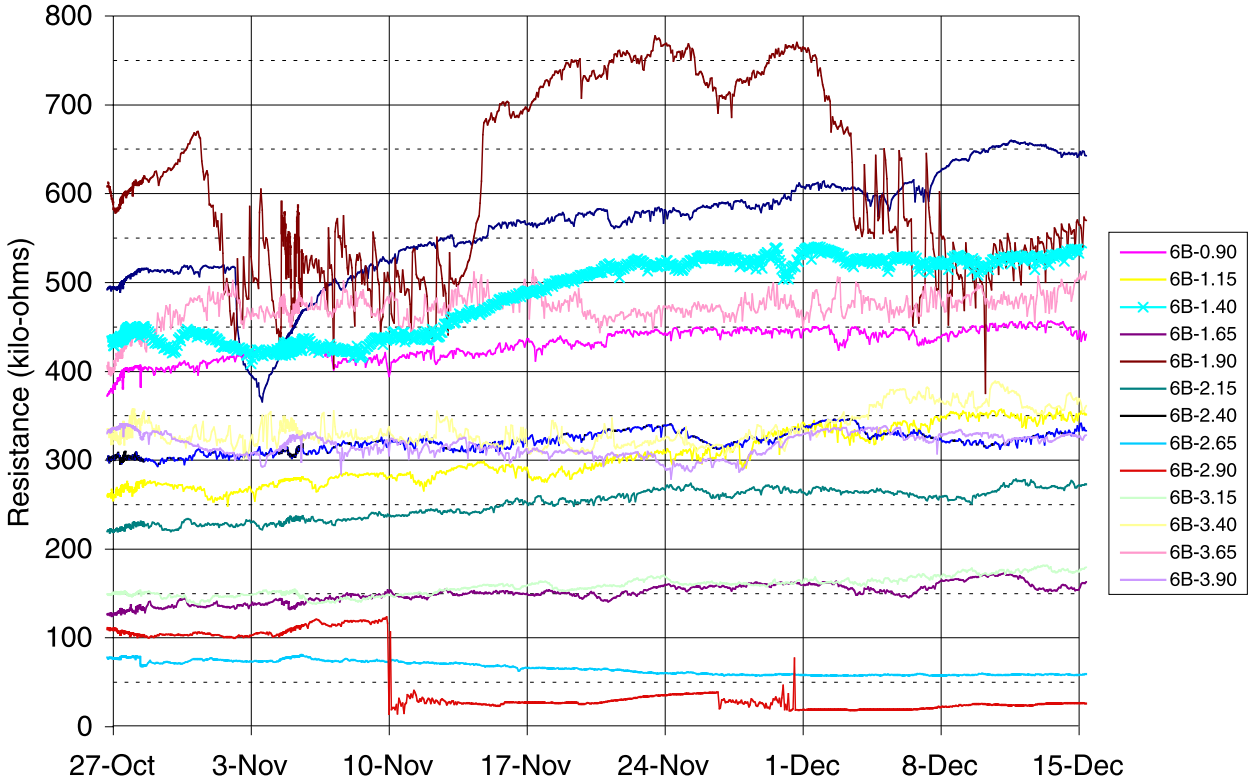

DTN: LB990901233124.005 [146884]

NOTE: The legend indicates the location of the measurement (in meters) from the collar. The 'B' indicates that these are measurements from the lower BSTs in the borehole.

Figure 6.7.2-6. Changes in Electrical Resistance in Borehole 6 in Response to Liquid Released in Borehole 5

6.8 COMPILATION OF WATER-POTENTIAL MEASUREMENTS IN NICHES

Measurements of water potentials from three niche sites in the ESF are presented. These sites are located on the west side of the ESF Main Drift at Niche 3566 (Niche 1), Niche 3650 (Niche 2), and Niche 3107 (Niche 3). Niche 3566 (Niche 1) lies between the Sundance fault and a cooling joint branching out from the fault. The primary objective of this effort was to determine the water potential at various points within the three niche sites to determine if wet conditions exist at Niche 3566 (Niche 1) near the fault while other niches are drier.

To meet this objective, we used psychrometers (a method to measure water potential, in boreholes). The psychrometers were also used in wetting-front detection, as described in Section 6.6 for Alcove 6 and Section 6.7 for Alcove 4. The sensitivity of psychrometer performance is described in Attachment VII. The results of this section need to take into account the uncertainties associated with the sensitivities of psychrometer readings (to operating conditions and to handling of the sensors, as discussed in Attachment VII.)

6.8.1 Location and Timing of Water-Potential Measurements at Niches

Water potentials were measured either along the length or at the ends of 0.0762 m diameter boreholes. Three different types of housing units were used to locate psychrometers in the boreholes. The main feature of the housings was the creation of a small air chamber that allowed for quick equilibration and measurements of humidity close to the borehole wall.

At Niche 3566 (Niche 1), two separate sets of measurements were made: before and after niche excavation. Pre-excavation measurements were made during May 1997 in three holes (U, M, and B) at a distance of 10 m from the borehole collar (Figure 6.8.1-1a). Between July and September 1997, two sets of measurements were made along borehole U at distances between 3.5 and 8.0 m from the collar. Post-excavation measurements of water potential were made in October 1997 in five boreholes extending radially along a horizontal plane from the niche cavity (Figure 6.8.1-1b).

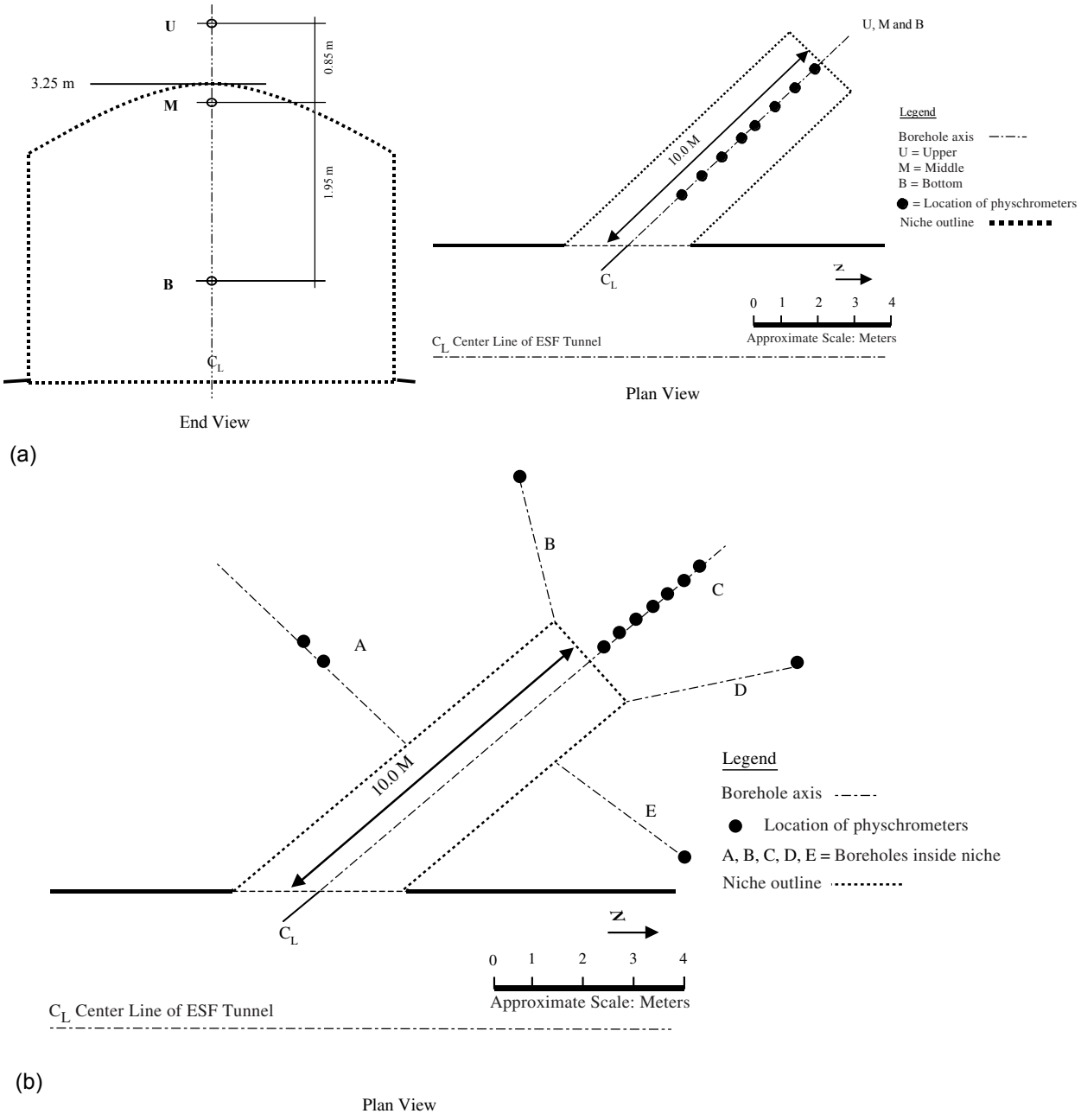

Figure 6.8.1-1. Schematic Illustration of the Location of Psychrometers in Niche 3566 (Niche 1) (a) in Pre-Excavation and (b) in Post-Excavation Conditions

At Niche 3650 (Niche 2), two separate sets of water-potential measurements were made in July 1997, before and after air-permeability tests were conducted in the boreholes. In three boreholes at this location (ML, BR, and BL), water potentials were measured at the end of the boreholes (10 m). In borehole UM, measurements were made close to the borehole collar, i.e., between 0.6 and 1.2 m (Figure 6.8.1-2).

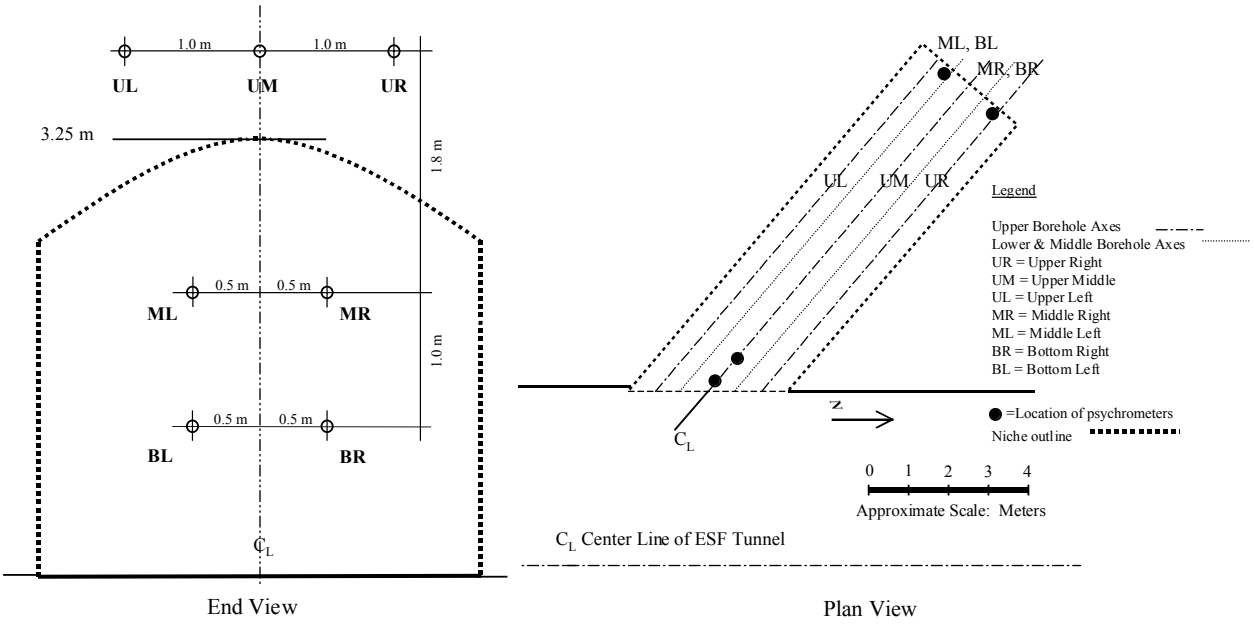

Figure 6.8.1-2. Schematic Illustration of Location of Psychrometers in Niche 3650 (Niche 2)

At Niche 3107 (Niche 3), four boreholes were instrumented with psychrometers (Figure 6.8.1-3). One set of potential measurements were made in December 1997 and January 1998. In the upper middle (UM) borehole, multiple measurements were made along the first 3.0 m, while in the remaining three boreholes (ML, UL, UR), single measurements were made using different lengths of borehole cavity. In the upper-right borehole (UR), sensors were located at the back of the borehole and sealed off with inflation packers such that the borehole cavity was less than 0.04 m long. In the upper-left borehole (UL), sensors were located 5 m from the borehole collar, with the cavity sealed off by inflation packers. In this case, the sensing cavity extended over 5 m of the borehole. In the middle-lower borehole (ML), sensors were located 0.3 m from the borehole collar, with an inflation packer installed to isolate the entire 10 m length of borehole from the ESF Main Drift.

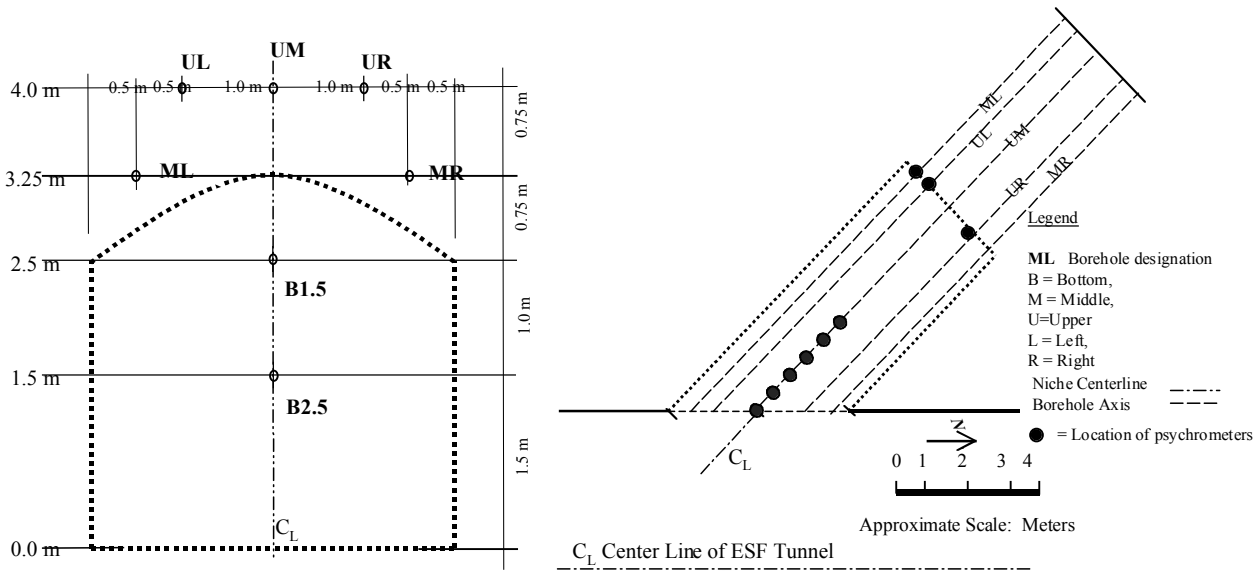

Figure 6.8.1-3. Schematic Illustration of Location of Psychrometers in Niche 3107 (Niche 3) (Pre-Excavation)

6.8.2 Observations of Dryout in Niche Boreholes

Water-potential measurements obtained from the three niches are summarized in Table 6.8.2-1 and Table 6.8.2-2. The time and duration of measurements are presented for each location.

Table 6.8.2-1. Water-Potential Measurements in Niche 3566 (Niche 1)

Borehole ID	Dist. from Collar (m)	Duration of Measurement	Psych #	Water Potential (m)
Pre-Excavation				
U	10.0	5/9-16/97	Psy -51	-13
U	10.0	5/9-16/97	Psy -52	-13
M	10.0	5/9-16/97	Psy -53	-7
M	10.0	5/9-16/97	Psy -54	0.4
B	10.0	5/9-16/97	Psy -55	-12
U	6.1	7/8-14/97	Psy -42	-49
U	5.5	7/8-14/97	Psy -43	-46
U	5.5	7/8-14/97	Psy -44	-34
U	4.9	7/8-14/97	Psy -45	-46
U	4.3	7/8-14/97	Psy -48	-68
U	3.7	7/8-14/97	Psy -50	-62
U	7.9	9/16-24/97	Psy -42	-49
U	7.3	9/16-24/97	Psy -60	-46
U	6.7	9/16-24/97	Psy -45	-71
U	6.1	9/16-24/97	Psy -48	-67
U	5.5	9/16-24/97	Psy -50	-36
Post-Excavation				
A	6.25	10/18-21/97	Psy-43a	-2
A	6.75	10/18-21/97	Psy-60	-30
B	6.00	10/18-21/97	Psy-51	-43
C	0.15	10/18-21/97	Psy-49	-132
C	0.76	10/18-21/97	Psy-42	-33
C	1.98	10/18-21/97	Psy-45	-22
C	1.98	10/18-21/97	Psy-47	-47
C	1.37	10/18-21/97	Psy-48	-40
C	2.60	10/18-21/97	Psy-43	-57
D	6.00	10/18-21/97	Psy-54	-22
D	6.00	10/18-21/97	Psy-56	-32
E	6.00	10/18-21/97	Psy-57	-75
E	6.00	10/18-21/97	Psy-59	-81

DTN: LB980001233124.001 [105800]

Table 6.8.2-2. Water-Potential Measurements in Niche 3650 (Niche 2)

Borehole ID	Dist. from Collar (m)	Duration of Measurement	Psych #	Water Potential (m)
Pre-Air-Injection Testing				
UM	1.2	7/1-8/97	Psy -48	-127
UM	0.6	7/1-8/97	Psy -49	-139
UM	0.6	7/1-8/97	Psy -50	-165
BR	10.0	7/1-8/97	Psy -51	-37
BR	10.0	7/1-8/97	Psy -52	-39
BR	10.0	7/1-8/97	Psy -53	-32
BL	10.0	7/1-8/97	Psy -54	-24
BL	10.0	7/1-8/97	Psy -55	-36
ML	10.0	7/1-8/97	Psy -57	-1
Post-Air-Injection Testing				
ML	10.0	7/24-28/97	Psy -51	-29
ML	10.0	7/24-28/97	Psy -52	-38
ML	10.0	7/24-28/97	Psy -53	-39
BR	10.0	7/24-28/97	Psy -54	-58
BR	10.0	7/24-28/97	Psy -55	-49
BR	10.0	7/24-28/97	Psy -56	-48
BL	10.0	7/24-28/97	Psy -57	-21
BL	10.0	7/24-28/97	Psy -58	-15
BL	10.0	7/24-28/97	Psy -59	-28

DTN: LB980001233124.001 [105800]

Table 6.8.2-3. Water-Potential Measurements in Niche 3107 (Niche 3)

Borehole ID	Dist. from Collar (m)	Duration of Measurement	Psych #	Water Potential (m)
UM	0.45	12/22/97-1/8/98	Psy-86	-273
UM	1.06	12/22/97-1/8/98	Psy-83	-154
UM	1.67	12/22/97-1/8/98	Psy-75	-83
UM	2.90	12/22/97-1/8/98	Psy-68	-28
UL	10.00	12/22/97-1/8/98	Psy-64	-15
ML	10.00	12/22/97-1/8/98	Psy-66	-84

DTN: LB980001233124.001 [105800]

6.8.2.1 Niche 3566 (Niche 1) Pre-Excavation

Water potentials measured at the ends of the three pre-excavation boreholes (U, M, and B) in Niche 3566 (Niche 1) were close to saturation values, indicating that approximately 10 m from

the ESF, the formation is relatively wet. Of the three, the end of the middle borehole appeared to be wettest, with water potentials between 0.4 and -7 m. Measurements made along the profile of borehole U (between 3.7 and 7.9 m from the collar) ranged between -34 and -71 m (Figure 6.8.2-1 and Table 6.8.2-1).

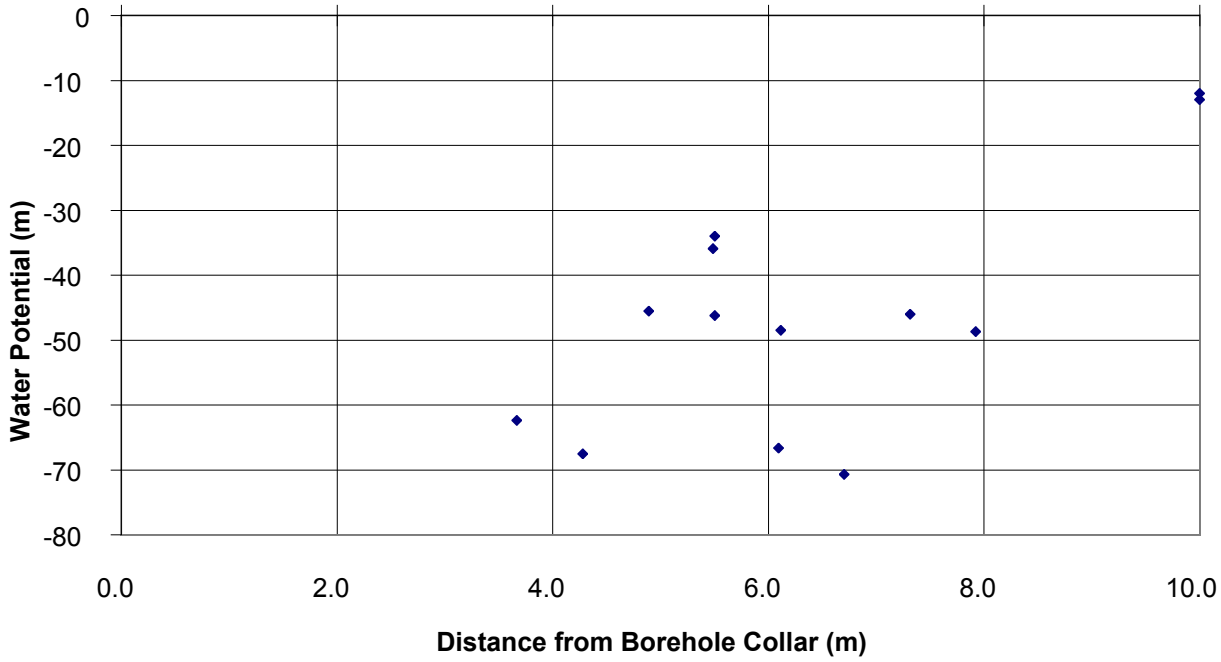

DTN: LB980001233124.001 [105800]

Figure 6.8.2-1. Pre-Excavation Water Potential Measured along Borehole U in Niche 3566 (Niche 1)

6.8.2.2 Niche 3566 (Niche 1) Post-Excavation

In the excavated niche cavity, water potentials were monitored in five boreholes. The monitored locations in borehole A (Figure 6.8.1-1b) were at 6.25 and 6.75 m from the collar. High water potentials were measured at these points (-2 and -30 m respectively). In three of the remaining boreholes (B, D, and E) water potentials measured at depths of 6.0 m varied significantly between boreholes. Borehole D (-27 m) was wettest, followed by B (-43 m) and then E (-78 m). These observations appear to be consistent with those made in the pre-excavation boreholes, which indicated that the formation tended to get wetter with increasing distance from the Main Drift.

Measurements made close to the collar in borehole C suggest that there was significant dryout in the rock surrounding the niches to a depth of at least 0.15 m, extending possibly to 2.6 m.

6.8.2.3 Niche 3650 (Niche 2) Pre-Excavation

Measurements were made at the end of three boreholes BR, BL, and ML (Figure 6.8.1-2, Table 6.8.2-2), each 10 m long, before and after a series of air-permeability tests. Pre-test water-potential values ranged between -1 and -39 m. However, following the test, water potentials in one hole (BR) dropped to between -48 and -58 m, while in another hole (BL) the measurements did not show significant changes. Closer to the borehole collar of borehole UM, readings made between 0.6 and 1.2 m indicate a relatively dry zone, with water potentials between -125 and -137 m.

6.8.2.4 Niche 3107 (Niche 3)

The observations made in Niche 3107 (Niche 3) in Table 6.8.2-3 indicate significant variability among the boreholes in the niche. Measurements made at the ends of boreholes UL (-15 m) and ML (-84 m) indicate that at a depth of 10 m, with a separation distance of 0.9 m (0.75 m vertically and 0.5 m horizontally, as illustrated in Figure 6.8.1-3), there is a steep potential gradient. Furthermore, from observations within borehole UM, it is clear that a prominent dryout zone (Figure 6.8.2-2) is associated with the Main Drift of the ESF.

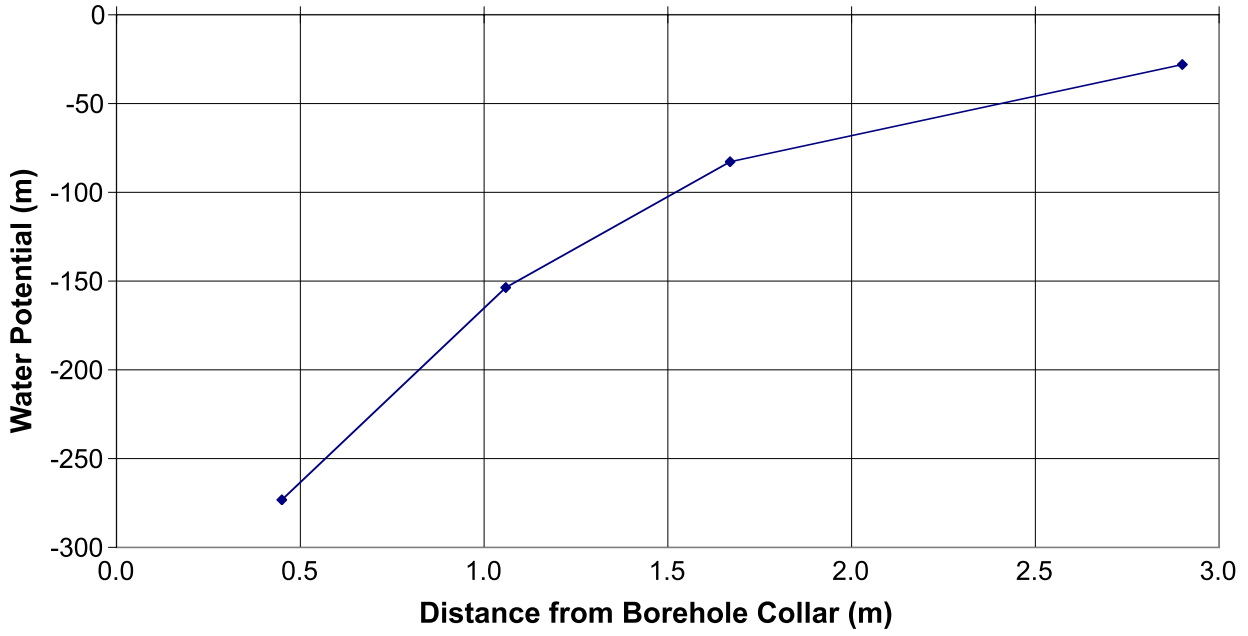

DTN: LB980001233124.001 [105800]

Figure 6.8.2-2. Water Potential Measured along Borehole UM in Niche 3107 (Niche 3)

6.9 OBSERVATIONS OF CONSTRUCTION-WATER MIGRATION

During the ECRB Cross Drift excavation, sensors and water-collection trays were placed in a borehole below the Starter Tunnel and along the ESF Main Drift at the cross-over point. This section summarizes the results of monitoring the migration of water plumes from tunneling activities. A secondary objective was to evaluate the performance of ERP as a tool to detect the migration of wetting fronts in the unsaturated zone of fractured tuffs. Time-domain reflectometry (TDR) was also used to monitor construction-water arrivals in drift walls. TDR is based on electric measurement of waveguide reflection signals from changes in dielectric constant associated with water-content changes.

6.9.1 Equipment Setup for Construction-Water Monitoring

6.9.1.1 Starter Tunnel Borehole

To monitor the migration of a water plume resulting from construction of the ECRB Cross Drift, a 30 m long borehole (0.10 m ID), at an angle of 30 degrees (from the horizontal), was constructed along the proposed path of the ECRB Cross Drift tunnel (Figure 6.9.1-1). This borehole was located in the Tptpul unit. The borehole originated at the end of a starter tunnel that was the launching pad for the Tunnel Boring Machine (TBM) used to excavate the ECRB Cross Drift. Changes in water saturation and potential were monitored along the entire length of theborehole, using psychrometers and ERPs, as the TBM advanced through the formation above.

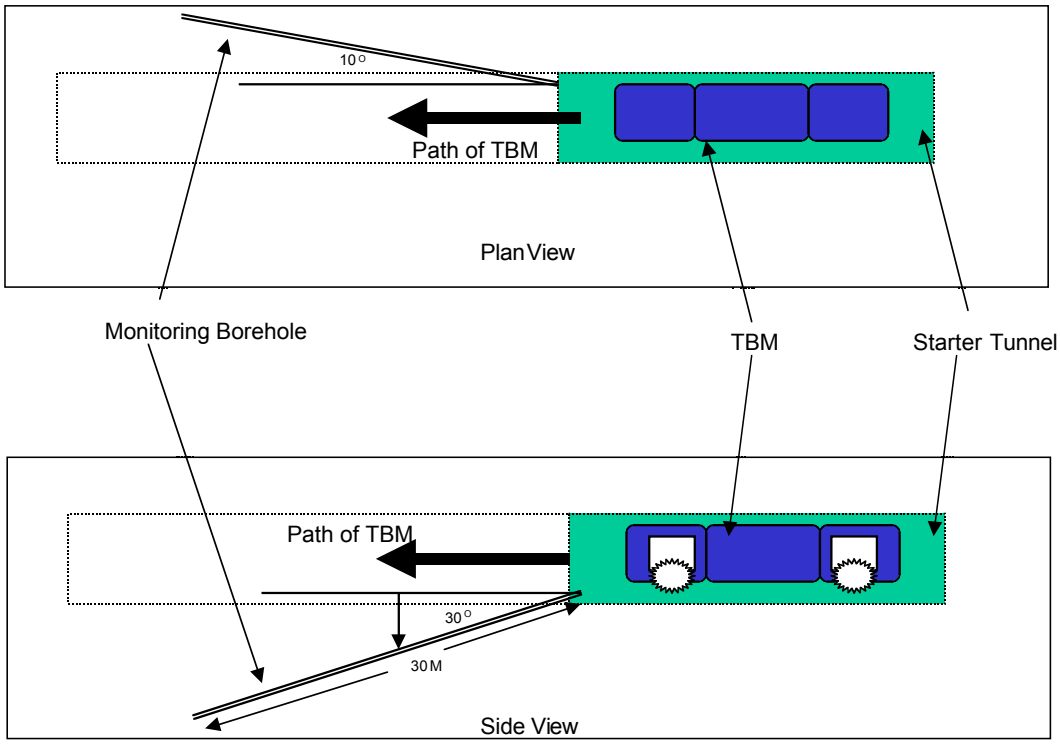

Figure 6.9.1-1. Schematic Illustration of the Location of Wetting-Monitoring Borehole at the Starter Tunnel of the ECRB Cross Drift

6.9.1.2. Electrical Resistivity Probes and Psychrometers

The psychrometers and ERPs were housed in PVC trays. These trays were fabricated from PVC pipes (0.10 m OD) bisected along the lengths. On each tray, psychrometers were installed at a spacing of 1.0 m along the borehole, while ERPs were located at 0.5 m intervals. To locate the psychrometers, squares of PVC (0.02 m) were glued at the 1.0 m mark and small diameter holes (~0.003 m ID) were drilled through the tray. Psychrometers were then installed in these holes (Figure 6.9.1-2). ERPs were attached to the outer surface of the PVC trays with strips of Velcro. This housing permitted close contact between the ERPs and borehole wall, while allowing the psychrometers to contact the borehole wall through a small cavity.

A steel spoon, 3.0 m long and having the same configuration as the trays, was used to locate each PVC tray along the borehole. Typically, each tray was placed on the steel spoon and carried to the desired location, at which point the spoon was slipped out, allowing the tray to settle snugly against the borehole wall.

Twenty-seven psychrometers and 54 electrical resistivity probes located on nine PVC trays were installed in the borehole (Figure 6.9.1-2) on February 26, 1998. Psychrometer data were collected at 1.5-hour intervals starting on February 28, 1998, for a period of four months. ER data collection started on March 25, 1998, and was collected at the same frequency and for the same duration as the psychrometers.

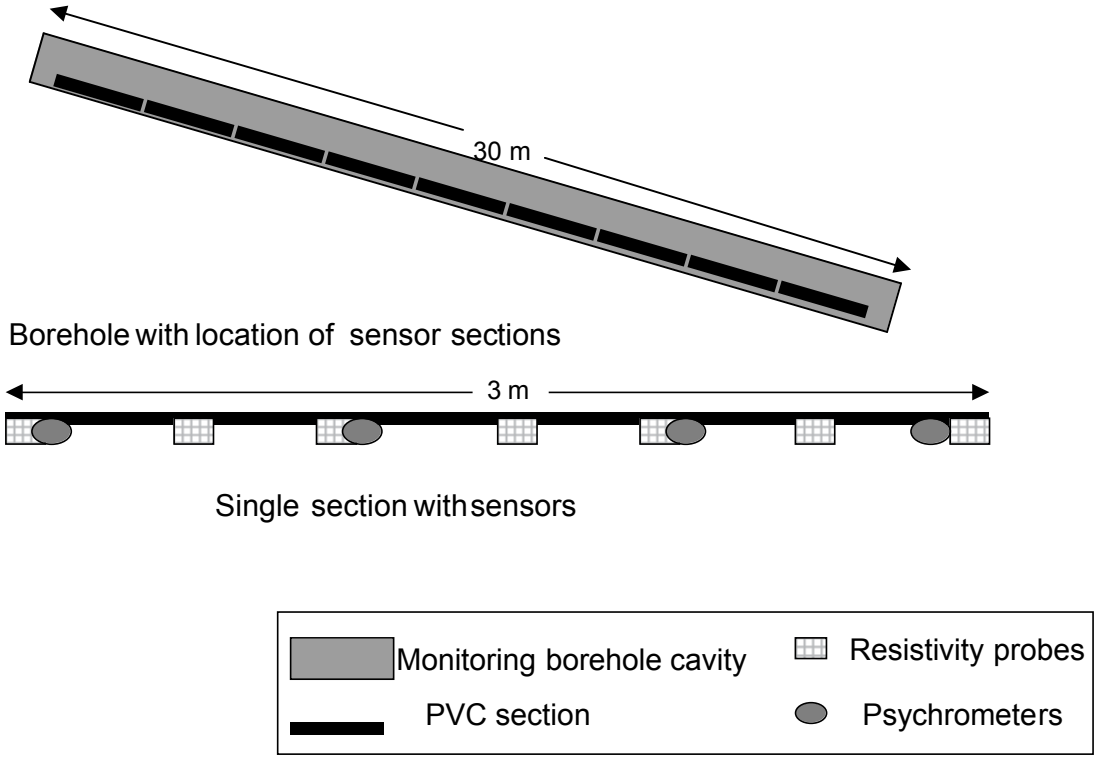

Figure 6.9.1-2. Schematic Illustration of the Borehole Wetting Front Monitoring System with Psychrometers and Electrical Resistivity Probes

6.9.1.3 Drift Monitoring at the Crossover Point

The schematics of the seepage detection system, with fluid collection trays hanging below the ceiling of the ESF Main Drift, are illustrated in Figure 6-2. The schematics of the associated sensor arrays are illustrated in Figure 6.9.1-3. The seepage monitoring system was used to detect the wetting front in the ESF Main Drift as the result of releases of traced water in the ECRB Cross Drift above.

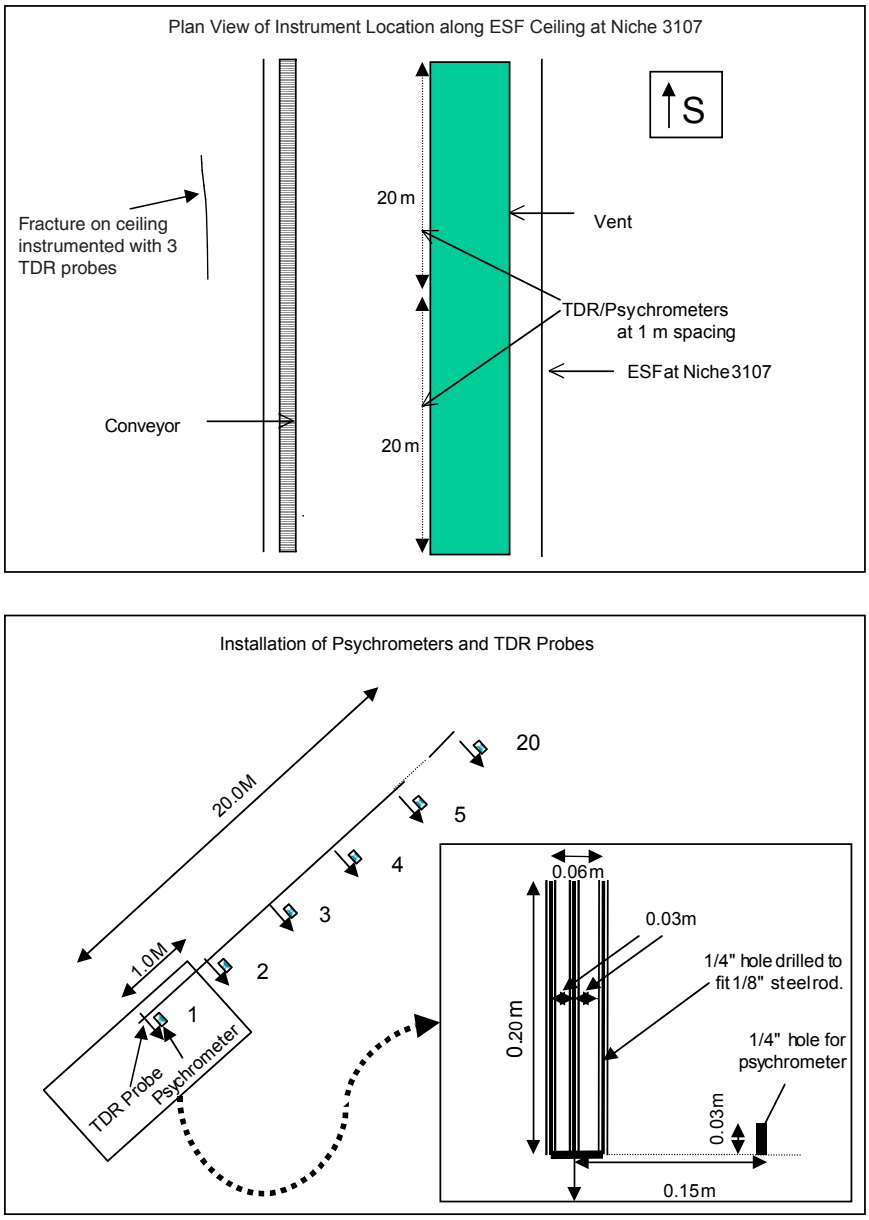

Figure 6.9.1-3. Schematic Illustration of Sensor Arrays for Wetting Front Monitoring

At the cross-over monitoring station, 132 collection trays were installed, each 0.3 m wide and 1.23 m long, from station 30+40 to 30+80 m. The trays were hung below the tunnel ceiling next to the ventilation duct along the ESF Main Drift. On the drift walls above the spring line (3.18 m

above the floor), psychrometers and TDR probes were installed. A horizontal sensor array with 40 psychrometer-TDR pairs at 1 m spacing was installed along the west wall (right rib). At the crossover location, vertically along the west wall, between the spring line and the ventilation duct, three psychrometers were installed. On the east wall (left rib), three TDR probes were installed along the trace of a major fracture. In addition to the sensor on the walls, an infrared camera and a video camera periodically monitored the area around one TDR probe on the fracture trace. Infrared images are sensitive to temperature changes associated with evaporation processes.

6.9.2 Wetting-Front Detection and Monitoring Below the ECRB Cross Drift

The following results are presented to show that the wetting front was detected up to 12.15 m below the ECRB Cross Drift Starter Tunnel, and no seepage was observed at the crossover point in the Main Drift 17.5 m below the ECRB Cross Drift. The Starter Tunnel is located in the upper lithophysal TSw tuff unit, and the crossover point is located in the middle nonlithophysal TSw tuff unit.

6.9.2.1 Wetting-Front Detection at the Starter Tunnel

The responses of all psychrometers and ERPs used in this investigation are summarized in Table 6.9.2-1 and Table 6.9.2-2. In the last columns of both tables, all working sensors with signals in response to construction-water usage are labeled “yes,” and those not in response are labeled “no.” With the arrival of a wetting front, the water potential measured by psychrometers and the electrical resistance measured by ERPs change to near-zero values.

Table 6.9.2-1. Psychrometers Response to Excavation at the Starter Tunnel of the ECRB Cross Drift

PSY_ID	Dist. Collar (m)	Vertical Depth (m)	Response to Tunneling
Psy_30.3	30.3	15.15	-
Psy_29.3	29.3	14.65	-
Psy_28.3	28.3	14.15	No
Psy_27.3	27.3	13.65	-
Psy_26.3	26.3	13.15	No
Psy_25.3	25.3	12.65	No
Psy_24.3	24.3	12.15	Yes
Psy_23.3	23.3	11.65	No
Psy_22.3	22.3	11.15	Yes
Psy_21.3	21.3	10.65	No
Psy_20.3	20.3	10.15	No
Psy_19.3	19.3	9.65	-
Psy_18.3	18.3	9.15	Yes
Psy_17.3	17.3	8.65	Yes
Psy_16.3	16.3	8.15	Yes
Psy_15.3	15.3	7.65	Yes
Psy_14.3	14.3	7.15	Yes
Psy_13.3	13.3	6.65	Yes
Psy_11.4	11.4	5.7	Yes
Psy_10.4	10.4	5.2	Yes
Psy_9.4	9.4	4.7	Yes
Psy_7.2	7.2	3.6	-
Psy_6.2	6.2	3.1	Yes
Psy_5.2	5.2	2.6	Yes
Psy_3.9	3.9	1.95	-
Psy_2.6	2.6	1.3	-
Psy_1.6	1.6	0.8	Yes

NOTE: This table summarizes the interpretation of water-potential data in DTN: LB98091233124.014 [105858] with detailed example curves shown in Figure 6.9.2-1.

Table 6.9.2-2. Electrical Resistivity Probe Responses to Excavation at the Starter Tunnel of the ECRB Cross Drift

ER_ID	Dist. Collar (m)	Vertical Depth (m)	Response to Tunneling
ER_30.3 m	30.3	15.2	No
ER_29.8 m	29.8	14.9	No
ER_29.3 m	29.3	14.7	No
ER_28.8 m	28.8	14.4	No
ER_28.3 m	28.3	14.2	No
ER_27.8 m	27.8	13.9	No
ER_27.3 m	27.3	13.7	Yes
ER_26.8 m	26.8	13.4	Yes
ER_26.3 m	26.3	13.2	No
ER_25.8 m	25.8	12.9	No
ER_25.3 m	25.3	12.7	No
ER_24.8 m	24.8	12.4	No
ER_24.3 m	24.3	12.2	Yes
ER_23.8 m	23.8	11.9	No
ER_23.3 m	23.3	11.7	No
ER_22.8 m	22.8	11.4	No
ER_22.3 m	22.3	11.2	Yes
ER_21.8 m	21.8	10.9	Yes
ER_21.3 m	21.3	10.7	Yes
ER_20.8 m	20.8	10.4	No
ER_20.3 m	20.3	10.2	Yes
ER_19.8 m	19.8	9.9	Yes
ER_19.3 m	19.3	9.7	Yes
ER_18.8 m	18.8	9.4	Yes
ER_18.3 m	18.3	9.2	Yes
ER_17.8 m	17.8	8.9	Yes
ER_17.3 m	17.3	8.7	Yes
ER_16.8 m	16.8	8.4	Yes
ER_16.3 m	16.3	8.2	Yes
ER_15.8 m	15.8	7.9	Yes
ER_15.3 m	15.3	7.7	Yes
ER_14.8 m	14.8	7.4	Yes
ER_14.3 m	14.3	7.2	Yes
ER_13.8 m	13.8	6.9	Yes
ER_13.3 m	13.3	6.7	Yes

Table 6.9.2-2. Electrical Resistivity Probe Responses to Excavation at the Starter Tunnel of the ECRB Cross Drift (continued)

ER_ID	Dist. Collar (m)	Vertical Depth (m)	Response to Tunneling
ER_12.8 m	12.8	6.4	Yes
ER_11.4 m	11.4	5.7	Yes
ER_10.9 m	10.9	5.5	Yes
ER_10.4 m	10.4	5.2	Yes
ER_9.9 m	9.9	5.0	Yes
ER_9.4 m	9.4	4.7	Yes
ER_8.9 m	8.9	4.5	Yes
ER_7.2 m	7.2	3.6	Yes
ER_6.7 m	6.7	3.4	Yes
ER_6.2 m	6.2	3.1	Yes
ER_5.7 m	5.7	2.9	Yes
ER_5.2 m	5.2	2.6	Yes
ER_4.7 m	4.7	2.4	Yes
ER_3.9 m	3.9	2.0	Yes
ER_3.1 m	3.1	1.6	Yes
ER_2.6 m	2.6	1.3	Yes
ER_2.1 m	2.1	1.1	Yes
ER_1.6 m	1.6	0.8	Yes
ER_1.1 m	1.1	0.6	Yes

NOTE: This table summarizes the interpretation of electrical resistivity data in DTN: LB98091233124.014 [105858] with detailed example curves shown in Figure 6.9.2-2.

6.9.2.1.1 Psychrometers

The data from the psychrometers illustrated in Figure 6.9.2-1 show that along the entire length of the borehole, the walls were at water potentials approximately -500 m when the sensors were installed in late February 1998. A uniform, steep increase in water-potential values over the first two weeks in March 1998 suggests the recovery of the borehole wall from drying that occurred during the dry drilling of this borehole. The following four months of data show all psychrometers approaching equilibrium values, with water potentials ranging from -70 to 0 m (Figure 6.9.2-1).

Superimposed on this asymptotic trend in water-potential values are periodic deviations, with psychrometers nearer the borehole collar showing a larger number of such events. These events were restricted to the first two months of monitoring, and by the third week of April, the last of these events had occurred. Three of the psychrometers (located at distances of 1.6, 6.2, and 9.4 m

from the borehole collar) showed evidence of wetting events, which increased water potential to (near) zero. The psychrometer at 1.6 m had near-zero water potential for three distinct periods. The first extended from the start of monitoring until March 3, and the second extended for four days beginning on March 8. A final period, significantly shorter, lasted for almost 24 hours on March 22. The psychrometer located at 6.2 m measured water potential close to zero for a three-day period starting on March 8th. The psychrometer located at 9.4 m detected water-potential values close to zero for a single event on March 13, for nearly eleven hours.

One concern that could arise from the use of a slanting borehole to measure wetting-front migration is the possibility of the bore cavity short-circuiting flow paths. For this particular investigation, this short-circuiting does not appear to be happening, as indicated by the analysis of recovery responses observed at the depth of 5.2 m. Here, the response to a wetting event was negligible when compared with other psychrometers close to this location (above and below), suggesting that this zone was well isolated (hydraulically) from the adjacent zones and did not detect the wetting front. In the remaining eight psychrometers located between 9.4 m and 17.3 m from the borehole collar, investigators found evidence of small increases in water potential that extend beyond the projected recovery rate. Some of these increases coincided with periods when the psychrometers at distances of 1.6, 6.2, and 9.4 m along the borehole showed near-zero potentials; the rest of the psychrometer data remained uncorrelated until the end of April 1998. The psychrometers up to a distance of 10.4 maintained a sinusoidal response, which fluctuated around a trend of slow water-potential increase.

By early May 1998, the rates at which water potential was increasing had decreased significantly, and by mid-June all psychrometer readings appeared to have stabilized. In the case of two deep psychrometers (i.e., at 18.3 m and 22.3 m), there appears to have been individual events that for brief periods increased the rate at which water potentials were increasing. The deep psychrometers maintained nearly constant readings once they approached equilibrium, without the oscillations observed for shallow psychrometers.

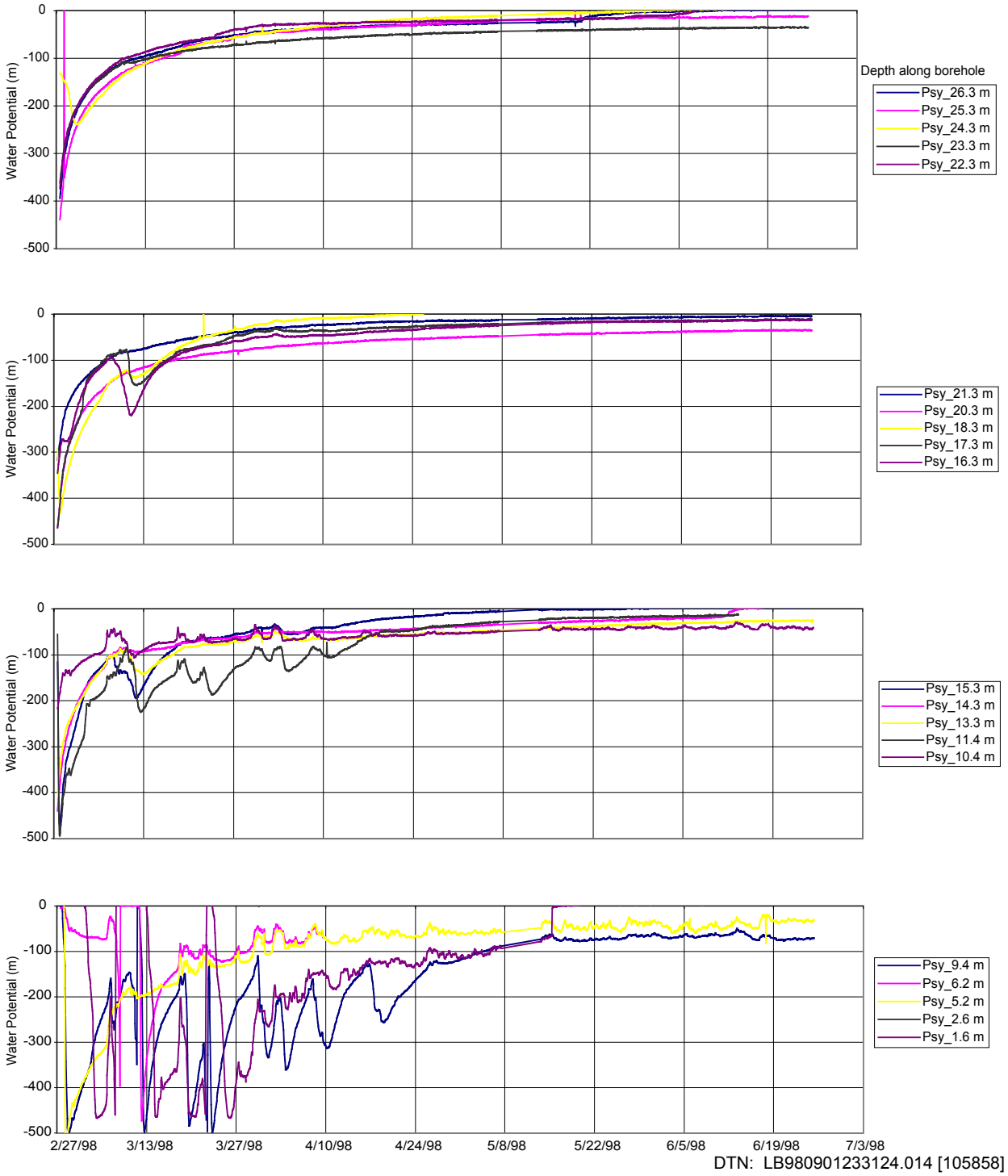

Figure 6.9.2-1. Changes in Water Potential Observed along the Wetting Front Monitoring Borehole at the Starter Tunnel of ECRB Cross Drift

6.9.2.1.2 Electrical Resistivity Probe

Measurements of electrical resistance were initiated in late March and continued until late June. Figure 6.9.2-2 summarizes the responses observed from probes located at 0.5 m intervals along the walls of the borehole between 17.3 and 29.8 m from the borehole collar.

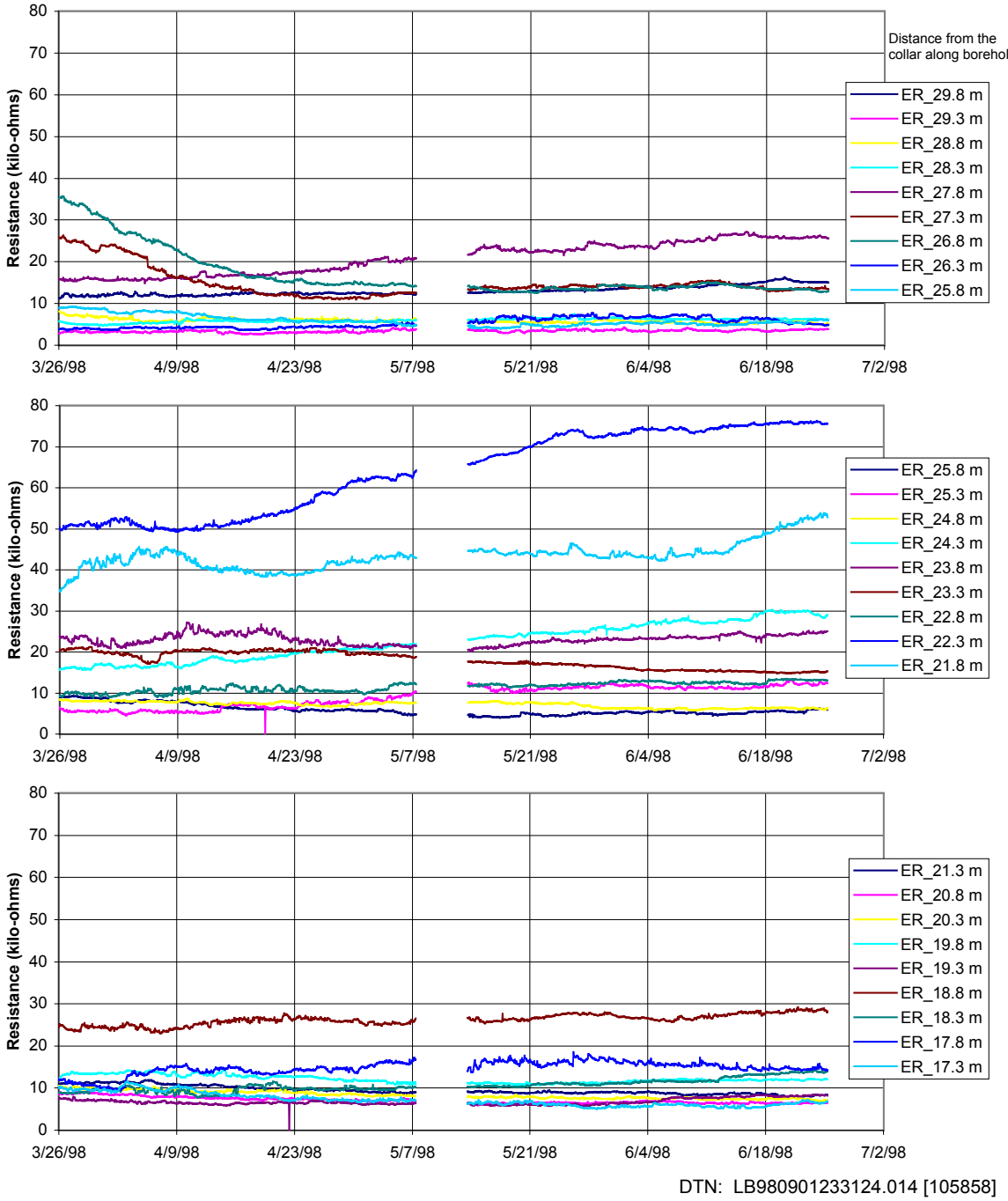

Figure 6.9.2-2. Changes in Electrical Resistance Observed along the Wetting-Front Monitoring Borehole at the Starter Tunnel of the ECRB Cross Drift

6.9.2.1.3 Potential Sensor Comparison

As part of an effort to evaluate the performance of ERPs as a sensor to monitor the arrival and movement of a wetting front, a series of probes was installed adjacent to psychrometers along the borehole length. The performance of the ERPs was compared with those of psychrometers.

From the psychrometer data collected between late March and June 1998, as illustrated in Figure 6.9.2-3, the events of interest were:

- Sinusoidal responses in the shallower psychrometers (e.g., psychrometers at a distance of 5.2 m)
- The wetting and drying cycles observed in the shallower zones as the borehole walls approached equilibrium (e.g., psychrometers at a distance of 9.4 m)
- Steady approaches to equilibrium as seen in the deeper psychrometers (i.e., at depths greater than 10.4 m).

Figure 6.9.2-3a to Figure 6.9.2-3c summarize responses of both psychrometers and ERPs for the three response patterns observed in the psychrometer data. (The y-axes for resistance were presented in decreasing scales, so that wetter sensors have higher y-values.) In two of the three cases, the ERPs responded in a pattern similar to that of psychrometers located adjacent to the probes. With the exception of the sensor at 5.2 m, the sinusoidal response observed by the psychrometer was well tracked by the ERPs, with points of changing trends fairly well synchronized. However, the direction of the trends between small time intervals is not consistent, suggesting that the response times of the probes are significantly different. The ERPs at shallow depths might be sensitive to air flows through the fractures in addition to moisture conditions in the vicinity of the probes. The psychrometers measure the moisture conditions in the vicinity of the probes.

(a)

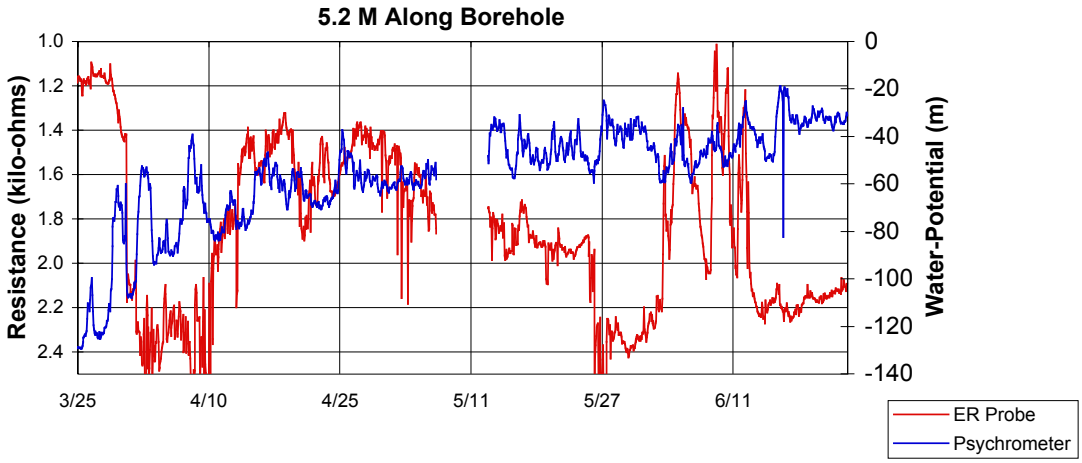

(b)

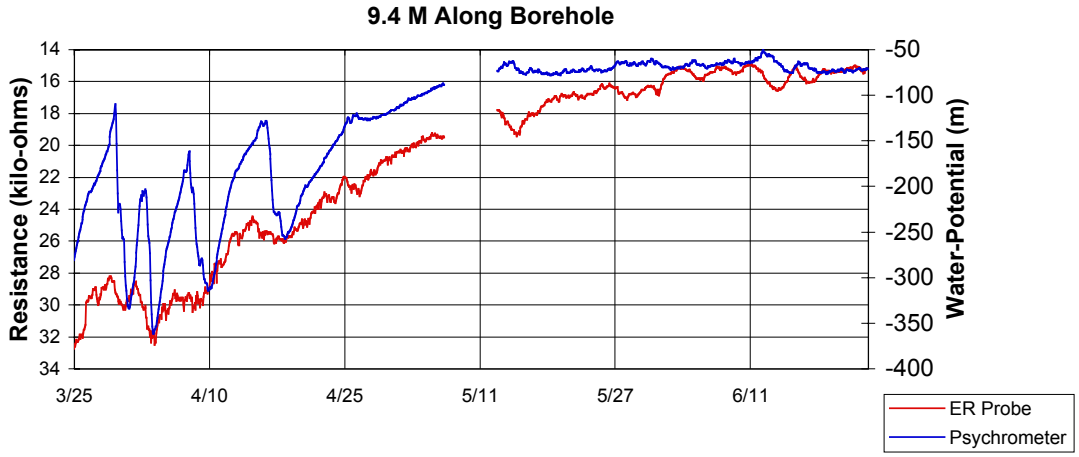

(c)

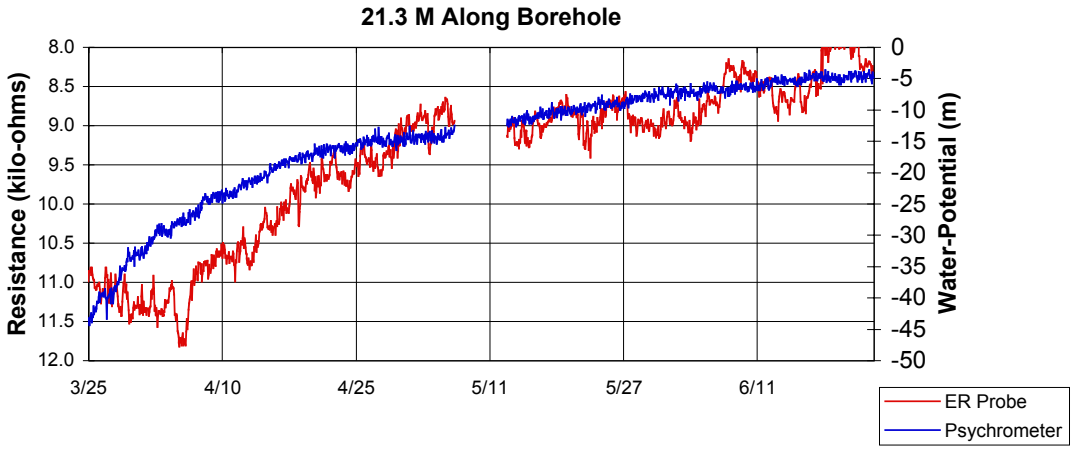

DTN: LB980901233124.014 [105858]

Figure 6.9.2-3. Comparison of Performance of Electrical Resistivity Probe and Psychrometer

At a distance of 9.4 m, the potential increased steadily from -400 m to -70 m between late March 1998 and June 1998, and the corresponding ERP measurements followed a similar pattern. Here, large fluctuations in water potentials in relatively short periods of time (-200 m in 4 days) were comparably detected by both types of probes. The slower, more gradual recovery observed by psychrometers deeper in the formation was generally well tracked by the ERPs (e.g., at 21.3 m).

6.9.2.2 Wetting-Front Monitoring at the Crossover Point

Figure 6-2 illustrates the potential movement from ECRB Cross Drift to the ESF Main Drift seepage collection system to study the migration of water and tracer flow from one drift to another. The seepage monitoring system was used to monitor the migration of construction water from the ECRB Cross Drift. Niche 3107 (Niche 3) is currently part of the drift-to-drift study as a monitoring station. The existing horizontal boreholes at Niche 3107 (Niche 3) are used in wetting-front monitoring for liquid released from a new alcove excavated horizontally from the ECRB Cross Drift and directly above the niche.

The ECRB Cross Drift passed over the ESF Main Drift on the second shift of July 1, 1998. No seepage was observed. The observers in the ESF Main Drift could hear rumbling noises from the TBM and feel vibrations on the railroad tracks and tunnel wall. However, no falling of loose rock was observed.

Figure 6.9.2-4 illustrates an example of the data collected by the TDR probes. No evident signals were associated with wetting-front arrivals. These null results from the sensors substantiated the field observations of no seepage associated with TBM passing over the ESF Main Drift. The confirmation of no seepage at the crossover point establishes the lower limit for the drift-to-drift flow and drift seepage processes associated with localized construction-water usage. It also provides a guide to the design of controlled drift-to-drift experiments at this unique location, with one drift above another drift.

The underground water usage in the ECRB Cross Drift is being monitored by YMP Science and Engineering Testing on a shift-by-shift basis; the tunnel-water use logs are being evaluated by the YMP Testing Safety Assurance group.

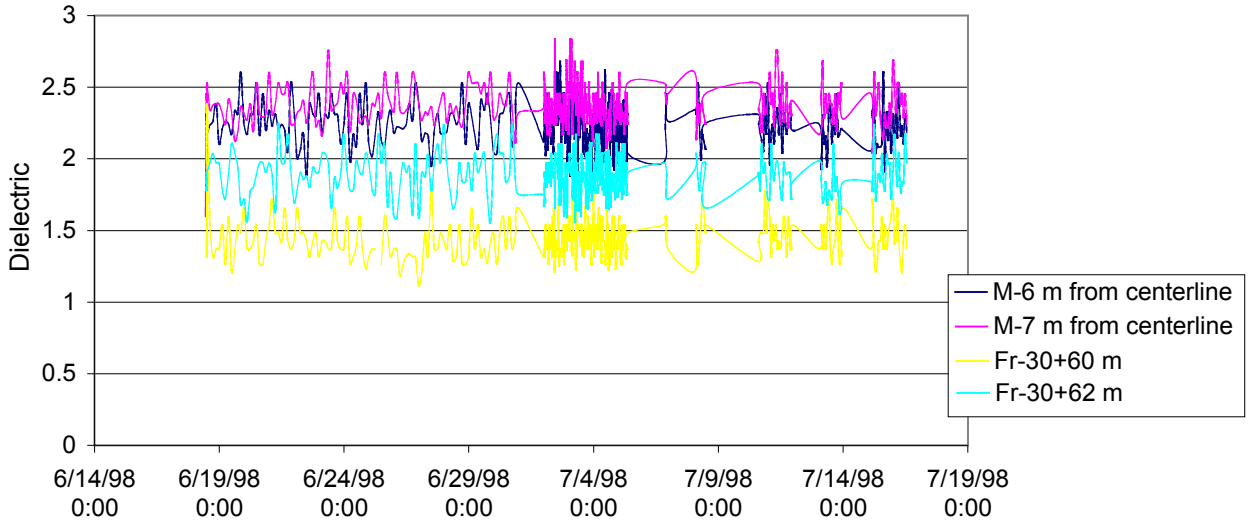

Measurement of Dielectric in Formation Matrix (M-6, M-7) and Fracture (Fr) at Crossover Point

DTN: LB980901233124.014 [105858]

Figure 6.9.2-4. Example of Time Domain Reflectometry Probe Data at the Crossover Point in the ESF Main Drift

6.10 MOISTURE MONITORING AND WATER ANALYSIS IN UNDERGROUND DRIFTS

In ventilated drift sections, no continuous dripping (or seepage) was observed in either the ESF Loop or in the ECRB Cross Drift. This lack of seepage may be explained by the capillary barrier mechanism, as described in Section 6.2, with capillary forces holding water within the rock mass. The other explanation is related to ventilation. Ventilation can remove large amounts of moisture, dry the rock behind the drift walls, and suppress seepage. To determine if seepage returns when ventilation effects are mitigated, the last one-third of the ECRB Cross Drift was sealed with multiple bulkheads. Section 6.10.1 summarizes the moisture conditions and construction-water migration associated with drift excavation. Section 6.10.2 describes the preliminary results from the ongoing moisture monitoring in the ECRB Cross Drift. This section summarizes the current information on both the moisture conditions during drift operation and the post-emplacement environment in sealed drifts.

6.10.1 Construction (Drift Excavation) Effects on Moisture Conditions

6.10.1.1 Status of the ESF Moisture Monitoring Study

The moisture conditions in the ESF tunnels were monitored at 17 stations in the ESF main tunnel (from station 7+20 to station 73+50) and 10 stations in the ECRB Cross Drift (from station 0+25 to station 25+55), as summarized in Table 6.10.1-1. Relative humidity, temperature, barometric pressure, and air velocity were measured at various stations. The moisture-monitoring stations were supplemented by measurements from sensors with humidity/temperature probes and barometers mounted on the TBM during excavations. Additionally, periodic surveys were conducted along the tunnels with these sensors, mounted on a mobile cart. An infrared camera was used in mobile surveys to measure the temperature changes on the tunnel walls.

Table 6.10.1-1. Moisture-Monitoring Stations in the Exploratory Studies Facility

Moisture-Monitoring Station Location/ ID*	Description**	DTN
21+00/LB20, 28+30/LB50, 35+00/LB40, 42+50/LB60, 47+00/LB70, 51+73/LB80, 57+50/LB90, 64+59, 67+00, 73+50, AOD5, BKH5	Relative Humidity, Temperature, and Pressure in ESF Monitoring Stations in Report "Evaluation of Moisture Evolution in the Exploratory Studies Facility." VA Supporting Data	LB960800831224.001 [105793]
	Moisture Data Report from October, 1996 to January, 1997	LB970300831224.001 [105794]
	Moisture-Monitoring Data Collected at ESF Sensor Stations, Moisture Monitoring Before and After the Completion of the ESF	LB970801233124.001 [105796]
	Moisture-Monitoring Data Collected at Stationary Moisture Stations	LB970901233124.002 [105798]
7+20/GS#3, 10+93/GS#4, 28+93, 51+64, 67+20, Operator-Shack/GS#1 (on TBM), Vent-Line-Intake/GS#2 (on TBM)	Moisture Monitoring in the ESF, Oct. 1, 1996 through Jan. 31, 1997	GS970208312242.001 [135119]
	Moisture Monitoring in the ESF, Feb. 1, 1997 through July. 31, 1997	GS970708312242.002 [135123]
	Moisture Monitoring in the ESF, August 1, 1997 through July. 31, 1998	GS980908312242.024 [135132]
ECRB Cross Drift GS: 0+25, 2+37, 2+88, 3+38, 10+03, 21+07, 24+75; LB: 14+35, 21+40, 25+55	Moisture Monitoring in the ECRB CROSS DRIFT, 04/08/98 to 7/31/98	GS980908312242.035 [135133] LB990901233124.006 [135137] (This Scientific Analysis Report/Section 6.10.2.2)

NOTES: * LB for stations maintained by LBNL, and GS for stations maintained by USGS in this cooperative moisture-monitoring study.

* From ATDT or equivalent description.

The moisture data in the drifts, together with ventilation data and construction-water usage data, can be used to evaluate the amounts of moisture removed from the ESF drifts and the net quantities of construction water drained into the surrounding tuff formations. In this scientific analysis report, examples of moisture-monitoring data collected right after excavation of the ECRB Cross Drift are presented. Simple observations are qualitatively discussed to highlight the importance of excavation and operation data for determining site perturbations. Potential sources for corroborative evidence of the induced effects are presented in Table 6.10.1-1 through Table 6.10.1-3.

Table 6.10.1-1 summarizes the data collected in moisture monitoring stations during and after drift excavations. Moisture removals in the drift dry up the surrounding tuffs. Water-potential measurements are listed in Table 6.10.1-2. Use of construction water changes the saturation of

the tuffs along flow paths. Table 6.10.1-3 summarizes the saturation measurements for both perturbed conditions and for ambient conditions.

Table 6.10.1-2. Water-Potential Measurements in the Exploratory Studies Facility

Potential Measurement	Description*	DTN
Niche 3566 (Niche 1)—psychrometer Niche 3650 (Niche 2)—psychrometer	3 main boreholes, 5 lateral boreholes in Niche 3566 (Niche 2), 5/9/97—10/21/97; 6 main boreholes in Niche 3650 (Niche 2), 7/1/97—7/28/97	LB980001233124.001 [105800]/ This Scientific Analysis Report/Section 6.8.2
Niche 3566 (Niche 1)—heat dissipation probe	21 heat dissipation probe drill holes, 11/4/97—7/31/98	GS980908312242.022 [135157]
Niche 3107 (Niche 3)—psychrometer	3 main boreholes, 12/22/97—1/8/98	LB980001233124.001 [105800]/ This Scientific Analysis Report/Section 6.8.2.4
Alcove 7—heat dissipation probe	Heat dissipation probe drill holes, 12/9/97—1/31/98	GS980908312242.022 [135157]
Alcove 3—filter paper Alcove 4—filter paper	1 core hole in Alcove 3, 2 core holes in Alcove 4	GS980908312242.033 [107168], GS980908312242.032 [107177]
North Ramp 7+27 to 10+70 South Ramp 69+65 to 76+33—filter paper	18 North Ramp boreholes, 3 Alcove 4 boreholes, and 46 South Ramp boreholes, HQ, 2-m length	GS980308312242.004 [107172]
South Ramp—heat dissipation probe	Heat dissipation probe drill holes, 8/1/97—1/4/98	GS980308312242.002 [135163]
Cross-Over Point 30+62 in the ESF Main Drift Below the ECRB Cross Drift—psychrometer	43 psychrometers on ESF drift walls, 6/19/98—7/16/98	LB980901233124.014 [105858]/ This Scientific Analysis Report/Section 6.9.2.2
ECRB Cross Drift Starter Tunnel—psychrometer & electrical resistivity probe	1 slant borehole below the invert	LB980901233124.014 [105858]/ This Scientific Analysis Report/Section 6.9.2.1
ECRB Cross Drift 0+50 to 7+75—heat dissipation probe	6 heat dissipation probe drill holes, 4/23/98—7/31/98	GS980908312242.036 [119820]
Surface Based Boreholes—psychrometer	USW NRG-7a, UE-25 UZ#4, UE-25 UZ#5, USW UZ-7a and USW SD-12; 1/1/97—6/30/97; 7/1/97—9/30/97; 10/1/98—3/31/98; 4/1/98—9/30/98	GS970808312232.005 [105978] GS971108312232.007 [105980] GS980408312232.001 [105982] GS981208312232.002 [156505]

NOTE: * ATDT or equivalent description.

Table 6.10.1-3. Saturation Measurements in the Exploratory Studies Facility

Saturation Measurement	Description*	DTN
Niche 3566 (Niche 1) - core Niche 3650 (Niche 2) - core	3 main boreholes, 6 lateral boreholes in Niche 3566 (Niche 1) and 7 main boreholes in Niche 3650 (Niche 2)	GS980908312242.018 [135170], GS980908312242.020 [135172]
Alcove 6 - core Alcove 7 - core	3 boreholes in Alcove 6, 1 borehole in Alcove 7	GS980908312242.029 [135175], GS980908312242.028 [135176]
Alcove 3 - core Alcove 4 - core	1 core hole in Alcove 3, 2 core holes in Alcove 4	GS980908312242.033 [107168], GS980908312242.032 [107177]
North Ramp 7+27 to 10+70 South Ramp 59+65 to 76+33 – core	Borehole samples	GS980308312242.005 [107165], GS980308312242.003 [135180]
South Ramp - time domain reflectometry	TDR measurements, 8/1/97 - 1/4/98	GS980308312242.001 [135181]
ECRB Cross Drift Starter Tunnel - Core	1 slant borehole core	GS980908312242.030 [135224]
Cross-Over Point 30+62 in the ESF Main Drift Below the ECRB Cross Drift - time domain reflectometry	43 TDR probes on ESF drift walls, 6/19/98 - 7/16/98	LB980901233124.014 [105858]/ This Scientific Analysis Report/Section 6.9.2.2

NOTE: * From ATDT or equivalent description.

6.10.1.2 Moisture Conditions and Perturbations Observed in Drifts

6.10.1.2.1 Observation of Moisture Conditions in Ventilated ESF Main Drift

Preliminary evaluation of the moisture data during ESF excavation showed that the moisture conditions were sensitive to construction activities. The daily usage of water for excavation, muck transport, dust-control, and other operations introduced rapid changes in moisture conditions throughout the tunnel atmosphere and in the wall rock. During weekends in 1996, when construction activities were absent, the tunnel atmosphere generally stabilized to either high-humidity conditions if the ventilation was turned off, or low-humidity conditions if the ventilation was left on (DTN: LB960800831224.001 [105793]). After completion of the ESF main tunnel with two portals for entrance and exit, high-humidity conditions were suppressed by natural ventilation through the portals (DTN: LB970801233124.001 [105796]).

The following order-of-magnitude estimate of moisture removal capacity represents the ESF system in August 1996 conditions when the ESF Main Drift was excavated but the ESF South Ramp was not, with the total length of 6,250 m. (The ESF was excavated from 1994 to 1997.) For a 6,250 m long tunnel with cross-sectional area of 40 m^2 (circular cross-sectional area with invert, vent line, and conveyor blockage areas subtracted), the humid tunnel air can contain 2,500 kilograms of excess water mass if we estimate that the tunnel is on average 50% higher in relative humidity than the outside air, with the corresponding vapor density difference on the

order of 0.01 kg/m^3. If the tunnel air is ventilated with a flow rate of 47 m^3/s or 100,000 ft^3/min (cubic feet per minute, or cfm), it will take 5,300 seconds or 1.5 hours to remove and replace the tunnel air. The water-removal rate of 2,500 kg over 1.5 hours corresponds to 285 m^3/week (285 kiloliter/week or 75,000 gallon/week). If all the moisture in the tunnel air is from evaporation, the equivalent evaporation rate from the tunnel walls and inverts (with area 6250 m × 23.7 m) is on the order of 100 mm/yr (Wang et al. 1996 [101309]).

More specific estimates were made for sections in different tuff units, using measured relative humidity changes. Vapor-density differences between different locations, together with a simple approximation of air flow in the tunnel, were used to estimate the moisture removal rate and the equivalent evaporation rate. Weekly rates of the amount of water removed by ventilation were a substantial fraction of water used in the tunnel. Estimated equivalent evaporation rates were on the order of 200 mm/yr, with standard deviation over 90 mm/yr, for both the Topopah Spring welded tuff units in a 1400 m section centered at Alcove 5 (the thermal test alcove) and the Paintbrush nonwelded units in a 380 m section between Alcove 3 and Alcove 4. The uncertainties were related to fluctuations in the moisture conditions introduced by construction activities, including air ventilation and water usage.

The equivalent evaporation rate over 100 mm/yr is an order of magnitude larger than the ambient percolation flux. The large evaporation rate could suppress the observations of active seeps and contribute to the apparent dry tunnel conditions. Rock temperatures near the TBM were observed to change spatially and temporally and could be related to evaporation from rock surfaces. Water potentials near the rock surfaces were measured with heat dissipation probes, and water potential profiles along boreholes were measured by psychrometers in niches and alcoves along the ESF Main Drift and along the ECRB Cross Drift, as summarized in Table 6.10.1-2. Field measurements in boreholes and laboratory measurements of physical and hydrological properties of cores were conducted to measure saturation distributions, as summarized in Table 6.10.1-3 and Section 6.8. The dryout zones could extend nominally 1 to 3 m into the walls, with fractures and faults likely extending the depths of drying influence.

The advances of the ESF tunnel excavations were detected pneumatically by sensors in 10 surface-based boreholes within 200 m of the ESF. In comparison to the damping of barometric signals from the ground surface, less attenuation and phase lag were observed for signals from the ESF. For the borehole NRG-7a, within 30 m in horizontal distance from the ESF tunnel, the changes in water potential could also be related to the ESF dryout (see last entry of Table 6.10.1-2 for DTNs of surface-based boreholes).

The main effects of ESF ventilation are the drying of rocks around the tunnel, the suppression of potential seepage into tunnels, and the perturbation of the gas flow field around the tunnel. Niche 3566 (Niche 1), Alcove 7, and the last section of the ECRB Cross Drift have been closed for long time periods to gain additional information on the rewetting processes and potential seepage events. Both the data collected during active ventilation phases and passive nonventilation phases will contribute to the assessment of UZ responses to large-scale perturbations at Yucca Mountain.

6.10.1.2.2 Observation of Moisture Effects in Alcove 3 and Alcove 4

Corroborating studies have been performed between Alcove 3 and Alcove 4 that quantified *in situ* water-potential, moisture, and temperature fluctuations in the nonwelded units of the Paintbrush Group (PTn), to identify gradients between the PTn and adjacent Tiva Canyon tuff and Topopah Spring tuff (DTN: GS021008312242.003 [162178]). The studies identified an effect of ventilation-induced drying to a depth of 4.9 m into the tuff from the ESF. As a result, water-potential values were more negative (lower moisture content) near the tunnel surface and greater (higher moisture content) beyond the zone influenced by ventilation. From surface to depth, water-potential values (in bars) were: Tiva Canyon -27.0 to –3.5 (ventilation effects), Paintbrush nonwelded –1.7 to –0.1, and Topopah Spring –1.4 to -0.6. The combined evidence of high moisture values at the Bt2/Tptrv3 contact (–0.1 and –0.3 bars), along with the 10-degree east dip of the beds, indicates a high potential for lateral water flow in the PTn (DTN: GS021008312242.003 [162178]; LeCain et al. 2002 [158511]).

6.10.1.2.3 Observation of Moisture Conditions in Ventilated ECRB Cross Drift

The drift conditions at the ECRB Cross Drift in 1998 were similar to the conditions of the ESF Main Drift in 1996. High-humidity conditions existed in the new sections just excavated. Relative humidity data from three moisture stations in the ECRB Cross Drift are illustrated in Figure 6.10.1-1 and Figure 6.10.1-2 for the month of November 1998, right after the completion of TBM excavation. The moisture sensor assembly at ECRB Cross Drift Construction Station CD 25+55 (2,555 m from the ECRB Cross Drift entrance) is located near the Solitario Canyon fault on the western boundary of the repository block. The other two stations, at CD 14+43 and CD 21+40, measured the moisture conditions in the middle part of the ECRB Cross Drift within the repository block.

The figures illustrate the temporal fluctuations and the spatial distributions of moisture conditions along the ECRB Cross Drift. The data were collected every 15 minutes. CD 25+55 was much more humid than the other two stations under the control of the same ventilation system. The day shifts had more activities than the other two shifts. During the week of the Thanksgiving holiday (November 26, 1998), there were increases in moisture conditions that might be correlated with ventilation shutdown. The monthly averaged relative-humidity values are 15 ± 3% for CD 14+43, 18±4% for CD 21+40, and 28±5% for CD 25+55.

The spatial variations illustrated in Figure 6.10.1-2 are based on weekly averaging over the day shifts. The differences in relative humidity are more clearly shown with the spatial distribution plot. While the magnitude varies from week to week, the spatial gradients were relatively constant. Average gradients for the two sections were 3.4% per kilometer between CD 14+35 and CD 21+40, and 25.2% per kilometer between CD 21+40 and CD 25+55. The section near the end of the tunnel apparently had more moisture removed than the section near the entrance.

The temporal and spatial distributions in Figure 6.10.1-1 and Figure 6.10.1-2 are presented to illustrate the characteristics of the moisture evolution in a newly excavated tunnel. Moisture gradients, together with the ventilation rates, are needed to calculate the moisture removal rates. The ECRB Cross Drift is a simple tunnel system compared to the ESF Main Drift. There is only one ventilation line operating along the ECRB Cross Drift, without any secondary branches separating the air flows into side alcoves and niches.

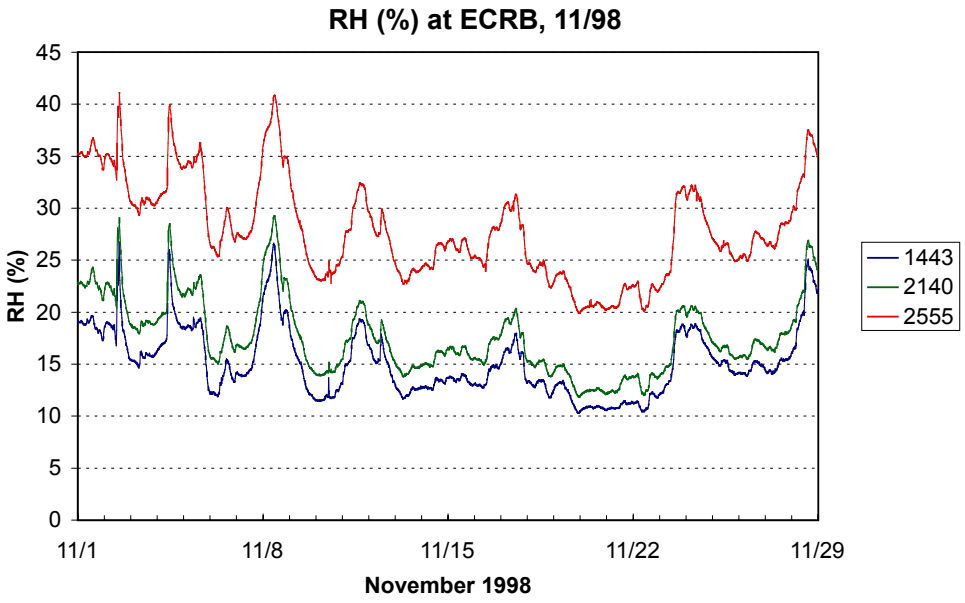

DTN: LB990901233124.006 [135137]

NOTE: The data were collected in November 1998 after completion of excavation. The legends are the distances in meters from the moisture station to the ECRB Cross Drift entrance.

Figure 6.10.1-1. Relative Humidity Temporal Variations in the ECRB Cross Drift

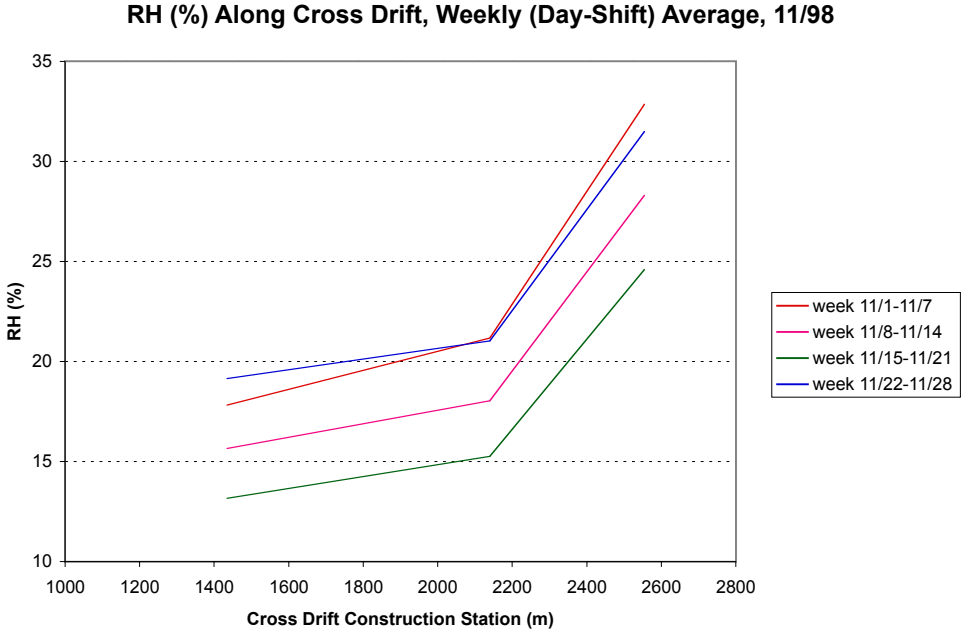

DTN: LB990901233124.006 [135137]

NOTE: The weekly averages of day shift data are presented for November 1998 after completion of excavation.

Figure 6.10.1-2. Relative Humidity Spatial Variations along the ECRB Cross Drift

6.10.1.3 Construction Water Migration Below Invert from Excavation

Construction water used in the excavation of the ESF contained lithium bromide as a tracer. The presence of the tracer (measured as bromide to chloride ratio, Br/Cl, leached out of crushed borehole samples) is illustrated in Figure 6.10.1-3 along three construction-water (CWAT) boreholes drilled in the ESF. The deepest tracer penetration was at borehole CWAT#2, in which construction water had reached the bottom of the borehole (30 m). CWAT#2 is located in an intensely fractured zone of the middle nonlithophysal zone of the TSw. In CWAT#1, the construction water was detected in all samples to a depth of 2.4 m, with two isolated peaks at greater depths. In CWAT#3, located in the upper lithophysal zone, the construction water was detected only in the top 2 m. Figure 6.10.1-3 also illustrates the areal distributions of three tuff units in the repository horizon: the middle nonlithophysal zone, the lower lithophysal zone, and the lower nonlithophysal zone, all of the Topopah Spring welded hydrogeologic unit. Both the variations in hydrological properties of different tuff units and in the construction usage rates could have affected the construction-water penetrations.

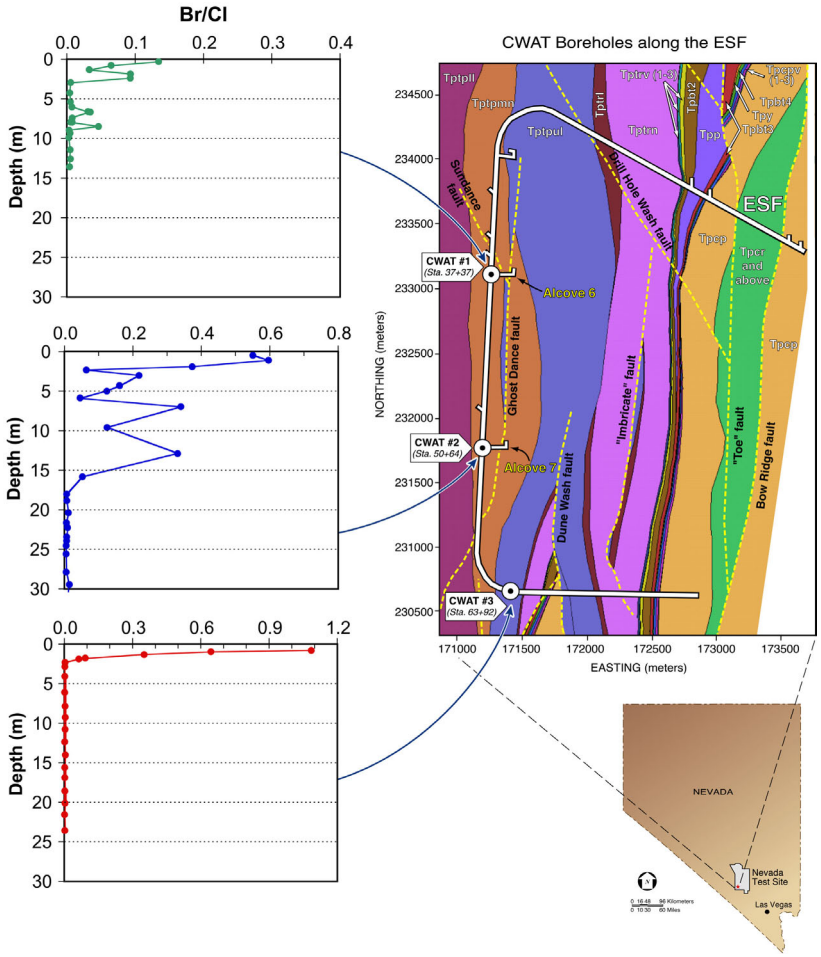

DTN: LAJF831222AQ98.007 [122730]

Source: Geological framework model GFM3.1 (BSC 2001 [154622]).

Figure 6.10.1-3. Construction Water Distribution below Exploratory Studies Facility Drift

6.10.2 Observation along the Nonventilated Sections of the ECRB Cross Drift

The moisture monitoring study conducted in the ECRB Cross Drift is designed to detect drips in sealed drift sections. To observe potential seepage, ventilation effects to the terminal section of the ECRB Cross Drift have been minimized with the construction of a series of four bulkheads (Figure 6.10.2-1). The nonventilated sections include the area below the Solitario Canyon wall and intercept the Solitario Canyon fault.

The first two bulkhead doors were located at Stations CD 17+63 and CD 25+03 on June 1999. A third bulkhead door was located at Station CD 25+99 on July 2000, and then a fourth bulkhead was located at Station CD 22+01 on November 2001.

Along seven boreholes in the ECRB Cross Drift shown in Figure 6.10.2-2, psychrometer measurements of water potential have been made. Within the drift opening, humidity, temperature, wind speed, and barometric pressure are being measured at various stations to provide information on moisture dynamics along the ECRB Cross Drift. During November 2002, Electrical Resistance Probes (ERPs) were laid out at 0.5 m intervals between Stations CD 24+00 and CD 26+36 to measure saturation changes along the drift wall. Additionally, relative humidity and temperature probes were located in Stations CD 15+02, CD 20+40, CD 21+40, CD 21+90, CD 22+50, CD 23+45, CD 24+40, CD 25+10, CD 25+36, CD 25+52, CD 25+90, CD 26+00, CD 26+30, and CD 26+60. Six water collection units were also installed between Stations CD 24+85 and CD 24+95. Figure 6.10.2-2 shows the location of moisture monitoring stations along sections of the ECRB.

Additional information on moisture conditions within the nonventilated zone has been gleaned during periods when the bulkhead doors were opened, including before 2003: (1) January 12–13, 2000; (2) May, June, and July 2000 to install the third bulkhead, (3) January 22–25, 2001, (4) May 22, 2001, to repair electrical power, (5) October 1–December 20, 2001, and (6) June 24-27, 2002. During most of the entries, the entire ECRB was accessible for visual inspection. The June 2002 entry was restricted to the area between bulkhead at CD 17+63 and bulkhead at CD 22+01. During each of these entries, observations of wet spots were documented, and water samples were manually collected from small pools of water if feasible.

Figure 6.10.2-3 provides a geological cross section at the terminal end of the ECRB Cross Drift, showing the locations of the last two bulkheads and the TBM. These sections have higher potential for seepage because of higher surface net-infiltration rates and higher percolation flux distributions in the repository level. The high flux region could be located especially in areas with no overlying nonwelded tuff. The section between Station CD 25+03 and Station CD 26+01 also intersects the Solitario Canyon fault at CD 25+84. The section behind the bulkhead at CD 25+99 contains the TBM used for ECRB Cross Drift excavation. The TBM is a heat source because of power being supplied to the TBM. Table 6.10.2-1 provides rock unit contacts intersected by the tunnel sections behind the bulkheads.

Section 6.10.2.1 summarizes the water potential and moisture monitoring data. Section 6.10.2.2 presents the observations in periodic entries behind the bulkheads to observe wet zones. Section 6.10.2.3 presents data from water samples collected during early entries.

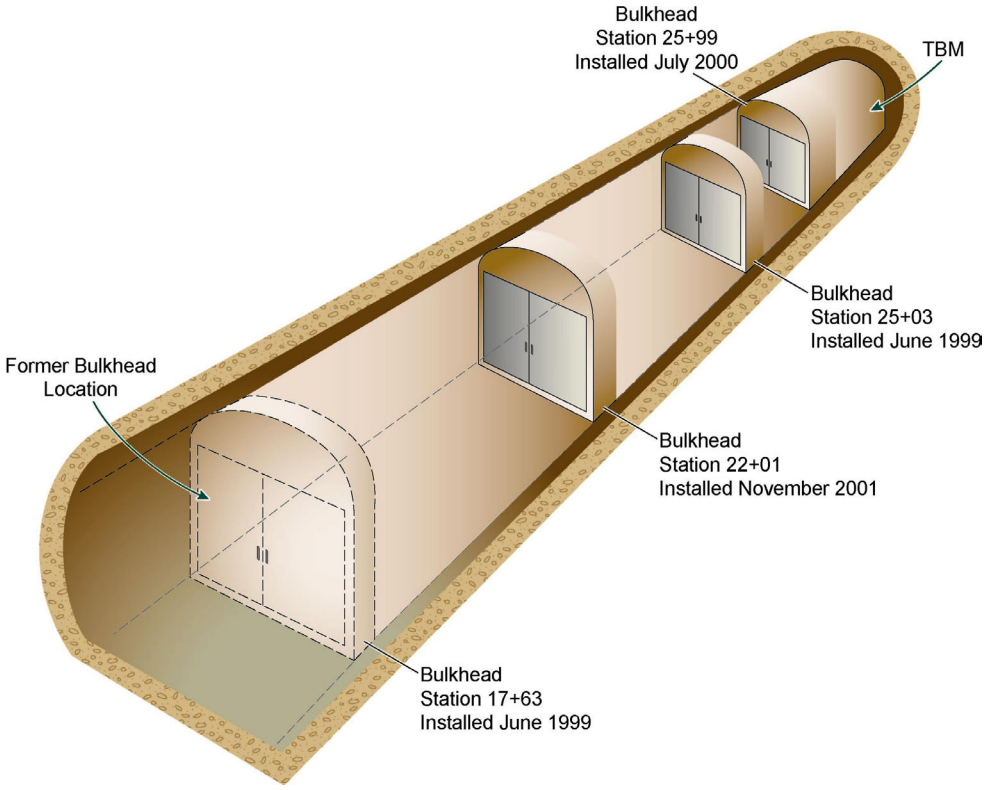

Figure 6.10.2-1. Schematic Illustration of Bulkhead Locations in the ECRB Cross Drift

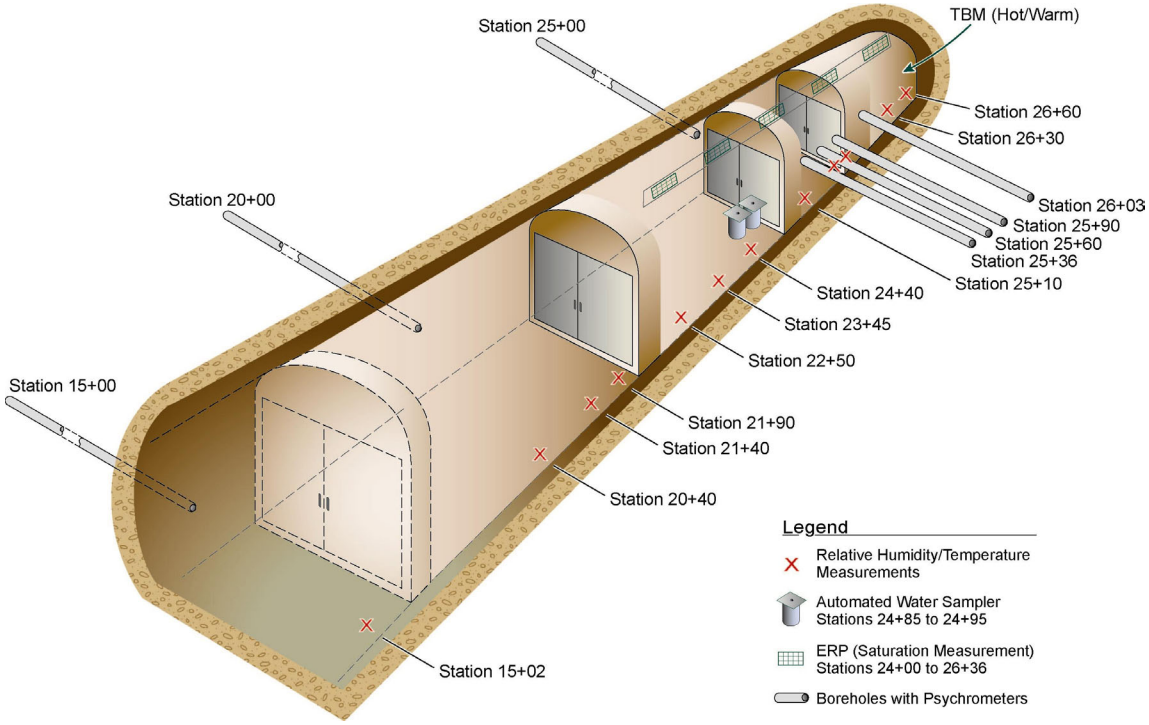

Figure 6.10.2-2. Schematic Illustration showing Berkeley Lab Monitoring Station in Locations in the ECRB Cross Drift

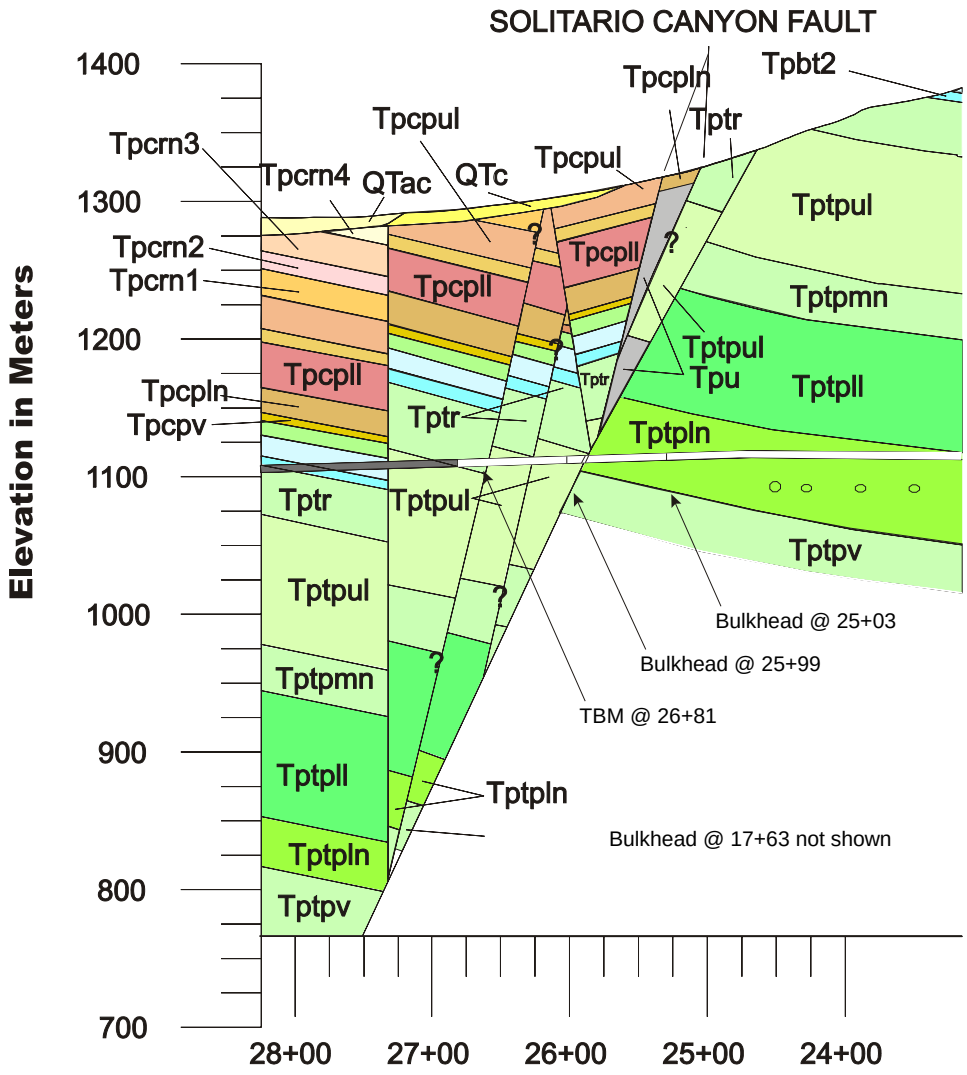

DTN: GS990908314224.010 [152631]

NOTE: For stratigraphic abbreviations, refer to Drawing OA-46-345 "Comparative Geologic Cross Section along the Cross Drift".

Figure 6.10.2-3 As-Built Cross Section of the Terminal End of the ECRB Cross Drift (23+00 m to 26+81 m) Showing the Bulkhead Locations

Table 6.10.2-1 Rock Unit Contacts Intersected by the Bulkhead Sections (All within the Topopah Spring Tuff)

Station	Mapped Contact
23+26	Tptpll / Tptpln (Topopah Spring Tuff lower lithophysal / lower nonlithophysal Contact)
25+84	Tptpln / Tptpul (Topopah Spring Tuff lower nonlithophysal / upper lithophysal Solitario Canyon Fault Zone)
26+64	Tptpul / Tptr (Topopah Spring Tuff upper lithophysal / crystal rich lithophysal Solitario Canyon Fault Zone)

DTN: GS990408314224.006 [108409]

6.10.2.1 Water-Potential Measurements and Drift Relative Humidity and Temperature Variations

Past observations have shown that, in an open tunnel, the evaporation potential of ventilation is much greater than any expected seepage. Observations from boreholes installed perpendicular to the tunnel wall suggest a clear dryout zone associated with ventilation of the tunnel. General conclusions from our understanding of the unsaturated zone suggest that if seepage into drifts were to occur, it would most likely be in the western portion of the repository block, where geological conditions are most conducive to infiltration, percolation, and seepage. The characteristics in this portion of the tunnel that make it most suitable for locating seeps are the absence of an overlying PTn past about CD 23+50 and the relatively high percolation rates, caused by high infiltration from shallow soils and higher elevation at the surface.

The 918 m long drift section (from bulkhead at CD 17+63 to the TBM end at CD 26+81) is located in the Topopah Spring lower lithophysal (Tptpll) and the lower nonlithophysal (Tptpln) tuff units, and includes the Solitario Canyon fault (the western boundary of the primary repository block) (Figure 6.10.2-1).

6.10.2.1.1 Water-Potential Measurements

Water-potential measurements along three horizontal boreholes in the ECRB Cross Drift are summarized in Figure 6.10.2-4. These three boreholes are located at CD 15+00, CD 20+00 and CD 25+00, and are 6 m long. The borehole at CD 15+00 is located before the first bulkhead, while the boreholes at CD 20+00 and CD 25+00 are located in bulkheaded sections.

There are three aspects to the water-potential measurements in the ECRB Cross Drift: (a) spatial variability within boreholes, (b) spatial variability between boreholes, and (c) the temporal variability within boreholes located between the first and second borehole. Spatial variability within boreholes begins with low water potentials close to the drift, increases rapidly over a distance of 1-2 m, and then remains close to saturated values along the deeper profile. Among the three monitored boreholes, the one located at CD 15+00 had its lowest water potential (i.e., driest) close to the drift wall. The borehole at CD 20+00 also had lower water potentials up to a distance of ~1.5 m from the borehole collar in (prior to the location of the bulkhead doors), which have since increased. The borehole located farthest into the ECRB Cross Drift at CD 25+00 did not show large drops in water potential closer to the collar, nor did the borehole show any increases in water potentials following the installation of the bulkhead doors.

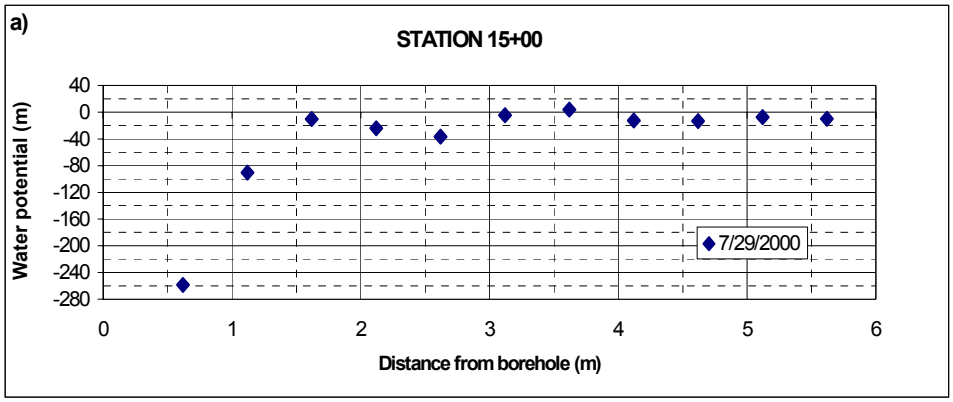

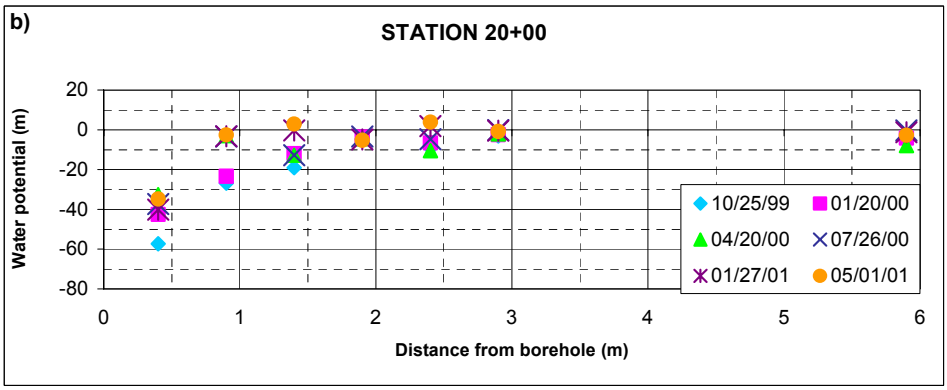

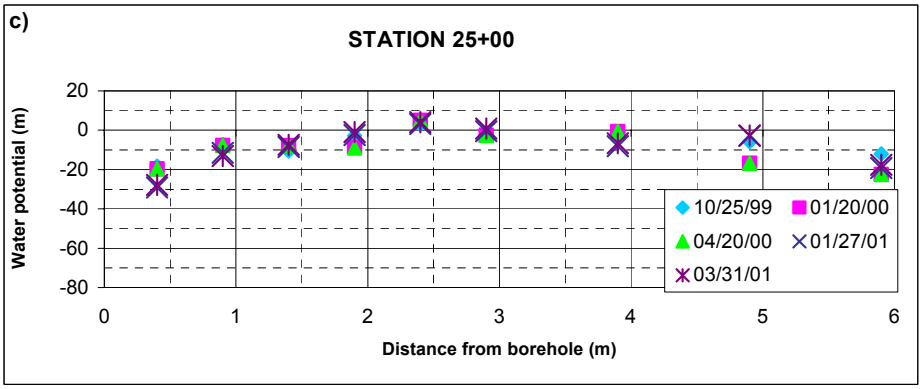

DTN: LB0110ECRBH2OP.001 [156883]

Figure 6.10.2-4. Water-Potential Measurements along the ECRB Cross Drift: (a) Station 15+00; (b) Station 20+00; (c) Station 25+00

6.10.2.1.2 Barometric Pressure Variations

Barometric pressure measured in the ECRB Cross Drift did not show any spatial variability, but had a pronounced change over time (Figure 6.10.2-5). The range of the temporal variability was between ~870 and ~905 millibars (mbars). From May to September 2000, the barometric pressure along the ECRB Cross Drift was restricted between ~880 and ~895 mbars. Larger fluctuations in the barometric pressure were observed between October 2000 and May 2001.

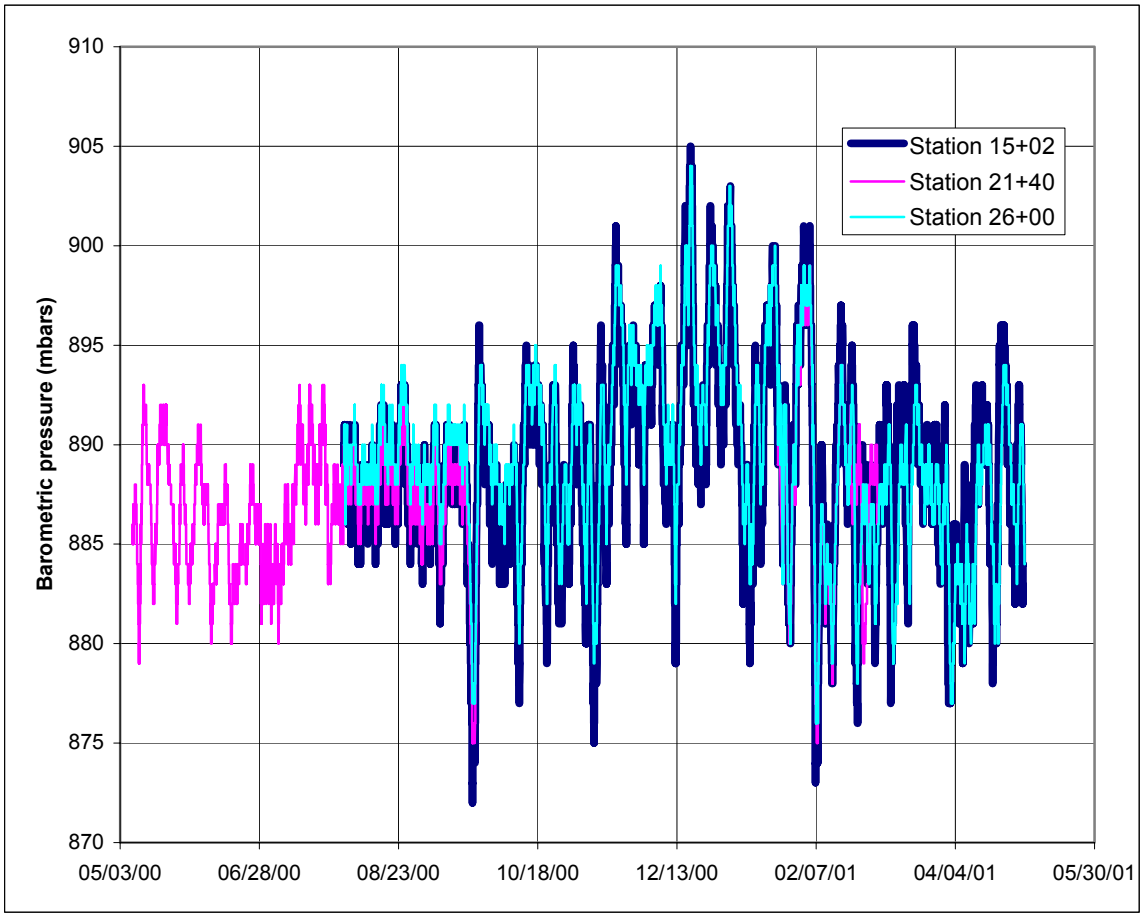

DTN: LB0307ECRBRHTB.001 [164843]

Figure 6.10.2-5. Barometric Pressure Measured along the ECRB Cross Drift

6.10.2.1.3 Temperature Variations between May 2000 and May 2001

Temperature measurements along the ECRB Cross Drift made over a period of nine months, starting in early August 2000, show a clear temperature gradient extending through the section of the ECRB Cross Drift behind the bulkhead doors (Figure 6.10.2-6).

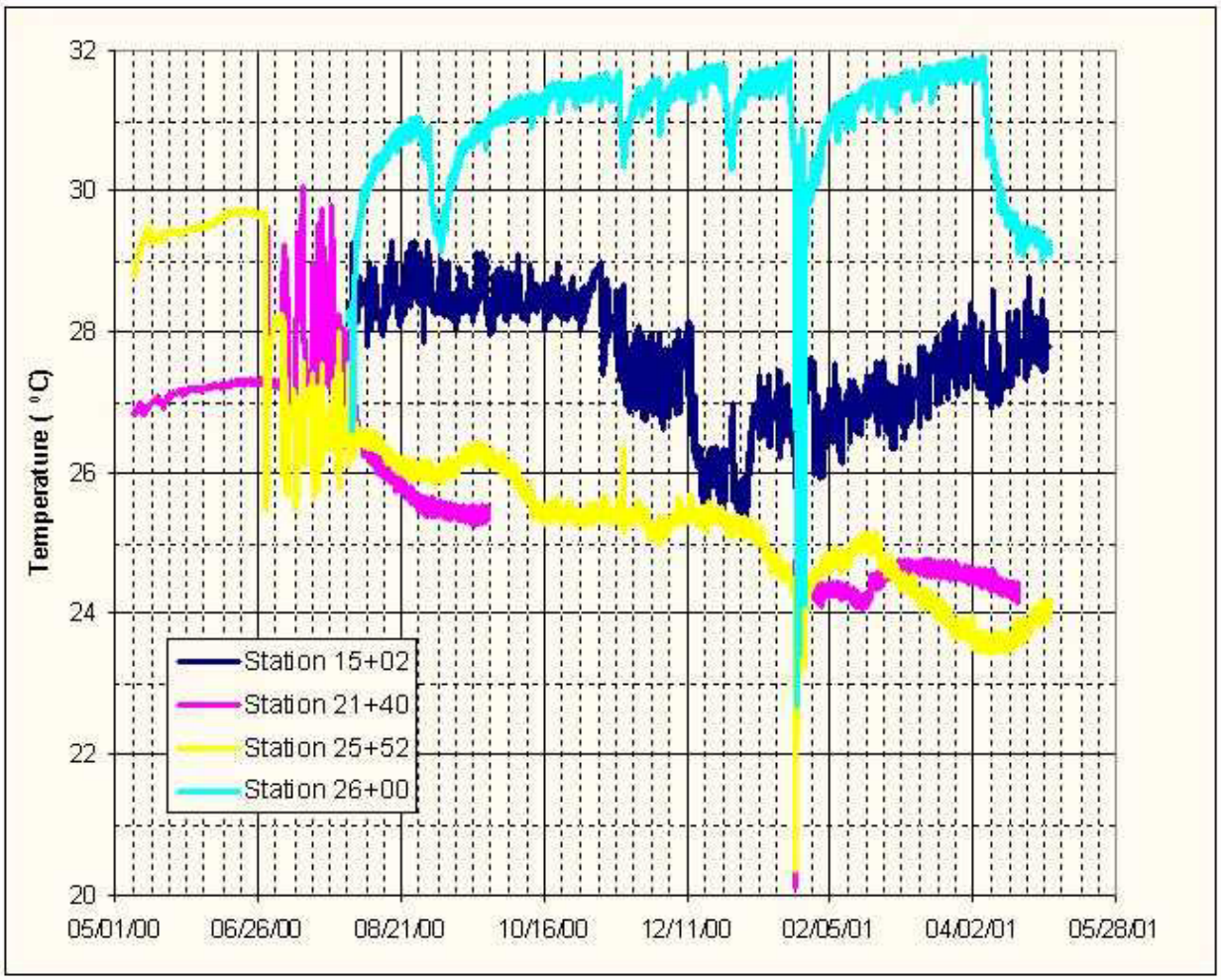

DTN: LB0307ECRBRHTB.001 [164843]

Figure 6.10.2-6. Temperature Measured in the Four ECRB Cross Drift Stations

The highest temperatures were recorded in the zone behind the last bulkhead, which houses the TBM. In this zone, the temperature fluctuated between 30˚ and 32˚C during most of the monitoring periods. However, there were three distinct periods when the temperature in this zone dropped below 30˚C. The first occurred in early September 2000 and was likely caused by power interruptions, which in turn caused the TBM to cool. The second temperature drop was in late January 2001, when all the bulkhead doors were opened. During this brief period, the temperature in the vicinity of the TBM dropped to ~22.5˚C. The temperature in this zone again dropped to below 30˚C in early April 2001, likely because of the powering-off of the TBM.

In the zone between the third and fourth bulkheads, the temperature tended to continuously drop from ~26.5˚C to ~ 24˚C between August 2000 and May 2001. Significant deviations from trend were observed in early September 2000, when the temperature increased briefly. These deviations coincide with the temperature decreases in the zone housing the TBM. Because similar observations were not recorded before the first bulkhead, it is likely that this perturbation was caused when the fourth bulkhead door was left open for a few days.

The temperature data collected between the first and second bulkhead shows the region steadily cooling immediately following the closure of the bulkhead doors in July 2000. (Because of the lack of temperature data from this location between late September 2000 and February 2001, temperature dynamics in this zone cannot be compared with the other two zones during this time.) Following the closure of the bulkhead doors in late January 2001, the temperature in this zone immediately reached ~24˚C and remained close to that value over the next two months.

Temperature in the ECRB Cross Drift measured immediately before the first bulkhead shows diurnal and seasonal fluctuations. While the diurnal fluctuations appear to be restricted to within 3˚C, the seasonal temperature changes from ~29˚C in late August 2000, to ~25˚C in late December 2000.

In summary, the zones defined by the bulkhead in the ECRB Cross Drift appear to be partially thermally isolated from each other and also from the area before the bulkhead *when the doors are closed*. The zone housing the TBM was warmer than the area before the first bulkhead, while the other two zones were consistently cooler when the doors were closed. During the period when the bulkhead doors were opened, the temperature in each of the zones rapidly approached that of the zone outside the bulkheads.

6.10.2.1.4 Relative Humidity Variations between May 2000 and May 2001

The relative humidity in the three zones defined by the bulkheads shows spatial variability similar to the temperature data (Figure 6.10.2-7). The lowest humidity was observed in the area before the first bulkhead, where it fluctuated between ~10 and 40%, with a few instances where the humidity was greater than 60%. In the two zones monitored behind the bulkheads, the relative humidity remained close to ~95%, with some changes observed in March 2001, when the humidity in the third zone gradually fell closer to ~90%.

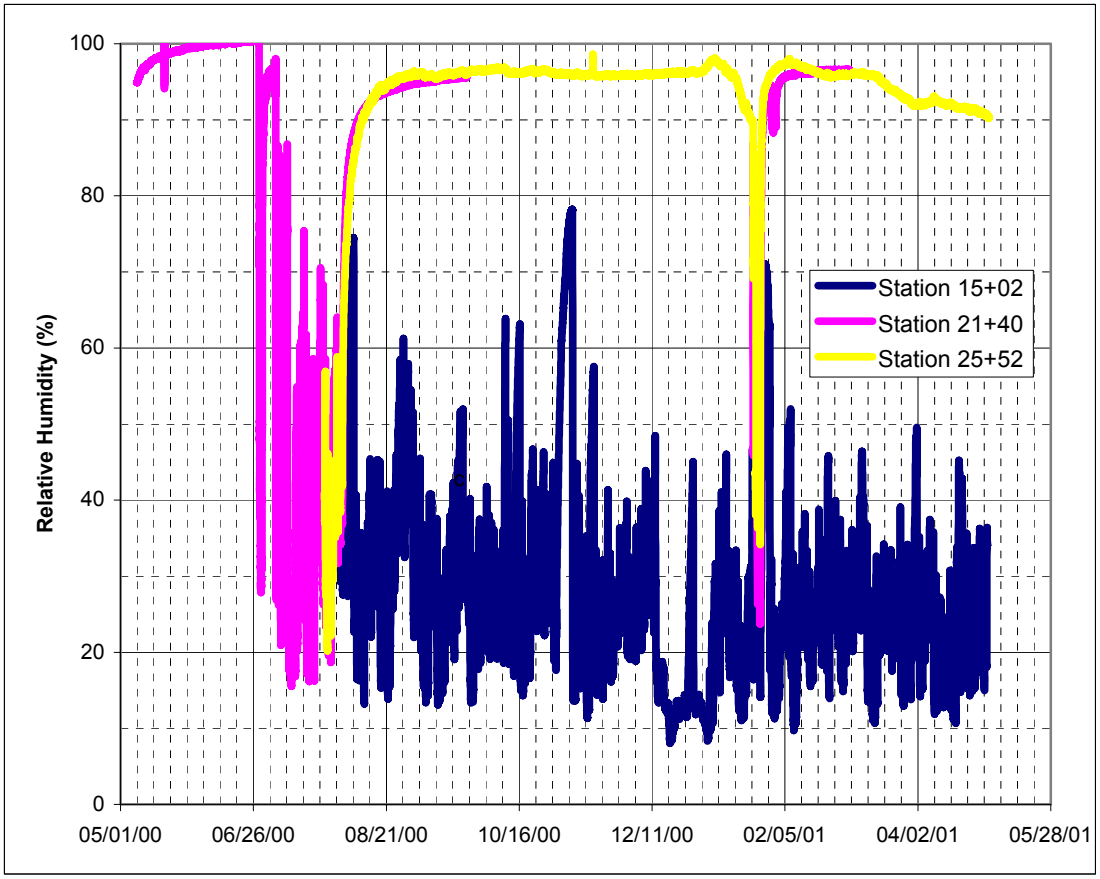

DTN: LB0307ECRBRHTB.001 [164843]

Figure 6.10.2-7. Relative Humidity Measured in the ECRB Cross Drift Stations

6.10.2.2 Observations of Wet Zones During Bulkhead Entries

Additional information on the moisture conditions within the nonventilated zone has been collected during periods when the bulkhead doors were opened. During periodic entries for visual inspection, wet spots were observed and water samples were manually collected. Observations have been made in the nonventilated sections that show the existence of liquid water, as well as rust spots and organic growths (i.e., indicators of the prolonged presence of water). While the presence of liquid water is evident, no continuous seepage from the rock into the closed sections of the ECRB Cross Drift has been observed to date. Figure 6.10.2-8 summarizes the timing and locations of liquid water observed during bulkhead entries, with details described in the following subsections. Photographic evidence is presented for the October 1-2, 2001 entry (DTN: LB0301ECRBRHTB.001 [164605]) to represent similar observations during other entries (DTN: GS030608312231.002 [165547] for additional images of ECRB moisture monitoring entries, January 22, 2002, to February 3, 2003).

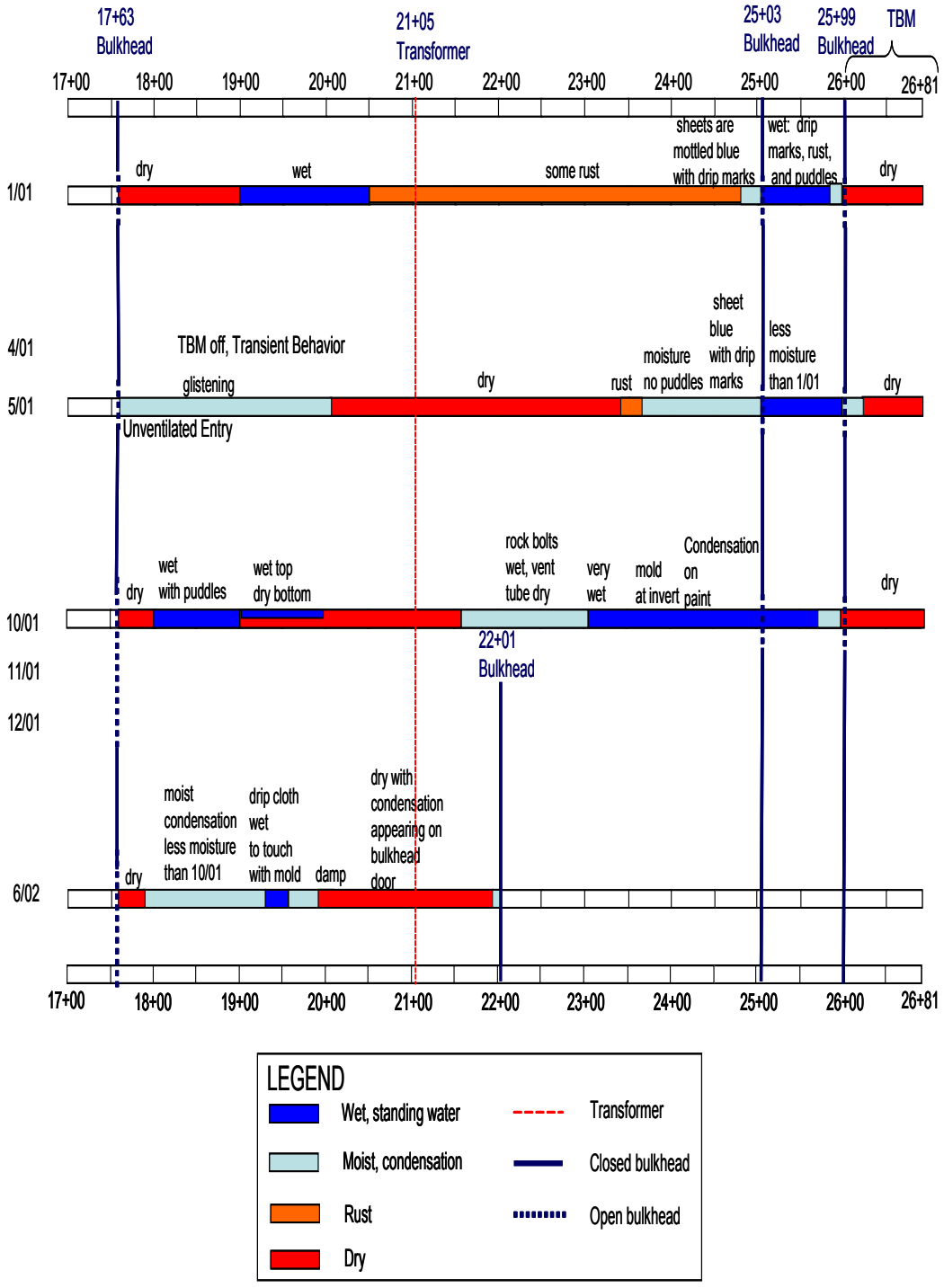

Sources: Entry 1/23/01 to 1/25/01: Hudson 2002 [165391] pp. 23-24, 91-98;
Entry 5/22/01: Hudson 2002 [165391] pp. 38-39, 140-150;
Entry 10/1/01 to 12/20/01: Hudson 2002 [165391] pp. 218-301;
Hudson 2002 [163398] pp. 1-47;
Entry 6/24/02 to 6/27/02: Hudson 2002 [163398] pp. 143-147.

Figure 6.10.2-8. Distribution of Wet Zones During ECRB Bulkhead Entries

6.10.2.2.1 Comparison of Observations During Nonventilated Entries in January 22–25, 2001 and May 22, 2001

In the entry on January 22-25, 2001, distinctly wet zones were observed, as shown in Figure 6.10.2-8. The power was off in April 2001. To avoid loss of data, an unventilated entry behind the bulkheads was done on May 22, 2001, to restore power to the dataloggers and to the TBM. The first bulkhead at CD 17+63 was opened at 11:10 am on May 22, 2001. No ventilation was established, and entry was permitted at 11:20 am. This entry was restricted to the same day, with bulkheads closed after the entry.

Less moisture was observed during the May 22, 2001, entry than had been observed during the January 22–25, 2001, entry. The moisture had not accumulated into puddles. The canvas drip detection sheet at CD 24+10 and the observed rust spots at CD 23+50 indicate that liquid moisture had been present at least this far up the tunnel. The continued power loss to the TBM resulted in a decreased temperature gradient within the tunnel. Moisture behind the third bulkhead and the smaller amount of moisture between the second and third bulkhead indicate that as the temperature gradient decreases, observable moisture tends to move toward the TBM.

The existence of water (glistening) was initially observed on the utility and vent lines in the first 250 m. The water appeared to be present only on the surface. Within two hours the moisture had evaporated. At CD 21+00, everything was dry. Moisture began reappearing on the utility and vent lines at about CD 23+50. There were rust spots on the steel channels and on the tracks. There was moisture at about a meter interval on the conveyor belt, but the water had not accumulated into puddles. A canvas sheet further up the tunnel than the others and hung on January 25, 2001, at CD 24+10, was mottled blue, with drip marks covering the entire sheets. The sheets between CD 24+75 and CD 24+95 were moist, and moisture also appeared on the utility and vent lines and on the bulkhead at CD 25+03, opened at 12:06 pm. Between the CD 25+03 and the CD 25+99 bulkhead, the canvas sheets were moist, but there was much less puddled water than for the January 22–25, 2001 entry. Moisture was evident on the canvas sheets, conveyor belt, and metal surfaces, and there were some small rocks on the conveyor belt. The bulkhead at CD25+99 was opened at 12:17 pm. There was moisture on utility lines and instruments cables to about 10 m behind the bulkhead. Beyond 10 m behind the bulkhead at CD 25+99, everything was dry.

6.10.2.2.2 Observations of Entry Made on October 1–2, 2001

An entry occurred on October 1 and a follow-up entry occurred on October 2, 2001. Four sections of alternating dry and wet conditions were observed between the first and second bulkhead on the first day, October 1, 2001 (12:03 pm to 13:37 pm). On the next day October 2, 2001, most water droplets had evaporated. Some of the rock and especially the in-filled fractures remained damp. Note that DTN: LB0301ECRBRHTB.001 [164605] includes photos for this entry.

On October 1 in the wet sections, the dampness was more pronounced on the upper part of the drift walls. The fault between the CD 25+03 and CD 25+99 bulkhead was dry. The last section behind the CD 25+99 bulkhead was also dry, with no rust was observed (implying that the section was not wet during the closure period). On the next day, October 2, 2001, most of water

droplets were evaporated, with some of the rock remaining damp. A patch of paint was observed to have beads of water drops on its surface, with no similar beads observed on the surrounding rock surfaces (Figure 6.10.2-9). Since the paint is impermeable, the observed beads are likely the results of condensation, not from seepage through the rocks below the painted patch. This observation substantiates the hypothesis that the observed water originates from condensation as the result of local temperature variations. This hypothesis is based on observations of early bulkhead entries and on chemical analyses (Section 6.10-3) from the limited water samples collected.

Detailed Descriptions of Visual and Photographic Observations

The bulkhead at CD 17+63 was entered on October 1, 2001, 12:03. Dry stalactites were observed on the vent tube just inside of the first bulkhead (Figure 6.10.2-10). The deposits were probably from redistribution of vent tube materials from dissolutions associated with early condensations, driven by temperature variations near the bulkhead. The lights in the same area have precipitate on them, but were dry during the observation. The drift was dry from the first bulkhead to about CD 18+00.

The drift was wet from CD 18+00 to about CD 19+00. First sign of moisture was observed on the left rib at CD 17+90, with condensate drips on utilities from overhead cables. The drops on the utilities were dry and a little bit rusty. Ventline and walls were very wet, and there were puddles on the belt and condensate all over the belt. There was a large puddle on the conveyer belt at CD 18+25 (Figure 6.10.2-11).

The wet sections conveyer belt had very clear water droplets (presumed to be condensate), all approximately evenly spaced on all rubber surfaces (top, bottom, in-between top bottom belts, etc.). The droplets sometimes ran together if there were depressions in the belt, creating puddles.

The surfaces of the rock in the wet areas were clearly damp but only on the top half of the drift. On the second day, the outer wet area was much drier. There was visual evidence of moisture retention in the little calcite infilled fractures but not in the matrix (Figure 6.10.2-12). This infill occurred more on the upper half of the drift than on the lower half. The infilled fractures looked like collapsed lithophysal cavities, even though the observation was in the lower nonlithophysal zone. In comparison with the observation first day, the inner wet area was not drier on the 2nd day. The main difference was that the droplets on the conveyer had mostly disappeared on the 2nd day.

Condensate was prevalent on the shotcrete after the CD 25+03 bulkhead (Figure 6.10.2-13) and behind the CD 25+99 bulkhead. The drift was dry again from CD 19+00 to about CD 21+50. The walls began to dry out moving towards the TBM. The Solitario Canyon fault appeared quite dry (Figure 6.10.2-14). The cloth tarp hanging on the portal side of the CD 25+99 bulkhead showed discoloration (blue for about 6 m or 20 feet from the bulkhead), indicating that it was wet at some point. Further towards the portal there was no discoloration (Figure 6.10.2-15). The water was likely located only near the bulkhead. Inside the CD 25+99 bulkhead, the drift was quite dry (Figure 6.10.2-16).

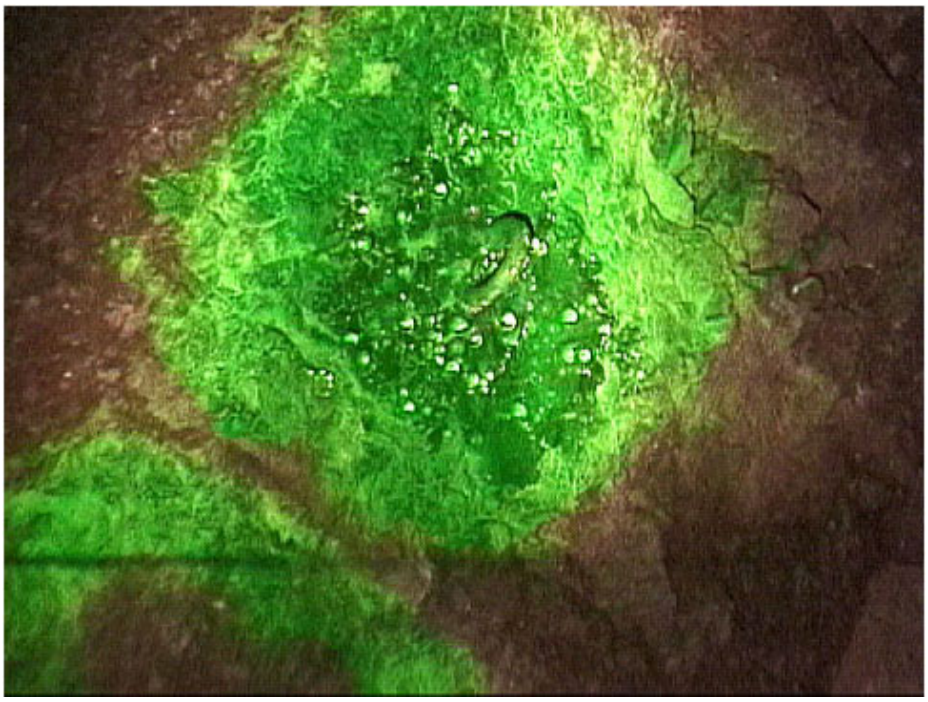

DTN: LB0301ECRBRHTB.001 [164605]

NOTE: Photo taken on 10/2/2001.

Figure 6.10.2-9. The Green Paint on the Crown of the ECRB Had Condensate Hanging from It, but Surrounding Rock Surface Did Not at CD 24+70.

DTN: LB0301ECRBRHTB.001 [164605]

NOTE: Photo taken on 10/1/2001 at 11:43.

Figure 6.10.2-10. Stalactites near 1st Bulkhead at CD 17+63

DTN: LB0301ECRBRHTB.001 [164605]

NOTE: Photo taken on 10/1/2001 at 12:26.

Figure 6.10.2-11. Water Puddle and Condensate on Conveyer at CD 18+25

DTN: LB0301ECRBRHTB.001 [164605]

NOTE: Photo taken on 10/2/2001 at 14:30.

Figure 6.10.2-12. Water Surrounding Inclusions

DTN: LB0301ECRBRHTB.001 [164605]

NOTE: Photo taken on 10/1/2001 at 13:19.

Figure 6.10.2-13. Condensate on Shotcrete after 2nd Bulkhead

DTN: LB0301ECRBRHTB.001 [164605]

NOTE: Photo taken on 10/1/2001 at 13:14.

Figure 6.10.2-14. Solitario Canyon Fault Left Rib

DTN: LB0301ECRBRHTB.001 [164605]

NOTE: Photo taken on 10/1/2001 at 13:15.

Figure 6.10.2-15. Tarp Discoloration before CD 25+99 Bulkhead

DTN: LB0301ECRBRHTB.001 [164605]

NOTE: Photo taken on 10/1/2001 at 13:13.

Figure 6.10.2-16. Inside Bulkhead at CD 25+99 (with TBM)—Quite Dry

6.10.2.2.3 Observations of Entry Made on June 24, 2002

During the nonventilated entry made on June 24, 2002, access to the ECRB was restricted to the areas between Station CD 17+63 and Station CD 22+01. During this entry, no standing pools of water were observed. However, there was some evidence of water at various locations. For example, at Station CD 19+15, a few brown spots of water were visible on plastic sheets that lay over the railroad tracks. Similar brown spots were visible on plastic sheets suspended from the ceiling at the same location. Mold was visible along certain sections of the rail tracks (e.g. Station CD 19+50) and on some of the canvas tarps suspended from the ceiling. Note that DTN: LB0301ECRBRHTB.001 [164605] also contains photos for this entry.

At Station CD 20+00, where a canvas sheet was located next to the transformer, a color contrast observed on the canvas sheet suggests the existence of a microclimate resulting from temperature gradients. Large quantities of water were observed as rivulets along the bulkhead doors at Station CD 22+01. However, immediately above the doors, the bulkhead remained dry.

6.10.2.3 Estimates of Mass of Vapor in Nonventilated Sections of the ECRB

From measurements of relative humidity (i.e., the ratio of the existing vapor pressure to the saturation vapor pressure at the same temperature), the density of water vapor (i.e., the mass of water vapor per unit volume of air) along the ECRB can be estimated from the relationship between temperature and the vapor density in saturated air (Figure 6.10.2-17). This relationship is accurately captured ($R^2 = 0.999$) by the second-order polynomial equation:

$$V_{\sigma s} = 0.00002t^2 + 0.0001t - 0.0053 \quad [6.10\text{-}1]$$

where $V_{\sigma s}$ is the vapor density of saturated air (kg m^{-3}) and t is the temperature (^{0}C) of the saturated air.

The actual vapor density ($V_{\sigma a}$) is then calculated from the relative humidity as:

$$V_{\sigma a} = V_{\sigma s} \times Rh \quad [6.10\text{-}2]$$

Subsequently, for a given length of drift, along which the temperature and relative humidity are approximated to be fairly constant, the flux of moisture in to or out of the drift, and the amount of moisture contained per unit length of drift at any given time can also be determined (see Attachment IX.4 for calculation).

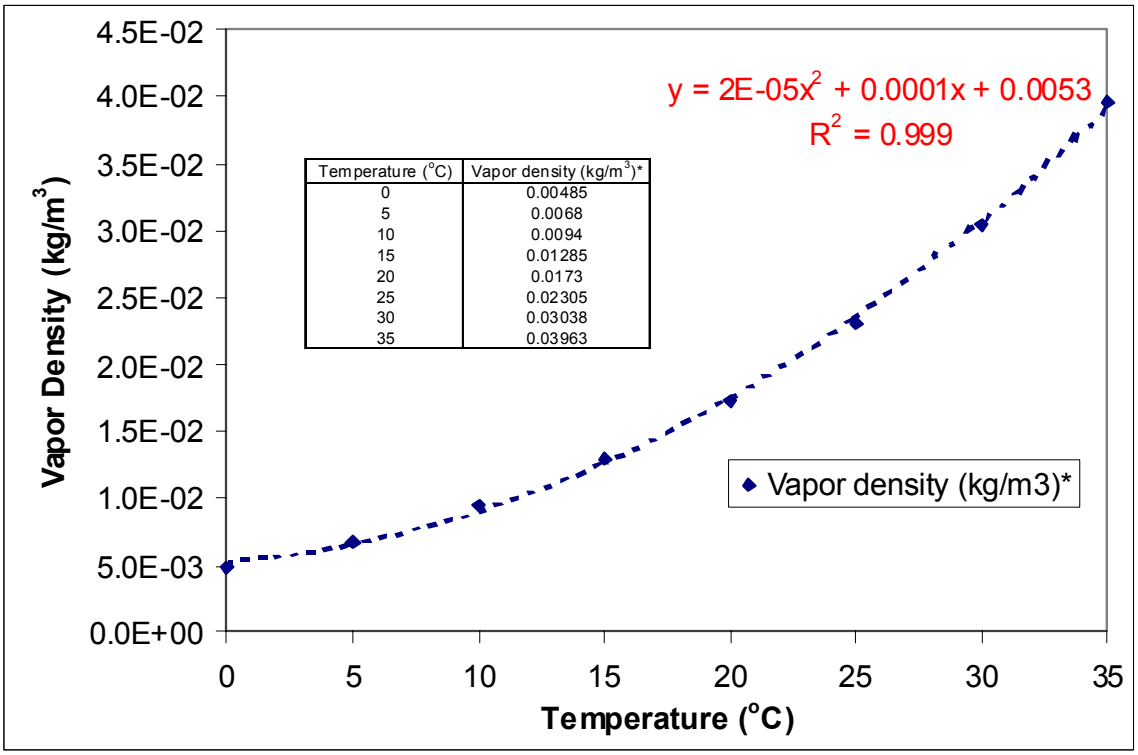

Temperature (°C)	Vapor density (kg/m^3)*
0	0.00485
5	0.0068
10	0.0094
15	0.01285
20	0.0173
25	0.02305
30	0.03038
35	0.03963

DTN: LB0307ECRBRHTB.001 [164843]

NOTE: Table shows the data from which the plot was developed. The polynomial equation describing this relationship is included in the plot. Data for table is from Hillel (1998 [165404], page 37).

Figure 6.10.2-17. Vapor Density at Various Temperatures

For example, after the bulkhead doors in the ECRB were closed during the last week of January 2001, the relative humidity measured at the monitoring stations CD 21+40, CD 25+52 (See DTN LB0307ECRBRHTB.001 [164843]) show a rapid rise in the in-drift humidity measurements (Figure 6.10.2-7).

A first-order estimate of the amount (mass) of vapor for the period immediately following the closure of the bulkhead doors can be made by determining the mass of vapor associated at a given temperature using Equation 6.10-1 and Figure 6.10-2. The temporal response of the mass of vapor is presented in Figure 6.10.2-18. This figure shows that once nonventilated conditions prevail behind closed bulkheads, the mass of vapor rapidly increases to ~37 kg per 100 m section of tunnel.

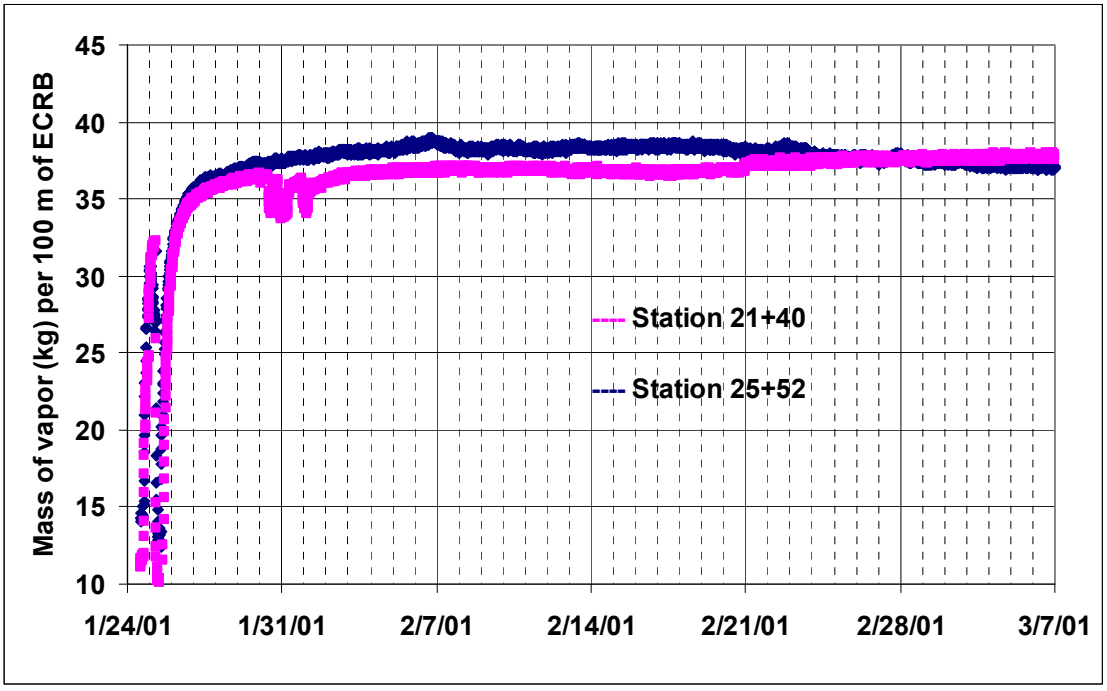

DTN: LB0307ECRBRHTB.001 [164843]

Figure 6.10.2-18. Mass of Vapor in Sections of ECRB Determined from Temperature and Relative Humidity Measurements at Station CD 21+40 and Station CD 25+52

6.10.3 Chemical and Isotopic Analysis of Water Samples Collected During Bulkhead Entries

The nonventilated sections of the ECRB Cross Drift were opened four times from January 2000 to January 2001, and water samples were collected. Both chemical analysis and isotopic measurements were conducted on the samples. The chemical analyses were on major anionic and cationic constituents (including bromide, chloride, and lithium) in the liquid samples. The hydrogen (δD) and oxygen ($\delta^{18}O$) isotope compositions were also analyzed.

6.10.3.1 Chemical Analysis

Most of the initial samples were collected directly from pools that had formed on the conveyor belt, and these samples were of brownish to dark-brown color, with some examples shown in Figure 6.10.3-1. Their chemical compositions show high and spurious concentrations of many constituents, as shown in Table 6.10.3-1. These samples are likely contaminated from the conveyor belt, resulting from the belt usage/operation before ECRB Cross Drift closure, with the degree of contamination unknown and unable to be quantified. Contamination of the conveyor belt may include salt accumulated from water evaporation following transportation of the tuff debris, as well as other miscellaneous contamination. Therefore, these samples may not yield useful information about the origin of the water (condensate or seepage) observed in the ECRB Cross Drift behind bulkheads.

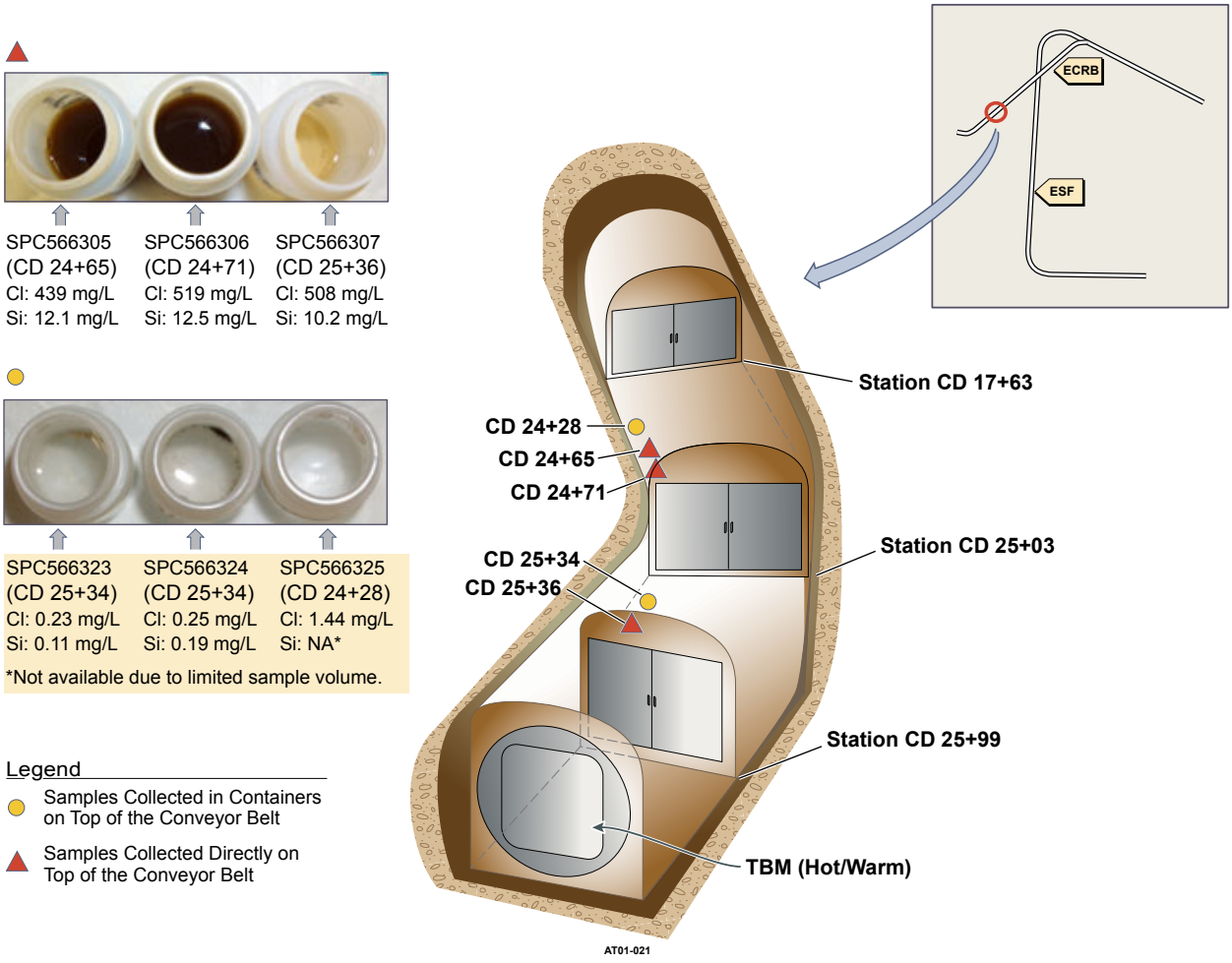

DTN: LB0110ECRBH2OA.001 [156886]

Figure 6.10.3-1. Chemical Analyses of Liquid Samples Collected during Bulkhead Entries

Subsequently, three samples were collected from collection containers placed on the top of the conveyor belt. These samples are clear (Figure 6.10.3-1). Their chemistry, particularly low chloride and silica contents, indicates that this water is condensate (Figure 6.10.3-2). The water does not have the chemical signature of the construction water, which contains about 20 mg/L of lithium bromide added to J-13 well water. Condensate, and subsequent dripping down, could

occur as a result of vapor-to-liquid transition associated with local temperature variations in a humid environment. The moisture conditions measured by humidity and temperature probes support the presence of drift moisture variations (Section 6.10.2.2). These clear samples also show a relatively high amount of calcium and a high sulfate/chloride ratio, suggesting some minor contamination from either rock grout or rock dust (Figure 6.10.3-2). (Some grout or dust present along the drift crown above the sampling containers may have dissolved in the condensate prior to collection.) Samples collected on the drift wall (using a needle syringe for SPC566308 in Table 6.10.3-1, and absorbent pad attached to the wall) show an even higher concentration of calcium and a larger sulfate/chloride ratio, resulting from the direct contact of the sample with the rock.

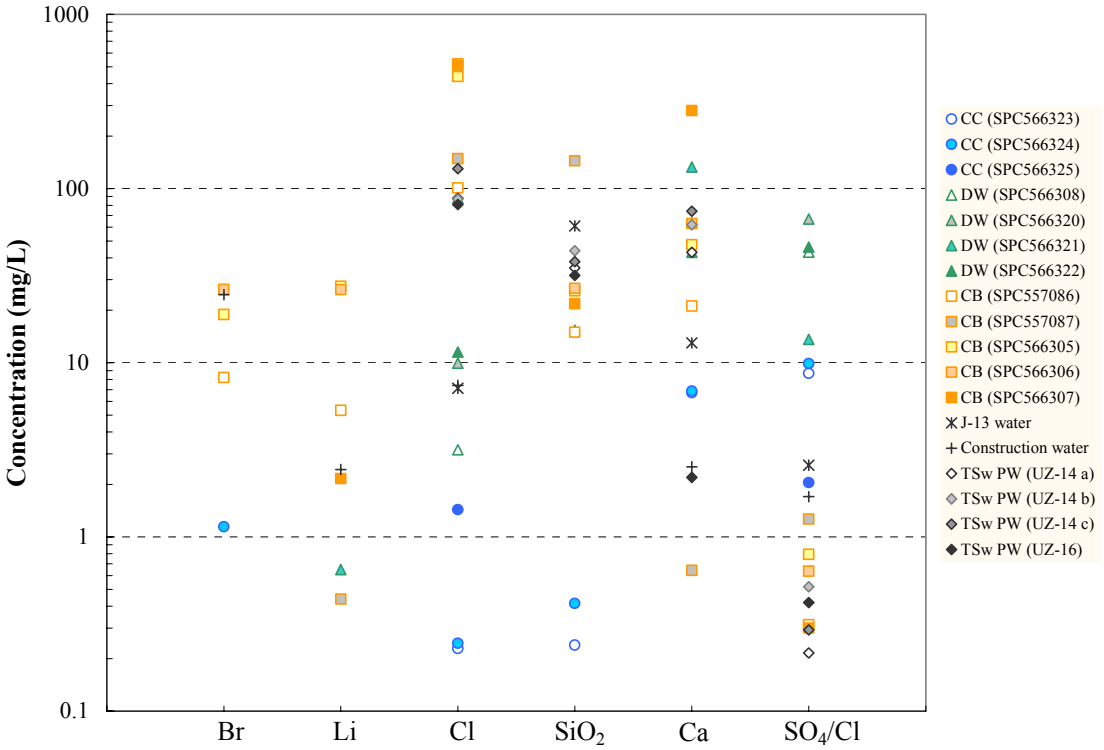

Source: J-13 well water composition from DTN: MO0006J13WTRCM.000 [151029].
TSw pore-water data from BSC 2001 [154874], Table 6.
ECRB water data from DTN: LB0110ECRBH2OA.001 [156886]

NOTE: Unit of the Y-axis is in mg/L, except for the ratio of sulfate to chloride (dimensionless).
ECRB Samples are grouped as follows: CC in collection container, DW on drift wall, and CB on conveyor belt.
Construction water data presented here are an average value from seven samples.
TSw PW: pore water in Topopah Spring welded tuff unit.

Figure 6.10.3-2. Comparison of Chemical Signatures

Table 6.10.3-1. Chemical and Isotopic Data for Liquid Samples Collected in the ECRB Cross Drift

Specimen ID#	Sample Location	Collection Date	Br^-	Cl^-	F^-	NO_3^-	SO_4^{2-}	Ca^{2+}	Li^+	Mg^{2+}	K^+	Na^+	SiO_2	δD	$\delta^{18}O$
			(mg/L)											(%)	
SPC557086	Conveyor belt - Station CD 24+83	1/31/00	8.23	101	ND	ND	31.7	21.2	5.33	3.10	19.0	88.6	15.0	-59	-7.1
SPC557087	Conveyor belt - Station CD 25+17	1/31/00	ND	149	29	ND	188	0.64	0.44	0.10	160	139733	144	-80	-9.3
SPC566305	Conveyor belt - Station CD 24+65	5/03/00	18.9	439	ND	ND	349	47.6	27.5	9.00	27.9	195	25.9	-79	-9.3
SPC566306	Conveyor belt - Station CD 24+71	5/03/00	26.3	519	9.19	ND	330	62.9	26.3	12.0	35.3	230	26.7	-80	-8.9
SPC566307	Conveyor belt - Station CD 25+36	5/03/00	ND	508	6.41	24.1	152	280	2.16	34.0	36.3	191	21.8	-79	-8.7
SPC566308	Shotcrete- Station CD 25+50	5/03/00	ND	3.16	ND	4.29	136	---	---	---	---	---	---	---	---
SPC566300	Construction Water	5/31/00	25.1	6.82	---	ND	13.4	6.64	2.02	---	5.94	59.1	---	---	---
SPC566320	Absorbent pad - Station CD 25+62	6/28/00	ND	9.95	7.05	3.99	665	63.5	ND	11.5	172	105	<1.0	---	---
SPC566321	Absorbent pad - Station CD 25+62	6/28/00	ND	88.0	15.8	5.79	1197	133	0.65	18.1	163	233	15.4	-69	-6.9
SPC566322	Absorbent pad - Station CD 25+62	6/28/00	ND	11.5	8.02	2.20	531	43.0	ND	6.50	141	78.6	<1.0	-71	-7.8
SPC566323	Collection container - Station CD 25+34	6/28/00	ND	0.23	ND	1.63	1.99	6.73	ND	0.40	0.84	1.56	0.24	-83	-9.4
SPC566324	Collection container - Station CD 25+34	6/28/00	1.14	0.25	ND	ND	2.42	6.87	ND	0.40	0.90	1.65	0.42	-84	-9.4
SPC566325	Collection container - Station CD 24+28	6/28/00	ND	1.44	ND	2.34	2.95	---	---	---	---	---	---	-67	-8.1

Table 6.10.3-1. Chemical and Isotopic Data for Liquid Samples Collected in the ECRB Cross Drift (Continued)

Specimen ID#	Sample Location	Collection Date	Br^-	Cl^-	F^-	NO_3^-	SO_4^{2-}	Ca^{2+}	Li^+	Mg^{2+}	K^+	Na^+	SiO_2	δD	$\delta^{18}O$
			(mg/L)											(%)	
SPC573600	Conveyor belt - ~5 m from 2nd bulkhead	1/22/01	45.4	---	---	---	---	---	0.11	---	---	---	---	-90	-10.6
SPC573602	Conveyor belt - Station CD 25+37	1/22/01	79.7	---	---	---	---	---	0.17	---	---	---	---	-74	---
SPC573604	Conveyor belt - ~7 m from 2nd bulkhead	1/22/01	56.3	---	---	---	---	---	12.31	---	---	---	---	-89	-10.7
SPC573605	Conveyor belt - Station CD 25+42	1/22/01	ND	---	---	---	---	---	0.22	---	---	---	---	-55	-3.7
SPC573601	Conveyor belt - Station CD 25+10	1/23/01	72.5	---	---	---	---	---	14.8	---	---	---	---	-48	-5.0
SPC573603	Conveyor belt - Station CD 25+21	1/23/01	52.5	---	---	---	---	---	0.13	---	---	---	---	-55	-4.9

DTN: LB0110ECRBH2OA.001 [156886]; LB0110ECRBH2OI.001 [156887]

NOTE: Liquid samples were filtered through 0.45 µm filters prior to chemical analyses. Phosphate was not detected in any of the liquid samples.
ND: not detected, e.g., below the analytical detection limit (about 0.1 mg/L).
---: Data not available.

6.10.3.2 Isotopic Analysis

Water samples collected were also used for isotopic analyses, with the results presented in Table 6.10.3-1 and illustrated in Figure 6.10.3-3. The δD values of the ECRB Cross Drift water range from -48‰ to -9‰, and the $\delta^{18}O$ values range from -3‰ to -10.7‰. These values are higher than those found in the construction water. The lag time between opening of bulkheads and allowing sample collection (3–4 hours) is sufficient to result in a significant degree of evaporation of the samples. In Figure 6.10.3-3, all samples from the ECRB Cross Drift are shifted from the global meteoric water line, similar to samples from Alcove 5. The offset is characteristic of waters that have undergone some degree of vapor loss. The same degree of shift for both the contaminated samples and the relatively clean samples may indicate that approximately the same degree of evaporation occurred for water collected in the ECRB Cross Drift.

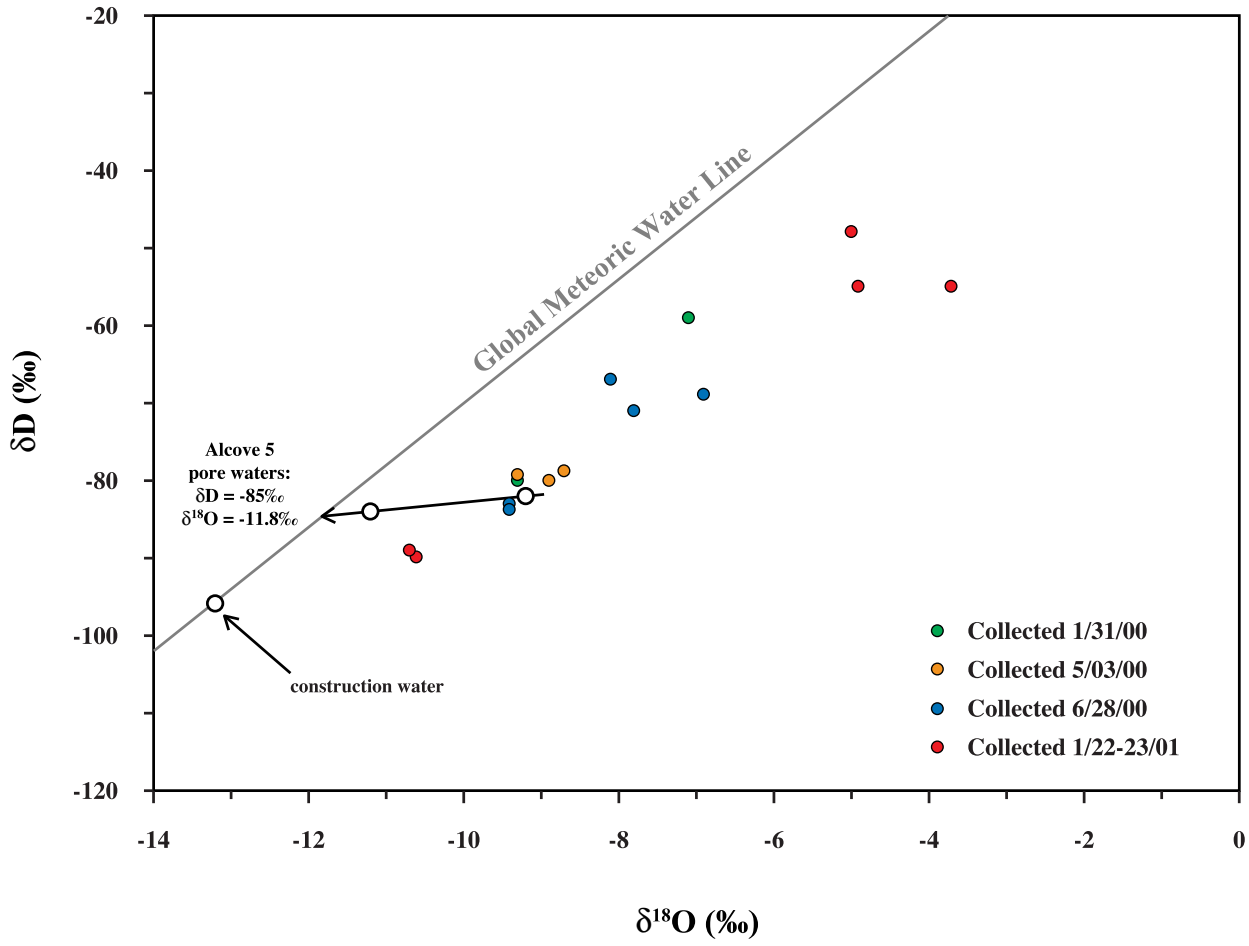

DTNs: LB0110ECRBH2OI.001 [156887], LB0108CO2DST05.001 [156888], LB0011CO2DST08.001 [153460]

NOTE: Also plotted is the isotopic composition of construction water, two pore water samples extracted from core samples from Alcove 5 and the location of the Global Meteoric Water Line.

Figure 6.10.3-3. Plot of the Hydrogen and Oxygen Isotope Compositions of Water Samples Collected from the ECRB Cross Drift

6.10.3.3 Summary of ECRB Entries

During most of the entries, the entire ECRB Cross Drift was accessible for visual inspection. Wet areas were observed and water samples were manually collected from small pools of water. The visual observations suggest that the water observed in the ECRB originated from condensation. (For example, water droplets were observed on the surface of a small patch of paint, an impermeable barrier to the rock.) Water collected from collection containers in the second entry (June 28, 2000) indicated that the water is low in chloride and silicate contents, characteristic of condensate. The water does not have the chemical signature of construction water (i.e., spiked with about 20 mg/L of lithium bromide). Condensates, and consequent dripping down, could occur by water phase transition from vapor to liquid associated with local temperature variations. The moisture conditions measured by humidity and temperature probes support the presence of drift moisture variations. The potential measurements in the boreholes indicate that the tuff matrix is still dry near the borehole collars.

6.10.4 Ambient Monitoring in Alcove 7

Ambient monitoring of temperature, barometric pressure, and relative humidity was also performed inside Alcove 7, located in the ESF at station 50+64. This alcove was constructed to a depth of 203 m and penetrated the Ghost Dance fault at 167 m. Bulkhead doors were installed 64 m and 132 m from the entrance of the alcove during the Fall of 1997 (Kurzmack et al. 2002 [162333]).

The Alcove 7 bulkhead door was first closed on December 11, 1997. Although there were many entries during the period from December 1997 to October 30, 2000, there were relative humidity measurements close to 100%. Fluctuating temperature and relative humidity measurements indicated that the bulkheads were not perfectly sealed (DTN: GS990108312242.005 [166000]).

On September 18, 2001 the bulkheads were opened after being closed since October 30, 2000. Evidence of moisture was observed during this entry. Signs of moisture included drip spots on the drip collection sheets, moisture drops on the utility lines, moisture drops on the shotcrete around the bulkheads, and moisture spots in the dust on an instrument enclosure. Also, the rock in the crown had a dark, moist appearance. The bulkhead doors were next opened on May 20, 2003. There were drip spots on the drip collection sheets, moisture drops on the utility lines, and moisture spots in the dust on an instrument enclosure. The rock in the crown had a dark, moist appearance and the fractures in the rib appeared wet (Hudson 2003 [165273]).

Between September 25, 2001 and June 10, 2002, the relative humidity behind the bulkhead doors was less than 95% (dry end of the thermocouple psychrometers) and was therefore not measured. Pressure monitoring indicated that the transmission of atmospheric pressure fluctuations across the bulkhead doors showed minimal dampening (< 5%) and short time lags (on the order of hours). Large temperature fluctuations (19.5 to 27.5 degrees Celsius) at the monitoring station located 4 m from the entrance of the alcove were caused by seasonal temperature fluctuations down the ESF by the ventilation system. This monitoring station is located outside the bulkhead doors. Diurnal temperature fluctuations caused by ventilation were as large as 1.2 degrees. Temperatures behind the bulkheads indicated no discernable annual fluctuation, and the diurnal temperature fluctuations were less than 0.05 degrees. Abrupt temperature decreases (up to 1.0

degree) were occasionally measured behind the bulkheads. These temperature decreases were correlated with the pressure recovery period following a low-pressure event. The temperature decrease may be caused by a pressure gradient driving warm-dry ESF air through the fractures around the bulkheads, evaporating water and cooling the air.

6.11 ANALYSES AND INTERPRETATIONS OF SYSTEMATIC HYDROLOGICAL CHARACTERIZATION

A systematic approach—testing at regular intervals regardless of specific features arising from spatial heterogeneity—has been chosen for performing hydrological characterization tests. These tests take place in boreholes drilled at regular intervals along the ECRB Cross Drift within the lower lithophysal zone of the TSw. The lower lithophysal welded tuff unit is intersected by many small fractures (less than 1 m long) and interspersed with many lithophysal cavities (ranging in size from 15 to 100 cm). The size and spacing of both the fractures and lithophysal cavities vary appreciably along the drift walls (the drift is 5 m in diameter) over an 800 m stretch. This indicates that hydrological characteristics at one particular location may not be representative of the entire unit. Therefore, a systematic approach of testing at regular intervals has been adopted to acquire knowledge of the heterogeneous hydrological characteristics of this unit, in which over 80% of the repository will reside. The systematic approach is to complement other hydrological testing in the ambient testing program, in which test locations are selected either by avoiding or focusing on specific features (such as large fractures or extra abundance of fractures or cavities). Systematic hydrological characterization investigates the hydrological properties that are important to repository performance. Field measurements include:

1. Air-injection tests that give a measure of fracture permeability

2. Liquid-release tests that determine the ability of the open drift to act as a capillary barrier (diverting water around itself) as well as the potential for water seeping into the drift

3. Crosshole gas-tracer tests to measure the effective porosity of the rock mass.

6.11.1 Systematic Borehole Testing Setup

6.11.1.1 Systematic Borehole Configuration

Figure 6.11.1-1 shows a schematic of the arrays of boreholes (all 20 m in length) drilled at regular intervals along the ECRB Cross Drift. The borehole arrays are divided into three groups. Group I consists of low-angled boreholes drilled from the crown of the 5 m diameter ECRB Cross Drift, inclined at 15^{o} from the drift-axis. These boreholes are intended for both air-injection and liquid-release tests, with the spacing of adjacent boreholes from collar to collar at 30 m. Group II consists of near-vertical boreholes drilled from the crown of the drift. Group III consists of pairs of parallel horizontal boreholes, spaced 3 m apart and drilled from the side of the drift. The former are intended for air-injection tests to determine the effect of drift excavation on fracture properties, and the latter are for gas-tracer tests to determine the effective porosity. Group II and III boreholes are in groups of three, spaced 90 m apart, as shown in Figure 6.11.1-1.

The Group I boreholes are the primary ones used for study in this investigation. To date, four of them have been tested. They have their collars located at CD 17+49, CD 17+26, CD 16+95, and CD 16+65, respectively, from the ECRB portal. Twenty meters separate the first two, because of the presence of a bulkhead at CD 17+63 precluding drilling any further into the ECRB than CD 17+63. All of the boreholes are inclined up towards the portal end of the ECRB.

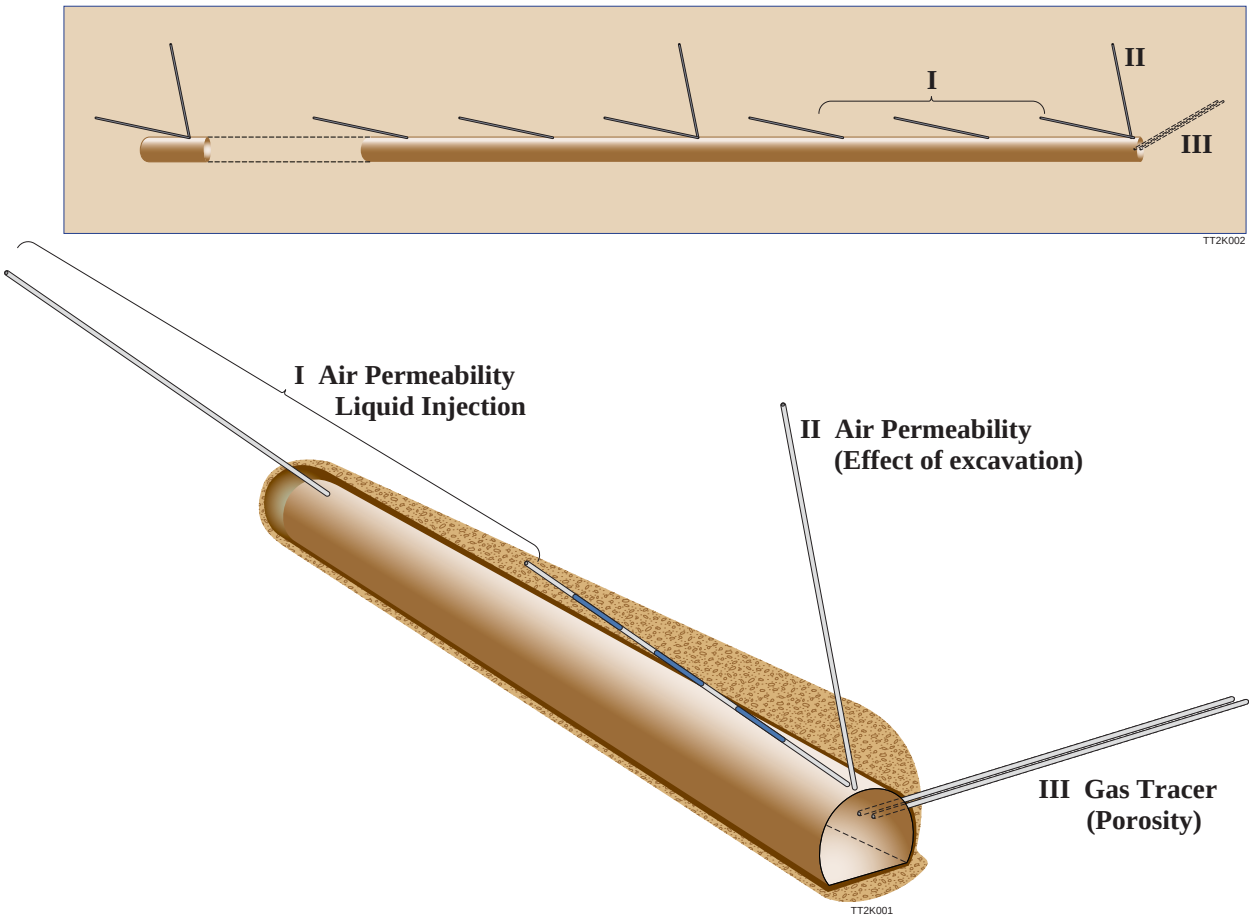

Figure 6.11.1-1. Schematic of Borehole Configuration in the ECRB Cross Drift for Systematic Characterization of the Lower Lithophysal Unit

6.11.1.2 Equipment

The equipment system has been custom-designed for the systematic characterization study, based on two criteria: automation and mobility. Field-scale measurements involving liquid flow in unsaturated rock require continuous testing, lasting for weeks to months, whereas the ECRB Cross Drift is open only for eight hours, four days every week. Therefore, the control of test equipment has been fully automated, allowing remote manipulation via computer network when there is no human presence at the field site. The second criterion of mobility is achieved by designing all equipment needed for the systematic characterization as a complete unit to fit on flatbed rail cars. This enables investigators to efficiently transport equipment from one test station to another along the ECRB Cross Drift.

A schematic of the testing equipment for air injection and liquid release is shown in Figure 6.11.1-2. The main function of the equipment is to distribute water at a specified rate along a specified length of borehole and to capture any water that makes its way from the borehole through the rock formation as seepage into the drift. The key components of the system are the packer assembly, water supply hardware, and seepage capture system.

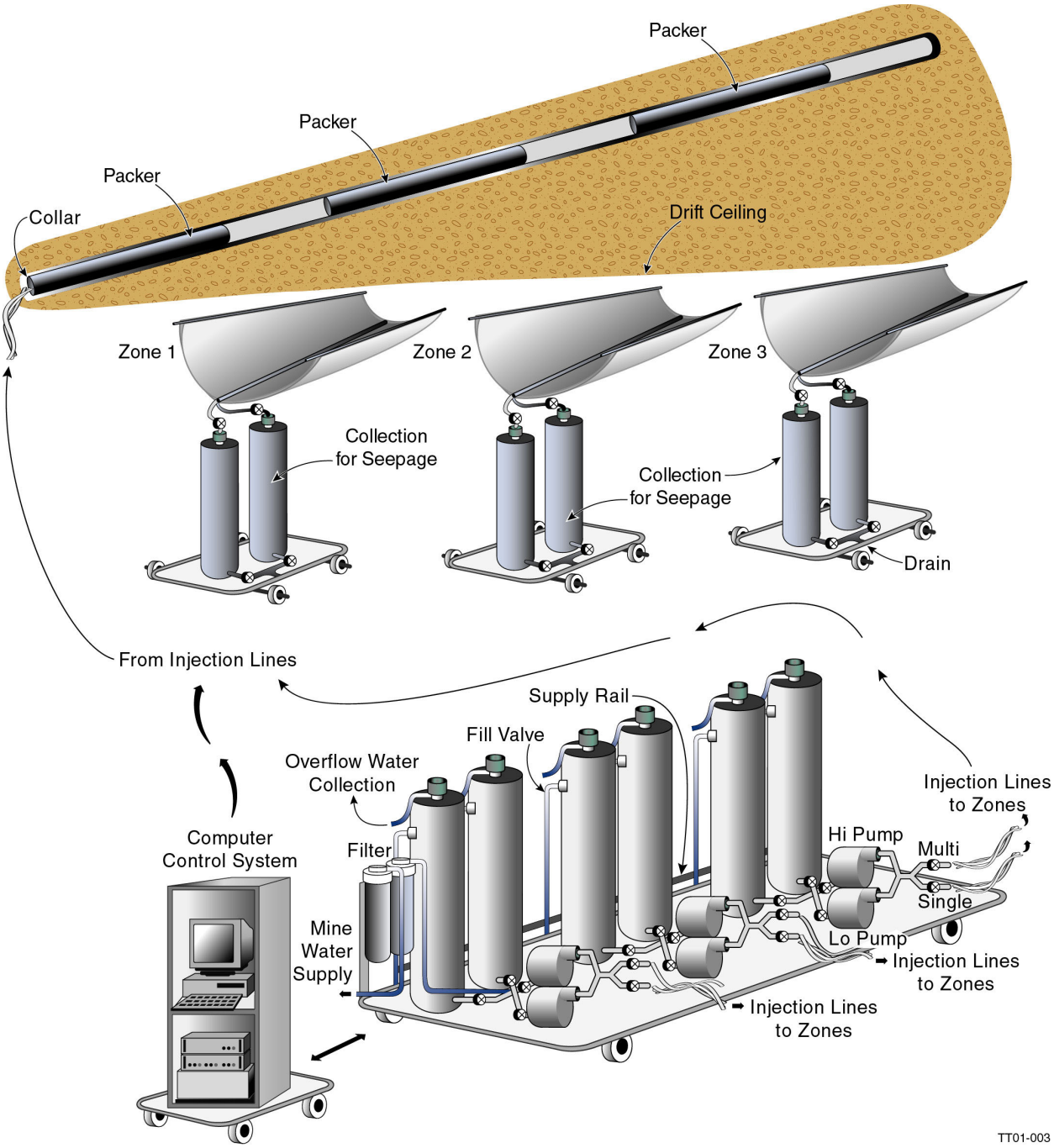

Figure 6.11.1-2 A Schematic of the Equipment System: Packer Assembly, Water Supply and Air-Injection Component, Seepage Collection Component, and Data Acquisition and Control

6.11.1.2.1 Packer Assembly

The packer assembly uses inflatable-rubber-packer units to seal off sections of borehole (so that released water cannot reach these sections) and isolates each borehole into three nonsealed 1.83 m water-release sections. The three sealing sections of the packer assembly use a 3 m, 0.64 cm

wall, and a soft inflatable rubber tubing supported by and clamped at each end onto a 5 cm stainless-steel core, for an overall diameter of 6.3 cm. The relatively long packers (3 m) are intended to provide effective sealing in a lithophysal unit, where the size of cavities can reach to 1 m. Cores of these rubberized sections contain internal tubing to inflate the rubber up to the borehole diameter (7.6 cm) using compressed air.

Of the three water-delivery sections, also made of 5 cm diameter stainless tubing, two lie between the three rubberized sections in the borehole, and the third lies beyond the farthest rubber section into the borehole. Because of the small-angle incline of the borehole, the vertical distance from the nearest section to the drift crown is about 1 m, whereas the vertical distance between the second and farthest (into the borehole) sections and the crown are on the order of 2.5 and 5 m, respectively. Water is released into these unsealed sections or zones by one of two means. One method uses a single release point close to the rubber sealing section at the far (upper) end of the unsealed zone. The other method uses multiple orifices along an unsealed section to enable water to be released at six evenly spaced locations along the entire unsealed section. Tubing resides inside each of the delivery sections for single-point injection, for multipoint injection at six evenly spaced locations, and for drainage of overflow, should the delivery rate prove to be too high for all the water to completely enter the formation. One additional tube from each delivery section connects it to a pressure transducer located outside the hole, to measure air pressure in each zone.

In keeping with the design requirements of the testing site, the sections of packer assembly are shipped as separate parts and assembled at the site. O-rings at the connections between sections assure that the annuli left around the water-delivery sections are sealed from atmospheric conditions inside the hollow, open-packer core. The packer inflation, water supply, and water drain tubing from all sections run through the core of the packer assembly to the outside of the borehole, where it is connected to the water supply system.

6.11.1.2.2 Water Supply System

Each delivery section in the borehole has its own water supply system. The triplicate design allows testing in all three zones of the same borehole simultaneously. The water supply hardware controls the amount of water delivered to a section and also measures the total quantity of water supplied to that section over time. In addition, the supply hardware also measures, over time, the quantity of any return flow through the drain port from the delivery section. Each supply system makes use of twin vertical, cylindrical bottles to supply and measure the water that is delivered. The bottles are 1.5 m tall and 20 cm in diameter, a size that enables mobility of the units between test locations without sacrificing volume resolution or supply volume. One bottle can fill from the tunnel water supply, while the other is pumped, so that the supply and measurement system can run without interruption. Located at the base of each bottle, differential-pressure transducers (which cancel atmospheric changes) measure the head of water in each bottle. These transducers, when multiplied by the known area of a bottle, yield the current water quantity residing in the bottle. One of two sizes of electronically controlled gear pumps pushes water from the bottom of the active supply bottle up to the packer assembly for water delivery. The two different-sized pumps are used to provide supply-rate range of 10 mL/min to 2,000 mL/min. The crossover from the small pump to the large pump is about 300 mL/min. Valves enable either bottle to supply either pump with the single-point delivery tube or the multipoint delivery tube. Another valve to

each bottle directs any return flow to run back into the inactive bottle, so that this flow can be measured. One more valve at each bottle supplies each with refill water from the tunnel supply when needed. All the valves are pneumatically actuated via air lines controlled by solenoids. Electronic relays under computer control operate the solenoids. Voltage signals delivered by digital-to-analog converters under computer control govern the pumps, and an analog-to-digital converter with multiplexor converts the transducers' current-loop output to digital format, which is recorded by the same computer used for valve and pump control.

6.11.1.2.3 Seepage-Capture System

Hardware for seepage capture at each zone consists of a horizontally mounted U-shaped PVC curtain, which captures seepage from the rock under the release zone and funnels it into twin collection bottles designed similarly to the supply bottles. Figure 6.11.1-2 shows the arrangement of the capture curtains relative to the packer system. The length of the capture curtain is four meters, twice over that of the release zone (1.83 m in length). A valve at the bottom of each bottle allows drainage into a continuous drain, while another valve at the top of each determines whether collected water can enter. This configuration allows drainage of one bottle without interruption of seepage collection and measurement in the other. The collection system also utilizes differential-pressure transducers to obtain head (and therefore quantity of water) in the bottles. The diameter of 20 cm for the collection system implies that a volume of 0.03 liters of seepage water needs to be accumulated for every mm rise of water level. As with the supply system, the collection system is serviced by computer recording and control system.

6.11.1.2.4 Air-Injection System

The water supply system supports an air-injection system for determining the air permeability of each delivery zone. Incorporated into the single-point delivery tubes are valves that allow water to drain from these tubes and that allow introduction of air into each zone. Mass-flow controllers deliver air at constant-mass flux through the single-point injection line. Dedicated absolute-pressure transducers for each zone enable air-pressure measurements during air injection and thus allow calculation of air permeability. The mass-flow controllers are computer-controlled, and air-flow rates are recorded by the data acquisition system.

6.11.1.2.5 Control and Recording System

In addition to continuous recording of all transducer outputs, the computer interface for the supply and collection systems enables the processes to be manually or automatically controlled. The computer incorporates remote-control capability, so that the systems can be started and controlled through computer networks.

Figure 6.11.1-3 shows the front panel from the user interface on the computer control. Depicted are the supply bottles at the top and the collection bottles at the bottom. There are three completely independent systems, one for each zone. The zone 1 system is shown operating on automatic control, using the low flow pump at 50% flow capacity from Bottle A. Return flow is being collected in Bottle B. Seepage is being collected in Bottle B while Bottle A is draining. Other zones are not operating. Paths for water highlight themselves with thicker lines when operational. The toggle switch on the zone 1 control panel is on, to enable automatic operation.

When this switch is enabled, manual operation of the valve and pump controls is disabled, and they merely function as indicators from which to monitor the automatic operation. A separate automation program then operates the controls much as an operator would.

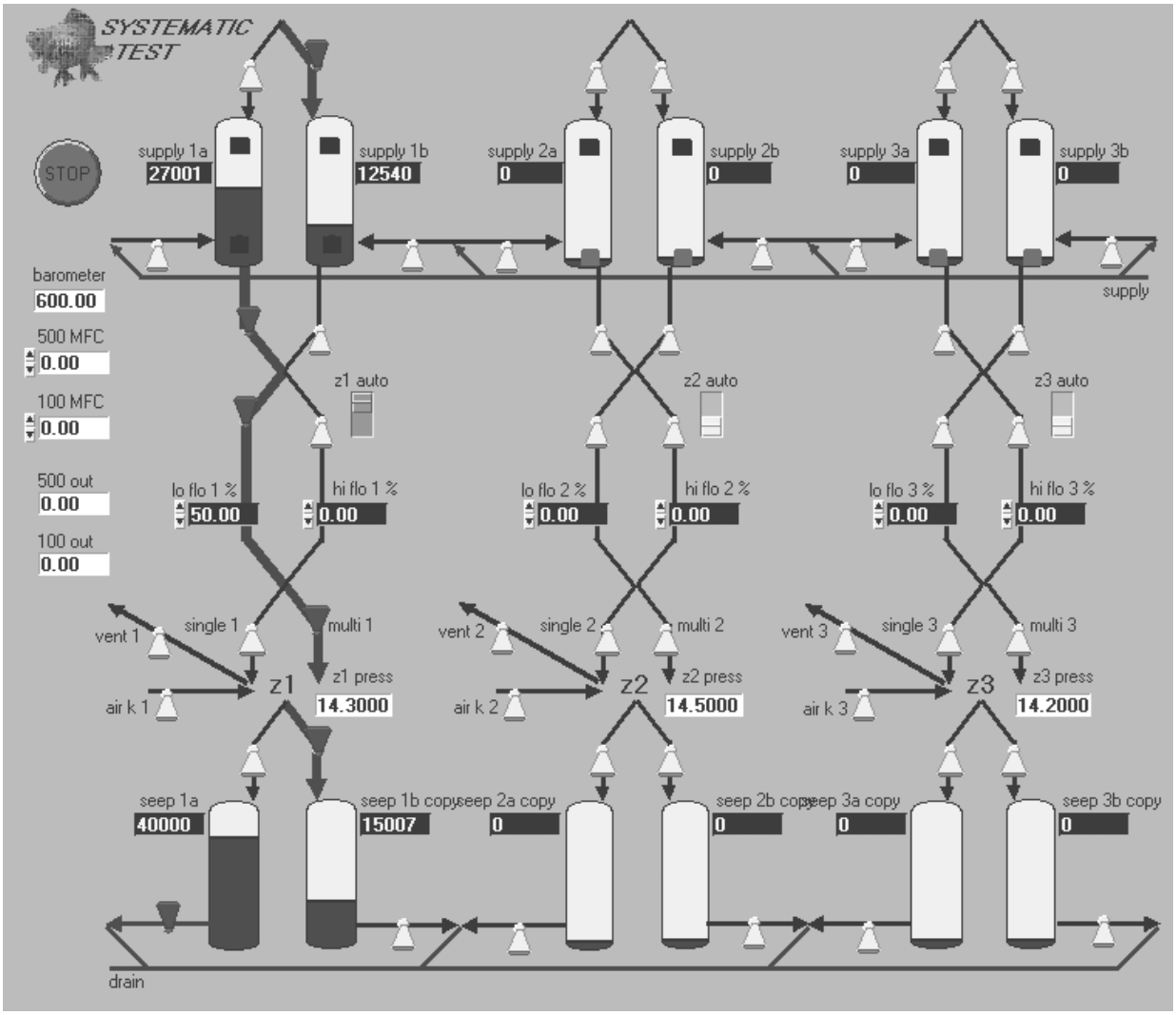

Figure 6.11.1-3. Schematic Illustration of Front Panel for Control Interface on Computer

6.11.1.2.6 Automation Program

The automation program takes two basic parameters from the operator, that of pump rate and that of water-delivery zone selection. All other aspects of control are performed automatically. Pumping starts in Bottle A, while Bottle B collects return water, until the water content read by the Bottle A transducer indicates that this bottle is nearly empty. At this point, Bottle B is filled to a preset limit (as read by the transducer) if it is not at this limit already. When Bottle B is filled, pumping is switched from Bottle A to Bottle B. Bottle A is now able to collect any return flow. While filling from the main water supply, bottles are unable to collect return flow. Because filling is a rapid event, this pause in collection does not affect data collection. If filling does not occur rapidly enough to prepare the second bottle before the first one runs dry, the pump is

switched to the second bottle even before it is completely full when a lower limit is passed (as read by the transducer of the first bottle). To obtain a smooth record of all the water delivered to a zone; the water content of a bottle being filled is subtracted from the water content at the start of that bottle's filling. This value is in turn added to the total recorded when the last bottle switch occurred. A similar arrangement works for the return-water record.

6.11.1.2.7 System Fail-Safes

To avoid overfilling of the bottles or the pumps running dry in the event of a failure in the automatic control system, or inadvertent use of the controls on manual setting, the system employs float switches at the top and bottom of the bottles as a backup to the automation. The bottom float switches when triggered (depicted in light gray in Figure 6.11.1-3) for the zone 2 and zone 3 systems, forcing the pumps on these to stay off even if requested by a user or automation system to operate. The top float switches interrupt the electrical current to the fill valves when triggered. In the event of a computer shutdown such as during a power failure, all the relays and pump controls are turned off, causing the system to default to a stand-by mode.

6.11.2 Systematic Testing Results and Observations

Sets of completed tests in four low-angle boreholes (belonging to Group I according to the nomenclature in Figure 6.11.1-1), ECRB-SYBT-LA#1, ECRB-SYBT-LA#2, ECRB-SYBT-LA#3, and ECRB-SYBT-LA#4, will be described below in the order in which they were performed.

6.11.2.1 Air-Injection Tests and Liquid-Release Tests in LA2, Initiated on May 11, 2000

ECRB-SYBT-LA#2 (hereafter referred to as LA2) is collared at ECRB Cross Drift Station CD 17+26. Three packers isolated the borehole into three zones, so that the distance from the middle of the 1.83 m liquid-release zone to drift crown is respectively 1.58 m, 2.84 m, and 4.10 m for zone 1, zone 2, and zone 3.

Air-permeability estimates for the three zones from the steady-state pressure response to constant-flow-rate air-injection tests is tabulated in Table 6.11.2-1 (DTN: LB00090012213U.001 [153141]).

Table 6.11.2-1. Air-Permeability Estimates for the Three Zones in Borehole LA2

Zone ID	Zone Length (m)	Air Permeability k (m^2), for Packer Inflation at 27.5 PSI	Air Permeability k (m^2), for Packer Inflation at 32.5 PSI
LA2 zone 1	1.83	2.5×10^{-11}	2.3×10^{-11}
LA2 zone 2	1.83	2.7×10^{-11}	2.5×10^{-11}
LA2 zone 3	5.18	1.1×10^{-11}	0.95×10^{-11}

DTN: LB00090012213U.001 [153141]

Pressure response and injection flow rates are shown in Figure 6.11.2-1. The fast rise and decay of the pressure in response to initiation and termination of air injection indicate very little storage effect. Zone 3 is longer than the designed 1.83 m liquid-injection section because the last zone for air injection begins at the end of the third packer and extends to the end of the borehole. The air-permeability measurements were repeated for a lower and higher inflation pressure. The repeatability of the two measurements for different packer inflation pressure indicates that there was little leakage between zones from possible improper sealing of the packers.

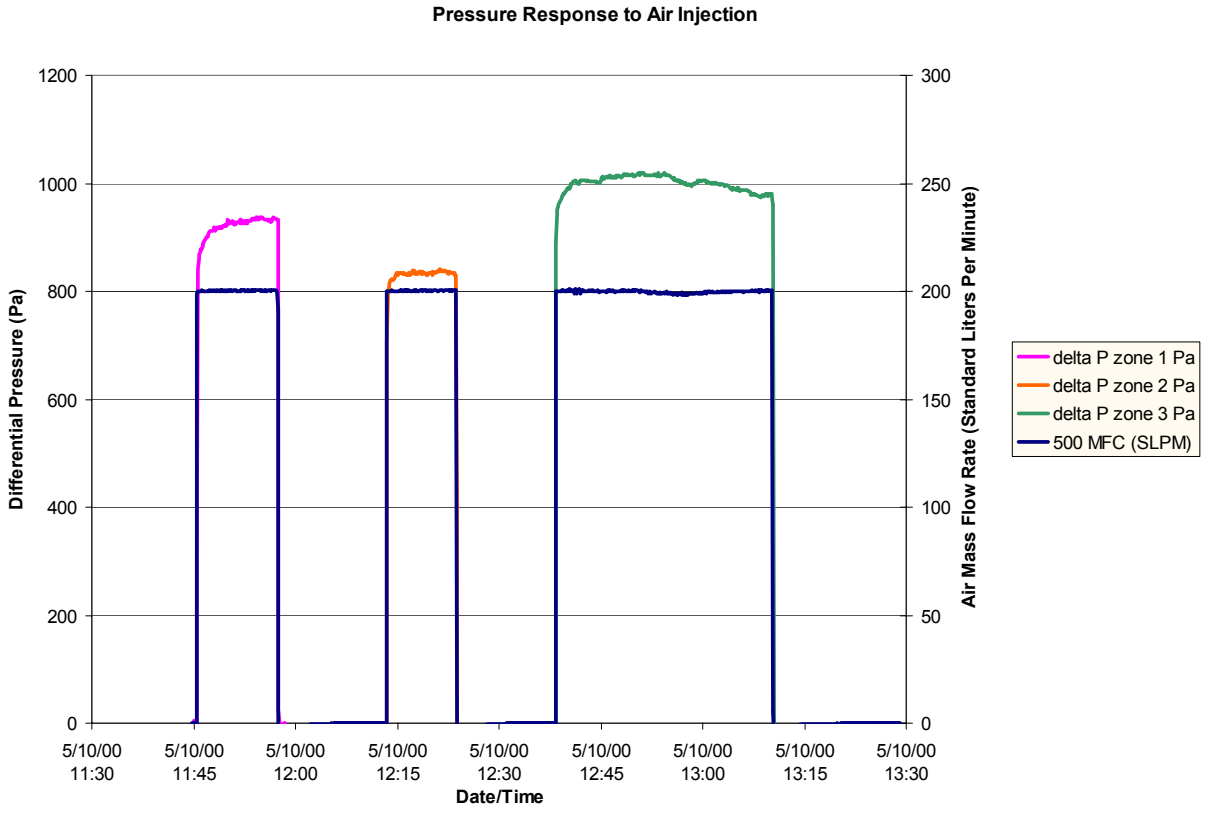

DTN: LB00090012213U.001 [153141];
Output-DTN: LB0110SYST0015.001

Figure 6.11.2-1. Pressure Responses (Red, Orange, and Green) to Constant Mass Flow of Air-Injection (Blue) for Estimation of Fracture Permeability in ECRB-SYBT LA#2

Following the air-injection tests in all three zones, a liquid-release test was conducted in zone 1 only. A large liquid release rate of ~450 mL/min was initiated in zone 1 through one single release point in the 1.83 m injection zone. No return flow was detected, indicating that all released water was able to enter the rock formation through the injection section. Figure 6.11.2-2 gives the cumulative volume of water supplied to zone 1 (left axis) and the cumulative volume of water collected in the seepage-collection system (right axis) as a function of time. Figure 6.11.2-2 indicates that the initiation of water release was at 9:31 and the start of seepage collection was at 12:00 (although a wet spot made its first appearance at the drift ceiling at 11:10, and water began to seep shortly after). Understandably, a time lapse existed between the first wetting of the drift ceiling and the time when enough water was collected in the seepage-collection cylinder to cause a measurable change in the water level (nominally, a 3 mm change in water level for every 100 mL of water). The wetting of the drift ceiling expanded with time, and by 15:15, the wetted area was on the order of 0.8 m^2. The following morning (May 12, 2000), it was noted that in addition to the seepage from the wetted drift ceiling directly below the injection zone, water was also seeping through a rock-bolt borehole beyond the edge of the capture curtain. The capture curtain was 4 m in length and was centered approximately below the 1.83 m liquid injection zone. Seeped water from the rock-bolt borehole was missed by the seepage collection data acquisition and may be related to the recorded decrease in seepage rate after ~20:00 on May 11 (as shown in Figure 6.11.2-2). The water release into zone 1 was terminated at 8:36 on May 12, 2000.

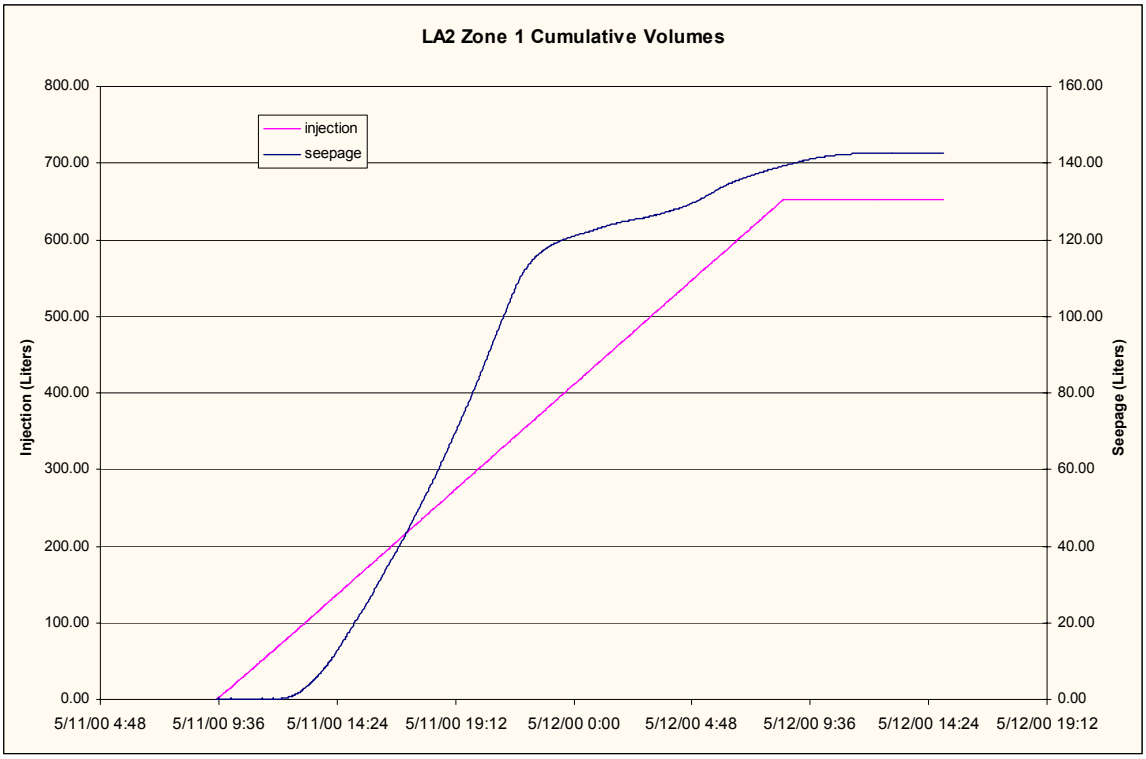

DTN: LB00090012213U.002 [153154];
Output-DTN: LB0110SYST0015.001

Figure 6.11.2-2 Cumulative Water Supplied to ECRB-SYBT-LA#2 Zone 1 and Cumulative Seeped Water into the ECRB Cross Drift for a Test Performed on May 11–May 12, 2000

6.11.2.2 Liquid-Release Test in Zone 1, Zone 2, and Zone 3 in LA2, Initiated on May 17, 2000

Between 11:45 and 11:49 on May 17, 2000, liquid release into zone 1, zone 2, and zone 3 was initiated (Figure 6.11.2-3). The multipoint mode of injection was used so that water was evenly spread along each 1.83 m zone. A liquid release rate of 30 mL/min was intended for every zone. However, for the same specified water-release pump rate, the actual release rate to each zone would differ because of the difference in zone height. Subsequent adjustments to the pump rate may be made as guided by the actual release rate recorded by the data acquisition system. Figure 6.11.2-3 shows the cumulative volume of water supplied to zone 1, zone 2, and zone 3 (left axis) and the cumulative volume of water seeped (right axis). Note that seepage from zone 1 was recorded beginning at 3:11 of May 18, 2000 (none from zone 2 or zone 3). The next morning (May 18, 2000), it was found that the software control of the filling function to supply Bottle B was not functioning properly. Delivery of water to all three zones was therefore terminated at 9:08, May 18, 2000. Note that data in Figure 6.11.2-3 as recorded by the data acquisition system show that the cumulative volume of supply water ceases to increase after May 17, 2000 (21:23), May 18, 2000 (0:39), and May 18, 2000 (7:13) respectively for zone 1, zone 2, and zone 3. These were the times at which Bottle A was "emptied," and water supply to the rock was switched to Bottle B. However, field observations showed that refill in Bottle B was being mechanically controlled by the float switches. Consequently, that bottle stayed at the full level and water was continually being released into the rock formation, presumably at the prevailing pumping rate prior to the fill problem. Therefore, although Figure 6.11.2-3 gives the false impression of no cumulative increase in supply water, in fact water was being supplied to the rock formation from Bottle B, possibly at the prevailing rate (as supplied by Bottle A), until May 18 at 9:08.

The noisy "swings" in the cumulative seepage data in Figure 6.11.2-3 (and in later figures) may be attributed to the slow response time in differential-pressure transducers to the atmospheric fluctuations. While the water level in the seepage-collection cylinders responded instantaneously to the atmospheric fluctuations, filters placed in the differential-pressure-transducer ports caused a delay response. The filters were originally put in place to keep the ports "clean"; they were removed from use in May 2001.

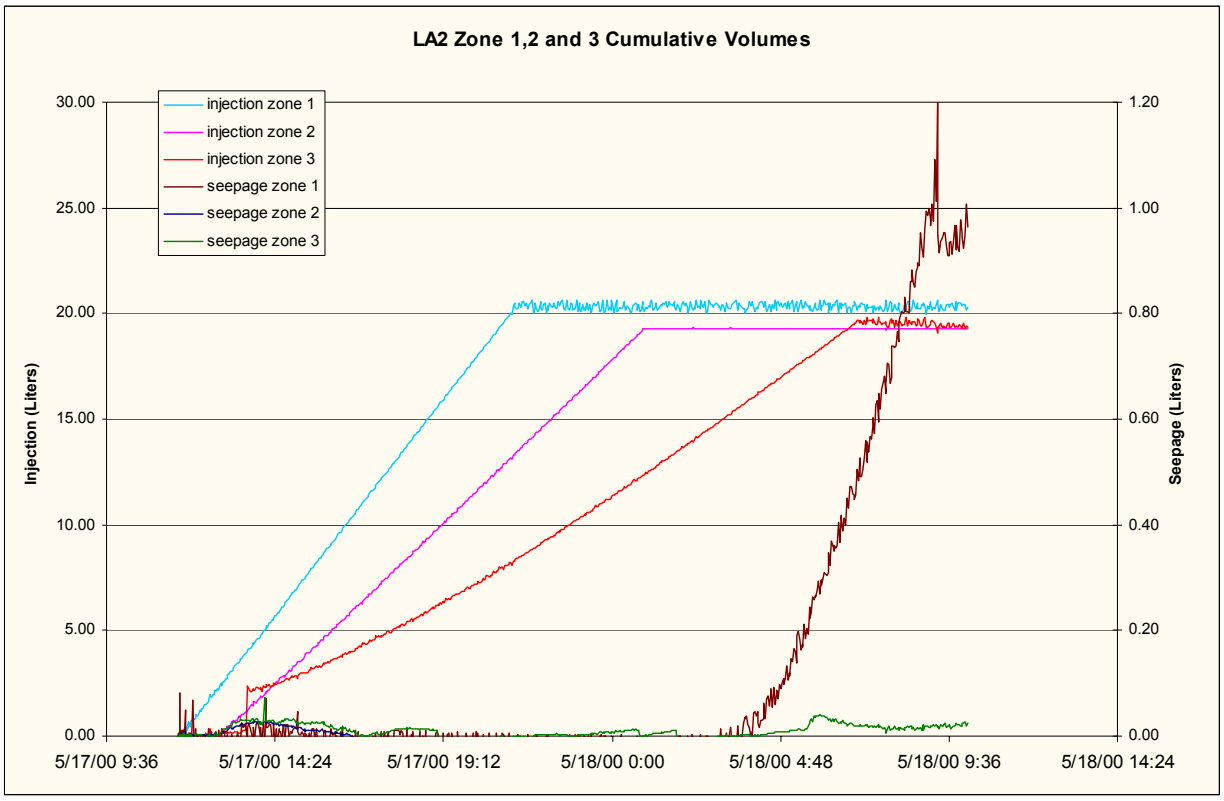

DTN: LB00090012213U.002 [153154];
Output-DTN: LB0110SYST0015.001

Figure 6.11.2-3. Cumulative Water Supplied to ECRB-SYBT-LA#2 Zone 1, Zone 2, and Zone 3 and Cumulative Seeped Water into the ECRB Cross Drift for Tests Performed on May 17–May 18, 2000

6.11.2.3 Liquid-Release Test in Zone 1, Zone 2, and Zone 3 in LA2, Initiated on May 23, 2000

The faulty software control of the filling function in the May 17, 2000, tests was resolved. Liquid-release tests from six multiple points in zone 1, zone 2, and zone 3 were resumed at 14:25 on May 23, 2000 at the intended rate of 30 mL/min. Data for the three zones will be discussed separately.

6.11.2.3.1 Zone 1

Figure 6.11.2-4 shows cumulative supply (left axis) and cumulative seepage volume (right axis) as a function of time from May 23, 2000, to June 1, 2000, 11:14, when water release was terminated. Data show that seepage collection initiated on May 24, 2000, 13:19, although a wetted spot ~0.5 m in diameter was observed as early as 8:40. The rate of supply water was on the order of 28 mL/min, and the rate of seepage stabilized to ~4 to 5 mL/min within a week.

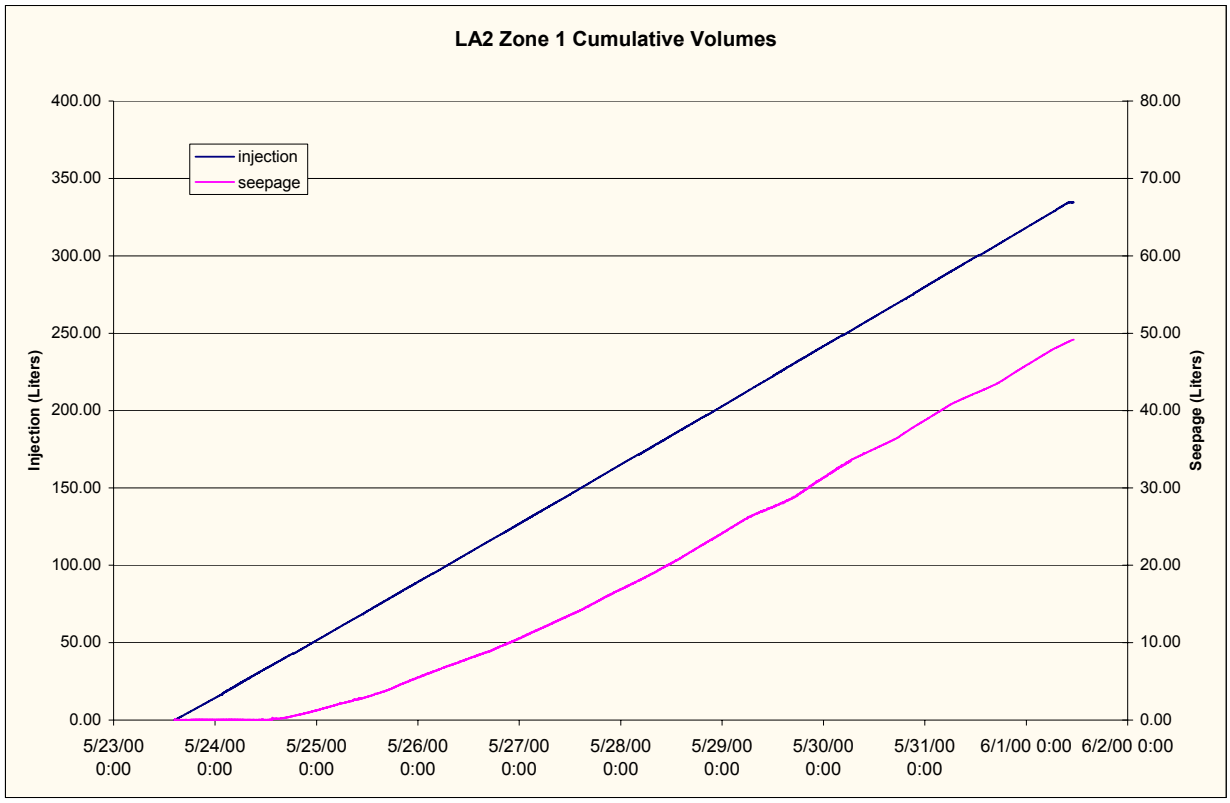

DTN: LB00090012213U.002 [153154];
Output-DTN: LB0110SYST0015.001

Figure 6.11.2-4. Cumulative Water Supplied to ECRB-SYBT-LA#2 Zone 1 and Cumulative Seeped Water into the ECRB Cross Drift for Tests Performed on May 23–June 1, 2000

6.11.2.3.2 Zone 2

Water release continued from May 23, 2000, through June 8, 2000. Multiweek liquid-release tests were stopped and restarted periodically to keep data files at a manageable size. Every time the software control routine was restarted, new data files with date/time stamp were generated, and cumulative supply and seepage reference was restarted at zero. Figure 6.11.2-5 shows cumulative supply (left axis) and cumulative seepage volume (right axis) in two graphs: (a) from May 23 to June 1 and (b) from June 1 to June 8, since the test was stopped on June 1, 2000, 11:14 and restarted at June 1, 11:23. Figure 6.11.2-5a shows that seepage from zone 2 initiates at 20:26, May 29, 2000. Step-like structures are very prominent in the cumulative volume of seepage water data in Figure 6.11.2-5b, indicating two different slopes and therefore different rates of seepage. The periods of larger slope (higher seepage rate of ~2-3 mL/min) in Figure 6.11.2-5b can be correlated to evenings and weekends when the underground tunnels were closed for access and the ventilation system was not in operation. Data in Figure 6.11.2-4 for zone 1 also give different slopes for seepage-water volume versus time, depending on whether ventilation is on or off. The step-like signature in Figure 6.11.2-4 is subtler than that in Figure 6.11.2-5b because of the higher seepage rate there. That water seeping into the drift has partly evaporated places uncertainty on the seepage data, because even when the ventilation is not in operation in the evenings and on weekends, the relative humidity in the underground tunnels is

still far below 100%. As a result, while data in Figure 6.11.2-4 and Figure 6.11.2-5 give a measure of the amount of water lost to evaporation resulting from active ventilation, they do not provide information on the amount of water lost to evaporation in the absence of active ventilation. In response to these initial results, we have (for subsequent tests) modified the systematic measuring system to incorporate measurements of relative humidity and evaporation rate (from an open pan) in the tunnel space between the drift crown and the seepage-collection PVC curtain enclosure. No direct measurement system exists to ascertain the evaporation rate from within the fracture system.

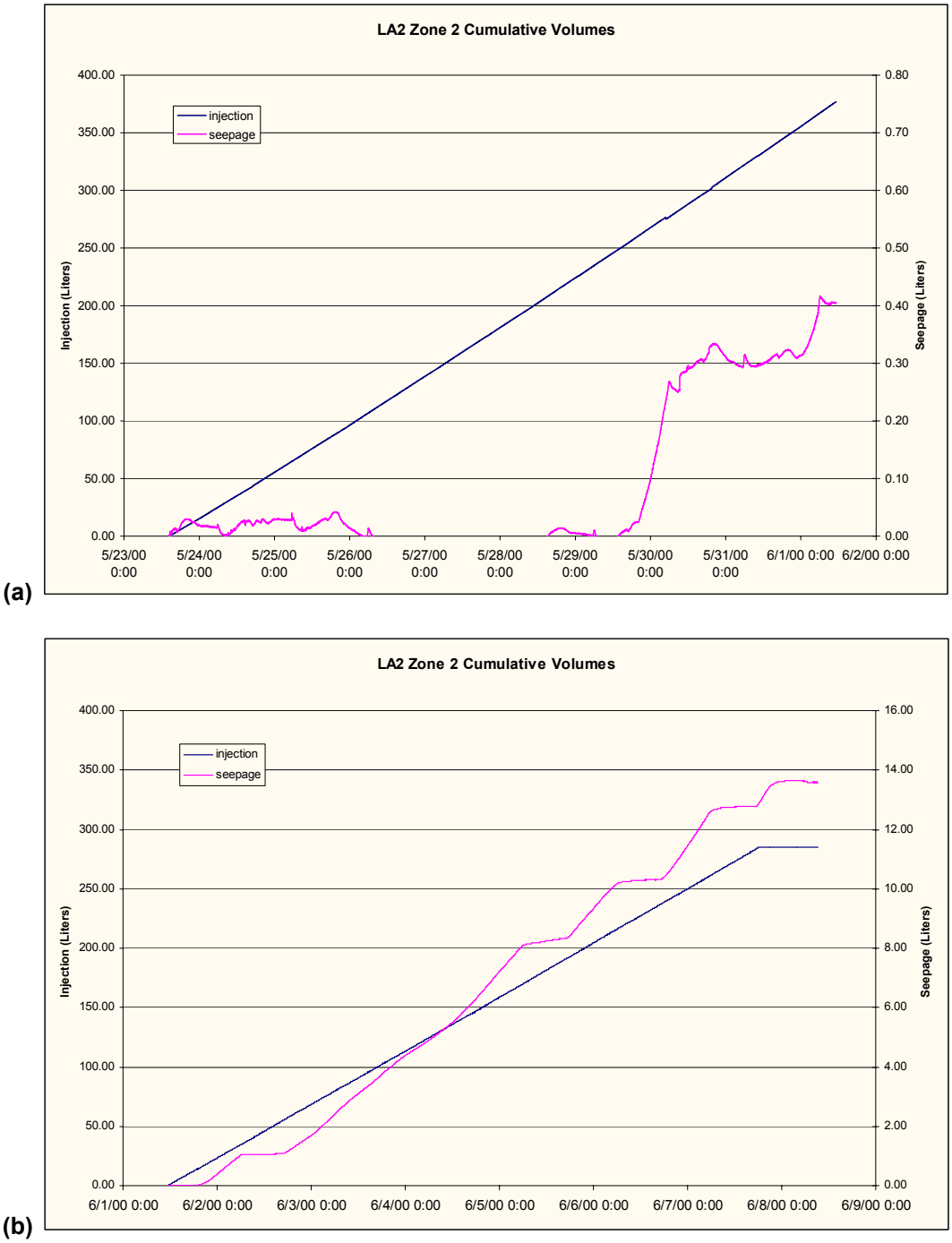

DTN: LB00090012213U.002 [153154];
Output-DTN: LB0110SYST0015.001

Figure 6.11.2-5. Cumulative Water Supplied to ECRB-SYBT-LA#2 Zone 2 and Cumulative Seeped Water into ECRB Cross Drift for Tests Performed on May 23–June 8, 2000: (a) May 23–June 1, 2000 (b) June 1–June 8, 2000

6.11.2.3.3 Zone 3

Cumulative supply and cumulative seepage data for zone 3 between May 23, 2000 and June 27, 2000, are presented in Figure 6.11.2-6a through Figure 6.11.2-6d. Because of unanticipated experimental problems concerning the interface between the software control and the valves controlling the water supply system for this zone, the release of water was interrupted for two periods over a total duration of 34 days of testing. The periods where no water was supplied were (1) two days between May 30 and June 1, and (2) 11 days between June 3 and June 14. The problem was fully corrected from June 14 onwards, and the first indication of seepage water being collected in the seepage bottles for zone 3 was recorded by the data acquisition system at 12:00a.m. June 26, 2000. Other testing activities in the underground tunnel necessitated the termination of water release in zone 3 (as well as monitoring of data), only about 8 hours after the first onset of seepage.

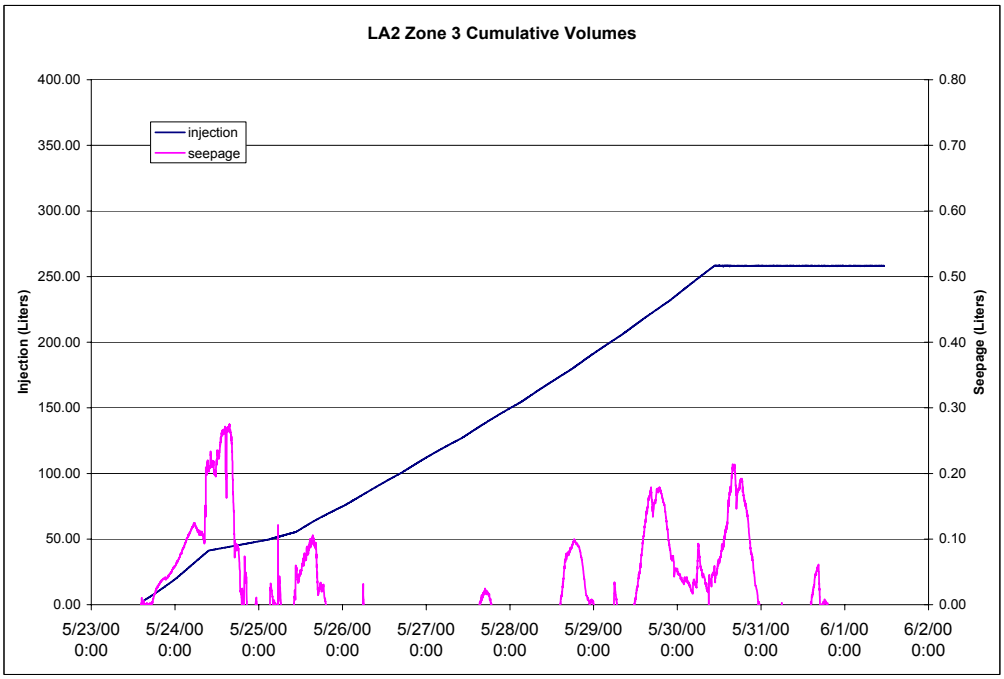

(a)

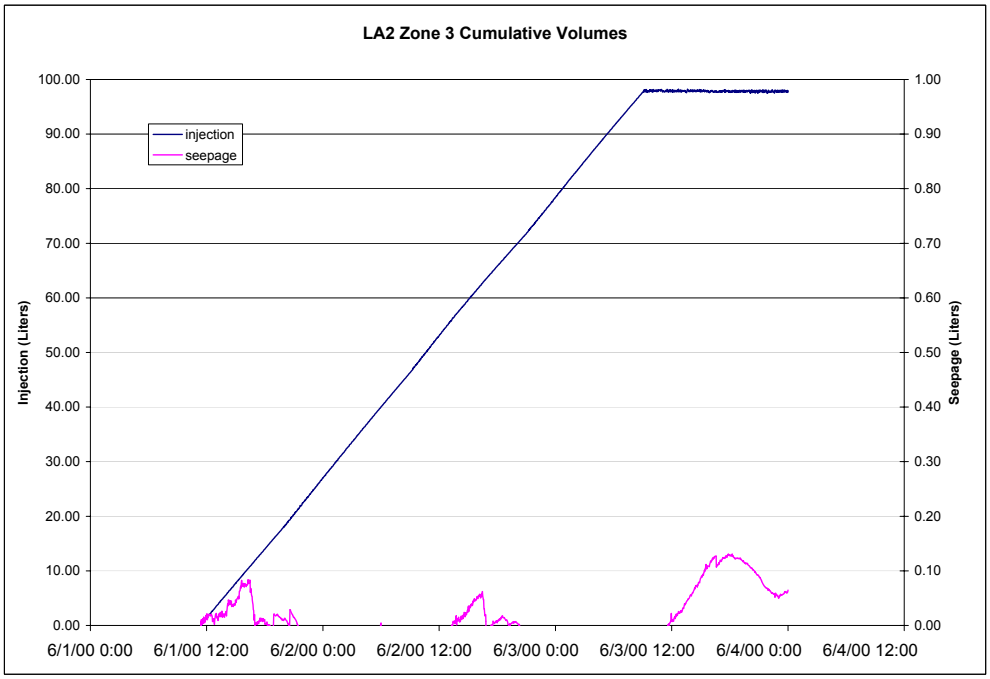

(b)

DTN: LB00090012213U.002 [153154];
Output-DTN: LB0110SYST0015.001

Figure 6.11.2-6. Cumulative Water Supplied to ECRB-SYBT-LA#2 Zone 3 and Cumulative Seeped Water into ECRB Cross Drift for Tests Performed on May 23–June 27, 2000: (a) May 23–June 1; (b) June 1–June 3; (c) June 14–June 18; and (d) June 18–June 27

(c)

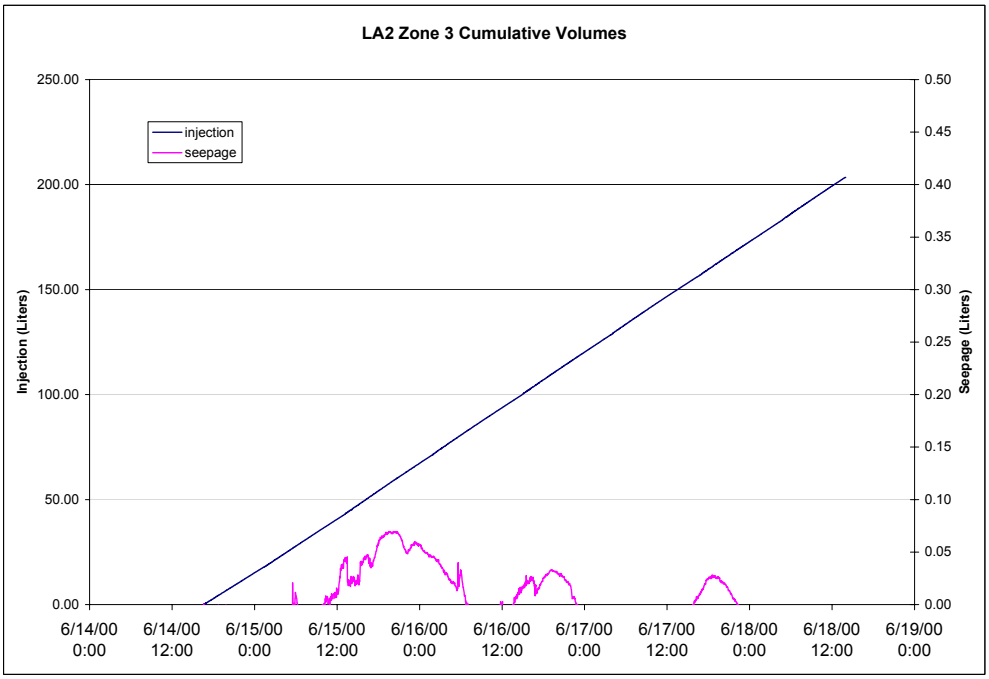

(d)

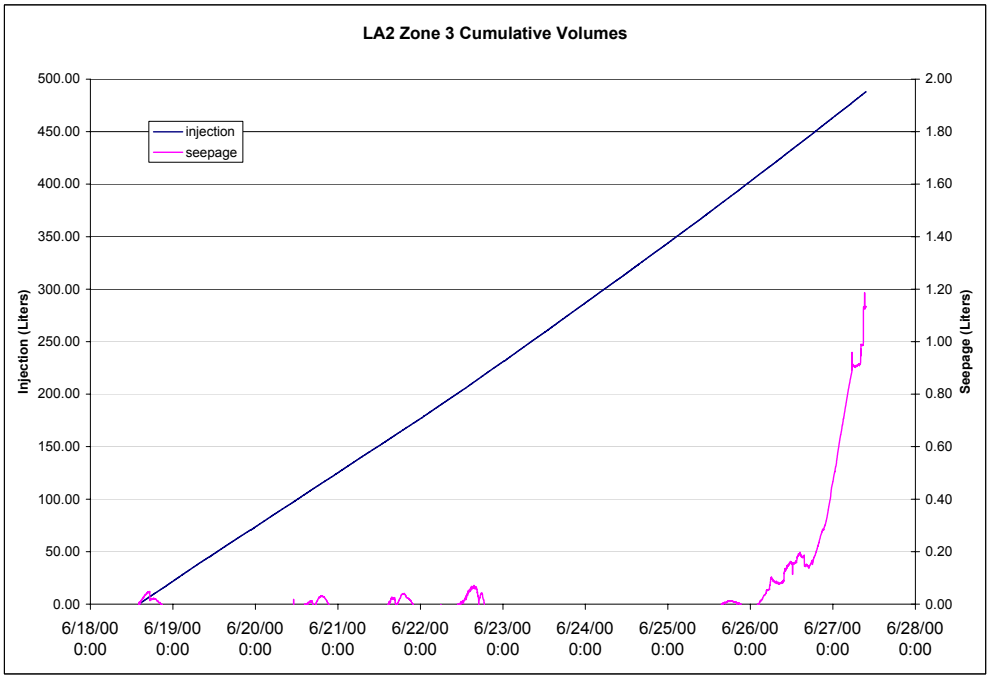

DTN: LB00090012213U.002 [153154];
Output-DTN: LB0110SYST0015.001

Figure 6.11.2-6. Cumulative Water Supplied to ECRB-SYBT-LA#2 Zone 3 and Cumulative Seeped Water into ECRB Cross Drift for Tests Performed on May 23–June 27, 2000: (a) May 23–June 1; (b) June 1–June 3; (c) June 14–June 18; and (d) June 18–June 27 (continued)

6.11.2.4 Liquid-Release Test in Zone 2 and Zone 3 in LA2: October 23–December 1, 2000

Other activities in the ECRB Cross Drift prevented the redeployment of systematic testing equipment for four months after the tests described in the previous section (6.11.2.3). In this later set of testing, liquid-release tests were repeated in zone 2 and zone 3 of LA2, specifically to evaluate the impact of evaporation from active ventilation and less-than-100% relative humidity on seepage data. The following modifications to the test design and measuring system were made since the completion of the previous test in June 2000. First, additional curtains were installed on the two ends of the V-shaped seepage-capture PVC curtains shown in Figure 6.11.1-2, to mitigate drying of the wetted drift crown from ventilation. Second, humidity and temperature sensors were placed within the curtain enclosures of zone 2 and zone 3 to investigate the correlation of humidity conditions to seepage data. Also, a camera was installed to observe the drift ceiling below the injection section of zone 2 to monitor the evolution of wetting.

Cumulative water supply and cumulative seepage data for zone 2 and zone 3 are shown in Figure 6.11.2-7. Data show that the first recorded seepage (as indicated by a rise in water level in the seepage collection cylinder) occurred on October 31 at ~20:00, for both zone 2 and zone 3. Observations taken periodically of the drift ceiling below zone 2 indicate that a wetted area first appeared on October 27 around 8:00 and expanded with time. The wetted area on the drift ceiling could be estimated by counting the number of ground-support wire-mesh grids it covered. Observations indicate that by November 7, 2000, the wetted area had stopped expanding and had become stabilized at 6.8 m^2. Derivatives of the cumulative supply and cumulative seepage from Figure 6.11.2-7 give the rates of supply and seepage. Supply rate, seepage rate, and relative humidity and temperature within the capture curtain enclosure for zone 2 and zone 3 are respectively shown in Figure 6.11.2-8 and Figure 6.11.2-9. Note that the relative humidity was on the order of 35% prior to initiation of seepage on October 31, 2000. Coincidentally, the vent line in the ECRB Cross Drift collapsed on October 31, 2000, cutting off the ventilation. Note that the humidity within the capture curtain enclosures of zone 2 and zone 3 rose to almost 90% by November 7, 2000. Since the collapse of the vent line, ventilation was restored in the ECRB Cross Drift only partially (on and off) throughout the current set of tests, and the humidity reading varied with time between the preseepage value of 35% to the high of 90%.

Figure 6.11.2-8 and Figure 6.11.2-9 show that the seepage rates in both zone 2 and zone 3 track the relative humidity; that is, seepage rates increase and decrease with the rise and fall of relative humidity values. The seepage rate in zone 3 is higher than that in zone 2, reaching a high of about 6 mL/min. This may result from the higher water-release rate in zone 3 (~38 mL/min, as compared to ~34 mL/min in zone 2). It is not known whether the smaller evaporation component (from a smaller wetted area on the drift ceiling than that within zone 2) that existed for zone 3 possibly led to the higher seepage in zone 3. This is because our measuring system had only one camera positioned to monitor zone 2, and the vent-line collapse and subsequent delay in repair has prevented access to the LA2 test site for direct observation of the drift ceiling. Note also that there were several brief periods of interruption of liquid release on November 26, 29, and 30 (these show up as data gaps in Figure 6.11.2-7) results from problems with network-connection power outages and the equipment-computer interface. These control-program shutdowns required a few restarts of liquid injection. Liquid release to zone 2 and zone 3 was terminated on December 1, 2001. Data in Figure 6.11.2-7 and Figure 6.11.2-8 indicate that recorded seepage ceased within 11 hours of liquid-release termination.

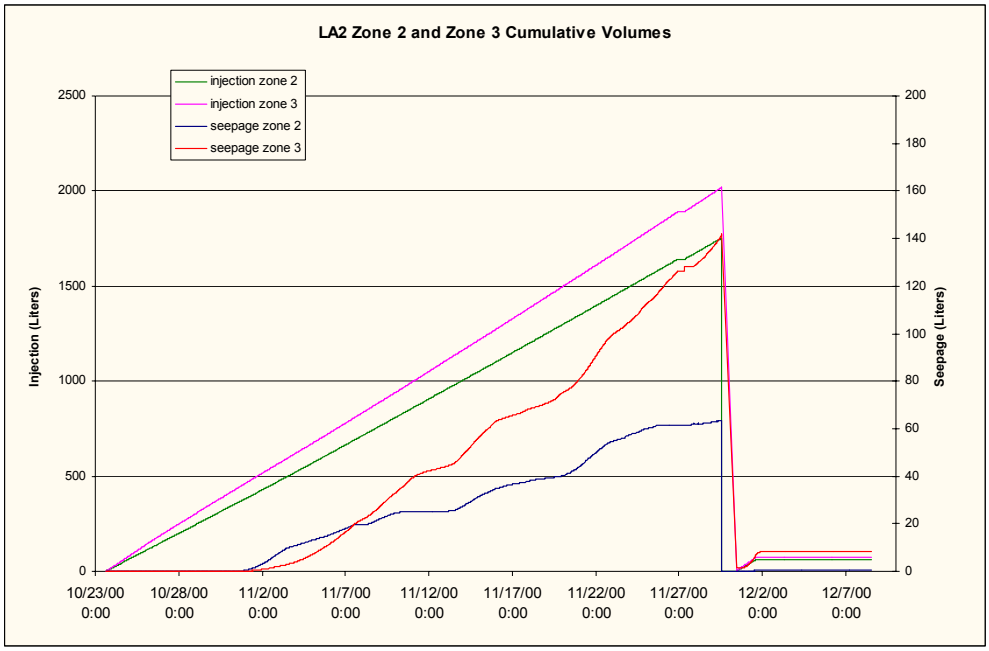

DTN: LB0110ECRBLIQR.003 [156877];
Output-DTN: LB0110SYST0015.001

Figure 6.11.2-7. Cumulative Water Supplied to ECRB-SYBT-LA#2 Zone 2 and Zone 3 and Cumulative Seeped Water into ECRB Cross Drift for Test Performed on October 23, 2000 to December 1, 2000

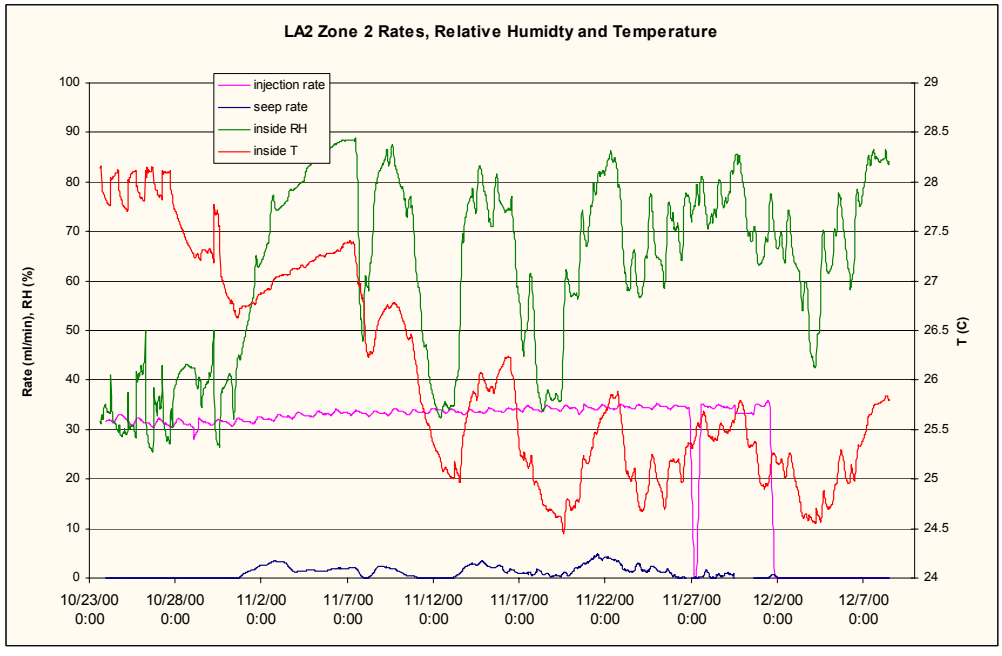

DTN: LB0110ECRBLIQR.003 [156877];
Output-DTN: LB0110SYST0015.001

Figure 6.11.2-8. Supply Rate, Seepage Rate and Relative Humidity and Temperature for Liquid-Release Test Performed in ECRB-SYBT-LA#2 Zone 2 on October 23, 2000, to December 1, 2000

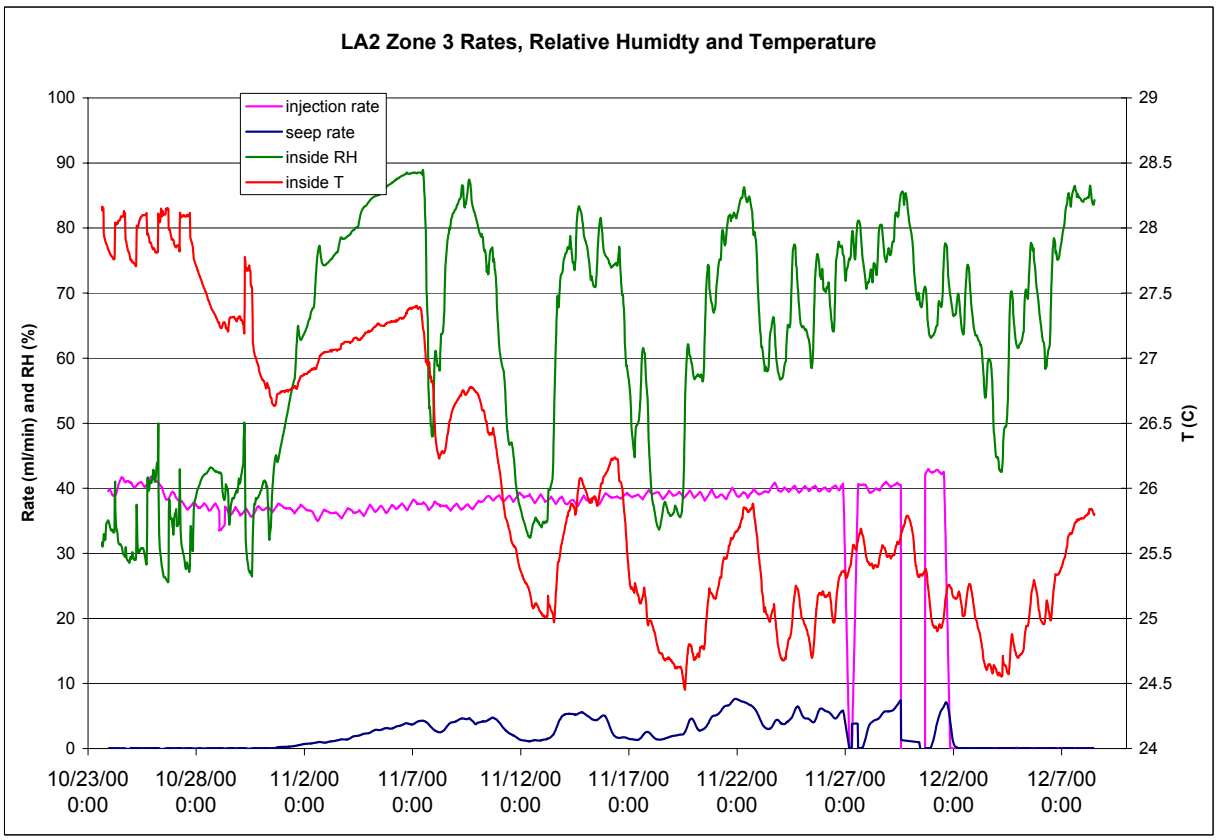

DTN: LB0110ECRBLIQR.003 [156877];
Output-DTN: LB0110SYST0015.001

Figure 6.11.2-9. Supply Rate, Seepage Rate, and Relative Humidity and Temperature for Liquid-Release Test Performed in ECRB-SYBT-LA#2 Zone 3 on October 23, 2000, to December 1, 2000

6.11.2.5 Liquid-Release Test in Zone 2 of LA1: December 20, 2000–January 2, 2001

Similar to ECRB-SYBT-LA#2, LA#1 is a low-angle near-horizontal borehole (inclination of 15^{o} from the Cross Drift axis), drilled from the ECRB Cross Drift crown. It is collared at ECRB Cross Drift Station CD 17+49, immediately outside of the first bulkhead. Rock fragments that fell into the borehole (postdrilling) caused the borehole to be totally obstructed 8.2 m from the collar to the end of the 20 m long hole. Therefore, only one zone instead of the intended three (as in LA2) was accessible for fluid testing.

Zone 2 was isolated by two inflated packers and nominally at 3.0–4.9 m from the collar. Therefore, height of mid-zone from drift crown was 1.03 m. Liquid release carried out in this zone (denoted as zone 2 in the data acquisition system) took place through the six equally spaced outlet nozzles. To better evaluate the impact of evaporation on the seepage data, investigators installed an evaporation pan within the space enclosed by the seepage capture and end curtains. A differential-pressure transducer monitored the drop in water level from evaporation. Liquid release into zone 2 started on December 20, 2000, 14:56, with a requested pump rate of 30 mL/min. Data (Figure 6.11.2-10) show that the actual water-release rate was 15 mL/min. ECRB Cross Drift was closed and not ventilated during the experimental period, so the test was run and

monitored remotely. A power outage shortly after 12:00 a.m. December 25th terminated the liquid injection and data acquisition at 0:22, December 26, 2000. Power was restored on December 28, 2000, and the data acquisition system was restarted remotely. Unfortunately, the pumps that deliver water could not be restarted properly. Also, observations taken periodically of the drift ceiling show the beginning of a wet spot the morning of December 25th prior to the power outage, indicating the first arrival of water to the drift ceiling. Figure 6.11.2-10a shows that ~103 liters of water has been released into zone 2 at the time of the sign of this first arrival of water at the drift ceiling. Since water release stopped about 15 hours later and could not be resumed, the test did not run long enough to generate seepage. Figure 6.11.2-10a and Figure 6.11.2-10b also show respectively that the relative humidity and temperature within the curtain enclosure remained at about 12% and 26°C throughout the data acquisition period. Figure 6.11.2-10b shows that the data from the evaporation pan indicate the evaporation rate was on the order of 3 mm/day.

The ECRB Cross Drift was reopened January 2, 2001, but other field activities (such as opening of the bulkhead) required the removal of systematic test equipment from the ECRB Cross Drift and prevented resumption of the liquid release test in LA1. Data acquisition in LA1 was terminated on January 2, 2001.

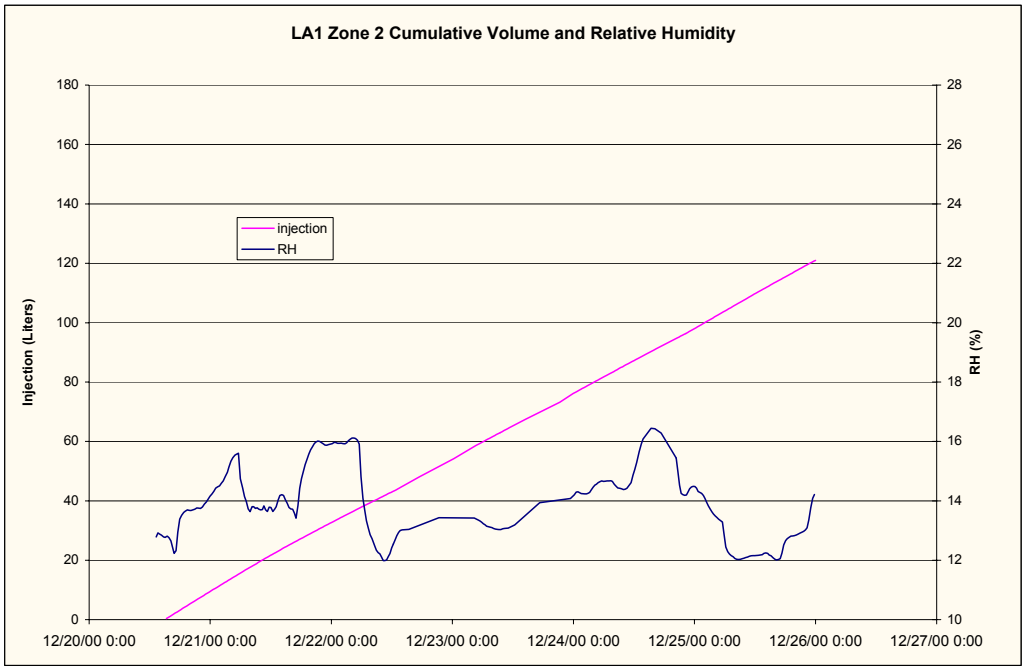

(a)

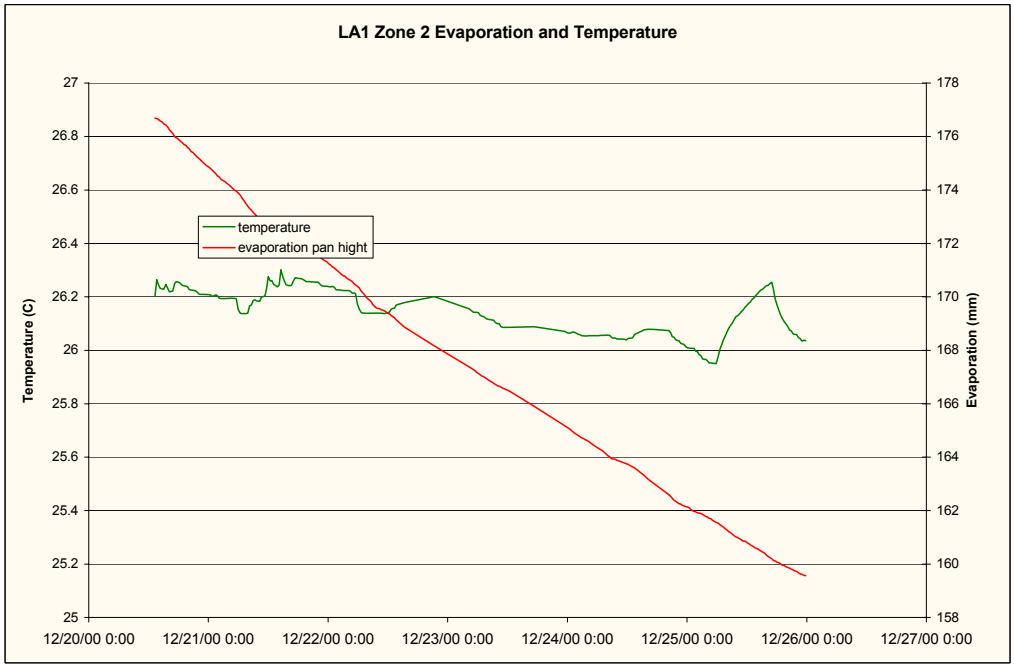

(b)

DTN: LB0110ECRBLIQR.001 [156878];
Output-DTN: LB0110SYST0015.001

Figure 6.11.2-10. (a) Cumulative Water Supplied to ECRB-SYBT-LA#1 Zone 2 for Test Performed on December 20, 2000 to January 2, 2001. Also shown are humidity and (b) temperature, and the water level in the evaporation pan.

6.11.2.6 Liquid-Release Test in Zone 2 of LA1: February 28–April 30, 2001

This test, initiated on February 28, 2001, was a resumption of the test conducted in December 2000. Line release of water over a 1.83 m zone was initially set at the same rate as that of the December tests, ~15 mL/min, actual. Observations show that the first appearance of a wet spot (water arriving at the drift ceiling) was on March 3, 2001, 16:23; that is, about 75 hours after initiation of water release. Figure 6.11.2-11a, which shows the cumulative supply and seepage of water, indicates that about 60 liters of water have been introduced into the formation at this time. The seepage collection system (rise in water level in the seepage collection cylinder) registered the initiation of seepage at ~22:00 on March 15, 12 days since the observation of the first wetting on the drift ceiling. Furthermore, in this period, the actual water-release rate had increased from 14 mL/min to above 20 mL/min. Following March 15, a Thursday, was a three-day weekend when ventilation was turned off, during which time the average injection remained at ~20 mL/min and average seepage was on the order of 1 mL/min. Figure 6.11.2-11b shows that on Monday, March 19 (when ventilation was resumed) the seepage rate decreased dramatically to almost zero. This was true even during the next three-day weekend (March 23 to March 25). Recorded seepage continued to be about zero through the following week. Observations also show that the wetted area on the drift ceiling had shrunk. A study of the plotted data (Figure 6.11.2-11b) indicates that the average release rate during this period has fallen below 20 mL/min to around 18 mL/min. That is, although the request pump rate was constant (at 30 mL/min), the actual injection rate went above 20 mL/min on the weekend of March 16 to 18, and then fell back to ~18 mL/min afterwards. Data therefore indicate that, in general, the actual water-release rate needed to be above 20 mL/min for recorded seepage.

An unplanned interruption of water release occurred on Thursday, March 29, 2001, 4:43, because of an air-compressor problem. Water release was resumed on Tuesday 4/3/2001 9:50, at a higher requested pump rate. Data (Figure 6.11.2-11b) show that the actual injection rate was on the order of 42 mL/min, and seepage-collection data acquisition began to record non-zero seepage at ~20 hours after resumption of water release.

A planned power outage caused another interruption of water release on April 5, 2001, 17:48. The negative slope on the cumulative volume plot indicates no data recorded during this period. (What appears as a positive rate on Figure 6.11.2-11b just before April 9, 2001, 12:08, has no data.) Water release to LA#1 resumed on April 9, 2001, 12:08 (Friday), at an actual rate of ~42 mL/min. Data indicate the onset of seepage at ~20 hours after resumption of water release. The seepage rate increases from ~7 mL/min to ~10 mL/min on April 16, 2001 (Monday). We carried out two planned, deliberate interruptions of water release for duration of less than a day. The first pause of water release occurred on April 16, 2001 (Monday), 15:22. After a pause of 18 hours and 20 minutes, water release was resumed, and seepage was observed ~16 hours afterwards. Then for a second time on April 24, 2001, (Tuesday) at 16:54, water release was interrupted, and then restarted on April 25, 2001, 11:39. Seepage began at ~16 hours afterwards. Following both these planned water-release pauses, the water-release rate was on the order of 42 mL/min, and seepage was on the order of ~ 10 mL/min.

Fall of water level in the evaporation pan indicated that the evaporation rate is on the order of 3 mm/day. Coupling this information with the largest (stable) wetted area estimated from observations of the drift ceiling (~4.5 m^2) would give an upper bound of the evaporation from the wetted drift surface a rate of 9.5 mL/min. Testing in LA1 was concluded on April 30, 2001.

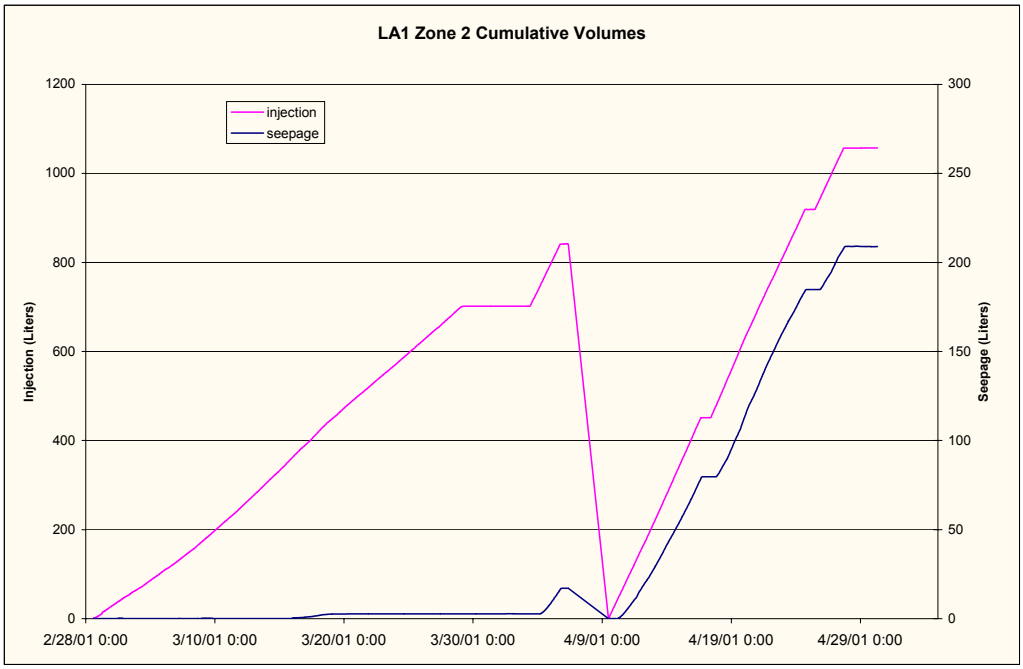

(a)

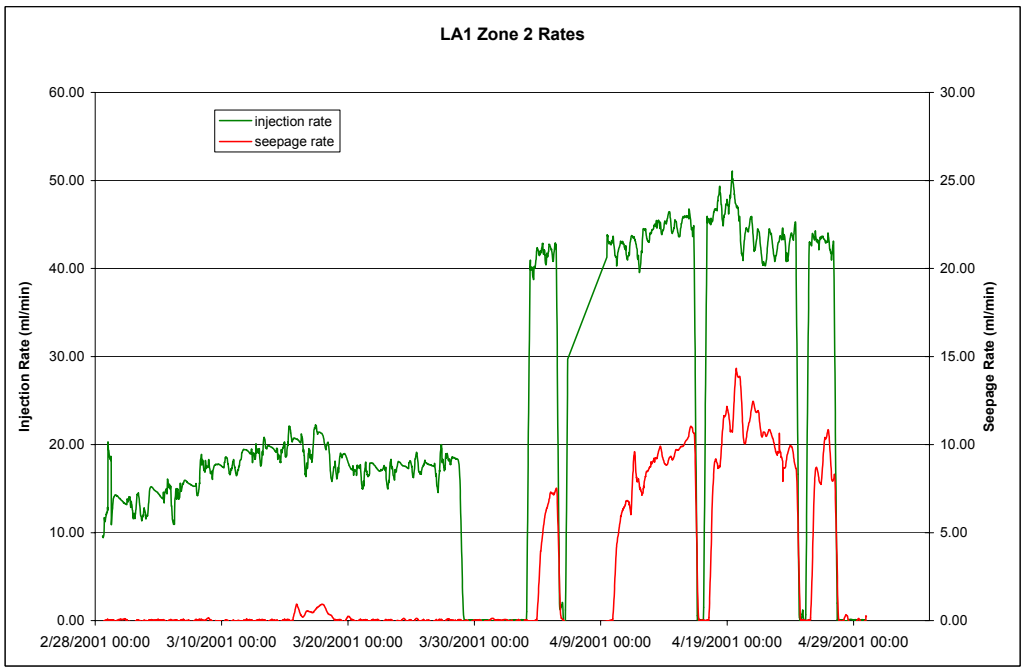

(b)

DTN: LB0110ECRBLIQR.002 [156879]

Figure 6.11.2-11. (a) Cumulative Water Supplied to and Seeped from ECRB-SYBT-LA#1 Zone 2 for Test Performed on February 28 to April 30, 2001; (b) Water Supply Rate and Seeped Rate; (c) Humidity, Temperature, and the Water Level in the Evaporation Pan

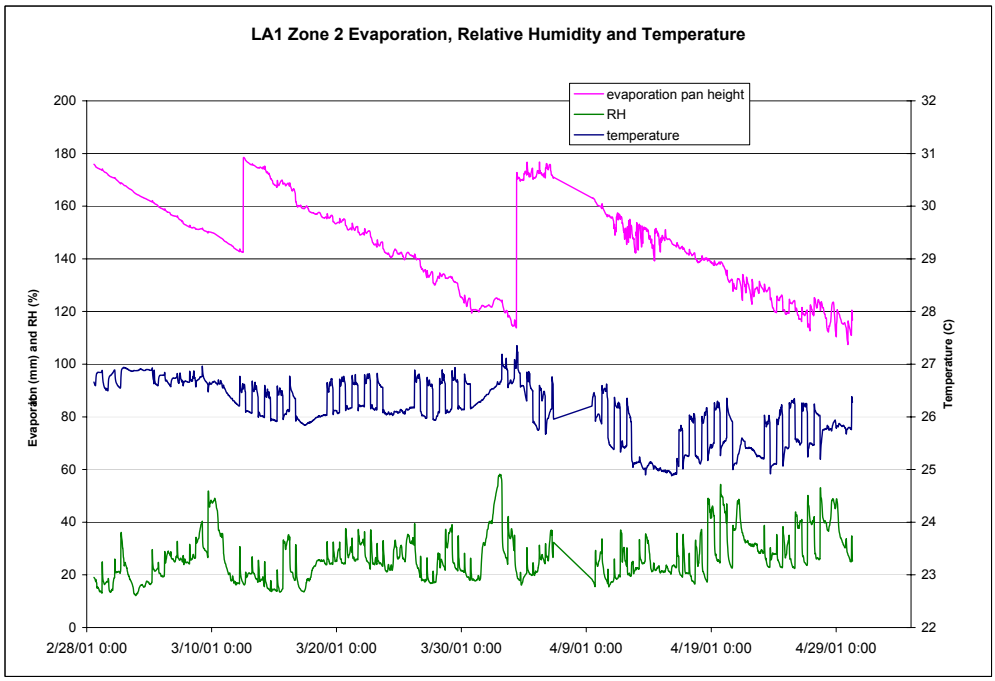

(c)

DTN: LB0110ECRBLIQR.002 [156879]

Figure 6.11.2-11. (a) Cumulative Water Supplied to and Seeped from ECRB-SYBT-LA#1 Zone 2 for Test Performed on February 28 to April 30, 2001; (b) Water Supply Rate and Seeped Rate; (c) Humidity, Temperature, and the Water Level in the Evaporation Pan (continued)

6.11.2.7 Borehole LA3 and Liquid-Release Test in Zone 1, LA3: May 10–June 18, 2001

Tests in borehole ECRB-SYBT-LA#3 (LA3) began on May 10, 2001. This is another 15° low angle hole that was collared at ECRB Station CD 16+95 in the drift crown. The borehole was divided into 3 sections for water release using the systematic hydrological packer system. The three sections for water release spanned 5.5–7.3 m, 10.4–12.2 m and 15.2–17.1 m, respectively, from the collar. The midpoints of each of the zones were therefore 1.7, 2.9, and 4.2 meters respectively above the crown of the drift. While there was no trouble this time with packer placement, the rubber on the first two packer sealing sections could not maintain inflation, due to piercing of the rubber, and therefore could not seal the first two zones of the borehole. It was considered at the time to be primarily a problem for performing successful air-permeability tests for this hole. The water release was thought not to be affected by the lack of inflation because the weight of the packers was thought to provide sufficient sealing by pressing down on the uniflated rubber material at the bottom of the borehole. For any water to get by this seal, there would have to be a head built up, but this would be prevented by the drain hole located at the bottom lower end of each release zone. This is located just on the edge of the rubber section, which would drain water out of the zone completely before it could get past the rubber in any quantity.

Plots of zone 1 injection and seepage from May 17 to May 23 show no seepage with a constant liquid injection rate of ~36 mL/min, but there was in fact some seep water that was missed by the collection system. When test was resumed on May 23, 2001 the injection rate was maintained at

a constant of about 24 mL/min, and the tarp for zone 1 was repositioned closer towards the collar to capture the seep entirely.

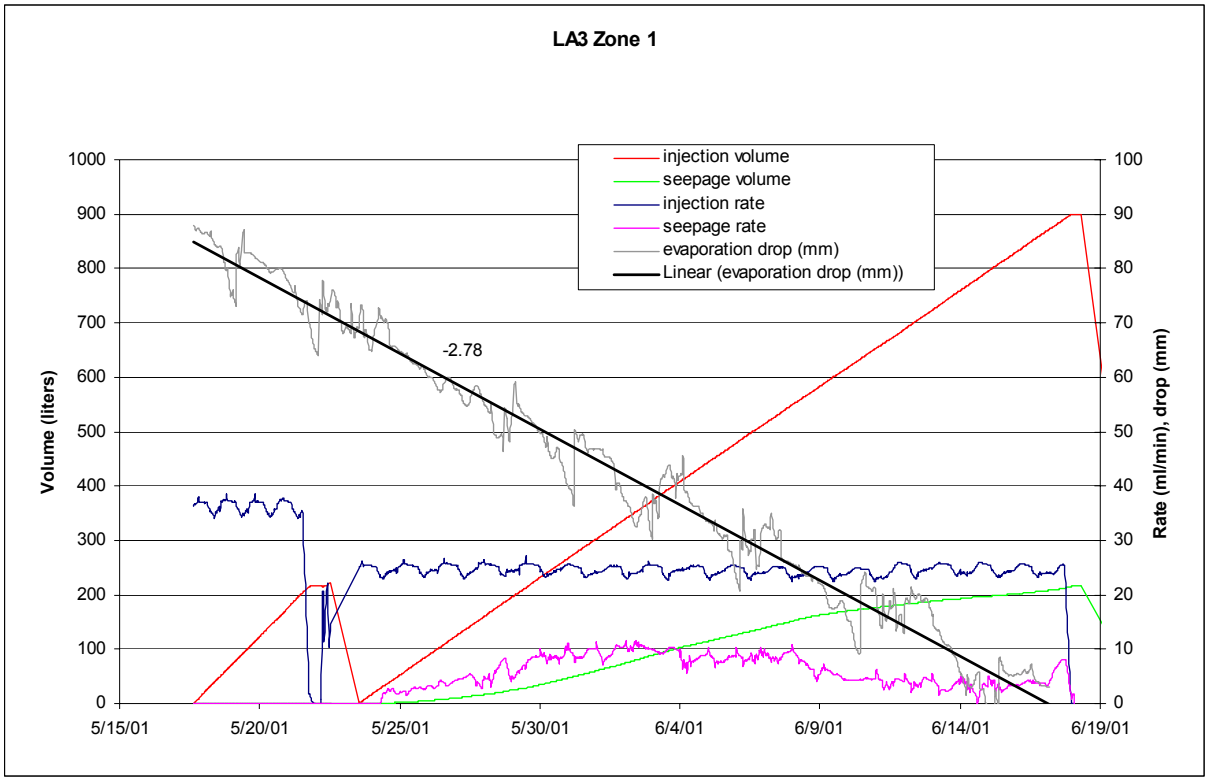

DTN: LB0203ECRBLIQR.001 [158462]

NOTE: Linear curve fit for evaporation uses Excel trendline option for putting a curve fit onto an existing plot. Slope is from the equation generated by Excel for the fit. See Attachment IX.6.3 for calculation details.

Figure 6.11.2-12. Cumulative Water Volume and Rate Supplied to and Seeped from ECRB-SYBT-LA#3 Zone 1 and Evaporation with Linear Fit and Slope (mm drop per day) for the Test Performed on May 17 to June 19, 2001

The plots in Figure 6.11.2-12 show that the seepage rate has reached steady state by May 31 at about 8 mL/min. (Volume drops in the plots indicate stoppage and restart of testing. Slopes for evaporation drop are listed on the evaporation linear fit curve and are in millimeter drop per day.) A wet spot on the ceiling was noted as early as May 24, 2001, at near the edge of the tarp closest to the borehole collar. Another wetted area developed towards the opposite end of the tarp and started seeping by May 29. This seeping wetted spot was 1.2 m in diameter, and on May 31 it increased to 1.37 m in diameter, extending from about 3.66 m to 5.03 m from the collar. The estimated rate lost to evaporation at this point from the 1.37 m diameter wet spot is as follows: Area of wetted spot $=3.1416 \times ((100*1.37)/2)^2 = 14{,}741$ cm^2 (Attachment IX.6). Data on drop of water level in the evaporation pan shows an average rate of 2.78 mm/day or 1.93E-4 cm/min from the slope of the evaporation line in Figure 6.11.2-12, so that the evaporation rate from the wetted area is $1.93\text{E-}4 \times 14741 = 2.85$ mL/min. With an injection rate of 25 mL/min, a recorded seepage of ~ 8 mL/min, and an evaporation loss of ~ 2.85 mL/min, the rate of water being diverted around the drift after "fast paths (or connected paths between water release at borehole to the drift ceiling) have been established is about 14 mL/min.

The decline in seepage rate starting on June 7, 2001, may in part be attributed to evaporation caused by a larger wetted area observed on the drift ceiling. The increasing size of the wetted area may itself be regarded as a form of surface water flow that suppresses the formation of seeps by both growing in size (and thus accommodating more water) and by contributing a larger evaporation area. On June 6, 2001, this wetted spot became 1.83 m in length (along the drift axis) and 2.44 m in width. On June 13, 11:25, the wetted spot that had first appeared on May 24, 2001 (that which was closer to the collar edge of the tarp and that had not seeped) had expanded to about 0.91 m in diameter and started to drip. By June 13, 2001, 15:45, the two wetted spots had merged and formed one spot about 3.05 m in length. When comparing the wetted area (on June 13, 2001) of one ellipse of 1.83 m and 2.44 m axes plus a circle of 0.91 m in diameter to that of one circle of diameter, 1.37 m (the previous wet spot from May 31, 2001), one arrives at the ratio of $[(2.44/2 \times 1.83/2) + (0.91/2)^2]/(1.37/2)^2 = 2.82$ (Attachment IX.6). If the evaporation rate from the wetted area on May 31, 2001 was 2.85 mL/min, then that on June 13 could be as high as $2.82 \times 2.85 = 8.04$ mL/min, or 5.2 mL/min higher than that on May 31. This is on the right order of magnitude as the observed seepage rate decline from ~8 mL/min in beginning of June to ~ 3.0 mL/min by mid-June. On June 17, injection to zone 1 was stopped. Seepage stopped within 40 minutes of turning off the injection. On June 19, all work was stopped, including seepage collection, so that the equipment could be temporarily moved to allow other tunnel activities to take place. The results from zone 1, LA3, highlighted some of the complexity of flow paths that are showing up during the course of systematic testing. They showed that subtle changes occur in the geometry and number of the wetted areas, even at steady water-release rates.

6.11.2.8 Liquid-Release Test in Zone 2, LA3: May 10–July 23, 2001

Liquid release in zone 2 was also initiated on May 17, 2001, during which seepage was missed by collection tarps immediately below zone 2. It was realized that there might be some test interference between release at zone 1 and release at zone 2, so testing at zone 2 was terminated on May 21 and resumed on June 20, following the conclusion of a liquid release test in zone 1. Seepage from water released in zone 2 was now expected to fall on collection tarp 1, which had been moved 2.7 m (9 feet) closer to the LA3 borehole collar on May 23, 2001. Collection tarp 2 was moved back on June 19, 2001, to directly under injection zone 2. (It had previously been repositioned under directly under zone 1 to take the place of the zone 1 tarp when it was placed near the collar.) Liquid injection in zone 2 started on June 20, 2001. There was a power outage on July 1, but testing was resumed on July 5.

For the May 17 release, there is release data only (seepage missed the collection tarps). For the June 20 and July 5 injections into zone 2, the seepage was collected from the zone 1 tarp. The fact that seepage from zone 2 water application appeared in the zone 1 collection tarp with no other seepage location evident, indicates that the packer system may indeed have failed to keep the zone 2 water release at the zone 2 location, and in fact had let water run through the borehole to the zone 1 location. This would be especially likely if the formation around zone 2 was nearly impermeable to released water.

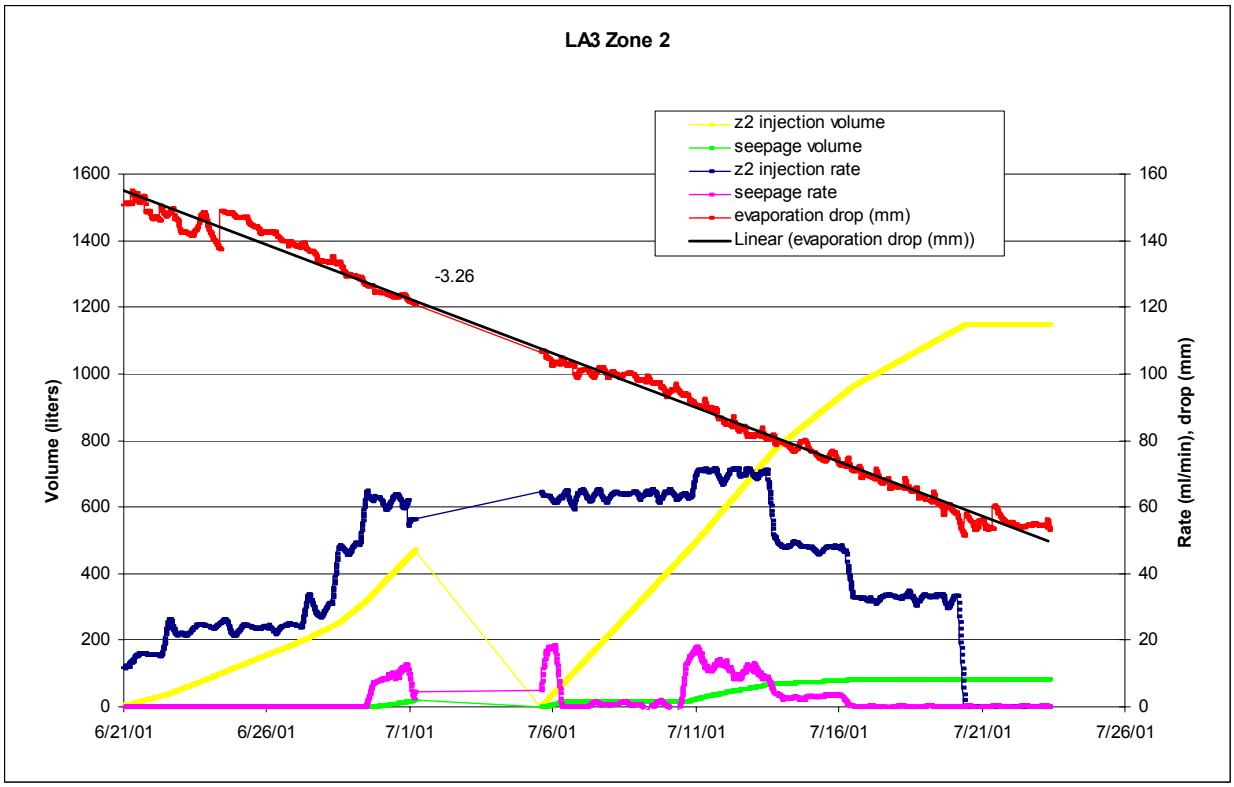

DTN: LB0203ECRBLIQR.001 [158462]

NOTE: Linear curve fit for evaporation uses Excel trendline option for putting a curve fit onto an existing plot. Slope is from the equation generated by Excel for the fit. See Attachment IX.6.3 for calculation details.

Figure 6.11.2-13. Cumulative Water Volume and Rate Supplied to and Seeped from ECRB-SYBT-LA#3 Zone 2 and Evaporation with Linear Fit and Slope (millimeter drop per day) for Test Performed on June 20 to July 24, 2001

The plots in Figure 6.11.2-13 show that the injection rate in zone 2 was increased step-wise. It started from the low of ~11 mL/min at the initiation of test on June 20, 2000, to ~25 mL/min between June 22 and June 27, to ~30 mL/min until June 28, 11:00, at which time the rate was increased to ~ 49 mL/min. Then, on June 29, 10:30, the rate was increased to 63 mL/min. Seepage collection initiated on June 29 at 16:11 and was on the order of 10–15 mL/min just before an unplanned power outage on July 1 at 3:16. When the work was restarted on July 5, 2001, testing continued at the higher rate of injection, ~65 mL/min, as before the power outage. The seepage resumed almost immediately, confirming that the fast paths (connected paths for liquid flow comprised mostly of fractures) between release point and drift ceiling, had been established. The seepage rate had increased to the pre-power-outage level within about five hours of resumption of water release. The drop of seepage to zero on July 6, 2001, turned out to be from a leak in the tubing of a collection bottle. The leak was repaired on July 10, 14:31, accompanied by a quick response of the seepage rate which increased to ~16 mL/min. In an attempt to estimate the seepage threshold, the liquid release was reduced stepwise. On July 13 17:04 the release rate was reduced from ~71 mL/min to ~48 mL/min. The seepage rate decreased from the average of ~16 mL/min to ~3 mL/min. Approximating that the loss due to evaporation had not changed (the evaporation flux appears similar) from before 7/13 to after 7/13, the data may indicate that the difference in diversion of release water around the drift opening caused by varying inflow rates is on the order of (71-16)–(48-3) = 10 mL/min (Attachment IX.6). The

water release rate was further decreased on July 16, 11:53, from 48 mL/min, to 33 mL/min and the recorded seepage has almost disappeared. However, field observations in the morning of July 16 also indicate the presence of a small seep between the tarps of zone 1 and zone 2. That small seep was missed by the data collection system. Field observations indicated that that missed seepage rate could still be on the order of 2 mL/min. That is, the prevailing release rate of 33 mL/min is still above the seepage threshold. Because of ECRB field schedule, there was no opportunity to investigate further the seepage threshold, and water release was terminated on July 20, 2001.

6.11.2.9 Liquid-Release Test in Zone 3, LA3: May 10–July 23, 2001

Testing at zone 3 LA3 took place from May 10 to July 23, 2001, concurrently with the testing at other zones in LA3. It was apparent that there would be no chance of test interference with the other zones from zone 3, because at the start of testing at zone 3, the liquid-release test data showed that there would be no seepage; results from zone 3 were different from any yet encountered in the systematic testing. Plots of injection, return, and net inflow rates are shown in Figure 6.11.2-14. Liquid release tests from May 17–22, May 23–June 18, June 21–July 1, and July 5–July 20 indicate that except for a brief period on May 17 and May 23, the formation essentially could not take in any significant amount of water, regardless of the rate of injection. The average rate of water intake was ~ 0.5 mL/min when the injection rate was set quite high. At lower injection rates, the net inflow was close to zero after steady state conditions had been reached. This seems to indicate that zone 3 possibly was lined with cavities that initially filled up, but whose bottoms are sealed so that little water can leave the cavities. In other words, the cavity population around injection zone 3 is so large and the fracture population so small that very little introduced water can access the connected fractures that form the “fast paths” that lead to the crown. The “fast paths” are those that allow intake of water at tens and even hundreds of mL/min in all the liquid release tests until this one.

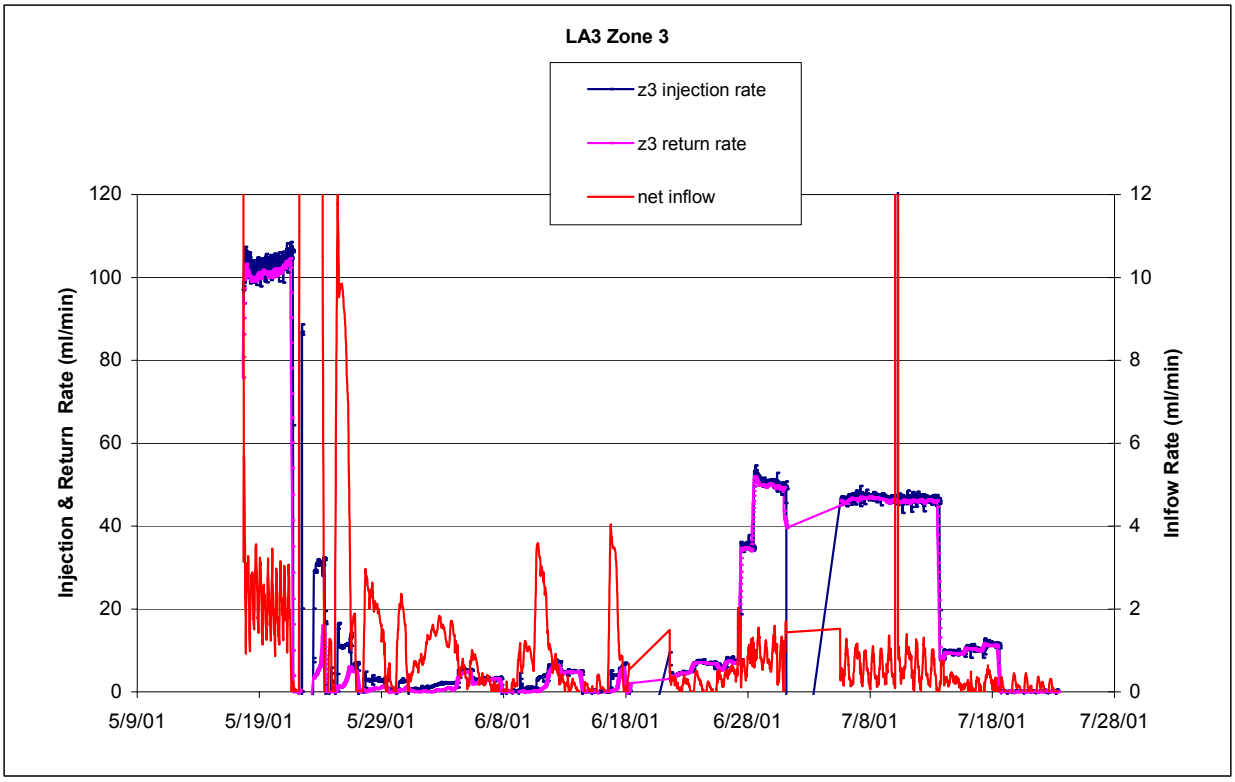

DTN: LB0203ECRBLIQR.001 [158462]

NOTE: See Attachment IX.6.3 for calculation details.

Figure 6.11.2-14. Rate Supplied to Returned from and Rate of Net Inflow ECRB-SYBT-LA#3 Zone 3 for Test Performed on May 17 to July 24, 2001

It can be seen from the testing at LA3 that there seems to be a spatial transition from a fast path type of formation to a very tight formation over a length scale from 2 to 10 meters as testing moves towards zone 3 closer to the portal of the ECRB. Seepage was seen only from zone 1, the zone closest to the previous borehole, which had multiple fast path characteristics. This seepage came both from zone 1 and zone 2 injections, indicating that the borehole may have participated in movement of water from the zone 2 release line to the seep seen at zone 1. Various patterns and rates of seepage were apparent on the zone 1 crown. In addition, there was near 100% water return from zone 3 testing, but zero return from zones 1 and 2 testing. It is, however, possible that zone 2 would have displayed properties of zero intake similar to zone 3 had the borehole not been acting as a drain for the water to reach zone 1 during zone 2 testing. In addition there appears to be no effect from relative humidity or temperature on evaporation rate, which is very steady over the course of LA3 testing.

6.11.2.10 Borehole LA4 and Liquid-Release Test in Zone 1, LA4: February 5–March 11, 2002

Tests in borehole ECRB-SYBT-LA#4 (LA4) began on February 5, 2002, and finished in November 2002. This is the fourth 15° low angle hole and was collared at ECRB CS 16+65 in the drift crown. The borehole was again divided into three sections for water release using the systematic hydrological packer system. The three sections for water release spanned 3.9–5.7 m, 8.8–10.6 m and 13.6–15.5 m respectively from the collar. The midpoints of each of the zones

were therefore 1.2, 2.5 and 3.8 m, respectively, above the crown of the drift. At LA4, a modification to the packer system whereby the durability of the rubber sections was enhanced, ensured that a proper seal formed between the rock and the inflated sealing sections in the borehole. Problems of water leaking by the sealing sections were thus not an issue at LA4 as they may have been at LA3.

Testing at zone 1, LA4 started on February 5 and proceeded through March 11, 2002. Plots for injection and water return volumes and rates into zone 1 at LA4 shown in Figure 6.11.2-15 show that it behaves somewhat similarly to zone 3 of LA3, in that there is a relatively high percentage of return flow. There is an initial high rate of inflow into the formation upon initiation of water release, after which the net inflow becomes quite small. As in zone 3, LA3, the net inflow increases slightly when the absolute injection rate is increased most likely because of the slight rate dependency of the water-delivery-system geometry in that the water is more evenly distributed at higher rates and thus is more likely to enter the formation. The combination of results from zone 3, LA3, and zone 1, LA4, indicate that the tight formation properties seen in both possibly continue through both zones over a distance of almost 18 meters. It has been noted that zone 2 of LA3 may have had similar flow characteristics to these two, observations of which were unfortunately confounded by the leaky packer system. If this is the case, then the property distance could be as large as 23. There was no seepage capture from the testing at zone 1, LA4. Unlike zone 3, LA3, however, some wetting occurs on the crown. During the course of testing, the evaporation averaged about 2.8 mm per day (the closest estimate for this time of year from Figure 6.11.2-12), which, combined with a maximum observed wetted area of 12,000 cm^2, gives 2.3 mL/min of evaporation from the crown. The maximum infiltration rate of about 30 mL/min was obtained at the maximum injection rate of 120 mL/min, so that the diversion around the crown measured 27.7 mL/min or 92% of inflow.

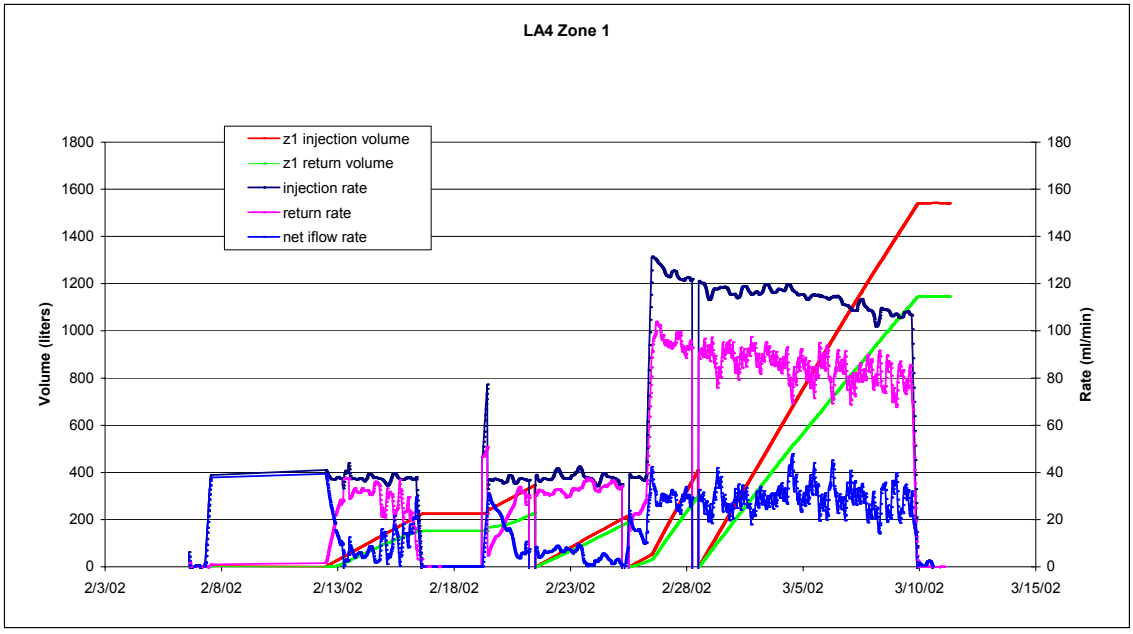

DTN: LB0301SYTSTLA4.001 [165227]

NOTE: See Attachment IX.6.3 for calculation details.

Figure 6.11.2-15. Volume and Rate Supplied to Returned from and Rate of Net Inflow ECRB-SYBT-LA#4 Zone 1 for Test Performed from February 6 to March 9, 2002

6.11.2.11 Liquid-Release Test in Zone 2, LA4: October 8 – November 18, 2002

Testing at zone 2, LA4 ran from October 8 to November 18, 2002. Owing to scheduling complexities, this was held some time after the other tests at LA4 but with no noticeable effects on the systematic type of testing. Figure 6.11.2-16 shows plots of volumes injected and captured with rates and evaporation drop during testing at zone 2, LA4. Included in the plots is a net loss rate that is the difference between the injection rate and capture rate. This curve indicates the rate of loss to diversion around the drift or to evaporation. There was no return flow at this location regardless of the injection rate, indicating that the character of the formation had changed again as the testing location moved towards the ECRB portal. The rate of evaporation measured 5.73 mm/day on average over the course of testing at zone 2. Observations indicated that on October 23, the wet patch on the crown had an area of 8.0477 m^2. Evaporation from the crown surface is therefore estimated to have been about 32 mL/day at this time. Combined with a loss rate of 40 mL/min and an injection rate of 44 mL/min, this makes the diversion rate 8.0 mL/min (discounting fracture evaporation losses), or about 18% of the injection rate and about 20% of the total loss rate.

From the plots, it can be seen that the loss rate (water diverted or evaporated) appears to be slightly higher (as a fraction of injection rate) at lower injection rates. This phenomenon suggests that at very high injection rates in zone 2, a higher percentage of introduced water would have seeped into the drift.

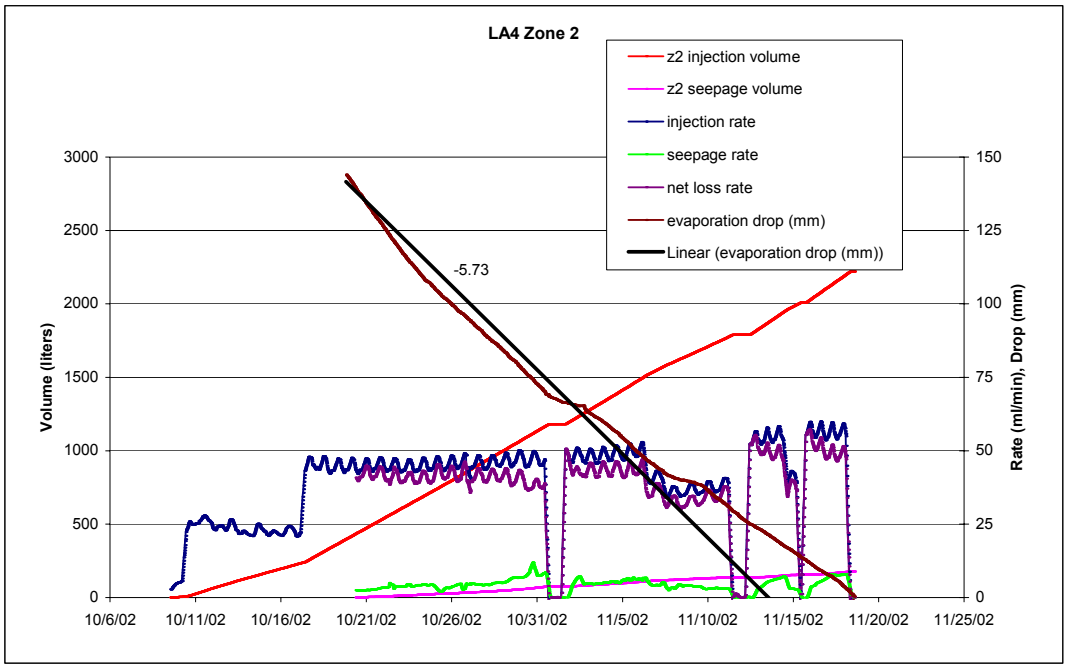

DTN: LB0301SYTSTLA4.001 [165227]

NOTE: Linear curve fit for evaporation uses Excel trendline option for putting a curve fit onto an existing plot. Slope is from the equation generated by Excel for the fit. See Attachment IX.6.3 for calculation details.

Figure 6.11.2-16. Volume and Rate Supplied to Returned from and Rate of Net Inflow ECRB-SYBT-LA#4 Zone 2 and Evaporation with Linear Fit and Slope (mm drop per day) for Test Performed from November 9 to September 18, 2002

6.11.2.12 Liquid-Release Test in Zone 3, LA4: February 5–February 28, 2002

During the zone 1 testing at LA4, zone 3 at LA4 also underwent some testing from February 5 to February 28. The two zones were sufficiently far apart along the drift to ensure that no test interference was likely. In contrast to the flow characteristics observed at LA4 zone 2, zone 3 provided an example of another as-yet-unseen flow characteristic. Again, like zone 2, there was no return flow, regardless of injection rate. However, all flow into the zone was accepted, and no seepage or wetted areas were observed. Even at inflow rates over 200 mL/min, no water flowed into the drift. Figure 6.11.2-15 shows plots of the injected volume and corresponding injection and inflow rates into zone 3.

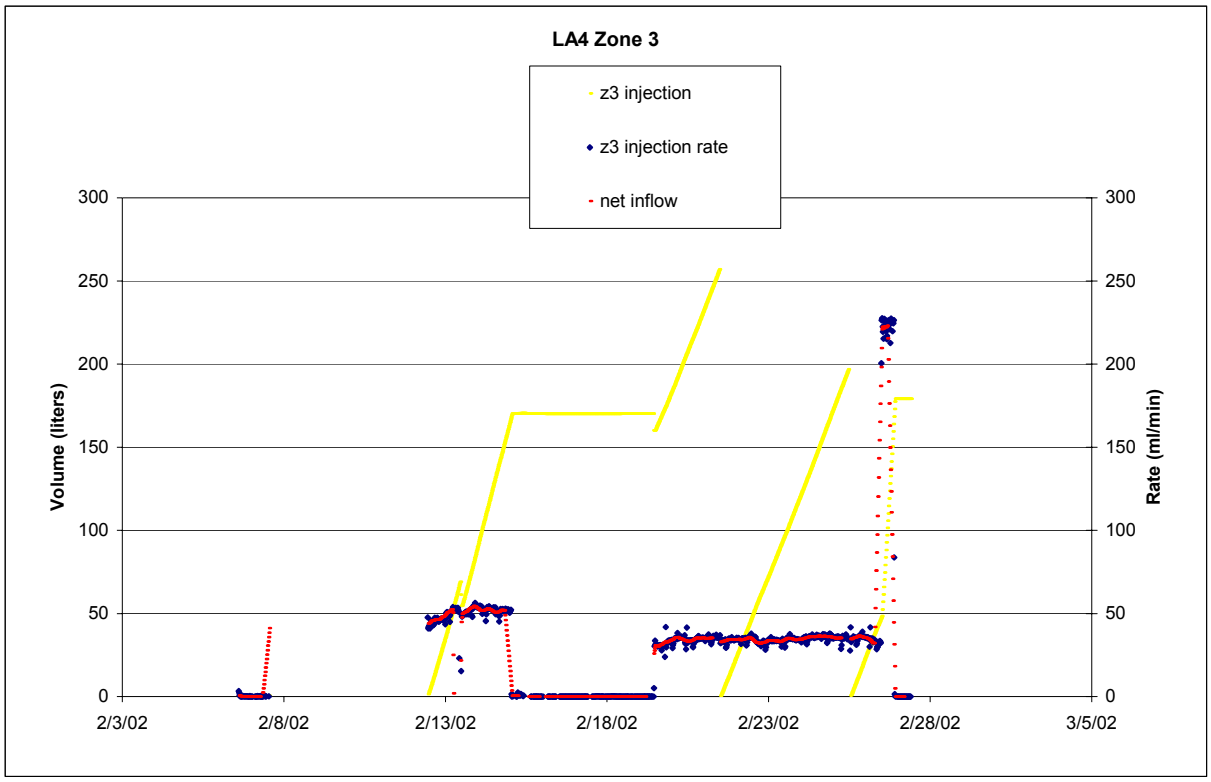

DTN: LB0301SYTSTLA4.001 [165227]

NOTE: See Attachment IX.6.3 for calculation details.

Figure 6.11.2-17. Volume and Rate Supplied to Returned from and Rate of Net Inflow ECRB-SYBT-LA#4 Zone 3 for Test Performed from February 6 to February 28, 2002

6.11.3 Systematic Testing Discussion and Interpretation

Several important results become apparent when examining the data presented above. One result is the insight into the role of fractures, matrix, and lithophysal cavities in liquid flow through the partially saturated lower lithophysal unit. Another is the assessment of the nonintersecting flow (a combination of diversion by capillary barrier and of alternate flow paths) around the drift excavation. A third important result is the estimation of a threshold flux at the water-release borehole, below which seepage into the drift does not occur. The first few locations that were tested allowed us to make significant progress in understanding these hydrological characteristics

of the lower lithophysal unit. In addition, it is now becoming apparent that as systematic testing continues in more locations at regularly spaced intervals, investigators have accumulated more valuable insight into the heterogeneity of fluid flow and the dimensions of this flow heterogeneity in the highly spatially heterogeneous, fractured, and porous lithophysal unit. Direct comparisons of the same type of data from location to location are providing knowledge applicable to a large portion of the ECRB Cross Drift.

6.11.3.1 Participation of Lithophysal Cavities in Storage and Flow Paths

Lithophysal cavities, fractures, and matrix contribute to the overall porosity of the lower lithophysal rock. Drift-wall mapping along the ECRB Cross Drift indicate a mean lithophysal cavity porosity of 0.125 in the lower lithophysal unit (Mongano et al. 1999 [149850]). Gas-tracer measurements of the effective porosity in the middle nonlithophysal units indicate that fracture porosity is on the order of 0.01 (DTN: LB980912332245.002 [105593]). Both cavities and fractures are expected to be essentially dry at ambient conditions. Laboratory measurements from 453 samples of surface-based boreholes give the mean matrix porosity of 0.13 and a mean saturation of 0.78 for the lower lithophysal unit (Flint 1998 [100033]). Fourteen measurements on cores from boreholes drilled for systematic testing at the ECRB Cross Drift Station CD 17+49 (DTN: LB0110COREPROP.001 [157169]) give results similar to that of Flint: mean values of 0.12 for matrix porosity and 0.72 for liquid saturation. Because of the high ambient liquid saturation, the matrix contributes only about 0.03 in porosity that is available for liquid storage from systematic testing.

In liquid-release tests such as those conducted for the systematic testing, it is anticipated that fractures and possibly large cavities will ultimately be responsible for the steady-state flow behavior of the fractures-matrix-lithophysal cavity system, while slow-draining cavities and matrix will contribute to the first-time storage. Of the first-time test storage features, slow-draining cavities and matrix will contribute to one-time storage, while only fractures and open cavities contribute to subsequent “steady-state” storage. Thus, in a flow test at a new borehole where no water has yet been introduced, all the storage components should be in full effect. The water released into the formation will partition into storage and steady flow paths. If the fast paths themselves contain a significant storage component, this should lengthen the first arrival time for water (from the delivery point in the borehole to the exit point in the drift) and also increase the amount of water needed to do so.

Data from niche liquid release tests (Section 6.2 in this scientific analysis report) with dye observations during excavation of Niche CD 1620 (Niche 5) at ECRB Cross Drift suggest that the shape of the flow plume in close vicinity to the release is roughly circular. During a liquid-release test, as soon as water is observed at the crown of the drift, the maximum distance of any flow can be interpreted to have reached (along fast paths) the surface of a cylinder (the diameter of the cylinder is the distance between the middle of the release zone and the crown). The cylinder length would be roughly that of the release zone. This cylindrical volume concept is applied during the first-time test period when the connected paths are being developed, as a bound to contain the fast, connected paths. At later times in the test, during the steady-state phase, water may have moved well beyond the bounds of this cylinder. The volume of water injected up to the point of first wetting at the drift ceiling, divided by the volume of this cylinder, gives the effective porosity for establishing fast paths. Note that the effective porosity measured

this way is very much injection-rate-dependent, because the degree to which different components of actual porosity participate in the flow path varies according to their time of exposure to the flow (and in this case, this is the time needed for water to reach the edge of the cylinder).

For the test in LA2 zone 1 (Section 6.11.2.1), Figure 6.11.2-2 shows that 46 liters (0.046 m^3) of water has been introduced at the first wetting of the drift crown. The volume of the cylindrical plume (diameter 1.58 m and length 1.83 m) is estimated to be 3.6 m^3. Hence, the estimated effective porosity for establishing fast paths is 0.046 m^3/3.6 m^3 = 0.013. Water was released into LA2 zone 1 at a relatively high rate of 450 mL/min.

For the test in LA1 (Section 6.11.2.5), the diameter of the cylinder is 1.03 m, and the length is 1.83 m, for a volume of 1.53 m^3. Flow volume for the initial wetting of LA1 was 103 liters (0.103 m^3), which gives an effective porosity of 0.067. In this case, the water was released at a much slower rate of 15 mL/min.

The two estimated effective-porosity values of 0.013 and 0.067 prior to the establishment of fast paths lead to the following interpretation. In the case of LA2 zone 1, when the release rate was as high as 450 mL/min, the fracture porosity was accessed with little imbibition into the matrix at the time of intersection with the drift. Also, for the lithophysal cavities that act as a capillary barrier with the very high release rate, little water would be expected to seep into these cavities. For LA1, when the release rate was about 30 times slower at 15 mL/min, the flowing water would have time to access the matrix porosity, and less would be diverted around the lithophysal cavities. The difference in effective-porosity results from these two tests could thus be a measure of the component of storage due to matrix and slow-filling cavities. Because cavities are the primary contributor to actual porosity in the system, even a little participation in the flow path would raise the effective porosity. In the case of LA1, they seem to contribute up to a maximum of about 0.057 (effective minus fracture porosity, not accounting for matrix participation) and a minimum of 0.027 (if all the available matrix porosity participates). These values indicate that only a quarter to one half of the lithophysal cavity volume (porosity of 0.125) participates in the liquid storage.

One refinement in the evaluation of effective porosity is to study the process of restarting a water-release test after some pauses in activity. For LA1, after slightly more than two months, a new release was made (Section 6.11.2.6). The first arrival was observed after only 60 liters, giving a new effective porosity of 0.039. Therefore, it appears that the liquid storage from the matrix and cavities filled in the initial test (Section 6.11.2.5) had not completely drained in this two-month lapse. The difference between the new value and that of 0.067 from the previous test in the same location is 0.028 and could be a measure of the capacity of the matrix and the slow-draining lithophysal cavities. Lastly, the difference between the storage measured from the already wet slow test (storage from fast-draining cavities and fractures) and the initially dry high-rate tests (storage by fractures only) gives the drainable cavity porosity of (0.039–0.013) or 0.026, or just less than a quarter of the cavity estimated porosity.

6.11.3.2 Estimation of the Steady-State Nonintersecting Flow around the Drift

One of the key outcomes of testing to investigate seepage into drifts is an estimation of the component of introduced water diverted around the mined opening during steady-state flow, following the establishment of connected paths between borehole and drift ceiling, as discussed in the previous section. A fraction of the water will miss the drift opening because of the nonuniform flow from heterogeneity. At the drift crown, additional lateral flow will be diverted around the drift, resulting from the drift acting as a capillary barrier. The total component of non-intersecting water (from flow channeling and capillary effects) can roughly be thought of as the difference between the rate of injection and the rate of seepage into the drift when the test has reached steady-state conditions, provided that there are no other losses. However, the systematic data (Section 6.11.2.3, Section 6.11.2.4 and Section 6.11.2.6) show clearly that evaporation contributes to the difference in the recorded injected and seeped volume of water. It is thus essential that evaporation be taken into account in any attempt to estimate the nonintersecting component.

The evaporation contribution to the wetted-drift ceiling can be estimated by multiplying the flux from an evaporation pan mounted just below the seep (to get accurate conditions) by the wetted area associated with the seep. All monitoring data for the water-level drop in the evaporation pan show that the evaporation flux is on the order of 3 mm/day, for the wide range (15 to 90%) of relative humidity encountered. The largest wetted area for all the systematic tests to date was 6.8 m^2 corresponding to the test in LA2 described in Section 6.11.2.4. An upper bound of evaporation rate from systematic testing may be obtained by multiplying the evaporation flux of 3 mm/day by the largest wetted area recorded by half-hourly observations (photographs) at LA2, 6.8 m^2. The resultant evaporation rate is about 14.4 mL/min. Clearly, uncertainty in this number remains, since potential for injected water to leave the test system from barometric pumping and from vapor transport in a drying front behind the drift wall has not been included.

During the period from February 28, 2001, to March 30, 2001 (Section 6.11.2.6), injection proceeded at an approximate rate of 17.5 mL/min at LA1. Observational evidence showed that the crown underneath the injected zone was wet, but no seepage was collected during this period. The exception was for the period from the afternoon of March 15, 2001, to the morning of March 19, 2001, corresponding to a weekend shutdown of the ventilation, during which collection occurred at a rate of 0.6 mL/min. The next weekend shutdown did not cause any seepage collection to occur. Slight variations in ventilation conditions, determined whether seepage collection occurred at a very low rate or none at all, indicated that the system was just on the verge of collecting or virtually seeping. The evaporation rate from the largest wetted area at LA1 (4.6 m^2) of 9.5 mL/min left 8 mL/min of flow from the injection unaccounted for; this can be interpreted to be the flow that has missed the drift. A conclusion can be drawn from testing during this period that at injection rates just high enough to cause active seeping at this location, about 46% of steady-state flow is diverted.

Section 6.11.2.6 (Figure 6.11.2-11b) also shows that a seepage collection rate of 8.5 mL/min was obtained at LA1 for a higher injection rate of about 40 mL/min during the period from 4/10/01 to 4/16/01. The nonintersecting flow is the evaporation rate and the seepage-collection rate subtracted from injection rate to give 22.0 mL/min. The nonintersecting flow estimated from this testing is therefore about 55%. Nonintersecting flow arises from both flow channeling and a

capillary barrier, but at those rates where seeps occur, the capillary barrier is likely overcome and no longer plays a significant role. Because the geometry of the channeled flow during "steady state" is likely independent of the water-release rate, the conceptual model of nonintersecting flow would seem to support the notion that at a given test location, diverted flow is a fixed percentage of the injected flow. The flow paths for diverting flow are probably similar in structure to those that are responsible for total seepage (including evaporation) and so respond linearly to an increase in injection rate. Because of the evaporation component, seepage collection rate (as opposed to total seepage rate) is not necessarily proportional to injection rate.

For another estimate of the lateral nonintersecting component, consider the seepage volume drained following the injection turn-off during "steady-state" testing and compare this volume to that required to initiate seepage after water release has been restarted. Water will drain out of the fast paths and be collected as seepage for some time after injection is terminated. (For all the systematic tests to date, the drainage period lasted less than 24 hours.) This is the storage volume of fast-path water connecting directly to the drift. Upon resumption of water release, the volume required to initiate seeping into the drift, the refill volume, is that which has to supply both the seepage fast path and the nonintersecting fast paths. The difference between the drainage seep volume and the refill volume suggests the volume of the nonintersecting fast paths.

Several pause studies were performed at LA1 to obtain this volume of nonintersecting fast paths that missed the drift opening. Correction for effects of rock-surface evaporation to both the drainage value and the volume to reinitiate seep is incorporated in this estimate. Evaporation increases the actual drainage value over that collected as seepage and decreases the refill volume from that recorded from the injection. During one test pause in LA1, on April 16, 2001, the seep drainage was 1.1 liters, but an additional 10.3 liters can be attributed to evaporation for the whole period that the injection is turned off. Evaporation is interpreted to be at its maximum of 9.5 mL/min for the duration of 18 hours. This interpretation is conservative, since observations of the drift ceiling indicate that drying of the wetted surface commences with the termination of water release, and evaporation would decrease and cease within this period. Consequently, longer duration pauses would cause about the same amount of surface evaporation. When injection is restarted on April 17, 2001, at the same rate as on April 10, 2001, it takes 16 hours to refill using a volume of 40 injection liters before the resumption of seepage. This volume is partly evaporated at a rate of 9.5 mL/min, so that the real refill volume is 34 liters. It might be argued that there is a volume component associated with the water hanging on the ceiling, contained in the wet spot, and contributing to drainage collection. There may well be such a component, but it should be fairly well cancelled out by a converse contribution to the wet spot during refill. It appears that, even when accounting for a very large estimate of evaporation, the refill volume is just over twice the drainage volume, meaning that more than half the flow is nonintersecting. This number agrees favorably with the rate method of obtaining nonintersection steady-state flow for the period of injection just before the April 16, 2001, pause and also for the earlier lower-rate test. Note that this method of calculating the nonintersecting component of flow, even though transient, will nevertheless be independent of injection rate because the time-dependent features (slow-filling cavities and matrix) no longer participate in a refill test.

6.11.3.3 Minimum Injection Rate Needed to Induce Seepage

At the scale of the drift, flow is more likely to progress in concentrated regions than as a uniformly spread front. A borehole line release occurs locally over the area projection of the borehole zone. This area emulates one of these concentrated regions at a given distance above the drift. During the testing at LA1 (Section 6.11.2.5) for the period from December 20, 2001, to December 26, 2001, observations (photographs) every half-hour confirmed that at the flow rate of 15 mL/min, with no ventilation, seepage on the ceiling was just observable as a tiny spot on the morning of December 25, 2001. It is postulated that there was little evaporation from the surface because there was no significant area to the spot. The spot stayed small for the remainder of the test, indicating that the system as a whole was approaching steady state. The 15 mL/min of injected flow in this case appear to just barely reach the crown. Thus, the threshold below which seepage into the drift does not occur is 15 mL/min.

6.11.3.4 Estimation of Evaporation from within the Fracture System

The observation of seepage was made within a day of water-injection resumption on April 3, 2001, and April 9, 2001, following a pause of 4 to 5 days; and also on April 17, 2001, following a pause of 18 hours. These observations indicated that "fast paths," connected paths comprised of flowing higher-permeability features, had been established as depicted in Figure 6.11.3-1(a). This delay in the onset of seepage after a pause-induced drainage (depicted in Figure 6.11.3-1(b)) enabled us to measure the capacity of water needed to refill the transient storage (that is, the storage volume needed before seepage occurs, depicted in yellow in Figure 6.11.3-1(c)) of these fast paths upon resumption of injection.

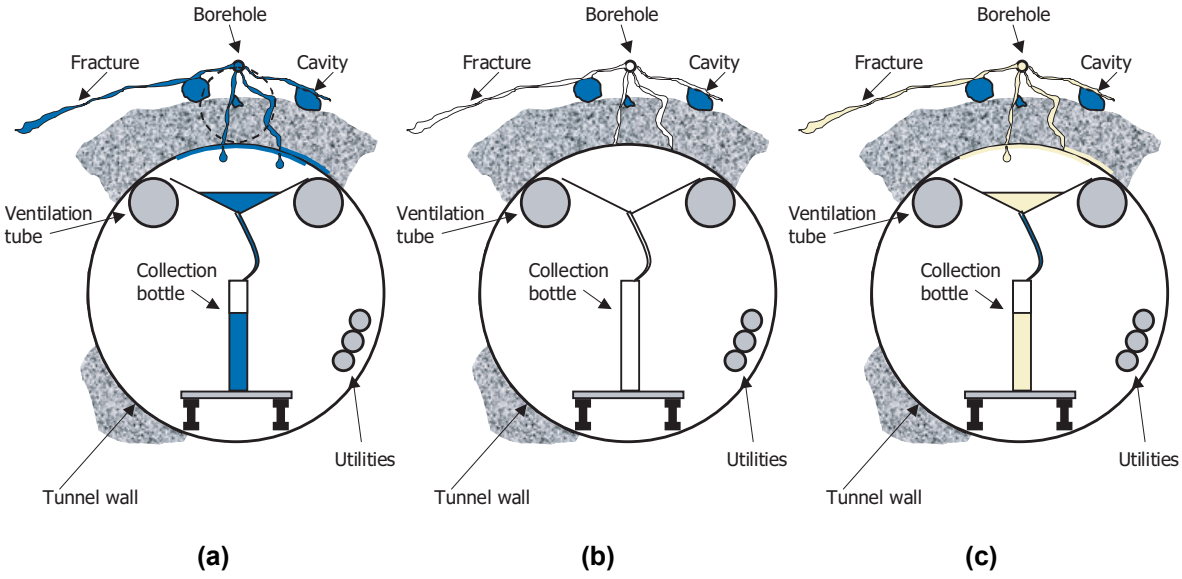

Figure 6.11.3-1. (a) Depiction of Fast Paths and Storage Areas for Flowing Seepage, (b) Pause in Flow and Subsequent Drainage and (c) Refill of Fast Paths

This volume exists because flow through fractures takes a finite amount of time to travel and needs to refill its paths before seepage again takes place. Because of the nature of fracture flow, once seepage occurs, the paths are essentially full and the system is again at steady state. This volume is the same as that of the water lost from all the paths during the pauses. After the 5-day pause, refill took 20 hours at a rate of 42 mL/min. The refill volume in this case was approximately 50 liters. For a pause of 18 hours, the refill volume was about 40 liters. The refill volume is thus seen as not very sensitive to the pause time. Drainage during each pause was the same and was complete long before the end of each of these pauses, so that any further loss was a result of longer-lasting processes (such as evaporation within the fracture system from hanging water, which would then require more refill volume). The small difference in refill volumes provides a measure of the rate of water moving out of the system by evaporation (or any other processes) after drainage. An estimate of this rate during the portion of pause time between 18 hours and 5 days can be made in dividing the difference in refill volumes by the difference in pause length. The result for this rate is 2.0 mL/min. If the surface area of the hanging water is not greatly different from that of the moving water, then this number also gives an indication of the rate of maximum evaporation from the fracture system at other times during the testing phase. No other quantifiable factors are included in the evaporation estimation.

6.11.3.5 Characteristics and Scale of Flow Heterogeneity along the Drift

As the systematic hydrological testing progresses towards the ECRB portal, a catalogue of flow characteristics for a growing length of drift is being developed. Not only can the various flow characteristics themselves be logged, but the distances for which they persist along the drift can now also be measured. Length scales as long as 23 m and flow characteristics such as 100% return flow and 100% diversion not yet observed in the detailed niche studies have now become apparent, due to the expansive coverage of drift that can be tested with the systematic approach. The results are starting to show the level and the physical dimensions of the heterogeneity at the drift scale. This flow heterogeneity and its scales are not immediately apparent by simple visual observation and feature mapping of the surface of the drift, and are only discernable with a systematic approach to hydrological testing.

6.11.3.6 Summary of Systematic Hydrological Testing

The following provides a summary of the work performed for the Systematic Hydrological Testing activities in the ECRB. A graphical summary of the results for nonintersecting (diverted) flow at steady state is provided in Figure 6.11.3-2. Thus far, arrays of 20 m long boreholes, collar to collar at 30 m, have been tested, with 10 tests reported. Additional curtains were installed on the two ends of the V-shaped seepage-capture PVC curtains, and a camera was installed to take observations of the drift ceiling below the injection section. After completion of LA2 zone 1, two evaporation pans were installed within the space enclosed by the seepage capture and end curtains (for remainder of testing, start of LA1 zone 2 through current LA4 zone 3). As a result of the LA2 and LA1 tests, effective porosity for one-time fill cavities was 0.028, for drainable cavities 0.027, and for fractures 0.013. Effective porosity here is defined as total volume water necessary to initiate seepage, divided by the potential volume of participating formation; thus it is rate dependent. The threshold flux from LA1 zone 2 was found to be 15 mL/min, with a corresponding flux at borehole of ~57,000 mm/year.

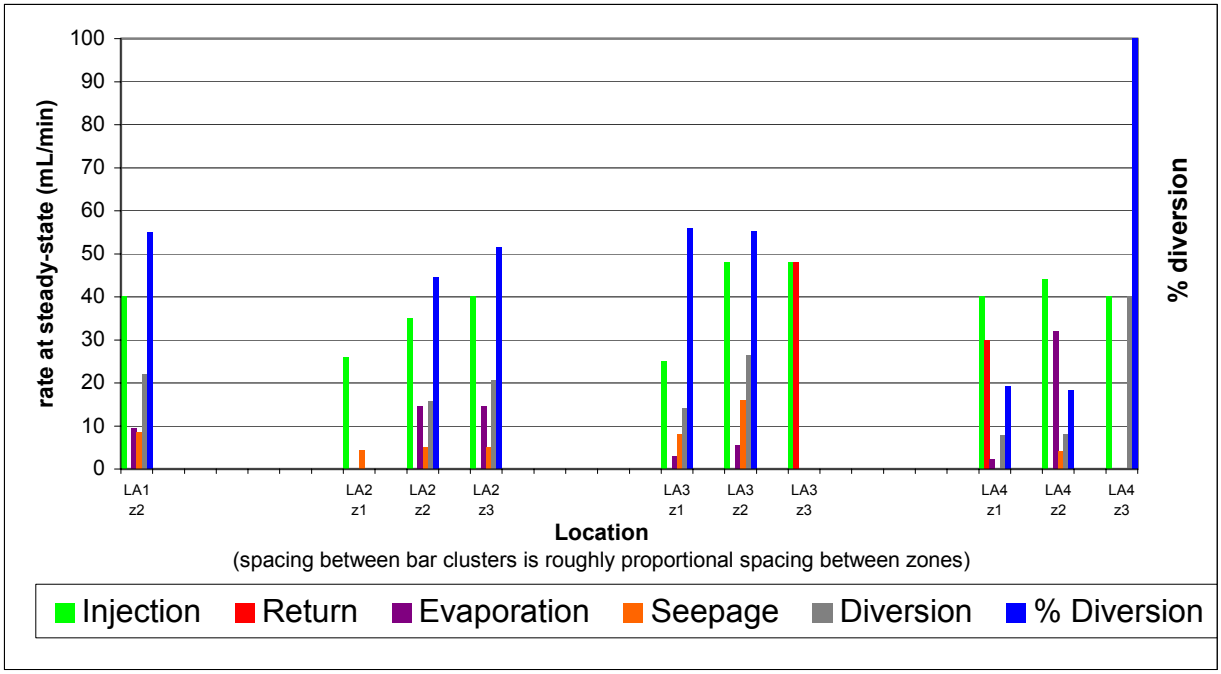

DTNs: LB0110ECRBLIQR.001 [156878]; LB0110ECRBLIQR.003 [156877]; LB0110ECRBLIQR.002 [156879]; LB00090012213U.001 [153141]; LB00090012213U.002 [153154]; LB0203ECRBLIQR.001 [158462] LB0301SYTSTLA4.001 [165227]

NOTES: Injection, return, evaporation and seepage are all either from the text in section 6.11 or are estimates based on the figures that have the relevant information. Diversion is return, evaporation, and seepage all subtracted from injection. % Diverted is diversion divided by (injection – return).

Testing for LA2 zone 1 is missing evaporation data (because there were no ventilation control curtains yet at this time) and therefore has no diversion or % diverted.

% Diverted for LA3 zone 3 is not quantifiable because there was 100 % return flow.

Some of the evaporation rates are estimates from tests run under similar conditions.

Figure 6.11.3-2. Summary Figure of Injection: Return Flow, Evaporation, and Diversion in All Systematic Hydrological Testing Studies

6.12 DRIFT-TO-DRIFT ALCOVE 8/NICHE 3107 (NICHE 3) AND SURFACE-TO-DRIFT ALCOVE 1 TESTS

Alcove 8-Niche 3107 (Niche 3) tests were designed based on experience gained from surface infiltration tests and niche seepage tests. Sections 6.12.1 is on the test setup between Alcove 8 in the ECRB Cross Drift and in Niche 3107 (Niche 3) directly below in the ESF Main Drift. Section 6.12.2 presents the results of a completed phase of a series of tests along a fault mapped in both Alcove 8 and Niche 3107 (Niche 3). Section 6.12.3 presents the results of geophysical imaging of the drift-to-drift test block between Alcove 8 and Niche 3107 (Niche 3). Section 6.12.4 presents available data from the ongoing plot tests. The available information from the early Alcove 1 tests and its implication for surface infiltration processes are summarized in Section 6.12.5.

The ongoing drift-to-drift tests at Alcove 8-Niche 3107 (Niche 3) and the completed surface-to-drift tests at Alcove 1 provide information over large scales in the range of 20 to 30 m. This is the relevant scale to relate site-scale processes of infiltration and percolation with drift-scale processes of diversion and seepage. Along long flow paths, fracture-matrix interaction is shown to be an important component to transport, with the matrix contributing to delays in water and tracer movements through the unsaturated units.

6.12.1 Drift-to-Drift Alcove 8/Niche 3107 (Niche 3) Tests

6.12.1.1 Test Sequence of Liquid and Tracer Releases

A series of tests broadly outlined in Figure 6.12.1-1 has been initiated in the Alcove 8/Niche 3107 (Niche 3) fault test bed. Broadly, this sequence of tests is being conducted in two phases. During the first phase, water was introduced along the fault under ponded conditions (with 2 cm of water head) until quasi-steady state seepage was observed in Niche 3107 (Niche 3). Then, a finite volume of water containing two tracers with different molecular diffusion coefficients (Br and PFBA) was introduced into the fault. Once the tracer-laced water had been released into the fault, more tracer-free water was released. Both tracer-laced and tracer-free releases occurred under the same ponded condition. This release of tracer-free water continued until a few months after breakthrough of the two tracers (Br and PFBA) was observed in the seepage collected in Niche 3107 (Niche 3).

The second phase of the test series involves the release water (laced with single and double tracers) under nonponded conditions. During this phase, water is to be released into the fault under controlled rates. It is proposed that the first release rate be set at ~75% of the intake rates observed under ponded conditions. Following the observation of steady seepage in Niche 3107 (Niche 3), the release rate will be stepped down to 50% and then 25% of the ponded intake rates.

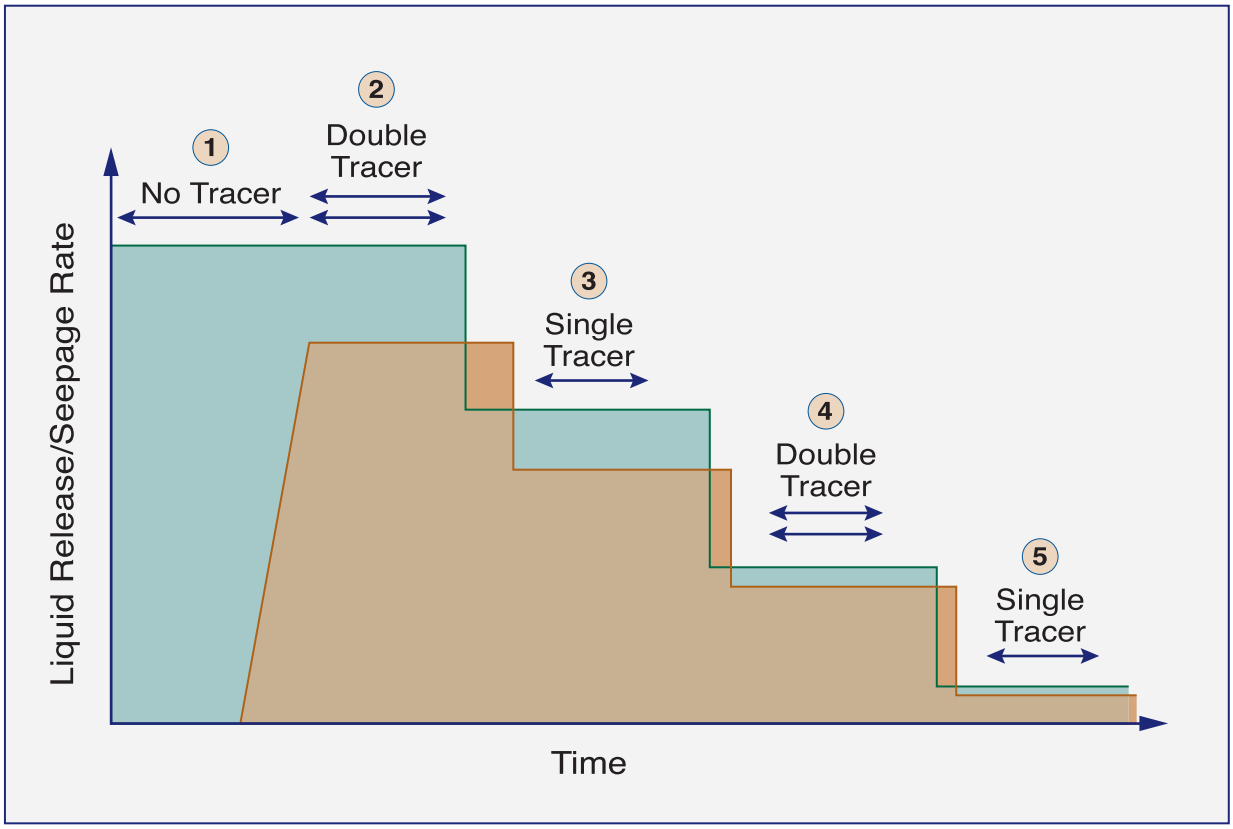

NOTE: Phase numbers in circles.
Blue = Introduced water.
Orange = Seepage

Figure 6.12.1-1. Schematic Illustration of Liquid Release and Seepage Collection Test Sequence

6.12.1.2 The Test Bed

Figure 6.12.1-2a shows the location of the test site within the ESF Main Drift and the ECRB Cross Drift. Figure 6.12.1-2b shows a three-dimensional representation of the test area, including several slanted (near-vertical) boreholes. Alcove 8 is excavated within the upper lithophysal zone of the TSw (Tplpul) in the ECRB Cross Drift, directly located above Niche 3107 (Niche 3) in the middle nonlithophysal zone (Tptpmn) in the ESF Main Drift. Shortly after Alcove 8 excavation, water was observed toward the end of Niche 3107 (Niche 3, DTN: GS030508312242.004 [165545]).

Alcove 8 begins at Cross Drift Station CD 7+98.236, (CRWMS M&O 1999 [156876]). An elevation of 1093.973 masl is calculated for CD 7+98.236 using the software ECRB-XYZ V.03 (CRWMS M&O 1999 [147402]). The elevation at STA 0+00 of Alcove 8 is approximately 0.510 m above CD 7+98.236 or 1094.483 (± 0.15 m) masl based on Alcove 8 design drawings (CRWMS M&O 1999 [156876]). Niche 3107 (Niche 3) is located in the middle nonlithophysal zone of the TSw (Tptpmn). The crown of Niche 3107 (Niche 3) is ~2–3 m lower than the 1076.7 masl crown elevation of the ESF at Station 31+07. The location of the Tptpul-Tptpmn contact is ~1080 masl, based on GFM3.1 data (DTN: MO9901MWDGFM31.000 [103769]).

The distinctive feature of the test bed in Alcove 8 is a near-vertical fault that cuts across the floor (Figure 6.12.1-3). It is open on the ceiling, and appears to be closed along the floor of the alcove. To facilitate ponded releases of water, a trench ~5 cm wide and ~5 cm deep was etched along this fault.

The physical set up of the trench is in two parts. The first part (trench 4) was the area that was dug out for the original cylinder (and box) experiments. It is a square approximately 1.4 x 1.5 meters with the fault running kitty corner through it. The rest of the fault was exposed in a trench that was 3.3 m long and 43 to 46 cm wide. The entire trench was divided into 4 sections. The area of each trench section is as follows: Trench 1 (left rib to right rib) 4005 cm^2, trench 2 is 4680cm^2, trench 3 is 5265 cm^2, and trench 4 is 21,000 cm^2 with the total area exposed to water application being 34,950 cm^2.

Niche 3107 (Niche 3) is approximately 4 m wide and extends to ~14 m from the centerline in the ESF Main Drift. The ceiling of the niche steps from 3.25 m at the opening to 2.5 m towards the midpoint of the niche. In addition to the near-vertical holes, three 9.0 m long, 0.0762 m in diameter horizontal boreholes were drilled ~0.5 m above the ceiling. Additionally, there are seven 6.0 m long, 0.0762 m diameter boreholes drilled inside the niche (Figure 6.12.1-4). The fault is visible along the ceiling of Niche 3107 (Niche 3), vertically below the trace along the floor in Alcove 8.

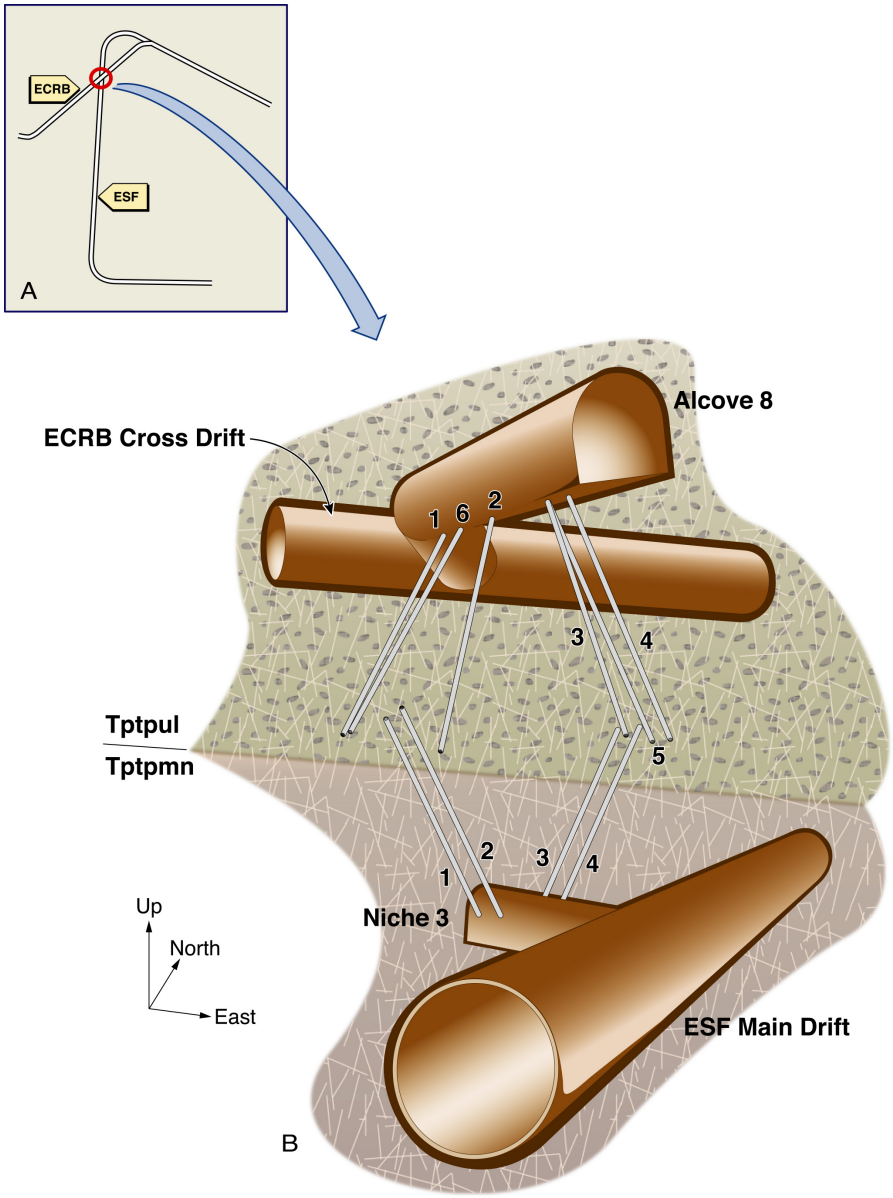

Figure 6.12.1-2. Schematic Illustration of the Test Bed for the Alcove 8/Niche 3107 (Niche 3) Tests

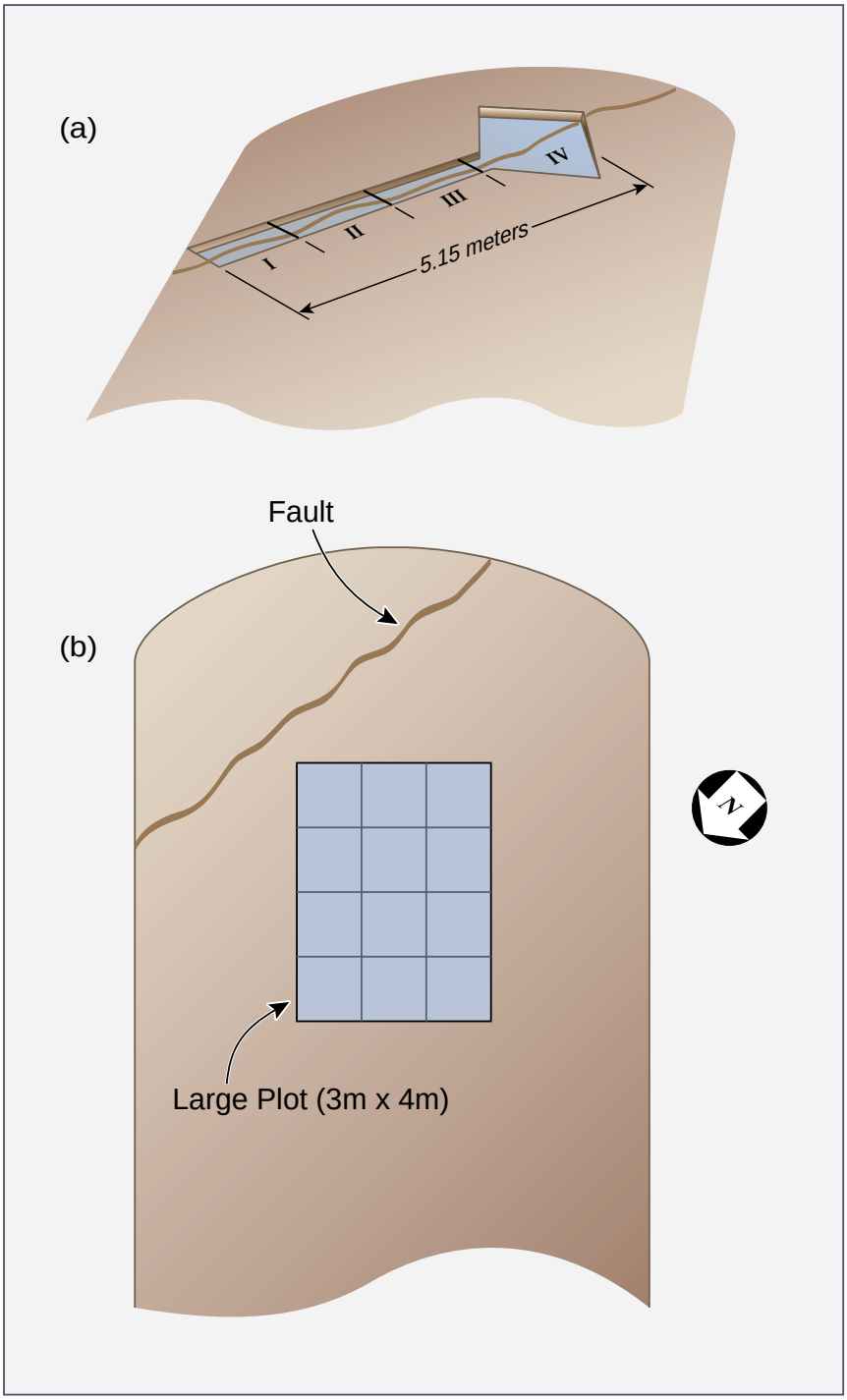

Figure 6.12.1-3. Schematic Illustration of the Infiltration Zones along the Floor of Alcove 8: (a) Fault Test and (b) Large Plot Test

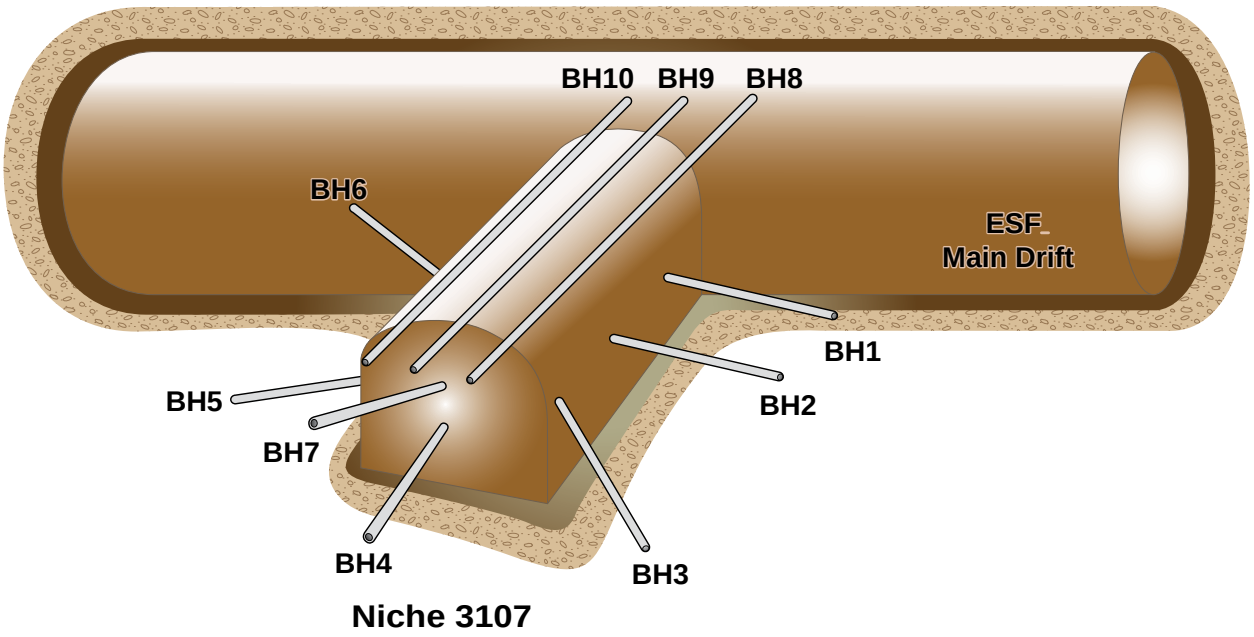

Figure 6.12.1-4. Schematic Illustration of the Monitoring Boreholes in Niche 3107 (Niche 3)

6.12.1.3 Instrumentation

There are three distinct components to the flow investigation: (1) controlled release of water into isolated zones along the fault in Alcove 8, (2) borehole monitoring for changes in saturation and water potential, and (3) collection of seepage from the ceiling of Niche 3107 (Niche 3). The key features of techniques used in this field investigation are presented below.

6.12.1.3.1 Fluid and Tracer Injection

Water was applied along the fault in Alcove 8 at three different times. Initially, the application area was over a small section of the fault. This was increased to 1.0 m and then to 5.15 m. In the small injection zone, water was first released with an infiltrometer, which is a cylinder 30 cm in diameter. During the second release, the infiltrometer cylinder was replaced with a box that measured 70 cm by 70 cm. These two releases are referred to as the small plot tests (DTN: GS010608312242.004 [165542], DTN: GS010608312242.002 [165543]). For the third set of water releases (along 5.15 m), the fault was divided into four sections, with each section serving as a separate release zone. In each of these applications, water along the release zone was ponded to a head of ~0.02 m.

A mix of conservative tracers (pentafluorobenzoic acid [PFBA] and lithium bromide [LiBr]) was released along the fault over a period of nine days, beginning on October 1, 2001.

The concentration of LiBr in the tracer-mix was ~500 ppm, while the concentration of the injected PFBA was ~25 ppm. These concentrations were achieved by dissolving 50 grams of PFBA and 1,000 grams of LiBr in a 1893 liter (500 gallon) tank of water that was used for supplying the water injected into the fault.

6.12.1.3.2 Borehole Monitoring

In nine monitoring boreholes (i.e., 1–7, 9, and 10 in Figure 6.12.1-4), changes in saturation were measured continuously with electrical resistivity probes (ERPs) located at 0.25 m intervals along the length of each borehole during the entire field investigation. Water-potential measurements were made with psychrometers along a single borehole (i.e., 8 in Figure 6.12.1-4).

The psychrometers and ERPs were housed in borehole sensor trays (BSTs) installed along the length of each monitoring borehole. The BSTs were fabricated from 0.10 m OD PVC pipes, 3.0 m in section length. Each pipe section was cut lengthwise to produce a 0.075 m wide curved tray. The BST housing permitted immediate contact between ERPs and the borehole wall. The psychrometers were installed inside small cavities (0.005 m in diameter) perforated through the BST wall to measure water potentials of the rock.

There are six boreholes (ECRB-COA-AL # 8-1 to 8-6) surrounding the large plot, 15 degrees out from vertical and drilled to an approximate depth of 15 m. There are two each on the right and left side of the large plot and one hole each in the front and back of the large plot, as illustrated in Figure 6.12.1-2. These six boreholes are monitored periodically with neutron meters for water content.

6.12.1.3.3 Seepage Collection

An automated water-collection system was designed to capture seepage from the niche ceiling. With this system, water dripping from the niche ceiling is collected in plastic trays and diverted to PVC collection bottles. These bottles have been installed with pressure transducers to periodically measure the collected amount of seepage water.

6.12.1.3.4 Tracer Sampling System

Immediately after the release of tracers into the fault in early October 2001, a water sampling device, the passive-discreet water sampler (PDWS), was connected to three of the collections trays in Niche 3107 (Niche 3) into which water was seeping. The PDWS, which was designed to isolate continuous seepage from each tray into discreet samples for chemical analysis, remained connected to the trays over a period of three months. During this time water that seeped into the three trays was captured sequentially into sampling bottles and analyzed for concentrations of PFBA and LiBr.

6.12.2 Phase I Observations from the Fault Liquid Test

Ponded release of water to the extended fault section began on March 6, 2001, and continued for more than a year. The fault was divided into four sections, each of which had a permeameter for water application measurement; all four permeameters were supplied by a single water tank. (Note that Trench Section #4 includes the area previously infiltrated during the Small Plot test.)

Observations from this phase of testing include the intake rates measured along the fault, the time taken for the wetting front to arrive at the monitoring boreholes immediately above Niche 3107 (Niche 3), seepage rates measured at various locations, and concentration of tracers in the seeping water.

6.12.2.1 Fault Intake Rates

During the first two months of water release (under ponded conditions), a stable boundary condition could not be maintained along the fault because of power interruptions and equipment failure. The resulting disruptions to the daily application rate are apparent in the intake data, which show large fluctuations from early March 2001 through mid-May 2001 (Figure 6.12.2-1). During this period, ~15,000 liters of water were applied in the four sections of the fault. Once the supply of water to the fault was stabilized, the variability in infiltriation rates was greatly reduced, ranging from ~25 liters/day to ~100 liters/day along the sections (DTNs: GS020508312242.001 [162129]; GS020908312242.002 [162141]; GS030208312242.003 [165544]).

Within the next nine months, as an additional 57,000 liters of water were released into the fault, there was large spatial and temporal variability in infiltration rates along the fault. In Trench 1, infiltration rates that were ~100 liters/day in early May 2001, steadily dropped to ~25 liters/day by the end of January 2002. In Trench 2, intake rates of ~25 liters/day in early May 2001, gradually decreased to 15 liters/day over a period of nine months. In both Trenches 3 and 4, the temporal fluctuations in the infiltration rates were much larger than Trenches 1 and 2. In both these trenches, the infiltration rates decreased from ~100 liters/day early in May 2001 to ~70 liters per day by late January 2002.

The observed infiltration rates reflect the permeability of the infill material that clogged the near-surface sections of the fault rather than an "open fault." The variability measured in the four sections was most likely determined by the depth to which this infill material had penetrated in each of the sections.

On April 8, 2002, the fault was switched from saturated application to unsaturated application. This was done by applying a known amount of water per minute by the use of pumps. On July 9, 2002, all the dividers were removed from the trench, two of the pumps were turned off, and the water to the entire fault unit was supplied by two pumps. The infiltration rates are illustrated in Figure 6.12.2-1 for the daily rates and in Figure 6.12.2-2 for the cumulative rate. On August 20, 2002, the water application to the trench was stopped and water application to the large plot started (as described in Section 6.12.4).

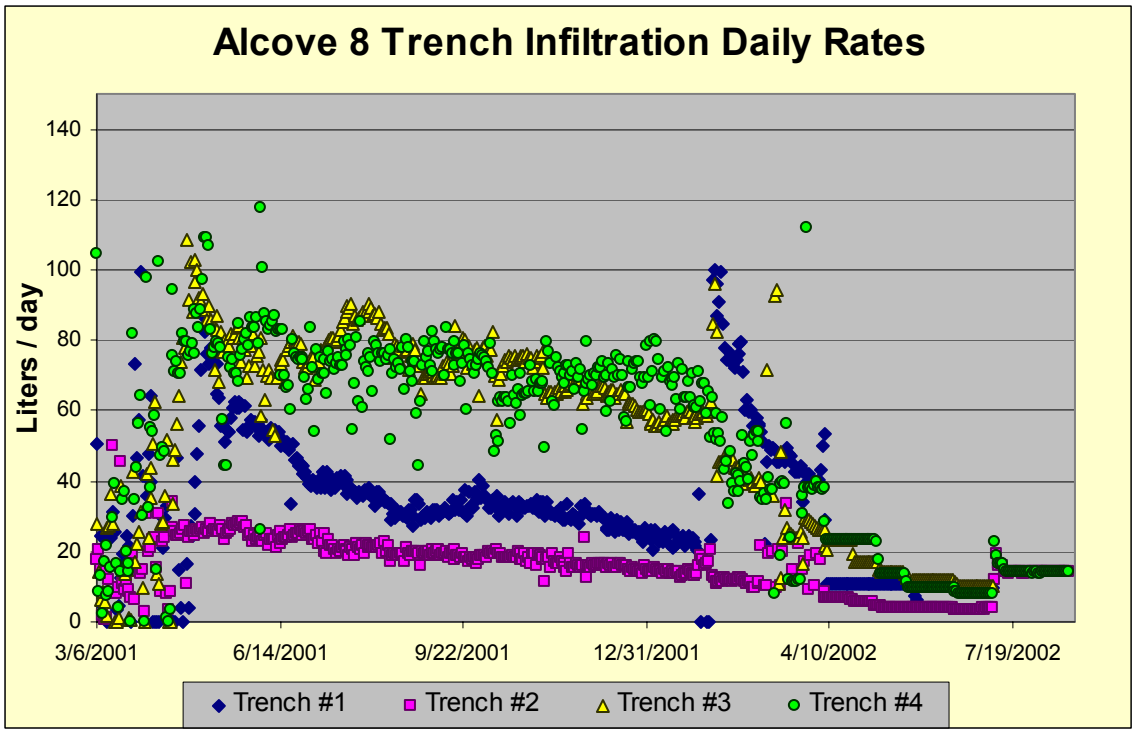

DTN: GS020508312242.001 [162129] for 3/5/2001 to 6/1/2001
DTN: GS020908312242.002 [162141] for 6/1/2001 to 3/26/2002
DTN: GS030208312242.003 [165544] for 3/26/2002 to 8/20/2002

Figure 6.12.2-1. Alcove 8 Trench Infiltration Daily Rates for Saturated and Unsaturated Conditions in the Fault Experiment

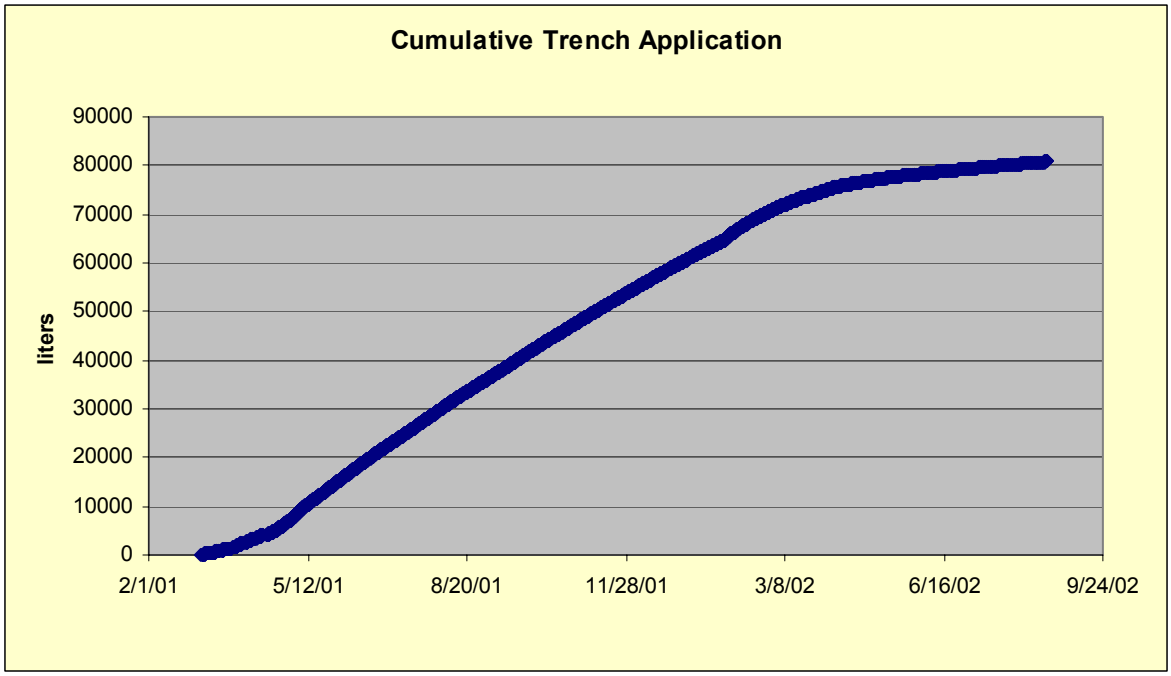

DTN: GS020508312242.001 [162129] for 3/5/2001 to 6/1/2001;
DTN: GS020908312242.002 [162141] for 6/1/2001 to 3/26/2002;
DTN: GS030208312242.003 [165544] for 3/26/2002 to 8/20/2002

Figure 6.12.2-2. Cumulative Trench Application from March 5, 200l, to August 20, 2002

6.12.2.2 Wetting-Front Migration and Development of the Wetting Plume

The three horizontal boreholes located immediately above the ceiling of Niche 3107 (Niche 3) (i.e., boreholes 8, 9, and 10), intercept the fault at a distance of 1.27, 1.93, and 2.08 m respectively from the collars (Figure 6.12.1-4). The vertical distance from the liquid-release zone in Alcove 8 to these boreholes is ~20 m.

The advancing edge of the wetting front was detected 1.9 m from the collar of borehole 10 on April 9, 2001, 34 days after the start of liquid releases along the fault in Alcove 8 (Figure 6.12.2-3). This plume was observed to extend between 1.65 and 2.40 m from the collar in borehole 10 over the next seven days. At this location, the ERP response suggests that wetting was quick, with measured resistance dropping to a relatively constant value within two days.

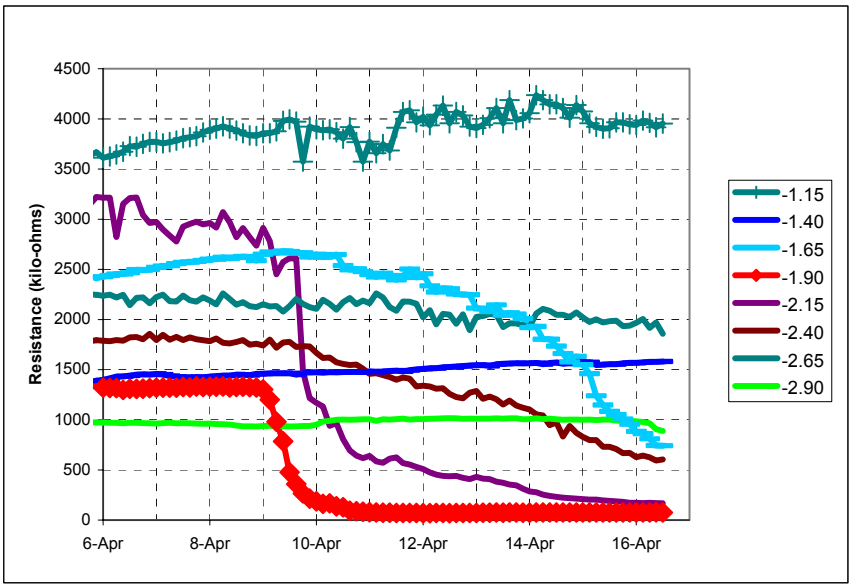

DTN: LB0110A8N3LIQR.001 [157001]

NOTE: Legend indicates the location of measurement (in meters) from borehole collar.

Figure 6.12.2-3. Wetting-Front Arrival Detected in Borehole 10 in Niche 3107 (Niche 3)

After water was detected along sections of the three boreholes intersecting the fault, the spread of the edge of the plume was recorded by ERPs located along boreholes 1, 9, and 10. Figure 6.12.2-4 shows the velocity of the wetting front of the plume in reaching various locations surrounding Niche 3107 (Niche 3). The response from ERPs located along the length of borehole 9 suggests that the fastest velocities (about 0.65 m/day) were observed along a ~0.75 m wide zone from 1.25 m to just below 2.0 m from the borehole collar. The second fastest velocities of ~0.6 m/day were detected over a ~1.0 m wide zone in borehole 10 that was centered 2.0 m from the borehole collar. In both boreholes 9 and 10, the velocity of the wetting front continued to linearly decrease with depth (i.e., further into the niche), dropping to 0.1–0.3 m/day at distances between 4 and 7 m from the borehole collars. Deeper in these boreholes changes in saturation were not detected during the 12 months of liquid release. In the sections of boreholes 9 and 10 close to the Main Drift (i.e., at depths from 0 to 1.0 m from the collars), the wetting front was detected 75–125 days after the start of water release along the fault. It is possible that this delayed signal is the result of evaporation effects closer to the drift.

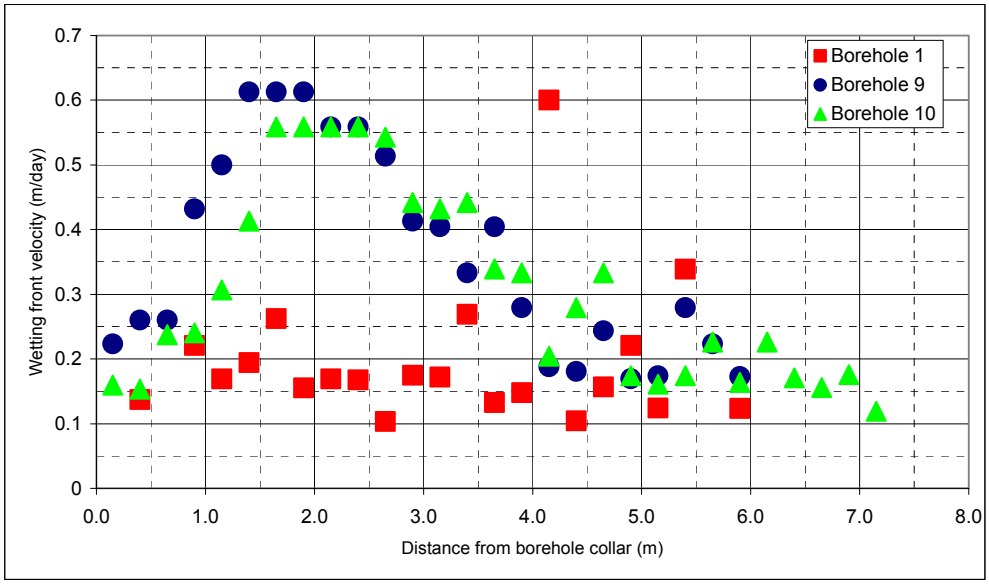

DTN: LB0110A8N3LIQR.001 [157001];
DTN: LB0209A8N3LIQR.001 [165461];
DTN: LB0303A8N3LIQR.001 [162570]

NOTE: See Attachment IX.6.5 for calculation details.

Figure 6.12.2-4. Wetting-Front Velocities as determined from Boreholes 1, 9 and 10 in Niche 3107 (Niche 3)

6.12.2.3 Seepage in Niche 3107 (Niche 3)

Water was first observed along the fault at Niche 3107 (Niche 3) on April 10, 2001. Over the next few weeks, the number of seeps along the fault exposed in Niche 3107 (Niche 3) gradually increased. By June 18, 2001, approximately 1,100 liters of water had been collected from seeps into Niche 3107 (Niche 3) (Figure 6.12.2-5). The seepage rate from a single seep collection tray suggests that following the first measurable seepage, which occurred by the middle of April 2001, seepage rates climbed to near-steady values in the next four weeks.

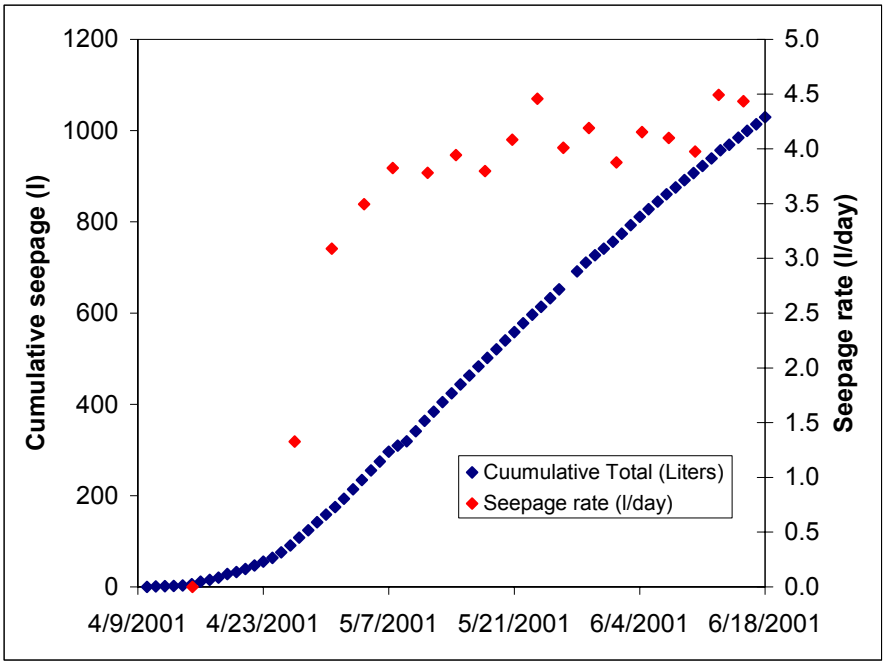

DTN: LB0110A8N3LIQR.001 [157001]

Figure 6.12.2-5. Cumulative Seepage (Blue) from All Collection Trays in Niche 3107 (Niche 3) and the Seepage Rate Observed (Red) along a Section of Fault in Niche 3107 (Niche 3) (as Measured in Tray U3-B4)

Over the next 7 months, measurable seepage was observed in 10 trays located close to the fault trace along the ceiling of Niche 3 (Figure 6.12.2-6). Further into the niche, the ceiling was visibly damp (though not dripping) up to a depth of 4 m into the niche.

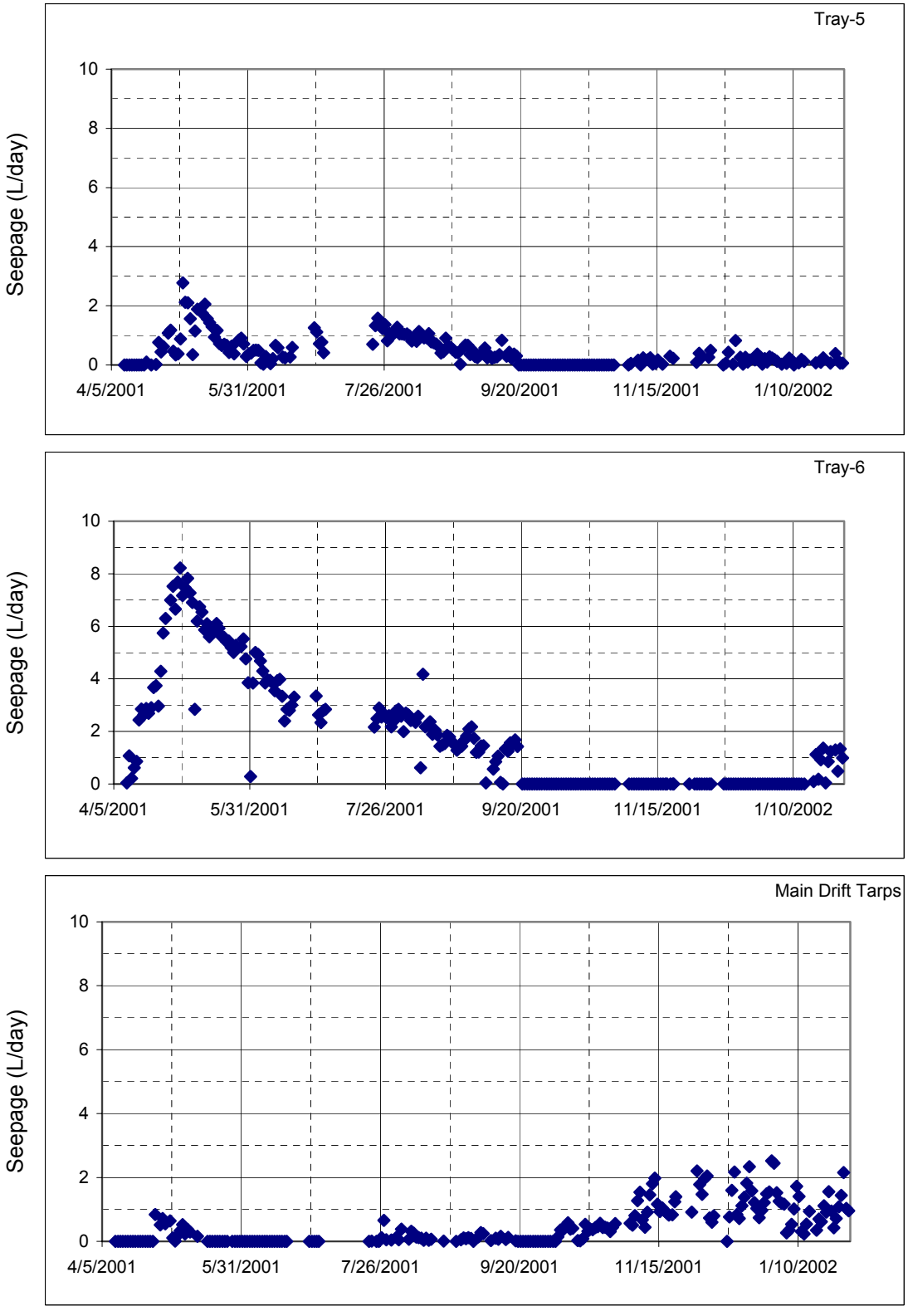

DTN: LB0303A8N3LIQR.001 [162570]

Figure 6.12.2-6. Seepage Rates Measured from 10 Trays Located along the Ceiling of Niche 3107 (Niche 3)

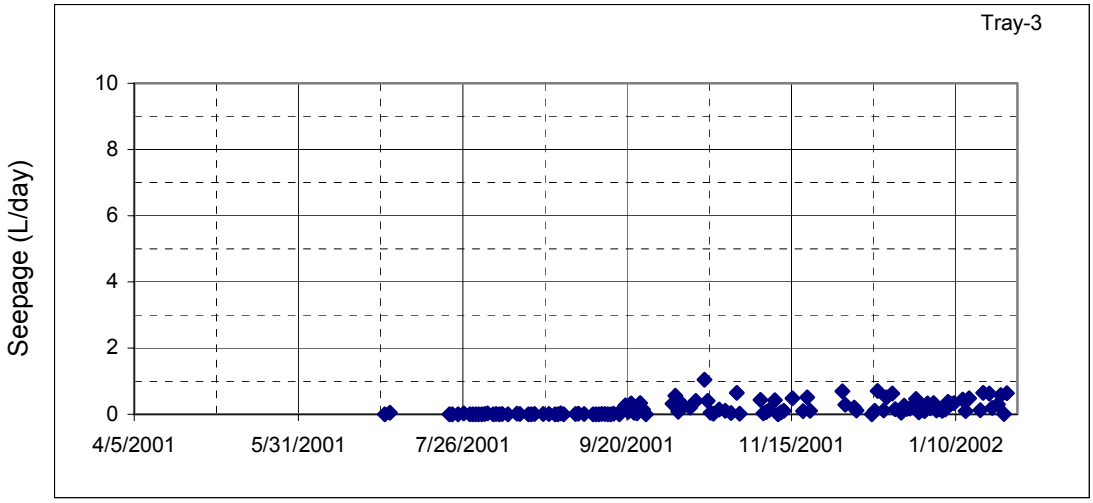

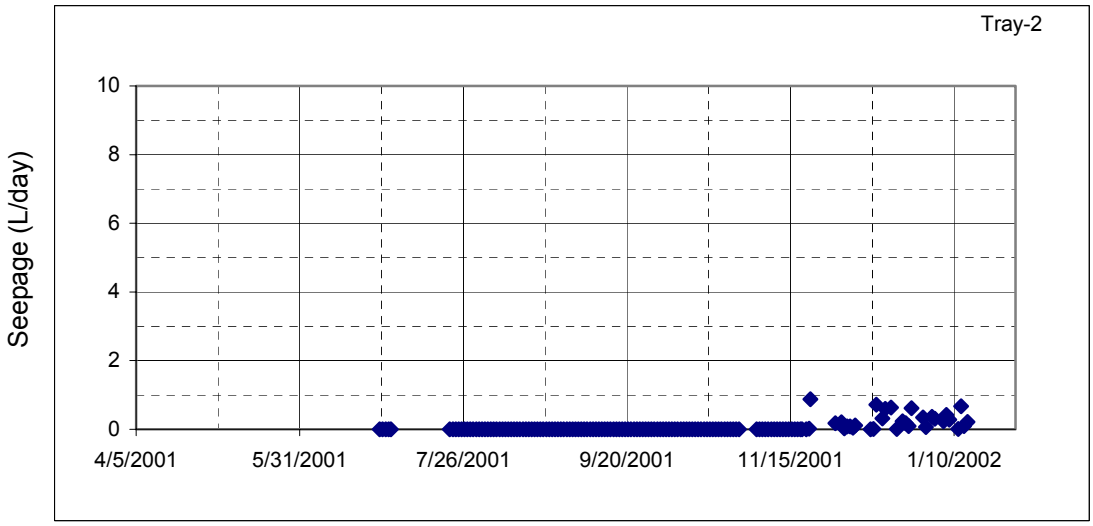

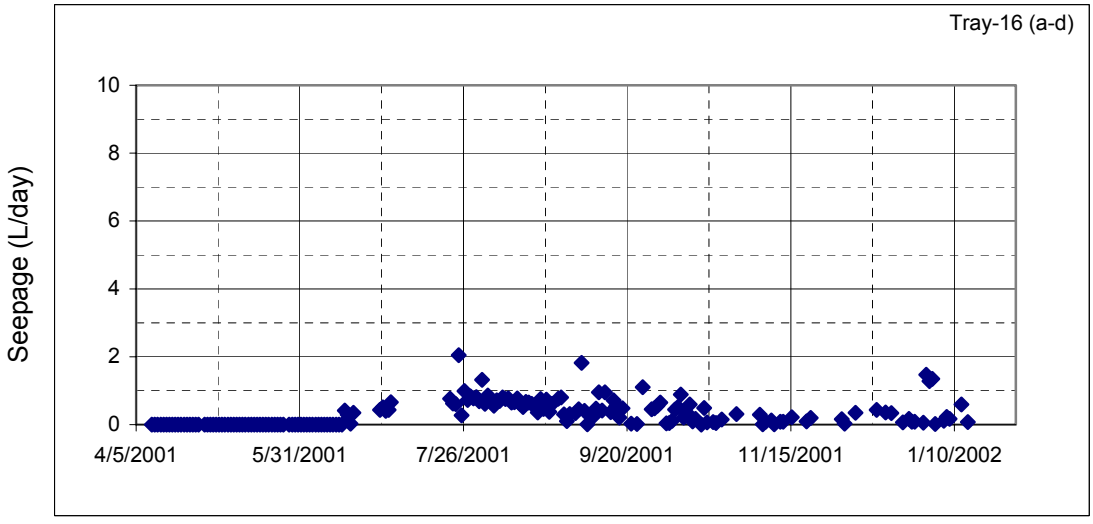

DTN: LB0303A8N3LIQR.001 [162570]

Figure 6.12.2-6. Seepage Rates Measured from 10 Trays Located along the Ceiling of Niche 3107 (Niche 3) (continued)

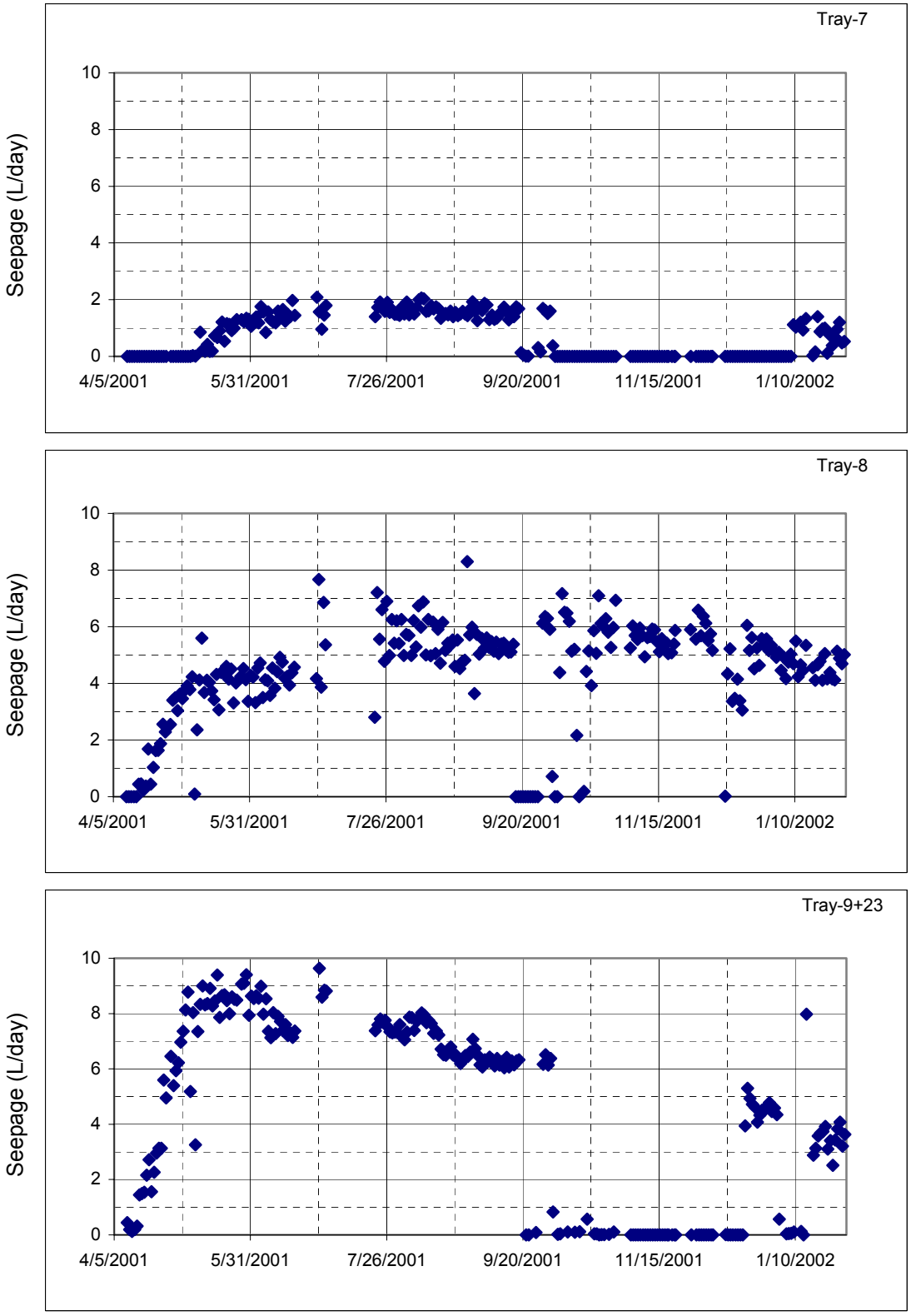

DTN: LB0303A8N3LIQR.001 [162570]

Figure 6.12.2-6. Seepage Rates Measured from 10 Trays Located along the Ceiling of Niche 3107 (Niche 3) (continued)

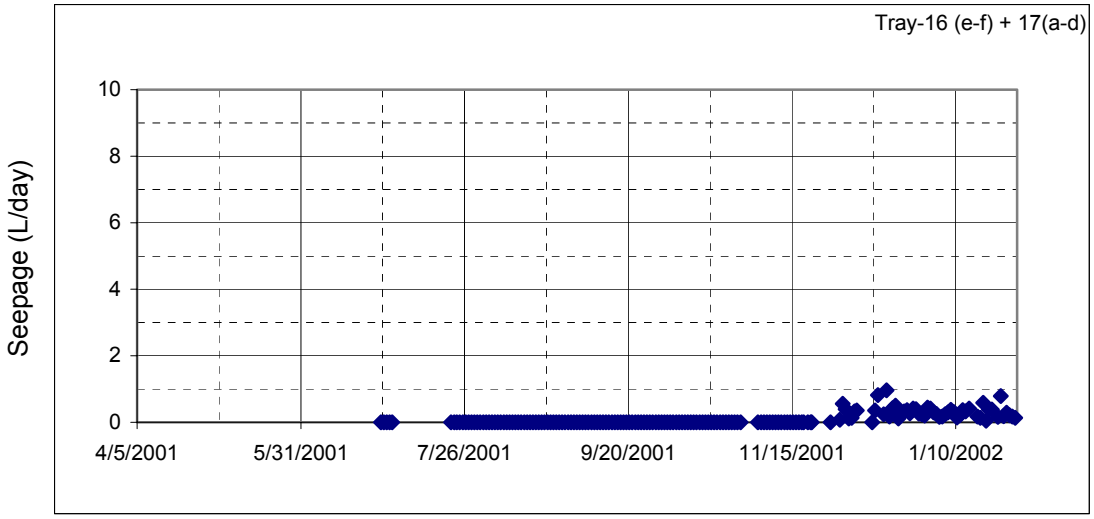

DTN: LB0303A8N3LIQR.001 [162570]

Figure 6.12.2-6. Seepage Rates Measured from 10 Trays Located along the Ceiling of Niche 3107 (Niche 3) (continued)

Seepage was first seen above Tray 6. At this location, seepage rates climbed rapidly to ~ 8 L/day over a period of two weeks, before dropping sharply to rates below 2 L/day by early August 2001. A similar temporal pattern was observed from Tray 9+23, where the seepage rates reached ~9 L/day over a period of 2–3 weeks before steadily decreasing to ~3 L/day by late January 2002. (For the period from October 2001 to early January 2002, seepage water into trays 6, 7, and 9+23 were diverted to tracer samplers, and the seepage rates were not measured.) The most consistent seepage rates (i.e., between ~4–7 L/day) were maintained at the location of Tray 8. At other locations along the niche ceiling, seeps were observed significantly later. At these locations, seepage was sporadic and occurred at rates that were consistently less than 3 L/day.

6.12.2.4 Tracer Recovery in Niche 3107 (Niche 3)

From the time that the first seep was observed in Niche 3 on April 9, 2001, water samples were periodically collected from the location of the first seep (Tray 6) and analyzed for LiBr concentrations. Six months later, when the tracer-mix comprising LiBr and PFBA was injected with the infiltrating water, seeping water from three locations along the Niche 3 ceiling were sampled. During this sampling, all water seeping from the three locations was collected as discrete 0.5 or 1.0 liter samples and analyzed for concentrations of Li, Br, and PFBA.

Figure 6.12.2-7 shows the concentration of Br measured in the seepage water along with the daily seepage rates for a 1.5 month period following arrival of the wetting front. The Br concentration was initially low (about 3 ppm), increasing gradually with time to a value of 30 ppm (that is the same as that for water applied at the infiltration plot) about 30 days after seepage occurred at Niche 3107 (Niche 3). This may be an indication of the importance of matrix diffusion. If there is no matrix diffusion at all, the Br arrival will not be developed and Br concentration should be a constant (30 ppm) with time. In addition to matrix diffusion, other mechanisms, such as sorption, may also contribute to the observed retardation of Br transport. However, Br is generally considered conservative, and the potential sorption is expected to play a minor role in the observed retardation.

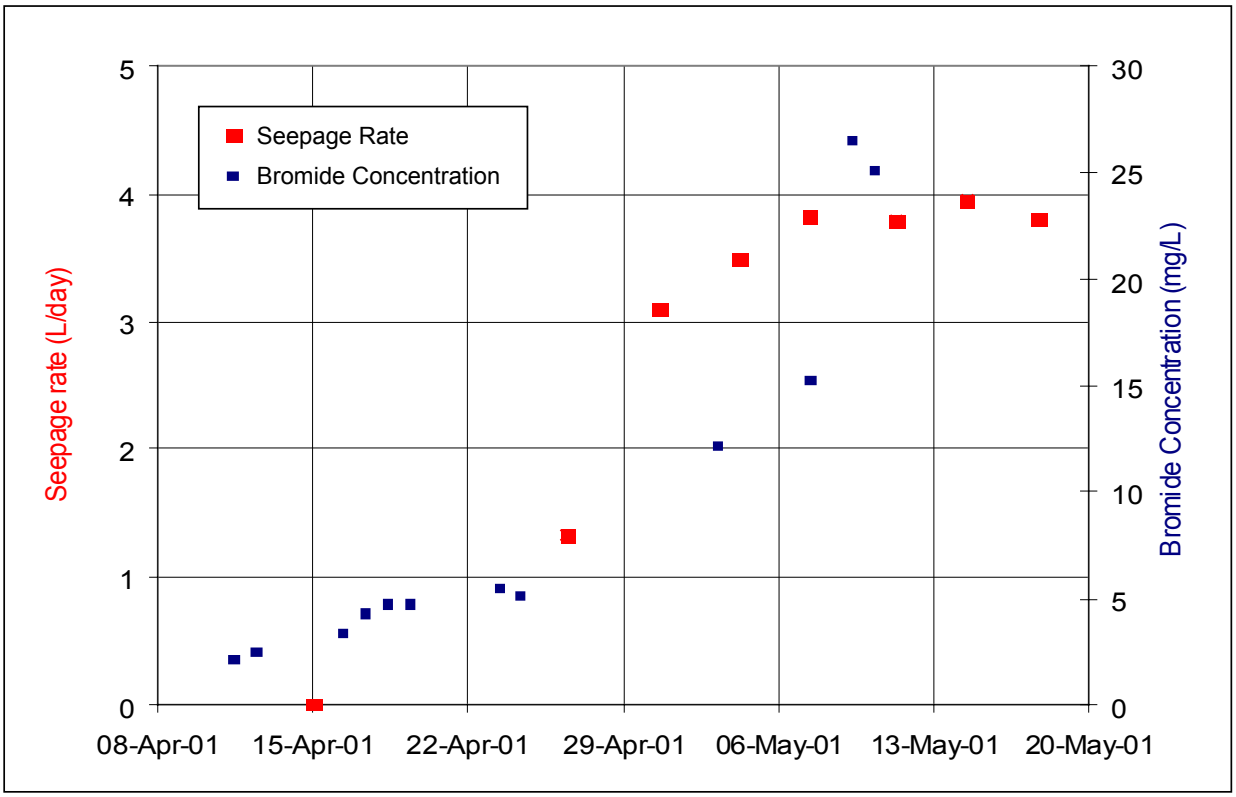

DTNs: LB0110A8N3LIQR.001 [157001]; LB0204NICH3TRC.001 [158478]

Figure 6.12.2-7. Concentration of Bromide and Seepage Rates Plotted for a Period of 45 Days After First Observations of Drips in Tray 6

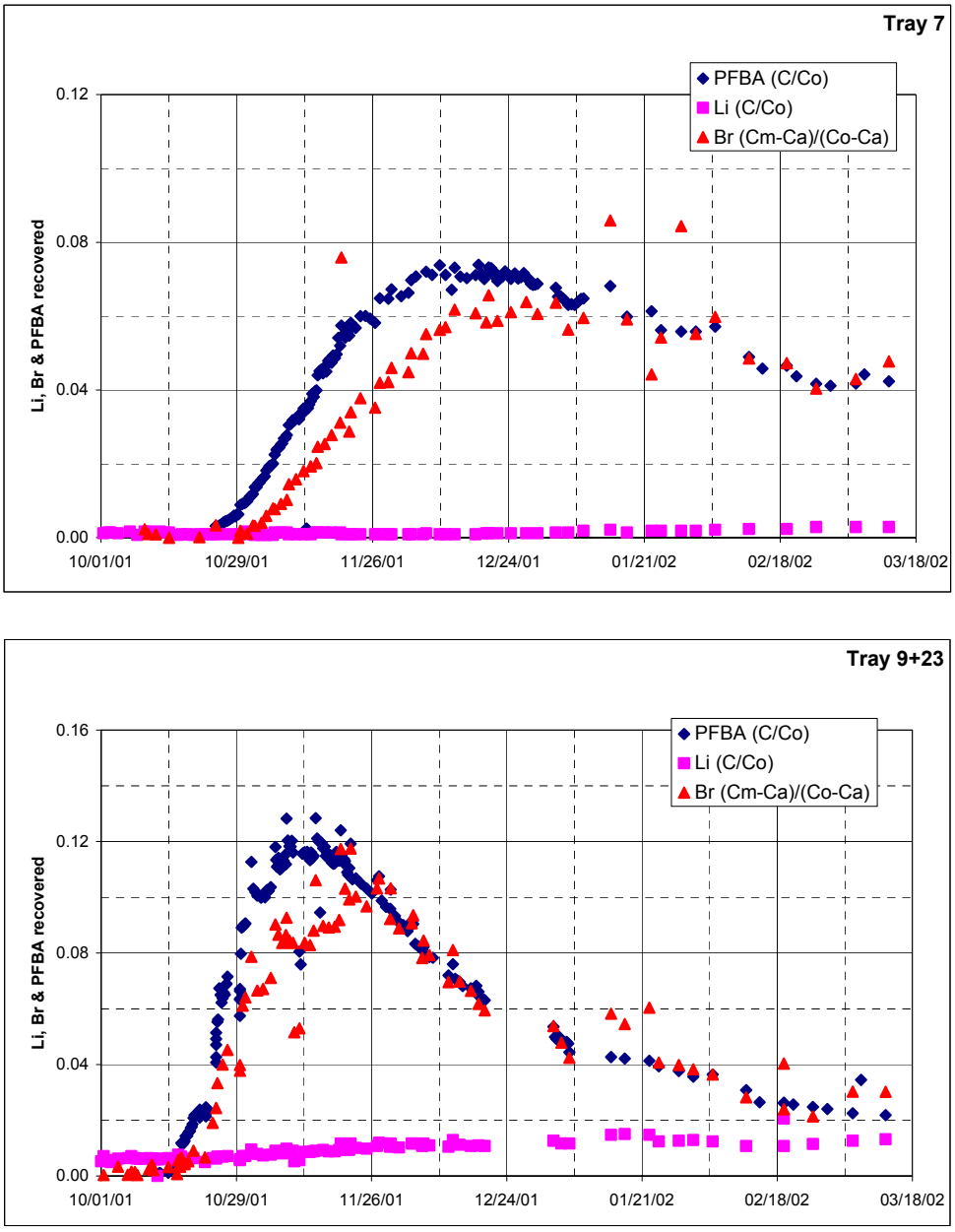

DTNS: LB0204NICH3TRC.001 [158478], LB0303A8N3LIQR.001 [162570]

Note: C_m is the measured concentration and C_a is the background concentration in the leachate.

Figure 6.12.2-8. Relative Mass Recovery of Tracers Measured in Seepage in Niche 3107 (Niche 3)

Figure 6.12.2-8 presents the tracer concentration in the seepage water collected from two sampling locations. In Tray 7, both bromide and PFBA were first detected three weeks after initial application of the tracers along the fault. In the following month, the concentration of both the tracers gradually increased, with the PFBA concentrations clearly preceding bromide. Peak concentrations of PFBA at this location were observed 61 days after the start of tracer release in Alcove 8. Over the next three months, the concentration of both tracers gradually decreased. During the final month of sampling, the tracer concentrations remained relatively constant.

In Tray 9+23, except for the period between mid-October and late November 2001, when the PFBA concentrations suggest faster travel through the fault zone, both tracers showed a similar temporal recovery pattern. The peak concentrations of tracers at this location were observed 43 days after the start of tracer release in Alcove 8, suggesting a transport velocity of ~ 0.46 m/day.

6.12.3 Geophysical Imaging of the Drift-to-Drift Test Block

Preliminary baseline images for the test block between Alcove 8 and Niche 3107 (Niche 3) have been collected with two different techniques: seismic tomography and ground-penetrating radar tomography (GPR-T). The objective of seismic tomography data acquisition was to acquire baseline data to help monitor the fluid infiltration tests. The GPR data are presented in detail within this scientific analysis report and compared with documented seismic tomography data. The comparison helps to constrain the interpretation of the local lithology. Both geophysical tomography studies used the slant (near-vertical) boreholes drilled around the test block, as illustrated in Figure 6.12.1-2 and Figure 6.12.1-3, around a large plot prepared for planar infiltration tests.

6.12.3.1 Background and Ground-Penetrating-Radar Experimental Approach

In the borehole radar method, modified surface radar antennas are emplaced into a rock formation, and high-frequency electromagnetic signals are transmitted through the formation to a receiving antenna. Electrical properties of the subsurface material greatly influence the transmitted electromagnetic signal. In particular, the dielectric permittivity (K) of the rock has a strong influence on the propagation of the signal and on whether it travels at a high or low velocity. Furthermore, moisture content also affects dielectric permittivity. The high dielectric permittivity of water (K ~80) or wet rock (K ~20–30) in contrast to drier rock (K ~3-6) typically results in greatly reduced signal velocities. Changing chemical compositions (i.e., tracers) may also alter the bulk dielectric permittivity of the rock and hence the propagation velocity of the radar wave. Any changes in signal character shall be measured over the course of the Alcove 8/Niche 3107 (Niche 3) infiltration experiment, and any increase (or decrease) in the background moisture content or chemical composition resulting from the fluid infiltration (or rock dryout) will result in changes in the received radar velocity.

The transmitted signals are represented as multiple ray paths crossing through a zone within the block. If sufficient ray paths are recorded, a tomographic image is obtained through computer processing. The information extracted from such data consists of the radar wave travel time, which depends on the wave velocity. This information, in the form of a processed radar velocity tomogram, offers a high-resolution approach to monitoring the changes occurring in the rock over the duration of the tracer-injection experiment. Previous experiments at Yucca Mountain

indicate that the radar method should provide relatively high-resolution imaging of the zone of interest. The peculiar orientation of the boreholes between Alcove 8 and Niche 3107 (Niche 3), however, may provide decreased image resolution relative to previous radar experiments (e.g., Busted Butte, Drift Scale Test, Single Heater Test).

A detailed description of the equipment used, the component specifications, the operating principles, and the GPR survey methodology can be found in the Technical Implementing Procedure, YMP-LBNL-TIP/GP 5.0, *Ground Penetrating Radar Data Acquisition*, governing all GPR data acquisition done in support of the Yucca Mountain site characterization effort.

6.12.3.2 Results of the Radar Data Acquisition

The radar data were acquired in all six of the boreholes located within Alcove 8. Additionally, two of the boreholes in Niche 3107 (Niche 3) were used in combination with two of the holes in Alcove 8. The eight boreholes include the following: 1–6 (Alcove 8) and 1–2 (Niche 3107 (Niche 3)). The configuration of and layout of the boreholes used are illustrated in Figure 6.12.1-2.

The radar data were acquired in the two-dimensional planes defined by the two boreholes, more commonly referred to as well pairs. The well pairs acquired in Alcove 8 include the following: 1-2, 3-4, 1-3, 2-4, and 5-6. The well pairs acquired between Alcove 8 and Niche 3107 (Niche 3) include the following: 1 (Alcove 8)—3 (Niche 3107 (Niche 3)) and 4 (Alcove 8)—2 (Niche 3107 (Niche 3)). The decision to acquire data between Alcove 8 and Niche 3107 (Niche 3) stemmed from the fact that an image of the boundary between the two lithologic units in this region was desired. By working only in the boreholes located in Alcove 8, this boundary was not penetrated and hence was not able to be imaged by using these boreholes alone.

Thus far, the data have been processed for travel times, with the result being radar velocity tomograms. Differencing or subtraction of the velocity tomograms will be conducted over the course of infiltration tests. Such differencing or subtraction allows for the highlighting of the moisture front as it changes spatially and temporally. In essence, the background formation remains static in those areas not affected by the changing moisture front. By subtracting one velocity tomogram from another, we will be able to discount those areas remaining static while emphasizing those areas where change (i.e., flow or wetting) is occurring.

The well pairs between Alcove 8 and Niche 3107 (Niche 3) differ slightly from the well pairs in Alcove 8 in their acquisition method. Because of the large distances between the well pairs (~20 m), the 100 MHz antenna frequency used for the Alcove 8 well pairs was found to be too high (i.e., too prone to signal attenuation), and so the well pairs were collected using the 50 MHz antennas. Higher frequencies generally result in data of higher resolution (approximately 25.0 cm for 100 MHz), so the highest frequency antennas should be used if at all possible. Unfortunately, higher frequencies also result in greater attenuation of radar energy with increasing distance, so a balance must be struck between resolution and well-pair distance. The 50 MHz data collected between Alcove 8 and Niche 3107 (Niche 3) resulted in very usable data, and for the purposes of this experiment, it is deemed perfectly acceptable.

6.12.3.2.1 Alcove 8 Well Pairs 1-2, 3-4, 1-3, 2-4, and 5-6

All of the radar data processed thus far between the boreholes in Alcove 8 show similar results, and as such are considered together in this section (Figure 6.12.3-1a through Figure 6.12.3-1e). The radar velocity images all appear to suggest that the lithologic formation directly underlying Alcove 8 varies little in regards to its dielectric properties. This is as expected, because none of the boreholes penetrates the lithologic contact between Alcove 8 and Niche 3107 (Niche 3). As far as smaller structures are concerned (e.g., lithophysal cavities), they may be of too small a size or of insignificant-enough dielectric contrast to be imaged. Close inspection of the images, however, reveals some zones of anomalous velocity that may or may not correspond to such small structures. What the data do suggest is that any changes resulting from wetting or fluid flow upon commencement of the infiltration experiment are not expected to follow any particular path. In previous experiments using this method, potential flow paths had been defined by the baseline radar velocity images prior to infiltration, and velocity change results from wetting were subsequently observed in these regions. Again, this is not observed for the baseline images acquired between the Alcove 8 boreholes.

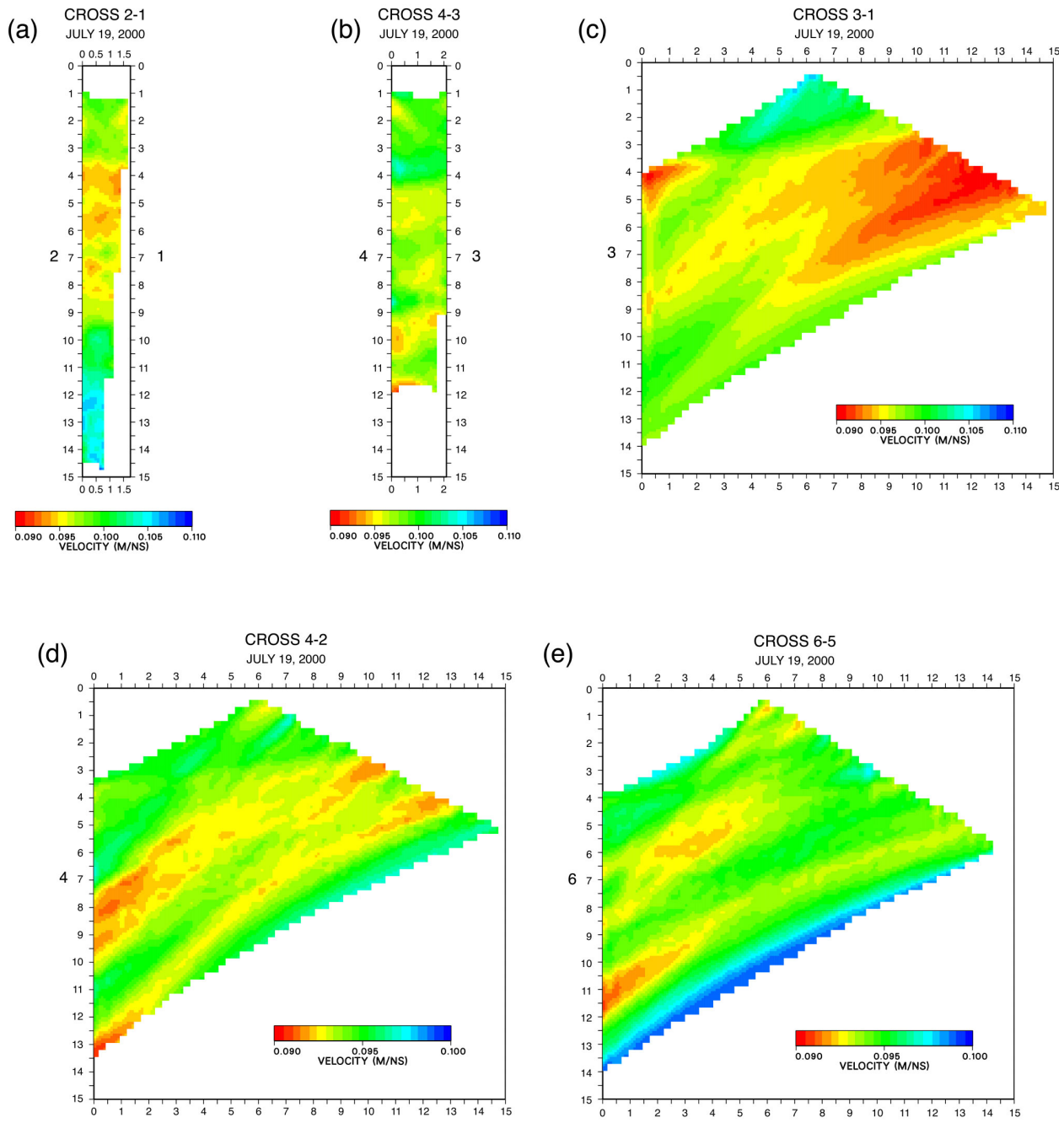

DTN: LB0110A8N3GPRB.001 [156912]

Note: All axes are distance in meters (m). Borehole IDs of the well pairs are placed next to the velocity labels.

Figure 6.12.3-1. Radar Velocity Tomograms between Alcove 8 Well Pairs

6.12.3.2.2 Well Pairs 1 (Alcove 8)—3 (Niche 3107 (Niche 3)) and 4 (Alcove 8)—2 (Niche 3107 (Niche 3))

After acquiring the radar data between the boreholes in Alcove 8, additional data were acquired in boreholes between Alcove 8 and Niche 3107 (Niche 3). The drift-to-drift tests imaged the lithologic contact occurring between the two locations and allowed for monitoring of this contact during the infiltration. Figure 6.12.3-2a and Figure 6.12.3-2b are the baseline radar velocity data for the two well pairs. Immediately obvious is the higher velocity subhorizontal interface near the upper portions of the Niche 3107 (Niche 3) boreholes. This region is inferred to be the lithologic contact between the two locations. Comparing the two radar velocity images, this contact is quite similar, although it appears to be dipping at slightly different angles from one image to the other. The imaged contact will be a point of focus in infiltration tests.

Seismic tomography is another geophysical technique that is sensitive to structure heterogeneity. The seismic method relies on differences in the mechanical properties of the rock to produce a tomographic image. Results of the seismic tomographic images are presented by Descour et al. (2001 [156869]).

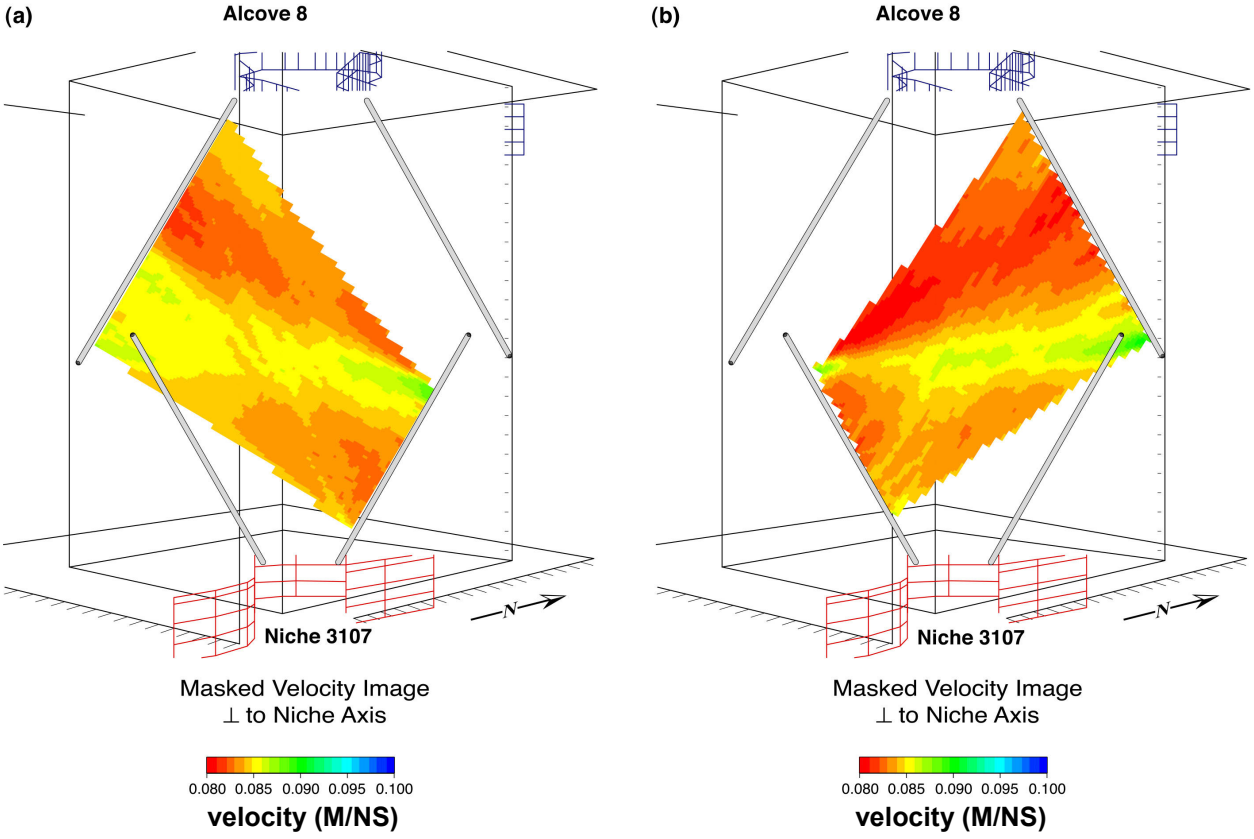

DTN: LB0110A8N3GPRB.001 [156912]

Figure 6.12.3-2. Radar Velocity Tomograms between Alcove 8 and Niche 3107 (Niche 3) Well Pairs

6.12.4 Large Plot Test

The ongoing test series involves the release water (laced with 1 or 2 tracers) under both ponded and nonponded conditions in a 4 m by 3 m plot (Figure 6.12.4-1). During this phase, water was released into the plot under a controlled rate. Details of the site, experimental setup, and monitoring for the large-plot test are the same as in the fault liquid test (Section 6.12.2) with the following test information. Ponded release of water to the 3 × 4 m section along the floor of Alcove 8 began on August 20, 2002 (DTN: GS031008312242.007 [166089]). The infiltration zone was divided into 12 sections, each 1 × 1 m (Figure 6.12.4-1).

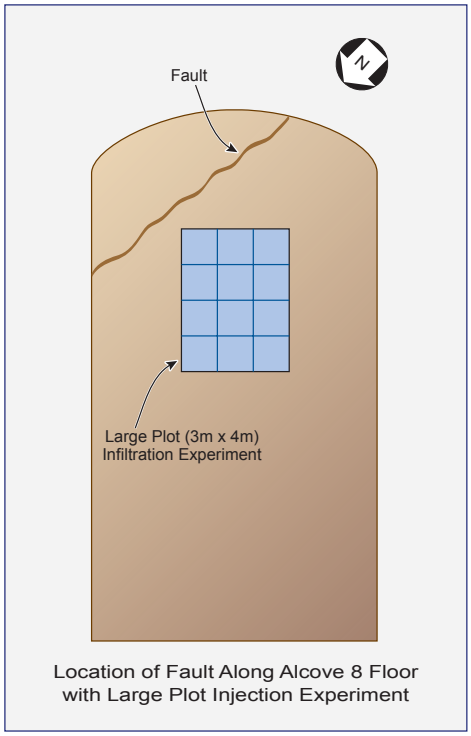

Figure 6.12.4-1. Schematic Illustration of the Infiltration Zones along the Floor of Alcove 8 Large-Plot Test with the numbers identifying the 12 infiltration sub-plots

The infiltration rates of individual plots are illustrated in Figure 6.12.4-2. The cumulative application of all 12 plots is illustrated in Figure 6.12.4-3 for the period from August 20, 2002 to November 12, 2002.

Infiltration was initiated in the large-plot on August 20, 2002 and this upper boundary condition was constrained to a ~2 cm head of ponded water. The amount of water necessary to maintain the 2 cm of ponding was continuously recorded. The resulting infiltration rates (measured over period of five months) in each of the 12 plots are plotted in Figure 6.12.4-2. Note the legend in the plots refers to the plot numbers, which increase sequentially along the rows beginning with the plot on the top left (i.e. the first plot is AL 810 and the last plot located at the bottom row last column is AL 821).

The data show that there was spatial and temporal variability in the infiltration rates. In most plots the early high fluctuations in infiltration rates gradually approached steady rates that ranged between ~ 120 to less than 10 L/day.

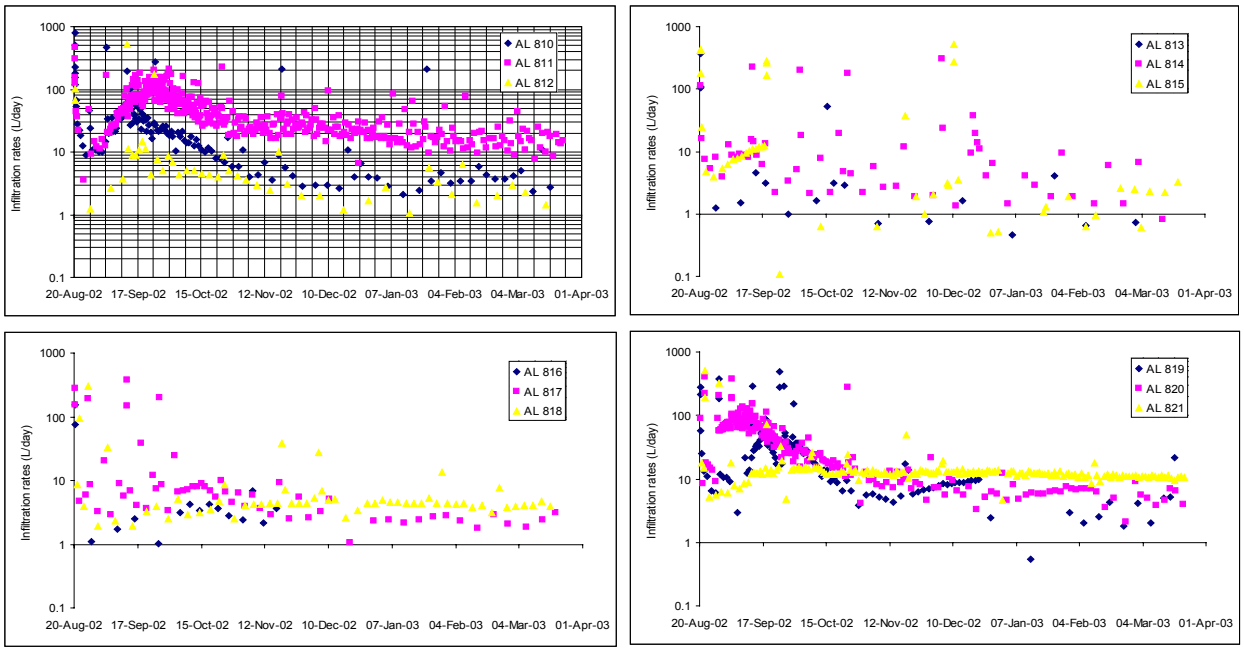

DTNs: GS031008312242.007 [166089] from 8/20/2002 to 11/19/2002;
GS030608312242.005 [166200] from 11/19/2002 to 3/21/2003

Figure 6.12.4-2. Infiltration Rates of Individual Plots from August 20, 2002, to November 19, 2002

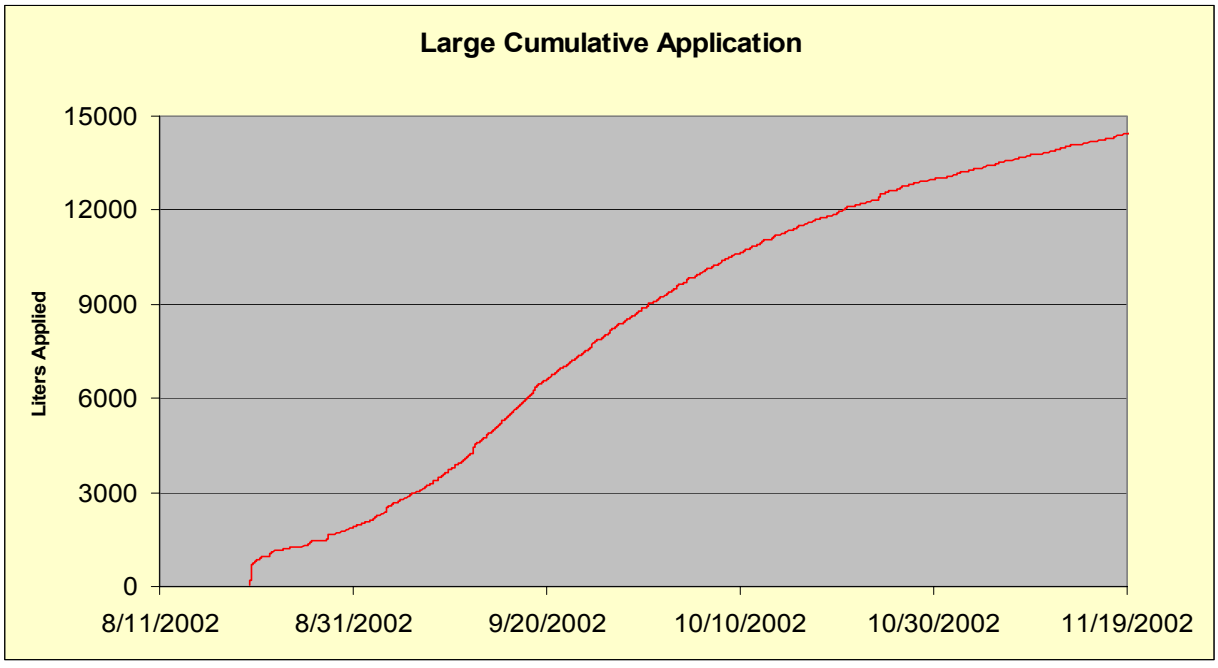

DTN: GS031008312242.007 [166089]

Figure 6.12.4-3. Cumulative Application of All Twelve Plots in Alcove 8 Large Plot Experiment

Observations from this phase of testing include the total seepage rates measured at Niche 3107 (Niche 3) during the preliminary phase of this test. Water was first observed along the fault at Niche 3107 (Niche 3) on September 10, 2002. Measurable seepage was recorded after a week. By the last week of September, the total daily seepage rate measured in Niche 3107 (Niche 3) was ~25 L/day (Figure 6.12.4-4). Over the next few weeks, the daily seepage rates remained fairly steady.

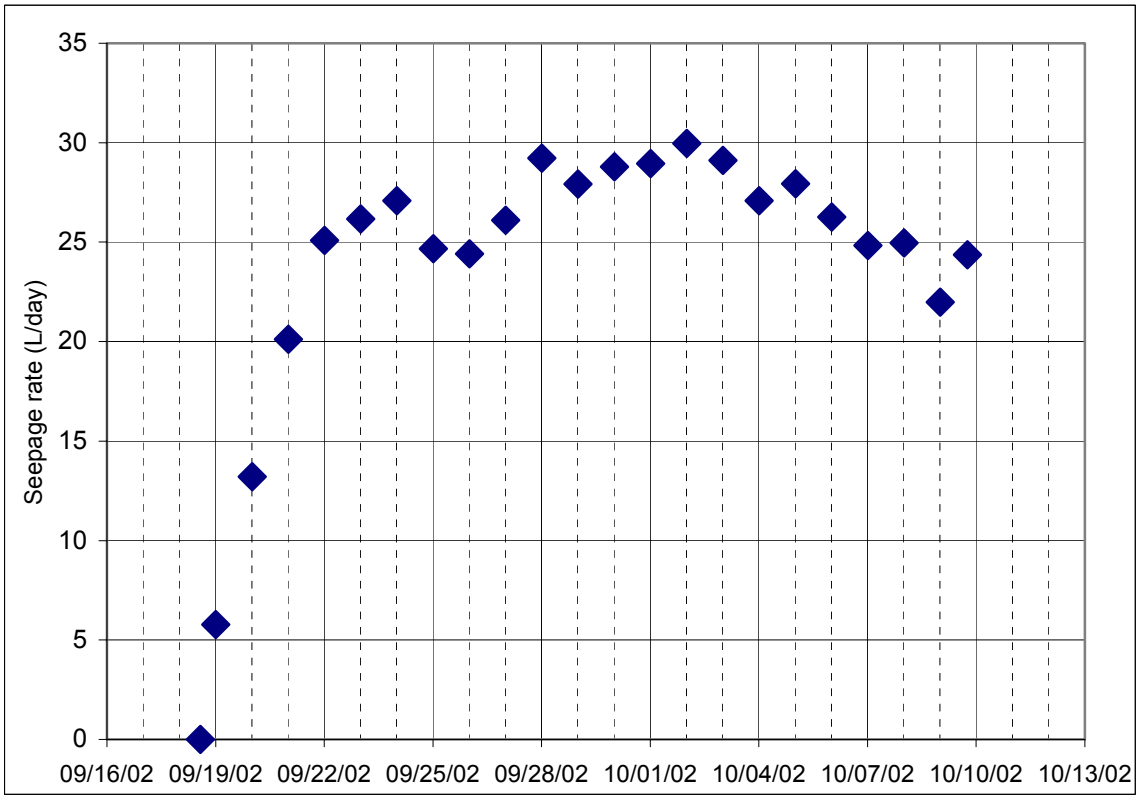

DTN: LB0306A8N3LIQR.001 [165405]

Figure 6.12.4-4. Daily Seepage Rates Measured in Niche 3107 (Niche 3) Following Release of Water in the Big Infiltration Plot in Alcove 8

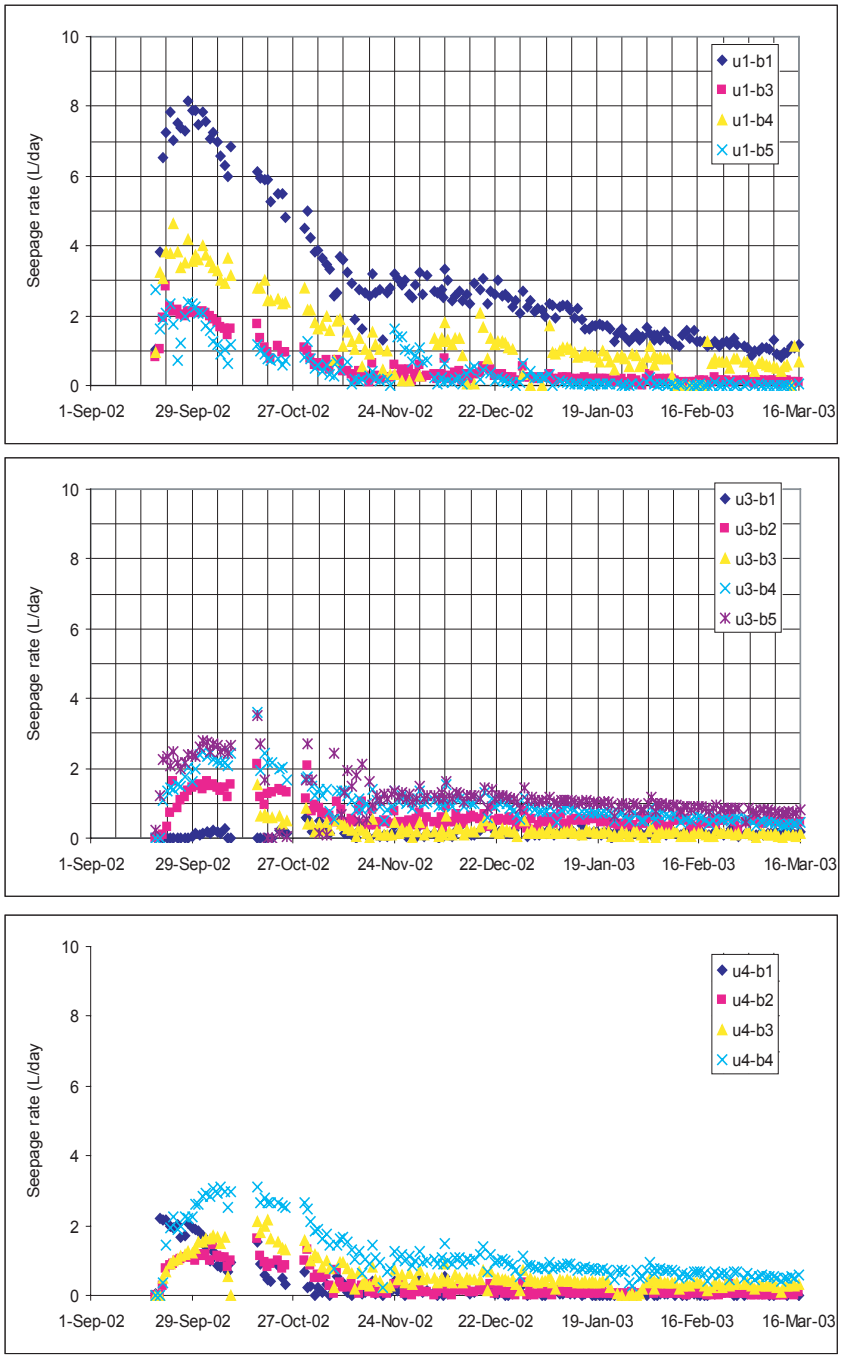

DTN: LB0306A8N3LIQR.001 [165405] from 9/18/2002 to 10/16/2002;
LB0308A8N3SEEP.001 [166090] from 10/16/2002 to 4/2/2003

NOTE: Sample bottle collection locations from designations “u1-b1, u1-b3, …” are documented in scientific notebook by Salve (2002 [165378], pp. 71, 88, 97).

Figure 6.12.4-5. Seepage Rates Measured in Niche 3107 (Niche 3) Following Release of Water in the Big Infiltration Plot in Alcove 8

Seepage was first visually observed in Niche 3 on September 10, 2002, on the back wall, where it meets the ceiling. Measurable seepage was recorded after a week after these initial observations.

The seepage measured over time from each tray for the period of 9/16/02 to 3/16/03 is plotted in Figure 6.12.4-5. Early seepage was measured approximately 30 days after the initial application of water along the infiltration plot. Following the arrival of the wetting front, seepage at most monitored locations appeared to increase over a period of ~1-4 weeks before gradually decreasing. The highest seepage rates measured during this peak event was ~ 8 L/day. Following peak values, the seepage rates at all locations continuously decreased with maximum rates measured at ~1 L/day by the second week of March, 2003.

6.12.5 Available Information of Alcove 1 Surface-to-Drift Tests and Implications for Infiltration Processes

6.12.5.1 Alcove 1 Test Data

Alcove 1 is located near the North Portal of ESF in the upper lithophysal zone of the Tiva Canyon Tuff. The alcove is about 5.5 m high and 5.8 m wide. In the Alcove 1 tests, water was applied in a plot ~30 m directly above the alcove. The size of the infiltration plot was 7.9 × 10.6 m (Liu et al. 2003 [162470], pp. 174–175). An irrigation drip tubing, with 490 drippers uniformly distributed within the infiltration plot, was used to apply the water. The vertical cross section and plan view of the test site is illustrated in Figure 6.12.5-1 (Guertal 2001 [164070], pp. 29–30). Table 6.12.5-1 summaries the data in the TDMS for two phases of tests.

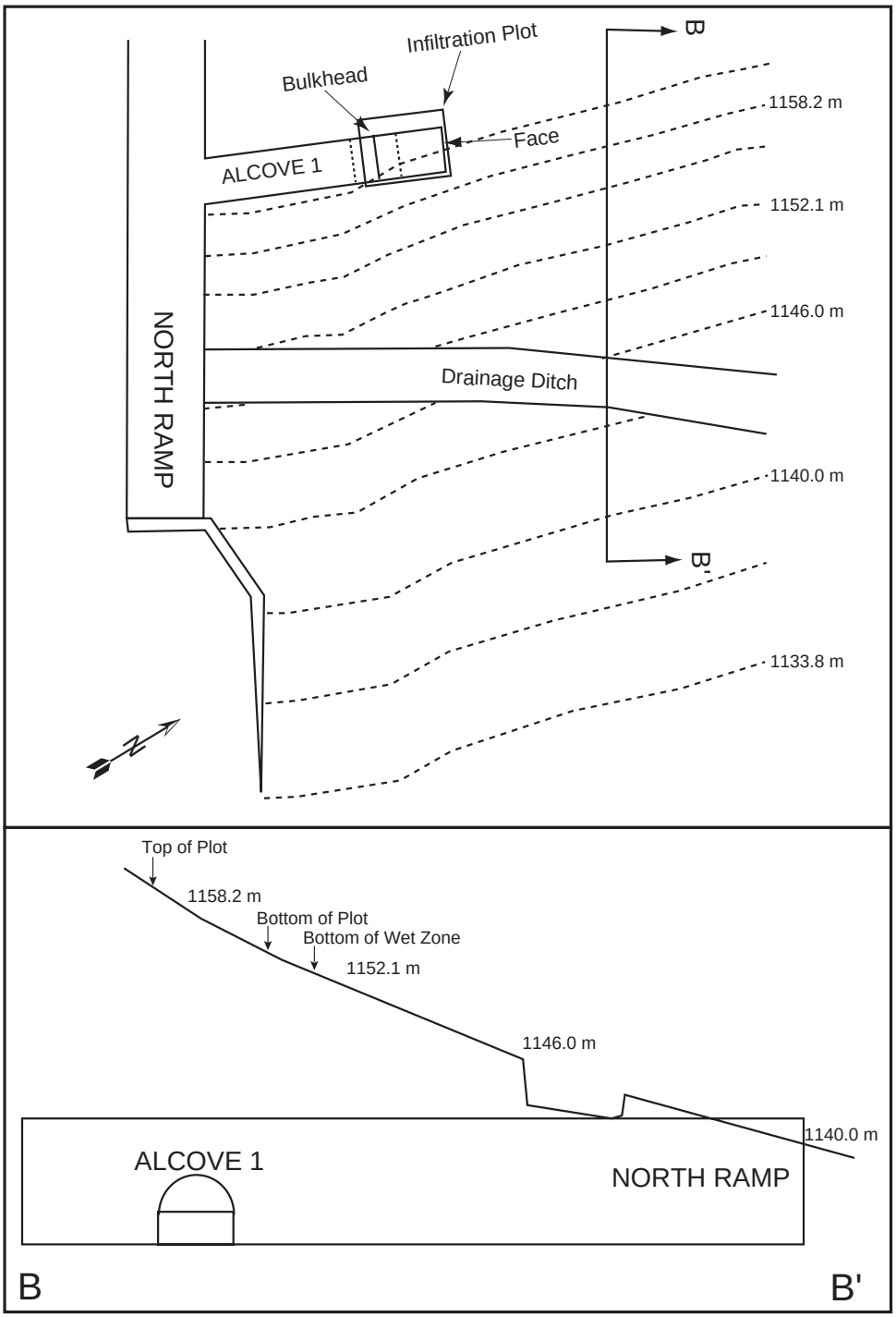

Source: Guertal (2001 [164070], pp. 29–30)

Figure 6.12.5-1. Schematic Illustration of Alcove 1 Test Site Inside the ESF North Portal

Table 6.12.5-1. Alcove 1 Infiltration Test Data

DTN	Description
GS990108312242.006 [162979]	Pulse flow meter data for infiltration on surface, Phase I, 3/9/98–12/4/98
GS000308312242.002 [156911]	Seepage data for water collected in Alcove 1, Phase I, 05/05/98–08/27/98
GS000808312242.006 [162980]	Pulse flow meter data for infiltration on surface, Phase II, 2/19/99–6/20/00
GS000399991221.003 [147024]	Preliminary infiltration, seepage, tracer data, Phase II, 2/19/99–12/15/99
GS001108312242.009 [165202]	Tracer data for water collected in Alcove 1, Phase II, 5/9/99–7/5/00

Phase I infiltration of infiltration and seepage is summarized in DTN: GS000308312242.002 [156911]. Water was applied at the surface with irrigation drip tubing (3/9/1998 – 8/13/1998) and collected by a series of 1-foot-square (~0.3 m × 0.3 m) drip trays inside Alcove 1 (5/5/1998–8/27/1998). The irrigated area was 83.7 m^2 and the collection area was 40.2 m^2. The amount of seepage as a percentage of the water applied on the surface depends on the areas chosen for comparison and on the time of observations: 2.9% of the total applied water seeped into Alcove 1; 6.1% of the water applied above the collection area seeped in Alcove 1; 5.4% of the total applied water seeped into Alcove 1 after the rock above Alcove 1 was wetted; and 11.1% of the water applied above the collection area seeped into Alcove 1 after the rock above Alcove 1 was wetted.

Both Phase I and Phase II data were used to interpret the test, with calibration using the seepage rate from Phase I of the test and prediction and comparison for Phase II (Liu et al. 2003 [162470], Figure 1 for infiltration rates, Figure 3 for seepage rates). The study of LiBr tracer data shows that matrix diffusion may have a significant effect on overall transport behavior in unsaturated fractured rocks.

6.12.5.2 Alcove 1 and Pagany Wash Infiltration Comparison

In addition to seepage and transport, Alcove 1 tests also have implications for the description of net infiltration processes through the bedrock. The upper surfaces of Yucca Mountain are either exposed bedrock with a thin veneer of soil cover, or in washes filled with alluvium. An Alcove 1 infiltration test result is compared to a Pagany Wash analysis results in this section.

The maintenance of rates at the infiltration plot is related to a controlling factor in determining net infiltration. The infiltration plot was located on a hill slope. The range of flux was from 0 to 30 mm/d during 2/19/99 to 12/15/99. The range of 18 mm/d to 25 mm/d was maintained from 9/21/99 to 10/15/99 before a test with tracer application began. In both the Phase I test (from 3/8/98 to 12/4/98) and the Phase II test (from 1/29/99 to 6/20/00), water applications were controlled such that no surface runoff occurred. Therefore, infiltration rate over 30 mm/d could induce surface runoff.

This range of infiltration rate (< 30 mm/d) is orders of magnitude smaller than the hydraulic conductivity values of the Tiva Canyon fractured rock, based on measured values from air-injection tests in boreholes drilled from the interior of the alcove, ranging from 169 mm/d to 7.20e4 mm/d, with the geometric mean of 1.36e4 mm/d (LeCain 1998 [100052], p. 1 and Tables 1-3). One implication is that the fractures on the surface in the infiltration plot are filled with

soils or other in-fill material, with the conductivity determined by the filling material. At depths below the zone of soil influence, fractures are open, with much higher conductivity values. The net infiltration is controlled by the filled fractures near the surface.

Such a discrepancy between near-surface conductivity and formation conductivity may not exist in alluvium, as evaluated in an analysis at Pagany Wash. Pagany Wash is an alluvium/colluvium filled channel located northeast of Yucca Mountain. An analytical estimation of infiltration was made using the temperature data between sensors at 3.0 and 6.1 m below the surface in borehole UZ #4 (LeCain et al. 2002 [158511], Table 1, p. 18). The hydraulic conductivity used in the solution is 149 mm/d. This value is of the same order of magnitude as the conductivity value of 500 mm/d used in the infiltration estimation (USGS 2001 [160355]). Alluvium can be treated as a porous medium without fractures, based on the relative close agreement between the alluvium conductivity value and the model parameter used in the interpretation of temperature signal propagation.

Both the Alcove 1 test result and Pagany Wash analysis suggest that surface soils have significant influence on the infiltration process.

6.13 BUSTED BUTTE UNSATURATED ZONE TRANSPORT TEST

This section presents the field data collected at the Unsaturated Zone Transport Test (UZTT) at Busted Butte in a distal extension of the Calico Hills formation below Yucca Mountain. The UZTT was described in the scientific analysis report *Unsaturated Zone and Saturated Zone Transport Properties (U0100)* (CRWMS M&O 2001 [154024]). Some of the early results are presented in this section for completeness. The overview in Section 6.13.1 in this scientific analysis report is equivalent to Section 6.8.1 and to test-related information in Section 6.8.2 of CRWMS M&O 2001 [154024]. The UZTT was conducted in two phases. The Phase 1 results in Section 6.13.2 in this scientific analysis report are equivalent to Section 6.8.5 of CRWMS M&O 2001 [154024]. An update of Phase 2 tracer test results is presented in Section 6.13.3 of this scientific analysis report. Early geophysical imaging results (CRWMS M&O 2001 [154024], Section 6.8.4) and updates of the GPR tomograph results from the Phase 2 test block are presented in Section 6.13.4 of this scientific analysis report. The neutron moisture measurements are summarized in Section 6.13.5. The laboratory test of radionuclide transport through blocks of Busted Butte tuff are summarized in Section 6.13.6. Because of the focus on the flow-and-transport-related results, the mineral evaluation of the Busted Butte samples and the geological implications regarding the applicability of Busted Butte results for Yucca Mountain study are presented in Attachment VIII (update of Section 6.8.3 of CRWMS M&O 2001 [154024]).

6.13.1 Overview of Unsaturated Zone Transport Test

6.13.1.1 Unsaturated Zone Transport Test Location

The Busted Butte test facility is located in Area 25 of the Nevada Test Site (NTS) approximately 160 km northwest of Las Vegas, Nevada, and 8 km southeast of the Yucca Mountain repository area. The site was chosen based on the presence of a readily accessible exposure of the Topopah Spring Tuff (Tpt) and the Calico Hills formation (Tac) and the similarity of these units to those beneath the repository horizon. The test facility consists of an underground excavation along a geologic contact between Tpt and Tac. The corresponding hydrogeologic contact between the Topopah Spring welded (TSw) unit and the Calico Hills nonwelded (CHn) unit is comprised of the nonwelded portion of the basal vitrophyre of Tac (Tptpv1) and of Tpt (Tptpv2).

6.13.1.2 Unsaturated Zone Transport Test Objectives

The principal objectives of the test are to address uncertainties associated with flow and transport in the UZ site-process models for Yucca Mountain. These include, but are not restricted to:

- The effect of heterogeneities on flow and transport in unsaturated and partially saturated conditions near the TSw-CHn contact; in particular, issues relevant to fracture-matrix interactions and permeability contrast boundaries.
- The validation through field testing of laboratory sorption experiments in unsaturated Calico Hills rocks.
- The effect of scaling from lab scale to field scale and site scale.

- The inputs to the evaluation of the 3-D site-scale flow and transport process model used in the performance assessment (PA) abstractions for licensing application (LA).

- The migration behavior of colloids in fractured and unfractured Calico Hills rocks.

6.13.1.3 Unsaturated Zone Transport Test Concept

The Unsaturated Zone Transport Test (UZTT) is comprised of three integrated efforts: the field test, a parallel laboratory-scale testing program, and validation and assessment of models used for PA. The field test involves design of the test, analysis of the geology, identification of tracer breakthrough using chemical analyses, *in situ* imaging of liquid and tracer migration through geophysical techniques, and ultimately, destructive testing to quantify tracer migration. Only the field test results are described in this scientific analysis report. The laboratory and modeling efforts are summarized in the next two paragraphs and reported in CRWMS M&O (2001 [154024]).

In addition to field testing, parallel laboratory analytical and testing programs in geochemistry, tracer evaluation, hydrology, and mineralogy are designed to help interpret the field results. The geochemistry program includes measurement of *in situ* pore-water chemistry and development of a synthetic injection matrix. The tracer evaluation program includes batch-sorption studies on Busted Butte rock samples using nonreactive and reactive surrogate tracers and radionuclides. The laboratory program also includes modeling of the geochemical behavior of those tracers in the ambient water chemistry, and tracer stability in the rock environments. The hydrology program involves the measurement of the matric potentials and conductivities as a function of saturation for core samples from Busted Butte with the porosity of each sample also characterized. Mineralogy/petrology (Min/Pet) activities involve the mineralogic characterization of the Busted Butte samples from cores.

The laboratory investigations undertaken are listed below for information purposes.

- Unsaturated hydraulic characterization of Busted Butte rocks (done by the USGS)
- Detailed mineralogic and oxide-coating characterization of Busted Butte rocks
- Batch measurements of radionuclide sorption to Busted Butte rocks
- Batch measurements of tracer sorption to Busted Butte rocks
- Short-term and long-term stability measurements of tracer solutions
- Short-term and long-term stability measurements of tracer-affected collection pads
- Short-term and long-term stability measurements of tracer-affected rock samples.

Geological, mineralogical, and hydrological properties form the basis for assessing the applicability of Busted Butte UZTT for the Calico Hills formation below the nuclear waste repository at Yucca Mountain, as depicted in detail in Attachment VIII.

The flow and transport modeling study is the third aspect of UZTT. The principal objective of the test is to evaluate the validity of the flow and transport site-scale process models used in PA abstractions. This effort makes it possible to improve or enhance the site-scale flow and transport

model by simulating and predicting experimental field results and by addressing the effects of scaling from laboratory to field scales.

6.13.1.4 Test Design

The UZTT is comprised of the main adit, which is 75 m in length, and a test alcove, which is 19 m in length. The configuration of the UZTT site is shown in Figure 6.13.1-1. Details of the design and construction criteria can be found elsewhere (SubTerra 1998 [147703], pp. 9–21, 33–44).

The UZTT was designed as two test phases. The first phase, including test Phases 1A and 1B, was designed as a scoping study to assist in design and analysis of Phase 2, and as a short-term experiment aimed at providing initial transport data on fracture near an interface. The second phase incorporated a larger region than Phase 1, with a broader, more complex scope of tracer injection, monitoring, and collection.

Test Phase 1—Test Phase 1 was comprised of two small scale scoping tests, Phase 1A and Phase 1B. Phase 1A was in Tac and Tptpv1, and Phase 1B in Tptpv2. Phase 1A was a "blind" single-point injection test using four boreholes, at either 1mL/hr or 10 mL/hr rates. Following the injection period, a “mini-mineback” was done to expose the distribution of the tracer in the rock mass.

Phase 1B involved two pairs of injection and collection boreholes in Tptpv2. Phase 1B also used two injection rates (1 mL/hr and 10 mL/hr). Because of the paucity of data on fracture-matrix interactions in these lithologies, this test was designed as a “calibration” test for fracture-matrix interactions to be used in Phase 2 simulations. The 2 m long Phase 1B collection boreholes, immediately below the injection boreholes, were used to capture arrival of tracers. At the culmination of injection, overcoring was done to collect rock samples for tracer analysis.

Test Phase 2—Phase 2 involved a large (7 m × 10 m × 10 m) block comprising all of the lithologies of Phase 1. Unlike the single-point injection geometries in Phase 1, the injection systems in Phase 2 were designed to activate large surfaces of the block. Phase 2 included 8 injection boreholes drilled from the test alcove and distributed in two horizontal, parallel planes. Injection boreholes were placed to test the properties of the lower Topopah Spring Tuff (Tptpv2) and the hydrological Calico Hills (Tptpv1 and Tac). In addition, there were 12 collection boreholes, drilled from the main adit. Collection holes were perpendicular in plan view to the injection holes and distributed at various distances from the injectors.

6.13.1.5 Site Characterization

The site characterization of the potential test block included core sampling from boreholes and grab samples from outcrops. Core samples were collected from the dry drilling of the boreholes from the main adit and the test adit for geological, hydrological, and geochemical laboratory investigations and scoping calculations. The boreholes were then surveyed and instrumented for the injection tests.

Design, construction, and scientific teams were all involved in ensuring that the test block itself remained undisturbed by construction activities. Minimal disturbance of the *in situ* test block in

the initial stages of UZTT was the foremost objective. Sodium silicate was applied to the wall of the test block to minimize evaporation.

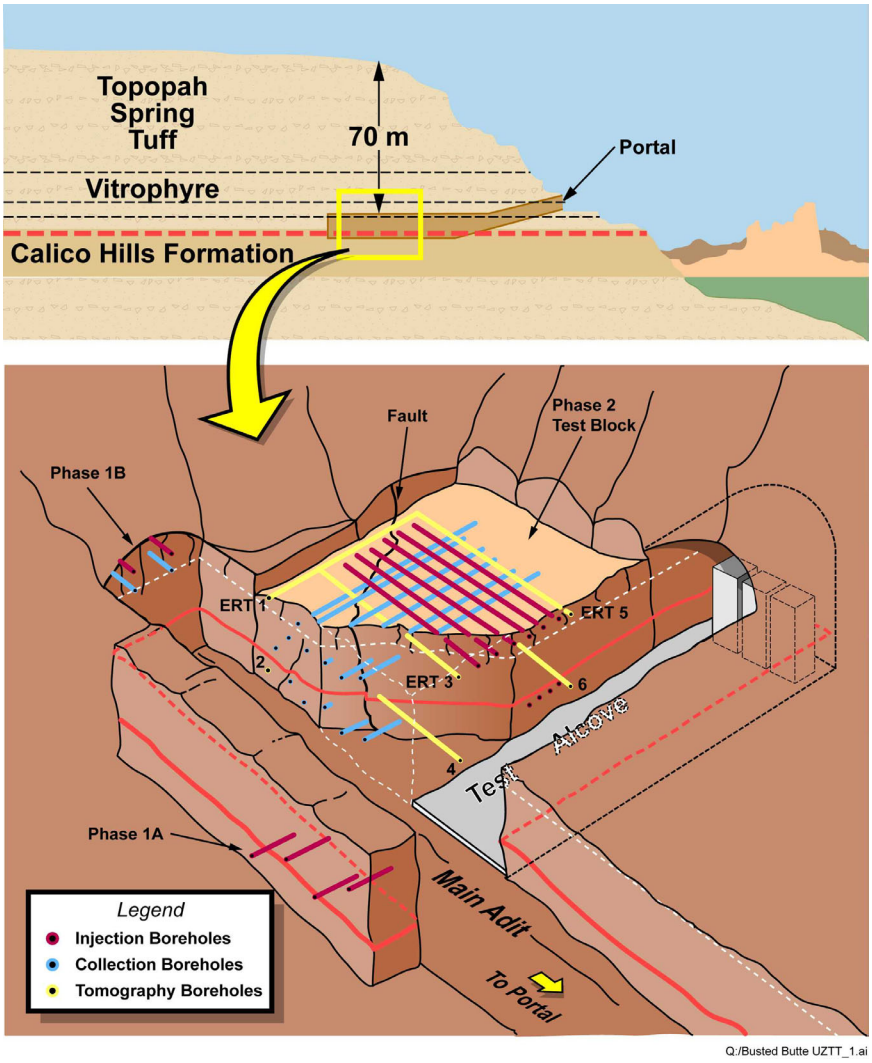

Source: Derived from CRWMS M&O 2001 [154024], Figure 34 (For illustration purposes only).

NOTE: This schematic of the Busted Butte UZTT shows the relative locations of the different experiment phases and borehole locations. Figure not drawn to scale.

Figure 6.13.1-1. Busted Butte Unsaturated Zone Transport Test

6.13.1.6 Borehole Injection and Sampling Systems

Injection and sampling of the liquid tracers was accomplished by two pneumatically inflated borehole sealing and measurement systems (Figure 6.13.1-2). To allow visual inspection of the injection points under both standard and ultraviolet (UV) illumination, a transparent packer system was developed for the tracer-injection systems. Moisture sensing and sampling were accomplished using pneumatically emplaced inverting membranes, which were fabricated with mesh pockets to retain absorbent sample pads. The inverting membranes are removed from the boreholes regularly (at interval ranging from daily to biweekly) for sample-pad removal and

replacement, whereas the injection packers remain in the holes for the duration of the test program. Each system was maintained at slight overpressure (1.7 to 3.5 kPa) to maintain contact between the sampling/injection pads and the tuff and to prevent circulation of air within the borehole.

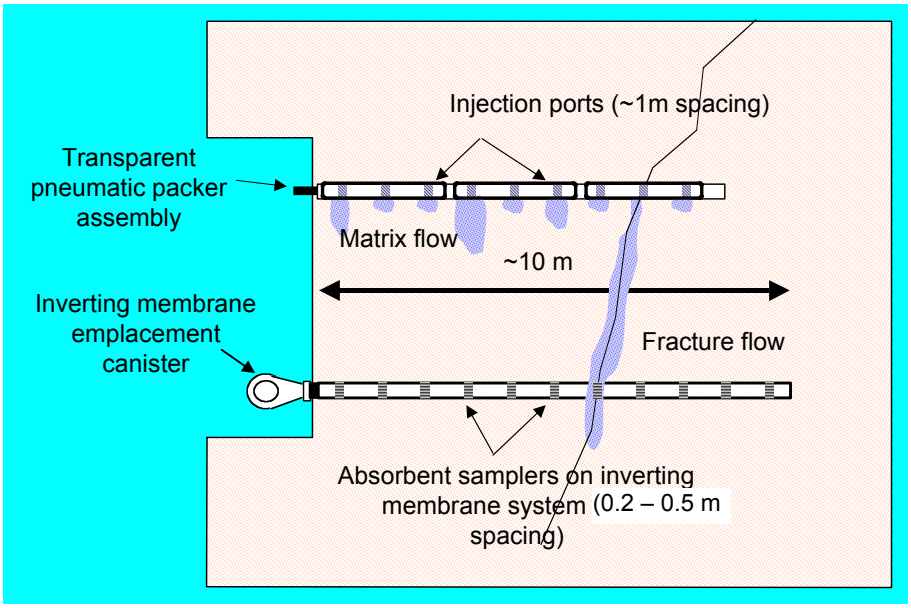

Source: CRWMS M&O 2001 [154024], Figure 35 (For illustration purposes only).

NOTE: Injection and collection boreholes are actually perpendicular in plan view. – Absorbent sampler spacing (0.25-0.50 m)

Figure 6.13.1-2. Vertical Cross Section of Injection and Collection System Configuration

6.13.1.7 Electrical-Resistance Moisture Sensors

Simple electrical-resistance moisture sensors were installed to monitor the relative moisture state of the injection pads and the arrival of liquid tracer at the sampling-pad data collection. Two Campbell Scientific dataloggers were used to collect measurement data from sensors and instrumentation.

Phase 1—For the Phase 1A test, the dataloggers measured the pressure in the injection/sampling manifold, 12 to 14 moisture sensors, the datalogger panel temperature and battery voltage, the number of times the syringe pumps cycled in a given period of time, and the relative humidity, air temperature, and atmospheric pressure in the experimental area. For the Phase 1B test, the same data was collected, except a total of 32 moisture sensors were logged, as well as an anemometer in the ventilation shaft.

Phase 2—For the Phase-2 experiment, over 200 different sensors were measured. The data that are (or can be) collected include:

- Environmental information, such as ambient pressure, temperature, and relative humidity and wind speed in the ventilation system

- Experimental control information, such as injection pressure, the number of times pumps are activated, and relative saturation at injection points, at the face of boreholes or along sampling membranes.

6.13.1.8 Nonreactive and Reactive Tracers and Microspheres

Measurements on a small scale can be conducted in the laboratory, but validating the extrapolation of these data in the presence of larger-scale heterogeneities requires field-tracer tests. The behavior of actual radionuclides of concern has been extensively studied in the laboratory, but regulatory and environmental concerns prevent the use of these materials in the field. For the Busted Butte field tests, nonreactive and reactive tracers are used as surrogates for radionuclides. The tracers were chosen so that nonreactive, reactive, and colloidal behaviors could be monitored in a single continuous injection scenario. They were mixed together to normalize the hydrological conditions of the injection. The tracer matrix was synthetic pore water, which is based on the measured composition of Busted Butte pore waters.

The tracers selected for the Busted Butte field experiments include nonreactive anionic tracers with a range of diffusivities, metal tracers displaying a range of reactivity, and organic dyes with a variety of characteristics (see extensive discussion in Turin et al. 2002 [164633]).

Nonreactive tracers used in the field experiments included bromide, iodide, five different fluorinated benzoic acids (FBAs), sodium fluorescein (uranine, acid yellow 73), and carbomoyl-2(1H)-pyridone (henceforth, "pyridone"). Bromide was used in all the injection boreholes since testing was initiated. Iodide has similar properties to bromide, and was introduced approximately one year into the experiment, after the system approached a hydraulic steady state. By comparing bromide and iodide field behavior, we were able to assess the impact of the strong hydraulic transients produced by the initiation of tracer injection.

The FBAs include 2,4-difluorobenzoic acid (2,4-diFBA), 2,6-difluorobenzoic acid (2,6-diFBA), 2,4,5-trifluorobenzoic acid (2,4,5-triFBA), 2,3,4,5-tetrafluorobenzoic acid (2,3,4,5-tetraFBA), and pentafluorobenzoic acid (PFBA) (Farnham et al. 2000 [165254]). The number of FBAs available makes them valuable for "tagging" individual injection boreholes. Each of the injection boreholes was tagged with a single FBA; FBA analyses enable us to determine the extent of mixing between the different tracer plumes and to estimate transverse dispersion.

Sodium fluorescein and "pyridone" are organic dye tracers. Sodium fluorescein's strong fluorescence under ultraviolet illumination enables qualitative determination of breakthrough during sample collection at the field site, but its susceptibility to photodegradation and the sensitivity of its fluorescence to matrix variations limit its usefulness as a quantitative tracer. "Pyridone" is an experimental tracer that has been used by the U.S. Geological Survey for saturated-zone tracer testing at the C-Wells (Geldon et al. 1997 [100397]), and was added to the Busted Butte tracer mixture to further evaluate its usefulness for future field studies.

Reactive metal tracers include Li, Mn, Co, Ni, Ce and Sm. Li is a weakly sorbing tracer whose value has been demonstrated in saturated-zone tracer tests at the Yucca Mountain C-Wells complex (Reimus et al. 1999 [126243]). Li is quite soluble, and the breakthrough concentrations at the collection boreholes are readily analyzed. The transition metals Mn, Co, and Ni sorb more strongly than Li, are far less soluble, and are less susceptible to transport. Therefore,

breakthrough concentrations are lower, and analytical difficulties abound. Furthermore, Mn, unlike the other metals, has a significant background level that may interfere with breakthrough detection. The rare-earth metals Sm and Ce were also added to the tracer mixture at Busted Butte. These metals have very low solubilities under field conditions, and it is likely that they precipitated within the tracer tanks (Kearney et al. 2000 [165255]).

Rhodamine WT (acid red 388) was also added to the Busted Butte tracer mixture. This intensely colored organic dye is known to sorb to rock and soil materials (Kasnavia et al. 1999 [164629]; Sabatini and Austin 1991 [164630]), and was used primarily to help locate tracer plumes in rock samples collected during post-test excavation.

6.13.1.9 Phase 1 Tracers

Phase 1 tracers were chosen based on the list of tracers permitted for use in the C-wells tests. Surrogate nonreactive and reactive tracers and colloids were mixed together to normalize the hydrological conditions they experience and provide for higher accuracy of the results. The tracers used in the Busted Butte experiments of Phase 1 included the following:

- Lithium bromide
- Fluorescent polystyrene latex microspheres
- Sodium fluorescein
- "Pyridone" (3-carbomoyl-2(1H)-pyridone)
- 2,6-difluorobenzoic acid (2,6-DFBA)
- Pentafluorobenzoic acid (PFBA).

The reactive sorbing tracer used is lithium, and the colloid analogs are fluorescent polystyrene latex microspheres of two sizes: 0.3 and 1 μm diameter. The 2,6-DFBA and PFBA are nonreactive tracers used to tag the various injection boreholes according to injection rates (i.e., 1 and 10 mL/hr rates). Sodium fluorescein and pyridone are UV fluorescent and are used as nonreactive tracer markers that can be detected in the field at a concentration level of approximately 10 ppm, using UV illumination. Borehole numbers are shown in Figure 6.13.1-3 for Phase 1A and Figure 6.13.1-4 for Phase 1B and Phase 2.

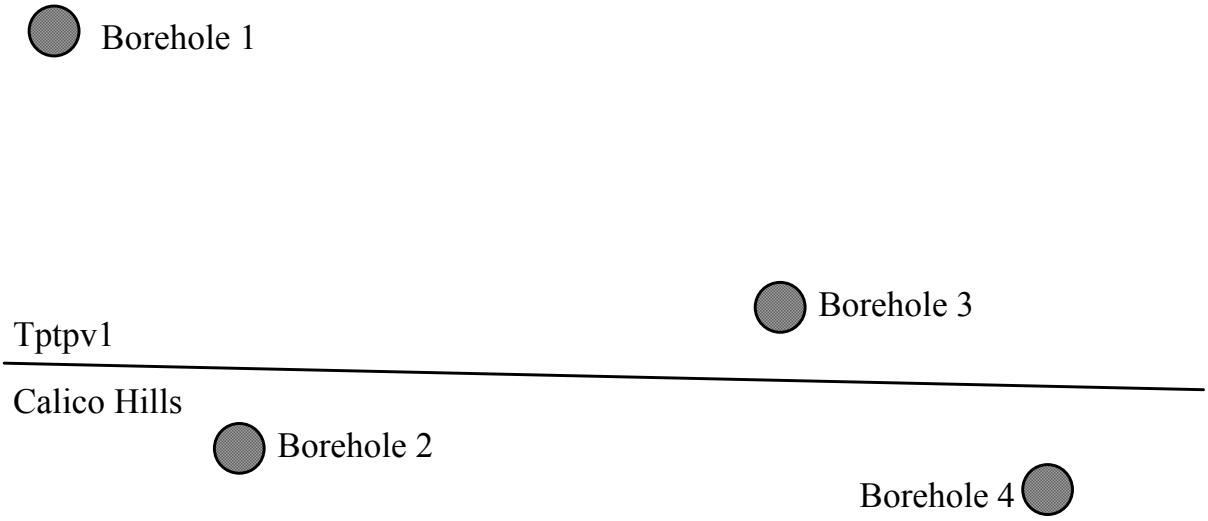

Source: CRWMS M&O 2001 [154024], Figure 37 (for illustration purposes only).

NOTE: Figure not drawn to scale.

Figure 6.13.1-3. Schematic of Phase-1A Borehole Numbers and Relative Locations

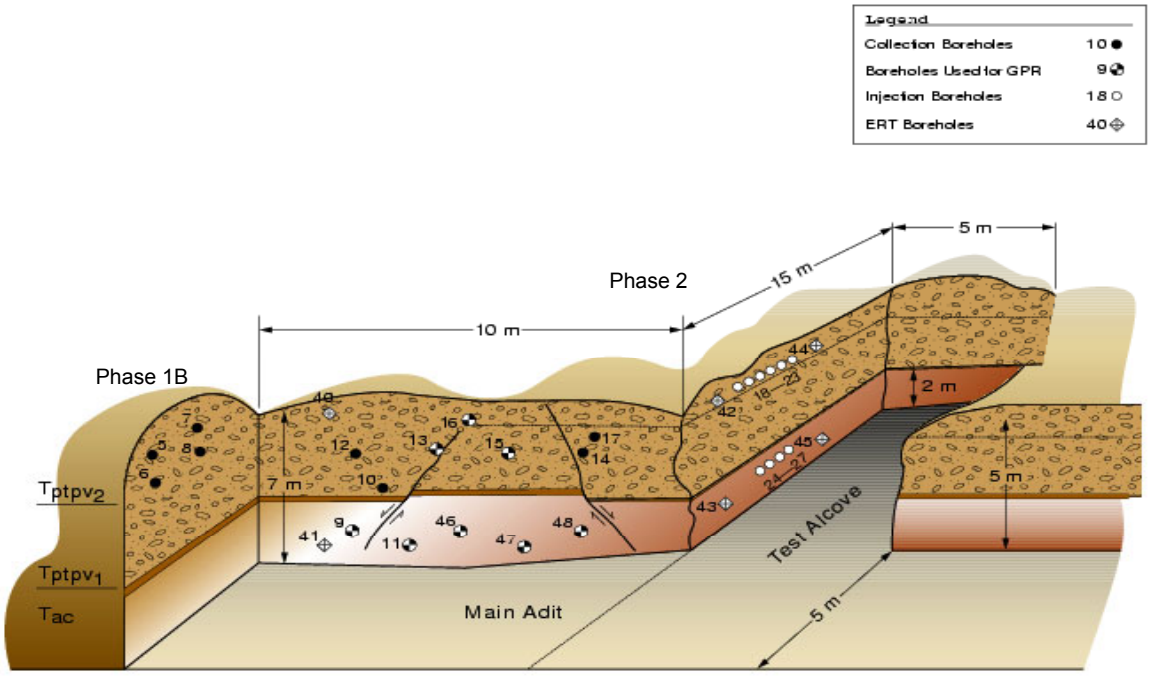

Source: CRWMS M&O 2001 [154024], Figure 38 (for illustration purposes only).

Figure 6.13.1-4. Phase-1B and Phase-2 Borehole Numbers and Relative Locations

Table 6.13.1-1 summarizes the initial concentrations of Phase 1B injection with the lithium and bromide elemental concentrations derived from the 500 mg/kg lithium bromide value, based on

the elemental atomic weights of lithium and bromide. Table 6.13.1-2 summarizes the concentrations used for Phase 1B injections.

Table 6.13.1-1. Tracer C0 Values for Phase 1B Injection

Tracer	C0 (mg/kg)
Lithium	40
Bromide	460
2,6-DFBA (Borehole 5 only)	100
Pyridone	100
Sodium fluorescein	500

Source: (CRWMS M&O 2001 [154024], Table 30)

Table 6.13.1-2. Summary of Concentrations Used for Phase 1 Injections

Phase 1A—10 mL/hr Injection Rate; Boreholes 1 and 3:
500 mg kg–1 lithium bromide
500 mg kg–1 sodium fluorescein
100 mg kg–1 2,6-DFBA
1 mL kg–1 fluorescent polystyrene microspheres
Phase 1A—1 mL/hr Injection Rate; Boreholes 2 and 4:
500 mg kg^{-1} lithium bromide
500 mg kg^{-1} sodium fluorescein
100 mg kg^{-1} PFBA
1 mL kg^{-1} fluorescent polystyrene microspheres
Phase 1B—10 mL/hr Injection Rate; Borehole 5:
500 mg kg^{-1} lithium bromide
500 mg kg^{-1} sodium fluorescein
100 mg kg^{-1} 2,6-DFBA
100 mg kg^{-1} pyridone
1 mL kg^{-1} fluorescent polystyrene microspheres
Phase 1B—1 mL/hr Injection Rate; Borehole 7:
500 mg kg–1 lithium bromide
500 mg kg–1 sodium fluorescein
100 mg kg–1 PFBA
100 mg kg–1 pyridone
1 mL kg–1 fluorescent polystyrene microspheres

Source: CRWMS M&O 2001 [154024], Section 6.8.2.4

6.13.1.10 Phase 2 Tracers

Phase 2 tracers include those used in Phase 1 but with three additional fluorinated benzoic acids (FBAs) (2,4-DFBA, 2,4,5-triFBA, 2,3,4,5-tetraFBA), iodide, a fluorescent reactive tracer (Rhodamine WT), and additional reactive ions that serve as analogs for neptunium, plutonium, and americium. (See Figure 6.13.1-4 for Phase-2 borehole locations.)

- Neptunium Analogs (NpO_2^+, Np(V)):

  Nickel (Ni^{2+})
  Cobalt (Co^{2+})
  Manganese (Mn^{2+}).

- Plutonium Analog (Pu3+):

  Samarium (Sm^{3+}).

- Plutonium Analogs (colloidal form):

  Polystyrene microspheres.

- Americium Analog (Am^{3+}):

  Cerium (Ce^{3+}).

The Phase 2 tracer recipes are presented in Table 6.13.1-3, Table 6.13.1-4, and Table 6.13.1-5.

Table 6.13.1-3. Summary of Concentrations Used for Phase 2A Injections

Phase 2A–1 mL/hr Injection Rate; Borehole 23:
1000 mg/kg lithium bromide
10 mg/kg sodium fluorescein
100 mg/kg 2,4,5-TriFBA
10 mg/kg pyridone
1 mL/kg microspheres
Starting October 7, 1998:
10 mg/L rhodamine WT
10 mg/kg $NiCl_2 \cdot 6H_2O$ (2.47 mg/kg of Ni^{2+})
10 mg/kg $MnCl_2 \cdot 4H_2O$ (2.78 mg/kg of Mn^{2+})
10 mg/kg $CoCl_2 \cdot 6H_2O$ (2.48 mg/kg of Co^{2+})
5 mg/kg $SmCl_3 \cdot 6H_2O$ (2.06 mg/kg of Sm^{3+})
5 mg/kg $CeCl_3 \cdot 7H_2O$ (1.88 mg/kg of Ce^{3+})

Source: CRWMS M&O 2001 [154024], Section 6.8.2.4

On September 30, 1999, the Phase-2A recipe was changed with the elimination of the microspheres and the addition of 500 mg/kg potassium iodide.

Table 6.13.1-4. Summary of Concentrations Used for Phase 2B Injections

Phase 2B–10 mL/hr Injection Rate; Boreholes 24, 25, 26, 27
1000 mg/kg lithium bromide
10 mg/kg sodium fluorescein
100 mg/kg 2,6-DFBA (Borehole 26, Borehole 27)
100 mg/kg 2,3,4,5-TetraFBA (Borehole 24, Borehole 25)
10 mg/kg pyridone
10 mg/kg rhodamine WT
1 mL/kg microspheres
Starting September 2, 1998:
10 mg/kg $NiCl_2 \cdot 6H_2O$ (2.47 mg/kg of Ni^{2+})
10 mg/kg $MnCl_2 \cdot 4H_2O$ (2.78 mg/kg of Mn^{2+})
10 mg/kg $CoCl_2 \cdot 6H_2O$ (2.48 mg/kg of Co^{2+})
5 mg/kg $SmCl_3 \cdot 6H_2O$ (2.06 mg/kg of Sm^{3+})
5 mg/kg $CeCl_3 \cdot 7H_2O$ (1.88 mg/kg of Ce^{3+})

Source: CRWMS M&O 2001 [154024], Section 6.8.2.4

On August 18, 1999, the Phase-2B recipe was changed with the elimination of the microspheres and the addition of 500 mg/kg potassium iodide.

Table 6.13.1-5. Summary of Concentrations Used for Phase 2C Injections

Phase 2C–50 mL/hr Injection Rate; Boreholes 18, 20, 21:
1000 mg/kg lithium bromide
10 mg/kg sodium fluorescein
100 mg/kg 2,6-DFBA (Borehole 18)
100 mg/kg PFBA (Borehole 20)
100 mg/kg 2,4-DFBA (Borehole 21)
10 mg/kg pyridone
10 mg/kg rhodamine WT
1 mL/kg microspheres
Starting September 2, 1998:
10 mg/kg $NiCl_2 \cdot 6H_2O$ (2.47 mg/kg of Ni^{2+})
10 mg/kg $MnCl_2 \cdot 4H_2O$ (2.78 mg/kg of Mn^{2+})
10 mg/kg $CoCl_2 \cdot 6H_2O$ (2.48 mg/kg of Co^{2+})
5 mg/kg $SmCl_3 \cdot 6H_2O$ (2.06 mg/kg of Sm^{3+})
5 mg/kg $CeCl_3 \cdot 7H_2O$ (1.88 mg/kg of Ce^{3+})

Source: CRWMS M&O 2001 [154024], Section 6.8.2.4

On August 18, 1999, the Phase-2C recipe was changed with the elimination of the microspheres and the addition of 500 mg/kg potassium iodide.

6.13.1.11 Synthetic Pore-Water Recipe

Composition of the UZTT pore water is found in DTNs: LA9909WS831372.015 [140089], LA9909WS831372.016[140093], LA9909WS831372.017[140097], and LA9909WS831372.018 [140101] and composition of the synthetic pore water used in the UZTT is found in Table 29 in Section 6.8.5.2 of CRWMS M&O 2001 [154024].

6.13.2 Field-Scale Tracer Transport—Phase 1

6.13.2.1 Test Phase 1A

Phase 1A was located in the nonwelded Calico Hills (CHn) hydrogeologic unit spanning both the geologic Calico Hills formation (Tac) and the nonwelded subzone of the lowermost Topopah Spring Tuff (Tptpv1). It was a noninstrumented or "blind" test consisting of four single-point injection boreholes. All Phase 1 boreholes were 2 m in length and 10 cm in diameter. The injection point was located 90 cm in from the borehole collar. Continuous injection started on April 2, 1998, and ended on January 12, 1999 (286 days). Injection rates were 10 mL/hr (boreholes 1 and 3) and 1 mL/hr (boreholes 2 and 4). A mixture of nonreactive tracers (bromide, fluorescein, pyridone, and fluorinated benzoic acids (FBAs)), a reactive tracer (lithium), and fluorescent polystyrene microspheres were used to track nonreactive transport, reactive transport, and colloid migration, respectively.

The field test was completed through excavation by "mineback" and auger sampling. Mineback of the Phase 1A test block began on January 15, 1999 and ended on March 3, 1999. During mineback, as successive layers of the adit wall were removed, digital photographs under visible and UV illumination were taken, and the exposed face was surveyed. In addition, rock samples were collected by augering for laboratory analysis of tracer and moisture content.

Results

The Phase 1A mineback consisted of four faces exposed 50, 90, 115, and 140 cm in from the adit wall. At each face, the stratigraphy was mapped and surveyed, and images of the fluorescein plume were taken under UV light. The visualization of the fluorescein tracer plume using UV illumination was very successful, and the digital imagery resulting from this effort serves as the primary result of Phase 1A. Recall that the concentration of fluorescein for this test phase was very high for just this purpose. Figure 6.13.2-1 (a through d) shows the fluorescein plume at each of the mineback faces.

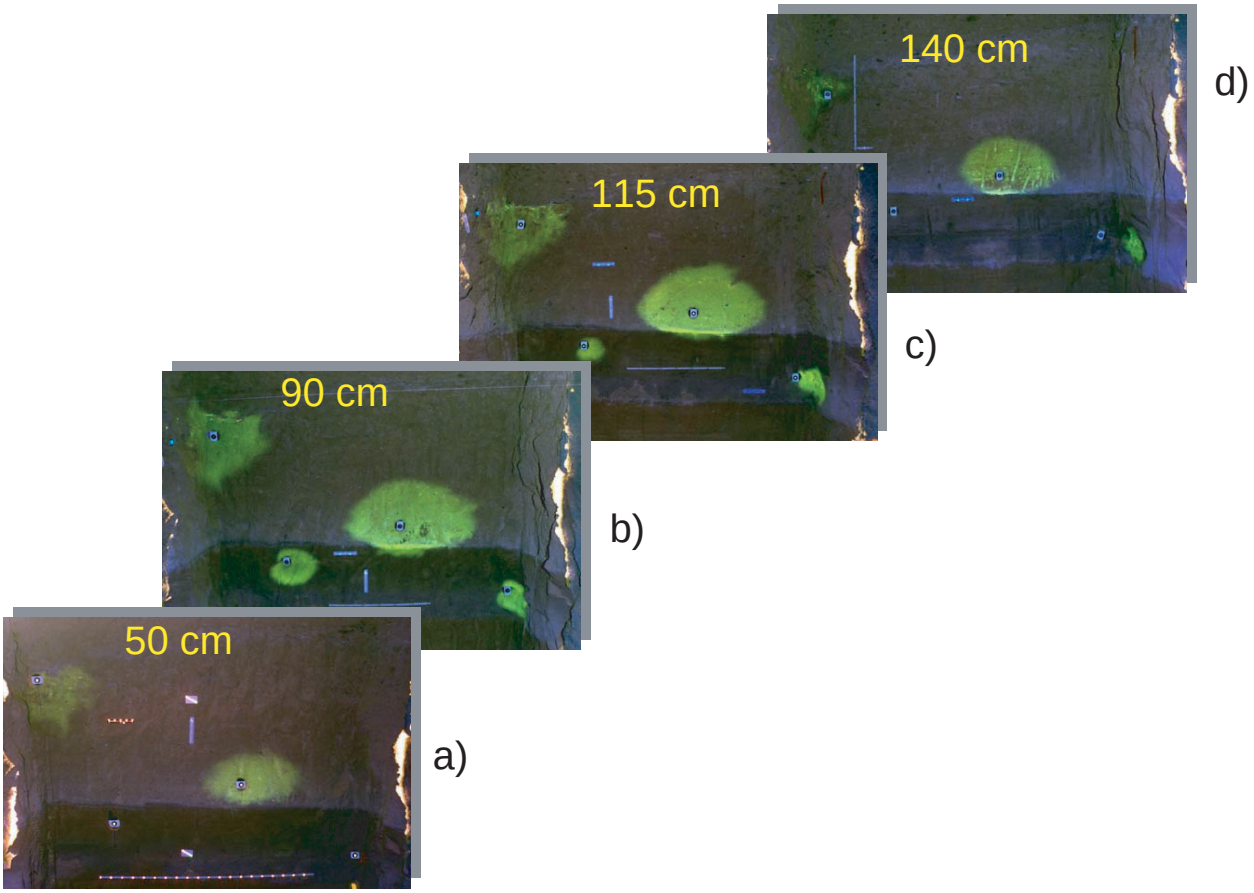

DTN: LA0302WS831372.001 [162765]

Figure 6.13.2-1. Fluorescein Plume at Each of the Four Phase-1A Mineback Faces

Observations from the Phase 1A test demonstrate strong capillary dominated flow for both the 1 and 10 ml hr^{-1} injection rates. Injection is at "3-o'clock" with respect to the borehole. The plumes are relatively uniformly distributed around the injection sites, though some borehole shielding effects (tracer blocked or delayed from moving in the direction of the borehole) can be seen. Lithological contacts, however, clearly influence the flow. At all of the mineback faces, the plumes are more oval than round. This reflects the ash layers just above boreholes 2 and 4 and just below borehole 3.

Although difficult to see from the image itself, Figure 6.13.2-2 shows the location of a small fracture near the injection point in borehole 3. This image demonstrates that fractures have a relatively minor effect on the flow in Tac and Tptpv1 units. There is a slight perturbation in the upper right that may have resulted from the presence of the fracture but indicates that under the Phase 1A conditions the fracture is acting as a permeability barrier rather than as a fast path.

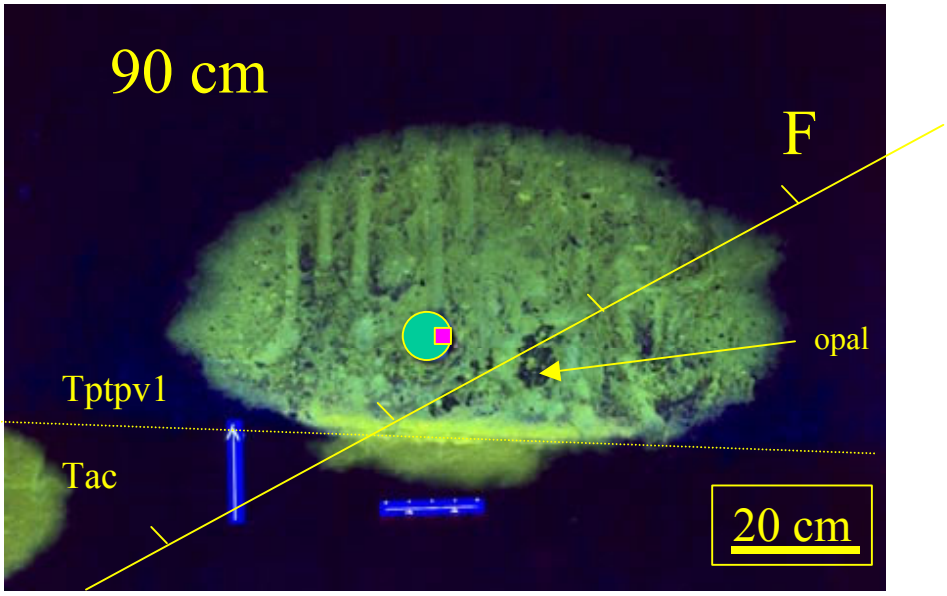

DTN: LA0302WS831372.001 [162765]

Figure 6.13.2-2. Fluorescein Plume at 90 cm Mineback Face at Borehole 3 (10 mL/h)

A small number of augered rock samples have been analyzed for bromide and moisture content (DTN: LA9910WS831372.008 [147156]). Table 6.13.2-1 reports measured data from these samples. Samples 1–4 are taken at increasing distance below borehole 3. Samples 1 and 2 are above the ash layer, while Samples 3 and 4 are located vertically beneath the injector. Samples 5 to 12 are taken at increasing lateral distance from the injection point.

Table 6.13.2-1. Phase 1A Samples Taken from the 90 cm Mineback Face at Borehole 3

Sample Name	X (m)	Y (m)	Z (m)	Gravimetric moisture content (g/g)	Bromide C/Co
Borehole Location	-3.929	59.093	-2.684	---	---
BBR-990204-3-1-B	-3.788	59.092	-2.825	0.078	0.74
BBR-990204-3-2-B	-3.790	59.089	-2.933	0.112	0.49
BBR-990204-3-3-B	-3.798	59.083	-3.056	0.115	0.00
BBR-990204-3-4-B	-3.807	59.070	-3.164	0.122	0.00
BBR-990205-3-5-HS	-3.831	59.147	-2.675	0.064	2.77
BBR-990204-3-6-B	-3.822	59.219	-2.652	0.081	0.87
BBR-990204-3-7-B	-3.806	59.336	-2.629	0.077	0.75
BBR-990204-3-8-B	-3.804	59.434	-2.637	0.074	0.75
BBR-990204-3-9-B	-3.819	59.528	-2.661	0.077	0.81
BBR-990204-3-10-B	-3.780	59.636	-2.666	0.078	0.79
BBR-990204-3-11-B	-3.763	59.765	-2.675	0.074	0.32
BBR-990204-3-12-B	-3.770	59.894	-2.693	0.077	0.01

DTN: LA9910WS831372.008 [147156]

NOTE: Samples were analyzed for moisture content and bromide concentration. Sample 5 was a hand sample of polystyrene microspheres at the injection point. Distance is in cm from the mineback face and into the wall.

6.13.2.2 Test Phase 1B

Phase 1B involved both injection of a tracer mixture and collection of pore-water/tracer samples in the lower section of the Topopah Spring Tuff (Tptpv2). Because of the paucity of data on fracture-matrix interactions in these lithologies, this test was designed to provide data on fracture-matrix interactions in the TSw. The results are being used to calibrate fracture properties for Phase 2 analysis. In addition, modeling and analysis were significant elements of this effort, for which the work is reported in the Model Report *Radionuclide Transport Models Under Ambient Conditions*, MDL-NBS-HS-000008 REV01 (BSC 2003 [163228]).

Phase 1B consisted of two 2 m injection boreholes (5 and 7) and two 2 m collection boreholes (6 and 8). The tracer mixture was injected at 10 mL/hr in borehole 5 and at 1 mL/hr in borehole 7. Phase 1B injection began on May 12, 1998. Borehole 7 injection was terminated on November 9, 1998, and borehole 5 injection was terminated on November 18, 1998. Throughout the experiment, rock pore-water samples were collected at regular intervals using collection pads installed in boreholes 6 and 8.

At the conclusion of the experiment, overcoring of the Phase-1B boreholes was conducted. Moisture pad collection was conducted in collection borehole 8 directly below injection hole 7, until injection shut down of borehole 7 on November 9, 1998. Tracer injection and moisture pad collection was continued in boreholes 5 and 6 while two 10-inch-diameter overcores were drilled approximately tangential to one another, with their centerlines in a vertical plane and contained in the area between the top of injection borehole 7 and the bottom of collection borehole 8. When injection hole 5 was shut down, three 10-inch-diameter overcores were drilled approximately tangential to one another with their centerlines in a vertical plane and contained in the area between the top of injection borehole 5 and 10 inches below the bottom of collection borehole 6. As soon as each of the injection holes was turned off, the injection and collection holes were surveyed, as well as video and neutron logged.

Results

There were 176 selected pads extracted for tracers, and the extracts were analyzed by ion chromatograph (IC), inductively coupled plasma/mass spectroscopy (ICP/MS), high pressure liquid chromatograph (HPLC), spectrofluorimetry, and epifluorescent microscopy. The extraction/analysis procedure is shown schematically in Figure 6.13.2-3. Altogether, 883 individual analyses were conducted, and full results were submitted (DTNs: LA9909WS831372.001 [122739] and LA9909WS831372.002 [122741]). Breakthrough of all 5 solute tracers was detected in borehole 6, directly below the 10 mL/hr injection site in borehole 5. No breakthrough was detected in borehole 8 below the 1 mL/hr injection site in borehole 7. No clear evidence of microsphere breakthrough was detected in either borehole, but this may be result from analytical difficulties, discussed below. The borehole 6 breakthrough results are summarized in Figure 6.13.2-4 (a through e), which shows tracer concentration in pad (C) normalized by the input tracer concentration (C_0) listed in Table 6.13.1-1 (see Section 6.13.1.9).

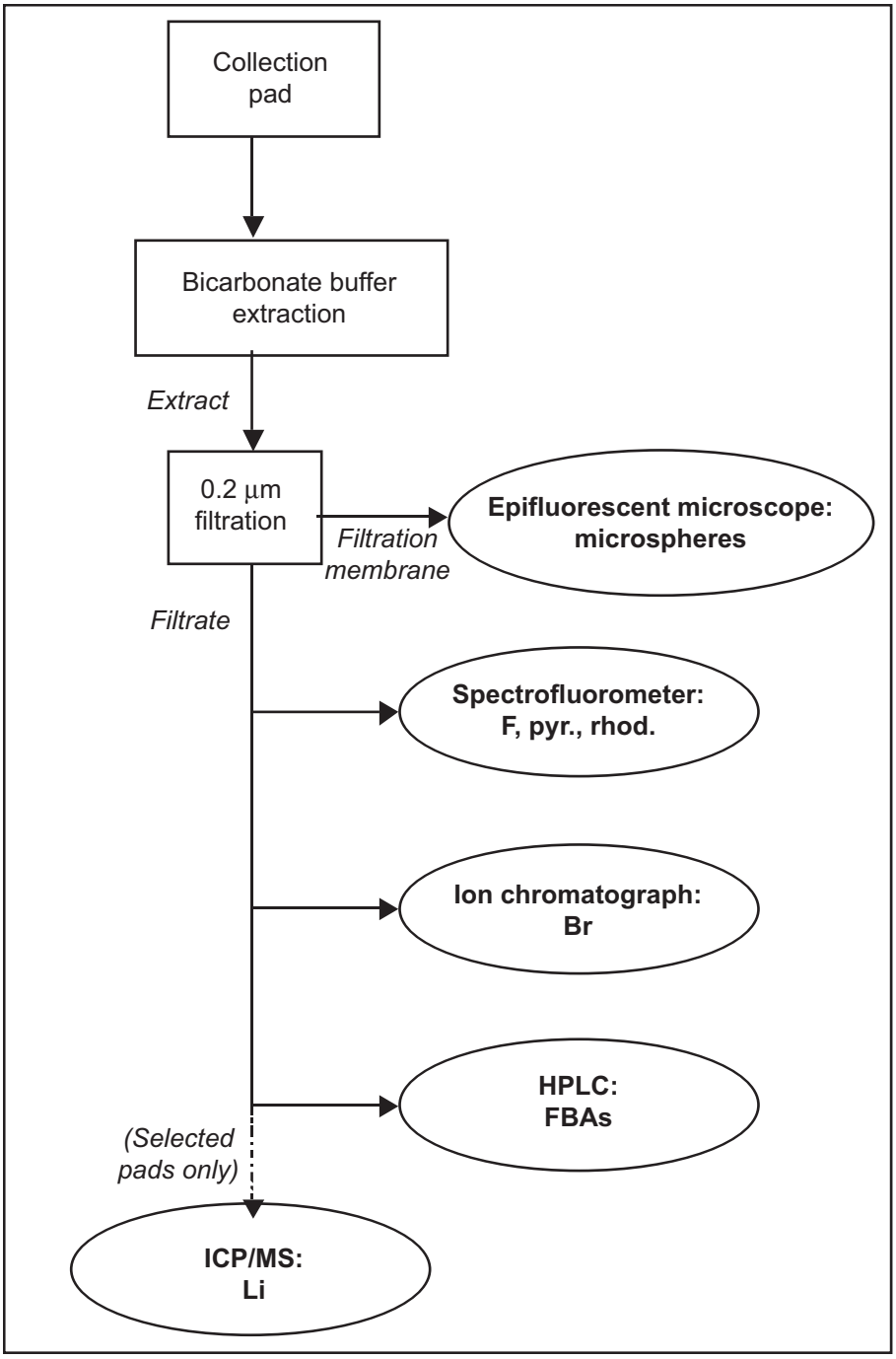

Source: CRWMS M&O 2001 [154024], Figure 57 (For illustration purposes only).

Figure 6.13.2-3. Phase-1B Pad Extraction/Analysis Scheme

All five tracers shown in Figure 6.13.2-4 give clear evidence of breakthrough by the end of the experiment. All of the figures show peak concentrations at a (horizontal) depth of approximately 130 cm, directly below the injection port in borehole 5; but maximum recovery varies greatly. Bromide and 2,6-DFBA, both nonreactive anionic tracers, show similar and reasonable breakthrough patterns, with initial breakthrough detected in mid-late June 1998, after approximately 1 month of injection. Both bromide and 2,6-DFBA reached 50% injection concentrations in mid-July, after 2 months of injection. The fluorescein breakthrough pattern is more erratic. In particular, the peak concentration measured is over twice the injected concentration, which is clearly not reasonable. These anomalies probably reflect analytical difficulties associated with the extremely high concentration of fluorescein injected. The high concentration succeeded in improving field visualization of the plumes during mineback and overcore, even though it hurt the laboratory quantification. This analytical problem will be less severe for Phase 2, in which injected fluorescein concentrations are just 1/50 of that used in Phase 1. The later breakthrough and lower detected concentrations of pyridone may also reflect analytical difficulties; if real, they may indicate either sorption or degradation of this supposedly nonreactive tracer. Finally, although detected lithium concentrations are quite low, their contrast with background levels and their consistent location both in time and space indicate that true lithium breakthrough was observed in the field. The low and late breakthrough indicate that lithium was sorbed quite significantly.

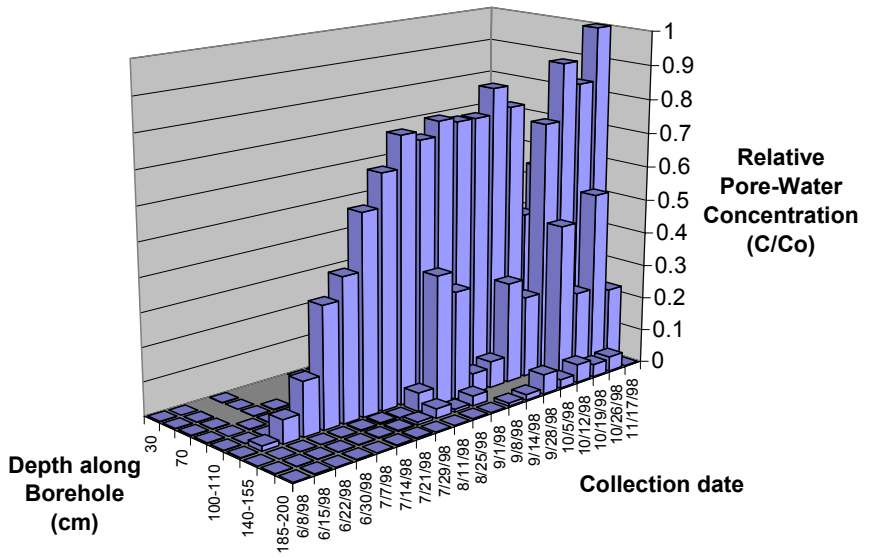

DTNs: LA9909WS831372.001 [122739]; LA9909WS831372.002 [122741]

Source: CRWMS M&O 2001 [154024], Figure 58a.

Figure 6.13.2-4a. Bromide Concentrations in Borehole 6 for Phase 1B

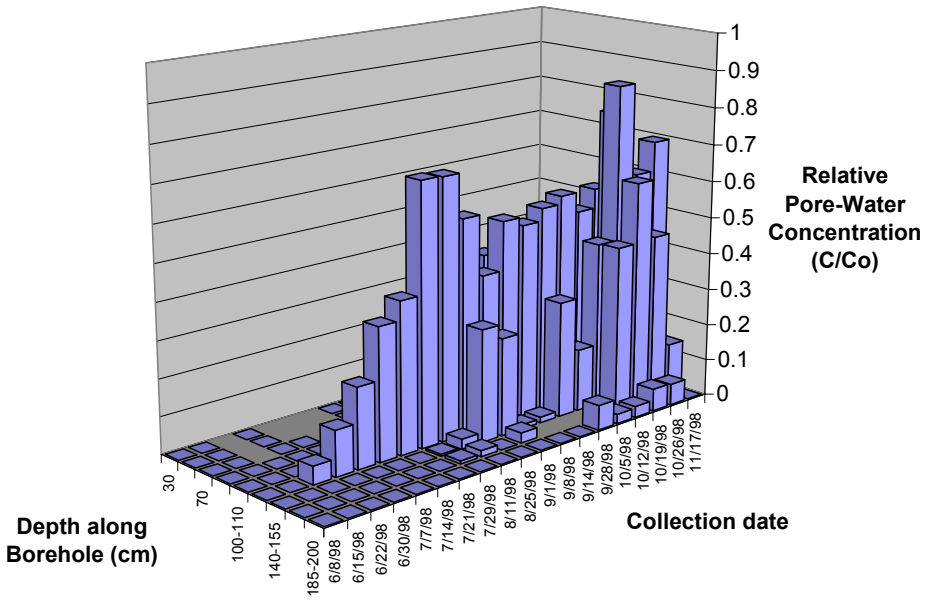

DTN: LA9909WS831372.001 [122739]; LA9909WS831372.002 [122741]

Source: CRWMS M&O 2001 [154024], Figure 58b.

Figure 6.13.2-4b. 2,6-DFBA Concentrations in Borehole 6 for Phase 1B

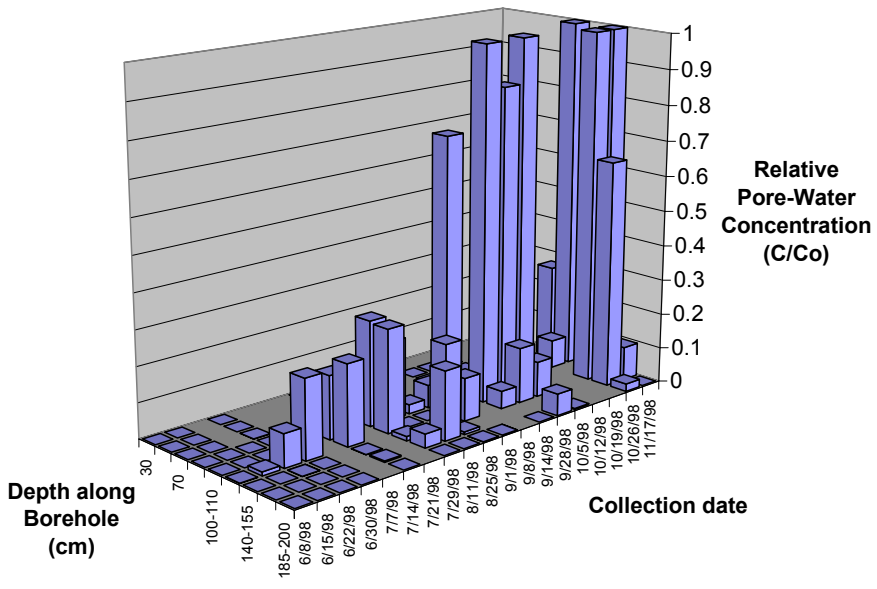

DTN: LA9909WS831372.001 [122739]; LA9909WS831372.002 [122741]

Source: CRWMS M&O 2001 [154024], Figure 58c.

Figure 6.13.2-4c. Fluorescein Concentrations in Borehole 6 for Phase 1B

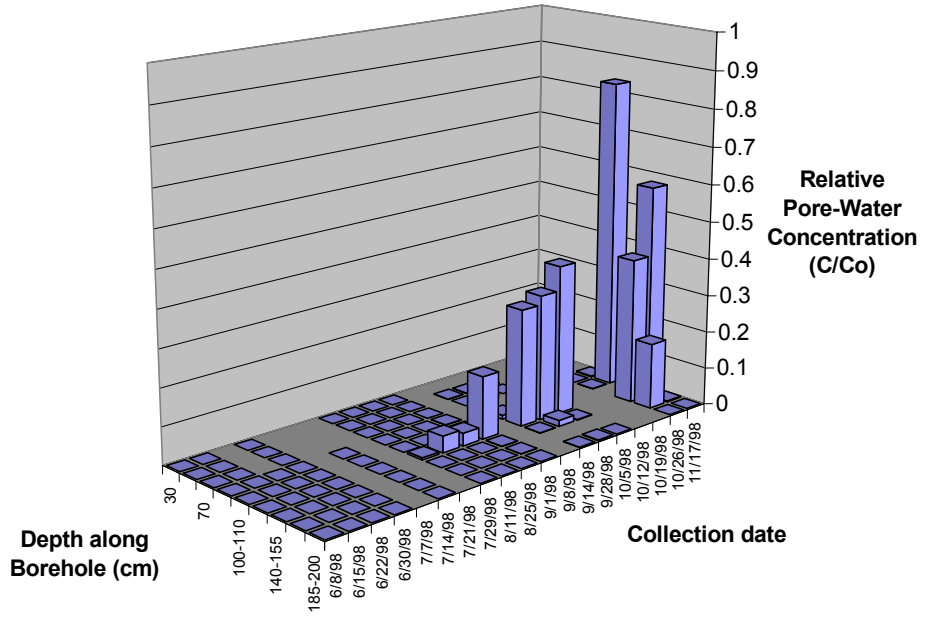

DTN: LA9909WS831372.001 [122739]; LA9909WS831372.002 [122741]

Source: CRWMS M&O 2001 [154024], Figure 58d

Figure 6.13.2-4d. Pyridone Concentrations in Borehole 6 for Phase 1B

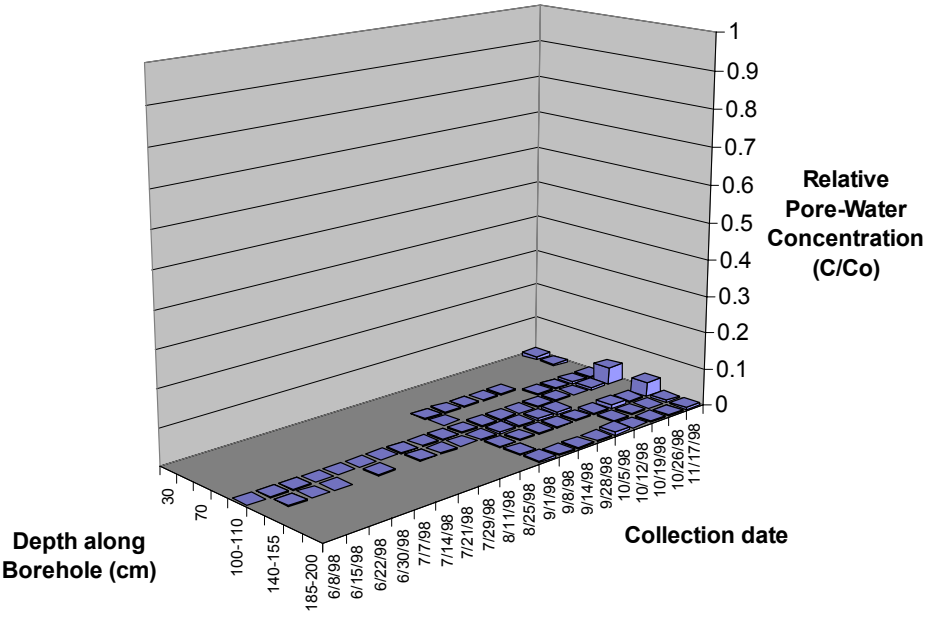

DTN: LA9909WS831372.001 [122739]; LA9909WS831372.002 [122741]

Source: CRWMS M&O 2001 [154024], Figure 58e

Figure 6.13.2-4e. Lithium Concentrations in Borehole 6 for Phase 1B

6.13.3 Field-Scale Tracer Transport – Phase 2

6.13.3.1 Test Configuration

Phase 2 testing involved a 7 m high, 10 m wide, and 10 m deep block comprising all of the lithologies of Phase 1 (Figure 6.13.1-4). The injection systems in Phase 2 were designed to activate large surfaces of the block. The injection points for this phase are distributed in two horizontal, parallel planes arranged to test the properties of the lower Topopah Spring Tuff (Tptpv2) and the hydrologic Calico Hills (Tptpv1 and Tac). There were 6 upper injection boreholes drilled (4 used for injection) and 4 lower injection boreholes drilled from the test alcove. The upper injection plane consists of fractured Topopah Spring Tuff Tptpv2. As in Phase 1B, this unit represents the base of the TSw basal vitrophyre and is characterized by subvertical fractured surfaces representing columnar joints. Thirty-seven injection points distributed along 4 injection holes approximately 8 m deep each were used for tracer injection along a horizontal surface. The natural fracture pattern present in this unit serves as the conduit for tracer migration into the nonwelded Calico Hills. The lower horizontal injection plane was located in the Calico Hills formation (Tac). There were 40 injection points distributed in four horizontal and parallel boreholes. These boreholes were designed to activate the lower part of the block in the event that the top injection system did not activate the entire block during the testing program.

Phase 2 included 15 collection boreholes drilled from the Main Adit, perpendicular to the injection boreholes. Twelve of the collection boreholes were drilled prior to the initiation of Phase 2 injection; 3 additional collection boreholes were drilled during injection. These boreholes were 8.5 to 10.0 m in length, and each contained 15 to 20 collection pads evenly distributed on inverted membranes.

Figure 6.13.3-1 is a view of the collection face, showing the positions of all the boreholes (to scale). It also shows the locations of the injection holes as horizontal lines. In describing the results of the field test, refer to Figure 6.13.3-1 to visualize the relative locations.

Phase 2 was subdivided into three subphases (2A, 2B, and 2C) according to location and injection rates used. Phase 2A consisted of a single borehole in the upper injection plane instrumented with 10 injection points and 10 moisture sensors, one at each injection point. The injection rate was 1 mL/hr per injection point. This borehole is restricted to the Tptpv2 lithology, which consists of fractured, moderately welded tuff from the basal vitrophyre. Phase 2A injection began on July 23, 1998, and was terminated on October 30, 2000.

Phase 2B consisted of four injection boreholes in the lower-injection plane, each instrumented with 10 injection points and 10 moisture sensors, one at each injection point. The injection rate was 10 mL/hr per injection point. This injection plane is restricted to the Calico Hills formation (Tac) and was planned to activate the lower section of the test block simultaneously with the upper section (Phases 2A and 2C). Phase 2B injection began on July 30, 1998, and was terminated on October 30, 2000.

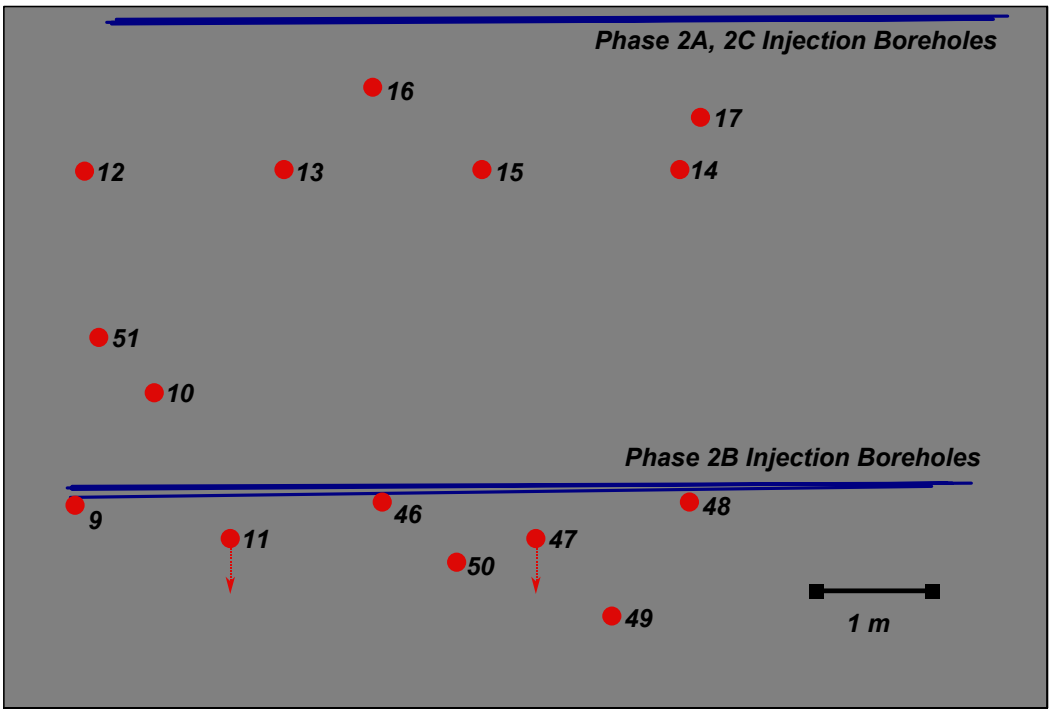

Source: CRWMS M&O 2001 [154024], Figure 59 (For illustration purposes only).
NOTE: Borehole 11 and borehole 47 with arrows are inclined.

Figure 6.13.3-1. Borehole Configuration on the Collection Face

Phase 2C consisted of three upper injection boreholes, each instrumented with nine injection points and 12 moisture sensors, one at each injection point, and two additional sensors located toward the borehole collar to detect tracer movement towards the front of the borehole. The injection rate was 50 mL/hr per injection point. This injection system was restricted to a horizontal plane in the Tptpv2 lithology. Phase 2C injection was initiated on August 5, 1998, and was terminated on October 30, 2000.

As discussed in Section 6.13.1.10, Phase 2 injected a mixed tracer solution that included those tracers used in Phase 1 plus three additional fluorinated benzoic acids (FBAs), a mixture of new reactive tracers (Ni^{2+}, Co^{2+}, Mn^{2+}, Sm^{3+}, Ce^{3+}, and Rhodamine WT). Beginning in August 1999, an additional nonreactive tracer (I^-) was added to the solution to study flow and transport response at higher system saturations.

Natural infiltration rates at Yucca Mountain vary between 0.01 and 250 mm yr^{-1}, with an average of 5 mm yr^{-1} (Flint et al. 1996 [100147]). Phase 2A falls within the range of natural present-day infiltration rates at Yucca Mountain, whereas Phase 2B lies at the high end of predicted values for a pluvial-climate scenario. Phase 2C infiltration rates are artificially higher than expected natural-infiltration rates for the region, but provide for the longest travel distances given the short duration of the experiment.

In addition to the tracer collection system, two geophysical imaging techniques [electrical resistance tomography (ERT) and ground-penetrating radar tomography (GPR-T)] were used to image the *in situ* 2- and 3-D saturation state of the block at approximately bimonthly intervals.

6.13.3.2 Additional Coring

During February–March 2000, three additional cores were extracted from the Phase 2 collection face (boreholes 49 to 51, Figure 6.13.3-1). These boreholes were located to sample volumes of the block that were not being captured by existing boreholes. The core from these boreholes was analyzed in the laboratory for tracers. The boreholes were also instrumented for pad collection, and these additional pads/locations were also analyzed. Results are presented later in this section.

Following termination of tracer injection, 5 overcores were taken around and below injection holes (Figure 6.13.3-2) to analyze the rock for tracers. These overcores were located to obtain the broadest spectrum of information on metals and microspheres, which had not been observed on any collection pads.

6.13.3.3 Mineback

A partial mineback of the Phase 2 block is currently underway. The purpose of the mineback is (1) to collect additional information about the geology of the block, particularly faults and permeability contrasts, and (2) to obtain rock samples for tracer analysis that cover a larger portion of the test block volume than the collection boreholes.

Observations of block geology at this point have identified at least one fault. An ash layer was observed in the lower Tptpv1 unit. At least one of the injection boreholes was fully contained within this layer. Observations of *in situ* fluorescing tracer indicate that this layer strongly affected flow by impeding movement of injected tracer mix into the remainder of the block.

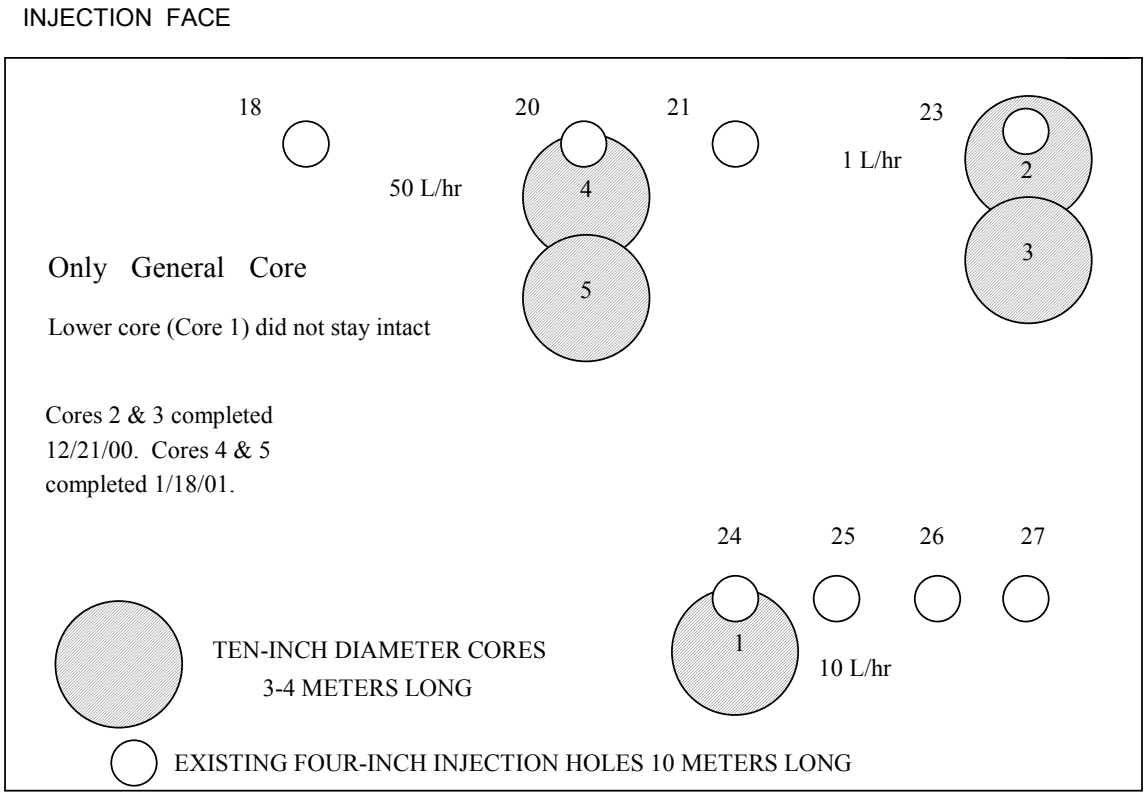

Figure 6.13.3-2. Schematic Illustration of Locations of Phase 2 Post-Test Overcores

6.13.3.4 Pad Analyses

Phase 2 injection began in July 1998 and was terminated on October 30, 2000. Almost 19,000 Phase 2 sampling pads were collected. Selected pads were analyzed via the tracer extraction process. Over 5,000 pads have been extracted, and over 32,000 individual analyses have been completed.

Pad analyses run thus far confirm breakthrough of nonreactive tracers in 14 of the 15 collection boreholes (all except borehole 10). Lithium breakthrough has been confirmed in 10 of the 15 collection boreholes (all except boreholes 10, 11, 47, 49, and 51). No other sorbing tracers have yet been unequivocally detected, but pad extract analysis in continuing.

Breakthrough information is presented in the following figures. These figures show distance in from the collection face on the horizontal axis, and time on the vertical axis, increasing from the top of the figure down. The location of injection boreholes is shown by vertical lines. Note that the location of the injection boreholes varies slightly at the different collection holes because the starting location of the collection boreholes varies: the collection face is not precisely perpendicular nor flat with respect to the injection face.

6.13.3.5 Moisture Movement

Figure 6.13.3-3 presents the moisture data at collection boreholes 10 and 15 compared with the bromide tracer breakthrough. As expected, the breakthrough of moisture onto the collection pads precedes the breakthrough of tracer. Initial saturation of the UZTT Phase 2 block was estimated at approximately 16%. Because the block was not totally dry, tracer displaced existing water ahead of it as it was injected. The contour maps in Section 6.13.3 were generated by using Excel to process the data and using NOeSYS V2.0 to interpolate irregularly-spaced data points into a regular grid for the plots.

6.13.3.6 Scaling/Travel Distance

The configuration of the injection and collection boreholes was designed to allow analysis of a variety of different processes. Collection boreholes were placed at different distances from the injection boreholes to assess the influence of travel distance. Differing travel distances also provide a range of scales for studying transport, from tens of centimeters to meters.

The effect of travel distance on tracer transport is shown in Figure 6.13.3-4. Collection boreholes 16, 17, 15, and 10 are all parallel and at increasing distance from the upper injection holes. All of the collection holes reside in unit Tptpv1 (hydrologic Calico Hills).

Breakthrough times at the different distances scale approximately linearly with travel distance. Fifty percent breakthrough of bromide in borehole 16 occurs at just under 125 days, whereas at borehole 15, almost twice as far from the injection boreholes, breakthrough occurs at approximately 250 days. Based on this, breakthrough at borehole 10 is expected at approximately 570 days. Pad analyses for borehole 10 at those dates are not yet available.

6.13.3.7 Heterogeneity

Boreholes 12, 13, 15, and 14 are all equidistant from the upper injection boreholes and parallel. They are all in the same unit. Difference in breakthrough pattern between these boreholes is thus a result of heterogeneities in the test block. Figure 6.13.3-5 demonstrates noticeable variability in both breakthrough times and concentrations for bromide in these boreholes.

The significant delay between breakthrough in borehole 12 versus boreholes 13 and 15 is possibly results from the presence of a fault that runs through the back of the block. This fault appears to cut between the injection boreholes and borehole 12.

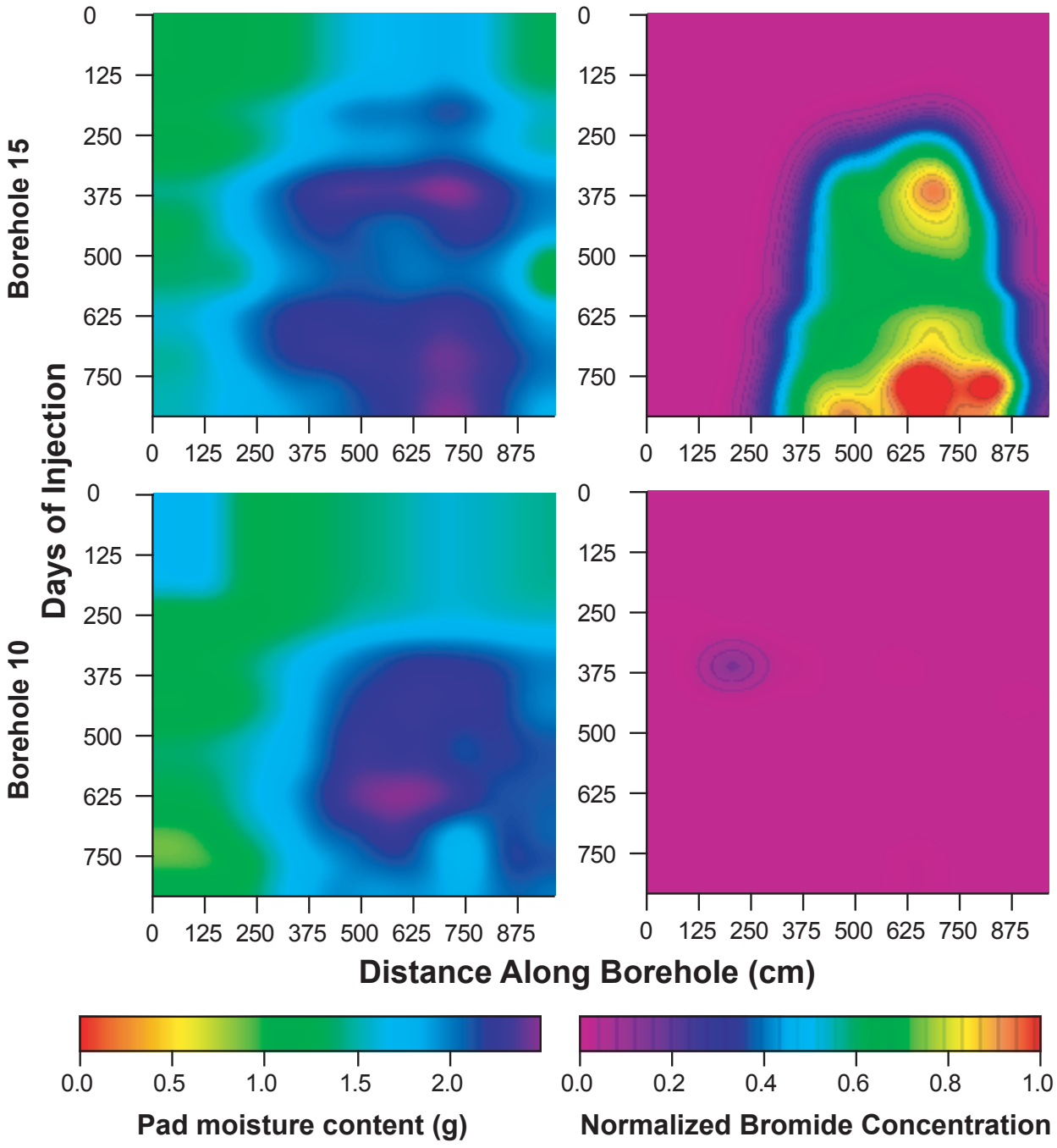

DTN: LA0112WS831372.001 [157100], LA0112WS831372.002 [157115], LA0112WS831372.003 [157106]

Figure 6.13.3-3. Moisture Front Precedes Tracer Front

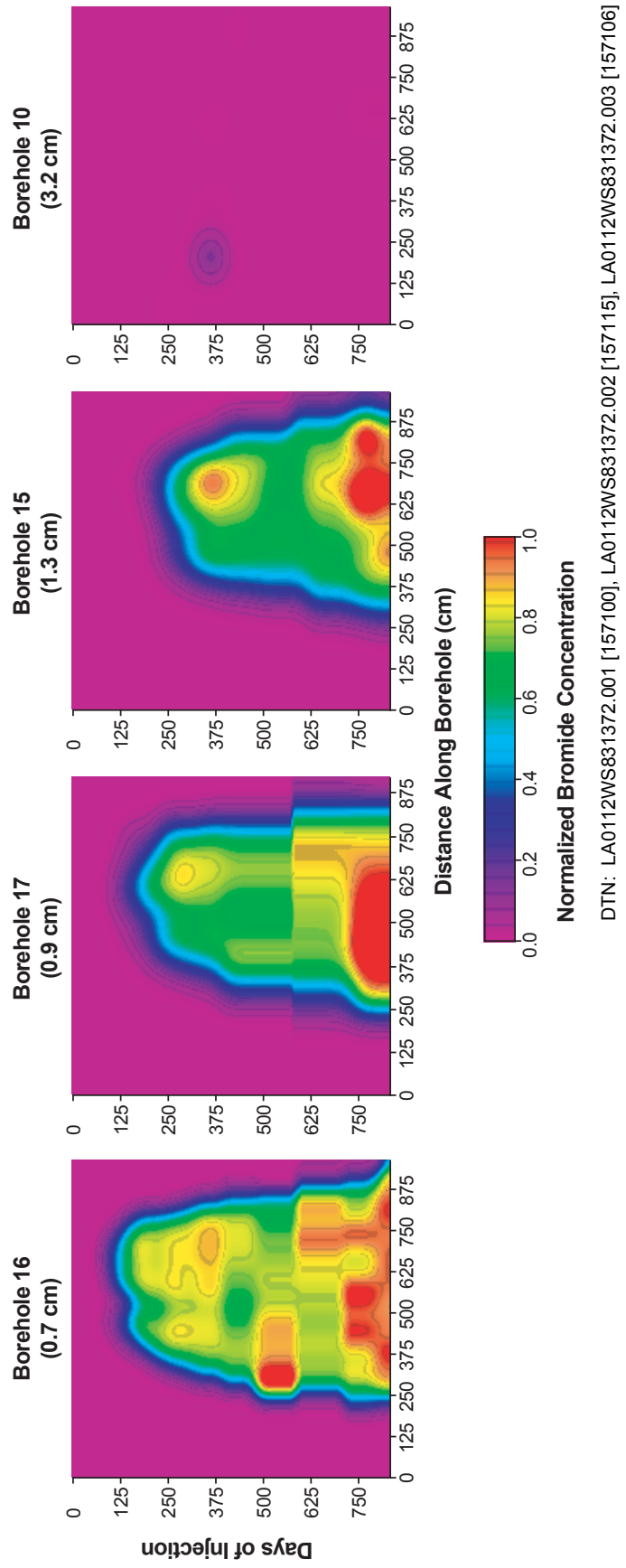

DTN: LA0112WS831372.001 [157100], LA0112WS831372.002 [157115], LA0112WS831372.003 [157106]

Figure 6.13.3-4. Influence of Scaling/Travel Distance on Tracer Transport in UZTT Phase 2

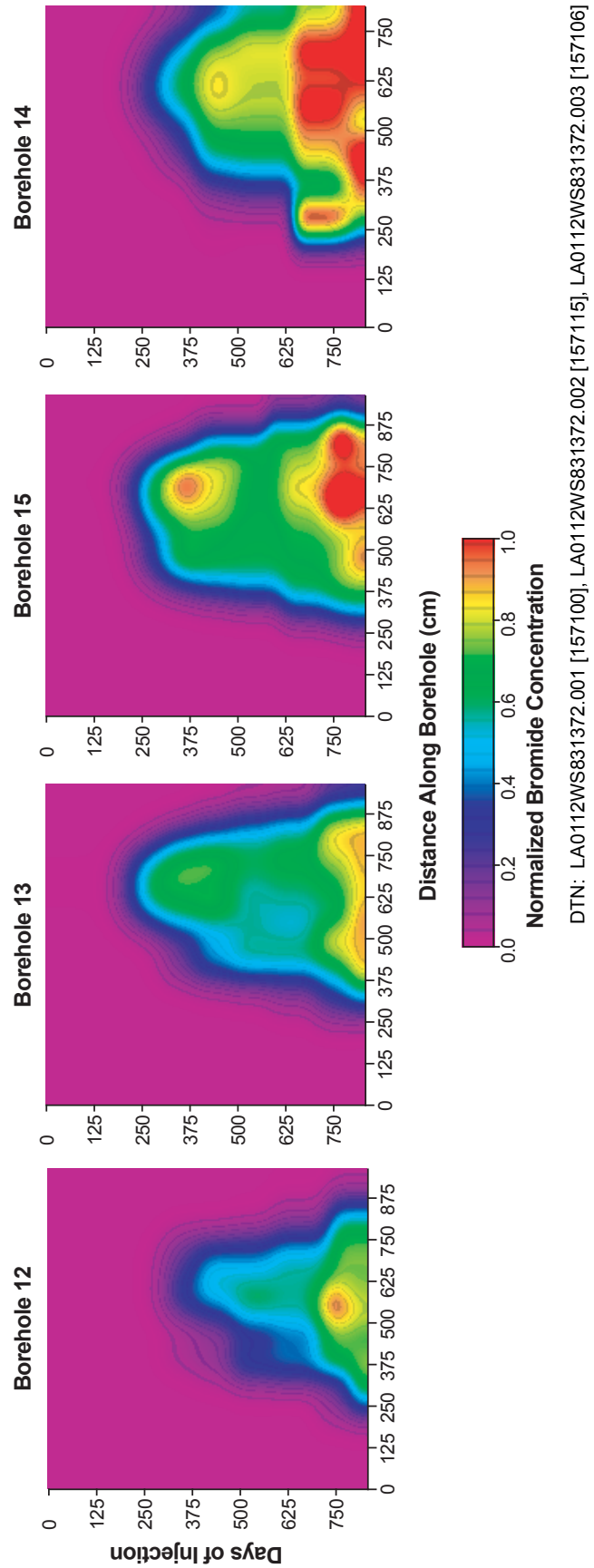

DTN: LA0112WS831372.001 [157100], LA0112WS831372.002 [157115], LA0112WS831372.003 [157106]

Figure 6.13.3-5. Influence of Rock Heterogeneity on Tracer Transport in UZTT Phase 2

6.13.3.8 Transverse Dispersion

In each of the injection holes, a mix of a number of tracers is introduced. The tracer mix is the same for all boreholes except with regard to the FBAs. Each injection borehole injects a different FBA to allow identification of the source of the tracer when collection pads are analyzed. Thus, by looking at tracer breakthrough patterns in a single collection borehole, the extent of lateral dispersion can be assessed.

Tracer breakthrough in borehole 16 is shown in Figure 6.13.3-6. Borehole 16 is 0.7 m below the injection boreholes. The vertical marks on Figure 6.13.3-6 show the location of the borehole that is injecting the particular FBA being plotted. Bromide is injected in all holes, so the bromide plot shows overall breakthrough in borehole 16.

The breakthrough pattern in borehole 16 indicates that there is little transverse dispersion or mixing of the tracer being injected at the various injection boreholes.

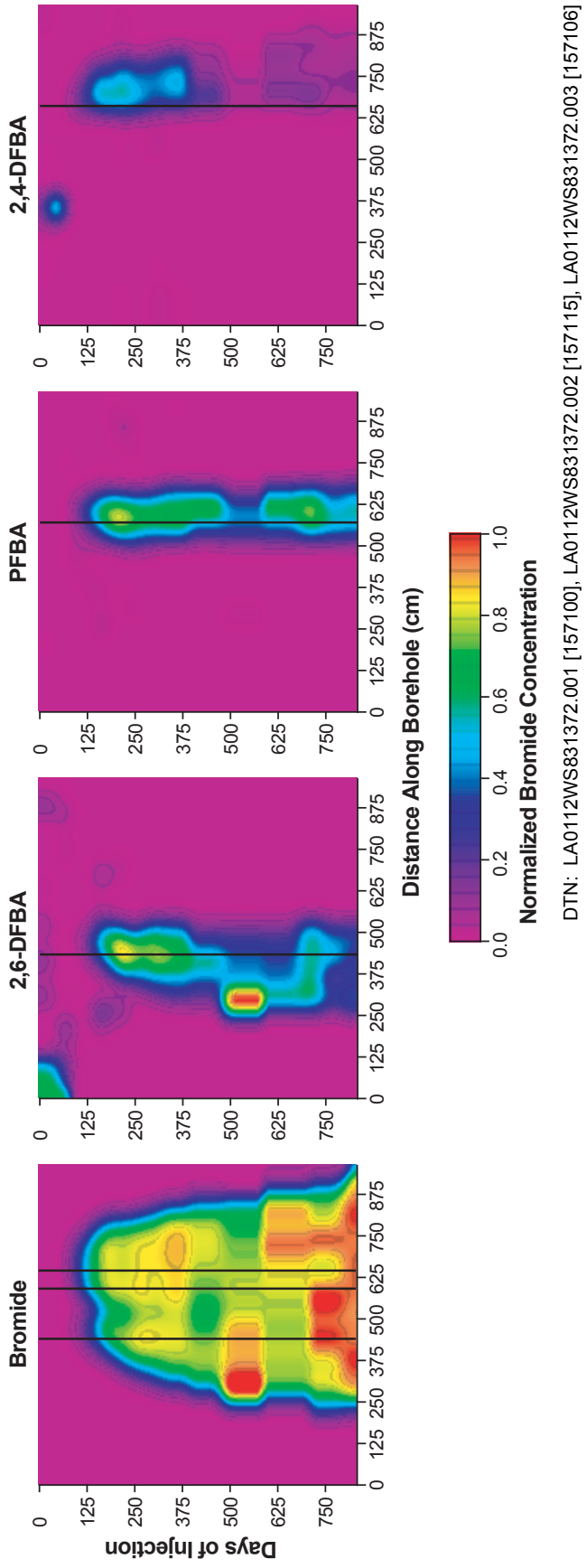

DTN: LA0112WS831372.001 [157100], LA0112WS831372.002 [157115], LA0112WS831372.003 [157106]

Figure 6.13.3-6. Extent of Transverse Dispersion on Tracer Transport Measured in Borehole 16 of the UZTT Phase 2

6.13.3.9 Sorption/Retardation

The influence of sorption/retardation is analyzed by comparing breakthrough curves for bromide versus lithium at various boreholes. Figure 6.13.3-7 shows breakthrough curves for the two tracers at three different boreholes. Borehole 16 and borehole 15 are below the upper injection boreholes (50 mL/hr), in Tptpv1, 0.7 m and 1.3 m, respectively. Borehole 48 is below the lower injection boreholes (10 mL/hr), located in the Tac.

As expected, lithium breakthrough is retarded with respect to bromide. Laboratory sorption measurements calculate lithium K_d values between 0.4 and 1.1 (DTN: LA9912WS831372.001 [156586]).

All of the other reactive tracers being used have significantly higher K_d values and were not expected to break through at any of the boreholes yet.

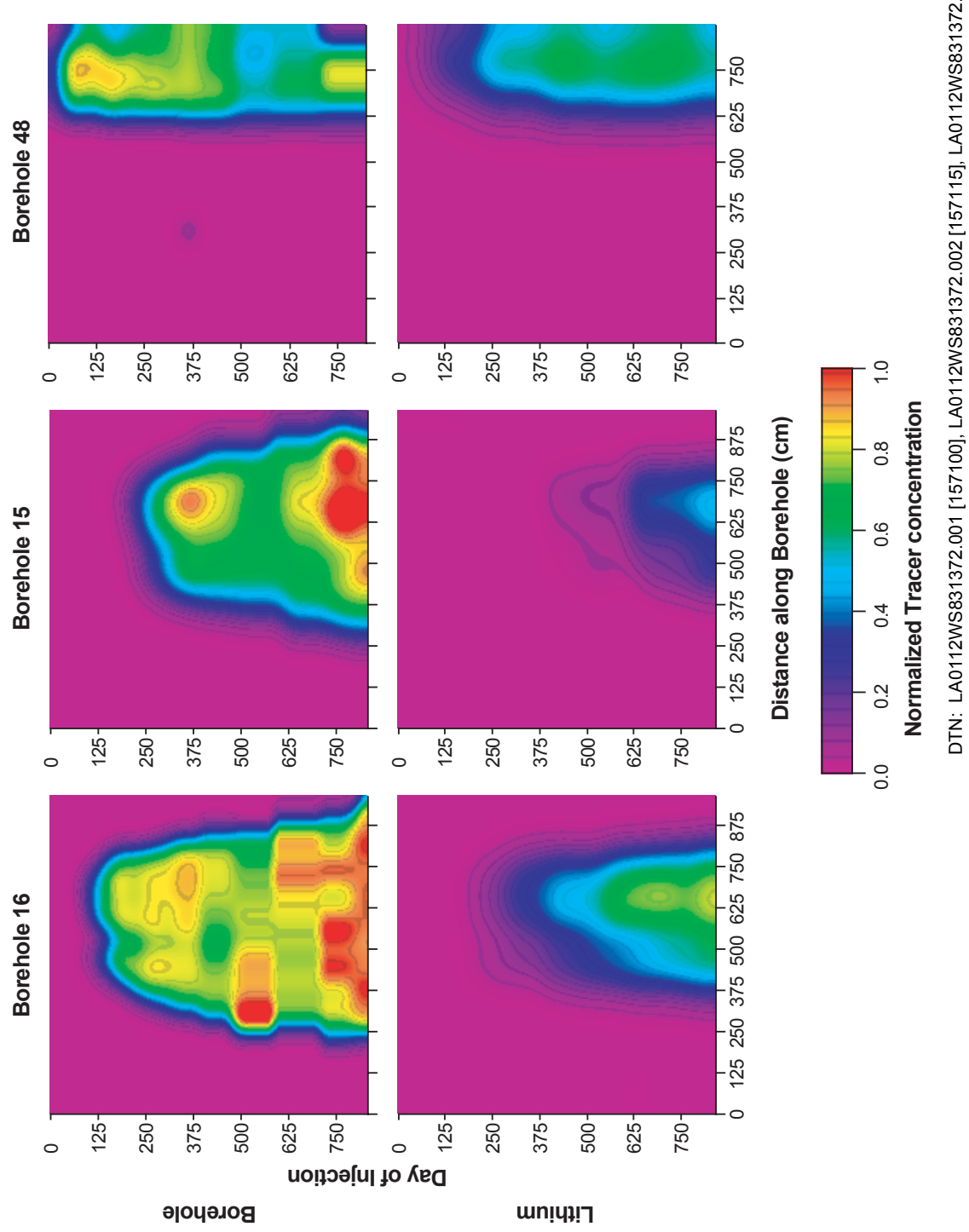

DTN: LA0112WS831372.001 [157100], LA0112WS831372.002 [157115], LA0112WS831372.003 [157106]

Figure 6.13.3-7. Effect of Sorption/Retardation on Tracer Transport in UZTT Phase 2

6.13.4 Tomographic Studies: Geophysical Techniques at the Busted Butte Unsaturated Zone Test Facility

Real-time geophysical monitoring techniques were used to provide real-time data on the advance of fluid fronts and tracer fronts through the block. Combining two geophysical techniques enables the collection of detailed, high-resolution, 3-D, calibrated, real-time monitoring of moisture and tracer movement through the unsaturated fractured medium. Specifically, electrical resistance tomography (ERT) provides 3-D global coverage, and ground-penetrating radar tomography (GPR-T) provides high spatial resolution.

6.13.4.1 Busted Butte Ground Penetrating Radar Tomography

The GPR data acquisition was conducted in the Phase 2 test block to monitor the tracer injection, both spatially and temporally, and to investigate the nature of fluid migration through the Calico Hills formation. The data collected, analyzed, and submitted to the Technical Data Management System (TDMS) thus far include the pre-injection/baseline radar velocity measurements as well as the subsequent velocity measurements made after the start of tracer injection (nine data collection visits though November 2000). All analyzed data were periodically compared to the other available geophysical data (as well as to the tracer breakthrough data) to constrain the interpretation of the fluid/tracer migration within the block.

6.13.4.1.1 Background and Experimental Approach

In the borehole radar method, modified surface radar antennas are emplaced into a rock formation, and high-frequency electromagnetic signals are transmitted through the formation to a receiving antenna. The electrical properties of the subsurface material greatly influence the transmitted electromagnetic signal. In particular, the dielectric permittivity (K) of the rock has a strong influence on the propagation of the signal and whether it travels at a high or low velocity. Moisture content also affects dielectric permittivity. The high dielectric permittivity of water (K ~80) or wet rock (K ~20-30) in contrast to drier rock (K ~3-6) typically results in greatly reduced signal velocities. Changing chemical compositions (i.e., tracers) may also alter the bulk dielectric permittivity of the rock and hence the propagation velocity of the radar waves. Because such changes in signal character are what are measured over the course of the Busted Butte UZTT, any increase (or decrease) in background moisture content or chemical composition resulting from the tracer injection (or rock dryout) should result in changes in the received radar velocity.

The transmitted signals are represented as multiple ray paths crossing through a zone of interest within the block. If sufficient ray paths are recorded, a tomographic image is obtained through computer processing. The information extracted from such data consists of the radar wave travel time, which depends on the wave velocity. This information, in the form of a processed radar velocity tomogram, offers a high-resolution approach to monitoring the changes occurring in the rock over the duration of the tracer-injection experiment.

A detailed description of the equipment used, the component specifications, the operating principles, and the GPR survey methodology can be found in the Technical Implementing Procedure, YMP-LBNL-TIP/GP 5.0, *Ground Penetrating Radar Data Acquisition*, governing all GPR data acquisition done in support of the Yucca Mountain site characterization effort.

6.13.4.1.2 Equipment Description, Component Specifications, Operating Principles, and Survey Methodology

A detailed description of the equipment used, the component specifications, the operating principles, and the GPR survey methodology can be found in Bussod et al. (1998 [131513], Section 5.1.6). Additional information can be found in the Technical Implementing Procedure governing all GPR data acquisition done in support of the Yucca Mountain site characterization effort (YMP-LBNL-TIP/GP 5.0).

6.13.4.1.3 Results of the Busted Butte Unsaturated Zone Transport Test Radar Data Acquisition

The radar data were acquired in eight of the Phase 2 collection boreholes orthogonal to the direction of the Phase 2 injection boreholes. Additionally, two of the Phase 2 injection boreholes were used to acquire data one time only after they were apparently affected by grout infiltration resulting from nearby ERT borehole grouting. The ten boreholes include the following: 9, 11, 13, 15, 16, 46, 47, and 48 (Phase 2 collection); 19 and 22 (Phase 2 injection). The configuration of and layout of the boreholes used are illustrated in Figure 6.13.3-1.

The radar data were acquired in the two-dimensional planes defined by the two boreholes, more commonly referred to as well pairs. The well pairs acquired include the following: 15-13, 48-46, 47-11, 46-9, 46-16, and 22-19 (one time only). The decision to acquire data in these particular well pairs was made based on the relative proximity to the injection boreholes. Data from both the upper horizontal well pair 15-13 and the vertical well pair 46-16 was acquired to monitor tracer injection associated with the upper injection boreholes 18, 20, 21, and 23. Data from the lower horizontal well pairs 46-9, 47-11, and 48-46 were acquired to monitor tracer injection associated with the lower injection boreholes 24, 25, 26, and 27. The vertical well pair 46-16 may also be used to image any tracer injection associated with the lower injection boreholes and the progress of the tracer beneath the horizontal well pair 15-13.

Thus far, the data have been processed for travel times, with the result being radar velocity tomograms. Differencing or subtraction of the velocity tomograms over time has also been completed for each of the well pairs. Such differencing or subtraction allows for the highlighting of the tracer or moisture front as it changes spatially and temporally. In essence, the background formation remains static in those areas not affected by the changing tracer or moisture front. By subtracting one velocity tomogram from another, we have been able to discount those areas remaining static, while emphasizing those areas where change is occurring.

Two of the well pairs differ slightly in the acquisition method used between the baseline and the post-injection surveys. These well pairs are 46-16 and 46-9. Data for well pair 46-16 was collected at a high frequency (200 MHz) during the post-injection surveys to better match the data collected in all of the other well pairs. Higher frequencies generally result in data of higher resolution (approximately 10.0 cm for 200 MHz), so the highest-frequency antennas should be used if at all possible. Data were not originally acquired in well pair 46-9 because it was believed that well pair 48-46 provided sufficient coverage in the area of the lower injection boreholes. A decision was subsequently made after tracer injection began to gather more spatial information below the lower injection boreholes and, therefore, well pair 46-9 was added to the GPR

acquisition list. Also, it should be noted that the pre-injection baseline data for several of the well pairs differs significantly from data acquired just one month after tracer injection began. The differences were likely the result of changes in the overall block assemblies (e.g., grouting of the ERT boreholes, addition of the injection apparatus) rather than the immediate consequence of the tracer injection. To enhance the subsequent differencing tomography, the "baseline" set of radar velocity tomograms chosen were those collected in August-September 1998, approximately one month after tracer injection began. Comparison with tracer breakthrough data on the collection pads indicated that tracer had not yet significantly entered those regions imaged by the GPR tomograms. Therefore, it was determined that the August–September 1998 data would provide an adequate starting point from which to evaluate the changes in the block over time.

Each of the well pairs witnessed some degree of velocity change over the course of the experiment. For the purposes of this AMR, however, only four of the well pairs will be discussed in detail: 46-16, 46-9, 11-47, and 15-13. Interpretation of the data suggested that the results for all of the well pairs are similar. Again, all data from each of the well pairs have been submitted to the TDMS and are available for review.

Well Pair 46-16

This well pair represents the only vertical slice through the block (approximately 9.5 m long and 3.5 m wide). It images tracer and moisture contributions from both the upper and the lower injection boreholes. When evaluating changes in velocity over time, one would expect such changes to occur in the regions directly surrounding the injection boreholes, with decreased velocities representing areas of increased moisture content. This is exactly what is seen in the differenced tomograms. Figures 6.13.4-1 represent several time steps throughout the course of the experiment (dates of data acquisition are noted above each tomogram). As can be seen, decreases in the velocity relative to the baseline (Aug.–Sept. 1998) data are immediately obvious surrounding the high and low injections boreholes (these locations are marked on the tomograms as small white dots). Furthermore, the zones of decreased velocity can be seen to expand away from the injection boreholes over time, both in a vertical as well as a horizontal direction. Such vertical and horizontal spreading is to be expected as a result of the matrix or capillary-driven flow and was, in fact, confirmed in the Phase 1A excavation. Until the results of a similar excavation in the Phase 2 block are analyzed, the GPR data would seem to indicate a similar mechanism of flow for this area.

Also of note is the seemingly large extent of decreased velocity. It should be restated that low velocities are indicative of zones of higher dielectric permittivity, which indicate zones of elevated moisture content. That being the case, those zones of decreased velocity may represent regions of elevated moisture content and simply the presence of tracer. This subtlety is borne out when comparing the tracer breakthrough data with the tomography results. The zones of increased moisture content (i.e. decreased velocity) do not directly overlay the tracer breakthrough within boreholes 46 or 16. In fact, the locations of tracer breakthrough are contained within the zones of decreased velocity. This implies that as the fluid front containing the tracer spreads away from the injection boreholes, some of the tracer may be retarded relative to the spread of the moisture front. In effect, the tracer may be moving more slowly through the block than its associated fluid or water component.

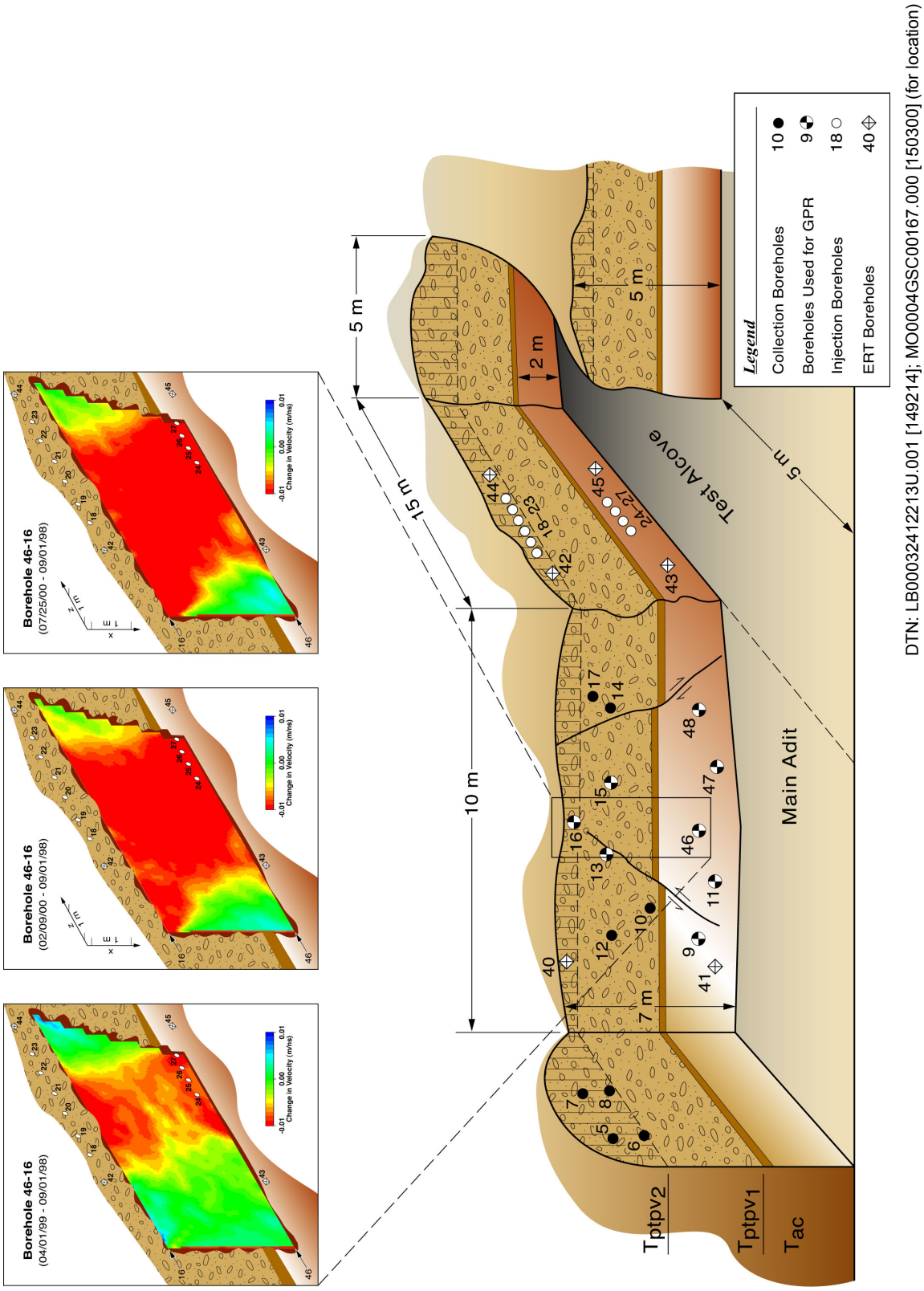

DTN: LB0003241221 3U.001 [149214]; MO0004GSC00167.000 [150300] (for location)

Figure 6.13.4-1. Tomography (GPR-T) Results for Well Pair 46-16 from December 1998; March 1999; and April 1999

Conversely, the fluid front leaving the injection boreholes may be simply displacing existing pore fluid and mobilizing it within the block. The radar velocities are insensitive to this effect and thus are incapable of distinguishing between existing pore fluid, introduced pore fluid, and tracer. Given the extent to which the velocities are decreasing, it seems unlikely at this time that sufficient natural pore water existed within the block prior to the experiment to account for all of the change observed. Again, comparing the tomography results with those recorded in the tracer breakthrough logs, it appears that some form of fluid breakthrough is occurring in the collection boreholes which is not comprised of tracer (so-called "contamination of pads" in the breakthrough logs). This is evidently what is being imaged by the differenced radar tomograms, and it is not an inconsequential finding.

Additionally, when compared to the radar results, the neutron probe data collected in these two boreholes imply a similar pattern of increased moisture content. Those zones that appear to be wetting as well as those that remain dry agree nicely with the same regions on the tomograms.

Well Pair 46-9

This well pair represents a horizontal slice (approximately 8.0 m long and 2.6 m wide) through the block and images the tracer/moisture front associated with the lower injection boreholes. Figures 6.13.4-2 represent several time steps throughout the course of the injection (dates of acquisition are noted above each tomogram). Decreases in velocity relative to the baseline (August–September 1998) data are immediately obvious surrounding the lower injection boreholes (these locations are marked on the tomograms as orthogonal tubes). Furthermore, the zones of decreased velocity expand away from the injection boreholes over time in a horizontal direction. Because a horizontal well pair cannot capture the vertical flow of moisture away from the boreholes, only the extent of the horizontal flow can be imaged. The decrease in velocity (i.e., the increase in moisture content) moves rapidly away from the injection boreholes early on in the experiment and then remains relatively constant (aside from localized changes). This would imply that much of the moisture front moves away from the injection apparatus to its greatest possible extent at which time it can no longer spread in such a direction. Presumably, the majority of fluid flow from the lower injection boreholes continues on in a vertical direction. Later in the course of the experiment, however, decreases in velocity (i.e., increases in moisture content) begin to show up at distances farther removed from the lower injection boreholes. This contribution possibly results from the upper injection boreholes. As the fluid/tracer front moves away from the upper injection boreholes in the downward direction, it ultimately comes into contact with the lower horizontal well pairs (i.e.,. 48-46, 46-9, 11-47). That this occurs is seen in the vertically oriented tomograms described for well pair 46-16.

The results implied by the radar tomograms support the tracer breakthrough logs for boreholes 48 and 9. Again, those zones of decreased velocity overlay those locations in the boreholes where tracer has been seen to break through onto the collection pads. The additional contribution of the moisture front relative to the tracer (as described above for well pair 46-16) does not appear to be as significant for this well pair. It is not yet clear whether this is because the region imaged is smaller or spatially close to the injection boreholes. Additionally, the neutron probe data collected in these two boreholes implies a very similar pattern of increased moisture content. Those zones that appear to be wetting as well as those that remain dry agree well with the same regions on the tomograms.

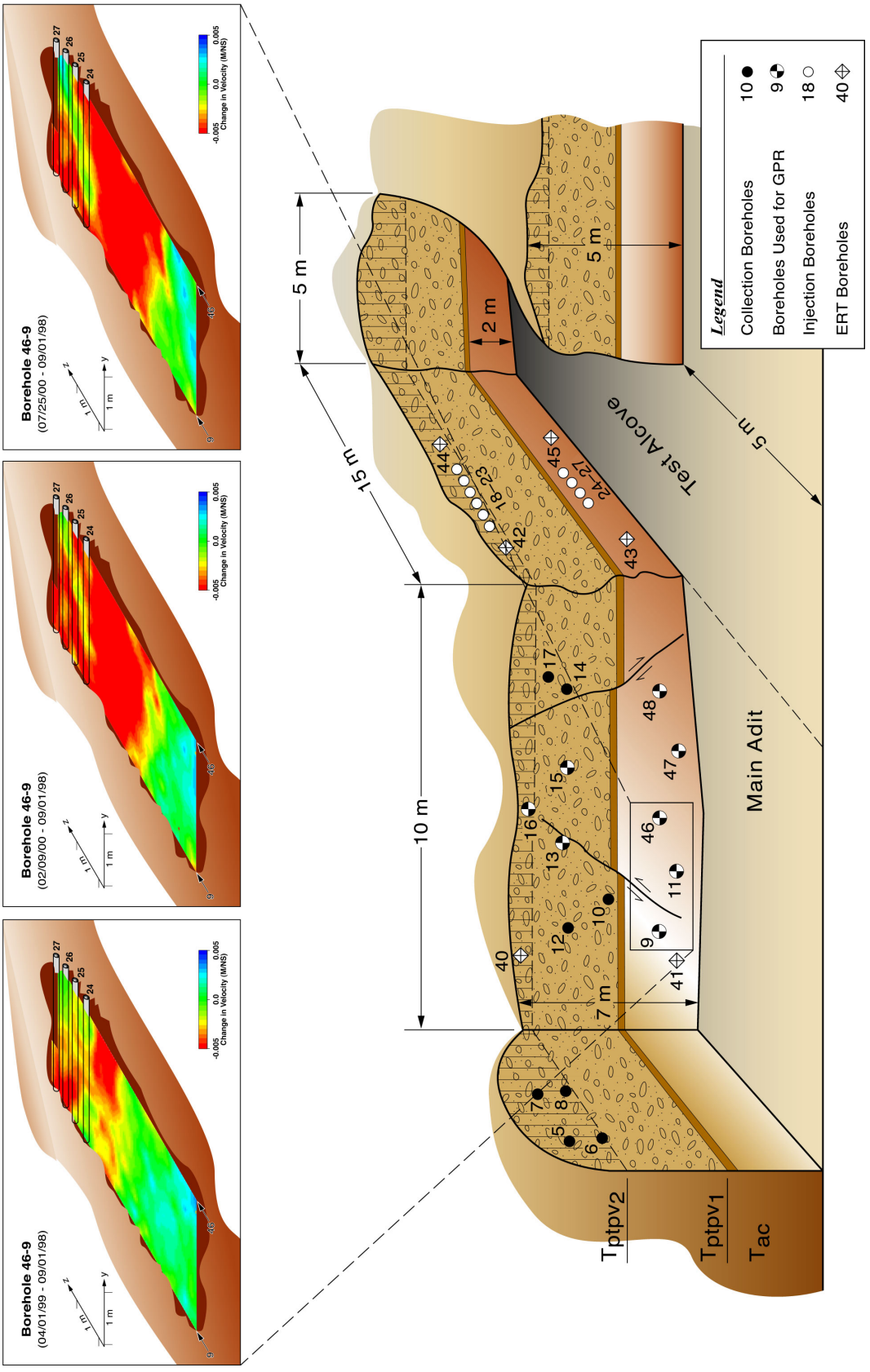

DTN: LB0003241221 3U.001 [149214]; MO0004GSC00167.000 [150300] (for location)

Figure 6.13.4-2. Tomography (GPR-T) Results for Well Pair 46-9 from April 1999; February 2000; and July 2000

Well Pair 11-47

This well pair represents a subhorizontal slice (approximately 10.0 m long and 2.6 m wide) through the block and images the tracer/moisture front associated with the lower injection boreholes. This well pair is of interest because of its component of dip, which allows the collection boreholes to get progressively farther away from the injection boreholes as a function of depth. Figure 6.13.4-3 represents several time steps throughout the course of the injection (dates of acquisition are noted above each tomogram). Decreases in velocity relative to the baseline (June 1998) data are immediately obvious surrounding the lower injection boreholes (these locations are marked on the tomograms as orthogonal tubes). The zones of decreased velocity expand away from the injection boreholes over time in a horizontal direction. Again, the dip of these two boreholes was designed to provide a means to measure sequential breakthrough down the length of the boreholes. The radar data does not appear to show such an effect. Because of either the time step chosen or to smearing inherent in the tomographic processing, there is no obvious "staggering" in the moisture/tracer breakthrough locations. The region of decreased velocity (i.e., the area of increased moisture content) moves away from the injection boreholes early on in the experiment and then continues in a similar fashion up to a point at which moisture spreading seems to cease. As for the other horizontal well pairs, this would imply that much of the moisture front moves away from the injection apparatus to the greatest possible extent, at which time it can no longer spread in such a direction. Presumably, the majority of fluid flow from the lower injection boreholes continues on in a vertical direction.

The results implied by the radar tomograms support the tracer breakthrough logs for boreholes 11 and 47. Again, those zones of decreased velocity overlay those locations in the boreholes where tracer has been seen to break through onto the collection pads. Additionally, the neutron probe data collected in these two boreholes implies a very similar pattern of increased moisture content. Those zones that appear to be wetting as well as those that remain dry agree well with the same regions on the tomograms.

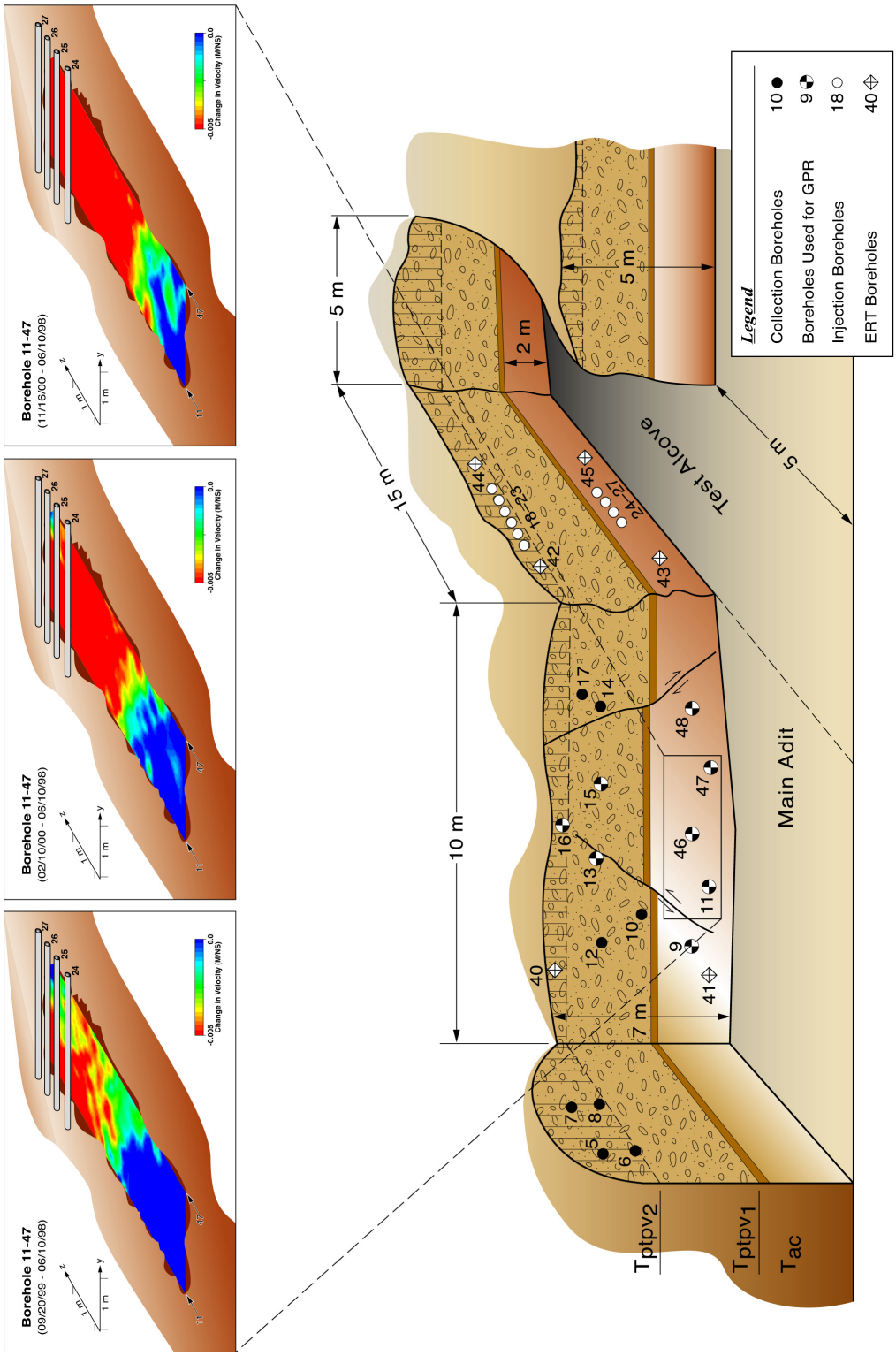

DTN: LB0003241221 3U.001 [149214]; LB0110BSTBTGPR.001 [156913]

Figure 6.13.4-3. Tomography (GPR-T) Results for Well Pair 11-47 from September 1999, February 2000, and November 2000

Well Pair 13-15

This well pair represents a horizontal slice (approximately 9.5 m long and 2.0 m wide) through the upper part of the block. Figure 6.13.4-4 represents several time steps throughout the course of the experiment (dates of data acquisition are noted above each tomogram). Decreases in the velocity relative to the baseline data (August–September 1998) are immediately obvious surrounding the upper injection boreholes (these locations are marked on the tomogram as orthogonal tubes). Furthermore, the zones of decreased velocity expand away from the injection boreholes over time in a horizontal direction. The decrease in velocity (i.e., the increase in moisture content) moves steadily away from the injection boreholes throughout the course of the experiment. This varies a bit from the analogous well pair 48-46. Rather than reaching a maximum extent, the moisture front appears to be continually expanding away from the boreholes. This is probably the result of the well pair's increased distance beneath the injection boreholes and the much larger volume of fluid being introduced by the upper injection boreholes (50mL/hr as compared to 10mL/hr).

The results implied by the radar tomograms are in concurrence with the tracer breakthrough logs for boreholes 13 and 15. Again, those zones of decreased velocity overlay those locations in the boreholes where tracer has been seen to break through onto the collection pads. The additional input of the moisture front relative to the tracer (as described for well pair 46-16) does not appear to be as significant for this well pair. As for well pair 48-46, it is not yet clear whether this is because the region imaged is smaller or spatially closer to the injection boreholes. Also, the much larger volume of tracer injected into the region of this well pair may account for the lack of a discrepancy (i.e., there is simply more tracer in the area of the collection boreholes). Additionally, the neutron-probe data collected in these two boreholes imply a very similar pattern of elevated moisture content. Those zones that appear to be wetting as well as those that remain dry agree nicely with the same regions on the tomograms.

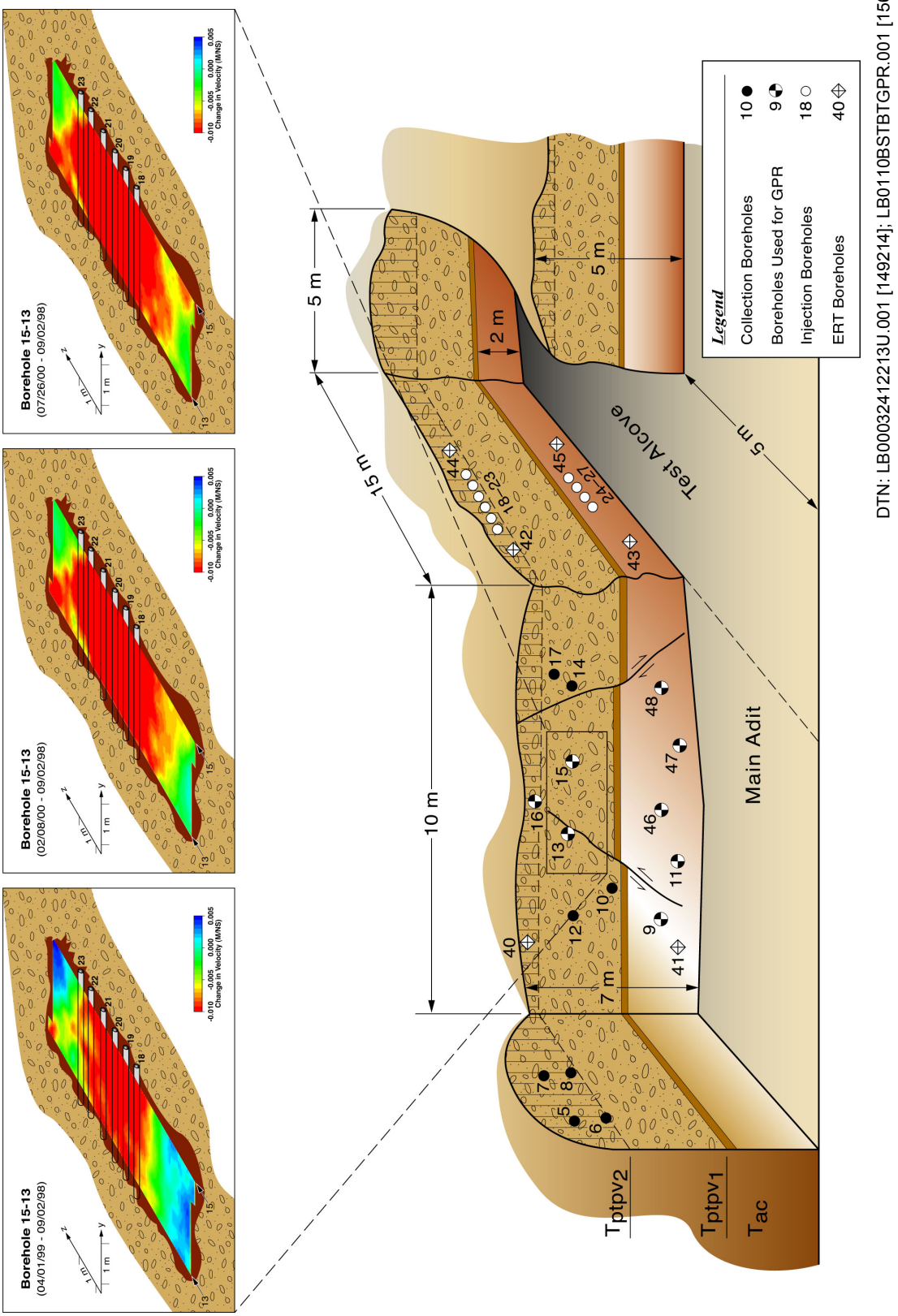

DTN: LB0003241221 3U.001 [149214]; LB0110BSTBTGPR.001 [156913]

Figure 6.13.4-4. Tomography (GPR-T) Results for Well Pair 13-15 from April 1999, February 2000, and July 2000

6.13.4.1.4 Summary of Ground-Penetrating Radar Tomography

The radar data collected thus far in support of the Busted Butte UZTT suggest that this method is appropriate for investigating subsurface velocity anomalies that may be related to tracer injection and moisture migration. Such anomalies are the result of changes in the dielectric permittivity of the rock mass. As noted above, such changes are most likely the result of some combination of the injected tracer and its associated fluid component. The regions of low velocity (i.e., elevated moisture content) appear to be in very close agreement with the other complementary evidence, including the tracer breakthrough logs and the neutron logging results. At this time, it appears likely that the differenced radar tomograms are defining the total extent of elevated moisture content within those zones defined by the radar well pairs. By defining the extent of this front, the radar tomography should provide an excellent control mechanism for the interpretation of the excavated Phase 2 block or any of the hydrological flow modeling done to date.

6.13.4.2 Electrical-Resistance Tomography

The objective of this work is to provide 3-D electrical-resistance tomography (ERT) images of the movement of a tracer through the test block at the UZTT at Busted Butte. This report describes the results obtained during four separate data collections starting in July and ending in early September 1998.

ERT is a new geophysical imaging technique that can be used to map subsurface liquids as flow occurs and to map geologic structure. ERT is a technique for reconstruction of subsurface electrical resistivity. The result of such a reconstruction is a 2- or 3-D map of the electrical resistivity distribution underground made from a series of voltage and current measurements from buried electrodes. The ERT approach followed here relies on detection and mapping of the changes in electrical resistivity associated with the movement of a tracer through the test block at the UZTT site.

6.13.4.2.1 Results of Data Collections—July to Early September 1998

ERT data were collected four times: July 2, July 14, August 19, and September 9, 1998. The intent was to make comparisons between the baseline condition on July 2 and data collected at later times. Comparisons between July 2 and August 19 and between July 2 and September 9 are presented because the data from July 14 were of questionable quality. These data have been submitted to the YMP Technical Data Management System (DTN: LL990612704244.098 [147168]).

Sixty ERT electrodes were installed in the test block as shown in Figure 6.13.4-5. The electrodes were placed in six drilled holes, ERT-1 though ERT-6, and two surface arrays (upper and lower). Holes ERT-3, 4, 5, and 6 and the surface arrays were drilled perpendicular to and from the instrumentation alcove. Holes ERT-1 and 2 were drilled from the main adit. The electrodes were grouped into boreholes 1 through 4 as shown in Figure 6.13.5-8. As is evident, each borehole is L-shaped and contains 15 electrodes. For example, borehole 1 is composed of the 8 electrodes in hole ERT-3 along with the 7 electrodes in the upper-surface array.

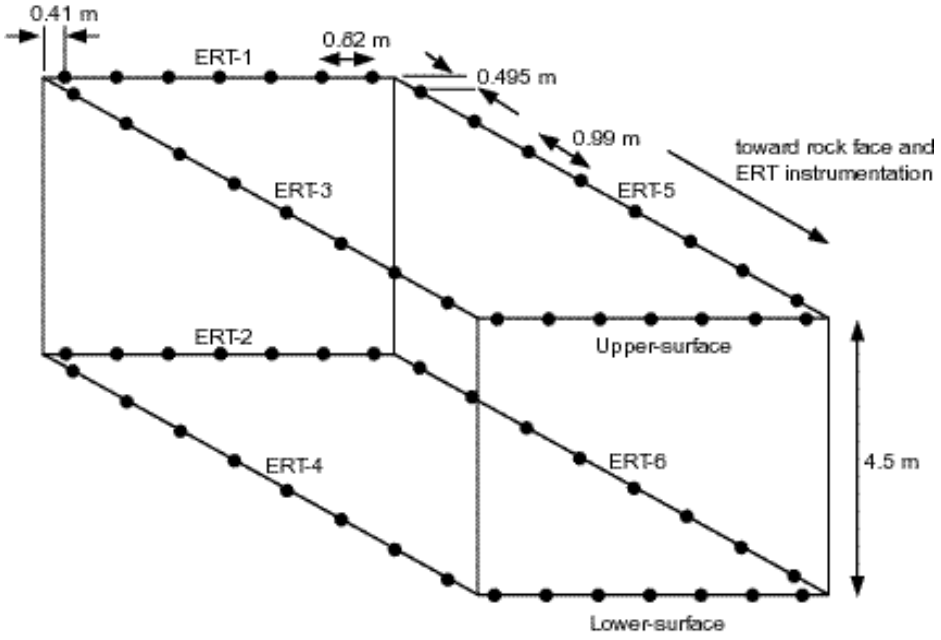

Source: CRWMS M&O 2000 [154024], Figure 53

NOTE: This diagram gives the layout of drilled holes, ERT electrode locations, and spacing in the UZTT test block at Busted Butte.

Figure 6.13.4-5. ERT Layout

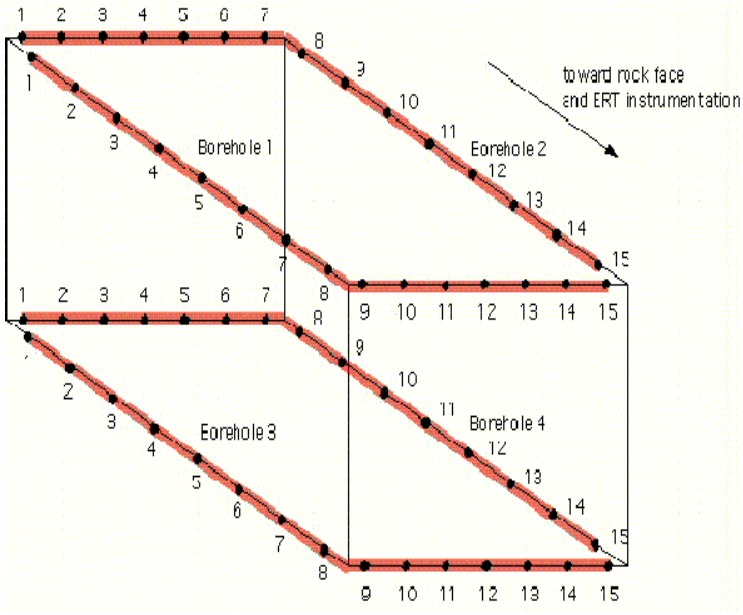

Source: CRWMS M&O 2000 [154024], Figure 54

NOTE: This diagram gives the layout of the ERT boreholes and electrode assignments in the UZTT test block at Busted Butte.

Figure 6.13.4-6. ERT Electrode Assignments

The ERT data were collected between borehole pairs: boreholes 1 and 2 (upper horizontal plane), 3 and 4 (lower horizontal plane), 1 and 3 (left vertical plane), 2 and 4 (right vertical plane), 1 and 4 (diagonal), and finally 2 and 3 (diagonal) for a total of six data sets. The total number of data values collected was 2,430. These values provided the 3-D sampling of the test block resistivity, and the 3-D inversion algorithm operated on these data to produce a 3-D ERT image of the block.

It is most useful to look at comparison images when changes are taking place over time. The results presented here consider difference images that compare the resistivity of the block on August 19 and September 9 to July 2. Because the tracer mixture injected during Phase 2 of the UZTT experiment was approximately eight times more conductive than the pore water, resistivity decreases in the images are of interest.

6.13.4.2.2 Absolute ERT Images of the Block

Figure 6.13.5-9 shows an absolute image of the baseline condition of July 2 (top) and the difference between August 19 and July 2 (bottom). The baseline image shows a layered structure consistent with the lithology in the rear half of the block-that is, a high-resistivity layer over most of the middle of the block, Tptpv1, with a lower-resistivity region, Tptpv2, at the top, and a low-resistivity region, Tac, at the bottom. The image also shows an anomalously low resistivity region in the front half of the block, particularly near the bottom. This is not well understood and should be confirmed, if possible, by other means.

6.13.4.2.3 Difference ERT Images of the Block

The difference image of Figure 6.13.4-7 shows regions of resistivity decrease near injection holes 18, 20, and 21, as one would expect from the injection of conductive tracer mixture. It is apparent that a pronounced resistivity decrease exists in the slice 2.66 m from the front of the block, which could be associated with water moving downward in the block. The region of the block between 1.33 and 4.0 m, which contains this slice, also appears to be a low-resistivity region in the absolute image.

The September 9 to July 2 difference (Figure 6.13.4-8) also shows regions of resistivity decrease near injection boreholes 18, 20, and 21. The effect is even stronger in the 5.33 m slice. Moreover, the effect of water moving down into the block seems to be more pronounced in the 4.0 m slice compared to August 19.

The difference images from August 19 and September 9 show clear and consistent resistivity decreases in the region near boreholes 18, 20, and 21 that can be associated with the injection of conductive water. This effect appears to be stronger on September 9 in the 5.33 m slice. The images show very little effect in the region around the other injection boreholes, 23 and 24 through 27, where far less water was injected.

In addition, the difference images from August 19 and September 9 show resistivity decreases that could be interpreted as water moving down into the block between the 1.33 m and 4.0 m slices. This is the same region that has an anomalously low resistivity in the baseline image.

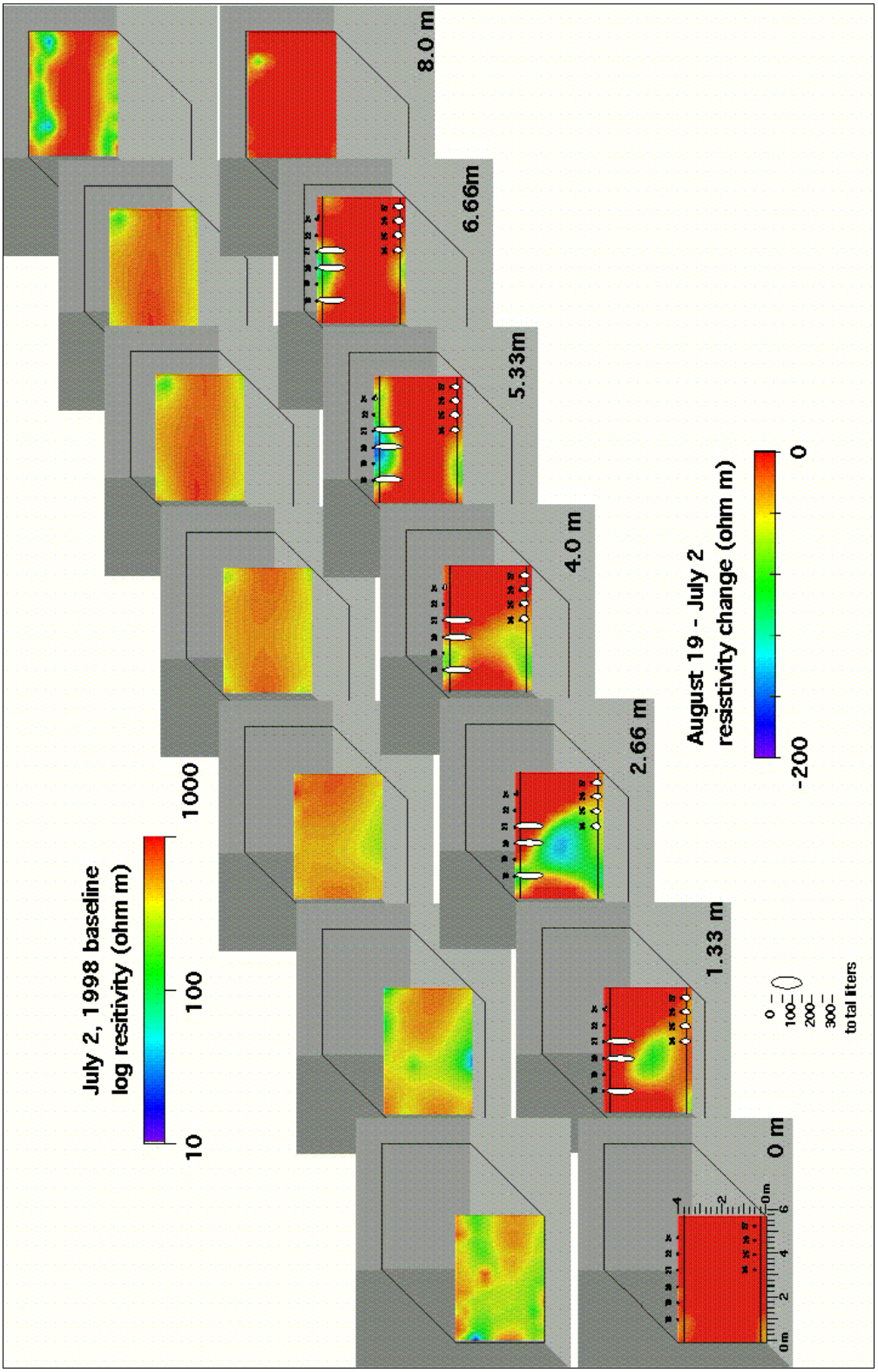

DTN: LL990612704244.098 [147168]

Source: CRWMS M&O 2000 [154024], Figure 55

NOTE: The diagram shows vertical slices through block at 0, 1.33, 2.66, 4.0, 5.33, 6.66, and 8.0 m. The top series is an absolute image (baseline, July 2), and the bottom series is the August 19–July 2 difference images.

Figure 6.13.4-7. ERT Images of the Test Block Viewed from Test Alcove: Baseline and August Differences

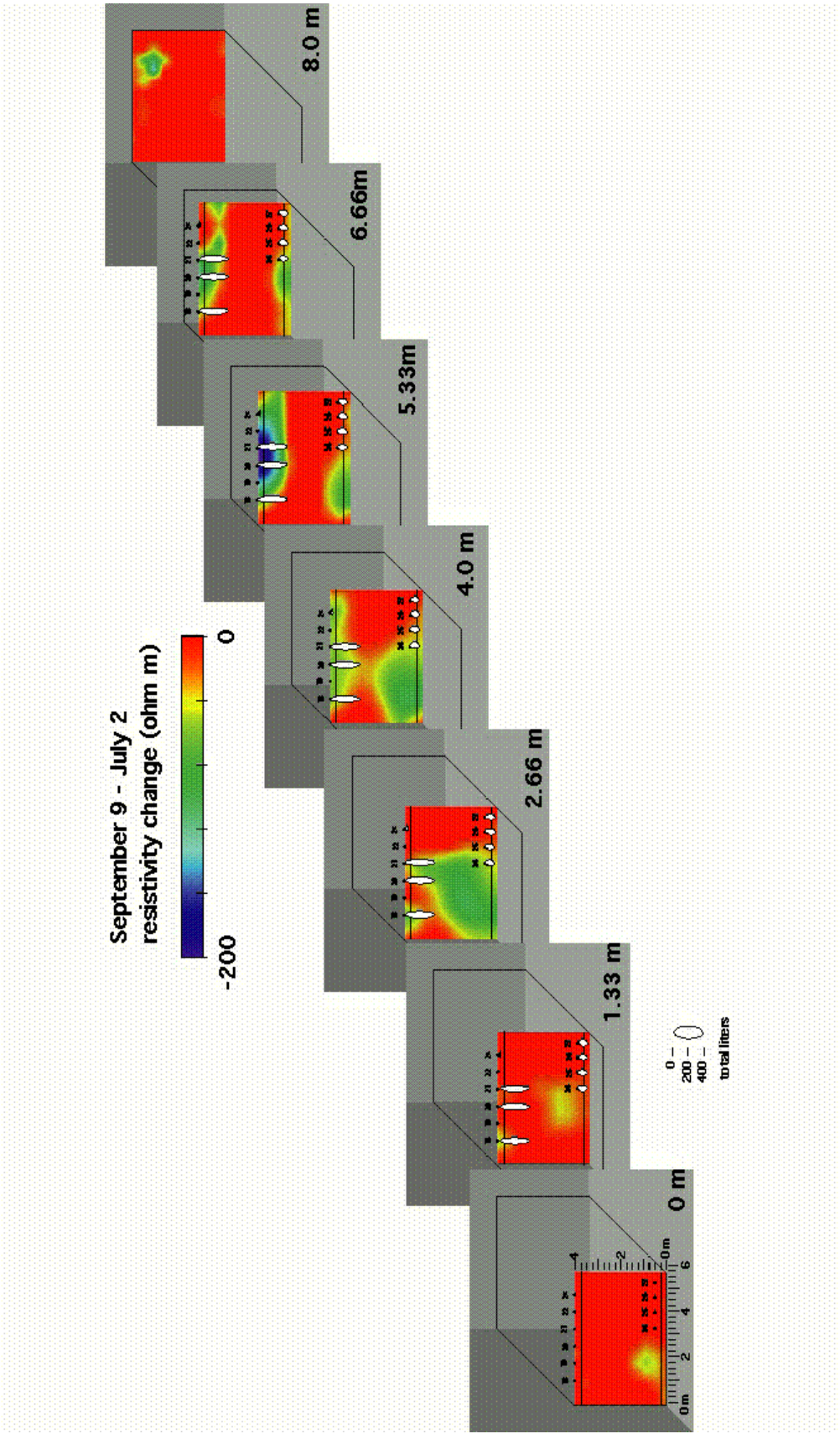

DTN: LL990612704244.098 [147168]

Source: CRWMS M&O 2000 [154024], Figure 56
NOTE: The diagram shows vertical slices through the block at 0, 1.33, 2.66, 4.0, 5.33, 6.66, and 8.0 m that represent September 9–July 2 difference images.

Figure 6.13.4-8. ERT Images of the Test Block Viewed from Test Alcove: September Differences

6.13.5 Neutron Moisture Measurements

Neutron probes were used to sample the moisture content in the UZTT test block using collection boreholes as sampling locations. Neutron moisture data was collected using the CPN 503DR Hydroprobe™ Moisture Depth Gauge (Lowry 2001 [164632]). This instrument has two major components. One is a source of fast neutrons. The other is a detector that counts slow neutrons. Neutron measurements were taken by inserting the probe into each selected borehole and taking readings at 10 cm intervals. At each position, the probe was held fixed for the required interval of time and recorded the number of slow neutrons that the probe detected.

6.13.5.1 Neutron Logging Background and Calibration

Collisions with hydrogen atoms are much more effective at reducing the speed of neutrons than are collisions with other atoms. It takes about 18 collisions with hydrogen atoms to slow a neutron sufficiently that it will react with the detector. A neutron would need at least two hundred collisions with other atoms to have the same effect. A material that contains many water molecules, which have two hydrogen atoms, is more efficient at slowing neutrons than the same material with less moisture content.

The emitted neutrons scatter through the neighboring ground material. Those that slow sufficiently and return to the detector will have followed various paths and traveled various distances from the source. The radius of measurement is that distance beyond which only 2% of the counted neutrons will have strayed; this radius is a function of the moisture content and the density.

Instrument calibration is necessary because other atoms, including the hydrogen atoms in rock compounds, will also slow neutrons. Twelve test cells with known density and water content were constructed to calibrate the neutron logging systems. Measurements taken on the test cells established calibration curves for use in converting neutron counts to moisture content. Spreadsheets document the recorded counts and the resulting values of water content (Lowry 2001 [164632]). Note, however, that if the composition of the rock varies from that used for calibration, the calibration curve may be in error at some locations in the borehole.

Most of the readings taken at the Busted Butte site measured moisture contents between 10% to 25% moisture by volume. The distance between measurements is about one-half of the distance sampled by a measurement. There is substantial overlap between the regions covered by the measurements. Each sampled region overlaps somewhat with three adjacent regions on each side. This reduces measurement error.

Both the emission of neutrons and their collisions with atoms are random processes. The uncertainty in the final count is approximately the square root of the number of measured counts. Most of the neutron measurements resulted in counts between 4,000 and 9,000. The uncertainty in counts results in a measurement error of 1.0% to 1.6%. The contribution of this uncertainty to the uncertainty in moisture content is 1.4 to 2.4 kg/m^3 (0.14% to 0.24% by volume).

6.13.5.2 Pre-injection Neutron Logging

Figure 6.13.5-1 shows the neutron moisture data taken in borehole #16 before Phase 2 injection began. Notice that the moisture content decreases near the opening of the borehole due to evaporation at the face. This discussion does not consider measurements taken within 1 meter of the face because of edge effects.

Moisture content (MC) down borehole #16 may be visually grouped into four distinct regions. A region about 1.5 meters thick next to the main adit face has a moisture content of about 9% by volume (90 kilograms per cubic meter). Next is a 2.3 m region of increasing MC, followed by a 1-meter region with a MC of 16.5% (165 kg/m^3). The last four meters of the borehole are in rock with a measured MC of 13.5% (135 kg/m^3). Within each region, fluctuations in MC are consistent with the measurement uncertainty of about 0.2% by volume (two kilograms per cubic meter). The initial MC in the lower region, as reflected in borehole #46 and shown in Figure 6.13.5-3, has much less variation with position than in the upper region.

Even before moisture injection began, the variations in measured MC from region to region in the rock are significantly larger than would be expected as a result of measurement error, Thus, we believe these variations are real, caused by variation in the retentive capacity of the rock.

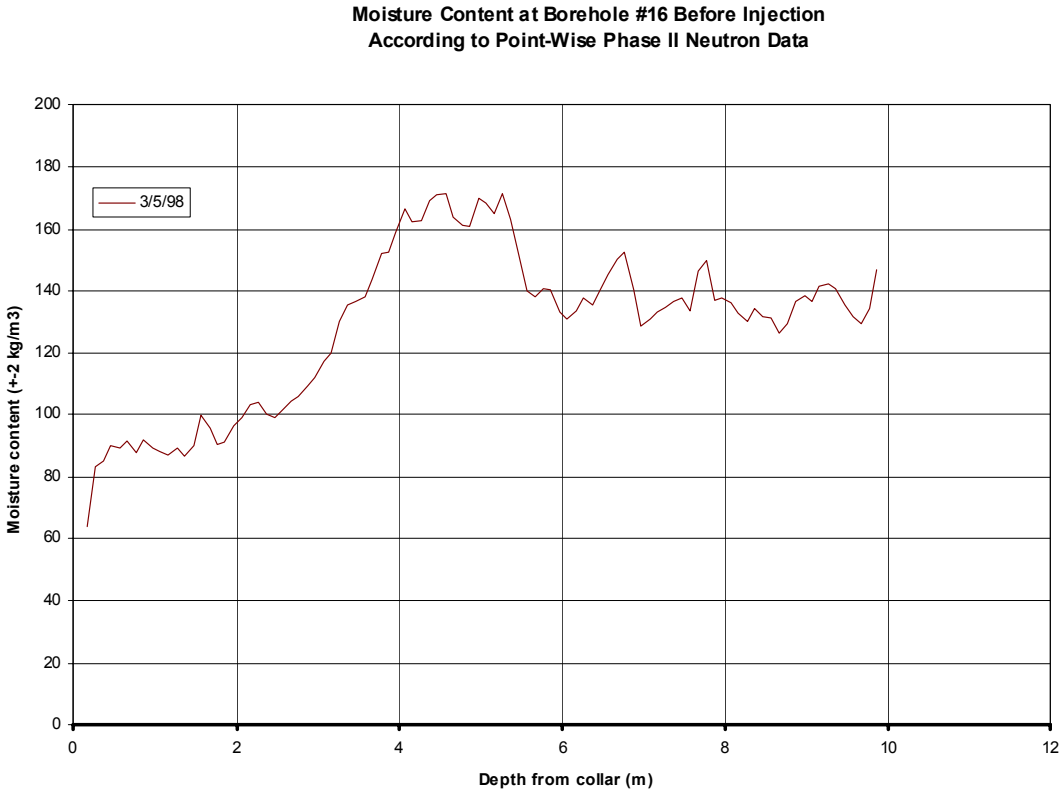

DTN: LA0201WS831372.004 [165422]

Figure 6.13.5-1. Initial Measurements of Moisture Content at Borehole #16 (before smoothing)

Figure 6.13.5-2 shows additional evidence of heterogeneity of hydraulic properties down the length of the borehole. The figure compares the neutron moisture data with the air permeability measurements obtained for borehole #16. These two sets of measurements together suggest the groupings shown in Figure 6.13.5-2.

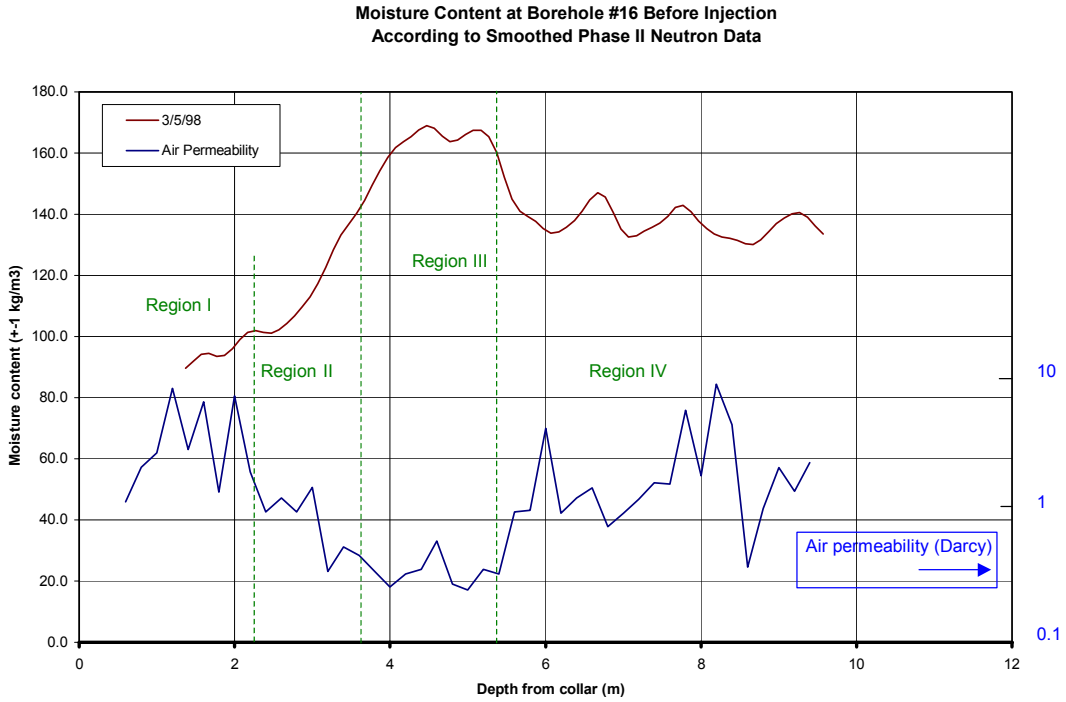

DTNs: LA0311SD831372.001 [166197]; LA0201WS831372.004 [165422]

NOTE: Darcy is a unit of intrinsic permeability where 1 darcy = 9.87×10^{-9} cm^2 (Fetter 2001 [156668], pp. 96-97).

Figure 6.13.5-2. Moisture Content at Borehole #16 before Injection Compared with Air Permeability

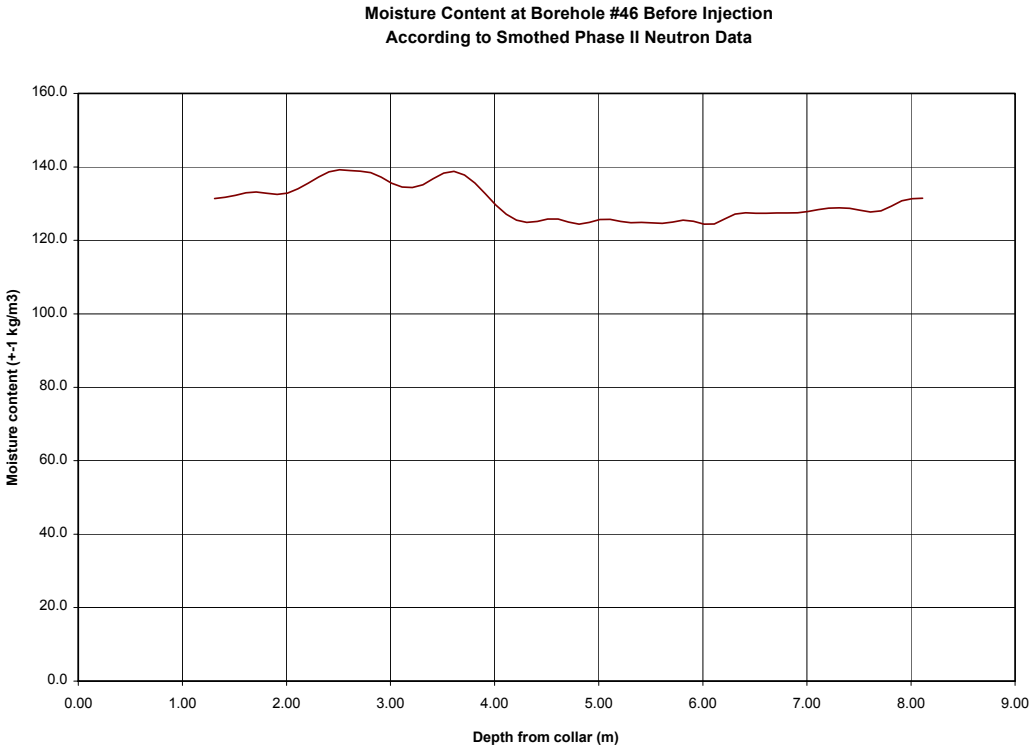

DTN: LA0201WS831372.004 [165422]

Figure 6.13.5-3. Moisture Content at Borehole #46 before Injection

6.13.5.3 After Beginning Injection

By subtracting the original measurements from later measurements, one may see the changes in the rock caused by the injected water. This section presents both spatial and temporal changes in moisture content in the Phase 2 block. Although the amount of hydrogen in the solid rock affects the absolute measurement, taking the difference in measurements cancels any systematic errors. In the example, the amount of uncertainty in the difference is 0.13% (1.3 kg/m^3). Because there are other sources of uncertainty (such as the calibration procedure), 0.2% (2 kg/m^3) is a reasonable estimate of the total measurement uncertainty for the change in moisture content.

Figure 6.13.5-4 shows the changes in moisture content at borehole #16 for each of the days that the measurements were taken. Also shown are the locations of the four upper-region injection boreholes. Each of these injection boreholes was perpendicular to borehole #16. The red circles represent the positions of these boreholes at their closest approach to borehole #16. According to the average flow rates (see Figure 6.13.5-4), borehole #23 provided less than 1% of the total moisture.

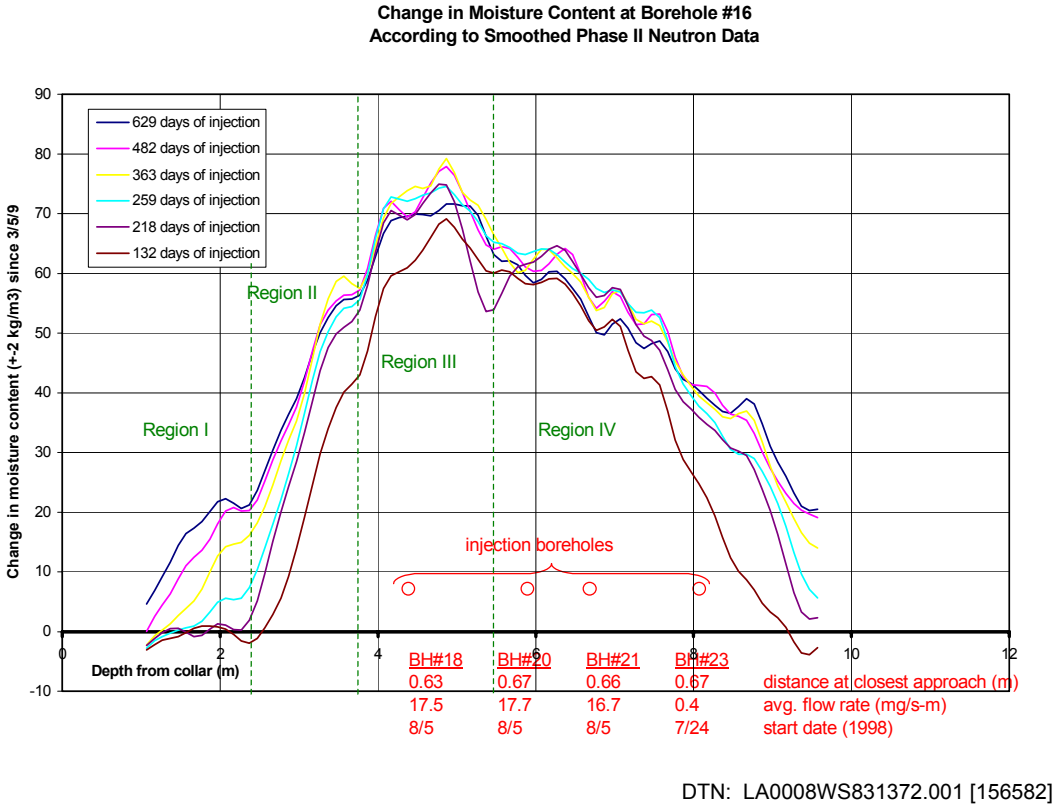

Figure 6.13.5-4. Moisture Increase at Borehole #16 at Various Times

For the lower region, Figure 6.13.5-5 displays the changes in moisture content at borehole #46 for each of the days that measurements were taken. Also shown are the locations of the four lower-region injection boreholes.

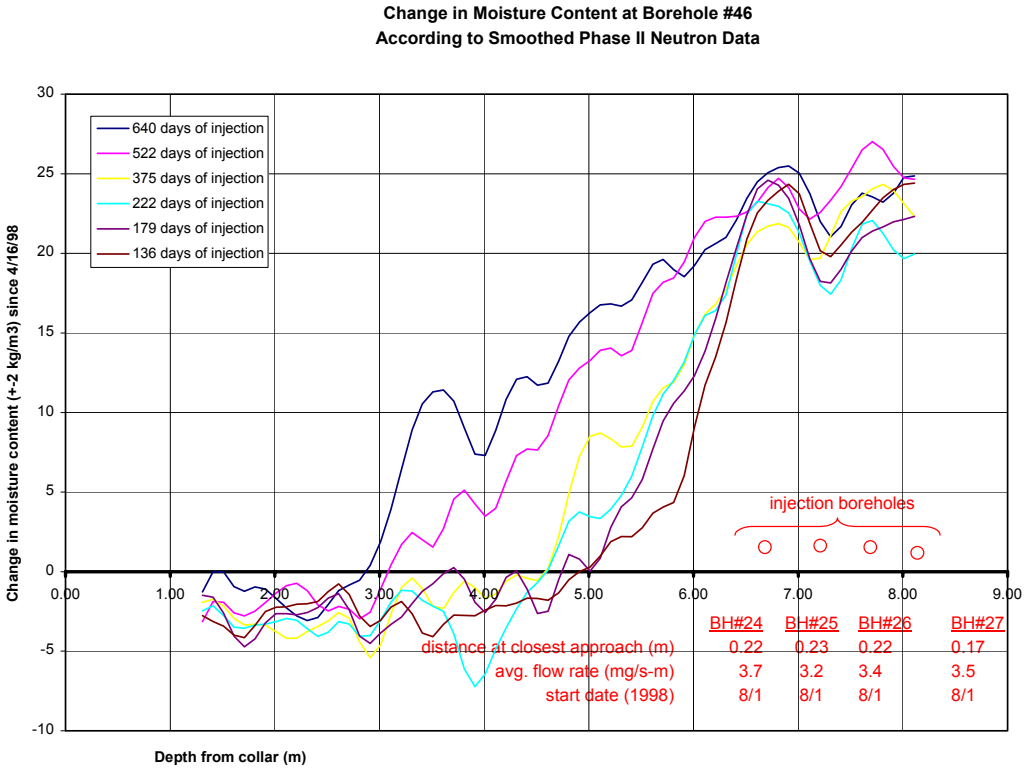

DTN: LA0008WS831372.001 [156582]

Figure 6.13.5-5. Moisture Increase at Borehole #46 at Various Times

6.13.6 Summary of Laboratory Radionuclide Migration Experiments

Migration experiments under unsaturated conditions have been conducted at the Atomic Energy of Canada Limited's Whiteshell Laboratories in Pinawa, Manitoba, on blocks excavated from the Busted Butte Test Facility. The following summary is based on an abstracts by Vandergraaf et al. (2002 [165133]) and a report by Vandergraaf et al. (2003 [165099]). The migration experiments were conducted with radionuclides to collaborate and compare with field experiments that use nonradioactive chemical analogs for tracers to evaluate flow and transport through nonwelded tuff.

The duration of the migration experiment on a trial block of nominally one cubic foot (~0.3 m × 0.3 m × 0.3 m) was 87 days. After a vertical flow of synthetic Busted Butte pore water as transport solution was set up under unsaturated conditions, a suite of conservative and chemically reactive radionuclide tracers was injected at volumetric flow rates of 20 mL/hr. Na-fluorescein dye, ^{3}H (as tritiated water), ^{22}Na, ^{60}Co, $^{95m+99}Tc$ (as the pertechnetate anion), ^{137}Cs, and ^{237}Np were used as tracers. Results showed that transport of $^{95m+99}Tc$ was slightly faster than that of the transport solution, using tritiated water ($^{3}H_2O$) as a flow indicator. The finding of Tc and dye tracer eluted ahead of triatiated water has been attributed to an anion exclusion effect. Retardation of ^{237}Np was consistent with that predicted from results obtained in supporting static-batch-sorption studies. Post-migration analysis of the flow field in the trial block showed that the front of the ^{22}Na had migrated approximately half the distance through the block and that ^{60}Co and ^{137}Cs had been retained near the inlet. This agrees qualitatively with that predicted from the results from static-batch-sorption studies.

The duration of the migration experiment on a nominally one cubic meter (~1 m × 1 m × 1 m) was over 700 days, initiated in April 2001. The tracer solution was injected continuously at two locations at the top of the block, at a flow rate of 10mL/h per injection point (20 mL/h with both injections). By June 2002, the normalized concentrations of ^{3}H, ^{99}Tc, and dye tracer in the water collected from the bottom of the block had reached a value of ~0.08. The transport behavior of Tc is very similar to that of the transport solution. None of the other tracers has been observed in the eluent from the larger block. This is consistent with the observations from the smaller block.

The static batch sorption coefficients and retardation coefficients of Tc and Np are available in TDMS: DTN: LA0108TV12213U.001 [161525]. The submittals of migration data are in progress.

6.14 GEOCHEMICAL AND ISOTOPIC OBSERVATIONS AND ANALYSIS OF THE UNSATURATED ZONE

A series of geochemical examinations have been performed using rock, mineral, and water samples collected from both the ESF and ECRB. These studies provide evidence of a long-term hydrological regime in the Yucca Mountain. The following sections will examine:

- Pore water and rock geochemistry (6.14.1)
- Isotope geochemical studies to examine evidence of fast-flow pathways for water infiltration and seepage into the drift, as well as a historical thermal regime (6.14.2)
- The application of uranium isotope ratios to indicate past climate conditions and examine infiltration flow paths in the unsaturated zone (UZ) (6.14.3)
- Determinations of mineralogy in fractures as evidence of water flow and mineral deposition (6.14.4).

The evidence and analysis provided in the following sections offer critical information on mineral formation and deposition, as well as indicating potential flow rates and pathways for water through the UZ.

6.14.1 Pore Water and Rock Geochemistry

6.14.1.1 Analysis and Interpretation of Pore-Water Data

Pore water in the welded Tiva Canyon tuff (TCw), the bedded tuff of the Paintbrush nonwelded (PTn), and the underlying welded Topopah Spring Tuff (TSw) is a calcium-chloride or calcium-sulfate type (Yang et al. 1996 [100194], pp. 13 and 55; Yang et al. 1998 [101441], p. 53; Yang et al 2003 [164631]; Peterman and Marshall 2002 [162992], p. 308). A major compositional change occurs in pore-water composition in the zeolitized Calico Hills nonwelded unit (CHn). Here, the pore water rapidly evolves to a sodium-bicarbonate type in which the relative abundances of alkalies (Na and K) and alkaline earths (Ca and Mg) reflect different degrees of ion exchange with zeolitized tuff (Yang et al. 2003 [164631]). The ion exchange process is clearly reflected in the alkaline earth and alkali contents of the zeolitized rocks (Vaniman et al. 2001 [157427]). The downward chemical evolution is shown clearly by analyses of pore water from USW SD-6 (Yang et al. 2003 [164631]) and by analyses of pore water extracted from core of the Topopah Spring welded (TSw) in the ECRB Cross Drift (Peterman and Marshall 2002 [162992], p. 308). The chemical changes from the TCw, PTn, and TSw, into the CHn include decreases in Ca, Mg, SO_4, and NO_3, and increases in HCO_3, Na, and K. The decrease in NO_3 and increase in HCO_3 are suggestive of microbially mediated denitrification and concomitant production of organic HCO_3. Most of the denitrification occurs in the TSw where NO_3 decreases by as much as three orders of magnitude relative to mean values in the PTn. Similarly, the decrease in SO_4 can be explained by microbially induced sulfate reduction. The processes of denitrification and sulfate reduction

processes would imply the presence of bacterially controlled reducing microenvironments at the pore-scale in the otherwise oxidizing environment of the Yucca Mountain UZ.

Early extractions of pore water were limited to compression of nonwelded or zeolitized units such as those of the PTn or the CHn (Calico Hills nonwelded). The analyses of these pore waters (Yang et al. 1996 [100194]; 1998 [101441]) are summarized in the Yucca Mountain Site Description (CRWMS M&O 2000 [151945], Table 5.3-4). Pore water data are also summarized in DTN: LA0002JF12213U.001 [154760] (surface-based boreholes), DTN: LA0002JF122123U.002 [156281] (underground drifts), DTN: LAJF831222AQ98.011 [145402] (waters), and DTN: LA9909JF831222.012 [122736] (Niche 3566 [Niche 1] and Niche 3650 [Niche 2]).

More recently, extractions being made by ultracentrifugation emphasize pore water from the welded Topopah Spring tuff (TSw), in which emplacement drifts of the repository will be constructed (Yang et al. 2003 [164631]; Peterman and Marshall 2002 [162992]). The most recent analyses of pore water from this unit are summarized as means and statistical parameters in Table 6.14.1-1. Normalcy tests for the cations and anions indicate that only Na, Mg, SiO_2, and perhaps Rb are close to being normally distributed. As more data are accumulated, distributions other than normal will be evaluated in determining the key statistics of the samples. For example, Cl appears to be lognormally distributed and the lognormal average is 38 mg/L, in comparison with the straight arithmetic average of 46 mg/L.

Table 6.14.1-1. Summary of the Most Recent Analyses of Pore Water from Topopah Spring Tuff (TSw), Means and Statistical Parameters

		ECRB and ESF (Alcove 7)					
n=29	**Units**	**Mean**	**Stdev**	**SE mean**	**Min**	**Max**	**n**
pH	--	7.5	0.4	0.1	6.7	8.2	24
SC	ms/cm	867	262	53	520	1490	24
Ca	mg/L	122	57	11	55	240	28
Mg	mg/L	16.8	9.6	1.8	3.3	44.2	28
Na	mg/L	88.3	27.3	5.2	39.0	140.0	28
K	mg/L	10.5	4.0	0.7	5.9	24.8	28
HCO_3 Calc	mg/L	559	215	41	287	1116	28
Cl	mg/L	35.8	19.8	3.7	17.0	97.0	28
SO_4	mg/L	56.8	34.7	6.6	13.0	147.0	28
NO_3	mg/L	6.0	7.7	1.5	0.0	25.0	27
F	mg/L	3.0	2.3	0.4	0.7	11.0	28
SiO_2	mg/L	51.8	7.2	1.4	40.0	70.0	28
Mn	mg/L	122	124	23	14	470	28
Rb	mg/L	21.8	9.3	1.8	9.3	51.2	28
Sr	mg/L	1539	909	172	480	4090	28
As	mg/L	7.2	2.9	0.7	3.4	15.0	17
Mo	mg/L	14.7	13.1	2.5	3.4	67.0	28
Ba	mg/L	97.1	117.1	35.3	23.0	420.0	11
U	mg/L	8.1	8.3	1.6	0.1	28.7	26

DTN: GS020408312272.003 [160899]; DTN: GS030408312272.002 [165226]

In addition to the downward compositional evolution, the dissolved ion composition of pore water from within hydrostratigraphic units shows considerable stratigraphic and lateral variability (Table 6.14.1-1). Coefficients of variation for the major cations and anions range from 13.4% for SiO_2 to 134% for NO_3 with most of the values between 35 and 67%. The existence of this compositional variability deep in the rock mass at the repository level, testifies to the inefficiency of advective or diffusional mixing in the downward percolation of pore water.

The strontium isotopic composition of pore water and pore water salts is summarized by Marshall and Futa (2003 [162717]). Pore water salts from the relatively shallow core samples of three drill holes have $^{87}Sr/^{86}Sr$ ratios between 0.7117 and 0.7124, which are consistent with values for soil carbonates (0.7113–0.7127) at Yucca Mountain. The variability in $^{87}Sr/^{86}Sr$ decreases with increasing depth, with salts from 35 core samples from TSw having $^{87}Sr/^{86}Sr$ values between 0.7122 and 0.7127. This range is consistent with seven samples of pore water extracted from core taken along the ECRB Cross Drift and yielding values of 0.7121 to 0.7127. The decrease in variability of pore-water $^{87}Sr/^{86}Sr$ ratios from the TCw to the TSw indicates that percolation through the PTn matrix is sufficiently slow to allow pore water to partially acquire a strontium isotope signature through water/rock interaction.

Yang et al. (1998 [164631], pp. 34–44) evaluated various water-extraction methods to determine which would be most suitable for stable isotope measurements of hydrologically active pore water. They concluded that vacuum distillation was suitable for densely welded tuffs or tuffs with little or no secondary alteration. However, vacuum distillation was not suitable for altered tuff in which the secondary minerals had fractionated oxygen isotopes, and water extracted from these rocks was relatively depleted in ^{2}H, with ^{18}O typically plotting to the left of the global meteoric water line.

The most comprehensive suite of $\delta^{2}H$ and $\delta^{18}O$ analyses is for pore water extracted from USW UZ-14 dry-drilled core samples (Yang et al. 1998 [164631], Figures 15 and 16) by both compression and by vacuum distillation. These data show that water extracted from the lower part of the Topopah Spring tuff is significantly depleted in ^{2}H and ^{18}O relative to water in the middle and upper part of the unit. The lower part of the Topopah Spring tuff in UZ-14 contains zeolite and clays, which probably explain the spurious stable isotope compositions. Despite these excursions, there appear to be real isotopic variations in pore water through the rock column. Considering the stable isotope compositions of water compressed from the PTn and from the CHn in UZ-14 (Yang et al. 1998 [164631], Figures 15 and 16), mean $\delta^{2}H$ and $\delta^{18}O$ values are -90.3 ± 2.6‰ and -12.3 ± 0.4‰ for the PTn (9 values); and -101.1 ± 1.5‰ and -13.3 ± 0.3‰ for the CHn (14 values), respectively. Most of the isotopic values for pore water distilled from the intervening TSw form a curvilinear continuum between the PTn and CHn values. The mean isotopic composition of pore water from the PTn is well within the range of values for snow collected at Yucca Mountain, which Benson and Klieforth (1989 [104370], p. 51) considered to be the likely source of recharge. The mean $\delta^{2}H$ and $\delta^{18}O$ values for the CHn are similar to mean values for Yucca Mountain saturated zone water of -101.1 ± 1.5‰ and -13.3 ± 0.3‰, respectively, based on analyses reported in Benson and Klieforth (1989 [104370], Table 1a).

Benson and Klieforth (1989 [104370], p. 50) calculated a best-fit line to the stable isotope compositions of snow at Yucca Mountain, and the following equation is considered to be a local meteoric water line for Yucca Mountain:

$$\delta^2H = 8.0*\delta^{18}O + 8.9$$

Pore water samples from the PTn and the TSw (excluding obvious outliers) have a mean deuterium excess of 8.3 ± 0.3‰ (uncertainty is standard error of the mean), with a median value of 8.1. Thus, the departure of the pore-water isotopic compositions from the local meteoric water line with a deuterium excess value of 8.9 is small, indicating that the effects of evaporation during infiltration were small. In contrast, the mean deuterium excess value for the CHn pore waters of 5.4 ± 0.5‰ and median of 5.9 is distinct from the local meteoric water line of Benson and Klieforth (1989 [104370], p. 50), and all of the individual values plot to the right of the line. Given the range of transport velocity of 0.8 to 3.2 cm/year calculated by Yang (2002 [160839], p. 814), the pore water in the Calico Hills and older tuffs in UZ-14 could be several tens of thousands of years old. Such old ages would be consistent with uncorrected radiocarbon ages for groundwater immediately beneath Yucca Mountain, which range from 12 ka to 18 ka (Benson and Klieforth 1989 [104370], Table 1a).

6.14.1.2 Compilation of Rock Chemistry in the Cross Drift

At the request of the YMP Waste Package Department, the U.S. Geological Survey conducted geochemical analyses of samples from various zones of the crystal-poor member of the Topopah Spring Tuff intersected by the Cross Drift. The chemical analyses were published by Peterman and Cloke (2002 [162576], pp. 683–698) and are in the TDMS (DTN: GS000308313211.001 [162015]). To represent the relevant lithostratigraphic zones, 20 samples were selected from existing holes cored to 2 m depth and located on 50 m centers throughout the Cross Drift. These drill holes are designated ECRB-SYS-CS (distance) where (distance) records the location of the drill holes in meters from a survey control point near the intersection of the Cross Drift and the ESF. Samples for analyses were selected at locations from station 10+00 to station 25+00 to represent the middle nonlithophysal zone, the lower lithophysal zone, and the lower nonlithophysal zone of the Topopah Spring Tuff. The core samples used for chemical analyses had been encapsulated in cans at the time of drilling to retain moisture. Core displaying vapor-phase minerals or calcite and opal were avoided in sampling.

Core samples are considered to be a reasonable size/volume representative of a larger portion of the sampled rock mass. The size of samples is commonly dictated by the grain size of the rock being sampled. A coarse-grained granite may require a few kilograms of samples, whereas a fine-grained volcanic rock, such as the crystal-poor Topopah Spring rhyolite, may be represented by samples of much smaller mass. For rock units with sparsely distributed heterogeneities, such as mineralized lithophysal cavities in certain zones of the Topopah Spring Tuff, direct sampling may be impractical for capturing these features in determining the large-scale chemical composition.

Core samples were removed from the cans and air dried overnight under a heat lamp. Each core was broken with a hammer on a steel anvil and crushed in a laboratory jaw crusher to fragments

of about 1 cm or smaller. The crushed material (typically 200 to 500 grams) was weighed, mixed by rolling on paper, split by cone, and quartered to yield a subsample of approximately 100 grams. The 100 gram subsample was then puliverized in a hardened steel mill for 2 minutes to yield a 200 mesh powder. Aliquots of the powder were taken for duplicate chemical analyses.

Previous analyses indicated limited chemical variability of the crystal-poor zone of the Topopah Spring Tuff (Lipman et al. 1966 [100773]; Broxton et al. 1989 [100024]; Flood et al. 1989 [164636]; Schuraytz et al. 1989 [107248]). Accordingly, duplicate analyses of each sample were used to assess analytical reproducibility and to compare with intersample variability (see Youden 1951 [153339]). Accuracy was assessed by five analyses, with each of two USGS reference materials (GSP-2 and RGM-1) submitted as blind standards interspersed with the samples. Results for the standards are given in Peterman and Cloke (2002 [162576], Tables 2 and 3).

The means, ranges, standard deviations, and standard errors (SDOM) for major and selected trace elements for the 20 analyses of crystal-poor rhyolite from the Cross Drift are given in Table 6.14.1-2. A more comprehensive suite of trace elements analyzed by inductively coupled plasma mass spectrometry are given in Table 6.14.1-3 from Peterman and Cloke (2001 [155696]). Mean normative mineral contents are given in Table 6.14.1-4. These tabulations show that the variability of the crystal-poor rhyolite in major and trace element contents is exceedingly small. The intersample variability of the 20 samples was compared with the analytical variability based on the duplicate analyses (Peterman and Cloke 2002 [162576], p. 692) using the Fisher (F) test (Youden 1951 [153339]) (Attachment IX.5). The intersample variability of SiO_2 and TiO_2 is commensurate solely with the estimated analytical uncertainty, based on duplicate samples. The other major oxides (Table 6.14.1-2) show greater variability, with CaO exhibiting an F value of 25.9 (intersample variance/analytical variance) versus the critical F value of 1.84 at the 0.05 significance level. The mean CaO concentration is 0.50% with a standard deviation of 0.03, whereas the standard deviation of the duplicates is only 0.005.

Table 6.14.1-2. Mean Composition of the Phenocryst-Poor Member of the Topopah Spring Tuff in the Cross Drift

Oxide or Element	Mean	σ_x	SDOM	Min	Max
	Major elements and oxides, in weight percent				
SiO_2	76.29	0.318	0.101	76.09	76.49
Al_2O_3	12.55	0.142	0.045	12.46	12.64
FeO	0.13	0.047	0.015	0.10	0.16
Fe_2O_3	0.97	0.070	0.022	0.93	1.01
MgO	0.12	0.020	0.006	0.11	0.13
CaO	0.50	0.027	0.008	0.48	0.52
Na_2O	3.52	0.109	0.035	3.45	3.59
K_2O	4.83	0.062	0.020	4.79	4.87
TiO_2	0.109	0.004	0.001	0.107	0.111
ZrO_2	0.016	0.001	0.000	0.015	0.017
P_2O_5	<0.05	---	---	---	---
MnO	0.068	0.008	0.002	0.063	0.073
Cl	0.017	0.004	0.001	0.014	0.020
F	0.038	0.008	0.003	0.033	0.043
S	<0.05	---	---	---	---
CO_2	0.011	0.003	0.001	0.009	0.01
H_2O-	0.24	0.072	0.023	0.19	0.29
H_2O+	0.40	0.090	0.029	0.34	0.46
SUM	99.81				
	Trace elements, in micrograms per gram				
Rb	188	5.3	1.7	185	191
Sr	25	3.4	1.1	23	27
Y	32	2.9	0.9	30	34
Zr	116	3.8	1.2	114	118
Nb	25	1.1	0.3	24	26
Ba	55	6.8	2.1	51	59
La	51	5.5	1.7	48	54
Ce	84	5.1	1.6	81	87

DTN: GS000308313211.001 [162015], see Attachment IX for calculations

NOTE: σ_x is standard deviation, SDOM is standard deviation of the mean, and Min and Max are the mean values plus and minus 2 times SDOM for each element.

Normative mineral compositions were calculated from the means of each pair of duplicate analyses (Table 6.14.1-4). The abundances of normative quartz and feldspars (orthoclase, albite, and anorthite) range from 95 to 97% of the total rock and closely approximate the abundances of silica polymorphs and feldspars actually in the rock (Bish and Vaniman 1985 [101196]).

Table 6.14.1-3. Mean Trace Element Concentrations of the Phenocryst-Poor Member of the Topopah Spring Tuff in the Cross Drift

Element	Mean	σ_x	SDOM	Min	Max
	Micrograms per gram (parts per million)				
Ag	<1	---	---	---	---
As	5.4	1.9	0.60	4.1	6.6
Ba	51.3	12.1	3.83	43.7	59.0
Be	3.4	0.1	0.03	3.4	3.5
Bi	0.06	0.03	0.01	0.04	0.08
Cd	0.07	0.03	0.01	0.05	0.09
Ce	70.8	5.84	1.85	67.1	74.5
Co	0.23	0.05	0.02	0.19	0.26
Cr	8.7	2.9	0.92	6.9	10.6
Cs	4.2	0.3	0.09	4.0	4.4
Cu	13.7	---	---	---	---
Ga	15.6	0.50	0.16	15.3	16.0
La	34.2	3.31	1.05	32.1	36.3
Li	25.1	8.9	2.82	19.4	30.7
Mo	2.21	0.95	0.30	1.61	2.82
Nb	20.6	1.4	0.45	19.7	21.5
Ni	1.4	0.3	0.11	1.2	1.6
Pb	27.2	1.1	0.36	26.5	27.9
Rb	185.6	8.8	2.78	180.0	191.1
Sb	0.33	0.06	0.02	0.29	0.37
Sc	2.45	0.10	0.03	2.39	2.51
Sr	27.1	3.3	1.06	25.0	29.2
Th	26.0	1.4	0.45	25.1	26.9
Tl	1.10	0.21	0.07	1.0	1.2
U	3.92	0.30	0.10	3.73	4.11
V	1.3	0.6	0.20	0.9	1.7
Y	30.1	3.06	0.97	28.2	32.1
Zn	35.9	4.3	1.35	33.2	38.6

DTN: GS000308313211.001 [162015]; see Attachment IX for calculations

NOTES: See Table 6.14.1-2 for explanation of columns

Table 6.14.1-4. Mean Normative Mineral Contents of the Phenocryst-Poor Rhyolite Member of the Topopah Spring Tuff in the Cross Drift

Normative Minerals	Mean	σ_x	SDOM	Min	Max
			Weight Percent		
Q (quartz)	36.41	0.899	0.201	36.01	36.81
or (orthoclase)	28.55	0.375	0.084	28.38	28.71
ab (albite)	29.65	0.930	0.208	29.24	30.07
an (anorthite)	1.92	0.138	0.031	1.85	1.98
C (corundum)	0.85	0.133	0.030	0.79	0.91
hy (hypersthene)	0.30	0.052	0.012	0.27	0.32
mt (magnetite)	0.19	0.171	0.038	0.11	0.26
il (ilmenite)	0.18	0.031	0.007	0.16	0.19
hem (hematite)	0.89	0.132	0.029	0.84	0.95
ap (apatite)	0.12	0.000	0.000	0.12	0.12
hl (halite)	0.03	0.007	0.002	0.02	0.03
zr (zircon)	0.03	0.000	0.000	0.03	0.03
fl (fluorite)	0.07	0.018	0.004	0.06	0.08
pr (pyrite)	0.09	0.000	0.000	0.09	0.09
ru (rutile)	0.04	0.017	0.004	0.03	0.04

DTN: GS000308313211.001 [162015], see Attachment IX for calculations

NOTE: See Table 6.14.1-2 for explanation of columns

Statistical analyses of major and trace element compositions indicate that the 200 to 500 gram core samples selected for analyses are representative of the crystal-poor Topopah Spring rhyolite (Table 6.14.1-2). However, no attempt was made in this approach to capture the compositional influence of localized deposits of vapor-phase minerals and low-temperature calcite and opal. Obviously, random sampling of the unit at the 200-to-500 gram scale would produce a number of samples with compositions within the range of those reported here (Table 6.14.1-2) and a few samples with widely divergent composition. Further, large numbers of samples would be required to capture this compositional variability solely by random sampling. Alternatively, large multi-ton bulk samples would have captured these features at the zonal scale, but would have to have been taken during construction of the tunnel. Neither of these approaches was feasible, but information on the amount of calcite present in the crystal-poor Topopah Spring tuff was used to assess the compositional effects of considering these heterogeneities in estimating the zonal compositions (Peterman and Cloke 2002 [162576], pp. 695–696). Using detailed analyses of CO_2 and calculated normative calcite abundances of cuttings from WT-24 (DTN: GS020608315215.002 [162126] and DTN: GS021008315215.007 [162127]), Peterman and Cloke (2002 [162576], p. 696) noted that the mean values of CaO and CO_2 determined from the rock analyses would only have to be increased slightly to incorporate the effects of calcite in cavities and fractures at the zonal scale. Similarly, the effect of opal ($SiO_2 \cdot nH_2O$) on the zonal compositions would be trivial. Further, Peterman and Cloke (2002 [162576], p. 696) argued that incorporation of vapor phase minerals in the estimate of zonal compositions would be negligible because the process of vapor-phase corrosion and deposition could be approximated as a closed system at the zonal scale.

6.14.2 Isoptope Geochemistry Examinations

Isotope geochemistry has been used to provide information about the "fast path" signals (Section 6.14.2.1 on $^{36}Cl/Cl$ ratios and Section 6.14.2.2 on tritium data) and about the inferred thermal history of Yucca Mountain (Section 6.14.2.3 on fluid inclusion data). Early results of geochemical and isotope studies were reported in the AMR *Analysis of Geochemical Data for the Unsaturated Zone (U0085)* (BSC 2002 [160247]).

The data submitted to the TDMS from the ^{36}Cl Validation Study (VS) are summarized in the following two subsections. The report on *Chlorine-36 Validation Studies at Yucca Mountain, Nevada* (BSC 2003 [166104]) is not finalized. This is a deviation from the UZ TWP (BSC 2002 [160819]) listed in Section 1.4. The description of analysis and interpretation by Paces et al. (2003 [162738]), together with ongoing development of alternative interpretations, are summarized.

6.14.2.1 Chlorine-36 Validation Studies

Elevated $^{36}Cl/Cl$ ratios have been reported from Yucca Mountain at the depth of the repository horizon during the late 1990s (Fabryka-Martin et al. 1996 [144839]; 1997 [100145]; 1998 [162737]).The $^{36}Cl/Cl$ values above $1{,}250 \times 10^{-15}$ (the upper limit for Pleistocene meteoric input) were attributed to atmospheric nuclear testing in the Pacific Ocean and interpreted as an indication that at least some meteoric water is capable of percolating rapidly through the UZ to depths of 300 m below the surface in the last 50 years (Fabryka-Martin et al. 1996 [144839]; 1997 [100145]; 1998 [162737]; Levy et al. 1999 [162740]). Because of the "fast path" hydrological implications for the repository, the VS was initiated in late 1999 to independently verify the presence of "bomb-pulse" ^{36}Cl in the ESF. The study primarily entailed analyses of core from 50 new boreholes drilled across two zones, the Sundance fault and the Drillhole Wash fault, where significant $^{36}Cl/Cl$ bomb-pulse ratios were identified in the late 1990s.

6.14.2.1.1 Results

Previous studies reported numerous samples from the ESF with elevated levels of ^{36}Cl in a 165 m wide zone associated with the Sundance fault (Figure 6.14.2-1). Ratios of $^{36}Cl/Cl$ near or above 1250×10^{-15} were obtained for 11 of 16 samples between 3,428 m and 3,593 m in the ESF ($^{36}Cl/Cl$ ratios from 1,339 to $4{,}105 \times 10^{-15}$). Also, 9 of 15 samples from Niche 3566 (Niche 1), also associated with the Sundance fault, had $^{36}Cl/Cl$ values from 1,235 to $2{,}038 \times 10^{-15}$. Therefore VS targeted this zone to maximize the probability of reproducing the commonly sporadic "bomb-pulse" ^{36}Cl signal.

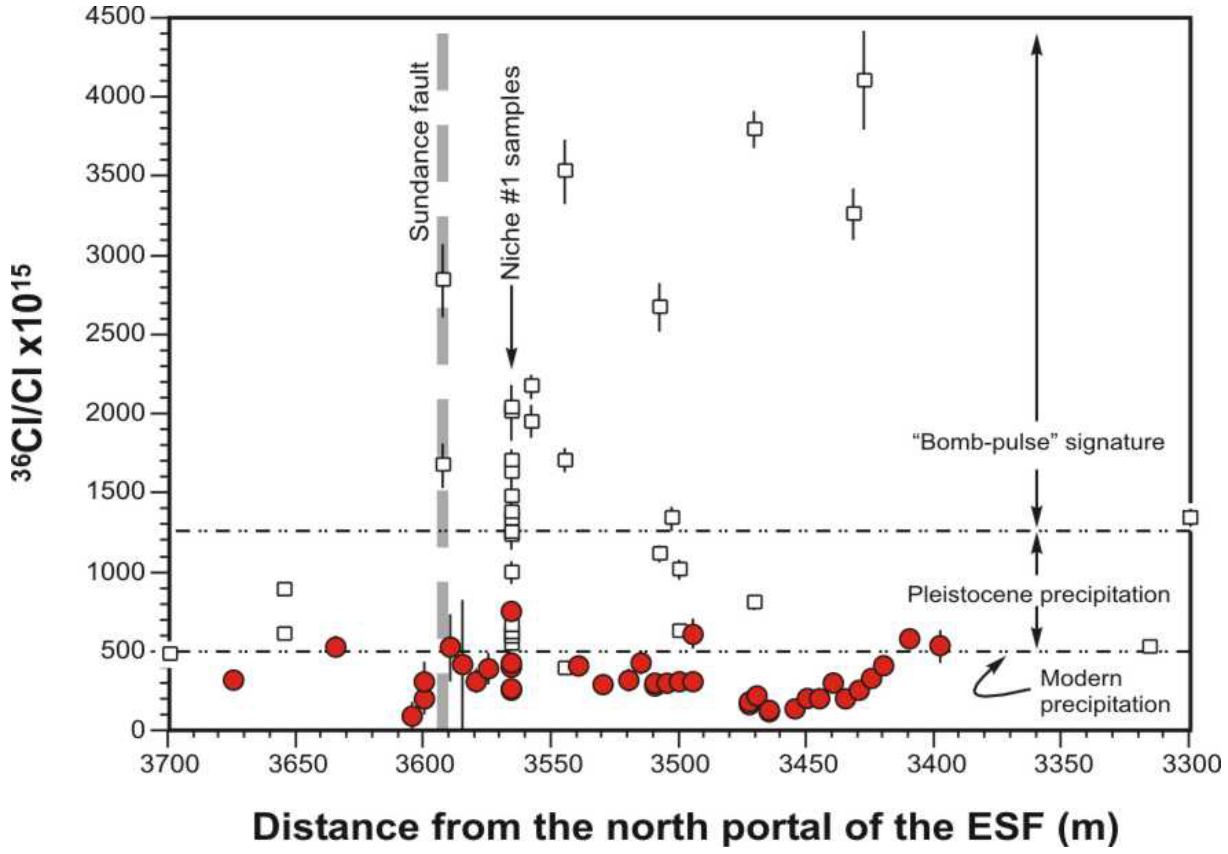

DTNs: LAJF831222AQ98.004 [107364]; LAJF831222AQ98.009 [145650]; LL030605223121.030 [163827]

NOTE: Although the main trace of the Sundance fault (shaded broad dashes) is exposed at a distance of 3,593 from the ESF north portal, the entire zone between about 3,400 and 3,650 m is pervasively fractured. Analytical errors (2σ) are shown as vertical lines if they are larger than the size of the symbol.The USGS-LLNL validation-study samples are shown as filled circles. Previously published LANL data (Fabryka-Martin et al. 1996 [144839]; 1997 [100145]; 1998 [162737]) are shown as open squares. Ranges for different ^{36}Cl/Cl signatures are from Fabryka-Martin et al. (1996 [144839]; 1997 [100145]).

Figure 6.14.2-1. ^{36}Cl/Cl Ratio Plotted against Sample Location in the Exploratory Studies Facility (ESF)

Initially, VS samples were crushed at LLNL and leached by deionized water in slowly rotating tumblers for 7 hours ("active" leach). Resulting leachates (Table 6.14.2-1) had high Cl concentrations (approximately 1 to 4.5 mg/kg) and low ^{36}Cl/Cl (approximately 40×10^{-15} to 275×10^{-15}) from overextraction of rock Cl, which is low in ^{36}Cl. Consequently, less-aggressive leach protocols were adopted. Subsequent samples were subjected to a "passive" leach method at USGS-Denver labs, where 1 to 2 kg of the 2 to 19 mm sized fraction of rock fragments was leached for 1 hour in an approximately equal weight of deionized water. This process approximated the passive-leaching methods used in earlier LANL studies except for a substantial reduction in the leach times (24 as opposed to 72 hours at LANL). Shorter leach times yield lower Cl concentrations (Gascoyne 2003 [162716]) with smaller contributions of rock Cl and greater contributions from labile meteoric Cl.

Table 6.14.2-1. Comparison of Chlorine-36 (^{36}Cl) Validation Study Results with Other ^{36}Cl Results

	Initial LLNL ^{36}Cl Validation Study[a]	**USGS-LLNL ^{36}Cl Validation Study[b]**	**LANL Previous Studies[c]**	**LANL ^{36}Cl Validation Study**
Sample locations [d]	ESF 3,398 to 3,470 and 3,580 to 3,675	ESF 3,398 to 3,675 and Niche 3566 (Niche 1)	ESF 3,300 to 3,768 and Niche 3566 (Niche 1)	ESF 3,300 to 3,768 and Niche 3566 (Niche 1), ECRB
Sample form	Drill core	Drill core	ESF tunnel walls and Niche 3566 (Niche 1) drill core	Drill core, ECRB tunnel walls, muck pile (EVAL)
Crushing	Jaw crusher	Jaw crusher and hammer/plate	Hammer/plate	Hammer/plate, jaw crusher
Size fraction	6 to 13 mm	2 to 19 mm	Typically 10 to 20 mm	Various sizes studied
Cl in Crushing blank	Not determined	<0.01 mg/kg	Not determined	Not determined
Leaching protocol	Active – 7 hr	Passive – 1 hr	Passive – 24 to 72 hr	Passive and Active
Cl in Leaching blank	Not determined	0.009 to 0.018 mg/kg	Unknown	Not determined
AMS Analytical facility	LLNL – CAMS lab	LLNL – CAMS lab	Purdue – PRIME lab	Purdue – PRIME lab LLNL – CAMS lab
Cl concentrations [e]	1.0 to 4.5 mg/kg	0.029 to 0.41 mg/kg	0.20 to 2.3 mg/kg	LANL 2003 DTNs
Average Cl concentration [e]	2.2 mg/kg	0.13 mg/kg	0.72 mg/kg	LANL 2003 DTNs
Minimum ^{36}Cl/Cl [e]	42 x10^{-15}	93 x10^{-15}	363 x10^{-15}	LANL 2003 DTNs
Maximum ^{36}Cl/Cl [e]	275 x10^{-15}	747 x10^{-15}	4,105 x10^{-15}	LANL 2003 DTNs
Average ^{36}Cl/Cl [e]	91 x10^{-15}	328 x10^{-15}	1,437 x10^{-15}	LANL 2003 DTNs
(Standard Deviation) [e]	(42 x10^{-15})	(146 x10^{-15})	(998 x10^{-15})	LANL 2003 DTNs
Median ^{36}Cl/Cl [e]	79 x10^{-15}	308 x10^{-15}	1,252 x10^{-15}	LANL 2003 DTNs
Number of analyses	44	40	39	LANL 2003 DTNs

DTN: LAJF831222AQ98.004 [107364]; DTN: LL030408023121.027 [162949]; DTN: LL030605223121.030 [163827]; DTN: LA0305RR831222.001 [163422]; DTN: LA0307RR831222.001 [164091]; DTN: LA0307RR831222.002 [164090]

NOTES: [a] Lawrence Livermore National Laboratory, unpublished data
[b] U.S. Geological Survey-Lawrence Livermore Laboratory, this study
[c] Los Alamos National Laboratory
[d] Exploratory Studies Facility (ESF) values are given in meters from the north portal.
[e] Cl concentrations and ^{36}Cl/Cl ratios have been corrected for contributions from spike, background, and blank in validation-study samples

The $^{36}Cl/Cl$ ratios were analyzed by accelerator mass spectrometry (AMS) and corrected for ^{36}S interference, background, and both spike and blank Cl contributions. None of the differences in measured blanks is sufficient to account for differences in measured bomb-pulse $^{36}Cl/Cl$ values.

The $^{36}Cl/Cl$ ratios in leachates from 34 of the 40 VS boreholes and from six leachates of Niche 3566 (Niche 1) boreholes range from $93 \pm 90 \times 10^{-15}$ to $747 \pm 43 \times 10^{-15}$ (Figure 6.14.2-1 and Table 6.14.2-1, USGS-LLNL study column). These values are considerably smaller than the values obtained in 1990s, with values of $363 \pm 22 \times 10^{-15}$ to $4{,}105 \pm 310 \times 10^{-15}$ (Table 6.14.2-1, LANL previous studies column). Only three of the 40 new VS analyses (USGS-LLNL study) are significantly greater (at 2σ error) than the modern precipitation value of 500×10^{-15}, compared to 33 of 39 analyses greater than 500×10^{-15}. The average $^{36}Cl/Cl$ ratio for VS samples is 328×10^{-15} (standard deviation of 146×10^{-15}, N=40), almost 5 times lower than the average of $1{,}437 \times 10^{-15}$ (standard deviation of 998×10^{-15}, N=39) for early samples collected from around the Sundance fault.

Cl concentrations in VS leachates (Table 6.14.2-1, USGS-LLNL study column) vary from 0.029 to 0.41 mg/kg (average of 0.13 mg/kg) and are systematically lower than early leachates (Table 6.14.2-1, LANL previous studies column) of 0.20 to 2.3 mg/kg (average of 0.72 mg/kg). These results are consistent with shorter leach times for VS samples (USGS-LLNL). Therefore, Cl leached from the VS samples (USGS-LLNL) should better represent the labile meteoric component present in the Sundance fault zone. Any "bomb-pulse" ^{36}Cl should be more readily identifiable in VS leachates (USGS-LLNL) than in previous leachates (LANL) with higher Cl concentrations.

Table 6.14.2-1 also includes information of additional and recent studies (in the LANL ^{36}Cl validation study column) with drill core samples, ECRB tunnel wall samples, and muck pile samples. This set of results in general supports the previous results with the presence of "bomb-pulse" signals. In additional to VS borehole samples, the results from different laboratories are also different on splits of Niche 3566 (Niche 1) core samples, as reported in different DTNs. At present, investigators are continuing the rigorous data verification and evaluation efforts necessary to develop a path forward for this important study. Due to the status of the VS, ^{36}Cl DTNs generated during the VS and cited in this section are presented for reference only. The VS conclusions will be documented in the final report of BSC (2003 [166104]).

6.14.2.2 Tritium Distribution in the ESF and ECRB

Low-level tritium measurements of pore water distilled from UZ core samples are used to identify the presence of fast pathways that allow the percolation of young water to the repository horizon. Natural tritium, with a half-life of 12.43 years, is produced in the atmosphere by neutron bombardment and enters the hydrological system as precipitation. Estimates of tritium activities in precipitation near Yucca Mountain prior to atmospheric testing of nuclear weapons (early 1950s) vary from 5 to 8 tritium units (TU). After weapons testing began, tritium activities in precipitation increased to thousands of TU. Water isolated from the atmosphere by entering the unsaturated zone prior to nuclear weapons testing, with a tritium activity of 8 TU, would currently contain less than 1 TU of tritium, based on radioactive decay alone. Therefore, the analysis of tritium data assumes that water with tritium activities in excess of 1 TU must contain some component of water that entered the UZ within the last 50 years.

All boreholes were dry-drilled using compressed air. After core was retrieved from each run, it was video logged and then wrapped in plastic film, inserted into Lexan tubing with caps tapped on each end, and finally sealed in ProtecCore™ packages. Core for ^{3}H analysis was selected from the deepest parts of the borehole where possible to minimize the effects of dryout and construction water contamination. Core was shipped and stored under refrigerated conditions until samples were ready for processing.

All pore water used for ^{3}H analyses was extracted from core samples by vacuum distillation, using the method described by Yang et al. (1998 [101441], pp. 25–27). Resulting water volumes ranged from 39 to 169 mL. Samples from Alcove #2 were processed and analyzed by the USGS in Denver. All other extracted pore water was processed by the USGS in Denver and sent to the University of Miami, Rosenstiel School of Marine and Atmospheric Science Tritium Laboratory for low-level analysis. Details of the analytical procedure are described by Ostlund 1987 [163335], pp. 8–10). Pore-water samples with low-level ^{3}H concentrations were processed through an electrolytic enrichment step, in which tritium concentrations are increased about 60-fold through volume reduction from the original starting volume to about 5 mL of sodium hydroxide solution. Low activities of ^{3}H were measured by internal gas proportional counting of H_2 gas made from the water sample. The counting equipment consists of nine proportional gas counters of various sizes, operating in anticoincidence with a surrounding cosmic-ray detector system. The whole system is encased in a 30-ton iron shield. Accuracy of the low-level measurement with enrichment is 0.10 TU (0.3 pCi L^{-1} of H_2O), or 3.5%, whichever is greater. All uncertainties for ^{3}H are given at 2σ.

Potential contamination effects increase as interpretations are made on lower levels of tritium. Prolonged exposure of the samples to the atmosphere could potentially increase tritium activity within the sample to that of the atmosphere (8–10 TU). Within the ESF and ECRB, the samples could be contaminated with construction water. The sampling techniques used are specifically designed to minimize any atmospheric exposure of the core or water samples, and the preponderance of samples with tritium activities below 1 TU indicates that the sampling techniques are sufficient in eliminating this effect. The effects of construction water contamination are more difficult to eliminate. The construction water used in the ESF and ECRB derives from water well UE 25 J-13, which has been sampled several times and has not contained measurable tritium. Therefore, the result of construction water contamination of the core samples would be to dilute any evidence of young water. During the process of selecting core for tritium analyses, core from the deepest part of the borehole, farthest from the application of construction water, is selected to minimize these effects.

Geogenic production of tritium in the subsurface does occur because of the spontaneous fission of uranium and thorium. However, in most groundwater, *in situ* production of tritium in the subsurface is assumed to be on the order of 0.1 TU (Clark and Fritz 1997 [105738]).

Because of the above considerations, interpretation of the number of fast pathways in the ESF and ECRB are conservatively lower than the actual number of pathways that have been active since the advent of weapons testing. However, because of the large number of samples analyzed, the general distribution of recently active pathways should be well represented by the tritium data.

6.14.2.2.1 Sample Collection and Low-level Analyses of Tritium Activity

Water samples for tritium analyses are obtained from core samples collected during the drilling of horizontal boreholes in the ESF and the ECRB. These boreholes are dry-drilled, and core is sealed from atmospheric contamination with plastic wrap and sealed tubing. Core selected for tritium analysis is taken from the deepest part of the hole to minimize the possibility of construction water contamination. The porewater from the core sample is removed by distillation and sent to the University of Miami, Rosenstiel School of Marine and Atmospheric Science Tritium Laboratory for analysis.

Samples were collected from several locations within the ESF and ECRB. Eleven samples were collected from boreholes crossing the Bow Ridge fault in Alcove 2, off the north ramp of the ESF. Seventeen samples were collected from the North Ramp of the ESF, with 10 of those coming from the Drill Hole Wash fault where other studies had indicated the presence of fast pathways. Forty samples were collected from the Sundance fault area within the main drift of the ESF, another location that other studies had indicated the presence of fast pathways. Eighteen samples were collected from the northern Ghost Dance fault access drift and alcove, and five from the southern Ghost Dance fault access drift along the main drift of the ESF. Twenty-eight samples were collected along the South Ramp of the ESF and 22 from the ECRB.

6.14.2.2.2 Results and Interpretation of Tritium Analyses

In the North Ramp of the ESF, the only tritium activities above the 1 TU threshold were found in samples from the Bow Ridge fault in Alcove 2. These samples are from the Tiva Canyon Tuff, which lies above the Paintbrush Tuff nonwelded units. Samples along the Drill Hole Wash fault, from the Topopah Spring Tuff which lies below the Paintbrush Tuff nonwelded units, contained no tritium activities above the 1 TU threshold.

All the results of tritium activities are listed in Table 6.14.2-2. In the ESF Main Drift along the Sundance fault, only 1 of 42 samples contained tritium in excess of 1 TU. Pore water from 12.3 to 13.5 feet deep in the borehole at Station 35+25 had tritium activity of 1.6 TU, but pore water from 10.9 to 11.8 feet deep in the same borehole had tritium activity below detection level. This indicates that although there appears to be a fast path present at this location, only a small amount of young water imbibed into the matrix.

The remaining 23 samples collected along the of the ESF Main Drift were all collected in the vicinity of the Ghost Dance fault near Alcoves 6 and 7. None of these samples contains tritium in excess of the 1 TU threshold, which would indicate the presence of young water.

In the South Ramp of the ESF, where the Paintbrush Tuff nonwelded units are faulted and offset in a number of locations, 16 of 28 samples contained tritium activities greater than 1 TU. The young pore water present along the South Ramp occurs both above and below the nonwelded units. This indicates significant, rapid infiltration in this part of the ESF that is able to quickly bypass the nonwelded units because of the extensive faulting.

In the ECRB, nine of 22 samples analyzed had tritium activities greater than 1 TU. All four of the samples between 750 and 950 m in the upper lythophysal unit of the Topopah Spring tuff in the ECRB indicated the presence of young porewater. Other more isolated locations indicating

the presence of young pore water occurred in the middle nonlithophysal and lower lithophysal units of the Topopah Spring tuff at 1350, 1500, and 2,150 m in the ECRB. Attempts to duplicate the high tritium activities at two locations met with mixed results. Three samples from the borehole at 1,500 m in the ECRB were analyzed, with two of the three samples containing elevated tritium activities. Two samples from the borehole at 2,150 m in the ECRB were analyzed, and one contained elevated tritium activity.

Only one of the 38 VS samples analyzed for tritium had a detectable signal just above the 1 TU detection limit (Patterson 2000 [154827]). VS cores from the Sundance fault zone also were analyzed for whole-rock $^{234}U/^{238}U$ compositions, assuming that fast pathways would result in long-term differences in the degree of uranium-series isotope disequilibrium. Results from samples within the highly fractured and faulted VS study area are statistically identical to samples of unfaulted tuff elsewhere in the repository (Gascoyne et al. 2002 [154800]). Strontium isotopic compositions of pore-water salts from six leachates of Niche 3566 (Niche 1) core also are identical to other areas in the repository and require substantial water/rock interaction in the overlying Sr-rich rock units. These Sr isotopic compositions are not consistent with rapid flow down faults (Marshall and Futa 2003 [162717]).

Table 6.14.2-2. Tritium Activities Found in Samples from Locations in the ESF and ECRB.

Borehole Name	Interval (Ft)	Tritium (TU)	Tritium Error (TU)
ESF-AL#2-HPF#1	16.4-16.7	<0.1	3.90
ESF-AL#2-HPF#1	23.2-23.5	2.00	3.90
ESF-AL#2-HPF#1	27.8-28.0	5.10	3.90
ESF-AL#2-HPF#1	34.3-34.6	28.80	4.20
ESF-AL#2-HPF#1	47.2-47.6	30.90	4.20
ESF-AL#2-HPF#1	50.5-50.7	118.30	9.40
ESF-AL#2-HPF#1	55.4-55.7	128.10	5.20
ESF-AL#2-HPF#1	58.9-59.0	78.60	4.70
ESF-AL#2-HPF#1	61.2-61.3	65.30	4.60
ESF-AL#2-HPF#1	68.6-68.9	154.60	5.50
ESF-AL#2-HPF#1	83.6-83.8	32.90	4.30
ESF-LPCA-MOISTSTDY#02	6.4-7.0	<0.1	0.29
ESF-NR-MOISTSTDY#03	4.4-5.0	0.20	0.40
ESF-NR-MOISTSTDY#04	4.2-6.9	0.76	0.12
ESF-NR-MOISTSTDY#04	4.-6.9	0.66	0.10
ESF-NR-MOISTSTDY#10	4.6-6.5	0.22	0.15
ESF-NR-MOISTSTDY#13	4.3-5.1	0.55	0.15
ESF-NR-MOISTSTDY#16	5.8-6.6	0.44	0.15
ESF-DHW-CIV#01	10.9-13.2	1.00	0.40
ESF-DHW-CIV#02	6.5-8.2	0.50	0.70
ESF-DHW-CIV#03	12.0-13.3	1.60	0.40
ESF-DHW-CIV#04	12.3-13.7	0.90	0.30
ESF-DHW-CIV#05	26.7-28.7	0.70	0.30
ESF-DHW-CIV#06	12.2-13.9	0.48	0.28
ESF-DHW-CIV#07	9.6-11.0	1.60	0.40
ESF-DHW-CIV#08	11.7-13.1	0.20	0.50
ESF-DHW-CIV#09	11.5-12.5	0.60	0.60
ESF-DHW-CIV#10	11.2-12.4	0.94	0.24
ESF-SD-CIV#01	11.5-12.6	0.50	0.40
ESF-SD-CIV#02	8.0-9.9	0.10	0.30
ESF-SD-CIV#03	10.7-11.4	0.60	0.30
ESF-SD-CIV#04	11.8-13.4	0.30	0.40
ESF-SD-CIV#05	7.9-9.7	0.71	0.23
ESF-SD-CIV#06	9.3-10.5	1.10	0.50
ESF-SD-CIV#07	8.1-9.7	0.30	0.40
ESF-SD-CIV#08	7.9-9.9	0.60	0.30
ESF-SD-CIV#09	10.1-11.5	0.20	0.30
ESF-SD-CIV#10	11.8-13.0	0.37	0.29
ESF-SD-CIV#11	11.0-12.5	0.15	0.28
ESF-SD-CIV#12	11.8-13.4	0.20	0.27
ESF-SD-CIV#13	30.5-32.3	0.60	0.40
ESF-SD-CIV#14	11.6-13.4	<0.1	0.15
ESF-SD-CIV#15	12.0-13.5	0.60	0.50
ESF-SD-CIV#16	12.0-13.2	0.20	0.30
ESF-SD-CIV#17	10.5-12.0	0.95	0.26

Table 6.14.2-2. Tritium Activities Found in Samples from Locations in the ESF and ECRB.(Continued)

Borehole Name	Interval (Ft)	Tritium (TU)	Tritium Error (TU)
ESF-SD-CIV#17	12.0-13.2	0.70	0.40
ESF-SD-CIV#18	10.9-11.8	1.40	0.80
ESF-SD-CIV#18	12.3-13.5	2.60	0.50
ESF-SD-CIV#19	11.7-13.1	0.60	0.40
ESF-SD-CIV#20	10.5-13.0	<0.1	0.24
ESF-SD-CIV#21	9.8-11.1	0.40	0.28
ESF-SD-CIV#22	10.4-11.2	0.15	0.27
ESF-SD-CIV#23	12.6-13.7	0.22	0.29
ESF-SD-CIV#24	12.1-13.4	0.40	0.30
ESF-SD-CIV#25	8.7-9.9	0.20	0.40
ESF-SD-CIV#26	12.2-13.2	0.10	0.40
ESF-SD-CIV#27	12.0-13.4	0.22	0.17
ESF-SD-CIV#28	8.0-11.3	1.14	0.26
ESF-SD-CIV#29	10.7-12.2	0.28	0.17
ESF-SD-CIV#30	12.2-13.4	0.20	0.30
ESF-SD-CIV#31	11.0-12.6	0.30	0.40
ESF-SD-CIV#32	11.6-13.2	0.31	0.23
ESF-SD-CIV#33	7.7-8.9	0.90	0.30
ESF-SD-CIV#34	10.5-12.0	0.46	0.21
ESF-SD-CIV#35	10.0-11.4	0.29	0.22
ESF-SD-CIV#36	6.7-8.1	<0.1	0.18
ESF-SD-CIV#37	9.7-11.2	0.28	0.13
ESF-SD-CIV#38	11.0-12.5	1.40	0.80
ESF-SD-CIV#39	11.2-12.7	0.23	0.14
ESF-SD-CIV#40	12.3-13.3	0.30	0.16
ESF/NAD/GTB#1A	114.0-115.0	0.50	0.30
ESF/NAD/GTB#1A	120.3-121.6	1.00	0.40
ESF/NAD/GTB#1A	122.1-123.8	1.20	0.40
ESF/NAD/GTB#1A	124.4-126.0	1.20	0.40
ESF/NAD/GTB#1A	127.0-129.0	1.60	0.60
ESF/NAD/GTB#1A	130.2-131.9	0.80	0.70
ESF/NAD/GTB#1A	137.0-142.0	0.30	0.40
ESF/NAD/GTB#1A	165.8-166.7	0.80	0.50
ESF/NAD/GTB#1A	168.0-169.8	0.80	0.50
ESF/NAD/GTB#1A	98.4-100	1.40	0.40
ESF-AL6-NDR-MF#01	44.2-46.0	1.60	0.50
ESF-AL6-NDR-MF#01	48.9-50.9	2.20	0.60
ESF-AL6-NDR-MF#01	53.9-55.6	1.30	0.50
ESF-AL6-NDR-MF#02	42.3-43.9	1.60	0.70
ESF-AL6-NDR-MF#02	47.3-49.0	1.16	0.20
ESF-AL6-NDR-MF#02	49.3-51.3	1.10	0.50
ESF-AL6-NDR-MF#02	55.3-57.0	1.00	0.60
ESF-AL6-NDR-MF#02	61.1-62.9	0.90	0.70
ESF/SAD/GTB#1	103.4-104.1	3.70	0.70
ESF/SAD/GTB#1	124.3-125.9	1.10	0.30
ESF/SAD/GTB#1	175.4-177.0	1.80	0.70
ESF/SAD/GTB#1	214.5-216.9	2.25	0.29
ESF/SAD/GTB#1	85.1-86.0	1.20	0.50
ESF-SR-MOISTSTDY#01	2.1-3.6	0.30	0.15
ESF-SR-MOISTSTDY#02	2.2-3.9	0.03	0.10

Table 6.14.2-2. Tritium Activities Found in Samples from Locations in the ESF and ECRB.(Continued)

Borehole Name	Interval (Ft)	Tritium (TU)	Tritium Error (TU)
ESF-SR-MOISTSTDY#03	2.9-5.7	1.70	0.40
ESF-SR-MOISTSTDY#05	3.6-6.5	0.42	0.15
ESF-SR-MOISTSTDY#06	2.6-7.0	0.81	0.14
ESF-SR-MOISTSTDY#07	3.8-7.0	3.18	0.18
ESF-SR-MOISTSTDY#10	2.4-6.4	28.60	1.80
ESF-SR-MOISTSTDY#11	3.2-6.9	4.80	0.40
ESF-SR-MOISTSTDY#13	6.0-6.8	3.09	0.27
ESF-SR-MOISTSTDY#16	4.6-6.8	8.20	0.50
ESF-SR-MOISTSTDY#17	5.8-6.7	3.80	0.30
ESF-SR-MOISTSTDY#17	5.8-6.7	3.50	0.50
ESF-SR-MOISTSTDY#18	4.6-6.7	1.10	0.40
ESF-SR-MOISTSTDY#19	4.5-6.9	14.30	1.00
ESF-SR-MOISTSTDY#20	4.2-6.8	7.40	0.40
ESF-SR-MOISTSTDY#23	16.2-17.0	0.45	0.15
ESF-SR-MOISTSTDY#23	16.2-17.0	0.25	0.16
ESF-SR-MOISTSTDY#25	5.0-6.9	4.40	0.40
ESF-SR-MOISTSTDY#26	7.4-9.6	4.94	0.27
ESF-SR-MOISTSTDY#27	5.9-6.8	1.50	0.40
ESF-SR-MOISTSTDY#28	2.5-6.8	3.20	0.40
ESF-SR-MOISTSTDY#29	4.5-6.8	0.77	0.23
ESF-SR-MOISTSTDY#30	3.8-6.7	12.50	0.60
ESF-SR-MOISTSTDY#31	4.7-7.0	5.39	0.28
ESF-SR-MOISTSTDY#33	5.9-6.9	2.65	0.28
ESF-SR-MOISTSTDY#34	5.9-6.8	1.24	0.24
ESF-SR-MOISTSTDY#38	5.9-6.8	1.70	0.30
ESF-SR-MOISTSTDY#40	5.9-6.9	0.58	0.16
ECRB-SYS-CS0600	3.2-6.0	0.79	0.29
ECRB-SYS-CS0750	3.6-6.2	6.2	0.5
ECRB-SYS-CS0800	2.9-5.8	1.7	0.3
ECRB-SYS-CS0900	3.5-6.4	6.5	0.6
ECRB-SYS-CS0950	2.8-5.6	6.1	0.4
ECRB-SYS-CS1000	17.4-18.2	0.5	0.3
ECRB-SYS-CS1200	2.9-6.9	0.41	0.23
ECRB-SYS-CS1300	3.0-5.5	0.7	0.7
ECRB-SYS-CS1350	3.6-6.4	3.8	0.5
ECRB-SYS-CS1450	4.0-6.5	0.3	0.5
ECRB-SYS-CS1500	14.4-17.4	2.5	0.4
ECRB-SYS-CS1500	4.3-7.1	10.3	0.9
ECRB-SYS-CS1500	9.5-12.1	1.5	0.4
ECRB-SYS-CS1600	3.4-4.3	1.7	0.9
ECRB-SYS-CS1750	5.5-5.9	0.6	0.4
ECRB-SYS-CS1800	3.6-6.1	0.1	0.8
ECRB-SYS-CS1950	4.0-6.5	3.6	0.5
ECRB-SYS-CS2000	11.0-11.9	0.1	0.5
ECRB-SYS-CS2150	3.4-4.1	<0.1	0.9
ECRB-SYS-CS2150	5.5-6.7	9.8	0.5
ECRB-SYS-CS2250	2.9-3.9	0.8	0.4
ECRB-SYS-CS2500	16.7-19.8	0.64	0.3

DTNs: GS951208312272.002 [151649]; GS990183122410.001 [146125]; GS990183122410.004 [146129]; GS020408312272.002 [162342]; GS021208312272.005 [162934]; GS030208312272.001 [162935]

6.14.2.3 Reconstruction of the Paragenetic Sequence and Thermal History of Fracture-Hosted Secondary Mineral Deposits

Detailed mapping of the secondary mineral deposits has shown that in high-angle fracture settings, the deposits generally are restricted to the fracture footwalls; in cavity settings, they are restricted to the cavity floors. The mineral coatings typically are (1) heterogeneously distributed and found on <10% of open fractures and cavities, (2) discontinuous and patchy within fractures, (3) of irregular thickness in cavities and without geopetal features indicating ponding, and (4) adjacent to or intersected by barren fractures and cavities (Paces et al. 2001 [156507]; Whelan et al. 2002 [160442]; Whelan et al. 2003 [163590]). This distribution of coatings is consistent with simulations of gravity-controlled fracture flow in UZ settings predicting that percolating waters will concentrate into only a small percentage of the available flow paths (Tokunaga and Wan 1997 [139195]; Pruess 1999 [104250]). Although some have argued that the deposits formed from upwelling of hydrothermal fluids (Dublyansky et al. 1996 [109204]; 2001 [161543]), the sparse and patchy distribution of the deposits on open-space lower surfaces, coupled with the lack of evidence that fluids filled open space (such as coatings on the hanging-walls of fractures or completely lining the interiors of cavities), indicates that the deposits formed from descending percolating water in a vadose setting (Paces et al. 2001 [156507]; Whelan et al. 2002 [160442]; Whelan et al. 2003 [163590]).

Most coatings are consistent with the following generalized paragenetic sequence. Many deposits begin with an early stage of calcite ± fluorite and, rarely, zeolites; this stage is commonly capped by botryoidal chalcedony ± drusy quartz. The intermediate stage is largely calcite and opal, rarely with minor fluorite, and the late stage consists of calcite and opal (Whelan et al. 2002 [160442]). Thin, patchy coatings of manganese -oxides are common on fracture walls where they may underlie the secondary mineral coatings (Carlos et al. 1993 [105210]).

6.14.2.3.1 Results

Some of the deposits contain early- or intermediate-stage calcite having two-phase, liquid + vapor, fluid inclusions (FI) suitable for thermometric determinations of depositional temperature. Based on measurements of T_h in about 4,000 FIs in samples from 52 underground locations, measured depositional temperatures range from 37 to 89°C in calcite and from 57 to 93°C in fluorite (Figure 6.14.2-2). Fluid inclusion T_h in calcite decreases: from east to west along the ESF North Ramp in the north bend (from about 90°C to about 60°C); from northeast to southwest along the ECRB Cross Drift from about 60 to 50°C; and from north to south along the ESF Main Drift from about 60°C to about 45°C (Figure 6.14.2-2). Temperature trends are not apparent in the south ramp data. Where paragenetic relations indicate that multiple generations of calcite in a deposit provide T_h data, depositional temperatures decrease with time. These results are in close agreement with measurements obtained from the same samples by Wilson et al. (2000 [154279]; [154280]) and Wilson and Cline (2001 [155426]).

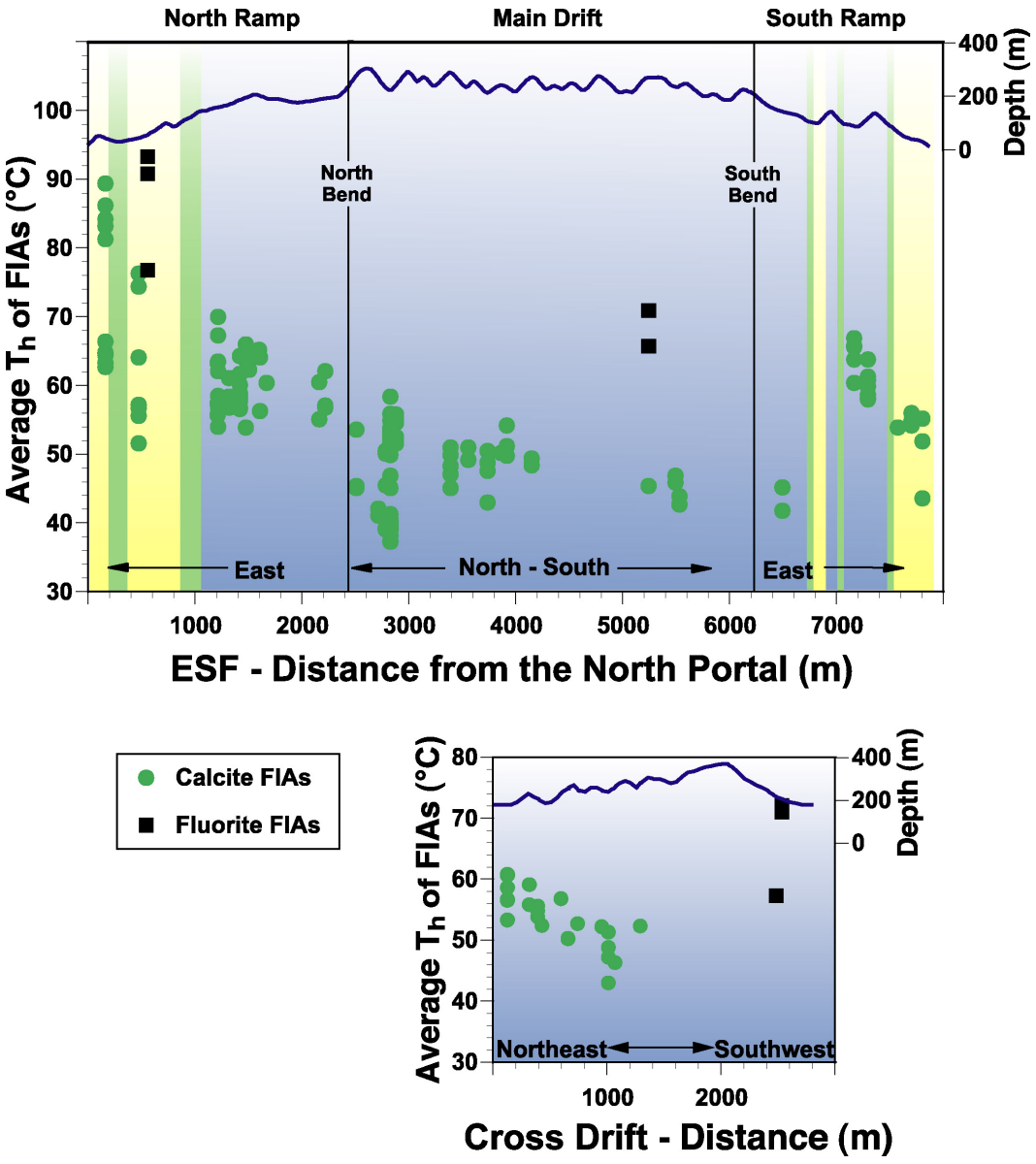

DTNs: GS010808315215.003 [164844]; GS020908315215.003 [164846]

NOTE: Yellow and blue backgrounds for the welded tuffs of the Tiva Canyon and Topopah Spring Tuffs, respectively, and a green background for the intervening bedded and nonwelded tuffs illustrate tunnel stratigraphy. Depth of the tunnel below ground surface is plotted along the tops of the graphs.

Figure 6.14.2-2. The Average Homogenization Temperatures (T_h) of Two-Phase Fluid Inclusions with Small and Consistent Vapor: Liquid Ratios in Fluid Inclusion Assemblages in Calcite and Fluorite from Secondary Mineral Coating Samples from the Exploratory Studies Facility (ESF) and Enhanced Characterization of the Repository Block (ECRB) Cross Drift Tunnels

Although FIs suitable for T_h determinations are common in the early stage and locally observed in the intermediate stage, they have not been observed in the late stage of deposits. Fluid inclusions in the late stage are largely all-liquid, with no two-phase inclusions that might indicate calcite deposition at higher than modern ambient temperatures.

Calcite $\delta^{18}O$ values from 135 ESF Main Drift and 34 ECRB Cross Drift locations range widely from about -1 to almost 24‰, with the lowest $\delta^{18}O$ values in the paragenetically older calcites (Figure 6.14.2-3). Most early-stage calcite $\delta^{18}O$ values range from 5 to 15‰. Minimum $\delta^{18}O$ values of early-stage calcite tend to increase westward along both the north and south ramps, from <10‰ to around 12‰ in the ESF Main Drift and the ECRB Cross Drift. Intermediate calcite $\delta^{18}O$ values range from 10.9 to 23.0‰, with most between 13 and 18‰, late-stage calcite $\delta^{18}O$ values range from 14.4 to 21.3‰, with most between 16 and 20‰ (Figure 6.14.2-3). Late-stage calcite values decrease systematically with depth and are relatively constant within the ESF Main Drift and ECRB Cross Drift locales.

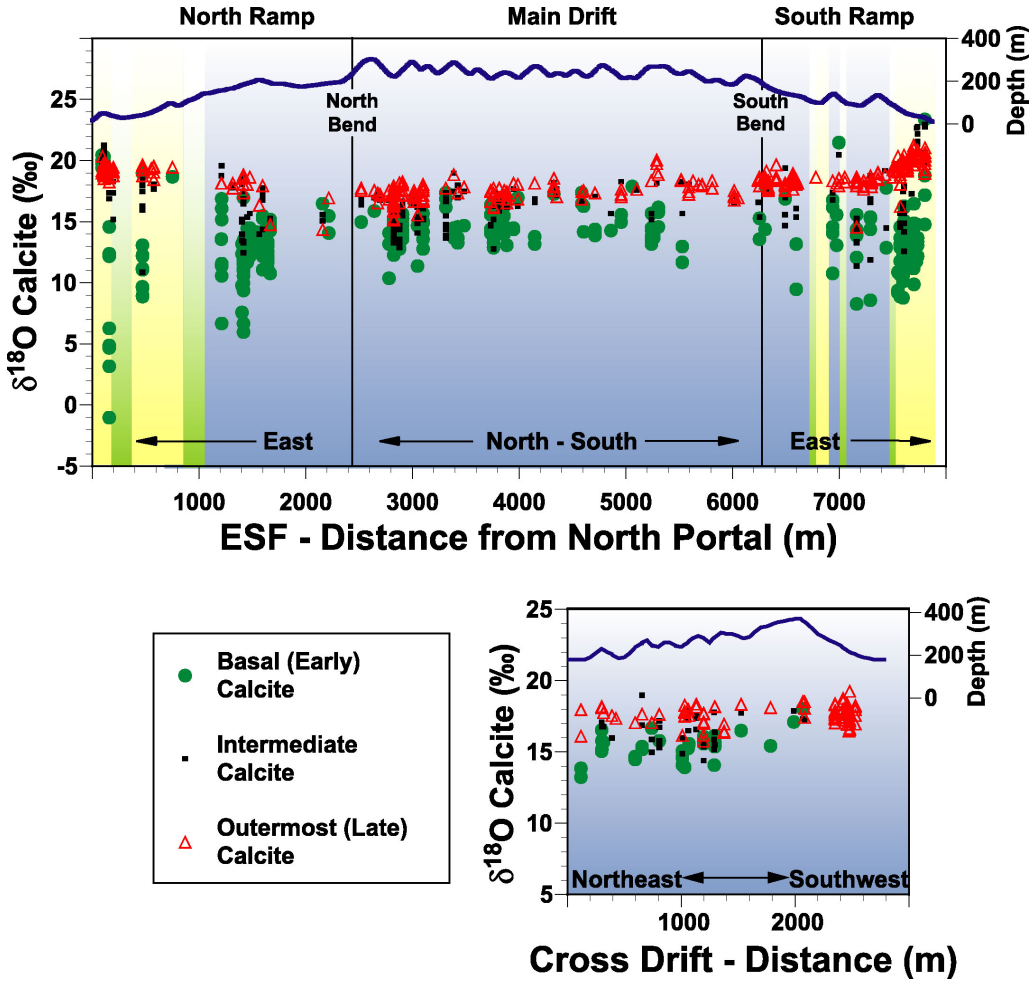

DTNs: GS020908315215.004 [164846]; GS970208315215.005 [107351]; GS970808315215.010 [145920]; GS980908315213.002 [146088]; GS990908315213.001 [153379]

NOTE: Yellow and blue backgrounds for the welded tuffs of the Tiva Canyon and Topopah Spring Tuffs, respectively, and a green background for the intervening bedded and nonwelded tuffs illustrate tunnel stratigraphy. Depth of the tunnel below ground surface is plotted near the tops of the graphs. Calcite $\delta^{18}O$ values are reported versus the SMOW scale wherein the $\delta^{18}O$ value of NBS-19 calcite is 28.65% (Coplen et al. 2002 [165235], pp. 36–37). The $\delta^{18}O$ value of water is estimated from $\delta^{18}O$ values from calcite as in Marshall et al. (2000 [151018]).

Figure 6.14.2-3. The $\delta^{18}O$ Values of Calcite from Secondary Mineral Coating Samples in the Exploratory Studies Facility (ESF) and Enhanced Characterization of the Repository Block (ECRB) Cross Drift Tunnels

The $\delta^{18}O$ values of the outermost (most recent) calcite in the UZ coatings decrease with depth (Figure 6.14.2-4). Assuming a $\delta^{18}O_{H2O}$ of -13‰, consistent with recent recharge in the tuffs (Yang et al. 1996 100194]), the decrease of the $\delta^{18}O$ value with depth in the TSw displayed by the latest calcite is consistent with a geothermal gradient of about 27°C/km (Figure 6 and Whelan et al. 2002 [160442]), slightly higher than the measured gradient of ~24°C determined from Sass et al. (1988 [100644]; 1995 [101288]). Within the overlying TCw, however, outermost calcite $\delta^{18}O$ values decrease rapidly with depth at a rate that, if solely a function of temperature, would suggest a geothermal gradient of over 100°C/km–a high gradient clearly at odds with that in the underlying TSw. It is more likely that much of the decrease of fracture-hosted calcite $\delta^{18}O$ values with depth in the TCw reflects decreasing amounts of evaporative ^{18}O-enrichment of water deeper in the fracture network. In the TSw, evaporation and ^{18}O-enrichment are inhibited by the much less fractured bedded tuffs of the overlying PTn, which inhibit upward transport of the vapor phase (Thorstenson et al. 1998 [126827]). The temperature estimates based on latest calcite $\delta^{18}O$ values support the conclusion that late-stage deposition has been at or near modern ambient temperatures.

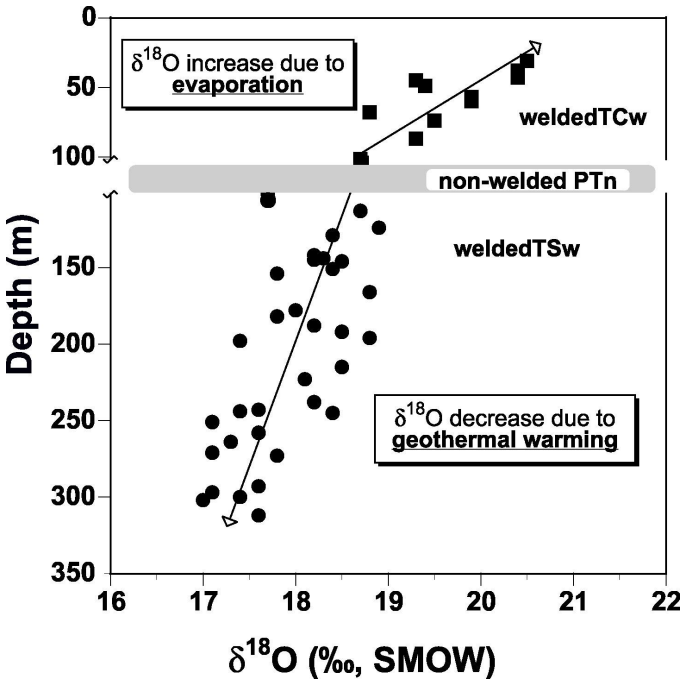

DTNs: GS020908315215.004 [164846]; GS970208315215.005 [107351]; GS970808315215.010 [145920]; GS980908315213.002 [146088]; GS990908315213.001 [153379]

NOTE: Modified from Whelan et al. 2002 [160442].

Figure 6.14.2-4. Latest Calcite $\delta^{18}O$ Values Plotted vs. Depth Below the Surface in the ESF, Reflecting Separate Trends in the TCw (squares) and TSw (circles) Welded Tuffs

Calcite and fluorite hosting elevated temperature FIs were typically the earliest minerals precipitated. The timing of trapping for those FIs is constrained only to after initial cooling of the tuffs to <100°C, and before deposition of the overlying chalcedony or opal that was dated. The $^{207}Pb/^{235}U$ ages of subsamples of silica collected above calcite containing fluid inclusions with

small and consistent vapor:liquid ratios range from 1.14 ± 0.16 to 8.99 ± 0.07 Ma. Similar data from four subsamples of opal/chalcedony overlying calcite with low $\delta^{18}O$ values indicative of higher depositional temperatures (Whelan et al. 2001 [154773]) have $^{207}Pb/^{235}U$ ages ranging from 3.97 ± 0.05 to 9.7 ± 1.5 Ma (Neymark et al. 2002 [158673]).

A graph of age versus temperature of deposition (Figure 6.14.2-5a) shows that the highest temperatures occurred ≥10 Ma, and that temperatures cooled gradually to near-modern ambient temperatures over the next 6 or more million years, where they have remained for the past 2 to 4 million years. The protracted cooling of the UZ since ~10 Ma is consistent with published thermal models (Marshall and Whelan 2000 [154415]; 2001 [163591]) that show that the large magma chamber <10 km to the north, which was responsible for the voluminous ash eruptions that formed the tuff sequence, could have supplied heat to the surrounding crust for that long.

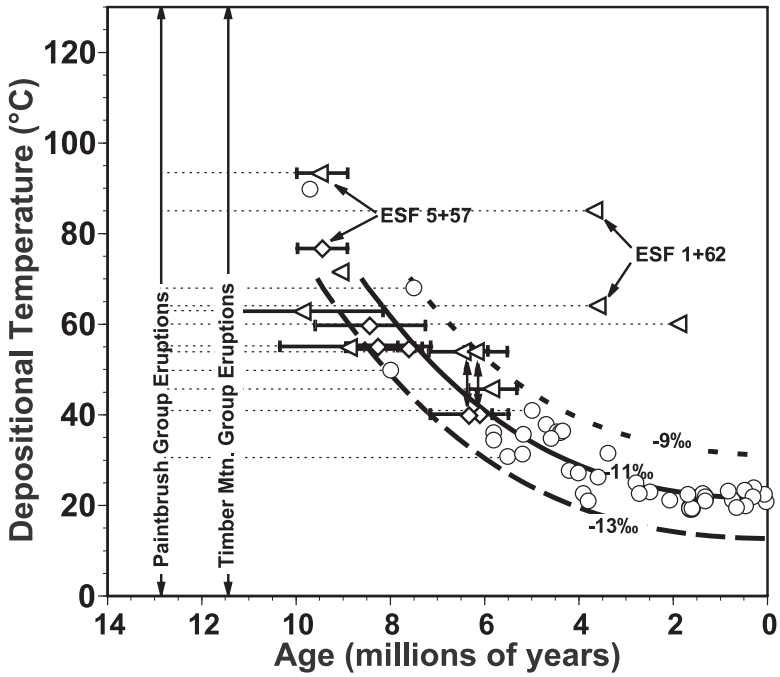

DTNs: GS020908315215.004 [164846]; GS021008315215.005 [164848]; GS970208315215.005 [107351]; GS010808315215.004 [164850]; GS970808315215.010 [145920]; GS980908315213.002 [146088]; GS990908315213.001 [153379]; GS010808315215.003 [164844]; GS020908315215.004 [164847]

NOTE: Temperatures determined from FIA T_h are shown as open triangles for calcite that is older than the associated chalcedony/opal, with dotted lines connecting the age to the eruptive age of the host tuffs; the true of the calcite lies somewhere along these dotted lines. Ages where paragenetic relations indicate the calcite and chalcedony/opal formed nearly contemporaneously are shown as open diamonds. Temperatures calculated from the $\delta^{18}O$ value of calcite, assuming a $\delta^{18}O$ for the depositing water of -11‰, are shown as open circles. A best-fit curve for a water of -11‰, as well as curves for waters of -13 and -9‰, are shown.

Figure 6.14.2-5. Graph of Calcite Depositional Temperatures versus $^{235}U/^{207}Pb$ or $^{230}Th/U$ (Paces et al. 2001 [156507]) Depositional Ages of Chalcedony or Opal Associated with the Calcite

ESF Stations 1+62, 4+73, and 5+57 (fluorite), appear anomalously hot, with maximum temperatures ranging from 76 to 93°C. These samples are only 40–60 m below the surface and do not appear to be compatible with subsurface magma-chamber-sourced heating. Geological relations and alteration rinds on the walls of the host fractures suggest that they formed from

fluids hot enough to alter the tuffs. Such alteration is not observed from other locations. These minerals are consistent with deposition from fumarolic systems, such as occur elsewhere near the tops of the ash flows. Formation from deeper-sourced hydrothermal systems cannot be ruled out, although no evidence exists of the hotter roots of such systems, such as alteration of the deeper stratigraphic units in the UZ, or of ^{18}O-enriched minerals that a fluid having undergone extensive water-rock interaction at hydrothermal temperatures would produce.

6.14.3 Uranium Isotope Studies

6.14.3.1 Mineral-Climate Records of UZ Flow

Although infiltrating water is expected to flow through connected fracture pathways in the tuffs (Bodvarsson and Bandurraga 1996 [100102]; Flint et al. 2001 [164506], Wu et al. 2001 [156399]), modern fracture flow has not been observed in extensive underground excavations. Coatings of hydrogenic calcite and silica in fractures and lithophysal cavities represent a record of past percolation and are being studied to determine the sources of solutions, timing of flow, thermal history of the rock mass, and amount of past seepage (Whelan et al. 1994 [100091]; Paces et al. 1998 [107408]; Whelan and Moscati 1998 [109179]; Whelan et al. 1998 [137305]; Marshall et al. 2000 [151018]; Neymark and Paces 2000 [127012]; Neymark et al. 2000 [162710]; Paces et al. 2001 [156507]; Neymark et al. 2002 [158673]; Whelan et al. 2002 [160442]; Wilson and Cline 2001 [155426]). Previous U-series and U-Pb dating of calcite and opal suggested uniform long-term average growth rates of fracture minerals at Yucca Mountain on the order of millimeters per million years (mm/m.y.) (Neymark and Paces 2000 [127012]; Paces et al. 2001 [156507]; Neymark et al. 2002 [158673]). However, to more directly assess mineral growth histories and inferred hydrological flow (seepage), improvements in the spatial resolution of age determinations are required. If hydrogenic mineral growth rates determined at finer scales of resolution can be established, growth histories may be compared to known cycles of Pleistocene climate variation at Yucca Mountain to help evaluate numerical models of UZ flow and seepage.

Recent U-series investigations use two analytical methods, ion microprobe (IMP) and *in situ* microdigestions followed by thermal-ionization mass spectrometry (TIMS). These methods result in ages for thinner layers (about 2 to 35 μm) of clear, hyalitic opal hemispheres. Opal reported here is from sample HD2074, an irregular mineral coating covering the floor of a large lithophysal cavity, 270 m below the land surface and 3,051 m from the north portal of the ESF tunnel. Total mineral coating thickness varies between 1 and 4 cm. Equant to elongated hemispheres up to 1 to 2 mm in diameter are present on the tips of thin calcite blades and show fine layering on micrometer scales.

6.14.3.1.1 Results

<u>*Ion-Microprobe Results:*</u> IMP traverses consisting of 7 to 10 spots were conducted across the outer 305 to 740 μm of two opal hemispheres (Figure 6.14.3-1). The primary beam of $^{16}O_2^-$ ions resulted in roughly circular ablation pits approximately 45 μm in diameter and 15 to 20 μm deep. However, given the uniform layering, 91% of the mass analyzed in each spot represents the central, 35 μm thick layers within the spot diameter. Resulting isotope ratios and $^{230}Th/U$ ages are given in Table 6.14.3-1. Measured U isotope activity ratios range from 1.1 to 6.7. In spite of

the relatively large analytical errors, IMP data follow paths expected for closed-system isotope evolution from a uniform initial $^{234}U/^{238}U$ of between 7 and 8 (cross-hatched area in Figure 6.14.3-2). In contrast, mechanically separated total digestions of hemispheres and sheets of Yucca Mountain opal determined by TIMS are offset towards lower $^{230}Th/^{238}U$ at a given value for $^{234}U/^{238}U$ (Neymark and Paces 2000 [127012], Figure 4; Paces et al. 2001 [156507], Figure 13). The differences between these two patterns of isotope behavior are caused by integrating materials of widely varying ages in mechanically separated TIMS subsamples compared to the greater spatial resolution offered by the IMP spots. Sample weights for the opal residues analyzed by total digestion varied from about 0.2 to 32 mg (Paces et al. 2001 [156507], Appendix 2b) compared to total masses less than 0.05 µg for IMP spots.

Table 6.14.3-1. Microstratigraphic Depth, Date and Initial $^{234}U/^{238}U$ Activity Ratios for HD2074 Opal Determined by Ion Probe

Spot No.	Spot ID	Micro-stratigraphic depth from outer surface, (µm)	$^{230}Th/U$ date[a] (ka)	Initial $^{234}U/^{238}U$	ρ[b]	$^{234}U/^{238}U$ estimated date (ka)
17	2074-g2-1.1	--	441 ±750	1.39 ±0.71	0.96	1426 ±379
18	2074-g2-2.1	27	51.9 ±8.2	7.57 ±0.33	0.11	42 ±29
19	2074-g2-3.1	75	137 ±19	7.53 ±0.35	0.63	128 ±27
20	2074-g2-4.1	135	183 ±36	6.62 ±0.51	0.81	228 ±32
21	2074-g2-5.1	237	268 ±110	6.0 ±1.4	0.95	353 ±48
22	2074-g2-6.1	340	298 ±120	4.5 ±1.1	0.97	516 ±46
23	2074-g2-7.1	467	560 ±600	5.4 ±7.2	1.00	693 ±39
24	2074-g2-8.1	740	Excess ^{230}Th	Undefined		1041 ±78
25	2074-g2-9.1	29	47.7 ±7.1	7.26 ±0.29	0.09	54 ±28
26	2074-g2-10.1	31	51.7 ±9.8	7.33 ±0.37	0.11	55 ±33
27	2074-g1-1.1	36	51.7 ±7.5	7.46 ±0.29	0.11	47 ±28
28	2074-g1-2.1	95	177 ±29	7.69 ±0.49	0.80	160 ±28
29	2074-g1-3.1	158	266 ±65	7.18 ±0.99	0.96	278 ±31
30	2074-g1-4.1	60	131 ±32	7.40±0.59	0.59	130 ±41
31	2074-g1-5.1	211	314 ±200	5.5 ±2.3	0.98	437 ±61
32	2074-g1-6.1	305	675 ±1700	9 ±38	1.00	584 ±52
33	2074-g1-7.1	10	34.4 ±7.6	7.32 ±0.48	-0.09	38 ±40

DTN: GS021208315215.008 [164851]

NOTE: [a] Date and 95% confidence errors calculated using decay-constants given by Cheng et al. 2000 [153475].
[b] Correlation coefficient between date and initial $^{234}U/^{238}U$.
Calculation of estimated $^{234}U/^{238}U$ ages is summarized in Attachment IX.4.2, using Eq. IX.4.2-1.

The $^{230}Th/U$ dates calculated for IMP spots range from 34.4 ± 7.6 to 675 ± 1,700 ka, and increase progressively with depth below the outermost surface (Table 6.14.3-1, Figure 6.14.3-1). The very large errors for spots older than 200 to 300 ka are a consequence of large uncertainties in measured $^{230}Th/^{238}U$ activity ratios (AR) and the reduced dating resolution as ^{230}Th approaches about five half lives. For the nine spots with dates <200 ka, calculated initial $^{234}U/^{238}U$ AR vary from 6.62 to 7.69 and yield a weighted average value of 7.38 ± 0.19. Approximating that percolating fracture water retained this $^{234}U/^{238}U$ AR over longer time periods, measured $^{234}U/^{238}U$ AR can be used to estimate model dates as old as several million years. Using the

average initial $^{234}U/^{238}U$ AR value for spots <200 ka, model $^{234}U/^{238}U$ dates between about 280 and 1,430 ka are estimated for spots with $^{230}Th/U$ dates >200 ka (Table 6.14.3-1). Relative uncertainties between 6 and 14% for most of these estimated dates are propagated using both the $^{234}U/^{238}U$ analytical errors and the error for the weighted initial $^{234}U/^{238}U$ AR, and may underestimate the true age uncertainty. Nevertheless, they allow further comparisons of data from younger and older parts of the hemispheres not possible with $^{230}Th/U$ dating alone. In most cases, estimated $^{234}U/^{238}U$ dates agree (within error overlap) with $^{230}Th/U$ dates over the entire dated range (Table 6.14.3-1).

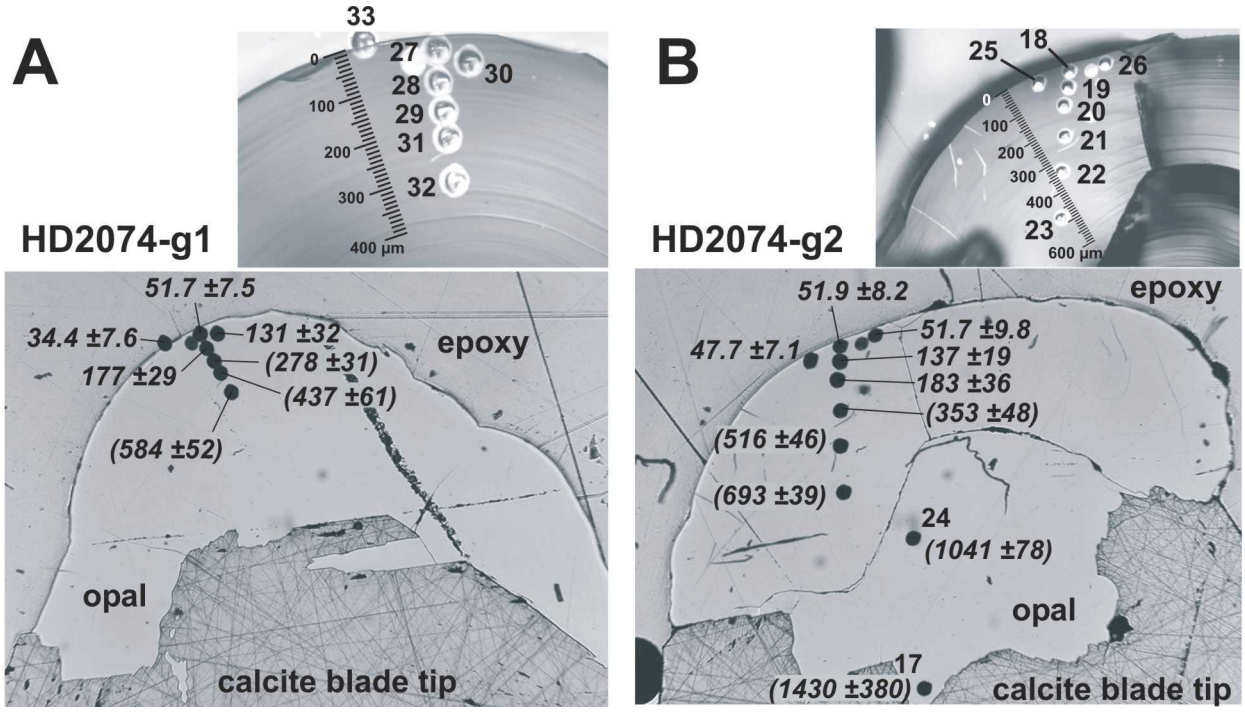

DTN: GS021208315215.008 [164851]

NOTE: Ablation pits are numbered for reference to Table 6.14.3-1. $^{230}TH/U$ dates in thousands of years are given for microstratigraphically higher pits, and model $^{234}U/^{238}U$ dates in thousands of years (in parentheses) are given for microstratigraphically lower pits. Calculation of estimated $^{234}U/^{238}U$ ages is summarized in Attachment IX.4.2, using Eq. IX.4.2-1.

Figure 6.14.3-1. Cross Sections of Two Opal Hemispheres Analyzed by Ion Microprobe Shown under Transmitted Light (Upper Images) and Reflected Light (Lower Images)

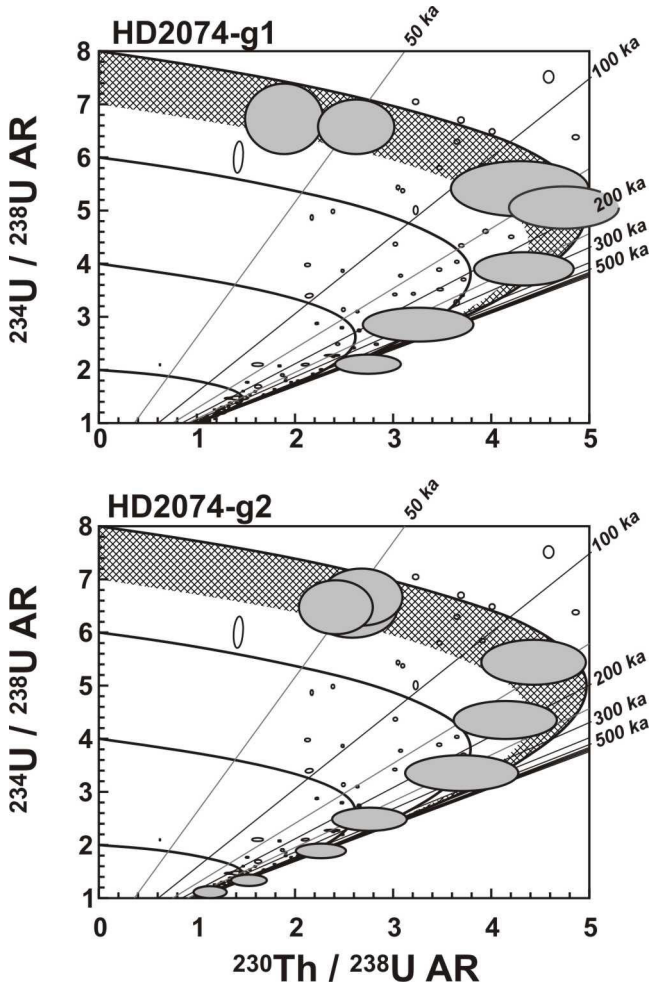

DTN: GS021208315215.008 [164851]

NOTE: Dark curved lines are the traces of activity ratios (AR) developed through time in a closed isotopic system. The Cross-hatched are as show the isotopic compositions of material evolving from initial $^{234}U/^{238}U$ AR values between 7 and 8. Thin straight lines represent isochrones with ages in thousands of years (ka). Analyses of whole opal hemispheres and sheets from Paces et al. 2001 [156507], Figure 13) are shown as small, open 2σ error ellipses. Calculation of estimated $^{234}U/^{238}U$ ages is summarized in Attachment IX.4.2, using Eq. IX.4.2-1.

Figure 6.14.3-2. U/Th Isotope Evolution Plot for Ion-Microprobe Analyses of Opal Hemispheres (Large, Shaded 2σ Error Ellipses)

The IMP dates are correlated with microstratigraphic depth within each transect of the two opal hemispheres analyzed (Figure 6.14.3-3). Both $^{230}Th/U$ dates and $^{234}U/^{238}U$ model dates were used to calculate slopes (Attachment IX.5) that represent average growth rates of 0.56 ± 0.14 µm/k.y. (equivalent to mm/m.y.) for HD2074-g1, and 0.683 ± 0.045 µm/k.y. for HD2074-g2. These rates are about 2 to 10 times smaller than the long-term average growth rates reported by Neymark et al. (1998 [109140]; 2002 [158673]) calculated from $^{207}Pb/^{235}U$ dates of interior opal and chalcedony. IMP data indicate that individual opal hemispheres take more than a million years to form, and that, at the scale of resolution used for IMP analyses, growth rates remained uniform throughout the late and middle Pleistocene.

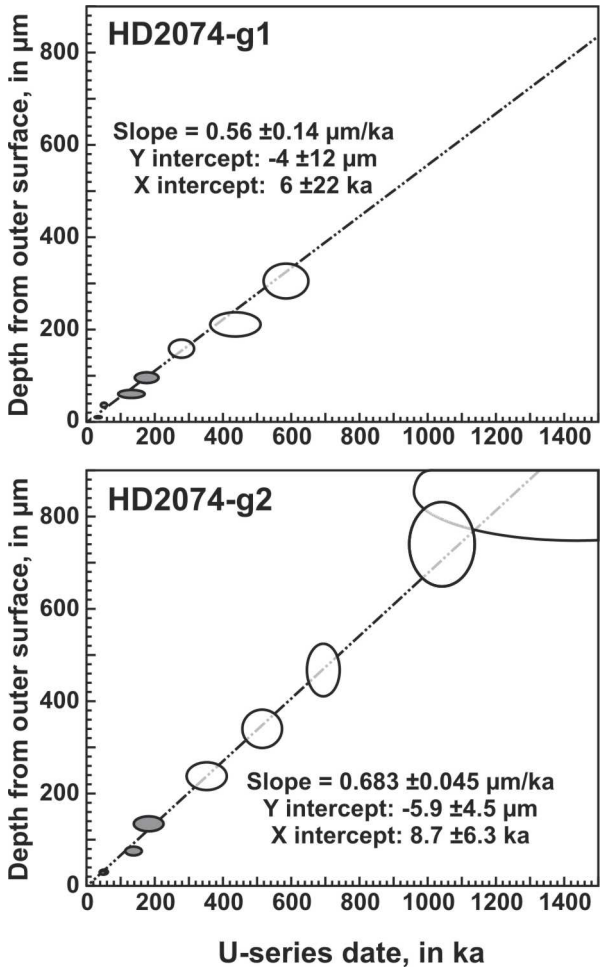

DTN: GS021208315215.008 [164851]

NOTE: ^{230}Th/U dates are shown as shaded symbols with 2σ error ellipses and mode ^{234}U/^{238}U dates (based on an initial ^{234}U/^{238}U ratio of 7.38 ± 0.19) are shown as open symbols with 2σ error ellipses. Errors for microstratigraphic depth are assumed to be 10% of the measured value. Calculation of estimated ^{234}U/^{238}U ages is summarized in Attachment IX.4.2, using Eq. IX.4.2-1.

Figure 6.14.3-3. Depth-Age Relations for Profiles of Opal Hemispheres Analyzed by Ion Microprobe (spot locations Shown in Figure 6.14.3-1)

Microdigestion TIMS Results: Previous conventional TIMS analyses of three 1 mm diameter whole opal hemispheres from sample HD2074 (Paces et al. 2001 [156507]) yield ^{230}Th/U dates ranging from 153.0 ± 1.9 to 226.8 ± 7.4 ka, with initial ^{234}U/^{238}U AR of 4.2 to 2.7 (Table 6.14.3-2). These initial ^{234}U/^{238}U ratios are much lower than those observed for opal analyses less than 100 ka (typically greater than 6, Paces et al. 2001 [156507]), or for IMP results presented above (7.38). In addition, initial ^{234}U/^{238}U AR for these three HD2074 whole-hemisphere digestions are negatively correlated with age. These features are indications that whole-hemisphere digestions represent mixtures of older and younger material (Neymark and Paces 2000 [127012]; Neymark et al. 2000 [158673]). Therefore, *in situ* microdigestions of similar materials were conducted to refine growth histories of individual hemispheres.

Table 6.14.3-2. U and Th Isotopic Results from HD2074 Opal Hemispheres

Sample Name[a]	Digestion duration, minutes	Estimated thickness (μm)[b]	Estimated weight (μg)[b]	Measured U abundance (ng)[b]	U concentration (μg/g)[b]	Th concentration (μg/g)[b]	Measured $^{230}Th/^{232}Th$ AR	$^{230}Th/^{238}U$ AR[c]	$^{234}U/^{238}U$ AR[c]	$^{230}Th/U$ date[d] (ka)	Initial $^{234}U/^{238}U$ AR[d]
Whole hemisphere total digestions											
HD2074-U1R	n.a.	~1,000	2870	467	162.64	0.009	641,700	2.629 ±0.014	3.089 ±0.012	153.0 ±1.9	4.220 ±0.016
HD2074-U3R	n.a.	~1,000	10090	1278	126.71	0.008	278,700	2.464 ±0.014	2.787 ±0.011	166.2 ±2.2	3.859 ±0.016
HD2074-U4R	n.a.	~1,000	9120	878	96.29	0.007	137,900	1.865±0.015	1.899 ±0.016	226.8 ±7.4	2.706 ±0.023
Single in situ microdigestions											
HD2074 - HF1	<3	n.d.	n.d.	0.474	n.d.	n.d.	20.0	0.525 ±0.12	6.80 ±0.14	8.7 ±2.0	6.95 ±0.14
HD2074-HF2	<3	n.d.	n.d.	0.043	n.d.	n.d.	3.34	0.25 ±0.11	6.80 ±0.63	4.0 ±1.9	6.86 ±0.63
HD2074-HF3	<3	n.d.	n.d.	0.571	n.d.	n.d.	99.5	0.68 ±0.03	6.63 ±0.13	11.6 ±0.6	6.82 ±0.13
HD2074-MD2	<3	n.d.	n.d.	0.519	n.d.	n.d.	1.72	0.57 ±0.17	8.41 ±0.98	7.6 ±2.8	8.57 ±0.97
Sequential in situ microdigestions											
HD2074-T1a	1-2	n.d.	n.d.	12.647	n.d.	n.d.	1,250	0.344 ±0.005	6.043 ±0.082	6.34 ±0.12	6.134 ±0.082
HD2074-T1b	3	n.d.	n.d.	0.744	n.d.	n.d.	130	0.901 ±0.069	6.421 ±0.058	16.2 ±1.3	6.674 ±0.061
HD2074-T1c	12	n.d.	n.d.	1.635	n.d.	n.d.	720	1.490 ±0.056	6.089 ±0.054	29.5 ±1.3	6.531 ±0.058
HD2074-T1d	12	n.d.	n.d.	1.220	n.d.	n.d.	1,430	2.393 ±0.076	5.213 ±0.049	61.4 ±2.5	6.011 ±0.059
HD2074-g2-L1	2	1.5	7.2	2.21	310	1.3	550	0.430 ±0.038	6.574 ±0.089	7.3 ±0.7	6.691 ±0.090
HD2074-g2-L2	2	1.5	7.2	3.13	430	2.7	580	0.671 ±0.074	6.561 ±0.058	11.6 ±1.3	6.747 ±0.062
HD2074-g2-L3	3	2.3	11	4.81	450	2.4	940	0.932 ±0.011	6.649 ±0.084	16.1 ±1.2	6.913 ±0.086
HD2074-g2-L4	3	2.3	11	4.50	420	0.9	3,300	1.350 ±0.077	6.435 ±0.041	24.9 ±1.6	6.831 ±0.048
HD2074-g2-L5	4	3.0	14	5.10	350	0.0	5,700	1.427 ±0.034	6.492 ±0.042	26.2 ±0.7	6.914 ±0.044
HD2074-g2-L6	5	3.8	18	6.89	380	1.2	2,800	1.620 ±0.023	6.375 ±0.036	30.7 ±0.5	6.862 ±0.037
HD2074-g2-L7	5	3.8	18	7.99	450	0.8	5,000	1.593 ±0.055	6.362 ±0.034	30.2 ±1.2	6.840 ±0.039
HD2074-g2-L8	5	3.8	18	9.37	530	0.6	10,200	1.908 ±0.071	6.347 ±0.039	37.1 ±1.6	6.938 ±0.047

DTN: GS021208315215.009 [164750]

[a] All subsamples are from station 30+51 in the Yucca Mountain Exploratory Studies Facility, at a depth of 270 m below land surface.

[b] Weights and concentrations for whole-hemisphere digestions are measured directly. Thicknesses, weights, and concentrations for in situ digestions are estimated by methods explained in the text.

[c] Isotope ratios are corrected for contributions from spike and blank and for mass fractionation. $^{230}Th/^{238}U$ and $^{234}U/^{238}U$ ratios are also corrected for contributions from a secular equilibrium detrital component with activity ratios of $^{232}Th/^{238}U = 1.9 \pm 0.95$, $^{230}Th/^{238}U = 1.0 \pm 0.5$, and $^{234}U/^{238}U = 1.0 \pm 0.2$. Uncertainties are given at the 95% confidence level.

[d] $^{230}Th/U$ date and initial $^{234}U/^{238}U$ calculated from ^{232}Th-corrected isotope ratios with uncertainties given at the 95% confidence level.

Not applicable (n.a.); not determined (n.d.)

Values for $^{230}Th/U$ dates are taken directly from Paces et al. (2001 [156507]). Ages are estimated from an approach similar to $^{234}U/^{238}U$ ages described in Attachment IX.4.2.

Initial microdigestion results yielded much younger ^{230}Th/U dates (4.0 ± 1.9 to 11.6 ± 0.6 ka; Table 6.14.3-2) and higher initial ^{234}U/^{238}U AR values (6.80 to 8.6) than those obtained for whole-hemisphere digestions (see Attachment IX.5 for calculations). A second set of experiments involving sequential microdigestions from a single opal hemisphere yielded ages ranging from 6.3 ± 0.1 to 61.4 ± 2.5 ka, with intial ^{234}U/^{238}U AR from 6.0 to 6.7. A third set of microdigestions was conducted on one of the same opal hemispheres used for IMP analysis (HD2074-g2). The remaining hemisphere was extracted from the microprobe mount and glued onto a glass slide, so that the outer surface was oriented upwards. In this series of sequential microdigestions, repeated measurements of surface elevation were made to yield surface profiles after each step. Dates for the HD2074-g2 sequential microdigestions range from 7.3 ± 0.7 to 37.1 ± 1.6 ka and initial ^{234}U/^{238}U AR vary from 6.69 to 6.94. The resulting ^{230}Th/U dates form a smooth pattern of increasing age when plotted against depth from the outermost surface (Figure 6.14.3-4), with a possible inflection point around 25 ka (Attachment IX.5). The four HD2074-g2 microdigestion analyses with dates less than 25 ka yield a regression with a shallower slope of 0.35 ± 0.23 μm/k.y., whereas the five microdigestion analyses with dates greater than 20 ka yield a regression with a steeper slope of 1.16 ± 0.35 μm/k.y. All data from microdigestions of HD2074-g2 yield a combined regression slope of 0.68 ± 0.22 μm/k.y (Attachment IX.5).

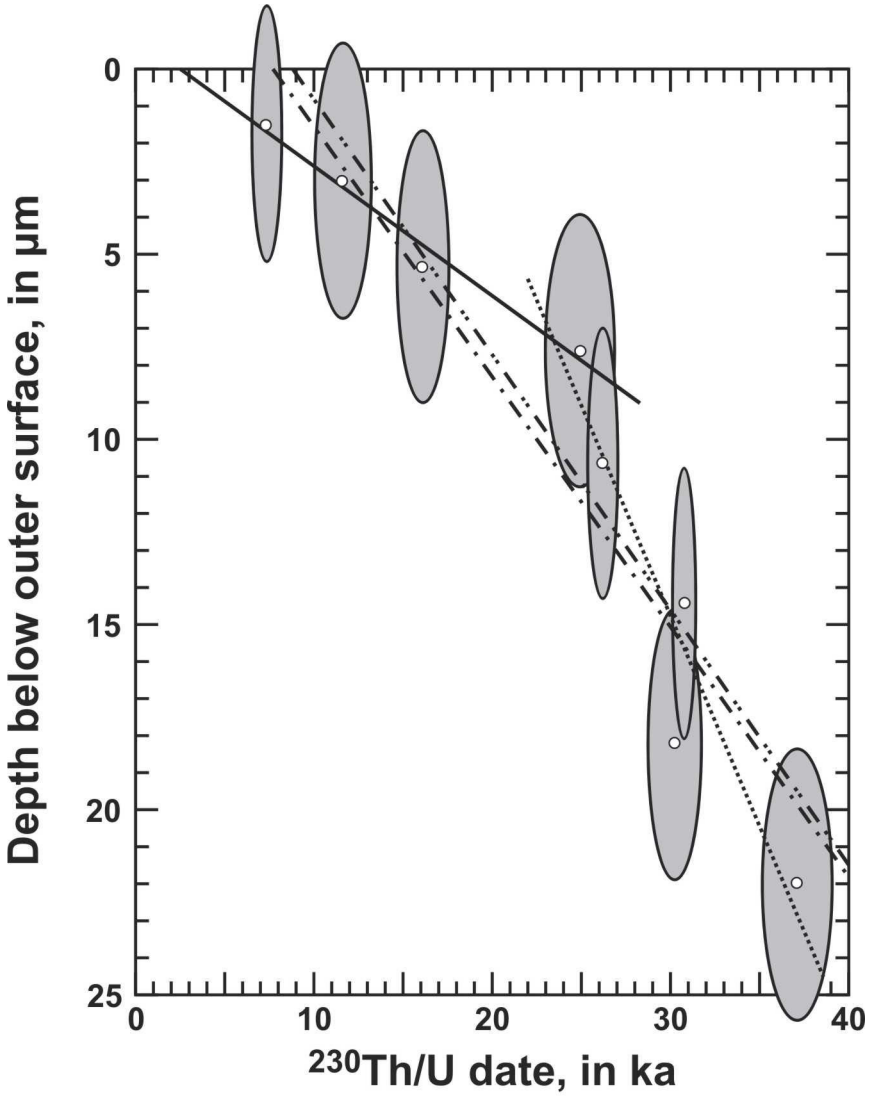

DTN: GS021208315215.009 [164750]

NOTE: Two-sigma error ellipses are shown, along with various regressions using 2σ age uncertainties from Table 6.14.3-2 and a constant 3 μm depth uncertainty. Also shown is the regression curve extrapolated from data older than 48 ka determined by ion microprobe for the same hemisphere (Figure 6.14.3-3). Values for ^{230}Th/U dates are taken directly from Paces et al. (2001 [156507]). Ages are estimated from an approach similar to ^{234}U/^{238}U ages described in Attachment IX.4.2.

Figure 6.14.3-4. Depth-Age Relations for Sequential Microdigestions of Opal Hemisphere HD2074-g2

Discussion: U-series dates and growth rates are determined at much finer scales of spatial resolution by IMP and microdigestion TIMS analyses than by previous whole-hemisphere TIMS

methods. IMP spots integrate material deposited over about 35 μm, whereas microdigestion TIMS analyses integrate opal deposited over thicknesses of less than 5 μm. Outermost IMP spots have ^{230}Th/U dates that cluster around 50 ka, whereas microdigestion TIMS analyses indicate that this same interval consists of layers deposited more recently. Conversely, IMP ^{234}U/^{238}U model dates for deeper layers show that material in the interior of the hemispheres is more than a million years old.

Data collected at higher spatial resolutions are consistent with the previously hypothesized model of long-term "continuous" deposition for Yucca Mountain secondary minerals, in the sense that secondary minerals formed slowly over extended periods of time. However, the microdigestion data imply that growth rates were not necessarily constant and that depositional hiatuses may occur during periods of low infiltration. These aspects were anticipated previously (Neymark and Paces 2000 [127012], p. 158; Paces et al. 2001 [156507], p. 55), but could not be demonstrated without finer spatial resolutions.

The limited data currently available suggest that Pleistocene growth rates were slower than those present during the Miocene. Compared with the long-term average growth rates of 1 to 5 mm/m.y. for Miocene-to-Pleistocene deposits (Neymark et al. 2002 [158673]), the average Pleistocene growth rate determined for the HD2074 opal (0.68 mm/m.y.) is almost 10 times lower than the Miocene-Pleistocene rate. Reduced Pleistocene growth rates may reflect a shift to increased aridity in the region over the last 2 million years (Axelrod 1979 [161531]; Winograd et al. 1985 [109187]; Thompson 1991 [109175]). Previous studies (Paces et al. 2001 [156507]) did not identify these small differences because of the averaging effects of the milligram- rather than microgram-sized samples.

The microdigestion TIMS data represent the first evidence that mineral growth rates in the Yucca Mountain UZ may have varied during the late Pleistocene. Age-depth relations imply faster growth rates under pluvial/glacial climate conditions between 20 and 40 ka, and slower growth rates during transitional and interpluvial climate conditions after that. The absence of reasonably precise dates for outermost layers less than 6.34 ± 0.12 to 7.3 ± 0.7 ka, plus the non-zero age intercept between 3 and 9 ka for depth-age regressions, imply that no opal has been added in the past several thousand years.

The correlation of growth rates with variable Pleistocene climates indicates that mineral growth is correlated with percolation flux. Infiltration and UZ percolation are likely to be greatest during episodes of greatest mean annual precipitation and coolest mean annual temperature when evaporation/evapotranspiration is minimized. Full pluvial/glacial climate conditions at Yucca Mountain resulted in greater surface- and groundwater fluxes up to about 15 to 20 ka (Spaulding 1985 [106883]; Paces et al. 1993 [106474]; Lundstrom et al. 1996 [136523]; Forester et al. 1999 [109425]; Paces and Whelan 2001 [154724]). Greater UZ fluxes during this time resulted in larger mineral growth rate (1.16 mm/m.y.) compared to the lower rates (0.35 mm/m.y.) associated with glacial transition conditions between about 10 and 20 ka. The possible absence of mineral growth over the last several k.y. implies that fracture flow supplying solute to the HD2074 depositional site may have ceased during the driest interglacial periods. Time lags between climate variability and percolation deep within Yucca Mountain of up to thousands of years may also complicate the relations between surface and UZ hydrology; however, these

initial results are encouraging evidence of a climate-percolation relation that warrants confirmation from additional sites.

Two methods of U-series dating were applied to finely laminated opal hemispheres formed within unsaturated felsic tuffs at Yucca Mountain. The first method used an ion microprobe to determine isotope compositions of 45 μm diameter spots on transects across two mm sized opal hemispheres; the second used *in situ* microdigestions to sequentially remove 2–5 μm thick layers of outermost material. Both methods substantially improved spatial resolution of the analyses relative to the millimeter-scale subsamples analyzed previously by standard total digestion techniques. As a result, more detailed reconstructions of the opal growth histories can be obtained.

6.14.3.2 U-series Delineation of UZ Flow Zones

Samples from two areas in the underground workings at Yucca Mountain (Figure 6.14.3-5) were selected for analysis of ^{234}U-^{230}Th-^{238}U by TIMS. Details of the analytical techniques are given in footnotes to Table 6.14.3-3, and are described in the data package DTN: GS021208312272.008 [164609] and in Paces and Neymark (2003 [162900]). Three samples of TSw tuff were collected from two sites in the ECRB Cross Drift within the repository block at depths of 220 to 300 m below land surface and 120 to 200 m below the base of the PTn (HD2423-HD2425, Figure 6.14.3-5). In addition, 11 samples of TCw tuff and post-TCw nonwelded tuff were collected along a profile across the Bow Ridge fault zone in the ESF tunnel at depths of only 20 to 30 m below land surface (HD2426-HD2436, Figure 6.14.3-5). The two different sample localities were selected to represent areas of lower percolation flux in the ECRB Cross Drift below the PTn and higher flux in the near-surface ESF environment that may be further focused along the Bow Ridge fault zone. In addition, samples were collected to represent hydrologically "active" sites (containing fractures clearly associated with visible secondary hydrogenic mineral deposits) and "inactive" sites (unfractured material or fractured rock lacking secondary minerals).

Table 6.14.3-3. Uranium and Thorium Concentrations and ^{234}U-^{230}Th-^{238}U-^{232}Th Isotopic Compositions for Whole Rock-Samples from the ECRB Cross Drift and ESF Tunnels, Yucca Mountain, Nevada

Subsample Name	Location	Distance from start of tunnel or alcove, m	Lith-ology[a]	Distance from fracture surface, mm	Concentrations, in µg/g[b]				$^{232}Th/^{230}$ Th atomic[c]	Activity Ratios[c,d]					
					U ±2σ		Th ±2σ			$^{230}Th/^{238}U$ ±2σ		$^{234}U/^{238}U$ ±2σ		$^{232}Th/^{238}U$ ±2σ	
HD2423-U1	ECRB Cross Drift	1,640.8	TptpII	0.2	4.316	0.019	24.05	0.15	334,800	1.016	0.022	1.002	0.005	1.837	0.012
HD2423-U2	ECRB Cross Drift	1,640.8	TptpII	0.5	4.341	0.025	22.7	1.1	321,700	0.991	0.024	0.989	0.006	1.722	0.083
HD2423-U3	ECRB Cross Drift	1,640.8	TptpII	3	4.447	0.015	22.22	0.11	321,800	0.947	0.010	0.989	0.007	1.647	0.009
HD2423-U4	ECRB Cross Drift	1,640.8	TptpII	10	4.530	0.016	21.96	0.11	315,100	0.939	0.010	0.987	0.005	1.598	0.009
HD2424-U1	ECRB Cross Drift	1,641.1	TptpII	0.5	4.513	0.019	25.74	0.21	362,700	0.959	0.023	0.973	0.006	1.879	0.016
HD2424-U2	ECRB Cross Drift	1,641.1	TptpII	5	4.564	0.017	24.35	0.14	330,000	0.986	0.011	0.973	0.004	1.759	0.011
HD2424-U3	ECRB Cross Drift	1,641.1	TptpII	20	4.471	0.018	22.57	0.12	332,700	0.926	0.009	0.960	0.005	1.664	0.010
HD2425-U1	ECRB Alcove#8	1.2	Tptpul	0.5	4.453	0.019	29.62	0.16	434,300	0.934	0.010	0.948	0.005	2.193	0.013
HD2425-U2	ECRB Alcove#8	1.2	Tptpul	2	4.466	0.018	25.20	0.14	349,700	0.985	0.010	0.961	0.005	1.860	0.011
HD2425-U3	ECRB Alcove#8	1.2	Tptpul	19	4.377	0.017	23.71	0.14	338,000	0.978	0.014	0.963	0.005	1.786	0.011
HD2426-U1	ESF North Ramp	183.4	TpcpII	3	4.794	0.018	24.41	0.13	321,800	0.965	0.009	0.961	0.005	1.678	0.010
HD2426-U2	ESF North Ramp	183.4	TpcpII	16	4.891	0.018	25.74	0.15	343,100	0.936	0.008	0.964	0.005	1.735	0.011
HD2427-U1	ESF North Ramp	187.1	TpcpII	3	4.820	0.019	25.37	0.24	333,000	0.965	0.021	0.986	0.005	1.735	0.017
HD2427-U2	ESF North Ramp	187.1	TpcpII	22	5.081	0.022	24.23	0.15	307,100	0.947	0.008	0.991	0.006	1.572	0.010
HD2428-U1	ESF North Ramp	197.0	TpcpII	3	5.085	0.023	25.43	0.14	335,800	0.909	0.008	0.940	0.007	1.649	0.010
HD2428-U2	ESF North Ramp	197.0	TpcpII	25	4.972	0.020	24.66	0.14	337,400	0.897	0.008	0.949	0.007	1.635	0.010
HD2429-U1	ESF North Ramp	198.3	TpcpII	2	4.890	0.020	22.77	0.13	318,400	0.892	0.014	0.968	0.007	1.535	0.010
HD2429-U2	ESF North Ramp	198.3	TpcpII	15	4.788	0.021	23.78	0.14	339,500	0.892	0.012	0.966	0.006	1.637	0.010
HD2430-U1	ESF North Ramp	199.8	TpcpII	0.25	4.468	0.018	26.56	0.17	322,800	1.123	0.015	0.986	0.006	1.959	0.013
HD2430-U2	ESF North Ramp	199.8	TpcpII	3	4.425	0.017	24.11	0.13	320,200	1.038	0.009	0.971	0.005	1.796	0.011
HD2430-U5	ESF North Ramp	199.8	TpcpII	13.5	4.660	0.017	28.87	0.19	326,700	1.157	0.023	0.951	0.004	2.042	0.015
HD2431-U1	ESF North Ramp	199.9	fault rock	--	4.169	0.018	22.31	0.18	354,400	0.921	0.006	0.944	0.004	1.764	0.014
HD2431-U2	ESF North Ramp	199.9	fault rock	--	4.377	0.018	24.51	0.12	333,500	1.024	0.011	0.955	0.006	1.846	0.010
HD2432-U1	ESF North Ramp	200.6	fault rock	--	4.755	0.019	25.73	0.15	372,800	0.886	0.008	0.892	0.004	1.783	0.011
HD2433-U1	ESF North Ramp	200.5	fault rock	--	4.369	0.017	23.28	0.18	352,500	0.922	0.008	0.945	0.004	1.756	0.014
HD2434-U1	ESF North Ramp	203.3	post-TCw	--	2.800	0.012	20.56	0.11	545,400	0.821	0.010	0.764	0.008	2.420	0.015
HD2435-U1	ESF North Ramp	213.0	post-TCw	--	5.436	0.021	19.48	0.11	227,400	0.962	0.008	0.962	0.006	1.181	0.008
HD2436-U1	ESF North Ramp	215.7	post-TCw	--	4.903	0.018	21.94	0.11	280,300	0.974	0.010	0.973	0.006	1.475	0.009

[a] Lithostratigraphic unit designations from Buesch et al. (1996 [100106]) include TptpII (Topopah Spring Tuff lower lithophysal unit) and Tptpul (Topopah Spring Tuff upper lithophysal unit) in the TSw, and TpcpII (Tiva Canyon Tuff lower lithophysal unit) in the TCw.

[b] Concentrations determined by isotope dilution using known amounts of a mixed ^{236}U-^{229}Th tracer solution.

[c] Corrected for mass fractionation and contributions from spike and blank.

[d] Activity ratios calculated using decay constants $\lambda_{230} = 9.158 \times 10^{-6}$ yr^{-1}, $\lambda_{234} = 2.8262 \times 10^{-6}$ yr^{-1} (Cheng et al., 2000 [153475]), $\lambda_{238} = 1.55125 \times 10^{-10}$ yr^{-1} (Jaffey et al. 1971 [164637]), and $\lambda_{232} = 4.9475 \times 10^{-11}$ yr^{-1} (Steiger and Jäger 1977 [133377]). DTN: GS021208312272.008 [164609]

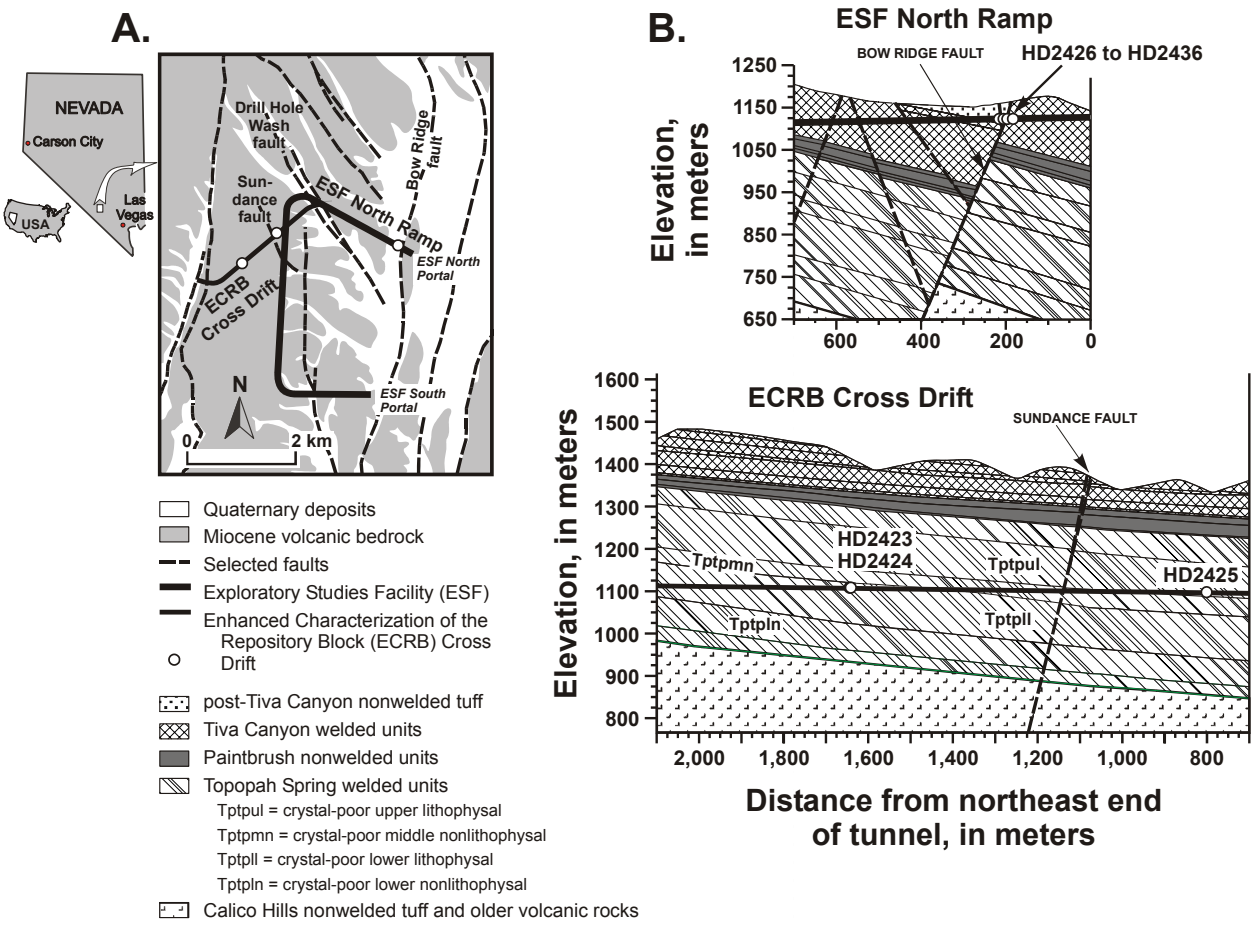

DTN: GS030808315215.001 [165426];
DTN: GS021208312272.008 [164609]; DTN: GS971108314224.020 [105561]; DTN: GS971108314224.021 [106007];
DTN: GS990408314224.001 [108396]; DTN: GS990408314224.001.002 [105625]

Figure 6.14.3-5. A. Generalized Geologic Map of Yucca Mountain Showing Sample Locations; B. Cross Sections along the Exploratory Studies Facility (ESF) North Ramp Tunnel Alignment (upper section) and the Enhanced Characterization of the Repository Block (ECRB) Cross Drift Tunnel Alignment (lower section) Showing Sample Locations

6.14.3.2.1 U-series Variations in Fracture Versus Matrix Samples

Both matrix and fracture flow may contribute to water/rock interactions and consequent U-series disequilibrium. To test for increased U mobility and $^{234}U/^{238}U$ fractionation on fracture surfaces relative to interiors of welded tuff fragments, investigators collected multiple subsamples at varying distances (0.2 to 25 mm) from discrete fracture surfaces. Distance profiles show constant or depleted U concentrations near fracture surfaces, whereas Th concentrations are commonly greatest for the subsamples closest to fracture surfaces (Table 6.14.3-3, Figure 6.14.3-6a). Given the very low solubility of Th in low temperature aqueous solutions (Kaufman 1969 [164722]; Langmuir and Herman 1980 [147527]), which is supported by the near absence of ^{232}Th in Yucca Mountain UZ secondary calcite and silica deposits (Paces et al. 2001 [156507]), the higher concentrations of Th on fracture surfaces are probably caused either by the removal of U

and more soluble cations while Th remained immobile, or by inclusion of small amounts of secondary manganese oxides, which preferentially concentrate Th (Neymark and Amelin 2002 [164725]). At the same time, $^{234}U/^{238}U$ AR remain constant across depth profiles whereas $^{230}Th/^{238}U$ AR show greater but nonsystematic variations (Figure 6.14.3-6b). Based on the small number of analyses for these subsamples, systematic differences in either the $^{234}U/^{238}U$ or $^{230}Th/^{238}U$ disequilibrium are not apparent between subsamples representing fracture surfaces and those obtained from the interiors of the same tuff fragments.

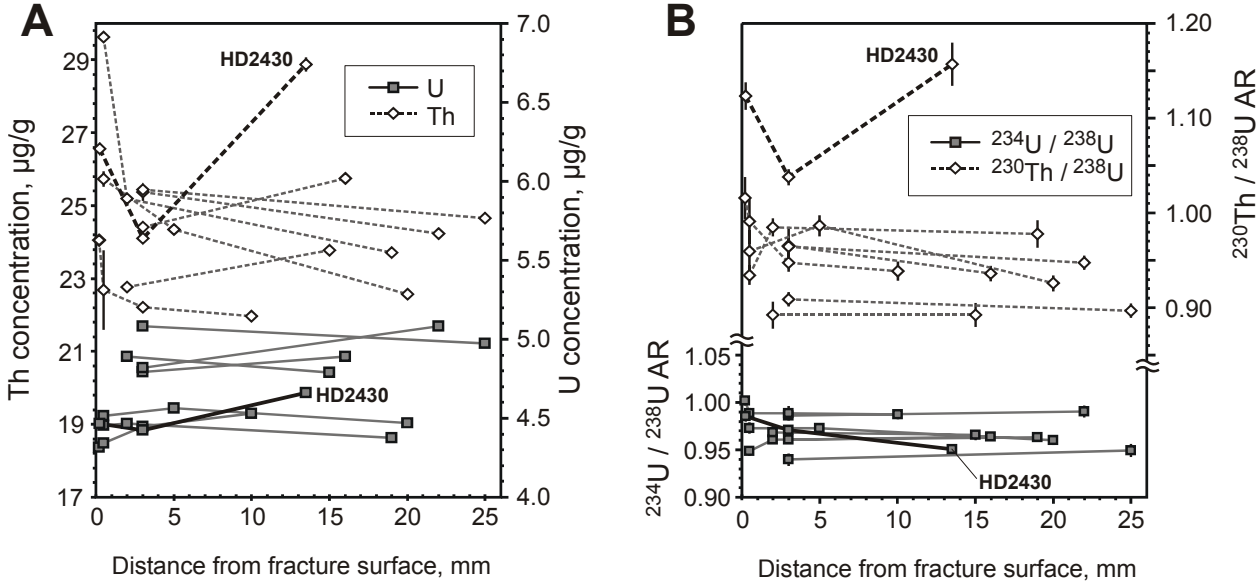

DTN: GS021208312272.008 [164609]

Figure 6.14.3-6. Variations of (A) Thorium and Uranium Concentration and (B) $^{234}U/^{238}U$ and $^{230}Th/^{238}U$ Activity Ratios (AR) in Yucca Mountain Whole-Rock Subsamples Plotted against Distance from the Fracture Surface

A notable exception to the observation of general consistency of both concentration and isotopic composition between fracture surfaces and interiors of individual tuff fragments was obtained for multiple subsamples of HD2430. This welded tuff sample was collected from the footwall surface of the Bow Ridge Fault (see "Shallow UZ samples" below). It shows not only the largest $^{230}Th/^{238}U$ AR values of all of the samples analyzed in this study, but also a large and erratic variation of both Th concentration and $^{230}Th/^{238}U$ AR with distance (Figure 6.14.3-6). In contrast, $^{234}U/^{238}U$ AR (Table 6.14.3-3) show a small but consistent decrease from the subsample representing the fracture surface (0.986 ± 0.006) to the innermost subsample (0.951 ± 0.004) at a distance of about 13.5 mm.

6.14.3.2.2 U-series Variations in Deep UZ Samples

Whole-rock $^{234}U/^{238}U$ and $^{230}Th/^{238}U$ AR show small but significant variations at depth within the TSw (Table 6.14.3-3 and Figure 6.14.3-7). Nearly all subsamples have $^{234}U/^{238}U$ AR between about 1.0 and 0.95; in most cases, values are statistically distinguishable from the secular equilibrium value of 1.0 that is expected for rocks undisturbed by water-rock interactions. Values of $^{230}Th/^{238}U$ AR are also lower than the secular equilibrium value of 1.0;

however, most analyses plot near the $^{234}U/^{230}Th$ "equiline" (equal ^{234}U and ^{230}Th activities), indicating that the observed ^{230}Th is in radioactive equilibrium with its immediate parent isotope, ^{234}U, present in the sample.

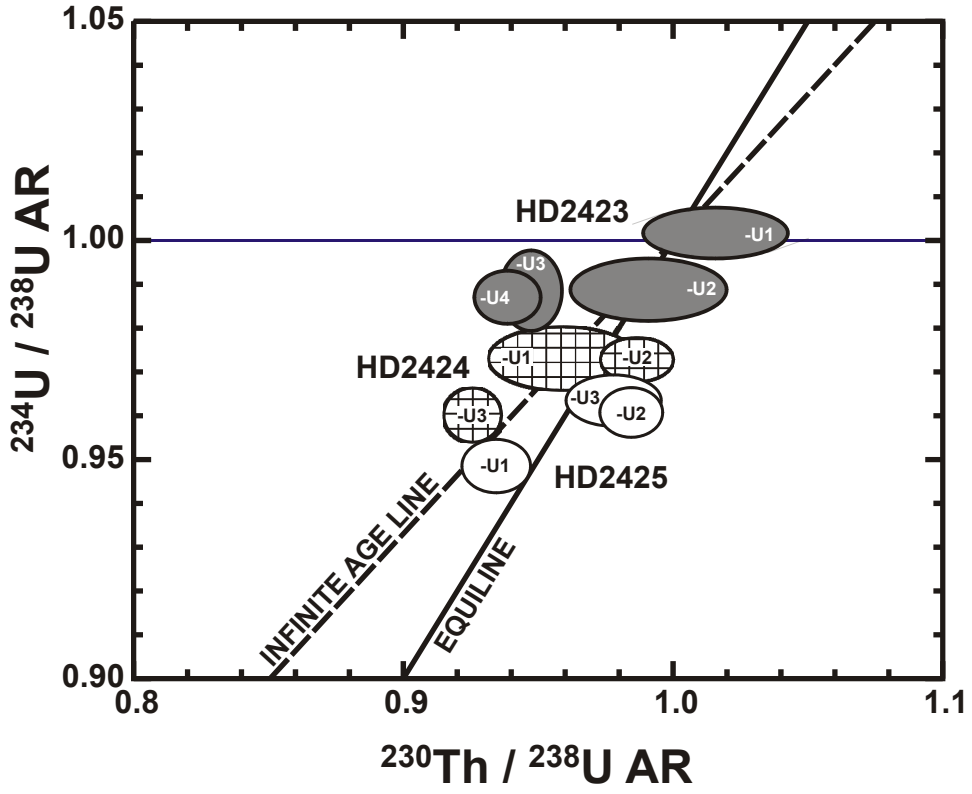

DTN: GS021208312272.008 [164609]

NOTES: Data are shown as 2σ error ellipses. Sample HD2423 (~300 m below land surface) shows no macroscopic evidence for fracture flow, whereas samples HD2424 (~300 m below land surface) and HD2425 (~220 m below land surface) are closely associated with hydrogenic calcite deposits indicating past fracture flow and seepage. The $^{230}Th/^{234}U$ equiline connects isotopic compositions with equal ^{230}Th and ^{234}U activities. The infinite-age line represents the loci of points for maximum $^{230}Th/^{238}U$ AR possible for a given $^{234}U/^{238}U$ AR under conditions of closed isotopic evolution.

Figure 6.14.3-7. Relations between $^{230}Th/^{238}U$ and $^{234}U/^{238}U$ Activity Ratios (AR) for Three Samples from the Cross Drift

Differences in the degree of radioactive disequilibrium between samples associated with sites supporting past fracture flow (as indicated by closely related secondary hydrogenic mineral deposits) also were compared with results from a sampling site lacking obvious evidence of fracture flow. Of the three TSw samples from the ECRB Cross Drift, HD2423 (at a distance of 1,640.8 m from the northeast end of the ECRB Cross Drift, Figure 1) is not associated with any visible secondary hydrogenic minerals, whereas samples HD2424 (at 1,641.1 m) and HD2425 (at 800 m) are both from sites with closely associated secondary calcite deposits. Resulting $^{234}U/^{238}U$ AR values (Table 6.14.3-3) for the "inactive" fracture (HD2423, shaded pattern in Figure 6.14.3-7) are closer to the secular equilibrium value of 1 compared to samples associated with "active" fracture flow (HD2424, hachured pattern and HD2425 open pattern in Figure 6.14.3-7), which have $^{234}U/^{238}U$ AR values in greater disequilibrium. In addition, sample HD2425 from a stratigraphically higher subunit of the TSw (crystal-poor upper lithophysal)

yields slightly greater $^{234}U/^{238}U$ disequilibrium than sample HD2424 from a stratigraphically lower subunit of the TSw (crystal-poor lower lithophysal). Therefore, these limited data support the expectation that water/rock interaction is greatest in areas that are associated with fracture flow and at shallower depths within the TSw.

6.14.3.2.3 U-Series Variations in Shallow UZ Samples

Samples from the ESF near the Bow Ridge fault zone consist of TCw in the footwall block, post-TCw nonwelded tuff in the hanging-wall block, and a mixture of the two lithologies in the 2 m wide fault zone (Figure 6.14.3-8). The sample traverse across the fault zone was intended to evaluate differences between normal fracture or matrix flow and focused flow within the highly brecciated fault zone within 30 m of the land surface.

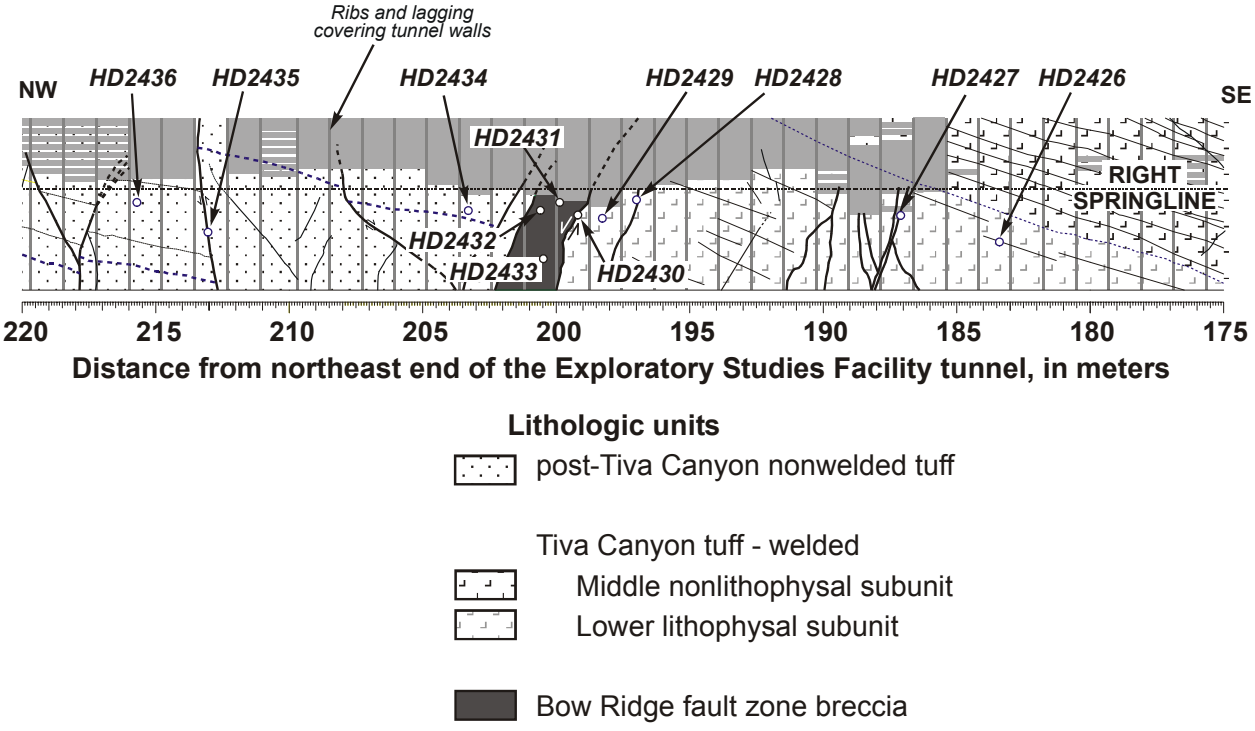

DTNs: GS950508314224.003 [107488]; GS021208312272.008 [164609]

NOTE: Map modified from Beason et al. 1996 [101191], pp. 175–220.

Figure 6.14.3-8. Map of the Right Rib of the Exploratory Studies Facility Tunnel Showing U-Series Sample Locations

In samples from the ESF near the Bow Ridge fault zone both $^{234}U/^{238}U$ and $^{230}Th/^{238}U$ AR span a wider range of values compared to analyses of the deeper TSw samples (Table 6.14.3-3). Eleven samples across the Bow Ridge fault zone all have $^{234}U/^{238}U$ AR values less than 1.0 (0.99 to 0.76), but $^{230}Th/^{238}U$ AR values that are both less than and greater than 1.0 (0.82 to 1.16; Figure 6.14.3-9). Samples from within the fault zone show the greatest degree of $^{230}Th/^{238}U$ disequilibrium with activity ratios between 1.04 and 1.16 for TCw sample HD2430 from the footwall surface. The surface of a centimeter-sized TCw clast within the fault zone (HD2431-U2) also has higher $^{230}Th/^{238}U$ AR (1.024 ±0.011) compared to values of 0.886 to 0.922 for bulk

samples of nonwelded matrix from within the fault zone (HD2431-U1, HD2432-U1, and HD2433-U1). These same samples with the highest $^{230}Th/^{238}U$ have relatively small amounts of ^{234}U depletion ($^{234}U/^{238}U$ AR of 0.951 to 0.986) that are comparable to other whole-rock samples from both the ESF and ECRB Cross Drift.

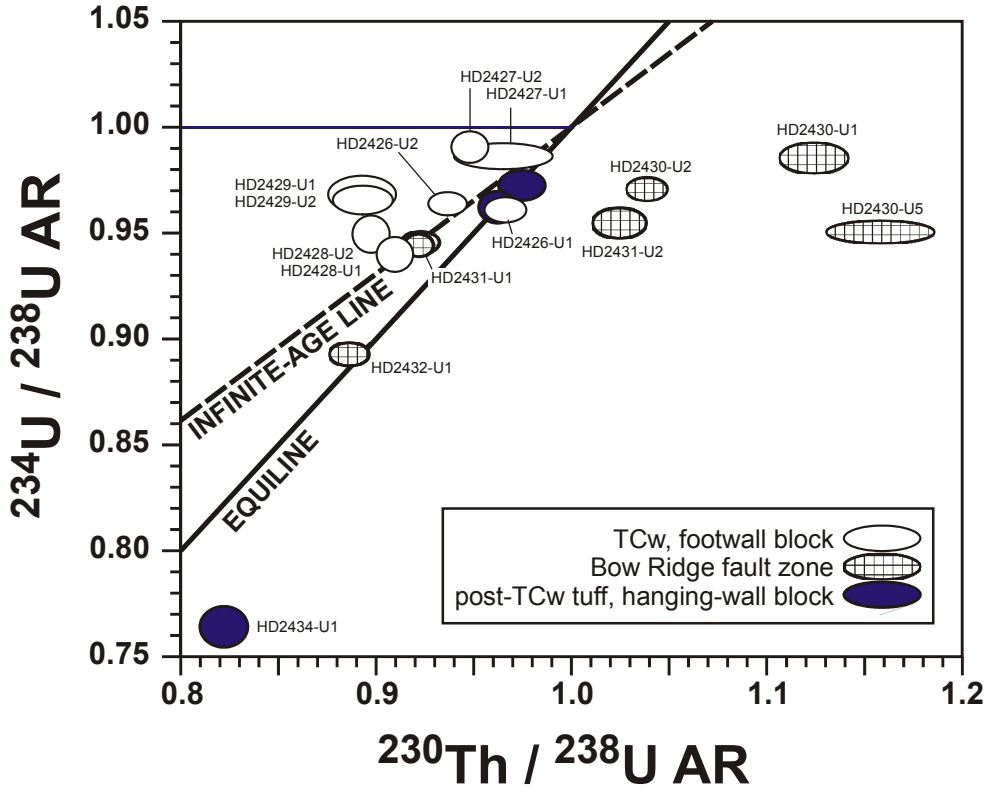

DTN: GS021208312272.008 [164609]

NOTE: All samples are from 20 to 30 m below land surface. $^{230}Th/^{234}U$ equiline and infinite-age line as in Figure 6.14.3-7.

Figure 6.14.3-9. U-series Isotopic Compositions (2σ Error Ellipses) for Samples from the Exploratory Studies Facility near the Bow Ridge Fault Zone

Two of three samples of post-TCw nonwelded tuff from the hanging-wall block have $^{234}U/^{238}U$ and $^{230}Th/^{238}U$ AR that plot along the equiline with only small amounts of ^{234}U depletion ($^{234}U/^{238}U$ AR of 0.962 and 0.973). Both analyses show overlapping compositions in spite of the fact that HD2435 is a sample of wall rock taken immediately adjacent to a 5–10 cm thick, near-vertical fracture filled with calcrete and tan pedogenic opal. In contrast, HD2434-U1, from 1 to 2 m west of the Bow Ridge fault zone, shows the greatest amount of ^{234}U depletion with a $^{234}U/^{238}U$ AR of 0.764 and a $^{230}Th/^{238}U$ offset somewhat from the equiline towards higher ^{230}Th.

6.14.3.2.4 Comparisons of Water-rock Environments

Preliminary results suggest that rates of ^{238}U loss are low in Yucca Mountain tuffs compared to crystalline rocks in other areas. The median value for the ^{238}U leach constant (c_8) is 1.3×10^{-7} yr^{-1}

for TSw samples and 6.2×10^{-7} yr^{-1} for TCw samples (Paces and Neymark 2003 [162900]). Calculated median c_4/c_8 values are 1.6 for TSw samples and 1.2 for TCw samples. These values support general geochemical arguments that the degree of fractionation between ^{234}U and ^{238}U is inversely proportional to the rate of U removal. In a study of U and Th in crystalline rocks from California, Wyoming, Colorado, and Illinois, Rosholt (1983 [164723]) found a wide range of U-series compositions. Median values of c_8 and c_4/c_8 calculated for these rocks using the same equations are 6.0×10^{-7} yr^{-1} and 1.05, respectively (Paces and Neymark 2003 [162900]). Higher values for c_8 were also calculated for Eye-Dashwa granite samples (1 to 2×10^{-6} yr^{-1}, Gascoyne and Schwarcz 1986 [164720]). Comparisons of these data sets are complicated by differences in analytical methods (TIMS versus alpha-decay counting) and the variety of sample types, including both surface and drill-core samples. In contrast to compositions of crystalline rock, fine-grained fluvial sediments exposed to extensive water/rock interactions have c_8 values ranging from 3 to 80×10^{-6} yr^{-1} (Vigier et al. 2001 [164719]).

6.14.4 Fracture Mineral Distribution and Mineralogy

Secondary (low-temperature) mineral deposits consist of ~1- to ~40 mm thick irregular coatings of predominantly calcite interlayered with lesser amounts of silica phases, including opal, chalcedony, and quartz. Other phases may also be present in minor amounts, including fluorite, clay minerals, zeolites, and manganese oxides; however, these phases are mostly present in older parts of the coatings (Paces et al. 2001 [156507], p. 8). Textural details of secondary minerals vary widely in both space and time (Paces et al. 2001 [156507], pp. 11–17; Whelan et al. 2002 [160442], p. 738). Calcite typically forms equant, blocky prisms on high-angle fracture surfaces, and unusually delicately bladed crystals in lithophysal cavities and in low-angle fractures. Opal typically forms water-clear solid-hemispheres, botryoidal masses, or thin sheets coating calcite substrates. Opal commonly occurs at the tops of calcite blades. Both opal and calcite are finely layered (micron to submicron) and commonly are intimately intergrown. Outermost surfaces of both minerals show little evidence of dissolution, although scattered patches of basal porous zones may be related to dissolution of early-formed calcite.

Most of the secondary mineralization within the UZ occurs as patchy coatings on the footwalls of fracture cavities or as irregular to hummocky accumulations on the floors of lithophysal cavities (Paces et al. 2001 [156507], p. 8; Whelan et al. 2002 [160442], p. 737). Hanging-wall surfaces and cavity ceilings are almost invariably devoid of calcite/silica deposits (Paces et al. 2001 [156507], pp. 10–11; Whelan, et al., 2002 [160442], p. 737). Although some small-aperture fractures may be completely filled with calcite, most secondary minerals are present in fractures and lithophysae with substantial open space. Calcite/silica deposits are present in only a small percentage of all fractures or lithophysae (Paces et al 2001 [156507], p. 11); more than 90% of the fractures and cavities exposed in the underground workings do not contain secondary minerals (Whelan et al. 2002 [160442], p. 738). This observation is considered strong evidence that secondary mineral deposits are related to fracture flow and seepage rather than to percolation through the matrix of the welded tuffs. Locations of secondary calcite/silica deposits within underground workings at Yucca Mountain are consistent with formation under hydrologically unsaturated conditions and are inconsistent with formation under even locally saturated conditions (Paces et al. 2001 [156507], p. 66; Whelan et al. 2002 [160442], p. 66).

The distribution of secondary minerals within the repository block has been estimated by two different methods. Mineral line-surveys based on visual observation were conducted along tunnel walls in both the ESF Main Drift and ECRB Cross Drift. The method involves visually estimating the physical dimensions of secondary mineral deposits within a 60 cm wide band of tunnel wall centered on a 30 m tape measure stretched at a height of 1.2 to 1.7 m above the concrete invert (floor) in the ESF, or between the conveyor belt and the right rib spring line in the ECRB Cross Drift. Thickness, length, and orientation of the mineral deposits were measured within the survey band, and cross-sectional areas of hydrogenic minerals were determined from these measurements. Sums of these areas are divided by the total surveyed area (30×0.6 m^2 less areas covered by ribs, lagging or muck) to obtain mineral abundances in percent. Local irregularities of the tunnel walls, the complex geometry of the mineral coatings, and the accumulation of rock dust obscuring mineral occurrences are sources of measurement error. Within the ESF, surveys typically were conducted on 100 m centers, resulting in 81 determinations for 78 stations. Within the shorter ECRB Cross Drift, surveys were conducted continuously from 750 m to 2,100 m in the drift. These surveys were partitioned into 38 separate 25 m or 30 m sections for comparison with the ESF surveys.

The second method of determining mineral abundances relied on the amount of CO_2 gas generated by acid treatment of cuttings produced during dry-drilling of two surface-based boreholes, USW WT-24 and USW SD-6. Cuttings were collected for each 5 feet of borehole advance, and representative splits were pulverized for CO_2 determination by gas chromatography (White et al. 1999 [151450]) and Ca determinations by x-ray fluorescence. Calcite abundances were calculated from measured CO_2 concentrations and compared to Ca contents from the same intervals. Concentrations of Ca and CO_2-derived calcite concentrations are highly correlated (R^2 values greater than 0.95) for compositionally uniform high-silica rhyolite in both the Tiva Canyon and Topopah Spring tuff units, and have slopes that are consistent with the addition of stoichometric calcite (dashed lines in Figure 6.14.4-1). In addition, calcite-free y-intercept Ca concentrations are similar to bulk-rock values of Ca reported for the Tiva Canyon high-silica rhyolite (average value of 1,800 µg/g Ca; Peterman and Futa 1996 [106494]) and Topopah Spring high-silica rhyolite (average value of 3,600 µg/g Ca; Peterman and Cloke 2002 [162576]).

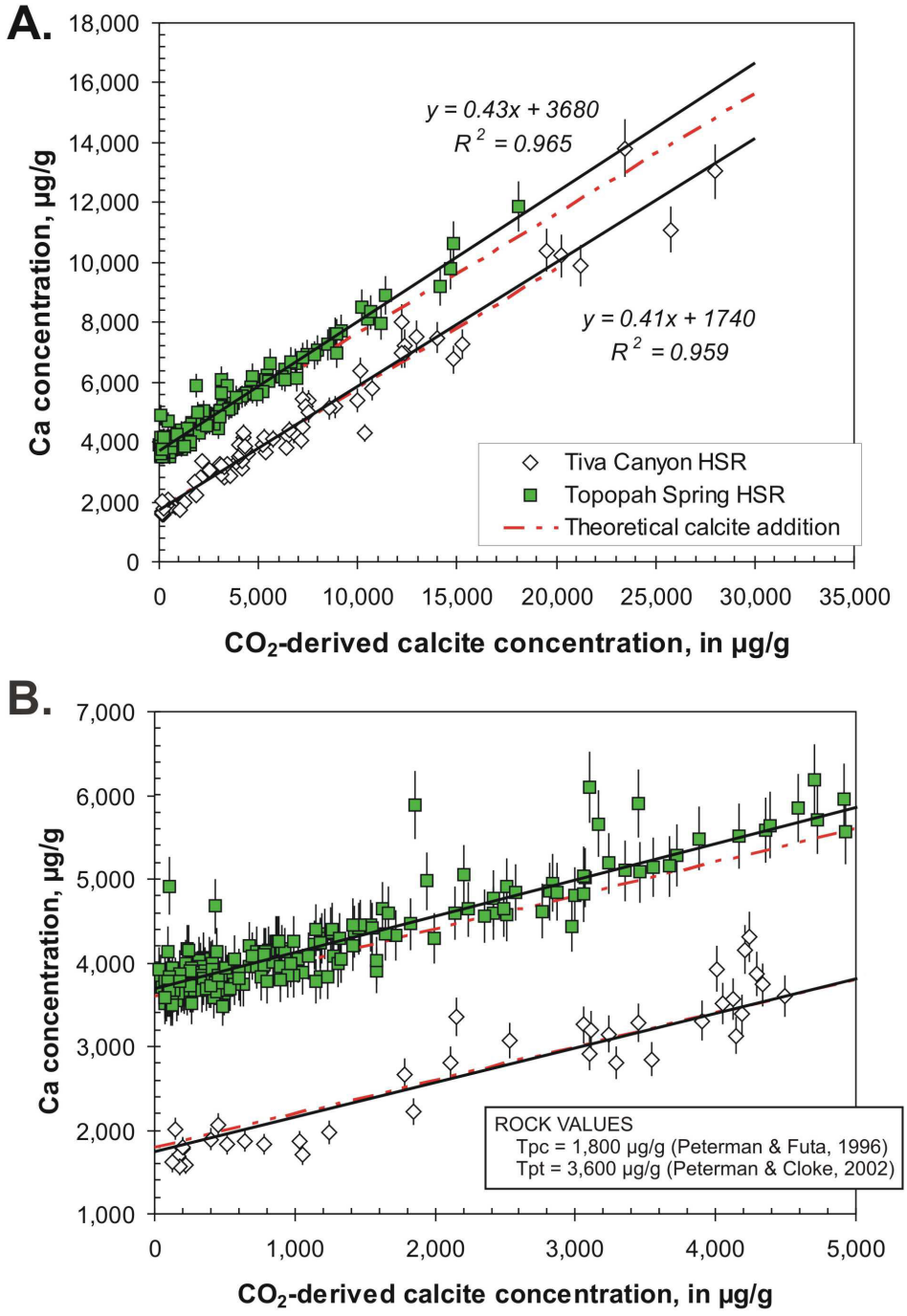

DTN: GS030908315215.002 [166097];
DTN: GS020608315215.002 [162126]; DTN: GS021008315215.007 [162127]

Figure 6.14.4-1. Relations between Ca Concentration Determined by X-ray Fluorescence and Calcite Concentration Determined by CO_2 Evolution for Cuttings of Tiva Canyon and Topopah Spring High-Silica Rhyolite from Boreholes USW SD-6 and USW WT-24

6.14.4.1 Results

ESF Line-Survey Results: Mineral abundances in the 78 ESF line-survey intervals ranged from no observed hydrogenic minerals to one that had 36 deposits yielding a total hydrogenic mineral abundance of 0.65% (Figure 6.14.4-2 and Figure 6.14.4-3). In general, nonwelded tuffs (PTn) with large matrix permeability and few open fractures or cavities have small hydrogenic mineral abundances compared to the welded tuffs (TCw and TSw). Abundance data for all intervals in welded tuffs (71 surveys) have an arithmetic mean of 0.084%; however, the frequency distribution is strongly skewed (Figure 6.14.4-4a). Logarithms of the mineral percentages are more symmetrically distributed around a mean value of 0.034% (Figure 6.14.4-4b), indicating that mineral populations averaged over 30-m intervals are better represented by lognormal distributions. In the following discussion, log means are used to represent the average mineral abundances when values for multiple survey intervals are given. See Attachment IX.1 and Attachment IX.2 for calculation details.

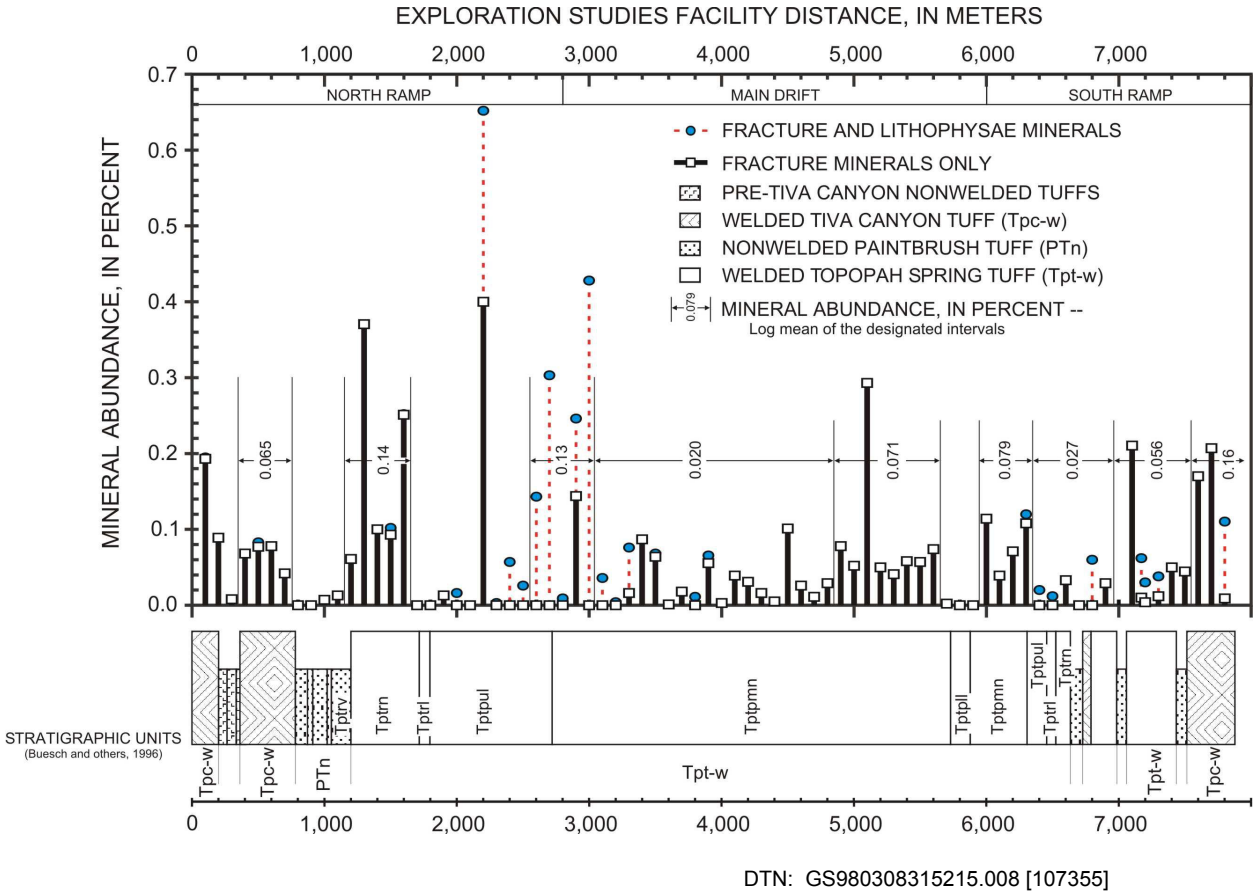

DTN: GS980308315215.008 [107355]

NOTE: Mineral abundances (log means in volume percent) are shown for selected intervals.

Figure 6.14.4-2. Hydrogenic Mineral Abundances for 30-m Surveys in the Exploratory Studies Facility (ESF) Plotted against Distance from the North Portal

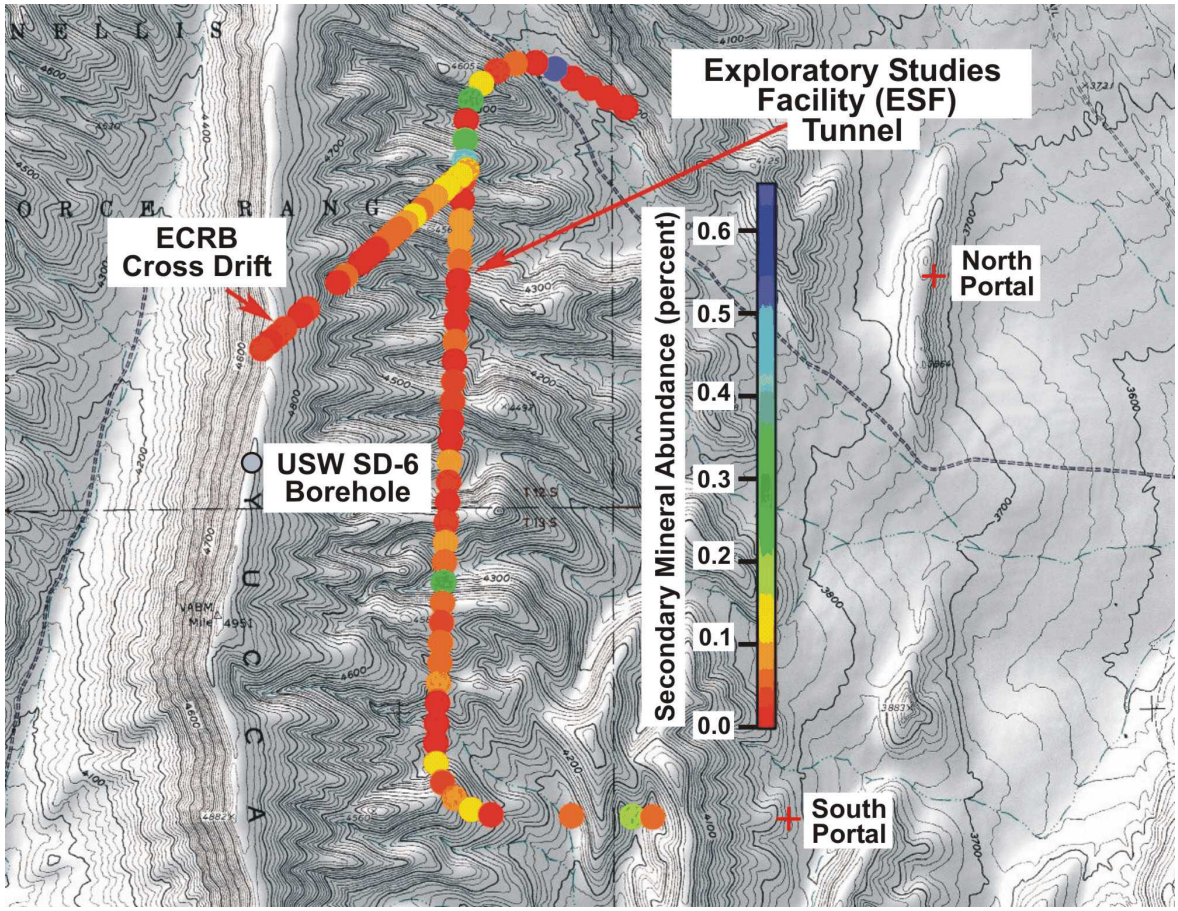

DTNs: GS980308315215.008 [107355]; GS030808315215.001 [165426]

NOTES: Calcite abundances (volume percent) estimated from line surveys in the TSw are shown by circles colored according to value. Base map is USGS Busted Butte quadrangle (7.5 minute series), contour interval is 20 feet (6.1 m).

Figure 6.14.4-3. Shaded Topographic Map of the Area Overlying the Underground Workings at the Repository Site

Several different factors may control the distribution of hydrogenic minerals in the subsurface, including topography, infiltration, fracture density, fault and shear frequency, and depth. None of these factors has a high degree of correlation with the measured mineral abundances, although the survey with the largest abundance is directly underneath Drill Hole Wash, the largest drainage overlying the underground workings (Figure 6.14.4-3). Models of infiltration generally predict greater infiltration over bedrock areas compared to alluvium-floored valleys (Flint et al. 2001 [156351]), resulting in the highest infiltration expected in the ESF main drift between 3,000 and 6,000 m. This ESF interval, however, generally contains low average mineral abundances (Figure 6.14.4-5c). Simulated infiltration values compared directly with the mineral-survey data (Marshall et al. 1998 [107415], Figure. 1) suggest a possible correlation in the TCw (r^2 value for linear regression = 0.43) based on a limited number (N = 7) of survey intervals; however, no correlation between simulated infiltration and mineral abundance is present in the TSw (r^2 = 0.009; N = 50, forced through zero). These observations are interpreted to indicate that other factors besides infiltration control the distribution of mineral abundances beneath the PTn.

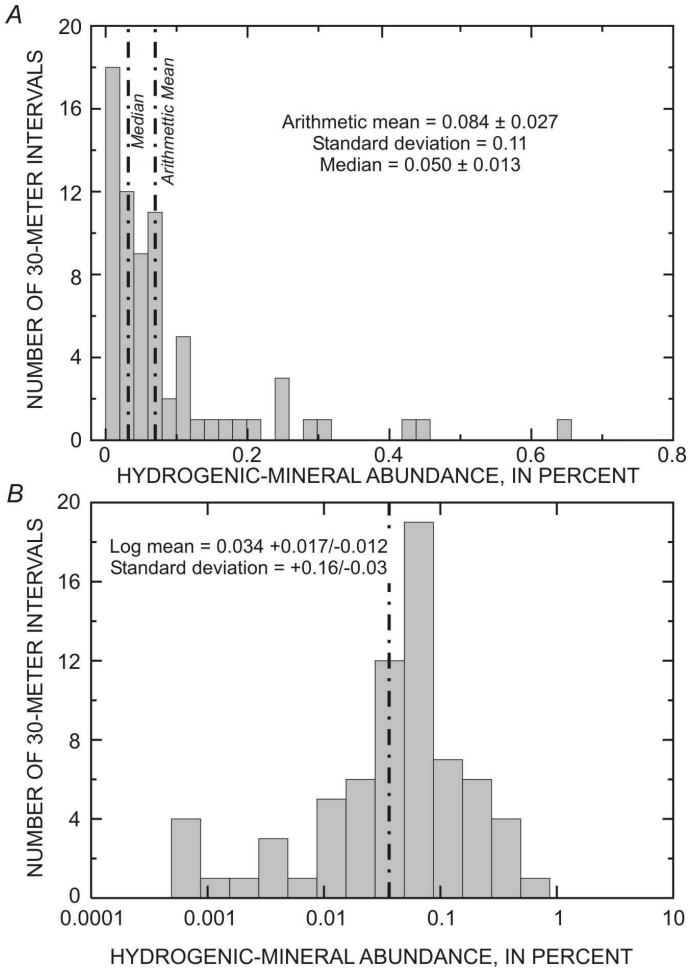

DTNs: GS980308315215.008 [107355]

NOTE: A total of 71 intervals are plotted and uncertainties for mean and median estimates are given at the 95% confidence level (Attachment IX.5).

Figure 6.14.4-4. Histograms Showing Hydrogenic Mineral Abundances in Welded Tuffs in the Exploratory Studies Facility on (A) Linear and (B) Log Scales

Mineral abundances also can be compared to structural features mapped in the ESF. The number of fractures per meter is generally low in the ESF North Ramp and increases substantially in the ESF Main Drift in the TSw middle nonlithophysal zone (Figure 6.14.4-5b). Many of these fractures are strata-bound features formed during cooling of the volcanic rock; therefore, they are unlikely to have long-range continuity that would facilitate UZ flow. Comparisons between data shown in Figures 6.14.4-5a and 5c imply that mineral abundances are not correlated with fracture frequency.

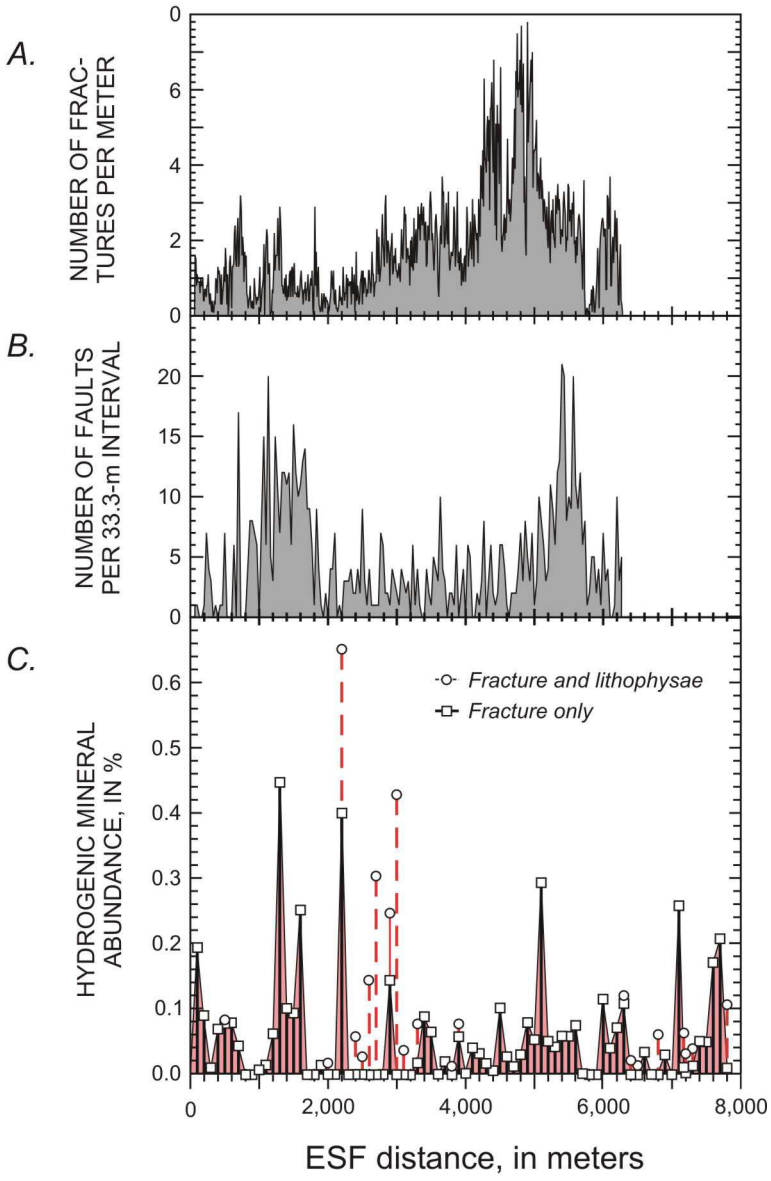

DTNs: GS960908314224.014 [106033]; GS970208314224.003 [106048]; GS971108314224.020 [105561]; GS971108314224.021 [106007]; GS971108314224.022 [106009]; GS971108314224.023 [106010]; GS971108314224.024 [106023]; GS971108314224.025 [106025]; GS971108314224.026 [106032]; GS971108314224.028 [106047]; GS980308315215.008 [107355]

Figure 6.14.4-5. Variations with Distance in the Exploratory Studies Facility from the North Portal for (A) Fracture Density; (B) Fault and Shear Density; and (C) Hydrogenic Mineral Abundance

In contrast to fractures, faults and shears may provide long-range connectivity for percolation. Distributions of these structures in the first 6,200 m of the ESF cluster in two areas between about 1,000 and 1,800 m and about 4,900 and 5,800 m (Figure 6.14.4-5b). These areas also have mineral abundances that are generally greater than the mean value for the ESF (Figure 6.14.4-2 and Figure 6.14.4-5c). Although some major faults are interpreted to be generally responsible

for greater mineral abundances in adjacent areas (the western splay of the Drill Hole Wash fault and associated ESF survey at 2,200 m being the most notable examples), other major faults have no closely related hydrogenic minerals. In spite of the qualitative observations, no correlation exists when mineral abundance data from the welded units of the Topopah Spring Tuff are plotted against the number of faults and shears in the corresponding ESF intervals (Figure 6.14.4-6). Correlation between these parameters may be lacking, in part, because some of the faults may not effectively transmit water. If faults do act as percolation conduits, they may lack the open space necessary for hydrogenic mineral deposition. Mineral deposits associated with faulting also may be offset from mapped fault planes. For example, large mineral abundances are observed in the ESF between 2,200 and 2,230 m, although the western splay of the fault intersects the ESF at approximately 2,270 m. Therefore, a relation, albeit a complex one, may exist between faulting, percolation, and mineral deposition.

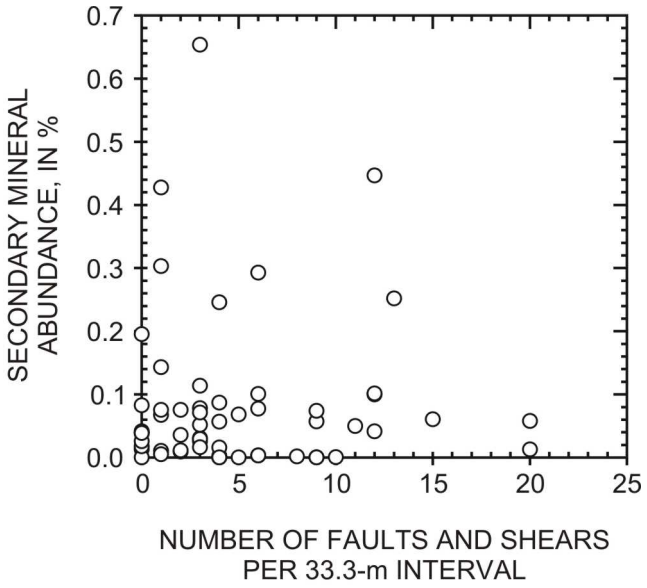

DTNs: GS960708314224.008 [105617]; GS960708314224.010 [106031]; GS000608314224.004 [152573]; GS960908314224.014 [106033]; GS970208314224.003 [106048]; GS971108314224.020 [105561]; GS971108314224.021 [106007]; GS971108314224.022 [106009]; GS971108314224.023 [106010]; GS971108314224.024 [106023]; GS971108314224.025 [106025]; GS971108314224.026 [106032]; GS971108314224.028 [106047]

Figure 6.14.4-6. Relation between Hydrogenic Mineral Abundance in Welded Units of the Topopah Spring Tuff and the Number of Faults and Shears Measured in the Corresponding Intervals in the Exploratory Studies Facility

Lithostratigraphic depth also may control the abundance of hydrogenic minerals. To evaluate this possibility, 30 m survey intervals were grouped by host lithology and separated among the ESF North Ramp, South Ramp, and Main Drift. Lithostratigraphic zones of the TCw have log means of the hydrogenic mineral abundances ranging from 0.053 to 0.16%. The small number of observations, plus the lack of large variation between percentages in the north and south ramps, justifies calculating an overall TCw log mean of 0.094 percent (N = 9). Percentages for welded zones in the TSw generally have mineral abundances lower than the TCw mean, although the TSw crystal-rich nonlithophysal unit in the ESF North Ramp area has a log mean of 0.14 (N = 5). The same zone in the ESF South Ramp has a lower percentage of 0.028 (N = 4). The TSw

upper lithophysal zone exposed in the ESF North Ramp has a small value of 0.014 percent (N = 11) with a large uncertainty because of the scatter of individual surveys. If the values for surveys under Drill Hole Wash (1,800 to 2,300 m) are excluded, the log mean increases to 0.090% (N = 4). The same zone exposed in the ESF South Ramp has a value of 0.047% (N = 6), and the log mean value for both areas (excluding surveys under Drill Hole Wash) is 0.060% (N = 10). This latter value is preferred, in part, because a similar value is obtained if the lithophysal-rich parts of the underlying middle nonlithophysal zone are combined with the ESF North Ramp upper lithophysal data (2,400 to 3,300 m). Mineral abundances for the TSw middle nonlithophysal zone in the ESF main drift are based on the largest number of surveys and have a log-mean value of 0.030% (N = 30), although this value varies from 0.020% towards the north to 0.071% towards the south (Figure 6.14.4-2). The TSw lower lithophysal zone was exposed only in one survey (5,700 m) and lacked macroscopic calcite or opal. Therefore, preferred estimates of mineral abundances grouped by stratigraphic position (filled symbols, Figure 6.14.4-7) suggest that values decrease with depth in the UZ, although substantial overlap exists in uncertainties among the groups.

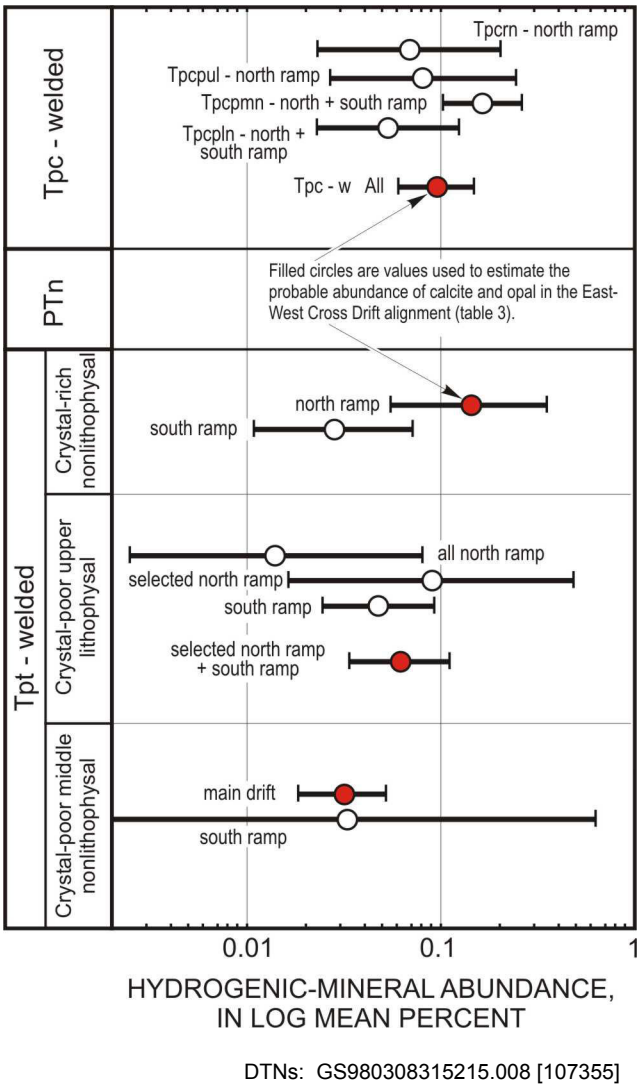

DTNs: GS980308315215.008 [107355]

Source: Stratigraphic units from Buesch et al. (1996 [100106]).

Figure 6.14.4-7. Summary of Hydrogenic-Mineral Abundances in Welded Tuffs in the Exploratory Studies Facility

Borehole Cutting Results: Stratigraphic controls on mineral distributions are further supported by data from USW WT-24 and USW SD-6 cuttings (Figure 6.14.4-8). In both cases, calcite concentrations are highest near the surface in the TCw. Concentrations decrease with increasing depth in the TCw and into the nonwelded tuffs of the PTn. At WT-24, calcite concentrations are very low within the thick PTn (median value of 46 µg/g) and remain low in the TSw until near the base of the upper lithophysal unit (Tptpul; median value = 270 µg/g). Concentrations increase dramatically in the TSw middle nonlithophysal unit (Tptpmn; median value = 2700 µg/g) and gradually decrease with depth in the lower lithophysal (Tptpll; median value = 1200 µg/g) and lower nonlithophysal (Tptpln; median value = 162 µg/g) units. At SD-6, a similar increase in calcite concentration is observed within the Tptpul (median value = 1700 µg/g); however, concentrations quickly decrease in the underlying welded units (Tptpmn median = 1100 µg/g; Tptpll median = 518 µg/g; Tptpln = 598 µg/g).

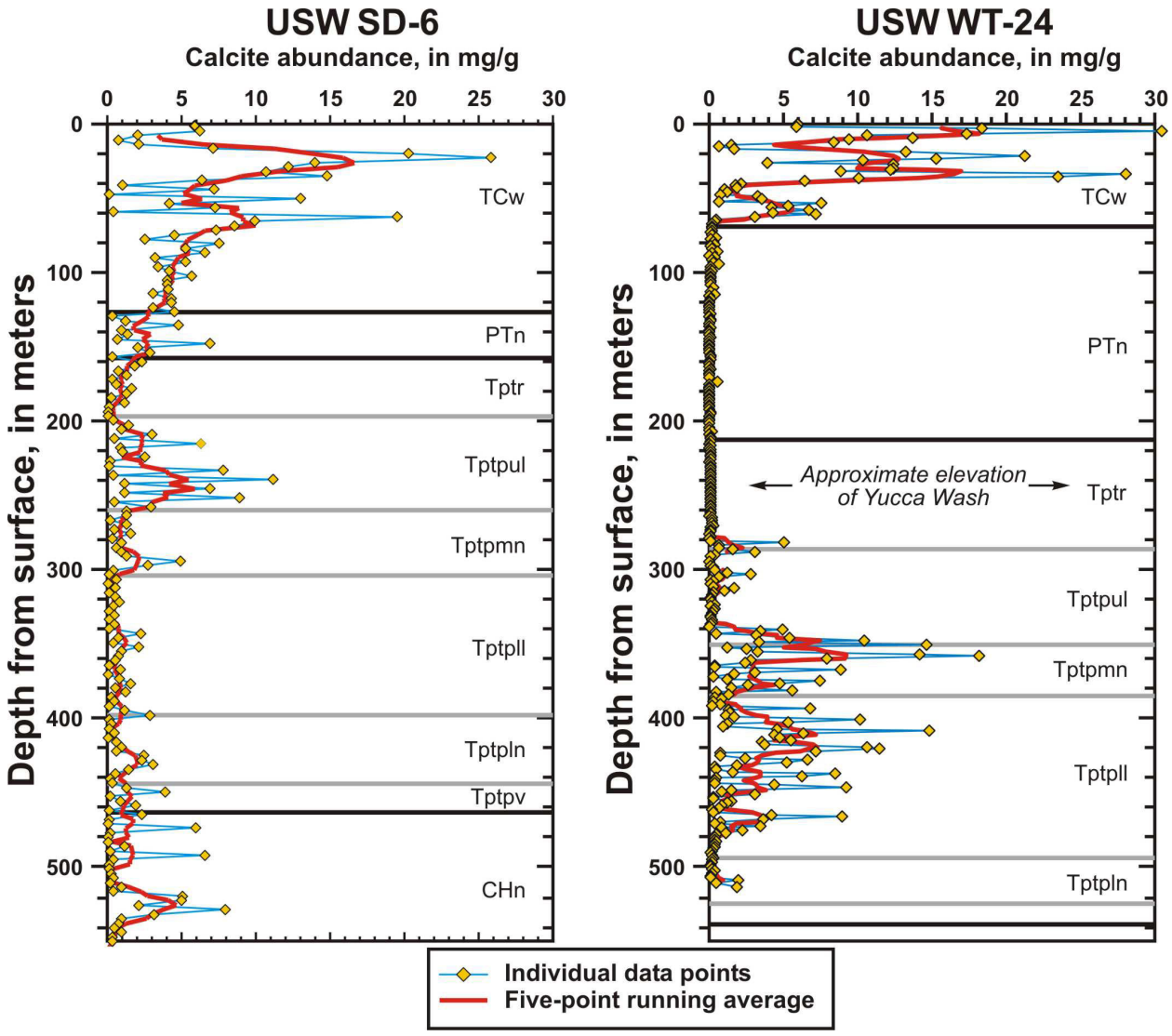

DTN: GS030908315215.002 [166097];
DTN: GS020608315215.002 [162126]; DTN: GS021008315215.007 [162127]

Figure 6.14.4-8. Profiles of Calcite Abundance Calculated from CO_2 Determinations on Cuttings from Boreholes USW SD-6 and USW WT-24

Interpretation of Results: These data show clear evidence for stratigraphic control on calcite concentration. The general trend of large decreases in calcite concentration through the TCw are pronounced in both boreholes and most likely reflect larger amounts of gas flow and consequent rates of evaporation in the shallow, fractured tuffs. Variations in oxygen-isotope compositions of late-stage calcite were also used as evidence for greater evaporative effects in the TCw relative to the TSw (Whelan et al. 2002 [160442], Figure. 8). Reduced gas fluxes within the PTn are a likely cause for lower calcite concentrations. Conceptual models of calcite deposition rely on interactions between independently migrating gas and liquid phases as a primary cause for both calcite and opal deposition (Paces et al. 2001 [156507]; Whelan et al. 2002 [160442]).

Decreased amounts of gas flow beneath the PTn are a likely cause for the overall lower calcite abundances in the TSw compared to the TCw. Variations in oxygen isotopes in TSw calcite are

interpreted as evidence for greater influence from geothermal effects than evaporative effects (Szabo and Kyzer 1990 [109172]; Whelan et al. 1994 [100091]; Whelan et al. 2002 [160442], p. 743). However, the causes for large observed variations in calcite concentration within TSw units are not obvious. Variations within the TSw are similar in both boreholes. Both profiles show marked increases in concentration well below the PTn/TSw boundary within the Tptpul or Tptpmn units. Both profiles also show distinct decreases in calcite concentrations below this peak, although overall abundances of calcite are much greater in the deeper TSw units in USW WT-24. Additional factors may affect UZ flow at this site, including the possibility of dispersal of UZ flow associated with overland recharge in Yucca Wash less than a kilometer to the northeast. Anomalously large calcite abundances have also been observed in drill core from nearby borehole USW G-2. Because of this complication, the calcite concentration profile from USW-SD-6 may better represent calcite distributions within the repository footprint.

Line surveys completed in the ECRB Cross Drift provide further support for the interpretations above, specifically that surface infiltration has little effect on seepage in the TSw and that there is an overall decrease in seepage with stratigraphic depth within the TSw. If the calcite abundance measurements from the Cross Drift and from USW SD-6 are divided into lithostratigraphic zones (Figure 6.14.4-9), it is apparent that both sets of data reveal similar decreases in calcite abundance with depth, implying decreasing seepage with depth. Also, the cross-drift data clearly do not show any increase in abundance under the crest of Yucca Mountain (Figure 6.14.4-3), further indicating the lack of correlation with simulated infiltration differences due to topographic effects.

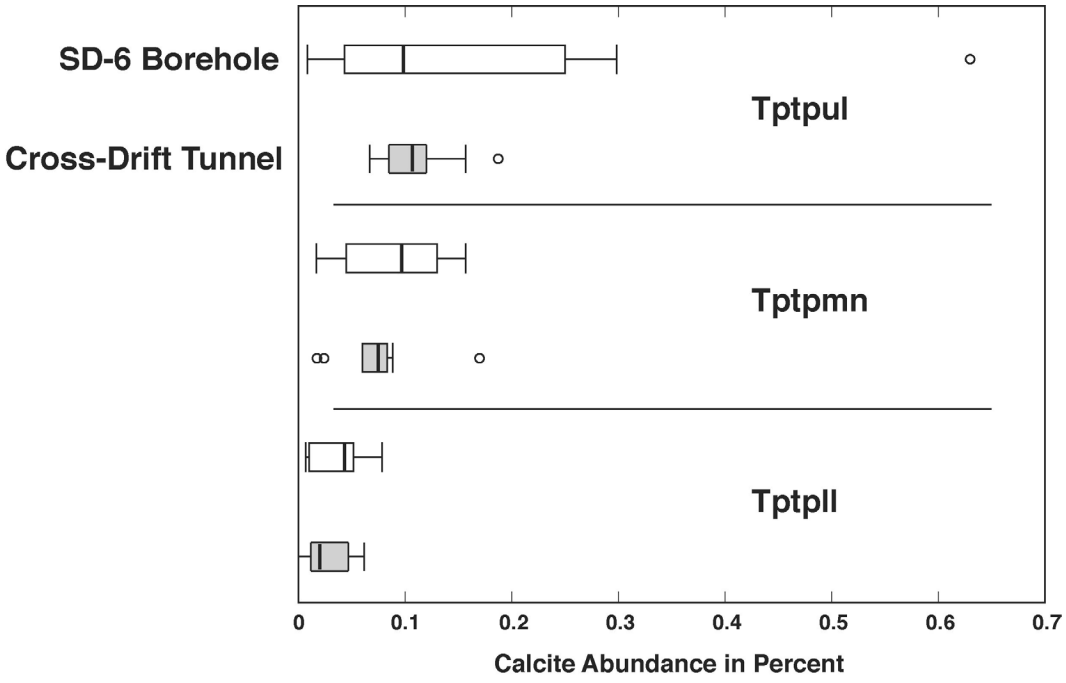

DTN: GS030908315215.002 [166097];
DTNs: GS030808315215.001 [165426]; GS020608315215.002 [162126]

NOTES: Note that two different methods were used to estimate calcite abundance as discussed in the text; borehole abundances are weight percent and cross-drift abundances are volume percent. Both sets of data clearly show a decrease in abundance with depth, especially in the lower lithophysal zone (Tptpll). See Attachment IX.5 for details of box and whisker plots.

Figure 6.14.4-9. Box and Whisker Plots for Distributions of Calcite Abundance Measurements in Borehole USW SD-6 and the ECRB Cross Drift (gray boxes) Divided into Three Lithostratigraphic Zones, Each Zone Deeper Than the One Above

In addition to variations in gas flux through the TSw, changes in percolation flux with depth may also influence calcite deposition. Increases in calcite concentrations in the Tptpul and upper parts of the Tptpmn may reflect fracture water that seeps into lithophysal cavities and is dispersed over very large surface areas exposed to open space. Interactions with an upward-migrating gas phase passing through these cavities causes slow growth of calcite and opal. As a consequence, less fracture water may be available for subsequent percolation to greater depths. The much lower calcite concentrations observed in the underlying Tptpll may reflect lower total fracture-water fluxes and reduced seepage.

Estimates of past seepage volume: Using calculated volumes of calcite at each surveyed site in the underground workings within the TSw, it is possible to estimate the volumes of water required to deposit the calcite. By scaling the individual volumes up to the volume that would correspond to a 5 m long waste package, estimates of past water seepage may be made on a per-waste-package basis (Marshall et al. 2003 [162891]). The information required to make these estimations includes the statistical distribution of coating thicknesses and cavity widths (Figure 6.14.4-10). The details of the estimations are presented in Marshall et al. (2003 [162891]).

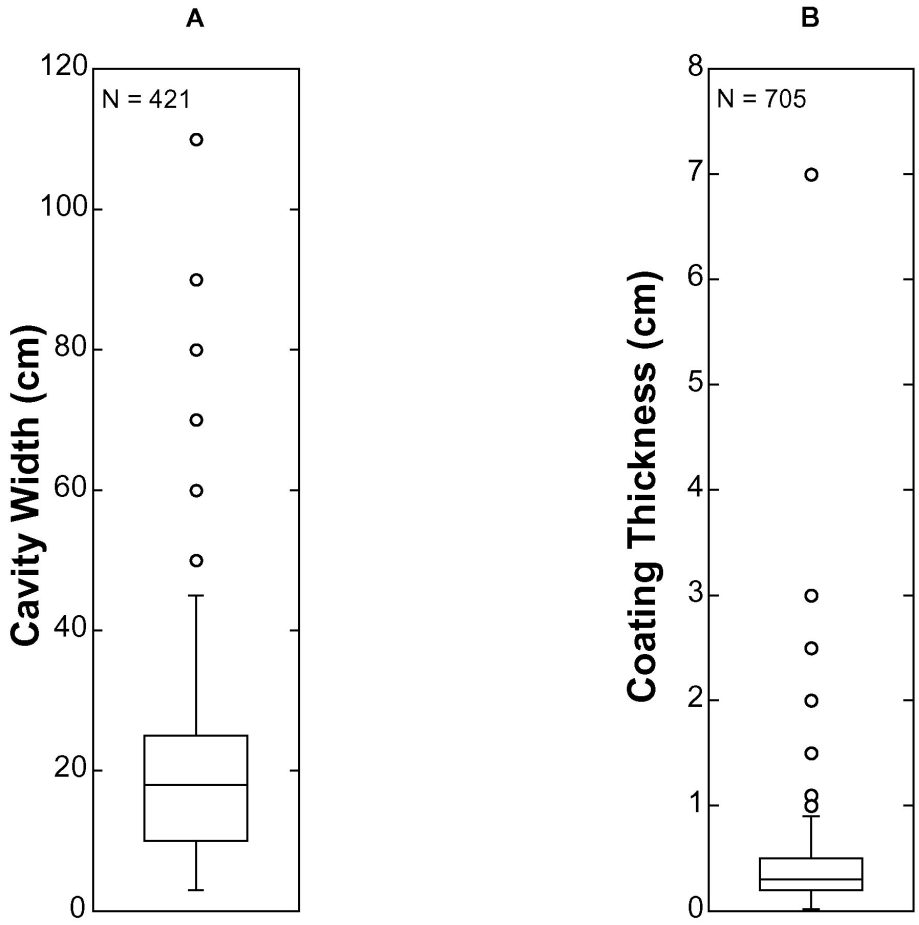

DTNs: GS030808315215.001 [165426]; GS980308315215.008 [107355]

NOTES: The upper and lower limits of the box are the 75th and 25th percentiles of the data, the line is the median, the whiskers indicate the total range of the data as calculated from the box range, and outliers are shown by circles. N is the number of measurements (Attachment IX.4).

Figure 6.14.4-10. (A) Box and Whisker Plots for Distributions of Lithophysal Cavity Widths and (B) Coating Thicknesses for Both Cavities and Fractures in the Topopah Spring Tuff Welded Unit (TSw)

INTENTIONALLY LEFT BLANK

7. CONCLUSIONS

Since the inception of the ambient field testing program in 1995 during the excavation of the Exploratory Studies Facility (ESF), progress was made in drift seepage studies in niches, systematic hydrological characterization, fracture/fault flow tests in alcoves, wetting-front and moisture monitoring along ESF drifts, drift-scale infiltration tracer testing, tracer transport testing at Busted Butte, and hydrochemical evaluations. This scientific analysis report focuses on *in situ* field testing of processes. The technical summary and conclusions for analyses in Section 6.1 through Section 6.14 are given in Section 7.1 through Section 7.14. In brief, the key findings include:

- Seepage thresholds were established for the middle nonlithophysal zone of TSw, with measured values at Niche 3650 (Niche 2) ranging from the borehole flux of 200 mm/yr to 136,000 mm/yr for flow paths through fractures and fracture network. Fracture characteristic curves were derived from the seepage threshold data, with the effective fracture porosity as high as 5% (Table 6.2.2-3). The fracture characteristic curves and effective fracture porosity, derived from seepage thresholds, are applicable for seepage-relevant processes within the test region between the air-injection/liquid-release point and the niche ceiling (this difference is less than 1 m). The tests were conducted through releases in 0.3 m borehole intervals, representing approximately the width of a flow path observed in the same tuff unit (Figure 6.2.1-1), to quantify seepage processes near the drift ceiling.

- Long-term seepage tests behind sealed bulkheads at Niche 4788 (Niche 4) confirmed the seepage results of early short-term transient tests at Niche 3650 (Niche 2).

- ECRB Cross Drift Niche 1620 (Niche 5) in the lower lithophysal zone of TSw has the characteristics of larger permeability and stronger capillarity, as indicated by air-permeability tests and flow-path patterns observed during niche excavation.

- The presence of a seepage threshold is confirmed in the lower lithophysal niche testing, with seepage reduced to zero as liquid release rate decreases.

- The borehole conditions in the lower lithophysal tuff are in general much worse than in middle nonlithophysal tuff, with loose rock pieces blocking several boreholes.

- The excavation and stability maintenance of a slot at the lower lithophysal Niche CD 1620 (Niche 5) is more difficult than anticipated.

- The mass balance tests at Niche CD 1620 (Niche 5) did not achieve the objective of quantifying the amount of water diverted by the drift, due to safety concerns preventing proper installation of the water collection system within the slot space.

- Cases of water flowing along niche sidewalls were observed.

- Systematic hydrological characterization along the ECRB Cross Drift through the lower lithophysal zone of TSw quantified the ventilation effects on measured seepage in this heterogeneous unit.

- Seepage diversion was shown to be nearly 100% effective in some tests, and less than 10% in other tests, as the results of spatial heterogeneity quantified along the lower lithophysal tuff with the the systematic hydrological characterization studies. Currently liquid release tests have been conducted in intervals along four slanted boreholes, covering a drift segment over 100 m long along the lower lithophysal zone.

- Heterogeneity was systematically evaluated with air-injection tests, with borehole-scale and drift-scale distributions and excavation-induced enhancements of permeability variations orders of magnitude larger than the site-to-site variations of average values along the ESF Main Drift. In addition to mechanical effects, some of the permeability increases could be related to the intersection of previously dead-ended fractures with the excavated free surface.

- Dyes and nonreactive tracers were confined locally (within a 1.0 m × 1.6 m area for the last test in Niche 3650 [Niche 2]) near the liquid-release points above the niche ceiling, with tracers released from multiple sequences of short-term seepage tests.

- Fracture flow paths were spatially heterogeneous and discrete in TSw. Fault zone flow paths and nonwelded tuff layers contributed to the complexity of pneumatic responses in PTn, with an argillic layer effectively dampening the pneumatic responses.

- Fracture flows in TSw were intermittent in nature, even when the flow boundary conditions were stable.

- In PTn both fault and matrix flows had large capacities for accommodating damping of infiltration pulses.

- Rock dryout zones were shown to extend approximately 3 m into the tunnel wall, construction water was detected nearly 10 m below the invert, and large changes in relative humidity conditions could be related to moisture removal by ventilation.

- After over two years of nearly continuous sealing of the last one-third of the ECRB Cross Drift, the rocks have not completely rewetted, based on water-potential measurements in boreholes.

- Wet areas and droplets were observed and liquid samples of condensate were collected during entries into sealed sections of the ECRB Cross Drift. The origin of water is attributed to the condensation process, based on limited chemical analyses of the relatively clean water collected. The temperature and relative humidity differences needed for condensation and moisture redistribution processes were indicated by variations in the in-drift moisture sensors.

- Infiltration, wetting-front detection, and seepage collection data for faults were collected at the drift-to-drift test between Alcove 8 in the ECRB Cross Drift and Niche 3107 (Niche 3) in the ESF Main Drift. The tuff interface between the test sites has been confirmed by baseline geophysical tomographies.

- The air-permeability data measured in the slanted boreholes from Alcove 8 have large variability associated with the transition from upper lithophysal zone to middle non-lithophysal zone across the tuff interface.

- Breakthrough curves of two tracers in the fault test clearly indicate that the molecular size of tracers has a large effect on transport, with larger tracer having faster transport and smaller tracers being delayed by effective matrix diffusion into tuff blocks next to the fractures.

- The Unsaturated Zone Transport Test (UZTT) at Busted Butte provided field-scale data on transport properties of the vitric Calico Hills hydrogeological unit and the basal vitrophyre at the tuff interface between Topopah Spring and Calico Hills units.

- Capillarity was shown to be strong in the vitric Calico Hills.

- Spatial heterogeneity was shown to affect transport through the vitrophyre.

- Sorbing tracers have been shown to move little. The plume migration has been evaluated by mine-back sample analyses and by periodic ground-penetrating-radar tomography (GPR-T).

- Neutron moisture data and laboratory radionuclide transport data corroborate the findings based on tracer pad analyses and mine-out images at UZTT.

- Along the ECRB, pore-water chemistry is relatively more heterogeneous than the rock mineral distribution.

- The validation study of bomb-pulse $^{36}Cl/Cl$ signals in fault/feature locations along the northern ramp and ESF Main Drift is not completed. High tritium samples are found at multiple locations along the south ramp of ESF.

- Uranium isotope data illustrate the sensitivity of redistribution and transport to percolation flux magnitude.

- Fracture calcite/opal data support the understanding that only a small fraction of fracture surfaces are coated primarily on the footwalls, lithophysal cavites have secondary precipitates only at the bottom, growth rates are low, and the inferred percolation and seepage rates are small.

These findings are used as inputs to other model reports. The unsaturated zone model reports are identified in the following on the current field status of testing and monitoring activities at different sites in the ESF.

- Extensive pneumatic air-permeability tests were conducted in borehole clusters before and after niche excavation, and in alcove test beds before liquid releases. The test results are inputs to *Seepage Calibration Model and Seepage Testing Data* (BSC 2003 [162267], *Seepage Model for PA Including Drift Collapse* (BSC 2003 [163226], and *Abstraction of Drift Seepage* (BSC 2003 [165564]).

- Niche 3566 (Niche 1), in the vicinity of the Sundance fault, was sealed for over two years. The first damp feature in the repository horizon was observed in this niche.

- Niche 3650 (Niche 2), in a fractured setting away from faults, had over 40 liquid-release tests conducted to quantify seepage thresholds. The core samples from the latest test were analyzed for tracer distribution.

- Niche 3107 (Niche 3), in a relatively uniform rock mass below the crossover point between the ESF Main Drift and Cross Drift, is the site of the drift-to-drift fault tests and ongoing large plot tests for matrix diffusion and active fracture model calibration and validation.

- Niche 4788 (Niche 4), in an intensely fractured zone, hosted completed phases of pre- and post-excavation characterization and several long-term seepage testing sequences.

- Niche CD 1620 (Niche 5), located near the center of the repository in the lower lithophysal zone, is the site of a series of consecutive seepage tests completed for inputs to *Seepage Calibration Model and Seepage Testing Data* (BSC 2003 [162267]). Evaporation losses were quantified and used to improve the seepage calibration model.

- Systematic hydrological characterization along the ECRB Cross Drift (1) provided the data set for *Seepage Calibration Model and Seepage Testing Data* (BSC 2003 [162267]) in the lower lithophysal zone of TSw, (2) quantified the ventilation effects along the open drift, and (3) provided observations of heterogeneity controls by fractures and lithophysal cavities.

- Alcove 6, in a fractured zone with relatively competent matrix blocks, has been used for series of tests, with water dripped into a slot below the test bed collected. The test results can be used to compare with the fracture flow fractions predicted by *UZ Flow Models and Submodels* (BSC 2003 [163045]).

- Alcove 4, in a layered zone with a fault bounded by porous PTn, has been used for series of tests to evaluate the migration of injected water. The test results can be used to evaluate the lateral diversion at the PTn addressed by *UZ Flow Models and Submodels* (BSC 2003 [163045]).

- Alcove 1, 30 m below the ground surface near the North Portal in the Tiva Canyon welded tuff unit, is the site for large infiltration tests at the ESF. The test results from two series of flow and tracer tests were analyzed in Liu et al. 2003 [162470]. Matrix diffusion is shown to be important in diluting the tracer concentration and reducing the tracer breakthrough at the Alcove 1 test site.

- The Alcove 8/Niche 3107 (Niche 3) data (liquid release rate, seepage rate, tracer breakthroughs) are inputs to *UZ Flow Models and Submodels* (BSC 2003 [163045]) and to *Radionuclide Transport Models under Ambient Conditions* (BSC 2003 [163228]).

- Water-potential measurements with heat dissipation probes, with psychrometers, and with tensiometers have been conducted in ESF boreholes at alcoves, at niches, and systematically along the ECRB Cross Drift. The results of potential data from ECRB have been used in *UZ Flow Models and Submodels* (BSC 2003 [163045]). The dryout zone data are also used to support repository design of ground support systems and to quantify vapor flux into drift for in-drift condition evaluation.

- Construction-water migration was monitored at the starter tunnel of the Cross Drift and below the crossover point. Data on the distributions of lithium bromide tracers from boreholes drilled into the drift floor (invert) are inputs to the Yucca Mountain site description document.

- Moisture monitoring stations continue to collect data to evaluate the impact of tunnel ventilation and moisture removal.

- Condensation observed in the sealed sections of the ECRB Cross Drift provides additional insights for in-drift redistribution of moisture under thermal and relative humidity variations.

- Busted Butte transport test data (plume configuration, tracer distributions and breakthrough) from Phase 1A, Phase 1B, and Phase 2 are inputs for *Radionuclide Transport Models under Ambient Conditions* (BSC 2003 [163228]) for model validation.

- The geochemistry and transport properties data are inputs to *UZ Flow Models and Submodels* (BSC 2003 [163045]) and to *Radionuclide Transport Models under Ambient Conditions* (BSC 2003 [163228]).

The ambient testing program has evolved from an initial focus on the middle nonlithophysal zone of TSw to the lower lithophysal zone of TSw, and to both the PTn above the repository horizon and CHn below the repository horizon. The tests confirm, validate, refine, or refute existing and alternative conceptual models for seepage into drifts, fracture flow, fracture-matrix interaction, and drainage and migration below the repository. With most of the repository horizon in the lower lithophysal unit of the TSw, it is critical to characterize this unit to determine if the presence of lithophysal cavities and friable tuff media change the seepage distributions and percolation characteristics. The seepage-threshold quantification is confirmed with long-term tests to address the concerns about the capillary barrier concept under steady-state conditions, the effects of evaporation, and the effects of moisture storage and flow-diversion capacities. Quantification of spatial distribution of fast flow paths and assessment of temporal variations of episodic percolation events require testing and monitoring refinements for *in situ* conditions.

The emphasis of this scientific analysis report is on active-flow testing in niches and alcoves. These activities, together with many other laboratory and field activities analyzed in other

analysis and model reports, provide data for inputs to other model reports for process evaluation, calibration, and validation. Since different activities and analyses for *in situ* field testing in processes are in different stages of progress, the summaries of test analyses presented in the following 14 sections are in different degrees of maturity. Section 7.n is the summary of data analyses in Section 6.n, with n = 1,..., 14. The data are summarized with minimal speculative interpretations. Credible interpretations can be achieved with close interactions between testing and modeling, as documented in the model reports and scientific analysis reports cited, and on an activity-by-activity basis.

This scientific analysis report may be affected by technical product input information that requires confirmation. The status of the technical product input information quality might be confirmed by review of the DIRS database.

Technical product outputs have been generated to document and summarize the results from analyses of some sets of DTNs. In some cases, the technical product outputs are directly used by downstream models. In other case, the technical product output has been generated as suggestions for potential uses. The authors of model reports are advised to use directly collected data with DTNs. Details of analyses are included in the current reports prepared for LA so that technical product outputs are no longer needed in most cases. The results of the analyses associated with each tests are documented directly in this scientific analysis report. The results in figures and tables are documented in sufficient details to eliminate the need to issue new technical output DTNs. For cases where technical output DTNs were issued associated with early analyses, the use of each technical product output is summarized, together with discussions of associated uncertainties and limitations of data and information.

Two YMRP acceptance criteria for this scientific analysis report are listed in Section 4.2: (1) data sufficiency for model justification, and (2) data uncertainty characterization for propagation through models. These criteria are addressed in this scientific analysis report by reporting the statistics of parameter distributions for cases of field measurements and laboratory experiments with sufficient data, by describing the challenges and chronologies of data collection issues during the testing and measuring periods, and by comparing different techniques if available for quantification of similar parameters for the same unsaturated processes over different scales. The measured results are analyzed and reported in this scientific analysis report for inputs to other unsaturated zone and coupled process models as summarized above. The process models form the basis for further abstractions, using the ranges of measured parameters and other sources of information. Summaries are presented in the following sections of different activities for data sufficiency and uncertainty evaluations.

7.1 SUMMARY AND CONCLUSIONS OF AIR-PERMEABILITY DISTRIBUTION AND EXCAVATION-INDUCED ENHANCEMENT IN NICHES

Using the pneumatic packer system developed with automated controls and data acquisition, extensive air-permeability tests were systematically conducted in borehole clusters at five niches and other test beds. Single-hole permeability data have proven their use in detecting changes in permeability (and boundary conditions) as a result of nearby excavation and in characterizing sites. Pre-excavation and post-excavation permeability profiles with 0.3 m spatial resolution are presented for boreholes used for drift-seepage and liquid-release tests. Air-permeability

distributions are used as inputs for the seepage calibration model (BSC 2003 [162267]) to assess the capillary-barrier and seepage-threshold mechanisms. Fractures immediately above the niches are important to the evaluation of seepage into drifts.

The approach summarized in Cook (2000 [165411]) and Wang and Ellsworth (1999 [104366]) are used to collect the air-permeability distribution data described in Section 6.1. The main results from air-permeability profile and distribution analyses are:

- The excavation-induced permeability enhancements in borehole intervals are large, with an average enhancement for boreholes of one to two orders of magnitude.

- Drift-scale variation of permeability values and permeability enhancement along boreholes and among different boreholes within the niches are larger than differences among different niche sites.

It is important in drift-scale assessment to characterize the permeability distributions controlling local flow path and seepage spatial variation. The results quantify the spatial variability associated with formation heterogeneity in fractured tuff. The relatively small difference in mean permeability values for different niches is encouraging for the reduction of uncertainties associated with site-scale spatial heterogeneity. If subsequent liquid-seepage tests in locally distinct niches result in seepage-threshold values within a relatively narrow range, the uncertainties for seepage into drifts could be greatly reduced for the middle nonlithophysal unit of TSw, where four existing niches were located. The seepage evaluation with nearly continuous releases has been carried out for the lower lithophysal tuff unit to acquire the necessary data for the majority of the repository horizon area.

Output-DTN: LB0310AIRK0015.001 (for computed ratios of post-excavation air-permeability over pre-excavation air-permeability data) is the technical product output from the analysis presented in Section 6.1 of this scientific analysis report.

The permeability ratios in this DTN are presented in Section 6.1.2.3. As shown in Figure 6.1.2-12 through Figure 6.1.2-16, the correlation coefficient R^2 of the ratio as a function of initial permeability has low values (from ~0.11 to ~0.17), representing poor fit. These results, together with permeability profiles in Section 6.1.1 and statistical analyses summarized in Table 6.1.2-1 through Table 6.1.2-5, provide the basis for understanding of the permeability-stress coupling and the measure of natural variability of the fractures of the tuff units. Heterogeneity quantification is important for other hydrological processes (discussed in other sections). Downstream users of the air-permeability data need to recognize the natural variability and spatial heterogeneity, and quantify the hydrological effects consistent with the air-permeability measures.

7.2 SUMMARY AND CONCLUSIONS OF LIQUID-RELEASE AND SEEPAGE TESTS IN NICHES

The approach of using liquid releases and seepage tests (Trautz and Wang 2002 [160335]; 2001 [165419]; and Wang et al. 1999 [106146]) has been used to collect seepage data, as described in Section 6.2 and summarized in the following sections.

7.2.1 Pre-Excavation Liquid-Release Testing and Niche Excavation Activities

Numerous liquid-release tests were conducted prior to the excavation of each niche to evaluate how far a finite pulse of water would travel through relatively undisturbed fractures located in the middle nonlithophysal zone of the TSw. Similar tests were conducted in the lower lithophysal zone of the TSw to identify the difference in capillary strengths between these two major repository host rocks.

The maximum depth of the wetting front increases with increasing mass of fluid injected. It appears that maximum-depth data cannot discriminate the type of flow (i.e., high-angle fracture versus network flow) observed during the test. Lateral spreading and the aspect ratio (i.e., ratio of depth to lateral spreading) may be stronger measures of the type of flow that predominates. Increased lateral spreading of the wetting front appears to be typical of well-connected fracture networks containing both high- and low-angle fractures, whereas large aspect ratios appear to be typical of flow in individual vertical fractures.

- The middle nonlithophysal zone is dominated by gravity, with large aspect ratios observed in most flow paths.

- The lower lithophysal zone has some flow paths with symmetric patterns, indicating potential strong capillarity in spreading the plumes.

DTN: LB0110LIQR0015.001 (for liquid-release test analyses and computed seepage rates) and DTN: LB0110NICH4LIQ.001 (for wetting front characterization in the ceiling of Niche 4788 [Niche 4]) are technical product outputs from the analyses presented in Section 6.2.1 of this scientific analysis report.

DTN: LB0110LIQR0015.001 is for the water retention curves for fractures illustrated in Figure 6.2.2-3 and summarized in Table 6.2.2-3. Various data sets were used to generate the water retention curves, with seepage threshold fluxes determined by the test data having relatively high correlation coefficients shown in Table 6.2.2-1. While the data for the seepage thresholds have high certainty, the analyses using analytic solutions do have uncertainties assoociated with the approximations of medium uniformity. Downstream models, such as the Seepage Calibration Model (BSC 2003 [162267]), recognize this limitation and formulate the heterogeneous numerical models, taking air-permeability distributions into account.

DTN: LB0110NICH4LIQ.001 is for the analyses of wetting-front movements observed on a niche ceiling, as illustrated in Figure 6.2.1-7. The relative uniform patterns at early times and the interferences by fractures at later times are presented to gain better understanding on the seepage and diversion mechanisms. The DTN was generated for potential use by models with fractures explicitly taken into account. Additional data of fracture characterstics for each discrete fractures may be needed if such an approach is used.

7.2.2 Post-Excavation Seepage Tests at Niche 3650 (Niche 2), Niche 4788 (Niche 4), and Niche CD 1620 (Niche 5)

The focus of the seepage tests at Niche 3650 (Niche 2) was to investigate the amount of water that would drip into a mined opening from a transient liquid-release event of short duration.

- Forty post-excavation liquid-release tests were conducted on 16 different test intervals located above Niche 3650 (Niche 2) within the middle nonlithophysal zone of the Topopah Spring welded unit.

- Of the 16 zones tested, water seeped into the capture system from 10 intervals, water appeared at the niche ceiling but did not drip in 3 cases, and water did not appear at all when introduced into the three remaining zones.

- The seepage percentage, defined as the amount of water captured in the niche divided by the amount released into the rock, ranged from 0 to 56.2%.

It was determined during the early stages of testing that the memory effect, or wetting history, had a profound impact on seepage. If the liquid-release tests were performed too close together in time, then it was found that the seepage percentage increased dramatically, as one would expect. This is because the fractures contained residual moisture, and their unsaturated conductivity was higher during subsequent tests. The test with seepage percentage of 56.2%, the third test in a series of four tests in the same interval, was conducted within 2 hours after the second test with 23.2% seepage. In comparison, the first test conducted 20 days before the second test had a fairly consistent result of 22.6% seepage.

- The seepage-threshold flux, defined as the flux of water that when introduced into the injection borehole results in zero seepage, was evaluated for the 10 zones that seeped in Section 6.2.2.1.

- The seepage-threshold fluxes measured at Niche 3650 (Niche 2) range from 6.35E-09 to 4.31E-06 m/s or 200 to 136,000 mm/yr.

- The seepage-threshold data were evaluated and interpreted using analytical techniques specific to a homogenous, unsaturated porous medium derived by Philip et al. (1989 [105743]).

Two types of flow paths were observed in the field during the mining operation, as described in Section 6.2.1.2. Estimates of the volumetric water content were produced in Section 6.2.2.3, using wetting-front arrival times recorded during the seepage tests. The α-values resulting from the analyses performed in Section 6.2.2.2 were used to estimate the water potentials of the fractures reported in Section 6.2.2.4. Water-potential estimates and the corresponding volumetric water contents were used to construct the fracture-water retention curves presented in Section 6.2.2.5. Examination of these plots indicates that:

- Fractures appear to drain very quickly, approaching a residual water content as low as 0.1 to 0.2% (Figure 6.2.2-3).

- Saturated water content or effective fracture porosity may be as high as 5% (Table 6.2.2-3).

The approach of using short-term tests at Niche 3560 (Niche 2) in ventilated conditions was replaced by long-term tests at both Niche 3107 (Niche 3) and Niche 4788 (Niche 4) under

controlled high-humidity conditions. The series of Niche 4788 (Niche 4) tests was more complete and was used by the seepage calibration model (BSC 2003 [162267]) to calibrate and validate the model. The analytic solution approach presented in this scientific analysis report indicated that:

- The seepage thresholds determined by the long-term tests are comparable to the seepage thresholds determined by short-term tests.

For Niche CD 1620 (Niche 5) in the lower lithophysal tuff, Test #2 demonstrated that:

- Seepage thresholds exist even with the series of tests conducted consecutively, with essentially no waiting periods between tests at different rates.

- The slot did not effectively capture lateral movement of water around the niche.

The lack of evidence that seepage occurred into the slot implies that the revised objectives of the test stated in Section 6.2.1.3.5.1 were not met in this study.

However, both at Niche 4788 (Niche 4) and Niche CD 1620 (Niche 5), photographic evidence showed that:

- A wetted area spread across the ceiling and down the terminal face and sidewall of Niche 4788 (Niche 4) in the middle nonlithophysal tuff (Trautz and Wang 2002 [160335]).

- A wetted area spread down the sidewall of Niche CD 1620 (Niche 5) in the lower lithophysal tuff (Figure 6.2.1-23).

7.2.3 Constraints and Limitations of the Niche Seepage Test Results

The seepage test results at Niche 3650 (Niche 2), including the determinations of the seepage thresholds, are based on multiple liquid-release tests conducted over short duration, with some of the rates high enough to induce artificial seepage. The tests were conducted in open-niche conditions with the humidity affected by the ventilation in the tunnel. The effects of evaporation can remove water from the rock through the vapor phase and may reduce the liquid seepage flux in determining the seepage threshold.

The tests at Niche 3107 (Niche 3) and at Niche 4788 (Niche 4) are conducted over longer test periods, with some at lower release rates and under better control of ventilation and humidity effects. Long duration tests do not practically allow long recovery periods between tests of different rates at the same borehole interval. The same long-duration approaches have been used in tests at the lower lithophysal TSw unit at Niche CD 1620 (Niche 5), with some tests conducted with essentially no recovery periods between tests of different rates. The constraints and limitations of the seepage test results in the middle nonlithophysal TSw unit with recovery periods, and in the lower lithophysal TSw unit with minimal recovery periods, should be carefully evaluated to assess their applicability. The intended use of niche test data is for seepage process evaluation.

7.3 SUMMARY AND CONCLUSIONS OF TRACER-MIGRATION DELINATION AT NICHE 3650 (NICHE 2)

Tracer distribution in cores after a liquid-release event at Niche 3650 (Niche 2) was analyzed in Section 6.3. Niche 3560 (Niche 2) is first of three niches (Niche 3560 [Niche 2], Niche 3107 [Niche 3], and Niche 4788 [Niche 4]) with series of seepage tests conducted in the middle nonlithophysal TSw unit. The results of multiple sequences of short-term seepage tests showed that:

- The tracer migration from the latest test was localized and possibly confined within the 1.0 m × 1.6 m area directly below the liquid-release interval, with a vertical scale of about 0.7 m. This result is based mainly on analyses of iodine as a conservative tracer.

- Spatial distributions of other dye tracers resulting from early liquid-release tests consistently point to localized flow with limited lateral spreading of tracer migration. The previous liquid release and seepage tests with dyes were conducted over six months before the latest test.

Liquid-release tests reported in Section 6.2 indicated that post-excavation seepage water was captured in most cases directly beneath the test zone or in capture cells immediately adjacent to the interval. Flow-path observations during niche excavations generally showed that the dyes did not spread laterally to great extents (also see Section 6.2 and preliminary results of Niche 3566 (Niche 1) and Niche 3650 (Niche 2) reported in Wang et al. 1999 [106146], pp. 329–332). Gravity-driven flow is the primary flow mechanism in fracture systems, either through individual fractures and/or through the fracture network connected to the release intervals. In Section 6.4 of this report, further laboratory tests of tracer sorption and fracture-matrix interactions are presented.

The absence of nonreactive tracers, especially iodine (introduced only at the latest pulse release), together with the localized spatial distributions of dyes long after the liquid releases, strongly suggested that the gravity-driven component was strong. Capillary imbibition and capillary barrier effects could promote lateral spreading. Longer-term tests with sampling over larger areas than the latest pulse test, as well as early liquid-release tests, could further quantify the migration and retention of tracers. Tracer-test results could be used to investigate the occurrence and significance of localized flow and to assess the mechanisms governing contaminant transport.

The results provide a data set for flow path distribution from multiple liquid releases using different tracers. The data set can be used to quantify natural variability and uncertainties of flow and transport in the scale of less than a few meters above the niche opening, with spatial confinement demonstrated. Since the tracer distributions are based on cores recovered from a cluster of boreholes, there are technical uncertainties associated with flow and transport out the domain between the boreholes. Ventilation drying may also contribute to the uncertainties in the test interpretation. These considerations should be taken into account in using the data set for detailed calculations of the flow and transport processes in this spatial scale of a few meters surrounded by the borehole array.

7.4 SUMMARY AND CONCLUSIONS ON TRACER PENETRATION AND WATER IMBIBITION INTO WELDED TUFF MATRIX

Field and laboratory tracer experiments have been conducted to investigate the flow partitioning between fracture flow and matrix imbibition in unsaturated conditions. During niche excavation, dye-stained rock samples were collected for laboratory analyses. Additional tuff samples collected from the repository horizon were machined as rock cores for laboratory studies of tracer penetration into the rock matrix under two initial water saturations. In the drift seepage tests using dye tracers, seepage-water samples were collected. A rock-drilling and sampling technique was developed to profile the tracer concentration in the rock matrix over distance in Section 6.4 and in Hu et al. (2002 [165412]). The samples were collected in Niche 3560 (Niche 2), the same site discussed in Section 7.3. The laboratory evaluation complements the evaluation documented in Section 6.3 for the site in middle nonlithophysal TSW unit.

- For rock samples, the sorbing dye-tracer penetration depths are on the order of several millimeters from the fractures permitting flow.

- In well-controlled laboratory tracer-imbibition tests under both high and low initial water saturations, the concentration profiles of sorbing dyes lag behind the nonreactive bromide front, with the travel distance for dyes being a few millimeters over the contact time of about 18 hours.

- The bromide front lags significantly behind the moisture front at high initial water saturation of 75.8%. The front is comparable to the moisture front in the rock core at the initial water saturation of 12.5%.

- Retardation of sorbing tracers increases with a decrease in saturation, as measured in the dry core and in the wet core, verifying the functional relationship between retardation and water content.

- Core measurements can be used to measure retardation factors in *in situ* conditions to check the results of batch experiments using crushed tuff in saturated conditions.

Data presented in Section 6.4 revealed interesting processes, especially at the interface boundary region between the core bottom and the water reservoir, simulating the contact of flow-permitting fractures with adjoining tuff matrix. Data of flow partitioning, front separation, and tracer retardation can be used for validation of fracture-matrix interaction and fracture flow models.

The uncertainties of the laboratory measurements are associated with the spatial resolution limitations of drilling and sampling techniques and analytic accuracy. Compared to field testing conditions, these measurement uncertainties are small. The findings are mainly for process understanding, and for alternative approaches for block rock characterization to complement crushed rock measurements.

7.5 SUMMARY AND CONCLUSIONS OF SINGLE-HOLE PERMEABILITY DISTRIBUTIONS AND CROSSHOLE CONNECTIVITY ANALYSES

Crosshole analyses of pneumatic air-permeability test data are presented for Niche 4788 (Niche 4), Alcove 6, and Alcove 4. Crosshole connectivity analyses for Niche 4788 (Niche 4) are used in the seepage tests in this intensely fractured zone. The pneumatic air-permeability test results were used for interval selection and test interpretation in the series of tests conducted for fracture flows and fracture-matrix interactions in TSw at Alcove 6, and for fault and matrix flows in PTn in Alcove 4. Niche 4788 (Niche 4) and Alcove 6 are in fractured middle nonlithophysal TSw unit. Alcove 4 is in porous Paintbrush nonwelded tuff PTn.

The main results from permeability distribution and crosshole analyses are:

- Welded-tuff test sites have distinct flow paths clearly identified by crosshole analyses from isolated injection intervals to observation intervals.

- The fracture flow connections are predominately one-way, with an injection interval inducing response in an observation interval, but with the interval not necessarily detecting injection into the original observation interval.

- The PTn test bed in Alcove 4 has many more connections than the corresponding TSw sites in niches and in Alcove 6. Weaker connections were trimmed out to reveal the stronger connections.

- The argillic layer in the test bed was shown from crosshole analyses to be a nearly impermeable barrier.

- Stronger connections were associated with a fault in the test bed at Alcove 4. A high-permeability zone near the end of the test block was identified by the air-permeability results and crosshole analyses.

The cross-hole analyses present the air-permability tests documented in Section 6.2 and Section 7.2 visually, primarily for the purpose to support the test design in selecting liquid injection intervals. The uncertatinties associated with permeability testing also apply to the evaluation of the cross-hole responses. The cross-hole analysis results can be used for heterogenous model evaluation over the spatial domain covered by the borehole clusters. Discrete fracture models can use the cross-hole analysis for inputs for the heterogeneity field.

7.6 SUMMARY AND CONCLUSIONS OF FRACTURE FLOW IN THE FRACTURE-MATRIX TEST BED AT ALCOVE 6

Fracture flow data were collected in a slotted test bed located at Alcove 6 of ESF within the TSw. With a slot below injection zones, it was possible to quantify both the inflow into the system and outflow at the lower boundary, and to better evaluate the flow field in underground test conditions, as described in Section 6.6, in Salve et al. 2002 [161318], and in Hu et al. 2001 [165413].

In this field study, techniques developed to investigate flow in fractured welded tuffs were evaluated. Results from field tests suggest that *in situ* characterization of certain fundamental flow parameters (such as travel times, percolation, and seepage rates) can be achieved with this approach. Alcove 6 is in the middle nonlithophysal TSw unit, with well-defined fracture network through competent welded tuff rock.

The test results revealed aspects of flow in unsaturated, fractured systems and provided insight towards the conceptualization of flow through unsaturated and fractured rock formations. The Alcove 6 test is the first test conducted in the ESF on unsaturated fractured tuff with attempts in taking liquid mass conservation explicitly into account. In field tests, it is frequently difficult to control the boundaries, and liquid can flow to unknown domains. Transient data collected at Alcove 6 also contribute to the evaluation of unsaturated flow in fractured tuffs.

Several sets of liquid-release tests were conducted with localized injections of liquid into a low permeability zone (LPZ) and into a high permeability zone (HPZ) along a borehole. The major test results were:

- For all injections into both LPZ and HPZ, changes in electrical resistance and psychrometer readings were detected in two monitoring boreholes ~0.6 m below the point of injection.
- For the LPZ tests, water did not seep into the slot located 1.65 m below.
- Liquid-release rate into the LPZ was observed to steadily decrease by two orders of magnitude (from >30 to < 0.1 mL/minute) over a period of 24 hours.
- In the HPZ, liquid-release rates under constant-head conditions were significantly higher (~100 mL/minute), with intermittent changes observed in the intake rate.
- For injection tests in HPZ, water was observed to drip into the slot in 3 to 7 minutes at high injection rates of ~28 to ~100 mL/min, in 1 hour at the low injection rate of 14 mL/min, and in 5 hours at the lowest rate of 5 mL/min.
- During the course of each test, seepage rates measured in the slot showed intermittent responses despite constant-head or constant-rate conditions imposed at the input boundary.
- The percentage of cumulative volume of water recovered in the slot was observed to increase in most tests, approaching steady-state values after ~10 liters of water had been injected.
- A maximum of 80% of the injected water was recovered for high-rate injection tests.
- The saturated volumes of fracture flowpaths were estimated for each test from measurements of fluid volume before wetting front arrivals and from measurements of drainage volume into the slot after termination of injection. The flowpath volumes were

found to increase from <0.2 liter initially to ~1.0 liter during recovery, with some stepped increments of 0.1 to 0.3 liter observed.

- Plug-flow processes were observed with tracer analyses. "New" water replaced "old" water from the previous test.

The stepped and intermittent changes could be associated with heterogeneous distribution of storage volumes in the connected fracture flow paths, in the dead-end fractures, and in the rock matrix blocks. The test results from Alcove 6 could be used to evaluate fracture flows and fracture-matrix interactions.

Uncertainties are associated with series of tests over relatively short durations in comparison with seepage tests in niches. With limited number of tests, uncertainties are expected to be larger than tests collecting more data. The understanding gained from Alcove 6 testing were used in designing other tests, such as the Alcove 8/Niche 3107 (Niche 3) tests described in Section 6.12. The later tests have much longer durations over larger scales.

7.7 SUMMARY AND CONCLUSIONS OF FLOW THROUGH THE FAULT AND MATRIX IN THE TEST BED AT ALCOVE 4

Fault and matrix flow data were collected in a test bed located in the PTn at Alcove 4 in the ESF. Using a series of horizontal boreholes, the intake rates and plume travel times in various locations within the test bed were determined, as described in Section 6.7, in Salve et al. 2003 [164470], and in Salve and Oldenburg 2001 [157316].

These test results revealed aspects of flow in a fault located within the nonwelded tuffs and provided insights into the flow properties of the PTn. With the exception of a well-defined fault trace, no visible fracture traces are evident in the bulk of the test bed in the Paintbrush nonwelded tuff test bed. A series of localized liquid-release tests helped determine that:

- Intake rates within a fault located in the PTn decreased as more water was introduced into the release zone (i.e., from an initial value of ~200 mL/min to ~50 mL/min after 193 liters of water entered the injection zone).

- The travel time of the wetting front resulting from water released in the fault decreased when the fault was wet (i.e., in closely timed tests, the plume traveled faster in subsequent releases).

- Over time, the hydrological properties of the fault appear to be altered, with water traveling along the fault at significantly slower rates.

- The matrix adjacent to the fault imbibed water that was introduced into the fault. Changes in saturation were seen more than 1.0 m from the point of release.

- The intake rates and wetting-front travel times in the matrix were significantly slower than in the fault. Water released into the matrix was observed to travel 0.45 m in 14 days.

Uncertainties are also associated with relative short durations in comparison with seepage tests in niches. With limited number of tests, uncertainties are expected to be larger than tests collecting more data. Not enough water was injected to induce seepage and water collection with the slot below. The tests were conducted to gain understanding of the flow through nonwelded tuff unit, with large damping capacities for modulating infiltrating pulses.

7.8 SUMMARY AND CONCLUSIONS OF WATER-POTENTIAL MEASUREMENTS CONDUCTED IN THREE NICHES WITHIN THE ESF MAIN DRIFT

Psychrometer measurements in the ESF suggest significant variability in water potentials between and within Niche 3566 (Niche 1), Niche 3650 (Niche 2), and Niche 3107 (Niche 3). All three niches are in the middle nonlithophysal TSw unit. The main observations are:

- The extent to which ventilation effects may have penetrated the rock is possibly greater than 3 m.

- Two possible zones were observed to have significantly high water potentials in Niche 3566 (Niche 1). The first was observed at the end of the middle borehole. The second was detected 6.25 m along borehole A in Niche 3566 (Niche 1). Borehole A was drilled from the niche toward the Sundance fault.

- There was large variability (-15 and -84 m) in the short distance of 0.9 m between two boreholes at Niche 3107 (Niche 3).

- In the zone beyond where ventilation effects of the ESF were observed (i.e., at 10 m depths), Niche 3566 (Niche 1, with potential 0.4 to –13 m) appeared to be wetter than Niche 3650 (Niche 2, with potential –1 to –39 m).

These potential measurements were conducted before the bulkhead closed in Niche 3566 (Niche 1) and before seepage measurements in Niche 3650 (Niche 2) and in Niche 3107 (Niche 3). The data are presented for future comparisons with potential measurements elsewhere in the ESF, including the Cross Drift.

Psychrometer measurements are sensitive to testing conditions, as discussed in Attachment VII. The measurement uncertainties associated with water potential in the field are relative large in comparison with other hydrological measurements, such as saturation from core measurements. The data from measurements before bulkhead closure are also greatly influenced by ventilation drying. The results indicate that wet conditions exist in the vicinity of Sundance fault. The absolute magnitude of the water potential should only be used with the measurement uncertainties and test site ventilating conditions taken into account.

7.9 SUMMARY AND CONCLUSIONS OF MONITORING THE CONSTRUCTION-WATER MIGRATION

The sensors in a borehole below the starter tunnel of the Cross Drift detected signals associated with wetting-front migration. In the other case, no seepage was observed at the crossover point along the ESF Main Drift below the ECRB Cross Drift. Cross Drift starter tunnel is located in

the upper lithophysal TSw unit. The crossover point in the ESF Main Drift is located in the middle nonlithophysal TSw unit.

The specific observations are

- At the starter tunnel, three events were observed along the borehole below the starter tunnel at depths close to 10 m. The ponding event that occurred on March 8, 1998, increased water-potential values up to a depth of 8.65 m (17.3 m along the borehole). During this event, the magnitude of the disturbance decreased farther into the borehole, with an interesting aberration observed at a depth of 9.4 m: the change in water potentials was significantly larger than the expected trend.

- At different times during the monitoring period, the impact on changes in water-potential values occurred at different locations along the borehole. Early in March 1998, the large impact was restricted to close to the borehole collar, whereas by early April 1998, this impact was relatively larger—between 9.4 and 11.4 m.

- One concern that could arise from the use of a slanting borehole to measure wetting-front migration is the possibility of the bore cavity short-circuiting flow paths. For this particular investigation, this short-circuiting does not appear to be happening, as indicated by the analysis of recovery responses observed at the depth of 5.2 m. Here, the response to a wetting event was negligible when compared with other psychrometers close to this location (above and below), suggesting that this zone was well isolated (hydraulically) from the adjacent zones and did not detect the wetting front.

- The response of the electrical resistivity probes when compared with the performance of psychrometers suggests that these probes (with their current design) can be effectively used as a qualitative tool to detect the arrival (or departure) of wetting fronts. Unlike psychrometers, these probes are relatively inexpensive, easy to maintain, and have a low failure rate. These advantages make them particularly useful for extensive downhole monitoring applications in fractured-rock environments such as found at Yucca Mountain.

- At the crossover point, no seepage was observed, nor were wetting-front signals detected at the crossover point when the Cross Drift tunnel boring machine (TBM) passed over the ESF Main Drift. The TBM apparently did not use enough water to induce dripping into the Main Drift, 17.5 m below. The confirmation of no seepage at the crossover point establishes the lower limit for the drift-to-drift flow and drift seepage processes associated with construction-water usage.

In the repository at Yucca Mountain, performance-confirmation drifts are planned to be located above (or below) the waste emplacement drifts to monitor the waste-induced impacts. It is therefore important to evaluate the drift-to-drift migration, drift seepage, and wetting-front detection to assess the potential impacts. The experience in the integrated monitoring station at the crossover point (with seepage collection trays, water-potential and wetting-front sensors, and thermal/visual imaging devices) can be applied to future testing and monitoring tasks.

Uncertainties are large for these observations of wetting front migrations associated with construction water usage, both from the sensor sensitivities and from the information needed for the total amount and rates used for the excavation. The findings did provide order of magnitude estimates on the migration below drifts.

7.10 SUMMARY AND CONCLUSIONS OF ANALYSES OF CONSTRUCTION EFFECTS

Some observations of ESF moisture conditions are presented in Section 6.10.1.1 and Section 6.10.1.2. The ESF Main Drift is in middle nonlithophysal TSw unit. The ECRB Cross Drift bullheaded sections are in the lower lithophysal, lower nonlithophysal TSW units, and the Solitario Canyon fault. From the observations:

- The newly excavated drift has high humidity conditions detected near the TBM.
- The relative humidity gradient near the end of the tunnel was greater than the gradient close to the entrance in the month after the excavation.
- Construction water migration results are presented in Section 6.10.1.3 and in Finsterle 2002 [165415]:
- The constuction water penetration reached 30 m depth at a borehole outside Alcove 7 (Figure 6.10-1-3).

In the ongoing moisture study of bulkheaded sections in the ECRB Cross Drift, observations were as follows:

- Water-potential measurements in boreholes suggest that the formation (in tuff matrix) is still relatively dry to a depth of 0.5–1.0 m.
- Moisture conditions (relative humidity and temperature) respond to bulkhead entries and TBM power fluctuations relatively quickly.
- Wet spots were observed and liquid water was collected in sections, with the water likely originating from condensation, based on chemical analyses of clean water collected. Isotopic signatures indicate that water collected has undergone an evaporation shift.

The major uncertainties are the interpretation if the observed moisture and wetness are associated with condensation or associated with seepage. The observations, the moisture evolution data, the drying profiles into the rocks, together with chamical analyses of collected water, are the basis to address this large uncertainty associated with the origin of water observed.

7.11. SUMMARY AND CONCLUSIONS OF SYSTEMATIC HYDROLOGICAL CHARACTERIZATION ALONG THE ECRB CROSS DRIFT

Hydrological characterization of the lower lithophysal zone of the Topopah Spring welded tuff unit was initiated in the ECRB Cross Drift, using the systematic approach of testing at regular intervals as described in Section 6.11 and in Cook et al. 2003 [165424]. Data and analyses from

several sets of completed tests were performed in 10 zones over four low-angle boreholes. The results to date indicate that:

- Small fractures (less than 1 m in length) are well connected, giving rise to air-permeability values on the order of 10^{-11} m^2. The connected fractures probably constitute the main contribution to fast paths for liquid flow.

- In the transient process of establishing the fast paths between the water release (at a vertical distance ranging from 1 to 5 m above the drift) to the drift ceiling, some water imbibes into the rock matrix, and some seeps into the lithophysal cavities. Out of the available storage porosity of 0.125 of the lithophysal cavities, about 20% to 50% participates in taking in water introduced when the rate of injection is tens of milliliters per minute. When the water-release rate is an order of magnitude higher, water flow occurs mainly in the fractures, with little participation from the matrix or lithophysal cavities during the time period it takes to intersect the drift.

- Under steady-state conditions, water introduced from one to several meters above the drift flows down toward the drift not in a uniform plume, but in preferential paths. A fraction of the water would miss the drift because of nonuniform flow from fracture heterogeneity, and a fraction of water would be diverted around the drift because of capillary effects. The former component of nonintersecting flow is controlled by geometry and is likely independent of the water-release rate.

- An estimate is made of the injection rate (from a borehole of a given area at a given distance above the drift) below which there is no seepage into the drift. Based on the discussion in Section 6.11.3.3 for borehole LA1, we arrive at a value of 15 mL/min for a projected borehole area of 0.13 m^2 at an average height of 1.3 m above the drift.

- Because of the low humidity inside the Cross Drift, and because of the drift ventilation system, effects of evaporation must be considered in interpreting seepage data from systematic testing. Relative humidity measurements and open-pan evaporation measurements were incorporated into the systematic-testing equipment system, following the completion of the first set of tests (when the significance of evaporation was first noted).

- Systematic testing at LA2 and LA1 revealed effective porosity for one-time fill cavities of 0.028, 0.027 for drainable cavities, and 0.013 for fractures. The threshold flux from LA1 zone 2 was found to be 15 mL/min, corresponding flux at borehole: ~57,000 mm/year.

- Systematic testing at LA3 and LA4 revealed very heterogeneous responses, ranging from tight zones with low capacities to accept water, to a zone with nearly 100% of all water diverted around the drift.

The fully automated feature of the systematic-testing equipment has served investigators well. There were some prolonged periods when field problems with the ventilation system prevented

the physical presence of investigators who were relying exclusively on being able to control the test from off-site.

As for all field-testing programs, the initial sets of measurements revealed many unforeseen items that provide insight into modification and improvement of the equipment system and testing protocol. Systematic testing is at a stage where all major experimental problems have been worked out. Such testing will be productive in providing hydrological characteristics of the heterogeneous lower lithophysal unit.

DTN: LB0110SYST0015.001 (computed comparisons from systematic testing) is technical product output from the analysis presented in Section 6.11 of this Scientific Analysis report.

DTN: LB0110SYST0015.001 was generated in 2001 for systematic testing results from raw data for the first two slanted boreholes drilled into the crown of the ECRB Cross Drift, as illustrated in Figure 6.11.2-1 through Figure 6.11.2-10. Later data sets include data processing and eliminate the needs for generating this type of technical product output. The strength of systematic testing is to gain insight on how spatial heterogeneity impacts seepage, flow, and transport processes. Uncertainties associated with ventilation effects are significant for the testing conditions in the periodically ventilated ECRB Cross Drift. The systematic testing data set was the first set available for seepage evaluation in the lower lithophysal zone in 2001 and is used in recent revision of the Seepage Calibration Model (BSC 2003 [162267]).

7.12 SUMMARY AND CONCLUSIONS OF DRIFT-TO-DRIFT TESTS BETWEEN ALCOVE 8 AND NICHE 3107 (NICHE 3)

Alcove 8 is located in the upper lithophysal tuff of TSw, ~20 m directly above Niche 3107 (Niche 3) in the middle nonlithophysal tuff of TSw. From fault testing and preliminary stages of the block test in this unique test bed Alcove 8-Niche 3107 (Niche 3), we have obtained data that describes the response of the system to releases of water under constant-head conditions. Specifically:

- Infiltration rates along the fault reached quasi-steady-state conditions ~45 days after water was introduced to the infiltration zones, and the infiltration rates varied at different locations along the fault.

- Observations of saturation changes within the fault indicate the velocity of the wetting front vertically along the fault to be ~0.65 m/s.

- Seepage observations indicate that quasi-steady state conditions may have been reached two months after the initial releases into the fault.

- Radar data collected thus far in support of the Alcove 8/Niche 3107 (Niche 3) infiltration experiment suggest that this method is appropriate for investigating subsurface anomalies that may be related to moisture migration.

- Experimental results indicate that matrix diffusion has an important effect on solute transport.

- Observed low seepage recovery rate from the fault implies good communication between the fault and the surrounding fracture networks.

- Similar tracer arrival times (corresponding to the peak concentration values) for most flow paths suggest that macrodispersion may not be important for solute transport in unsaturated fractured rock.

- The observation of the first seepage spot in Niche 3107 (Niche 3), 21 days after water was introduced along the nonfaulted section of Alcove 8, suggests that wetting-front velocity was ~1.0 m/day below the large plot test bed.

7.13 SUMMARY AND CONCLUSIONS OF BUSTED BUTTE UNSATURATED ZONE TRANSPORT TEST

The UZTT at Busted Butte was designed to address uncertainties associated with flow and transport in the UZ. The UZTT is comprised of three tightly integrated efforts: the field test, a parallel laboratory program, and assessment and validation of computational models. Section 6.13 and Attachment VIII present the results of the field test and associated laboratory analyses. The model assessment and validation is reported in *Radionuclide Transport Models under Ambient Conditions* (BSC 2003 [163228]). The tracer sorption to vitric tuffs of Busted Butte is also described in Turin et al. 2002 [164633].

The design of the UZTT began in 1997. Injection of tracers for Phase 1 began in April 1998, and Phase 2 injection was completed in October 2000. The mineback excavation of Phase 2 continued in 2001. Results to date provide important information for the UZ transport performance of Calico Hills hydrological units, with the following key conclusions:

- Flow and transport in the Calico Hills hydrological units (Tac and Tptpv1) are strongly capillary dominated, as observed from fluorescein distributions in the Phase 1A test.

- Fractures at Busted Butte do not act as fast flow paths, as observed in Phase 1A. However, they appear to play a role as a barrier or permeability contrast boundary.

- Heterogeneity appears to have a significant effect on flow, as observed in Phase 1A for layer contacts and in Phase 2 for faults.

- Breakthrough times of nonreactive bromide are approximately linear with travel distance.

- Sorption can delay chemical transport, as shown from the breakthrough curves of lithium.

- Neutron moisture data corroborate with plume and breakthrough data in moisture changes associated with injections into the test block.

- Laboratory measurements with radionuclides collaborate with field tracer testing, with technetium (as pertechneate anion) moving slightly faster than tritiated water in a small

cubic foot block and at approximately the same velocity in a cubic meter block from the Busted Butte site.

7.14 SUMMARY AND CONCLUSIONS FOR GEOCHEMICAL AND ISOTOPIC OBSERVATIONS AND ANALYSIS OF THE UNSATURATED ZONE

Section 6.14 and references therein describes the geochemical and isotopic observations and analyses of samples collected primarily along the underground drifts in the unsaturated zone. The summaries are presented in the following sections on pore water and rock geochemistry (Section 7.4.1 for Section 6.14.1), isotopic examination of chloride-36 and tritium for potential fast flow signals and fluid inclusion temperature signals for thermal history at Yucca Mountain (Section 7.14.2 for Section 6.14.2), uranium isotopic studies of past climate records and delineation of UZ flow zones (Section 7.14.3 for Section 6.14.3), and fracture mineral distributions and implications (Section 7.14.4 for Section 6.14.4). Some model interpretations and detailed analyses are documented in cited references.

7.14.1 Pore Water and Bulk Repository Rock Unit Geochemistry

Analysis and interpretation of pore-water data are described in Section 6.14.1.1. Rock chemistry in the Cross Drift is compiled in Section 6.14.1.2. In the TSw, the results indicate:

- The dissolved ion composition of pore water shows considerable stratigraphic and lateral variability (Table 6.14.1-1).
- The variability in major and trace elements and in mineral contents of the rocks is exceedingly small (Table 6.14.1-2, Table 6.14.1-3, Table 6.14.1-4)

The existence of pore-water variability in the repository deep underground testifies to the inefficiency of advective or diffusional mixing in the downward percolation of pore water.

The rock samples from the Cross Drift include both lithophysal and nonlithophysal zones. The analyses indicate the chemical homogeneity of the phencryst-poor rhyolite unit, excluding localized deposits of vapor-phase minerals and low-temperature calcite and opal in fractures, cavities, and faults (Peterman and Cloke 2002 [162576]).

7.14.2 Isotope Geochemical Studies

Fast-flow paths and the thermal history at Yucca Mountain have been evaluated in Section 6.14.2.

7.14.2.1 Isotope Geochemical Studies of ^{36}Cl/Cl Signatures

As acknowledged in Section 6.14.2, the ^{36}Cl validation study report has not been finalized. The conclusions will be documented in the final report of BSC (2003 [166104]).

7.14.2.2 Trituim in Porewater

The analyses of tritium in pore water from several locations within the ESF and ECRB indicate that substantial amounts of young pore exist water:

- In the Bow Ridge fault above the Paintbrush Tuff nonwelded units
- In the South Ramp of the ESF, where the Paintbrush Tuff nonwelded units are faulted and offset
- From 750 to 950 m, in the ECRB in the upper lithophysal unit of the Topopah Spring Tuff.

The occurrences in the Bow Ridge fault and in the South Ramp of the ESF are clearly linked to the absence of the Paintbrush Tuff nonwelded units or the inability of these units to impede downward percolation of young water at those locations. In the ECRB, it is unclear what features may provide the pathways for the percolation of young water. The investigation into the presence of tritium in pore water from the ECRB is in progress.

The distribution of the percolation of young water in the ESF and ECRB does not generally agree with that determined from chlorine isotopes (Fabryka-Martin et al. 1998 [162737]).

- Analyses of chlorine-36 indicate significant percolation of young water at the Drill Hole Wash fault and Sundance fault, where only 1 of 52 samples contained tritium in excess of the 1 TU threshold that indicates the presence of young water.
- Analyses of chlorine-36 in the ESF South Ramp did not identify the presence of young water where 16 of 28 samples contained tritium in excess of the 1 TU threshold.

It is possible that in the Drill Hole Wash fault and Sundance fault, the pore water near the fractures that provided the fast pathways evaporated, due to the barometric pumping of relatively dry air. If this did occur, the evaporated water could leave behind chloride salts containing post-weapons-testing isotope ratios, while the tritium evidence would evaporate with the water. In the South Ramp, where numerous samples contained post-weapons-testing levels of tritium, it is possible that large amounts of old chloride were dissolved during percolation of the young water, such that any post-weapons-testing chlorine-36 ratios would be unrecognizable.

7.14.2.3 Thermal Regime

- Depositional temperature of fluid inclusion, oxygen isotope evaluation, and U-Th geochronologic study are used to reconstruct the sequence of thermal history at Yucca Mountain.
- Depositional temperatures of secondary mineral deposits in the UZ at Yucca Mountain, estimated from fluid inclusion temperature T_h and calculated from calcite $\delta^{18}O$ values, range from present-day ambient to as high as 93°C.

- Coupled with depositional ages interpolated or extrapolated from U-Pb geochronologic studies of associated chalcedony or opal, these temperature estimates demonstrate a thermal history generally consistent with regional heating from the deep magmatic sources responsible for the silicic volcanism 15 to 11 million years ago.

- Maximum temperatures in the UZ occurred more than 10 million years ago, followed by slow cooling to near-modern ambient temperatures between 2 and 4 millions years ago.

- The UZ appears to have been at or near present-day ambient temperatures for the past 2 to 4 million years.

- Several deposits in the North Ramp, however, appear to have formed at temperatures too high to reflect conductive heating from a magmatic heat source. These deposits are associated with fractures present since early cooling of the Tiva Canyon Tuff and may record fumarolic activity during posteruptive cooling of the tuffs 12.7 million years ago.

The implications are as follows:

- None of the thermal data requires or is consistent with, deposition from upwelling hydrothermal fluids, as some have proposed.

- The sparse and scattered distribution of the secondary mineral deposits and their restriction to fracture footwalls and cavity floors is incompatible with deposition from upwelling of hydrothermal fluids. Upwelling would cause local flooding of the open spaces and result in a pervasive deposition of secondary minerals that is not observed.

- The distribution and morphology, as well as the geochemical characteristics of the deposits, are fully consistent with deposition from meteoric waters infiltrating at the surface and percolating through the UZ, but at temperatures greater than modern ambient temperatures until 2 to 4 million years ago.

7.14.3 Uranium Studies

Uranium isotope ratios are used to indicate past climate conditions and flow paths in the UZ in Section 6.14.3.

7.14.3.1 Uranium-Series Dating

Two methods of U-series dating were applied to finely laminated opal hemispheres formed within unsaturated felsic tuffs at Yucca Mountain.

1. An ion microprobe was used to determine isotope compositions of 45 μm diameter spots on transects across two millimeter-sized opal hemispheres.

2. *In situ* microdigestions were used to sequentially remove 2–5 μm thick layers of outermost material.

Both methods substantially improved spatial resolution of the analyses relative to the millimeter-scale subsamples analyzed previously by standard total digestion techniques. As a result, more detailed reconstructions of the opal growth histories can be obtained.

Ion-microprobe ^{230}Th/U and model ^{234}U/^{238}U dates from traverses across two opal hemispheres indicate that:

- Age increases progressively with microstratigraphic depth. Spots near the base of the hemispheres have ages of more than a million years.
- The age-depth relations define average opal growth rates of 0.56 and 0.683 mm/m.y. for two separate hemispheres. *In situ* microdigestions resulted in even finer spatial resolution (2 to 5 μm per analysis) as well as the youngest dates.
- Reliable ^{230}Th/U dates for the outermost layers of several hemispheres range from 6.34 ± 0.12 to 11.6 ± 1.4 ka.

Sequential microdigestions from the outer 22 μm of one hemisphere yield:

- Dates that increase progressively to 37.1 ± 1.6 ka and result in an average growth rate of 0.68 mm/m.y.
- However, opal growth rates appear to have been faster between about 25 and 40 ka (1.16 mm/m.y.) and slower between about 5 and 25 ka (0.35 mm/m.y.).
- Both the lack of outermost opal dates less than about 6 ka and age-depth intercepts of 3 to 10 ka imply that opal was not deposited in the last several thousand years.

Although dates determined by these two methods are not determined at the highest levels of precision, they are considered reliable because of the overall consistency of both ages and initial ^{234}U/^{238}U ratios in both data sets, and because of the identical average growth rates calculated for the two different scales of sample resolution. Collectively, these data:

- Confirm the previously hypothesized conceptual model of "continuous" deposition for Yucca Mountain UZ secondary minerals (Neymark and Paces 2000 [127012]; Neymark et al. 2000 [162710]; Paces et al. 2001 [156507]).
- Demonstrate that material is added at very slow rates from solutions seeping into air-filled cavities, and that these rates are likely correlated with climate-controlled percolation flux.
- Absence of mineral growth over the last several thousand years implies that seepage may cease completely during the most arid parts of Pleistocene climate cycles.

It is not conclusive whether the growth patterns observed in HD2074 opal hemispheres can be correlated with other UZ mineral deposits, and whether these patterns can be correlated more reliably with other climate signals.

7.14.3.2 U-series Flow Paths in the UZ

New TIMS analyses of ^{234}U-^{238}U-^{230}Th-^{232}Th in whole-rock samples confirm earlier indications of ^{234}U-^{230}Th-^{238}U disequilibria in the Yucca Mountain UZ tuffs.

- Initial results indicate that radioactive disequilibria are present as a result of both matrix and fracture flow, and that the degree of disequilibria between these two environments is similar.

- Results also show systematic differences in $^{234}U/^{238}U$ and $^{230}Th/^{238}U$ ratios that are consistent with sample location within the UZ and with hydrological concepts of higher percolation fluxes in the shallow Bow Ridge fault zone (20–30 m depth) and lower fluxes at the repository horizon (220–300 m depth).

Data from most samples of welded tuff at the repository horizon experienced lesser rates of ^{238}U removal and greater loss of ^{234}U relative to ^{238}U. In contrast, samples from the shallow Bow Ridge fault zone show a higher degree of ^{238}U loss and smaller preferential ^{234}U loss, indicating isotopic evolution in an environment with greater amounts of water/rock interaction. Samples in the footwall block of the Bow Ridge fault zone show some evidence for U-gain that may be coupled to water/rock interactions within the fault zone.

Amounts of water/rock interaction estimated from these U-series data may be lower for rocks in the repository horizon at Yucca Mountain than they appear to be in other crystalline rock environments. This may reflect the lower long-term effective moisture present in the Yucca Mountain setting.

Results from these samples suggest that U-series data may provide a tool for identifying zones of lesser and greater percolation flux within the Yucca Mountain UZ. These types of data may therefore offer a means of independently testing numerical models of flow and transport.

7.14.4 Fracture Mineralogy

Low-temperature deposits of calcite and opal are present in open cavities and fractures within the volcanic rocks at Yucca Mountain. The abundances of these minerals have been estimated in Section 6.14.4 by surveying underground tunnels and by direct measurement of carbonate in borehole cuttings.

- The abundances are log-normally distributed about a mean value of 0.03% of the rock volume, based on ESF line survey data.

- The abundance of calcite and opal is generally not correlated with faults, fracture density, or topography, although one line survey with a large abundance is located beneath Drill Hole Wash, possibly associated with a nearby fault.

- Both line survey data collected in the Cross Drift and estimates of calcite abundance from the nearby borehole USW SD-6 show a decrease in calcite with stratigraphic depth. This is interpreted as indicating a decrease in seepage with depth (Marshall et al. 2003 [162891]).

8. INPUTS AND REFERENCES

The following is a list of the references cited in this document. Column 1 represents the unique six digit numerical identifier (the Document Input Reference System [DIRS] number), which is placed in the text following the reference callout (e.g., BSC 2002 [160819]). The purpose of these numbers is to assist the reader in locating a specific reference. Within the reference list, multiple sources by the same author (e.g., BSC 2002) are sorted alphabetically by title.

8.1 DOCUMENTS CITED

106071 Andreini, M.S. and Steenhuis, T.S. 1990. "Preferential Paths of Flow Under Conventional and Conservation Tillage." *Geoderma, 46*, 85-102. Amsterdam, The Netherlands: Elsevier. TIC: 245381.

161531 Axelrod, D.I. 1979. "Age and Origin of Sonoran Desert Vegetation." *Occasional Papers of the California Academy of Sciences*. Number 132. San Francisco, California: California Academy of Sciences. TIC: 218991.

100029 Barr, D.L.; Moyer, T.C.; Singleton, W.L.; Albin, A.L.; Lung, R.C.; Lee, A.C.; Beason, S.C.; and Eatman, G.L.W. 1996. *Geology of the North Ramp — Stations 4+00 to 28+00, Exploratory Studies Facility, Yucca Mountain Project, Yucca Mountain, Nevada*. Denver, Colorado: U.S. Geological Survey. ACC: MOL.19970106.0496.

156269 Bear, J. 1972. *Dynamics of Fluids in Porous Media*. Environmental Science Series. Biswas, A.K., ed. New York, New York: Elsevier. TIC: 217356.

101191 Beason, S.C.; Turlington, G.A.; Lung, R.C.; Eatman, G.L.W.; Ryter, D.; and Barr, D.L. 1996. *Geology of the North Ramp - Station 0+60 to 4+00, Exploratory Studies Facility, Yucca Mountain Project, Yucca Mountain, Nevada*. Denver, Colorado: U.S. Geological Survey. ACC: MOL.19970106.0449.

104370 Benson, L. and Klieforth, H. 1989. "Stable Isotopes in Precipitation and Ground Water in the Yucca Mountain Region, Southern Nevada: Paleoclimatic Implications." [*Aspects of Climate Variability in the Pacific and the Western Americas*. Peterson, D.H., ed.]. Geophysical Monograph 55. Pages 41-59. Washington, D.C.: American Geophysical Union. TIC: 224413.

101196 Bish, D.L. and Vaniman, D.T. 1985. *Mineralogic Summary of Yucca Mountain, Nevada*. LA-10543-MS. Los Alamos, New Mexico: Los Alamos National Laboratory. ACC: MOL.19950412.0041.

100102 Bodvarsson, G.S. and Bandurraga, T.M., eds. 1996. *Development and Calibration of the Three-Dimensional Site-Scale Unsaturated Zone Model of Yucca Mountain, Nevada*. LBNL-39315. Berkeley, California: Lawrence Berkeley National Laboratory. ACC: MOL.19970701.0692.

155682 Bouwer, H. 1966. "Rapid Field Measurement of Air Entry Value and Hydraulic Conductivity of Soil as Significant Parameters in Flow System Analysis." *Water Resources Research, 2*, (4), 729-738. [Washington, D.C.]: American Geophysical Union. TIC: 225260.

106088 Braester, C. 1973. "Moisture Variation at the Soil Surface and the Advance of the Wetting Front During Infiltration at Constant Flux." *Water Resources Research, 9*, (3), 687-694. Washington, D.C.: American Geophysical Union. TIC: 242383.

107386 Broxton, D.E.; Chipera, S.J.; Byers, F.M., Jr.; and Rautman, C.A. 1993. *Geologic Evaluation of Six Nonwelded Tuff Sites in the Vicinity of Yucca Mountain, Nevada for a Surface-Based Test Facility for the Yucca Mountain Project.* LA-12542-MS. Los Alamos, New Mexico: Los Alamos National Laboratory. ACC: NNA.19940224.0128.

100024 Broxton, D.E.; Warren, R.G.; Byers, F.M.; and Scott, R.B. 1989. "Chemical and Mineralogic Trends Within the Timber Mountain–Oasis Valley Caldera Complex, Nevada: Evidence for Multiple Cycles of Chemical Evolution in a Long-Lived Silicic Magma System." *Journal of Geophysical Research, 94*, (B5), 5961-5985. Washington, D.C.: American Geophysical Union. TIC: 225928.

154874 BSC (Bechtel SAIC Company) 2001. *Analysis of Geochemical Data for the Unsaturated Zone*. ANL-NBS-HS-000017 REV 00 ICN 01. Las Vegas, Nevada: Bechtel SAIC Company. ACC: MOL.20010405.0013.

154622 BSC (Bechtel SAIC Company) 2001. *Geologic Framework Model Analysis Model Report*. MDL-NBS-GS-000002 REV 00 ICN 02. Las Vegas, Nevada: Bechtel SAIC Company. ACC: MOL.20010313.0505.

158200 BSC (Bechtel SAIC Company) 2001. *Test Plan for: Niche 5 Seepage Testing*. SITP-02-UZ-002 REV 00. Las Vegas, Nevada: Bechtel SAIC Company. ACC: MOL.20020117.0200.

156609 BSC (Bechtel SAIC Company) 2001. *Unsaturated Zone Flow Patterns and Analysis.* MDL-NBS-HS-000012 REV 00. Las Vegas, Nevada: Bechtel SAIC Company. ACC: MOL.20011029.0315.

160247 BSC (Bechtel SAIC Company) 2002. *Analysis of Geochemical Data for the Unsaturated Zone*. ANL-NBS-HS-000017 REV 00 ICN 02. Las Vegas, Nevada: Bechtel SAIC Company. ACC: MOL.20020314.0051.

158794 BSC (Bechtel SAIC Company) 2002. *Guidelines for Developing and Documenting Alternative Conceptual Models, Model Abstractions, and Parameter Uncertainty in the Total System Performance Assessment for the License Application*. TDR-WIS-PA-000008 REV 00, ICN 01. Las Vegas, Nevada: Bechtel SAIC Company. ACC: MOL.20020904.0002.

160819 BSC (Bechtel SAIC Company) 2002. *Technical Work Plan for: Performance Assessment Unsaturated Zone*. TWP-NBS-HS-000003 REV 02. Las Vegas, Nevada: Bechtel SAIC Company. ACC: MOL.20030102.0108.

160146 BSC (Bechtel SAIC Company) 2002. *Total System Performance Assessment-License Application Methods and Approach*. TDR-WIS-PA-000006 REV 00. Las Vegas, Nevada: Bechtel SAIC Company. ACC: MOL.20020923.0175.

165564 BSC (Bechtel SAIC Company) 2003. *Abstraction of Drift Seepage*. MDL-NBS-HS-000019 REV 00 ICN 01. Las Vegas, Nevada: Bechtel SAIC Company. ACC: DOC.20031112.0002.

166104 BSC (Bechtel SAIC Company) 2003. *Chlorine-36 Validation Studies at Yucca Mountain, Nevada*. TDR-NBS-HS-000017 REV 00A-Draft. Las Vegas, Nevada: Bechtel SAIC Company. ACC: MOL.20031105.0082.

164889 BSC (Bechtel SAIC Company) 2003. *Drift-Scale Radionuclide Transport*. MDL-NBS-HS-000016 REV 00. Las Vegas, Nevada: Bechtel SAIC Company. ACC: DOC.20030902.0009.

164873 BSC (Bechtel SAIC Company) 2003. *Features, Events, and Processes in UZ Flow and Transport*. ANL-NBS-MD-000001 REV 02A. Las Vegas, Nevada: Bechtel SAIC Company. ACC: MOL.20031016.0004.

165179 BSC (Bechtel SAIC Company) 2003. *Q-List*. TDR-MGR-RL-000005 REV 00. Las Vegas, Nevada: Bechtel SAIC Company. ACC: DOC.20030930.0002.

163228 BSC (Bechtel SAIC Company) 2003. *Radionuclide Transport Models Under Ambient Conditions*. MDL-NBS-HS-000008 REV 01. Las Vegas, Nevada: Bechtel SAIC Company. ACC: DOC.20031201.0002.

164491 BSC (Bechtel SAIC Company) 2003. *Repository Design Project, Repository/PA IED Subsurface Facilities*. 800-IED-WIS0-00103-000-00Ab. Las Vegas, Nevada: Bechtel SAIC Company. ACC: MOL.20030813.0178.

161726 BSC (Bechtel SAIC Company) 2003. *Repository Design, Repository/PA IED Subsurface Facilities*. 800-IED-EBS0-00401-000-00B. Las Vegas, Nevada: Bechtel SAIC Company. ACC: MOL.20030109.0145.

162267 BSC (Bechtel SAIC Company) 2003. *Seepage Calibration Model and Seepage Testing Data.* MDL-NBS-HS-000004 REV 02. Las Vegas, Nevada: Bechtel SAIC Company. ACC: DOC.20030408.0004.

163226 BSC (Bechtel SAIC Company) 2003. *Seepage Model for PA Including Drift Collapse*. MDL-NBS-HS-000002 REV 02. Las Vegas, Nevada: Bechtel SAIC Company. ACC: DOC.20030709.0001.

163045 BSC (Bechtel SAIC Company) 2003. *UZ Flow Models and Submodels*. MDL-NBS-HS-000006 REV 01. Las Vegas, Nevada: Bechtel SAIC Company. ACC: DOC.20030818.0002.

101433 Buesch, D.C. and Spengler, R.W. 1998. "Character of the Middle Nonlithophysal Zone of the Topopah Spring Tuff at Yucca Mountain." *High-Level Radioactive Waste Management, Proceedings of the Eighth International Conference, Las Vegas, Nevada, May 11-14, 1998*. Pages 16-23. La Grange Park, Illinois: American Nuclear Society. TIC: 237082.

100106 Buesch, D.C.; Spengler, R.W.; Moyer, T.C.; and Geslin, J.K. 1996. *Proposed Stratigraphic Nomenclature and Macroscopic Identification of Lithostratigraphic Units of the Paintbrush Group Exposed at Yucca Mountain, Nevada*. Open-File Report 94-469. Denver, Colorado: U.S. Geological Survey. ACC: MOL.19970205.0061.

146978 Bussod, G. 1999. Busted Butte On-Site Logbook #2, UZ Transport Field Test (LA-EES-5-NBK-98-020). Scientific Notebook SN-LANL-SCI-039-V1. ACC: MOL.20000307.0380.

165281 Bussod, G. 2001. LA-EES-1-NBK-98-005, UZ Transport Test Notebook 2. Scientific Notebook SN-LANL-SCI-038-V1. ACC: MOL.20010830.0382.

165300 Bussod, G. and Turin, H.J. 2000. LA-CST-NBK-98-017, Busted Butte Project IC/ICPAES Notebook. Scientific Notebook SN-LANL-SCI-127-V1. ACC: MOL.20001219.0010.

165306 Bussod, G. and Wolfsberg, L. 2000. LA-CST-NBK-98-002, Busted Butte Project #1. Scientific Notebook SN-LANL-SCI-159-V1. ACC: MOL.20001219.0004.

165312 Bussod, G. and Wolfsberg, L. 2000. LA-CST-NBK-98-009, Busted Butte Project Fluorimetry Notebook. Scientific Notebook SN-LANL-SCI-169-V1. ACC: MOL.20000926.0186.

165308 Bussod, G. and Wolfsberg, L. 2000. LA-CST-NBK-98-012, Busted Butte Project Notebook # 2. Scientific Notebook SN-LANL-SCI-160-V1. ACC: MOL.20001219.0008.

165310 Bussod, G. and Wolfsberg, L. 2000. LA-CST-NBK-98-015, Busted Butte Pad Processing Notebook # 1. Scientific Notebook SN-LANL-SCI-161-V1. ACC: MOL.20001219.0002.

165311 Bussod, G. and Wolfsberg, L. 2000. LA-CST-NBK-98-016, Busted Butte Project Sample Tracking Forms. Scientific Notebook SN-LANL-SCI-163-V1. ACC: MOL.20000926.0192.

165303 Bussod, G. and Wolfsberg, L. 2000. LA-CST-NBK-98-017, Busted Butte Project IC/ICPAES Notebook. Scientific Notebook SN-LANL-SCI-136-V1. ACC: MOL.20001023.0241.

165301 Bussod, G. and Wolfsberg, L. 2000. LA-CST-NBK-98-018, Busted Butte Project Microscopy Notebook. Scientific Notebook SN-LANL-SCI-133-V1. ACC: MOL.20000926.0199.

165319 Bussod, G. and Wolfsberg, L. 2000. LA-CST-NBK-99-003, Busted Butte ICPMS. Scientific Notebook SN-LANL-SCI-192-V1. ACC: MOL.20000926.0201.

165305 Bussod, G.; Turin, H.J.; and Wolfsberg, L. 2000. Busted Butte Tracer Preparation Notebook #1. Scientific Notebook SN-LANL-SCI-145-V1. ACC: MOL.20000710.0325; MOL.19991109.0060.

165317 Bussod, G.; Turin, H.J.; and Wolfsberg, L. 2000. LA-CST-NBK-99-004; YMP Busted Butte Sorption. Scientific Notebook SN-LANL-SCI-191-V1. ACC: MOL.20001219.0012.

149129 Bussod, G.Y. 1998. Busted Butte On-Site Logbook #1, UZ Transport Field Test (LA-EES-5-NBK-98-010). Scientific Notebook SN-LANL-SCI-040-V1. ACC: MOL.20000321.0288.

165324 Bussod, G.Y. and Stockton, J. 1999. J. Stockton SEA-YMP Notebook #1. Scientific Notebook SN-LANL-SCI-043-V1. ACC: MOL.19990719.0103; MOL.19991109.0114.

165321 Bussod, G.Y. and Turin, H.J. 2001. LA-CST-NBK-98-004, Busted Butte Collection Pad Notebook. Scientific Notebook SN-LANL-SCI-199-V1. ACC: MOL.20010718.0258.

165364 Bussod, G.Y. and Wolfsberg, L. 2000. LA-EES-5-NBK-98-019, UZTT Cylinder Volume Notebook - Phase 1. Scientific Notebook SN-LANL-SCI-228-V1. ACC: MOL.20000926.0182; MOL.20001219.0023.

131513 Bussod, G.Y.; Coen, K.; and Eckhardt, R.C. 1998. *LA Testing Status Report: Busted Butte Unsaturated Zone Transport Test FY 98*. SPU85M4. Los Alamos, New Mexico: Los Alamos National Laboratory. TIC: 246363.

155695 Bussod, G.Y.; Turin, H.J.; and Lowry, W.E. 1999. *Busted Butte Unsaturated Zone Transport Test: Fiscal Year 1998 Status Report*. LA-13670-SR. Los Alamos, New Mexico: Los Alamos National Laboratory. TIC: 250657.

161770 Canori, G.F. and Leitner, M.M. 2003. *Project Requirements Document*. TER-MGR-MD-000001 REV 01. Las Vegas, Nevada: Bechtel SAIC Company. ACC: DOC.20030404.0003.

105210 Carlos, B.A.; Chipera, S.J.; Bish, D.L.; and Craven, S.J. 1993. "Fracture-Lining Manganese Oxide Minerals in Silicic Tuff, Yucca Mountain, Nevada, U.S.A." *Chemical Geology, 107*, 47-69. Amsterdam, The Netherlands: Elsevier. TIC: 208629.

153475 Cheng, H.; Edwards, R.L.; Hoff, J.; Gallup, C.D.; Richards, D.A.; and Asmerom, Y. 2000. "The Half-Lives of Uranium-234 and Thorium-230." *Chemical Geology, 169*, 17-33. [Amsterdam, The Netherlands]: Elsevier. TIC: 249205.

101331 Chipera, S.J.; Vaniman, D.T.; and Bish, D.L. 1996. *Zeolite Abundances and the Vitric-to-Zeolitic Transition in Drill Holes USW SD-7, 9, and 12, Yucca Mountain, Nevada*. LA-EES-1-TIP-96-005. Los Alamos, New Mexico: Los Alamos National Laboratory. ACC: MOL.19970407.0339.

105738 Clark, I.D. and Fritz, P. 1997. *Environmental Isotopes in Hydrogeology*. Boca Raton, Florida: Lewis Publishers. TIC: 233503.

165411 Cook, P. 2000. "In Situ Pneumatic Testing at Yucca Mountain." *International Journal of Rock Mechanics and Mining Sciences, 37*, ([1-2]), 357-367. [New York, New York]: Pergamon. TIC: 254967.

156902 Cook, P. 2001. Drift Scale Seepage Test. Scientific Notebook YMP-LBNL-JSW-PJC-6.2. ACC: MOL.20011105.0080.

165424 Cook, P.J.; Salve, R.; Freifeld, B.M.; and Tsang, Y.T. 2003. "Measurement System for Systematic Hydrological Characterization of Unsaturated Fractured Welded Tuff in a Mined Underground Tunnel." *Ground Water, 41*, (4), 449-457. Westerville, Ohio: National Ground Water Association. TIC: 211670.

165235 Coplen, T.B.; Hopple, J.A.; Böhlke, J.K.; Peiser, H.S.; Rieder, S.E.; Krouse, H.R.; Rosman, K.J.R.; Ding, T.; Vocke, R.D., Jr.; Révész, K.M.; Lamberty, A.; Taylor, P.; and De Bièvre, P. 2003. *Compilation of Minimum and Maximum Isotope Ratios of Selected Elements in Naturally Occurring Terrestrial Materials and Reagents*. Water-Resources Investigations Report 01-4222. Reston, Virginia: U.S. Geological Survey. TIC: 255203.

156876 CRWMS M&O (Civilian Radioactive Waste Management Management and Operating Contractor) 1999. *Exploratory Studies Facility, Cross Drift Alcove #8 Plan and Sections.* BABEAF000-01717-2100-40312 REV 00. Las Vegas, Nevada: CRWMS M&O. ACC: MOL.19990608.0041.

138960 CRWMS M&O 2000. *Mineralogical Model (MM3.0)*. MDL-NBS-GS-000003 REV 00 ICN 01. Las Vegas, Nevada: CRWMS M&O. ACC: MOL.20000120.0477.

151940 CRWMS M&O 2000. *Unsaturated Zone Flow and Transport Model Process Model Report*. TDR-NBS-HS-000002 REV 00 ICN 02. Las Vegas, Nevada: CRWMS M&O. ACC: MOL.20000831.0280.

151945 CRWMS M&O 2000. *Yucca Mountain Site Description*. TDR-CRW-GS-000001 REV 01 ICN 01. Las Vegas, Nevada: CRWMS M&O. ACC: MOL.20001003.0111.

154024 CRWMS M&O 2001. *Unsaturated Zone and Saturated Zone Transport Properties (U0100)*. ANL-NBS-HS-000019 REV 00 ICN 1. Las Vegas, Nevada: CRWMS M&O. ACC: MOL.20010201.0026.

165380 Daily, B. and Buettner, M. 2002. *Electrical Resistance Tomography at the Unsaturated Zone Transport Test at Busted Butte*. Scientific Notebook SN-LLNL-SCI-421-V1. ACC: MOL.20010522.0183; MOL.20020418.0126.

156869 Descour, J.M.; Hanna, K.; Conover, D.; and Hoekstra, B. 2001. *Seismic Tomography Technology for the Water Infiltration Experiment*. TDR-EBS-MD-000017 REV 00. Las Vegas, Nevada: Bechtel SAIC Company. ACC: MOL.20010508.0194.

100550 DOE (U.S. Department of Energy) 1998. *Total System Performance Assessment. Volume 3 of Viability Assessment of a Repository at Yucca Mountain*. DOE/RW-0508. Washington, D.C.: U.S. Department of Energy, Office of Civilian Radioactive Waste Management. ACC: MOL.19981007.0030.

165362 Drew, D. 2002. AECL Busted Butte Experiment General Laboratory Notebook - 3. Scientific Notebook SN-LANL-SCI-208-V3. ACC: MOL.20021023.0183.

165333 Drew, D. 2002. AECL Busted Butte Saturated Experiment Laboratory Notebook - 6. Scientific Notebook SN-LANL-SCI-206-V6. ACC: MOL.20021104.0186.

165330 Drew, D. 2002. AECL Busted Butte Saturated Experiment Laboratory Notebook-5. Scientific Notebook SN-LANL-SCI-206-V5. ACC: MOL.20020827.0022.

165338 Drew, D. 2002. AECL Busted Butte Unsaturated Experiment Laboratory Notebook - 10. Scientific Notebook SN-LANL-SCI-207-V10. ACC: MOL.20020827.0025.

165340 Drew, D. 2002. AECL Busted Butte Unsaturated Experiment Laboratory Notebook - 11. Scientific Notebook SN-LANL-SCI-207-V11. ACC: MOL.20021023.0178.

165344 Drew, D. 2002. AECL Busted Butte Unsaturated Experiment Laboratory Notebook - 12. Scientific Notebook SN-LANL-SCI-207-V12. ACC: MOL.20030313.0074.

165335 Drew, D. 2003. AECL Busted Butte Saturated Experiment Laboratory Notebook - 7. Scientific Notebook SN-LANL-SCI-206-V7. ACC: MOL.20030717.0441.

165346 Drew, D. 2003. AECL Busted Butte Unsaturated Experiment Laboratory Notebook - 13. Scientific Notebook SN-LANL-SCI-207-V13. ACC: MOL.20030904.0343.

165360 Drew, D.J. 2001. AECL Busted Butte Experiment General Notebook - 1. Scientific Notebook SN-LANL-SCI-208-V1. ACC: MOL.20010830.0390.

165361 Drew, D.J. 2001. AECL Busted Butte Experiment General Notebook - 2. Scientific Notebook SN-LANL-SCI-208-V2. ACC: MOL.20011219.0336.

166105 Drew, D.J. 2001. AECL Busted Butte Field Notebook - 1. Scientific Notebook SN-LANL-SCI-205-V1. ACC: MOL.20010716.0243.

165323 Drew, D.J. 2001. AECL Busted Butte Saturated Experiment Laboratory Notebook - 1. Scientific Notebook SN-LANL-SCI-206-V1. ACC: MOL.20010830.0375.

165325 Drew, D.J. 2001. AECL Busted Butte Saturated Experiment Laboratory Notebook - 2. Scientific Notebook SN-LANL-SCI-206-V2. ACC: MOL.20011219.0343.

165336 Drew, D.J. 2001. AECL Busted Butte Unsaturated Experiment Laboratory Notebook - 1. Scientific Notebook SN-LANL-SCI-207-V1. ACC: MOL.20010830.0387.

165348 Drew, D.J. 2001. AECL Busted Butte Unsaturated Experiment Laboratory Notebook - 2. Scientific Notebook SN-LANL-SCI-207-V2. ACC: MOL.20010830.0378.

165349 Drew, D.J. 2001. AECL Busted Butte Unsaturated Experiment Laboratory Notebook - 3. Scientific Notebook SN-LANL-SCI-207-V3. ACC: MOL.20010830.0380.

165350 Drew, D.J. 2001. AECL Busted Butte Unsaturated Experiment Laboratory Notebook - 4. Scientific Notebook SN-LANL-SCI-207-V4. ACC: MOL.20010910.0212.

165351 Drew, D.J. 2001. AECL Busted Butte Unsaturated Experiment Laboratory Notebook - 5. Scientific Notebook SN-LANL-SCI-207-V5. ACC: MOL.20010910.0214.

165352 Drew, D.J. 2001. AECL Busted Butte Unsaturated Experiment Laboratory Notebook - 6. Scientific Notebook SN-LANL-SCI-207-V6. ACC: MOL.20011219.0346.

165354 Drew, D.J. 2001. AECL Busted Butte Unsaturated Experiment Laboratory Notebook - 7. Scientific Notebook SN-LANL-SCI-207-V7. ACC: MOL.20020417.0399.

165328 Drew, D.J. 2002. AECL Busted Butte Saturated Experiment Laboratory Notebook - 4. Scientific Notebook SN-LANL-SCI-206-V4. ACC: MOL.20020628.0360.

165326 Drew, D.J. 2002. AECL Busted Butte Saturated Experiment Laboratory Notebook - 3. Scientific Notebook SN-LANL-SCI-206-V3. ACC: MOL.20020625.0175.

165356 Drew, D.J. 2002. AECL Busted Butte Unsaturated Experiment Laboratory Notebook - 8. Scientific Notebook SN-LANL-SCI-207-V8. ACC: MOL.20020625.0181.

165358 Drew, D.J. 2002. AECL Busted Butte Unsaturated Experiment Laboratory Notebook - 9. Scientific Notebook SN-LANL-SCI-207-V9. ACC: MOL.20020625.0178.

161543 Dublyansky, Y.; Ford, D.; and Reutski, V. 2001. "Traces of Epigenetic Hydrothermal Activity at Yucca Mountain, Nevada: Preliminary Data on the Fluid Inclusion and Stable Isotope Evidence." *Chemical Geology, 173*, (1-3), 125-149. [New York, New York]: Elsevier. TIC: 253849.

109204 Dublyansky, Y.; Reutsky, V.; and Shugurova, N. 1996. "Fluid Inclusions in Calcite from the Yucca Mountain Exploratory Tunnel." *Sixth Biennial Pan American Conference on Research in Fluid Inclusions, May 30 - June 1, 1996*. Brown, P.E. and Hagemann, S.G., eds. Madison, Wisconsin: Department of Geology, University of Wisconsin. TIC: 237704.

165297 Dunn, S. 2001. LA-EES-5-NBK-98-012: SEA: S. Salvit-Dunn, 03/23/98, SEA-YMP Lab Notebook #1. Scientific Notebook SN-LANL-SCI-042-V1. ACC: MOL.19991109.0078; MOL.20011119.0378; MOL.20011119.0379; MOL.20011119.0380.

144839 Fabryka-Martin, J.; Wolfsberg, A.V.; Dixon, P.R.; Levy, S.; Musgrave, J.; and Turin, H.J. 1996. *Summary Report of Chlorine-36 Studies: Sampling, Analysis and Simulation of Chlorine-36 in the Exploratory Studies Facility*. Milestone 3783M. Los Alamos, New Mexico: Los Alamos National Laboratory. ACC: MOL.19970103.0047.

162737 Fabryka-Martin, J.T.; Turin, H.J.; Wolfsberg, A.V.; Brenner, D.L.; Dixon, P.R.; and Musgrave, J.A. 1998. *Summary Report of Chlorine-36 Studies as of August 1996.* LA-13458-MS. Los Alamos, New Mexico: Los Alamos National Laboratory. ACC: MOL.20031119.0395.

100145 Fabryka-Martin, J.T.; Wolfsberg, A.V.; Dixon, P.R.; Levy, S.S.; Musgrave, J.A.; and Turin, H.J. 1997. *Summary Report of Chlorine-36 Studies: Sampling, Analysis, and Simulation of Chlorine-36 in the Exploratory Studies Facility*. LA-13352-MS. Los

Alamos, New Mexico: Los Alamos National Laboratory. ACC: MOL.19980812.0254.

165254 Farnham, I.M.; Meigs, L.C.; Dominguez, M.E.; Lindley, K.; Daniels, J.M.; and Stetzenbach, K.J. 2000. "Evaluation of Tracers Used for the WIPP Tracer Tests." Appendix H of *Interpretations of Tracer Tests Performed in the Culebra Dolomite at the Waste Isolation Pilot Plant Site*. Meigs, L.C.; Beauheim, R.L.; and Jones, T.L., eds. SAND97-3109. Albuquerque, New Mexico: Sandia National Laboratories. TIC: 255153.

105559 Faure, G. 1986. *Principles of Isotope Geology*. 2nd Edition. New York, New York: John Wiley & Sons. TIC: 237212.

156668 Fetter, C.W. 2001. *Applied Hydrogeology*. 4th Edition. Upper Saddle River, New Jersey: Prentice Hall. TIC: 251142.

165415 Finsterle, S.; Fabryka-Martin, J.T.; and Wang, J.S.Y. 2002. "Migration of a Water Pulse Through Fractured Porous Media." *Journal of Contaminant Hydrology, 54*, ([1-2]), 37-57. [New York, New York]: Elsevier. TIC: 254968.

156351 Flint, A.L.; Flint, L.E.; Bodvarsson, G.S.; Kwicklis, E.M.; and Fabryka-Martin, J. 2001. "Evolution of the Conceptual Model of Unsaturated Zone Hydrology at Yucca Mountain, Nevada." *Journal of Hydrology, 247*, ([1-2]), 1-30. [New York, New York]: Elsevier. TIC: 250932.

164506 Flint, A.L.; Flint, L.E.; Kwicklis, E.M.; Bodvarsson, G.S.; and Fabryka-Martin, J.M. 2001. "Hydrology of Yucca Mountain, Nevada." *Reviews of Geophysics, 39*, (4), 447-470. Washington, D.C.: American Geophysical Union. TIC: 254964.

100147 Flint, A.L.; Hevesi, J.A.; and Flint, L.E. 1996. *Conceptual and Numerical Model of Infiltration for the Yucca Mountain Area, Nevada*. Milestone 3GUI623M. Denver, Colorado: U.S. Geological Survey. ACC: MOL.19970409.0087.

165381 Flint, L. 2001. Busted Butte Hydrologic Properties. Scientific Notebook SN-USGS-SCI-117-V1. ACC: MOL.20020214.0398.

165382 Flint, L. 2001. Busted Butte Hydrologic Properties. Scientific Notebook SN-USGS-SCI-117-V2. ACC: MOL.20020214.0399.

165383 Flint, L.; Hudson, D.; and Kostalek, T. 2002. Busted Butte Hydrologic Properties. Scientific Notebook SN-USGS-SCI-117-V3. ACC: MOL.20020926.0130.

100033 Flint, L.E. 1998. *Characterization of Hydrogeologic Units Using Matrix Properties, Yucca Mountain, Nevada*. Water-Resources Investigations Report 97-4243. Denver, Colorado: U.S. Geological Survey. ACC: MOL.19980429.0512.

164636 Flood, T.P.; Vogel, T.A.; and Schuraytz, B.C. 1989. "Chemical Evolution of a Magmatic System: The Paintbrush Tuff, Southwest Nevada Volcanic Field." *Journal of Geophysical Research, 94*, (B5), 5943-5960. [Washington, D.C.]: American Geophysical Union. TIC: 235505.

109425 Forester, R.M.; Bradbury, J.P.; Carter, C.; Elvidge-Tuma, A.B.; Hemphill, M.L.; Lundstrom, S.C.; Mahan, S.A.; Marshall, B.D.; Neymark, L.A.; Paces, J.B.; Sharpe, S.E.; Whelan, J.F.; and Wigand, P.E. 1999. *The Climatic and Hydrologic History of Southern Nevada During the Late Quaternary*. Open-File Report 98-635. Denver, Colorado: U.S. Geological Survey. TIC: 245717.

154365 Freeze, G.A.; Brodsky, N.S.; and Swift, P.N. 2001. *The Development of Information Catalogued in REV00 of the YMP FEP Database.* TDR-WIS-MD-000003 REV 00 ICN 01. Las Vegas, Nevada: Bechtel SAIC Company. ACC: MOL.20010301.0237.

101173 Freeze, R.A. and Cherry, J.A. 1979. *Groundwater*. Englewood Cliffs, New Jersey: Prentice-Hall. TIC: 217571.

162716 Gascoyne, M. 2003. "Soluble Salts in the Yucca Mountain Tuff and their Significance." *Proceedings of the 10th International High-Level Radioactive Waste Management Conference (IHLRWM), March 30-April 2, 2003, Las Vegas, Nevada*. Pages 340-347. La Grange Park, Illinois: American Nuclear Society. TIC: 254202.

164720 Gascoyne, M. and Schwarcz, H.P. 1986. "Radionuclide Migration over Recent Geologic Time in a Granitic Pluton." *Chemical Geology, 59*, 75-85. [New York, New York]: Elsevier. TIC: 254779.

154800 Gascoyne, M.; Miller, N.H.; and Neymark, L.A. 2002. "Uranium-Series Disequilibrium in Tuffs from Yucca Mountain, Nevada, as Evidence of Pore-Fluid Flow Over the Last Million Years." *Applied Geochemistry, 17*, ([6]), 781-792. [New York, New York]: Elsevier. TIC: 251901.

100397 Geldon, A.L.; Umari, A.M.A.; Fahy, M.F.; Earle, J.D.; Gemmell, J.M.; and Darnell, J. 1997. *Results of Hydraulic and Conservative Tracer Tests in Miocene Tuffaceous Rocks at the C-Hole Complex, 1995 to 1997, Yucca Mountain, Nye County, Nevada*. Milestone SP23PM3. [Las Vegas, Nevada]: U.S. Geological Survey. ACC: MOL.19980122.0412.

106099 Ghuman, B.S. and Prihar, S.S. 1980. "Chloride Displacement by Water in Homogeneous Columns of Three Soils." *Soil Science Society of America Journal, 44*, (1), 17-21. Madison, Wisconsin: Soil Science Society of America. TIC: 246698.

164642 Grim, R.E. 1968. "Clay-Water System." *Clay Mineralogy*. 2nd Edition. Pages 234-277. New York, New York: McGraw Hill. TIC: 247447.

105787 GSA (Geological Society of America) 1995. *Rock Color Chart with Genuine Munsell® Color Chips*. Boulder, Colorado: Geological Society of America. TIC: 242285.

164070 Guertal, W. 2001. Seepage into Alcove 1. Scientific Notebook SN-USGS-SCI-108-V1. ACC: MOL.20011219.0325.

165384 Guertal, W. and Flint, A. 2000. ESF Niche Studies. Scientific Notebook SN-USGS-SCI-110-V1. ACC: MOL.20000512.0035.

165369 Haga, M. 2001. Marc Haga Busted Butte Personal Laboratory Notebook. Scientific Notebook SN-LANL-SCI-253-V1. ACC: MOL.20020128.0171.

165404 Hillel, D. 1998. *Environmental Soil Physics*. San Diego, California: Academic Press. TIC: 254422.

101134 Hillel, D. 1980. *Fundamentals of Soil Physics*. New York, New York: Academic Press. TIC: 215655.

156557 Hinds, J. 2000. Percolation and Seepage. Scientific Notebook YMP-LBNL-JSW-JJH-1. ACC: MOL.20000307.0066; MOL.20000419.0645.

156539 Hu, M.Q. 1999. Characterization of Yucca Mountain Percolation in the Unsaturated Zone-ESF Study. Scientific Notebook YMP-LBNL-JSW-QH-1. ACC: MOL.19991013.0463.

156540 Hu, M.Q. 1999. Characterization of Yucca Mountain Percolation in the Unsaturated Zone-ESF Study. Scientific Notebook YMP-LBNL-JSW-QH-1A. ACC: MOL.20000107.0345.

156541 Hu, M.Q. 1999. Characterization of Yucca Mountain Percolation in the Unsaturated Zone-ESF Study. Scientific Notebook YMP-LBNL-JSW-QH-1B. ACC: MOL.20000107.0346.

156542 Hu, M.Q. 1999. Characterization of Yucca Mountain Percolation in the Unsaturated Zone-ESF Study. Scientific Notebook YMP-LBNL-JSW-QH-1C. ACC: MOL.19991210.0212.

155691 Hu, M.Q. 1999. Characterization of Yucca Mountain Percolation in the Unsaturated Zone-ESF Study. Scientific Notebook YMP-LBNL-JSW-QH-1D. ACC: MOL.19991013.0467.

156473 Hu, M.Q. 2000. Characterization of Yucca Mountain Percolation in the Unsaturated Zone-ESF Study. Scientific Notebook YMP-LBNL-JSW-QH-1E. ACC: MOL.19991013.0468; MOL.20010201.0419.

165412 Hu, Q.; Kneafsey, T.J.; Trautz, R.C.; and Wang, J.S.Y. 2002. "Tracer Penetration into Welded Tuff Matrix from Flowing Fractures." *Vadose Zone Journal, 1*, 102-112. [Madison, Wisconsin: Soil Science Society of America]. TIC: 254966.

165413 Hu, Q.; Salve, S.; Stringfellow, W.T.; and Wang, J.S.Y. 2001. "Field Tracer-Transport Tests in Unsaturated Fractured Tuff." *Journal of Contaminant Hydrology, 51*, ([1-2]), 1-12. [New York, New York]: Elsevier. TIC: 254969.

165385 Hudson, D. 2002. Crossover Alcove - Seepage into Niche 3 and Tracer Testing. Scientific Notebook SN-USGS-SCI-120-V1. ACC: MOL.20020513.0380.

165386 Hudson, D. 2002. Crossover Alcove - Seepage into Niche 3 and Tracer Testing. Scientific Notebook SN-USGS-SCI-120-V2. ACC: MOL.20020513.0381.

165387 Hudson, D. 2002. Crossover Alcove - Seepage into Niche 3 and Tracer Testing. Scientific Notebook SN-USGS-SCI-120-V3. ACC: MOL.20020513.0382.

166103 Hudson, D. 2002. Crossover Alcove - Seepage into Niche 3 and Tracer Testing. Scientific Notebook SN-USGS-SCI-120-V5. ACC: MOL.20020920.0307.

165389 Hudson, D. 2002. Crossover Alcove - Seepage into Niche 3 and Tracer Testing. Scientific Notebook SN-USGS-SCI-120-V6. ACC: MOL.20030106.0357.

165390 Hudson, D. 2003. Crossover Alcove - Seepage into Niche 3 and Tracer Testing. Scientific Notebook SN-USGS-SCI-120-V7. ACC: MOL.20030402.0103.

165388 Hudson, D. and Guertal, W. 2002. Crossover Alcove - Seepage into Niche 3 and Tracer Testing. Scientific Notebook SN-USGS-SCI-120-V4. ACC: MOL.20020513.0383.

163398 Hudson, D.B. 2002. Bulkhead Moisture Monitoring in the Cross Drift. Scientific Notebook SN-USGS-SCI-133-V1. ACC: MOL.20021125.0122.

165391 Hudson, D.B. 2002. Moisture Monitoring in the Exploratory Studies Facility (ESF) and Cross Drift. Scientific Notebook SN-USGS-SCI-128-V1. ACC: MOL.20020520.0349.

165392 Hudson, D.B. 2002. Moisture Monitoring in the Exploratory Studies Facility (ESF) and Cross Drift. Scientific Notebook SN-USGS-SCI-128-V2. ACC: MOL.20021125.0124.

165393 Hudson, D.B. 2003. Bulkhead Moisture Monitoring in the Cross Drift. Scientific Notebook SN-USGS-SCI-133-V2. ACC: MOL.20030711.0158.

165273 Hudson, D.B. 2003. Moisture Monitoring in the Exploratory Studies Facility (ESF) and Cross Drift. Scientific Notebook SN-USGS-SCI-128-V3. ACC: MOL.20030821.0214.

164637 Jaffey, A.H.; Flynn, K.F.; Glendenin, L.E.; Bentley, W.C.; and Essling, A.M. 1971. "Precision Measurement of Half-Lives and Specific Activities of {superscript 235}U and {superscript 238}U." *Physical Review C, 4*, (5), 1889-1906. [Ridge, New York]: American Institute of Physics. TIC: 254712.

164629 Kasnavia, T.; Vu, D.; and Sabatini, D.A. 1999. "Fluorescent Dye and Media Properties Affecting Sorption and Tracer Selection." *Ground Water, 37*, (3), 376-381. [Westerville, Ohio]: Association of Ground Water Scientists & Engineers. TIC: 254708.

164722 Kaufman, A. 1969. "The Th{superscript 232} Concentration of Surface Ocean Water." *Geochimica et Cosmochimica Acta, 33*, ([6]), 717-724. [New York, New York]: Pergamon. TIC: 254837.

165255 Kearney, M.L.; Wolfsberg, L.E.; Groffman, A.R.; Jones, C.L.; and Turin, H.J. 2000. "Solubility of Rare Earth Elements and Transition Metals as a Function of Increasing pH During Unsaturated-Zone Transport Tests at Busted Butte, Nevada." *Abstracts with Programs - Geological Society of America, 32*, (7), A-209. Boulder, Colorado: Geological Society of America. TIC: 249113.

106105 Klinkenberg, L.J. 1942. "The Permeability of Porous Media to Liquids and Gases." *Drilling and Production Practice 1941*. New York, New York: American Petroleum Institute. TIC: 217454.

162333 Kurzmack, M.; LeCain, G.D.; and Hudson, D. 2002. "Relative Humidity, Pressure, and Temperature Values from the Ghost Dance Fault Alcove 7, Yucca Mountain, Nevada." *Abstracts with Programs - Geological Society of America, 34*, (6), 59. Boulder, Colorado: Geological Society of America. TIC: 254868.

147527 Langmuir, D. and Herman, J.S. 1980. "The Mobility of Thorium in Natural Waters at Low Temperatures." *Geochimica et Cosmochimica Acta, 44*, 1753-1766. New York, New York: Pergamon Press. TIC: 237029.

101700 LeCain, G.D. 1995. *Pneumatic Testing in 45-Degree-Inclined Boreholes in Ash-Flow Tuff Near Superior, Arizona*. Water-Resources Investigations Report 95-4073. Denver, Colorado: U.S. Geological Survey. ACC: MOL.19960715.0083.

100052 LeCain, G.D. 1998. *Results from Air-Injection and Tracer Testing in the Upper Tiva Canyon, Bow Ridge Fault, and Upper Paintbrush Contact Alcoves of the Exploratory*

Studies Facility, August 1994 through July 1996, Yucca Mountain, Nevada. Water-Resources Investigations Report 98-4058. Denver, Colorado: U.S. Geological Survey. ACC: MOL.19980625.0344.

158511 LeCain, G.D.; Lu, N.; and Kurzmack, M. 2002. *Use of Temperature, Pressure, and Water Potential Data to Estimate Infiltration and Monitor Percolation in Pagany Wash Associated with the Winter of 1997–98 El Niño Precipitation, Yucca Mountain, Nevada*. Water Resources Investigations Report 02-4035. Denver, Colorado: U.S. Geological Survey. TIC: 252641.

162740 Levy, S.; Chipera, S.; WoldeGabriel, G.; Fabryka-Martin, J.; Roach, J.; and Sweetkind, D. 1999. "Flow-Path Textures and Mineralogy in Tuffs of the Unsaturated Zone." *Faults and Subsurface Fluid Flow in the Shallow Crust. Geophysical Monograph 113*. 159-183. [Washington, D.C.]: American Geophysical Union. TIC: 254128.

165363 Levy, S.S. 2001. LA-EES-1-NBK-94-002, Mineralogic/Petrologic/Structural Studies in Support of Unsaturated Zone Flow and Transport Test. Scientific Notebook SN-LANL-SCI-220-V1. ACC: MOL.20010705.0124.

165370 Levy, S.S. 2002. Busted Butte Applicability Studies. Scientific Notebook SN-LANL-SCI-256-V1. ACC: MOL.20021104.0185.

104158 Lipman, P.W. and McKay, E.J. 1965. *Geologic Map of the Topopah Spring SW Quadrangle, Nye County, Nevada.* Geologic Quadrangle Map GQ-439. Denver, Colorado: U.S. Geological Survey. TIC: 212352.

100773 Lipman, P.W.; Christiansen, R.L.; and O'Connor, J.T. 1966. *A Compositionally Zoned Ash-Flow Sheet in Southern Nevada*. Professional Paper 524-F. Washington, D.C.: U.S. Geological Survey. TIC: 219972.

162470 Liu, H-H.; Haukwa, C.B.; Ahlers, C.F.; Bodvarsson, G.S.; Flint, A.L.; and Guertal, W.B. 2003. "Modeling Flow and Transport in Unsaturated Fractured Rock: An Evaluation of the Continuum Approach." *Journal of Contaminant Hydrology, 62-63*, 173-188. New York, New York: Elsevier. TIC: 254205.

164632 Lowry, W. 2001. LA-EES-5-NBK-98-016; SEA: W.Lowry, 03/23/98, SEA-YMP, Lab Notebook #1. Scientific Notebook SN-LANL-SCI-046-V1. ACC: MOL.20011212.0024.

136523 Lundstrom, S.C.; Paces, J.B.; and Mahan, S.M. 1996. "Late Quaternary History of Fortymile Wash, Southern Nevada: A Record of Geomorphic Response to Climate Change in the Yucca Mountain Region." *Abstracts with Programs - Geological Society of America, 28*, (7), A-552. Boulder, Colorado: Geological Society of America. TIC: 247474.

162717 Marshall, B.D. and Futa, K. 2003. "Strontium in Pore Water from the Topopah Spring Tuff, Yucca Mountain, Nevada." *Proceedings of the 10th International High-Level Radioactive Waste Management Conference (IHLRWM), March 30-April 2, 2003, Las Vegas, Nevada*. Pages 373-376. [La Grange Park, Illinois]: American Nuclear Society. TIC: 254204.

154415 Marshall, B.D. and Whelan, J.F. 2000. "Isotope Geochemistry of Calcite Coatings and the Thermal History of the Unsaturated Zone at Yucca Mountain, Nevada." *Abstracts with Programs - Geological Society of America, 32*, (7), A-259. Boulder, Colorado: Geological Society of America. TIC: 249113.

163591 Marshall, B.D. and Whelan, J.F. 2001. "Simulating the Thermal History of the Unsaturated Zone at Yucca Mountain, Nevada." *Abstracts with Programs - Geological Society of America, 33*, (6), A-375. Boulder, Colorado: Geological Society of America. TIC: 252701.

162891 Marshall, B.D.; Neymark, L.A.; and Peterman, Z.E. 2003. "Estimation of Past Seepage Volumes from Calcite Distribution in the Topopah Spring Tuff, Yucca Mountain, Nevada." *Journal of Contaminant Hydrology, 62-63*, 237-247. [New York, New York]: Elsevier. TIC: 254210.

151018 Marshall, B.D.; Neymark, L.A.; Paces, J.B.; Peterman, Z.E.; and Whelan, J.F. 2000. "Seepage Flux Conceptualized from Secondary Calcite in Lithophysal Cavities in the Topopah Spring Tuff, Yucca Mountain, Nevada." *SME Annual Meeting, February 28-March 1, 2000, Salt Lake City, Utah*. Preprint 00-12. [Littleton, Colorado]: Society for Mining, Metallurgy, and Exploration. TIC: 248608.

107415 Marshall, B.D.; Paces, J.B.; Neymark, L.A.; Whelan, J.F.; and Peterman, Z.E. 1998. "Secondary Minerals Record Past Percolation Flux at Yucca Mountain, Nevada." *High-Level Radioactive Waste Management, Proceedings of the Eighth International Conference, Las Vegas, Nevada, May 11-14, 1998*. Pages 127-129. La Grange Park, Illinois: American Nuclear Society. TIC: 237082.

149850 Mongano, G.S.; Singleton, W.L.; Moyer, T.C.; Beason, S.C.; Eatman, G.L.W.; Albin, A.L.; and Lung, R.C. 1999. *Geology of the ECRB Cross Drift - Exploratory Studies Facility, Yucca Mountain Project, Yucca Mountain, Nevada*. [Deliverable SPG42GM3]. Denver, Colorado: U.S. Geological Survey. ACC: MOL.20000324.0614.

101269 Moyer, T.C. and Geslin, J.K. 1995. *Lithostratigraphy of the Calico Hills Formation and Prow Pass Tuff (Crater Flat Group) at Yucca Mountain, Nevada*. Open-File Report 94-460. Denver, Colorado: U.S. Geological Survey. ACC: MOL.19941208.0003.

100162 Moyer, T.C.; Geslin, J.K.; and Flint, L.E. 1996. *Stratigraphic Relations and Hydrologic Properties of the Paintbrush Tuff Nonwelded (PTn) Hydrologic Unit, Yucca Mountain, Nevada*. Open-File Report 95-397. Denver, Colorado: U.S. Geological Survey. ACC: MOL.19970204.0216.

134132 Muskat, M. 1982. *The Flow of Homogeneous Fluids through Porous Media*. Boston, Massachusetts: International Human Resources Development Corporation. TIC: 208295.

164725 Neymark, L.A. and Amelin, Y. 2002. "Extreme U-Th-Pb Fractionation Among Hydrogenic Fracture-Coating Minerals in Felsic Tuffs at Yucca Mountain, Nevada, USA: Implications for Geochronlogy." *Geochimica et Cosmochimica Acta, 66*, (15A), Page A552. New York, New York: Pergamon. TIC: 254805.

127012 Neymark, L.A. and Paces, J.B. 2000. "Consequences of Slow Growth for 230Th/U Dating of Quaternary Opals, Yucca Mountain, NV, USA." *Chemical Geology, 164*, 143-160. Amsterdam, The Netherlands: Elsevier. TIC: 246316.

158673 Neymark, L.A.; Amelin, Y.; Paces, J.B.; and Peterman, Z.E. 2002. "U-Pb Ages of Secondary Silica at Yucca Mountain, Nevada: Implications for the Paleohydrology of the Unsaturated Zone." *Applied Geochemistry, 17*, ([6]), 709-734. [New York, New York]: Elsevier. TIC: 252598.

162710 Neymark, L.A.; Amelin, Y.V.; and Paces, J.B. 2000. "{superscript 206}Pb–{superscript 230}Th–{superscript 234}U–{superscript 238}U and {superscript 207}Pb–{superscript 235}U Geochronology of Quaternary Opal, Yucca Mountain, Nevada." *Geochimica et Cosmochimica Acta, 64*, (17), 2913-2928. [New York, New York]: Pergamon. TIC: 253360.

109140 Neymark, L.A.; Amelin, Y.V.; Paces, J.B.; and Peterman, Z.E. 1998. "U-Pb Age Evidence for Long-Term Stability of the Unsaturated Zone at Yucca Mountain." *High-Level Radioactive Waste Management, Proceedings of the Eighth International Conference, Las Vegas, Nevada, May 11-14, 1998*. Pages 85-87. La Grange Park, Illinois: American Nuclear Society. TIC: 237082.

163274 NRC (U.S. Nuclear Regulatory Commission) 2003. *Yucca Mountain Review Plan, Final Report. NUREG-1804, Rev. 2*. Washington, D.C.: U.S. Nuclear Regulatory Commission, Office of Nuclear Material Safety and Safeguards. TIC: 254568.

162418 NRC (U.S. Nuclear Regulatory Commission) 2003. *Yucca Mountain Review Plan, Information Only. NUREG-1804, Draft Final Revision 2*. Washington, D.C.: U.S. Nuclear Regulatory Commission, Office of Nuclear Material Safety and Safeguards. TIC: 254002.

156558 Oldenburg, C. 2000. Percolation and Seepage. Scientific Notebook YMP-LBNL-JSW-CMO-1. ACC: MOL.20000922.0075.

163335 Ostlund, H.G. 1987. "Tritium." Volume 7 of *GEOSECS Atlantic, Pacific, and Indian Ocean Expeditions.* Shorebased Data and Graphics. Pages 7-10. Washington, D.C.: National Science Foundation. TIC: 254317.

162900 Paces, J.B. and Neymark, L.A. 2003. "U-Series Disequilibrium as a Test for Unsaturated-Zone Hydrologic Models at Yucca Mountain, Nevada." *Proceedings of the 10th International High-Level Radioactive Waste Management Conference (IHLRWM), March 30-April 2, 2003, Las Vegas, Nevada*. Pages 27-38. [La Grange Park, Illinois]: American Nuclear Society. TIC: 254201.

154724 Paces, J.B. and Whelan, J.F. 2001. "Water-Table Fluctuations in the Amargosa Desert, Nye County, Nevada." "Back to the Future - Managing the Back End of the Nuclear Fuel Cycle to Create a More Secure Energy Future," *Proceedings of the 9th International High-Level Radioactive Waste Management Conference (IHLRWM), Las Vegas, Nevada, April 29-May 3, 2001*. La Grange Park, Illinois: American Nuclear Society. TIC: 247873.

107408 Paces, J.B.; Neymark, L.A.; Marshall, B.D.; Whelan, J.F.; and Peterman, Z.E. 1998. "Inferences for Yucca Mountain Unsaturated-Zone Hydrology from Secondary Minerals." *High-Level Radioactive Waste Management, Proceedings of the Eighth International Conference, Las Vegas, Nevada, May 11-14, 1998*. Pages 36-39. La Grange Park, Illinois: American Nuclear Society. TIC: 237082.

156507 Paces, J.B.; Neymark, L.A.; Marshall, B.D.; Whelan, J.F.; and Peterman, Z.E. 2001. *Ages and Origins of Calcite and Opal in the Exploratory Studies Facility Tunnel, Yucca Mountain, Nevada*. Water-Resources Investigations Report 01-4049. Denver, Colorado: U.S. Geological Survey. TIC: 251284.

162738 Paces, J.B.; Peterman, Z.E.; Neymark, L.A.; Nimz, G.J.; Gascoyne, M.; and Marshall, B.D. 2003. "Summary of Chlorine-36 Validation Studies at Yucca Mountain, Nevada." *Proceedings of the 10th International High-Level Radioactive Waste Management Conference (IHLRWM), March 30-April 2, 2003, Las Vegas, Nevada*. Pages 348-356. La Grange Park, Illinois: American Nuclear Society. TIC: 254253.

106474 Paces, J.B.; Taylor, E.M.; and Bush, C. 1993. "Late Quaternary History and Uranium Isotopic Compositions of Ground Water Discharge Deposits, Crater Flat, Nevada." *High Level Radioactive Waste Management, Proceedings of the Fourth Annual International Conference, Las Vegas, Nevada, April 26-30, 1993*. 2, 1573-1580. La Grange Park, Illinois: American Nuclear Society. TIC: 208542.

154827 Patterson, G.L. 2000. "Low-Level Measurements of Tritium in the Unsaturated Zone from the Exploratory Studies Facility Beneath Yucca Mountain, Nevada." *Abstracts with Programs - Geological Society of America, 32*, (7), A-479–A-480. Boulder, Colorado: Geological Society of America. TIC: 249113.

155696 Peterman, Z.E. and Cloke, P.L. 2001. "Geochemical Homogeneity of Tuffs at the Potential Repository Level, Yucca Mountain, Nevada." "Back to the Future - Managing the Back End of the Nuclear Fuel Cycle to Create a More Secure Energy Future," *Proceedings of the 9th International High-Level Radioactive Waste Management Conference (IHLRWM), Las Vegas, Nevada, April 29-May 3, 2001*. La Grange Park, Illinois: American Nuclear Society. TIC: 247873.

162576 Peterman, Z.E. and Cloke, P.L. 2002. "Geochemistry of Rock Units at the Potential Repository Level, Yucca Mountain, Nevada (includes Erratum)." *Applied Geochemistry, 17*, ([6, 7]), 683-698, 955-958. New York, New York: Pergamon. TIC: 252516; 252517.

106494 Peterman, Z.E. and Futa, K. 1996. *Geochemistry of Core Samples of the Tiva Canyon Tuff from Drill Hole UE-25 NRG#3, Yucca Mountain, Nevada*. Open-File Report 95-325. Denver, Colorado: U.S. Geological Survey. ACC: MOL.19961118.0132.

162992 Peterman, Z.E. and Marshall, B.D. 2002. "Geochemistry of Pore Water from Densely Welded Topopah Spring Tuff at Yucca Mountain, Nevada." *GSA Abstracts with Programs, 34*, (6), Page 308. Boulder, Colorado: Geological Society of America. TIC: 254868.

106498 Peterman, Z.E.; Spengler, R.W.; Singer, F.R.; and Dickerson, R.P. 1993. "Isotopic and Trace Element Variability in Altered and Unaltered Tuffs at Yucca Mountain, Nevada." *High Level Radioactive Waste Management, Proceedings of the Fourth Annual International Conference, Las Vegas, Nevada, April 26-30, 1993*. 2, 1940-1947. La Grange Park, Illinois: American Nuclear Society. TIC: 208542.

165379 Peterson, J. 2002. Busted Butte (YMP-LBNL-ELM-JP-1). Scientific Notebook SN-LBNL-SCI-193-V1. ACC: MOL.20030115.0004.

106133 Philip, J.R. 1986. "Linearized Unsteady Multidimensional Infiltration." *Water Resources Research, 22*, (12), 1717-1727. Washington, D.C.: American Geophysical Union. TIC: 239826.

156974 Philip, J.R. 1989. "The Scattering Analog for Infiltration in Porous Media." *Reviews of Geophysics, 27*, (4), 431-448. [Washington, D.C.]: American Geophysical Union. TIC: 251332.

105743 Philip, J.R.; Knight, J.H.; and Waechter, R.T. 1989. "Unsaturated Seepage and Subterranean Holes: Conspectus, and Exclusion Problem for Circular Cylindrical Cavities." *Water Resources Research, 25*, (1), 16-28. Washington, D.C.: American Geophysical Union. TIC: 239117.

134083 Porro, I. and Wierenga, P.J. 1993. "Transient and Steady-State Transport through a Large Unsaturated Soil Column." *Ground Water, 31*, (2), 193-200. Dublin, Ohio: National Ground Water Association. TIC: 246899.

104250 Pruess, K. 1999. "A Mechanistic Model for Water Seepage Through Thick Unsaturated Zones in Fractured Rocks of Low Matrix." *Water Resources Research, 35*, (4), 1039-1051. Washington, D.C.: American Geophysical Union. TIC: 244913.

106141 Pullan, A.J. 1990. "The Quasilinear Approximation for Unsaturated Porous Media Flow." *Water Resources Resources, 26*, (6), 1219-1234. Washington, D.C.: American Geophysical Union. TIC: 239824.

155683 Raats, P.A.C. and Gardner, W.R. 1971. "Comparison of Empirical Relationships Between Pressure Head and Hydraulic Conductivity and Some Observations on Radially Symmetric Flow." *Water Resources Research, 7*, (4), 921-928. [Washington, D.C.]: American Geophysical Union. TIC: 239815.

100642 Rautman, C.A. and Engstrom, D.A. 1996. *Geology of the USW SD-12 Drill Hole Yucca Mountain, Nevada*. SAND96-1368. Albuquerque, New Mexico: Sandia National Laboratories. ACC: MOL.19970613.0101.

101008 Rautman, C.A. and Engstrom, D.A. 1996. *Geology of the USW SD-7 Drill Hole Yucca Mountain, Nevada*. SAND96-1474. Albuquerque, New Mexico: Sandia National Laboratories. ACC: MOL.19971218.0442.

126243 Reimus, P.W.; Adams, A.; Haga, M.J.; Humphrey, A.; Callahan, T.; Anghel, I.; and Counce, D. 1999. *Results and Interpretation of Hydraulic and Tracer Testing in the Prow Pass Tuff at the C-Holes*. Milestone SP32E7M4. Los Alamos, New Mexico: Los Alamos National Laboratory. TIC: 246377.

164723 Rosholt, J.N. 1983. "Isotopic Composition of Uranium and Thorium in Crystalline Rocks." *Journal of Geophysical Research, 88*, (B9), 7315-7330. [Washington, D.C.]: American Geophysical Union. TIC: 254838.

155697 Russo, R.E.; Mao, X.; Borisov, O.V.; and Liu, H. 2000. "Laser Ablation in Atomic Spectroscopy." *Encyclopedia of Analytical Chemistry*. Meyers, R.A., ed. Pages 9485-9506. Chichester, England: John Wiley & Sons. TIC: 250479.

164630 Sabatini, D.A. and Austin, T.A. 1991. "Characteristics of Rhodamine WT and Fluorescein as Adsorbing Ground-Water Tracers." *Ground Water, 29*, (3), 341-349. [Westerville, Ohio]: Association of Ground Water Scientists & Engineers. TIC: 254709.

155692 Salve, R. 1999. Fracture Flow, Fracture-Matrix Interaction. Scientific Notebook YMP-LBNL-JSW-RS-1. ACC: MOL.19991013.0470.

156547 Salve, R. 1999. Fracture Flow, Fracture-Matrix Interaction. Scientific Notebook YMP-LBNL-JSW-RS-1A. ACC: MOL.19991013.0471.

156555 Salve, R. 1999. Measurements of Moisture Potential in P Tunnel Calico Hills using Tensiometers and Psychrometers. Scientific Notebook YMP-LBNL-JW-1.2A. ACC: MOL.19991013.0473.

156552 Salve, R. 1999. Measurements of Moisture Potential in P Tunnel/Calico Hills using Tensiometers and Psychrometers. Scientific Notebook YMP-LBNL-JW-1.2. ACC: MOL.20000215.0229.

156548 Salve, R. 2000. Percolation and Seepage. Scientific Notebook YMP-LBNL-JSW-RS-2. ACC: MOL.20000908.0236.

165378 Salve, R. 2002. YMP-LBNL-JSW-RS-4 UZ Investigations-ESF/Drift-FY00. Scientific Notebook SN-LBNL-SCI-182-V1. ACC: MOL.20020708.0384.

165377 Salve, R. 2003. Moisture Monitoring in the ESF, YMP-LBNL-JSW-RS-5-UZ Investigations-ESF/XDrift. Scientific Notebook SN-LBNL-SCI-181-V1. ACC: MOL.20030430.0281.

157316 Salve, R. and Oldenburg, C.M. 2001. "Water Flow Within a Fault in Altered Nonwelded Tuff." *Water Resources Research, 37*, (12), 3043-3056. [Washington, D.C.]: American Geophysical Union. TIC: 251485.

164470 Salve, R.; Oldenburg, C.M.; and Wang, J.S.Y. 2003. "Fault-Matrix Interactions in Nonwelded Tuff of the Paintbrush Group at Yucca Mountain." *Journal of Contaminant Hydrology, 62-63*, 269-286. New York, New York: Elsevier. TIC: 254205.

161318 Salve, R.; Wang, J.S.Y.; and Doughty, C. 2002. "Liquid-Release Tests in Unsaturated Fractured Welded Tuffs: I. Field Investigations." *Journal of Hydrology, 256*, ([1-2]), 60-79. [New York, New York]: Elsevier. TIC: 253774.

101288 Sass, J.H.; Dudley, W.W., Jr.; and Lachenbruch, A.H. 1995. "Regional Thermal Setting." Chapter 8 of *Major Results of Geophysical Investigations at Yucca Mountain and Vicinity, Southern Nevada*. Oliver, H.W.; Ponce, D.A.; Hunter, W.C., eds. Open-File Report 95-74. Menlo Park, California: U.S. Geological Survey. ACC: MOL.19980305.0122.

100644 Sass, J.H.; Lachenbruch, A.H.; Dudley, W.W., Jr.; Priest, S.S.; and Munroe, R.J. 1988. *Temperature, Thermal Conductivity, and Heat Flow Near Yucca Mountain, Nevada: Some Tectonic and Hydrologic Implications*. Open-File Report 87-649. [Denver, Colorado]: U.S. Geological Survey. TIC: 203195.

100075 Sawyer, D.A.; Fleck, R.J.; Lanphere, M.A.; Warren, R.G.; Broxton, D.E.; and Hudson, M.R. 1994. "Episodic Caldera Volcanism in the Miocene Southwestern Nevada Volcanic Field: Revised Stratigraphic Framework, {superscript 40}Ar/{superscript 39}Ar Geochronology, and Implications for Magmatism and Extension." *Geological Society of America Bulletin, 106*, (10), 1304-1318. Boulder, Colorado: Geological Society of America. TIC: 222523.

107248 Schuraytz, B.C.; Vogel, T.A.; and Younker, L.W. 1989. "Evidence for Dynamic Withdrawal from a Layered Magma Body: The Topopah Spring Tuff, Southwestern Nevada." *Journal of Geophysical Research, 94*, (B5), 5925-5942. Washington, D.C.: American Geophysical Union. TIC: 225936.

104181 Scott, R.B. and Bonk, J. 1984. *Preliminary Geologic Map of Yucca Mountain, Nye County, Nevada, with Geologic Sections*. Open-File Report 84-494. Denver, Colorado: U.S. Geological Survey. ACC: HQS.19880517.1443.

101291 Scott, R.B. and Castellanos, M. 1984. *Stratigraphic and Structural Relations of Volcanic Rocks in Drill Holes USW GU-3 and USW G-3, Yucca Mountain, Nye County, Nevada*. Open-File Report 84-491. Denver, Colorado: U.S. Geological Survey. ACC: NNA.19870519.0095.

106143 Selby, S.M., ed. 1975. *CRC Standard Mathematical Tables*. 23rd Edition. Cleveland, Ohio: CRC Press. TIC: 247118.

165371 Soll, W. 2001. Busted Butte UZTT Phase 2A Tracer Level Records. Scientific Notebook SN-LANL-SCI-257-V1. ACC: MOL.20010605.0371.

165372 Soll, W. and Aldrich, M.J. 2002. Mineralogic/Petrologic/Structural Studies in Support of Busted Butte Unsaturated Zone Flow and Transport Test. Scientific Notebook SN-LANL-SCI-261-V1. ACC: MOL.20020517.0132.

165299 Soll, W. and Bussod, G.Y. 2001. LA-EES-5-NBK-99-003 Busted Butte On-Site Logbook #3, UZ Transport Field Test. Scientific Notebook SN-LANL-SCI-106-V1. ACC: MOL.20010531.0104.

165316 Soll, W. and Wolfsberg, L. 2000. Busted Butte Project IC/ICP-AES Notebook #2. Scientific Notebook SN-LANL-SCI-188-V1. ACC: MOL.20001023.0243.

165365 Soll, W. and Wolfsberg, L. 2000. Busted Butte Project Tracking Forms # 3. Scientific Notebook SN-LANL-SCI-232-V1. ACC: MOL.20001219.0006.

165320 Soll, W. and Wolfsberg, L. 2000. Pad Concentration and Loading Calculations. Scientific Notebook SN-LANL-SCI-193-V1. ACC: MOL.20000926.0190.

165313 Soll, W. and Wolfsberg, L. 2000. The Busted Butte Project Sample Tracking Forms # 2. Scientific Notebook SN-LANL-SCI-184-V1. ACC: MOL.20000926.0188.

165367 Soll, W. and Wolfsberg, L. 2002. Busted Butte Research and Development Notebook for Chemical Analyses. Scientific Notebook SN-LANL-SCI-241-V1. ACC: MOL.20021104.0176.

165296 Soll, W.; Bussod, G.; and Mason, N.G. 2001. LA-EES-5-NBK-98-011, Sensor Design / N. Mason SEA-YMP Notebook #1. Scientific Notebook SN-LANL-SCI-041-V1. ACC: MOL.20011212.0020.

165366 Soll, W.; Turin, H.J.; and Wolfsberg, L. 2002. Busted Butte Master Notebook for Chemical Analyses. Scientific Notebook SN-LANL-SCI-239-V1. ACC: MOL.20030121.0082.

106883 Spaulding, W.G. 1985. *Vegetation and Climates of the Last 45,000 Years in the Vicinity of the Nevada Test Site, South-Central Nevada*. Professional Paper 1329. Washington, D.C.: U.S. Geological Survey. TIC: 203210.

133377 Steiger, R.H. and Jager, E. 1977. "Subcommission on Geochronology: Convention on the Use of Decay Constants in Geo- and Cosmochronology." *Earth and Planetary Science Letters, 36*, 359-362. Amsterdam, The Netherlands: Elsevier. TIC: 236817.

156561 Stepek, J. 2000. Characterization of Yucca Mountain Percolation in the Unsaturated Zone - ESF Study. Scientific Notebook YMP-LBNL-JSW-JS-1. ACC: MOL.19991013.0476; MOL.20010724.0086.

147703 SubTerra. 1998. *Final Report, TRW Environmental Safety Systems, Inc., Busted Butte Test Facility*. Project: 97-35. Kirkland, Washington: SubTerra. TIC: 247628.

109172 Szabo, B.J. and Kyser, T.K. 1990. "Ages and Stable-Isotope Compositions of Secondary Calcite and Opal in Drill Cores from Tertiary Volcanic Rocks of the Yucca Mountain Area, Nevada." *Geological Society of America Bulletin, 102*, 1714-1719. Boulder, Colorado: Geological Society of America. TIC: 221927.

109175 Thompson, R.S. 1991. "Pliocene Environments and Climates in the Western United States." *Quaternary Science Reviews, 10*, 115-132. Oxford, United Kingdom: Pergamon Press. TIC: 234260.

126827 Thorstenson, D.C.; Weeks, E.P.; Haas, H.; Busenberg, E.; Plummer, L.N.; and Peters, C.A. 1998. "Chemistry of Unsaturated Zone Gases Sampled in Open Boreholes at the Crest of Yucca Mountain, Nevada: Data and Basic Concepts of Chemical and Physical Processes in the Mountain." *Water Resources Research, 34*, (6), 1507-1529. Washington, D.C.: American Geophysical Union. TIC: 246315.

139195 Tokunaga, T.K. and Wan, J. 1997. "Water Film Flow Along Fracture Surfaces of Porous Rock." *Water Resources Research, 33*, (6), 1287-1295. Washington, D.C.: American Geophysical Union. TIC: 242739.

166248 Trautz, R. 2003. YMP-LBNL-RCT-5 Moisture Monitoring in the ESF (Phase 2)/Drift Seepage Test. SN-LBNL-SCI-221-V1. ACC: MOL.20011029.0234; MOL.20020923.0235; MOL.20030929.0011.

156563 Trautz, R.C. 1999. Moisture Monitoring in the ESF (Phase 2)/Drift Seepage Test. Scientific Notebook YMP-LBNL-RCT-1. ACC: MOL.20000306.0470; MOL.20001121.0084.

156903 Trautz, R.C. 2001. Moisture Monitoring in the ESF (Phase 2)/Drift Seepage Test. Scientific Notebook YMP-LBNL-RCT-2. ACC: MOL.20011030.0706.

161208 Trautz, R.C. 2001. Moisture Monitoring in the ESF (Phase 2)/Drift Seepage Test. Scientific Notebook YMP-LBNL-RCT-4. ACC: MOL.20020508.0272.

157022 Trautz, R.C. 2001. Niche Excavation; Liquid Flow Testing; Borehole Drilling and Pneumatic Testing; Drift Seepage Testing. Scientific Notebook YMP-LBNL-RCT-3. ACC: MOL.20011116.0083.

165419 Trautz, R.C. and Wang, J.S.Y. 2001. "Evaluation of Seepage into an Underground Opening Using Small-Scale Field Experiments, Yucca Mountain, Nevada." *Mining Engineering, 53*, (12), 41-44. Littleton, Colorado: Society for Mining, Metallurgy and Exploration. TIC: 253862.

160335 Trautz, R.C. and Wang, J.S.Y. 2002. "Seepage into an Underground Opening Constructed in Unsaturated Fractured Rock Under Evaporative Conditions." *Water Resources Research, 38*, (10), 6-1 through 6-14. [Washington, D.C.]: American Geophysical Union. TIC: 253348.

165375 Tsang, Y. and Wang, J. 2000. ECRB Systematic Hydrological Testing. Scientific Notebook SN-LBNL-SCI-179-V1. ACC: MOL.20001016.0017.

165368 Turin, H.J. 2001. Busted Butte Phase II Overcore and Mineback Activities. Scientific Notebook SN-LANL-SCI-252-V1. ACC: MOL.20020204.0180.

164633 Turin, H.J.; Groffman, A.R.; Wolfsberg, L.E.; Roach, J.L.; and Strietelmeier, B.A. 2002. "Tracer and Radionuclide Sorption to Vitric Tuffs of Busted Butte, Nevada." *Applied Geochemistry, 17*, (6), 825-836. New York, New York: Pergamon. TIC: 254046.

160355 USGS (U.S. Geological Survey) 2001. *Simulation of Net Infiltration for Modern and Potential Future Climates*. ANL-NBS-HS-000032 REV 00 ICN 02. Denver, Colorado: U.S. Geological Survey. ACC: MOL.20011119.0334.

165099 Vandergraaf, T.T.; Drew, D.J.; and Ticknor, K.V. 2002. *Busted Butte Report on Laboratory Radionuclide Migration Experiments in Non-Welded Tuff Under Unsaturated Conditions*. AECL-12170. Pinawa, Manitoba, Canada: Atomic Energy of Canada Limited. ACC: MOL.20030919.0118.

165133 Vandergraaf, T.T.; Drew, D.J.; Ticknor, K.V.; and Seddon, W.A. 2002. "Radionuclide Migration Experiments at a Scale of up to 1 Metre in Tuff Blocks Under Unsaturated Conditions." *Abstracts with Programs - Geological Society of America, 34*, (6), 237. Boulder, Colorado: Geological Society of America. TIC: 254868.

157427 Vaniman, D.T.; Chipera, S.J.; Bish, D.L.; Carey, J.W.; and Levy, S.S. 2001. "Quantification of Unsaturated-Zone Alteration and Cation Exchange in Zeolitized Tuffs at Yucca Mountain, Nevada, USA." *Geochimica et Cosmochimica Acta, 65*, (20), 3409-3433. [New York, New York]: Elsevier. TIC: 251574.

164719 Vigier, N.; Bourdon, B.; Turner, S.; and Allègre, C.J. 2001. "Erosion Timescales Derived from U-Decay Series Measurements in Rivers." *Earth and Planetary Science Letters, 193*, ([3-4]), 549-563. [New York, New York]: Elsevier. TIC: 254755.

156530 Wang, J. 1997. Characterization of Yucca Mountain Percolation in the Unsaturated Zone - ESF Study. Scientific Notebook YMP-LBNL-JSW-6. ACC: MOL.19991013.0459.

156534 Wang, J. 1997. Characterization of Yucca Mountain Percolation in the Unsaturated Zone - ESF Study. Scientific Notebook YMP-LBNL-JSW-6A. ACC: MOL.19991013.0460.

156538 Wang, J. 1999. Characterization of Yucca Mountain Percolation in the Unsaturated Zone - ESF Study. Scientific Notebook YMP-LBNL-JSW-6B. ACC: MOL.19991013.0461.

153449 Wang, J. 1999. Characterization of Yucca Mountain Percolation in the Unsaturated Zone - ESF Study. Scientific Notebook YMP-LBNL-JSW-6C. ACC: MOL.19991013.0462.

156559 Wang, J. 2000. Characterization of Yucca Mountain Percolation in the Unsaturated Zone - Exploratory Shaft Facility Study. Scientific Notebook YMP-LBNL-JSW-4.3. ACC: MOL.19991018.0187; MOL.20000808.0010.

165376 Wang, J.S. 2003. "Scientific Notebooks Referenced in Scientific Analysis Report U0015, In-Situ Field Testing Processes, ANL-NBS-HS-000005 REV02." Memorandum from J.S. Wang (BSC) to File, December 2, 2003, with attachments. ACC: MOL.20031202.0097.

104366 Wang, J.S.Y. and Elsworth, D. 1999. "Permeability Changes Induced by Excavation in Fractured Tuff." *Rock Mechanics for Industry, Proceedings of the 37th U.S. Rock Mechanics Symposium, Vail, Colorado, USA, 6-9 June 1999*. Amadei, B.; Kranz, R.L.; Scott, G.A.; and Smeallie, P.H., eds. 2, 751-757. Brookfield, Vermont: A.A. Balkema. TIC: 245246.

106793 Wang, J.S.Y. and Narasimhan, T.N. 1993. "Unsaturated Flow in Fractured Porous Media." Chapter 7 of *Flow and Contaminant Transport in Fractured Rock*. Bear, J.; Tsang, C-F.; and de Marsily, G., eds. San Diego, California: Academic Press. TIC: 235461.

101309 Wang, J.S.Y.; Flint, A.L.; Nitao, J.J.; Chesnut, D.A.; Cook, P.; Cook, N.G.W.; Birkholzer, J.; Freifeld, B.; Flint, L.E.; Ellet, K.; Mitchell, A.J.; Homuth, E.F.; Griego, G.J.; Cerny, J.A.; and Johnson, C.L. 1996. *Evaluation of Moisture Evolution in the Exploratory Studies Facility*. Milestone TR31K6M. Berkeley, California: Lawrence Berkeley National Laboratory. ACC: MOL.19961231.0089.

106146 Wang, J.S.Y.; Trautz, R.C.; Cook, P.J.; Finsterle, S.; James, A.L.; and Birkholzer, J. 1999. "Field Tests and Model Analyses of Seepage into Drift." *Journal of Contaminant Hydrology, 38*, (1-3), 323-347. New York, New York: Elsevier. TIC: 244160.

106150 Warrick, A.W.; Biggar, J.W.; and Nielsen, D.R. 1971. "Simultaneous Solute and Water Transfer for an Unsaturated Soil." *Water Resources Research, 7*, (5), 1216-1225. Washington, D.C.: American Geophysical Union. TIC: 245674.

109179 Whelan, J.F. and Moscati, R.J. 1998. "9 M.Y. Record of Southern Nevada Climate from Yucca Mountain Secondary Minerals." *High-Level Radioactive Waste Management, Proceedings of the Eighth International Conference, Las Vegas, Nevada, May 11-14, 1998*. Pages 12-15. La Grange Park, Illinois: American Nuclear Society. TIC: 237082.

137305 Whelan, J.F.; Moscati, R.J.; Allerton, S.B.M.; and Marshall, B.D. 1998. *Applications of Isotope Geochemistry to the Reconstruction of Yucca Mountain, Nevada, Paleohydrology—Status of Investigations: June 1996*. Open-File Report 98-83. Denver, Colorado: U.S. Geological Survey. ACC: MOL.19981012.0740.

163590 Whelan, J.F.; Neymark, L.A.; Roedder, E.; and Moscati, R.J. 2003. "Thermochronology of Secondary Minerals from the Yucca Mountain Unsaturated Zone." *Proceedings of the 10th International High-Level Radioactive Waste Management Conference (IHLRWM), March 30-April 2, 2003, Las Vegas, Nevada*. Pages 357-366. [La Grange Park, Illinois]: American Nuclear Society. TIC: 254368.

160442 Whelan, J.F.; Paces, J.B.; and Peterman, Z.E. 2002. "Physical and Stable-Isotope Evidence for Formation of Secondary Calcite and Silica in the Unsaturated Zone, Yucca Mountain, Nevada." *Applied Geochemistry, 17*, ([6]), 735-750. [New York, New York]: Elsevier. TIC: 253462.

154773 Whelan, J.F.; Roedder, E.; and Paces, J.B. 2001. "Evidence for an Unsaturated-Zone Origin of Secondary Minerals in Yucca Mountain, Nevada." "Back to the Future - Managing the Back End of the Nuclear Fuel Cycle to Create a More Secure Energy Future," *Proceedings of the 9th International High-Level Radioactive Waste Management Conference (IHLRWM), Las Vegas, Nevada, April 29-May 3, 2001*. La Grange Park, Illinois: American Nuclear Society. TIC: 247873.

100091 Whelan, J.F.; Vaniman, D.T.; Stuckless, J.S.; and Moscati, R.J. 1994. "Paleoclimatic and Paleohydrologic Records from Secondary Calcite: Yucca Mountain, Nevada." *High Level Radioactive Waste Management, Proceedings of the Fifth Annual International Conference, Las Vegas, Nevada, May 22-26, 1994*. 4, 2738-2745. La Grange Park, Illinois: American Nuclear Society. TIC: 210984.

151450 White, A.F.; Bullen, T.D.; Vivit, D.V.; Schulz, M.S.; and Clow, D.W. 1999. "The Role of Disseminated Calcite in the Chemical Weathering of Granitoid Rocks." *Geochimica et Cosmochimica Acta, 63*, (13/14), 1939-1953. [New York, New York]: Pergamon Press. TIC: 248634.

106152 White, I. and Sully, M.J. 1987. "Macroscopic and Microscopic Capillary Length and Time Scales from Field Infiltration." *Water Resources Research, 23*, (8), 1514-1522. Washington, D.C.: American Geophysical Union. TIC: 239821.

165373 Williams, K. 2000. Busted Butte. Scientific Notebook SN-LBNL-SCI-119-V1. ACC: MOL.20001011.0059.

165374 Williams, K. 2002. YMP-LBNL-ELM-KHW-2 UZ Busted Butte. Scientific Notebook SN-LBNL-SCI-119-V2. ACC: MOL.20021126.0232.

154279 Wilson, N.S.F.; Cline, J.S.; and Lundberg, S.A.W. 2000. "Paragenesis and Chemical Composition of Secondary Mineralization at Yucca Mountain, Nevada." *Abstracts with Programs - Geological Society of America, 32*, (7), A-260. Boulder, Colorado: Geological Society of America. TIC: 249113.

154280 Wilson, N.S.F.; Cline, J.S.; Rotert, J.; and Amelin, Y.V. 2000. "Timing and Temperature of Fluid Movement at Yucca Mountain, NV: Fluid Inclusion Analyses and U-Pb and U-Series Dating." *Abstracts with Programs - Geological Society of America, 32*, (7), A-260. Boulder, Colorado: Geological Society of America. TIC: 249113.

155426 Wilson, S.F. and Cline, J.S. 2001. "Paragenesis, Temperature and Timing of Secondary Minerals at Yucca Mountain." "Back to the Future - Managing the Back End of the Nuclear Fuel Cycle to Create a More Secure Energy Future," *Proceedings of the 9th International High-Level Radioactive Waste Management Conference (IHLRWM), Las Vegas, Nevada, April 29-May 3, 2001*. La Grange Park, Illinois: American Nuclear Society. TIC: 247873.

109187 Winograd, I.J.; Szabo, B.J.; Coplen, T.B.; Riggs, A.C.; and Kolesar, P.T. 1985. "Two-Million-Year Record of Deuterium Depletion in Great Basin Ground Waters." *Science, 227*, 519-522. Washington, D.C.: American Association for the Advancement of Science. TIC: 216799.

156399 Wu, Y.S.; Liu, H.H.; Bodvarsson, G.S.; and Zellmer, K.E. 2001. *A Triple-Continuum Approach for Modeling Flow and Transport Processes in Fractured Rock*. LBNL-48875. Berkeley, California: Lawrence Berkeley National Laboratory. TIC: 251297.

165298 Wyckoff, D. 1999. Unsaturated Zone Transport Test (LA-EES-5-NBK-98-014). Scientific Notebook SN-LANL-SCI-044-V1. ACC: MOL.20001023.0116.

160839 Yang, I.C. 2002. "Percolation Flux and Transport Velocity in the Unsaturated Zone, Yucca Mountain, Nevada." *Applied Geochemistry, 17*, ([6]), 807-817. [New York, New York]: Elsevier. TIC: 253605.

164631 Yang, I.C.; Peterman, Z.E.; and Scofield, K.M. 2003. "Chemical Analyses of Pore Water from Boreholes USW SD-6 and USW WT-24, Yucca Mountain, Nevada." *Journal of Contaminant Hydrology, 62-63*, 361-380. New York, New York: Elsevier. TIC: 254205.

100194 Yang, I.C.; Rattray, G.W.; and Yu, P. 1996. *Interpretation of Chemical and Isotopic Data from Boreholes in the Unsaturated Zone at Yucca Mountain, Nevada*. Water-Resources Investigations Report 96-4058. Denver, Colorado: U.S. Geological Survey. ACC: MOL.19980528.0216.

101441 Yang, I.C.; Yu, P.; Rattray, G.W.; Ferarese, J.S.; and Ryan, J.N. 1998. *Hydrochemical Investigations in Characterizing the Unsaturated Zone at Yucca Mountain, Nevada*. Water-Resources Investigations Report 98-4132. Denver, Colorado: U.S. Geological Survey. ACC: MOL.19981012.0790.

153339 Youden, W.J. 1951. *Statistical Methods for Chemists*. New York, New York: John Wiley & Sons. TIC: 248814.

Software Cited

147402 CRWMS M&O 1999. *Software Routine: ECRB-XYZ*. V.03. PC. 30093-V.03.

140259 Lawrence Berkeley National Laboratory 1/26/2000. *Software Macro: Mettler Double Scale 1.vi*. V1.0. PC. MOL.19991018.0189.

152835 LBNL (Lawrence Berkeley National Laboratory) 1998. *Software Code: EARTHVISION*. V4.0. SGI, IRIX 6.4. 30035-2 V4.0.

161229 LBNL (Lawrence Berkeley National Laboratory) 2000. *Software Code: Mettler Single Scale 9-27-00.vi*. V1.0. PC, Windows 95/98/NT. 10399-1.0-00.

161226 LBNL (Lawrence Berkeley National Laboratory) 2002. *Software Code: Auto packer inflation.vi*. V1.0. PC, Windows 95/98/NT/2000. 10754-1.0-00.

161227 LBNL (Lawrence Berkeley National Laboratory) 2002. *Software Code: Auto pinch valve box.vi*. V1.0. PC, Windows 95/98/NT/2000. 10755-1.0-00.

161221 LBNL (Lawrence Berkeley National Laboratory) 2002. *Software Code: Auto refill water supply.vi*. V1.0. PC, Windows 95/98/NT/2000. 10756-1.0-00.

161222 LBNL (Lawrence Berkeley National Laboratory) 2002. *Software Code: Automated return pump.vi*. V1.0. PC, Windows 95/98/NT/2000. 10757-1.0-00.

161219 LBNL (Lawrence Berkeley National Laboratory) 2002. *Software Code: Combined System Box.vi*. V1.0. PC, Windows 95/98/NT/2000. 10758-1.0-00.

161224 LBNL (Lawrence Berkeley National Laboratory) 2002. *Software Code: Manual packer inflation.vi*. V1.0. PC, Windows 95/98/NT/2000. 10759-1.0-00.

161225 LBNL (Lawrence Berkeley National Laboratory) 2002. *Software Code: Manual pinch valve box.vi*. V1.0. PC, Windows 95/98/NT/2000. 10760-1.0-00.

161230 LBNL (Lawrence Berkeley National Laboratory) 2002. *Software Code: Mettler Quad Scale 8-23-01.vi*. V2.0. PC, Windows 2000. 10345-2.0-00.

161228 LBNL (Lawrence Berkeley National Laboratory) 2002. *Software Code: Mettler Single Scale 8-31-01.vi*. V2.0. PC, Windows 2000. 10399-2.0-00.

161220 LBNL (Lawrence Berkeley National Laboratory) 2002. *Software Code: Pump box.vi*. V1.0. PC, Windows 95/98/NT/2000. 10761-1.0-00.

161218 LBNL (Lawrence Berkeley National Laboratory) 2002. *Software Name: Nistime-32 bit.exe*. V3.12. PC, Windows 2000. 10664-3.12-00.

8.2 CODES, STANDARDS, REGULATIONS, AND PROCEDURES

156605 10 CFR 63. Energy: Disposal of High-Level Radioactive Wastes in a Geologic Repository at Yucca Mountain, Nevada. Readily available.

AP-2.22Q, Rev. 1, ICN 0. *Classification Analyses and Maintenance of the Q-List.* Washington, D.C.: U.S. Department of Energy, Office of Civilian Radioactive Waste Management. ACC: DOC.20030807.0002.

AP-12.1Q, Rev. 0, ICN 2. *Control of Measuring and Test Equipment and Calibration Standards*. Washington, D.C.: U.S. Department of Energy, Office of Civilian Radioactive Waste Management. ACC: MOL.20020207.0111..

AP-SI.1Q, Rev. 5, ICN 12 *Software Management*. Washington, D.C.: U.S. Department of Energy, Office of Civilian Radioactive Waste Management. ACC: DOC.20030902.0003.

YMP-LBNL-TIP/GP 5.0, Rev. 1, Mod. 0. *Ground Penetrating Radar Data Acquisition.* Berkeley, California: Lawrence Berkeley National Laboratory. ACC: MOL.20000419.0583.

8.3 SOURCE DATA, LISTED BY DATA TRACKING NUMBER

156911 GS000308312242.002. Phase 1 of Water Collection in Alcove 1 from 05/05/98 to 08/27/98. Submittal date: 03/01/2000.

162015 GS000308313211.001. Geochemistry of Repository Block. Submittal date: 03/27/2000.

147024 GS000399991221.003. Preliminary Alcove 1 Infiltration Experiment Data. Submittal date: 03/10/2000.

152573 GS000608314224.004. Provisional Results: Geotechnical Data for Station 35+00 to Station 40+00, Main Drift of the ESF. Submittal date: 06/20/2000.

162980 GS000808312242.006. Pulse Flow Meter Data for the Alcove 1 Infiltration Experiment from 02/19/99 to 06/20/00. Submittal date: 09/07/2000.

165202 GS001108312242.009. Tracker Data for the Alcove 1 Infiltration Experiment, Phase II 05/09/99 to 07/05/00. Submittal date: 11/07/2000.

165543 GS010608312242.002. Small Plot Infiltration in Alcove 8 Using a Box Permeameter from August 28, 2000 to December 14, 2000. Submittal date: 06/27/2001.

165542 GS010608312242.004. Crossover Alcove/Seepage into Niche 3; Small Plot Infiltration Using a Cylinder Permeameter from August 9, 2000 to August 21, 2000. Submittal date: 06/28/2001.

164844 GS010808315215.003. Fluid Inclusion Homogenization Temperatures from the ESF, ECRB, and EWCD, 12/99 to 4/01. Submittal date: 09/04/2001.

164850 GS010808315215.004. Uranium and Lead Concentrations, Lead Isotopic Compositions, and U-Pb Isotope Ages for the ESF Secondary Minerals Determined at the Royal Ontario Museum between April 20, 2000 and April 19, 2001. Submittal date: 08/29/2001.

162342 GS020408312272.002. Tritium Abundance Data from Pore-Water in Core Samples from Yucca Mountain ESF Boreholes for the Period of April 30, 1998 through March 21, 2001. Submittal date: 05/08/2002.

160899 GS020408312272.003. Collection and Analysis of Pore Water Samples for the Period from April 2001 to February 2002. Submittal date: 04/24/2002.

162129 GS020508312242.001. Trench Fault Infiltration in Alcove 8 Using Permeameters from March 5, 2001 to June 1, 2001. Submittal date: 05/22/2002.

162126 GS020608315215.002. Carbon Dioxide Abundances, Carbon Dioxide Concentrations, and Normative Calcite Concentrations for Cuttings from Borehole USW SD-6, USW WT-24, and ECRB Cross Drift Boreholes, Determined by Carbon Dioxide Evolution, May 25, 2000 and September 8, 2000. Submittal date: 06/26/2002.

162141 GS020908312242.002. Trenched Fault Infiltration in Alcove 8 Using Permeameters from June 1, 2001 to March 26, 2002. Submittal date: 09/17/2002.

164846 GS020908315215.003. Fluid Inclusion Homogenization Temperatures from the ESF and ECRB, 10/01 to 5/02. Submittal date: 09/26/2001.

164847 GS020908315215.004. Stable Carbon and Oxygen Isotope Analyses of ESF/ECRB Calcite and USW SD-6 and USW WT-24 Whole Rock; 1/1999-6/2002. Submittal date: 10/16/2002.

162178 GS021008312242.003. Moisture Monitoring in ESF, Alcoves 3 and 4, from April 1, 2000 through March 31, 2002. Submittal date: 01/15/2003.

164848 GS021008315215.005. Uranium, Thorium, and Lead Concentrations, Lead Isotopic Compositions, U-Pb Isotope Ages and 234U/238U and 230TH/238U Activity Ratios for the ESF and ECRB Secondary Minerals Determined at the Royal Ontario Museum between 11/16/01 and 4/7/02. Submittal date: 10/21/2002.

162127 GS021008315215.007. Carbon Dioxide and Normative Calcite Concentrations in Powdered Cuttings from Borehole USW WT-24 Determined by CO2 Evolution between July 1998 and August 1999. Submittal date: 11/07/2002.

162934 GS021208312272.005. Tritium Abundance Data from Pore-Water in Core Samples from Yucca Mountain ESF ECRB. Submittal date: 12/19/2002.

164609 GS021208312272.008. Uranium and Thorium Concentrations and 234U-230TH-238U-232TH Isotopic Compositions from Whole Rock Samples from the ECRB Cross-Drift and ESF Analyzed between February and June, 2002. Submittal date: 01/28/2003.

164851 GS021208315215.008. 238U-234U-230TH-232TH Isotope Ratios and Calculated Ages for Opal Hemispheres from Sample HD2074 (SPC00506577) at Station 30+51 in the Exploratory Studies Facility Determined Using Ion-Probe Mass Spectrometry. Submittal date: 12/19/2002.

164750 GS021208315215.009. U Abundances, 238U-234U-230TH-232TH Activity Ratios, and Calculated 230TH/U Ages, and Initial 234U/238U Activity Ratios Determined for Sequential In-Situ Microdigestions of Opal Hemispheres from the ESF by Thermal Ionization Mass Spectrometry. Submittal date: 12/19/2002.

165544 GS030208312242.003. Trenched Fault Infiltration in Alcove 8 Using Permeameters from March 26, 2002 to August 20, 2002. Submittal date: 03/10/2003.

162935 GS030208312272.001. Gas and Water Vapor Chemistry Data in Yucca Mountain ESF ECRB Bulkheads. Submittal date: 03/11/2003.

165226 GS030408312272.002. Analysis of Water-Quality Samples for the Period from July 2002 to November 2002. Submittal date: 05/07/2003.

165545 GS030508312242.004. Photographs from Niche 3 of the Alcove 8/Niche 3 Seepage Experiment During Construction Showing Construction Water in Niche 3, March 6, 2000. Submittal date: 06/03/2003.

165547 GS030608312231.002. Digital Image Data from the Moisture Monitoring Tests in the ECRB Bulkheaded Cross Drift from January 22, 2001 to February 3, 2003. Submittal date: 07/09/2003.

166200 GS030608312242.005. Surface Infiltration in a Large Plot in Alcove 8 Using Permeameters from November 19, 2002 to March 24, 2003. Submittal date: 06/24/2003.

165426 GS030808315215.001. Line Survey Information from the East-West Cross-Drift Obtained to Estimate Secondary Mineral Abudance. Submittal date: 09/23/2003.

166097 GS030908315215.002. X-Ray Fluorescence Elemental Compositions Determined on Cuttings from USW SD-6 and USW WT-24 Analyzed from May 20, 1998 to March 13, 2001. Submittal date: 10/20/2003.

166089 GS031008312242.007. Surface Infiltration in a Large Plot in Alcove 8 Using Permeameters from August 20, 2002 to November 19, 2002. Submittal date: 10/31/2003.

107488 GS950508314224.003. Provisional Results: Geotechnical Data - Full Periphery Map Data from North Ramp of the Exploratory Studies Facility, Stations 0+60 to 4+00. Submittal date: 05/24/1995.

108984 GS951108312231.009. Physical Properties, Water Content, and Water Potential for Borehole USW SD-7. Submittal date: 09/26/1995.

151649 GS951208312272.002. Tritium Analyses of Porewater from USW UZ-14, USW NRG-6, USW NRG-7A and UE-25 UZ#16 and of Perched Water from USW SD-7, USW SD-9, USW UZ-14 and USW NRG-7A from 12/09/92 to 5/15/95. Submittal date: 12/15/1995.

105617 GS960708314224.008. Provisional Results: Geotechnical Data for Station 30 + 00 to Station 35 + 00, Main Drift of the ESF. Submittal date: 08/05/1996.

106031 GS960708314224.010. Provisional Results: Geotechnical Data for Station 40+00 to Station 45+00, Main Drift of the ESF. Submittal date: 08/05/1996.

108985 GS960808312231.004. Physical Properties, Water Content and Water Potential for Samples from Lower Depths in Boreholes USW SD- 7 and USW SD-12. Submittal date: 08/30/1996.

108995 GS960808312231.005. Water Permeability and Relative Humidity Calculated Porosity for Samples from Boreholes USW SD-7, USW SD-9, USW SD-12 and USW UZ-14. Submittal date: 08/30/1996.

106033 GS960908314224.014. Provisional Results - ESF Main Drift, Station 50+00 to Station 55+00. Submittal date: 09/09/1996.

106059 GS960908314224.020. Analysis Report: Geology of the North Ramp - Stations 4+00 to 28+00 and Data: Detailed Line Survey and Full-Periphery Geotechnical Map - Alcoves 3 (UPCA) and 4 (LPCA), and Comparative Geologic Cross Section - Stations 0+60 to 28+00. Submittal date: 09/09/1996.

135119 GS970208312242.001. Moisture Monitoring in the ESF, Oct. 1, 1996 through Jan. 31, 1997. Submittal date: 02/19/1997.

106048 GS970208314224.003. Geotechnical Data for Station 60+00 to Station 65+00, South Ramp of the ESF. Submittal date: 02/12/1997.

107351 GS970208315215.005. Carbon and Oxygen Stable Isotope Kiel Analyses of Calcite from the ESF and USW G-1, G-2 and G-4, UE-25 A#1, USW NRG-6 and NRG-7/7A, and UE-25 UZ#16, April 1996 – January 1997. Submittal date: 02/27/1997.

135123 GS970708312242.002. Moisture Monitoring in the ESF, Feb. 1, 1997 through July 31, 1997. Submittal date: 07/18/1997.

105978 GS970808312232.005. Deep Unsaturated Zone Surface-Based Borehole Instrumentation Program Data from Boreholes USW NRG-7A, UE-25 UZ#4, UE-25 UZ#5, USW UZ-7A and USW SD-12 for the Time Period 1/1/97 - 6/30/97. Submittal date: 08/28/1997.

145920 GS970808315215.010. Carbon and Oxygen Stable Isotope Analyses of Calcite from the ESF and USW G-1, G-2, and G-3/GU-3, from 01/16/97 to 07/18/97. Submittal date: 08/18/1997.

105980 GS971108312232.007. Deep Unsaturated Zone Surface-Based Borehole Instrumentation Program Data from Boreholes USW NRG-7A, UE-25 UZ #4, UE-25 UZ #5, USW UZ-7A and USW SD-12 for the Time Period 7/1/97 - 9/30/97. Submittal date: 11/18/1997.

105561 GS971108314224.020. Revision 1 of Detailed Line Survey Data, Station 0+60 to Station 4+00, North Ramp Starter Tunnel, Exploratory Studies Facility. Submittal date: 12/03/1997.

106007 GS971108314224.021. Revision 1 of Detailed Line Survey Data, Station 4+00 to Station 8+00, North Ramp, Exploratory Studies Facility. Submittal date: 12/03/1997.

106009 GS971108314224.022. Revision 1 of Detailed Line Survey Data, Station 8+00 to Station 10+00, North Ramp, Exploratory Studies Facility. Submittal date: 12/03/1997.

106010 GS971108314224.023. Revision 1 of Detailed Line Survey Data, Station 10 + 00 to Station 18 + 00, North Ramp, Exploratory Studies Facility. Submittal date: 12/03/1997.

106023 GS971108314224.024. Revision 1 of Detailed Line Survey Data, Station 18+00 to Station 26+00, North Ramp, Exploratory Studies Facility. Submittal date: 12/03/1997.

106025 GS971108314224.025. Revision 1 of Detailed Line Survey Data, Station 26+00 to Station 30+00, North Ramp and Main Drift, Exploratory Studies Facility. Submittal date: 12/03/1997.

106032 GS971108314224.026. Revision 1 of Detailed Line Survey Data, Station 45+00 to Station 50+00, Main Drift, Exploratory Studies Facility. Submittal date: 12/03/1997.

106047 GS971108314224.028. Revision 1 of Detailed Line Survey Data, Station 55+00 to Station 60+00, Main Drift and South Ramp, Exploratory Studies Facility. Submittal date: 12/03/1997.

135181 GS980308312242.001. Time Domain Reflectometry Measurements in the South Ramp of the ESF, August 1, 1997 to January 4, 1998. Submittal date: 03/04/1998.

135163 GS980308312242.002. Heat Dissipation Probe Measurements in the South Ramp of the ESF, August 1, 1997 to January 31, 1998. Submittal date: 03/09/1998.

135180 GS980308312242.003. Physical Properties of Borehole Samples from the ESF South Ramp (ESF Station 59+65M to ESF Station 76+33M). Submittal date: 03/16/1998.

107172 GS980308312242.004. Water Potential Measurements Using the Filter Paper Technique for Borehole Samples from the ESF North Ramp (ESF Station 7+27 M to ESF Station 10+70 M) and the ESF South Ramp (ESF Station 59+65 M to 76+33 M). Submittal date: 03/19/1998.

107165 GS980308312242.005. Physical Properties of Lexan-Sealed Borehole Samples from the PTN Exposure in the ESF North Ramp (ESF Station 7+27 M to ESF Station 10+70 M). Submittal date: 03/11/1998.

107355 GS980308315215.008. Line Survey Information from the Exploratory Studies Facility Obtained to Estimate Secondary Mineral Abundance. Submittal date: 03/24/1998.

105982 GS980408312232.001. Deep Unsaturated Zone Surface-Based Borehole Instrumentation Program Data from Boreholes USW NRG-7A, UE-25 UZ #4, USW NRG-6, UE-25 UZ #5, USW UZ-7A and USW SD-12 for the Time Period 10/01/97 - 03/31/98. Submittal date: 04/16/1998.

135170 GS980908312242.018. Physical Properties of Borehole Core Samples from ESF-MD-NICHE3566#1, ESF-MD-NICHE3566#2, ESF-MD-NICHE3566#3A, ESF-MD-NICHE3566LT#1, ESF-MD-NICHE3566LT#2, ESF-MD-NICHE3566LT#3, ESF-MD-NICHE3566LT#4, ESF-MD-NICHE3566LT#5, and ESF-MD-NICHE3566LT#6. Submittal date: 09/03/1998.

135172 GS980908312242.020. Physical Properties of Borehole Core Samples from ESF-MD-NICHE3650#1, ESF-MD-NICHE3650#2, ESF-MD-NICHE3650#3, ESF-MD-NICHE3650#4, ESF-MD-NICHE3650#5, ESF-MD-NICHE3650#6, and ESF-MD-NICHE3650#7. Submittal date: 09/05/1998.

135157 GS980908312242.022. Water Potentials Measured with Heat Dissipation Probes in Twenty-One Drill Holes in Niche 1 (ESF-NICHE3566) from 11/04/97 to 07/31/98. Submittal date: 09/11/1998.

135132 GS980908312242.024. Moisture Monitoring in the ESF, August 1, 1997 to July 31, 1998. Submittal date: 09/15/1998.

135176 GS980908312242.028. Physical and Hydrologic Properties of Borehole Core Samples from ESF-SAD-GTB#1. Submittal date: 09/16/1998.

135175 GS980908312242.029. Physical and Hydrologic Properties of Borehole Core Samples from ESF-NDR-MF#1, ESF-NDR-MF#2, and ESF-NDR-MF#4 in Alcove 6 of the ESF. Submittal date: 09/17/1998.

135224 GS980908312242.030. Physical Properties of Borehole Core Samples from ESF-ECRB-SLANT#2. Submittal date: 09/17/1998.

107177 GS980908312242.032. Physical and Hydrologic Properties of Borehole Core Samples and Water Potential Measurements Using the Filter Paper Technique for Borehole Samples from ESF-LPCA-PTN#1 and ESF-LPCA-PTN#2 in Alcove 4. Submittal date: 09/17/1998.

107168 GS980908312242.033. Physical and Hydrologic Properties of Borehole Core Samples and Water Potential Measurements Using the Filter Paper Technique for Borehole Samples from ESF-UPCA-PTN#1 in Alcove 3 of the ESF. Submittal date: 09/17/1998.

135133 GS980908312242.035. Moisture Monitoring in the ECRB, 04/08/98 to 07/31/98. Submittal date: 09/24/1998.

119820 GS980908312242.036. Water Potentials Measured with Heat Dissipation Probes in ECRB Holes from 4/23/98 to 7/31/98. Submittal date: 09/22/1998.

146088 GS980908315213.002. Carbon and Oxygen Stable Isotopic Compositions of Exploratory Studies Facility Secondary Calcite Occurrences, 10/01/97 to 08/15/98. Submittal date: 09/16/1998.

156505 GS981208312232.002. Deep UZ Surface-Based Borehole Instrumentation Program Data from Boreholes USW NRG-7A, UE-25 UZ#4, USW NRG-6, UE-25 UZ#5, USW UZ-7A and USW SD-12 for the Time Period 4/1/98 through 9/30/98. Submittal date: 12/03/1998.

166000 GS990108312242.005. Temperature, Relative Humidity and Barometric Pressure Data for Alcove 7 of the ESF from 12/08/97 to 12/12/98. Submittal date: 01/28/1999.

162979 GS990108312242.006. Pulse Flow Meter Data for the Alcove 1 Infiltration Experiment from 03/08/98 to 12/04/98. Submittal date: 01/29/1999.

146125 GS990183122410.001. Tritium Data from Pore Water from ESF Borehole Cores, 1997 Analyses by USGS. Submittal date: 01/06/1999.

146129 GS990183122410.004. Tritium Data from Pore Water from ESF Borehole Cores, 1998 Analyses by University of Miami. Submittal date: 10/14/1999.

107185 GS990308312242.007. Laboratory and Centrifuge Measurements of Physical and Hydraulic Properties of Core Samples from Busted Butte Boreholes UZTT-BB-INJ-1, UZTT-BB-INJ-3, UZTT-BB-INJ-4, UZTT-BB-INJ-6, UZTT-BB-COL-5 and UZTT-BB-COL-8. Submittal date: 03/22/1999.

108396 GS990408314224.001. Detailed Line Survey Data for Stations 00+00.89 to 14+95.18, ECRB Cross Drift. Submittal date: 09/09/1999.

105625 GS990408314224.002. Detailed Line Survey Data for Stations 15+00.85 to 26+63.85, ECRB Cross Drift. Submittal date: 09/09/1999.

108409 GS990408314224.006. Full-Periphery Geologic Maps for Station 20+00 to 26+81, ECRB Cross Drift. Submittal date: 09/09/1999.

109822 GS990708312242.008. Physical and Hydraulic Properties of Core Samples from Busted Butte Boreholes. Submittal date: 07/01/1999.

164604 GS990708314224.007. Detailed Line Survey Data for Busted Butte Access Drift and Busted Butte Cross Drift. Submittal date: 11/02/1999.

152631 GS990908314224.010. Geology of the ECRB Cross Drift: Graphical Data. Submittal date: 09/14/1999.

153379 GS990908315213.001. Stable Carbon and Oxygen Isotope Data for Calcite from the ESF and Analyzed 2/96 - 5/99. Submittal date: 10/28/1999.

154760 LA0002JF12213U.001. Chemistry Data for Porewater Extracted from Drillcore from Surface-Based Boreholes USW NRG-6, USW NRG-7A, USW UZ-7A, USW UZ-14, UE-25 UZ#16, USW UZ-N55, USW SD-6, USW SD-7, USW SD-9, USW SD-12, and USW WT-24. Submittal date: 02/15/2000.

156281 LA0002JF12213U.002. Chemistry Data for Porewater Extracted from ESF, Cross Drift and Busted Butte Drill Core. Submittal date: 02/15/2000.

156582 LA0008WS831372.001. Calculated Daily Injection Rates for the Busted Butte Unsaturated Zone Transport Tests. Submittal date: 08/23/2000.

161525 LA0108TV12213U.001. Static Batch Sorption Coefficients and Retardation Coefficients. Submittal date: 08/14/2001.

157100 LA0112WS831372.001. Busted Butte UZ Transport Test: Phase II Collection Pad Tracer Loading. Submittal date: 12/06/2001.

157115 LA0112WS831372.002. Busted Butte UZ Transport Test: Phase II Collection Pad Tracer Concentrations. Submittal date: 12/06/2001.

157106 LA0112WS831372.003. Busted Butte UZ Transport Test: Phase II Normalized Collection Pad Tracer Concentrations. Submittal date: 12/06/2001.

165422 LA0201WS831372.004. Calculated Moisture Content for the Busted Butte Site Phase II Collection Boreholes. Submittal date: 01/03/2002.

164749 LA0204SL831372.001. Mineralogy of the Busted Butte Phase 2 Test Block. Submittal date: 04/17/2002.

160824 LA0207SL831372.001. Lithostratigraphic Classification of Hydrologic-Property Core-Sampling Depths, Busted Butte Phase 2 Test Block. Submittal date: 07/16/2002.

162765 LA0302WS831372.001. Fluorescein Plume Images from the Phase 1A Mineback at Busted Butte. Submittal date: 02/26/2003.

163422 LA0305RR831222.001. Chlorine-36 and Cl in Salts Leached from Rock Samples for the Chlorine-36 Validation Study. Submittal date: 05/22/2003.

164091 LA0307RR831222.001. Chloride, Bromide, Sulfate, and Chlorine-36 Analyses of Salts Leached from Cross Drift Rock Samples in FY99 and FY00. Submittal date: 07/09/2003.

164090 LA0307RR831222.002. Chloride, Bromide, Sulfate, and Chlorine-36 Analyses of Salts Leached from ESF 36Cl Validation Drillcore Samples in FY99. Submittal date: 07/09/2003.

166197 LA0311SD831372.001. In-Situ Air Permeability Measurements at Busted Butte. Submittal date: 11/19/2003.

122736 LA9909JF831222.012. Chloride, Bromide, and Sulfate Analyses of Porewater Extracted from ESF Niche 3566 (Niche #1) and ESF 3650 (Niche #2) Drillcore. Submittal date: 09/29/1999.

122739 LA9909WS831372.001. Busted Butte UZ Transport Test: Phase I Collection Pad Extract Concentrations. Submittal date: 09/29/1999.

122741 LA9909WS831372.002. Busted Butte UZ Transport Test: Phase I Collection Pad Tracer Loading and Tracer Concentrations. Submittal date: 09/30/1999.

140089 LA9909WS831372.015. ICPAES Porewater Analysis for Rock Samples from Busted Butte, NV. Submittal date: 10/01/1999.

140093 LA9909WS831372.016. ION Chromatography Porewater Analysis for Rock Samples from Busted Butte, NV. Submittal date: 09/30/1999.

140097 LA9909WS831372.017. pH of Porewater of Rock Samples from Busted Butte, NV. Submittal date: 09/30/1999.

140101 LA9909WS831372.018. Gravimetric Moisture Content of Rock Samples from Busted Butte, NV. Submittal date: 09/30/1999.

147156 LA9910WS831372.008. Busted Butte UZ Transport Test: Gravimetric Moisture Content and Bromide Concentration in Selected Phase 1A Rock Samples. Submittal date: 11/03/1999.

156586 LA9912WS831372.001. Sorption of Fluorinated Benzoic Acids and Lithium on Rock Samples Form Busted Butte, NV. Submittal date: 02/22/2000.

107364 LAJF831222AQ98.004. Chloride, Bromide, Sulfate, and Chlorine-36 Analyses of Salts Leached from ESF Rock Samples. Submittal date: 09/10/1998.

122730 LAJF831222AQ98.007. Chloride, Bromide, and Sulfate Analyses of Salts Leached from ECRB-CWAT#1, #2, and #3 Drill Core. Submittal date: 09/09/1998.

145650 LAJF831222AQ98.009. Chlorine-36 Analyses of Salts Leached from ESF Niche 3566 (Niche #1) Drillcore. Submittal date: 09/09/1998.

145402 LAJF831222AQ98.011. Chloride, Bromide, Sulfate and Chlorine-36 Analyses of Springs, Groundwater, Porewater, Perched Water and Surface Runoff. Submittal date: 09/10/1998.

149214 LB00032412213U.001. Busted Butte Ground Penetrating Radar Data Collected June 1998 through February 2000 at the Unsaturated Zone Transport Test (UZTT): GPR Velocity Data. Submittal date: 03/24/2000.

153141 LB00090012213U.001. Air K Testing in Borehole SYBT-ERCB-LA#2 at CS 17+26 in Cross Drift. Submittal date: 11/03/2000.

153154 LB00090012213U.002. Liquid Release Tests from Borehole SYBT-ECRB-LA#2 at CS 17+26 in Cross Drift. Submittal date: 11/09/2000.

153144 LB0010NICH3LIQ.001. Niche 3107 Seepage Test. Submittal date: 11/02/2000.

153145 LB0010NICH4LIQ.001. Niche 4788 Seepage Test. Submittal date: 11/02/2000.

153155 LB0011AIRKTEST.001. Air Permeability Testing in Niches 3566 and 3650. Submittal date: 11/08/2000.

153460 LB0011CO2DST08.001. Isotope Data for CO2 from Gas Samples Collected from Hydrology Holes in Drift-Scale Test. Submittal date: 12/09/2000.

154586 LB0012AIRKTEST.001. Niche 5 Air K Testing 3/23/00-4/3/00. Submittal date: 12/21/2000.

146878 LB002181233124.001. Air Permeability and Pneumatic Pressure Data Collected Between October 27, 1999 through November 7, 1999 from Niche 5 (ECRB Niche 1620) of the ESF. Submittal date: 02/18/2000.

155681 LB0102NICH5LIQ.001. Niche 5 Seepage Tests - Pre Excavation. Submittal date: 02/28/2001.

156888 LB0108CO2DST05.001. Concentration and Isotope Data for CO2 and H2O from Gas Samples Collected from Hydrology Holes in Drift-Scale Test - May and August 1999, April 2000, January and April 2001. Submittal date: 08/27/2001.

156912 LB0110A8N3GPRB.001. Alcove 8/Niche 3 GPR Baseline Data. Submittal date: 11/12/2001.

157001 LB0110A8N3LIQR.001. Preliminary Observations from the Fault Test at Alcove8/Niche3. Submittal date: 11/12/2001.

156905 LB0110AK23POST.001. AK2 and AK3 Post-Excavation Air-K. Submittal date: 11/12/2001.

156904 LB0110AKN5POST.001. Niche 5 (1620 in ECRB) Post-Excavation Air-K. Submittal date: 11/12/2001.

156913 LB0110BSTBTGPR.001. Busted Butte GPR Data. Submittal date: 11/12/2001.

157169 LB0110COREPROP.001. Lab Measurements of 14 Matrix Cores. Submittal date: 11/12/2001.

156886 LB0110ECRBH2OA.001. ECRB Water Analyses. Submittal date: 11/12/2001.

156887 LB0110ECRBH2OI.001. Isotope Data for Water Samples Collected from the ECRB. Submittal date: 11/12/2001.

156883 LB0110ECRBH2OP.001. Water Potential Data from Three Locations in the ECRB. Submittal date: 11/12/2001.

156878 LB0110ECRBLIQR.001. Systematic Testing in ECRB-SYBT-LA#1, 12/20/2000. Submittal date: 11/12/2001.

156879 LB0110ECRBLIQR.002. Systematic Testing in ECRB-SYBT-LA#1, 2/28/2001. Submittal date: 11/12/2001.

156877 LB0110ECRBLIQR.003. Systematic Testing in ECRB-SYBT-LA#2, 10/23/2000. Submittal date: 11/12/2001.

156979 LB0110TUFTRACR.001. Using Laser Ablation to Study Tracer Movement in Tuff. Submittal date: 11/12/2001.

158462 LB0203ECRBLIQR.001. Systematic Testing in ECRB-SYBT-LA#3(May-July 2001). Submittal date: 03/20/2002.

158478 LB0204NICH3TRC.001. Fault Infiltration Test Tracer Sampling Apr 2001-Mar 2002. Submittal date: 04/30/2002.

160408 LB0207NICH5LIQ.001. Niche 5 Seepage Tests (CD 1620). Submittal date: 07/09/2002.

161210 LB0208NICH5LIQ.001. Niche 5 Seepage Tests (CD 1620), July-August 2002. Submittal date: 08/22/2002.

165461 LB0209A8N3LIQR.001. Resistance Measurements from Borehole 10 in Niche3 (5/23/2001 - 9/3/2002). Submittal date: 09/11/2002.

160796 LB0209NICH5LIQ.001. Niche 5 Seepage Tests (CD 1620), June-August 2002. Submittal date: 09/11/2002.

161211 LB0210NICH5LIQ.001. Niche 5 Seepage Tests (CD 1620), August-October 2002. Submittal date: 10/25/2002.

160792 LB0211NICH5LIQ.001. Niche 5 Seepage Tests (CD 1620), August-October 2002. Submittal date: 11/14/2002.

164605 LB0301ECRBRHTB.001. Moisture Monitoring at Four Locations in the ECRB. Submittal date: 01/31/2003.

165227 LB0301SYTSTLA4.001. Systematic Testing in ECRB-SYBT-LA#4. Submittal date: 01/31/2003.

164748 LB0302ALC8AIRK.001. Alcove 8 Air Permeability Testing. Submittal date: 02/28/2003.

162570 LB0303A8N3LIQR.001. Alcove 8 - Niche 3 Seepage Data Compilation. Submittal date: 03/19/2003.

165405 LB0306A8N3LIQR.001. Fault Infiltration Test from Alcoves to Niche3 (9/18/2002 - 10/16/2002). Submittal date: 06/19/2003.

164843 LB0307ECRBRHTB.001. Moisture Monitoring at Four Locations in the ECRB. Submittal date: 07/30/2003.

166090 LB0308A8N3SEEP.001. Niche 3 Seepage (10/16/2002-04/02/2003). Submittal date: 08/29/2003.

105793 LB960800831224.001. Relative Humidity, Temperature, and Pressure in ESF Monitoring Stations. Submittal date: 08/23/1996.

105794 LB970300831224.001. Moisture Data Report from October, 1996 to January, 1997. Submittal date: 03/13/1997.

105796 LB970801233124.001. Moisture Monitoring Data Collected at ESF Sensor Stations. Submittal date: 08/27/1997.

105798 LB970901233124.002. Moisture Monitoring Data Collected at Stationary Moisture Stations. Submittal date: 09/30/1997.

105800 LB980001233124.001. Water Potential Measurements in Niches 3566, 3650, and 3107 of the ESF. Submittal date: 04/23/1998.

136583 LB980001233124.004. Liquid Release Test Data from Niche 3566 and Niche 3650 of the ESF in Milestone Report, "Drift Seepage Test and Niche Moisture Study: Phase 1 Report on Flux Threshold Determination, Air Permeability Distribution, and Water Potential Measurement. Submittal date: 11/23/1999.

105592 LB980901233124.003. Liquid Release and Tracer Tests in Niches 3566, 3650, 3107, and 4788 in the ESF. Submittal date: 09/14/1998.

105855 LB980901233124.004. Pneumatic Pressure and Air Permeability Data from Alcove 6 in the ESF. Submittal date: 09/14/1998.

105856 LB980901233124.009. Pneumatic Pressure and Air Permeability Data from Alcove 4 in the ESF. Submittal date: 09/14/1998.

105858 LB980901233124.014. Borehole Monitoring at the Single Borehole in the ECRB and ECRB Crossover Point in the ESF. Submittal date: 09/14/1998.

136593 LB980901233124.101. Pneumatic Pressure and Air Permeability Data from Niche 3107 and Niche 4788 in the ESF from Chapter 2 of Report SP33PBM4: Fracture Flow and Seepage Testing in the ESF, FY98. Submittal date: 11/23/1999.

110828 LB980912332245.001. Air Injection Data from Niche 3107 of the ESF. Submittal date: 09/30/1998.

105593 LB980912332245.002. Gas Tracer Data from Niche 3107 of the ESF. Submittal date: 09/30/1998.

105888 LB990601233124.001. Seepage Data Feed to UZ Drift-Scale Flow Model for TSPA-SR. Submittal date: 06/18/1999.

106051 LB990601233124.003. Seepage Data Feed to UZ Drift-Scale Flow Model for TSPA-SR. Submittal date: 06/18/1999.

155694 LB990901233124.001. Alcove 6 Tracer Tests for AMR U0015, "In Situ Field Testing of Processes.". Submittal date: 11/01/1999.

146883 LB990901233124.002. Alcove 6 Flow Data for AMR U0015, "In Situ Field Testing of Processes". Submittal date: 11/01/1999.

155690 LB990901233124.003. Tracer Lab Analyses of Dye Penetration in Niches 3650 and 4788 of the ESF for AMR U0015, "In Situ Field Testing of Processes.". Submittal date: 11/01/1999.

123273 LB990901233124.004. Air Permeability Cross-Hole Connectivity in Alcove 6, Alcove 4, and Niche 4 of the ESF for AMR U0015, "In Situ Testing of Field Processes". Submittal date: 11/01/1999.

146884 LB990901233124.005. Alcove 4 Flow Data for AMR U0015, "In Situ Field Testing of Processes". Submittal date: 11/01/1999.

135137 LB990901233124.006. Moisture Data from the ECRB Cross Drift for AMR U0015, "In Situ Testing of Field Processes". Submittal date: 11/01/1999.

162949 LL030408023121.027. Cl Abundance and Cl Ratios of Leachates from ESF Core Samples. Submittal date: 04/17/2003.

163827 LL030605223121.030. Cl Abundance and Cl Ratios of Leachates from ESF Core Samples. Submittal date: 06/13/2003.

147168 LL990612704244.098. ERT Data for Busted Butte. Submittal date: 06/21/1999.

150300 MO0004GSC00167.000. As-Built Coordinate of Boreholes in the Test Alcove and Running Drift, Busted Butte Test Facility (BBTF). Submittal date: 04/20/2000.

151029 MO0006J13WTRCM.000. Recommended Mean Values of Major Constituents in J-13 Well Water. Submittal date: 06/07/2000.

166198 MO0008GSC00269.000. As-Built ECRB Alcove 8, Construction Observation Alcove (COA) - Boreholes (#1 through 7). Submittal date: 08/01/2000.

153777 MO0012MWDGFM02.002. Geologic Framework Model (GFM2000). Submittal date: 12/18/2000.

155369 MO0107GSC01061.000. As-Built Profile of Bat-Wing Excavation, Niche #5 ECRB. Submittal date: 07/03/2001.

156941 MO0107GSC01069.000. ESF Niche #4 (Niche 4788) Borehole As-Built Information. Submittal date: 07/19/2001.

160407 MO0209GSC02116.000. Enhanced Characterization of the Repository Block (ECRB) Niche 5 (Niche 1620), Borehole As-Built Information. Submittal date: 09/23/2002.

164527 MO0307SEPFEPS4.000. LA FEP List. Submittal date: 07/31/2003.

103769 MO9901MWDGFM31.000. Geologic Framework Model. Submittal date: 01/06/1999.

8.4 OUTPUT DATA, LISTED BY DATA TRACKING NUMBER

LB0110LIQR0015.001. Developed Data for Liquid Release/Seepage Tests and Systematic Testing. Submittal date: 11/12/2001.

LB0110NICH4LIQ.001. Niche 4788 Ceiling - Wetting Front Data. Submittal date: 11/12/2001.

LB0110SYST0015.001. Developed Data for Systematic Testing. Submittal date: 12/06/2001.

LB0310AIRK0015.001. Developed data for Air-K Tests. Submittal date: 10/07/2003.

ATTACHMENT I

AUTOMATED AIR-INJECTION SYSTEM

Attachment I is referred to in Section 6.1.2 and Section 6.1.2.1 on air-permeability determination. Attachment Section I.4 on automation is referred to in Section 6.1.2.1 and Section 6.1.2.2.1 on permeability profile measurements. Attachment I is also referred to in Section 6.5 on crosshole air-injection tests.

INTENTIONALLY LEFT BLANK

ATTACHMENT I—AUTOMATED AIR-INJECTION SYSTEM

The pneumatic-testing equipment is a specially designed packer system fabricated to take specific testing needs into account. Many boreholes at several sites need to be tested in a controlled fashion to allow site-to-site and borehole-to-borehole comparisons to be meaningful. For determination of connectivity between boreholes, all permutations of injection and response zones at a site need to be examined, so the boreholes must be instrumented for simultaneous measurements. In heterogeneous rock, such as that at the ESF, it is difficult to compensate for variations in results caused by different test configurations, such as test interval length or test scale. It is therefore important to keep the testing as consistent as possible by varying only one parameter when performing the tests, namely the location of the test zones. These needs were accommodated not only in the design and operation of the packer system, but also in planning the borehole patterns and drilling. To ensure that the air permeability of unaltered rock would be measured, boreholes were drilled dry and at low speed, a process that minimizes damage to the formation and thereby allows the packer systems to be placed along the entire length of each borehole.

I.1 AUTOMATIC PNEUMATIC INJECTION PACKERS

In light of the need for consistency, the same packer design is used for injection and observation. This approach is amenable to the automation and remote control necessary for establishing consistent testing regimens and accommodating the large number of tests. Inflatable rubber sealing bladders on a packer string can be manipulated independently and divide a borehole into 14 different possible zones over the length of the string. Zone resolution is 0.3, and the bladders cover the entire length of the string. This configuration allows 4.8 meters of borehole to be covered by one string. One 3.2 mm diameter port for pressure measurement and one 6.4 mm diameter port for air-injection service each zone. Up to seven boreholes can be instrumented at one time. The packer inflation and air-injection lines can all be controlled automatically. A modular design allows partial dismantling of the packer strings in the field for repair or work in tight quarters. Figure I-1 shows a diagram of part of a packer assembly.

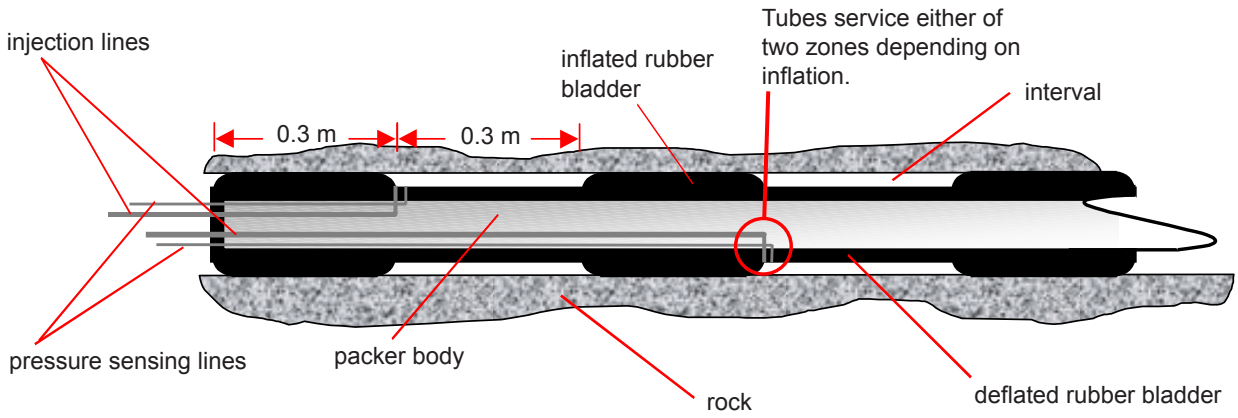

Figure I-1. Schematic Sketch of Automatic Packer Design

If the bladders are all inflated at once, then the packer string would seal the entire section of borehole occupied by the string. However, by inflating every other bladder and allowing the remainder to remain deflated, an alternating sequence of open and closed (sealed) intervals is produced. Depending on the injection control valves, an open interval becomes either an observation zone used to monitor pressure, or an injection zone where air is introduced under pressure during a test. Once tests have been performed with these open zones, the inflated bladders are deflated and deflated bladders are inflated, causing those zones that were once closed to become open and those that were originally open to become closed. In this manner, close to the entire length of the packer string is usable for testing every 0.3 without having to move the string. By changing the zones on the injection packer independently from those on the observation packers, there are four possible zone configurations available during a given packer installation. All permutations of these injection and observation positions are used to ensure that all positions within each observation borehole are allowed a chance to respond to a given injection zone. Figure I-2 shows schematically how this process is implemented. The observation packer zones are usually changed in unison because the locations of the observation zones are thought not to perturb the flow field significantly. Permutations between them would cause only second-order effects in the response system.

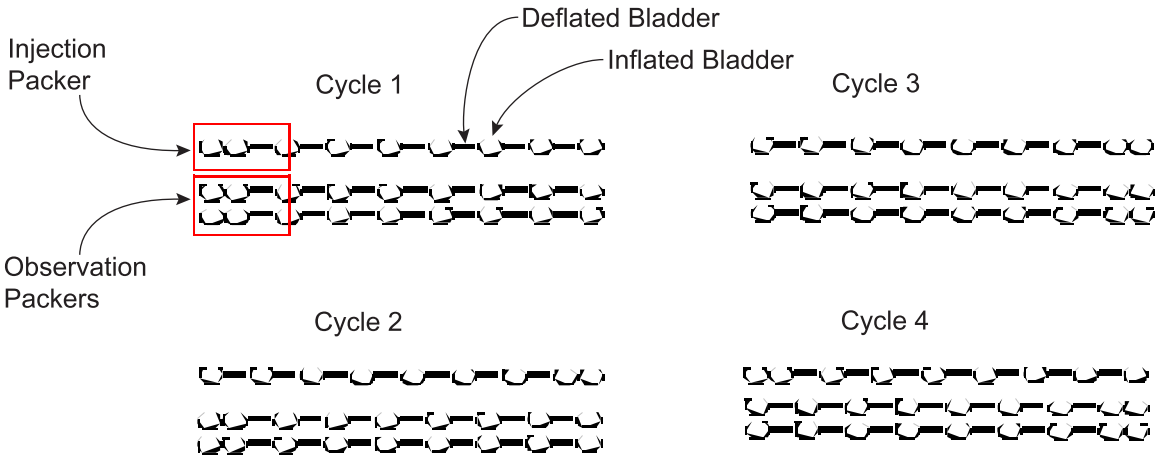

Figure I-2. Schematic Illustration of the Permutation Scheme for Automatic Packers

I.2 AIR-INJECTION FLOW INSTRUMENTATION

Pressure monitoring for each zone was accomplished using pressure transducers accurate to a resolution of 0.3 kilopascals (kPa). Mass-flow controllers (MFCs) with voltage control and output were used to inject a constant mass-flow rate of air during each permeability test. Four sizes of these controllers, from 1 to 500 standard liters per minute (SLPM), were employed to span the anticipated flow-rate ranges. The pressure transducer and MFC outputs were continually monitored and digitally recorded throughout testing, using a 27-bit voltmeter and an accompanying computer. Time resolution for the data from all sources was set nominally at five seconds.

I.3 INITIAL SETUP IN TESTING REGIMEN

Initially, by performing some manually operated tests for a given site, the operator determined under what conditions steady state was reached and at what injection pressure packer leak-by could occur. (Leak-by is the condition of injected air forcing its way past the packer and breaking its seal with the rock.) The information from these initial tests was used to plan the automatic controls. The operator determined packer leak-by pressure by observing the pressure response in the observation zones axially adjacent to the injection zone. When leak-by occurs, a distinct and sudden pressure response occurs in the guard zone as the packer seal with the borehole is broken. The packer inflation pressure was set at roughly 240 kPa above the ambient pressure to ensure adequate contact with the borehole without risk of damage to the rubber bladders. The leak-by pressure at this inflation was usually about 138 kPa above the ambient pressure, depending on rock conditions, and the limit for any injection pressure was typically set to 80 kPa above the ambient pressure.

I.4 AUTOMATION AND MULTI-RATE APPROACH

Utilization of the automatic controls ensured that the tests would reach steady state yet allow them to be completed in minimal time. In addition, automation enabled testing to be run 24 hours a day (referred to in Section 6.1.2.2.1). The automation scheme allotted a minimum time to every individual injection test. This time period allowed enough data points to be collected to determine the slope of the injection pressure response. Steady state was defined in the automation routine as that condition when the slope of pressure change over time is less than a certain set point for the recent readings. If, after the minimum time, the criterion of steady state had not been met, the test was allowed to continue until it had been met. Pauses between tests left time to monitor recovery pressure. Any excess pressure was bled off from all zones for sufficient time to allow residual pressure in the formation to reach ambient conditions at the site before further testing. Confirmation of this bleed-off was seen in all cases.

The automation routine allowed multiple flow rates at each test interval and also ensured that injection pressure did not exceed the packer leak-by pressure. The test would be shut off if the injection pressure came within about 60% of the packer leak-by pressure, and the data would automatically be annotated to note that steady state had not been attained. To save time, injections at higher rates would not be attempted in a zone with this situation. Conversely, if pressure in an injection zone did not rise above a certain threshold value after a short time, then the test at this rate was cut short and a higher flow rate test attempted. The multirate strategy ensured that, by utilizing higher flow rates, highly permeable injection intervals would more likely have sufficient pressure to generate a measurable response in the observation intervals. It also ensured that, by using low flow rates, the very tight intervals could be measured without possible interference of packer leak-by. Theoretically, the same permeability value should result for a given interval location, regardless of the flow rate used. Small differences in permeability may result at different flow rates and between repeat tests, possibly caused by movement of residual water within the fractures. In the case of water redistribution, permeability will be seen to go up slightly for higher rates as testing progresses, with injection pressures overcoming the capillary forces holding the water in the formation. A small decrease of apparent permeability with increasing flow rate can be seen in areas that are drier, on account of turbulence at higher

air injection rate. Any large discrepancy between permeabilities at different flow rates and in repeat tests for a given zone can be attributed to compromised packer sealing. The maximum flow rate that did not cause the zone pressure to exceed the packer leak-by pressure during a test was chosen for single-hole permeability calculation and for crosshole response detection.

ATTACHMENT II

COMPUTATION TABLES FOR NICHE STUDIES

Table II-1 on aspect ratio is referred to in Section 6.2.1.2 on flow paths observed during niche excavation. Table II-2 on distance from borehole to niche ceiling is referred to in Section 6.2.1.3 on seepage tests. Table II-3a through Table II-4e on liquid-release fluxes are referred to in Section 6.2.2.1 on seepage threshold determinations. Table II-5 on alpha values is the computation summarized in Table 6.2.2-2. Table II-4 and Table II-6 are referred to in Figure 6.2.2-2 on seepage threshold. Table II-7 and Table II-8 are referred to in Figure 6.2.2-3 and Figure 6.2.2-4 on water retention curves.

INTENTIONALLY LEFT BLANK

ATTACHMENT II—COMPUTATION TABLES FOR NICHE STUDIES

Table II-1. Computation of Aspect Ratio (depth to lateral distance)

Observed Dye Observed	Injection Borehole	Injection Interval (m)	Mass Injected (g)	Input Maximum Lateral Distance (m)	Input Maximum Penetration Depth (m)	Output Ratio of Depth to Lateral Dist.
Niche 3566 (Niche 1 in Tptpmn)						
FD&C Red No. 40	M	2.13 - 2.44	941.7	0.73	1.52	2.08
Acid Yellow 7	M	2.77 - 3.05	120.3	0.16	0.3	1.90
FD&C Blue No. 1	M	4.57 - 4.88	474	0.30	1.3	4.33
Niche 3650 (Niche 2 in Tptpmn)						
FD&C Red No. 40	UL	7.01 - 7.31	694.5	0.99	1.42	1.43
FD&C Blue No. 1	UM	4.27 - 4.57	675.8	0.58	1.68	2.90
FD&C Red No. 40	UM	4.88 - 5.18	937.4	0.28	0.86	3.07
FD&C Blue No. 1	UM	6.70 - 7.01	438.7	1.05	1.82	1.74
FD&C Red No. 40	UR	1.52 - 1.82	369.9	0.76	1.41	1.86
FD&C Blue No. 1	UR	2.13 - 2.43	999.8	0.32	2.57	8.03
Sulfo Rhodamine B	ML	4.88 - 5.18	151.6	0.08	0.02	0.25
Sulfo Rhodamine B	ML	6.7 - 7.01	170.9	0.25	1.02	4.06
Niche 3107 (Niche 3 in Tptpmn)						
Green	B1.5	3.35-3.66	391.3	0.54	0.87	1.61
FD&C Blue No. 1	UM	4.88-5.18	111.7	0.27	1.19	4.41
Niche 4788 (Niche 4 in Tptpmn)						
FD&C Red No. 40	UM	4.27-4.57	151.1	0.31	0.955	3.08
Green	UM	4.88-5.18	401.8	0.51	1.79	3.50
FD&C Blue No. 1	UM	6.40-6.70	1019.7	0.78	1.25	1.61
						Ave. Tptpmn = 2.87
Niche CD1620 (Niche 5 in Tptpll)						
Green	#1	1.48-1.78	1184.7	0.76	1.25	1.64
Rhodamine	#1	2.54-2.84	1342.8	0.22	1.37	6.23
Green	#1	3.31-3.61	804.7	0.21	0.28	1.33
Rhodamine	#1	4.54-4.84	826.9	0.15	0.19	1.27
FD&C Blue No. 1	#1	5.44-5.74	1001.8	0.33	0.18	0.55
Rhodamine	#1	6.54-6.84	1041.3	0.16	0.07	0.44
FD&C Blue No. 1	#1	7.58-7.88	1555.9	0.17	0.18	1.06
Rhodamine	#1	8.54-8.84	1142.2	0.26	0.15	0.58
						Ave. Tptpll = 1.64
A	**B**	**C**	**D**	**E**	**F**	**G**

A through E from DTN: LB980001233124.004 [136583] for Niche 3566 (Niche 1) and Niche 3650 (Niche 2).
A through E from DTN: LB980901233124.003 [105592] for Niche 3107 (Niche 3) and Niche 4788 (Niche 4).
A through E from DTN: LB0102NICH5LIQ.001 [155681] for Niche 3107 (Niche 3) and Niche 4788 (Niche 4).
D for Niche CD1620 (Niche 5) are reported in kg and converted to g in table by multiplying by 1000 g/kg
G = F/E
Ave. Tptpmn and Ave. Tptpll computed using Excel 2000 arithmetic average (AVERAGE) function.

Table II-2. Computation of Distance from Borehole to Niche Ceiling at Niche 4788 (Niche 4), a Niche Study

Niche	Borehole & Depth (m)	Input Vertical distance from horizontal scanline to borehole UM (m)	Input Elevation of borehole UM at collar (m)	Input Elevation of borehole collar (m)	Output Difference in elevation between borehole and UM (m)	Output Elevation of borehole collar above horizontal scanline (m)	Input Borehole Inclination minutes	Input Borehole Inclination seconds	Output Borehole inclination (radians)	Output Sine(J)	Output Cosine(J)	Input Local horizontal coordinate for borehole collar (m)
4788	UL 7.62-7.93	1.505	1096.57	1096.58	0.01	1.515	-41	-13	-0.0120	-0.0120	0.9999	4.17
	UM 6.10-6.40	1.505	1096.57	1096.57	0.00	1.505	-41	-23	-0.0120	-0.0120	0.9999	4.87
	UR 5.18-5.48	1.505	1096.57	1096.57	0.00	1.505	-10	-26	-0.0030	-0.0030	1.0000	5.82
A	**B**	**C**	**D**	**E**	**F**	**G**	**H**	**I**	**J**	**K**	**L**	**M**

C a horizontal scanline or datum measured along the center line of the niche was used to relate known survey stations to the boreholes and a local coordinate system setup inside the niche. Nodes spaced 0.6 X 0.6 m apart were marked on the niche ceiling using the frame holding the seepage capture trays as the basis for the grid–see Scientific Notebook by Trautz (2001 [156903], p. 36) for details.

D, E from survey data DTN: MO0107GSC01069.000 [156941]

F=E-D

G=C+F

H, I from survey data DTN: MO0107GSC01069.000 [156941]

K=sin(J)

L=cos(J)

M from survey data DTN: MO0107GSC01069.000 [156941], local coordinate system see note for T & U.

Table II-2. Computation of Distance from Borehole to Niche Ceiling at Niche 4788 (Niche 4), a Niche Study (Continued)

Niche	Input Distance along inclined borehole from collar to start of test interval (m)	Input Distance along inclined borehole from collar to end of test interval (m)	Output Distance along inclined borehole from collar to center of test interval (m)	Output Vertical distance from borehole collar to the center of test interval (m)	Output Vertical distance from horizontal scanline to center of test interval (m)	Output Local horizontal coordinate for center of test interval (m)	Input Local horizontal coordinate for start of capture node (m)	Input Local horizontal coordinate for end of capture node (m)	Input Vertical distance from horizontal scanline to ceiling above start node (m)	Input Vertical distance from horizontal scanline to ceiling above end node (m)	Output Interpolated vertical distance from horizontal scanline to the ceiling beneath the center of the test interval (m)	Output Distance from borehole bottom to Ceiling (m)
4788	7.62	7.93	7.775	-0.09	1.42	11.944	11.905	11.905	0.81	0.84	0.820	0.60
	6.10	6.40	6.25	-0.08	1.43	11.12	10.955	11.26	0.84	0.855	0.848	0.58
	5.18	5.48	5.33	-0.02	1.49	11.15	10.615	11.905	0.76	0.73	0.748	0.74
	N	**O**	**P**	**Q**	**R**	**S**	**T**	**U**	**V**	**W**	**X**	**Y**

N and O from DTN: LB0010NICH4LIQ.001 [153145]

P = N+(O-N)/2

Q=K*P

R=G+Q

S=M+(P*L)

T, U represent local coordinates. They are horizontal distances from the ESF centerline taken parallel to the niche axis to the starting node and ending node of the capture system, respectively, that bracket the center of the overlying test interval, S. Note that the center of the interval lies between two nodes at the same horizontal coordinate, 11.905 m, for UL 7.62-7.93. Values from Scientific Notebook by Trautz (2001 [156903], p. 36).

V,W are the vertical distances from the horizontal scanline plane to the ceiling of the niche at the start and end node at the horizontal coordinate T and U, respectively. Values from Scientific Notebook by Trautz (2001 [156903], pp. 36, 38, 40, 41).

X is the interpolated distance to ceiling determined using V and W. X = V+(W-V)*(S-T)/(U-T) except for UL 7.62-7.93 where X = V+(W-V)*(0.3-0.2)/0.3 and 0.3 is the distance between nodes (2,12) and (3,12).

Y = R-X

Table II-3a. Computation of Liquid Release Flux for Post-Excavation Seepage Tests at Niche 3107 (Niche 3), Niche Studies

Borehole	Depth (m)	Test Name	Input Liquid-Release Rate Qs (kg/s)	Input Seepage Percentage y' (%)	Computed Cross-Sectional area A (m^2)	Output Liquid-Release Flux qs (m/s)	Output Liquid-Release flux qs (mm/yr)
UM	4.88-5.18	Test #1 3/4/99	1.4266E-05	0	0.053	2.67E-07	8420
		Test #1 4/7/99	9.7304E-05	--	0.053	1.82E-06	57430
		Test #1 4-27-99	3.9897E-05	5.465	0.053	7.47E-07	23548
		Test #1 4-30-99	1.4113E-05	0	0.053	2.64E-07	8330
		Test #1 5/6/99	9.0739E-05	47.271	0.053	1.70E-06	53555
		Test #1 9-21-99	8.39647E-05	42.975	0.053	1.57E-06	49557
		Test #1 9-23-99	8.7576E-05	46.08	0.053	1.64E-06	51689
		Test #1 9-27-99	9.0044E-05	59.5915	0.053	1.69E-06	53145
		Test #1 10-11-99	9.03981E-05	70.0857	0.053	1.69E-06	53354
A	**B**	**C**	**D**	**E**	**F**	**G**	**H**

UM = upper middle

A through E from DTN LB0010NICH3LIQ.001 [153144]

F through H computed in Excel 2000 spreadsheet using formulae below:

F = wetted area of borehole up to return port of packers = [2π-(2Arccosine(d/r))] hr where d = nominal vertical distance from center of borehole to return port on packer system = 2.54 cm r = nominal radius of borehole = 3.81 cm = 0.0381 m h = nominal test interval length = 1 ft = 0.3048 m

G = D*(1000 g/kg)/(1,000,000 g/m^3 *F) = D/(1000*F), where density of water is assumed = 1,000,000 g/m^3

H = G *(1000 mm/m)*(86400 s/day)*(365 days/year)

Table II-3b. Computation of Liquid Release Flux for Post-Excavation Seepage Tests at Niche 4788 (Niche 4), Niche Studies

Borehole	Depth (m)	Test Name	Input Liquid-release rate Q_s (kg/s)	Input Seepage percentage y' (%)	Computed Cross-sectional area A (m^2)	Output Liquid-release flux q_s (m/s)	Output Liquid-release flux q_s (mm/yr)
UL	7.62-7.93	Test #1 11/3/99	8.8095E-05	24.159	0.053	1.65E-06	51995
		Test #1 11-30-99 Niche 4788	4.9246E-05	17.964	0.053	9.22E-07	29066
		Test #1 01-24-00	7.81146E-06	0.000	0.053	1.46E-07	4610
		Test #1 6-26-2000	1.91662E-05	14.4488	0.053	3.59E-07	11312
UM	6.10-6.40	Test #1 Niche 4788 11/16/99	9.16384E-05	35.383	0.053	1.72E-06	54086
		Test #1 Niche 4788 12-10-99	3.91451E-05	23.405	0.053	7.33E-07	23104
		Test #1 02-09-2000	8.819E-06	0	0.053	1.65E-07	5205
		Test #1 3-10-2000	9.681E-06	0	0.053	1.81E-07	5714
		Test #1 3-14-2000	8.8479E-06	0	0.053	1.66E-07	5222
		Test #1 06-08-2000	2.0489E-05	8.5381	0.053	3.83E-07	12093
UR	5.18-5.48	Test #1 Niche 4788 12/7/99	9.00855E-05	68.6623	0.053	1.69E-06	53170
		Test #1 1/5/2000	3.79689E-05	56.4895	0.053	7.11E-07	22410
		Test #1 02-14-2000	8.80016E-06	11.092	0.053	1.65E-07	5194
A	**B**	**C**	**D**	**E**	**F**	**G**	**H**

UL = upper left

UM = upper middle

UR = upper right

A through E from DTN LB0010NICH4LIQ.001 [153145]

F through H computed in Excel 2000 spreadsheet using formulae below:

F = wetted area of borehole up to return port of packers = $[2\pi-(2\text{Arccosine}(d/r))]hr$ where:

d = nominal vertical distance from center of borehole to return port on packer system = 2.54 cm

r = nominal radius of borehole = 3.81 cm = 0.0381 m

h = nominal test interval length = 1 ft = 0.3048 m

G = D*(1000 g/kg)/(1,000,000 g/m^3 *F) = D/(1000*F), where density of water is assumed = 1,000,000 g/m^3

H = G *(1000 mm/m)*(86400 s/day)*(365 days/year)

Table II-4. Summary of Regression Equations and Computation of Seepage Threshold Fluxes (K o*) and Saturated Hydraulic Conductivities (K l), a Niche Study

Niche	Borehole & Depth (m)	Output Linear Regression Equation	Input Data Points	Output Correlation Coefficient (R2)	Input Slope	Input intercept	Output/Input Seepage Threshold Flux K_o* (m/s)	Output Seepage Threshold Flux K_o* (mm/yr)	Input Air Permeability k (m2)	Output Saturated Hydraulic Conductivity Kl (m/s)
3107	UM 4.88-5.18	y = 30.440Ln(K_o) + 456.085	8	0.820	30.440	456.085	3.11E-07	9.81E+03	NA	NA
3650	UL 7.01-7.32	y = 0.6833Ln(K_o) + 8.5742	2	NR	--	--	3.55E-06	1.12E+05	--	8.98E-05
	UL 7.62-7.92	y = 5.7394Ln(K_o) + 92.627	3	0.979	--	--	9.80E-08	3.09E+03	--	1.51E-04
	UM 4.27-4.57	y = 5.2757Ln(K_o) + 79.443	4	0.921	--	--	2.89E-07	9.11E+03	--	2.62E-05
	UM 4.88-5.18	y = 2.304Ln(K_o) + 31.767	3	0.975	--	--	1.03E-06	3.25E+04	--	2.52E-03
	UM 5.49-5.79	y = 5.8876Ln(K_o) + 87.528	4	0.963	--	--	3.50E-07	1.10E+04	--	2.16E-05
	UR 4.27-4.57	y = 0.314Ln(K_o) + 4.3283	2	NR	--	--	1.03E-06	3.25E+04	--	4.08E-05
	UR 4.88-5.18	y = 0.3165Ln(K_o) + 4.3751	2	NR	--	--	9.92E-07	3.13E+04	--	9.87E-05
	UR 5.49-5.79	y = 28.419Ln(K_o) + 351.09	2	NR	--	--	4.31E-06	1.36E+05	--	1.71E-05
	UR 6.10-6.40	y = 4.2169Ln(K_o) + 79.596	2	NR	--	--	6.35E-09	2.00E+02	--	3.01E-05
	UR 6.71-7.01	y = 10.574Ln(K_o) + 165.28	3	0.974	--	--	1.63E-07	5.14E+03	--	2.28E-04
4788	UL 7.62-7.93	y = 9.273Ln(K_o) + 148.119	4	0.929	9.273	148.119	1.16E-07	3.65E+03	2.51E-12	2.46E-05
	UM 6.10-6.40	y = 15.697Ln(K_o) + 243.611	4	0.980	15.697	243.611	1.82E-07	5.74E+03	2.50E-11	2.45E-04
	UR 5.18-5.48	y = 25.415Ln(K_o) + 410.285	3	0.970	25.415	410.285	9.75E-08	3.07E+03	4.00E-13	3.92E-06
A	B	C	D	E	F	G	H	I	J	K

NA = not available, the test could not be completed as planned because of rock properties outside the equipment's measurable range.

NR = not reported because two data points result in perfect correlation (R^2 =1.0), therefore, correlation coefficient is meaningless Intermediate computations not performed for Niche 3650 (Niche 2) because they were performed in earlier technical products using the same formulae / methods shown below. Output shown in Table for Niche 3650 (Niche 2) was obtained directly from TDMS except where noted.

C for Niche 3650 (Niche 2) from DTN LB980001233124.004 [136583]

C for Niche 3107 (Niche 3) and Niche 4788 (Niche 4) computed below using Excel 2000 built-in Regression Analysis Tool pack (see Tables II-4b - II-4e). y = predicted seepage percentage (%). Derived from measured seepage percentages (y') in Table II-4a (E). K_o = net downward liquid-release flux (m/s) from regression model. Derived from computed liquid-release fluxes (ln[q_s]) in Table II-4a (G).

D = number of data points used in linear regression

E for Niche 3650 (Niche 2) from DTN: LB980001233124.004 [136583]

E for Niche 3107 (Niche 3) and Niche 4788 (Niche 4) = correlation coefficient from Excel 2000 built-in Regression Analysis Tool pack (see Tables II-4b - II 4e). F = slope of regression line C

G = intercept of regression line C

H for Niche 3650 (Niche 2) from DTN: LB980901233124.003 [105592]

H for Niche 3107 (Niche 3) and Niche 4788 (Niche 4) are computed by setting y=0 in C and solving $K_o(0) = K_o^* = \exp(-G/F)$

I = 1000 mm/m * 86400 s/day * 365 days/year for all the niches

J for Niche 3107 (Niche 3) and Niche 4788 (Niche 4) from DTN: LB990601233124.001 [105888]

K = J * (100*100 cm^2/m^2) * 980 m/s/cm^2; the conversion factor 980 is from Freeze and Cherry 1979 [101173].

K for Niche 3650 (Niche 2) from DTN LB980901233124.003 [105592]

Table II-4a. Data Used in Linear Regression Analysis (y' vs. ln q_s)

Niche	Borehole	Depth (m)	Test name	Input Seepage Percentages y' (%)	Input Liquid-Release Flux q_s (m/s)	Output Natural Log of Liquid Release Flux ln(q_s)
3107	UM	4.88-5.18	Test #1 3/4/99	0.0	2.67E-07	-15.136
			Test #1 4-27-99	5.5	7.47E-07	-14.108
			Test #1 4-30-99	0.0	2.64E-07	-15.147
			Test #1 5/6/99	47.3	1.70E-06	-13.286
			Test #1 9-21-99	43.0	1.57E-06	-13.364
			Test #1 9-23-99	46.1	1.64E-06	-13.321
			Test #1 9-27-99	59.6	1.69E-06	-13.294
			Test #1 10-11-99	70.1	1.69E-06	-13.290
4788	UL	7.62-7.93	Test #1 11/3/99	24.2	1.65E-06	-13.315
			Test #1 11-30-99 Niche 4788	18.0	9.22E-07	-13.897
			Test #1 01-24-00	0.0	1.46E-07	-15.738
			Test #1 6-26-2000	14.4	3.59E-07	-14.841
	UM	6.10-6.40	Test #1 Niche 4788 11/16/99	35.4	1.72E-06	-13.276
			Test #1 Niche 4788 12-10-99	23.4	7.33E-07	-14.127
			Test #1 3-14-2000	0.0	1.66E-07	-15.614
			Test #1 06-08-2000	8.5	3.83E-07	-14.774
	UR	5.18-5.48	Test #1 Niche 4788 12/7/99	68.7	1.69E-06	-13.293
			Test #1 1/5/2000	56.5	7.11E-07	-14.157
			Test #1 02-14-2000	11.1	1.65E-07	-15.619
A	**B**	**C**	**D**	**E**	**F**	**G**

A through F from Table II-3a and Table II-3b

G = ln(F)

Table II-4b. Linear Regression Summary (Output) for Niche 3107 (Niche 3) UM 4.88-5.18

ANOVA								
	df	***SS***	***MS***	***F***	***Significance F***			
Regression	1	4500.737	4500.737	27.411	0.002			
Residual	6	985.173	164.195					
Total	7	5485.910						
	Coefficients	***Standard Error***	***t Stat***	***P-value***	***Lower 95%***	***Upper 95%***	***Lower 95.0%***	***Upper 95.0%***
Intercept	456.085	80.759	5.647	0.001	258.474	653.695	258.474	653.695
X Variable 1	30.440	5.814	5.236	0.002	16.214	44.667	16.214	44.667

All output shown in this table was obtained using Microsoft Excel 2000 built-in regression analysis tool package.

Intercept = y-intercept of linear regression equation

X Variable 1 = slope of linear regression equation

Data used in regression analysis are from Table II-4a.

Regression Statistics: Multiple R = 0.906; R Square = 0.820; Adjusted R Square = 0.790; Standard Error = 12.814; Number of Observations = 8.

Table II-4c. Linear Regression Summary (Output) for Niche 4788 (Niche 4) UL 7.62-7.93

ANOVA								
	df	***SS***	***MS***	***F***	***Significance F***			
Regression	1	292.815	292.815	26.353	0.036			
Residual	2	22.223	11.111					
Total	3	315.038						
	Coefficients	***Standard Error***	***t Stat***	***P-value***	***Lower 95%***	***Upper 95%***	***Lower 95.0%***	***Upper 95.0%***
Intercept	148.119	26.152	5.664	0.030	35.597	260.640	35.597	260.640
X Variable 1	9.273	1.806	5.133	0.036	1.501	17.045	1.501	17.045

All output shown in this table was obtained using Microsoft Excel 2000 built-in regression analysis tool package.

Intercept = y-intercept of linear regression equation

X Variable 1 = slope of linear regression equation

Data used in regression analysis are from Table II-4a.

Regression Statistics: Multiple R = 0.964; R Square = 0.929; Adjusted R Square = 0.894; and number of Observations = 4.

Table II-4d. Linear Regression Summary (Output) for Niche 4788 (Niche 4) UM 6.10-6.40

ANOVA								
	df	***SS***	***MS***	***F***	***Significance F***			
Regression	1	724.849	724.849	99.295	0.010			
Residual	2	14.600	7.300					
Total	3	739.449						
	Coefficients	***Standard Error***	***t Stat***	***P-value***	***Lower 95%***	***Upper 95%***	***Lower 95.0%***	***Upper 95.0%***
Intercept	243.611	22.798	10.685	0.009	145.517	341.704	145.517	341.704
X Variable 1	15.697	1.575	9.965	0.010	8.919	22.474	8.919	22.474

All output shown in this table was obtained using Microsoft Excel 2000 built-in regression analysis tool package.

Intercept = y-intercept of linear regression equation

X Variable 1 = slope of linear regression equation

Data used in regression analysis are from Table II-4a.

Regression Statistics: Multiple R = 0.990; R Square = 0.980; Adjusted R Square = 0.970; Standard Error = 2.702; Number of Observations = 4

Table II-4e. Linear Regression Summary (Output) for Niche 4788 (Niche 4) UR 5.18-5.48

ANOVA								
	df	***SS***	***MS***	***F***	***Significance F***			
Regression	1	1785.798	1785.798	32.263	0.111			
Residual	1	55.352	55.352					
Total	2	1841.150						
	Coefficients	***Standard Error***	***t Stat***	***P-value***	***Lower 95%***	***Upper 95%***	***Lower 95.0%***	***Upper 95.0%***
Intercept	410.285	64.381	6.373	0.099	-407.747	1228.317	-407.747	1228.317
X Variable 1	25.415	4.474	5.680	0.111	-31.438	82.268	-31.438	82.268

All output shown in this table was obtained using Microsoft Excel 2000 built-in regression analysis tool pak.

Intercept = y-intercept of linear regression equation

X Variable 1 = slope of linear regression equation

Data used in regression analysis are from Table II-4a.

Regression Statistics: Multiple R = 0.985; R Square = 0.970; Adjusted R Square = 0.940; Standard Error = 7.440; Number of Observations = 3

Table II-5. Computation of α-Values, a Niche Study

Niche	Borehole & Depth (m)	Input Seepage Threshold Flux K_o^* (m/s)	Input Saturated Hydraulic conductivity K_l (m/s)	Intermediate Output K_o^* / K_l (dim.less)	Intermediate Output Inverse of Dimensionless Potentials $[\vartheta_{max}\,(s)]^{-1}$	Output Sorptive Number α (m^{-1})	Output Capillary Strength α^{-1} (m)	Output Error (%)
3650	UL 7.01-7.32	3.55E-06	8.98E-05	--	--	11.7	0.0855	--
	UL 7.62-7.92	9.80E-08	1.51E-04	--	--	771.9	0.0013	--
	UM 4.27-4.57	2.89E-07	2.62E-05	--	--	44.4	0.0225	--
	UM 4.88-5.18	1.03E-06	2.52E-03	--	--	1225.5	0.0008	--
	UM 5.49-5.79	3.50E-07	2.16E-05	--	--	29.9	0.0334	--
	UR 4.27-4.57	1.03E-06	4.08E-05	--	--	18.8	0.0532	--
	UR 4.88-5.18	9.92E-07	9.87E-05	--	--	48.8	0.0205	--
	UR 5.49-5.79	4.31E-06	1.71E-05	--	--	1.4	0.71	--
	UR 6.10-6.40	6.35E-09	3.01E-05	--	--	2373.7	0.0004	--
	UR 6.71-7.01	1.63E-07	2.28E-04	--	--	699.2	0.0014	--
4788	UL 7.62-7.93	1.16E-07	2.46E-05	4.70E-03	4.70E-03	105.4	0.0095	-3.66E-04
	UM 6.10-6.40	1.82E-07	2.45E-04	7.43E-04	7.43E-04	672.3	0.0015	-1.80E-04
	UR 5.18-5.48	9.75E-08	3.92E-06	2.49E-02	2.49E-02	19.1	0.0523	-9.41E-05
Theoretical limit						521.7	0.0019	
A	B	C	D	E	F	G	H	I

Intermediate computations not performed for Niche 3650 (Niche 2) because they were performed in other technical products using the same formulae shown below. Output shown in Table for Niche 3650 (Niche 2) was obtained directly from TDMS except where noted.

C from Table II-4 (H)

D from Table II-4 (K)

E = C/D

F = $1/(2*G+2-(1/G)) = [\vartheta_{max}\,(s)]^{-1}$, where ϑ_{max} is defined by Equation (84) and s is defined by Equation (14) in Philip et al. 1989 [105743]. In our case, $s = 0.5*\alpha*r = 0.5*\alpha*2 = \alpha$ since the nominal radius of the niche (r) is approximately 2 meters.

G = α, sorptive number, where α is selected such that absolute value of Error (i.e., column I) is < 1E-03 %

G for Niche 3650 (Niche 2) from DTN: LB980901233124.003 [105592]

G (Theoretical limit) = α = maximum sorptive number = $(2*\rho*g/\gamma)^{1/2}$, where ρ = density of water assumed equal to 1000 kg/m^3, g = acceleration of gravity 9.8 m/s^2, and γ = surface tension of water assumed equal to 0.072 kg/s^2

Equation G (theoretical limit) can be derived by substituting the maximum aperture (β_{max}) that can sustain a fluid meniscus because of capillary forces ($\beta_{max} = (2\gamma/\rho g)^{1/2}$) into the capillary height of rise equation $2\alpha^{-1} = 2\gamma/(\rho g \beta_{max})$.

Expression for β_{max} from Wang and Narasimhan 1993 [106793]. Expression for capillary height of rise equation from Philip 1989 [156974].

H = $1/G = \alpha^{-1}$, capillary strength of the porous medium computed for all niches

I = 100*(E-F)/E, Note that $K_o^* / K_l = [\vartheta_{max}\,(s)]^{-1}$ as noted in Section 3.4 of Philip et al. 1989 [105743].

Table II-6. Computed Values of Seepage Threshold Values

Output K_l (mm/yr)	Input K_l (m/s)	Input s (dim.less)	Input 2s (dim.less)	Output/Input ϑ_{max} (dim.less)	Output $[\vartheta_{max}]^{-1}$ (dim.less)	Output/Input K_o^* (m/s)	Output K_o^* (mm/yr)
3.154E+01	1.000E-09	521.7	1043.5	1045.50	9.56E-04	9.56E-13	3.02E-02
4.730E+01	1.500E-09			1045.50	9.56E-04	1.43E-12	4.52E-02
6.307E+01	2.000E-09			1045.50	9.56E-04	1.91E-12	6.03E-02
9.461E+01	3.000E-09			1045.50	9.56E-04	2.87E-12	9.05E-02
1.261E+02	4.000E-09			1045.50	9.56E-04	3.83E-12	1.21E-01
1.577E+02	5.000E-09			1045.50	9.56E-04	4.78E-12	1.51E-01
1.892E+02	6.000E-09			1045.50	9.56E-04	5.74E-12	1.81E-01
2.208E+02	7.000E-09			1045.50	9.56E-04	6.70E-12	2.11E-01
2.523E+02	8.000E-09			1045.50	9.56E-04	7.65E-12	2.41E-01
2.838E+02	9.000E-09			1045.50	9.56E-04	8.61E-12	2.71E-01
3.154E+02	1.000E-08			1045.50	9.56E-04	9.56E-12	3.02E-01
4.730E+02	1.500E-08			1045.50	9.56E-04	1.43E-11	4.52E-01
6.307E+02	2.000E-08			1045.50	9.56E-04	1.91E-11	6.03E-01
9.461E+02	3.000E-08			1045.50	9.56E-04	2.87E-11	9.05E-01
1.261E+03	4.000E-08			1045.50	9.56E-04	3.83E-11	1.21E+00
1.577E+03	5.000E-08			1045.50	9.56E-04	4.78E-11	1.51E+00
1.892E+03	6.000E-08			1045.50	9.56E-04	5.74E-11	1.81E+00
2.208E+03	7.000E-08			1045.50	9.56E-04	6.70E-11	2.11E+00
2.523E+03	8.000E-08			1045.50	9.56E-04	7.65E-11	2.41E+00
2.838E+03	9.000E-08			1045.50	9.56E-04	8.61E-11	2.71E+00
3.154E+03	1.000E-07			1045.50	9.56E-04	9.56E-11	3.02E+00
4.730E+03	1.500E-07			1045.50	9.56E-04	1.43E-10	4.52E+00
6.307E+03	2.000E-07			1045.50	9.56E-04	1.91E-10	6.03E+00
9.461E+03	3.000E-07			1045.50	9.56E-04	2.87E-10	9.05E+00
1.261E+04	4.000E-07			1045.50	9.56E-04	3.83E-10	1.21E+01
1.577E+04	5.000E-07			1045.50	9.56E-04	4.78E-10	1.51E+01
1.892E+04	6.000E-07			1045.50	9.56E-04	5.74E-10	1.81E+01
2.208E+04	7.000E-07			1045.50	9.56E-04	6.70E-10	2.11E+01
2.523E+04	8.000E-07			1045.50	9.56E-04	7.65E-10	2.41E+01
2.838E+04	9.000E-07			1045.50	9.56E-04	8.61E-10	2.71E+01
3.154E+04	1.000E-06			1045.50	9.56E-04	9.56E-10	3.02E+01
4.730E+04	1.500E-06			1045.50	9.56E-04	1.43E-09	4.52E+01
6.307E+04	2.000E-06			1045.50	9.56E-04	1.91E-09	6.03E+01
9.461E+04	3.000E-06			1045.50	9.56E-04	2.87E-09	9.05E+01
1.261E+05	4.000E-06			1045.50	9.56E-04	3.83E-09	1.21E+02
1.577E+05	5.000E-06			1045.50	9.56E-04	4.78E-09	1.51E+02
1.892E+05	6.000E-06			1045.50	9.56E-04	5.74E-09	1.81E+02
2.208E+05	7.000E-06			1045.50	9.56E-04	6.70E-09	2.11E+02
2.523E+05	8.000E-06			1045.50	9.56E-04	7.65E-09	2.41E+02
2.838E+05	9.000E-06			1045.50	9.56E-04	8.61E-09	2.71E+02

Table II-6. Computed Values of Seepage Threshold Values (Continued)

Output K_l (mm/yr)	Input K_l (m/s)	Input s (dim.less)	Input 2s (dim.less)	Output/Input ϑ_{max} (dim.less)	Output $[\vartheta_{max}]^{-1}$ (dim.less)	Output/Input K_o^* (m/s)	Output K_o^* (mm/yr)
3.154E+05	1.000E-05			1045.50	9.56E-04	9.56E-09	3.02E+02
4.730E+05	1.500E-05			1045.50	9.56E-04	1.43E-08	4.52E+02
6.307E+05	2.000E-05			1045.50	9.56E-04	1.91E-08	6.03E+02
9.461E+05	3.000E-05			1045.50	9.56E-04	2.87E-08	9.05E+02
1.261E+06	4.000E-05			1045.50	9.56E-04	3.83E-08	1.21E+03
1.577E+06	5.000E-05			1045.50	9.56E-04	4.78E-08	1.51E+03
1.892E+06	6.000E-05			1045.50	9.56E-04	5.74E-08	1.81E+03
2.208E+06	7.000E-05			1045.50	9.56E-04	6.70E-08	2.11E+03
2.523E+06	8.000E-05			1045.50	9.56E-04	7.65E-08	2.41E+03
2.838E+06	9.000E-05			1045.50	9.56E-04	8.61E-08	2.71E+03
3.154E+06	1.000E-04			1045.50	9.56E-04	9.56E-08	3.02E+03
4.730E+06	1.500E-04			1045.50	9.56E-04	1.43E-07	4.52E+03
6.307E+06	2.000E-04			1045.50	9.56E-04	1.91E-07	6.03E+03
9.461E+06	3.000E-04			1045.50	9.56E-04	2.87E-07	9.05E+03
1.261E+07	4.000E-04			1045.50	9.56E-04	3.83E-07	1.21E+04
1.577E+07	5.000E-04			1045.50	9.56E-04	4.78E-07	1.51E+04
1.892E+07	6.000E-04			1045.50	9.56E-04	5.74E-07	1.81E+04
2.208E+07	7.000E-04			1045.50	9.56E-04	6.70E-07	2.11E+04
2.523E+07	8.000E-04			1045.50	9.56E-04	7.65E-07	2.41E+04
2.838E+07	9.000E-04			1045.50	9.56E-04	8.61E-07	2.71E+04
3.154E+07	1.000E-03			1045.50	9.56E-04	9.56E-07	3.02E+04
4.730E+07	1.500E-03			1045.50	9.56E-04	1.43E-06	4.52E+04
6.307E+07	2.000E-03			1045.50	9.56E-04	1.91E-06	6.03E+04
9.461E+07	3.000E-03			1045.50	9.56E-04	2.87E-06	9.05E+04
1.261E+08	4.000E-03			1045.50	9.56E-04	3.83E-06	1.21E+05
1.577E+08	5.000E-03			1045.50	9.56E-04	4.78E-06	1.51E+05
1.892E+08	6.000E-03			1045.50	9.56E-04	5.74E-06	1.81E+05
2.208E+08	7.000E-03			1045.50	9.56E-04	6.70E-06	2.11E+05
2.523E+08	8.000E-03			1045.50	9.56E-04	7.65E-06	2.41E+05
2.838E+08	9.000E-03			1045.50	9.56E-04	8.61E-06	2.71E+05
3.154E+08	1.000E-02			1045.50	9.56E-04	9.56E-06	3.02E+05
A	**B**	**C**	**D**	**E**	**F**	**G**	**H**

Refer to Philip et al. (1989 [105743]) for an explanation of nomenclature.

A=B*1000 mm/m * 86400 s/day * 365 days/year; dim.less = dimensionless

B = saturated hydraulic conductivity whose values are arbitrary set in this column to span the range of values measured during air k tests performed at Niche 3650 (Niche 2) and Niche 4788 (Niche 4).

C = G (Theoretical limit) from bottom of Table II-5.

D = 2*C

E = 2s +2 -1/s

F = 1/E

G = B*F

H = G*1000 mm/m * 86400 s/day * 365 days/year.

Table II-7. Computation of Estimated Water Potentials, a Niche Study

Niche	Borehole Depth (m)	Test Name	Input Liquid-Release Flux q_s (m/s)	Input Saturated Hydraulic Conductivity K_l (m/s)	Input Alpha Value α (m^{-1})	Output Absolute Value of the Water Potential $x\psi x$ (m)
3650	UL 7.62-7.92	Test #2 1-6-98	9.49E-06	1.51E-04	771.9	3.59E-03
	UL 7.62-7.92	Test #1 2-12-98	1.89E-06	1.51E-04	771.9	5.68E-03
	UL 7.62-7.92	Test #1 3-4-98	2.33E-07	1.51E-04	771.9	8.39E-03
	UM 4.27-4.57	Test 5 Niche 3650 (11-13-97)	3.78E-05	2.62E-05	44.4	8.26E-03
	UM 4.27-4.57	Test #1 12-3-97	9.42E-06	2.62E-05	44.4	2.30E-02
	UM 4.27-4.57	Test #2 12-3-97	9.47E-06	2.62E-05	44.4	2.29E-02
	UM 4.27-4.57	Test #1 1-7-98	8.82E-07	2.62E-05	44.4	7.64E-02
	UM 4.27-4.57	Test #2 2-10-98	3.09E-07	2.62E-05	44.4	1.00E-01
	UM 4.88-5.18	Test 1 Niche 3650 (11-12-97)	5.41E-05	2.52E-03	1225.5	3.13E-03
	UM 4.88-5.18	Test #1 12-4-97	9.49E-06	2.52E-03	1225.5	4.56E-03
	UM 4.88-5.18	Test #2 12-5-97	2.70E-06	2.52E-03	1225.5	5.58E-03
	UM 4.88-5.18	Test #1 1-8-98	8.75E-07	2.52E-03	1225.5	6.50E-03
	UM 4.88-5.18	Test #1 3-6-98	2.48E-07	2.52E-03	1225.5	7.53E-03
	UM 5.49-5.79	Test 4 Niche 3650 (11-13-97)	3.87E-05	2.16E-05	29.9	1.95E-02
	UM 5.49-5.79	Test #2 12-4-97	9.43E-06	2.16E-05	29.9	2.77E-02
	UM 5.49-5.79	Test #1 1-9-98	1.08E-06	2.16E-05	29.9	1.00E-01
	UM 5.49-5.79	Test #1 2-11-98	2.55E-07	2.16E-05	29.9	1.48E-01
	UR 6.71-7.01	Test #1 1-13-98	3.68E-06	2.28E-04	699.2	5.90E-03
	UR 6.71-7.01	Test #1 2-3-98	1.91E-06	2.28E-04	699.2	6.84E-03
	UR 6.71-7.01	Test #1 3-5-98	2.48E-07	2.28E-04	699.2	9.76E-03
4788	UL 7.62-7.93	Test #1 11/3/99	1.65E-06	2.46E-05	105.4	2.56E-02
	UL 7.62-7.93	Test #1 11-30-99 Niche 4788	9.22E-07	2.46E-05	105.4	3.12E-02
	UL 7.62-7.93	Test #1 6-26-2000	3.59E-07	2.46E-05	105.4	4.01E-02
	UL 7.62-7.93	Test #1 01-24-00	1.46E-07	2.46E-05	105.4	4.86E-02
	UM 6.10-6.40	Test #1 Niche 4788 11/16/99	1.72E-06	2.45E-04	672.3	7.38E-03
	UM 6.10-6.40	Test #1 Niche 4788 12-10-99	7.33E-07	2.45E-04	672.3	8.65E-03
	UM 6.10-6.40	Test #1 06-08-2000	3.83E-07	2.45E-04	672.3	9.61E-03
	UM 6.10-6.40	Test #1 3-14-2000	1.66E-07	2.45E-04	672.3	1.09E-02
	UR 5.18-5.48	Test #1 Niche 4788 12/7/99	1.69E-06	3.92E-06	19.1	4.41E-02
	UR 5.18-5.48	Test #1 1/5/2000	7.11E-07	3.92E-06	19.1	8.93E-02
	UR 5.18-5.48	Test #1 02-14-2000	1.65E-07	3.92E-06	19.1	1.66E-01
A	**B**	**C**	**D**	**E**	**F**	**G**

D for Niche 3650 (Niche 2) from DTN: LB980901233124.003 [105592]; D for Niche 4788 (Niche 4) computed in Table II-3b (G), respectively.

E from Table II-4 (K).

F from Table II-5 (G)

G = $x\ln(D/E)/Fx$; G for Niche 3650 (Niche 2) from DTN: LB980901233124.003 [105592] using same formula

Table II-8. Computation of Estimated Water Content Change, Niche Studies

Niche	Depth (m)	Test Name	Input Liquid Release Flux q_s, (m/s)	Input Arrival Time of Wetting Front at Ceiling, t (s)	Input Distance to Ceiling z_p, (m)	Output Average Water Content Change $\theta_{ave} - \theta_n$ (m^3/m^3)
3650	UL 7.62-7.92	Test #2 1-6-98	9.49E-06	690	0.65	0.0101
	UL 7.62-7.92	Test #1 2-12-98	1.89E-06	570	0.65	0.0017
	UL 7.62-7.92	Test #1 3-4-98	2.33E-07	2610	0.65	0.0009
	UM 4.27-4.57	Test 5 Niche 3650 (11-13-97)	3.78E-05	416	0.65	0.0242
	UM 4.27-4.57	Test #1 12-3-97	9.42E-06	1008	0.65	0.0146
	UM 4.27-4.57	Test #2 12-3-97	9.47E-06	514	0.65	0.0075
	UM 4.27-4.57	Test #1 1-7-98	8.82E-07	8811	0.65	0.0120
	UM 4.27-4.57	Test #2 2-10-98	3.09E-07	13375	0.65	0.0063
	UM 4.88-5.18	Test 1 Niche 3650 (11-12-97)	5.41E-05	180	0.65	0.0150
	UM 4.88-5.18	Test #1 12-4-97	9.49E-06	298	0.65	0.0043
	UM 4.88-5.18	Test #2 12-5-97	2.70E-06	952	0.65	0.0040
	UM 4.88-5.18	Test #1 1-8-98	8.75E-07	6060	0.65	0.0082
	UM 4.88-5.18	Test #1 3-6-98	2.48E-07	21690	0.65	0.0083
	UM 5.49-5.79	Test 4 Niche 3650 (11-13-97)	3.87E-05	208	0.65	0.0124
	UM 5.49-5.79	Test #2 12-4-97	9.43E-06	420	0.65	0.0061
	UM 5.49-5.79	Test #1 1-9-98	1.08E-06	2750	0.65	0.0046
	UM 5.49-5.79	Test #1 2-11-98	2.55E-07	10130	0.65	0.0040
	UR 6.71-7.01	Test #1 1-13-98	3.68E-06	416	0.65	0.0024
	UR 6.71-7.01	Test #1 2-3-98	1.91E-06	626	0.65	0.0018
	UR 6.71-7.01	Test #1 3-5-98	2.48E-07	4457	0.65	0.0017
4788	UL 7.62-7.93	Test #1 11/3/99	1.65E-06	7057	0.60	0.0193
	UL 7.62-7.93	Test #1 11-30-99 Niche 4788	9.22E-07	3602	0.60	0.0055
	UL 7.62-7.93	Test #1 6-26-2000	3.59E-07	16445	0.60	0.0098
	UL 7.62-7.93	Test #1 01-24-00	1.46E-07	45697	0.60	0.0111
	UM 6.10-6.40	Test #1 Niche 4788 11/16/99	1.72E-06	16572	0.58	0.0489
	UM 6.10-6.40	Test #1 Niche 4788 12-10-99	7.33E-07	39938	0.58	0.0503
	UM 6.10-6.40	Test #1 06-08-2000	3.83E-07	50190	0.58	0.0331
	UM 6.10-6.40	Test #1 3-14-2000	1.66E-07	124800	0.58	0.0355
	UR 5.18-5.48	Test #1 Niche 4788 12/7/99	1.69E-06	4034	0.74	0.0092
	UR 5.18-5.48	Test #1 1/5/2000	7.11E-07	5707	0.74	0.0055
	UR 5.18-5.48	Test #1 02-14-2000	1.65E-07	24900	0.74	0.0055
A	**B**	**C**	**D**	**E**	**F**	**G**

D for Niche 3650 (Niche 2) from DTN: LB980901233124.003 [105592]

D for Niche 4788 (Niche 4) computed in Table II-3b (G), respectively.

E in hr:minute:second format for Niche 4788 (Niche 4) from DTN: LB0010NICH4LIQ.001 [153145]

E conversion from hr:minute:second format to seconds = hours*3600+minutes*60+seconds in table

E in seconds for Niche 3650 (Niche 2) from DTN: LB980901233124.003 [105592] using same conversion

F for Niche 3650 (Niche 2) from Scientific Notebook by Wang (1999 [153449], p. 84).

F for Niche 4788 (Niche 4) from Table II-2

G = D*E/F for Niche 4788 (Niche 4)

G for Niche 3650 (Niche 2) from DTN: LB980901233124.003 [105592] using same formula

ATTACHMENT III

SUPPLEMENTAL INFORMATION ON SEEPAGE TESTS AT NICHE CD 1620 (NICHE 5)

Attachment III is referred to in Section 6.2.1.3.5.2 on seepage tests at Niche CD 1620 (Niche 5) with Attachment III.1 on as-built slot profiles to supplement Figure 6.2.1-13, Attachment III.2 on details of test operation on control equipment, Attachment III.3 on software of measuring and testing equipment, and Attachment III.4 on test sequence and scientific notebooks.

INTENTIONALLY LEFT BLANK

ATTACHMENT III – SUPPLEMENTAL INFORMATION ON SEEPATE TESTS OF NICHE CD 1620 (NICHE 5)

III.1 SURVEY DATA

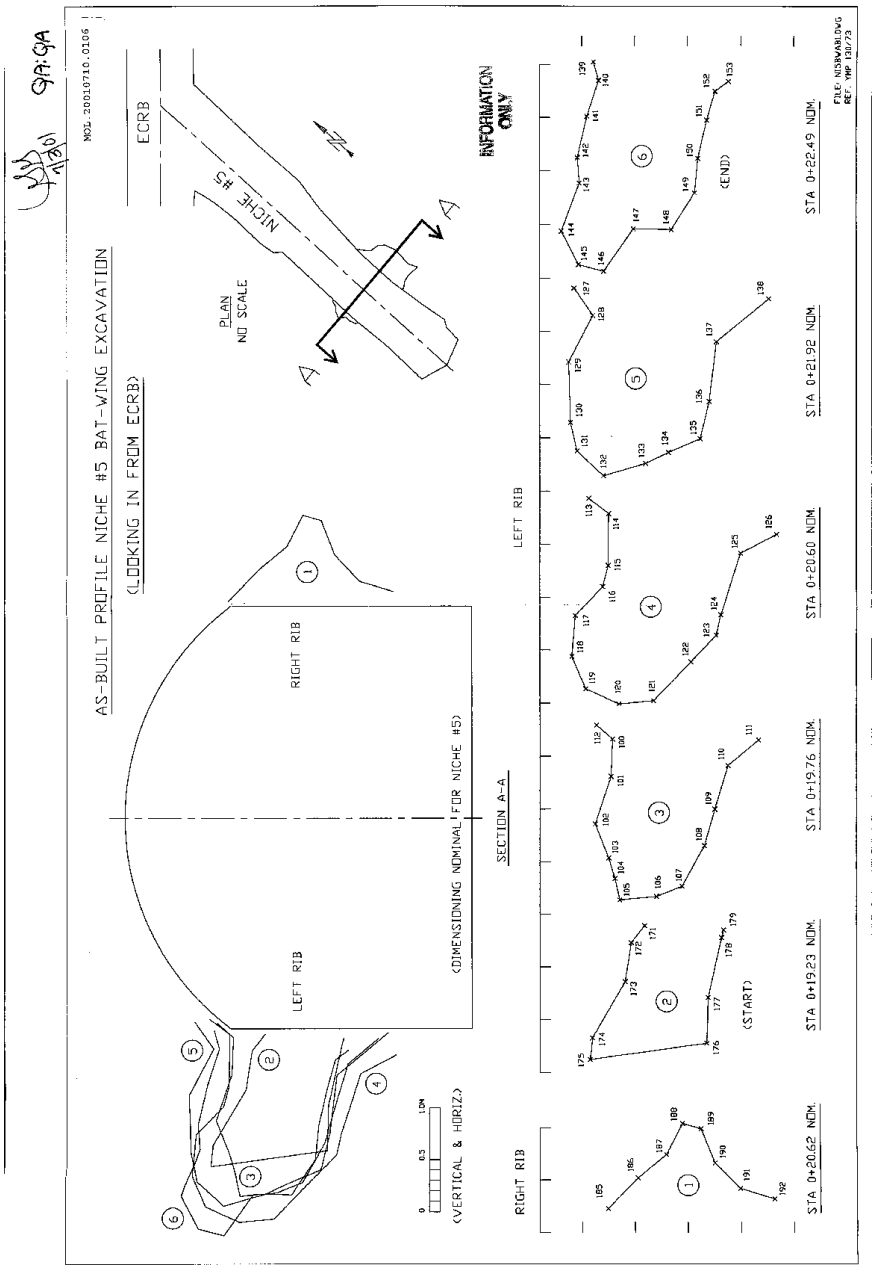

DTN: MO0107GSC01061.000 [155369]

III.2 TEST OPERATION AND CONTROL EQUIPMENT

The test operation and control equipment can be categorized into three general functional groups, as follows:

1. Valves and pumps that allow the user to control the direction, speed, and duration of fluid (air and water) movement through the manifolds, transmission lines, and straddle packers. Two pumps are used to control the release rate into the test interval, and valves are used to fill the release reservoir with more water once it is depleted. High-capacity pumps are periodically used to empty the capture and return reservoirs, where seepage and return waters, respectively, accumulate during an experiment.

2. Instruments and sensors including electronic balances, pressure transducers, and water level sensors provide system feedback. The operator uses feedback from these sensors to manipulate control variables by manually or programmatically changing corresponding process variables. Automated equipment control software was also used to continually poll these sensors and automatically change process variables (e.g., start and stop a pump) to effect a change in a corresponding control variable (e.g., release rate). Once the test is started, it can run for long periods of time without an operator, using the automated control routines.

3. National Instruments' FieldPoint (FP) modular distributed input/output system is used to monitor and control process variables. Several FP modules are used as controllers allowing the user to open and close valves, start or stop pumps, etc., using the front panel controls found in the software described in Attachment III.3.

Detailed process control diagrams associated with the test equipment are provided in Figure III.2-1 for the release and return manifolds and in Figure III.2-2 for the capture manifold.

The primary components of the test operation and control equipment consist of Aro solenoid valves, Nupro pneumatic valves, Richway air pinch valves, straddle packers, pumps, Kavlico pressure transducers, Gems water level sensors, and Mettler Toledo balances.

Solenoid valves are used to control the flow of compressed air to the pneumatic and pinch valves, and the straddle packers as shown in Figure III.2-1 and Figure III.2-2. A FP control module is used to send a voltage signal to the input terminal of a solenoid valve, causing the valve to open, and allowing compressed air to pass through the valve body. If the solenoid valve is opened, and it is connected to a pneumatic or pinch valve, then the air pressure will open or close these valves depending upon their initial state (i.e., normally open [N.O.] or normally closed [N.C.]). Solenoid valves are also used to directly control the air pressure needed to inflate the rubber glands of the straddle packer as shown in Figure III.2-1.

Pneumatic and pinch valves are used to control the movement of fluid through the release manifold. Water is pumped from the release reservoir resting on a Model SG 16001 Mettler Toledo balance (capacity 16.1 kg) through the release manifold and straddle packers via tubing to the test interval. Changing the pump speed changes the rate that water is released into the test zone. Two pumps having different pumping speed (high and low) can be used for this purpose including a MASTERFLEX® L/S® variable-speed digital peristaltic pump (0.1 to 340 g/min)

and a Scilog piston pump (0.02 to 11 g/min). A FP control module is used to send a 3.5 to 20 mAmp electrical signal to either pump, which changes the pump speed from 0 to 100% of the pump's full-scale output. The rate that water is pumped into the borehole is monitored using the balance. When the release reservoir is depleted, based on its mass, a pneumatic valve is opened on the water supply line to replenish the water in the release reservoir. Replenishing the release reservoir can be performed manually or automatically using equipment control software. A Gems float switch is used as a high-water-level indicator in the release reservoir to close the water supply valve and to turn off the release pumps if the release reservoir accidentally overfills.

The return port and return line connect the test interval through the straddle packer to the return manifold and the return reservoir sitting on another balance (Figure III.2-1 and Figure III.2-2). If the pumping rate exceeds the infiltration capacity of the rock, then water will pond in the borehole and eventually flow out through the return line to the return reservoir sitting on a second Model SG16001 Mettler Toledo balance. Pneumatic and pinch valves are used to control the movement of fluid through the return manifold and transmission lines. The rate that water returns by gravity to the return reservoir is monitored using the balance. Once the return reservoir is full (based on its mass), a high capacity (0.12–17 kg/min) MASTERFLEX® I/P® variable speed peristaltic pump is used to remove the water from the return reservoir. An FP control module is used to actuate the pump either manually or automatically, using equipment control software.

Water introduced into the test interval is expected to move from the borehole through the rock to the niche ceiling, where it drips into the niche (Figure III .2-1 and Figure III.2-2). A capture system, consisting of 0.30 m wide by 1.20 m long trays constructed of transparent lexan plastic hung from an aluminum frame, is used to collect the water dripping from the niche ceiling (Figure 6.2.1-17). Each plastic tray is about 0.2 m deep and divided into four separate compartments, each 0.30 by 0.30 m square. Each compartment drains from the bottom through a pinch valve and associated tubing to a capture reservoir sitting on a third Model SG16001 Mettler Toledo balance. The pinch valve can be opened or closed by closing and opening, respectively, its corresponding solenoid valve. The spatial distribution of seepage can be determined by sequentially opening and closing the different pinch valves and measuring the cumulative mass collected in a given compartment using the capture balance. Once the capture reservoir is full (based on its mass), a second MASTERFLEX® I/P® variable speed peristaltic pump is used to remove the water from the capture reservoir. Again, an FP control module is used to actuate the pump either manually or automatically, using the software listed in Attachment III.3.

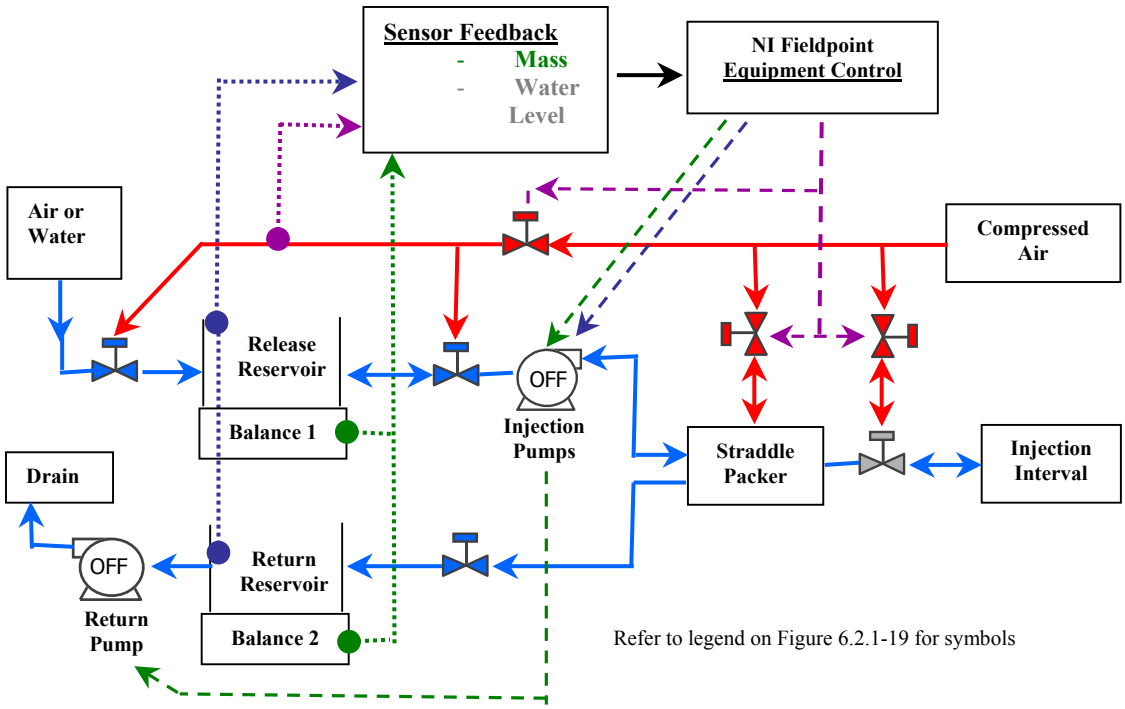

Figure III.2-1. Process Diagram for the Release and Return Manifolds Used to Control Fluid Flow to and from the Test Interval

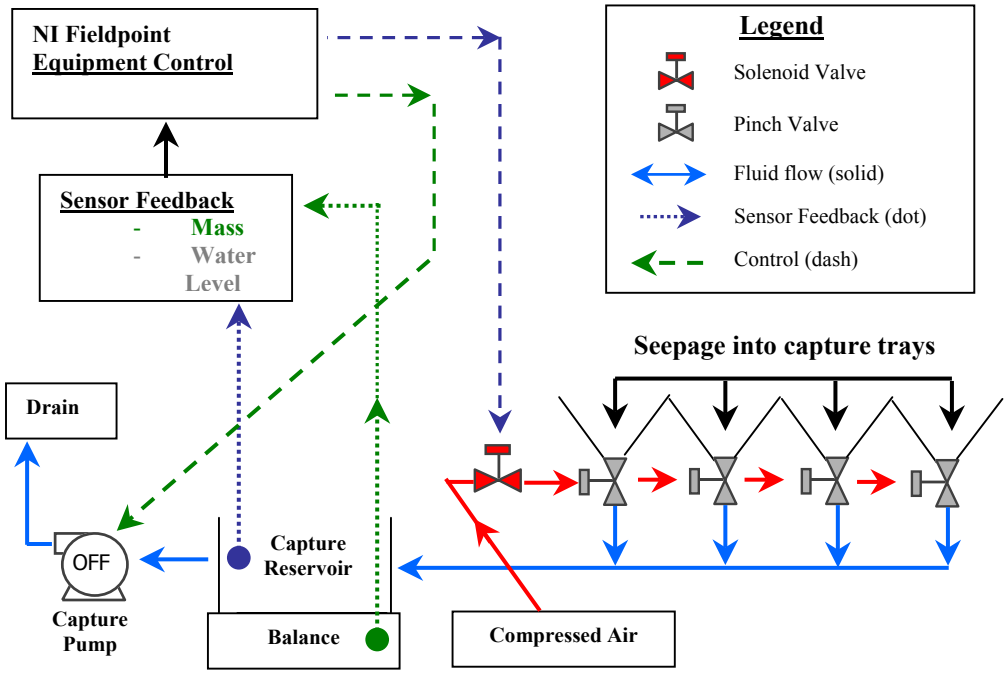

Figure III.2-2. Process Diagram for the Capture Manifold Used to Measure and Control Seepage Collected Inside the Niche

III.3 EQUIPMENT CONTROL AND DATA ACQUISITION SOFTWARE

Custom-designed software was developed for the PC using National Instruments LabVIEW graphical development environment to control the seepage test equipment, allowing both manual or automated manipulation and control of the test equipment and parameters described in the Test operation of Control Equipment subsection above. LabVIEW provides a convenient platform on which to interface with equipment and sensors. The control (e.g., valve icon) and indicator (e.g., graph) functions provided in LabVIEW allow the software developer to build custom "virtual instruments" (vi's) that can be viewed and operated from a PC. The operator interfaces with the equipment by clicking on icons representing valves, buttons, knobs, etc., that control processes or by viewing indicators showing data, including graphs, gauges, and tanks, shown on the PC's video display. Figure III.3-1 shows part of the front panel display for "Combined system box.vi," with V1.0 the main program used to control valves and monitor test equipment.

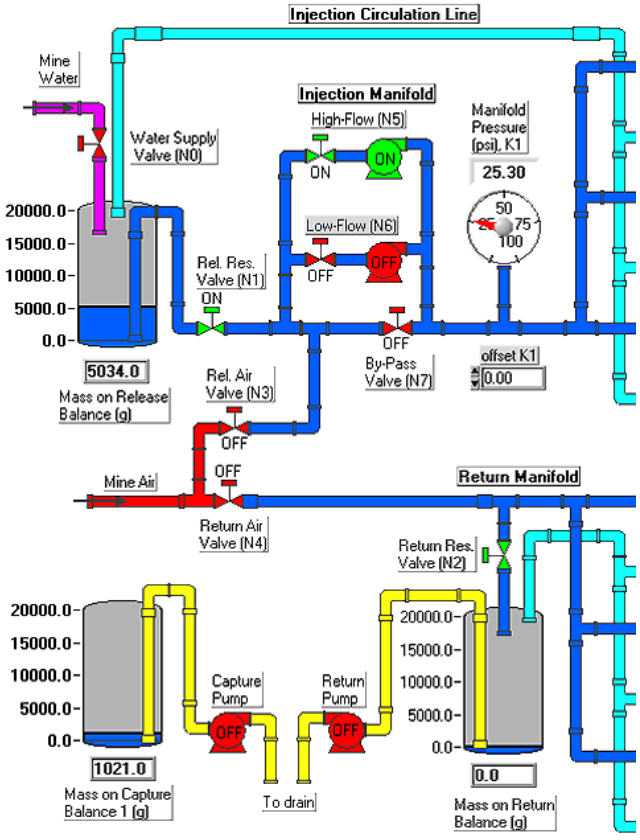

Figure III.3-1. Front Panel Display for LabVIEW Virtual Instrument 'Combined system box.vi' V1.0, Showing Example of Equipment Control Parameters

Table III.3-1 summarizes the equipment control software routines used during the seepage tests. Additional details regarding software use, limitations, and testing can be found in the software management reports developed and submitted in accordance with applicable Software Quality Assurance procedures.

The software programs allow the test operator to open and close valves, start and stop pumps, change the pump speed and direction, inflate and deflate packers, fill and empty water reservoirs, and monitor test parameters. This is accomplished by running the software on a PC connected directly to the sensors and FP modules used to monitor and control the test equipment. The user interfaces with the equipment on site, in real time, using traditional keyboard/mouse entries, or off site by controlling the PC remotely over the Internet, using readily available commercial software (e.g., Timbuktu Pro), which controls data acquisition equipment and has not been developed or modified.

Table III.3-1. Software Used to Control Seepage Test Equipment

Software Name	STN	Function	Citation
Nistime-32 bit.exe V.3.12 *	10664-3.12-00	Synchronizes PC clock with time maintained by NIST	LBNL 2002 [161218]
Combined System Box.vi V.1.0	10758-1.0-00	Operates main valves and monitor process variables. This is the main vi that calls the sub vi's listed below	LBNL 2002 [161219]
Pump box.vi V1.0	10761-1.0-00	Manually operates release, return and capture pumps	LBNL 2002 [161220]
Auto refill water supply.vi V.1.0	10756-1.0-00	Automatically refills release reservoir during long-duration tests	LBNL 2002 [161221]
Automated return pump.vi V.1.0	10757-1.0-00	Automatically operates return pump during long-duration tests	LBNL 2002 [161222]
Manual packer inflation.vi V.1.0	10759-1.0-00	Manually inflates and deflates packers	LBNL 2002 [161224]
Manual pinch valve box.vi V1.0	10760-1.0-00	Manually opens and closes pinch valves that control the flow of seepage into the capture reservoir	LBNL 2002 [161225]
Auto packer inflation.vi V.1.0	10754-1.0-00	Automatically inflates the packers each time the pressure drops below a user defined setpoint	LBNL 2002 [161226]
Auto pinch valve box.vi V.1.0	10755-1.0-00	Automatically opens and closes the pinch valves that control seepage into the capture reservoir. Also automatically controls the capture pump.	LBNL 2002 [161227]

NOTE: * Nistime-32 bit.exe is distributed as freeware by the National Institute of Standards and Technology (NIST).

Automation of the test equipment allows unattended operation of the tests. Unattended operation and remote access to the equipment was critical to the success of the seepage tests because of the long duration of the experiments and limited access to the equipment during routine (e.g., weekend and holidays) and unexpected (e.g., power failures) closure of the ESF.

Custom-designed software was also developed for the PC using LabVIEW to acquire release, return, capture, and evaporation mass and rate data collected during the tests, using the Mettler Toledo balances noted in Section 6.2.1.3.5.2, Data Acquisition Equipment. Table III.3-2 summarizes the data acquisition software used to collect the evaporation and seepage test data. Additional details regarding the software use, limitations, and testing can be found in the software routine reports or software management reports created in accordance with applicable software quality assurance procedures in effect at the time of software development.

Table III.3-2. Software Used to Acquire Evaporation and Seepage Test Data

Software Name	STN or ACC**	Function	Citation
Nistime-32 bit.exe V.3.12 *	10664-3.12-00	Synchronizes PC clock with time maintained by NIST, providing accurate time stamp for acquired data	LBNL 2002 [161218]
Mettler Single Scale 9-27-00.vi V1.0	10399-1.0-00	Measures evaporation using a single Mettler Toledo balance	LBNL 2000 [161229]
Mettler Single Scale 8-31-01.vi V2.0	10399-2.0-00	Measures evaporation using a single Mettler Toledo balance	LBNL 2002 [161228]
Mettler double Scale 1.vi V1.0	MOL.19991018.0189**	Measures evaporation using a single Mettler Toledo balance	LBNL 2000 [140259]
Mettler Quad Scale 8-23-01.vi V2.0	10345-2.0-00	Measures the release, return, seepage, and evaporation masses and rates using four Mettler Toledo balances during a seepage test	LBNL 2002 [161230]
Auto pinch valve box.vi V.1.0	10755-1.0-00	Records the mass, rate, and seepage percentage each time individual seepage compartments drain water into the reservoir on the capture balance(s).	LBNL 2002 [161227]

NOTE: * Nistime-32 bit.exe is distributed as freeware by the National Institute of Standards and Technology (NIST).

** Documentation before M&TE software registration with STN assignment.

The three software routines ("Mettler Single Scale 9-27-00.vi V1.0," "Mettler Double Scale 1.vi V1.0," and "Mettler Single Scale 8-31-01.vi V2.0") were initially used to record the evaporation rate prior to 7/15/02. After 7/15/02, only one balance was used to measure seepage into the niche, and a fourth balance was available to record the water loss to evaporation. "Mettler Quad Scale 8-23-01.vi V2.0" was used to measure the evaporation mass and rate from this date forward. Therefore, test data files generated after 7/15/02 not only contain the cumulative mass and rate of water released (Balance 1), returned (Balance 2), and captured (Balance 3), but also the loss caused by evaporation from the evaporation pan (Balance 4).

III.4 NICHE CD 1620 (NICHE 5) DATA FILES AND SCIENTIFIC NOTEBOOKS

Five sets of data were submitted to the Technical Database Management System (TDMS). Three of the data sets including LB0207NICH5LIQ.001 [160408], LB0209NICH5LIQ.001 [160796], and LB0211NICH5LIQ.001 [160792] contain native data files (in comma-delimited ASCII format) and are summarized in Table III.4-1. The remaining data sets including LB0208NICH5LIQ.001 [161210] and LB0210NICH5LIQ.001 [161211] contained preliminary data and were subsequently superseded by LB0209NICH5LIQ.001 [160796] and LB0211NICH5LIQ.001 [160792], respectively. Table III.4-1 also identifies the scientific notebook pages pertinent to each test, which provide test-specific details including the serial number and location of instruments and sensors used during the experiment, test operating conditions, etc. Copies of the pertinent scientific notebook pages were reviewed and sent to the Records Processing Center for inclusion in the project records.

The name of the native electronic files containing the test data generated using the data acquisition equipment and software are listed in the table. Test data files consist of four types. Three of these types include the suffix "…(seep)," "…(smass)," and "…(srate)" in their filename. These files contain the seepage percentage, seep mass, and seepage rate data, respectively, from individual capture compartments draining seepage water to the capture balance(s) during the test (Figure III.2-1 and Figure III.2-2). These files were generated using the software routine "Auto pinch valve box.vi V.1.0" (LBNL 2002 [161227]). The remaining test files that do not contain these suffixes in the filename (e.g., "Test#1_BH#2_21-22_ft_5-6-02.csv") contain the cumulative mass and rate of water released (Balance 1), returned (Balance 2), and the total seepage captured (Balance 3 and/or 4) during a given experiment. These files were generated using the software routine "Mettler Quad Scale 8-23-01.vi V2.0" (LBNL 2002 [161230]), which recorded the mass on the Mettler Toledo balances used during the experiments. As noted in Attachment III.3, after 7/15/02, only one balance was used to measure seepage into the niche (i.e., Balance 3) and Balance 4 was used to measure evaporation.

Table III.4-1. General Test Information for Post-Excavation Seepage Tests at Niche CD 1620 (Niche 5)

Borehole	Depth (m)	Test Name	Start Date	End Date	Source of Data	
					Scientific Notebook	Electronic Filename (see footnote)
#2	6.40-6.70	Test#1 5-6-02	5/6/2002	5/10/2002	Trautz 2003 [166248], pp. 154-160, 162-167, 169-171,178-190, 193-196, 199, 201-202, 220, 226-229, 233	Test#1_BH#2_21-22_ft_5-6-02.csv
#2	6.10-6.40	Test #2 5-17-02	5/17/2002	5/17/2002	Trautz 2003 [166248], pp. 154-160, 162-167, 169-171, 178-190, 201-203, 205-208, 220 226-229, 233.	Test#2_BH#2_20-21_ft_5-17-02.csv Test#2_BH#2_20-21_ft_5-17-02 (seep)_#1.csv Test#2_BH#2_20-21_ft_5-17-02 (smass)_#1.csv Test#2_BH#2_20-21_ft_5-17-02 (srate)_#1.csv
#5	8.53-8.83	Test #1 5-3-02	5/3/2002	5/14/2002	Trautz 2003 [166248], pp. 154-160, 162-166, 168-178, 184-192, 195-202, 220, 229-233.	Test#1_b5_28-29_ft_5-3-02_#1.csv Test#1_b5_28-29_ft_5-3-02_#2.csv Test#1_b5_28-29_ft_5-3-02_#3.csv Test#1_b5_28-29_ft_5-3-02_#4.csv Test#1_b5_28-29_ft_5-3-02_(seep).csv Test#1_b5_28-29_ft_5-3-02_(smass).csv Test#1_b5_28-29_ft_5-3-02_(srate).csv
#5	8.53-8.83	Test #2 5-16-02	5/16/2000	5/31/2002	Trautz 2003 [166248], pp. 154-160, 162-166, 168-178, 184-190, 201-222, 226-234.	Test#2_b5_28-29_ft_5-16-02.csv Test#2_b5_28-29_ft_5-16-02_(seep)_#1.csv Test#2_b5_28-29_ft_5-16-02_(seep)_#2.csv Test#2_b5_28-29_ft_5-16-02_(seep)_#3.csv Test#2_b5_28-29_ft_5-16-02_(seep)_#4.csv Test#2_b5_28-29_ft_5-16-02_(smass)_#1.csv Test#2_b5_28-29_ft_5-16-02_(smass)_#2.csv Test#2_b5_28-29_ft_5-16-02_(smass)_#3.csv Test#2_b5_28-29_ft_5-16-02_(smass)_#4.csv Test#2_b5_28-29_ft_5-16-02_(srate)_#1.csv Test#2_b5_28-29_ft_5-16-02_(srate)_#2.csv Test#2_b5_28-29_ft_5-16-02_(srate)_#3.csv Test#2_b5_28-29_ft_5-16-02_(srate)_#4.csv Test#2_BH#2_20-21_ft_5-17-02.csv Test#2_BH#2_20-21_ft_5-17-02 (seep)_#1.csv Test#2_BH#2_20-21_ft_5-17-02 (seep)_#2.csv

Table III.4-1. General Test Information for Post-Excavation Seepage Tests at Niche CD 1620 (Niche 5) (continued)

Borehole	Depth (m)	Test Name	Start Date	End Date	Source of Data	
					Scientific Notebook	Electronic Filename (see footnote)
						Test#2_BH#2_20-21_ft_5-17-02 (seep)_#3.csv Test#2_BH#2_20-21_ft_5-17-02 (smass)_#1.csv Test#2_BH#2_20-21_ft_5-17-02 (smass)_#2.csv Test#2_BH#2_20-21_ft_5-17-02 (smass)_#3.csv Test#2_BH#2_20-21_ft_5-17-02 (srate)_#1.csv Test#2_BH#2_20-21_ft_5-17-02 (srate)_#2.csv Test#2_BH#2_20-21_ft_5-17-02 (srate)_#3.csv
Evaporation Pan Data		Pre-tests	12/7/2000 2/7/2001 2/21/2001 4/2/2001 7/12/2001	12/12/2000 2/8/2001 4/2/2001 4/3/2001 8/25/2001	Trautz 2001 [161208], pp. 90-91, 116-117, 120, 130-131, 156-157, 195, 298-299.	Evap Niche CD1620 12-7-00.csv Evap Niche CD1620 start2-07-01.csv Evap Niche CD1620 start 2-21-01.csv Evap Niche CD1620 start 4-02-01.csv Evap Niche CD1620 start 7-12-01.csv
Evaporation Pan Data		All tests	5/2/2002 5/6/2002 5/10/2002 5/2/2002 5/6/2002	5/3/2002 5/10/2002 6/13/2002 5/3/2002 6/13/2002	Trautz 2003 [166248], pp. 187, 192, 193, 198, 199, 203, 220, 223, 226-230, 233	N5 Evap inside start 5-2-02.csv N5 Evap inside start 5-6-02.csv N5_Evap_inside_start_5-10-02.csv N5 Evap out start 5-2-02.csv N5_Evap_out_start 5-6-02.csv
Relative Hum. and Temp. inside niche		Pre-tests	12/7/2000 1/23/2001 2/26/2001 3/21/2001 3/22/2001 7/12/2001 7/24/2001 8/25/2001	12/21/2000 2/26/2001 3/21/2001 3/22/2001 4/3/2001 7/24/2001 8/25/2001 9/12/2001	Trautz 2001 [156903], p. 47. Trautz 2001 [161208], pp. 90-91, 116, 134-135, 143, 158, 190-195, 219-221, 298-299.	N51-23.csv N52-26.csv N53-21.csv N54-3-01.csv N54-3.csv N57-24.csv N58-25.csv N59-12.csv
Relative Hum. and Temp. inside and outside niche, and liquid pressure in release lines		All tests	5/2/2002 5/2/2002 5/2/2002 5/2/2002	5/6/2002 5/9/2002 5/22/2002 6/3/2002	Trautz 2003 [166248], pp. 162-164, 170-171, 186, 188-190, 192, 197, 210, 220-222, 226-230, 233	N5_RH-T-P_5-6-02.csv N5_RH-T-p_5-9-02.csv N5_RH-T-p_5-22-02.csv N5_RH-T-p_6-3-02.csv

DTN: LB0207NICH5LIQ.001 [160408], native data file Niche CD1620 data sources rev 8-9-02.xls

NOTE: .csv file extension = comma delimited ASCII formatted file.

Table III.4-1. General Test Information for Post-Excavation Seepage Tests at Niche CD 1620 (Niche 5) (continued)

Borehole	Depth (m)	Test Name	Start Date	End Date	Source of Data	
					Scientific Notebook	Electronic Filename (see footnote)
#3	6.40-6.70	Test#1 7-16-02	7/16/2002	8/14/2002	Trautz 2003 [166248], pp. 154-159, 162-164, 170-183, 201, 239-258, 262-273, 297-301.	Test#1_BH#3_21-22_ft_7-16-02_#1.csv Test#1_BH#3_21-22_ft_7-16-02_#1 (seep).csv Test#1_BH#3_21-22_ft_7-16-02_#1 (smass).csv Test#1_BH#3_21-22_ft_7-16-02_#1 (srate).csv
#3	6.40-6.70	Test #1 8-14-02	8/14/2002	8/26/2002	Trautz 2003 [166248], pp. 154-159, 162-164, 170-183, 201, 239-258, 273-285, 297-301.	Test#1_BH#3_21-22_ft_8-14-02_#1.csv Test#1_BH#3_21-22_ft_8-14-02_#1 (seep).csv Test#1_BH#3_21-22_ft_8-14-02_#1 (smass).csv Test#1_BH#3_21-22_ft_8-14-02_#1 (srate).csv Test#1_BH#3_21-22_ft_8-14-02_#2.csv Test#1_BH#3_21-22_ft_8-14-02_#2 (seep).csv Test#1_BH#3_21-22_ft_8-14-02_#2 (smass).csv Test#1_BH#3_21-22_ft_8-14-02_#2 (srate).csv
#5	8.53-8.83	Test #1 7-15-02	7/15/2002	8/26/2002	Trautz 2003 [166248], pp.154-159, 162-164, 170-183, 201, 239-262, 267-273, 275-285 297-301.	Test#1_b5_28-29_ft_7-15-02_#1.csv Test#1_b5_28-29_ft_7-15-02_#1_(seep).csv Test#1_b5_28-29_ft_7-15-02_#1_(smass).csv Test#1_b5_28-29_ft_7-15-02_#1_(srate).csv Test#1_b5_28-29_ft_7-15-02_#2.csv Test#1_b5_28-29_ft_7-15-02_#2 (seep).csv Test#1_b5_28-29_ft_7-15-02_#2 (smass).csv Test#1_b5_28-29_ft_7-15-02_#2 (srate).csv
Evaporation Pan Data inside and outside Niche CD 1620 (Niche 5)		Pre-tests	7/2/2002 7/3/2002 6/27/2002 7/3/2002	7/3/2002 7/15/2002 7/3/2002 7/16/2002	Trautz 2003 [166248], pp. 242, 244-246, 260, 263, 272-273.	N5_Evap_inside_start_7-2-02.csv N5_Evap_inside_start_7-3-02.csv N5_Evap_out_start 6-27-02.csv N5_Evap_out_start_7-3-02.csv
Evaporation Pan Data inside and outside Niche CD 1620 (Niche 5)		During tests	7/15/2002 7/15/2002 7/16/2002 8/13/2002 8/14/2002 8/23/2002	7/15/2002 8/26/2002 8/12/2002 8/14/2002 8/22/2002 8/26/2002	Trautz 2003 [166248], pp. 240-241, 247-250, 258, 260, 263, 265, 272-274, 281-282, 283-285.	Test#1_b5_28-29_ft_7-15-02_#1.csv Test#1_b5_28-29_ft_7-15-02_#2.csv Test#1_BH#3_21-22_ft_7-16-02_#1.csv Test#1_BH#3_21-22_ft_8-13-02_#1.csv Test#1_BH#3_21-22_ft_8-14-02_#1.csv Test#1_BH#3_21-22_ft_8-14-02_#2.csv

Table III.4-1. General Test Information for Post-Excavation Seepage Tests at Niche CD 1620 (Niche 5) (continued)

Borehole	Depth (m)	Test Name	Start Date	End Date	Source of Data	
					Scientific Notebook	Electronic Filename (see footnote)
Relative Hum. and Temp. inside and outside niche, and liquid pressure in release lines		All tests	7/3/2002	8/19/2002	Trautz 2003 [166248], pp. 162-164, 170-171, 186, 188-190, 220-222, 224-226, 239-243, 245 278, 280-281, 297-299.	N5_RH-T-p_8-19-02.csv

DTN: LB0209NICH5LIQ.001 [160796], native data file Niche CD1620 data sources rev 9-13-02 #2.xls

NOTE: .csv file extension = comma delimited ASCII formatted file.

Table III.4-1. General Test Information for Post-Excavation Seepage Tests at Niche CD 1620 (Niche 5) (continued)

Borehole	Depth (m)	Test Name	Start Date	End Date	Source of Data	
					Scientific Notebook	Electronic Filename (see footnote)
#4	6.40-6.70	Test#1 9-17-02	9/17/2002	10/1/2002	Trautz 2003 [166248], pp.154-159, 162-163, 165, 170-183, 243-245, 284, and 287. Trautz 2001 [161208], pp. 14-15, 18-41, 54-56, 61-62, 65.	Test#1_BH#4_10-11_ft_9-17-02_#1.csv Test#1_BH#4_10-11_ft_9-17-02_#1a_(seep).csv Test#1_BH#4_10-11_ft_9-17-02_#1a_(smass).csv Test#1_BH#4_10-11_ft_9-17-02_#1a_(srate).csv Test#1_BH#4_10-11_ft_9-17-02_#2_(seep).csv Test#1_BH#4_10-11_ft_9-17-02_#2_(smass).csv Test#1_BH#4_10-11_ft_9-17-02_#2_(srate).csv
#4	6.40-6.70	Test #1 10-1-02	10/1/2002	10/28/2002	Trautz 2003 [166248], pp.154-159, 162-163, 165, 170-183, 243-245, 284, and 287. Trautz 2001 [161208], pp. 14-15, 18-40, 42-60, 63-66.	Test#1_BH#4_10-11_ft_9-17-02_#1.csv
#5	8.53-8.83	Test #2 9-17-02	9/17/2002	10/28/2002	Trautz 2003 [166248], pp.154-159, 162-163, 165, 170-183, 243-245, 284, 286-287. Trautz 2001 [161208], pp. 14-17, 20-41, 43-47, 49-53, 55-62, 65, 67.	Test#2_b5_20-21_ft_9-17-02_#2 (seep).csv Test#2_b5_20-21_ft_9-17-02_#2 (smass).csv Test#2_b5_20-21_ft_9-17-02_#2 (srate).csv Test#2_b5_20-21_ft_9-17-02_#1.csv Test#2_b5_20-21_ft_9-17-02_#1a (seep).csv Test#2_b5_20-21_ft_9-17-02_#1a (smass).csv Test#2_b5_20-21_ft_9-17-02_#1a (srate).csv
Evaporation Pan Data inside and outside Niche CD1620 (Niche 5)		All tests	9/17/2002	10/28/2002	Trautz 2003 [166248], pp. 240-241, 247-250, 260, 263, 265, 272-274, 281-282, 283-285. Trautz 2001 [161208], pp. 14-19, 28, 41-42, 45-46, 55-56, 59.	Test#1_BH#4_10-11_ft_9-17-02_#1.csv Test#2_b5_20-21_ft_9-17-02_#1.csv
Relative Hum. and Temp. inside and outside niche, and liquid pressure in release lines		All tests	8/20/2002 9/18/2002 10/18/2002	9/18/2002 10/18/2002 10/29/2002	Trautz 2003 [166248], pp. 162-164, 170-171, 186, 188-190, 221-222, 224-225, 239-243, 245, 280-281. Trautz 2001 [161208], pp. 16, 18,20, 52, 54-56.	N5_RH-T-p_9-18-02.csv N5_RH-T-p_10-18-02.csv N5_RH-T-p_10-29-02.csv

DTN: LB0211NICH5LIQ.001 [160792], native data file Niche CD1620 data sources rev 11-15-02.xls
NOTE: .csv file extension = comma delimited ASCII formatted file

INTENTIONALLY LEFT BLANK

ATTACHMENT IV

SEEPAGE PARAMETER EVALUATION

Attachment IV.1 on approach used to determine seepage parameters and Attachment IV.2 on estimation of saturated hydraulic conductivity using air-permeability are referred to in Section 6.2.2.1 on seepage thresholds. Attachment IV.3 on water-content-profile evaluation is referred to in Section 6.2.2.3 on water content in estimating water retention curves in fractures.

INTENTIONALLY LEFT BLANK

ATTACHMENT IV—SEEPAGE PARAMETER EVALUATION

IV.1 APPROACH TO EVALUATION SEEPAGE PARAMETERS

In liquid tests for seepage quantification, the saturated conductivities are estimated from air permeability values, the fracture capillarities are estimated from the seepage threshold fluxes, and the water potentials are estimated for the flow paths from the liquid-release interval to the niche ceiling. The following paragraphs discuss the approach used to derive the seepage parameters.

Permeability is an intrinsic parameter characterizing the resistance to flow by the rock medium. For laboratory test conditions with a well-defined unidirectional flow path through a core specimen, the permeability value is independent of the fluid used in the measurement. In the field conditions associated with localized injections, the flow path followed by the air is different from the flow path followed by the liquid. The following approximations, together with detailed evaluation in Attachment IV.2, address the relationship between air permeability and liquid permeability in the niche seepage tests.

For locally saturated conditions such as in the immediate vicinity of a liquid-filled borehole interval, the saturated permeability to liquid flow is approximately equal to the permeability measured in air-injection tests. The saturated liquid flux is then estimated from the measured air-permeability value and the wetted area of the borehole, as described in Attachment IV.2.

The estimations of saturated liquid permeability are evaluated in Attachment IV.2 from available data collected in the niche studies. The evaluation compares the estimated flux values with measured flux values for cases where there is evidence that the borehole intervals tested are actually saturated, with return flows observed. With liquid flow mainly through fractures below the borehole interval (resulting from gravity drainage and air flow into fractures all around the borehole interval driven by pressure gradient), the liquid permeability and air permeability represent the effective values of different fracture flow paths. The evaluation of the difference between liquid permeability and air permeability is documented in Attachment IV.2, where it is shown that the saturated liquid permeability is within one order of magnitude of the air permeability.

Also in this section, gravity-driven flow is considered the primary flow mechanism in fractures with weak capillarity, and liquid fracture flows are governed by Darcy's law. Under unsaturated conditions, capillary forces and gravity are the driving mechanisms for flow. Because fracture apertures are much larger than tuff matrix pores, the effect of capillarity is much less than the effect of gravity on liquid fracture flow. This justifies neglecting fracture capillarity and the use of gravity gradient to estimate flux. The small fracture capillarity is evaluated in Section 6.2.2.2.

Philip et al. (1989 [105743]) developed an analytical solution describing under what conditions water will flow from an unsaturated porous medium into a buried cylindrical cavity. The solution is used in Section 6.2.2.2 to compute the sorptive number, α, a hydraulic parameter that is related to the strength of the capillary forces exerted by the porous medium. In the approach taken by Philip et al. (1989 [105743], pp. 16–18), the approximation of steady downward flow of water through a homogeneous, isotropic, unsaturated porous medium is used. Far from the cavity, the

flow velocity is spatially uniform. The flow region is considered infinite in extent. These conditions underlie the derivation of Philip's capillary barrier solution. Furthermore, Philip et al. (1989 [105743], Section 1.5, p. 17) note that the requirement for homogeneity is relatively weak. Analytic solutions are generally derived in most cases with simplified descriptions and approximations about the flow domain in the surrounding medium. Results derived from an analytic solution represent effective values. The description, evaluation, and justification of Philip's capillary barrier solution are presented in Section 6.2.2.2.

Braester (1973 [106088]) derived a time-dependent solution for the average volumetric-water-content distribution in a porous medium caused by the water release from a surface source of constant flux. This solution is described and used to estimate the volumetric water content of the fractures in Section 6.2.2.3. The following simplifications were used by Braester (1973 [106088]) to derive the solution. A one-dimensional (1-D) formulation of Richards' equation, which includes both gravity and capillary-driven components of flow, is used to describe flow through an unsaturated porous medium.

The 1-D flow approximation can be evaluated and justified by (1) the weak fracture capillarity values described in Section 6.2.2.2, (2) the roughly 1-D flow paths observed during niche excavation described in Section 6.2.1.2, and (3) the limited spatial spread of seepage fluxes observed during post-excavation seepage tests described in Section 6.2.1.3.1.

The downward translation of a wetted profile is at constant velocity. The average value of the water content at the infiltrating surface over time is used by Braester (1973 [106088], p. 688) to be equal to the average value of water content over the wetted depth. This approximation becomes valid if the solution of water content takes the form of a downward translation of the entire wetted profile at constant velocity. This would generally occur after the capillary forces near the source have diminished, and the volumetric water content at the soil surface reaches its steady-state limit, with the gravity gradient driving the liquid flux. The times needed to reach steady state and the evaluations of this requirement of downward translation of wetted profiles at constant velocity are addressed further in Attachment IV.3.

IV.2 COMPARISON OF LIQUID AND AIR-DERIVED SATURATED HYDRAULIC CONDUCTIVITIES

The liquid-release rate, Q_s, measured during each test (Section 6.2.1.3.1) was converted to a liquid-release flux, q_s, using the following equation:

$$q_s = \frac{Q_s}{A \rho_w} \qquad \text{(Eq. IV.2-1)}$$

where A is the cross-sectional area of flow and ρ_w is the density of water (set at 1.0E+6 g/m^3). The q_s data are tabulated in DTN: LB980001233124.004 [136583] for the seepage tests conducted at Niche 3650 (Niche 2).

The cross-sectional area was derived by the water level that could rise to a maximum elevation of 0.0635 m in the borehole, equal to the maximum ponding depth within the borehole. The ponding depth is controlled by the elevation of the liquid-return line, which prevents the buildup of excess pressure in the test interval by allowing water to flow from the test interval back to the surface. If water rises to the level of the return line, then wetted area A is less than the surface area of the entire test interval and equal to that portion of the curved surface area of a right circular cylinder lying below the water line as follows (Selby 1975 [106143], pp. 12, 16):

$$A = \left[2\pi - \left(2\,\text{Arccosine}\left(d / r\right)\right)\right] h\, r \qquad \text{(Eq. IV.2-2)}$$

where d is equal to the vertical distance from the center of the cylinder to the water line (0.0254 m), r is equal to radius of the borehole (0.0381 m), and h is equal to the test interval length (0.3048 m). With these parameters, the cross-sectional area of flow A is equal to 5.343E-02 m^2.

With the approach described in Attachment IV.1, we estimate the saturated hydraulic conductivity for liquid flow through the fractured porous medium by equating the air permeability (k) derived from the air-injection tests to the water permeability (k_l) of the porous medium. In turn, k_l is related to the saturated hydraulic conductivity (K_l) of a porous medium through the functional relation defined by Darcy's law (Freeze and Cherry 1979 [101173], Equation (2.28), p. 27):

$$K_l = \frac{k_l\, \rho_w g}{\mu} \qquad \text{(Eq. IV.2-3)}$$

where g is the acceleration of gravity and μ is the viscosity of water. Air-permeability values reported in DTN: LB980001233124.004 [136583] were converted to the equivalent saturated hydraulic conductivity values ($K_l \approx K_{air\text{-}sat}$) reported in DTN: LB980901233124.003 [105592] as shown in Scientific Notebook by Wang (1999 [153449], p. 38). This conversion allows us to compare the $K_{air\text{-}sat}$ values to the q_s values, which are also summarized in DTN: LB980901233124.003 [105592]. The q_s values were computed using Equation III-1 and the liquid-release rates (Q_s) from the pre-excavation tests performed at Niche 3566 (Niche 1) and Niche 3650 (Niche 2) (DTN: LB980001233124.004 [136583]), the pre-excavation tests performed at Niche 3107 (Niche 3) and Niche 4788 (Niche 4) (DTN: LB980901233124.003 [105592]), and the post-excavation seepage tests from Niche 3650 (Niche 2) (DTN: LB980001233124.004 [136583]). [1]

Under slightly ponded conditions in the borehole (i.e., saturated conditions), q_s may initially exceed the saturated hydraulic conductivity of the test interval during the early stages of the test. During the later stages of the test, gravity-driven flow will dominate, a unit hydraulic gradient

[1] The entire cross-sectional area of the borehole was used to compute the air-permeability values reported in LB980001233124.002 [136583] because gravitational effects on air are negligible and, thus, the entire cross-sectional area of the borehole is typically available for airflow. A smaller wetted area, as calculated by Equation III-2, was used to compute the liquid-release flux values.

will be established near the borehole wall in the porous material, and q_s will approach K_l for the interval. Based on the approach described in Attachment IV.1, gravity-driven flow is approximated to be the primary flow mechanism operating in fracture systems tested at Niche 3650 (Niche 2). Therefore, one would expect capillary effects to be short-lived, and for all practical purposes the q_s for a given interval should be equal to K_l. Theoretically, q_s can exceed K_l if water ponds to a significant depth or is injected under high pressure, creating a steep hydraulic gradient within the porous material near the borehole wall. However, the packer system used in the seepage tests was designed so that water could not pond more than 0.0635 m; otherwise, return flow to the surface would occur.

Return flow provides direct evidence that the liquid pumping rate exceeded the infiltration capacity of the test interval, implying that $q_s = K_l$, which in turn should equal $K_{air\text{-}sat}$, using the approximation that $K_{air\text{-}sat}$ is a reasonable estimate of K_l. The $K_{air\text{-}sat}$ and q_s values from DTN: LB980901233124.003 [105592] for those tests that exhibited return flow are plotted in Figure III-1, along with a solid line that represents the relation $K_{air\text{-}sat} = K_l = q_s$. A data point located above the solid line indicates that $K_{air\text{-}sat} > K_l$, and a data point below the solid line indicates that $K_{air\text{-}sat} < K_l$. One would expect the data values to fall on the $K_{air\text{-}sat} = q_s$ line if air-permeability and liquid-release tests are directly correlated.

Figure IV.2-1 indicates that the data points are equally distributed above and below the $K_{air\text{-}sat} = q_s$ line, with the majority of points falling within a factor of 10 of $K_{air\text{-}sat} = q_s$. Therefore, the equivalent saturated hydraulic conductivity derived from the air-injection tests appears to approximately characterize the saturated hydraulic conductivity represented by q_s. The scattering of the individual data points around the line is a measure of the simplifying estimations, approximations, and experimental uncertainties in relating air-flow processes with liquid-flow processes.

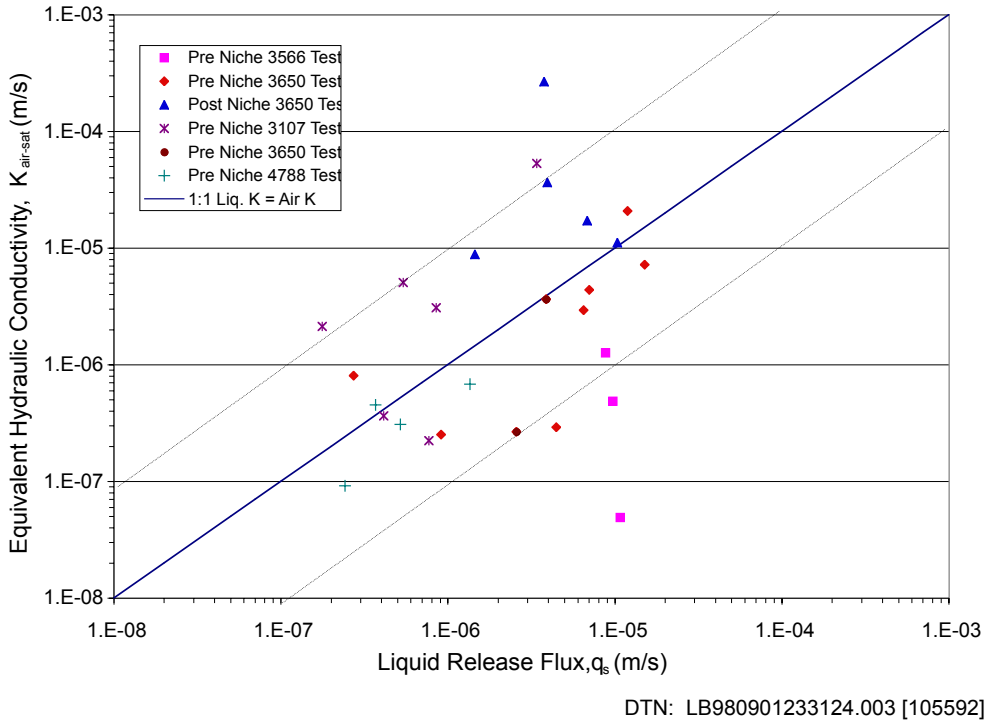

Figure IV.2-1. Comparison of Liquid and Air-Derived Saturated Hydraulic Conductivities

IV.3 WATER-CONTENT PROFILE EVALUATION

IV.3.1 EVALUATION OF APPROXIMATION OF ONE-DIMENSIONAL (1-D) FLOW

Large α-values calculated in Section 6.2.2.2 indicate that gravity-driven flow predominates in the fractures tested at Niche 3650 (Niche 2). Although the large α-values in themselves do not collectively imply that flow is strictly 1-D, they do imply limited lateral spreading of the wetting front in the fractures, because capillary forces will probably be negligible during the early stages of liquid release. Once the wetting front arrives at the niche ceiling, however, capillary forces become very important as water saturations begin to increase because of the capillary barrier, resulting in water being diverted laterally around the cavity. Therefore, flow will change from 1-D to 2-D or 3-D once the wetting front arrives at the ceiling. This implies that the θ_{ave} values calculated using Braester's model are no longer valid after the wetting front arrives at the niche ceiling.

Field observations made during the pre-excavation liquid release and post-excavation seepage tests provide stronger evidence that flow is roughly 1-D. Examination of Figure 6.2.1-2 described in Section 6.2.1.2 for the pre-excavation liquid-release tests shows that the average aspect ratio (i.e., depth to lateral distance traveled by the wetting front) is slightly less than 2 for the tests representing fracture networks and about 4.5 for the high-angle fracture data. This implies that for a 0.65 m travel distance, we would expect lateral spreading to be on average within 0.32 m of the borehole for the fractured network case and within 0.15 m for the near-vertical fracture case. The mean angle of wetting-front migration is only 26° from the vertical (Arctan(0.32/0.65)). This analysis is supported further by two field observations made during the post-excavation seepage tests as described in Section 6.2.1.3.1: (1) the majority of water was typically captured in only one or two 0.305 × 0.305 m cells located directly beneath the test interval; (2) the wetting front typically arrived at the niche ceiling directly below the test zone.

IV.3.2 EVALUATION OF APPROXIMATION OF DOWNWARD TRANSLATION OF THE WETTED PROFILE AT CONSTANT VELOCITY

Earth scientists and engineers have recognized for a number of years that during infiltration tests, the liquid-release rate approaches an asymptotic value equal to the hydraulic conductivity as time progresses. And in fact, steady moisture conditions are obtained rather rapidly in the vicinity of the source, typically with geometric mean of 1.7 hr when water is introduced at a water potential equal to or greater than zero (White and Sully 1987 [106152], pp. 1514, 1521). In our case, water is introduced at a flux that is often much lower than the saturated hydraulic conductivity of the fractured interval and, therefore, reliance on generalities such as those in the preceding sentence may not be appropriate. Instead, the solution developed for unsteady multidimensional infiltration by Philip (1986 [106133], p. 1725) and summarized by White and Sully (1987 [106152], p. 1521) is used herein to determine the time to steady moisture conditions. In this manner, we will check the validity of the approach in Attachment IV.1 on downward translation of wetting profile at constant velocity, and determine whether the volumetric water contents presented in Section 6.2.2.3 are derived using an appropriate model.

Philip (1986 [106133]) developed an analytical solution for unsteady 2-D unsaturated flow from a buried horizontal cylinder into an infinite porous medium with uniform initial water content θ_n. We approximate that this solution is also valid for flow through unsaturated, fractured media. Richards' equation was linearized with a constant D and the exponential relation between hydraulic conductivity and water potential, given by Equation 6.2.2-2 in Section 6.2.2.2. Philip (1986 [106133], p. 1719) found that regardless of the cavity shape and dimensionality of the flow field, the solution is approximately reducible to the product of the steady solution (ϑ_∞) and a function of dimensionless time (t_D) and radial coordinates (r_D dimensionless radius, $0 \le \varphi \le \pi$ polar angle) as follows:

$$\vartheta(r_D, \varphi; s; t_D) \approx G(r_D; s; t_D)\, \vartheta_\infty(r_D, \varphi; s; \infty) = G(r_D; s; t_D)\, \vartheta_\infty \qquad \text{(Eq. IV.3-1)}$$

Philip (1986 [106133]) defines ϑ, r_D, and t_D, by Equation (15), G by Equation (29), ϑ_∞ by Equation (62), and φ in Section 4 in his paper on flow from a buried horizontal cylinder. Equation IV-1 is valid for large s (the dimensionless characteristic cavity length defined by Equation 6.2.2-3 in Section 6.2.2.2) and for any value of t_D.

The significance of Equation IV.3-1 is that the function G ranges in value from 0 to 1. This implies that at large dimensional times (corresponding to large t_D), the unsteady solution approaches the steady solution ($G \rightarrow 1$). Using the same approach employed by Philip (1986 [106133], Section 8, p. 1725) for a spherical source, we computed the time to obtain 95% of the steady-state moisture conditions ($t_{D\ 95\%}$) for flow from a buried horizontal cylinder at a radial distance that is slightly larger than the borehole ($r_D = 1.1$) and at radial distance to the niche ceiling ($r_D = 17.1 = 0.65$ m / 0.0381 m). The details of the analysis can be found in Scientific Notebook YMP-LBNL-JSW-6c (Wang 1999 [153449], pp. 85–91) and the $t_{D\ 95\%}$ values are tabulated in DTN: LB980901233124.003 [105592] for each group of tests where seepage was observed.

The dimensional time ($t_{95\%}$) at which the moisture profile reaches 95% of its steady value can be calculated using $t_{D\ 95\%}$ (Philip 1986 [106133], Equation (15), p. 1718). Again, the details of the analysis can be found in Scientific Notebook by Wang (1999 [153449], pp. 91–92) and the $t_{95\%}$ values are tabulated in Table IV.3-1 and DTN: LB980901233124.003 [105592], along with the arrival time of the wetting front at the niche ceiling.

Examination of the $t_{95\%}$ values in Table IV.3-1 indicates that for all the tests, steady-state moisture conditions (i.e., constant θ) are reached near the borehole wall within 6 minutes (344 s) of starting the test and before pumping ceased (pumping times are tabulated in DTN: LB980001233124.004 [136583]). This demonstrates the original point of this discussion, that approximation for downward translation of wetting profile at constant velocity is valid. That is, q_s approached the unsaturated hydraulic conductivity of the fractured media, resulting in the downward migration of the wetted profile at a constant velocity within the time limit of each test. In addition, it is important to note that in all cases, steady-state moisture conditions are obtained near the borehole prior to the arrival of the wetting front. After the wetting front arrives at the ceiling, the moisture conditions will begin to change again near the release borehole as the water saturation increases because of the capillary barrier. Based on this analysis, the use of Equation

6.2.2-7 in Section 6.2.2.3 to estimate the change of volumetric water contents appears to be reasonable.

Table IV.3-1. Time to Steady-State Moisture Conditions

Borehole	Test Name	Test Date	Test Interval (m)	Time to Steady State[1]		Wetting Front[2] Arrival Time (hr)
				r_D = 1.1 (hr)	r_D = 17.1 (hr)	
Fracture Networks						
UR	Test #1 1-15-98	1/15/98	4.88-5.18	0.0129	0.691	0.497
	Test #1 2-6-98	2/6/98	4.88-5.18	0.0317	1.696	1.221
UL	Test #1 12-10-97	12/10/97	7.01-7.32	0.0012	0.127	0.067
	Test #1 1-6-98	1/6/98	7.01-7.32	0.0160	1.740	0.914
UR	Test #1 1-14-98	1/14/98	4.27-4.57	0.0200	1.580	0.936
	Test #1 2-5-98	2/5/98	4.27-4.57	0.0590	4.650	2.753
UM	Test 5 Niche 3650	11/13/97	4.27-4.57	0.0030	0.163	0.116
	Test 5 Niche 3650	12/3/97	4.27-4.57	0.0072	0.396	0.280
	Test #2 12-3-97	12/3/97	4.27-4.57	0.0037	0.202	0.143
	Test #1 1-7-98	1/7/98	4.27-4.57	0.0630	3.458	2.448
	Test #2 2-10-98	2/10/98	4.27-4.57	0.0957	5.249	3.715
UM	Test 4 Niche 3650	11/13/97	5.49-5.79	0.0014	0.088	0.058
	Test #2 12-4-97	12/4/97	5.49-5.79	0.0028	0.178	0.117
	Test #1 1-9-98	1/9/98	5.49-5.79	0.0186	1.164	0.764
	Test #1 2-11-98	2/11/98	5.49-5.79	0.0684	4.289	2.814
UR	Test #2 1-13-98	1/13/98	5.49-5.79	0.0005	0.527	0.150
	Test #2 2-10-98	2/10/98	5.49-5.79	0.0002	0.224	0.064
Individual or Small Groups of Vertical Fractures						
UM	Test 1 Niche 3650	11/12/97	4.88-5.18	0.0007	0.051	0.050
	Test #1 12-4-97	12/4/97	4.88-5.18	0.0011	0.085	0.083
	Test #2 12-5-97	12/5/97	4.88-5.18	0.0035	0.272	0.264
	Test #1 1-8-98	1/8/98	4.88-5.18	0.0225	1.729	1.683
	Test #1 3-6-98	3/6/98	4.88-5.18	0.0807	6.189	6.025
UR	Test #1 1-13-98	1/13/98	6.71-7.01	0.0018	0.122	0.116
	Test #1 2-3-98	2/3/98	6.71-7.01	0.0027	0.184	0.174
	Test #1 3-5-98	3/5/98	6.71-7.01	0.0195	1.307	1.238
UL	Test #2 1-6-98	1/6/98	7.62-7.92	0.0029	0.201	0.192
	Test #1 2-12-98	2/12/98	7.62-7.92	0.0024	0.166	0.158
	Test #1 3-4-98	3/4/98	7.62-7.92	0.0111	0.761	0.725
UR	Test #2 1-14-98	1/14/98	6.10-6.40	0.0030	0.267	0.267
	Test #1 2-4-98	2/4/98	6.10-6.40	0.0116	1.046	1.043

DTNs: [1] LB980901233124.003 [105592], [2] LB980001233124.004 [136583]

INTENTIONALLY LEFT BLANK

ATTACHMENT V

LABORATORY MEASUREMENTS OF RETARDATION AND FRONT SEPARATION

Attachment V is referred to in Section 6.3.1.2 on tracer migration test, in Section 6.4.1 on penetration of dyes into rocks, in Section 6.4.2.1 on dye retardation factor determined by front separation, and in Section 6.4.3 on chemical transport and sorption.

INTENTIONALLY LEFT BLANK

ATTACHMENT V—LABORATORY MEASUREMENTS OF RETARDATION AND FRONT SEPARATION

Laboratory analyses are described for dyed samples collected from the niches and core samples for tracer retardation and front separation measurements.

V.1 WATER IMBIBITION

Rock cores, 5.08 cm in diameter and 2.0 cm in length, were used for the imbibition experiments to examine tracer penetration into the unsaturated rock matrix. Cores were cut and machined from a clean sample block from the same stratigraphic unit as the niche locations where tracer release tests were conducted. Porosity, bulk-density and particle-density measurements were based on the core dry weight at a temperature of 60°C.

Partial saturation of cores was obtained by equilibrating cores within relative humidity chambers controlled by different saturated brines and/or water until they reached constant weights. Cores with two different levels of initial water saturation S_w, approximately 15% and 80%, were used in this work to investigate and compare tracer penetration behavior with respect to saturation levels.

The core was hung inside a humidity-controlled chamber, with the core bottom submerged in a water reservoir containing tracers to a depth of about 1 mm. The core weight gain was continuously recorded by a data acquisition system. This study was designed to simulate the imbibition and penetration of tracers into the matrix from a continuously flowing fracture, modeled here as the core bottom. After a predetermined period of time (about 16–20 hrs), the core was lifted out of the reservoir, and the moisture front was routinely examined. Rock sampling was immediately conducted as described below. The water contained about 10 g/L LiBr, 1 g/L FD&C Blue No. 1, and 1g/l Sulpho Rhodamine B. These tracers were selected to compare the behavior of nonreactive bromide with the dyes used in the field tracer work.

V.2 ROCK SAMPLING AND TRACER EXTRACTION

Tracer-stained rock samples were drilled, drill cuttings eluted, and the supernatant analyzed to profile tracer location and concentration. A mill (Bridgeport Series II) (Hu 1999 [156540], pp. 37–38) was used for drilling, with the rock sample firmly stabilized on the working platform and the rock surface covered with tape except for the location to be drilled. A series of drills of different sizes with flat-bottom, carbide-end mill cutters were used to sample different depths from the same location. The largest drill was used for the drilling at the rock surface, and the size gradually decreased with increased drilling depth to minimize carry-over powder contamination from previous depths. A tube was placed around the carbide-end mill cutter to reduce powder loss and to maximize sample recovery. The drilling was carried out slowly and steadily in 1 mm increments, as indicated by a digital caliper (Mitutoyo, precision 0.01 mm).

Drill cuttings were collected at each 1 mm interval using a stainless steel needle attached to a stainless steel filter holder, connected to a vacuum source. The vacuum intensity was tested and adjusted before actual sample collection. Two pieces of cellulose nitrate membrane (with the membrane pore size of 0.45 μm) were used inside the filter holder to trap the sample powder.

The powder was suctioned and trapped into the collection device by pointing the needle to the drilled hole and applying the vacuum. Collected cuttings were transferred to an amber-glass vial before tracer extraction. Before drilling the next interval, the drilled hole was cleaned using an air stream just strong enough to remove any powder that might be left from the collection, and the cutter was cleaned with premoistened wipes and dried with a gentle air stream.

Samples of dye-stained rocks having a flat face were selected for rock drilling. Three samples were identified as suitable for this work. The flat surfaces with dye stains were approximated to be fracture surfaces of active flow paths induced by dye-water releases. For these three samples, no visible fracture coatings were observed.

Sampling of cylinder-shaped machined cores for the laboratory studies was performed from both the top and bottom of the core, first from the cleaner top (i.e., core side not in physical contact with liquid) to 16 mm, then from the bottom to 10 mm. This sampling scheme allows a comparison and evaluation of powder contamination of the drilling method. Drilling from the two sides was conducted so that the drill holes did not intersect each other.

Dye tracers were extracted from the drill cuttings into the aqueous phase by mixing 5 mL Nanopure water with 0.1 g of powder sample, mixing nominally for 15 seconds at the speed of 1,400 rpm. The mixture was then filtered, and the concentration of the tracer in the clear aqueous phase was measured. Either Gelman Supor® hydrophilic polyethersulfone membrane filter or Whatman cellulose nitrate membrane was used for the filtration. Testing showed negligible mass loss to both membranes for FD&C Blue No. 1 and Sulpho Rhodamine B.

Extraction efficiency was evaluated by spiking a known amount of tracers into the rock powder (<104 μm) for one day. The results show the extraction efficiency of 98.0 ± 4.6% (average plus and minus standard deviation, 5 replicates) for bromide, 94.1 ± 3.8% for FD&C Blue No. 1 (6 replicates), and 55.2 ± 0.7% for Sulpho Rhodamine B (7 replicates). The extraction procedure was not designed to be exhaustive for the maximum mass extraction. Relative comparisons with identical procedures were used in this study.

V.3 MEASUREMENT OF AQUEOUS TRACER CONCENTRATION

The aqueous concentration of FD&C Blue No. 1 dye was measured using a UV/vis Spectrophotometer (Hitachi, Model U-2001) at the characteristic wavelength of 630 nm. Sulpho Rhodamine B concentration was measured using a Spectrofluorophotometer (Shimadzu, Model RF-1501) at the excitation wavelength of 565 nm and emission wavelength of 590 nm. Depending upon the tracer concentration present in the samples, samples were diluted appropriately until the final solution measurement fell into the linear range of the calibration curve. Bromide concentration was measured by Ion Specific Electrode (Orion, Ionplus design) with the addition of an ion strength adjuster having a volume ratio of 50:1. Background levels for all tracers were measured with powders from clean tuff samples. The clean powder was obtained from a clean rock sample that was crushed for size reduction to pass through a 104 μm opening sieve, similar to the powder size of the drill cuttings. Refer to the associated scientific notebook pages, Hu (1999 [156540], pp. 20–22, 37–48, 54, 68–82, 86–99, and 103–126), Hu (1999 [156541], pp. 9, 27, 42, 77, 118, 123–140, and 149), and Hu (1999 [156542], pp. 13, 17–25, 39–

41, 51–102, and 105–112), for detailed entries about instrument calibration and tracer measurements.

V.4 EVALUATION OF DRILLING TECHNIQUE

Tracer cross-contamination during drilling was evaluated by drilling from both the top and bottom for machined cores. For both drilling directions, measured tracer concentration are compared over distance in Figure V-1 (for Core D with lower initial water saturation $S_{w)}$ and Figure V-2 (for Core H with high initial S_w). Note that the core bottom was the core side in physical contact with the tracer solution. For the lower S_w case, the tracer concentration is comparable for both drilling directions, showing no significant powder carryover (Figures V-1a and V-1b). A slight difference at the 4–5 mm interval is observed in Figure V-1b for Sulpho Rhodamine B. This difference could be real, since the fluorometer used for measurement had a low detection limit of about 0.021 mg/kg. Overall, the drilling technique yielded reliable concentration profile results.

For the case with the higher initial S_w, the difference in measured concentration from the two drilling directions is noticeable (Figure V-2a). After the tracer-rock contact and experiments were completed, the drilling was conducted first from the core top (cleaner side), then from the bottom after the core was inverted. Nominally, it took about 1 hour to finish drilling and sample collection for 10 depth intervals. The difference in concentrations shown in Figure V-2a for the two drilling directions may result from any or a combination of (1) gravitational flow during the second drilling phase, (2) heterogeneity, (3) flow resulting from exposure to the atmosphere, (4) evaporation loss resulting from heating caused by drilling. The spreading of tracer front at the high initial S_w makes the flow redistribution effects more pronounced than the case with sharp tracer front at low initial S_w. For Sulpho Rhodamine B, the difference is less evident (Figure V-2b). Results from the core top were utilized if the data were available.

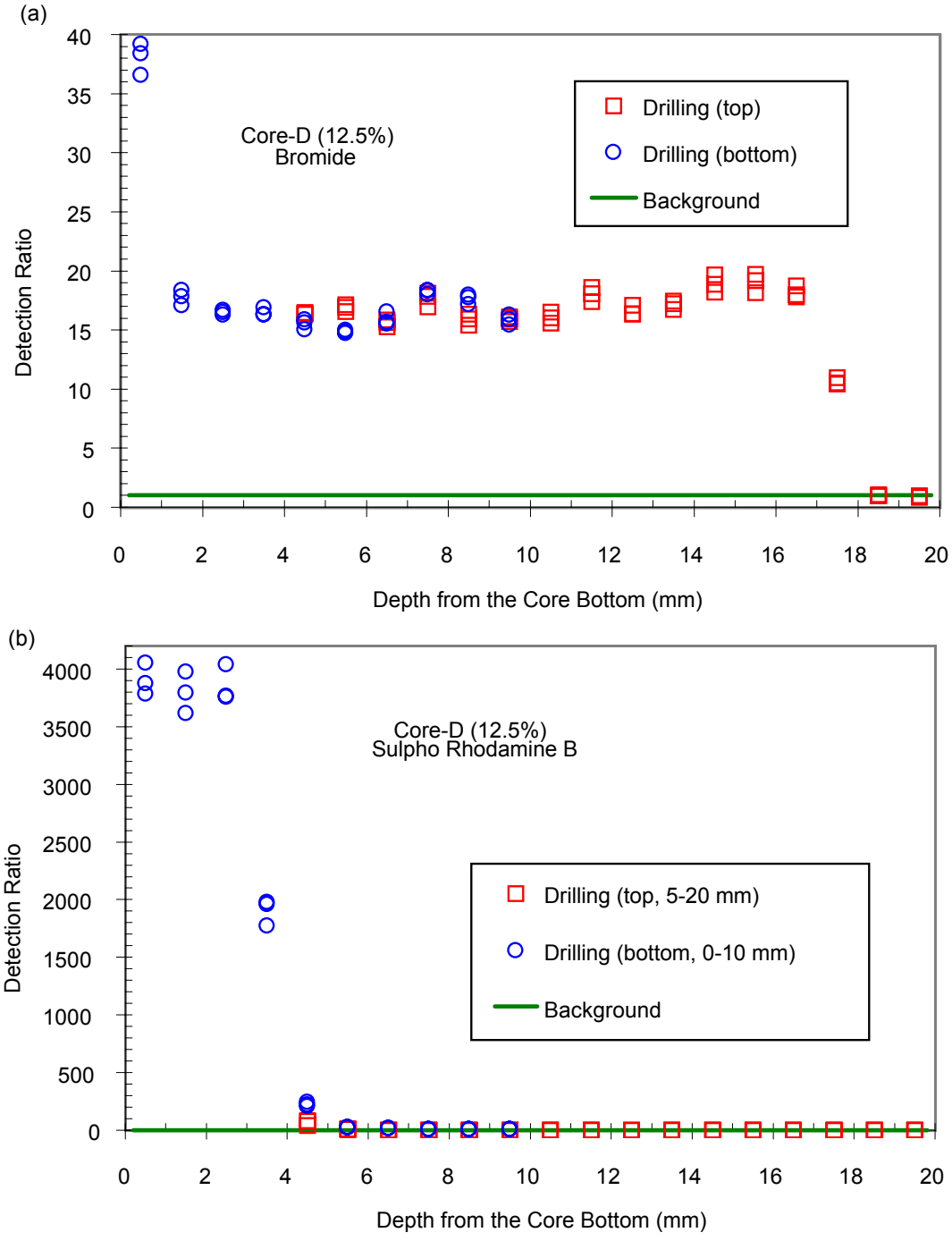

DTN: LB990901233124.003 [155690]

NOTE: The core ID and the initial core saturation (in parentheses) are presented in the figures.

Figure V-1. Comparison of Measured Detection Ratio from the Opposite Drilling Directions for Core D with Lower Initial S_w: (a) Bromide, (b) Sulpho Rhodamine B

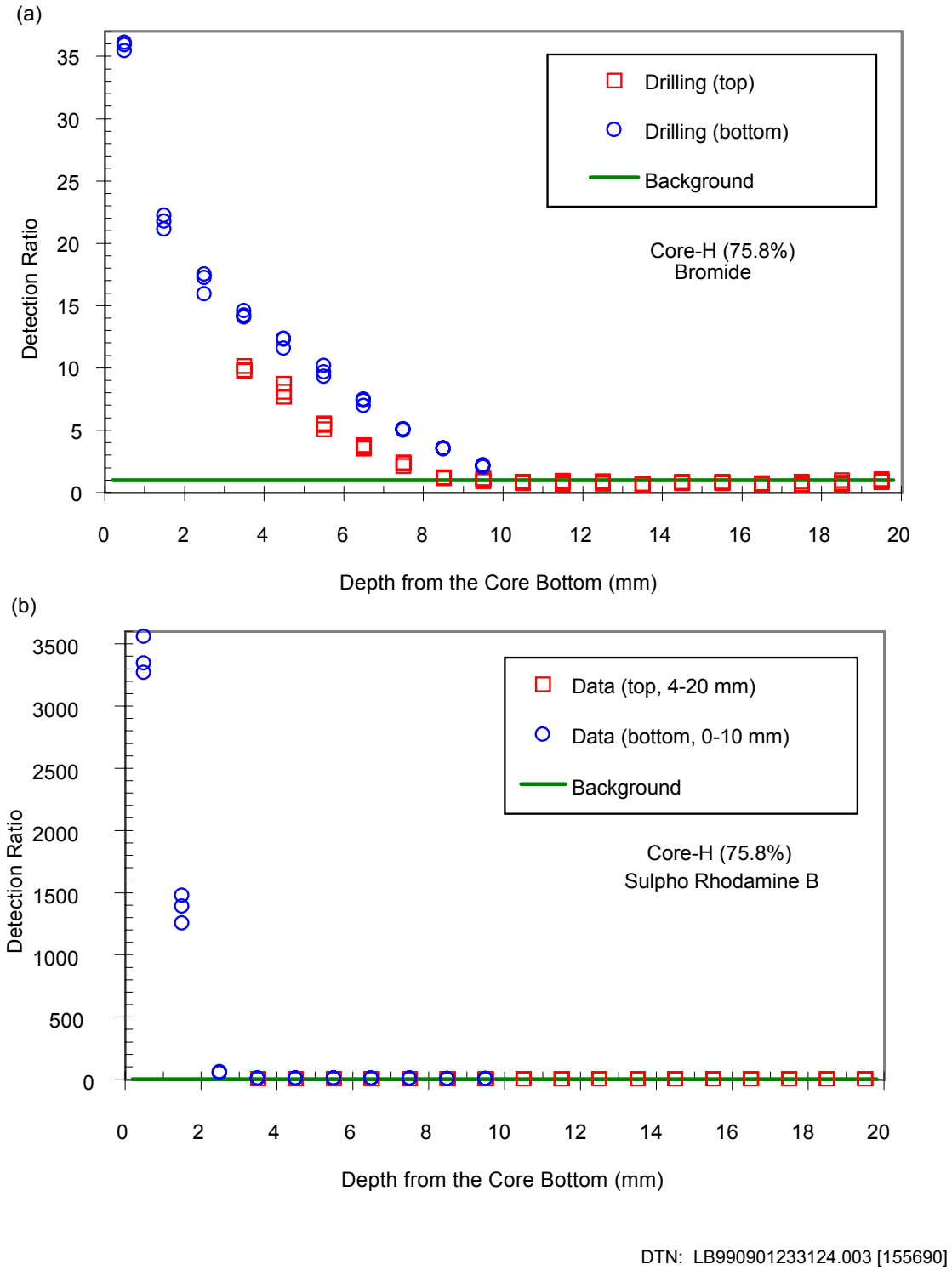

DTN: LB990901233124.003 [155690]

Figure V-2. Comparison of Measured Detection Ratio from the Opposite Drilling Directions for Core H with Higher Initial S_w: (a) Bromide, (b) Sulpho Rhodamine B

INTENTIONALLY LEFT BLANK

ATTACHMENT VI

FIELD EQUIPMENT FOR CONTROLLED WATER RELEASE, WETTING-FRONT DETECTION, AND SEEPAGE COLLECTION

Attachment VI is referred to in Section 6.6.1.2 on instrumentation used in the fracture-matrix interaction test at Alcove 6, and in Section 6.7.1.2 on instrumentation used in fault and matrix tests at Alcove 4. Attachment Section VI.1 on fluid injection is referred to in Section 6.6.1.3 on liquid release experiments. Attachment Section VI.2 is referred to in Section 6.7.1.2.2 on borehole monitoring.

INTENTIONALLY LEFT BLANK

ATTACHMENT VI—FIELD EQUIPMENT FOR CONTROLLED WATER RELEASE, WETTING-FRONT DETECTION, AND SEEPAGE COLLECTION

Equipment for controlled release of water into isolated zones, borehole monitoring for changes in saturation and water potential, and collection of seepage in an excavated slot are presented for the new instruments developed for this field investigation of fracture flow and fracture matrix interaction.

During this time period, five sets of data were submitted to the Technical Database Management System (TDMS) to fulfill scheduling and planning document requirements. Three of the data sets, including LB0207NICH5LIQ.001 [160408], LB0209NICH5LIQ.001 [160796], and LB0211NICH5LIQ.001 [160792], contain native data files (in comma-delimited ASCII format) and are summarized in Table 6.2.1-4. The remaining data sets, including LB0208NICH5LIQ.001 [161210] and LB0210NICH5LIQ.001 [161211], contained preliminary data and were subsequently superseded by LB0209NICH5LIQ.001 [160796] and LB0211NICH5LIQ.001 [160792], respectively. Table 6.2.1-4 also identifies the scientific notebook pages pertinent to each test, which provide test-specific details, including the serial number and location of instruments and sensors used during the experiment, and test operating conditions. Copies of the pertinent scientific notebook pages were reviewed and sent to the YMP Records Processing Center for inclusion in the project records.

The name of the native electronic files containing the test data generated using the data acquisition equipment and software identified in Sections 6.2.1.3.5.2. and 6.2.1.3.5.2. are listed in the table. Test data files consist of four types. Three of these types include the suffix "…(seep)," "…(smass)," and "…(srate)" in their filename. These files contain the seepage percentage, seep mass, and seepage rate data, respectively, from individual capture compartments draining seepage water to the capture balance(s) during the test (Figure 6.2.1-19 and Figure 6.2.1-20). These files were generated using the software routine "Auto pinch valve box.vi V.1.0" (LBNL 2002 [161227]). The remaining test files that do not contain these suffixes in the filename (e.g., "Test#1_BH#2_21-22_ft_5-6-02.csv") contain the cumulative mass and rate of water released (Balance 1), returned (Balance 2), and the total seepage captured (Balance 3 and/or 4) during a given experiment. These files were generated using the software routine "Mettler Quad Scale 8-23-01.vi V2.0" (LBNL 2002 [161230]), which recorded the mass on the Mettler Toledo balances used during the experiments. As noted in Section 6.2.1.3.5.3, after 7/15/02, only one balance was used to measure seepage into the niche (i.e., Balance 3) and Balance 4 was used to measure evaporation.

VI.1 FLUID INJECTION

The liquid-release experiments required water to be injected into the formation over a 0.3 m zone in the borehole under constant-head or constant-rate conditions. The constant-head tests were conducted first to determine the maximum rates at which the zone could take in water. The subsequent set of experiments required that water be released to the formation at predetermined rates ranging from ~ 5 mL/min to ~ 100 mL/min. Both the constant-head method and the constant-rate method of injection were incorporated in the fluid-release apparatus. The main components of the fluid-release apparatus included an inflatable packer system for isolating the

injection zone, a pump for delivering water, and a reservoir for providing a continuous supply of water (Figure VI-1a).

The inflation packer system consisted of two rubber packers, each 0.60 m long, connected to an inflation line (Figure VI-1b). Two stainless tubes (0.95 cm and 0.31 cm ID) passed through one of the packers to provide fluid (air and water) access into the injection zone. The 0.95 cm tube was used to deliver fluid into the injection zone, while the 0.31 cm tube was used as a siphon to remove excess water from the injection zone. Before liquid was released into the formation, the packer system was located to straddle the zone of interest (determined from air-permeability measurements) and then inflated to a pressure of ~200 kPa. The 0.95 cm ID stainless steel tube was then connected to a water supply line from a constant-head or a constant-rate system. During the entire period of injection, pressure in the inflation packers was continuously monitored to ensure that the injection zone remained isolated from adjacent zones of the borehole.

To capture the temporal variability in vertical flux of water from the injection zone, an automated liquid-release system was developed. This system allowed for continuous measurement of local liquid-release rates. The unit consisted of a storage tank (~4.5 liters) for water supply to a clear-acrylic, constant-head chamber. The chamber, 0.15 m ID and 0.30 m tall, served to maintain a constant head of water above the liquid-release surface within the injection zone (Figure VI-1c). The head maintenance was achieved with a level switch that activated the pump when the water level dropped below the control level. The control level was nominally set at or slightly above the elevation of the horizontal injection borehole. Two pressure transducers continuously recorded the height of water in each tank. A pulse damper was installed between the pump and tank to reduce any pulsating effects (caused by the pump) from migrating to the storage tank and influencing the pressure readings.

The constant-rate injection system included all the components used in the constant-head system without the constant-head chamber. To allow for easy regulation of flow rates in the field, the pump was calibrated before field deployment to relate flow rates with displayed numbers on a 10-turn speed control. In the field, the speed control was set at the desired flow rate before the pump was activated. The actual flow rate was determined from transducers located at the bottom of the water reservoir. A data acquisition system was used to record changes in head of water (water level) in the reservoir.

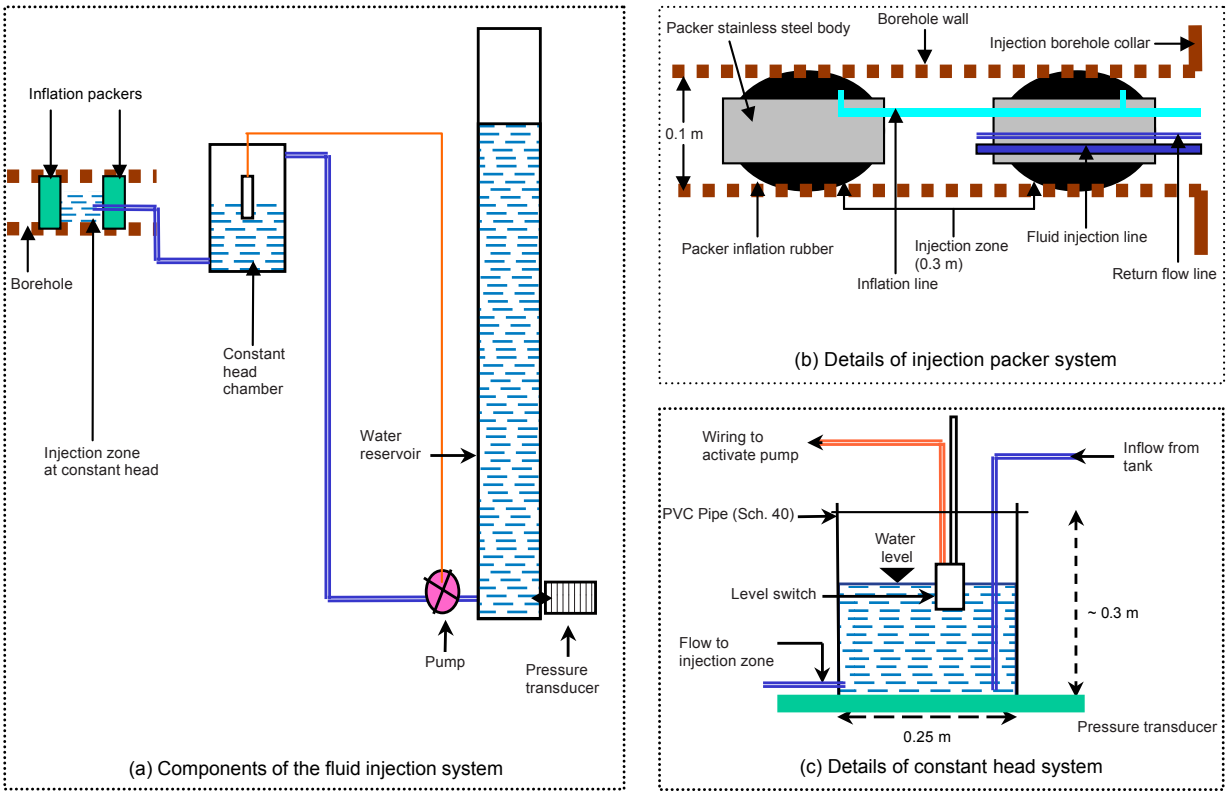

Figure VI-1. Schematic Illustration of Liquid Release System for Constant-Head and Constant-Rate Injections

VI.2 BOREHOLE MONITORING

In three monitoring boreholes (B, C, and D in Figure 6.6.1-1), changes in saturation and water potential were measured continuously during the entire field investigation. Changes in saturation were measured with electrical-resistivity probes (ERPs) located at 0.25 m intervals along the 6.0 m length of each borehole. These ERPs consisted of two electrical leads sandwiched between pieces of filter paper. Water-potential measurements were made with psychrometers. With the multiplexing capabilities of the data logger (model CR7, Campbell Scientific Inc.), hourly measurements of up to 80 psychrometers (model PST-55, Wescor Inc.) were automated. The chromel-constantan junction in the psychrometer was cooled with an electric current to a temperature below dew point to first induce condensation, followed by evaporation without electric current. Temperature depression resulting from evaporation was recorded and used to determine water potentials in the vicinity of the psychrometers.

The psychrometers and ERP were housed in borehole sensor trays (BSTs), installed along the length of each monitoring borehole (Figure VI-2a). The BSTs were fabricated from 0.10 m outside diameter (OD) PVC pipes, 3.0 m in section length. Each pipe section was cut lengthwise to produce a 0.075 m wide curved tray (Figure VI-2b). On each tray, psychrometers were installed at 0.5 m intervals along the borehole while ERPs were located at 0.25 m intervals (Figures VI-2b and VI-2c). BST housing permitted immediate contact between ERPs and the

borehole wall. The psychrometers were installed inside small cavities (0.005 m in diameter) perforated through the BST wall to measure water potentials of the rock. A steel spoon, 3.0 m long with the same configuration as the trays, was used to guide each BST to the assigned location along the borehole. Two BSTs were located along each section of borehole, one in contact with the top of the borehole and the other with the bottom. Each pair of BSTs was separated by a wedge that pressed the BSTs tight against the borehole wall. The double BST configuration improved the contacts between ERPs with the borehole wall and allowed two sensors, one on the upper BST and one on the lower BST, to detect wetting-front advances at each given location along the borehole.

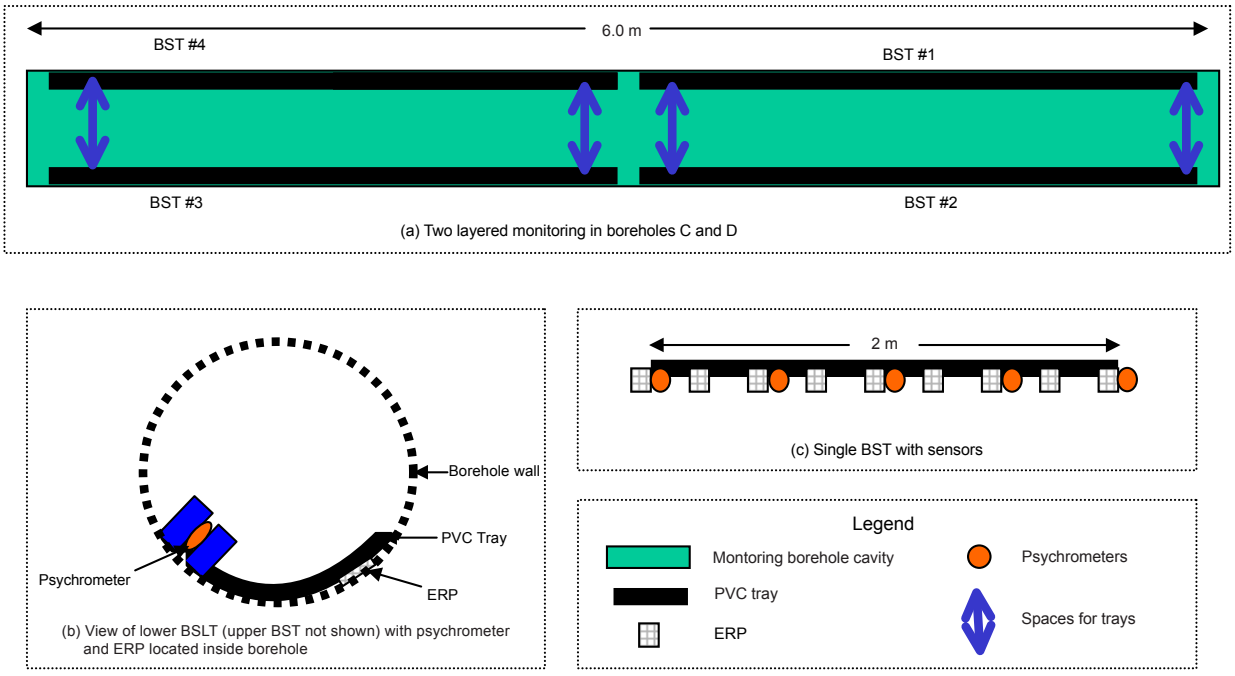

Figure VI-2. Schematic Illustration of Borehole Monitoring System

VI.3 SEEPAGE COLLECTION

To measure water seeping into the slot following liquid release into the injection borehole, a water collection system was designed to capture seepage from the slot ceiling (Figure VI-3). Design of this system was dictated by the slot geometry and locations of 'I' beam supports. A row of stainless steel trays was fabricated for each of the four accessible compartments between the I-beams. Each tray was an inverted pyramid 0.46 m long and 0.40 m wide and tapered to a single point 0.20 m from the top. For each compartment, seven trays were assembled along a single steel frame, allowing for easy installation inside the slot. Water captured in the stainless steel trays was transferred into clear PVC collection bottles (0.076 m ID, 0.45 m tall). Water falling onto the trays was drained to the collection bottles through Teflon tubes (0.635 cm OD). An intermittent vacuum was applied to the collection bottles such that water stored on the trays or in Teflon tubes could be sucked into the collection bottles. The amounts of seepage water in

the collection bottles were periodically recorded with sampling intervals determined in the field by the rates observed.

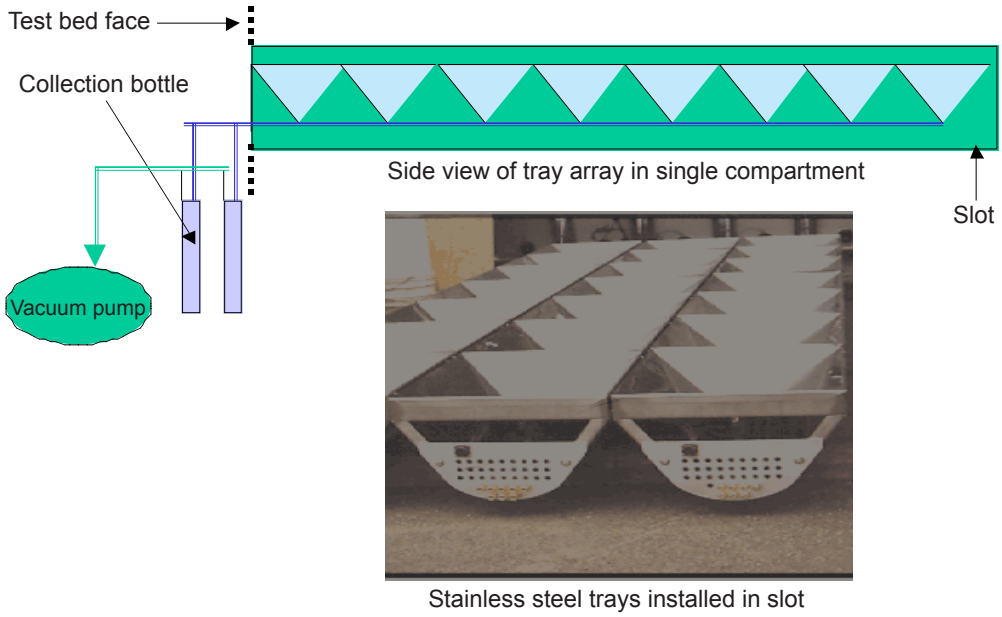

Figure VI-3. Schematic Illustration of Water Collection System Installed in Slot

INTENTIONALLY LEFT BLANK

ATTACHMENT VII

MEASUREMENT OF WATER POTENTIAL USING PSYCHROMETERS

Attachment VII is referred to in Section 6.8 on water-potential measurements in niches.

INTENTIONALLY LEFT BLANK

ATTACHMENT VII—MEASUREMENT OF WATER POTENTIAL USING PSYCHROMETERS

Prior to field use, all psychrometers were calibrated in the laboratory, using potassium chloride solutions (0.1–1.0 molal or mole of solute per 1,000 grams of solvent). A second calibration was done in the laboratory after psychrometers had been used for field measurements, if feasible and practical. During the calibration procedure, psychrometers were isolated in an insulated box to minimize temperature fluctuations. Automated measurements were then made using the multiplexing capabilities of the CR7 data logger. When the psychrometers were observed to have reached equilibrium, they were removed from the calibration solution, washed in distilled water, air-dried, and immersed in the next solution. After calibrations were completed, all psychrometers were washed and air-dried before installation in the field.

During laboratory calibrations and preliminary field measurements, the shape of the psychrometer output curve was significantly influenced by the size of the cooling voltage and cooling duration for a given water potential (Figure VII-1). This curve was also dramatically altered when the psychrometers became contaminated with dust particles (Figure VII-2). Given the high rate of failure of psychrometers in the field, it was therefore important to optimize both the cooling voltage and duration for a given water potential to help identify psychrometers that were contaminated or otherwise malfunctioning. Optimization was accomplished by increasing the cooling voltage and/or increasing the time over which the cooling voltage was applied until a well-defined plateau resulted for the psychrometer output. Data from contaminated or malfunctioning psychrometers are not for interpretation and are labeled as such in Salve (1999 [156552], pp. 103–152).

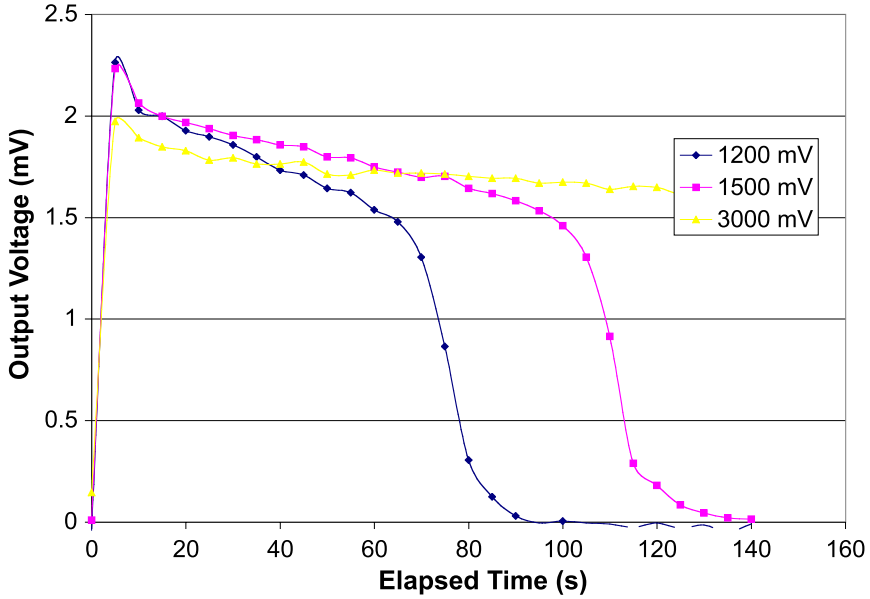

DTN: LB980001233124.001 [105800]

Figure VII-1. Effect of Cooling Current on Psychrometer Output Curve (PSY-732)

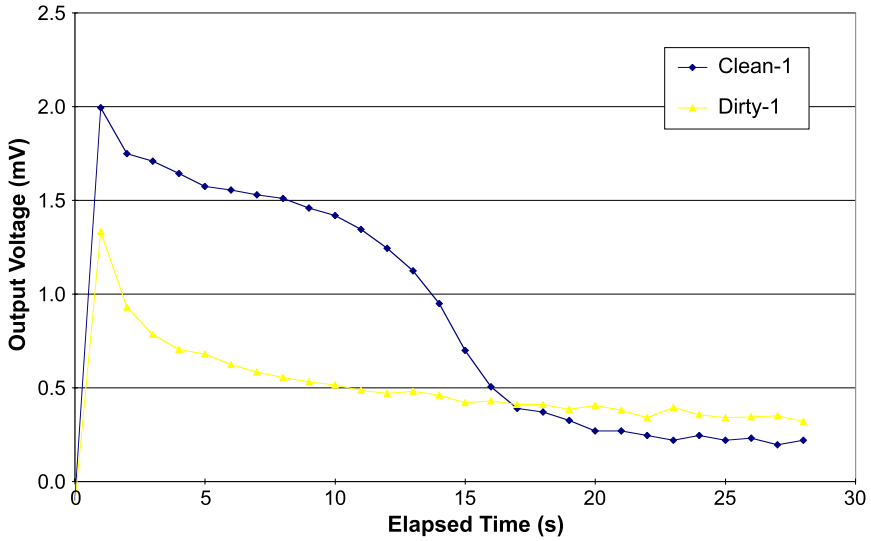

DTN: LB980001233124.001 [105800]

Figure VII-2. Effect of Dust Coating on Psychrometer Output Curve (PSY-731)

ATTACHMENT VIII

GEOLOGY, MINERALOGY, AND HYDROLOGICAL PROPERTIES—BUSTED BUTTE APPLICABILITY

INTENTIONALLY LEFT BLANK

ATTACHMENT VIII—GEOLOGY, MINERALOGY, AND HYDROLOGICAL PROPERTIES—BUSTED BUTTE APPLICABILITY

The selection of southeastern Busted Butte, 8 km southeast of the repository area at Yucca Mountain, to site a field test facility was based on a presumption that the test results could be appropriately used in numerical studies of flow and transport in the Calico Hills Formation at Yucca Mountain (Bussod et al. 1999 [155695], p. 2). The presumption of applicability relies on the equivalence of stratigraphic units at Busted Butte and Yucca Mountain.

The Calico Hills section at southeastern Busted Butte, a thin distal residue of deposits, cannot completely represent the variability of the Calico Hills Formation below the nuclear waste repository. Because of this limitation, it is important to know more specifically what portion of the Calico Hills section occurs in the test facility. Existing and new data are examined here to document the extent of lithostratigraphic correspondence between the Busted Butte and Yucca Mountain sections. These studies focus on the portion of the Busted Butte section where tracer tests have been conducted.

VIII.1 Geology of the Busted Butte Test Facility

Busted Butte is a small (2.5 km by 1 km) north-trending mountain block primarily made up of thick, ignimbrite deposits of the Paintbrush Group. This fault-block uplift is bound by northeast- and north-trending normal faults, and it is split by a north-trending down-to-the-west normal fault that gives Busted Butte its distinctive appearance. The test facility is located within a small (300 to 350 m wide) horst on the southeast side of Busted Butte. Geological units exposed in the vicinity of the test facility include, in ascending stratigraphic order: the Wahmonie Formation, the Calico Hills Formation, and the Topopah Spring Tuff (Figure VIII-1). The test facility is constructed in the Topopah Spring Tuff and the Calico Hills Formation. The Wahmonie Formation, which is not present below the repository, is also absent from the UZTT test block itself.

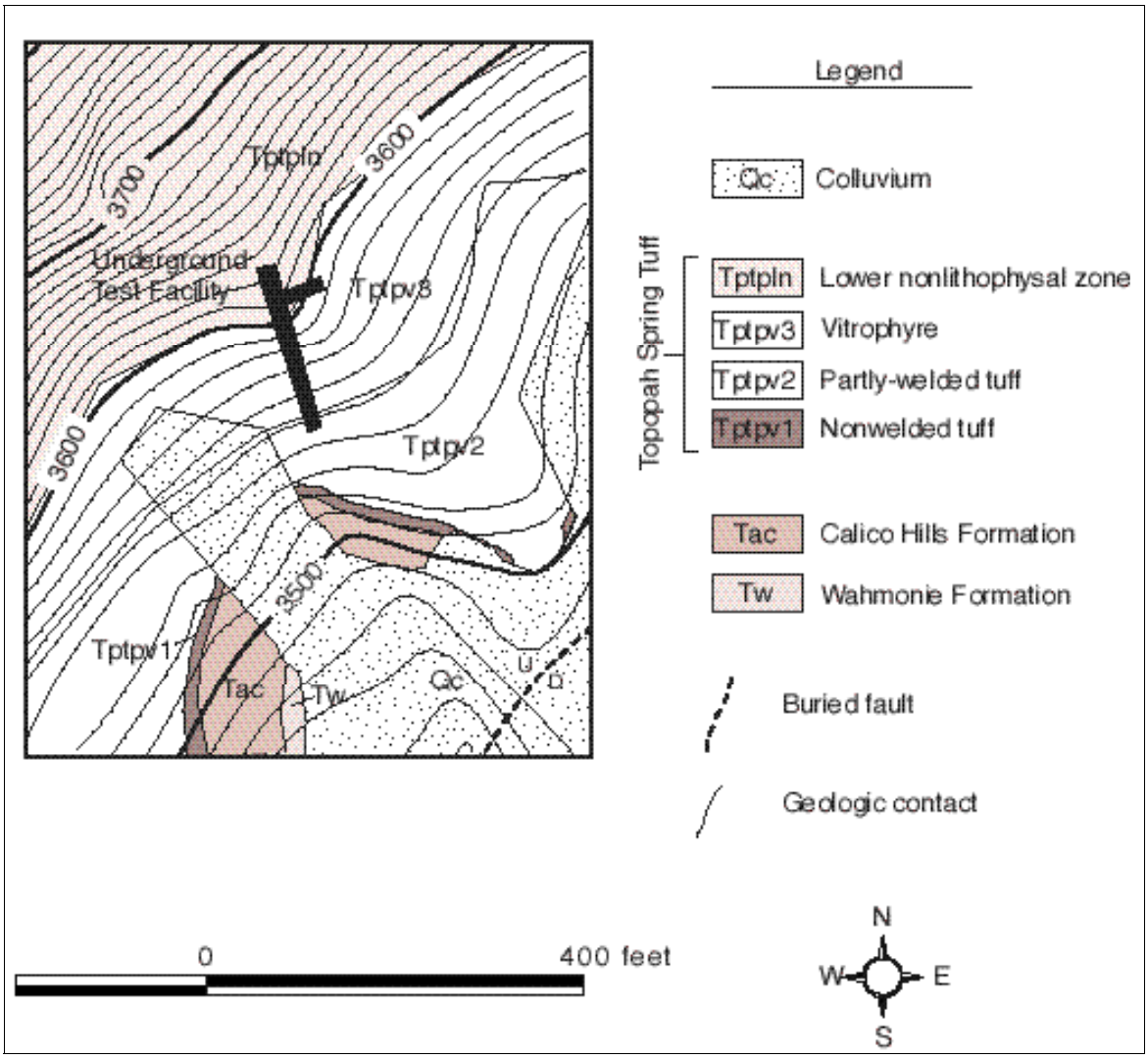

N/A - For illustration purposes only

NOTE: The plot is a geologic map of the area around the underground test facility in the southeastern part of Busted Butte. The contour interval is 10 feet. The tunnel entrance is at the southern end of the facility.

Figure VIII-1. Busted Butte Geologic Map (CRWMS M&O 2001 [154024], Figure 44)

VIII.2 Stratigraphic Setting of Busted Butte

The stratigraphic succession at Busted Butte was originally mapped by Lipman and McKay (1965 [104158]), who recognized the widespread principal units of the Paintbrush Group and small local exposures of underlying nonwelded tuffs not attributed to specific formations (undivided tuffs, Tt, according to their nomenclature). Broxton et al. (1993 [107386], pp. 6, 9) assigned the nonwelded tuffs to the Calico Hills Formation, the Wahmonie Formation, and the Prow Pass Tuff in order of increasing age and depth. This report follows the stratigraphic assignments of Broxton et al. (1993 [107386]), but all of the stratigraphic nomenclature has been updated from the original sources to the usage of Sawyer et al. (1994 [100075], Table 1).

The Calico Hills, Wahmonie, and Prow Pass tuffs were derived from different volcanic centers (Sawyer et al. 1994 [100075], Table 1). The pattern of decreasing unit thickness from north to south along Yucca Mountain (Moyer and Geslin 1995 [101269], Figure 3) is consistent with derivation of the Calico Hills pyroclastic material from an eruptive center north of the mountain (Sawyer et al. 1994 [100075], p. 1307). Thickness of the Calico Hills tuff decreases over a distance of about 13 km from more than 947.7 ft (288.86 m) at the northern end of Yucca Mountain (Moyer and Geslin 1995 [101269], Figure 3) to 21 ft (6.40 m) at the southeastern Busted Butte outcrop adjacent to the flow-and-transport test facility (Broxton et al. 1993 [107386], p. 9). At Raven Canyon, about 15 km southwest of Busted Butte, the Calico Hills Formation is absent and the Paintbrush Tuff rests on the Wahmonie Formation (Peterman et al. 1993 [106498], Figure 2).

VIII.3 Lithology of the Calico Hills Formation

The predominant rock types of the Calico Hills Formation in the Yucca Mountain area are an upper section of ash-flow and air-fall tuffs and a lower section of bedded tuffs and sandstones (Moyer and Geslin 1995 [101269], p. 5). All of these rocks originally consisted predominantly of glassy pyroclasts (volcanic ash, shards, and pumice clasts that formed as the lava was erupted and fragmented). The rocks also contained smaller amounts of phenocrysts (crystals from the lava) and lithic inclusions (crystalline or glassy rock fragments).

In the northeastern portion of the Yucca Mountain region, the glassy constituents of the Calico Hills tuffs have been altered to a mixture of zeolites (mostly clinoptilolite), smectite clay, and secondary silica. The Calico Hills Formation in the southeastern and southwestern Yucca Mountain region (including Busted Butte) remains mostly glassy, although some intervals contain appreciable amounts of smectite, clinoptilolite, and other secondary minerals. The areal distribution of zeolitic Calico Hills tuff is depicted in CRWMS M&O (2000 [138960], Figures 14 to 18). Areas of low zeolite content in the cited figures generally show where the tuff is vitric.

VIII.4 Criteria of Unit Identification

Positive recognition of the units depends heavily on observing the entire stratigraphic sequence in drill core or outcrop and identifying the distinctive contacts (boundaries) between adjacent units (Moyer and Geslin 1995 [101269], pp. 50–51). Moyer and Geslin (1995 [101269], pp. 5–8) also define typical values for color and for phenocryst content, lithic grains, and pumice clasts associated with each unit. Their summaries of chemical and mineralogic/petrographic data show that the data for some of these parameters, taken alone, are sufficient only to distinguish the upper ash flow/air fall tuff section from the lower bedded tuff and sandstone. Within the ash flow/air fall section, however, the phenocryst data do not reliably distinguish among units 3, 4, and 5 because of the large overlaps in parameter-value populations (e.g., Moyer and Geslin 1995 [101269], Figures 4 and 5).

Drill hole USW GU-3 is the fully cored hole closest to Busted Butte. It is also the source of the only drill core studied by Moyer and Geslin (1995 [101269]) in which the Calico Hills section is vitric, like the section at Busted Butte. Unit identification in this hole was considered very ambiguous by Moyer and Geslin (1995 [101269], pp. 8–9), due to poor core recovery of the vitric Calico Hills interval. The main problem in making unit identifications in the Calico Hills section of drill core USW GU-3 is that contacts are missing because of incomplete core recovery.

Moyer and Geslin (1995 [101269], pp. 8–9) tentatively recognized unit 3 and underlying bedded tuffs in this core, but did not rule out the presence of additional units. The absence of well-supported unit correlations in USW GU-3, along with a paucity of data from other drill sites where the Calico Hills Formation is vitric, increases the difficulty of comparison between Busted Butte and Yucca Mountain based solely on existing data.

The identification of lithostratigraphic units at southeastern Busted Butte is based on a combination of characteristics common to other locations where the units are exposed. Moyer and Geslin (1995 [101269], pp. 8, 10) noted lithologic similarities between the Calico Hills section exposed at Busted Butte and the USW GU-3 section, especially the presence of black, perlitic-glass lithic clasts [glass chunks with distinctive rounded surfaces, described by Moyer and Geslin (1995 [101269], p. 8) as "black obsidian" or "obsidian lithic clasts"]. The restricted occurrence of these clasts was considered a basis for identification and intersite correlation of unit 3 by Moyer and Geslin (1995 [101269], p. 8). They did not have much data to support this interpretation because such data could only come from locations where the perlite clasts have escaped zeolitic alteration. At the time their report was produced, the USW GU-3 and USW UZ-14 cores were the only sources of data for the vitric or partly vitric Calico Hills Formation.

As a follow-up to the observations and interpretations of Moyer and Geslin (1995 [101269]), new petrographic data on rock color, lithic-clast content, and black perlitic-clast content were collected for a vertical suite of samples from the Busted Butte test facility. Comparable data were collected for drill-hole samples from USW GU-3, USW H-5, and USW SD-12, all holes with predominantly vitric Calico Hills sections. These data are used to document the comparison of Calico Hills sections between Busted Butte and Yucca Mountain.

VIII.5 Evaluation of Petrographic Parameters

Because Moyer and Geslin (1995 [101269], pp. 8, 10) proposed that the Busted Butte section represents unit 3, efforts reported here concentrated on collection and evaluation of data most useful to distinguish unit 3 from other units of the Calico Hills Formation, particularly the adjacent units 2 and 4. Given that the Busted Butte section appears to contain only one pyroclastic-flow unit, the identification of that unit must be based on observable petrographic parameters without recourse to examination of the contacts of a multi-unit sequence. The parameters deemed to have the most characteristic values for unit 3 are the total lithic-clast content and the presence of black perlitic lithic clasts. Moyer and Geslin (1995 [101269], pp. 6 to 7) found that the lithic-clast content of unit 3 is in the range of 5 to 10% (excluding localized zones of higher concentration), higher than the ranges of 1 to 5% in units 2 and 4. New information on lithic-clast content in vitric Calico Hills tuff is presented in VIII-2. In keeping with the presumed usage of Moyer and Geslin (1995 [101269], p. 8), the lithic-clast abundances determined for this study include both crystalline and vitric lithic clasts. This usage differs from some published data (e.g., Broxton et al. 1993 [107386], p. 43) that include only crystalline clasts in the lithic-abundance determination.

Moyer and Geslin (1995 [101269], p. 8) believed that the black perlitic lithic clasts might be unique to unit 3, but had few data to support this interpretation. For this criterion to be used with confidence at Busted Butte, it should be supported by data from additional sites. Table 2 summarizes new observations of black perlitic clast distribution in vitric Calico Hills tuff, taken

from samples on hand. The table also contains new matrix-color data for vitric samples only. Moyer and Geslin (1995 [101269], pp. 5, 6, 8, 51) consider color a useful factor to help distinguish units. Most of their color observations are for zeolitized tuffs that may differ in color from unaltered tuffs of equivalent stratigraphic position.

Lithic clast content: Lithic-clast content may be the consistently most useful discriminant to identify unit 3 within a vertical sequence of samples where more than one unit is present. The data suite for USW SD-12 (VIII-1) defines an interval in the middle of the Calico Hills Formation with lithic-clast content of 5 to 10%.

Black, perlitic clast content: The distribution of black perlitic clasts in USW SD-12 is reasonably, but not perfectly, congruent with the interval containing 5 to 10% total lithic clasts (VIII-1). Data for the smaller sample suites from drill holes USW GU-3 and USW H-5 also suggest a correspondence between black perlite occurrence and total lithic-clast content characteristic of unit 3. The existence of samples without black perlite clasts—bedded tuff below the perlite interval in USW GU-3 and USW SD-12 and the tuff section above the perlite interval in USW SD-12—confirms that black perlite content can be used to discriminate among units.

Color: The color data for predominantly vitric Calico Hills samples show some similarities to the colors of zeolitic tuff in unit 3, although the zeolitic tuff is more likely to have yellow or orange tints (Moyer and Geslin 1995 [101269], p. 51). The data also indicate that color alone is not a useful interunit discriminant in every case. For example, the data for USW SD-12 show little difference between the unit 3 samples and samples inferred to be from overlying unit 4. In contrast, the USW GU-3 suite shows a reliable color difference between the orange pink of unit 3 and the yellowish brown of the underlying bedded tuff.

The 2 m section of uppermost Calico Hills tuff in the Busted Butte test facility shares the two most characteristic lithologic attributes of unit 3: lithic-clast content in the 5–10% range and the presence of black perlitic clasts. Note that the observations for drill-hole samples, intended to confirm the applicability of Moyer and Geslin's (1995 [101269]) unit-discrimination criteria to vitric tuff, were derived from small suites of discrete samples. To achieve greater certainty of unit identification, it would be desirable to make a direct examination of the entire vitric Calico Hills section, complete with contacts, in drill core USW SD-12.

VIII. 6 Stratigraphy and Mineralogy of the Busted Butte Test Facility

Busted Butte is a small (2.5 km by 1 km) mountain block primarily made up of ignimbrite deposits of the Paintbrush Group. This fault-block uplift is bounded by northeast- and north-trending normal faults, and it is split by a north-trending down-to-the-west normal fault that gives Busted Butte its distinctive appearance. Tuff units generally have dips less than 10° except where affected by drag near large faults. Small exposures of older volcanic units, including the Calico Hills Formation, Wahmonie Formation, and Prow Pass Tuff, occur near the base of the butte on the north and southeast sides (Broxton et al. 1993 [107386], pp. 5–10).

The test facility is located within a small horst on the southeast side of Busted Butte. The horst is 300 to 350 m wide and is bounded by the down-to-the-west Paintbrush Canyon fault on the west and by a down-to-the-east splay of the Busted Butte fault on the east (Scott and Bonk 1984

[104181]). Geologic units exposed in the vicinity of the test facility include, in order of ascending position and decreasing age, the Wahmonie Formation, the Calico Hills Formation, and the Topopah Spring Tuff. The test facility is constructed in the Topopah Spring Tuff and the Calico Hills Formation.

Brief descriptions of the formal and informal lithologic units in the underground test facility, with emphasis on the Phase 2 test block, are given below. A representative stratigraphic and lithologic section is shown in Figure VIII-2. Characterization of the lithologic units was accomplished by examining and sampling the walls of the test block, by examination of drill core collected before and during the test, and by studying and sampling the mineback faces excavated into the test block following completion of the test. All color descriptions are based on the Munsell system (Geological Society of America 1995 [105787]). Descriptions and nomenclature of subunits within the Calico Hills Formation are strictly informal usage. We have followed the criteria of Buesch et al. (1996 [100106]) for definition and recognition of lithologic zones within the Topopah Spring Tuff. Because lithologic zones were used to define numerical model units, it was necessary to replace the gradational transitions between the zones with no-thickness boundaries. The rationale and consequences of this substitution are discussed below.

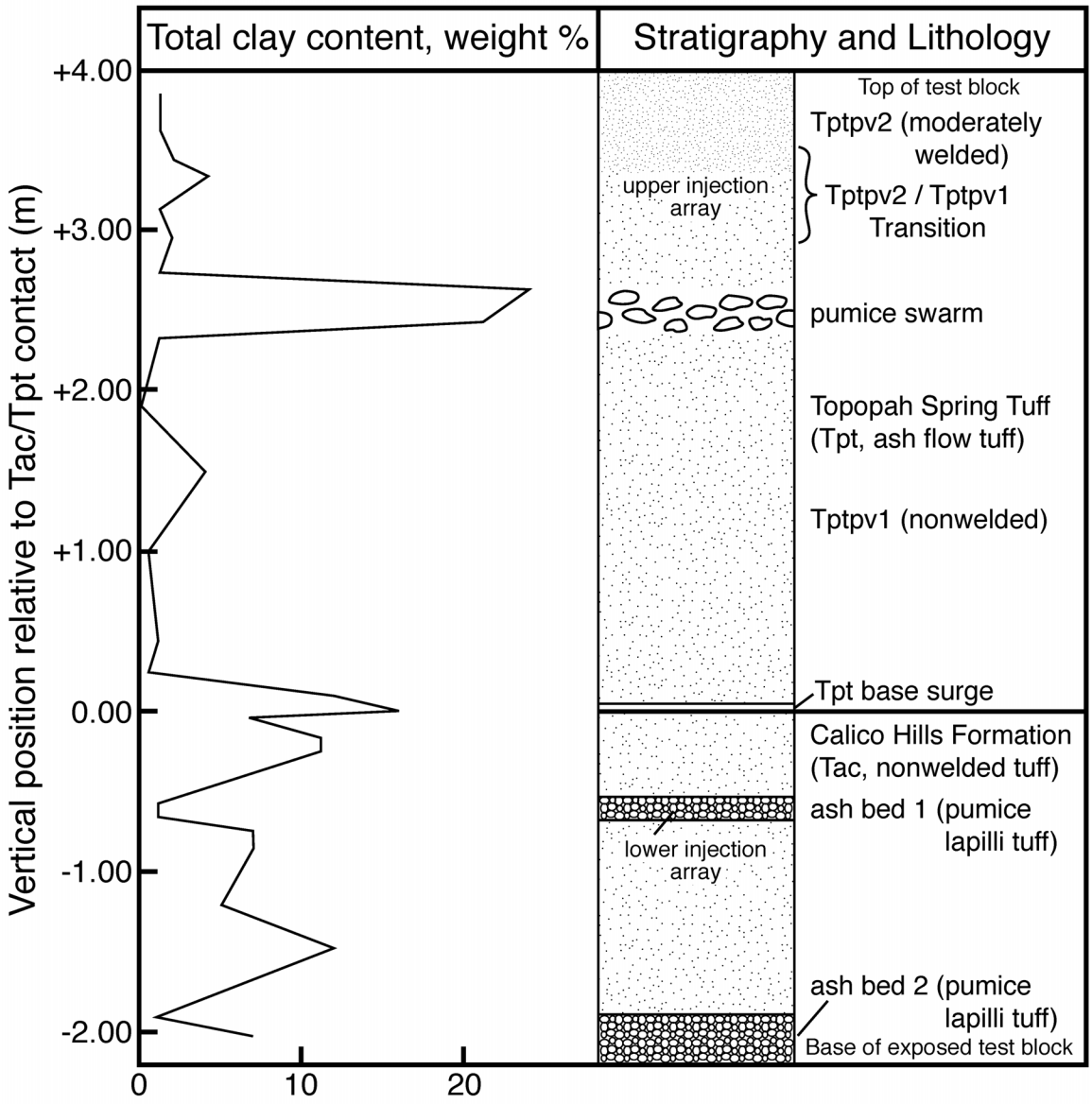

DTN: LA0204SL831372.001 [164749]

Figure VIII-2. Stratigraphy and Clay Content of the Phase 2 Test Block

Calico Hills Formation

A little more than 2 m of Calico Hills Formation (Tac) is exposed in the test area of the facility in the lower walls of both the main adit and the test alcove. The exposed unit consists predominantly of light brown (5YR 6/4), nonwelded vitric tuffs. Fine ash (particles less than one millimeter) is the principal constituent of the tuffs. Other constituents include varicolored crystalline lithic grains and glass chunks (5 to 25% by volume), feldspar, quartz, and biotite phenocrysts (5 to 10%), and pumice lapilli of centimeter size or less (≤ 5%). The tuff is uncemented, but variable cohesion is provided by the clay alteration described below.

Interspersed with the light brown tuffs are two beds of pumice-lapilli tuff, each about 20 cm thick. The upper layer is known informally as "ash bed 1," "ash layer 1," or "ash 1" and the lower layer is known as "ash bed 2," "ash layer 2," or "ash 2." Neither bed is composed principally of ash, but the names have gained sufficient currency within the field-test project that they are retained here. Ash bed 1 is pinkish gray (5YR 8/1), nonwelded, and vitric. Amorphous opal cement comprises about 5% of the tuff and contributes to its resistant, cohesive character.

Topopah Spring Tuff

Buesch et al. (1996 [100106], pp. 43–44) defined the crystal-poor vitric zone (Tptpv) in the lowermost Topopah Spring Tuff (Tpt) and subdivided it into three subzones distinguished by a downward decrease in degree of welding (compaction through viscous flow of the glassy components as the tuff cooled). The two lower subzones are present in the Phase 2 test block. The moderately welded subzone (Tptpv2), as described by Buesch et al. (1996 [100106], p. 44), has moderately to strongly deformed pumice clasts in a moderately welded matrix. Near-vertical fractures are present. The nonwelded subzone below (Tptpv1) is characterized by partially to nondeformed pumice clasts in a partially welded to nonwelded matrix.

At Busted Butte, there is no bedded tuff between the base of the Topopah Spring Tuff and the underlying Calico Hills Formation comparable to the 2 m thick unit observed in drill core by Scott and Castellanos (1984 [101291], p. 101). The lowermost part of the Topopah Spring Tuff, included within Tptpv1, is a base surge deposit up to about seven centimeters thick and resting directly on the Tac. The base surge is finely laminated on a millimeter scale and contains well aligned pumice lapilli (≤ 2 cm across, elongations ≤ 4:1) and black glass chunks in a matrix of vitric ash.

The Tptpv1 contains many texturally distinctive layers, although none is so well defined as the beds in the underlying Tac. Layers may be defined by concentrations or sizes of pumice lapilli, by the presence of abundant vitric shards, or similar characteristics. A mixed pumice population, indicated by variations in color, size, flattening, and alteration, is present in the upper portion of the Tptpv1 and in the Tptpv2. Heterogeneity of layering is absent from the Tptpv2 in the test block.

Defining the Tptpv1/Tptpv2 Boundary

The boundary between the two subzones can be gradational across a 0.5–2 m thick vertical interval (Buesch et al. 1996 [100106], p. 44). It is important to note that the subzones are defined

on the basis of a syngenetic property—the degree of welding—rather than on depositional criteria. Within the context of the Busted Butte flow and transport test, the Tptpv1/Tptpv2 boundary is important as a marker separating two hydrogeologic modeling units that are defined to correspond to the lithologic subzones described above. The boundary must therefore be defined as a discrete surface suitable for numerical modeling, rather than as a gradational transition. The challenge is to determine whether consistent and significant hydrogeologic differences exist between the two subzones, and then to correlate the location of the hydrogeologic change with well defined, mappable lithologic changes. This is an iterative process that was accomplished satisfactorily for test purposes, but without resolving the geological uncertainties.

Lithologic criteria for distinguishing Tptpv2 and Tptpv1 subzones could not be applied uniformly throughout the test block. For example, one criterion was the presence of vertical cooling joints in the Tptpv2 that terminated at the boundary with Tptpv1. This was a useful criterion for mapping the boundary within the Phase 2 test alcove, but the first mineback faces were devoid of similar fractures in what was otherwise recognizable as Tptpv2. In the last two mineback faces, joints were present, but the joint terminations had been extended downward due to tectonic modification.

The chief recognition criterion for the Tptpv1/Tptpv2 boundary in the Phase 2 mineback was the uppermost occurrence of undeformed, subequant, vitric pumice lapilli up to about 10 cm across. For the first seven mineback faces, the boundary defined on this basis is at essentially the same elevation as the boundary mapped on the test alcove injection face. Between Face 7 and Face 8, the boundary rises about 0.6 m in a westerly direction, whereas the boundary mapped on the injection face remains level. No attempt has been made to investigate the differences, and both sets of data have been accepted for modeling purposes.

The ambiguities described above have led to minor inconsistencies in defining the boundary for modeling purposes and in selection of samples for properties characterization. The modeled boundary surface is slightly more irregular because of the inconsistencies. Three samples designated as Tptpv1/Tptpv2 in Table VIII-1 span an approximately 40 cm vertical range of identified boundary locations, based on different criteria for defining the boundary. This range may be taken as an estimate of the uncertainty in boundary location due to differing criteria at any particular location within the Phase 2 block.

Table VIII-1. Mineralogy of the Busted Butte Phase 2 Test Block (weight percent)

LANL number	SPC number	Vertical position relative to Tpt/Tac contact (m)	Stratigraphic/ Lithologic designation	Smectite	Kaolinite	Quartz	Cristobalite	Feldspar	Hematite	Amorphous	Mica	Cryptomelane	Total
3692,p1	575100	+3.86	Tptpv2	n.d.	1(1)	n.d.	n.d.	2(1)	n.d.	97(1)	n.d.	n.d.	100(1)
3693,p1	575101	+3.64	Tptpv2	trace	1(1)	1(1)	n.d.	1(1)	n.d.	97(2)	n.d.	n.d.	100(2)
3693,p2	575101	+3.44	Tptpv2	trace	2(1)	trace	n.d.	2(1)	n.d.	96(1)	n.d.	n.d.	100(1)
3594,p1	525159	+3.40	Tptpv2	3(1)	1(1)	trace	n.d.	1(1)	n.d.	95(2)	trace	n.d.	100(2)
3695,p1	575103	+3.15	Tptpv1/Tptpv2	n.d.	1(1)	n.d.	trace?	1(1)	n.d.	98(1)	n.d.	n.d.	100(1)
3593,p2	525158	+3.00	Tptpv1/Tptpv2	trace	2(1)	trace	n.d.	2(1)	trace	96(1)	trace	n.d.	100(1)
3593,p1	525158	+2.80	Tptpv1/Tptpv2	trace	1(1)	n.d.	n.d.	2(1)	n.d.	97(1)	trace	n.d.	100(1)
3698,p1	575106	+2.65	Tptpv1	11(3)	13(3)	1(1)	n.d.	5(1)	trace	70(4)	n.d.	n.d.	100(4)
3699,p1	575107	+2.44	Tptpv1	13(4)	8(2)	trace	n.d.	4(1)	trace	75(5)	n.d.	n.d.	100(5)
3699,p2	575107	+2.36	Tptpv1	n.d.	1(1)	n.d.	n.d.	3(1)	trace	96(1)	trace	n.d.	100(1)
3702,p1	575110	+1.92	Tptpv1	n.d.	n.d.	trace	trace	1(1)	trace	99(1)	trace	n.d.	100(1)
3591,p1	525156	+1.65	Tptpv1	2(1)	1(1)	trace	n.d.	2(1)	trace	95(2)	trace	n.d.	100(2)
3589,p1	525154	+1.55	Tptpv1	3(1)	1(1)	trace	n.d.	2(1)	n.d.	94(2)	trace	n.d.	100(2)
3707,p1	575115	+1.00	Tptpv1	trace	n.d.	trace	trace	2(1)	trace	98(1)	trace	n.d.	100(1)
3582,p1	525147	+0.45	Tptpv1	1(1)	n.d.	trace	n.d.	1(1)	trace	98(1)	trace	n.d.	100(1)
3583,p1	525148	+0.25	Tptpv1	trace	n.d.	trace	trace	2(1)	trace	98(1)	trace	n.d.	100(1)
3583,p2	525148	+0.10	Tptpv1	12(4)	n.d.	trace	trace	3(1)	trace	85(4)	trace	n.d.	100(4)
3583,p3	525148	+0.01	Tpt, base surge	16(5)	n.d.	3(1)	1(1)	6(1)	trace	74(5)	trace	n.d.	100(5)
3584,p1	525149	-0.01	Tac	7(2)	n.d.	3(1)	1(1)	9(1)	trace	80(3)	trace	n.d.	100(3)
3584,p2	525149	-0.15	Tac	11(3)	n.d.	3(1)	1(1)	8(1)	1(1)	76(4)	trace	n.d.	100(4)
3587,p1	525152	-0.25	Tac	11(3)	n.d.	4(1)	1(1)	8(1)	trace	76(3)	trace	n.d.	100(3)
3585,p1	525150	-0.57	Tac, ash bed 1	1(1)	n.d.	6(1)	trace	11(2)	trace	82(2)	trace	n.d.	100(2)
3585,p2	525150	-0.65	Tac, ash bed 1	1(1)	n.d.	4(1)	1(1)	13(2)	trace	81(3)	trace	n.d.	100(3)
3585,p3	525150	-0.72	Tac	7(2)	n.d.	4(1)	1(1)	11(2)	trace	77(3)	trace	n.d.	100(3)
3586,p1	525151	-0.83	Tac	7(2)	n.d.	5(1)	1(1)	11(2)	trace	76(3)	trace	n.d.	100(3)
3598,p1	527826	-1.20	Tac	5(2)	n.d.	4(1)	1(1)	10(1)	trace	80(3)	trace	n.d.	100(3)
3598,p2	527826	-1.45	Tac	12(4)	n.d.	5(1)	1(1)	11(2)	trace	71(5)	trace	n.d.	100(5)
3596,p1	527827	-1.87	Tac, ash bed 2	1(1)	n.d.	5(1)	1(1)	9(1)	n.d.	84(2)	trace	5*	100(2)
3596,p2	527827	-2.07	Tac, ash bed 2	7(2)	n.d.	6(1)	1(1)	10(1)	n.d.	76(3)	trace	n.d.	100(3)

DTN: LA0204SL831372.001 [164749]

NOTES: LANL number is an internal tracking number assigned to mineralogy-petrology samples. SPC number is the number used by the Sample Management Facility to identify and track samples.

Tptpv1 = Topopah Spring Tuff crystal-poor vitric zone, nonwelded subzone. Tptpv2 = Topopah Spring Tuff crystal-poor vitric zone, moderately welded subzone. Tpt = Topopah Spring Tuff.

Tac = Calico Hills Formation. Ash beds 1 and 2, also known as ash layers 1 and 2, are informally designated layers of pumice-lapilli tuff.

Estimated 2-sigma errors are in parentheses

trace = less than 0.5 weight percent, queried ("?") where presence of phase is uncertain. n.d. = not detected.

Cristobalite diffraction peaks, where detected, are broad, indicating the presence of poorly crystalline cristobalite or opal-C.

"Amorphous" principally denotes volcanic glass, but small amounts of opal-A also may be present. Opal-A is most abundant in Tac ash beds 1 and 2, where it is estimated to comprise a few weight percent.

*This sample also contains a possible trace amount of lithiophorite. No error is given for the cryptomelane abundance because no standard reference intensity was used, and the value is an estimate. Because the value is an estimate, it is not included in the total.

Faults

Test objectives included investigating the influence of faults on fluid movement. However, the distribution of faults within the Phase 2 test block was largely unknown at the time the test facility was constructed. The location and orientation of the test block were driven by the need to penetrate as much of the Calico Hills Formation as possible. Locating the test block to optimize fault-transport studies was a lower priority. The test block, as sited, contained two faults that were exposed on the collection face in the main adit. The injection face in the test alcove included no identifiable faults (DTN: GS990708314224.007 [164604]). At the beginning of the test, nothing more was known about the presence of faults within the test block.

The two unnamed normal faults exposed in the collection face are both near-vertical and dip away from each other, defining a narrow horst block oriented diagonally across the rectangular test block. One of the faults was projected to extend slightly into the rock volumes below the upper and lower injection arrays within the boundaries of the test block. The other fault was located a least several meters laterally beyond either injection array and was therefore less likely to encounter fluid injected during the test.

The mineback through the Phase 2 test block revealed that the fault below the injection arrays extends about 6 m into the block, as far back as the fifth mineback face. The fault includes at least two branches, and the amount of offset decreases inward from the collection face. It does not intersect any of the injection boreholes. A fault (or faults) of similar orientation and sense of offset was observed on mineback faces 2, 3, and 4. This fault intersects injection holes UZTT-BB-INJ-9 (borehole 26) and -10 (borehole 27).

Directly visible effects of faults on tracer movement are minor. No concentrations of fluorescent tracer were observed along fault traces exposed in the mineback, except within clay-rich pumice lapilli cut by the fault. The same effect was observed in lapilli away from the fault. The other fault effect was observed in damp zones above and below ash bed 1. The damp zones, visible in newly completed mineback faces, are parallel to bedding and have fairly uniform and flat upper and lower margins. Where the damp zones are crossed by faults, the upper margins of the zones extend upward along the fault trace or have a mounded appearance centered on the fault trace. This is particularly noticeable in the damp zone above ash bed 1.

Mineralogic Variability of the Phase 2 Test Block

Mineralogic data were collected to help verify stratigraphic-unit assignments and to identify potential effects of mineralogy on the flow-and-transport test results. The mineralogy of a composite vertical section through the southwestern portion of the test block is presented in Table VIII-1, with all abundances in weight percent. The analyzed aliquots were taken from block samples of intact rock, rather than from drill core, to provide better representation and vertical coverage of the lithologic subunits present in the test block. The use of block samples also avoided potential problems with disturbed core.

Primary-Phase Mineralogic Variation

The primary pyroclastic constituents of the Tptpv1 (crystal-poor vitric nonwelded subzone of the Topopah Spring Tuff), Tptpv2 (crystal-poor vitric moderately welded subzone of the Topopah Spring Tuff), and Tac (Calico Hills Formation) are volcanic glass (shards, ash, and pumice clasts) plus quartz and feldspar in phenocrysts and xenoliths. The Tpt subzones contain ≤1% quartz and ≤2% feldspar except in two intervals with higher abundances of crystalline pyroclasts. The pumice swarm is characterized by feldspar contents of 4 to 5%, although it contains no more quartz than the bulk of the Tptpv1 and Tptpv2. The base surge directly above the Tac contains 3% quartz and 6% feldspar.

The Tac contains more crystalline pyroclasts than the overlying Tpt subzones, with 3 to 6% quartz and 8 to 13% feldspar. From ash layer 1 downward, the crystalline pyroclast content is slightly higher (13 to 19% quartz + feldspar) than in the uppermost Tac above ash layer 1 (11–13%).

Secondary Alteration

As noted above, volcanic glass is the most abundant constituent of the partially welded to nonwelded tuffs of the Busted Butte test facility. Glass is relatively susceptible to alteration by groundwater and is rarely preserved wherever the tuffs have been below the water table. The glassy rocks of Busted Butte are mostly unaltered, typical of nonwelded tuffs in the unsaturated zone of the Yucca Mountain region. Smectite and kaolinite clays are the principal alteration products of volcanic glass in the test facility. Figure VIII-2 highlights the vertical variability of clay content and associations of clay content with specific stratigraphic/lithologic features.

Clay content of the Topopah Spring Tuff in the test block is 4% or less, except in two layers within the Tptpv1. One of the layers is a primary depositional feature informally called the pumice swarm, pumice layer, or pumice zone. The pumice layer contains 30 to 50% (Levy 2001 [165363], p. 31) large (~10 cm long; Bussod 1999 [146978], p. 85), elongate pumice clasts aligned with the flow fabric of the ash flow. This layer is present throughout the Busted Butte test facility, but the layer thickness and the abundance of pumice clasts within the layer are variable. Alteration of the pumice clasts and perhaps the matrix as well has produced bulk smectite + kaolinite contents as high as 24%.

A smectite clay content of 12 to 16% was documented within and just above the base surge deposit of the Topopah Spring Tuff. This is a higher clay content than is present in either the overlying Tptpv1 tuff or the immediately underlying Calico Hills tuff. The localization of stronger alteration above the contact may have resulted from perching of downward-percolating water due to a permeability contrast at the contact.

Clay content is generally higher in the Tac than in the overlying Tpt subzones. Smectite is the only clay mineral present. Except in the ash layers, the total smectite content of Tac samples is between 5 and 12%. Smectite content of the ash layers is 1 to 7%. The lower clay content of the ash layers (actually pumice-lapilli tuffs) may be a consequence of early opal-A (amorphous silica) deposition that filled pores and cemented the pumice clasts. The cementation restricted

fluid access to the volcanic glass of which the pumice clasts are composed and protected it from the alteration that affected adjacent uncemented tuff.

Effects of Mineralogy on Test Results

The influence of clay content on the movement of introduced moisture is expected to be the predominant observable mineralogic effect on test performance. All of the tuff in the test block contains at least a little smectite clay, a mineral with a strong affinity for water that is held in a partially ordered condition between the clay tetrahedral lattice layers. The ambient water content of the tuff probably is less than the capacity of the smectite to hold water. Smectite-rich stratigraphic layers that are close to an injection array, like the pumice swarm in the upper Tptpv1, may capture and concentrate the tracer fluid. Kaolinite is less effective than smectite in attracting water (based on discussion and data in Grim 1968 [164642], pp. 251–254, 264–266), but it also contributes to the overall effect in the pumice swarm where it is abundant. The combined smectite+kaolinite content of the bulk rock within the pumice swarm is 21 to 24%, and the pumice swarm is within about one meter below the Phase 2 upper injection array. This fluid-imbibition effect may be detectable in neutron logs of collection boreholes that traverse the pumice swarm and in auger samples collected during the mineback.

A thinner, relatively smectite-rich interval in and above the Tpt base surge may behave like the pumice swarm with respect to tracer fluid. This interval is about 0.1 m thick and contains 12 to 16% smectite. The base surge is located about 70 cm above the Phase 2 lower injection array. In this position, a thin smectitic interval may have less of an effect on moisture retention than the pumice swarm. Data from the collection borehole UZTT-BB-COL-2, centered on the base surge, may document any moisture effects of the clay-rich rock.

VIII.7 APPLICABILITY OF BUSTED BUTTE HYDROLOGICAL DATA TO YUCCA MOUNTAIN

The Busted Butte UZTT included both field tests of aqueous tracer transport and laboratory measurements of hydrologic, tracer-sorption, and matrix-diffusion properties of rock samples from the field-test facility (Bussod et al. 1999 [155695]). The selection of southeastern Busted Butte, 8 km southeast of the repository area at Yucca Mountain, to site a field test facility was based on a presumption that the test results could be appropriately used in numerical studies of flow and transport in the Calico Hills Formation (Tac) at Yucca Mountain (Bussod et al., 1999 [155695], p. 2). Equivalence of stratigraphic units at Busted Butte and Yucca Mountain is the fundamental criterion for a presumption of applicability. Additional criteria for applicability are similarities of lithology and mineralogy, particularly mineralogic changes due to alteration. Final criteria are similarities of measured hydrologic properties between the Calico Hills Formation at Busted Butte and Yucca Mountain Calico Hills sections of corresponding stratigraphy, lithology, and mineralogy.

The Calico Hills section at southeastern Busted Butte, a thin distal residue of deposits with an aggregate thickness of one hundred to several hundred feet at Yucca Mountain, cannot completely represent the variability of the Calico Hills Formation below the nuclear waste repository. Thickness of the Calico Hills tuff decreases over a distance of about 13 km from more than 947.7 ft (288.86 m) at the northern end of Yucca Mountain (Moyer and Geslin

[101269] 1995, Figure 3) to 21 ft (6.40 m) at the southeastern Busted Butte outcrop adjacent to the flow-and-transport test facility (Broxton et al. 1993 [107386], p. 9). Because the Busted Butte section is so thin, it is important to know more specifically what portion of the Calico Hills section occurs in the test facility.

Lithostratigraphic Correspondence

An informal internal lithostratigraphy of the Calico Hills Formation devised by Moyer and Geslin (1995 [101269], pp. 5–9) provides a useful basis for comparing the Busted Butte and Yucca Mountain rock sections. The Calico Hills Formation is divided into five ash-flow/air-fall tuff units, plus a bedded tuff and volcaniclastic sandstone at the base of the formation. The majority of units (other than bedded tuff/sandstones) are laterally discontinuous, but pyroclastic unit 3 is present in most, and perhaps all, of the drill cores examined by Moyer and Geslin (1995 [101269], pp. 6, 8–9). Moyer and Geslin (1995 [101269], pp. 8, 10) noted lithologic similarities between the Calico Hills section exposed at Busted Butte and the USW GU-3 drill core section, especially the presence of black, perlitic-glass lithic clasts (glass chunks with distinctive rounded surfaces, described by Moyer and Geslin (1995 [101269], p. 8) as “black obsidian” or “obsidian lithic clasts”). The restricted occurrence of these clasts, in addition to a lithic-inclusion content of 5 to 10 volume % (Moyer and Geslin 1995 [101269], Table 3), was considered a basis for identification and intersite correlation of unit 3 by Moyer and Geslin (1995 [101269], p. 8).

The slightly more than 2 m thick section of uppermost Calico Hills Formation in the Busted Butte Phase 2 test block shares the two most characteristic lithologic attributes of unit 3: lithic-clast content in the 5–10% range and the presence of black perlitic clasts (Table VIII.2). This is the section from which hydrological-properties samples were collected. Yucca Mountain vitric Tac sections from boreholes USW SD-7 and SD-12, used for comparison with the Busted Butte Tac data, have been identified as parts of unit 3 (Rautman and Engstrom 1996 [101008]; [100642])

Table VIII-2. Calico Hills Formation Lithostratigraphy

Unit 5 – Non- to partially welded, pumiceous pyroclastic-flow deposit Slightly elongated pumice clasts; bimodal distribution of pumice clast sizes; 20 to 30 percent pumice. Light colored pumice clasts; moderate reddish-orange to grayish-pink matrix. Base marked by thinly bedded fall deposits.
Unit 4 – Nonwelded, pumiceous pyroclastic-flow deposit Volcanic lithic clasts are large (20 to 70 mm), isolated orin swarms; prominent clasts of moderate reddish-orange tuff. Light colored pumice clasts; very pale orange to grayish orange-pink matrix. Lithic-poor sections appear similar to unit 2. Base marked by a heterolithologic sequence of fall deposits.
Unit 3 – Nonwelded, lithic-rich pyroclastic flow deposit Lithic clasts comprise 5 to 10 percent, locally 10 to 30 percent (near the base and in several intervals within the unit); predominantly devitrified volcanic rocks with local obsidian. Grayish-orange to grayish-yellow or pinkish-gray matrix. The basal lithic-rich fallout is an excellent stratigraphic marker.
Unit 2 – Nonwelded, pumiceous pyroclastic-flow deposit 20 to 40 percent light colored pumice clasts; moderate pink or moderate orange-pink matrix. The fall deposit at the base of the unit contains porcelaneous ash layers.
Unit 1 – Nonwelded, lithic-rich pyroclastic-flow deposit 15 to 20 percent devitrified volcanic lithic clasts near base; lithic clasts decrease upward to 3 to 7 percent. Light colored pumice clasts; grayish orange-pink to light greenish-gray matrix; 7 to 12 percent phenocrysts.
Bedded tuff unit Interbedded coarse-grained fallout deposits, pyroclastic-flow deposits (many reworked or with paleosols), and thinly bedded porcelaneous ash-fall deposits. Pyroclastic-flow deposits have 13 to 25 percent phenocrysts.
Basal sandstone unit Massive to laminated, immature volcaniclastic sandstone; very pale orange to moderate red; medium to coarse grained; accumulations of argillic pumice clasts and rare sedimentary structures including load casts, pinch-and-swell structures, and flame structures. Locally interbedded with reworked pyroclastic-flow deposits.

Mineralogic Correspondence

For hydrological purposes, the Calico Hills Formation at Yucca Mountain is categorized as either vitric or zeolitic (containing clinoptilolite). The downward change from vitric to zeolitic Tac has been defined by hydrological criteria as a 5% reduction in the porosity (Flint 1998 [100033], p. 29). Zeolitization reduces the saturated hydraulic conductivity by several orders of magnitude relative to the conductivity of less altered vitric tuff (Flint 1998 [100033], p. 35). The Busted Butte section of the Tac is predominantly vitric, and its hydrological properties should therefore most resemble those of vitric Tac in the southern and western parts of Yucca Mountain.

In Tac sections at Yucca Mountain that are mostly vitric, exemplified by the section in drill hole USW SD-12 (Chipera et al. 1996 [101331], Table 3), smectite clay comprises as much as two weight percent in tuffs that contain 1–10% clinoptilolite. The vitric Tac section in the Busted Butte test facility contains two lithologic varieties, both nonwelded: pyroclastic-flow tuff and pumice-lapilli (air-fall) tuff. Neither lithology is zeolitic, but the pyroclastic-flow tuff contains 7-12% smectite clay and the pumice air-fall tuff contains 1-7% smectite (DTN: LA0204SL831372.001 [164749]). Thus, the ranges of secondary hydrous-mineral contents in the predominantly vitric Tac of Busted Butte and USW SD-12 are very similar. Whether it makes a significant difference that the Busted Butte secondary mineralogy is smectite whereas the Yucca Mountain secondary mineralogy is dominated by zeolite has not been investigated.

Borehole USW SD-7 is the only other source of qualified vitric Tac core. Four samples from the uppermost vitric portion of the Tac section of this core contain only up to one percent each of

smectite and zeolite (Chipera et al. 1996 [101331], Table 1). They differ in this respect from the mostly more altered Busted Butte and USW SD-12 vitric Tac.

Within-Site Variability of Hydrologic Properties

Within the slightly more than 2 m thickness of the Tac in the Phase 2 test block, pyroclastic-flow tuff comprises about 80% of the section and pumice air-fall tuff accounts for about 20% in two beds. The data set of 37 Tac hydrological-properties samples contains 16 samples of pyroclastic-flow tuff and 21 samples from a single bed of pumice air-fall tuff. The subset of samples for which saturated hydraulic conductivity has been measured includes five pyroclastic-flow tuff samples and 19 pumice air-fall samples. This means that the permeability data set is heavily skewed toward a less common lithology, with about 80% of the measurements representing about 20% of the Tac section in the test block.

The potential effect of this uneven sample coverage may be assessed from the data in Table VIII-3. The mean porosities and standard deviations of the two lithologies are the same. Geometric mean saturated hydraulic conductivity of the pumice air-fall is a factor of two higher than the comparable value for the pyroclastic-flow tuff. This finding raises questions about whether this difference reflects consistent and characteristic attributes of the two lithologies at Busted Butte and Yucca Mountain, and whether a difference of this magnitude is meaningful for modeling purposes. If the representation error is a problem, this under-representation is even more strongly exacerbated. Further studies would be required to address both questions.

Table VIII-3. Hydrological Properties of Calico Hills Formation, Busted Butte

Borehole UZTT-BB-	Sampling Depth, ft	Stratigraphic Category	RH Oven Porosity, cm^3/cm^3	Saturated Hydraulic Conductivity, m/s
COL-1	10.5	Tac pyroclastic flow	0.34	
COL-1	16.8	Tac pyroclastic flow	0.33	
COL-2	6.5	Tac pyroclastic flow	0.34	7.2E-05
COL-2	7.6	Tac pyroclastic flow	0.34	4.6E-05
COL-10	6.7	Tac pyroclastic flow	0.31	
COL-10	10.6	Tac pyroclastic flow	0.32	
COL-10	21.5	Tac pyroclastic flow	0.49	
COL-10	25.5	Tac pyroclastic flow	0.34	
COL-11	20.9	Tac pyroclastic flow	0.32	
COL-11	30.5	Tac pyroclastic flow	0.36	
COL-12	7.5	Tac pyroclastic flow	0.34	1.9E-05
COL-12	9.5	Tac pyroclastic flow	0.32	3.7E-05
COL-12	11.0	Tac pyroclastic flow	0.31	
COL-12	22.2	Tac pyroclastic flow	0.32	
COL-12	23.5	Tac pyroclastic flow	0.33	
COL-12	25.8	Tac pyroclastic flow	0.32	1.5E-05
	Arithmetic mean	Tac pyroclastic flow	0.34	
	Standard deviation	Tac pyroclastic flow	0.04	
	Geometric mean	Tac pyroclastic flow		3.2E-05

Table VIII-3. Hydrological Properties of Calico Hills Formation, Busted Butte (continued)

Borehole UZTT-BB-	Sampling Depth, ft	Stratigraphic Category	RH Oven Porosity, cm^3/cm^3	Saturated Hydraulic Conductivity, m/s
INJ-7	11.9	Tac pumice air-fall	0.37	4.3E-05
INJ-7	14.7	Tac pumice	0.34	2.1E-05
INJ-7	18.7	Tac pumice	0.31	4.5E-05
INJ-7	20.3	Tac pumice	0.32	1.1E-05
INJ-8	8.6	Tac pumice	0.33	1.0E-05
INJ-8	11.6	Tac pumice	0.32	3.1E-05
INJ-8	14.1	Tac pumice	0.32	8.4E-06
INJ-8	19.4	Tac pumice	0.33	8.3E-06
INJ-8	25.0	Tac pumice	0.46	5.1E-07
INJ-9	6.0	Tac pumice	0.31	
INJ-9	10.5	Tac pumice	0.35	5.5E-05
INJ-9	12.3	Tac pumice	0.34	2.4E-05
INJ-9	18.6	Tac pumice	0.31	3.1E-06
INJ-9	19.7	Tac pumice	0.27	2.0E-06
INJ-9	21.5	Tac pumice	0.35	8.8E-06
INJ-10	8.7	Tac pumice	0.36	8.8E-06
INJ-10	11.8	Tac pumice	0.33	
INJ-10	15.7	Tac pumice	0.31	4.2E-05
INJ-10	17.4	Tac pumice	0.36	4.2E-05
INJ-10	20.6	Tac pumice	0.33	4.2E-05
INJ-10	22.8	Tac pumice	0.33	4.3E-05
	Arithmetic mean	Tac pumice	0.34	
	Standard deviation	Tac pumice	0.04	
	Geometric mean	Tac pumice		1.4E-05
	Geometric mean	All Busted Butte Tac		1.7E-05

Input DTN's: GS990708312242.008 [109822] (hydrologic properties), LA0207SL831372.001 [160824] (stratigraphic category).

Comparison of Busted Butte and Yucca Mountain Hydrological Properties

Table VIII-4 contains porosity data for a portion of the Tac section in borehole USW SD-12 at Yucca Mountain. This portion shares petrologic characteristics used to identify the Busted Butte Tac section as unit 3 in Moyer and Geslin's (1995 [101269]) classification. The depth interval identified here as unit 3 in USW SD-12 differs from the interval designated as unit 3 by Rautman and Engstrom (1996 [100642], page 51), but the difference is not considered important for the purpose of this analysis.

The comparison of hydrological properties is limited to porosity data, because saturated hydraulic conductivity data are not available for the USW SD-12 Tac section. The mean porosity of the USW SD-12 section is slightly lower than for the Busted Butte section, including both pyroclastic-flow and pumice air-fall lithologies. The standard deviations are the same for USW SD-12 and for both Busted Butte lithologies. This is an indication that the very restricted provenance of the Busted Butte samples may not have seriously biased the variability of that data set.

Table VIII-4. Porosity Data for the Calico Hills Formation in USW SD-12

Borehole	Sample Depth, ft	Stratigraphic Category	RH Oven Porosity, cm^3/cm^3
USW SD-12	1500.6	Tac unit 3, Busted Butte equivalent	0.295
USW SD-12	1504.0	Tac unit 3, Busted Butte equivalent	0.361
USW SD-12	1507.0	Tac unit 3, Busted Butte equivalent	0.336
USW SD-12	1509.8	Tac unit 3, Busted Butte equivalent	0.333
USW SD-12	1513.0	Tac unit 3, Busted Butte equivalent	0.335
USW SD-12	1515.7	Tac unit 3, Busted Butte equivalent	0.324
USW SD-12	1519.1	Tac unit 3, Busted Butte equivalent	0.304
USW SD-12	1522.2	Tac unit 3, Busted Butte equivalent	0.308
USW SD-12	1524.5	Tac unit 3, Busted Butte equivalent	0.260
USW SD-12	1528.2	Tac unit 3, Busted Butte equivalent	0.308
USW SD-12	1531.0	Tac unit 3, Busted Butte equivalent	0.340
USW SD-12	1534.4	Tac unit 3, Busted Butte equivalent	0.309
USW SD-12	1537.2	Tac unit 3, Busted Butte equivalent	0.333
USW SD-12	1539.8	Tac unit 3, Busted Butte equivalent	0.318
USW SD-12	1542.5	Tac unit 3, Busted Butte equivalent	0.312
USW SD-12	1546.0	Tac unit 3, Busted Butte equivalent	0.327
USW SD-12	1549.0	Tac unit 3, Busted Butte equivalent	0.280
USW SD-12	1557.1	Tac unit 3, Busted Butte equivalent	0.321
USW SD-12	1558.1	Tac unit 3, Busted Butte equivalent	0.304
USW SD-12	1560.4	Tac unit 3, Busted Butte equivalent	0.310
USW SD-12	1563.5	Tac unit 3, Busted Butte equivalent	0.272
USW SD-12	1567.0	Tac unit 3, Busted Butte equivalent	0.257
USW SD-12	1570.0	Tac unit 3, Busted Butte equivalent	0.260
USW SD-12	1573.2	Tac unit 3, Busted Butte equivalent	0.313
USW SD-12	1575.2	Tac unit 3, Busted Butte equivalent	0.307
USW SD-12	1578.8	Tac unit 3, Busted Butte equivalent	0.330
USW SD-12	1581.6	Tac unit 3, Busted Butte equivalent	0.318
	Arithmetic mean	Tac unit 3, Busted Butte equivalent	0.310
	Standard deviation	Tac unit 3, Busted Butte equivalent	0.04

Input DTN: GS960808312231.004 [108985].

The mineralogic differences between the relatively unaltered upper Tac section in USW SD-7 and the somewhat more altered Busted Butte and USW SD-12 vitric Tac sections were noted above. Hydrological-properties data for four samples in Table VIII.5 also are distinctive. All porosity values are below the mean porosity values for Busted Butte and USW SD-12. Similarly, the saturated hydraulic conductivity values are all below the mean value of 1.7E-05 for all Busted Butte test facility Tac. The combination of lower porosity and hydraulic conductivity in a minimally altered tuff may reflect an increased degree of compaction relative to the two other sites. Alternatively, the differences may be a function of what is recoverable in the coring (a known problem). An additional potential difference might result if the Tac is non-unifrom and has different transverse and longitudinal properties. The reported difference might then partially result from measurement of properties from vertically extracted core versus horizontally extracted core.

Table VIII-5 Porosity and Permeability Data for the Calico Hills Formation in USW SD-7

Borehole	Sample depth, ft.*	Stratigraphic category†	RH oven porosity, cm^3/cm^3	Saturated hydraulic conductivity, m/s
USW SD-7	1396.4/1396.0	Tac subunit 3	0.298	1.60E-05
USW SD-7	1410.3/1410.7	Tac subunit 3	0.272	3.30E-06
USW SD-7	1422.0/1422.2	Tac subunit 3	0.308	7.10E-06
USW SD-7	1428.0/1428.0	Tac subunit 3	0.221	2.80E-09

DTN's: GS951108312231.009 [108984] (porosity), GS960808312231.005 [108995] (saturated hydraulic conductivity).

*The first depth is the porosity sample; the second depth is the saturated hydraulic conductivity sample.
†Based on Rautman and Engstrom (1996 [101008], p. 12). The 1396 ft samples are above the Tac, according to this reference.

Samples of the Calico Hills Formation and Topopah Spring Tuff exposed in Busted Butte outcrops were used to determine the hydrological properties of the formations in the test block. Table VIII-6 presents the mean and standard deviation for porosity, saturated conductivity, and van Genuchten parameters for samples taken from the three units at Busted Butte.

Table VIII-6. Hydrogeologic Properties of Busted Butte Units

Unit	# Samples	Porosity Mean	Porosity Std Dev	K_{sat} [m/s] Arith. Mean	K_{sat} [m/s] Std Dev	K_{sat} [m/s] Geom. mean
Tac	35	0.354	0.042	2.363E-05	1.720E-05	1.523E-05
Tptpv1	25	0.420	0.040	1.073E-05	1.853E-05	3.372E-06
Tptpv2	19	0.387	0.032	4.397E-06	4.387E-06	2.651E-06

Unit	# Samples	van Genuchten alpha [1/m] Mean	van Genuchten alpha [1/m] Std Dev	van Genuchten *n* Mean	van Genuchten *n* Std Dev
Tac	35	3.014	2.632	1.279	0.205
Tptpv1	25	0.685	0.365	1.385	0.278
Tptpv2	19	0.633	0.015	1.309	0.109

NOTE: Mean and standard deviation of values calculated from the following DTNs: GS990308312242.007 [107185]; GS990708312242.008 [109822]

Conclusions

The amount of existing hydrological-properties data for the vitric Tac at Yucca Mountain is insufficient to make a quantitative assessment of vitric Tac data from Busted Butte relative to Yucca Mountain data. The use of Busted Butte vitric Tac hydrological properties to model hydrological processes at Yucca Mountain is based on an approximation that no additional data from Yucca Mountain proper will be available. Examination of existing data suggests that Busted Butte property values probably lie within the range of Yucca Mountain values, but the variation of Yucca Mountain values is almost certainly greater than at Busted Butte. Values of Busted Butte hydrological properties (such as porosity and saturated hydraulic conductivity) may be near the high end of the range for these property values at Yucca Mountain. If this is correct, one possible explanation may be that the Tac tends to be slightly more compacted at Yucca Mountain than at Busted Butte, with its thinner overburden. Another possible explanation is that

recovery in the Yucca Mountain cores was limited to rock that was more intact and thus had smaller values of hydrological properties. The smectitic alteration at Busted Butte differs from zeolitic alteration at Yucca Mountain, but the data are insufficient to test for a relationship between alteration mineralogy and variations in hydrological properties.

ATTACHMENT IX

CALCULATIONS PERFORMED USING EXCEL SPREADSHEETS AND FUNCTIONS

INTENTIONALLY LEFT BLANK

ATTACHMENT IX—CALCULATIONS PERFORMED USING EXCEL SPREADSHEETS AND FUNCTIONS

Much of the data presented in this report have been analyzed and presented using the spreadsheet program Microsoft Excel. This appendix clarifies some of the common calculations and analyses performed using the functions provided in Excel. Brief information is provided so that with the detailed help files provided with the software, the calculations presented in this report can be repeated.

In the spreadsheet software program Excel, each place into which a single datum may be entered is referred to as a cell. A vertical group of cells is a column and a horizontal group of cells is a row. As in many spreadsheet programs the columns are labeled with letters and the rows with numbers, so that Cell A1 would be Column A in the first row (1). A list of rows in Column A would be (for example, A1:A34, which are cells in rows 1 through 34 in Column A. The pull-down menus along the top of the program may be used to insert functions. By selecting the INSERT pull-down menu and selecting FUNCTION as the option, the user elicits Excel's complete list of functions available. These are the functions that will be discussed below. The functions in the cells use the column-row nomenclature mentioned above (see examples below).

This attachment contains explanations for various spreadsheet calculations. The formula or explanations for calculations, the inputs, and the outputs will be found in the text of the main sections. The additional information required for the work to be reproducible is presented in this attachment. In some cases, greater explanation of a calculation was required than was appropriate for main-section text, so those have also been included in this attachment for clarity.

IX.1 MEAN: GEOMETRIC AND ARITHMETIC

The difference between geometric and arithmetic mean is in the underlying statistical distribution used in mean calculation. The arithmetic mean gives equal weight to all data and uses the normal (bell-shaped) distribution. The arithmetic mean is the most common and is therefore equivalent to classic averaging. The geometric mean, which is calculated for data in Section 6.1.2, is used to describe the mean for a different distribution than the normal distribution used in the arithmetic mean (geometric distribution). Unless specifically called out in the text (as in Section 6.1.2) the average or mean values presented in this report are calculated using the arithmetic mean. As mentioned, the geometric mean is appropriately calculated for data in Section 6.1.2. In all cases, the DTN listed in the text of the section (or as a note to a table or figure) contains the input values, and the output values are produced using the following functions:

If the following function is typed into Excel:

=AVERAGE(A1: A34) (Eq. IX-1)

then the arithmetic mean or average value will be returned for all the data in cells A1 through A34.

If the following function is typed into Excel:

=GEOMEAN(A1: A34) (Eq. IX-2)

then the geometric mean value will be returned for all the data in cells A1 through A34.

A log-mean value may also be calculated using Excel (as in Section 6.14.4) by taking the output from the function in Equation IX-1 and using the following:

=log(B1: B34) (Eq. IX-3)

This FUNCTION returns the log base ten values for cells in row 1 through 34 in Column B.

IX.2 MEDIAN, MODE, AND STANDARD DEVIATION

Data in some of the sections (e.g., Section 6.1 and Section 6.14) have been used to calculate median, mode, and standard deviation summary statistics. The median is the middle point of the probability distribution, where 50% of the observations lie on one side and 50% on the other of the median. The mode is the portion of the distribution with the greatest frequency of occurrence. In a normal distribution, the mean media and the mode should be equivalent. The standard deviation (σ), also referred to as error and variability in this report, is a measure of the spread of the probability distribution around the arithmetic mean. In Excel, these values were calculated for this report using the following functions:

=MEDIAN(A1: A34), (Eq. IX-4)

which returns the median value for all the data in cells A1 through A34,

=MODE(A1: A34), (Eq. IX-5)

which returns the mode, and

=STDEV(A1: A34), (Eq. IX-6)

which returns the standard deviation for a normal distribution for all the data in cells A1 through A34.

IX.3 SPREADSHEET CALCULATIONS

In addition to the preset functions in Excel, equations may be entered and calculated. Section 6.1 (Equation 6.1.2-1), Section 6.2 (Equation 6.2.2-1 to Equation 6.2.2-8), Section 6.4 (Equation 6.4.1-1), and Section 6.10 (Equation 6.10.3-1 to Equation 6.10.3-2) contain equations that were calculated using data for analyses in that section. For example, Equation IX-7 was used to calculate air-permeability from pressure differences during steady-state air injection using the following modified Hvorslev's formula (LeCain 1995 [101700], Equation 15, p. 10):

$$k = \frac{P_{sc} Q_{sc} \mu \ln\left(\frac{L}{r_w}\right) T_f}{\pi L \left(P_2^2 - P_1^2\right) T_{sc}} \qquad \text{(Eq. IX-7)}$$

k	permeability, m^2
P_{sc}	standard pressure, Pa
Q_{sc}	flow-rate at standard conditions, m^3/s
μ	dynamic viscosity of air, Pa-s
L	length of zone, m
r_w	radius of bore, m
T_f	temperature of formation, K
P_2	injection zone pressure at steady-state, Pa
P_1	ambient pressure, Pa
T_{sc}	standard temperature, K
ln	natural log

In Excel, the input data for this example DTN LB0011AIRKTEST.001 [153155] (first 9 entries shown) used in the calculations would appear as seen in Table IX.3-1.

Table IX.3-1. Calculation Spreadsheet for Permeability (Output) from Input in DTN: LB0011AIRKTEST.001 [153155]

	A	B	C	D	E	F	G	H	I	J
1	**P1**	**P2**	**L**	**Qsc**	**u**	**rw**	**Tf**	**Tsc**	**Psc**	**k -permeability**
2	89515.40	215482.27	0.3048	8.30E-04	1.78E-05	0.0381	288.1	288.1	101352.9	8.46E-14
3	92174.57	146320.52	0.3048	1.69E-05	1.78E-05	0.0381	288.1	288.1	101352.9	5.12E-15
4	89023.91	124321.86	0.3048	1.69E-05	1.78E-05	0.0381	288.1	288.1	101352.9	8.78E-15
5	90593.25	129981.18	0.3048	1.69E-05	1.78E-05	0.0381	288.1	288.1	101352.9	7.61E-15
6	88695.51	165094.52	0.3048	8.37E-05	1.78E-05	0.0381	288.1	288.1	101352.9	1.69E-14
7	89190.80	118626.97	0.3048	1.69E-05	1.78E-05	0.0381	288.1	288.1	101352.9	1.08E-14
8	89843.76	107377.01	0.3048	8.36E-05	1.78E-05	0.0381	288.1	288.1	101352.9	9.47E-14
9	89755.15	115576.75	0.3048	8.29E-04	1.78E-05	0.0381	288.1	288.1	101352.9	6.12E-13

DTN: LB0011AIRKTEST.001 [153155]

NOTE: In cell: Equation for permeability (Eq. 6.1.2-1):

J2	(I2*D2*E2*LN(C2/F2)*G2)/(3.14*C2*((B2^2)-(A2^2))*H2)
J3	(I3*D3*E3*LN(C3/F3)*G3)/(3.14*C3*((B3^2)-(A3^2))*H3)
J4	(I4*D4*E4*LN(C4/F4)*G4)/(3.14*C4*((B4^2)-(A4^2))*H4)
J5	(I5*D5*E5*LN(C5/F5)*G5)/(3.14*C5*((B5^2)-(A5^2))*H5)
J6	(I6*D6*E6*LN(C6/F6)*G6)/(3.14*C6*((B6^2)-(A6^2))*H6)
J7	(I7*D7*E7*LN(C7/F7)*G7)/(3.14*C7*((B7^2)-(A7^2))*H7)
J8	(I8*D8*E8*LN(C8/F8)*G8)/(3.14*C8*((B8^2)-(A8^2))*H8)
J9	(I9*D9*E9*LN(C9/F9)*G9)/(3.14*C9*((B9^2)-(A9^2))*H9)

Data have been truncated and are presented here as an example calculation only.

The input DTN in this case contains P_2 injection zone pressure at steady-state, (in Pa), P_1 ambient pressure (in Pa), and Q_{sc} flow-rate at standard conditions (in m^3/s). The remainder of the values in the calculations are standard constants obtained from reference books or site-specific values (e.g., borehole radius and length), all of which have been documented in the scientific notebooks referenced for the section. The output for this equation are the permeability values (k) in column J.

Other calculations have been performed in a similar manner using equations presented in this report in Section 6.1, Section 6.2, and Section 6.4. Details on the calculations in Section 6.2 are listed as notes to the tables in Attachment II. Please refer to Attachment II for details: only the general information related to calculations in Excel are discussed here.

IX.4 PLOTTING AND TREND-LINES

Using Excel, it is also possible to plot data organized in to columns and rows. This is performed by highlighting the data columns to be plotted (e.g., sample date column and seepage volume column) and then going to the INSERT pull-down menu and selecting the CHART option. The Excel Chart Wizard will then appear on screen and guide the user through the options to format the plot as desired. The following is provided as an example, with data from Section 6.10.2 and using input corroborating information from Hillel (1980 [101134], p. 37).

Temperature (ºC)	Vapor Density (km/m^3)
0	0.00485
5	0.0068
10	0.0094
15	0.01285
20	0.0173
25	0.02305
30	0.03038
35	0.03963

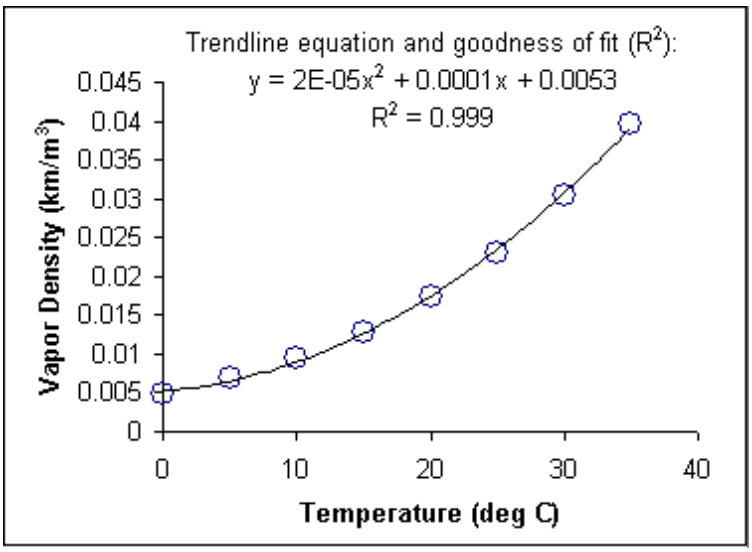

Figure IX.4-1. Example of Plotting and Trendline Addition in Excel Based on Figure 6.10.2-17

Once a chart exists and is selected (activated), a CHART file appears as a pull down menu and can be used to adjust chart format. From the CHART pull down menu ADD TRENDLINE may be selected to have Excel add a line to the data, based upon a least-squares best-fit technique. This means that a line is added that minimizes the sum of the squared differences between the line and the actual data. This feature of Excel has been used in this report in Figure 6.1.2-12 through Figure 6.1.2-16, Figure 6.10.2-17, Figure 6.11.2-12, Figure 6.11.2-13, and Figure 6.11.2-16. It is a calculation based upon data similar to the others performed in Excel. It is also possible to display box plots of data (Figure 6.14.4-9 and Figure 6.14.4-10), which are boxes on a graph with a line through the mean value and the upper and lower boundaries of the box at 2

times the standard deviation level. The outer lines (known as whiskers) of the box plot indicate the total range of data values, and individual points indicate outlier data.

IX.4.1 Excel Smoothing Function

Some of the plotted data figures displayed in this report are presented using *smoothed* lines to connect data points—Figures 6.6.2-2, 6.6.2-5, 6.6.2-6, 6.13.5-2, 6.13.5-3, 6.13.5-4, and 6.13.5-5. Display of data in this manner may be appropriate for various reasons, including that the continuity of the processes under observation is better characterized. The following discussion summarizes the smoothing function calculation in Excel.

In Excel, plots of data may be *smoothed*, which means that the lines between data points are made nonlinear to round the edges of sharp peaks in the data. The data itself remains unchanged, but the lines between the data are calculated using an exponential smoothing formula included in the Excel program. This formula is designed to predict a value based on the forecast for the prior period (data point). The tool uses the smoothing constant *a*, the magnitude of which determines how strongly forecasts respond to errors in the prior forecast. The function estimates the plotted result *F*, from each time step F_t, for the following time step F_{t+1}. The function is:

$$F_{t+1} = F_t + a*(A_t - F_t) = F_t + (1 - dampFact)*(A_t - F_t) \qquad \text{(Eq. IX.4.1-1)}$$

where A_t are the actual data points used to constrain the function. The damping factor (*dampFact*) is a corrective factor that minimizes the instability of data collected across a population. Larger constants yield a faster response, but can produce erratic projections. Smaller constants can result in long lags for forecast values. The default damping factor is 0.3.

IX.4.2 Calculation of Estimated $^{234}U/^{238}U$ ages

The following calculation is performed in an Excel spreadsheet as described previously and is used in Section 6.14.3 to estimate the ages of opal mineral deposits from uranium isotope ratios. This ratiometric calculation is a standard approach in geochemical analyses. The activity of ^{234}U at any time in a closed mineral system consists of the ^{234}U activity generated in place by decay of ^{238}U in the sample, and the amount of excess ^{234}U activity remaining from the ^{234}U incorporated into the mineral at the time of formation. The mathematical expression for this relation is given by Faure (1986 [105559], Equation 21.22, page 369). Rearranging to solve for the age of the system, *t*:

$$t = \frac{\ln\left(\frac{\left(\frac{^{234}U}{^{238}U}\right)_{measured} - 1}{\left(\frac{^{234}U}{^{238}U}\right)_{initial} - 1}\right)}{-\lambda_{234}} \qquad \text{Eq. IX.4.2-1}$$

where λ_{234} is the radioactive decay constant for ^{234}U of 2.8262×10^{-6} yr^{-1} (Cheng et al. 2000 [153475]). Therefore, estimated $^{234}U/^{238}U$ ages are calculated from measured $^{234}U/^{238}U$ ratios

and an assumed initial $^{234}U/^{238}U$, estimated, in the present case, using the average of initial $^{234}U/^{238}U$ activity ratios calculated using ^{238}U-^{234}U-^{230}Th data for SHRIMP (the ion microprobe technique) spots younger than 200 ka. The resulting estimated $^{234}U/^{238}U$ ages are presented in Table 6.14.3-1 and Figures 6.14.3-1, 6.14.3-2, and 6.14.3-3.

IX.5 OTHER STATISTICS

Additional statistical analyses are possible using functions in Excel. These include Students t-tests, normality tests, correlations tests, coefficient of variation calculations, F-tests, and linear regression. There are yet more preset functions in Excel, however, they are not applied in calculations in this report. These statistical functions can be calculated for arrays of data (in rows and columns) using the INSERT pull-down menu and FUNCTION command. The details of the analyses are unnecessary to cover in this attachment.

In Section 6.14.1.2 a Fisher (F) test is performed to examine intersample variability. The analysis was performed as described in Youden, (1951 [153339]) and in Peterman and Cloke (2002 [162576], p. 692):

$$F = [\Sigma (x_m-\mu)^2/(n_m-1)]/[\Sigma (x_a-x_b)^2/n] \quad \text{(Eq. IX-8)}$$

Where:

x_m =	means of duplicate analyses
μ =	overall mean of the analyses
n_m =	number of samples (20)
x_a and x_b	are the duplicate analyses
n_m =	number of duplicate analyses
n =	total number of analyses

A critical F-value is defined by Youden (1951 [153339]) for a given level of probability (in this case 95%). When the F statistic calculated with Equation IX-7 exceeds the critical F-value, then this is statistical evidence for environmental sources to the variability in addition that in the analytical method. This equation may be calculated in Excel as in the example in Attachment IX.3 using DTN: GS000308313211.001 [162015] as input data.

In Section 6.14.3, a discussion on the slopes of a regression line is provided for input DTN: GS021208315215.009 [164750]. In this regression, the isotope ratios for data $^{230}Th/U$ are analyzed in a linear regression with Excel. This is done by plotting the data in this case $^{230}Th/U$ ratio (column F) by distance from the outer most surface of the mineral. Then by adding a TRENDLINE as discussed in Section IX.4, the slope of the regression may be obtained from the equation as displayed in Figure IX.5-1.

Table IX.5-1. Calculation Excel Spreadsheet for Output in Table 6.14.3-2 and Figure 6.14.3-4

A	B	C	D	E	F	G	H	I
ROW	SAMPLE DESIGNATION	ELAPSED TIME (min)	URANIUM ABUNDANCE (ng)	^{230}THORIUM/ ^{232}THORIUM RADIOACTIVITY RATIO	^{230}THORIUM/ ^{238}URANIUM ISOTOPIC RATIO	^{234}URANIUM/ ^{238}URANIUM RADIOACTIVITY RATIO	MINERAL AGE (ka)	INITIAL ^{234}URANIUM/ ^{238}URANIUM RADIOACTIVITY RATIO
1	HD2074-T1a	1–2	12.6	1,250 ±400	0.3436 ±0.0045	6.043 ±0.082	6.34 ±0.12	6.134 ±0.082
2	HD2074-T1b	3	0.744	134 ±32	0.901 ±0.069	6.421 ±0.058	16.2 ±1.3	6.674 ±0.061
3	HD2074-T1c	12	1.64	720 ±220	1.490 ±0.056	6.089 ±0.054	29.5 ±1.3	6.531 ±0.058
4	HD2074-T1d	12	1.22	1,400 ±4,200	2.393 ±0.076	5.213 ±0.049	61.4 ±2.5	6.011 ±0.059
5	HD2074-g2-L1	2	2.21	550 ±340	0.430 ±0.038	6.574 ±0.089	7.3 ±0.7	6.691 ±0.090
6	HD2074-g2-L2	2	3.13	580 ±180	0.671 ±0.074	6.561 ±0.058	11.6 ±1.3	6.747 ±0.062
7	HD2074-g2-L3	3	4.81	940 ±220	0.932 ±0.064	6.649 ±0.084	16.1 ±1.2	6.913 ±0.086
8	HD2074-g2-L4	3	4.5	3,300 ±1,900	1.350 ±0.077	6.435 ±0.041	24.9 ±1.6	6.831 ±0.048
9	HD2074-g2-L5	4	5.1	5,700 ±4,700	1.427 ±0.034	6.492 ±0.042	26.2 ±0.7	6.914 ±0.044
10	HD2074-g2-L6	5	6.89	2,770 ±720	1.620 ±0.023	6.375 ±0.036	30.7 ±0.5	6.862 ±0.037

DTN: GS021208315215.009 [164750]

NOTE: Data have been truncated and are presented here as an example calculation only.

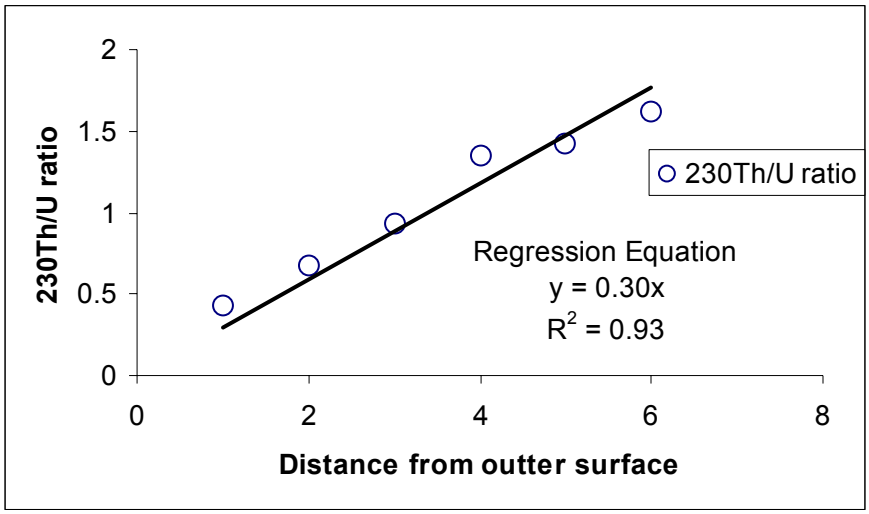

DTN: GS021208315215.009 [164750]

NOTE: The results are discussed in section 6.14.3 and are related to Table 6.14.3-2 and Figure 6.14.3-4.

Figure IX.5-1: Example of Linear Regression in Excel with the y=mx Equation, Where m is the Regression-Slope

The resulting slope in Figure IX.5-1 of 0.30 is not exactly the same as the 0.35 reported in Section 6.14.3, because a truncated data list was used for demonstration purposes in this calculation attachment.

For another example, see Section 6.2. A standard analysis of variance (ANOVA) statistical procedure is presented that has been calculated using Excel. Please refer to Attachment II for calculation details and references necessary for performing ANOVA.

IX.6 CALCULATIONS FOR SPECIFIC FIGURES

The following subsections document specific calculations used to create figures that require additional explanation to that provided in Attachment X.4.

IX.6.1 Descriptors for Evaporation-Pan Data in Figure 6.2.1-19 (DTN: LB0211NICH5LIQ.001 [160792])

As discussed in Section 6.2.1.3.5.3.1, evaporation-pan data identified in Table 6.2.1-4 were measured using a single balance loaded with a container filled with water. A "Mettler Single Scale 8-31-01.vi V2.0" referred to as Balance 4, was used to record the evaporation rate after 7/15/02. Figure 6.2.1-19 shows the evaporation rate inside and outside the niche during Test #2 9-17-02. The plot indicates that the average evaporation flux outside of the niche is about a factor of 20 greater than the average evaporation flux inside the niche. The input evaporation data (DTN: LB0211NICH5LIQ.001 [160792]) collected during the study and contained in the original data files are the evaporation rates [g/s]. These were converted to output evaporation fluxes [g/s-m^2] shown in the spreadsheet below in Column I. These outputs were obtained by dividing the evaporation rate (measured water-mass loss over time [in Column G]) by the surface area of the evaporation pan (i.e., πr^2, where r is the radius of the pan [in Column H]). The radius of the evaporation pan inside the niche was 0.075 m, as reported in Scientific Notebook by Trautz (2003 [166248], p. 187).

Table IX.6-1. Calculation Excel Spreadsheet for Output in Figure 6.2.1-19

A	B	C	D	E	F	G	H	I
Date	Time	Elapsed Time (s)	Weight	Units	Status	Mass Rate (g/s)	Area (πr^2)	Evaporation (g/s-m^2)
9/17/2002	2:01:01 PM	0	2163.3	g	S D	0	0.01767146	0
9/17/2002	2:01:04 PM	3.695	2163.5	g	S D	0.054127	0.01767146	3.062961637
9/17/2002	2:01:21 PM	20.029	2162.2	g	S D	-0.079589	0.01767146	-4.503816094
9/17/2002	2:01:37 PM	36.362	2163.3	g	S D	0.067348	0.01767146	3.811117194
9/17/2002	2:01:54 PM	52.746	2162.9	g	S D	-0.024414	0.01767146	-1.381549789
9/17/2002	2:02:10 PM	69.079	2163.3	g	S D	0.02449	0.01767146	1.385850509
9/17/2002	2:02:27 PM	86.134	2163.2	g	S D	-0.005863	0.01767146	-0.331777931
9/17/2002	2:02:43 PM	102.467	2163.5	g	S D	0.018368	0.01767146	1.039416176
9/17/2002	2:03:00 PM	118.791	2163.4	g	S D	-0.006126	0.01767146	-0.346660687
9/17/2002	2:03:16 PM	135.124	2162.9	g	S D	-0.030613	0.01767146	-1.73234143
9/17/2002	2:03:32 PM	151.457	2163.5	g	S D	0.036735	0.01767146	2.078775763

-- Balance 4 data

DTN: LB0211NICH5LIQ.001 [160792]

NOTE: Data have been truncated and are presented here as an example calculation only.

IX.6.2 Descriptor for Data in Figure 6.11.2-11(b) (DTN: LB0110ECRBLIQR.002 [156879])

The rate data for plotting is computed as follows: cumulative volume from column B and D, which are from Columns B and C in input data from LB0110ECRBLIQR.002 [156879], respectively, are divided by 1,000 (to convert milliliters to liters and written to Columns C and E respectively of the plotting worksheet. Rate data is written to Column F in this worksheet by taking the difference of sequential row data in Column C and dividing this difference by sequential row data from Column A (time stamp data). Rate data are written to Column H by taking the difference of sequential row data in Column E and dividing this difference by sequential row data from Column A (time stamp data). The rate data is smoothed for plotting by taking a 20-point moving average (using Excel 'AVERAGE' function in Equation IX-1) and writing the result to the row corresponding to the time stamp of the first data point of the 20-point averaging series. The averaging results are performed in this fashion on the rate data from Columns F and H and written to Output Columns G and I for plotting against Column A.

Table IX.6-2. Calculation Excel Spreadsheet for Output in Figure 6.11.2-11(b)

A	B	C	D	E	F	G	H	I
time	injection	liters	seepage	liters	inj rate	injection rate	seep rate	seepage rate
2/28/2001 13:59	376.4733	0.376473	8.269747	0.00827	9.50	9.54	0.00	-0.07
2/28/2001 14:19	566.9406	0.566941	8.269747	0.00827	12.83	9.64	0.00	-0.07
2/28/2001 14:39	823.9857	0.823986	8.269747	0.00827	11.57	9.57	-0.07	-0.07
2/28/2001 14:59	1055.978	1.055978	6.891456	0.006891	10.13	9.42	-0.07	-0.06
2/28/2001 15:19	1259.144	1.259144	5.513165	0.005513	10.31	9.51	0.00	-0.06
2/28/2001 15:39	1465.741	1.465741	5.513165	0.005513	9.94	9.55	-0.03	-0.06
2/28/2001 15:59	1665.131	1.665131	4.824019	0.004824	8.04	9.64	-0.10	-0.06
2/28/2001 16:19	1826.771	1.826771	2.756582	0.002757	1.52	9.86	-0.31	-0.05
2/28/2001 16:39	1857.314	1.857314	-3.44573	-0.00345	-4.18	10.45	-0.45	-0.03
2/28/2001 16:59	1773.577	1.773577	-12.4046	-0.0124	3.73	11.28	0.00	-0.01
2/28/2001 17:20	1848.391	1.848391	-12.4046	-0.0124	14.22	11.72	0.00	-0.01
2/28/2001 17:40	2133.234	2.133234	-12.4046	-0.0124	14.05	11.60	0.00	-0.01
2/28/2001 18:00	2414.989	2.414989	-12.4046	-0.0124	14.25	11.38	-0.03	-0.01

DTN: LB0110ECRBLIQR.002 [156879]

NOTE: Data have been truncated and are presented here as an example calculation only.

IX.6.3 Descriptor for Data in Figures 6.11.2-12 through 6.11.2-14 (DTN: LB0203ECRBLIQR.001 [158462])

Column B, C, and D contain the data from LB0203ECRBLIQR.001 [158462] for LA3 zone 1 with injection, return, and seepage volume, respectively, and are already divided by 1,000 to convert milliliters to liters. Columns E and G have the rates calculated using Columns B and D respectively in combination with time data from Column A. Rate data are calculated by taking the difference of sequential row data in a column and dividing this difference by sequential row data from column A (time stamp data). Columns F and H have a 17-point moving average (using Equation IX-1) calculated from data in Columns E and G, respectively. The data from this

calculation are written to the row corresponding to the first row of the series for each average. Return data is not plotted (they are zero).

Table IX.6-3. Calculation Excel Spreadsheet for Output in Figure 6.11.2-12

A	B	C	D	E	F	G	H
	injection volume	return volume	seepage volume	injection rate	Averaged injection rate	seepage rate	Averaged seepage rate
5/17/2001 15:33	0.42967	-0.00892	-0.00276	34.5923	36.25259193	-0.06874	0.040454465
5/17/2001 15:53	1.12324	-0.0151	-0.00413	32.5041	36.41670827	-0.05156	0.040454465
5/17/2001 16:13	1.77495	-0.01922	-0.00517	35.13798	36.65835198	-0.05143	0.041465388
5/17/2001 16:33	2.48122	-0.02196	-0.0062	39.05319	36.76620501	-0.0342	0.040446921
5/17/2001 16:54	3.26815	-0.02951	-0.00689	35.45289	36.63771063	0.034343	0.040436887
5/17/2001 17:14	3.97957	-0.03775	-0.0062	36.69389	36.77217985	0.1376	0.036393193
5/17/2001 17:34	4.71467	-0.03432	-0.00345	36.56069	36.73816646	0.618684	0.02829909
5/17/2001 17:54	5.44771	-0.01853	0.00896	37.87866	36.84489242	0.274971	-0.008094107
5/17/2001 18:14	6.20718	-0.01441	0.01447	34.57519	36.79052259	-0.03437	-0.024268861
5/17/2001 18:34	6.90041	-0.01441	0.01378	33.18211	36.9455773	-0.0344	-0.022247016
5/17/2001 18:54	7.56516	-0.01682	0.01309	26.39353	37.19951427	0.017186	-0.020223488

DTN: LB0203ECRBLIQR.001 [158462]

NOTE: Data have been truncated and are presented here as an example calculation only.

Column J, K, and L contain the data from LB0203ECRBLIQR.001 [158462] for LA3 zone 2 with injection, return and seepage volume, respectively, and are already divided by 1,000 to convert milliliters to liters. Columns M and O have the rates calculated using columns J and L respectively in combination with time data from Column I. Rate data are calculated by taking the difference of sequential row data in a column and dividing this difference by sequential row data from Column A (time stamp data). Columns N and P have a 17-point moving average (using Equation IX-1) calculated from data in Columns M and O, respectively. The data from this calculation are written to the row corresponding to the first row of the series for each average. Return data are not plotted (they are zero).

Table IX.6-4. Calculation Excel Spreadsheet for Output in Figure 6.11.2-13

I	J	K	L	M	N	O	P
	injection volume	return volume	seepage volume	injection rate	Averaged injection rate	seepage rate	Averaged seepage rate
5/17/2001 15:33	0.26597	-0.00069	-0.00069	73.03580223	70.10880015	-0.03437	0.034428271
5/17/2001 15:53	1.73034	-0.01167	-0.00138	66.30904562	70.10880014	-0.03437	0.032406423
5/17/2001 16:13	3.05983	-0.01922	-0.00207	69.11494788	70.49140268	-0.06857	0.028362738
5/17/2001 16:33	4.44904	-0.02471	-0.00345	57.02140797	70.69082885	-0.1368	0.030374522
5/17/2001 16:54	5.59802	-0.035	-0.0062	58.62638488	71.58049591	-0.06869	0.036399916
5/17/2001 17:14	6.77446	-0.03844	-0.00758	67.83744879	72.36819868	0.1032	0.040440248
5/17/2001 17:34	8.13347	-0.03569	-0.00551	70.02331071	72.60853901	0.171857	0.036391514
5/17/2001 17:54	9.53744	-0.03226	-0.00207	68.51706506	72.7384225	0.206228	0.026282293
5/17/2001 18:14	10.9112	-0.035	0.00207	72.45384363	72.9861073	0.481199	0.014151227
5/17/2001 18:34	12.3639	-0.03741	0.01172	73.88457489	73.51470289	0.0688	-0.014154591

DTN: LB0203ECRBLIQR.001 [158462]

NOTE: Data have been truncated and are presented here as an example calculation only.

Linear curve fit for evaporation uses the Excel trendline (see X.4 in this attachment) option for putting a curve fit onto an existing plot. Slope is from the equation generated by Excel for the fit.

Column R, S, and T contain the data from LB0203ECRBLIQR.001 [158462] for LA3 zone 3 with injection, return and seepage volume, respectively, and are already divided by 1,000 to convert milliliters to liters. Columns U and W have the rates calculated using Columns R and S (not T) respectively in combination with time data from Column Q. Rate data are calculated by taking the difference of sequential row data in a column and dividing this difference by sequential row data from Column A (time stamp data). Columns V and X have a 17 point moving average (using Equation IX-1) calculated from data in Columns U and W respectively. The data from this calculation are written to the row corresponding to the first row of the series for each average. Rows in column Y = V - X. Seepage data are not plotted (they are zero).

Table IX.6-5. Calculation Excel Spreadsheet for Output in Figure 6.11.2-14

Q	R	S	T	U	V	W	X	Y
	Injection volume	return volume	seepage volume	injection rate	Average injection rate	return rate	Average return rate	net inflow
5/17/2001 15:33	0.12492	-0.00275	1.40724	96.84475	102.1661207	7.223133	75.80776078	26.35835987
5/17/2001 15:53	2.06666	0.14208	1.42446	97.08438	102.7208943	28.03671	80.82287446	21.89801987
5/17/2001 16:13	4.0132	0.70421	1.43618	97.91853	103.0088531	33.77208	86.27193995	16.73691311
5/17/2001 16:34	5.98136	1.38303	1.44962	98.90518	103.342388	41.31827	90.16232341	13.18006459
5/17/2001 16:54	7.97595	2.21628	1.43825	99.00142	103.6813166	39.71012	93.70043656	9.980880038
5/17/2001 17:14	9.96093	3.01247	1.40103	98.75831	104.0469133	35.87162	97.41368893	6.633224337
5/17/2001 17:34	11.9394	3.7311	1.40276	93.72956	104.3823991	135.0315	101.2510492	3.131349904
5/17/2001 17:54	13.8187	6.43848	1.4224	103.6229	105.0438988	98.0429	99.35414615	5.689752607
5/17/2001 18:14	15.8963	8.40424	1.42929	104.2733	105.0831659	97.37536	99.56860494	5.514560925
5/17/2001 18:34	17.987	10.3566	1.42171	105.011	105.0539672	94.11589	99.85555683	5.198410416

DTN: LB0203ECRBLIQR.001 [158462]

NOTE: Data have been truncated and are presented here as an example calculation only.

IX.6.4 Descriptor for Data in Figures 6.11.2-15 through 6.11.2-17 (DTN: LB0301SYTSTLA4.001 [165227])

Column B, C, and D contain the data from for LA4 zone 1 with injection, return, and seepage (seepage is for zone 2 as per the TDMS notes) volume, respectively, and are already divided by 1,000 to convert milliliters to liters. Columns E and G have the rates calculated using Columns B and C, respectively, in combination with time data from Column A. Rate data are calculated by taking the difference of sequential row data in a column and dividing this difference by the difference in sequential row data from Column A (time stamp data) times conversion factors (1,000/1,440) to get mL/min. Columns F and H have a 17-point moving average (using Equation IX-1) calculated from data in Columns E and G, respectively. The data from this calculation are written to the row corresponding to the first row of the series for each average. Rows in Column I = F – H. Seepage data are not plotted (the one in this table is for zone 2 and seepage was zero for zone 1).

Table IX.6-6. Calculation Excel Spreadsheet for Output in Figure 6.11.2-15

A	B	C	D	E	F	G	H	I
	z1 injection volume	z1 return volume	z2 seepage volume	injection rate	Average injection rate	return rate	Average return rate	net inflow rate
2/6/2002 14:26	0.82193	0.01785	0.0062	35.12291	6.149953688	0.171164	1.539103191	4.610850497
2/6/2002 14:46	1.52614	0.02128	0.0062	35.99585	4.057721964	3.252121	1.527021005	2.530700959
2/6/2002 15:06	2.24786	0.08648	0.00551	30.71529	1.918149921	9.353345	1.329673623	0.588476297
2/6/2002 15:26	2.86319	0.27386	0.00345	19.78659	0.0267929	9.379803	0.77343575	-0.74664285
2/6/2002 15:46	3.25991	0.46193	0.00276	-0.822272	-1.0827092	4.316929	0.228736438	-1.311445637
2/6/2002 16:06	3.24344	0.54841	0.00207	-2.516115	-1.00713272	0.71889	-0.025200537	-0.981932188
2/6/2002 16:26	3.19299	0.56282	0.00276	-2.398294	-0.84100268	0.034261	-0.068495033	-0.772507647
2/6/2002 16:46	3.14494	0.56351	0.00276	-4.039477	-0.69488815	0	-0.070510406	-0.624377742
2/6/2002 17:06	3.06395	0.56351	0.00345	-0.907925	-0.48143621	-0.13705	-0.074537802	-0.406898408
2/6/2002 17:26	3.04576	0.56076	0.00345	-0.633308	-0.55902806	-0.13693	-0.078568549	-0.480459515

DTN: LB0301SYTSTLA4.001 [165227]

NOTE: Data have been truncated and are presented here as an example calculation only.

Column B, C, and M contain the data from LB0301SYTSTLA4.001 [165227] for LA4 zone 2 with injection, return, and seepage volume, respectively, and are already divided by 1,000 to convert milliliters to liters. Note that Column A has the traditional time stamp corresponding to zone 2 injection and return (B, C), but that Column I has times corresponding to seepage data in Column M. This is because the injection and seepage data come from different files with slightly different time stamps, as per the notes from the TDMS. Columns E and P have the rates calculated using Columns B and M, respectively, in combination with time data from Columns A and I, respectively. Rate data are calculated by taking the difference of sequential row data in a column and dividing this difference by the difference in sequential row data from Column A (time stamp data), or I in the case of seepage data in M, times conversion factors (1,000/1,440) to get mL/min. Columns F and Q have a 17-point moving average (using Equation IX-1) calculated from data in Columns E and P, respectively. The data from this calculation are written to the row corresponding to the first row of the series for each average. Column J = F – Q. Return data are

not plotted (they are zero). Zone 1 data (in columns D, K, J, N, O) are not plotted in this figure. It is just a placeholder in the worksheets.

Table IX.6-7. Calculation Excel Spreadsheet for Output in Figure 6.11.2-16

A	B	C	D	E	F	I
	z2 injection volume	z2 return volume	z1 seepage volume	Z2 injection rate	Z2 Average injection rate	
10/20/2002 09:02	435.465	-2.18094	-0.00138	46.2318	43.26999709	10/20/2002 09:04
10/20/2002 09:23	436.395	-2.18403	-0.00138	45.82622	43.09739301	10/20/2002 09:24
10/20/2002 09:43	437.316	-2.18403	-0.00207	45.87355	42.96269607	10/20/2002 09:45
10/20/2002 10:03	438.239	-2.18265	-0.00138	45.78825	42.84528516	10/20/2002 10:05
10/20/2002 10:23	439.16	-2.17236	-0.00138	45.97591	42.66257286	10/20/2002 10:25
10/20/2002 10:43	440.085	-2.15829	-0.00138	45.70295	42.48394771	10/20/2002 10:45
10/20/2002 11:03	441.004	-2.1449	-0.00138	46.56039	42.33743495	10/20/2002 11:05
10/20/2002 11:23	441.94	-2.13049	-0.00069	46.55594	42.16545265	
10/20/2002 11:43	442.877	-2.12534	-0.00069	30.01583	41.98482048	

J	K	L	M	N	O	P	Q
net loss rate	z1 injection volume	z1 return volume	z2 seepage volume	z1 injection rate	Average z1 injection rate	Z2 seepage rate	Average z2 seepage rate
40.79148803	-0.0048	0.00137	0.04893	-0.170597	-0.24282589	2.500793	2.478509058
40.62380401	-0.00824	0.00275	0.09924	-0.170597	-0.24082552	2.517922	2.473588999
40.49829032	-0.01167	0.00343	0.14989	-0.068239	-0.24081722	2.466536	2.464405749
40.38893998	-0.01304	0.00412	0.19951	-0.204886	-0.24683829	2.605725	2.456345175
40.22762295	-0.01716	0.0048	0.25188	-0.204716	-0.24080225	2.483665	2.434949909
40.06008109	-0.02128	0.00618	0.30185	-0.170597	-0.24080225	2.483665	2.423866617
39.91457591	-0.02471	0.00755	0.35181	-0.204716	-0.24080225	2.500793	2.422859045

DTN: LB0301SYTSTLA4.001 [165227]

NOTE: Data have been truncated and are presented here as an example calculation only.

Linear curve fit for evaporation (Figure 6.11.2-16) uses the Excel trendline option for putting a curve fit onto an existing plot. Slope is from the equation generated by Excel for the fit.

Rate calculations for Figure 6.11.2-17: Column S, T, and U contain the data from LB0203ECRBLIQR.001 [158462] for LA4 zone 3 with injection, return, and seepage volume respectively and are already divided by 1,000 to convert milliliters to liters. Columns V and X have the rates calculated using Columns S and T (not U), respectively, in combination with time data from Column R. Rate data are calculated by taking the difference of sequential row data in a column and dividing this by the difference of sequential row data from Column R (time stamp data) times conversion factors (1,000/1,440) to get mL/min. Columns W and Y have a 17-point moving average (using Equation IX-1) calculated from data in Columns U and W, respectively. The data from this calculation are written to the row corresponding to the first row of the series for each average. Rows in Column Z = W - Y. Seepage data are not plotted (they are zero).

Table IX.6-8. Calculation Excel Spreadsheet for Output in Figure 6.11.2-17

R	S	T	U	V	W	X	Y	Z
	z3 injection volume	z3 return volume	z3 seepage volume	z3 injection rate	average injection rate	z3 return rate	average return rate	net inflow
2/6/2002 14:27	0.32671	0.00549	-0.00034	3.237696	0.522815012	-0.29122	-0.128931088	0.6517461
2/6/2002 14:48	0.39157	-0.00034	-0.00207	2.276485	0.337400713	-0.59907	-0.112808103	0.450208816
2/6/2002 15:08	0.43722	-0.01235	-0.00551	0.788011	0.211551322	0.034261	-0.080591458	0.29214278
2/6/2002 15:28	0.453	-0.01167	-0.01447	0.222514	0.17123884	0	-0.084620527	0.255859367
2/6/2002 15:48	0.45746	-0.01167	-0.01792	0.25696	0.152103686	-0.17131	-0.076559036	0.228662722
2/6/2002 16:08	0.46261	-0.0151	-0.01999	0.205397	0.141015786	-0.13693	-0.06849587	0.209511657
2/6/2002 16:28	0.46673	-0.01785	-0.02067	0.017131	0.132964347	0.068523	-0.062456454	0.195420802
2/6/2002 16:48	0.46707	-0.01647	-0.02067	0.119815	0.131956662	0.034233	-0.066487201	0.198443863

DTN: LB0203ECRBLIQR.001 [158462]

NOTE: Data have been truncated and are presented here as an example calculation only.

IX.6.5 Wetting-Front Velocity Calculation in Figure 6.12.2-4 Observed in Boreholes 1, 9 and 10 in Niche 3107 (Niche 3)

The data used for this calculation is from DTNs: LB0110A8N3LIQR.001 [157001] and LB0209A8N3LIQR.001 [165461]. Each of these files includes the resistance measurements in the boreholes following the application of water along the fault. The decreasing resistance measured by ERPs located along the wall of each of these boreholes indicates increased wetting of the borehole walls.

The arrival time of the wetting front was determined to be the time when the resistance in a sensor first began to decrease following the application of water in the fault in early March 2001. For each of the boreholes, the date of the first observed decrease in resistance is noted in each of the measure locations in Boreholes 1, 9, and 10 in Niche 3107 (Niche 3) (Table IX.6-9a to Table IX.6-9c). The values in this table are used as inputs in this calculation.

Table IX.6-9a. Date of First Response in Borehole 1

Date/Time	First Response	Time (days) to First Response (from 03/06/01)
BH#1-0.15		
BH#1-0.40	8/6/01	153
BH#1-0.65	2/17/01	-17
BH#1-0.90	6/9/01	95
BH#1-1.15	7/8/01	124
BH#1-1.40	6/22/01	108
BH#1-1.65	5/25/01	80
BH#1-1.90	7/19/01	135
BH#1-2.15	7/8/01	124
BH#1-2.40	7/9/01	125
BH#1-2.65	9/25/01	203
BH#1-2.90	7/4/01	120
BH#1-3.15	7/6/01	122
BH#1-3.40	5/23/01	78
BH#1-3.65	8/11/01	158
BH#1-3.90	7/26/01	142
BH#1-4.15	4/10/01	35
BH#1-4.40	9/23/01	201
BH#1-4.65	7/18/01	134
BH#1-4.90	6/9/01	95
BH#1-5.15	8/22/01	169
BH#1-5.40	5/7/01	62
BH#1-5.65	3/23/01	17
BH#1-5.90	8/23/01	170

DTN: LB0110A8N3LIQR.001 [157001]

Table IX.6-9b. Date of First Response in Borehole 9

Date/Time	First Response	Time (days) to First Response (from 03/06/01)
BH#9-0.15	5/30/01	85
BH#9-0.40	5/18/01	73
BH#9-0.65	5/18/01	73
BH#9-0.90	4/19/01	44
BH#9-1.15	4/13/01	38
BH#9-1.40	4/6/01	31
BH#9-1.65	4/6/01	31
BH#9-1.90	4/6/01	31
BH#9-2.15	4/9/01	34
BH#9-2.40	4/9/01	34
BH#9-2.65	4/12/01	37
BH#9-2.90	4/21/01	46
BH#9-3.15	4/22/01	47
BH#9-3.40	5/2/01	57
BH#9-3.65	4/22/01	47
BH#9-3.90	5/13/01	68
BH#9-4.15	6/15/01	101
BH#9-4.40	6/19/01	105
BH#9-4.65	5/23/01	78
BH#9-4.90	6/26/01	112
BH#9-5.15	6/23/01	109
BH#9-5.40	5/13/01	68
BH#9-5.65	5/30/01	85
BH#9-5.90	6/24/01	110
BH#9-6.15	Not Known	Not Known
BH#9-6.40	Not Known	Not Known
BH#9-6.65	Not Known	Not Known
BH#9-6.90	Not Known	Not Known
BH#9-7.15	Not Known	Not Known
BH#9-7.40	Not Known	Not Known
BH#9-7.65	Not Known	Not Known
BH#9-7.90	Not Known	Not Known
BH#9-8.15	Not Known	Not Known
BH#9-8.40	Not Known	Not Known
BH#9-8.65	Not Known	Not Known
BH#9-8.90	Not Known	Not Known

DTN: LB0110A8N3LIQR.001 [157001]

Table IX.6-9c. Date of First Response in Borehole 10

Date/Time	First Response	Time (days) to First Response (from 03/06/01)
BH#10-0.15	7/3/01	119
BH#10-0.40	7/8/01	124
BH#10-0.65	5/25/01	80
BH#10-0.90	5/24/01	79
BH#10-1.15	5/7/01	62
BH#10-1.40	4/21/01	46
BH#10-1.65	4/9/01	34
BH#10-1.90	4/9/01	34
BH#10-2.15	4/9/01	34
BH#10-2.40	4/9/01	34
BH#10-2.65	4/10/01	35
BH#10-2.90	4/18/01	43
BH#10-3.15	4/19/01	44
BH#10-3.40	4/18/01	43
BH#10-3.65	5/1/01	56
BH#10-3.90	5/2/01	57
BH#10-4.15	6/7/01	93
BH#10-4.40	5/13/01	68
BH#10-4.65	5/2/01	57
BH#10-4.90	6/23/01	109
BH#10-5.15	7/2/01	118
BH#10-5.40	6/23/01	109
BH#10-5.65	5/29/01	84
BH#10-5.90	6/30/01	116
BH#10-6.15	5/29/01	84
BH#10-6.40	6/25/01	111
BH#10-6.65	7/6/01	122
BH#10-6.90	6/22/01	108
BH#10-7.15	8/12/01	159
BH#10-7.40	No wetting	
BH#10-7.65	No wetting	
BH#10-7.90	No wetting	
BH#10-8.15	No wetting	
BH#10-8.40	No wetting	
BH#10-8.65	No wetting	
BH#10-8.90	No wetting	

DTN: LB0209A8N3LIQR.001 [165461]

Given that the horizontal plane along which borehole 1 lies is ~21 m below the water release zone in Alcove 8, the wetting-front velocity is calculated by dividing the travel distance (21 m), by the travel time (days) for the wetting front to reach the sensor location along the borehole. Since the horizontal plane along which boreholes 9 and 10 lie is ~19 m below the injection zone in Alcove 8, the wetting-front velocity is calculated by dividing the travel distance (19 m) by the travel time (days) for the wetting front to reach the sensor location along the borehole. By setting this calculation up in Excel in the manner discussed in the previous sections of this attachment, the following table has the wetting-front velocity calculated for locations along the three boreholes.

Table IX.6-10. Wetting-Front Velocity Calculated for Locations along the Three Boreholes (1, 9, and 10)

	Travel time in days since start of liquid release on 03/06/01			Velocity of Wetting Front (meters/day)			
Distance from collar	Borehole 1	Borehole 9	Borehole 10	Distance from collar	Borehole 1	Borehole 9	Borehole 10
0.15		85	119	0.15		0.2	0.2
0.40	153	73	124	0.40	0.1	0.3	0.2
0.65	-17	73	80	0.65		0.3	0.2
0.90	95	44	79	0.90	0.2	0.4	0.2
1.15	124	38	62	1.15	0.2	0.5	0.3
1.40	108	31	46	1.40	0.2	0.6	0.4
1.65	80	31	34	1.65	0.3	0.6	0.6
1.90	135	31	34	1.90	0.2	0.6	0.6
2.15	124	34	34	2.15	0.2	0.6	0.6
2.40	125	34	34	2.40	0.2	0.6	0.6
2.65	203	37	35	2.65	0.1	0.5	0.5
2.90	120	46	43	2.90	0.2	0.4	0.4
3.15	122	47	44	3.15	0.2	0.4	0.4
3.40	78	57	43	3.40	0.3	0.3	0.4
3.65	158	47	56	3.65	0.1	0.4	0.3
3.90	142	68	57	3.90	0.1	0.3	0.3
4.15	35	101	93	4.15	0.6	0.2	0.2
4.40	201	105	68	4.40	0.1	0.2	0.3
4.65	134	78	57	4.65	0.2	0.2	0.3
4.90	95	112	109	4.90	0.2	0.2	0.2
5.15	169	109	118	5.15	0.1	0.2	0.2
5.40	62	68	109	5.40	0.3	0.3	0.2
5.65	17	85	84	5.65	1.2	0.2	0.2
5.90	170	110	116	5.90	0.1	0.2	0.2
6.15			84	6.15			0.2
6.40			111	6.40			0.2
6.65			122	6.65			0.2
6.90			108	6.90			0.2
7.15			159	7.15			0.1
7.40				7.40			
7.65				7.65			
7.90				7.90			
8.15				8.15			
8.40				8.40			
8.65				8.65			
8.90				8.90			

DTNs: LB0110A8N3LIQR.001 [157001], LB0209A8N3LIQR.001 [165461]

Using Table IX.6-10, the following is a plot of the velocity data determined from boreholes 1, 9 and 10 (Figure IX.6-1). This is essentially Figure 6.12.2-4, as presented in Section 6.12.

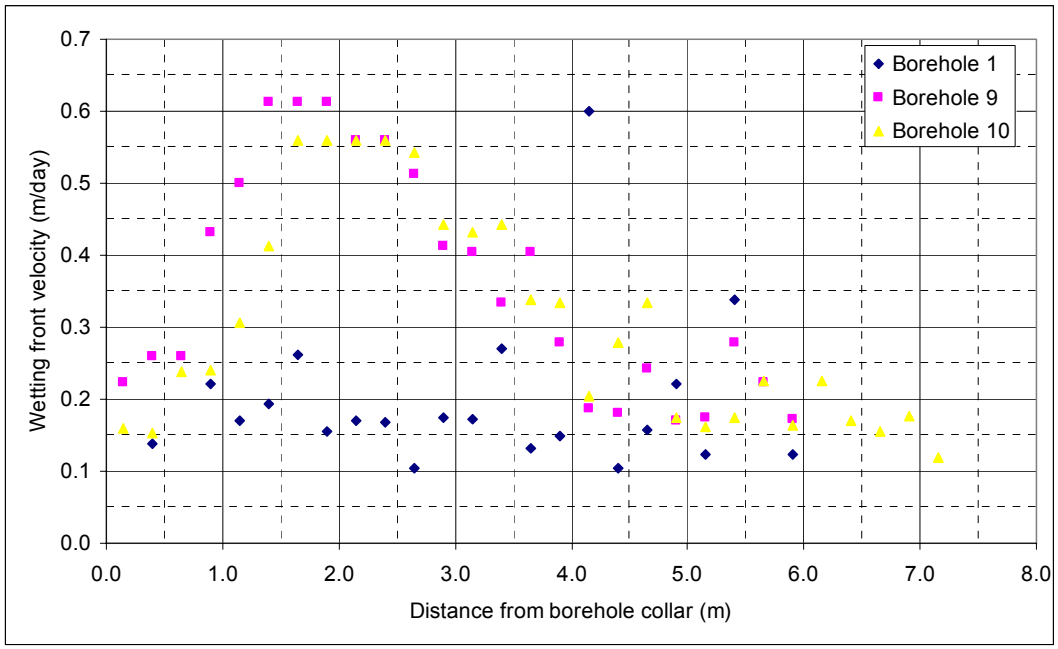

DTN: LB0110A8N3LIQR.001 [157001], LB0209A8N3LIQR.001 [165461], LB0303A8N3LIQR.001 [162570]

Figure IX.6-1. Wetting-Front Velocities for Boreholes 1, 9, and 10 as Presented in Figure 6.12.2-4